
組織的研究体系による次世代型感染症治療薬の開発

平成23年度～平成27年度「私立大学戦略的研究基盤形成支援事業」

研究成果報告書

平成28年5月

学校法人名 学校法人大阪医科薬科大学

大学名 大阪薬科大学

研究組織名 分子構造・機能解析学領域

研究代表者 辻坊 裕

(大阪薬科大学薬学部教授)

はしがき

大阪薬科大学では、平成 23 年度に文部科学省の私立大学戦略的研究基盤形成支援事業として採択されました「組織的研究体系による次世代型感染症治療薬の開発」と題したプロジェクト研究を推進してまいりました。この間平成 25 年度に 3 年目の中間評価を受け、平成 27 年度に 5 年目の最終年度を迎えました。最終年度を迎え、ひとことご挨拶申し上げます。

我々の研究プロジェクトチームは、大阪薬科大学大学院薬科学専攻博士前期・後期課程における分子構造・機能解析学領域に属する薬品物理化学研究室、生化学研究室、薬品分析化学研究室、微生物学研究室および中央機器研究施設の教員から構成されており、これらの研究室および施設の全教員が目的を達成するための具体的な研究課題に取り組み、効率的に研究を遂行する体制をとっています。最終年度を迎えられますことは、チームメンバーのご理解・ご協力のお陰であり、ここに感謝申し上げます次第でございます。

近年、腸管出血性大腸菌をはじめとする新興感染症、結核などの再興感染症、緑膿菌をはじめとする日和見感染症、さらには多剤耐性菌による院内感染などの問題から、新たな作用機作を有する新規抗菌薬の開発が待ち望まれています。今日使用されている多くの抗菌薬は、タンパク質や細胞壁などの生合成を阻害することにより細菌を殺滅します。細菌は抗菌薬による殺滅から逃れるために耐性化します。当研究プロジェクトでは、細菌を殺滅するのではなく、宿主生体内での増殖を抑制する次世代型の新規抗菌薬を開発することを目的としています。これにより耐性化を低く抑えることが期待できます。

ここに、5 年間の研究プロジェクトの研究成果をまとめ、皆様方からのご批判やご助言を仰ぐとともに、さらなる発展を目指して研鑽に励みたく、メンバー全員が決意を新たにしているところです。

結びにあたり、本研究基盤形成支援事業の推進にお世話になった学内外の共同研究者の各位にお礼を申し上げますとともに、今後とも益々のご支援・ご指導を賜りますようお願いいたします。

研究代表者 辻坊 裕

法人番号	271001
プロジェクト番号	S1101031

平成 23 年度～平成 27 年度「私立大学戦略的研究基盤形成支援事業」
研究成果報告書概要

1 学校法人名 大阪医科薬科大学 2 大学名 大阪薬科大学

3 研究組織名 分子構造・機能解析学領域

4 プロジェクト所在地 大阪府高槻市奈佐原4丁目20番1号

5 研究プロジェクト名 組織的研究体系による次世代型感染症治療薬の開発

6 研究観点 研究拠点を形成する研究

7 研究代表者

研究代表者名	所属部局名	職名
辻坊 裕	微生物学研究室	教授

8 プロジェクト参加研究者数 11 名

9 該当審査区分 理工・情報 生物・医歯 人文・社会

10 研究プロジェクトに参加する主な研究者

研究者名	所属・職名	プロジェクトでの研究課題	プロジェクトでの役割
辻坊 裕	薬学部・教授	細菌の増殖機構に関する新規タンパク質の探索	標的タンパク質の特定
宮本 勝城	薬学部・准教授	細菌の増殖機構に関する新規タンパク質の探索	標的タンパク質の特定
土屋 孝弘	薬学部・講師	細菌の増殖機構に関する新規タンパク質の探索	標的タンパク質の特定
友尾 幸司	薬学部・准教授	細菌の増殖機構に関する新規タンパク質の構造解析および新規感染症治療薬の分子設計	標的分子の三次構造の提示
尹 康子	薬学部・准教授	細菌の増殖機構に関する新規タンパク質の構造解析および新規感染症治療薬の分子設計	標的分子阻害剤の三次構造の提示
箕浦 克彦	薬学部・准教授	細菌の増殖機構に関する新規タンパク質の構造解析および新規感染症治療薬の分子設計	標的分子阻害剤の三次構造の提示
福永 理己郎	薬学部・教授	細菌の増殖機構に関するタンパク質の機能解析および酵素科学的解析	標的分子のタンパク質化学的解析結果に基づく機能の提示
井上 晴嗣	薬学部・准教授	細菌の増殖機構に関するタンパク質の機能解析および酵素科学的解析	標的分子のタンパク質化学的解析結果に基づく機能の提示
藤井 忍	薬学部・講師	細菌の増殖機構に関するタンパク質の機能解析および酵素科学的解析	標的分子と阻害剤の相互作用における酵素学的解析結果の提示
三野 芳紀	薬学部・教授	細菌の無機元素輸送体を標的とする新規阻害剤の探索	無機元素輸送体の特定
佐藤 卓史	薬学部・講師	細菌の無機元素輸送体を標的とする新規阻害剤の探索	無機元素輸送体に対する標的分子阻害剤の特定

法人番号	271001
プロジェクト番号	S1101031

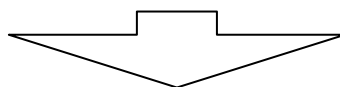
(共同研究機関等)			

<研究者の変更状況(研究代表者を含む)>

旧

プロジェクトでの研究課題	所属・職名	研究者氏名	プロジェクトでの役割
細菌の増殖機構に関する新規タンパク質の構造解析および新規感染症治療薬の分子設計	薬学部・教授	石田 寿昌	標的分子と阻害剤の相互作用に基づく阻害剤の分子設計

(変更の時期:平成 24 年 3 月 31 日)



新

変更前の所属・職名	変更(就任)後の所属・職名	研究者氏名	プロジェクトでの役割

11 研究の概要(※ 項目全体を10枚以内で作成)

(1) 研究プロジェクトの目的・意義及び計画の概要

近年、大腸菌 O-157 を病原体とする出血性大腸炎をはじめとする新興感染症、結核などの再興感染症、病院やデイケアセンター内などでの日和見感染症、さらには医療現場での抗菌薬の濫用が原因とも考えられる多剤耐性菌の発生など多くの問題から、新たな作用機作を有する新規抗菌薬の開発が待ち望まれている。今日使用されている多くの抗菌薬は、タンパク質や細胞壁等の生合成を阻害することにより細菌を殺滅する。当研究プロジェクトでは、細菌を殺滅するのではなく、宿主生体内での増殖を抑制する次世代型の新規抗菌薬を開発することを目的とする。すなわち、細菌の増殖機構の阻害へのアプローチとして、(1)増殖機構に関する新規タンパク質の特定とその機能阻害剤の探索、ならびに(2)シデロフォアなどの必須無機元素輸送体およびその機能阻害剤の探索を通して、従来の抗菌薬創製に係るアプローチとは異なる、新たな作用機作を有する新規感染症治療薬を開発する。

研究計画として、まず、重篤な敗血症の原因菌である *Vibrio vulnificus* の鉄欠乏下におけるプロテオーム解析を行い、ヒト体内での増殖に必要な標的タンパク質を探索し、特定する。既に明らかにしている標的タンパク質については、その構造および機能解析を行う。また、鉄および他の無機元素輸送体を標的とする阻害剤についても探索する。次に、それらの成果に基づき、種々の標的分子とその阻害剤との相互作用に関して、構造化学的、生化学的、および生物無機化学的解析を行い、得られた情報から最適な阻害剤を分子設計する。また、他の病原菌に対する新規標的分子やその阻害剤の探索は、申請期間中継続して行う。完成年度には、これまでの研究成果に基づき、候補となる一連の阻害剤の有効性を *in vitro* および *in vivo* で評価する。さらに、阻害剤の体内動態や代謝経路なども考慮に入れ、直ちに実用可能で新たな作用機作を有する新規感染症治療薬を開発する。

(2) 研究組織

研究代表者の所属研究室である微生物学研究室(3名)が中核となり、大阪薬科大学大学院・薬学研究科薬科学専攻の分子構造・機能解析学領域に所属する、薬品物理化学研究室(2名)、生化学研究室(3名)および薬品分析化学研究室(2名)によって実施されるため、プロジェクトを組織的に遂行し、効率よく研究成果を挙げることができる体制が整備されている。さらに、研究者のプロジェクトにおける役割を研究代表者が具体的に設定することによ

法人番号	271001
プロジェクト番号	S1101031

り、各自の目標および責任体制が明確にされている。プロジェクト開始当初は 2 名のポスドクを採用し、「細菌の増殖機構に関与する新規タンパク質の構造解析」、および「細菌の増殖機構に関与する新規タンパク質の探索」のテーマの基で本プロジェクト研究を円滑に推し進めることができた。また、プロジェクト構成員は、研究進捗状況ならびに研究成果を互いに共有し、最終目標である「細菌の増殖機構に関与する新規タンパク質の探索およびそれを標的とする感染症治療薬の開発」の達成を可能にするべく研究を進めている。

(3) 研究施設・設備等

本プロジェクト研究を遂行する本学中央機器研究施設(総面積 706 m²)には、Ettan DIGE システム、MALDI TOF-MS、蛍光イメージアナライザー、X 線解析装置、円二色性分散計、Biacore T200、共焦点レーザースキャン顕微鏡に加えて、本プロジェクトで導入された、超高感度示差走査型熱量計(DSC)と超高感度等温滴定型熱量計(ITC)で構成される「生体高分子熱エネルギー解析システム」および 2012 年度私立学校施設整備費補助金で導入された、Applied Biosystems 3500 ジェネティックアナライザと StepOne Plus リアルタイム PCR システムで構成される「ハイスループット遺伝子発現解析システム」が新たに整備された。研究プロジェクトに参加する、ポスドクを含む 13 名の研究者が、本研究施設内の研究装置を各研究目的に応じて効率的に利用することにより、円滑にプロジェクトを遂行することができる。今回導入された研究装置「生体高分子熱エネルギー解析システム」の稼働時間は、進捗状況報告書提出時には 160 時間だったが、その後は 400 時間と利用時間が倍増し、本プロジェクト研究において重要な研究装置となっている。現在、8 名の研究者が活用している。

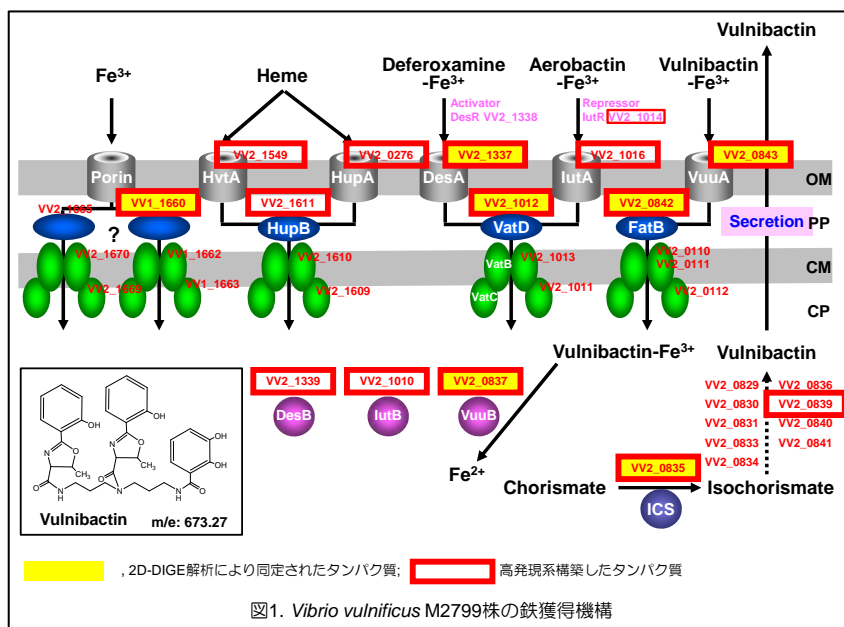
(4) 研究成果の概要 ※下記、13及び14に対応する成果には下線及び*を付すこと。

研究プロジェクトの計画や目的・意義と関連づけて、当初の目標をどれだけ達成したか記述するとともに、新たに得られた知見などについても具体的に記述してください。

臨床分離株 *Vibrio vulnificus* M2799 株の鉄獲得系タンパク質を網羅的に明らかにする目的で、プロテオーム解析

を行った。その結果、対数増殖前期、中期、後期に発現差異が認められたタンパク質のうち、それぞれ 18、31、26 種類のタンパク質を同定し、KEGG (<http://www.genome.jp/kegg/>)に基づいて機能分類を行った。それらのタンパク質遺伝子を、suicide vector である pKTN701 (Nishibuchi M, *et al.*, *Microb. Pathog.*, 11:453-460, 1991)に連結して相同組換えにより挿入変異株を作製し、鉄欠

乏下における増殖能について検討した。その結果、 Δ FeADH (鉄依存性アルコール脱水素酵素、VV2_0211)株、 Δ VuuA (Vulnibactin-Fe³⁺外膜レセプター、VV2_0843)株、 Δ FatB (Vulnibactin-Fe³⁺結合タンパク質、VV2_0842)株、 Δ VuuB (Vulnibactin-Fe³⁺還元酵素、VV2_0837)株、 Δ ICS (Vulnibactin 合成酵素、VV2_0835)株、および Δ VV2_1400 (オリゴエンドペプチダーゼ F) 株は、鉄欠乏下において増殖能が顕著に抑制された(*1)。そこで、それら遺伝子産物の生理的役割を明らかにする目的で、また、多重変異株を作製する目的で、遺伝

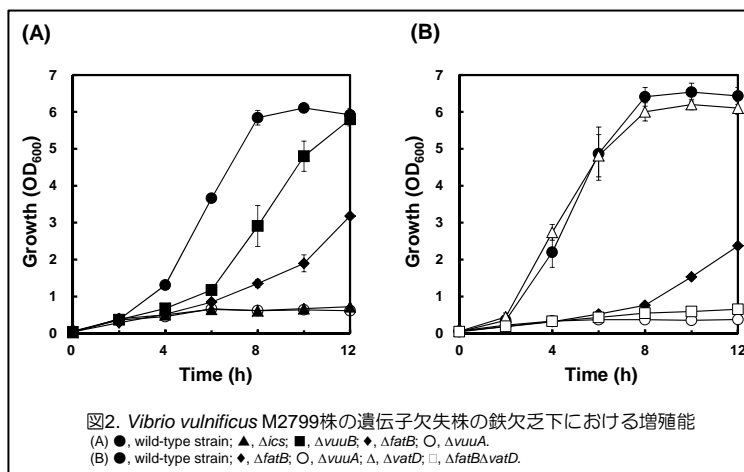


法人番号	271001
プロジェクト番号	S1101031

子欠失株の作製を試みた。なお、図 1 にはプロテオーム解析で明らかにされた M2799 株の鉄取り込み機構を模式的に示している。

遺伝子欠失株の作製は、suicide vector pDM4 (Milton DL, *et al.*, J. Bacteriol., 178:1310-1319, 1996)を用いて行った。まず、鉄獲得機構に関与する遺伝子のグローバルレギュレーターである *fur* 遺伝子の欠失株を作製した。欠失目的領域の上流および下流域それぞれ 500 bp を PCR で増幅し、これらを DNA リガーゼで連結後、PCR を行い増幅した。増幅した DNA を pDM4 に連結し、大腸菌 SY327 λ pir 株を形質転換後、得られた組換えプラスミドを用いて、M2799 株に対する遺伝子伝達能を有する大腸菌 SM10 λ pir 株を形質転換した。SM10 λ pir 形質転換株と M2799 株をそれぞれ培養し、メンブレンフィルター上で接合させることでプラスミドの伝達を行わせて 1 回目の相同組換えを誘発した。得られた相同組換え体を 15%スクロース、100 units/ml ポリミキシン B 含有 LB 寒天培地に塗抹して 2 回目の相同組換えを誘発し、目的とする遺伝子欠失株が得られたことを確認した(*2)。そこで、本菌株の産生するシデロフォアである

Vulnibactin を介する鉄取り込み機構に関与する遺伝子欠失株の作製を試みた。すなわち、VuuA、VuuB、ICS、および FatB について作製した。これらの欠失株の鉄欠乏下における増殖能について検討したところ、*ics* および *vuuA* 遺伝子欠失株では増殖が顕著に抑制されたが、*vuuB* および *fatB* 遺伝子欠失株においては遅いながらも増殖が確認された(図 2A、



*3)。この結果から、VuuB および FatB にはそれぞれ代替タンパク質が存在することが示唆された。

まず、ゲノム情報が明らかにされている *V. vulnificus* CMCP6 株において、FatB ホモログを探索した結果、FatB はハイドロキサメート型シデロフォアである Deferoxamine-Fe³⁺に対するペリプラズム結合タンパク質(VatD)に17%の相同性を示した。そこで、*vatD* 遺伝子欠失株、および *fatB* と *vatD* の二重遺伝子欠失株を作製し、鉄欠乏下における増殖能について検討した結果、*vatD* 遺伝子欠失株は野生株とほぼ同様の増殖能を示したが、二重欠失株では *fatB* 遺伝子欠失株よりも顕著に増殖が抑えられた(図 2B)。また、二重欠失株に、pRK415 をベクターとして用いて *vatD* 遺伝子を回復させたところ、*fatB* 遺伝子欠失株と同様の増殖が認められた。以上のことから、Vulnibactin-Fe³⁺に対するペリプラズム結合タンパク質は FatB が中心となって機能するが、FatB が機能しない場合、VatD で代替可能であることが明らかにされた(*3)。ハイドロキサメート型シデロフォアのペリプラズム結合タンパク質が、他のハイドロキサメート型シデロフォアの代替が可能であるという報告例はあるが、カテコール型シデロフォアを結合するのは今回が初めてである。本研究成果は、Microbial Pathogenesis (Elsevier)に掲載された(*3)。

次に、FatB および VatD タンパク質の高発現系を構築した。すなわち、His タグ融合タンパク質として発現する高発現系ベクター pProEX HTa にそれらの遺伝子を導入し、大腸菌 BL21 株を形質転換した。得られた形質転換株から目的タンパク質の発現を試みた結果、HisFatB は封入体を形成したが、HisVatD は、20°C で 18 時間誘導することにより可溶化状態で回収することができた。そこで、HisVatD タンパク質を Ni-Sepharose 6FF および HiLoad Superdex 75pg クロマトグラフィーにより、電気泳動的に均一にまで精製し、AcTEV プロテアーゼで処理することにより His タグを切断後、再度 Ni-Sepharose 6FF カラムクロマトグラフィーを行い、非吸着

法人番号	271001
プロジェクト番号	S1101031

画分から VatD タンパク質を回収した。VatD 精製標品を、Amicon Ultra-15 遠心式フィルターユニット(10,000 NMWL)により 10 mg/ml まで濃縮し、これを VatD-Apo 体の結晶化サンプルとした。また、Deferoxamine に FeCl_3 溶液を用いて Deferoxamine- Fe^{3+} を作製し、VatD:Deferoxamine- $\text{Fe}^{3+}=1:3$ になるように混合して、これを VatD-Deferoxamine- Fe^{3+} 複合体の結晶化サンプルとした。蒸気拡散法によりこれらの結晶を

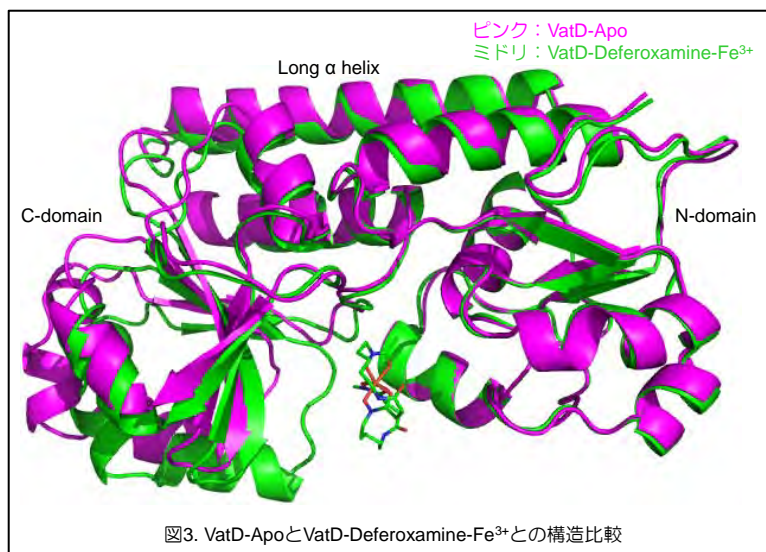


図3. VatD-ApoとVatD-Deferoxamine- Fe^{3+} との構造比較

作製し、リガク社製X線回折装置 (R-AXIS VII) および SPring-8 (BL38B1) により X 線回折強度測定を行った。これらのデータから分子置換法により初期位相を決定し、それを基に構造精密化を行い、構造を決定した(*4)。その結果、VatD-Apo 体では、分解能 2.6 Å、 R factor = 17.4%、VatD-Deferoxamine- Fe^{3+} 複合体では分解能 1.85 Å、 R factor = 21.9% で構造を決定した。本研究成果は、Acta Crystallographica Section F Structural Biology Communications (Wiley) に掲載された(*4)。X 線解析データから構造解析を行ったところ、VatD の全体構造は N-domain と C-domain から構成されており、両ドメインは long α -helix で繋がっていた。VatD-Deferoxamine- Fe^{3+} 複合体の解析により、それらのドメイン間に Deferoxamine- Fe^{3+} が結合していることが明らかとなった(未発表データ)。Deferoxamine- Fe^{3+} は VatD の Arg69 および Arg177 と直接および水分子を介した水素結合を形成していることが確認できた。また、本結合領域はトリプトファンやフェニルアラニンなどの疎水性残基が多く確認でき、Trp53、Trp205 および Phe263 の 3 残基で疎水性相互作用を形成していた。さらに、Apo 体と複合体との構造比較により、両構造において N-domain から long α -helix までは、良く一致した構造であったのに対して、Apo 体の C-domain は外側にシフトしていることが明らかとなった(図 3、*5)。Apo 体において、本結合領域近隣に存在する Gly227、Pro228 の温度因子が高く不安定であることから、Deferoxamine- Fe^{3+} の結合に伴い、VatD の Trp53、Pro228、Arg169、Thr262 の各アミノ酸残基および隣接する水分子と相互作用ネットワークを形成することにより、C-domain が Deferoxamine- Fe^{3+} 側に動き、結合サイトの構造を安定化しているのではないかと推測された。今後、FatB についても同様に精製し、構造解析を行う予定である。また、今回導入した、「生体高分子熱エネルギー解析システム」の超高感度等温滴定型熱量計 (ITC) を用いて、Vulnibactin を含む各種シデロフォア- Fe^{3+} 錯体との結合能について詳細に検討する予定である。

次に、VuuB について代替タンパク質の探索を試みた。本酵素は細胞内に取り込んだ Vulnibactin- Fe^{3+} 錯体の Fe^{3+} を Fe^{2+} に還元する酵素である。*V. vulnificus* M2799 株は、本菌が産生する Vulnibactin 以外のヒドロキサメート型シデロフォアである Aerobactin あるいは Deferoxamine を介する取り込み機構を有しており(図 1)、それらの遺伝子クラスターに、大腸菌のヒドロキサメート型シデロフォア鉄錯体の還元酵素である PhuF と相同性を

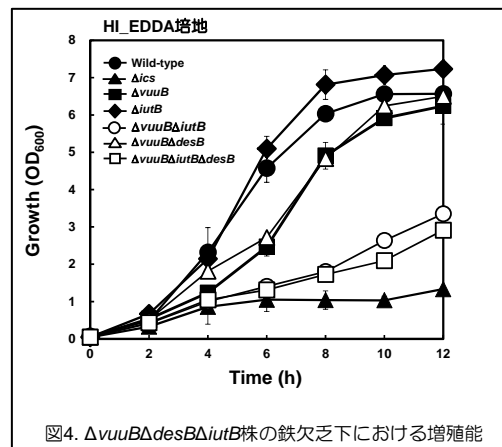


図4. $\Delta vuuB\Delta desB\Delta iutB$ 株の鉄欠乏下における増殖能

法人番号	271001
プロジェクト番号	S1101031

有するタンパク質(VV2_1010 および VV2_1339)をコードする遺伝子を見出した。クラスターの遺伝子名から、それぞれ IutB および DesB と命名し、それらの遺伝子欠失株を作製した。すなわち $\Delta vuuB$ 、 $\Delta iutB$ 、 $\Delta vuuB\Delta iutB$ 、 $\Delta vuuB\Delta desB$ 、 $\Delta vuuB\Delta iutB\Delta desB$ 株を作製し、鉄欠乏下での増殖能について検討した。なお、*ics* 遺伝子欠失株をネガティブコントロールとして用いた。その結果、IutB が代替タンパク質として機能することが明らかとなった (図 4、*6)。しかしながら Δics 株と比較して、遅いながらも増殖が認められたことから、更なる代替タンパク質が存在する可能性が示唆された。そこで、近縁菌である *V. vulnificus* CMCP6 株のゲノム情報を基に 25 還元

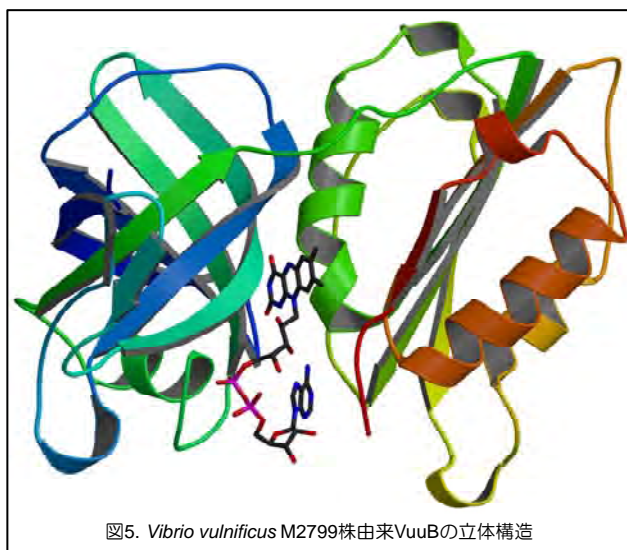


図5. *Vibrio vulnificus* M2799株由来VuuBの立体構造

酵素遺伝子を選択し、現在、それら遺伝子欠失株の作製を行っている。

VuuB、IutB および DesB の高発現系を構築した。現在までに、VuuB タンパク質を精製し、フラビンアデニンジヌクレオチド(FAD)共存下での結晶を得、構造解析を行い、その立体構造を明らかにした(図 5、*7)。今後、Vulnibactin-Fe³⁺複合体との共結晶化を行うとともに、本タンパク質の機能を抑制する、最適な阻害剤を分子設計する予定である。さらに、超高感度等温滴定型熱量計(ITC)を用いて、VuuB と Vulnibactin-Fe³⁺複合体との相互作用についても、詳細に解析する予定である。

さらに、これまでに明らかにされていない Vulnibactin の分泌機構について検討を行った。大腸菌において、Enterobactin の分泌に外膜チャネルタンパク質 TolC が関与することが明らかにされており、TolC を外膜チャネルとする resistance nodulation cell division (RND) 型排出システムが分泌に関与すると推測されている。M2799 株における TolC ホモログを探索した結果、VV1_0612 および VV2_1007 を見出した。そこで、これらの遺伝子の欠失株を作製し、鉄欠乏下での増殖能について検討したところ、VV1_0612 タンパク質遺伝子欠失株の鉄欠乏下での生育が顕著に抑制された(図 6A)。さらに、pRK415 を用いて VV1_0612 遺伝子を回復させたところ、野生株と同様の増殖が認められた(図 6B)。また、 Δics 株を用いたバイオアッセイを行ったところ、鉄欠乏下において、VV1_0612 タンパク質遺伝子欠失株の培養上清では Δics 株は増殖しなかった。以上のことから、*V. vulnificus* M2799 株において、VV1_0612 タンパク質が TolC であることが認められた(*8)。次に、M2799 株にコードされている 12 種類の RND タンパク質のうち、Vulnibactin の分泌に関与するタンパク質を探索した。まず、本タンパク質は鉄欠乏下で遺伝子発現が増大することが推測されることから、それらの逆転写産物について、定量的リアルタイム PCR を行った。その結果、鉄欠乏下において、VV1_0719、VV1_3156、VV2_0029、VV2_0195 および VV2_1320 の遺伝子発現量が増大した。そこで、それら遺伝子の欠失株を作製し、鉄欠乏下における増殖能について検討した結果、野生株と比較して、増殖能についてほとんど影響がないことが明らかとなっ

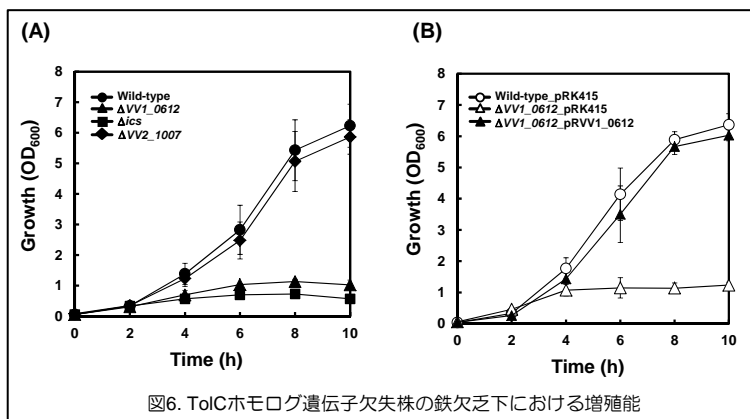


図6. TolCホモログ遺伝子欠失株の鉄欠乏下における増殖能

法人番号	271001
プロジェクト番号	S1101031

た(図 7A)。そこで、すべての RND ホモログについて遺伝子欠損株を作製した結果、VV1_1681 が RND タンパク質として Vulnibactin の分泌に関与することが明らかとなった(図 7B、*8)。しかしながら、遅いながらも増殖が確認されたことから、今回解析対象とした RND タンパク質以外の代替タンパク質の存在が示唆された。本研究成果は Microbial Pathogenesis (Elsevier) に掲載された。

類縁菌である *V. vulnificus* CMCP6 株には、ヘム取り込み機構に関与する外膜レセプターとして HupA (VV2_0276)3)および HvtA (VV2_1549)4)が存在することが明らかにされている。そこで、M2799 株のそれら遺伝子欠失($\Delta hupA$ および $\Delta hvtA$)株を作製した。鉄キレーターである EDDA と、単一鉄源としてヘミンを添加した CM9 培地を用いて、 Δics 、 $\Delta ics\Delta hupA$ 、 $\Delta ics\Delta hvtA$ および $\Delta ics\Delta hupA\Delta hvtA$ 株の増殖試験を行った。本培養条件において、 Δics 株は Vulnibactin 非産生菌であるため、ヘム取り込み機構を介しての増殖は可能であるが、ヘミンを利用できない欠失株では増殖できない。増殖試験の結果、 $\Delta ics\Delta hvtA$ 株は Δics 株と同様に増殖したが、 $\Delta ics\Delta hupA$ 株では増殖がやや抑制された。さらに、 $\Delta ics\Delta hupA\Delta hvtA$ 株では顕著に増殖が抑制された(図 8)。以上のことから、本菌株のヘム取り込み機構において、外膜レセプターは HupA が中心となって機能するが、HvtA は補助的役割を有しており、本取り込み機構において、これら 2 つのレセプターは必須であることが明らかとなった。また、ヘム取り込み機構に関与する新規タンパク質を探索した結果、VV2_1611 が唯一のペリプラズム結合タンパク質であり、VV2_1610 および VV2_1609 が細胞内膜に存在する ABC トランスポーターであることを明らかにした。

<優れた成果があがった点>

ヒトに感染症を起こす病原細菌は、宿主生体内で増殖するために鉄を必要とする。したがって、病原細菌の鉄取り込み機構を阻害することにより、ヒトの体内での増殖を抑制することができる。一般に、グラム陰性病原細菌は、ヒトの体内に存在する鉄を獲得するためにカテコール型、ハイドロキサメート型など、様々な構造を有するシデロフォアを産生する。細胞外に分泌されたシデロフォアは、 Fe^{3+} と結合して外膜レセプターを介してペリプラズム間隙に運ばれた後、ペリプラズム結合タンパク質と複合体を形成し、さらに細胞内膜に存在する ABC transporter を介して細胞内に取り込まれる。細胞内では、鉄還元酵素により二価鉄に還元されて利用される。一方、グラム陽性病原細菌は、外膜レセプターを有さず、それ以降はグラム陰性菌とほぼ同様の機構で鉄を獲得する。これまでの研究結果から、グラム陰性菌である *V. vulnificus* の鉄獲得機構の概要を明らかにするとともに、シデロフォア外膜レセプターの基質特異性は高いが、ペリプラズム結合タンパク質の特異性は比較的低いことが推測された。したがって、FatB、VatD 等のペリプラズム結合タンパク質の高発現系を構築して、それらの立体構造を明らかにし、Vulnibactin- Fe^{3+} 結合領域をターゲットとする分子設計を行うことにより、

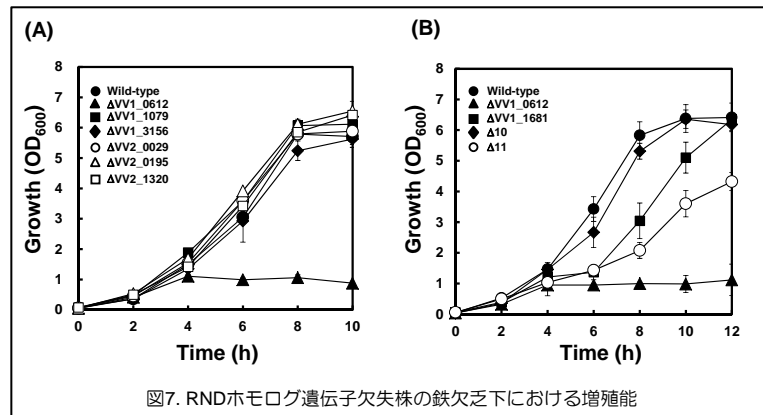


図7. RNDホモログ遺伝子欠失株の鉄欠乏下における増殖能

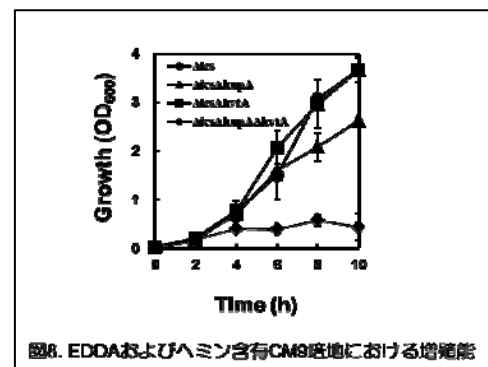


図8. EDDAおよびヘミン含有CM9培地における増殖能

法人番号	271001
プロジェクト番号	S1101031

新規感染症治療薬のリーダー化合物を開発できる可能性が考えられた。

<問題点>

高発現系を構築する際、封入体として宿主内で不溶化することがしばしばある。得られた封入体を塩酸グアニジンにより可溶化後、精製して立体構造を巻き戻すことが可能なタンパク質も存在するが、構造解析には適さない。したがって、可溶化状態で発現する条件を詳細に検討しなければならない。上述した VatD および VuuB タンパク質は 37°C で誘導すると封入体となったが、20°C では可溶化状態で回収することができた。さらに、それらタンパク質の結晶化に成功し、構造解析を行うことができた。以上のことから、今回導入した、「生体高分子熱エネルギー解析システム」の超高感度示差走査型熱量計(DSC)を用いて、可溶化状態で高発現させる温度や誘導条件などについて詳細に検討したい。さらに、タグの種類を変更する、カイコ由来無細胞タンパク質合成系を構築する等、あらゆる方法を駆使し、この問題点を克服したい。また、類似タンパク質の構造情報から阻害剤を分子設計し、細菌増殖抑制効果を繰り返し評価しつつ、設計分子と増殖抑制との構造活性相関を確立させる。以上の研究を繰り返して実験を収斂させることで、新規感染症治療薬を効率よく開発することができる。

<評価体制>

(研究プロジェクトの目標等に照らした自己評価の実施や、その結果を研究費等の資源の配分へ反映させるためのルール of 適切な設定、また、本プロジェクトに係る費用対効果(かけた費用に見合う効果が見られるか)について、どのように分析しているか。また、それらについて、外部(第三者)による評価を受ける体制ができているか等について記述してください。)

毎月第 4 金曜日に、全構成員が集まり、各研究室に課された研究の進捗状況を報告することによりデータの共有化および自己評価を行い、PDCA サイクルを活用して今後の研究内容について議論している。また、毎年 12 月には、学内外の研究者、学生を対象に公開シンポジウムを開催し、1 年間の主な研究成果の口頭発表と、メンバー全員のポスター発表を行っている。その際、本プロジェクトに関連した先駆的な研究を展開している研究者を招き講演いただくと同時に、我々の研究成果に対する意見交換を行い、費用対効果についても、外部からの評価および指導を得ている。また、本シンポジウムの要旨集を広く配布することにより学内外の研究者からも評価を受けている。

<研究期間終了後の展望>

(本プロジェクト終了後における研究の継続の有無、有の場合は今後の研究方針、無の場合は当該研究施設・装置・設備の活用方針を記述してください。)

カテコール型シデロフォアである Vulnibactin-Fe³⁺に対するペリプラズム結合タンパク質である FatB タンパク質の構造解析を行い、すでに明らかにしたハイドロキサメート型シデロフォアである deferroxamine-Fe³⁺に対するペリプラズム結合タンパク質である VatD タンパク質の構造と比較して、Vulnibactin-Fe³⁺結合領域をターゲットとする分子設計を行う。また、化合物ライブラリーから共通阻害剤を探索し、標的タンパク質との分子間相互作用を Biacore T200 および本プロジェクトで導入された iTC200 を用いて解析する。得られた相互作用解析のデータに基づいて、より高活性な阻害剤を分子設計し、アクセルリス社分子設計プログラム Discovery Studio を用いて標的タンパク質との結合シミュレーションや分子動力的計算を行い、最適構造化合物のスクリーニングを行う。スクリーニングされた阻害剤を用い、*V. vulnificus* を被検菌とし、最小発育阻止濃度を測定する。

V. vulnificus は肝機能障害有するヒトに感染し、高い割合で死に至らしめる。そこで、神戸朝日病院との共同研究で、B 型、C 型、アルコール性および非アルコール性の代償性肝硬変患者からの血清あるいは正常血清を用いた *in vitro* での阻害活性と、種々の感染モデル動物を用いた *in vivo* での阻害剤の効果との相関性を、投与方法等を含めて評価する。さらには

法人番号	271001
プロジェクト番号	S1101031

阻害剤の体内動態や、代謝経路なども考慮に入れた感染症治療薬の開発を行う。

<研究成果の副次的効果>

(研究成果の活用状況又は今後の活用計画(実用化・企業化の見通しや、特許の申請があればその申請状況・取得状況等)について、記述してください。)

本菌株の産生するシデロフォアである Vulnibactin を介する鉄取り込み・利用機構に関与する FatB、VatD、VuuB を始めとする標的タンパク質の立体構造を原子レベルで明らかにし、それらの機能を阻害する分子を設計することにより、特許はもとより実用化に繋がる可能性が十分に秘められている。また、本プロジェクトで得られた研究方法や結果を、緑膿菌やアシネトバクター菌などの多剤耐性グラム陰性細菌に適用する副次的効果も十分に考えられる。

12 キーワード(当該研究内容をよく表していると思われるものを8項目以内で記載してください。)

- (1) 感染症治療薬 (2) プロテオーム (3) Vibrio vulnificus
 (4) 鉄 (5) シデロフォア (6) ABC トランスポーター
 (7) _____ (8) _____

13 研究発表の状況(研究論文等公表状況。印刷中も含む。)

上記、11(4)に記載した研究成果に対応するものには*を付すこと。

<雑誌論文>

1. Tanabe T, Miyamoto K, Tsujibo H, Yamamoto S, Funahashi T.
The small RNA Spot 42 regulates the expression of the type III secretion system 1 (T3SS1) chaperone protein VP1682 in *Vibrio parahaemolyticus*.
FEMS Microbiol. Lett., 362. pii: fnv173 (2015). 査読有り
2. Miyano N, Igarashi T, Kawano H, Miyamoto K, Tsuchiya T, Tomoo K, Tsujibo H.
Expression, purification, crystallization and X-ray crystallographic analysis of the periplasmic binding protein VatD from *Vibrio vulnificus* M2799. (*4)
Acta Crystallogr. F Struct. Biol. Commun., 71:1078-1082 (2015). 査読有り
3. Funahashi T, Tanabe T, Maki J, Miyamoto K, Tsujibo H, Yamamoto S.
Identification and characterization of *Aeromonas hydrophila* genes encoding the outer membrane receptor of ferrioxamine B and an AraC-type transcriptional regulator.
Biosci. Biotechnol. Biochem., 78:1777-1787 (2014). 査読有り
4. Kawano H, Miyamoto K, Yasunobe M, Murata M, Myojin T, Tsuchiya T, Tanabe T, Funahashi T, Sato T, Azuma T, Mino Y, Tsujibo H.
The RND protein is involved in the vulnibactin export system in *Vibrio vulnificus* M2799. (*8)
Microb. Pathog., 75:59-67 (2014). 査読有り
5. Tanabe T, Kato A, Shiuchi K, Miyamoto K, Tsujibo H, Maki J, Yamamoto S, Funahashi T
Regulation of the expression of the *Vibrio parahaemolyticus* *peuA* gene encoding an alternative ferric enterobactin receptor.
PLoS One, 9:e105749 (2014). 査読有り
6. Kawano H, Miyamoto K, Yasunobe M, Murata M, Myojin T, Tsuchiya T, Tanabe T, Funahashi T, Sato T, Azuma T, Mino Y, Tsujibo H.

法人番号	271001
プロジェクト番号	S1101031

Role of periplasmic binding proteins, FatB and VatD, in the vulnibactin utilization system of *Vibrio vulnificus* M2799. (*3)

Microb. Pathog., 65:73-81 (2013). 査読有り

7. Kobayashi T, Hirose J, Wu H, Sano K, Katsumata T, Tsujibo H, Nakano T.
Application of electrolysis for inactivation of an antiviral drug that is one of possible selection pressure to drug-resistant influenza viruses.
J. Virol. Methods., 194:154-60 (2013). 査読有り
8. Funahashi T, Tanabe T, Miyamoto K, Tsujibo H, Maki J, Yamamoto S.
Characterization of a gene encoding the outer membrane receptor for ferric enterobactin in *Aeromonas hydrophila* ATCC 7966(T).
Biosci. Biotechnol. Biochem., 77, 353-360 (2013). 査読有り
9. Funahashi T, Tanabe T, Maki J, Miyamoto K, Tsujibo H, Yamamoto S.
Identification and characterization of a cluster of genes involved in biosynthesis and transport of acinetoferrin, a siderophore produced by *Acinetobacter haemolyticus* ATCC 17906T.
Microbiol., 159, 678-690 (2013). 査読有り
10. Tanabe T, Funahashi T, Shiuchi K, Okajima N, Nakao H, Miyamoto K, Tsujibo H, Yamamoto S.
Characterization of *Vibrio parahaemolyticus* genes encoding the systems for utilization of enterobactin as a xenosiderophore.
Microbiol., 158, 2039-2049 (2012). 査読有り
11. Funahashi T, Tanabe T, Mihara K, Miyamoto K, Tsujibo H, Yamamoto S.
Identification and characterization of an outer membrane receptor gene in *Acinetobacter baumannii* required for utilization of desferricoprogen, rhodotorulic acid, and desferrioxamine B as xenosiderophores.
Biol. Pharm. Bull., 35, 753-760 (2012). 査読有り
12. Tsuchiya T, Nakao N, Yamamoto S, Hirai Y, Miyamoto K, Tsujibo H.
NK1.1(+) cells regulate neutrophil migration in mice with *Acinetobacter baumannii* pneumonia.
Microbiol. Immunol., 56, 107-116 (2012). 査読有り
13. Tanabe T, Funahashi T, Miyamoto K, Tsujibo H, Yamamoto S.
Identification of genes, *desR* and *desA*, required for utilization of desferrioxamine B as a xenosiderophore in *Vibrio furnissii*.
Biol. Pharm. Bull., 34, 570-574 (2011). 査読有り
14. Tanabe T, Funahashi T, Okajima N, Nakao H, Takeuchi Y, Miyamoto K, Tsujibo H, Yamamoto S.
The *Vibrio parahaemolyticus pvuAI* gene (formerly termed *psuA*) encodes a second ferric vibrioferrin receptor that requires *tonB2*.
FEMS Microbiol. Lett., 324, 73-79 (2011). 査読有り
15. Xie C, Soeda Y, Shinzaki Y, In Y, Tomoo K, Ihara Y, Miyasaka T.
Identification of key amino acids responsible for the distinct aggregation properties of microtubule-associated protein 2 and tau.
J. Neurochem. 135(1):19-26 (2015). 査読有り
16. Kikuchi T, Masumoto Y, In Y, Tomoo K, Yamada T, Tanaka R.
Eringiacetal A, 5,6-seco-(5S,6R,7R,9S)-5,6:5,7:6,9-triepoxyergosta-8(14),22-diene-3 β ,7 β -diol, an unusual ergostane sterol from the fruiting bodies of *Pleurotus eryngii*.
European Journal of Organic Chemistry, 2015(21), 4645-4649 (2015). 査読有り

法人番号	271001
プロジェクト番号	S1101031

17. Inoue T, Matsui Y, Kikuchi T, Yamada T, In Y, Muraoka O, Sakai C, Ninomiya K, Morikawa T, Tanaka R.
Carapanolides M-S from seeds of andiroba (*Carapa guianensis*, Meliaceae) and triglyceride metabolism-promoting activity in high glucose-pretreated HepG2 cells.
Tetrahedron 71(18), 2753-2760 (2015). 査読有り
18. Sogawa K, Minoura K, In Y, Ishida T, Taniguchi T, Tomoo K.
CH- π interaction in VQIVYK sequence elucidated by NMR spectroscopy is essential for PHF formation of tau.
Biopolymers. **102**(3), 288-95 (2014). 査読有り
19. Inoue T, Matsui Y, Kikuchi T, In Y, Muraoka O, Yamada T, Tanaka R.
Carapanolides C-I from the seeds of andiroba (*Carapa guianensis*, Meliaceae).
Fitoterapia **96**, 56-64 (2014). 査読有り
20. Kim Y, In Y, Ishida T, Onaka H, Igarashi Y.
Biosynthetic origin of alchivemycin A, a new polyketide from *Streptomyces* and absolute configuration of alchivemycin B.
Organic Lett., 15, 3514-3517 (2013). 査読有り
21. Inoue T, Matsui Y, Kikuchi T, In Y, Yamada T, Muraoka O, Matsunaga S, Tanaka R.
Guianolides A and B, new carbon skeletal limonoids from the seeds of *Carapa guianensis*.
Organic Lett., 15, 3018-3021 (2013). 査読有り
22. Saeki D, Yamada T, In Y, Kajimoto T, Tanaka R, Iizuka Y, Nakane T, Takano A, Masuda K.
Officinatrione: an unusual (17S)-17,18-seco-lupane skeleton, and four novel lupane-type triterpenoids from the roots of *Taraxacum officinale*.
Tetrahedron, 69, 1583-1589 (2013). 査読有り
23. Okitsu T, Yumitate S, Sato K, In Y, Wada A.
Substituent Effect of bis(pyridines) iodonium complexes as iodinating reagents: control of the iodocyclization/oxidation process.
Chemistry, 19, 4992-4996 (2013). 査読有り
24. Paku K, Umenaga Y, Usui T, Fukuyo A, Mizuno A, In Y, Ishida T, Tomoo K.
A conserved motif within the flexible C-terminus of the translational regulator 4E-BP is required for tight binding to the mRNA cap-binding protein eIF4E.
Biochem. J., 441, 237-245 (2012). 査読有り
25. Sogawa K, Okuda R, In Y, Ishida T, Taniguchi T, Minoura K, Tomoo K.
C-H ... π interplay between Ile308 and Tyr310 residues in the third repeat of microtubule binding domain is indispensable for self-assembly of three- and four-repeat tau.
J. Biochem., 152, 221-229 (2012). 査読有り
26. Ishida T.
Overview of structural study on conformations and intermolecular interactions of biomolecules.
Yakugaku Zasshi, 132, 785-816 (2012). 査読無し
27. Ishida T.
Attracted by the structure of tryptophan which has molecular recognition ability.
Farumashia, 48, 725-727 (2012). 査読無し
28. Sogawa K, Okuda R, Minoura K, In Y, Ishida T, Taniguchi T, Tomoo K.
CH- π interaction between I308 and Y310 residues is required for self assembly of full length tau.

法人番号	271001
プロジェクト番号	S1101031

- Pept. Sci., 48th, 165-168 (2011). 査読無し
29. Umenaga Y, Paku K, In Y, Ishida T, Tomoo K.
Identification and function of the second eIF4E-binding region in N-terminal domain of eIF4G: comparison with eIF4E-binding protein.
Biochem. Biophys. Res. Commun., 414, 462-467 (2011). 査読有り
30. Fukuyo A, In Y, Ishida T, Tomoo K.
Structural scaffold for eIF4E binding selectivity of 4E-BP isoforms: crystal structure of eIF4E binding region of 4E-BP2 and its comparison with that of 4E-BP1.
J. Pept. Sci., 17, 650-657 (2011). 査読有り
31. Tanaka Y, Yamada T, In Y, Muraoka O, Kajimoto T, Tanaka R.
Absolute stereo structure of andirolides A-G from the flower of *Carapa guianensis* (Meliaceae).
Tetrahedron, 67, 782-792 (2011). 査読有り
32. In Y, Minoura K, Ishida T, Fujioka S, Takeda M, Murashima T, Yamada T.
Synthesis and conformational analysis of Dcp-containing homo-oligopeptides.
Pept. Sci., 48th, 205-208 (2011). 査読無し
33. Miyake T, Ishimoto S, Ishimatsu N, Higuchi K, Minoura K, Kikuchi T, Yamada T, Muraoka O, Tanaka R
Carapanolides T-X from *Carapa guianensis* (andiroba) seeds.
Molecules, 20, 20955-20966 (2015). 査読有り
34. Nakanishi K, Doi M, Usami Y, Amagata T, Minoura K, Tanaka R, Numata A, Yamada T.
Anthcolorins A-F, novel cytotoxic metabolites from a sea urchin-derived *Aspergillus versicolor*.
Tetrahedron, 69, 4617-4623 (2013). 査読有り
35. Amagata T, Xiao J, Chen YP, Holsopple N, Oliver AG, Gokey T, Guliaev AB, Minoura K.
Creation of an HDAC-based yeast screening method for evaluation of marine-derived actinomycetes: discovery of Streptosetin A.
J. Nat. Prod., 75, 2193-2199 (2012). 査読有り
36. Kitano M, Yamada T, Amagata T, Minoura K, Tanaka R, Numata A.
Novel pyridino-a-pyrone sesquiterpene type pileotin produced by a sea urchin-derived *Aspergillus* sp..
Tetrahedron Lett., 53, 4192-4194 (2012). 査読有り
37. Cebdriwski J, Lobo VJSA, Sandler M, Salas A, Kuhn JP, Molero X, Fukunaga R, Mayerle J, Lerch MM, Real FX
Mnk1 is a novel acinar cell specific kinase required for exocrine pancreatic secretion and response to pancreatitis in mice.
Gut, 64, 937-947 (2015). 査読有り
38. Chevillard-Briet M, Quaranta M, Grezy A, Mattera L, Courilleau C, Philippe M, Mercier P, Corpet D, Lough J, Ueda T, Fukunaga R, Trouche D, Escaffit F
Chevillard-Briet M, Quaranta M, Grezy A, Mattera L, Courilleau C, Philippe M, Mercier P, Corpet D, Lough J, Ueda T, Fukunaga R, Trouche D, Escaffit F
Interplay between chromatin-modifying enzymes controls colon cancer progression through Wnt signaling.
Human Molecular Genetics, 23, 2120-2131 (2014). 査読有り
39. Shi Y, Frost P, Hoang B, Yang Y, Fukunaga R, Gera J, Lichtenstein A.

法人番号	271001
プロジェクト番号	S1101031

- MNK kinases facilitate c-myc IRES activity in rapamycin-treated multiple myeloma cells. *Oncogene*, 32, 190-197 (2013). 査読有り
40. Gorentla BK, Krishna S, Shin J, Inoue M, Shinohara ML, Grayson JM, Fukunaga R, Zhong X-P. Mnk1 and 2 are dispensable for T cell development and activation but important for the pathogenesis of experimental autoimmune encephalomyelitis. *J. Immunol.*, 190, 1026-1037 (2013). 査読有り
41. Sharma B, Joshi S, Sassano A, Majchrzak B, Kaur S, Aggarwal P, Nabet B, Bulic M, Stein BL, McMahon B, Baker DP, Fukunaga R, Altman JK, Licht JD, Fish E. N, Platanius LC. Sprouty proteins are negative regulators of interferon (IFN) signaling and IFN-inducible biological responses. *J. Biol. Chem.*, 287, 42352-42360 (2012). 査読有り
42. Joshi S, Sharma B, Kaur S, Majchrzak B, Ueda T, Fukunaga R, Verma AK, Fish EN, Platanius LC. Essential role for Mnk kinases in type II interferon (IFN γ) signaling and its suppressive effects on normal hematopoiesis. *J. Biol. Chem.*, 286, 6017-6026 (2011). 査読有り
43. Mino Y, Azuma T, Sato T. Amino acid sequences of ferredoxins from several species of genus *Ephedra*. *Bull. Osaka Univ. Pharm. Sci.* 9, 53-60 (2015). 査読有り
44. Azuma T, Ishiuchi H, Inoyama T, Teranishi Y, Yamaoka M, Sato T, Yamashita N, Tanaka H, Mino Y. Detection of peramivir and laninamivir, new anti-influenza drugs, in sewage effluent and river waters in Japan. *PLoS One*, 10, 1-11 (2015). 査読有り
45. Azuma T, Ishiuchi H, Inoyama T, Teranishi Y, Yamaoka M, Sato T, Mino Y. Occurrence and fate of selected anticancer, antimicrobial and psychotropic pharmaceuticals in an urban river in a subcatchment of the Yodo River Basin, Japan. *Environ. Sci. Pollut. Res.*, 22, 18676-18686 (2015). 査読有り
46. Uemura M, Yoshikawa Y, Yoshikawa K, Sato T, Mino Y, Chikuma M, Komeda S, Inorg J. Second- and higher-order structural changes of DNA induced by antitumor-active tetrazolate-bridged dinuclear platinum (II) complexes with different types of 5-substituent. *Biochem.*, 127, 169-174 (2013). 査読有り
47. Tanaka T, Yamamoto D, Sato T, Tanaka S, Usui K, Manabe M, Aoki Y, Iwashima Y, Saito Y, Mino Y, Deguchi H. Adenosine thiamine triphosphate (AThTP) inhibits poly (ADP-ribose) polymerase-1 (PARP-1) activity. *J. Nutr. Sci. Vitaminol.*, 57, 192-196 (2011). 査読有り
48. Azuma T, Mino Y. Chemical degradation of polychlorinated biphenyls by the UV-Fe²⁺/Fe³⁺-H₂O₂ system and its application for polychlorinated biphenyl-polluted electric insulating oil. *J. Health Sci.*, 57, 442-447 (2011). 査読有り
49. 東 剛志、三野芳紀. 硫酸を用いた低温・低 pH 条件における UV-Fe²⁺/Fe³⁺-H₂O₂ 系による PCBs の化学分解. *環境衛生工学研究*, 25, 14-21 (2011). 査読有り

法人番号	271001
プロジェクト番号	S1101031

<図書>

なし

<学会発表>

1. 宮本勝城、河野広朗、土屋孝弘、田邊知孝、舟橋達也、辻坊 裕.
臨床分離株 *Vibrio vulnificus* M2799 株における Vulnibactin 分泌機構の解明. (*6)
第 65 回日本薬学会近畿支部総会・大会 大阪 (2015 年 10 月).
2. 栗山善成、奥田峻太、成瀬香奈美、成尾侑紀、岩本遼太郎、野口恭平、品川彩、小川悟史、土屋孝弘、宮本勝城、良原栄策、辻坊 裕.
Bam 複合体を標的とした新規抗菌物質の開発.
第 65 回日本薬学会近畿支部総会・大会 大阪 (2015 年 10 月).
3. 宮本勝城、河野広朗、知名秀泰、宮野菜央、五十嵐智子、友尾幸司、土屋孝弘、田邊知孝、舟橋達也、辻坊 裕.
Vibrio vulnificus M2799 株の鉄獲得機構の解明. (*5)
第 27 回微生物シンポジウム 岡山 (2015 年 9 月).
4. 宮本勝城、平野紋華、新田貴志、隈元由香、福井淳一、土屋孝弘、辻坊 裕.
Pseudoalteromonas piscicida O-7 株のキチン分解機構に関する新規タンパク質の解析.
日本キチン・キトサン学会第 29 回大会 熊本 (2015 年 8 月).
5. 河野広朗、宮本勝城、土屋孝弘、田邊知孝、舟橋達也、辻坊 裕.
Vibrio vulnificus M2799 株の Vulnibactin 分泌機構に RND タンパク質が関与する. (*8)
第 88 回日本細菌学会総会 岐阜 (2015 年 3 月).
6. 宮野菜央、宮本勝城、土屋孝弘、田邊知孝、舟橋達也、辻坊 裕.
Vibrio vulnificus M2799 株のペリプラズム結合タンパク質 VatD の構造解析. (*4)
第 88 回日本細菌学会総会 岐阜 (2015 年 3 月).
7. 良原栄策、後藤理和、岩本遼太郎、野口恭平、小川悟史、土屋孝弘.
Bam 複合体を標的とした緑膿菌およびアシネトバクターに対する新規抗菌物質の開発.
第 88 回日本細菌学会総会 岐阜 (2015 年 3 月).
8. 宮野菜央、五十嵐智子、河野広朗、宮本勝城、土屋孝弘、辻坊 裕.
臨床分離株 *Vibrio vulnificus* M2799 株の鉄獲得機構の解明. (*4)
日本結晶学会平成 26 年度年会 東京 (2014 年 11 月).
9. 宮本勝城、河野広朗、宮野菜央、土屋孝弘、田邊知孝、舟橋達也、辻坊 裕.
Vibrio vulnificus M2799 株の鉄獲得機構の解明. (*3)
第 38 回日本鉄バイオサイエンス学会学術集会 仙台 (2014 年 9 月).
10. 河野広朗、宮本勝城、土屋孝弘、田邊知孝、舟橋達也、辻坊 裕.
Vibrio vulnificus M2799 株における Vulnibactin 分泌機構. (*3)
第 26 回微生物シンポジウム 東京 (2014 年 9 月).
11. 宮野菜央、五十嵐智子、友尾幸司、宮本勝城、土屋孝弘、田邊知孝、舟橋達也、辻坊 裕.
Vibrio vulnificus M2799 株のペリプラズム結合タンパク質 VatD の構造解析. (*4)
第 26 回微生物シンポジウム 東京 (2014 年 9 月).
12. 宮本勝城、矢野 翼、山田貴大、山下拓起、前田沙梨、土屋孝弘、辻坊 裕.
Pseudoalteromonas piscicida O-7 株のキチン分解機構に関する新規タンパク質の解析.
日本キチン・キトサン学会第 28 回シンポジウム 東京 (2014 年 8 月).

法人番号	271001
プロジェクト番号	S1101031

13. 河野広朗、宮本勝城、土屋孝弘、田邊知孝、舟橋達也、辻坊 裕.
Vibrio vulnificus M2799 株のバルニバクチンを介する鉄獲得機構におけるペリプラズム結合タンパク質 FatB と VatD の役割. (*3)
 第 87 回日本細菌学会総会 東京 (2014 年 3 月).
14. 土屋孝弘、宮本勝城、良原栄策、辻坊 裕.
 Bam 複合体を標的とした新規抗菌物質の開発.
 第 87 回日本細菌学会総会 東京 (2014 年 3 月).
15. 宮本勝城、長谷川真耶、稲田涼子、北村健太、山本 優、土屋孝弘、辻坊 裕.
 Analysis of the novel proteins involved in the chitinolytic system of *Pseudoalteromonas piscicida* strain O-7.
 日本キチン・キトサン学会第 27 回シンポジウム 米子 (2013 年 10 月).
16. 宮本勝城、河野広朗、廣本武史、五十嵐智子、土屋孝弘、田邊知孝、山本重雄、辻坊 裕.
Vibrio vulnificus M2799 株の鉄獲得機構の解明(*7).
 日本鉄バイオサイエンス学会 第 37 回学術集会 東京 (2013 年 9 月).
17. 河野広朗、宮本勝城、廣本武史、五十嵐智子、土屋孝弘、田邊知孝、山本重雄、辻坊 裕.
Vibrio vulnificus M2799 株の鉄獲得機構の解明(*3).
 第 25 回微生物シンポジウム 静岡 (2013 年 9 月).
18. 土屋孝弘、栗野大輔、河野広朗、宮本勝城、辻坊 裕.
Vibrio vulnificus の病原因子の解析.
 第 25 回微生物シンポジウム 静岡 (2013 年 9 月).
19. 宮本勝城.
2D-DIGE 解析を用いた *Vibrio vulnificus* M2799 株の鉄取り込み機構に關与するタンパク質群の網羅的解析(*1).
 第 63 回日本電気泳動学会シンポジウム 東京 (2013 年 6 月).
20. 河野広朗、宮本勝城、土屋孝弘、田邊知孝、山本重雄、辻坊 裕.
Vibrio vulnificus M2799 株における鉄獲得関連遺伝子欠失株の作製(*2).
 第 86 回日本細菌学会総会 千葉 (2013 年 3 月).
21. 栗野大輔、土屋孝弘、河野広朗、宮本勝城、辻坊 裕.
Vibrio vulnificus の病原因子の解析.
 第 86 回日本細菌学会総会 千葉 (2013 年 3 月).
22. 宮本勝城、河野広朗、廣本武史、土屋孝弘、田邊知孝、山本重雄、辻坊 裕.
Vibrio vulnificus M2799 株の鉄獲得機構の解明(*1).
 第 24 回微生物シンポジウム 大阪 (2012 年 9 月).
23. 宮本勝城、尾上涼馬、中村有貴、小澤舞祈子、土屋孝弘、辻坊 裕.
Pseudoalteromonas piscicida O-7 株のキチン分解機構に關与する新規タンパク質の解析.
 日本キチン・キトサン学会第 26 回シンポジウム 札幌 (2012 年 7 月).
24. Tsuchiya T, Miyamoto K, Yamamoto S, Tsujibo H.
 Role of infiltrating cells in the lung of *Acinetobacter pneumonia* model mice.
 第 85 回日本細菌学会総会 長崎 (2012 年 3 月).
25. 宮本勝城、土屋孝弘、辻坊 裕.
Siderophore (acinetobactin) is involved in biofilm formation by *Acinetobacter baumannii* ATCC19606.
 第 84 回日本細菌学会総会 札幌 (2011 年 9 月).

法人番号	271001
プロジェクト番号	S1101031

26. 土屋孝弘、宮本勝城、山本重雄、辻坊 裕.
Analysis of infiltrating cells in the lung of *Acinetobacter pneumonia* model mice.
第 84 回日本細菌学会総会 札幌 (2011 年 9 月).
27. 田邊知孝、舟橋達也、宮本勝城、辻坊 裕、山本重雄.
Utilization of xenosiderophores by *Vibrio parahaemolyticus*: identification and characterization of genes, *irgA*, *vctA* and *vpa0150*, encoding ferric enterobactin receptors.
第 84 回日本細菌学会総会 札幌 (2011 年 9 月).
28. 田邊知孝、舟橋達也、中尾浩志、宮本勝城、辻坊 裕、山本重雄.
The *Vibrio parahaemolyticus psuA* gene encodes a second ferric vibrioferrin receptor exclusively dependent on the TonB2 system.
第 84 回日本細菌学会総会 札幌 (2011 年 9 月).
29. 土屋孝弘、宮本勝城、辻坊 裕.
Vibrio vulnificus の病原因子の解析.
第 23 回微生物シンポジウム 千葉 (2011 年 9 月).
30. 宮本勝城、高山加奈子、中西良子、東 えり子、土屋孝弘、辻坊 裕.
Pseudoalteromonas piscicida O-7 株のキチン分解機構に關与する新規タンパク質の解析.
日本キチン・キトサン学会第 25 回シンポジウム 奈良 (2011 年 8 月).
31. 友尾幸司、知名秀泰、宮野菜央、河野広朗、尹 康子、箕浦克彦、宮本勝城、土屋孝弘、辻坊 裕
臨床分離株 *Vibrio vulnificus* M2799 由来シデロフォア結合タンパク質 VatD のシデロフォア結合機構の解明. (*4)
第 65 回日本薬学会近畿支部総会・大会 大阪大谷大学 (2015 年 10 月)
32. 菊地 崇、榎本 有季、尹 康子、友尾 幸司、山田 剛司、田中 麗子
エリンギ (*Pleurotus eryngii*) 子実体に含まれる新規 ergostane 型ステロイド
第 62 回日本生薬学会年会 岐阜 (2015 年 9 月)
33. 菊地 崇、榎本 有季、尹 康子、友尾 幸司、山田 剛司、田中 麗子
エリンギ (*Pleurotus eryngii*) 子実体の ergostane 型ステロイド
第 59 回香料・テルペンおよび精油化学に関する討論会 大阪 (2015 年 9 月)
34. 若原章夫、尹 康子
Temperature-dependent structural change of 1D-ice, water nanopipe, in crystal.
第 23 回国際結晶学会 カナダ (2014 年 8 月)
35. 曾川甲子郎、奥田良平、箕浦克彦、尹 康子、宮崎杏奈、谷口泰造、石田寿昌、友尾幸司
Tau の分子会合における VQIVYK 配列の構造安定性について
日本薬学会第 134 年会 熊本 (2014 年 3 月)
36. 生野将史、宮本陽菜、曾川甲子郎、箕浦克彦、尹 康子、谷口泰造、石田寿昌、友尾幸司
Tau タンパク質の自己重合抑制能を有する Tau 認識抗体の構造機能解析
日本薬学会第 134 年会 熊本 (2014 年 3 月)
37. 曾川甲子郎、宮崎杏奈、箕浦克彦、尹 康子、谷口泰造、友尾幸司.
Tau の自己重合には微小管結合部位 R3 に存在する Ile308 と Tyr310 の側鎖間が形成する CH- π 相互作用が不可欠である.
日本薬学会第 133 年会 横浜 (2013 年 3 月).
38. 臼井常悟、齋藤 慧、尹 康子、友尾幸司、石田寿昌、宮本勝城、辻坊 裕.
好熱性放線菌 *Streptomyces thermoviolaceus* OPC-520 株由来細胞内キシラン分解酵素

法人番号	271001
プロジェクト番号	S1101031

- β -xylosidase (BxlA)の X 線結晶構造解析.
日本薬学会第 133 年会 横浜 (2013 年 3 月).
39. 篠原愛花、紙本香奈、上垣内みよ子、石田寿昌、友尾幸司.
小青竜湯成分の AGE 生成阻害活性と阻害機構の解明.
日本薬学会第 133 年会 横浜 (2013 年 3 月).
40. 臼井常悟、斎藤 慧、尹 康子、友尾幸司、石田寿昌、宮本勝城、辻坊 裕.
好熱性放線 *Streptomyces thermoviolaceus* OPC-520 株由来細胞内キシラン分解酵素
 β -xylosidase (BxlA) の結晶化と X 線結晶構造解析.
第 62 回日本薬学会近畿支部総会・大会 西宮 (2012 年 10 月).
41. 曾川甲子郎、箕浦克彦、尹 康子、友尾幸司.
Tau タンパク質阻害分子と R3N 末端 6 残基 VQIVYK との相互作用解析.
第 62 回日本薬学会近畿支部総会・大会 西宮 (2012 年 10 月).
42. 曾川甲子郎、奥田良平、箕浦克彦、尹 康子、友尾幸司、石田寿昌.
Tau タンパク質の自己重合における Ile308 と Tyr310 が形成する CH- π 相互作用の重要性.
日本薬学会第 132 年会 札幌 (2012 年 3 月).
43. 須佐匡樹、土屋孝弘、箕浦克彦、尹 康子、友尾幸司、谷口泰造、辻坊 裕、石田寿昌.
Tau タンパク質の自己凝集抑制能を有する特異的認識抗体の作成とその複合体結 晶化による
構造機能解析.
日本薬学会第 132 年会 札幌 (2012 年 3 月).
44. 篠原愛花、向 高弘、上垣内みよ子、尹 康子、友尾幸司、石田寿昌.
Vanillin 化合物類の構造と AGE 生成阻害活性の関係について.
日本薬学会第 132 年会 札幌 (2012 年 3 月).
45. 臼井常悟、斎藤 慧、石田寿昌、友尾幸司、辻坊 裕、宮本勝城.
好熱性放線菌 *Streptomyces thermoviolaceus* OPC-520 株由来細胞内キシラン分解酵素
 β -xylosidase (BxlA)の X 線結晶構造解析.
日本薬学会第 132 年会 札幌 (2012 年 3 月).
46. 須佐匡樹、土屋孝弘、箕浦克彦、尹 康子、友尾幸司、谷口泰造、辻坊 裕、石田寿昌.
Tau タンパク質の自己凝集抑制能を有する特異的認識抗体の作成とその構造機能解析.
第 61 回日本薬学会近畿支部総会・大会 神戸 (2011 年 10 月).
47. 曾川甲子郎、箕浦克彦、尹 康子、友尾幸司、石田寿昌.
Tau タンパク質の自己重合における Ile308 と Tyr310 が形成する CH- π 相互作用の重要性.
第 61 回日本薬学会近畿支部総会・大会 神戸 (2011 年 10 月).
48. 曾川甲子郎、奥田良平、箕浦克彦、尹 康子、石田寿昌、谷口泰造、友尾幸司.
CH- π interaction between I308 and Y310 residues is required for self-assembly of full length tau.
第 48 回ペプチド討論会 札幌 (2011 年 9 月).
49. 尹 康子、箕浦克彦、石田寿昌.
Synthesis and conformational analysis of a dcp-containing homooligopeptides.
第 48 回ペプチド討論会 札幌 (2011 年 9 月).
50. 紙本佳奈、川西和子、上垣内みよ子、友尾幸司、石田寿昌.
生薬煎液のタンパク質糖化反応阻害/促進活性と機能性添加物として Cyclodextrins の活性への
影響.
日本生薬学会第 58 回年会 東京 (2011 年 9 月).
51. 友尾幸司、石田寿昌.

法人番号	271001
プロジェクト番号	S1101031

- Protein structure determination using Saturn A200 CCD at SPring-8 by MAD phasing.
第 22 回国際結晶学会 スペイン (2011 年 8 月).
52. 若原章夫、石田寿昌.
The structure of 1D ice, water nanowire, in crystal host.
第 22 回国際結晶学会 スペイン (2011 年 8 月).
53. 友尾幸司、齋藤 慧、臼井常悟、石田寿昌、宮本勝城、辻坊 裕.
Structural studies of β -D-xylosidase from *Streptomyces thermoviolaceus* OPC-520.
第 22 回国際結晶学会 スペイン (2011 年 8 月).
54. 上田 健、福永理己郎、Roumiana Alexandrova、Theo Goh、Tak W. Mak、本田浩章.
Identification of interacting partners for MAP kinase-interacting kinase 1.
第 86 回日本生化学会 横浜 (2013 年 9 月).
55. 中村舞音、松村有紗、矢野可央里、藤井忍、福永理己郎、池田潔、井上晴嗣.
マウスロイシンリッチ α_2 -グリコプロテインとシトクロム c の相互作用.
第 87 回 日本生化学会大会 京都 (2014 年 10 月).
56. 井上晴嗣、松村有紗、矢野可央里、藤井忍、福永理己郎、池田潔.
ロイシンリッチ α_2 -グリコプロテインとシトクロム c の相互作用.
日本薬学会第 134 年会 熊本 (2014 年 3 月).
57. 西村恵子、宮地由香里、村上弦大、伊狩 光、土屋孝弘、藤井 忍、福永理己郎、池田 潔、井上晴嗣.
新規シグナル分子としての細胞外シトクロム c の機能.
第 86 回日本生化学会 横浜 (2013 年 9 月).
58. 矢野可央里、松村有紗、藤井 忍、福永理己郎、池田 潔、井上晴嗣.
ロイシンリッチ α_2 -グリコプロテインとシトクロム c の相互作用.
第 86 回日本生化学会 横浜 (2013 年 9 月).
59. 井上晴嗣、村上弦大、伊狩 光、土屋孝弘、藤井 忍、福永理己郎、池田 潔.
新規シグナル分子としての細胞外シトクロム c の役割.
日本薬学会第 133 年会 横浜 (2013 年 3 月).
60. 東 剛志、井ノ山智美、寺西裕亮、山岡美里、石打浩隆、佐藤卓史、三野芳紀.
都市河川における抗がん剤成分の存在実態.
第 16 回水環境学会シンポジウム 沖縄 (2013 年 11 月).
61. 東 剛志、三野芳紀、中田典秀、山下尚之、田中宏明、菅原民枝、大日康史.
下水処理場流入水中に存在する抗インフルエンザ薬成分を用いた疫学調査手法の検討.
第 48 回日本水環境学会年会 仙台 (2014 年 3 月).
62. 東 剛志、中田典秀、山下尚之、佐藤卓史、三野芳紀、田中宏明.
下水及び河川中に存在する抗インフルエンザ薬タミフル及びその活性代謝物、リレンザの定量解析.
フォーラム 2012 衛生薬学・環境トキシコロジー 名古屋 (2012 年 10 月).
63. 三野芳紀、林 大喜、藤田紀子、東 剛志、佐藤卓史.
環境中の医薬品類の Fe^{3+} - H_2O_2 混合試薬による化学分解 - 医療廃液のタミフル (oseltamivir phosphate) の分解 -.
フォーラム 2012 衛生薬学・環境トキシコロジー 名古屋 (2012 年 10 月).

法人番号	271001
プロジェクト番号	S1101031

<研究成果の公開状況>(上記以外)

シンポジウム・学会等の実施状況、インターネットでの公開状況等

※ホームページで公開している場合には、URL を記載してください。

<既に実施しているもの>

2011 年 12 月 3 日(土) 14:50-17:40 大阪薬科大学

http://www.oups.ac.jp/gakujutsu/kenkyukiban/kk_ayumi.html

文部科学省私立大学戦略的研究基盤形成支援事業「組織的研究体系による次世代型感染症治療薬の開発」第 1 回シンポジウム

・宮本勝城(大阪薬科大学 准教授)

「病原細菌 *Vibrio vulnificus* の宿主生体内における生存戦略」

・飯田哲也(大阪大学微生物病研究所 特任教授)

「下痢原因細菌の病原性解析と新規治療法への試み」

ポスターセッション

研究プロジェクトに参加する研究者全員による研究成果報告と討論

2012 年 12 月 8 日(土) 13:50-16:50 大阪薬科大学

http://www.oups.ac.jp/gakujutsu/kenkyukiban/kk_symposium.html

文部科学省私立大学戦略的研究基盤形成支援事業「組織的研究体系による次世代型感染症治療薬の開発」第 2 回シンポジウム

・宮本勝城(大阪薬科大学 准教授)

「病原細菌 *Vibrio vulnificus* の宿主生体内における生存戦略」

・友尾幸司(大阪薬科大学 准教授)

「好熱性放線菌由来キシロオリゴ糖輸送に関与するタンパク質群の構造機能解析」

・良原栄策(東海大学医学部基礎医学系分子生命科学 准教授)

「多剤耐性グラム陰性菌に対する新規抗菌分子の開発」

・塩見和朗(北里大学大学院感染制御科学府 北里生命科学研究所 教授)

「微生物の生産する新しいターゲットをもつ抗生物質の探索～抗寄生虫・抗細菌～」

ポスターセッション

研究プロジェクトに参加する研究者全員による研究成果報告と討論

2013 年 12 月 7 日(土) 13:00-17:00 大阪薬科大学

http://www.oups.ac.jp/gakujutsu/kenkyukiban/kk_symposium.html

文部科学省私立大学戦略的研究基盤形成支援事業「組織的研究体系による次世代型感染症治療薬の開発」第 3 回シンポジウム

・河野広朗(大阪薬科大学 博士研究員)

「病原細菌 *Vibrio vulnificus* の宿主生体内における生存戦略」

・佐藤卓史(大阪薬科大学 講師)

「次世代型感染症治療薬開発への生物無機化学的アプローチ」

・堀口安彦(大阪大学 微生物病研究所 分子細菌学分野 教授)

「なぜ百日咳菌はヒトだけに感染して激しい咳発作を起こすのか？その基礎細菌学的アプローチ」

・山口明人(大阪大学 産業科学研究所 生体防御学研究分野 特任教授)

「多剤排出トランスポーターによる多剤排出機構とその阻害の構造的基礎」

ポスターセッション

研究プロジェクトに参加する研究者全員による研究成果報告と討論

法人番号	271001
プロジェクト番号	S1101031

2014 年 12 月 6 日(土) 13:00-17:00 大阪薬科大学

http://www.oups.ac.jp/gakujutsu/kenkyukiban/kk_symposium.html

文部科学省私立大学戦略的研究基盤形成支援事業「組織的研究体系による次世代型感染症治療薬の開発」第 4 回シンポジウム

- ・河野広朗(大阪薬科大学 博士研究員)
「病原細菌 *Vibrio vulnificus* の宿主生体内における生存戦略」
- ・友尾幸司(大阪薬科大学 准教授)
「*Vibrio vulnificus* における鉄獲得機構関連タンパク質の構造と機能」
- ・山口高広(塩野義製薬(株) コア疾患創薬研究所 研究員)
「緑膿菌の抗菌薬耐性とカルバペネム」
- ・村田武士(千葉大学大学院理学研究科 生体構造化学研究室 教授)
「創薬標的膜タンパク質の X 線結晶構造解析に向けた技術開発」

ポスターセッション

研究プロジェクトに参加する研究者全員による研究成果報告と討論

2015 年 12 月 5 日(土) 13:00-17:00 大阪薬科大学

http://www.oups.ac.jp/gakujutsu/kenkyukiban/kk_symposium.html

文部科学省私立大学戦略的研究基盤形成支援事業「組織的研究体系による次世代型感染症治療薬の開発」第 5 回シンポジウム

- ・河野広朗(大阪薬科大学 博士研究員)
「病原細菌 *Vibrio vulnificus* の宿主生体内における生存戦略」
- ・知名秀泰(大阪薬科大学 技術補佐員)
「*Vibrio vulnificus* M2799 株のペリプラズム結合タンパク質 VatD の構造解析」
- ・井上晴嗣(大阪薬科大学 准教授)
「VatD と Siderophore との相互作用」
- ・三野芳紀(大阪薬科大学 教授)
「微生物の鉄獲得系に作用する新規抗菌剤の開発研究」
- ・和地正明(東京工業大学 大学院生命理工学研究科 生物プロセス専攻 教授)
「新規作用標的を有する抗生物質の探索」
- ・西野邦彦(大阪大学産業科学研究所 生体分子制御科学研究分野 教授)
「細菌の多剤排出機構と新規治療戦略」

<これから実施する予定のもの>

現在のところ未定

14 その他の研究成果等

なし

法人番号	271001
プロジェクト番号	S1101031

15 「選定時」及び「中間評価時」に付された留意事項とそれへの対応

<「選定時」に付された留意事項>

研究計画から次世代型感染症治療薬開発が達成できるかやや不安が残る。より確実性のある計画を見直し改善されたい。

<「選定時」に付された留意事項への対応>

当初の研究計画より、やや計画に遅れが認められるものの、<特に優れた研究成果>に記載した通り、予想外の研究成果を得ることができたと考えている。今後、*V. vulnificus* M2799株の鉄獲得・利用系を中心に研究を効率よく加速し、本プロジェクト期間内に感染症治療薬有力候補化合物の創製と創薬への可能性について検討したい。

<「中間評価時」に付された留意事項>

1 研究組織について

・拠点を形成する事業なので、PD、RA、大学院生の関与についても明記してほしい。

2 研究施設・設備等について

・本支援事業により設置された研究装置がさらに十分に活用されることを期待する。

3 研究プロジェクトの進捗状況・研究成果等について

・研究の進展が認められるが、更なる研究の推進を期待する。本プロジェクトの研究成果に関しての論文発表を今後積極的に行ってほしい。

・構想調書に沿って研究が進捗していると思われるが、「実用可能で新たな作用機作を有する新規感染症治療薬の開発」を目標としているので、実用化を含め、今後は具体的成果を創出することが期待される。

<「中間評価時」に付された留意事項への対応>

付された留意事項に対し、どのような対応策を講じ、また、それにより、どのような成果があがったか等について、詳細に記載してください。

1 研究組織について

・11 研究の概要(2)研究組織の項に記載した通り、1名のポスドクは「細菌の増殖機構に関与する新規タンパク質の探索」、1名の研究補助員は「細菌の増殖機構に関与する新規タンパク質の構造解析」の具体的なテーマの下に精力的に研究を行った。

2 研究施設・設備等について

・11 研究の概要(3)研究施設・設備等の項に記載した通り、今回導入された研究装置「生体高分子熱エネルギー解析システム」の稼働時間は、進捗状況報告書提出時には160時間だったが、その後は400時間と利用時間が倍増した。また、本プロジェクト最終年度以降も、新規感染症治療薬の開発を目的として、精力的に利用し、その実用化を目指す。

3 研究プロジェクトの進捗状況・研究成果等について

・本プロジェクトの研究成果に関しての論文発表については精力的に行ってきた。

・11 研究の概要(4)研究成果の概要<研究期間終了後の展望>の項に記載した通り、本プロジェクト最終年度以降、新規感染症治療薬の実用化を目指す。

法人番号	271001
プロジェクト番号	S1101031

16 施設・装置・設備・研究費の支出状況(実績概要)

(千円)

年度・区分	支出額	内 訳						
		法人負担	私学助成	共同研究機関負担	受託研究等	寄付金	その他()	備考
平成二三年度	施設	0						
	装置	40,036	20,036	20,000				
	設備	0						
	研究費	26,187	14,449	11,738				
平成二四年度	施設	0						
	装置	0						
	設備	0						
	研究費	37,482	27,735	9,747				
平成二五年度	施設	0						
	装置	0						
	設備	0						
	研究費	33,231	25,429	7,802				
平成二六年度	施設	0						
	装置	0						
	設備	0						
	研究費	28,790	23,872	4,918				
平成二七年度	施設	0						
	装置	0						
	設備	0						
	研究費	19,035	14,125	5,416				
総額	施設	0	0	0	0	0	0	0
	装置	40,036	20,036	20,000	0	0	0	0
	設備	0	0	0	0	0	0	0
	研究費	144,725	105,610	39,621	0	0	0	0
総計	184,761	125,646	59,621	0	0	0	0	

※ 最終年度は予定額。

17 施設・装置・設備の整備状況 (私学助成を受けたものはすべて記載してください。)

《施設》(私学助成を受けていないものも含め、使用している施設をすべて記載してください。)(千円)

施設の名 称	整備年度	研究施設面積	研究室等数	使用者数	事業経費	補助金額	補助主体

※ 私学助成による補助事業として行った新增築により、整備前と比較して増加した面積

0 m²

《装置・設備》(私学助成を受けていないものは、主なもののみを記載してください。)

(千円)

装置・設備の名称	整備年度	型番	台数	稼働時間数	事業経費	補助金額	補助主体
(研究装置) 生体高分子熱エネルギー解析システム	平成23年度	・超高感度示差走査型熱量計VP-DSC	1	} 560 h	40,036	20,000	私学助成
		・超高感度等温滴定型熱量計ITC200	1				
		・電源安定化装置 AA660F	2				
微小構造解析システム (MALDI TOF-MS Bruker)	平成27年度	・Microflex-OPS	1	10 h	87,470	0	校費
生体分子の微小環境動態測定と薬剤スクリーニングシステム (卓上型超遠心機)	平成25年度	・Optima MAX-XP	1	100 h	44,939	22,469	私学助成
ハイスループット遺伝子発現解析システム (DNAシーケンサー)	平成24年度	・ABI3500-150	1	100 h	} 19,943	9,971	私学助成
ハイスループット遺伝子発現解析システム (リアルタイムPCR装置)	平成24年度	・StepOne Plus-01C	1	150 h			
分子間相互作用の高感度微量検出システム (Biacore T100 System)	平成21年度	・Biacore T100System	1	792 h	45,234	22,617	私学助成
生体高分子用X線解析装置	平成19年度	・FR-E+ SUPER BIRGHT	1	2,664 h	105,249	44,730	私学助成
微量生理活性物質の構造解析・生物影響高感度抽出システム (ルミノ・イメージアナライザー)	平成17年度	・OP LAS-3000 Multi-Color	1	1,404 h	82,362	41,181	私学助成
定量的ディファレンス解析システム (Ettan DIGE System)	平成16年度	・Ettan DIGE, Ettan Spot Pickerパッケージ	1	710 h	43,207	21,603	私学助成
共焦点レーザースキャン顕微鏡	平成14年度	・LSM510	1	418 h	41,439	20,719	私学助成
タンパク質解析トータルシステム (MALDI TOF-MS Voyager)	平成14年度	・Voyager-DE STR	1	35,040 h	40,493	20,246	私学助成
(研究設備) 遺伝子情報発現解析システム (高感度プロテインシーケンサー)	平成12年度	・491-YS	1	43,800 h	} 38,760	20,672	私学助成
遺伝子情報発現解析システム (高速定量PCR装置) (情報処理関係設備)	平成12年度	・LightCycler Work Station V3	1	700 h			

法人番号

271001

18 研究費の支出状況

(千円)

年 度	平成 23 年度			
小 科 目	支 出 額	積 算 内 訳		
		主 な 使 途	金 額	主 な 内 容
教 育 研 究 経 費 支 出				
消 耗 品 費	20,430	試薬・器具類、その他	13,522,690	試薬、グローブ、ファイル 等
光 熱 水 費				
通 信 運 搬 費	18	郵送料	18	郵送料
印 刷 製 本 費	36	印刷費	36	シンポジウムポスター、封筒
旅 費 交 通 費	1,048	出張旅費	1,048	研究発表、資料収集 等
報 酬 ・ 委 託 料	311	英文校正、謝礼	256,55	英文校正、講演謝礼
(その他)	752	修繕費、会費、その他	493,214,45	機器等の修理、会費 等
計	22,595			
ア ル バ イ ト 関 係 支 出				
人件費支出 (兼務職員)				
教育研究経費支出 計	0			
設 備 関 係 支 出 (1個又は1組の価格が500万円未満のもの)				
教育研究用機器備品	3,485	機器備品	3,485	CO2インキュベーター、小型ルミノメーター 等
図 書	107	図書	107	書籍
計	3,592			
研 究 ス タ ッ フ 関 係 支 出				
リサーチ・アシスタント				
ポスト・ドクター				
研究支援推進経費 計	0			

年 度	平成 24 年度			
小 科 目	支 出 額	積 算 内 訳		
		主 な 使 途	金 額	主 な 内 容
教 育 研 究 経 費 支 出				
消 耗 品 費	17,534	試薬・器具類、実験動物、その他	10,856,790,588	試薬、チューブ、マウス 等
光 熱 水 費				
通 信 運 搬 費	25	郵送料	25	郵送料
印 刷 製 本 費	54	印刷費	54	シンポジウムポスター、封筒
旅 費 交 通 費	1,152	出張旅費	1,152	研究発表、資料収集 等
報 酬 ・ 委 託 料	163	謝礼、英文校正	111,52	講演謝礼、英文校正 等
(その他)	2,425	修繕・保守費、その他	2,091,366	機器等の修理・保守、会費 等
計	21,353			
ア ル バ イ ト 関 係 支 出				
人件費支出 (兼務職員)	608	研究補助(タンパク質の精製)		時給 1,450円、年間時間数 360.5時間 実人数 1人 (交通費込)
教育研究経費支出 計	608			
設 備 関 係 支 出 (1個又は1組の価格が500万円未満のもの)				
教育研究用機器備品	10,989	機器備品	10,989	HPLCポンプ、微量高速冷却遠心機 等
図 書	32			
計	11,021			
研 究 ス タ ッ フ 関 係 支 出				
リサーチ・アシスタント				
ポスト・ドクター	3,300	研究支援(遺伝子欠損株の作製)		学外1人
研究支援推進経費 計	4,500	研究支援(タンパク質の結晶化)		学外1人 学外2人

法人番号	271001
------	--------

年 度	平成 25 年度		
小 科 目	支 出 額	積 算 内 訳	
		主 な 使 途	金 額
教 育 研 究 経 費 支 出			
消 耗 品 費	17,000	試薬・器具類、実験動物、その他	9,390,550、7,060
光 熱 水 費			
通 信 運 搬 費	12	郵送料	12
印 刷 製 本 費	268	印刷費	268
旅 費 交 通 費	1,167	出張旅費	1,167
報 酬 委 託 料	234	謝礼、英文校正	234
(その他)	1,735	修繕・保守費、その他	1,317、418
計	20,416		
ア ル バ イ ト 関 係 支 出			
人 件 費 支 出 (兼務職員)	2,776	研究補助(タンパク質の精製)	時給 1,450円、年間時間数 1,411時間 実人数 1人 (交通費込)
教育研究経費支出			
計	2,776		
設 備 関 係 支 出(1個又は1組の価格が500万円未満のもの)			
教育研究用機器備品	6,439	機器備品	1,592,943
図 書			
計	6,439		
研 究 ス タ ッ フ 関 係 支 出			
リサーチ・アシスタント			
ポスト・ドクター	3,600	研究支援(遺伝子欠損株の作製)	学外1人
研究支援推進経費			
計	3,600		

年 度	平成 26 年度		
小 科 目	支 出 額	積 算 内 訳	
		主 な 使 途	金 額
教 育 研 究 経 費 支 出			
消 耗 品 費	17,459	試薬・器具類、実験動物、その他	12,436、476、4,547
光 熱 水 費			
通 信 運 搬 費	4	郵送料	4
印 刷 製 本 費			
旅 費 交 通 費	780	出張旅費	780
報 酬 委 託 料	572	謝礼、英文校正	572
(その他)	760	修繕・保守費、会費	612、148
計	19,575		
ア ル バ イ ト 関 係 支 出			
人 件 費 支 出 (兼務職員)			
教育研究経費支出			
計	0		
設 備 関 係 支 出(1個又は1組の価格が500万円未満のもの)			
教育研究用機器備品	1,681	機器備品	1,570、111
図 書			
計	1,681		
研 究 ス タ ッ フ 関 係 支 出			
リサーチ・アシスタント			
ポスト・ドクター	7,534	研究支援(タンパク質の精製)	学外2人
研究支援推進経費			
計	7,534		

法人番号

271001

年 度	平成 27 年度		
小 科 目	支 出 額	積 算 内 訳	
		主 な 使 途	金 額
主 な 内 容			
教 育 研 究 経 費 支 出			
消 耗 品 費	8,310	試薬・器具類、実験動物、その他	8,310 試薬・実験器具 等
光 熱 水 費			
通 信 運 搬 費	9	郵送料	9 郵送料
印 刷 製 本 費	53	印刷費	53 シンポジウムポスター
旅 費 交 通 費	160	出張旅費	160 研究発表 等
報 酬 委 託 料	503	謝礼、英文校正	503 講演謝礼、英文校正 等
(その他)	548	修繕・保守費、会費	521、27 機器等の修理・保守、会費 等
計	9,583		
ア ル バ イ ト 関 係 支 出			
人 件 費 支 出 (兼務職員)	2,941	研究補助(タンパク質の精製)	時給 1,450円 実人数 1人 (交通費込)
教 育 研 究 経 費 支 出			
計	2,941		
設 備 関 係 支 出 (1個又は1組の価格が500万円未満のもの)			
教 育 研 究 用 機 器 備 品	2,311	機器備品	606、657 低温パスサーキュレーター、超低温フリーザー 等
図 書			
計	2,311		
研 究 ス タ ッ フ 関 係 支 出			
リサーチ・アシスタント			
ポスト・ドクター	4,200	研究支援(タンパク質の精製)	学外1人
研 究 支 援 推 進 経 費			
計	4,200		

RESEARCH LETTER – Physiology & Biochemistry

The small RNA Spot 42 regulates the expression of the type III secretion system 1 (T3SS1) chaperone protein VP1682 in *Vibrio parahaemolyticus*

Tomotaka Tanabe^{1,*}, Katsushiro Miyamoto², Hiroshi Tsujibo²,
Shigeo Yamamoto¹ and Tatsuya Funahashi¹¹Laboratory of Hygienic Chemistry, College of Pharmaceutical Sciences, Matsuyama University, Matsuyama, Ehime, Japan and ²Department of Microbiology, Osaka University of Pharmaceutical Sciences, Takatsuki, Osaka, Japan

*Corresponding author: Laboratory of Hygienic Chemistry, College of Pharmaceutical Sciences, Matsuyama University, Matsuyama, Ehime, Japan.

Tel: +81-89-926-7283; Fax: +81-89-926-7162; E-mail: ttanabe@cc.matsuyama-u.ac.jp**One sentence summary:** The *Vibrio parahaemolyticus* sRNA Spot 42 inhibits the expression of VP1682 by base pairing with the region encompassing the RBS and initiation codon of the *vp1682* mRNA and thereby reduces cytotoxicity.

Editor: Olga Ozoline

ABSTRACT

The cytotoxicity of *Vibrio parahaemolyticus* has been related to the type III secretion system 1 effector protein VP1680, which is secreted and translocated into host cells with the help of the specific chaperone protein, VP1682. This study sought to confirm the *in silico* analysis, which predicted that a small regulatory RNA (Spot 42) could base pair with the region encompassing the ribosomal-binding site and initiation codon of the *vp1682* mRNA. Electrophoresis mobility shift assays indicated that Spot 42 could bind to the *vp1682* mRNA with the help of Hfq. Consistent with these results, the translation of the *vp1682* mRNA was inhibited when both Hfq and Spot 42 were added to the *in vitro* translation reaction. The cytotoxic activity against infected Caco-2 cells was significantly increased in the Spot 42 deletion mutant (Δ *spf*) at 4 h after infection as compared with the parental strain. Additionally, we observed that both VP1682 and VP1680 were more highly expressed in Δ *spf* mutants than in the parental strain. These results indicate that Spot 42 post-transcriptionally regulates the expression of VP1682 in *V. parahaemolyticus*, which contributes to cytotoxicity *in vivo*.

Keywords: *Vibrio parahaemolyticus*; small RNA; Spot 42; type III secretion system; chaperone; effector

INTRODUCTION

Bacterial small RNAs (sRNAs) are non-coding, small-sized molecules (50–500 nt) that are engaged in post-transcriptional regulation (Gottesman and Storz 2011). sRNAs are generally produced in response to various environmental stimuli, for example, changes in carbon source and osmolarity, and play an important role in the regulation of genes associated with cellular adaptation and microbial pathogenesis (Michaux *et al.* 2014).

Most sRNAs bind adjacent to or overlap with the ribosomal-binding sites (RBSs) of their target mRNAs with imperfect base pairing (Richards and Vanderpool 2011). By binding to the target mRNA, sRNAs prevent ribosomes from binding or promote the decay of their target mRNAs, so that the translation of the corresponding mRNAs is suppressed (Caron, Lafontaine and Massé 2010; Richards and Vanderpool 2011). However, some sRNAs can also bind to the coding sequence of a target mRNA (Bouvier *et al.*

Received: 9 July 2015; Accepted: 19 September 2015

© FEMS 2015. All rights reserved. For permissions, please e-mail: journals.permissions@oup.com

2008; Pfeiffer et al. 2009) or to the intergenic region of a target polycistronic mRNA (Balasubramanian and Vanderpool 2013) in order to downregulate the translation of these mRNAs. In addition, base pairing between sRNA and mRNA is often engaged in an upregulatory effect on its target mRNA because the base pairing contributes in a relief of an intrinsic translation-inhibitory structure in the mRNA or a protection of the mRNA from ribonuclease attack (Richards and Vanderpool 2011). Many sRNAs often require the aid of the RNA-binding chaperone Hfq, which forms a ring-shaped homohexamer to modulate the stability of and binding to their target mRNAs (Valentin-Hansen, Eriksen and Udesen 2004; Vogel and Luisi 2011).

Spot 42, encoded by the *spf* gene, was initially identified in *Escherichia coli* as a cellular RNA that is highly abundant in the presence of glucose (Sahagan and Dahlberg 1979a,b) and was later shown to serve as an Hfq-binding sRNA (Møller et al. 2002). In contrast, in the presence of less favorable carbon sources (i.e. when cellular cAMP levels are elevated), the transcription of the *spf* gene is abolished by the cAMP–cAMP receptor protein (CRP) complex (Polayes et al. 1988). *galK*, the third gene in the galactose operon (*galETKM*), was first identified as the target gene of Spot 42, which can bind to the region around the RBS of *galK* mRNA in order to block its translation without significantly affecting the stability of the *galETKM* mRNA (Møller et al. 2002). Recently, microarray analyses in *E. coli* have revealed that Spot 42 regulates the expression of at least 14 different operons, many of which appear to be associated with the uptake and catabolism of non-preferred carbon sources (Beisel and Storz 2011).

Vibrio parahaemolyticus, a halophilic Gram-negative bacterium, inhabits sea and brackish water, and causes watery diarrhea and acute gastroenteritis through the consumption of contaminated fish and shellfish (Shinoda 2011). The genome sequencing of a pandemic *V. parahaemolyticus* strain, RIMD2210633, revealed two sets of gene clusters encoding the type III secretion system (T3SS) on chromosomes 1 and 2 (T3SS1 and T3SS2, respectively) (Makino et al. 2003). By both T3SSs, their respective effector proteins are directly injected into the cytosol of the target host cells in order to trigger virulence (Troisfontaines and Cornelis 2005; Dean 2011). It has been reported that in *V. parahaemolyticus*, the T3SS1 causes cytotoxicity, whereas T3SS2 is mainly associated with enterotoxicity (Ono et al. 2006;

Kodama et al. 2010; Broberg, Calder and Orth 2011; Ham and Orth 2012; Kodama et al. 2015). Interestingly, several genes involved in *V. parahaemolyticus* pathogenesis, such as the *tdh* encoding thermostable direct hemolysin and *vp1680* encoding one of the T3SS1 effectors, have recently been reported to be upregulated in the *hfq* deletion mutant when compared with the wild-type strain (Nakano et al. 2008). This finding implies that the expression of some virulence genes in *V. parahaemolyticus* is downregulated by sRNAs, because Hfq generally mediates the binding of sRNAs to their target mRNAs.

In this paper, we report that the *V. parahaemolyticus* Spot 42 represses the expression of VP1682, which functions as a chaperone for the T3SS1 effector VP1680 (Akedo et al. 2009), by base pairing with the 5'-untranslated region of the *vp1682* mRNA. VP1680 is shown to be cytotoxic against cultured cells (Broberg, Calder and Orth 2011; Matsuda et al. 2012). We also report that the deletion mutant of the *spf* gene encoding Spot 42 significantly elevates cytotoxicity against Caco-2 cells as compared with the parental wild type.

MATERIALS AND METHODS

Bacterial strains, plasmids, growth conditions and primers

The bacterial strains and plasmids used in this study are listed in Table 1. *Escherichia coli* β 2155 (Demarre et al. 2005) was grown in Luria-Bertani (LB) medium (pH 7.0) containing 0.5% NaCl and 0.5 mM 2,6-diaminopimelic acid. *V. parahaemolyticus* RIMD2210633 (Makino et al. 2003) and its deletion mutants were routinely incubated in LB medium (pH 7.0) containing 3% NaCl. When appropriate, chloramphenicol was added at a final concentration of 10 μ g mL⁻¹. The oligonucleotide primers used in this study are listed in Table S1 (Supporting Information).

In silico analysis

We carried out *in silico* analysis on the genomic sequence of *V. parahaemolyticus* RIMD2210633 using the TargetRNA2 (Tjaden et al. 2006) and IntaRNA (Busch, Richter and Backofen 2008) to

Table 1. Strains and plasmids used in the present study.

Strains and plasmids	Description	Reference or source
<i>V. parahaemolyticus</i>		
RIMD2210633	Clinical isolate of serotype O3:K6	(Makino et al. 2003)
Δ <i>spf</i>	<i>spf</i> deletion mutant	Present study
<i>vp1682flag</i>	Translational fusion of <i>flag</i> to the 3' end of <i>vp1682</i>	Present study
<i>vp1682flag</i> / Δ <i>spf</i>	Translational fusion of <i>flag</i> to the 3' end of <i>vp1682</i> and <i>spf</i> deletion mutant	Present study
<i>vp1680flag</i>	Translational fusion of <i>flag</i> to the 3' end of <i>vp1680</i>	Present study
<i>vp1680flag</i> / Δ <i>spf</i>	Translational fusion of <i>flag</i> to the 3' end of <i>vp1680</i> and <i>spf</i> deletion mutant	Present study
<i>E. coli</i>		
β 2155	<i>thrB1004 pro thi strA hsdS Δ(lacZ)ΔM15 (F' Δ(lacZ)M15 lacI^q traD36 proA⁺ proB⁺) ΔdapA::erm(Em^r), pir::RP4(::kan(Km^r))</i> from SM10)	(Demarre et al. 2005)
Plasmids		
pXAC623	Suicide vector derived from pKTN701 containing <i>sacB</i> gene of <i>B. subtilis</i> ; Cm ^r	(Kuroda et al. 2005)
pXAC Δ <i>spf</i>	pXAC623 containing 1146-bp <i>XhoI</i> - <i>XhoI</i> fragment with 71-bp deletion in <i>spf</i> ; Cm ^r	Present study
pXAC <i>vp1682flag</i>	pXAC623 containing 1213-bp <i>XbaI</i> - <i>XbaI</i> fragment with a flag sequence in-frame at the 3' end of <i>vp1682</i> ; Cm ^r	Present study
pXAC <i>vp1680flag</i>	pXAC623 containing 986-bp <i>XbaI</i> - <i>XbaI</i> fragment with a flag sequence in-frame at the 3' end of <i>vp1680</i> ; Cm ^r	Present study

Cm^r, chloramphenicol resistance.

detect potential interactions of the mRNAs encoding T3SS components with sRNAs, which are annotated in the Rfam database (Griffiths-Jones et al. 2005).

Construction of Δ spf, and vp1682flag and vp1680flag fusion strains of *V. parahaemolyticus*

The deletion mutant of *spf* (Δ spf) and translational fusions of *flag* to the 3' ends of *vp1682* and *vp1680* (*vp1682flag* and *vp1680flag*) were generated by allelic exchange using the R6K-ori suicide vector pXAC623 (Kuroda, Mizushima and Tsuchiya 2005), as previously described (Tanabe et al. 2011). DNA fragments with a deletion in the *spf* gene or *flag* sequences in-frame at the 3' end of *vp1682* and *vp1680* were prepared by PCR-driven overlap extension (Heckman and Pease 2007) using the primers listed in Table S1 (Supporting Information), as previously described (Tanabe et al. 2011). DNA fragments were then ligated into appropriately digested pXAC623 vectors to yield pXAC Δ spf, pXACvp1682flag and pXACvp1680flag (Table 1).

Mapping the 5' RNA ends

Overnight cultures of *V. parahaemolyticus* RIMD2210633 were inoculated at an OD₆₀₀ of 0.005 into LB medium containing 3% NaCl and 0.2% glucose, and then shaken at 70 rpm for 4 h at 37°C. Cells were harvested and treated with the RNAProtect Bacteria Regent (Qiagen, Venlo, Netherlands), according to the manufacturer's instructions. Total RNA or sRNA-enriched RNA (<200 nt) was prepared using ISOGEN II (Nippon Gene, Tokyo, Japan), according to the manufacturer's instructions, and was used for the following experiments.

Primer extension of *vp1682* was carried out using the primer VP1682-PE (Table S1, Supporting Information) having a 5' Texas Red label and 10 μ g of total RNA, and the extension product was then analyzed with an SQ5500E DNA sequencer (Hitachi High-Tech, Tokyo, Japan), as previously described (Tanabe et al. 2014).

5'-Rapid amplification of cDNA ends (5' RACE) was performed using a GeneRacer kit (Life Technologies, Carlsbad, CA). Briefly, 4 μ g of sRNA-enriched RNA was treated with 0.5 U of tobacco acid pyrophosphatase, ligated with a GeneRacer RNA oligo using T4 RNA ligase and was then used as a template for a reverse transcriptase reaction with the Spot 42 5' primer (Table S1, Supporting Information). The resulting cDNA was used as a template for PCR amplification with the primer pair, Spot 42 5'/GeneRacer 5' (Table S1, Supporting Information), and the PCR product was then used as a template for nested PCR with the primer pair, Spot 42 5'Nested/GeneRacer 5'Nested (Table S1, Supporting Information). The nested PCR product was subcloned into pCR4-TOPO (Life Technologies) for sequencing.

Detection of Spot 42 RNA by northern blot

Overnight cultures of *V. parahaemolyticus* RIMD2210633 and Δ spf were inoculated at an OD₆₀₀ of 0.005 into LB medium containing 0.5% NaCl with or without 0.2% glucose, and the medium was then shaken at 70 rpm for 6 h at 37°C. Total RNAs were prepared as described above. Northern blot was performed using 3 μ g aliquots of the total RNA samples, as previously described (Tanabe et al. 2014). Spot 42 RNA was detected by a digoxigenin (DIG)-labeled RNA probe, which had been transcribed *in vitro* from PCR templates amplified with the primer pair T7-Spot 42-DIG-F/T7-Spot 42-DIG-R (Table S1, Supporting Information) using a T7 RNA polymerase (Roche, Basel, Switzerland) and a DIG RNA Labeling Mix (Roche).

Monitoring vp1682' RNA-Spot 42 interactions using electrophoretic mobility shift assays

Spot 42 RNA was synthesized by *in vitro* transcription using a T7 RNA polymerase. A truncated *vp1682* (*vp1682'*) RNA labeled with fluorescein was also generated by T7 transcription with a Fluorescein RNA Labeling Mix (Roche), as previously described (Tanabe et al. 2013). DNA templates for T7 transcription were produced by PCR using the primer pairs T7-VP1682-F/T7-VP1682-R (for *vp1682'* fragment) and T7-Spot 42-F/T7-Spot 42-R (for *spf* fragment) (Table S1, Supporting Information). Electrophoretic mobility shift assays (EMSA) were performed with fluorescein-labeled *vp1682'* RNA probes, as previously described (Tanabe et al. 2013). The His-tag fused Hfq protein was purified, as previously described (Tanabe et al. 2013), and the concentrations with respect to its hexameric form are indicated throughout this study.

In vitro RNA transcription followed by in vitro translation

A truncated *vp1682* DNA fragment (T7-*vp1682'*-*flag* DNA) flanked by the T7 promoter and *flag* sequences and a full-length *spf* DNA fragment (T7-*spf* DNA) that contains the T7 promoter were amplified by PCR with the primer pairs T7-VP1682-F/T7-VP1682-FLAG-R and T7-Spot 42-F/T7-Spot 42-R (Table S1, Supporting Information), respectively. The *vp1682'*-*flag* and Spot 42 RNAs were synthesized using *in vitro* transcription with a T7 RNA polymerase from the T7-*vp1682'*-*flag* and T7-*spf* DNAs, respectively. As a positive control, the *fur*-*flag* RNA was also transcribed *in vitro* using a T7 RNA polymerase, as previously described (Tanabe et al. 2014). The *fur* gene encodes a ferric uptake regulation protein. *In vitro* translation was performed using a PURESYSTEM classic II kit (BioComber, Tokyo, Japan), as previously described (Tanabe et al. 2014), with a mixture of *vp1682'*-*flag* RNA (15 pmol)/*fur*-*flag* RNA (1.5 pmol) as a template. As needed, Spot 42 RNA (30 pmol) and Hfq (15 pmol) was added to the PURESYSTEM (BioComber, Tokyo, Japan) reactions. The samples were separated on a 15% SDS-polyacrylamide gel, and western blots were carried out using mouse anti-FLAG M2 antibody (Sigma-Aldrich, St. Louis, MO) as previously described (Tanabe et al. 2014). Moreover, northern blots were performed using the DIG-labeled *vp1682* RNA probe for specific detection of the *vp1682'*-*flag* RNA, as previously described (Tanabe et al. 2014). The DIG-labeled *vp1682* RNA probe was synthesized *in vitro* with a T7 RNA polymerase and a DIG RNA Labeling Mix from the PCR template that was amplified with the primer pair, T7-VP1682-DIG-F/T7-VP1682-DIG-R (Table S1, Supporting Information).

Cell culture and cytotoxicity assays

Caco-2 cells were provided by the RIKEN BRC through the National Bio-Resource Project of the MEXT, Japan. Caco-2 cells were maintained in Eagle's minimal essential medium (MEM) (Sigma-Aldrich) containing 10% fetal bovine serum (FBS), 100 units mL⁻¹ penicillin and 100 μ g mL⁻¹ streptomycin at 37°C with 5% CO₂ and 95% room air.

For the evaluation of *V. parahaemolyticus* cytotoxicity, the lactose dehydrogenase (LDH) release was determined using a CytoTox 96 Non-Radioactive Cytotoxicity Assay kit (Promega). Briefly, Caco-2 cells were seeded in 96-well plates (5×10^3 cells well⁻¹) and incubated for 48 h in MEM supplemented with 10% FBS. The cells were washed three times with phosphate-buffered saline and incubated for 1 h in high glucose (0.45%) Dulbecco's

modified Eagles medium (DMEM) without phenol red (Life Technologies). The *V. parahaemolyticus* strains were added to the Caco-2 cell cultures at a multiplicity of infection of 10. At indicated times after infection, the supernatants were collected,

and experimental LDH release was measured. Maximum LDH release was achieved by lysing infected Caco-2 cells with 0.8% Triton X-100. Spontaneous LDH release in the supernatant of uninfected Caco-2 cells was also quantified. The percent

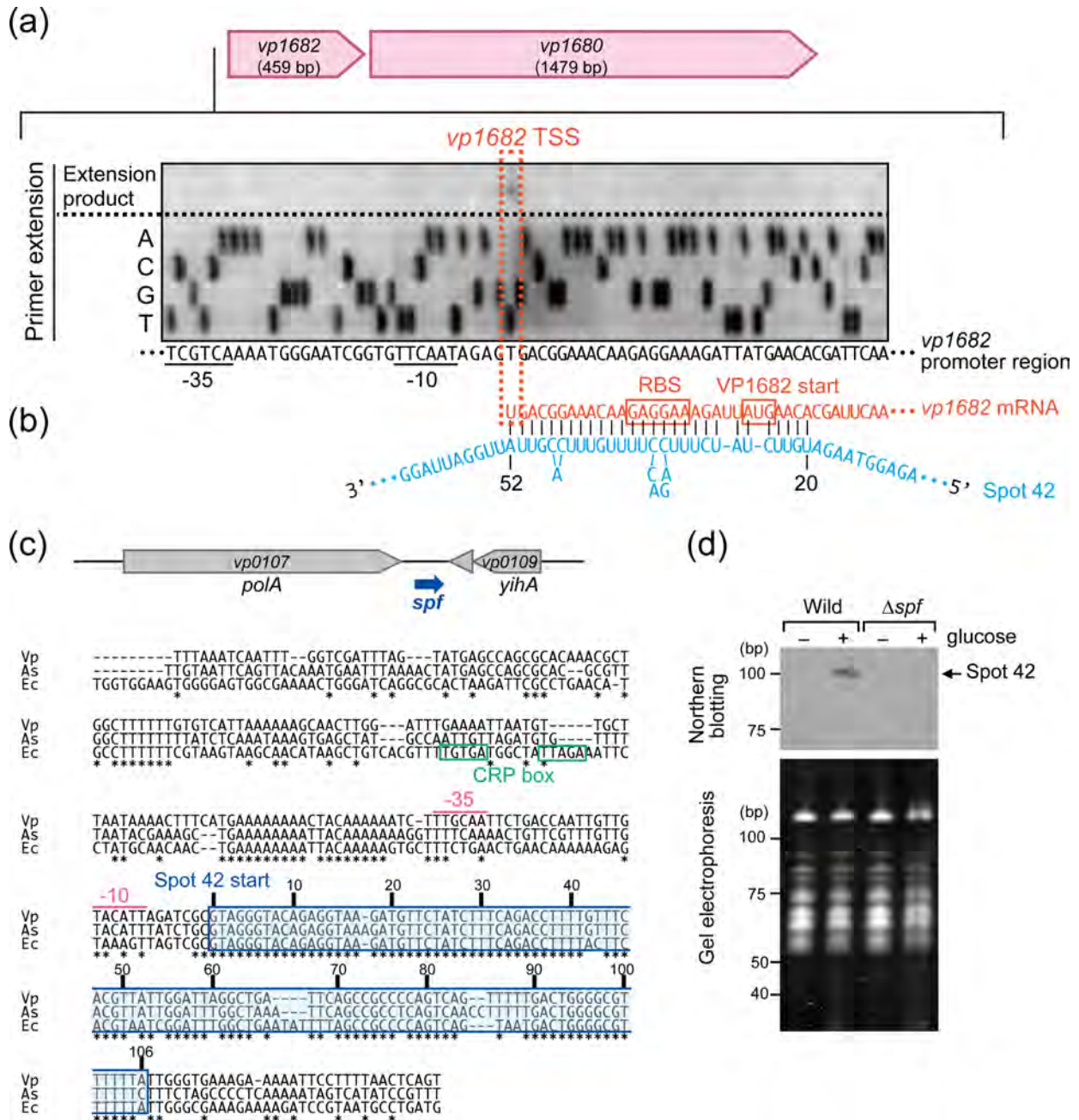


Figure 1. (a) Arrangement of *vp1682* and *vp1680* genes, which are located on chromosome 1 of *V. parahaemolyticus* RIMD2210633, and the nucleotide sequence of the *vp1682* promoter region. The transcription start site (TSS) of *vp1682* was determined by primer extension. The putative -10 and -35 promoter elements of *vp1682* are underlined. (b) The partial nucleotide sequence of the *vp1682* mRNA and its potential base pairing with Spot 42. The RBS and initiation codon of the *vp1682* mRNA are in boxes. Potential base pairing between Spot 42 and the *vp1682* mRNA was determined using the TargetRNA2 (<http://cs.wellesley.edu/~btjaden/TargetRNA2/advanced.html>) and IntaRNA (<http://rna.informatik.uni-freiburg.de/IntaRNA/Input.jsp>). (c) Location and alignment of the *V. parahaemolyticus spf* gene. The *V. parahaemolyticus spf* gene is located between the *vp0107* and *vp0109* genes. Sequences for the *spf* genes and their upstream regions in *V. parahaemolyticus* (Vp), *A. salmonicida* (As) and *E. coli* (Ec) were aligned using the ClustalW program (<http://www.genome.jp/tools/clustalw/>). Asterisks denote identical bases at that position in all three species. The *spf* sequences are indicated with a blue box. The putative -10 and -35 promoter elements of the *spf* gene are indicated with pink lines. The *E. coli* CRP box (Berg and von Hippel 1988) is indicated with a green box; however, the CRP boxes of the *spf* genes in some *Vibrionaceae* species are not well characterized (Hansen et al. 2012). (d) Northern blot of Spot 42 in *V. parahaemolyticus* wild-type strain and Δspf , grown with or without glucose (upper panel). Lower panel shows ethidium bromide staining of the RNAs that were used for the northern blot.

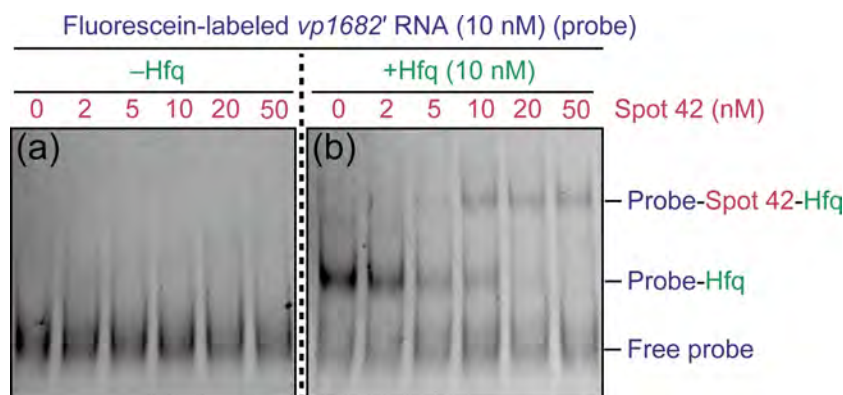


Figure 2. Base pairing between Spot 42 and the *vp1682* mRNA with (a) or without (b) the help of Hfq. Complex formation of the *vp1682* mRNA with Spot 42 and Hfq was analyzed by EMSA. EMSAs were carried out in the presence of an Hfq hexamer at 10 nM and Spot 42 at 0, 2, 5, 10, 20 and 50 nM. In both conditions, the fluorescein-labeled truncated *vp1682* (*vp1682'*) RNA was used as a probe at 10 nM.

cytotoxicity was calculated as follows: [(experimental LDH release – spontaneous LDH release)/(maximum LDH release – spontaneous LDH release)] × 100.

Preparation and western blot analysis of whole cell lysates from *V. parahaemolyticus* strains after infection against Caco-2 cells

Caco-2 cells seeded in 6-well plates (1.5×10^5 cells well⁻¹) were prepared as described above and incubated for 1 h in high glucose DMEM without phenol red. The *V. parahaemolyticus* strains (*vp1682flag*, *vp1682flag/Δspf*, *vp1680flag* and *vp1680flag/Δspf*) were added to the Caco-2 cell culture at a multiplicity of infection of 100. At 4 h after infection, *V. parahaemolyticus* cells (both floating in the medium and attached to Caco-2 cells) were harvested and resuspended in 1/100 volume of Laemmli buffer. Each cell lysate (5 μl) was separated on a 15% (for VP1682-FLAG detection) or 10% (for VP1680-FLAG detection) SDS-polyacrylamide gel, and expression of the VP1682-FLAG and VP1680-FLAG proteins was evaluated by western blot using mouse anti-FLAG M2 antibody, as previously described (Tanabe et al. 2014).

RESULTS AND DISCUSSION

Predicting the base pairing of the VP1682 chaperone mRNA with Spot 42 in *V. parahaemolyticus*

In silico analyses using the TargetRNA2 (Tjaden et al. 2006) and IntaRNA (Busch, Richter and Backofen 2008) revealed that the *V. parahaemolyticus* Spot 42 likely formed an RNA–RNA duplex with the *vp1682* mRNA (Fig. S1, Supporting Information). Primer extension analysis mapped the 5'-terminus of *vp1682* mRNA (+1) at the T residue, which is 23 bp upstream of the AUG translation initiation codon (Fig. 1a), and we determined that nucleotides 1–30 of the *vp1682* mRNA (including its RBS and translation initiation codon) can form a potential duplex with nucleotides 20–52 of Spot 42 (Fig. 1b). Therefore, there is a possibility that translation of the *vp1682* mRNA can be blocked by Spot 42.

The *spf* gene is highly conserved in some *Vibrionaceae* species (Hansen et al. 2012). The *spf* gene of *V. parahaemolyticus* is located on chromosome 1 between the *polA* (*vp0107*) and *yihA* (*vp0109*) genes, which encode a DNA polymerase I and ribosome biogenesis GTP-binding protein, respectively (Fig. 1c). The transcriptional start site of *spf* was determined by 5' RACE (data not shown), and the results showed that the 5' end of *V. para-*

haemolyticus Spot 42 agreed with those of *E. coli* and *Aliivibrio salmonicida* (Fig. 1c). We next examined the expression of Spot 42 in *V. parahaemolyticus* by northern blot. Like the *E. coli* Spot 42 (Polayes et al. 1988), *V. parahaemolyticus* Spot 42 was also detected at an appropriate size (approximately 100 bp) in the wild-type strain, but not in the Δspf strain, when grown in the glucose-containing medium (Fig. 1d).

Detection of Hfq-mediated Spot 42-*vp1682* mRNA duplex formation using EMSAs

To assess whether Spot 42 can base pair with the *vp1682* mRNA, EMSAs were performed using fluorescein-labeled *vp1682* RNAs as a probe. As shown in Fig. 2a, the *vp1682* RNA was unable to bind to Spot 42 in the absence of Hfq. While only the *vp1682* RNA-Hfq complex was detected when Hfq was present without Spot 42, the *vp1682* RNA-Spot 42-Hfq complex was detected when increasing concentrations of Spot 42 were added (Fig. 2b). These observations indicate that the base pairing between Spot 42 and the *vp1682* mRNA is accomplished with the aid of Hfq, which appears to function as a Spot 42-*vp1682* mRNA-Hfq ternary complex.

Effect of Spot 42 on the translation of *vp1682* mRNA

To examine whether Spot 42 affects the translation of *vp1682* mRNA, an *in vitro* translation assay was performed, in which the *fur-flag* and *vp1682'-flag* RNAs were used as templates. The *in vitro* translation products were analyzed by SDS-PAGE followed by western blots, using anti-FLAG IgG (Fig. 3, upper panel). The presence of the previously synthesized *vp1682'-flag* RNA from each *in vitro* translation reaction was also validated by northern blot, using a DIG-labeled *vp1682* RNA probe (Fig. 3, lower panel). As shown Fig. 3 (lanes 1 and 2), when Hfq is absent, VP1682'-FLAG was detected regardless of the presence or absence of Spot 42. However, VP1682'-FLAG was not detected in the presence of both Hfq and Spot 42 in the reaction mixture, although the positive control (Fur-FLAG) was detected (Fig. 3, lane 3). These findings strongly support the notion that only the Spot 42-*vp1682* mRNA-Hfq ternary complex (Fig. 2b) contributes to the translation block of *vp1682* mRNA. In addition, VP1682'-FLAG was synthesized in a reaction mixture containing Hfq, but without Spot 42 (Fig. 3, lane 4), suggesting that although Hfq can form a binary complex with the *vp1682* mRNA (Fig. 2b), this complex is unable to block the translation of *vp1682* mRNA.

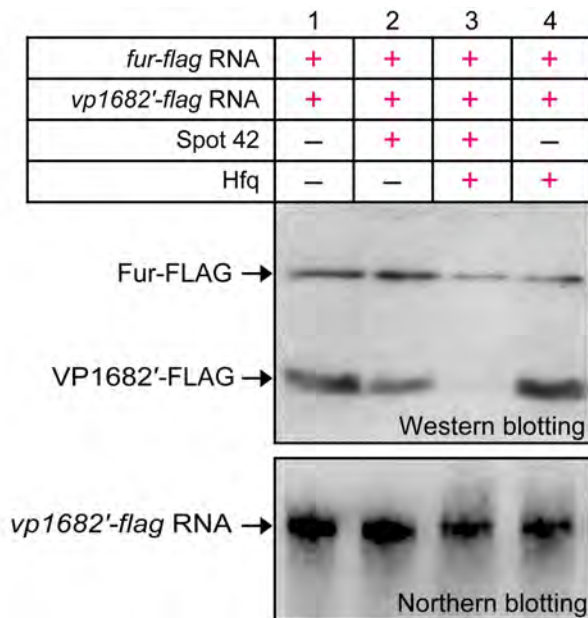


Figure 3. *In vitro* translation assay of the *vp1682*'-flag RNA. The *vp1682*'-flag RNA and *fur*-flag RNA were used as templates at 15 and 1.5 pmol, respectively. As needed, Spot 42 RNA (30 pmol) and Hfq (15 pmol as a hexamer) was added to the reactions. The *fur*-flag RNA was used as a reference reaction. The translated FLAG-fused proteins were separated on a 15% SDS-polyacrylamide gel and were analyzed by western blot (upper panel). To confirm the presence of the *vp1682*'-flag RNA in the *in vitro* translation reactions, northern blots were carried out using a DIG-labeled *vp1682* RNA probe (lower panel). A representative result from two independent experiments is shown.

Involvement of Spot 42 in *V. parahaemolyticus* cytotoxicity

It is known that a T3SS1 chaperone, VP1682, is required for the translocation of a T3SS1 effector, VP1680, and that the *vp1682* deletion mutant shows less cytotoxicity in Caco-2 cells relative to the wild-type RIMD2210633 strain (Akedo et al. 2009). In this study, the *in vitro* translation assays indicated that the *V. para-*

haemolyticus Spot 42 was involved in the inhibition of VP1682 production; hence, we performed cytotoxicity assays in order to test whether this sRNA can attenuate cytotoxicity of this bacterium against Caco-2 cells. Under the conditions used for cytotoxicity assay, the wild-type strain showed a maximum cytotoxic activity against Caco-2 cells after ca. 4 h coincubation. At 4 h after infection, the Δ *spf* strain showed significantly increased cytotoxicity levels as compared with the wild-type strain (Fig. 4a). Furthermore, the VP1682-FLAG and VP1680-FLAG proteins were more highly expressed in Δ *spf* at 4 h after infection than in the wild-type strain (Fig. 4b). Incidentally, in the assay medium (high glucose DMEM without phenol red), the growth rates of the mutant strains, Δ *spf*, *vp1682*'flag/ Δ *spf* and *vp1680*'flag/ Δ *spf*, were exactly similar to that of the wild-type strain (data not shown). Taken together, these data indicate that Spot 42 represses production of the VP1682 chaperone in the presence of glucose, thereby decreasing secretion and translocation of the VP1680 effector into the target cells, and subsequently reduces cytotoxicity of the wild-type strain as compared with that of Δ *spf*. In other words, in response to glucose starvation, *V. parahaemolyticus* increases levels of the VP1682 chaperone in order to mediate translocation of VP1680, which increases the rate of cytotoxicity.

In conclusion, we show that *V. parahaemolyticus* Spot 42 post-transcriptionally prevents the expression of VP1682 by binding to the *vp1682* mRNA with the help of Hfq, thereby increasing production of VP1682 and VP1680 compared to the wild-type strain. Nakano et al. (2008) have demonstrated that the Δ *hfq* strain leads to increased production of VP1680 relative to the wild-type strain. This together with our present finding strongly suggests that Hfq-dependent sRNAs, including Spot 42, add an additional level of regulation to a tightly controlled virulence pathway in *V. parahaemolyticus*. Pathogenic bacteria require adequate expression of their virulence factors for survival, growth and pathogenesis. In this context, it is reasonable that changes in available carbon sources in the host milieu are used by *V. parahaemolyticus* as an environmental signal to regulate the Spot 42-mediated expression of a T3SS1 chaperone, VP1682. In addition, a recent study has revealed that the absence of Spot 42 in *V. parahaemolyticus* reduces levels of VtrB, which is the

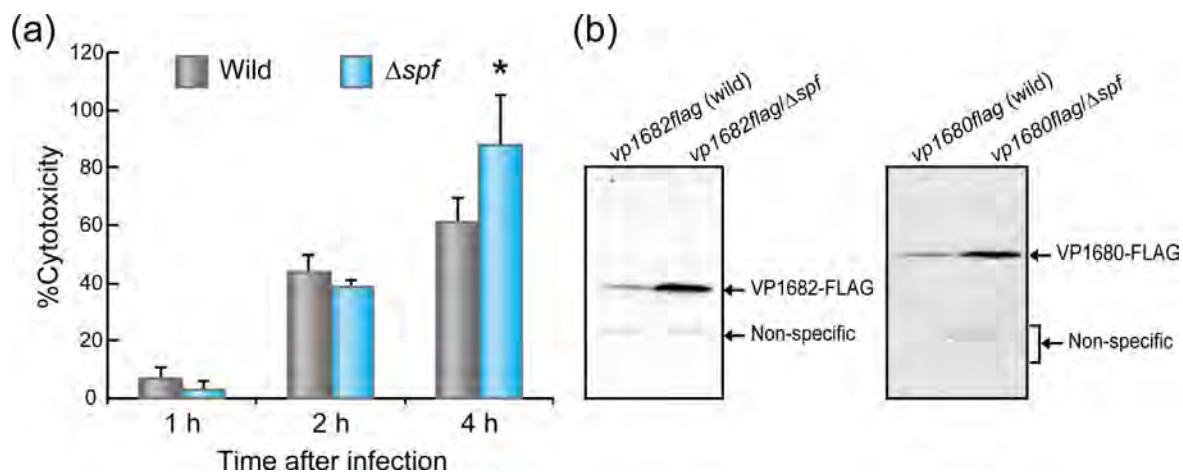


Figure 4. (a) Increased cytotoxicity of Δ *spf* mutants against Caco-2 cells. Caco-2 cells were infected with the wild-type or Δ *spf* mutant strains at a multiplicity of infection of 10. The percent cytotoxicity was determined as described in the section 'materials and methods'. Averages and standard errors of the mean (error bars) were calculated from five independent experiments. An asterisk indicates a P value of <0.05 as compared to the wild-type strain at the same timepoint. (b) Production of VP1682 and VP1680 in the wild-type and Δ *spf* mutant strains were monitored with western blots. The *vp1682*'flag, *vp1682*'flag/ Δ *spf*, *vp1680*'flag and *vp1680*'flag/ Δ *spf* strains were used to infect Caco-2 cells for 4 h, pelleted and then analyzed by western blot. The VP1682-FLAG and VP1680-FLAG proteins were detected with an antibody directed against the FLAG tag. The non-specific bands indicated were used as a possible internal control.

transcriptional regulatory protein involved in bile-mediated expression of T3SS2 effectors (Gotoh et al. 2010; Kodama et al. 2010, 2015), and leads to an attenuation in the production and secretion of translocators and effector proteins that are specific to T3SS2 (Livny et al. 2014). Therefore, it is tempting to speculate that *V. parahaemolyticus* Spot 42 controls the relative expression rate between T3SS1- and T3SS2-related proteins in response to environmental changes. Further studies are needed to better understand the post-transcriptional regulatory mechanisms of genes encoding *V. parahaemolyticus* T3SS-related proteins through Hfq-dependent sRNAs, including Spot 42.

SUPPLEMENTARY DATA

Supplementary data are available at FEMSLE online.

FUNDING

This work was supported in part by a Grant-in-Aid for Young Scientists (B) (25870987) from the Ministry of Education, Culture, Sports, Science and Technology of Japan.

Conflict of interest. None declared.

REFERENCES

- Akeda Y, Okayama K, Kimura T, et al. Identification and characterization of a type III secretion-associated chaperone in the type III secretion system 1 of *Vibrio parahaemolyticus*. *FEMS Microbiol Lett* 2009;**296**:18–25.
- Balasubramanian D, Vanderpool CK. New developments in post-transcriptional regulation of operons by small RNAs. *RNA Biol* 2013;**10**:337–41.
- Beisel CL, Storz G. The base-pairing RNA spot 42 participates in a multioutput feedforward loop to help enact catabolite repression in *Escherichia coli*. *Mol Cell* 2011;**41**:286–97.
- Berg OG, von Hippel PH. Selection of DNA binding sites by regulatory proteins. II. The binding specificity of cyclic AMP receptor protein to recognition sites. *J Mol Biol* 1988;**200**:709–23.
- Bouvier M, Sharma CM, Mika F, et al. Small RNA binding to 5' mRNA coding region inhibits translational initiation. *Mol Cell* 2008;**32**:827–37.
- Broberg CA, Calder TJ, Orth K. *Vibrio parahaemolyticus* cell biology and pathogenicity determinants. *Microbes Infect* 2011;**13**:992–1001.
- Busch A, Richter AS, Backofen R. IntaRNA: efficient prediction of bacterial sRNA targets incorporating target site accessibility and seed regions. *Bioinformatics* 2008;**24**:2849–56.
- Caron MP, Lafontaine DA, Massé E. Small RNA-mediated regulation at the level of transcript stability. *RNA Biol* 2010;**7**:140–4.
- Dean P. Functional domains and motifs of bacterial type III effector proteins and their roles in infection. *FEMS Microbiol Rev* 2011;**35**:1100–25.
- Demarre G, Guérout AM, Matsumoto-Mashimo C, et al. A new family of mobilizable suicide plasmids based on broad host range R388 plasmid (IncW) and RP4 plasmid (IncP α) conjugative machineries and their cognate *Escherichia coli* host strains. *Res Microbiol* 2005;**156**:245–55.
- Gotoh K, Kodama T, Hiyoshi H, et al. Bile acid-induced virulence gene expression of *Vibrio parahaemolyticus* reveals a novel therapeutic potential for bile acid sequestrants. *PLoS One* 2010;**5**:e13365.
- Gottesman S, Storz G. Bacterial small RNA regulators: versatile roles and rapidly evolving variations. *Cold Spring Harb Perspect Biol* 2011;**3**:a003798.
- Griffiths-Jones S, Moxon S, Marshall M, et al. Rfam: annotating non-coding RNAs in complete genomes. *Nucleic Acids Res* 2005;**33**:D121–4.
- Ham H, Orth K. The role of type III secretion system 2 in *Vibrio parahaemolyticus* pathogenicity. *J Microbiol* 2012;**50**:719–25.
- Hansen GA, Ahmad R, Hjerde E, et al. Expression profiling reveals Spot 42 small RNA as a key regulator in the central metabolism of *Aliivibrio salmonicida*. *BMC Genomics* 2012;**13**:37.
- Heckman KL, Pease LR. Gene splicing and mutagenesis by PCR-driven overlap extension. *Nat Protoc* 2007;**2**:924–32.
- Kodama T, Gotoh K, Hiyoshi H, et al. Two regulators of *Vibrio parahaemolyticus* play important roles in enterotoxicity by controlling the expression of genes in the Vp-PAI region. *PLoS One* 2010;**5**:e8678.
- Kodama T, Hiyoshi H, Okada R, et al. Regulation of *Vibrio parahaemolyticus* T3SS2 gene expression and function of T3SS2 effectors that modulate actin cytoskeleton. *Cell Microbiol* 2015;**17**:183–90.
- Kuroda T, Mizushima T, Tsuchiya T. Physiological roles of three Na⁺/H⁺ antiporters in the halophilic bacterium *Vibrio parahaemolyticus*. *Microbiol Immunol* 2005;**49**:711–9.
- Livny J, Zhou X, Mandlik A, et al. Comparative RNA-Seq based dissection of the regulatory networks and environmental stimuli underlying *Vibrio parahaemolyticus* gene expression during infection. *Nucleic Acids Res* 2014;**42**:12212–23.
- Makino K, Oshima K, Kurokawa K, et al. Genome sequence of *Vibrio parahaemolyticus*: a pathogenic mechanism distinct from that of *V. cholerae*. *Lancet* 2003;**361**:743–9.
- Matsuda S, Okada N, Kodama T, et al. A cytotoxic type III secretion effector of *Vibrio parahaemolyticus* targets vacuolar H⁺-ATPase subunit c and ruptures host cell lysosomes. *PLoS Pathog* 2012;**8**:e1002803.
- Michaux C, Verneuil N, Hartke A, et al. Physiological roles of small RNA molecules. *Microbiology* 2014;**160**:1007–19.
- Møller T, Franch T, Udesen C, et al. Spot 42 RNA mediates discordant expression of the *E. coli* galactose operon. *Gene Dev* 2002;**16**:1696–706.
- Nakano M, Takahashi A, Su Z, et al. Hfq regulates the expression of the thermostable direct hemolysin gene in *Vibrio parahaemolyticus*. *BMC Microbiol* 2008;**8**:155.
- Ono T, Park KS, Ueta M, et al. Identification of proteins secreted via *Vibrio parahaemolyticus* type III secretion system 1. *Infect Immun* 2006;**74**:1032–42.
- Pfeiffer V, Papenfort K, Lucchini S, et al. Coding sequence targeting by MicC RNA reveals bacterial mRNA silencing downstream of translational initiation. *Nat Struct Mol Biol* 2009;**16**:840–6.
- Polayes DA, Rice PW, Garner MM, et al. Cyclic AMP-cyclic AMP receptor protein as a repressor of transcription of the *spf* gene of *Escherichia coli*. *J Bacteriol* 1988;**170**:3110–4.
- Richards GR, Vanderpool CK. Molecular call and response: the physiology of bacterial small RNAs. *Biochim Biophys Acta* 2011;**1809**:525–31.
- Sahagan BG, Dahlberg JE. A small, unstable RNA molecule of *Escherichia coli*: spot 42 RNA. I. Nucleotide sequence analysis. *J Mol Biol* 1979a;**131**:573–92.
- Sahagan BG, Dahlberg JE. A small, unstable RNA molecule of *Escherichia coli*: spot 42 RNA. II. Accumulation and distribution. *J Mol Biol* 1979b;**131**:593–605.

- Shinoda S. Sixty years from the discovery of *Vibrio parahaemolyticus* and some recollections. *Biocontrol Sci* 2011;**16**:129–37.
- Tanabe T, Funahashi T, Nakao H, et al. The *Vibrio parahaemolyticus* small RNA RyhB promotes production of the siderophore vibrioferrin by stabilizing the polycistronic mRNA. *J Bacteriol* 2013;**195**:3692–703.
- Tanabe T, Funahashi T, Okajima N, et al. The *Vibrio parahaemolyticus* *pvuA1* gene (formerly termed *psuA*) encodes a second ferric vibrioferrin receptor that requires *tonB2*. *FEMS Microbiol Lett* 2011;**324**:73–9.
- Tanabe T, Kato A, Shiuchi K, et al. Regulation of the expression of the *Vibrio parahaemolyticus* *peuA* gene encoding an alternative ferric enterobactin receptor. *PLoS One* 2014;**9**:e105749.
- Tjaden B, Goodwin SS, Opdyke JA, et al. Target prediction for small, noncoding RNAs in bacteria. *Nucleic Acids Res* 2006;**34**:2791–802.
- Troisfontaines P, Cornelis GR. Type III secretion: more systems than you think. *Physiology* 2005;**20**:326–39.
- Valentin-Hansen P, Eriksen M, Udesen C. The bacterial Sm-like protein Hfq: a key player in RNA transactions. *Mol Microbiol* 2004;**51**:1525–33.
- Vogel J, Luisi BF. Hfq and its constellation of RNA. *Nat Rev Microbiol* 2011;**9**:578–89.



Expression, purification, crystallization and X-ray crystallographic analysis of the periplasmic binding protein VatD from *Vibrio vulnificus* M2799

Nao Miyano,^a Tomoko Igarashi,^a Hiroaki Kawano,^a Katsushiro Miyamoto,^a Takahiro Tsuchiya,^a Koji Tomoo^{b*} and Hiroshi Tsujibo^{a*}

Received 3 March 2015

Accepted 18 June 2015

Edited by A. Nakagawa, Osaka University, Japan

Keywords: *Vibrio vulnificus*; periplasmic binding protein; siderophore; iron; desferrioxamine B.

^aDepartment of Microbiology, Osaka University of Pharmaceutical Sciences, 4-20-1 Nasahara, Takatsuki, Osaka 569-1094, Japan, and ^bDepartment of Physical Chemistry, Osaka University of Pharmaceutical Sciences, 4-20-1 Nasahara, Takatsuki, Osaka 569-1094, Japan. *Correspondence e-mail: tomoo@gly.oups.ac.jp, tsujibo@gly.oups.ac.jp

Vibrio vulnificus is a halophilic marine microorganism which causes gastroenteritis and primary septicaemia in humans. An important factor that determines the survival of *V. vulnificus* in the human body is its ability to acquire iron. VatD is a periplasmic siderophore-binding protein from *V. vulnificus* M2799. The current study reports the expression, purification and crystallization of VatD. Crystals of both apo VatD and a VatD–desferrioxamine B–Fe³⁺ (VatD–FOB) complex were obtained. The crystal of apo VatD belonged to space group *P*6₄22, while the crystal of the VatD–FOB complex belonged to space group *P*2₁. The difference in the two crystal forms could be caused by the binding of FOB to VatD.

1. Introduction

Vibrio vulnificus is a halophilic marine microorganism which causes gastroenteritis and primary septicaemia in humans. The septicaemia is often acquired by eating raw oysters or shellfish, and wound infections are associated with the exposure of wounds to seawater (Blake *et al.*, 1979; Tacket *et al.*, 1984; Klontz *et al.*, 1988). Primary septicaemia is often associated with patients who have diseases predisposing them to iron overload, such as liver cirrhosis, haemochromatosis and alcoholism, or who are immunocompromised (Johnston *et al.*, 1985). *V. vulnificus* sequesters iron through the biosynthesis and secretion of a low-molecular-weight chelating compound called a siderophore (Morris *et al.*, 1987; Litwin *et al.*, 1996). *V. vulnificus* M2799 produces a catecholate siderophore called vulnibactin (Okujo *et al.*, 1994). The vulnibactin-mediated iron-uptake system plays an important role in the growth of *V. vulnificus* M2799 under low iron-concentration conditions (Kawano *et al.*, 2013). Furthermore, the vulnibactin export system is composed of VV1_0612 TolC and several resistance nodulation-division proteins, including the VV1_1681 protein (Kawano *et al.*, 2014). Vulnibactin chelates ferric iron in the environment, and vulnibactin–Fe³⁺ is imported to the periplasm through the specific outer membrane receptor VuuA (Webster & Litwin, 2000). Subsequently, vulnibactin–Fe³⁺ is captured by a periplasmic binding protein (PBP), FatB, and is transported through the inner membrane by an ABC transporter. In a previous study, we clarified that the VatD protein, which functions as a periplasmic ferric aerobactin-binding protein, participates in the ferric vulnibactin-uptake system in the absence of FatB (Kawano *et al.*, 2013). VatD can capture both ferric aerobactin and ferric vulnibactin. Therefore, the

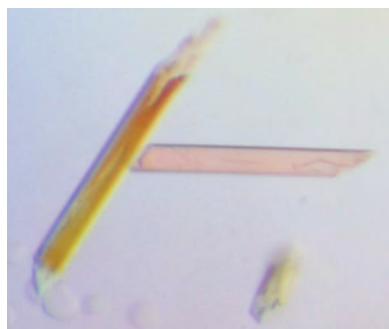


Table 1
Macromolecule-production information.

Source organism	<i>V. vulnificus</i> M2799
DNA source	Genomic DNA
Forward primer (vatD_Nc)	ATGTCCATGGACATCACCACGAAATG
Reverse primer (vatD_Xh)	ATGACTCGAGTCATTGTGGCTGGGT
Expression vector	pProEX HTa
Expression host	<i>E. coli</i> BL21(DE3)pLysS
Complete amino-acid sequence of the construct produced	MSYYHHHHHDYDIPPTTENLYFQGAMDPDITHEM-GTTSFETTPKVVVALDWLVTETVLSLGIIELEG-VANISGYQQWVAEPHLNADAI DVGSRREP NLE-LLSNIKPDVILISKHLAAAYEPLSKIAPVLVY-SVYSEDKQPLES AKRITRSLGKLFDEKQAEQ-VIAQTDQRLTANGAKITSAGKADKPLL FARFI-NDKTLRIHSEGLAQDTINAMGLKNDWQEPTN-LWGFTTTGTEKLAHQKANVMIFGPLSQEERQ-QLTQSPLWQAMEFSRTDSVYELPAI WTFGGLL-AAQR LSDHITGR L TQPQ

structural analysis of VatD will be important for elucidation of the iron-uptake system in *V. vulnificus* M2799. Here, we report the expression, purification, crystallization and preliminary X-ray crystallographic analysis of *V. vulnificus* VatD. Furthermore, the complex of VatD with desferrioxamine B-Fe³⁺ (FOB) was also analysed.

2. Materials and methods

2.1. Macromolecule production

The expression plasmid pProVatD coding for the mature VatD protein was constructed as follows. Two oligonucleotide primers (vatD_Nc and vatD_Xh) were synthesized which were modified to contain NcoI and XhoI recognition sites to facilitate in-frame cloning into the His-tagged protein expression vector pProEX HTa (Invitrogen). PCR was performed by KOD -Plus- DNA polymerase (Toyobo) with the genome of *V. vulnificus* M2799 as a template for 30 cycles consisting of 367 K for 15 s, 333 K for 30 s and 341 K for 1 min. The amplified DNA was digested by NcoI and XhoI, and the resulting fragment (857 bp) was inserted into the corresponding sites of pProEX HTa. The nucleotide sequence of the PCR fragment was confirmed by DNA sequencing. *Escherichia coli* BL21(DE3)pLysS cells harbouring pProVatD were induced with 1.0 mM isopropyl β-D-1-thiogalactopyranoside at an OD₆₀₀ of 0.7 and further incubated overnight at 293 K. The cells were disrupted by sonication and the lysate was centrifuged at 30 000 rev min⁻¹ for 30 min at 277 K. The supernatant was loaded onto an Ni Sepharose 6 Fast Flow column (GE Healthcare) equilibrated with 20 mM Tris-HCl pH 7.5 containing 300 mM NaCl and 50 mM imidazole. The column was washed with five bed volumes of the same buffer. The His-tagged VatD (HisVatD) protein was eluted with 20 mM Tris-HCl pH 7.5 containing 300 mM NaCl and 300 mM imidazole, and treated with AcTEV protease (Invitrogen) overnight at 277 K to obtain VatD. To remove the His tag, the sample was reloaded onto an Ni Sepharose column and the non-adsorbed fraction was pooled. The fraction was dialyzed against 20 mM Tris-HCl pH 8.0 and applied onto a RESOURCE Q column (GE Healthcare). The column was

eluted with a linear gradient of 0–1.0 M NaCl in 20 mM Tris-HCl pH 8.0. The VatD protein was collected and further purified by HiLoad 16/600 Superdex 75 pg (GE Healthcare) column chromatography. The N-terminal amino-acid sequence of VatD was confirmed by protein sequencing. The purified apo VatD protein was concentrated to 9 mg ml⁻¹ in 20 mM Tris-HCl pH 7.5 containing 150 mM NaCl using an Amicon Ultra-15 centrifugal filter device (molecular-weight cutoff 10 kDa). Macromolecule-production information is summarized in Table 1.

2.2. Crystallization

Initial crystallization trials were carried out with the commercially available sparse-matrix screening kits Index (Hampton Research), Wizard 1, Wizard 2 (Emerald Bio), MCSG-1 and MCSG-2 (Microlytic) using the sitting-drop vapour-diffusion method at 293 K. The protein solution (0.5 μl) was mixed with an equal volume of reservoir solution and then equilibrated against 60 μl reservoir solution. Crystals of apo VatD appeared under condition No. 4 from MCSG-1 (the same condition as No. 17 in Wizard 2), condition No. 56 from MCSG-1 and condition No. 32 from MCSG-2. The best crystals were obtained using a reservoir consisting of 0.1 M Tris-HCl pH 7.0, 0.2 M MgCl₂, 2.5 M NaCl.

For the crystallization of VatD-FOB, apo VatD was mixed with the FOB complex, which was prepared from iron(III) chloride and desferrioxamine B mesylate (Sigma-Aldrich), in a 1:3 molar ratio overnight at 277 K. Formation of the VatD-FOB complex was verified by the spectral changes in the tryptophanyl fluorescence. Crystallization screening of VatD-FOB was carried out in the same way as for apo VatD. Crystals of VatD-FOB appeared using a reservoir consisting of 0.1 M bis-tris pH 6.5, 50 mM MgCl₂, 30% (w/v) polyethylene glycol (PEG) 3350. Crystallization information is summarized in Table 2.

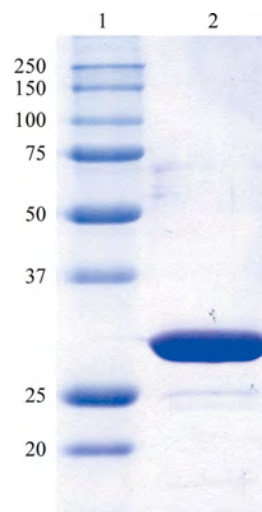


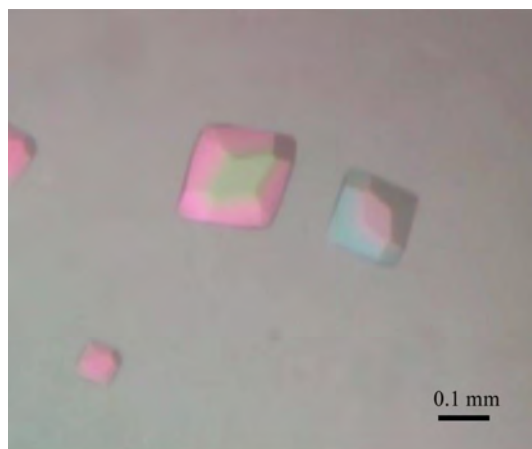
Figure 1
SDS-PAGE of purified VatD. Lane 1 contains molecular-weight marker (labelled in kDa). Lane 2 contains purified apo VatD (31 kDa).

Table 2
Crystallization.

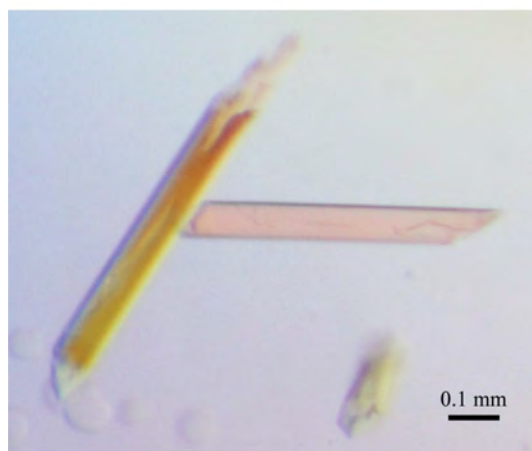
	Apo VatD	VatD-FOB
Method	Sitting-drop vapour diffusion	Sitting-drop vapour diffusion
Plate type	96-well	96-well
Temperature (K)	293	293
Protein concentration (mg ml ⁻¹)	9	9
Buffer composition of protein solution	20 mM Tris pH 7.5, 150 mM NaCl	20 mM Tris pH 7.5, 150 mM NaCl
Composition of reservoir solution	0.1 M Tris pH 7.0, 0.2 M MgCl ₂ , 2.5 M NaCl	0.1 M bis-tris pH 6.5, 50 mM MgCl ₂ , 30%(w/v) PEG 3350
Volume and ratio of drop	1.0 µl (1:1)	1.0 µl (1:1)
Volume of reservoir (µl)	60	60

2.3. Data collection and processing

Crystals of apo VatD and VatD-FOB were soaked in the crystallization solution supplemented with 20%(v/v) glycerol and were mounted in a cryoloop and flash-cooled in a stream of gaseous nitrogen at 100 K. X-ray diffraction data were collected from apo VatD crystals on beamline BL38B1 at SPring-8, Japan, which was equipped with an ADSC Quantum 315r CCD detector. Data collection was performed at a wavelength of 1.0 Å with a total oscillation range of 180°. Each diffraction image was obtained with an oscillation angle of 1.0°



(a)



(b)

Figure 2
(a) Crystals of apo VatD. The dimensions of the crystals are 0.2 × 0.2 × 0.1 mm. (b) Crystals of VatD-FOB. The dimensions of the crystals are 0.4 × 0.2 × 0.1 mm.

Table 3
Data collection and processing.

Values in parentheses are for the outer shell.

	Apo VatD	VatD-FOB
Diffraction source	BL38B1, SPring-8	Rigaku FR-E ⁺
Wavelength (Å)	1.0000	1.54
Temperature (K)	100	100
Detector	ADSC Quantum 315r CCD	R-Axis VII
Crystal-to-detector distance (mm)	320	115
Rotation range per image (°)	1	0.5
Total rotation range (°)	180	180
Exposure time per image (s)	30	360
Space group	<i>P</i> 6 ₄ 22	<i>P</i> 2 ₁
<i>a</i> , <i>b</i> , <i>c</i> (Å)	151.76, 151.76, 76.14	34.80, 57.90, 62.70
α, β, γ (°)	90, 90, 120	90, 95, 90
Mosaicity (°)	0.3	0.3
Resolution range (Å)	50.0–2.60 (2.69–2.60)	26.3–1.85 (1.92–1.85)
Total No. of reflections	98928	72517
No. of unique reflections	59929	20814
Completeness (%)	100 (100)	97.6 (95.4)
Multiplicity	5.8 (5.7)	3.48 (3.32)
<i>I</i> /σ(<i>I</i>)	13.6 (3.7)	10.6 (2.4)
<i>R</i> _{merge} †	0.061 (0.379)	0.085 (0.413)
Overall <i>B</i> factor from Wilson plot (Å ²)	37.9	22.2

† $R_{\text{merge}} = \frac{\sum_{hkl} \sum_i |I_i(hkl) - \langle I(hkl) \rangle|}{\sum_{hkl} \sum_i I_i(hkl)}$, where $I_i(hkl)$ is the *i*th measurement of reflection *hkl* and $\langle I(hkl) \rangle$ is the weighted mean of all measurements of reflection *hkl*.

and an exposure time of 30 s. The diffraction data for apo VatD were processed and scaled with the *HKL-2000* program package (Otwinowski & Minor, 1997). Data for VatD-FOB were collected on a Rigaku FR-E⁺ rotating copper-anode X-ray generator equipped with an Osmic confocal mirror and an R-Axis VII image-plate scanner. The diffraction data for VatD-FOB were processed and scaled with *CrystalClear* (Rigaku). Details of the data collection and processing and statistics describing the quality of the data are given in Table 3.

3. Results and discussion

Recombinant VatD was purified to homogeneity using Ni-affinity, anion-exchange and gel-filtration chromatography. The purity of the protein was checked by SDS-PAGE with Coomassie staining (Fig. 1). The molecular mass of VatD calculated from the deduced amino-acid sequence is in reasonable agreement with that estimated by SDS-PAGE (31 kDa). The protein solution was concentrated to a sufficient level for crystallization. Crystals of apo VatD and VatD-FOB

were obtained under several conditions from commercial screening kits. After a series of optimization experiments, the quality of the crystals was improved to a suitable level for X-ray analysis (Fig. 2).

X-ray diffraction data for apo VatD and VatD–FOB were collected to resolutions of 2.60 and 1.85 Å, respectively, from flash-cooled crystals (Fig. 3). The crystals of apo VatD belonged to space group $P6_422$, with unit-cell parameters

$a = b = 151.8$, $c = 76.1$ Å. According to the unit-cell parameters and the molecular weight of VatD, solvent-content analysis suggested one molecule per asymmetric unit, with a V_M value of $4.03 \text{ \AA}^3 \text{ Da}^{-1}$ and a solvent content of 69.5% (Matthews, 1968). The crystals of VatD–FOB belonged to space group $P2_1$, with unit-cell parameters $a = 34.8$, $b = 57.9$, $c = 62.7$ Å, $\alpha = 90.0$, $\beta = 95.0$, $\gamma = 90.0^\circ$. The V_M value of $2.03 \text{ \AA}^3 \text{ Da}^{-1}$ indicated that the VatD–FOB crystal contained one protein molecule per asymmetric unit. The data-collection statistics are shown in Table 3. Interestingly, the crystallization condition and crystal form of VatD–FOB were different from those of apo VatD. These differences could be caused by a conformational change of VatD owing to the binding of FOB.

The molecular-replacement procedure was applied to the structure determination of apo VatD and VatD–FOB and was performed using FhuD from *E. coli* (PDB entry 1efd; Clarke *et al.*, 2000) as a search model with *MOLREP* (Vagin & Teplyakov, 2010) from the *CCP4* suite (Winn *et al.*, 2011). The initial maps of both models showed clear electron density. The structures of both apo VatD and VatD–FOB are under construction.

Acknowledgements

We thank the beamline staff members at BL38B1 of SPring-8, Hyogo, Japan for their support during data collection. The synchrotron-radiation experiments were performed at BL38B1 of SPring-8, Japan with the approval of the Japan Synchrotron Radiation Research Institute (JASRI; Proposal Nos. 2014B1176 and 2014A1139). This study was supported in part by a Grant-in-Aid for the Strategic Research Foundation Grant-aided Project for Private Universities from the Ministry of Education, Culture, Sports, Science and Technology (MEXT), Japan, 2011–2015 (S1101031). We thank Professor Shin-ichi Miyoshi for supplying the *V. vulnificus* clinical isolate strain M2799.

References

- Blake, P. A., Merson, M. H., Weaver, R. E., Hollis, D. G. & Heublein, P. C. (1979). *N. Engl. J. Med.* **300**, 1–5.
- Clarke, T. E., Ku, S.-Y., Dougan, D. R., Vogel, H. J. & Tari, L. W. (2000). *Nature Struct. Biol.* **7**, 287–291.
- Johnston, J. M., Becker, S. F. & McFarland, L. M. (1985). *JAMA*, **253**, 2850–2853.
- Kawano, H., Miyamoto, K., Sakaguchi, I., Myojin, T., Moriwaki, M., Tsuchiya, T., Tanabe, T., Yamamoto, S. & Tsujibo, H. (2013). *Microb. Pathog.* **65**, 73–81.
- Kawano, H., Miyamoto, K., Yasunobe, M., Murata, M., Myojin, T., Tsuchiya, T., Tanabe, T., Funahashi, T., Sato, T., Azuma, T., Mino, Y. & Tsujibo, H. (2014). *Microb. Pathog.* **75**, 59–67.
- Klontz, K. C., Lieb, S., Schreiber, M., Janowski, H. T., Baldy, L. M. & Gunn, R. A. (1988). *Ann. Intern. Med.* **109**, 318–323.
- Litwin, C. M., Rayback, T. W. & Skinner, J. (1996). *Infect. Immun.* **64**, 2834–2838.
- Matthews, B. W. (1968). *J. Mol. Biol.* **33**, 491–497.
- Morris, J. G., Wright, A. C., Simpson, L. M., Wood, P. K., Johnson, D. E. & Oliver, J. D. (1987). *FEMS Microbiol. Lett.* **40**, 55–59.
- Okujo, N., Saito, M., Yamamoto, S., Yoshida, T., Miyoshi, S. & Shinoda, S. (1994). *Biometals*, **7**, 109–116.
- Otwinowski, Z. & Minor, W. (1997). *Methods Enzymol.* **276**, 307–326.

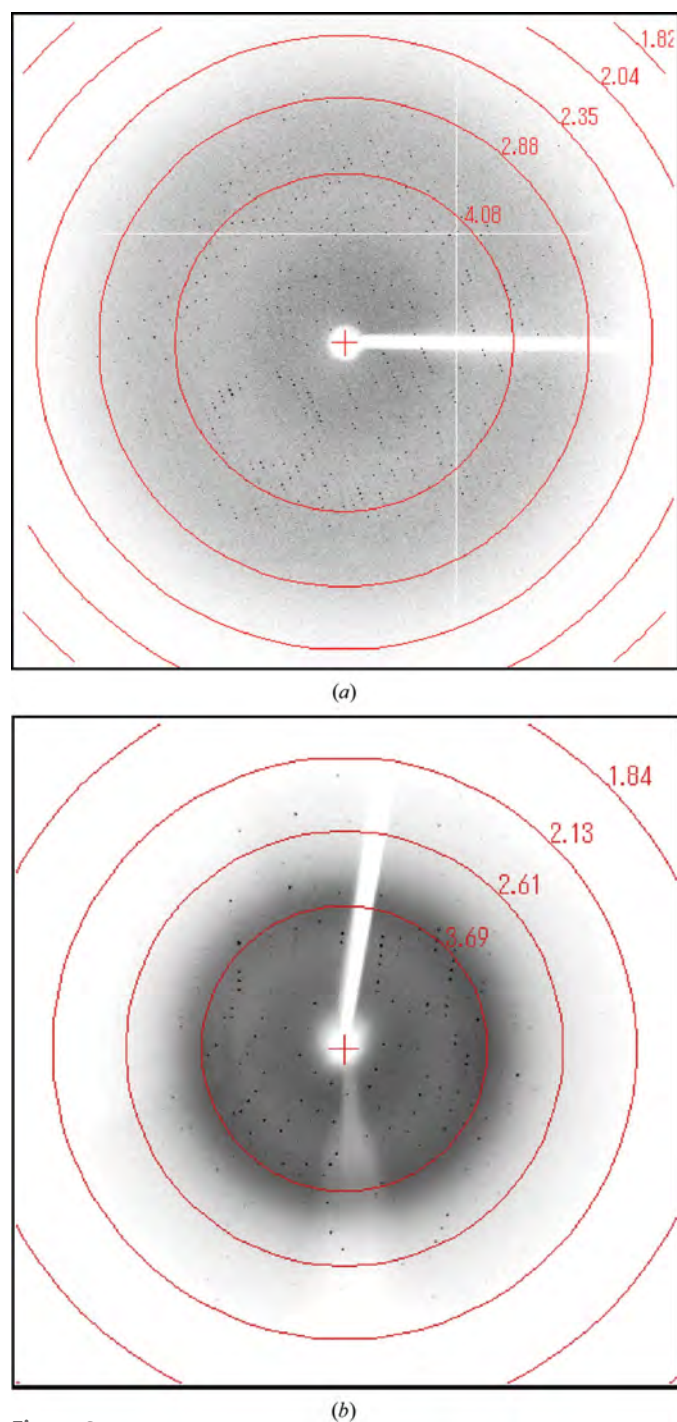


Figure 3
(a) A diffraction image from an apo VatD crystal obtained on BL38B1 at SPring-8. (b) A diffraction image from a VatD–FOB crystal obtained using an in-house X-ray source (Rigaku FR-E⁺, Cu K α radiation).

Tackett, C. O., Brenner, F. & Blake, P. A. (1984). *J. Infect. Dis.* **149**, 558–561.

Vagin, A. & Teplyakov, A. (2010). *Acta Cryst.* **D66**, 22–25.

Webster, A. C. D. & Litwin, C. M. (2000). *Infect. Immun.* **68**, 526–534.

Winn, M. D. *et al.* (2011). *Acta Cryst.* **D67**, 235–242.



Identification and characterization of *Aeromonas hydrophila* genes encoding the outer membrane receptor of ferrioxamine B and an AraC-type transcriptional regulator

Tatsuya Funahashi, Tomotaka Tanabe, Jun Maki, Katsushiro Miyamoto, Hiroshi Tsujibo & Shigeo Yamamoto

To cite this article: Tatsuya Funahashi, Tomotaka Tanabe, Jun Maki, Katsushiro Miyamoto, Hiroshi Tsujibo & Shigeo Yamamoto (2014) Identification and characterization of *Aeromonas hydrophila* genes encoding the outer membrane receptor of ferrioxamine B and an AraC-type transcriptional regulator, *Bioscience, Biotechnology, and Biochemistry*, 78:10, 1777-1787, DOI: 10.1080/09168451.2014.932669

To link to this article: <http://dx.doi.org/10.1080/09168451.2014.932669>



Published online: 10 Jul 2014.



Submit your article to this journal [↗](#)



Article views: 140



View related articles [↗](#)



View Crossmark data [↗](#)

Identification and characterization of *Aeromonas hydrophila* genes encoding the outer membrane receptor of ferrioxamine B and an AraC-type transcriptional regulator

Tatsuya Funahashi^{1,*}, Tomotaka Tanabe¹, Jun Maki², Katsushiro Miyamoto³, Hiroshi Tsujibo³ and Shigeo Yamamoto¹

¹Laboratory of Hygienic Chemistry, College of Pharmaceutical Sciences, Matsuyama University, Matsuyama, Japan;

²Laboratory of Infectious Disease, College of Pharmaceutical Sciences, Matsuyama University, Matsuyama, Japan;

³Department of Microbiology, Osaka University of Pharmaceutical Sciences, Takatsuki, Japan

Received March 12, 2014; accepted April 25, 2014

<http://dx.doi.org/10.1080/09168451.2014.932669>

We found that, under iron-limiting conditions, *Aeromonas hydrophila* ATCC 7966¹ could utilize the xenosiderophore desferrioxamine B (DFOB) for growth by inducing the expression of its own outer membrane receptor. Two consecutive genes, *desR* and *desA*, were selected as candidates involved in DFOB utilization. The presence of the ferric-uptake regulator boxes in their promoters suggested that these genes are under iron-dependent regulation. Mutation of *desA*, a gene that encodes the outer membrane receptor of ferrioxamine B, disrupted the growth of the amonabactin-deficient mutant in the presence of DFOB. β -Galactosidase reporter assays and reverse transcriptase-quantitative PCR demonstrated that *desR*, a gene that encodes an AraC-like regulator homolog is required for the induction of *desA* transcription in the presence of DFOB and under iron-limiting conditions. The functions of *desA* and *desR* were analyzed using complementation experiments. Our data provided evidence that DesA is powered primarily by the TonB2 system.

Key words: *Aeromonas hydrophila*; desferrioxamine B; outer membrane receptor; AraC-type regulator; TonB

Iron is an essential element for the survival and growth of nearly all bacteria. However, in an aerobic environment at neutral pH, iron is highly insoluble and therefore scarcely available to bacteria.¹⁾ To acquire iron from their environment, bacteria have developed specific strategies that permit them to scavenge the element. Most bacteria produce low-molecular mass chelators, siderophores that have a high affinity for ferric iron, allowing bacteria to scavenge iron from their surroundings.¹⁾ In addition to their own siderophores,

some bacteria have evolved the ability to utilize heterologous siderophores (xenosiderophores) of bacterial or fungal origin. In Gram-negative bacteria, iron-bound siderophores (ferric siderophores) are transported across the outer and inner membranes by specific iron-repressible outer membrane protein (IROMP) receptors and ATP-binding cassette transport systems, respectively.^{1–3)} Transport of ferric siderophores by using specific IROMP receptors is an energy-dependent process. Proton-motive force created by the inner membrane is transduced to IROMP receptors through the TonB system, which generally consists of the integral inner membrane proteins, TonB, ExbB, and ExbD. The TonB system activates by altering their structure to one that recognizes ferric siderophores.^{2,3)} Therefore, these IROMPs are referred to as TonB-dependent receptors. When the cytoplasmic Fe²⁺ concentration increases, the ferric uptake regulator protein (Fur) binds to Fe²⁺ as a cofactor, repressing the expression of iron acquisition genes including those involved in siderophore biosynthesis, ferric-siderophore transport, and virulence.^{4,5)} The Fur–Fe²⁺ complex binds to the Fur box consensus sequence that is located near the –10 and –35 elements of Fur-targeted genes. Binding of the Fur–Fe²⁺ to the Fur box leads to the transcriptional repression of target genes. AraC-type regulators reportedly control the transcription of iron acquisition genes in bacteria including *Pseudomonas aeruginosa*,⁶⁾ *Yersinia pestis*,⁷⁾ *Bordetella* species,^{8,9)} *Vibrio vulnificus*,¹⁰⁾ and *Vibrio furnissii*.¹¹⁾ In these species, the cognate siderophores or xenosiderophores can serve as co-activators of transcriptional regulators, and the transcription of the AraC-type regulator genes is generally under the control of Fur.

Aeromonas hydrophila is a facultative anaerobic invasive motile Gram-negative bacterium associated with a variety of human infections, including water-borne traumatic secondary wound infections,

*Corresponding author. Email: tfunahas@cc.matsuyama-u.ac.jp

Abbreviations: DFOB, desferrioxamine B; EDDA, ethylenediamine-di(o-hydroxyphenylacetic acid); FOB, ferrioxamine B; Fur, ferric uptake regulator; FURTA, Fur titration assay; IROMP, iron-repressible outer membrane protein; OMP, outer membrane protein; LB, Luria-Bertani; PAGE, polyacrylamide gel electrophoresis; RT-qPCR, reverse transcriptase-quantitative PCR.

septicemia, and gastroenteritis,^{12,13}) In response to iron starvation, *A. hydrophila* typically secrete and utilize amonabactins, a group of four peptide-based catecholate siderophores with two 2,3-dihydroxybenzoic acid Fe³⁺-binding moieties.^{14,15}) Recently, we reported that *entA*, which encodes 2,3-dihydro-2,3-dihydroxybenzoate dehydrogenase, is essential for the production of amonabactin, and the 66.2 kDa IROMP encoded by *irgA* functions as the ferric enterobactin receptor, which is dependent solely on the TonB2 system.¹⁶)

Here, we report that, under iron-limiting conditions, *A. hydrophila* ATCC 7966^T can utilize the xenosiderophore, desferrioxamine B (DFOB) by regulating the expression of its own outer membrane receptor encoded by *desA*. In addition, we show the involvement of *desR*, which encodes an AraC-type regulator, in the transcriptional induction of *desA* in the presence of DFOB and under iron-limiting conditions. Furthermore,

we demonstrate that DesA function depends on energy transduced by the TonB1 and, to a lesser extent, by TonB2 systems.

Materials and methods

Bacterial strains, plasmids, primers, and growth conditions. Bacterial strains and plasmids used in this study are listed in Table 1. *A. hydrophila* and *Escherichia coli* were grown at 30 and 37 °C, respectively, in Luria-Bertani (LB) media (with shaking) or grown on LB agar plates (1.5% agar) containing 0.5% NaCl. *E. coli* β2155, a diaminopimelic acid auxotroph, was grown in LB media containing 1 mM diaminopimelic acid. LB media with or without an iron chelator, ethylenediamine-di(*o*-hydroxyphenylacetic acid) (EDDA; 250 μM; Sigma-Aldrich, St. Louis, MO, USA) were used as iron-limiting (−Fe) and iron-replete (+Fe)

Table 1. Bacterial strains and plasmids used in this study.

Strains or plasmids	Relevant feature*	Reference or source
Strains		
<i>A. hydrophila</i>		
ATCC 7966 ^T	Wild-type, isolated from a tin of milk with a fishy odor	ATCC 16)
<i>ΔentA</i>	<i>entA</i> (amonabactin biosynthesis gene) deletion mutant derived from ATCC 7966 ^T	This study
<i>ΔdesA</i>	<i>desA</i> (FOB receptor gene) deletion mutant derived from ATCC 7966 ^T	This study
<i>ΔdesB</i>	<i>desB</i> (unknown function) deletion mutant derived from ATCC 7966 ^T	This study
<i>ΔdesR</i>	<i>desR</i> (AraC-like regulator gene) deletion mutant derived from ATCC 7966 ^T	This study
<i>ΔdesRΔlacZ</i>	<i>lacZ</i> (β-galactosidase gene) deletion mutant derived from <i>ΔdesR</i>	This study
<i>ΔentAΔdesA</i>	<i>desA</i> deletion mutant derived from <i>ΔentA</i>	This study
<i>ΔentAΔdesB</i>	<i>desB</i> deletion mutant derived from <i>ΔentA</i>	This study
<i>ΔentAΔdesR</i>	<i>desR</i> deletion mutant derived from <i>ΔentA</i>	This study
<i>ΔentAΔtonB1</i>	<i>tonB1</i> deletion mutant derived from <i>ΔentA</i>	16)
<i>ΔentAΔtonB2</i>	<i>tonB2</i> deletion mutant derived from <i>ΔentA</i>	16)
<i>ΔentAΔtonB3</i>	<i>tonB3</i> deletion mutant derived from <i>ΔentA</i>	16)
<i>ΔentAΔtonB1ΔtonB2</i>	<i>tonB1</i> and <i>tonB2</i> double deletion mutant derived from <i>ΔentA</i>	This study
<i>ΔentAΔtonB1ΔtonB3</i>	<i>tonB1</i> and <i>tonB3</i> double deletion mutant derived from <i>ΔentA</i>	This study
<i>ΔentAΔtonB2ΔtonB3</i>	<i>tonB2</i> and <i>tonB3</i> double deletion mutant derived from <i>ΔentA</i>	This study
<i>E. coli</i>		
β2155	<i>thrB1004 pro thi strA hsdS Δ(lacZ)ΔM15</i> [F' <i>Δ(lacZ)ΔM15 lacI^d traD36 proA⁺ proB⁺</i>] <i>ΔdapA::erm</i> (Em ^r), <i>pir::RP4[::kan</i> (Km ^r) from SM10]	24)
DH5α	<i>endA1 hsdR17</i> (r _g ⁺ m _g ⁺) <i>supE44 thi-1 recA1 gyrA96 relA1 Δ(argF-lacZYA)U169 deoR</i> [Φ80d <i>lac Δ(lacZ)M15</i>]	Promega
H1717	<i>araD139 rpsL150 Δ(argF-lac) relA1 U169 ffbB5301 deoC1 ptsF25 rbsR aroB fhfF::λplacMu</i> ; host strain for FURTA	20)
Plasmids		
pXAC623	Suicide vector derived from pKTN701 containing <i>sacB</i> gene of <i>Bacillus subtilis</i> ; Cm ^r	21)
pBluescript II KS(+)	High-copy-number cloning vector; Ap ^r	Stratagene 25)
pRK415	Broad-host-range plasmid; Tc ^r	26)
pHRP309	Broad-host-range plasmid (low-copy number) with promoterless <i>lacZ</i> gene; Gm ^r	26)
pXACΔdesA	pXAC623 containing 1132 bp <i>XbaI-XbaI</i> fragment with 2063 bp deletion in <i>desA</i> ; Cm ^r	This study
pXACΔdesB	pXAC623 containing 1016 bp <i>XbaI-XbaI</i> fragment with 791 bp deletion in <i>desB</i> ; Cm ^r	This study
pXACΔdesR	pXAC623 containing 1248 bp <i>XbaI-XbaI</i> fragment with 872 bp deletion in <i>desR</i> ; Cm ^r	This study
pXACΔlacZ	pXAC623 containing 1088 bp <i>XbaI-XbaI</i> fragment with 3045 bp deletion in <i>lacZ</i> ; Cm ^r	This study
pXACΔtonB1	pXAC623 containing 1129 bp <i>XbaI-XbaI</i> fragment with 704 bp deletion in <i>tonB1</i> ; Cm ^r	16)
pXACΔtonB2	pXAC623 containing 1094 bp <i>XbaI-XbaI</i> fragment with 606 bp deletion in <i>tonB2</i> ; Cm ^r	16)
pXACΔtonB3	pXAC623 containing 1069 bp <i>XbaI-XbaI</i> fragment with 491 bp deletion in <i>tonB3</i> ; Cm ^r	16)
pHRP-desA	pHRP309 containing 708 bp <i>XbaI-EcoRI</i> fragment with <i>desA</i>	This study
pHRP-desAR	pHRP309 containing 1554 bp <i>KpnI-EcoRI</i> fragment with full-length <i>desR</i> and <i>desA</i> promoter region; Gm ^r	This study
pRK415-desA	pRK415 containing 2393 bp <i>HindIII-XbaI</i> fragment with full-length <i>desA</i> ; Tc ^r	This study
pRK415-desR	pRK415 containing 1226 bp <i>HindIII-XbaI</i> fragment with full-length <i>desR</i> ; Tc ^r	This study
pBC-desAfur	pBluescript II KS(+) containing 250 bp <i>HindIII-EcoRI</i> fragment with <i>desA</i> promoter region; Ap ^r	This study
pBC-desRfur	pBluescript II KS(+) containing 318 bp <i>KpnI-SacI</i> fragment with <i>desR</i> promoter region; Ap ^r	This study

*Ap^r, ampicillin resistance; Cm^r, chloramphenicol resistance; Gm^r, gentamicin resistance; Tc^r, tetracycline resistance.

media, respectively. Appropriate antibiotics were added to the media as needed at the following concentrations: ampicillin (50 µg/mL), chloramphenicol (10 µg/mL), gentamicin (10 µg/mL), and tetracycline (10 µg/mL). PCR primers used in this study are listed in Table 2.

Growth assay. To avoid the effect of the endogenous siderophore amonabactin on growth in $-Fe$ medium, all deletion mutants used for this assay were generated from an *entA* deletion mutant ($\Delta entA$) derived from *A. hydrophila* ATCC 7966^T strain.¹⁶⁾ The mutant strains were grown overnight in LB medium. Fresh $+Fe$ and $-Fe$ media (5 mL) were inoculated with an aliquot of the preculture (OD₆₀₀ of 0.005). While the cultures were shaking at 70 rpm at 30 °C, OD₆₀₀ was automatically measured every 1 h by using an Advantec TVS062CA biophotorecorder (Advantec, Tokyo, Japan). When required, DFOB (Sigma-Aldrich) was added to $-Fe$ medium at 20 µM ($-Fe/+DFOB$).

DNA manipulations. Standard DNA manipulations were carried out as described by Sambrook et al.¹⁷⁾ Chromosomal DNA and plasmid DNA were extracted using the Wizard® Genomic DNA Purification Kit (Promega, Madison, WI, USA) and High Pure Plasmid Isolation Kit (Roche Diagnostics, Mannheim, Germany), respectively. Restriction enzymes were purchased from Roche Diagnostics. The Ligation-Convenience Kit (Wako Pure Chemical Industries, Osaka, Japan) was used for DNA ligation. DNA fragments were purified from agarose gels by using the MagExtractor-PCR & Gel Clean-Up DNA Fragment Purification Kit (Toyobo, Osaka, Japan). *E. coli* was transformed by electroporation using a MicroPulser™ apparatus (Bio-Rad, Benicia, CA, USA). The oligonucleotide primers used in this study (Table 2) were designed based on the *A. hydrophila* ATCC 7966^T genome sequence.¹⁸⁾ Homology searches were performed using the National Center for Biotechnology Information Basic Local Alignment Search Tool (BLAST; <http://blast.ncbi.nlm.nih.gov/>). A putative AraC-binding site (AraC box) sequence was identified using the Virtual Footprint promoter analysis software based on the PRODORIC Release 8.9 (<http://www.prodoric.de/>) online database.

IROMP analysis. *A. hydrophila* ATCC 7966^T cells grown in the presence or absence of DFOB for 12 h in LB media under $-Fe$ conditions were harvested. The outer membrane protein (OMP)-rich fractions were prepared and analyzed by SDS-polyacrylamide gel electrophoresis (PAGE), according to a procedure described previously.¹⁹⁾ The resulting gel was stained with Coomassie Brilliant Blue R-250, and visualized using a Gel Doc XR system (Bio-Rad). The protein was electroblotted onto a pre-wetted polyvinylidene difluoride membrane (ProBlott®; Applied Biosystems, Carlsbad, CA, USA) by using a Trans-Blot® semi-dry electrophoretic transfer cell (Bio-Rad). Their N-terminal amino acid sequences were determined by the automated Edman degradation method using a Procise® Model 491 protein sequencer (Applied Biosystems).

Fur titration assay. The Fur titration assay (FURTA)²⁰⁾ was used to assess whether Fur box sequences were present in the promoter regions of *A. hydrophila* *desA* and *desR* genes. PCR amplicons encoding the putative Fur boxes of *desA* and *desR* were generated using DesA-7/8, and DesR-7/8 primer pairs. The resulting *HindIII-EcoRI* *desA* (250 bp) and *KpnI-SacI* *desR* (418 bp) promoter inserts were used to construct pBC-desA_{Fur} and pBC-desR_{Fur} plasmids, respectively. The pBC-desA_{Fur} and pBC-desR_{Fur} plasmids were electroporated into *E. coli* H1717 bearing a Fur-repressible *shuF::lacZ* fusion. Transformants were incubated for 15 h on MacConkey lactose agar plates (BD, Franklin Lakes, NJ, USA) containing ampicillin (50 µg/mL) and ferric chloride (100 µM), and the phenotype of the colonies was examined. The FURTA-positive phenotype, denoted by red colonies (Lac+), indicated that the Fur protein bound to the promoter regions contained within the pBC-desA_{Fur} and pBC-desR_{Fur} plasmids that had been transformed into the *E. coli* H1717.

Construction of *A. hydrophila* ATCC 7966^T deletion mutants and complementing strains. Deletion mutants were generated by allelic exchange using the R6K-ori suicide vector pXAC623, as described previously.^{16,21)} DNA fragments carrying deletions in the *A. hydrophila* *desA*, *desB*, *desR*, and *lacZ* (AHA_4101) genes were prepared by PCR-driven overlap extension^{22,23)} using two primer sets for each gene (DesA1–4, DesB1–4, DesR1–4, and LacZ1–4, respectively). The fragments were digested using *XbaI* and were ligated into *XbaI*-digested pXAC623. The resulting plasmids (Table 1) were transformed into *E. coli* β2155,²⁴⁾ and then mobilized into the appropriate *A. hydrophila* strains by filter mating. The resulting merodiploids were selected on LB agar plates containing chloramphenicol (10 µg/mL) in the absence of diaminopimelic acid and were then incubated at room temperature for 48 h on LB agar plates containing 10% sucrose in the absence of both NaCl and chloramphenicol. Sucrose-resistant and chloramphenicol-sensitive colonies were selected. The deletions were confirmed by PCR using chromosomal DNA as template and the following primer pairs: DesA-5/6, DesB-5/6, DesR-5/6, LacZ-5/6, TonB1-5/6, TonB2-5/6, and TonB3-5/6. To complement mutants carrying a deletion in *desA* or *desR*, PCR amplicons containing the full-length genes were prepared using the primer pairs DesA-comp-F/R and DesR-comp-F/R and ligated into appropriately digested pRK415.²⁵⁾ The complementing plasmids were transformed into *E. coli* β2155 and then mobilized into the appropriate *A. hydrophila* mutants by filter mating.

Construction of *lacZ* fusions used in β-galactosidase reporter assays. Two varieties of DNA fragments containing the upstream regions of *desA* were amplified by PCR using two primer pairs, DesR-7/DesA-8 and DesA-1/8. PCR fragments were digested with *XbaI-EcoRI* and *KpnI-XbaI*, respectively, and ligated into the digested pHRP309.²⁶⁾ The resulting promoter-*lacZ* reporter plasmids, pHRP-desA and pHRP-desAR, were

Table 2. PCR primers used in this study.

Purpose	Primer name	Sequence (5'–3')*
Construction of $\Delta desA$ fragment	DesA-1 (including <i>Xba</i> I site)	TAGATGTTTCTAGAGCCGGCGAGTCGC
	DesA-2	gtcgtagcaggcggtacatcTGATCCTCGAATGC
	DesA-3	gatgtacgacctgctacacCAGAACAAGTCTGG
	DesA-4 (including <i>Xba</i> I site)	TCAAACCTAGATTGATCATGGGTTCGG
Confirmation of <i>desA</i> deletion	DesA-5	TCCGACTTTCAGCAGACGG
	DesA-6	TGCACCTGCCCGAGTTGTGC
Construction of full-length <i>desA</i>	DesA-comp-F (including <i>Hind</i> III site)	CGCCAACAAGCTTCAAATTGTTAATTCAAGGG
	DesA-comp-R (including <i>Xba</i> I site)	AGCCGACTCTAGAGGGGACGGGATAAGCC
Construction of <i>desA</i> promoter fragment for FURTA	DesA-7 (including <i>Hind</i> III site)	CGCCAACAAGCTTCAAATTGTTAATTCAAGGGC
	DesA-8 (including <i>Eco</i> RI site)	GAGCCGGGAATTCGTGCGGGTGTTCGG
Construction of $\Delta desR$ fragment	DesR-1 (including <i>Xba</i> I site)	GGCATCGTCTAGAGGCTGGGTACCG
	DesR-2	actccatcgcggtatctggcCTGTGCGCAAGGC
	DesR-3	cccagatccgcatggagtACTGGCTGCC
	DesR-4 (including <i>Xba</i> I site)	GTAGTTGTCTAGACCGGGATGTTGAACAGATCC
Confirmation of <i>desR</i> deletion	DesR-5	GAGGAGATGTTGATGATGCG
	DesR-6	AGTCGTTGTACTGCAGCAGC
Construction of full-length <i>desR</i>	DesR-comp-F (including <i>Hind</i> III site)	ATGCGATAAGCTTGGGCCAGCAAGGCGG
	DesR-comp-R (including <i>Xba</i> I site)	CAGGCGATCTAGAATGGATAGCAAAGCC
Construction of <i>desR</i> promoter fragment for FURTA	DesR-7 (including <i>Kpn</i> I site)	CATAAAAAGGTACCAACGAGGACTTTATGG
	DesR-8 (including <i>Sac</i> I site)	GGATGTACTCGAGCACCCGCTCGATGCG
Construction of full-length <i>desR</i> and <i>desA</i> promoter fragment for β -galactosidase assay	DesR-7	See above
	DesA-8	See above
Construction of <i>desA</i> promoter fragment for β -galactosidase assay	DesA-1	See above
	DesA-8	See above
Construction of $\Delta desB$ fragment	DesB-1 (including <i>Xba</i> I site)	AAGGGGGTCTAGATGGAGGGGCGCGTCC
	DesB-2	gttcaagccccgctcatggGGTGAGAGAG
	DesB-3	ccatgagcggggcctgaacAGAGAAACCC
	DesB-4 (including <i>Xba</i> I site)	GCGGCATCTAGACTTGTCTACCTCG
Confirmation of <i>desB</i> deletion	DesB-5	GATCCGGACAATGTCTACGG
	DesB-6	GGGCTTTGATTCCATCAGCG
Construction of $\Delta lacZ$ fragment	LacZ-1 (including <i>Xba</i> I site)	TCTCGGTTCTAGAGGACAACGGCCTCAAGG
	LacZ-2	cagcgtagaagggccactatCTCCCTGAGC
	LacZ-3	atagtggccttctacgetgAATCTGAGCG
	LacZ-4 (including <i>Xba</i> I site)	ATAGCTGTCTAGATCGGACGGCTCGG
Confirmation of <i>lacZ</i> deletion	LacZ-5	CCTACAACGATGCCATGGC
	LacZ-6	CTCCTTGGAGTCGGTACCC
Confirmation of <i>tonB1</i> deletion	TonB1-1	GTTCAGATCAAGGACGAGCC
	TonB1-2	TTGTCCAGACTGCTGTACC
Confirmation of <i>tonB2</i> deletion	TonB2-1	TTAACC CGGAGAGCATGGC
	TonB2-2	AGCACTGCCTAGTCGAGACG
Confirmation of <i>tonB3</i> deletion	TonB3-1	GGGGCACAGAAACGAAGG
	TonB3-2	GAGCAGATACCAGGACTCCG
qPCR for <i>desA</i>	desA-qF	GTTGCCGGAGCAGTTCAAG
	desA-qR	GCCAGGAAGAGGACGGTATG
qPCR for <i>desR</i>	desR-qF	ACCCAGTCCGAGCAGAAGAG
	desR-qR	GAAGTTGACCCGTGACCAGAG
qPCR for 16S rRNA	16S-qF	GCAACGCGAAGAACCTTACC
	16S-qR	GCGGGACTTAACCCAACATC
RT for <i>desAB</i>	desB-R	GCGCACATAACCGACCAAG
RT for <i>desR</i>	desR-R	GGATGAACCAAGTTGAGGGTCTG
RT for 16S rRNA	16S-R	TCCCTTGAGTTCCACCAATTAC
PCR for <i>desA</i> amplification	desA-F	AGTTTGCTATCGGCTGGTG
	desA-R	TTGTAGGTGTTCTGCTGGTTGG
PCR for <i>desB</i> amplification	desB-F	CAAGGGAGAGTTTGAGGTGTTG
	desB-R	See above
PCR for <i>desR</i> amplification	desR-F	TGGTACAGGTGCGGATCGAG
	desR-R	See above
PCR for 16S rRNA amplification	16S-F	GATTTGGAGGCTGTGTCCTTG
	16S-R	See above

*Underlined sequences indicate restriction enzyme sites; lowercase sequences within primer 2 and 3 are complementary.

individually introduced into *A. hydrophila* $\Delta desR\Delta lacZ$, which was constructed by deleting *lacZ* from $\Delta desR$ (described above). The resulting strains, $\Delta desR\Delta lacZ/pHRP-desA$ and $\Delta desR\Delta lacZ/pHRP-desAR$, were grown at 30 °C in +Fe, –Fe, and –Fe/+DFOB media

for 12 h. The β -galactosidase activities in their cell lysates were measured using the Miller method.²⁷⁾

Reverse transcriptase (RT)-PCR and quantitative (q)-PCR. *A. hydrophila* ATCC 7966^T and $\Delta entA$

were grown in LB medium to an OD₆₀₀ of 0.3. Each culture was split into two aliquots. One aliquot was left untreated (+Fe medium) and the other was supplemented with 250 μM EDDA (-Fe medium). Both cultures were further incubated until they reached an OD₆₀₀ of 0.5. Total RNA was extracted from each cell pellet using the RNeasy® Protect Bacteria Mini Kit (Qiagen, Valencia, CA, USA) and then treated with RNase-free DNase I (Ambion, Austin, TX, USA), following the manufacturer's instruction to eliminate trace chromosomal DNA contamination. These DNase I-treated total RNA preparations were used for RT-PCR and RT-qPCR. To generate cDNA for RT-PCR, 1 μg of the total RNA preparation was incubated at 42 °C for 1 h with primers complementary to the internal sequence of *desR* and *desB*, *desR*-R and *desB*-R. PCR was performed using 1 μL of the RT reaction mixture and gene-specific primer pairs, *desA*-F/R for *desA*, *desB*-F/R for *desB*, and *desR*-F/R for *desR*. The PCR conditions were as follows: after initial denaturation at 94 °C for 2 min, DNA was amplified by 30 cycles, with each cycle consisting of denaturation at 98 °C for 10 s, annealing at 58 °C for 30 s, and extension at 68 °C for 1 min. Total RNA not treated with RT was used as a negative control in the PCR reaction to confirm the absence of genomic DNA contamination. 16S rRNA was used as an endogenous internal control. RT-PCR products were run on a 1.5% agarose gel stained with ethidium bromide and visualized using a Gel Doc XR.

To perform RT-qPCR, 0.5 μg of the total RNA preparation was used to generate cDNA using ReverTra Ace® RT (Toyobo) and a random hexamer primer (Takara Bio, Otsu, Japan). The qPCR was performed using a Chromo4 Real-Time PCR detection system (Bio-Rad) and Thunderbird® SYBR® qPCR Mix (Toyobo). The following primer pairs were used: *desA*-qF/qR for *desA*; *desR*-qF/qR for *desR*; and 16S-qF/qR for 16S rRNA. Values were quantified using the comparative threshold cycle method and were normalized to the levels of 16S rRNA.

Results and discussion

Utilization of DFOB as a xenosiderophore by A. hydrophila ATCC 7966^T

The amonabactin-deficient mutant, *ΔentA*, did not grow in -Fe medium; however, the addition of 20 μM DFOB to the same medium restored the growth of *ΔentA* (Fig. 1). This indicates that *A. hydrophila* ATCC 7966^T can utilize DFOB as a xenosiderophore.

Identification of candidate genes involved in DFOB utilization in A. hydrophila ATCC 7966^T

To identify candidate *A. hydrophila* ATCC 7966^T genes involved in DFOB utilization, we performed BLAST searches on the *A. hydrophila* genome sequence¹⁸ using the amino acid sequence of the TonB-dependent ferrioxamine B (FOB; Fe³⁺-loaded form of DFOB) receptor DesA (VV2_1337) from *V. vulnificus*.¹⁰ We identified a *desA* ortholog (*AHA_1953*) that encodes a 714 amino acid protein

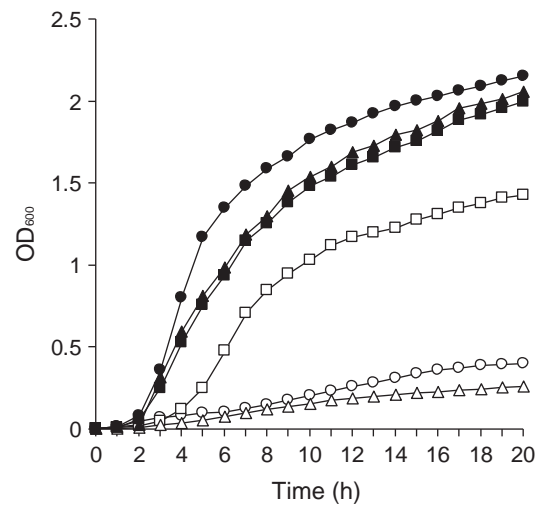


Fig. 1. Growth assays of *A. hydrophila* *ΔentA*, *ΔdesA*, *ΔdesR* and complementing strains.

Notes: *ΔentA*, a mutant deficient in the cognate siderophore amonabactin, was grown in iron-limiting DFOB negative medium (-Fe/-DFOB; open circle) and iron-limiting medium containing DFOB (-Fe/+DFOB; filled circle). *ΔentAΔdesA* and *ΔdesRΔentA*, generated from the *entA* deletion mutant (*ΔentA*), and their complementing strains were grown in -Fe/+DFOB medium. *ΔentAΔdesA/pRK415* (empty), open triangle; *ΔentAΔdesA/pRK415-desA*, filled triangle; *ΔentAΔdesR/pRK415* (empty), open square; and *ΔentAΔdesR/pRK415-desR*, filled square. OD₆₀₀ was measured every hour for 20 h. A representative example from three independent experiments is shown.

sharing 48% amino acid identity with *V. vulnificus* DesA. The product of *AHA_1953* was annotated as a ferrichrome receptor.¹⁸ An additional open reading frame (*AHA_1954*), *desB*, was found just downstream of *desA*. The predicted protein product of *desB* shared 33% amino acid identity with a *V. vulnificus* protein with unknown function (VV2_1339). *A. hydrophila* DesB was homologous to *E. coli* FluF, which is reportedly involved in the removal of iron from cytoplasmic FOB through the reduction of Fe³⁺.²⁸ The protein product of *desR* (*AHA_1952*), an upstream gene adjacent to *desA*, shared 51% amino acid identity with *V. vulnificus* DesR (VV2_1338),¹⁰ which encodes an AraC-type transcriptional activator of *V. vulnificus* DesA. A genetic map of the candidate genes in *A. hydrophila* ATCC 7966^T involved in DFOB utilization is shown in Fig. 2(A).

Using homology searches, we revealed that *Aeromonas salmonicida* also possessed the DesR (ASA_2342), DesA (ASA_2341), and DesB (ASA_2340) orthologs that shared 80, 90, and 75% identity to their respective proteins in *A. hydrophila*. The *desR*, *desA*, and *desB* are also found in *V. vulnificus*. In *A. hydrophila* and *A. salmonicida*, the genes appear in the same order (*desR-desA-desB*) and each gene is in the same orientation. However, the genes in *V. vulnificus* were arranged in a different order (*desB-desR-desA*) and *desB* was in the reverse orientation. The DesA and DesR proteins in *A. hydrophila* also showed similarities to their *V. furnissii* counterparts. However, no orthologs of *A. hydrophila* and *V. vulnificus* *desB* were found in the *V. furnissii* genome.²⁹

Characterization of DesA as an IROMP by SDS-PAGE and N-terminal amino acid sequence determination

To analyze the OMP profiles of *A. hydrophila* ATCC 7966^T grown in +Fe, -Fe, and -Fe/+DFOB media, sarkosyl-insoluble OMP fractions were prepared¹⁹⁾ and then separated by SDS-PAGE. In *A. hydrophila* grown in -Fe medium, we detected two major and one minor IROMP bands ranging in size from 66 to 80 kDa (Fig. 3, lane 2). These bands were not detected in *A. hydrophila* grown in +Fe medium (Fig. 3, lane 1). In

contrast, when grown in -Fe/+DFOB medium, the strain robustly expressed a novel 76.7 kDa IROMP (Fig. 3, lane 3). This band was not detected under +Fe conditions, even in the presence of DFOB (data not shown). We determined the sequence of the first 10 N-terminal amino acids belonging to the 76.7 kDa IROMP AATERPTQTL. This sequence was consistent with the N-terminal region encoded by *desA*. These results indicate that a 76.7 kDa IROMP is induced by the presence of DFOB under -Fe conditions to serve as the receptor for FOB.

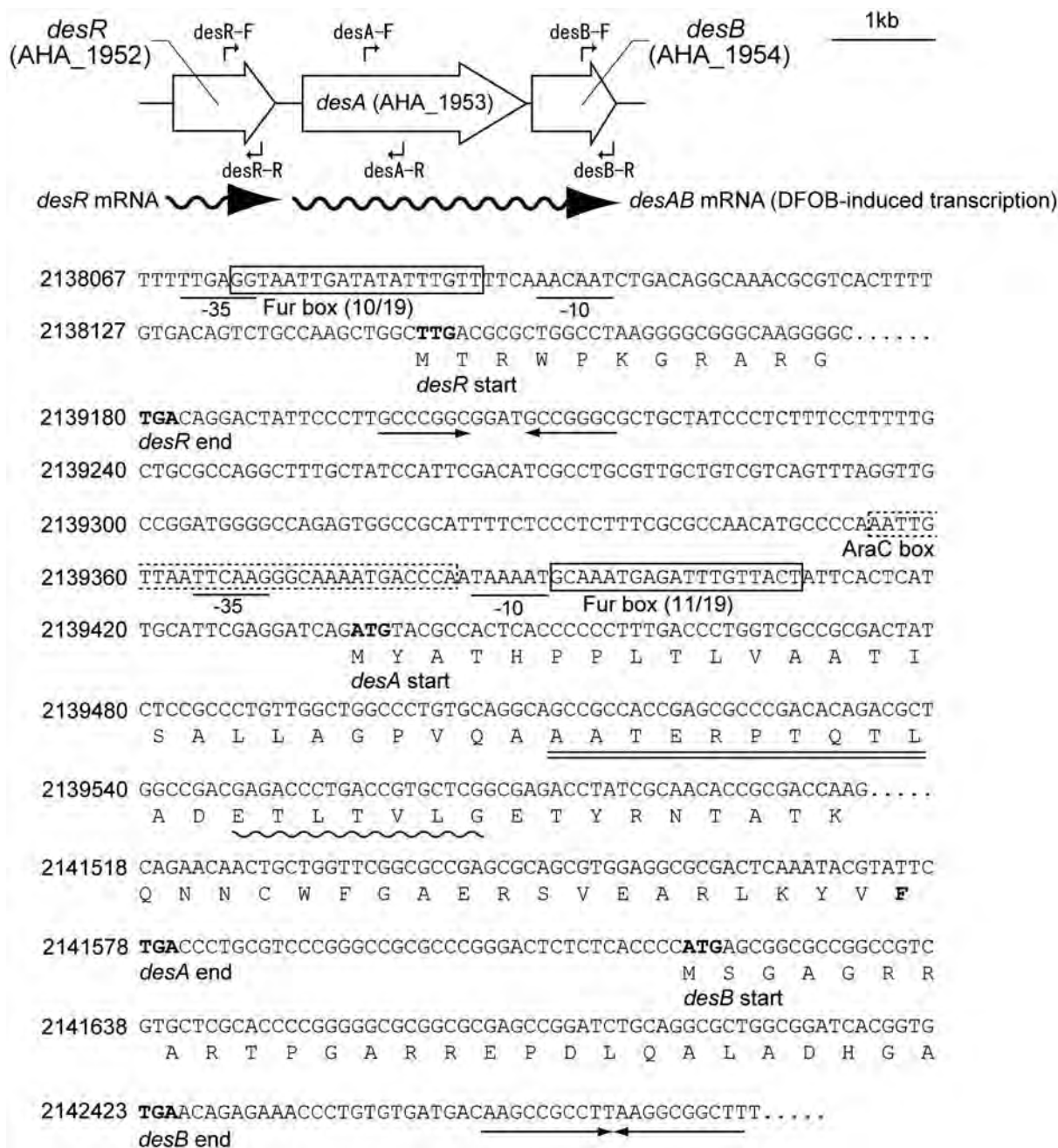


Fig. 2. Genetic map and the partial nucleotide and deduced amino acid sequences of the *desRAB* region.

Notes: (A) The gene nomenclature annotated in the *A. hydrophila* ATCC 7966^T genome sequence database¹⁰⁾ and the primers used for RT-PCR are illustrated. The wavy lines with arrowheads indicate the RNA messages. (B) The putative Fur boxes and AraC box are boxed with solid and dashed lines, respectively. The putative promoter sequences are labeled with -10 and -35. The predicted amino acid sequence of *desA* is double-underlined. This sequence is in accordance with the N-terminal amino acid sequence determined for the mature DesA. The putative TonB box sequence and the highly conserved C-terminal F residue in DesA are indicated with a wavy line and a bold letter, respectively. The terminator signal is indicated by converging arrows. Nucleotide numbers correspond to nucleotide sequence positions in the *A. hydrophila* Kyoto Encyclopedia of Genes and Genomes Database (http://www.genome.jp/kegg-bin/show_organism?org=aha).

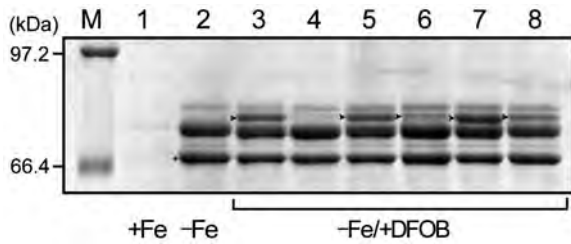


Fig. 3. Detection of DesA in *A. hydrophila* by SDS-PAGE. Notes: *A. hydrophila* ATCC 7966^T was grown in iron-replete (+Fe), -Fe, and -Fe/+DFOB media for 12 h. $\Delta desA$, $\Delta desR$, and their complementing strains were grown in -Fe/+DFOB media for 12 h. $\Delta entA\Delta desR/pRK415$ was also grown under the same conditions. SDS-PAGE was carried out by using a 7.5% polyacrylamide running gel (130 mm). The resulting gel was stained with Coomassie Brilliant Blue R-250. The amount of protein loaded in each lane was 25 μ g. Only the relevant part of the SDS-PAGE gel is shown. Arrowheads in lanes 3, 5, 6, 7, and 8 indicate DesA. Lanes 1, 2, and 3, *A. hydrophila* ATCC 7966^T; lanes 4, $\Delta desA$; lane 5, $\Delta desA/pRK415-desA$; lane 6, $\Delta desR$; lane 7, $\Delta desR/pRK415-desR$; lane 8, $\Delta entA\Delta desR$; and lane M, molecular mass marker proteins. *, ferric enterobactin receptor (IrgA).¹⁶⁾

The desA and desB genes constitute a DFOB-induced operon

The consecutive location of *desA* and *desB* in the same orientation, and the single set of putative promoter elements and Rho-independent transcription terminator suggest that the two genes are transcriptionally linked (Fig. 2(B)). To determine whether *desA* and *desB* are arranged in an operon, RT-PCR was carried out. cDNA was generated from total RNA collected

from cells grown in +Fe, -Fe, and -Fe/+DFOB media by using a primer complementary to the internal sequence of *desB* (Fig. 2(A)). The *desA* and *desB* amplicons from the cells grown in -Fe/+DFOB medium were of the expected size and had similar intensities (Fig. 4), indicating that a polycistronic mRNA, composed of *desA* and *desB*, was expressed in response to DFOB under -Fe conditions (Fig. 2(A)). As expected, *desR* was expressed as a monocistronic message under -Fe conditions, but was not induced in the presence of DFOB (Fig. 4). These data are consistent with the existence of a putative Fur box and a putative Rho-independent transcriptional terminator for *desR* in the intergenic region between *desR* and *desA* (Fig. 2(B)).

Features of des cluster genes and their protein products in A. hydrophila

The partial nucleotide sequences of the three *des* genes and their deduced amino acid sequences are shown in Fig. 2(B). Based on an *in silico* analysis, *desR* and *desA* promoters were shown to contain putative Fur boxes sharing 10/19 and 11/19 nucleotide matches, respectively, to the consensus Fur box of *E. coli*.³⁰⁾ To unequivocally determine the functions of the Fur boxes, FURTA was carried out. The promoter regions of *desR* and *desA*, including the potential Fur boxes, were cloned into the FURTA indicator strain *E. coli* H1717.²⁰⁾ Both of the cloned promoter regions showed a typical FURTA-positive phenotype as evidenced by the presence of Lac⁺ colonies on

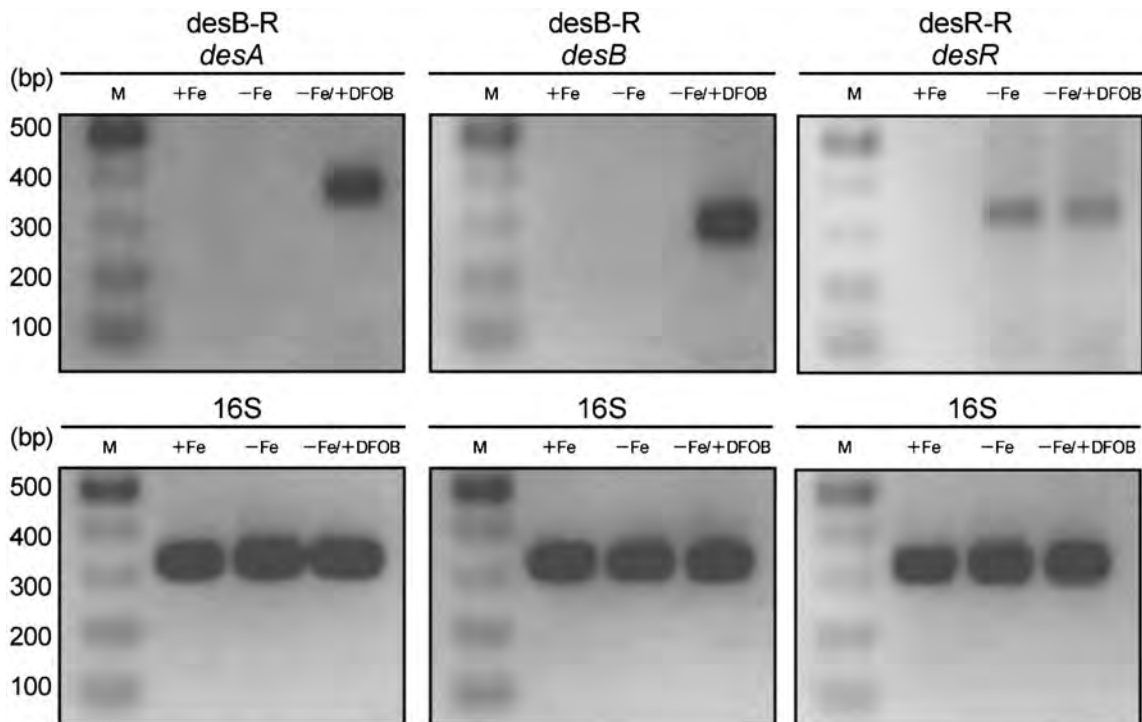


Fig. 4. Confirmation of *desA* and *desB* as a DFOB-induced operon by RT-PCR.

Notes: Total RNA was isolated from *A. hydrophila* ATCC 7966^T cells grown in +Fe, -Fe, and -Fe/+DFOB media and was used for RT-PCR analysis. The primers desR-R and desB-R used for the preparation of cDNA are indicated in Fig. 2(A). PCR was carried out under the conditions described in the Materials and Methods and the amplicons were analyzed by agarose gel electrophoresis. The primers used for PCR are also indicated in Fig. 2(A). The predicted sizes of the amplicons derived from the representative genes are as follows: *desA*, 376 bp; *desB*, 304 bp; and *desR*, 345 bp. As an internal control, a 333 bp fragment of the 16S rRNA gene was included. Lane M, molecular size markers.

MacConkey agar plates (data not shown), indicating that the cloned regions harbor the binding sites of the *E. coli* Fur protein.

The molecular mass of the mature DesA protein was estimated to be 76,756 Da, consistent with the 76.7 kDa mass estimated by the electrophoretic mobility on SDS-PAGE (Fig. 3). These data indicated that the N-terminal 25 amino acid residues of the premature DesA are indeed excluded as a signal peptide. Near its N terminus, DesA contains a putative TonB box sequence (₃₈ETLTVLG₄₄; highly conserved residues are underlined) (Fig. 2(B)).^{31,32} In addition, DesA possesses a C-terminal phenylalanine residue characteristic of TonB-dependent siderophore receptors.³³ Members of the AraC-like family have been described as positive transcriptional regulators.³⁴ Therefore, we compared the promoter sequences of *desA* and *desR* to the PRODORIC database by using the Virtual Footprint promoter analysis software. This software has been used to predict the existence of a putative AraC-type regulator binding site in the *V. anguillarum fvtA* gene promoter.³⁵ A putative AraC-type regulator binding site (AraC box; AATTGTTAATTCAAGGGCAAATGACCCA) was identified in the promoter of *desA*, overlapping with the -35 element (Fig. 2(B)), but was not found in the promoter of *desR*. However, it remains to be determined whether the predicted AraC box is functional and directly binds DesR. Using a homology search, we revealed that a putative helix-turn-helix DNA binding motif is present in the N-terminal portion of DesR. Because the majority of the proteins belonging to the AraC family have the helix-turn-helix DNA-binding motifs at the C-terminal portion,³⁴ this finding suggests that DesR belongs to a discrete subset of AraC family regulators, which includes Rob from *E. coli*.³⁶ Similar to Rob, the C-terminal segment of DesR is likely involved in binding with the co-activator, which is presumably FOB rather than DFOB. DesB was also found to contain a conserved Cys-Cys-Xaa₁₀-Cys-Xaa₂-Cys motif containing four consensus cysteine residues (underlined) in its C-terminal domain, as part of a 2Fe-2S cluster.³⁷ These data suggest that DesB exerts a reductase activity on Fe³⁺ bound to DFOB.

Phenotypic analysis and complementation of the *desA* and *desR* deletion mutants

To clarify the role of *A. hydrophila* DesA in DFOB utilization, we generated the $\Delta entA\Delta desA$ deletion mutant from $\Delta entA$.¹⁶ In contrast to $\Delta entA$, $\Delta entA\Delta desA$ failed to grow in $-Fe$ medium despite the presence of DFOB (Fig. 1). In accordance with this finding, no protein band corresponding to DesA was detected for $\Delta desA$ (Fig. 3, lane 4). The complementing strain, $\Delta entA\Delta desA/pRK415-desA$, showed restored growth to a level similar to that of $\Delta entA$ (Fig. 1) and considerable expression of DesA (Fig. 3, lane 5). These results demonstrate that DesA is the outer membrane receptor for FOB. In $-Fe$ medium, growth of $\Delta desA$ (able to synthesize amonabactin) was indistinguishable from that of wild-type *A. hydrophila* ATCC 7966^T (data not shown), indicating that DesA does not serve as a receptor for ferric amonabactin. DFOB-induced DesA expression was considerably lower in $\Delta desR$

(Fig. 3, lane 6). The production of DesA was restored in the complementing strain $\Delta desR/pRK415-desR$ (Fig. 3, lane 7). Taken together, these results suggest that DesR under iron-limiting conditions and in the presence of DFOB is involved in the induction of DesA expression. As shown in Fig. 1, $\Delta entA\Delta desR/pRK415$ showed reduced, but moderate growth in $-Fe/+DFOB$ medium. The growth of $\Delta entA\Delta desR/pRK415$ correlated with the expression of DesA (Fig. 3, lane 8). The more prominent expression of DesA in $\Delta entA\Delta desR$ compared to $\Delta desR$ may be attributed to the background of *entA* deletion. We speculate that an alternative or redundant activator able to recognize FOB as a co-activator enhances DesA expression and allows cells to overcome severe iron deficiency. Although our data suggest that DesB is a Fe³⁺ reductase for FOB, DFOB caused no significant difference in growth promotion between $\Delta entA\Delta desB$ and $\Delta entA$ (data not shown). This does not signify that *desB* is not involved in DFOB utilization. Instead, we speculate

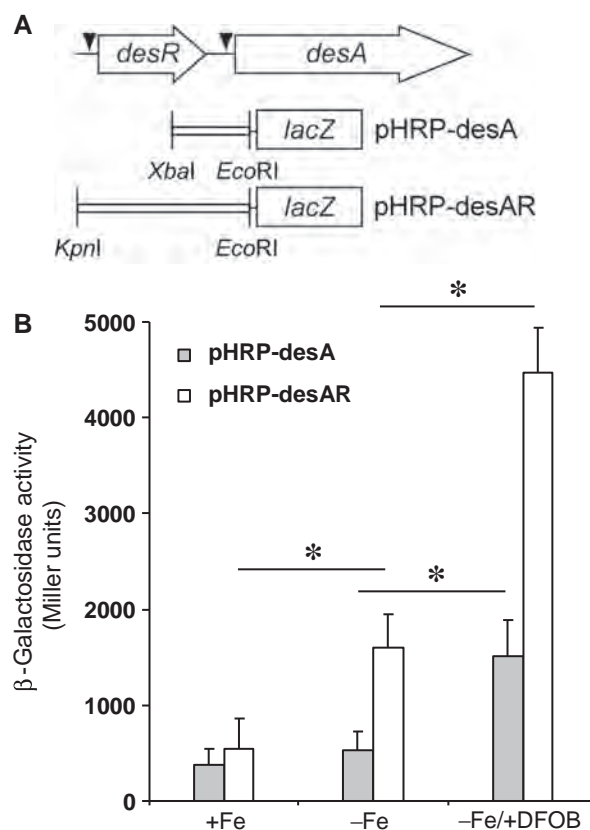


Fig. 5. Effects of *desR* and DFOB on the expression of *lacZ* fusions.

Notes: (A) Schematic representation of *desA* and *desR*, and the plasmids pHRP-*desA* and pHRP-*desAR* that were constructed for the β -galactosidase reporter assay. The restriction enzyme sites used to insert the DNA fragments into pHRP309 are shown. An arrowhead indicates a putative Fur box. (B) The transcriptional levels of *desA-lacZ* fusions as measured by β -galactosidase activities. *A. hydrophila* $\Delta desR\Delta lacZ$ carrying pHRP-*desA* and pHRP-*desAR* were grown in +Fe, -Fe, and -Fe/+DFOB media, and the β -galactosidase activities of their cell lysates were then assayed. $\Delta desR\Delta lacZ/pHRP309$ (empty plasmid) was grown in the same media. Its enzyme activity was subtracted from that obtained for strains carrying pHRP-*desA* and pHRP-*desR*. The mean β -galactosidase activities \pm SD ($n=3$) are shown in Miller units. p values were estimated using the Student's t -test (* $p < 0.05$).

that an alternative or redundant reductase present in this species can compensate for the deletion of *desB*.

Assessment of the function of DesR by lacZ transcriptional fusions

A putative AraC box found in the promoter region of *desA* suggests that *desA* expression is positively regulated by DesR. To define the functions of DesR and Fur boxes in *desR* and *desA* expression, β -galactosidase reporter assays were performed in *A. hydrophila* $\Delta desR\Delta lacZ$ grown in $-Fe$ and $-Fe/+DFOB$ media. *A. hydrophila* $\Delta desR\Delta lacZ$ carried the following plasmids: pHRP-*desA* (encoding a *lacZ* fused to the promoter region of *desA*), and pHRP-*desAR* (encoding a *lacZ* fused to the promoter regions of *desA* and *desR* in addition to *desR*) (Fig. 5(A)). As shown in Fig. 5(B), there was no significant difference in β -galactosidase activity in $\Delta desR\Delta lacZ$ /pHRP-*desA* cells grown in $-Fe$ and $+Fe$ media, suggesting that the promoter activity of *desA* might be very weak. When grown in $-Fe/+DFOB$ medium, $\Delta desR\Delta lacZ$ /pHRP-*desA* showed a significant increase in enzyme activity. This implied a possible contribution of an activator protein in addition to FOB. On the other hand, $\Delta desR\Delta lacZ$ /pHRP-*desAR* had a more pronounced enzyme activity in $-Fe$ medium than in $+Fe$ medium. This may be due to the potential action of apo-DesR (DesR not bound with FOB) that is expressed by the cloned *desR*, because DFOB was not present in the medium. Furthermore, the enzyme activity of $\Delta desR\Delta lacZ$ /pHRP-*desAR* grown in $-Fe/+DFOB$ medium increased approximately three times compared with that grown in $-Fe$ medium. This demonstrates that the *lacZ* fusion in $\Delta desR\Delta lacZ$ /pHRP-*desAR* is activated by both the plasmid-derived DesR and the presence of DFOB.

Analysis of the desR and desA transcriptional levels by RT-qPCR

RT-qPCR was performed to measure the transcript levels of *desR* and *desA* in wild-type *A. hydrophila*

ATCC 7966^T. *desR* transcript levels were increased by approximately threefold in *A. hydrophila* ATCC 7966^T grown in both $-Fe$ and $-Fe/+DFOB$ media compared to those grown in $+Fe$ medium (Fig. 6(A)). These data indicate that *desR* transcription is dependent on iron limitation, but is not affected by the presence of DFOB. The transcript levels of *desA* exhibited a pattern different from that of *desR* (Fig. 6(B)). Pronounced levels of *desA* transcript were observed in the wild-type cells grown in $-Fe/+DFOB$ medium, indicating that *desA* is highly inducible in the presence of DFOB under $-Fe$ conditions. RT-qPCR was also performed on $\Delta desR$ grown in $+Fe$, $-Fe$, and $-Fe/+DFOB$ media. When grown in $-Fe/+DFOB$ medium, $\Delta desR$ showed a drastic reduction in *desA* transcription. Thus, these results indicate that the transcriptional activation of *desA* under $-Fe$ conditions is mediated through DesR and the co-activator DFOB (FOB). Notably, the wild-type strain showed an approximate sixfold increase in *desA* transcription when grown in $-Fe$ medium vs. in $+Fe$ medium; however, there was no detectable DesA protein (Fig. 3, lane 2). Therefore, low levels of DesA may play a role in the initial uptake of FOB prior to induction of *desA* expression. Moreover, *desA* transcription was more significantly activated when $\Delta desR$ was grown in $-Fe/+DFOB$ medium than in $-Fe$ medium; this may be explained by the existence of an alternative or redundant DFOB-dependent activator. However, this potential alternative activator might be much less active than DesR. These data are consistent with the results for mutants carrying a *desR* deletion (Fig. 1; Fig. 3, lanes 6 and 8; and Fig. 5(B)).

TonB specificity of DesA

Previously, the presence of three TonB clusters, TonB1 (AHA_1987-1985), TonB2 (AHA_4251-4248), and TonB3 (AHA_3435-3438), was identified in *A. hydrophila* ATCC 7966^T.¹⁶⁾ To determine which TonB protein is involved in DesA-mediated transport of FOB, we generated a set of *tonB* double deletion mutants derived from $\Delta entA$. The growth of the

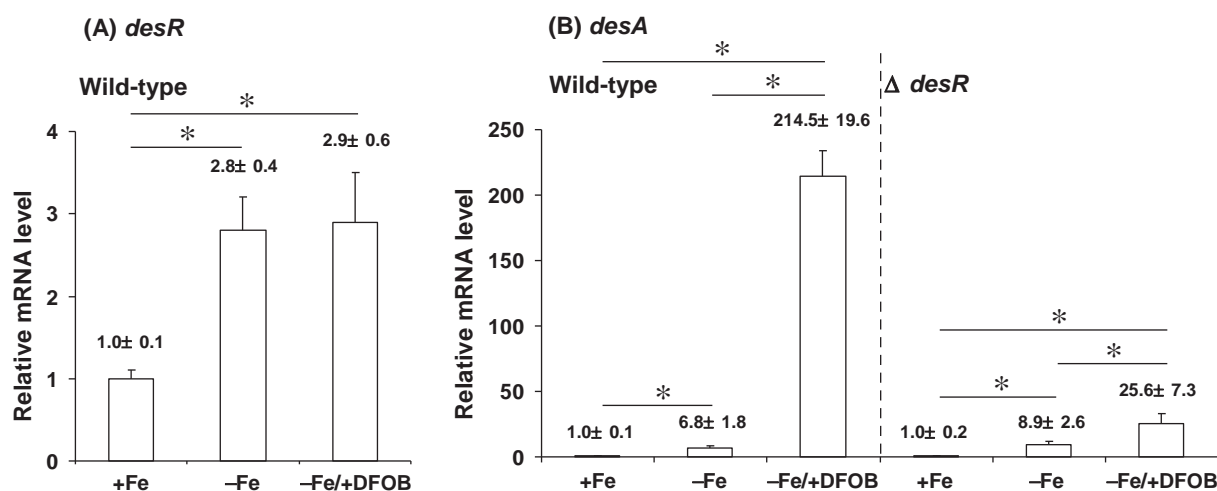


Fig. 6. RT-qPCR analysis of *desA* and *desR* transcript levels in *A. hydrophila* ATCC 7966^T and $\Delta desR$.

Notes: The levels of *desA* and *desR* mRNAs were assessed by RT-qPCR for the total RNA samples extracted from wild-type *A. hydrophila* ATCC 7966^T and $\Delta desR$ grown in $+Fe$, $-Fe$, and $-Fe/+DFOB$ media. mRNA levels of *desR* and *desA* were normalized to 16S rRNA, and bars represent mean values \pm SD ($n = 5$). p values were estimated using the Student's t -test ($*p < 0.05$).

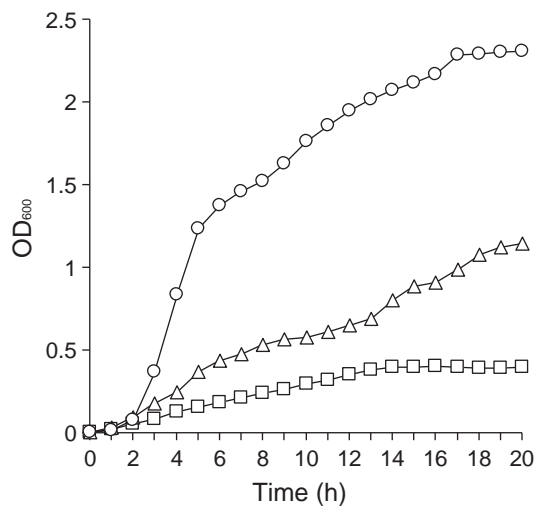


Fig. 7. Determination of TonB specificity of DesA by performing growth assays of *tonB* double mutants.

Notes: $\Delta entA\Delta tonB1\Delta tonB3$ (circle), $\Delta entA\Delta tonB2\Delta tonB3$ (triangle), and $\Delta entA\Delta tonB1\Delta tonB2$ (square) were grown in the $-Fe/+DFOB$. OD₆₀₀ was measured every hour for 20 h. A representative example from three independent experiments is shown.

deletion mutants was then measured in $-Fe/+DFOB$ medium (Fig. 7). $\Delta entA\Delta tonB1\Delta tonB3$ cells grew effectively, whereas $\Delta entA\Delta tonB2\Delta tonB3$ showed moderate growth and $\Delta entA\Delta tonB1\Delta tonB2$ failed to grow. These results indicate that TonB2, and to a lesser extent, TonB1 supplied energy necessary for the DesA-mediated transport of FOB into the periplasmic space. TonB3, on the other hand, is not associated with this process. Therefore, DesA is distinct from the *A. hydrophila* ferric enterobactin receptor, IrgA, which is powered exclusively by the TonB2 system.¹⁶⁾

In conclusion, we identified the *desA* and *desR* genes in *A. hydrophila* ATCC 7966^T, which encode the outer membrane receptor for FOB and the AraC-type transcriptional regulator of *desA*, respectively. The function of *desA* was confirmed by growth assays of the *desA* deletion mutant and its complementing strain. Moreover, the IROMP expression profile and RT-qPCR analysis of the *desR* deletion mutant showed that DesR is responsible for the induction of *desA* under $-Fe$ conditions. This occurs in the presence of DFOB, which serves both as a xenosiderophore and as a co-activator of its own IROMP receptor expression. Meanwhile, we found that unlike *V. furnissii*, *A. hydrophila* possesses *desB* which constitutes an operon with *desA*. Since DesB is homologous to *E. coli* FhuF that has been proposed to be involved in the reduction of ferric iron in cytoplasmic FOB,³⁷⁾ an enzymatic study of DesB would give a clue for a better understanding of the subsequent utilization of FOB-bound iron in this species.

Bacteria typically express genes at considerable levels only when the encoded functions are beneficial for them to save energy. Considering that *A. hydrophila* commonly inhabits soil and freshwater, utilization of DFOB for iron acquisition may represent an important strategy that the bacterium has adopted to compete with neighboring micro-organisms for survival and proliferation within its various niches. In fact, different

microbes that produce hydroxamate-type siderophores, including ferrioxamine species, are widely distributed in aquatic and terrestrial environments.^{38–42)} Future studies are required to characterize the inner membrane FOB transport system and elucidate the molecular mechanism by which *desA* transcription is induced by DesR in the presence of DFOB.

Acknowledgment

We thank Ms Y. Ido for assistance in the experiments.

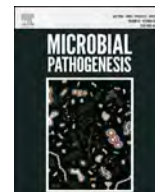
Funding

This study was supported by a Grant-in-Aid for Young Scientists (B) from the Ministry of Education, Culture, Sports, Science, and Technology of Japan [20790124 to TF].

References

- [1] Ratledge C, Dover LG. Iron metabolism in pathogenic bacteria. *Annu. Rev. Microbiol.* 2000;54:881–941.
- [2] Miethke M, Marahiel MA. Siderophore-based iron acquisition and pathogen control. *Microbiol. Mol. Biol. Rev.* 2007;71:413–451.
- [3] Krewulak KD, Vogel HJ. Structural biology of bacterial iron uptake. *Biochim. Biophys. Acta.* 2008;1778:1781–1804.
- [4] Escolar L, Pérez-Martin J, de Lorenzo V. Opening the iron box: transcriptional metalloregulation by the Fur protein. *J. Bacteriol.* 1991;181:6223–6229.
- [5] Carpenter BM, Whitmire JM, Merrell DS. This is not your mother's repressor: the complex role of Fur in pathogenesis. *Infect. Immun.* 2009;77:2590–2601.
- [6] Heinrichs DE, Poole K. Cloning and sequence analysis of a gene (*pchR*) encoding an AraC family activator of pyochelin and ferripyochelin receptor synthesis in *Pseudomonas aeruginosa*. *J. Bacteriol.* 1993;175:5882–5889.
- [7] Fetherston JD, Bearden SW, Perry RD. YbtA, an AraC-type regulator of the *Yersinia pestis* pesticin/yersiniabactin receptor. *Mol. Microbiol.* 1996;22:315–325.
- [8] Beaumont FC, Kang HY, Brickman TJ, Armstrong SK. Identification and characterization of *alcR*, a gene encoding an AraC-like regulator of alcaligin siderophore biosynthesis and transport in *Bordetella pertussis* and *Bordetella bronchiseptica*. *J. Bacteriol.* 1998;180:862–870.
- [9] Pradel E, Guiso N, Loch C. Identification of AlcR, an AraC-type regulator of alcaligin siderophore synthesis in *Bordetella bronchiseptica* and *Bordetella pertussis*. *J. Bacteriol.* 1998;180:871–880.
- [10] Tanabe T, Takata N, Naka A, Moon Y-H, Nakao H, Inoue Y, Narimatsu S, Yamamoto S. Identification of an AraC-like regulator gene required for induction of the 78 kDa ferrioxamine B receptor in *Vibrio vulnificus*. *FEMS Microbiol. Lett.* 2005;249:309–314.
- [11] Tanabe T, Funahashi T, Miyamoto K, Tsujibo H, Yamamoto S. Identification of genes, *desR* and *desA*, required for utilization of desferrioxamine B as a xenosiderophore in *Vibrio furnissii*. *Biol. Pharm. Bull.* 2011;34:570–574.
- [12] Semel JD, Trenholme G. *Aeromonas hydrophila* water-associated traumatic wound infections: a review. *J. Trauma Injury Infect. Crit. Care.* 1990;30:324–327.
- [13] Janda JM, Abbott SL. The genus *Aeromonas*: taxonomy, pathogenicity, and infection. *Clin. Microbiol. Rev.* 2010;23:35–73.
- [14] Barghouthi S, Young R, Olson MO, Arceneaux JE, Clem LW, Byers BR. Amonabactin, a novel tryptophan- or phenylalanine-containing phenolate siderophore in *Aeromonas hydrophila*. *J. Bacteriol.* 1989;171:1811–1816.

- [15] Telford JR, Raymond KN. Amonabactin: a family of novel siderophores from a pathogenic bacterium. *J. Biol. Inorg. Chem.* 1997;2:750–761.
- [16] Funahashi T, Tanabe T, Miyamoto K, Tsujibo H, Maki J, Yamamoto S. *Biosci. Biotechnol. Biochem.* 2013;77:353–360.
- [17] Sambrook J, Fritsch EF, Maniatis T. *Molecular cloning, a laboratory manual.* Cold Spring Harbor (NY): Cold Spring Harbor Laboratory Press; 1989.
- [18] Seshadri R, Joseph SW, Chopra AK, Sha J, Shaw J, Graf J, Haft D, Wu M, Ren Q, Rosovitz MJ, Madupu R, Tallon L, Kim M, Jin S, Vuong H, Stine OC, Ali A, Horneman AJ, Heidelberg JF. Genome sequence of *Aeromonas hydrophila* ATCC 7966^T: jack of all trades. *J. Bacteriol.* 2006;188:8272–8282.
- [19] Yamamoto S, Akiyama T, Okujo N, Matsu-ura S, Shinoda S. Demonstration of a ferric vibrioferrin-binding protein in the outer membrane of *Vibrio parahaemolyticus*. *Microbiol. Immunol.* 1995;39:759–766.
- [20] Stojiljkovic I, Bäumlner AJ, Hantke K. Fur regulon in Gram-negative bacteria. *J. Mol. Biol.* 1994;236:531–545.
- [21] Kuroda T, Mizushima T, Tsuchiya T. Physiological roles of three Na⁺/H⁺ antiporters in the halophilic bacterium *Vibrio parahaemolyticus*. *Microbiol. Immunol.* 2005;49:711–719.
- [22] Heckman KL, Pease LR. Gene splicing and mutagenesis by PCR-driven overlap extension. *Nat. Protoc.* 2007;2:924–932.
- [23] Tanabe T, Funahashi T, Okajima N, Nakao H, Takeuchi Y, Miyamoto K, Tsujibo H, Yamamoto S. The *Vibrio parahaemolyticus pvuA1* gene (formerly termed *psuA*) encodes a second ferric vibrioferrin receptor that requires *tonB2*. *FEMS Microbiol. Lett.* 2011;324:73–79.
- [24] Demarre G, Guérout AM, Matsumoto-Mashimo C, Rowe-Magnus DA, Marlière P, Mazel D. A new family of mobilizable suicide plasmids based on broad host range R388 plasmid (IncW) and RP4 plasmid (IncPa) conjugative machineries and their cognate *Escherichia coli* host strains. *Res. Microbiol.* 2005;156:245–255.
- [25] Keen NT, Tamaki S, Kobayashi D, Trollinger D. Improved broad-host-range plasmids for DNA cloning in Gram-negative bacteria. *Gene.* 1988;70:191–197.
- [26] Parales RE, Harwood CS. Construction and use of a new broad-host-range *lacZ* transcriptional fusion vector, pHRP309, for Gram⁻ bacteria. *Gene.* 1993;133:23–30.
- [27] Miller JH. *Experiments in molecular genetics.* Cold Spring Harbor (NY): Cold Spring Harbor Laboratory Press; 1972. p. 352–355.
- [28] Matzanke BF, Anemüller S, Schünemann V, Trautwein AX, Hantke K. FhuF, part of a siderophore-reductase system. *Biochemistry.* 2004;43:1386–1392.
- [29] Lux TM, Lee R, Love J. Complete genome sequence of a free-living *Vibrio furnissii* sp. nov. strain (NCTC 11218). *J. Bacteriol.* 2011;193:1487–1488.
- [30] de Lorenzo V, Wee S, Herrero M, Neilands JB. Operator sequences of the aerobactin operon of plasmid ColV-K30 binding the ferric uptake regulation (*fur*) repressor. *J. Bacteriol.* 1987;169:2624–2630.
- [31] Postle K, Larsen RA. TonB-dependent energy transduction between outer and cytoplasmic membranes. *Biometals.* 2007;20:453–465.
- [32] Sean Peacock R, Weljie AM, Peter Howard S, Price FD, Vogel HJ. The solution structure of the C-terminal domain of TonB and interaction studies with TonB box peptides. *J. Mol. Biol.* 2005;345:1185–1197.
- [33] Steuyvé M, Moons M, Tommassen J. Carboxy-terminal phenylalanine is essential for the correct assembly of a bacterial outer membrane protein. *J. Mol. Biol.* 1991;218:141–148.
- [34] Gallegos MT, Schleif R, Bairoch A, Hofmann K, Ramos JL. AraC/XylS family of transcriptional regulators. *Microbiol. Mol. Biol. Rev.* 1997;61:393–410.
- [35] Balado M, Osorio CR, Lemos ML. Biosynthetic and regulatory elements involved in the production of the siderophore vanchrobactin in *Vibrio anguillarum*. *Microbiology.* 2008;154:1400–1413.
- [36] Kwon HJ, Bennik MHJ, Demple B, Ellenberger T. Crystal structure of the *Escherichia coli* Rob transcription factor in complex with DNA. *Nat. Struct. Biol.* 2000;7:424–430.
- [37] Muller K, Matzanke BF, Schunemann V, Trautwein AX, Hantke K. FhuF, an iron-regulated protein of *Escherichia coli* with a new type of [2Fe–2S] center. *Eur. J. Biochem.* 1998;258:1001–1008.
- [38] Tortell PD, Maldonado MT, Granger J, Price NM. Marine bacteria and biogeochemical cycling of iron in the oceans. *FEMS Microbiol. Ecol.* 1999;29:1–11.
- [39] Winkelmann G. Ecology of siderophores. In: Crosa JH, Mey AR, Payne SM, editors. *Iron transport in bacteria.* Washington (DC): ASM Press; 2004. p. 437–450.
- [40] Essén SA, Bylund D, Holmström SJ, Moberg M, Lundström US. Quantification of hydroxamate siderophores in soil solutions of podzolic soil profiles in Sweden. *BioMetals.* 2006;19:269–282.
- [41] Mawji E, Gledhill M, Milton JA, Tarran GA, Ussher S, Thompson A, Wolff GA, Worsfold PJ, Achterberg EP. Hydroxamate siderophores: occurrence and importance in the Atlantic Ocean. *Environ. Sci. Technol.* 2008;42:8675–8680.
- [42] Gledhill M, Buck KN. The organic complexation of iron in the marine environment. *Front. Microbiol.* 2012;3:1–17.



The RND protein is involved in the vulnibactin export system in *Vibrio vulnificus* M2799



Hiroaki Kawano^a, Katsushiro Miyamoto^a, Megumi Yasunobe^a, Masahiro Murata^a, Tomoka Myojin^a, Takahiro Tsuchiya^a, Tomotaka Tanabe^b, Tatsuya Funahashi^b, Takaji Sato^c, Takashi Azuma^c, Yoshiki Mino^c, Hiroshi Tsujibo^{a,*}

^a Department of Microbiology, Osaka University of Pharmaceutical Sciences, 4-20-1 Nasahara, Takatsuki, Osaka 569-1094, Japan

^b Laboratory of Hygienic Chemistry, College of Pharmaceutical Sciences, Matsuyama University, 4-2 Bunkyo-cho, Matsuyama, Ehime 790-8578, Japan

^c Department of Analytical Chemistry, Osaka University of Pharmaceutical Sciences, 4-20-1 Nasahara, Takatsuki, Osaka 569-1094, Japan

ARTICLE INFO

Article history:

Received 8 April 2014

Received in revised form

28 August 2014

Accepted 1 September 2014

Available online 6 September 2014

Keywords:

Vibrio vulnificus

Vulnibactin secretion

RND-type efflux system

ABSTRACT

Vibrio vulnificus, an opportunistic marine bacterium that causes a serious, often fatal, infection in humans, requires iron for its pathogenesis. This bacterium exports vulnibactin for iron acquisition from the environment. The mechanisms of vulnibactin biosynthesis and ferric-vulnibactin uptake systems have recently been reported, while the vulnibactin export system has not been reported. Mutant growth under low-iron concentration conditions and a bioassay of the culture supernatant indicate that the VV1_0612 protein plays a crucial role in the vulnibactin secretion as a component of the resistance-nodulation-division (RND)-type efflux system in *V. vulnificus* M2799. To identify which RND protein(s) together with VV1_0612 ToIC constituted the RND efflux system for vulnibactin secretion, deletion mutants of 11 RND protein-encoding genes were constructed. The growth inhibition of a multiple mutant ($\Delta 11$) of the RND protein-encoding genes was observed 6 h after the beginning of the culture. Furthermore, $\Delta VV1_{1681}$ exhibited a growth curve that was similar to that of $\Delta 11$, while the multiple mutant except $\Delta VV1_{1681}$ showed the same growth as the wild-type strain. These results indicate that the VV1_1681 protein is involved in the vulnibactin export system of *V. vulnificus* M2799. This is the first genetic evidence that vulnibactin is secreted through the RND-type efflux systems in *V. vulnificus*.

© 2014 Elsevier Ltd. All rights reserved.

1. Introduction

Vibrio vulnificus is a gram-negative halophilic marine pathogen associated with human diseases such as septicemia and serious wound infections [1,2]. Septicemia is often acquired by eating raw oysters or shellfish, and wound infections are associated with the exposure of wounds to seawater. Primary septicemia is often associated with patients who have diseases predisposing them to iron overload, such as cirrhosis, hemochromatosis, and alcoholism,

or who are immunocompromised [3]. To date, several potential virulence factors of *V. vulnificus*, such as metalloprotease [4,5], hemolysin [6], RTX toxin [7–9], capsular polysaccharide [10,11], and iron acquisition factors including a siderophore [12] have been identified. Among the above-mentioned factors, the iron acquisition system is a well-known crucial virulence factor [12]. In our previous report, we showed that *V. vulnificus* M2799, a clinical isolate, possesses 100-fold higher lethality in mice than an environmental isolate, strain JCM3731 [13]. The cytotoxicity of *V. vulnificus* M2799 toward various cultured cells was high compared with strain JCM3731 [13].

Iron is an essential micronutrient for almost all life forms, and its acquisition from the environment is vital to bacteria [14]. At physiological pH, iron is rapidly oxidized to the ferric state [Fe(III)] as an insoluble hydroxide. Within human tissues, most iron is tightly bound to high-affinity iron-binding proteins, such as hemoglobin, transferrin, lactoferrin, and ferritin [15]. Because iron availability is limited in the human body, pathogenic bacteria possess intricate mechanisms to scavenge iron from the host.

Abbreviations: RND, resistance-nodulation-division; DHBA, 2,3-dihydroxybenzoic acid; ICS, isochorismate synthase; VuuB, vulnibactin utilization protein; FatB, a periplasmic ferric-vulnibactin-binding protein; VuuA, ferric-vulnibactin receptor protein; VatD, a periplasmic ferric-aerobactin-binding protein; MFP, membrane fusion protein; LB, Luria-Bertani; HI, heart infusion containing 2% NaCl; EDDA, ethylenediamine-di (*o*-hydroxyphenylacetic acid); Cm, chloramphenicol; Tet, tetracycline; RT-PCR, reverse transcription-PCR; ABC, ATP-binding cassette; MFS, major facilitator superfamily; Fur, ferric uptake regulator.

* Corresponding author. Tel./fax: +81 72 690 1057.

E-mail address: tsujibo@gly.oups.ac.jp (H. Tsujibo).

Table 1
Strains and plasmids used in this study.

Strain or plasmid	Description	Reference
Bacterial strains		
<i>V. vulnificus</i> M2799	Clinical isolate; virulent	–
ΔV2_0029	M2799ΔV2_0029	This study
ΔV1_0612	M2799ΔV1_0612	This study
Δics	M2799Δics (ΔV2_0835)	[20]
ΔV2_1007	M2799ΔV2_1007	This study
ΔV1_1079	M2799ΔV1_1079	This study
ΔV1_1681	M2799ΔV1_1681	This study
ΔV1_3156	M2799ΔV1_3156	This study
ΔV2_0029	M2799ΔV2_0029	This study
ΔV2_0195	M2799ΔV2_0195	This study
ΔV2_0340	M2799ΔV2_0340	This study
ΔV2_1320	M2799ΔV2_1320	This study
Δ2	ΔV2_0340, ΔV2_0529	This study
Δ3	ΔV2_0340, ΔV2_0529, ΔV2_1320	This study
Δ4	ΔV2_0340, ΔV2_0529, ΔV2_1320, ΔV2_0195	This study
Δ5	ΔV2_0340, ΔV2_0529, ΔV2_1320, ΔV2_0195, ΔV2_0928	This study
Δ6	ΔV2_0340, ΔV2_0529, ΔV2_1320, ΔV2_0195, ΔV2_0928, ΔV2_0029	This study
Δ7	ΔV2_0340, ΔV2_0529, ΔV2_1320, ΔV2_0195, ΔV2_0928, ΔV2_0029, ΔV1_1079	This study
Δ8	ΔV2_0340, ΔV2_0529, ΔV2_1320, ΔV2_0195, ΔV2_0928, ΔV2_0029, ΔV1_1079, ΔV1_3156	This study
Δ9	ΔV2_0340, ΔV2_0529, ΔV2_1320, ΔV2_0195, ΔV2_0928, ΔV2_0029, ΔV1_1079, ΔV1_3156, ΔV1_2874	This study
Δ10	ΔV2_0340, ΔV2_0529, ΔV2_1320, ΔV2_0195, ΔV2_0928, ΔV2_0029, ΔV1_1079, ΔV1_3156, ΔV1_2874, ΔV2_0852	This study
Δ11	ΔV2_0340, ΔV2_0529, ΔV2_1320, ΔV2_0195, ΔV2_0928, ΔV2_0029, ΔV1_1079, ΔV1_3156, ΔV1_2874, ΔV2_0852, ΔV1_1681	This study
<i>E. coli</i>		
SY327λpir	<i>araD</i> Δ (<i>lac-pro</i>) <i>argE</i> (Am) <i>nalA</i> <i>recA56</i> λpirR6K	[28]
SM10λpir	<i>thi thr leu tonA lacY supE recA::RP4-2-Tc::Mu</i> λpirR6K; Km ^r ; conjugal donor	[28]
Plasmids		
Gene deletion		
pDM4	R6K <i>ori sacB</i> ; suicide vector; <i>oriT</i> of RP4; Cm ^r	[29]
pDdV1_0612	pDM4 ΔV1_0612 fragment; for marker less deletion	This study
pDdV1_1079	pDM4 ΔV1_1079 fragment; for marker less deletion	This study
pDdV1_1681	pDM4 ΔV1_1681 fragment; for marker less deletion	This study
pDdV1_2874	pDM4 ΔV1_2874 fragment; for marker less deletion	This study
pDdV1_3156	pDM4 ΔV1_3156 fragment; for marker less deletion	This study
pDdV2_0029	pDM4 ΔV1_0029 fragment; for marker less deletion	This study
pDdV2_0195	pDM4 ΔV1_0195 fragment; for marker less deletion	This study
pDdV2_0340	pDM4 ΔV1_0340 fragment; for marker less deletion	This study
pDdV2_0529	pDM4 ΔV2_0529 fragment; for marker less deletion	This study
pDdV2_0852	pDM4 ΔV2_0852 fragment; for marker less deletion	This study
pDdV2_0928	pDM4 ΔV2_0928 fragment; for marker less deletion	This study
pDdV2_1007	pDM4 ΔV2_1007 fragment; for marker less deletion	This study
pDdV2_1320	pDM4 ΔV2_1320 fragment; for marker less deletion	This study
Complementation		
pRK415	Broad-host-range plasmid; Tet ^r	[30]
pRVV1_0612	V1_0612 locus in pRK415	This study

Cm^r, chloramphenicol resistance; Km^r, kanamycin resistance; Tet^r, tetracycline resistance.

V. vulnificus sequesters iron through the biosynthesis and secretion of a low molecular weight compound called siderophore [12,16]. *V. vulnificus* M2799 produces a catechol siderophore called vulnibactin [17]. Vulnibactin consists of one residue of 2,3-dihydroxybenzoic acid (DHBA), two residues of salicylic acid, and two residues of L-threonine on a norspermidine backbone. Vulnibactin is a siderophore with a structure that is similar to that of vibriobactin from *Vibrio cholerae* [17,18], except that vulnibactin contains two salicylic acid residues plus one DHBA molecule, whereas vibriobactin contains three DHBA residues. Tan et al. suggested that salicylic acid serves as a scavenger of hydroxyl radicals and plays an important role in the virulence of *V. vulnificus* [19]. It has been reported that isochorismate synthase (ICS) and isochorismatase were essential for the biosynthesis of vulnibactin [12,20]. Furthermore, the vulnibactin-mediated iron uptake system plays an essential role in the use of transferrin-bound iron and the virulence of *V. vulnificus* in animal models [12,21].

In our previous report, we used a proteomic approach to study the differential expression of proteins from *V. vulnificus* M2799 under iron-repleted and low-iron concentration conditions during

the early-, mid-, and late-logarithmic growth phases. A total of 32, 53, and 42 iron-regulated spots were detected by two-dimensional differential gel electrophoresis in the early-, mid-, and late-logarithmic growth phases, respectively [22]. Furthermore, we constructed deletion mutants of the genes encoding the proteins involved in the vulnibactin-mediated iron uptake system, ICS, ferric-vulnibactin utilization protein (VuuB), periplasmic ferric-vulnibactin-binding protein (FatB), and ferric-vulnibactin receptor protein (VuuA). The Δics and ΔvuuA mutants were unable to grow under low-iron concentration conditions compared with the isogenic wild-type strain, indicating that the involvement of ICS in the vulnibactin biosynthesis pathway and uptake of ferric-vulnibactin through the VuuA receptor protein are essential for *V. vulnificus* M2799 growth under low-iron concentration conditions. A similar growth impairment was also observed in ΔfatB, and the growth recovery of this mutant was observed 6 h after the beginning of the culture. These results indicate that there must be other periplasmic ferric-vulnibactin-binding proteins in *V. vulnificus* M2799 that complement the defective fatB gene. Complementary growth studies confirmed that VatD protein, which functions as a

periplasmic ferric-aerobactin-binding protein, participated in the ferric-vulnibactin uptake system in the absence of FatB [20]. However, the vulnibactin export system of *V. vulnificus* remains to be clarified.

In *Escherichia coli*, TolC protein was implicated in the export of newly synthesized enterobactin siderophore across the outer membrane [23]. Resistance nodulation cell division (RND) proteins are a typical type I secretion system of gram-negative bacteria and function as a huge protein complex spanning the inner and outer membrane. The protein complex is composed of an outer membrane channel protein, a membrane fusion protein (MFP), and an RND inner membrane protein. In *E. coli*, it is known that the major multidrug RND-type efflux system is a TolC–AcrAB complex, which is composed of TolC, AcrA, and AcrB as an outer membrane channel protein, an MFP, and an RND inner membrane protein. There are seven RND proteins (AcrB, AcrD, AcrF, MdtB, MdtC, MdtF, and CusA) in *E. coli*, whereas only two outer membrane channel proteins, TolC and CusC, have been shown to be responsible for the efflux [24,25]. RND-type efflux complexes such as TolC–AcrAB transport a very broad variety of substances, including antibiotics, dyes, detergents, and heavy metal cations [26,27].

In this study, to identify the genes encoding the proteins involved in the vulnibactin export system, we constructed the mutants of genes encoding the outer membrane channel proteins and their cognate RND proteins. Growth analyses of these mutants were investigated under low-iron concentration conditions.

2. Materials and methods

2.1. Strains, plasmids, media, and growth conditions

The bacterial strains and plasmids used in this study are listed in Table 1. The competent *E. coli* SY327λpir [28] was used for the construction of recombinant plasmids. Plasmids pDM4 [29] and pRK415 [30] were used for gene deletion and complementation analysis, respectively. The recombinant plasmids were subsequently transformed into *E. coli* SM10λpir [28] possessing conjugal activity to *V. vulnificus* cells. The suicide plasmid pDM4 was kindly provided by Prof. Debra L. Milton (Department of Molecular Biology, Umea University, Umea, Sweden).

E. coli strains were cultured in Luria-Bertani (LB) medium with the appropriate antibiotics. The medium used for the conjugation of *V. vulnificus* M2799 was LB medium containing 1.5% NaCl. For growth examination and RNA isolation, *V. vulnificus* M2799 was precultured in a heart infusion broth (Eiken Chemical, Tokyo, Japan) containing 2% NaCl (HI medium) at 37 °C and 200 rpm overnight. The culture was diluted 1:100 into fresh broth and then shaken at 37 °C at 200 rpm. HI medium with the iron chelator ethylenediamine-di (*o*-hydroxyphenylacetic acid) (EDDA, Sigma, St. Louis, MO, USA) at a final concentration of 10 µg/ml was used for growth examination under the low-iron concentration condition. To purify vulnibactin, *V. vulnificus* M2799 was cultured in T medium [17] containing 0.15 µM FeCl₃ for 28 h. In the vulnibactin detection test of culture supernatant, 10 µM purified vulnibactin was added to HI medium with EDDA as a control.

2.2. Antibiotics

The concentrations of antibiotics for *E. coli* strains were as follows: chloramphenicol (Cm), 10 µg/ml; and tetracycline (Tet), 15 µg/ml. The concentrations of antibiotics for the *V. vulnificus* strains were as follows: Cm, 5 µg/ml; polymyxin B, 100 U/ml; and Tet, 15 µg/ml. When used in the preculture for the complementation

analysis, the Tet concentration for the *V. vulnificus* strains was reduced to 5 µg/ml to maintain growth.

2.3. BLAST search and nucleotide sequencing

BLAST search for outer membrane channel proteins was performed based on the amino acid sequence of *E. coli* TolC, a representative outer membrane channel protein, against the currently available genome sequence of *V. vulnificus* CMCP6 [31]. Nucleotide sequencing of *tolC* homologs was carried out by the dideoxy chain termination method employing the BigDye Terminator v3.1 Cycle Sequencing Kit (Applied Biosystems, Foster City, CA, USA) on a DNA sequencer (ABI Prism 310 Genetic Analyzer, Applied Biosystems). Sequence data were analyzed using the GENETYX-WIN program (Software Development Co., Ltd., Tokyo, Japan). Chromosomal DNA was extracted from the M2799 culture using a Blood & Cell Culture DNA Midi Kit (Qiagen, Hilden, Germany). The PCR primers were designed based on the nucleotide sequences of *V. vulnificus* CMCP6. The PCR primers (VV1_0612_del_check_F and VV1_0612_del_check_R and VV2_1007_del_check_F and VV2_1007_del_check_R) were synthesized based on VV1_0612 and VV2_1007, respectively (Table 2). PCR amplification was performed by KOD-Plus-DNA polymerase (Toyobo, Osaka, Japan) for 30 cycles consisting of 94 °C for 15 s, 55 °C for 30 s, and 68 °C for 1 min. The 2440 bp and 2100 bp products were amplified and analyzed by direct sequencing. The nucleotide sequence data have been deposited in the DDBJ, EMBL, and GenBank nucleotide sequence databases under the accession numbers AB921202 and AB921203. Similarly, a search for possible RND proteins was performed based on the amino acid sequence of *E. coli* AcrB. The nucleotide sequences of RND protein-encoding genes were directly referred from CMCP6 genome sequence information.

2.4. Construction of gene-deletion mutants by marker exchange and complementation analysis

Plasmid construction, filter mating, and complementation analyses were done as reported previously [20]. The plasmids that were constructed for this study and the details of the deletion mutants are summarized in Table 1. The primers were constructed based on the *V. vulnificus* CMCP6 genome sequence [31] (Table 2).

2.5. Purification of vulnibactin

The purification of vulnibactin from *V. vulnificus* M2799 culture supernatant was performed according to the method of Okujo et al. with slight modifications [17]. The culture supernatant (2.5 l), adjusted to pH 4.0 with 60% citric acid, was adsorbed onto XAD-7 resin and eluted with 300 ml methanol. The eluant was evaporated and redissolved in 1 ml methanol. The resulting fraction was subjected to HPLC on an ODS column (Cosmosil 5C₁₈ ARII, 10 × 250 mm, Nacalai Tesque, Kyoto, Japan; 50–100% acetonitrile containing 0.05% trifluoroacetic acid in 20 min; flow rate, 2.0 ml/min; UV detection at 307 nm) to yield vulnibactin (ca. 1.0 mg). The retention time of vulnibactin by HPLC was 15.0 min.

2.6. Detection of vulnibactin in the culture supernatants using the *Dics* strain

V. vulnificus M2799 (wild-type) and ΔVV1_0612 were grown in HI medium containing EDDA (HI-EDDA) at 37 °C and 200 rpm for 6 h until the optical densities (OD₆₀₀) reached approximately 0.9. Culture supernatants were separated by centrifugation and filtered

Table 2
Primers used in this study.

Primer names	Nucleotide sequences ^a (5'-3')
Construction of deletion mutants of <i>tolC</i> homologs	
VV1_0612_upF	GATGCTCGAGTGTCCGACACGAAATTTGTT
VV1_0612_upR	GGCTACGGATCCCTGCACCAATAAGTAGTG
VV1_0612_dnF	CAGCGGATCCTACACTGAGCGAGCAAGAT
VV1_0612_dnR	ACCGCATGCTTGTGGCGTGAATACCGATG
VV1_0612_del_check_F	CCGAAACAAGTTGCCGACTTCTAGGCCAG
VV1_0612_del_check_R	ACTAATGGCTGCTTCCGACATCTCATGCA
VV2_1007_upF	TTCTGCTCGAGTTGCTCCCTATCTGATG
VV2_1007_upR	ATGGGGATCCCATGGCTGGCAAACACTCAGC
VV2_1007_dnF	CTCAGGATCCGATCAACTGGAACCAAGTGT
VV2_1007_dnR	TACATCGATCCGGCGTCCGGAAGGAAGCC
VV2_1007_del_check_F	GCTGCGACGGAAATGATGCTGTAGCCGAC
VV2_1007_del_check_R	TTGGCGTACACACTGAGGCTGCTTTTCC
Construction of deletion mutants of RND protein homologs	
VV1_1079_upF	TTTGTCTCGAGCTTCGCCAAGTCGAACGAGA
VV1_1079_upR	CTGAGGATCCCATGATGATGAAACACC
VV1_1079_dnF	TTGAGGATCCCGAAGCGCAGCGTAATGAGC
VV1_1079_dnR	CGCTGCATCCAGTGGAGGAGAAGCGTCGCCA
VV1_1079_del_check_F	GTGAAGTTGGCTACTCAACAATATTGAAG
VV1_1079_del_check_R	GGTAGAGGCTGTTGTCACTTTGTCTCAC
VV1_1681_upF	GATGCCCTCGAGCTCGCAAGCCGAATTTG
VV1_1681_upR	AAAAGGATCCCGATCCGCGAAGGCTCTCCG
VV1_1681_dnF	ATGCAGGATCCCGAGTGGAGCATGACTTTG
VV1_1681_dnR	AAGTGCATGCATCTACAAAAGAATAATGGT
VV1_1681_del_check_F	VV1_1681AAAATTGGTGATTGAGCCGACTC
VV1_1681_del_check_R	CTAATTTAATCCGCGTCACTGCATCCCG
VV1_2874_upF	GCTTCTCGAGCAGCTGATGTAATCGACC
VV1_2874_upR	TGGTGGATCCCTCATTTGCCCTCTGAG
VV1_2874_dnF	GTGGCGGATCCGAAAATAATTAATCCGGCCTA
VV1_2874_dnR	CTTTAGCATGCTCCGTGACCGCGGCACCT
VV1_2874_del_check_F	AATTTGAAAACGTTCAAGTTGGGCGAGCAAG
VV1_2874_del_check_R	CATCAACCATCCCGACCCGCTTGACGTAAGG
VV1_3156_upF	GGGCATTGACTCGAGGATTAACCCGAAAC
VV1_3156_upR	CTTTCGGGATCCGGCATCTCCGCGACTGCC
VV1_3156_dnF	GGCGGATCCGAAAAGCCGGTTCGCTGTTGG
VV1_3156_dnR	TTTTGCGATGCTTGTCGGGTTTAAATCACCC
VV1_3156_del_check_F	TATGCTGTGACAGCAACATCCAGCGCTTG
VV1_3156_del_check_R	CTGCTCTCCAGCGGAACTTAGGGGATACC
VV2_0029_upF	CAAATCCGAGCCGTGACGCTGGCGTTTACC
VV2_0029_upR	ACACGGATCCGCTTTGCAATGGTATAGCCA
VV2_0029_dnF	TTGACGGATCCACCAAGCAAGCAAAACACC
VV2_0029_dnR	CCTAGCATGCTGGCGCTCTTCTTTGGCGC
VV2_0029_del_check_F	TGACCTTGAAGCAATTAATCCCAAGCGGG
VV2_0029_del_check_R	AACCCGGTCACTATAAACCAAGGTGTTTTT
VV2_0195_upF	TGAATCCGAGCACACAAGTATGGATTACC
VV2_0195_upR	ATAAGGATCCAGCTGATGACTTTGTCTTGG
VV2_0195_dnF	GGCAGGATCCGGTTTCGCGACGGTACTAAC
VV2_0195_dnR	CGTTGCATGCAAACTTGGTTACACCTTTG
VV2_0195_del_check_F	TACGTGGCAATTGAGTTGTCGCAACAGTG
VV2_0195_del_check_R	CGCGTTACGGTATATTACAGTAAAGACG
VV2_0340_upF	TTGCTCGAGTGATATATCCCGTTTCCGGGG
VV2_0340_upR	AGCGGGGATCCGCTGATGGCAACACTTGGT
VV2_0340_dnF	ACCGGGATCCCGAGCAAGTATCCAATCCCG
VV2_0340_dnR	CAACAAGCATGCCAGGCATCACACCAAT
VV2_0340_del_check_F	CTGTGGCGCAAGCGAAAGAATCTCTCGGT
VV2_0340_del_check_R	CGAACTCCGACTTGAAAGCAAGCAACTG
VV2_0529_upF	AACGCTCGAGAGAATGATCTACATGTGC
VV2_0529_upR	CCCTTGGATCTAGGTTGAACCTCAACTTC
VV2_0529_dnF	CCTCTGGATCCATGGTGCACCTCAGTACAC
VV2_0529_dnR	GCCACTCGCATGCCCTTCCCTTGTCTTGG
VV2_0529_del_check_F	TACCGCATTCAGCATTAGCGAGCGTGGCG
VV2_0529_del_check_R	TGCGGATGAAAGTTCTGCTTACCGACCGC
VV2_0852_upF	CGCCCTCGAGGCGCTTCCCTCTCTCTCT
VV2_0852_upR	TTGCTGGATCCTTAAGTTGTAAGCACGCAA
VV2_0852_dnF	CCCAGTCAGGATCCAGTCTCAACGGTGTG
VV2_0852_dnR	GCTGGCATGCCAACGTACAGACATGCCCTTC
VV2_0852_del_check_F	TCTGGCACTTATGCTCGATTCTGAATCC
VV2_0852_del_check_R	TTTTTGAAGGTGATTTTTCATGTCACTC
VV2_0928_upF	TTTGTCCGAGTTCGCCAAGTCGAACGAGA
VV2_0928_upR	CTGAGGATCCCATGATGATGAACACC
VV2_0928_dnF	TTGAGGATCCCGAAGCGCAGCGTAATGAGC
VV2_0928_dnR	CGCTGCATGCAGTGGAGGAGCAAGCTCCGCCA
VV2_0928_del_check_F	GTGAAGTTGGCTACTCAACAATTTGAAG
VV2_0928_del_check_R	GCGTAGAGGCTGTTGACTATTTGCTCAC

Table 2 (continued)

Primer names	Nucleotide sequences ^a (5'-3')
VV2_1320_upF	TCCCCTCGAGTGCAGGAGCTTGATTGGAAC
VV2_1320_upR	AACGGGATCCTTGTATGCGCAGGGCGTCTC
VV2_1320_dnF	GATGGGATCCAACTCGCGCTGGAGAATATT
VV2_1320_dnR	TTGGCATGCTCAGCGAATGGCCAAAGCAGAA
VV2_1320_del_check_F	TGGTACCAGCGCACGGTATTGATGTGATGG
VV2_1320_del_check_R	ACGGCGGAAAACGCTCAGGCTCGCTTTC
Complementation analysis	
VV1_0612_Fw	CGATGATCTCTGCTGGCAAAATTTCCAAC
VV1_0612_Rv	AAAGGAATTCATTGCTGACCTTTTCTT
Real-time RT-PCR	
VV1_0612 RTPCR_Fw	GAAGTCCGAGCGCAAAACA
VV1_0612 RTPCR_Rv	CGCGCAGAAAACAACAGATTG
VV1_1079 RTPCR_Fw	TCCAGTTTTAGCGGTATCCATCA
VV1_1079 RTPCR_Rv	ATTTCTCGACCTGATCTTTGA
VV1_1681 RTPCR_Fw	CGCTTGAATGCCAAAGATTG
VV1_1681 RTPCR_Rv	TTGCCCTCGAATCCGAAAC
VV1_2874 RTPCR_Fw	GCGTTGGAAAGCTGGTTAGC
VV1_2874 RTPCR_Rv	ATGAAACGCTGCAAAACCTTA
VV1_3156 RTPCR_Fw	CGGCTACCCAGTGGAA
VV1_3156 RTPCR_Rv	GCGCGGTGCGAACAG
VV2_0029 RTPCR_Fw	GAGCATCGTTCGGAACCTT
VV2_0029 RTPCR_Rv	CCCCATAAACAGCAGCAACA
VV2_0195 RTPCR_Fw	TTCAAGAAAAGCCGCAATG
VV2_0195 RTPCR_Rv	CAGCCTGAAGCAAATGAAAC
VV2_0340 RTPCR_Fw	GCAAAAATGTGTGACTAGCGATAA
VV2_0340 RTPCR_Rv	CTATTCCGCGCCCTT
VV2_0529 RTPCR_Fw	CGTGTCCGCAAAATTGAGT
VV2_0529 RTPCR_Rv	AAGTCCGGAGAGCGTTTTTTT
VV2_0852 RTPCR_Fw	GCGCGTTACTCGTTTTTTT
VV2_0852 RTPCR_Rv	GAGAGCCGCCAATACAT
VV2_0928 RTPCR_Fw	TGGCTCTGTGGCTTATGACT
VV2_0928 RTPCR_Rv	TTCCGCCCATAAAACTG
VV2_1007 RTPCR_Fw	GGCTATTACCCGACCTCAGA
VV2_1007 RTPCR_Rv	GTCAGGCCCGCATTAACCTC
VV2_1320 RTPCR_Fw	GGAGTTTATCCGCGCTACA
VV2_1320 RTPCR_Rv	GCAGAAATGCTCTCTCCACT
16S RTPCR_Fw	GGGACAGCTCAAGTCTATCA
16S RTPCR_Rv	AGTTGGCCGCTCTGTAT

^a The mutagenized restriction sites are underlined.

with a 0.22- μ m pore size filter to remove living cells. The supernatants were stored at -30°C until use. The ICS mutant (Δ ics) was cultured on the above-mentioned culture-filtrates and then shaken at 37°C at 200 rpm for 8 h. The mutant was also cultured on HI-EDDA medium containing $10\ \mu\text{M}$ purified vulnibactin.

2.7. Quantitative RT-PCR

Cells were cultured in HI medium in the presence and absence of EDDA until the OD_{600} reached approximately 1.0. Then, the cells were treated with RNA Protect Bacteria Reagent (Qiagen) to maintain the stability of the RNA. Total cellular RNA was isolated using an RNeasy Kit (Qiagen). During isolation, RNA was treated with DNase I to avoid DNA contamination. Total RNA ($1\ \mu\text{g}$) and $1\ \mu\text{g}$ random primers (Invitrogen, Carlsbad, CA, USA) were used to generate the reverse transcripts. The reaction was carried out at 37°C for 60 min with Moloney murine leukemia virus reverse transcriptase (RNase H minus, Promega, Madison, WI, USA) and terminated by heating at 70°C for 15 min. PCR amplification of the reverse transcript was monitored using SYBR Premix Ex Taq (Takara, Shiga, Japan) in a Thermal Cycler Dice Real Time System (Takara). The reverse transcript ($1\ \mu\text{l}$) was used in the real-time PCR. After the initial denaturation of 30 s at 95°C , the DNA was amplified up to 40 cycles, with each cycle consisting of denaturation at 95°C for 5 s and annealing and extension at 60°C for 30 s. Specific primers (Table 2) amplifying the mean products of approximately 80 bp were designed with Primer Express software, version 3.0.1 (Applied Biosystems). Copy numbers of mRNA transcripts were

created using each PCR product, which was amplified with the primer set del_check_F and del_check_R (Table 2). The amount of target mRNA was normalized relative to an endogenous control of 16S rRNA.

3. Results

3.1. BLAST search and nucleotide sequencing

To determine the proteins functioning as outer and inner membrane proteins of the RND-type efflux system for vulnibactin transport, proteins homologous to *E. coli* TolC and AcrB were screened by BLAST. *E. coli* TolC was homologous to two putative outer membrane channel proteins, VV1_0612 and VV2_1007, of *V. vulnificus* CMCP6. Eleven putative RND proteins (VV1_1079, VV1_1681, VV1_2874, VV1_3156, VV2_0029, VV2_0195, VV2_0340, VV2_0529, VV2_0852, VV2_0928, and VV2_1320) were encoded in the *V. vulnificus* CMCP6 genome. BLAST results are summarized in Table 3.

To amplify the VV1_0612 and VV2_1007 genes, PCR was performed with the primers designed based on the sequences of the *V. vulnificus* CMCP6 genome. The nucleotide sequences of PCR products of *V. vulnificus* M2799 were determined by the dideoxy chain termination method. The identities of *E. coli* TolC and other closely related *Vibrio* strains are shown in Fig. 1. The open reading frames (ORFs) of the *V. vulnificus* M2799 VV1_0612 and VV2_1007 genes consist of 1326 and 1272 bp, respectively, and encode proteins consisting of 441 and 423 amino acid residues with molecular masses of 48 and 46 kDa, respectively. Significant identities were found when these proteins were compared with those from *E. coli* TolC [VV1_0612 (46%) and VV2_1007 (24%)], *V. vulnificus* CMCP6 VV1_0612 TolC [VV1_0612 (99%) and VV2_1007 (24%)] and VV2_1007 TolC [VV1_0612 (25%) and VV2_1007 (99%)], and *V. cholerae* TolC [VV1_0612 (79%) and VV2_1007 (24%)].

3.2. Growth of the deletion mutants of tolC homologs under low-iron concentration conditions

To obtain sufficient iron, many bacteria have developed the ability to synthesize low-molecular weight, high-affinity iron chelators known as siderophores to scavenge iron with high efficiency. *V. vulnificus* M2799 acquires iron through the secretion of a

catechololate siderophore called vulnibactin [17]. To investigate whether the VV1_0612 or/and the VV2_1007 protein(s) participate in vulnibactin secretion as the outer membrane channel protein, we constructed the deletion mutants (Δ VV1_0612 and Δ VV2_1007) and examined the growth of these mutants under low-iron concentration conditions. The Δ ics strain was unable to grow under low-iron concentration conditions as previously reported ([20], Fig. 2A). The Δ VV1_0612 strain was also unable to grow under low-iron concentration conditions compared with the wild-type and Δ VV2_1007 strains (Fig. 2A), suggesting that the VV1_0612 protein plays a crucial role in the iron utilization of M2799 cells. To confirm whether the VV1_0612 protein is involved in the iron acquisition system, complementation analysis of Δ VV1_0612 was performed. The growth of the recombinant mutant was restored to the level of the wild-type strain (Fig. 2B). These results suggest that the VV1_0612 protein is actually involved in the iron acquisition system via vulnibactin.

3.3. Vulnibactin secretion in the Δ VV1_0612 by bioassay

In *E. coli*, siderophore enterobactin has been shown to be secreted via the outer membrane channel protein TolC. Therefore, the TolC mutant did not export enterobactin into the extracellular milieu [23]. To investigate whether the vulnibactin can be secreted via the VV1_0612 protein, the growth of Δ ics under low-iron concentration conditions was examined. Although Δ ics cannot synthesize vulnibactin, the strain has the vulnibactin-mediated iron acquisition system. Therefore, when vulnibactin is supplemented exogenously, this strain can grow via the vulnibactin-mediated iron acquisition system. Okujo et al. showed that 0.8 μ M vulnibactin was purified from 1 l of the culture supernatant of *V. vulnificus* M2799 [17]. Then, vulnibactin that was purified from the strain was added to the medium at the final concentration of 10 μ M. As shown in Fig. 3, the growth of Δ ics was recovered by the addition of purified vulnibactin or the culture supernatant from the wild-type strain. However, the strain was unable to grow with the addition of the culture supernatant from Δ VV1_0612. These results indicate that Δ VV1_0612 is unable to export vulnibactin into the extracellular milieu.

3.4. Gene expression of RND protein-encoding genes under the iron-repleted and the low-iron concentration conditions

To investigate the regulation of the RND protein-encoding genes, quantitative RT-PCR was performed under the iron-repleted and the low-iron concentration conditions (Fig. 4). Of these genes, the copy numbers of VV1_1079 and VV2_0928 transcripts were relatively high under iron-repleted conditions compared with the other RND protein-encoding genes. In contrast, the copy numbers of the VV1_3156, VV2_0029, VV2_0529, and VV2_0852 transcripts were remarkably lower than those of the other genes. The expression level of the VV1_1079, VV1_3156, VV2_0029, VV2_0195, and VV2_1320 genes increased under the low-iron concentration conditions whereas that from VV2_0340 decreased. These results suggest that the VV1_1079, VV1_3156, VV2_0029, VV2_0195, and VV2_1320 genes are negatively regulated but the VV2_0340 gene is positively regulated by iron.

3.5. Growth of the mutants of genes encoding RND proteins under low-iron concentration conditions

To investigate which RND protein(s) together with the VV1_0612 outer membrane channel protein constitutes the RND-type efflux system for vulnibactin secretion, deletion mutants of genes encoding RND proteins whose gene expression increased

Table 3
Putative RND-type efflux system in *Vibrio vulnificus* CMCP6.

VV number	Description	Identity against <i>E. coli</i> TolC or AcrB (%)
TolC homolog		
VV1_0612	Type I secretion outer membrane protein, TolC	46
VV2_1007	Type I secretion outer membrane protein, TolC	24
RND protein homolog		
VV1_1079	RND multidrug efflux transporter	34
VV1_1681	Multidrug resistance protein	23
VV1_2874	Transporter, AcrB/D/F family	23
VV1_3156	RND multidrug efflux transporter	30
VV2_0029	Transporter, AcrB/D/F family	24
VV2_0195	Acriflavin resistance protein	24
VV2_0340	Acriflavin resistance protein	15
VV2_0529	RND family multidrug efflux inner membrane protein	40
VV2_0852	Cobalt–zinc–cadmium resistance protein CzcA/cation efflux system protein CusA	24
VV2_0928	Multidrug resistance protein	22
VV2_1320	Cation/multidrug efflux pump	13

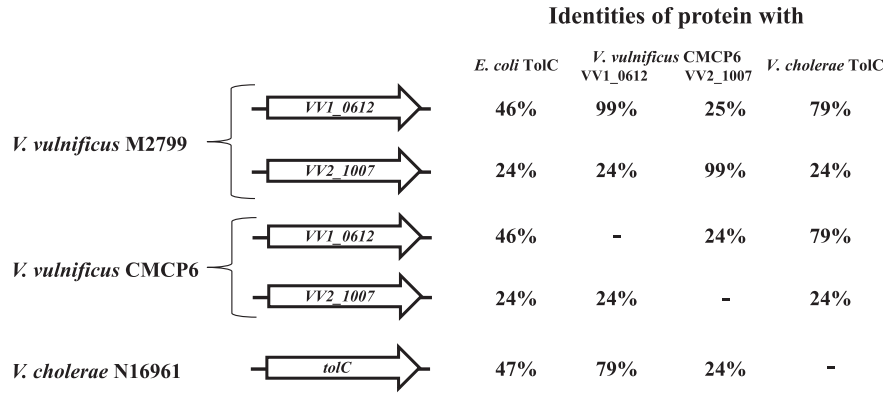


Fig. 1. TolC homologs in *Vibrio vulnificus* M2799 and their amino acid sequence identities with those from *Escherichia coli* and other closely related *Vibrio* strains. The orientation of the open reading frames (ORFs) is shown by arrows.

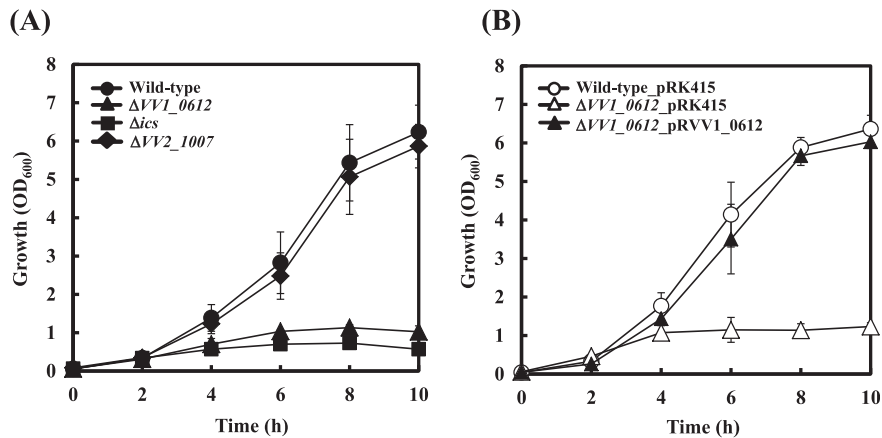


Fig. 2. Growth of the deletion mutants of *tolC* homologs (A) and its complementation analysis (B) under low-iron concentration conditions. (A) The deletion mutants of the gene encoding TolC homologs were cultured in heart infusion containing 2% NaCl (HI) medium containing 10 μ g/ml ethylenediamine-di (*o*-hydroxyphenylacetic acid) (EDDA), and the optical density (OD_{600}) was measured at the indicated time points. Data from three independent experiments are shown; standard deviations are indicated by vertical lines. (B) Plasmid pRVV1_0612 was transferred into $\Delta VV1_{0612}$.

under low-iron concentration conditions were constructed. We constructed the mutants of the iron-regulated genes, VV1_1079, VV1_3156, VV2_0029, VV2_0195, and VV2_1320 (Table 1), and the growth of these mutants under low-iron concentration conditions was investigated. As shown in Fig. 5A, no significant growth impairment was observed in the five mutants compared with the wild-type strain. These results imply that an individual gene is not essential as the RND protein for vulnibactin secretion.

We next constructed the multiple genes mutant of all RND protein-encoding genes, VV1_1079, VV1_1681, VV1_2874, VV1_3156, VV2_0029, VV2_0195, VV2_0340, VV2_0529, VV2_0852, VV2_0928, and VV2_1320. The mutant with 11 deleted genes was designated as $\Delta 11$. The growth of $\Delta 11$ was also investigated under low-iron concentration conditions. As shown in Fig. 5B, the growth inhibition of $\Delta 11$ was observed 6 h after the beginning of the culture. Furthermore, the multiple mutant except $\Delta VV1_{1681}$ ($\Delta 10$) and $\Delta VV1_{1681}$ were constructed. The $\Delta VV1_{1681}$ strain exhibited a growth curve that was similar to that of $\Delta 11$, while $\Delta 10$ showed the same growth as the wild-type strain. These results indicate that the VV1_1681 protein is involved in the vulnibactin export system of *V. vulnificus* M2799.

4. Discussion

Iron is essential for the growth of most bacteria. However, soluble iron in the human body is quite limiting because it is

normally bound with high affinity to iron-chelating proteins such as transferrin and lactoferrin. Many bacteria possess specialized iron acquisition systems to scavenge iron from the chelating molecules. *V. vulnificus* acquires iron through the secretion of a catecholate siderophore called vulnibactin [17]. The mechanisms of iron uptake, such as vulnibactin synthesis [12,20,32] and ferric-vulnibactin uptake systems [20,33], have recently been reported. However, the export system of vulnibactin from intracellular to extracellular milieu has not been reported until now. In this study, we focused on the RND-type efflux system and tried to identify the proteins constituting the system involved in the secretion of vulnibactin.

RND-type efflux systems are typical transporters of gram-negative bacteria and function as a huge protein complex spanning the cytoplasmic membrane and the outer membrane. This system is composed of an outer membrane channel protein, an MFP, and an RND protein [34]. Because the RND efflux complex requires a channel protein, the outer membrane protein is essential for the transportation of substrates across the outer membrane. If the RND-type efflux systems are actually involved in vulnibactin secretion through the outer membrane, the mutants of the corresponding genes would not export vulnibactin into the milieu. BLAST analysis revealed that two outer membrane channel proteins (VV1_0612 and VV2_1007) and 11 putative RND proteins were encoded by the *V. vulnificus* CMCP6 genome (Table 3). The MFPs for RND-type efflux systems and major facilitator superfamily (MFS)

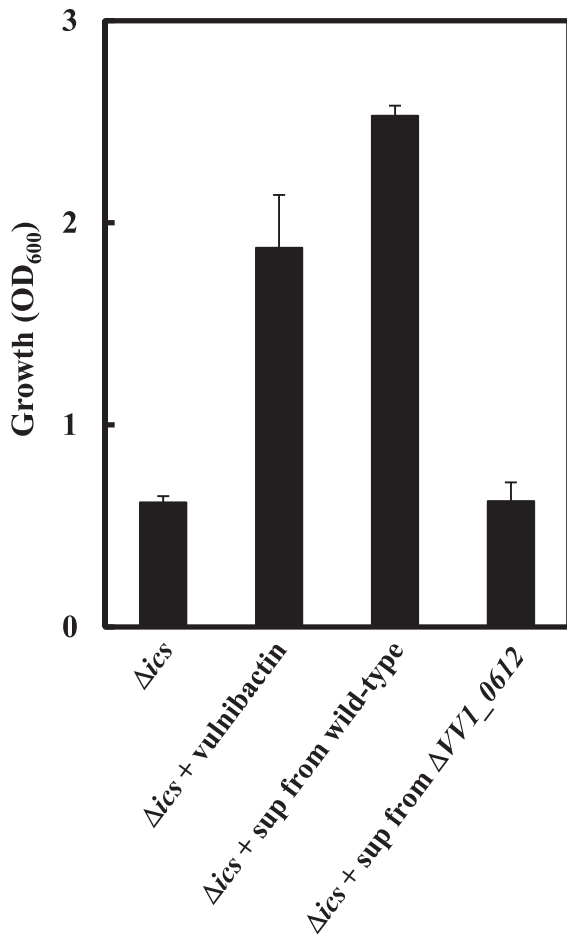


Fig. 3. Detection of vulnibactin in the culture supernatants by bioassay. The Δ ics strain was cultured on medium containing purified vulnibactin, the culture supernatant of the wild-type strain, and the culture supernatant of Δ VV1_0612. Data from three independent experiments are shown; standard deviations are indicated by vertical lines.

protein, which are considered to be involved in vulnibactin efflux across the cytoplasmic membrane, were not examined in this study.

The growth of Δ VV1_0612 but not Δ VV2_1007 under low-iron concentration conditions was significantly impaired, which was similar to Δ ics, and the growth was restored by the complementation of VV1_0612 (Fig. 2). In addition, no growth retardation was observed in Δ VV1_0612 under iron-repleted conditions (data not shown). Furthermore, culture supernatant from Δ VV1_0612 did not compensate the growth defect of Δ ics that could not synthesize vulnibactin. The Δ ics strain could be rescued with vulnibactin and the culture supernatant from the wild-type strain (Fig. 3). The growth ability of Δ VV1_0612 under low-iron concentration conditions was reverted by the addition of the purified vulnibactin (data not shown). These results indicate that the VV1_0612 protein plays a crucial role in vulnibactin secretion as a component of RND-type efflux systems in M2799 cells under low-iron concentration conditions.

In *E. coli*, the outer membrane protein TolC, which is used by several RND proteins, has been shown to be involved in enterobactin secretion [23]. To identify which RND protein(s) together with the VV1_0612 TolC constituted the RND efflux complex(s), we constructed the multiple mutants of RND inner membrane proteins, and the growth of the mutants was assessed under low-iron concentration conditions. The growth defect was observed in Δ VV1_1681. The growth inhibition of this mutant was observed 6 h

after the beginning of the culture. The growth ability was also reverted by the addition of the purified vulnibactin (data not shown). These results indicate that the VV1_1681 protein was involved in the vulnibactin export system of *V. vulnificus* M2799. Additionally, there must be unidentified RND protein(s) that complement the defect of the VV1_1681 gene. The VV1_0612 protein is the TolC homolog and thereby may also interact with different types of transporters such as the ATP-driven ABC transporters [35–37]. We focused on the TolC/MacAB efflux transporter system, which has been shown to export macrolide-type antibiotics from bacterial cells [36]. BLAST results indicated that the *E. coli* MacB homolog was composed of three ORFs (VV2_1004, VV2_1005, and VV2_1006). The deletion mutant of VV2_1005 and VV2_1006 was constructed, and the growth was tested under low-iron concentration conditions. However, the mutant did not show any growth impairment under the low-iron concentration conditions (data not shown). This result also strengthens our hypothesis that there is an unknown RND protein(s) in *V. vulnificus* M2799. This is the first genetic evidence that vulnibactin is secreted through the RND-type efflux systems in *V. vulnificus*.

Furthermore, the TolC proteins have been shown to contribute to the pathogenicity of *V. vulnificus*. VV1_0612 TolC was revealed to be responsible for RtxA toxin secretion in *V. vulnificus* MO6-24/O [38]. Similarly, it has been shown that *V. cholerae* RTX toxin is secreted by a four-component type I secretion system composed of RtxB, RtxD, RtxE, and TolC [39]. In addition, the cytotoxicity and biofilm formation in Δ VV2_1007 were both decreased, indicating that the VV2_1007 protein is associated with the virulence of *V. vulnificus* MO6-24/O [40]. Therefore, the TolC proteins in *V. vulnificus* seem to fulfill the function as the access point for the export pathway of several virulence factors including vulnibactin and RtxA. In *V. vulnificus* M2799, VV1_0612 TolC plays a crucial role in the vulnibactin export system (Fig. 2A). A model for the export and the uptake of vulnibactin in *V. vulnificus* M2799 cell is presented in Fig. 6. This is the simplest model that is consistent with our present and previous data, but more complex models involving additional factors are also possible.

In vulnibactin-mediated iron uptake system, VuuA was the only vulnibactin outer membrane receptor, whereas VatD could replace

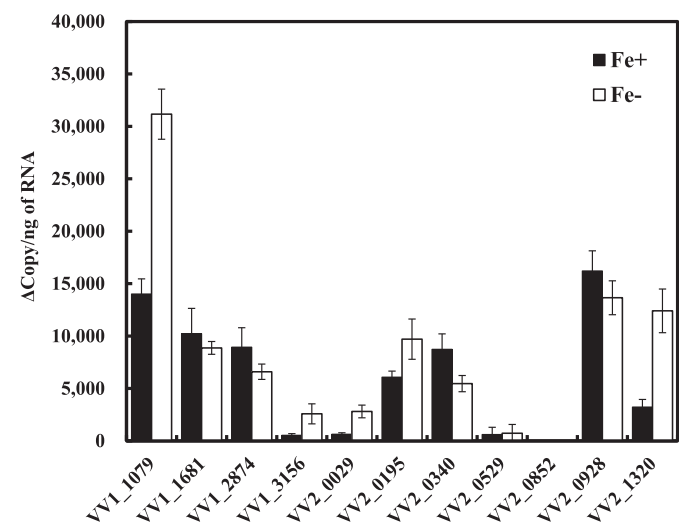


Fig. 4. Gene expression of the resistance-nodulation-division (RND) protein-encoding genes under the iron-repleted and low-iron concentration conditions. Total RNA was isolated and converted to the reverse transcript, which was analyzed for specific mRNA transcript levels by real-time RT-PCR. Copy numbers of mRNA transcripts were determined using each PCR product. The values are normalized to the 16S rRNA gene expression. Data from three independent experiments are shown; standard deviations are indicated by vertical lines.

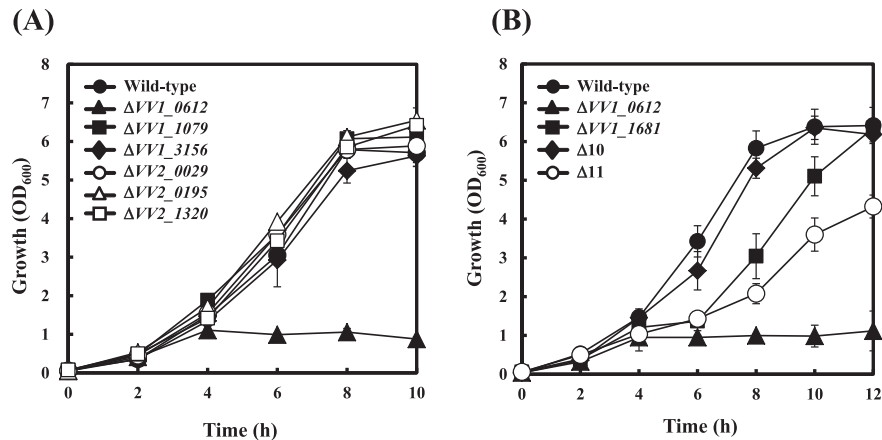


Fig. 5. Growth of the deletion mutants of RND protein-encoding genes under low-iron concentration conditions. (A) The deletion mutants of the RND protein-encoding genes were cultured in HI medium containing 10 $\mu\text{g/ml}$ EDDA, and the OD_{600} was measured at the indicated time points. Data from three independent experiments are shown; standard deviations are indicated by vertical lines. (B) The multiple deletion mutants of the RND protein-encoding genes were cultured in the same medium.

the function of FatB as a periplasmic ferric-vulnibactin binding protein [20]. Similarly, vulnibactin export systems of this strain seem to be composed of a single common outer membrane channel protein, VV1_0612 TolC, and several RND proteins including VV1_1681. Furthermore, when the *E. coli tolC* mutant was grown under low-iron concentration conditions, enterobactin accumulated in the periplasmic space. As a consequence, the bacterial morphology was impaired, possibly by sequestering iron and inhibiting iron-dependent reactions involved in cell division or peptidoglycan synthesis [41]. In addition, the ΔVV1_{0612} strain of *V. vulnificus* M2799 was unable to grow under low-iron concentration conditions. These results indicate that the TolC proteins might be a new target for the treatment of gram-negative bacterial infections.

It has been reported that Fur, a transcriptional repressor that responds to iron utilization [42], represses the expression of several genes such as *desA*, *vuuA*, and *vatD* under iron-repleted conditions [33,43,44]. In our data, the gene expression of

VV1_1079, VV1_3156, VV2_0029, VV2_0195, and VV2_1320 was remarkably upregulated under low-iron concentration conditions (Fig. 4). Judging from the nucleotide sequences of these gene-operon-promoter regions, a putative Fur box (GAA-TAATTAATCAATATTT) was identified only in the upstream region (VV2_1322 promoter) of the VV2_1320 gene (data not shown). These results suggest that the gene expression of VV2_1320 in *V. vulnificus* M2799 is regulated by Fur.

5. Conclusions

We proposed a model of a vulnibactin-export system in *V. vulnificus* M2799 whereby vulnibactin is exported from the cytoplasm to the extracellular milieu through RND-type efflux systems. The systems are composed of VV1_0612 TolC and several RND proteins including the VV1_1681 protein (Fig. 6). VV1_0612 TolC is essential for the vulnibactin export system. However, the other RND protein(s) involved in the system remains to be investigated. Genetic approaches to identify the RND-type efflux systems are currently underway.

Acknowledgments

This study was supported in part by a Grants-in-Aid for the Strategic Research Foundation Grant-aided Project for Private Universities from the Ministry of Education, Culture, Sports, Science and Technology (MEXT), Japan, 2011–2015 (S1101031).

We thank Prof. Shin-ichi Miyoshi for supplying the *V. vulnificus* clinical isolate strain M2799.

References

- [1] Klontz KC, Lieb S, Schreiber M, Janowski HT, Baldy LM, Gunn RA. Syndromes of *Vibrio vulnificus* infections. Clinical and epidemiologic features in Florida cases, 1981–1987. *Ann Intern Med* 1988;109:318–23.
- [2] Tacket CO, Brenner F, Blake PA. Clinical features and an epidemiological study of *Vibrio vulnificus* infections. *J Infect Dis* 1984;149:558–61.
- [3] Johnston JM, Becker SF, McFarland LM. *Vibrio vulnificus*. Man and the sea. *J Am Med Assoc* 1985;253:2850–3.
- [4] Kothary MH, Kreger AS. Purification and characterization of an elastolytic protease of *Vibrio vulnificus*. *J Gen Microbiol* 1987;133:1783–91.
- [5] Miyoshi N, Shimizu C, Miyoshi S, Shinoda S. Purification and characterization of *Vibrio vulnificus* protease. *Microbiol Immunol* 1987;31:13–25.
- [6] Fan JJ, Shao CP, Ho YC, Yu CK, Hor LI. Isolation and characterization of a *Vibrio vulnificus* mutant deficient in both extracellular metalloprotease and cytolysin. *Infect Immun* 2001;69:5943–8.

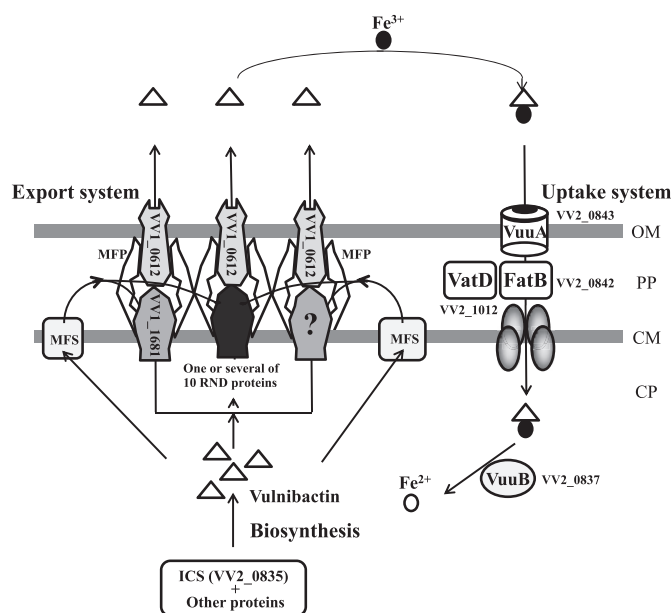


Fig. 6. Schematic representation of the vulnibactin-mediated iron uptake system of *V. vulnificus* M2799.

- [7] Chung KJ, Cho EJ, Kim MK, Kim YR, Kim SH, Yang HY, et al. RtxA1-induced expression of the small GTPase Rac2 plays a key role in the pathogenicity of *Vibrio vulnificus*. *J Infect Dis* 2010;201:97–105.
- [8] Kim YR, Lee SE, Kook H, Yeom JA, Na HS, Kim SY, et al. *Vibrio vulnificus* RTX toxin kills host cells only after contact of the bacteria with host cells. *Cell Microbiol* 2008;10:848–62.
- [9] Kwak JS, Jeong HG, Satchell KJ. *Vibrio vulnificus* rtxA1 gene recombination generates toxin variants with altered potency during intestinal infection. *Proc Natl Acad Sci U S A* 2011;108:1645–50.
- [10] Simpson LM, White VK, Zane SF, Oliver JD. Correlation between virulence and colony morphology in *Vibrio vulnificus*. *Infect Immun* 1987;55:269–72.
- [11] Wright AC, Powell JL, Kaper JB, Morris Jr JG. Identification of a group 1-like capsular polysaccharide operon for *Vibrio vulnificus*. *Infect Immun* 2001;69:6893–901.
- [12] Litwin CM, Rayback TW, Skinner J. Role of catechol siderophore synthesis in *Vibrio vulnificus* virulence. *Infect Immun* 1996;64:2834–8.
- [13] Tsuchiya T, Mitsuo E, Hayashi N, Hikita Y, Nakao H, Yamamoto S, et al. *Vibrio vulnificus* damages macrophages during the early phase of infection. *Infect Immun* 2007;75:4592–6.
- [14] Wooldridge KG, Williams PH. Iron uptake mechanisms of pathogenic bacteria. *FEMS Microbiol Rev* 1993;12:325–48.
- [15] Ratledge C, Dover LG. Iron metabolism in pathogenic bacteria. *Annu Rev Microbiol* 2000;54:881–941.
- [16] Morris JG, Wright AC, Simpson LM, Wood PK, Johnson DE, Oliver JD. Virulence of *Vibrio vulnificus*: association with utilization of transferrin-bound iron, and lack of correlation with levels of cytotoxin or protease production. *FEMS Microbiol Lett* 1987;40:55–9.
- [17] Okujo N, Saito M, Yamamoto S, Yoshida T, Miyoshi S, Shinoda S. Structure of vulnibactin, a new polyamine-containing siderophore from *Vibrio vulnificus*. *Biometals* 1994;7:109–16.
- [18] Griffiths GL, Sigel SP, Payne SM, Neilands JB. Vibriobactin, a siderophore from *Vibrio cholerae*. *J Biol Chem* 1984;259:383–5.
- [19] Tan W, Verma V, Jeong K, Kim SY, Jung CH, Lee SE, et al. Molecular characterization of vulnibactin biosynthesis in *Vibrio vulnificus* indicates the existence of an alternative siderophore. *Front Microbiol* 2014;5:1–11.
- [20] Kawano H, Miyamoto K, Sakaguchi I, Myojin T, Moriwaki M, Tsuchiya T, et al. Role of periplasmic binding proteins, FatB and VatD, in the vulnibactin utilization system of *Vibrio vulnificus* M2799. *Microb Pathog* 2013;65:73–81.
- [21] Kim CM, Park RY, Park JH, Sun HY, Bai YH, Ryu PY, et al. *Vibrio vulnificus* vulnibactin, but not metalloprotease VvpE, is essentially required for iron-uptake from human holotransferrin. *Biol Pharm Bull* 2006;29:911–8.
- [22] Miyamoto K, Kosakai K, Ikebayashi S, Tsuchiya T, Yamamoto S, Tsujibo H. Proteomic analysis of *Vibrio vulnificus* M2799 grown under iron-repleted and iron-depleted conditions. *Microb Pathog* 2009;46:171–7.
- [23] Bleuel C, Grosse C, Taudte N, Scherer J, Wesenberg D, Krauss GJ, et al. TolC is involved in enterobactin efflux across the outer membrane of *Escherichia coli*. *J Bacteriol* 2005;187:6701–7.
- [24] Whitney EN. The tolC locus in *Escherichia coli* K12. *Genetics* 1971;67:39–53.
- [25] Franke S, Grass G, Rensing C, Nies DH. Molecular analysis of the copper-transporting efflux system CusCFBA of *Escherichia coli*. *J Bacteriol* 2003;185:3804–12.
- [26] Nies DH. Efflux-mediated heavy metal resistance in prokaryotes. *FEMS Microbiol Rev* 2003;27:313–39.
- [27] Nikaido H. Multidrug efflux pumps of gram-negative bacteria. *J Bacteriol* 1996;178:5853–9.
- [28] Miller VL, Mekalanos JJ. A novel suicide vector and its use in construction of insertion mutations: osmoregulation of outer membrane proteins and virulence determinants in *Vibrio cholerae* requires toxR. *J Bacteriol* 1988;170:2575–83.
- [29] Milton DL, O'Toole R, Horstedt P, Wolf-Watz H. Flagellin A is essential for the virulence of *Vibrio anguillarum*. *J Bacteriol* 1996;178:1310–9.
- [30] Keen NT, Tamaki S, Kobayashi D, Trollinger D. Improved broad-host-range plasmids for DNA cloning in gram-negative bacteria. *Gene* 1988;70:191–7.
- [31] Kim YR, Lee SE, Kim CM, Kim SY, Shin EK, Shin DH, et al. Characterization and pathogenic significance of *Vibrio vulnificus* antigens preferentially expressed in septicemic patients. *Infect Immun* 2003;71:5461–71.
- [32] Kim IH, Shim JI, Lee KE, Hwang W, Kim JJ, Choi SH, et al. Nonribosomal peptide synthase is responsible for the biosynthesis of siderophore in *Vibrio vulnificus* MO6-24/O. *J Microbiol Biotechnol* 2008;18:35–42.
- [33] Webster ACD, Litwin CM. Cloning and characterization of *vuuA*, a gene encoding the *Vibrio vulnificus* ferric vulnibactin receptor. *Infect Immun* 2000;68:526–34.
- [34] Koronakis V, Andersen C, Hughes C. Channel-tunnels. *Curr Opin Struct Biol* 2001;11:403–7.
- [35] Lomovskaya O, Lewis K. Emr, an *Escherichia coli* locus for multidrug resistance. *Proc Natl Acad Sci U S A* 1992;89:8938–42.
- [36] Kobayashi N, Nishino K, Yamaguchi A. Novel macrolide-specific ABC-type efflux transporter in *Escherichia coli*. *J Bacteriol* 2001;183:5639–44.
- [37] Nishino K, Yamaguchi A. EvgA of the two-component signal transduction system modulates production of the YhiUV multidrug transporter in *Escherichia coli*. *J Bacteriol* 2002;184:2319–23.
- [38] Hwang W, Lee NY, Kim J, Lee MA, Kim KS, Lee KH, et al. Functional characterization of EpsC, a component of the type II secretion system, in the pathogenicity of *Vibrio vulnificus*. *Infect Immun* 2011;79:4068–80.
- [39] Boardman BK, Satchell KJ. *Vibrio cholerae* strains with mutations in an atypical type I secretion system accumulate RTX toxin intracellularly. *J Bacteriol* 2004;186:8137–43.
- [40] Lee KE, Bang JS, Baek CH, Park DK, Hwang W, Choi SH, et al. IVET-based identification of virulence factors in *Vibrio vulnificus* MO6-24/O. *J Microbiol Biotechnol* 2007;17:234–43.
- [41] Vega DE, Young KD. Accumulation of periplasmic enterobactin impairs the growth and morphology of *Escherichia coli* tolC mutants. *Mol Microbiol* 2014;91:508–21.
- [42] Hantke K. Iron and metal regulation in bacteria. *Curr Opin Microbiol* 2001;4:172–7.
- [43] Tanabe T, Takata N, Naka A, Moon YH, Nakao H, Inoue Y, et al. Identification of an AraC-like regulator gene required for induction of the 78-kDa ferrioxamine B receptor in *Vibrio vulnificus*. *FEMS Microbiol Lett* 2005;249:309–14.
- [44] Tanabe T, Naka A, Aso H, Nakao H, Narimatsu S, Inoue Y, et al. A novel aerobactin utilization cluster in *Vibrio vulnificus* with a gene involved in the transcription regulation of the *iutA* homologue. *Microbiol Immunol* 2005;49:823–34.



Regulation of the Expression of the *Vibrio parahaemolyticus* *peuA* Gene Encoding an Alternative Ferric Enterobactin Receptor

Tomotaka Tanabe^{1*}, Ayaka Kato¹, Keiichi Shiuchi², Katsushiro Miyamoto³, Hiroshi Tsujibo³, Jun Maki⁴, Shigeo Yamamoto¹, Tatsuya Funahashi¹

1 Laboratory of Hygienic Chemistry, College of Pharmaceutical Sciences, Matsuyama University, Matsuyama, Ehime, Japan, **2** Graduate School of Medicine, Dentistry and Pharmaceutical Sciences, Okayama University, Okayama, Japan, **3** Department of Microbiology, Osaka University of Pharmaceutical Sciences, Takatsuki, Osaka, Japan, **4** Laboratory of Infectious Diseases, College of Pharmaceutical Sciences, Matsuyama University, Matsuyama, Ehime, Japan

Abstract

A *pvsB-vctA-irgA* triple deletion mutant of *Vibrio parahaemolyticus* can utilize enterobactin under iron-limiting conditions by inducing a previously undescribed receptor, *PeuA* (VPA0150), in response to extracellular alkaline pH and enterobactin. *In silico* analyses revealed the existence of a two-component regulatory system operon, *peuRS*, immediately upstream of *peuA*, which constitutes an operon with the *TonB2* system genes. Both the *peuRS* and *peuA-tonB2* operons were found to be upregulated under iron-limiting conditions in a ferric uptake regulator (Fur)-dependent manner. The involvement of *peuA* and *peuRS* in enterobactin utilization was analyzed by complementation experiments using deletion mutants. Primer extension analysis indicated that, under iron-limiting conditions, the transcription of *peuA* was initiated from the +1 site at pH 7.0 and from both the +1 and +39 sites at pH 8.0 in the presence of enterobactin. The +39 transcript was absent from the *peuRS* deletion mutant. Secondary structure prediction of their 5'-untranslated regions suggested that translation initiation is blocked in the +1 transcript, but not in the +39 transcript. Consistent with this, *in vitro* translation analysis demonstrated that production of *PeuA* was determined only by the +39 transcript. These studies establish a novel gene regulation mechanism in which the two-component regulatory system *PeuRS* enhances expression of the alternative +39 transcript that possesses non-inhibitory structure, allowing the *peuA* expression to be regulated at the translation stage.

Citation: Tanabe T, Kato A, Shiuchi K, Miyamoto K, Tsujibo H, et al. (2014) Regulation of the Expression of the *Vibrio parahaemolyticus* *peuA* Gene Encoding an Alternative Ferric Enterobactin Receptor. PLoS ONE 9(8): e105749. doi:10.1371/journal.pone.0105749

Editor: Dongsheng Zhou, State Key Laboratory of Pathogen and Biosecurity, Beijing Institute of Microbiology and Epidemiology, China

Received: June 4, 2014; **Accepted:** July 27, 2014; **Published:** August 22, 2014

Copyright: © 2014 Tanabe et al. This is an open-access article distributed under the terms of the Creative Commons Attribution License, which permits unrestricted use, distribution, and reproduction in any medium, provided the original author and source are credited.

Data Availability: The authors confirm that all data underlying the findings are fully available without restriction. All relevant data are within the paper and its Supporting Information files.

Funding: This work was supported in part by a Grant-in-Aid for Young Scientists (B) (25870987) from the Ministry of Education, Culture, Sports, Science and Technology of Japan. The funders had no role in study design, data collection and analysis, decision to publish, or preparation of the manuscript.

Competing Interests: The authors have declared that no competing interests exist.

* Email: ttanabe@cc.matsuyama-u.ac.jp

Introduction

Iron is essential for the growth of nearly all forms of life, but its very limited solubility makes iron scarce. The predominant type (ferric iron) preferentially forms barely soluble hydroxide complexes under aerobic conditions and at neutral and alkaline pH [1–3]. To solubilize iron from these complexes and to acquire adequate levels, bacteria as well as other microorganisms frequently secrete siderophores, including catecholates, hydroxamates, and polycarboxylates [2,4], all of which exhibit high affinity for ferric iron. In Gram-negative bacteria, ferric siderophore complexes thus formed in the extracellular milieu are conveyed into the bacterial cell by a high-affinity active transport system composed of an outer membrane receptor (OMR) coupled with both a TonB-ExbBD protein complex (known as a TonB system) and an ATP-binding cassette (ABC) transporter system [5,6]. The TonB system transduces the proton-motive force of the cytoplasmic membrane to the OMRs [5,6], which are therefore known as TonB-dependent receptors. It is well known that, in these processes, the siderophore specificity resides mainly in the

OMRs [2,7]. Furthermore, expression of the genes responsible for iron acquisition is regulated by the cellular pool of iron through a ferric uptake regulator (Fur), which is ubiquitous in Gram-negative bacteria and usually acts as a repressor with ferrous iron as a co-repressor [8,9]. When the intracellular iron concentration increases, the Fur-Fe²⁺ complex binds to a consensus sequence, termed the Fur box, located in the promoter regions of the Fur target genes, thereby leading to repression of transcription initiation. In contrast, when iron becomes scarce in the cell, Fur is inactivated by release of the iron cofactor, and the target genes are transcribed to efficiently scavenge iron from the surroundings.

In addition to their own siderophores, some bacteria have evolved transport systems for ferric complex that use exogenous siderophores (xenosiderophores) produced by other bacterial or fungal species [10]. This strategy, called siderophore piracy [11], may be highly advantageous for survival and proliferation of these bacteria, because it allows them to escape any bacteriostatic or competitive effects caused by xenosiderophores likely to coexist under various environmental conditions [12]. In *Pseudomonas aeruginosa*, the ferric enterobactin (Ent) receptor PfeA is induced

in the presence of Ent combined with iron-starvation via the PfeRS two-component regulatory system [13,14]. This system typically comprises an inner membrane-integrated histidine sensor kinase and a cytoplasmic response regulator that together form a signal transduction pathway to regulate gene expression; environmental stimuli, including a wide range of physical and chemical signals, trigger autophosphorylation of a histidine sensor kinase, and its phosphoryl group is subsequently transferred to a response regulator, which activates or represses transcription of the target gene required for the appropriate physiological response [15–17].

Vibrio parahaemolyticus is a Gram-negative and halophilic human pathogen that naturally inhabits marine and estuarine environments. It is a significant cause of acute gastroenteritis worldwide, acquired through the consumption of raw or undercooked seafood [18–20]. Under iron-limiting conditions, this bacterium secretes its own siderophore, vibrioferrin [21], which is biosynthesized by four enzymes encoded by *pvsABDE* [22], and transports extracellular iron as ferric vibrioferrin back to the cell via two OMRs specific to ferric vibrioferrin and the ABC transporter complex, which are encoded by *pvuA1-pvuA2* and *pvuBCDE*, respectively [22–24]. In addition to producing vibrioferrin, *V. parahaemolyticus* can utilize aerobactin [25], ferrichrome [26], and Ent [27] as xenosiderophores by expressing their cognate OMRs.

In this report, we show that the *V. parahaemolyticus* *peuA* gene encoding the ferric Ent receptor is responsible for Ent utilization under iron-limiting conditions at pH 8.0. We also present evidence that the expression of *PeuA* is determined by an alternative transcript (+39 transcript) of *peuA* that is induced under iron-limiting conditions via a two-component regulatory system encoded by *peuRS* in response to extracellular alkaline pH and Ent.

Materials and Methods

Bacterial Strains, Plasmids, Growth Conditions, and Primers

The bacterial strains and plasmids used in this study are listed in Table 1 and S1, respectively. *Escherichia coli* β 2155 [29], which is a diamino-pimelic acid auxotroph, was grown under routine conditions and maintained in Luria-Bertani (LB) medium containing 0.5% NaCl and 0.5 mM 2,6-diamino-pimelic acid. *V. parahaemolyticus* RIMD2210633 [28] and its deletion mutants were incubated in LB medium containing 3% NaCl or in LB medium containing 3% NaCl and 100 mM Tris-HCl (LB-Tris medium) at pH 7.0 and 8.0. To impose iron limitation on *V. parahaemolyticus* strains, they were grown in LB-Tris medium containing 25 μ M ethylenediamine-di(*o*-hydroxyphenylacetic acid) (EDDA; Sigma-Aldrich) (LB-Tris/+EDDA medium). When required, the siderophore Ent (Sigma-Aldrich) was added to the LB-Tris/+EDDA medium at a final concentration of 5 μ M (LB-Tris/+EDDA/+Ent medium). Antibiotics were added at the following concentrations: 10 μ g/mL chloramphenicol and 10 μ g/mL tetracycline. The oligonucleotide primers used in this study are listed in Table S2.

Growth Assay

The growth assay was performed using a TVS062CA biophotorecorder (Advantec Toyo, Tokyo, Japan). Briefly, *V. parahaemolyticus* cells grown overnight in LB medium were diluted with LB-Tris/+EDDA or LB-Tris/+EDDA/+Ent medium to an optical density at 600 nm (OD_{600}) of 0.005. The cultures were shaken at 70 rpm at 37°C, and the OD_{600} was measured every 3 h for 18 h.

DNA Manipulation and *in silico* Sequence Analysis

Chromosomal DNA was extracted with a Wizard genomic DNA purification kit (Promega), and plasmid DNA was routinely prepared with a High Pure Plasmid Isolation Kit (Roche), according to the manufacturer's instructions. Standard DNA manipulation was performed as described [30]. Homology searches were performed using the BLAST program of the National Center for Biotechnology Information (<http://blast.ncbi.nlm.nih.gov/>) [31].

Preparation of Outer Membrane Protein (OMP)-Rich Fractions and Sodium Dodecyl Sulfate-Polyacrylamide Gel Electrophoresis (SDS-PAGE)

Stationary-phase *V. parahaemolyticus* cells were inoculated at a final OD_{600} of 0.005–0.01 into LB-Tris, LB-Tris/+EDDA, and LB-Tris/+EDDA/+Ent media at pH 7.0 and 8.0, and the cultures were shaken at 37°C for 4 h. Sarkosyl-insoluble OMPs were prepared and analyzed by SDS-PAGE, as previously described [32]. Separated OMPs were electroblotted onto a wet polyvinylidene difluoride membrane, and the N-terminal amino acid sequence was determined using the Edman degradation method with a Procise 491 HT protein sequencer (Applied Biosystems).

Gene Deletion and Complementation

Gene deletions in the *V. parahaemolyticus* genome were constructed by allelic exchange using the suicide plasmid pXAC623, according to the procedure described by Kuroda *et al.* [33]. Briefly, DNA fragments with deletions in the *peuA*, *peuRS*, *hutA*, *nutA*, *fhuA*, and *VPO168* genes were prepared by overlap extension PCR [34], as previously described [24]. The deleted gene fragments were ligated into appropriately digested pXAC623 to yield pXAC623 Δ *peuA*, pXAC623 Δ *peuRS*, pXAC623 Δ *hutA*, pXAC623 Δ *nutA*, pXAC623 Δ *fhuA*, and pXAC623 Δ *VPO168* (Table S1), which were then transformed into *E. coli* β 2155 to generate the respective donor strains. After filter mating between each donor strain and an appropriate *V. parahaemolyticus* strain, merodiploid recombinants were selected on LB plates containing chloramphenicol, but not diamino-pimelic acid. Each merodiploid recombinant was spread on VDS-broth agar plates (1% polypeptone, 0.5% yeast extract, 30 mM NaCl, 55 mM KCl, 10% sucrose, and 2.5% agar) [33] and incubated at 25°C for 30 h, at which point sucrose-resistant and chloramphenicol-sensitive colonies were selected. The deletions were verified by PCR, using chromosomal DNA isolated from each deletion mutant (data not shown). To complement the *peuA* and *peuRS* deletion mutants, PCR amplicons containing the respective genes were ligated into appropriately digested pRK415 [35], and the resulting complementing plasmids were transformed into the respective *V. parahaemolyticus* mutant strains.

RNA Analysis

Stationary-phase *V. parahaemolyticus* cells were inoculated as described for the preparation of OMP-rich fractions, and the cultures were then shaken at 37°C until they reached OD_{600} 0.3–0.6. Each cell pellet was treated with the RNeasy Protect Bacteria Reagent (Qiagen), according to the manufacturer's instructions, and total RNA was prepared from each cell sample using the RNeasy Mini kit (Qiagen) or TriPure Reagent (Roche), according to the manufacturer's instructions. Total RNA samples thus obtained were used for primer extension, reverse transcriptase (RT)-PCR, and RT-quantitative (q) PCR.

Primer extension analysis of *peuA* and *peuR* was performed with the oligonucleotide primers *peuA*-PE and *peuR*-PE (see

Table 1. Bacterial strains used in this study.

Strain	Description	Reference or source
<i>V. parahaemolyticus</i>		
RIMD2210633	Clinical isolate of serotype O3:K6; wild-type strain	[28]
VPD5	RIMD2210633 Δ pv s B (vibrioferri n -deficient mutant)	[24]
VPD54	VPD5 Δ vctA Δ irgA	[27]
VPD55	VPD5 Δ vctA Δ peuA	This study
VPD56	VPD5 Δ irgA Δ peuA	This study
VPD57	VPD5 Δ vctA Δ irgA Δ peuA	This study
VPD72	VPD5 Δ vctA Δ irgA Δ tonB1	This study
VPD73	VPD5 Δ vctA Δ irgA Δ tonB2	This study
VPD74	VPD5 Δ vctA Δ irgA Δ tonB3	This study
VPD102	VPD5 Δ vctA Δ irgA Δ peuRS	This study
VPD107	VPD5 Δ pvuA1 Δ pvuA2 Δ hutA Δ fhuA Δ iutA Δ vctA Δ irgA	This study
VPD108	VPD5 Δ pvuA1 Δ pvuA2 Δ hutA Δ fhuA Δ iutA Δ vctA Δ irgA Δ peuA	This study
VPD109	VPD5 Δ pvuA1 Δ pvuA2 Δ hutA Δ fhuA Δ iutA Δ vctA Δ irgA Δ peuRS	This study
VPD110	VPD5 Δ vctA Δ irgA Δ VP0168	This study
<i>E. coli</i>		
β 2155	<i>thrB1004 pro thi strA hsdS Δ(lacZ)ΔM15 (F' Δ(lacZ)M15 lac^f traD36 proA⁺ proB⁺) ΔdapA::erm(Em^r), pir::RP4(::kan(Km^r))</i> from SM10	[29]

doi:10.1371/journal.pone.0105749.t001

Table S2), respectively, which had been 5'-labeled with Texas Red prior to use. Each labeled primer was annealed to 10 μ g or 150 μ g of total RNA and extended with avian myeloblastosis virus RT XL (TaKaRa Biochemicals, Shiga, Japan) at 50°C for 90 min. The primer extension products were separated on a sequencing gel using an SQ5500E DNA sequencer (Hitachi High-Tech, Tokyo, Japan) alongside the DNA sequence ladder of the control region synthesized using the same primers used for the primer extension analysis.

For RT-PCR analysis, total RNA samples prepared from RIMD2210633 cells grown in LB-Tris/+EDDA medium at pH 7.0 were treated with TURBO DNase (Ambion) to remove contaminating chromosomal DNA. ReverTra Ace RT (Toyobo, Osaka, Japan) and the gene-specific primer VPA0156-R or peuS-R (see Table S2) was used to synthesize cDNA. cDNA synthesis was performed by incubating 0.5 μ g of DNase-treated RNA in a 20- μ l reaction for 60 min at 42°C. One microliter of the cDNA reaction mixture was then used as a template for PCR with the specific PCR primer pairs (see Table S2). PCR conditions were as follows: after an initial denaturation for 2 min at 95°C, DNA was amplified for 30 cycles, with each cycle consisting of denaturation at 95°C for 30 s, annealing at 55°C for 30 s, and extension at 72°C for 1 min. As a negative control, PCR omitting prior reverse transcription was performed directly for the same RNA template to confirm the absence of contaminating chromosomal DNA. PCR products were electrophoresed through 1.5% agarose gels, stained with ethidium bromide, and visualized with UV light.

For RT-qPCR analysis, total RNA samples were treated with TURBO DNase, and a 0.5- μ g aliquot of RNA was reverse transcribed with the ReverTra Ace RT and random hexamer primers (TaKaRa Biochemicals) for 60 min at 37°C. qPCR was performed using the *peuA*-specific primer pair VppeuA-qF/VppeuA-qR (see Table S2) and the Thunderbird SYBR qPCR Mix (Toyobo) in a Chromo4 Real-Time PCR detection system (Bio-Rad) under the conditions specified in the manufacturer's protocol. Relative mRNA expression levels were determined by

the comparative threshold cycle method, using the 16S rRNA expression level as an internal control. The RT-qPCR primers for 16S rRNA are listed in Table S2.

Preparation of DNA Templates and *in vitro* RNA Synthesis

Both a longer form of the truncated *peuA* fragment (+1 to +402) flanked by the T7 promoter and *flag* sequences (+1-*peuA'*-*flag* DNA) and a shorter form of the truncated *peuA* fragment (+39 to +402) flanked by T7 promoter and *flag* sequences (+39-*peuA'*-*flag* DNA) were amplified from *V. parahaemolyticus* chromosomal DNA by PCR. The primer pairs T7-VppeuA-F/T7-VppeuA-FLAG-R and T7-VppeuA-F/T7-VppeuA-FLAG-R (see Table S2) were used to amplify the longer form and the shorter form, respectively. A full-length *fur* fragment flanked by the T7 promoter and *flag* sequences (*fur*-*flag* DNA) was amplified by first-step PCR using *V. parahaemolyticus* chromosomal DNA and the primer pair T7-Vpfur-F/T7-Vpfur-FLAG-R (see Table S2), and subsequently by second-step PCR using the first-step amplicon and the primer pair UNIVERSAL/T7-Vpfur-FLAG-R (see Table S2). The amplified DNA fragments were purified by agarose gel electrophoresis and used as templates for *in vitro* RNA synthesis. The +1-*peuA'*-*flag*, +39-*peuA'*-*flag*, and *fur*-*flag* RNAs were synthesized from the +1-*peuA'*-*flag*, +39-*peuA'*-*flag*, and *fur*-*flag* DNAs, respectively, by *in vitro* transcription with T7 RNA polymerase (Roche). Following the *in vitro* transcription reaction, the reaction mixtures were treated with 1 U RQ1 DNase (Promega) and purified on a ProbeQuant G50 Micro column (GE Healthcare), followed by ethanol precipitation.

In vitro Translation Assay and Western Blotting

In vitro translation was performed using a PURESYSTM classic II (BioComber, Tokyo, Japan). For the RNA template for *in vitro* translation, either a +1-*peuA'*-*flag* RNA (30 pmol)/*fur*-*flag* RNA (3 pmol) mixture or a +39-*peuA'*-*flag* RNA (30 pmol)/*fur*-*flag* RNA (3 pmol) mixture was used. The PURESYSTM

reaction mixture (20 μ l) was incubated at 37°C for 2 h, and the reaction was then terminated by adding an equal volume of 2 \times SDS-PAGE sample buffer. The samples were separated on a 15% SDS-polyacrylamide gel, and the protein bands were transferred to a Clear Blot Membrane-P (Atto, Tokyo, Japan). The membrane was blocked with Tris-buffered saline with Tween 20 (TBST) containing 0.3% skim milk and incubated overnight at 4°C with mouse anti-FLAG M2 antibody (Sigma) diluted 1,000-fold with blocking solution. The membrane was then washed four times with TBST, incubated for 1 h at room temperature with horseradish peroxidase-conjugated anti-mouse secondary antibody (GE Healthcare), diluted 20,000-fold with blocking solution, and washed four times with TBST. Immunoreactive bands were detected with an ECL Select Western Blotting Detection Reagent (GE Healthcare) and visualized with a LAS-3000 gel imager (Fujifilm, Tokyo, Japan).

Northern Blotting

The reaction mixtures (2.5 μ l) obtained after *in vitro* translation of +1-*peuA'*-*flag* and +39-*peuA'*-*flag* RNAs were separated by electrophoresis on a 5% polyacrylamide/8 M urea gel in Tris-borate-EDTA buffer (90 mM Tris, 90 mM boric acid, 2 mM EDTA, pH 8.3), blotted onto a Biodyne B positively charged nylon membrane (Pall Corporation), and fixed to the membrane by baking for 30 min at 80°C. The digoxigenin (DIG)-labeled *peuA* probe was prepared with a primer pair, VppeuA-F/VppeuA-R (see Table S2), internal to the *peuA* gene using a DIG PCR Probe Synthesis Kit (Roche). Hybridization was performed overnight at 65°C, and the hybridized DIG-labeled *peuA* probe was detected using a DIG Luminescent Detection Kit (Roche) with a LAS-3000 image analyzer.

Results

Identification of the OMR Gene Responsible for Alkaline pH-Dependent Utilization of Ent in *V. parahaemolyticus*

We previously reported that *V. parahaemolyticus* can utilize ferric Ent as an iron source via the *VctA* and *IrgA* receptors [27]. Although the VPD54 mutant with deletion of *vctA* and *irgA* that was generated from the VPD5 vibrioferrin-deficient mutant failed to grow in LB-Tris/+EDDA medium at pH 7.0 and 8.0, it showed normal growth when Ent was added to LB-Tris/+EDDA medium (LB-Tris/+EDDA+Ent) at pH 8.0, but not at pH 7.0 (Figure 1). These data indicate that *V. parahaemolyticus* possesses a ferric Ent receptor gene that is specifically induced in response to extracellular alkaline pH and Ent. Several ferric siderophore receptors have already been identified and characterized in *V. parahaemolyticus* [23–27]; VPA0150 and VP0168 [28] have been documented as putative TonB-dependent receptors, but neither has been proven to be functional. To determine whether these receptors are involved in Ent utilization at pH 8.0, the two genes were deleted from the VPD54 mutant, and the resulting mutants, VPD57 and VPD110, were subjected to a growth assay. VPD110 grew in LB-Tris/+EDDA/+Ent medium at pH 8.0 (data not shown). In contrast, VPD57 showed no growth in LB-Tris/+EDDA/+Ent medium at pH 8.0, and the VPD57/pRK415-*peuA* complementing strain exhibited growth similar to the wild-type RIMD2210633 in the same medium (Figure 2). These data suggest that the VPA0150 gene encodes a receptor engaged in the uptake of ferric Ent at pH 8.0. In this paper, the VPA0150 gene is termed *peuA* (*peu* stands for *V. parahaemolyticus* Ent utilization).

Identification of *PeuA* by SDS-PAGE and Determination of Its N-Terminal Amino Acid Sequence

To assess whether extracellular alkaline pH and Ent affect OMP profiles, OMP fractions prepared from *V. parahaemolyticus* mutants were analyzed by SDS-PAGE. The wild-type *V. parahaemolyticus* expresses several iron-repressible OMRs under iron-limiting conditions, as shown in Figure 3, lane 2. We used a VPD107 mutant lacking all of the known iron-repressible OMPs for this experiment, to eliminate potential interference by these OMPs. In LB-Tris/+EDDA medium at pH 7.0, VPD107 was unable to produce *PeuA*, regardless of Ent presence (Figure 3, lanes 3 and 4). In contrast, when VPD107 was grown in LB-Tris/+EDDA medium at pH 8.0, a faint protein band was detected (Figure 3, lane 5); the sequence of its first 10 N-terminal amino acids was determined to be NVQTDEHLVV. This sequence exactly matched the N-terminal sequence deduced from *peuA* (see Figure 4A), indicating that *peuA* indeed encodes the ferric Ent receptor. The production of *PeuA* in VPD107 was remarkably increased in LB-Tris/+EDDA+Ent medium at pH 8.0 (Figure 3, lane 6). These results indicate that *PeuA* is not produced in significant amounts, even under iron-limiting conditions at pH 8.0, unless Ent is present in the growth medium. In addition, VPD108, a *peuA* deletion mutant derived from VPD107, failed to produce *PeuA* in LB-Tris/+EDDA/+Ent medium at pH 8.0, whereas the complementing strain VPD108/pRK415-*peuA* restored the ability to produce *PeuA* (Figure 3, lanes 7 and 8).

In silico Sequence Analyses of *peuA* and Its Adjacent Genes

A map of *peuA* and the neighboring genes is shown in Figure 4A, accompanied by partial nucleotide and deduced amino acid sequences [28]. *PeuA* shared amino acid similarity with many ferric hydroxamate-type siderophore receptors, such as FhuE (25% identity over 751 amino acids) of *E. coli* [36]; however, it displayed lower sequence similarity with FepA (20% identity over 729 amino acids) and PfeA (23% identity over 226 amino acids), the ferric Ent receptors of *E. coli* [37] and *P. aeruginosa* [13], respectively. A putative Fur box sequence resembling the consensus binding site for the Fur protein in *E. coli* [38] was detected in the promoter region of *peuA* (Figure 4A), and indeed this region cloned on pUC19 was positive in the Fur titration (FURTA) *in vivo* assay [39] (data not shown), indicating that the cloned region harbor the binding site of the *E. coli* Fur protein. Moreover, a tandem repeat of 5'-A(N)₃GCAAA(N)₄GTAAA-3' (the conserved nucleotides are underlined), termed the CpxR-box [40,41], which is typical of the CpxR-binding site, was identified in the promoter region of *peuA* (Figure 4A).

Homology searches revealed the existence of putative two-component regulatory system genes (VPA0148-0149), collectively named *peuRS*, immediately upstream of *peuA* (Figure 4A). *PeuR* and *PeuS* showed amino acid sequence similarity to components of the CpxAR signaling system [42], such as the *P. aeruginosa* PfeR response regulator (36% identity over 225 amino acids) [14] and the *E. coli* CpxA histidine sensor kinase (24% identity over 447 amino acid residues) [43]. The consensus amino acid sequences in the conserved domains of the response and sensor components [13,15] were also determined for *PeuR* and *PeuS*. In addition, they displayed striking structural features, including the presence of invariant amino acid residues, aspartic acid-9 in *PeuR* and histidine-244 in *PeuS*, both of which probably serve as phosphorylation sites. The hydropathy profile revealed that *PeuS* contains two transmembrane-spanning regions and an intervening 115-amino acid extracytoplasmic loop domain that is exposed to

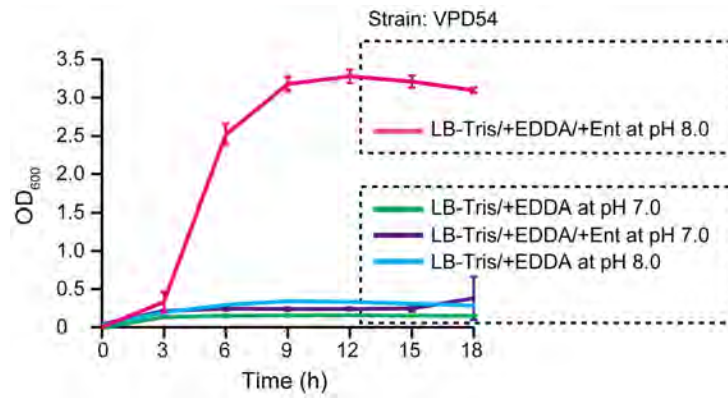


Figure 1. Alkaline pH-dependent utilization of Ent in VPD54. VPD54, which is a *vctA* and *irgA* deletion mutant generated from the VPD5 vibrioferrin-deficient mutant, was grown in LB-Tris/+EDDA medium (at indicated pH) at 37°C for 18 h with shaking at 70 rpm. When required, Ent was added at 5 μM. Cultures were monitored by measuring the OD₆₀₀ every 3 h. Data are shown as means ± SD from 3 separate experiments. doi:10.1371/journal.pone.0105749.g001

the cytoplasmic space. These features of PeuRS are illustrated in Figure S1. Moreover, the cloned promoter region of *peuR* also showed a FURTA-positive phenotype (data not shown), indicative of the presence of the Fur binding site.

Identification of *peuA/VPA0151-0156* and *peuRS* as Iron-Repressible Operons by RT-PCR

The *VPA0151-0156* genes, including the *ttpC2-tonB2* system genes, are located downstream of the *peuA* gene, and the open reading frames of the *VPA0151-0156* genes have overlapping stop and start codons, an arrangement typical of transcription unit boundaries in prokaryotic genomes [44]. Although there is a 53-bp gap, including an inverted repeat, immediately downstream of *peuA*, this region contains no potential promoter sequences for the downstream *tonB2* operon (data not shown). As expected, RT-PCR using the primer pairs designed to cover the respective intergenic regions of the *peuA* and *VPA0151-0156* genes produced extension bands of the expected size for total RNA prepared from the wild-type strain grown in LB-Tris/+EDDA at pH 7.0 (Figure 4B and C), indicating that these genes are co-transcribed in an iron-regulated operon.

The stop codon of *peuR* overlaps with the start codon of *peuS*, and no definitive promoter sequence was detected upstream of *peuS*. An RT-PCR product of the expected size was also detected

for total RNA prepared from the wild-type strain grown in LB-Tris/+EDDA at pH 7.0 when the primer pair VppeuR-F/VppeuS-R was used to amplify the intergenic region between the *peuRS* genes (Figure 4B and C), indicating that these genes also comprise an iron-regulated operon.

Involvement of the *peuRS* Genes in Ent Utilization at pH 8.0

To investigate the requirement of *peuRS* for Ent utilization at pH 8.0 under iron-limiting conditions, we generated the *peuRS* mutant VPD102 from VPD54, which possesses the *peuA* gene but not the *vctA* and *irgA* genes, for use in a growth assay. While VPD102 abolished the Ent-mediated growth observed for VPD54 in LB-Tris/+EDDA medium at pH 8.0, the complementing strain VPD102/pRK415-*peuRS* grew well in the same medium (Figure 2). Furthermore, to examine the effect of *peuRS* on *PeuA* production by SDS-PAGE, the VPD109 mutant with the *peuRS* operon deleted was constructed from VPD107. VPD109 showed a complete lack of *PeuA*, even in LB-Tris/+EDDA/+Ent medium at pH 8.0 (Figure 3, lane 9); however, the complementing strain VPD109/pRK415-*peuRS* restored the ability to produce *PeuA* in the same medium (Figure 3, lane 10). Taken together, these data highlight a possible role of the *PeuRS* two-component regulatory system in the production of *PeuA* induced by alkaline pH and Ent.

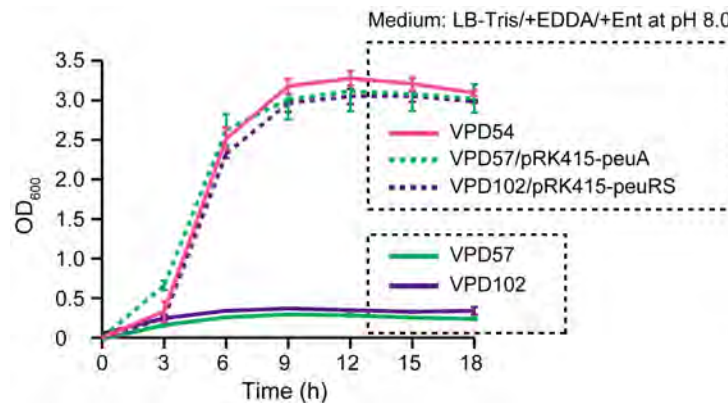


Figure 2. Involvement of *peuA* and *peuRS* in Ent utilization. The growth assay was performed as described in Figure 1. Data are shown as means ± SD from 3 separate experiments. doi:10.1371/journal.pone.0105749.g002

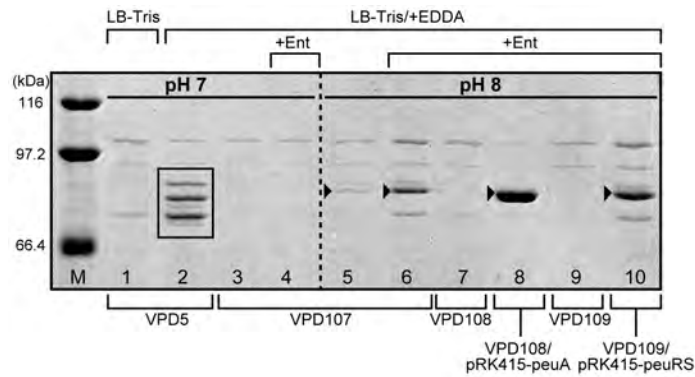


Figure 3. SDS-PAGE analysis of Sarkosyl-insoluble OMPs of *V. parahaemolyticus*. SDS-PAGE analysis was performed with VPD5, VPD107 (seven iron-repressible OMRs-deficient mutant derived from VPD5), VPD108 (*peuA*-deficient mutant derived from VPD107), VPD108/pRK415-*peuA*, VPD109 (*peuRS*-deficient mutant derived from VPD107), and VPD109/pRK415-*peuRS*. The OMP fractions were prepared from cells grown in LB-Tris medium at pH 7.0, LB-Tris/+EDDA media at pH 7.0 and 8.0, or LB-Tris/+EDDA/+Ent media at pH 7.0 and 8.0. Lanes 1–7 and 9–10 were loaded with 20 μ g OMPs, and lane 8 was loaded with 3 μ g OMPs. Electrophoresis was performed on 7.5% SDS-polyacrylamide gels (130 mm long) at a constant current of 15 mA at 4°C. The gel was stained with Coomassie Brilliant Blue. The figure shows only the relevant portions of the gel. The iron-repressible OMPs expressed by VPD5 at pH 7.0 under iron-limiting conditions are boxed in lane 2. Lane M, molecular weight marker proteins; closed arrowheads, *PeuA*.

doi:10.1371/journal.pone.0105749.g003

Iron-Repressible Transcription of *peuR*

To determine the transcriptional start site for *peuR*, and to test whether its expression is iron-regulated, primer extension analysis was also performed for total RNA samples of VPD54 cells grown in LB-Tris and LB-Tris/+EDDA media. The transcription of *peuR* was unambiguously derepressed in LB-Tris/+EDDA medium, independent of pH (Figure 5A), and the transcription start site (+1) of *peuR* was determined to be 29 nucleotides upstream of its start codon (Figure 4A). It is evident from these data that the *peuRS* operon is constitutively expressed under iron-limiting conditions.

Induction of an Alternative Transcript of *peuA* under Iron-Limiting Conditions in Response to Extracellular Alkaline pH and Ent

Primer extension analyses were performed with total RNA samples of both VPD54 and its *peuRS* deletion mutant VPD102. Two primer extension products were detected, when total RNA samples prepared from VPD54 grown in LB-Tris/+EDDA media at pH 7.0 and 8.0 or LB-Tris/+EDDA/+Ent medium at pH 7.0 were used as the templates. However, the growth of VPD54 was not promoted under the same conditions. Two probable transcription start sites of *peuA* were mapped to 105 bp and 104 bp upstream of the *peuA* ATG start codon (Figure 5B); hereafter, the transcripts from the +1 and +2 sites are collectively referred to as the +1 transcript. Another transcription start site for *peuA* (+39 transcript) was detected 67 bp upstream of its start codon, when VPD54 was grown in LB-Tris/+EDDA/+Ent medium at pH 8.0 (Figure 5B). In addition, the growth of VPD54 was promoted under the same conditions. These results suggested that the +1 transcript is not responsible for the growth of VPD54 as shown in Figure 1. Interestingly, the primer extension product of the +39 transcript was not detected when VPD102 was grown in the same medium at pH 7.0 (Figure 5B). However, when primer extension analysis was performed using a 15-fold excess of RNA, a small amount of the primer extension product of the +39 transcript was also detected in VPD54 cells grown in LB-Tris/+EDDA medium at pH 8.0, even when Ent was absent from the medium (Figure 5C). This is consistent with the expression of *PeuA* in VPD107 grown under the same conditions (Figure 3, lane

5), and this low level of *PeuA* expression in VPD107 under iron-limiting conditions may contribute to the initial uptake of ferric Ent for stimulation of *PeuS* prior to induction of *peuA* expression at pH 8.0. However, no extension band was detected for total RNA prepared from VPD54 grown in LB-Tris medium, suggesting that the putative Fur box detected in the promoter region of *peuA* (Figure 4A) was functional for the iron-repressive regulation of *peuA*. Collectively, these findings indicate that *peuA* mRNA is transcribed as the +1 transcript under iron-limiting conditions irrespective of Ent and pH, while the +39 transcript responsible for the expression of *PeuA* is expressed in trace amounts in LB-Tris/+EDDA medium at pH 8.0 and is significantly increased by the presence of Ent under the same conditions. These data also suggested that the increase in the +39 transcript was absolutely dependent on the *PeuRS* two-component regulatory system. In addition, two sets of the -35 and -10 promoter sequences are properly positioned for transcription from the +1 and +39 sites (Figure 4A).

To confirm the iron-regulated expression of *peuA*, RT-qPCR analysis was performed. At pH 7.0 and 8.0, the transcription of *peuA* was strongly induced in VPD54 and VPD102 in LB-Tris/+EDDA medium (10- to 20-fold increases compared to the level in LB-Tris medium) (Figure 6). Moreover, in LB-Tris/+EDDA medium at pH 7.0, VPD54 produced *peuA* mRNA at similar levels in the presence and absence of Ent; however, the addition of Ent to LB-Tris/+EDDA medium at pH 8.0 conspicuously increased the level of *peuA* mRNA (Figure 6). Considering the results of primer extension analysis (Figure 5B), these data suggested that the increase in the *peuA* mRNA was due to transcription from the +39 site. No such effect of Ent on *peuA* transcription at pH 8.0 was observed for the *peuRS*-deletion mutant VPD102 (Figure 6), implying that the *peuRS* operon is responsible for the transcription of *peuA* from the +39 site.

mRNA Secondary Structure Prediction

The results shown in Figure 3 indicate that remarkable amounts of *PeuA* are produced under iron-limiting conditions in response to an extracellular pH of 8.0, but not 7.0, and Ent. This corresponds with appearance of the +39 transcript, in addition to +1 transcription, under the same growth conditions. These

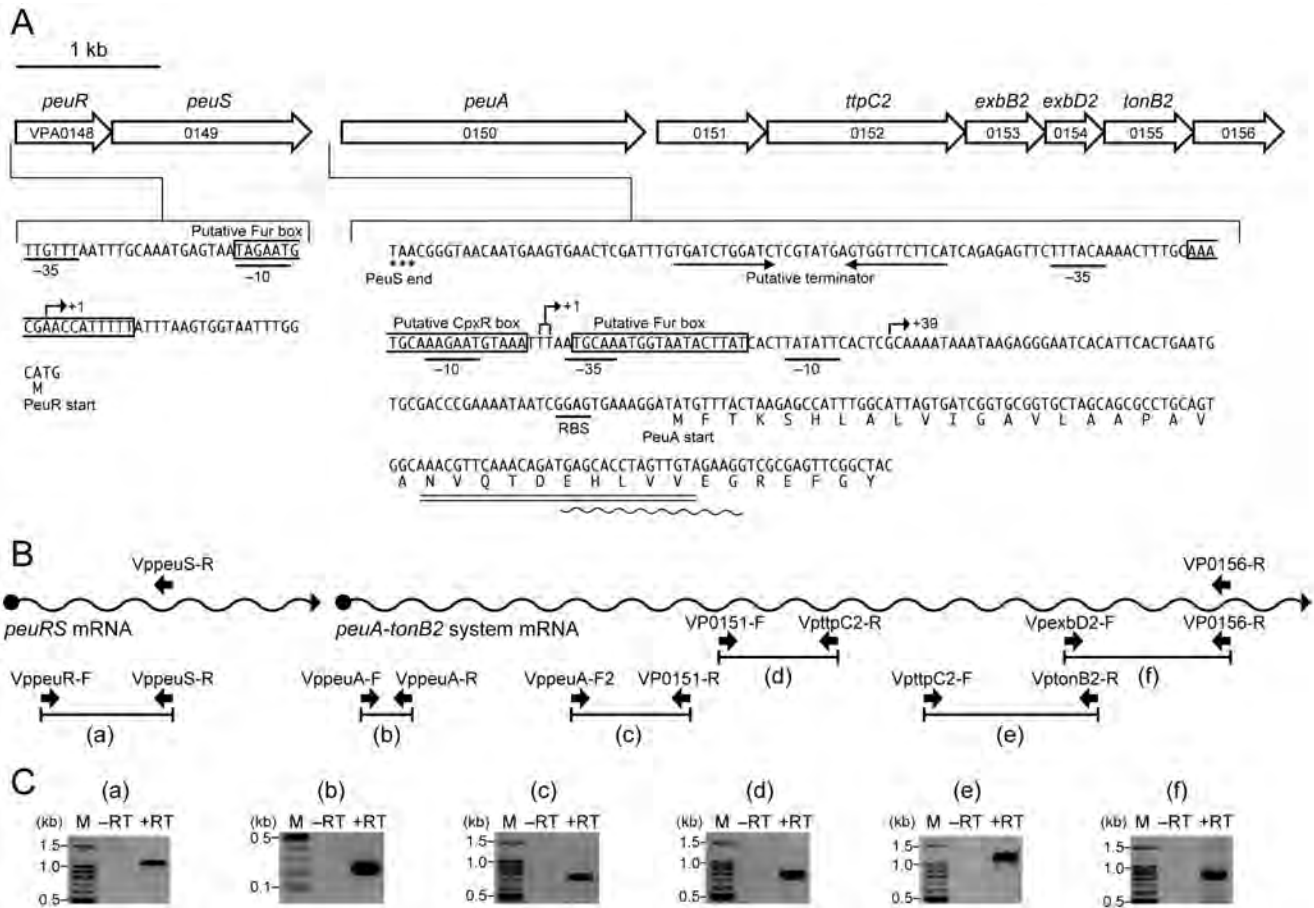


Figure 4. Genetic map and operon structure of VPA0148-VPA0156 locus. (A) Genetic map of the *peuA* gene and the flanking genes. Thick arrows indicate genes and their orientations. The -35 and -10 promoter elements and putative Fur box sequences in the promoter regions of *peuR* (VPA0148) and *peuA* (VPA0150) are indicated. The transcription start sites for *peuR* (+1) and *peuA* (+1 and +39) are indicated by right-angled arrows. The putative terminator signal between the *peuS* and *peuA* genes, the predicted RBS for the *peuA* gene, the start codons for *peuR* and *peuA* genes, and the stop codon for *peuS* are also indicated. The amino acid sequence consistent with the N-terminal sequence determined for the iron-repressible OMR induced in LB-Tris/+EDDA and LB-Tris/+EDDA/+Ent media at pH 8.0 (see Figure 3) is indicated by a double underline. (B) Schematic representation of mRNAs transcribed from the VPA0148-VPA0156 genes and the primer pairs used for RT-PCR. For preparation of cDNAs by RT, VPpeuS-R and VP0156-R were used. (C) RT-PCR analysis of RT-PCR products. +RT and -RT, RT-PCR was performed with and without reverse transcriptase, respectively. M, 100-bp DNA ladder. doi:10.1371/journal.pone.0105749.g004

findings led us to hypothesize that these transcripts might contain regulatory signals in their 5'-untranslated regions (UTRs) that couple transcription to translation. Thus, to better define the nature of these transcripts, the secondary structures of their 5'-UTRs were predicted using the CENTROIDFOLD program (<http://www.ncrna.org/centroidfold/>) [45]. Figure 7A shows that the first 40 nucleotides of the 5'-UTR of the +1 transcript are folded into the secondary structure with the ribosomal binding site (RBS) and the start codon of *peuA* to block initiation of translation. As opposed to the +1 transcript, the +39 transcript does not form an inhibitory structure in its 5'-UTR, thus allowing initiation of translation (Figure 7B). Therefore, we hypothesized that PeuA production might be dependent on the translation of the +39 *peuA* transcript.

The +39 Transcript is Responsible for PeuA Production

To test the above hypothesis, an *in vitro* translation assay was performed. The RNA templates for *in vitro* translation, i.e., +1-*peuA'*-*flag* (Figure 7A), +39-*peuA'*-*flag* (Figure 7B), and *fur*-*flag* RNAs, were constructed by *in vitro* transcription using DNA

templates containing the T7 promoter. The *in vitro* translation products were analyzed by SDS-PAGE followed by western blotting using anti-FLAG IgG. The PeuA'-FLAG product was not detected when a mixture of +1-*peuA'*-*flag* RNA and *fur*-*flag* RNA was used for *in vitro* translation, even though Fur-FLAG, a positive control for *in vitro* translation, was detected; however, when a mixture of +39-*peuA'*-*flag* RNA and *fur*-*flag* RNA was used as the template, a significant amount of PeuA'-FLAG was detected along with Fur-FLAG (Figure 8A). Simultaneously, the +1-*peuA'*-*flag* RNA and +39-*peuA'*-*flag* RNA in each reaction mixture for *in vitro* translation were validated by northern blotting using a DIG-labeled *peuA* probe (Figure 8B). These data are concordant with the secondary structures predicted for the +1 and +39 transcripts of *peuA*.

TonB Specificity of PeuA

V. parahaemolyticus contains up to three TonB clusters encoding TonB1 and TonB2 systems on the small chromosome and a TonB3 system on the large chromosome, and the TonB2 system is located downstream of *peuA*. To determine which TonB

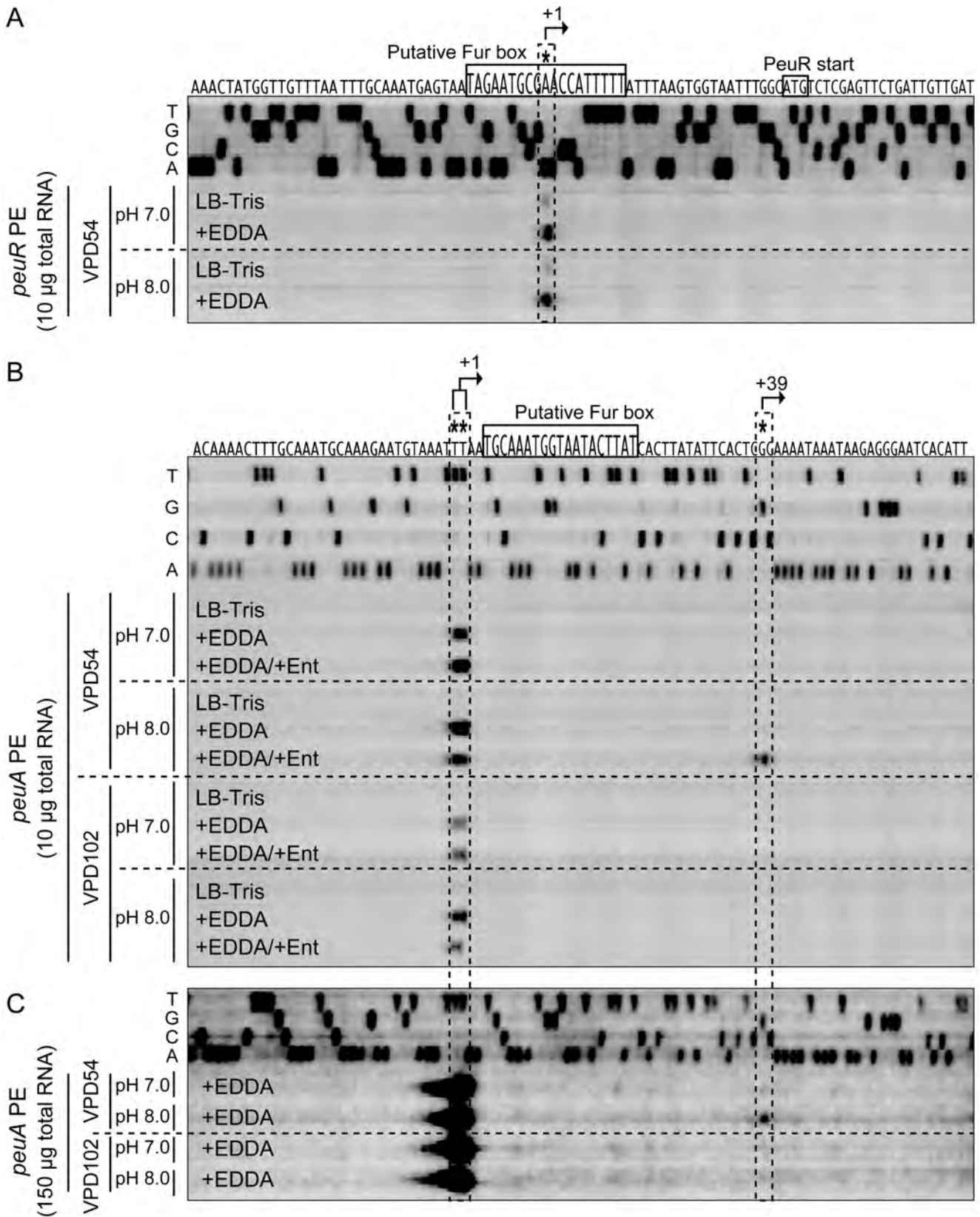


Figure 5. Primer extension analyses of total RNA from VPD54 or VPD102 to determine the transcription start sites of *peuR* (A) and *peuA* (B and C). Total RNAs were isolated from VPD54 (*vctA*- and *irgA*-deficient mutant derived from VPD5) and VPD102 (*peuRS*-deficient mutant derived from VPD54) grown at pH 7.0 and 8.0 in LB-Tris, LB-Tris/+EDDA, and LB-Tris/+EDDA/+Ent media. The amounts of total RNA and primers used for reverse transcription were as follows: (A) 10 µg *Vp*peuR-PE, (B) 10 µg *Vp*peuA-PE, and (C) 150 µg *Vp*peuA-PE. The same primers used for primer extension analysis were used to generate the sequence ladders (A, C, G, T). The transcription start sites and putative Fur boxes are indicated at the top of panels A and B (also see Figure 3A).

doi:10.1371/journal.pone.0105749.g005

systems are involved in the transport of ferric Ent via PeuA, a set of isogenic *tonB* deletion mutants were constructed from VPD54. A growth assay showed that only the VPD73 mutant deficient in *tonB2* lost the ability to grow in LB-Tris/+EDDA/+Ent medium at pH 8.0; however, the VPD72 and VPD74 mutants deficient in *tonB1* and *tonB3*, respectively, grew as well as their parental strain, VPD54, in the same medium (Figure S2). These observations show that the TonB2 system functions as an energy modulator for PeuA.

Distribution of Orthologs of the *V. parahaemolyticus* *PeuRSA-VPA0151-VPA0156* Genes Among Other *Vibrio* Species

Using BLAST analyses, we examined whether orthologs to the *V. parahaemolyticus* *peuRSA-VPA0151-VPA0156* locus genes are distributed among the whole-genome sequences of other *Vibrio* species. Although the *VPA0151-VPA0156* (the *tpC2-tonB2* system genes) cluster was identified in all *Vibrio* species examined, *peuRS* and *peuA* orthologs were identified only in *V. alginolyticus*, *V. harveyi*, and *V. campbellii*, which belong to the same phylogenetic group (the *V. harveyi* group) as *V. parahaemolyticus* [20] (Figure 9). However, all *peu* orthologs are absent from *V. cholerae* and *V. vulnificus*, and *V. fischeri* and *V. splendidus* possess the *peuA* ortholog, but not the *peuRS* orthologs.

Discussion

Based on the results obtained in this study, we propose a mechanism for enhanced expression of the *V. parahaemolyticus* *peuA* through the action of PeuRS in response to extracellular alkaline pH and Ent (Figure S3). Our data showed that *peuA* is transcribed in a polycistronic mRNA with the *VPA0151-VPA0156* genes under iron-limiting conditions (Figure 4B). However, at neutral pH, translation of the +1 *peuA* transcript appeared to be inhibited by the formation of a secondary structure in its 5'-UTR that blocks the RBS and start codon of *peuA* (Figure 7A); in contrast, the *VPA0151-VPA0156* mRNA responsible for the TonB2 system was expected to be translated normally under the same conditions, because the RBSs and start codons of their genes are available for ribosomal access. This expectation is supported by the fact that the *V. parahaemolyticus* PvuA1 is exclusively dependent on the energy transduced by the TonB2

system [24] and remains fully functional as the ferric vibrioferrin receptor under iron-limiting conditions at neutral pH. When grown under iron-limiting conditions at pH 8.0, *V. parahaemolyticus* expressed the *peuA-VPA0151-VPA0156* polycistronic mRNA from the +39 start site that was induced via the two-component regulatory system, PeuRS (Figure 5B). No inhibitory secondary structure was identified in the 5'-UTR of the +39 transcript; in other words, PeuA is synthesized owing to the translation of the +39 transcript (Figure 7B). Moreover, as shown in Figures 3, 5, and 6, the levels of PeuA and the +39 transcript expressed under iron-limiting conditions were more markedly elevated in the presence than in the absence of Ent. These observations indicate that Ent functions as a potent inducer for transcription from the +39 site, with the aid of PeuRS.

A number of Gram-negative bacteria, including *P. aeruginosa* [46], *Bordetella* spp. [47], *V. cholerae* [48], *V. anguillarum* [49], *V. parahaemolyticus* [27], and *Neisseria gonorrhoeae* [50], are known to utilize Ent as a xenosiderophore, which induces the cognate ferric Ent receptors under iron-limiting conditions. Such a wide distribution of this system in bacteria may be explained by the fact that Ent has an exceptionally high affinity for ferric iron, and its production by bacterial species is wider than previously thought [51]; Ent has been reported to be synthesized and excreted by most enterics [52], as well as two Gram-positive *Streptomyces* species [53]. Moreover, ferric Ent is more stable at alkaline pH than ferric hydroxamate-type siderophores [54]. In the pathogens described above, except for *P. aeruginosa*, the AraC-like or LysR-like transcriptional regulators operate to induce these ferric Ent receptors. *P. aeruginosa* has been reported to utilize Ent through the two-component regulatory system PfeRS [13,14]; however, expression of the ferric Ent receptor (PfeA) in this species is enhanced in response to Ent under iron-limiting conditions [46], and only a single set of promoter sequences (-10 and -35) are present in the region upstream of *pfeA* [14]. Another unique two-component regulatory system, operating through heme-dependent regulation, has been described in the Gram-positive bacterium *Corynebacterium diphtheriae* for the expression of a heme oxygenase gene responsible for the utilization of heme as an iron source [55]. In these systems, the signal molecules likely interact with the sensors, leading to activation of the response regulators.

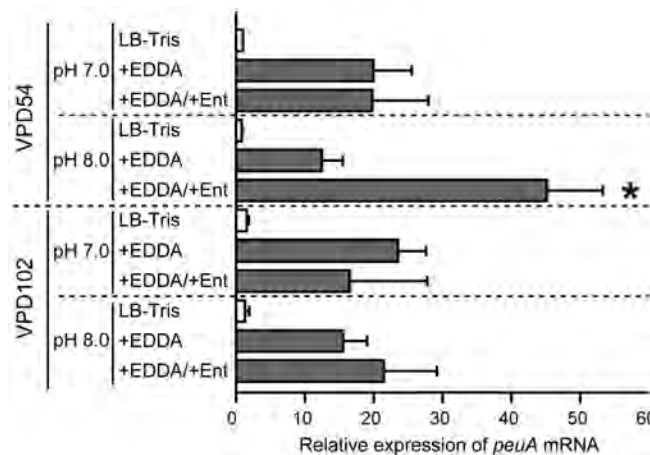


Figure 6. Relative levels of *peuA* mRNA, assessed by RT-qPCR. Total RNA samples were prepared from VPD54 (*vctA*- and *irgA*-deficient mutant derived from VPD5) and VPD102 (*peuRS*-deficient mutant derived from VPD54) grown at pH 7.0 and 8.0 in LB-Tris, LB-Tris/+EDDA, and LB-Tris/+EDDA/+Ent media. Data are shown as means ± SD from 3 separate experiments. An asterisk indicates $P < 0.05$ compared to other samples. doi:10.1371/journal.pone.0105749.g006

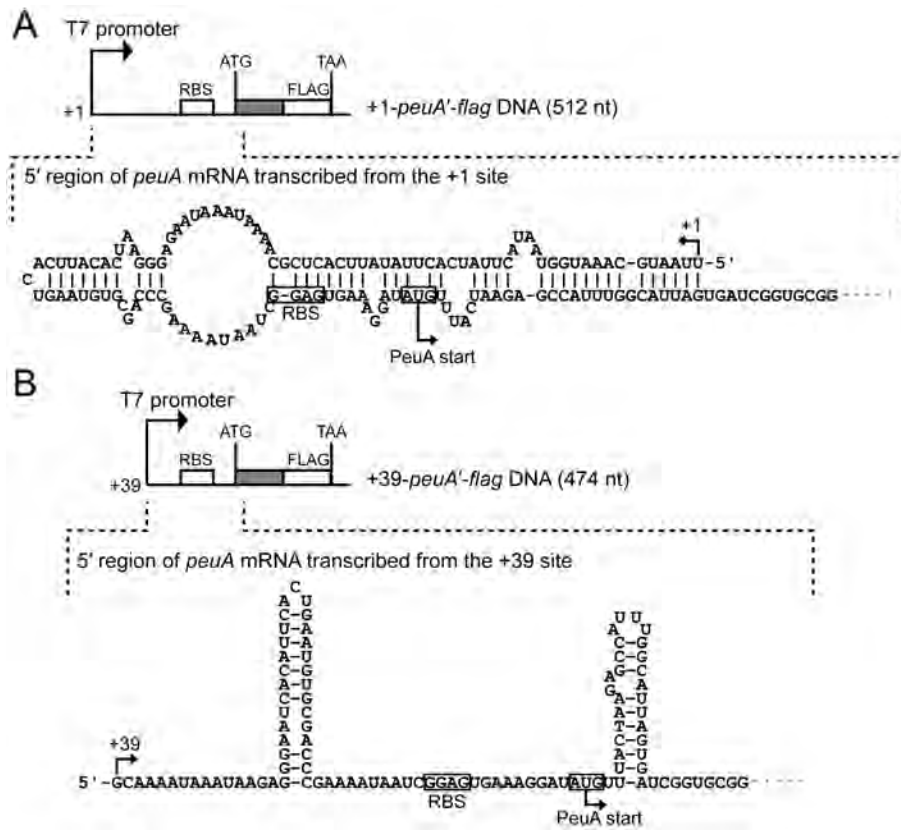


Figure 7. Schematic representation of the +1-*peuA'*-flag (A) and +39-*peuA'*-flag (B) DNA fragments. Each of these DNA fragments includes a nucleotide sequence corresponding to the *peuA* 5'-UTR from the +1 or +39 sites and the nucleotide sequence for the N-terminal 99 amino acid residues (in gray), in addition to a T7 promoter and a FLAG tag preceding the stop codon (TAA). The secondary structures of the 5'-UTRs of the +1 transcript (A) and the +39 transcript (B) of *peuA* are shown, both of which were predicted by the CentroidFold software (<http://www.ncrna.org/centroidfold/>). The RBS and start codon of *peuA* mRNA are boxed in the secondary structures. doi:10.1371/journal.pone.0105749.g007

The *E. coli* CpxAR two-component regulatory system is well known to be involved in counteracting extracellular stresses, including alkaline pH exposure [56,57]. Extracellular signals cause a conformational change in CpxA, stimulating the autophosphorylation of a conserved histidine residue. Once this residue is

phosphorylated, CpxA acts as a kinase and phosphorylates a conserved aspartate residue on CpxR. Phosphorylated CpxR acts on its target gene as a transcriptional activator [42]. Considering that PeuRS is homologous to members of the Cpx signaling system, it seems likely that the conformation of PeuS is altered to

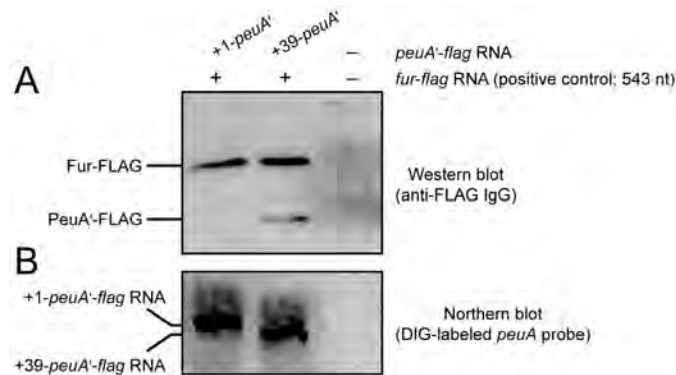


Figure 8. *In vitro* translation of *peuA* mRNA. (A) *In vitro* translation analysis of the +1 and +39 *peuA* transcripts labeled with the FLAG tag. The +1-*peuA'*-flag RNA and +39-*peuA'*-flag RNA were first synthesized by *in vitro* transcription, as described in the MATERIALS AND METHODS, and a mixture containing either the +1-*peuA'*-flag RNA (30 pmol)/*fur*-flag RNA (3 pmol) or the +39-*peuA'*-flag RNA (30 pmol)/*fur*-flag RNA (3 pmol) as the template was subjected to *in vitro* translation. The FLAG-fused proteins translated were separated on 15% SDS-polyacrylamide gels, and were detected by western blotting using anti-FLAG IgG. (B) Confirmation of the presence of +1-*peuA'*-flag RNA and +39-*peuA'*-flag RNA in the reaction mixture for *in vitro* translation. These RNA fragments were detected in the reaction mixture by northern blotting using a DIG-labeled *peuA* probe. doi:10.1371/journal.pone.0105749.g008

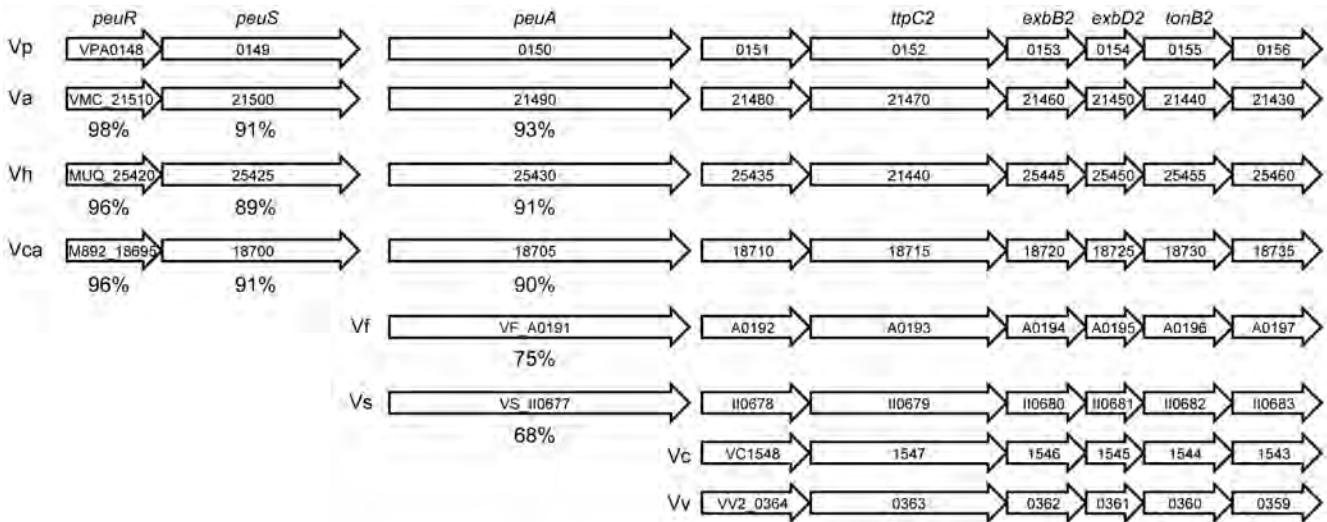


Figure 9. Distribution of the *Vibrio parahaemolyticus* VPA0148–VPA0156 orthologs in other *Vibrio* species for which whole-genomic sequences have been reported. Arrows represent genes and their orientations. The numbers below the genes indicate percent amino acid sequence similarities to *V. parahaemolyticus* PeuRS and PeuA. Vp, *V. parahaemolyticus*; Va, *V. alginolyticus*; Vh, *V. harveyi*; Vca, *V. campbellii*; Vf, *V. fischeri*; Vs, *V. splendidus*; Vc, *V. cholerae*; Vv, *V. vulnificus*. doi:10.1371/journal.pone.0105749.g009

initiate the signal transduction cascade in response to an extracellular alkaline pH and Ent, although it is not known whether these stimuli interact with PeuS separately or cooperatively. The activated PeuS phosphorylates PeuR, and the resulting phosphorylated PeuR is expected to bind to the *peuA* promoter region to induce transcription from the +39 site. However, it remains unclear whether additional factor(s) are required to transduce the signals of extracellular alkaline pH and Ent.

V. parahaemolyticus has also been reported to utilize Ent through two other ferric Ent receptors, VctA and IrgA [27]. In this study, these receptors were ascertained to operate under iron-limiting conditions at pH 8.0 (see Figure S4). Therefore, it is likely that the PeuA-mediated Ent utilization system is substituted and/or supplemented by Ent utilization via VctA and IrgA, and vice versa, signifying that, in bacteria, the expression of multiple siderophore receptors may be a common strategy or a backup system to capture the iron essential for survival and proliferation. Moreover, from evolutionary and ecological points of view, it is of interest that the *peuRSA* cluster is restrictively distributed in the phylogenetic group that includes *V. alginolyticus*, *V. harveyi*, and *V. campbellii* in addition to *V. parahaemolyticus*, all of which live in marine or estuarine environments at a pH of approximately 8.1 [58], often in association with plankton or animals, including fish and shellfish [19,20]. However, it is uncertain whether *V. parahaemolyticus* and the other species naturally encounter Ent. Alternatively, the authentic ligand for PeuA and PeuS could be another siderophore structurally similar to Ent that is produced by microorganisms inhabiting the same niches as *V. parahaemolyticus*.

In conclusion, our study establishes that under iron-limiting conditions, the *V. parahaemolyticus* two-component regulatory system PeuRS functions in concert with extracellular alkaline pH and Ent for the induction of *peuA* transcription at the +39 site, leading to production of PeuA. Further studies are needed to clarify the molecular mechanisms by which the PeuRS two-component system is activated in response to extracellular alkaline pH and Ent to induce transcription beginning at the +39 site.

Supporting Information

Figure S1 Amino acid sequences of PeuR (A) and PeuS (B). Consensus amino acid residues in the conserved regions are boxed, and invariant amino acid residues (proposed to be important for the function of PeuRS) are indicated by asterisks. In panel B, transmembrane (TM) helices proposed by the HMMTOP transmembrane topology prediction server (<http://www.enzim.hu/hmmtop/index.php>) are underlined. (C) A hydrophathy plot of PeuS. The hydrophatic index was calculated by the method of Kyte and Doolittle using a window of 21 amino acid residues. Solid bars correspond to the TM helices shown in panel B. (PDF)

Figure S2 TonB specificity of PeuA in Ent utilization. The growth assay was performed as described in Figure 1. Data are shown as means ± SD from 3 separate experiments. (PDF)

Figure S3 Proposed expression mechanism for *V. parahaemolyticus* PeuA ferric Ent receptor under iron-limiting conditions in response to extracellular alkaline pH and Ent. Thick arrows and wavy arrows represent the open reading frames and the direction of transcription and mRNAs, respectively. (A) Under iron-limiting conditions at pH 7.0, *peuA* is co-transcribed with VPA0151–VPA0156 from the +1 transcription start site. However, the transcript from the +1 site forms a secondary structure within its 5'-UTR, leading to inhibition of translation of the *peuA* mRNA, although the remaining VPA0151–VPA0156 mRNA is translated. (B) Under iron-limiting conditions at pH 8.0 in the absence of Ent, transcription of the *peuA/VPA0151–VPA0156* operon from the +39 site also occurs to a slight extent, combined with normal transcription beginning at the +1 site. The presence of Ent under iron-limiting conditions at pH 8.0 is proposed to result in induction of transcription from the +39 site, and thereby leads to enhanced expression of the ferric Ent receptor PeuA, because the RBS and start codon of *peuA* in the +39 transcript are available for translation initiation. The *peuA* gene, therefore, is optimally expressed under iron-limiting

conditions in response to extracellular alkaline pH and Ent. In addition, the two-component regulatory system, *PeuRS*, is proposed to be necessary to activate *peuA* transcription in response to these signals. (PDF)

Figure S4 Growth assays of the VPD54, VPD55, VPD56, and VPD57 mutants in LB-Tris/+EDDA/+Ent medium at pH 8.0. The growth assay was performed as described in Figure 1. Data are shown as means ± SD from 3 separate experiments. (PDF)

References

1. Andrews SC, Robinson AK, Rodriguez-Quinones F (2003) Bacterial iron homeostasis. *FEMS Microbiol Rev* 27: 215–237.
2. Braun V, Hantke K, Koster W (1998) Bacterial iron transport: mechanisms, genetics, and regulation. *Met Ions Biol Syst* 35: 67–145.
3. Ratledge C, Dover LG (2000) Iron metabolism in pathogenic bacteria. *Annu Rev Microbiol* 54: 881–941.
4. Hider RC, Kong X (2010) Chemistry and biology of siderophores. *Nat Prod Rep* 27: 637–657.
5. Noijnaj N, Guillier M, Barnard TJ, Buchanan SK (2010) TonB-dependent transporters: regulation, structure, and function. *Annu Rev Microbiol* 64: 43–60.
6. Postle K, Larsen RA (2007) TonB-dependent energy transduction between outer and cytoplasmic membranes. *Biometals* 20: 453–465.
7. Koster W (2001) ABC transporter-mediated uptake of iron, siderophores, heme and vitamin B12. *Res Microbiol* 152: 291–301.
8. Escolar L, Perez-Martin J, de Lorenzo V (1999) Opening the iron box: transcriptional metalloreulation by the Fur protein. *J Bacteriol* 181: 6223–6229.
9. Hantke K (2001) Iron and metal regulation in bacteria. *Curr Opin Microbiol* 4: 172–177.
10. Miethke M, Marahiel MA (2007) Siderophore-based iron acquisition and pathogen control. *Microbiol Mol Biol Rev* 71: 413–451.
11. Schubert S, Fischer D, Heesemann J (1999) Ferric enterochelin transport in *Yersinia enterocolitica*: molecular and evolutionary aspects. *J Bacteriol* 181: 6387–6395.
12. Brickman TJ, Armstrong SK (2009) Temporal signaling and differential expression of *Bordetella* iron transport systems: the role of ferrimones and positive regulators. *Biometals* 22: 33–41.
13. Dean CR, Poole K (1993) Expression of the ferric enterobactin receptor (*PfeA*) of *Pseudomonas aeruginosa*: involvement of a two-component regulatory system. *Mol Microbiol* 8: 1095–1103.
14. Dean CR, Neshat S, Poole K (1996) *PfeR*, an enterobactin-responsive activator of ferric enterobactin receptor gene expression in *Pseudomonas aeruginosa*. *J Bacteriol* 178: 5361–5369.
15. Albright LM, Huala E, Ausubel FM (1989) Prokaryotic signal transduction mediated by sensor and regulator protein pairs. *Annu Rev Genet* 23: 311–336.
16. Hoch JA, Varughese KI (2001) Keeping signals straight in phosphorelay signal transduction. *J Bacteriol* 183: 4941–4949.
17. Rowley G, Spector M, Kormanec J, Roberts M (2006) Pushing the envelope: extracytoplasmic stress responses in bacterial pathogens. *Nat Rev Microbiol* 4: 383–394.
18. Broberg CA, Calder TJ, Orth K (2011) *Vibrio parahaemolyticus* cell biology and pathogenicity determinants. *Microbes Infect* 13: 992–1001.
19. Igbinoza EO, Okoh AI (2008) Emerging *Vibrio* species: an unending threat to public health in developing countries. *Res Microbiol* 159: 495–506.
20. Thompson FL, Iida T, Swings J (2004) Biodiversity of vibrios. *Microbiol Mol Biol Rev* 68: 403–431.
21. Yamamoto S, Okujo N, Yoshida T, Matsuura S, Shinoda S (1994) Structure and iron transport activity of vibrioferrin, a new siderophore of *Vibrio parahaemolyticus*. *J Biochem* 115: 868–874.
22. Tanabe T, Funahashi T, Nakao H, Miyoshi S, Shinoda S, et al. (2003) Identification and characterization of genes required for biosynthesis and transport of the siderophore vibrioferrin in *Vibrio parahaemolyticus*. *J Bacteriol* 185: 6938–6949.
23. Funahashi T, Moriya K, Uemura S, Miyoshi S, Shinoda S, et al. (2002) Identification and characterization of *pvuA*, a gene encoding the ferric vibrioferrin receptor protein in *Vibrio parahaemolyticus*. *J Bacteriol* 184: 936–946.
24. Tanabe T, Funahashi T, Okajima N, Nakao H, Takeuchi Y, et al. (2011) The *Vibrio parahaemolyticus pvuA1* gene (formerly termed *psuA*) encodes a second ferric vibrioferrin receptor that requires *tonB2*. *FEMS Microbiol Lett* 324: 73–79.
25. Funahashi T, Tanabe T, Aso H, Nakao H, Fujii Y, et al. (2003) An iron-regulated gene required for utilization of aerobactin as an exogenous siderophore in *Vibrio parahaemolyticus*. *Microbiology* 149: 1217–1225.
26. Funahashi T, Tanabe T, Shiuchi K, Nakao H, Yamamoto S (2009) Identification and characterization of genes required for utilization of desferri-

Table S1 Plasmids used in this study. (PDF)

Table S2 PCR primers used in this study. (PDF)

Author Contributions

Conceived and designed the experiments: TT AK JM SY TF. Performed the experiments: TT AK KS. Analyzed the data: TT AK KM HT. Contributed reagents/materials/analysis tools: KM HT. Contributed to the writing of the manuscript: TT SY.

- ferrichrome and aerobactin in *Vibrio parahaemolyticus*. *Biol Pharm Bull* 32: 359–365.
27. Tanabe T, Funahashi T, Shiuchi K, Okajima N, Nakao H, et al. (2012) Characterization of *Vibrio parahaemolyticus* genes encoding the systems for utilization of enterobactin as a xenosiderophore. *Microbiology* 158: 2039–2049.
28. Makino K, Oshima K, Kurokawa K, Yokoyama K, Uda T, et al. (2003) Genome sequence of *Vibrio parahaemolyticus*: a pathogenic mechanism distinct from that of *V. cholerae*. *Lancet* 361: 743–749.
29. Demarre G, Guéroul AM, Matsumoto-Mashimo C, Rowe-Magnus DA, Marlière P, et al. (2005) A new family of mobilizable suicide plasmids based on broad host range R388 plasmid (*IncW*) and RP4 plasmid (*IncPα*) conjugative machineries and their cognate *Escherichia coli* host strains. *Res Microbiol* 156: 245–255.
30. Sambrook J, Russell DW (2001) Molecular cloning: a laboratory manual. vol. 1 to 3, 3rd ed. Cold Spring Harbor, NY: Cold Spring Harbor Laboratory Press.
31. Altschul SF, Madden TL, Schaffer AA, Zhang J, Zhang Z, et al. (1997) Gapped BLAST and PSI-BLAST: a new generation of protein database search programs. *Nucleic Acids Res* 25: 3389–3402.
32. Yamamoto S, Akiyama T, Okujo N, Matsuura S, Shinoda S (1995) Demonstration of a ferric vibrioferrin-binding protein in the outer membrane of *Vibrio parahaemolyticus*. *Microbiol Immunol* 39: 759–766.
33. Kuroda T, Mizushima T, Tsuchiya T (2005) Physiological roles of three Na⁺/H⁺ antiporters in the halophilic bacterium *Vibrio parahaemolyticus*. *Microbiol Immunol* 49: 711–719.
34. Heckman KL, Pease LR (2007) Gene splicing and mutagenesis by PCR-driven overlap extension. *Nat Protoc* 2: 924–932.
35. Keen NT, Tamaki S, Kobayashi D, Trollinger D (1988) Improved broad-host-range plasmids for DNA cloning in gram-negative bacteria. *Gene* 70: 191–197.
36. Hantke K (1983) Identification of an iron uptake system specific for coprogen and rhodotorulic acid in *Escherichia coli* K12. *Mol Gen Genet* 191: 301–306.
37. Lundrigan MD, Kadner RJ (1986) Nucleotide sequence of the gene for the ferrienterochelin receptor *FepA* in *Escherichia coli*. Homology among outer membrane receptors that interact with TonB. *J Biol Chem* 261: 10797–10801.
38. Braun V, Hantke K (1991) Genetics of bacterial iron transport. In: Winkelman G, editor. *Handbook of microbial iron chelates*. Boca Raton, Fla: CRC Press. pp. 107–138.
39. Stojiljkovic I, Baumler AJ, Hantke K (1994) Fur regulon in gram-negative bacteria: Identification and characterization of new iron-regulated *Escherichia coli* genes by a Fur titration assay. *J Mol Biol* 236: 531–545.
40. Poghiano J, Lynch AS, Belin D, Lin EC, Beckwith J (1997) Regulation of *Escherichia coli* cell envelope proteins involved in protein folding and degradation by the Cpx two-component system. *Genes Dev* 11: 1169–1182.
41. Yamamoto K, Ishihama A (2006) Characterization of copper-inducible promoters regulated by CpxA/CpxR in *Escherichia coli*. *Biosci Biotechnol Biochem* 70: 1688–1695.
42. Vogt SL, Raivio TL (2012) Just scratching the surface: an expanding view of the Cpx envelope stress response. *FEMS Microbiol Lett* 326: 2–11.
43. Weber RF, Silverman PM (1988) The Cpx proteins of *Escherichia coli* K12: Structure of the CpxA polypeptide as an inner membrane component. *J Mol Biol* 203: 467–478.
44. Salgado H, Moreno-Hagelsieb G, Smith TF, Collado-Vides J (2000) Operons in *Escherichia coli*: genomic analyses and predictions. *Proc Natl Acad Sci USA* 97: 6652–6657.
45. Sato K, Hamada M, Asai K, Mituyama T (2009) CENTROIDFOLD: a web server for RNA secondary structure prediction. *Nucleic Acids Res* 37: W277–280.
46. Dean CR, Poole K (1993) Cloning and characterization of the ferric enterobactin receptor gene (*pfeA*) of *Pseudomonas aeruginosa*. *J Bacteriol* 175: 317–324.
47. Anderson MT, Armstrong SK. (2004) The BfeR regulator mediates enterobactin-inducible expression of *Bordetella* enterobactin utilization genes. *J Bacteriol* 186: 7302–7311.
48. Mey AR, Wyckoff EE, Oglesby AG, Rab E, Taylor RK, et al. (2002) Identification of the *Vibrio cholerae* enterobactin receptors VctA and IrgA: IrgA is not required for virulence. *Infect Immun* 70: 3419–3426.

49. Naka H, Crosa JH (2012) Identification and characterization of a novel outer membrane protein receptor FetA for ferric enterobactin transport in *Vibrio anguillarum* 775 (pJM1). *Biometals* 25: 125–133.
50. Hollander A, Mercante AD, Shafer WM, Cornelissen CN (2011) The iron-repressed, AraC-like regulator MpeR activates expression of *fetA* in *Neisseria gonorrhoeae*. *Infect Immun* 79: 4764–4776.
51. Raymond KN, Dertz EA, Kim SS (2003) Enterobactin: an archetype for microbial iron transport. *Proc Natl Acad Sci USA* 100: 3584–3588.
52. Earhart CF (2004) Iron uptake via the enterobactin. In: Crosa JH, Mey AR, Payne SM, editors. *Iron transport in bacteria*. Washington, DC: American Society for Microbiology. pp. 133–146.
53. Fiedler HP, Krastel P, Muller J, Gebhardt K, Zceck A (2001) Enterobactin: the characteristic catecholate siderophore of Enterobacteriaceae is produced by *Streptomyces* species. *FEMS Microbiol Lett* 196: 147–151.
54. Valdebenito M, Crumbliss AL, Winkelmann G, Hantke K (2006) Environmental factors influence the production of enterobactin, salmochelin, aerobactin, and yersiniabactin in *Escherichia coli* strain Nissle 1917. *Int J Med Microbiol* 296: 513–520.
55. Schmitt MP (1999) Identification of a two-component signal transduction system from *Corynebacterium diphtheriae* that activates gene expression in response to the presence of heme and hemoglobin. *J Bacteriol* 181: 5330–5340.
56. Danese PN, Silhavy TJ (1998) CpxP, a stress-combative member of the Cpx regulon. *J Bacteriol* 180: 831–839.
57. Nakayama S, Watanabe H (1995) Involvement of *cpxA*, a sensor of a two-component regulatory system, in the pH-dependent regulation of expression of *Shigella sonnei virF* gene. *J Bacteriol* 177: 5062–5069.
58. Dore JE, Lukas R, Sadler DW, Church MJ, Karl DM (2009) Physical and biogeochemical modulation of ocean acidification in the central North Pacific. *Proc Natl Acad Sci USA* 106: 12235–12240.



Role of periplasmic binding proteins, FatB and VatD, in the vulnibactin utilization system of *Vibrio vulnificus* M2799



Hiroaki Kawano^a, Katsushiro Miyamoto^a, Itsumi Sakaguchi^a, Tomoka Myojin^a, Masamitsu Moriwaki^a, Takahiro Tsuchiya^a, Tomotaka Tanabe^b, Shigeo Yamamoto^b, Hiroshi Tsujibo^{a,*}

^a Department of Microbiology, Osaka University of Pharmaceutical Sciences, 4-20-1 Nasahara, Takatsuki, Osaka 569-1094, Japan

^b Laboratory of Hygienic Chemistry, College of Pharmaceutical Sciences, Matsuyama University, 4-2 Bunkyo-cho, Matsuyama, Ehime 790-8578, Japan

ARTICLE INFO

Article history:

Received 6 June 2013

Received in revised form

4 September 2013

Accepted 3 October 2013

Available online 14 October 2013

Keywords:

Vibrio vulnificus

Vulnibactin

Iron acquisition

ABC-type transporter

ABSTRACT

Vibrio vulnificus, an opportunistic marine bacterium that causes a serious, often fatal, infection in humans, requires iron for its pathogenesis. This bacterium uses iron from the environment via the vulnibactin-mediated-iron-uptake system. In this study, we constructed the deletion mutants of the genes encoding the proteins involved in the vulnibactin-mediated-iron-uptake system, isochorismate synthase (ICS), vulnibactin utilization protein (VuuB), periplasmic ferric-vulnibactin binding protein (FatB), and ferric-vulnibactin receptor protein (VuuA). The Δics and $\Delta vuuA$ mutants were unable to grow under low-iron concentration conditions compared with the isogenic wild-type, indicating that the involvement of ICS in the vulnibactin biosynthesis pathway and uptake of ferric-vulnibactin through the VuuA receptor protein are essential for *V. vulnificus* M2799 growth under low-iron concentration conditions. Similar growth impairment was also observed in $\Delta fatB$, with growth recovery of this mutant observed 6 h after the beginning of the culture. These results indicate that there must be other periplasmic ferric-vulnibactin binding proteins in *V. vulnificus* M2799 that complement the defective *fatB* gene. Complementary growth studies confirmed that VatD protein, which functions as a periplasmic ferric-aerobactin binding protein, was found to participate in the ferric-vulnibactin uptake system in the absence of FatB. Furthermore, the expression of *ics*, *vuuB*, *fatB*, *vuuA*, and *vatD* genes was found to be regulated by iron and the ferric uptake regulator.

© 2013 Elsevier Ltd. All rights reserved.

1. Introduction

Vibrio vulnificus is a Gram-negative halophilic marine bacterium capable of causing gastroenteritis and primary septicemia in humans [1,2]. The septicemia is often acquired by eating raw oysters or shellfish and the symptoms rapidly escalate despite early medical treatment. Primary septicemia is often associated with immunocompromised people and those with underlying conditions such as liver cirrhosis, hemochromatosis, and alcoholism. In our previous report, we showed that *V. vulnificus* M2799, a clinical isolate, possesses 100-fold higher lethality in mice than an environmental isolate, strain JCM3731 [3]. The cytotoxicity of *V. vulnificus* M2799 toward various cultured cells was high compared with an environmental isolate [3].

To date, several potential virulence factors of *V. vulnificus*, such as metalloprotease [4,5], hemolysin [6], RTX toxin [7–9], capsular polysaccharide [10,11], and iron acquisition factors including a siderophore [12] have been identified. Among the above-mentioned factors, the iron acquisition system is a well-known crucial virulence factor [12].

Iron is an essential micronutrient for almost all living organisms and its acquisition from the environment is vital to bacteria [13]. At physiological pH, iron is rapidly oxidized to the ferric state [Fe(III)] as an insoluble hydroxide. Within human tissues, most Fe(III) is tightly bound to high-affinity iron-binding proteins, such as hemoglobin, transferrin, lactoferrin, and ferritin [14]. Therefore, the level of freely available iron (10^{-18} M) within the human body is too low to sustain bacterial growth. Pathogenic bacteria growing within the human body express highly specific iron-uptake systems, including siderophores and specific receptors, which are essential for bacterial growth. In addition to the siderophore-mediated iron uptake system, *V. vulnificus* can directly take up iron either from free heme or from heme-containing proteins, such

* Corresponding author. Tel./fax: +81 72 690 1057.

E-mail address: tsujibo@gly.oups.ac.jp (H. Tsujibo).

Abbreviations			
ICS	isochorismate synthase	2D-DIGE	two-dimensional differential gel electrophoresis
VuuB	vulnibactin utilization protein	RT-PCR	reverse transcription-PCR
FatB	ferric-vulnibactin ABC transporter substrate-binding protein	LB	Luria–Bertani
VuuA	ferric-vulnibactin receptor protein	LBS	LB containing 1.5% NaCl
VatD	a periplasmic ferric-aerobactin binding protein	HI	heart infusion containing 2% NaCl
HupA	heme receptor protein	EDDA	ethylenediamine-di (o-hydroxyphenylacetic acid)
VenB	isochorismatase	Cm	chloramphenicol
Fur	ferric uptake regulator	Tet	tetracycline
DHBA	2,3-dihydroxybenzoic acid	PMB	polymyxin B
		desA	deferoxamine B siderophore receptor gene
		ABC	ATP-binding cassette
		SIPs	siderophore-interacting proteins

as hemoglobin or hemopexin via its heme receptor protein HupA [15]. The heme-uptake system in Gram-negative bacteria involves a single outer membrane heme receptor, a periplasmic heme transport protein and inner membrane proteins typical for an ABC transport system. The *V. vulnificus hupA* mutant showed reduced virulence in both mice and in tissue cultures due to the significant growth impairment [15,16]. Therefore, iron uptake from heme via the heme receptor-mediated transport system is also important for *V. vulnificus* pathogenesis. Furthermore, TtpC2-TonB2 systems in *V. vulnificus* have been shown to be important for both uptake of endogenously produced iron-bound siderophores as well as siderophores produced by other organism [17].

Synthesis of many enzymes, toxins, and virulence determinants is also regulated by the intracellular iron concentration, which is mediated mainly by a global transcriptional regulator, the ferric uptake regulator (Fur) [18]. Fur forms a complex with ferrous ions as a dimer, which can bind to a 19-bp inverted repeat sequence, called the Fur box. The Fur box is present in the target promoter regions of iron-regulated genes and leads to transcriptional repression of the genes by competing with RNA polymerase in the promoter regions [19]. In *V. vulnificus*, the Fur regulator has previously been shown to repress the transcription of several genes, including *desA* [20,21], *hupA* [15], *sodA* [22,23], *vatD* [24], and *vuuA* [25]. Recently, some reports addressed the response of *V. vulnificus* to iron [26,27].

V. vulnificus produces a catechol siderophore (vulnibactin) and hydroxamate siderophore [28]. The hydroxamate siderophore has not been fully characterized. The catechol siderophore vulnibactin consists of one residue of 2,3-dihydroxybenzoic acid (DHBA), two residues of salicylic acid, and two residues of L-threonine on a norspermidine backbone. Vulnibactin is a siderophore with a structure similar to that of vibriobactin from *Vibrio cholerae* [29,30], except that vulnibactin contains two salicylic acid residues plus one DHBA molecule, whereas vibriobactin contains three DHBA residues. It has been reported that isochorismate synthase (ICS) and isochorismatase (VenB) involved in biosynthesis of vulnibactin in *V. vulnificus*. The *ics* or *venB* mutant lost the ability to use transferrin as an iron source and reduced the virulence [12,31]. Similarly, Kim et al. showed that the mutants of gene encoding nonribosomal peptide synthases reduced vulnibactin production and reduced virulence [32]. In addition, Webster and Litin revealed ferric-vulnibactin receptor protein (VuuA) in *V. vulnificus* of which gene expression has been shown to be regulated by Fur [25]. The *vuuA* mutant lost the ability to utilize transferrin or ferric-vulnibactin as an iron source and lost the virulence. Hence, the vulnibactin-mediated iron-uptake system plays an essential role in the use of transferrin-bound iron and the virulence of *V. vulnificus* in animal models [12,31].

We used a proteomic approach to study the differential expression of proteins from *V. vulnificus* M2799 under iron-repleted and low-iron concentration conditions during the early, mid-, and late logarithmic growth phases. A total of 32, 53 and 42 iron-regulated spots were detected by two-dimensional differential gel electrophoresis (2D-DIGE) in the early, mid-, and late logarithmic growth phases, respectively. Of these, 18 (early logarithmic growth phase), 31 (mid logarithmic growth phase), and 26 (late logarithmic growth phase) proteins were subsequently identified by matrix-assisted laser desorption/ionization-time of flight analysis. The expression of proteins involved in the iron acquisition system increased from the early to the mid-logarithmic growth phases, while that of proteins involved in other metabolic pathways increased from the mid- to the late logarithmic growth phases. Furthermore, when the protein expression profile of the wild-type bacterium was compared with that of the *fur* insertion mutant grown under the iron-repleted condition, the expression of 18 proteins was found to be regulated by iron and Fur [26].

We constructed the deletion mutants of genes encoding the proteins involved in the vulnibactin-mediated iron-uptake system, ICS, ferric-vulnibactin utilization protein (VuuB), periplasmic ferric-vulnibactin binding protein (FatB), and VuuA. Growth analyses of these mutants were investigated under iron-repleted and low-iron concentration conditions. Furthermore, the expression level of these proteins in *fur* deletion mutants was confirmed at a transcriptional level by reverse transcription-polymerase chain reaction (RT-PCR).

2. Materials and methods

2.1. Strains, plasmids and media and growth conditions

The bacterial strains and plasmids used in this study are listed in Table 1. The clinical isolate of *V. vulnificus* M2799 was kindly provided by Prof. Shin-ichi Miyoshi (Okayama University, Okayama, Japan). The competent *Escherichia coli* SY327 λ pir [33] was used for construction of recombinant plasmids. Plasmids pDM4 [34] and pRK415 [35] were used for gene deletion and for complementation analysis, respectively. The recombinant plasmids were subsequently transformed into *E. coli* SM10 λ pir [33] possessing a conjugal activity to *V. vulnificus* cells. Suicide plasmid pDM4 was kindly gifted by Prof. Debra L. Milton (Department of Molecular Biology, Umea University, Umea, Sweden).

E. coli strains were cultured in Luria–Bertani (LB) medium with the appropriate antibiotics. The medium used for conjugation of *V. vulnificus* M2799 was LB medium containing 1.5% NaCl (LBS medium). For growth examination and RNA isolation *V. vulnificus* M2799 was precultured in a heart infusion broth (Eiken Chemical,

Table 1
Strains and plasmids used in this study.

Strain or plasmid	Description	Reference
Bacterial strains		
<i>V. vulnificus</i> M2799	Clinical isolate; virulent	–
Δfur	M2799 Δfur	This study
Δics	M2799 Δics	This study
$\Delta vuuB$	M2799 $\Delta vuuB$	This study
$\Delta fatB$	M2799 $\Delta fatB$	This study
$\Delta vuuA$	M2799 $\Delta vuuA$	This study
$\Delta vatD$	M2799 $\Delta vatD$	This study
$\Delta fatB\Delta vatD$	M2799 $\Delta fatB\Delta vatD$	This study
<i>Escherichia coli</i> SY327 λpir	<i>araD</i> $\Delta(lac-pro)$ <i>argE</i> (Am) <i>nalA</i> <i>recA56</i> $\lambda pirR6K$	[33]
SM10 λpir	<i>thi</i> <i>thr</i> <i>leu</i> <i>tonA</i> <i>lacY</i> <i>supE</i> <i>recA</i> ::RP4-2-Tc::Mu $\lambda pirR6K$; Km ^r ; conjugal donor	[33]
Plasmids		
Gene deletion		
pDM4	R6K <i>ori sacB</i> ; suicide vector; <i>oriT</i> of RP4; Cm ^r	[34]
pDdfur	pDM4 Δfur fragment; for marker less deletion	This study
pDdics	pDM4 Δics fragment; for marker less deletion	This study
pDdvuuB	pDM4 $\Delta vuuB$ fragment; for marker less deletion	This study
pDdfatB	pDM4 $\Delta fatB$ fragment; for marker less deletion	This study
pDdvuuA	pDM4 $\Delta vuuA$ fragment; for marker less deletion	This study
pDdvatD	pDM4 $\Delta vatD$ fragment; for marker less deletion	This study
Complementation		
pRK415	Broad-host-range plasmid; Tet ^r	[35]
pRfatB	<i>fatB</i> and upstream acyl carrier protein locus from original promoter in pRK415	This study
pRvuuA	<i>vuuA</i> locus from original promoter in pRK415	This study
pRvatD	<i>vatCD</i> locus from original promoter in pRK415	This study

*Cm^r, chloramphenicol resistance; Km^r, kanamycin resistance; Tet^r tetracycline resistance.

Tokyo, Japan) containing 2% NaCl (HI medium) at 37 °C at 200 rpm overnight. The culture was diluted 1:100 into a fresh broth and then shaken at 37 °C at 200 rpm. HI medium with the iron chelator ethylenediamine-di (*o*-hydroxyphenylacetic acid) (EDDA; Sigma (St. Louis, MO, USA)) at a final concentration of 10 µg/ml was used for growth examination under the low-iron concentration condition.

2.2. Antibiotics

The concentrations of antibiotics for *E. coli* strains were as follows: chloramphenicol (Cm), 10 µg/ml; and tetracycline (Tet), 15 µg/ml. The concentrations of antibiotics for the *V. vulnificus* strains were as follows: Cm, 5 µg/ml; polymyxin B (PMB), 100 U/ml; and Tet, 15 µg/ml. When used in the preculture for the complementation analysis, the Tet concentration for the *V. vulnificus* strains was reduced to 5 µg/ml to maintain growth.

2.3. Nucleotide sequencing of *ics*, *vuuB*, *fatB*, and *vuuA*

Nucleotide sequencing was carried out by the dideoxy chain termination method employing the DYEnamic ET terminator cycle sequencing premix kit (GE Healthcare, Uppsala, Sweden) on a DNA sequencer (ABI Prism 310 Genetic Analyzer; Applied Biosystems,

Foster City, CA, USA). Sequence data were analyzed by using the GENETYX-WIN program (Software Development Co., Ltd., Tokyo, Japan). Chromosomal DNA was extracted from the M2799 culture using a Blood Cell Culture DNA Midi Kit (Qiagen, Hilden, Germany). The PCR primers were designed based on the nucleotide sequences of *V. vulnificus* CMCP6 [36] of which the genome sequence has already been determined (GenBank Accession No. AE066796.2). The PCR primers (*ics*_upF and *ics*_dnR), (*vuuB*_upF and *vuuB*_dnR), (*fatB*_Fw and *fatB*_Rv), and (*vuuA*_Fw and *vuuA*_Rv) were synthesized based on VV2_0835, VV2_0837, VV2_0842, and VV2_0843, respectively (Table 2). PCR amplification was performed by KOD-Plus-DNA polymerase (Toyobo, Osaka, Japan) for 30 cycles

Table 2
Primers used in this study.

Primer names	Nucleotide sequences (5'–3')
Construction of deletion mutants	
<i>fur</i> _upF	GAGAAAATACTCGAGCCATACTGAGTACG
<i>fur</i> _upR	AAGGGTAACTTTGGATCCAGCATCTTTAG
<i>fur</i> _dnF	CAACATCACCATGGGATCCCTAGTTGTCTC
<i>fur</i> _dnR	CATCAATCCGCATGCTTTAACGGGTGATG
<i>fur</i> _del_check_F	ATGCTCGTCTCTTGTCCAGACATAGTAC
<i>fur</i> _del_check_R	CGTCTATTACCGGTACCAAATCCAGCAGCC
<i>ics</i> _upF	CGACCACCTCGAGCCCCCGCTCAAGTAGAT
<i>ics</i> _upR	AACGGATCCCTCTAGATATTTTCGATCGTGG
<i>ics</i> _dnF	AAAGGATCCGGGATTCACATCACTGAACGAATG
<i>ics</i> _dnR	ACATGCATGCTCTTTGAGAAGTTTTTCGGC
<i>ics</i> _del_check_F	TCACTGTCTGCTTGTAGTCGCACITCATCG
<i>ics</i> _del_check_R	TGAGATTGCAGCAGCTCGGAGTGATTGGCT
<i>vuuB</i> _upF	GATTTTACTCGAGAAGATCAITTTGCGGACC
<i>vuuB</i> _upR	CGATATTGTGGATCCGAGTAAAGCTCTCGGA
<i>vuuB</i> _dnF	CGCAGGATCCAAGGCGATTAAAGCAACTACC
<i>vuuB</i> _dnR	TAACAGAGGATGCAATATCATCTGTCACAG
<i>vuuB</i> _del_check_F	GCCATATCGGCATACTTTTCGACCACGTTAG
<i>vuuB</i> _del_check_R	CACACACAACGGTTTTTATCCGACTCGCGCA
<i>fatB</i> _upF	ACTGGCCGTAGCACCTCGAGATGAGTAACCC
<i>fatB</i> _upR	ATGCTCGATCACAGGATCCCTTCGCCATTGC
<i>fatB</i> _dnF	TCCGACATCAAAGGATCCGTCGAACTGTAG
<i>fatB</i> _dnR	TAGAGGCATGCACAGTGTGATGCCACAG
<i>fatB</i> _del_check_F	GTTGTCCGACGACCATATCTACTCTTGGCC
<i>fatB</i> _del_check_R	ACTGCTTCCCAATGGTGTATGATTTCATTAC
<i>vuuA</i> _upF	CTCTACTCAATCTCGAGGTAGAAAGACCAC
<i>vuuA</i> _upR	GGCATGCTGGATCCCTTGGCCAGAGTCCACC
<i>vuuA</i> _dnF	CCACGTATGATTGGATCCCTCATTGCGAGTTG
<i>vuuA</i> _dnR	CCAAGTGGATGCGCATGCCATCATGACATC
<i>vuuA</i> _del_check_F	ACATGCTTTTGTAGCGTACTCTATAGTGC
<i>vuuA</i> _del_check_R	CTTGACAACGATCTGTCTCAAGCCACCAAC
<i>vatD</i> _upF	CCGTCTCGAGGGGCTTTTGGTGTATATGGC
<i>vatD</i> _upR	CAGGAGGATCCCTTTTACAAACAGATTCTCT
<i>vatD</i> _dnF	ACACCGGATCCATCACAGCCAGTCAAGG
<i>vatD</i> _dnR	GCCCCAAAAGCATGCTCACCCATGCCCCGC
<i>vatD</i> _del_check_F	CCTACCTTCCCCAACATCCCCCATCACAG
<i>vatD</i> _del_check_R	CCCCACAAAAAATGCTGGTCAGCGGCTGC
Complementation	
<i>fatB</i> _Fw	CCTATCAGGGATCCGCTCTACTCCCTGATG
<i>fatB</i> _Rv	ATGTGTTTGAATTCGGCCGAGTACTCTGTG
<i>vuuA</i> _Fw	CAAGAGGATCCACCATCTCAGTGAAGCAG
<i>vuuA</i> _Rv	TCTGAATTCAGGATTTCTGCAACGGAAAA
<i>vatD</i> _Fw	AGGTGGATCCAGAAGGCAATCTCAAGCCG
<i>vatD</i> _Rv	GCAGGAATCAATAAGTAAACCCGCCGCG
RT-PCR	
<i>dnaA</i> _RTPCR_Fw	ACAAGCCCAACGCCAAAGTG
<i>dnaA</i> _RTPCR_Rv	GGAAAGAACTTCTCTGCGAA
<i>ics</i> _RTPCR_Fw	AACCCGACATCAACAGCAAG
<i>ics</i> _RTPCR_Rv	TGATTTTGTGCTCAGACTC
<i>vuuB</i> _RTPCR_Fw	AAGCAAGTGGCATTCTCCAG
<i>vuuB</i> _RTPCR_Rv	AACCAATCTGCGAGCCGATG
<i>fatB</i> _RTPCR_Fw	CAGTGCCGATCTCAAGCAAG
<i>fatB</i> _RTPCR_Rv	TGTATTGTTTGTATGGCGGCA
<i>vuuA</i> _RTPCR_Fw	ACTCTTCTAAACAGAAATGAG
<i>vuuA</i> _RTPCR_Rv	TTCTTCTCATAGCGCCCTG
<i>vatD</i> _RTPCR_Fw	CGGAGCAAGTATTGTCACAA
<i>vatD</i> _RTPCR_Rv	CTTGAGCCAAAGAGCCTTCA

The mutagenized restriction sites are underlined.

consisting of 94 °C for 15 s, 55 °C for 30 s, and 68 °C for 1 min. The 2,640, 1,818, 1,719, and 2,130 bp products were amplified and analyzed by direct sequencing. The nucleotide sequence data have been deposited in the DDBJ, EMBL, and GenBank nucleotide sequence databases under the accession numbers AB822514, AB822515, AB822516, and AB822517.

2.4. Construction of gene-deletion mutants by a marker exchange

Construction of plasmid and filter mating was done as reported by Milton et al., (1996) [34] with some modifications. The plasmids constructed for this study and the details of the deletion mutants are summarized in Table 1. First, to generate a plasmid for homologous recombination, the upstream regions (approximately 500 bp) flanking the genes were amplified by PCR with forward and reverse primers that were modified *Xho*I and *Bam*HI restriction sites, respectively. The downstream regions were amplified with the primers that were modified with *Bam*HI and *Sph*I restriction sites, respectively. The resulting two fragments were purified by a Wizard SV Gel and PCR cleanup system (Promega, Madison, WI, USA). The purified fragments were digested *Bam*HI and ligated, and then used as templates for the next PCR reaction. The second PCR was performed using the forward primer of the upstream fragment and the reverse primer of the downstream fragment in the first PCR step. The second PCR fragments were digested with *Xho*I and *Sph*I, and were cloned into the pDM4 suicide plasmid possessing a *sacB* counter-selection marker. The recombinant plasmids were subsequently transformed into *E. coli* SY327 λ *pir* cells, and a single colony was picked and cultured in LB medium containing Cm. Plasmids were purified from the cells and subsequently transformed into *E. coli* SM10 λ *pir* cells having conjugal activity to *V. vulnificus* M2799. Plasmid transfer from *E. coli* SM10 λ *pir* cells to M2799 cells was done by filter mating. *E. coli* SM10 λ *pir* harboring a pDM4 or pRK415 derivative was used as a donor strain. *E. coli* SM10 λ *pir* and recipient M2799 cells were grown at 37 °C at 150 rpm until the optical density at 600 nm (OD₆₀₀) reached 0.15 and 0.2, respectively. One milliliter of each culture was filtered using a 0.45 μ m pore size membrane filter (Millipore, Billerica, MA, USA), which was pre-equilibrated with 5 ml of LBS medium. The resulting membrane was transferred onto a LBS agar plate and incubated at 37 °C for 3 h to allow for conjugation. The membrane was picked and immersed in 5 ml of LBS medium and shaken at 37 °C for 1 h and then the culture was spread onto a LBS agar plate containing Cm and PMB to enhance the single-crossover event. Stable transconjugants were selected and then plated onto a LBS agar plate containing 15% sucrose to allow the second crossover to occur. The deletion was confirmed by PCR using the primers designed based on the up and downstream sequences of the deletion region.

2.5. Complementation analysis

Genes of *fatB*, *vuua*, and *vatD* were amplified by PCR using the following primers: *fatB*_Fw and *fatB*_Rv, *vuua*_Fw and *vuua*_Rv, and *vatD*_Fw and *vatD*_Rv, respectively. The amplicons of each of the genes were digested with *Bam*HI and *Eco*RI, and were cloned into pRK415, and the resulting recombinant plasmids were designated as pR*fatB*, pR*vuua*, and pR*vatD*, respectively. Of these, *vuua* was cloned from the original M2799 promoter including a putative Fur box whereas the *fatB* and *vatD* genes, consisting of an operon with an upstream aryl carrier domain-containing protein coding gene and the *vatC* gene respectively, were cloned from the corresponding upstream promoter so as to include a putative Fur box. The generated constructs were transferred to the corresponding *V. vulnificus* M2799 mutants by filter mating as described in the previous section. A Tet-resistant recombinant was precultured in HI

medium containing Tet and cultured at 37 °C overnight. The growth assay in the presence of EDDA was done as described in the growth conditions section without the addition of antibiotics.

2.6. RT-PCR

Cells were cultured in HI medium in the presence and absence of EDDA until the OD₆₀₀ reached approximately 1.0, then the cells were treated with RNA Protect bacteria reagent (Qiagen) to maintain the stability of the RNA. Total cellular RNA was isolated using an RNeasy Kit (Qiagen). During isolation, RNA was treated with DNase I to avoid DNA contamination. Total RNA (1 μ g) and 1 μ g of random primers (Invitrogen, CA, USA) were used to generate the reverse transcripts. The reaction was carried out at 55 °C for 60 min with Moloney murine leukemia virus reverse transcriptase (RNase H minus; Promega) and terminated by heating at 70 °C for 15 min. PCR was performed using 1 μ l of the reverse transcripts in 10 μ l of buffer containing 10 pmol of each primer and KOD dash DNA polymerase (Toyobo). After the initial denaturation of 2 min at 94 °C, the DNA was amplified for 30 cycles, with each cycle consisting of denaturation at 94 °C for 30 s, annealing at 54 °C for 5 s, and extension at 72 °C for 5 s. For detection of *ics*, *vuub*, *fatB*, *vuua*, and *vatD* transcripts by PCR, primer sets of *ics*_RTPCR_Fw and *ics*_RTPCR_Rv, *vuub*_RTPCR_Fw and *vuub*_RTPCR_Rv, *fatB*_RTPCR_Fw and *fatB*_RTPCR_Rv, *vuua*_RTPCR_Fw and *vuua*_RTPCR_Rv, and *vatD*_RTPCR_Fw and *vatD*_RTPCR_Rv, respectively were used. As an internal control, the *dnaA* expression level was also analyzed using the primer set *dnaA*_RTPCR_Fw and *dnaA*_RTPCR_Rv. The RT-PCR products were analyzed by agarose gel electrophoresis and stained with ethidium bromide.

3. Results

3.1. Nucleotide sequences of *ics*, *vuub*, *fatB*, and *vuua*

To amplify the genes of *ics*, *vuub*, *fatB*, and *vuua*, PCR was performed with the primers designed based on the sequences of currently available *V. vulnificus* CMCP6 genome data. The nucleotide sequences of DNA fragments were determined by the dideoxy chain termination method. The localization and function of each disrupted gene product and identities of these encoded proteins with other closely-related *Vibrio* strains are shown in Fig. 1. The open reading frames (ORFs) of *ics*, *vuub*, *fatB*, and *vuua* genes consist of 1,182, 816, 909, and 2,058 bp, respectively, and encode proteins consisting of 393, 271, 302, and 685 amino acid residues with molecular masses of 43, 30, 34, and 76 kDa. Significant identities were found when these proteins were compared with those from *V. vulnificus* CMCP6 [*ICS* (99%), *Vuub* (99%), *FatB* (100%) and *Vuua* (98%)], *Vibrio anguillarum* 775 [*VAA_02393* (66%), *VAA_01637* (30%), *FatB* (53%) and *VAA_02079* (30%)], and *V. cholerae* N16961 [*VC0773* (67%), *ViuB* (80%), *ViuP* (14%), and *VC2211* (69%)]. We also determined the nucleotide sequence of the upstream regulatory region of each ORF. The putative Fur box sequences (ATTAATGATAATTATTATC for *ics*, GATTATTATTACCATTTGC for *vuub*, GCAAATGGTAATAATAATC for *fatB*, and GCAAATGAGAATGCTTTAC for *vuua*) overlapping putative promoter regions were identified (Fig. 2). The 19-bp nucleotide sequence located on the upstream region of *vuua* in strain M2799 was 63% identical to the sequence that was confirmed in *V. vulnificus* MO6-24 [37].

3.2. Growth of the deletion mutants under low-iron concentration conditions

To obtain sufficient iron, many bacteria have developed the ability to synthesize low-molecular weight, high-affinity iron chelators known as siderophores to scavenge iron with high efficiency.

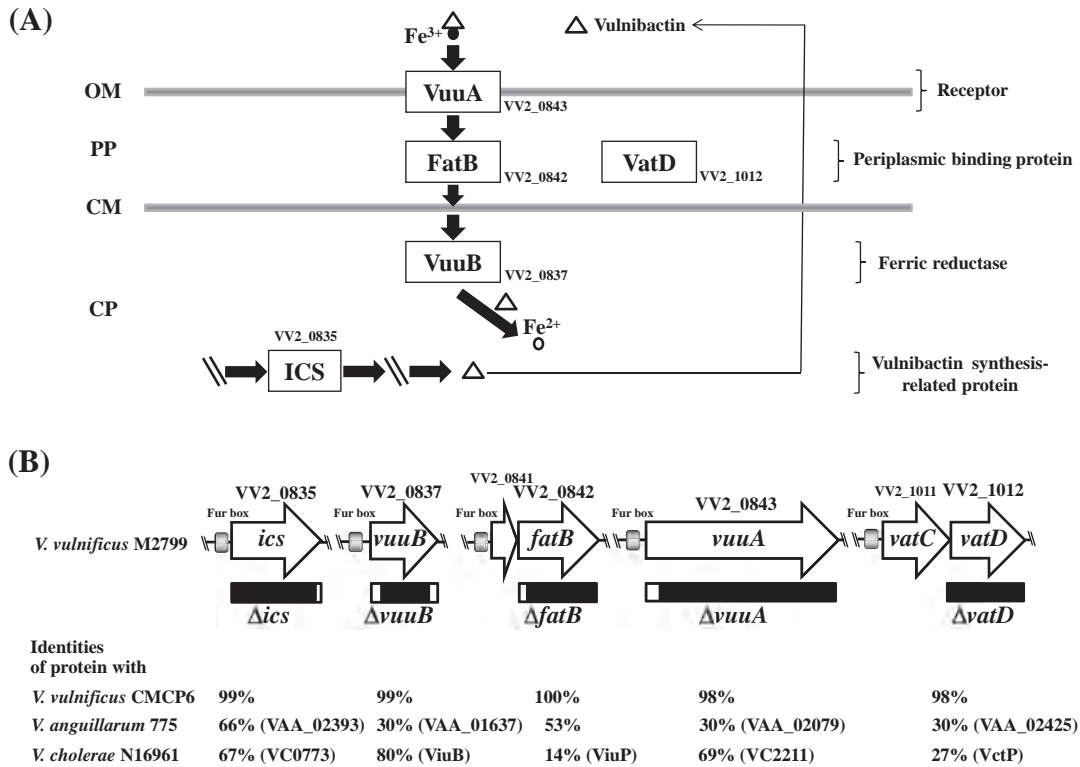


Fig. 1. The localization and function of the proteins involved in the vulnibactin-mediated iron-uptake system (A) and their amino acid sequence identities with those from other closely-related *Vibrio* strains (B). (A) Isochorismate synthase (ICS), ferric-vulnibactin utilization protein (VuuB), periplasmic ferric-vulnibactin binding protein (FatB), ferric-vulnibactin receptor protein (VuuA), and ferric-aerobactin binding protein (VatD) are shown. Each gene number referred from *V. vulnificus* CMCP6 database is also shown. (B) The orientation of the ORFs is shown by arrows. The putative Fur boxes are indicated as small gray-boxes. The deleted region of each gene is shown with black bar as illustrated in each ORF.

(A)
 tggccgtagcactagcagcatgagtaacccaacaaatcacgcaaatcagtgatattaataac
 accaaatGCAAATGGTAATAATAATcatttgaacaaatcaatcaagtaatgatattggtta
 attcctacacttagccgcaaaagaaatcggcaataagtcacgaaaatgaaaggaatta
 VV2_0841
 tttTGTGTCAGAACCTCTAAAAGAGTTTGTATTGCTTGCCACGCTCAGCGAGTTACTGCGAG
 TCAGCGAAGTGAAATTCAGTCCGACACCAACCTGATTGAACTGGGCCTCGACTCCATCA
 GTTTAATGCGCCTCACCTGGTCGCTTCGCCAAGTGGGTATCGAAGTCAACTTTGCCAAC
 TGATGAACTCACCCAGTTCAGCTCTTGGCAAACCATCATTTTCAATGCAAAGGCCTTG
 CCTAAAGcaccacggacatgggctatttggctgaaatagccttttcaataggacaaaaa
FatB
 ATGAAACTAAAATTAAGCGTTATGTTGGTCAGCACCTGATTCTGGTGGTGAATGGCG
 M K L K L S V M L V S T L I S G G A M A

(B)
 ttatgcataatcactcaataccttagccgaacagaactcaggacaatgaaggcatctca
 tgccggtgagtagcctatatcttcacaaaGCAAATGAGAATGCTTTACattttaaattgtc
 aataaattagaatgcgcttggtaactacgttggtaataccactcgatagttgagttatgctt
 -10
 ttggcctgaatcagcccccgcttggaaacgtatgtcagtcggaatatttgaatcaagcac
 atggcctttgagcgtgactctatagtgcaacgctgttcagtttcggtctctttacgcctc
 tctactcaatctcagagtagaagcaccactcgctatgcctgtgcacctgaaatgtaatca
 VuuA
 gttgcttattagatgaaggagaaattcaaatGGCAGCTTTACGCCACGCGGAACGAGC
 M A A L R P A R T S

Fig. 2. Nucleotide sequences of the promoter regions of *fatB* (A) and *vuuA* (B). The deduced amino acid sequence FatB and VV2_0841 (aryl carrier domain-containing protein) (A), and VuuA (B) are shown below the nucleotide sequence. The putative Fur box like sequences are shown by boxes. The putative -35 promoter regions are underlined.

V. vulnificus M2799 acquires iron through secretion of a catecholate siderophore called vulnibactin [30]. To investigate the roles of ICS, VuuB, FatB, and VuuA in the vulnibactin-mediated iron-uptake system, we constructed the deletion mutants (Δics , $\Delta vuuB$, $\Delta fatB$, and $\Delta vuuA$) and examined the growth of mutants under low-iron concentration conditions. As shown in Fig. 3A, the Δics and $\Delta vuuA$ mutants were unable to grow under low-iron concentration conditions compared with the wild-type, indicating that the vulnibactin synthesis pathway via the ICS protein and the ferric-vulnibactin uptake through the VuuA receptor play crucial roles in the growth of M2799 cells under low-iron concentration conditions. Similar growth impairment was also observed in $\Delta vuuB$ or $\Delta fatB$, but growth was restored 6 h after the beginning of the culture. These results indicate that there must be other proteins in *V. vulnificus* M2799 that complement the defect of the genes. The BLAST search program revealed that FatB is homologous to a putative periplasmic ferric-aerobactin binding protein, VatD (VV2_1012) in the *V. vulnificus* CMCP6 genome database. The VatD protein showed sequence similarity with FatB (17% identity). To examine whether VatD is used instead of FatB in strain M2799, the double mutant of *fatB* and *vatD* ($\Delta fatB\Delta vatD$) was constructed (Fig. 1B). The double mutant ($\Delta fatB\Delta vatD$) exhibited further growth impairment compared with the single mutant ($\Delta fatB$) under the low-iron concentration condition, while $\Delta vatD$ showed the same growth curve as the wild-type (Fig. 3B).

To determine whether FatB, VuuA, and VatD proteins are involved in the iron-acquisition system, complementation analyses of $\Delta fatB$, $\Delta vuuA$, and $\Delta fatB\Delta vatD$ strains were performed. The growth of each recombinant mutant was restored to the level of wild-type (Fig. 4). We did not perform the complementation

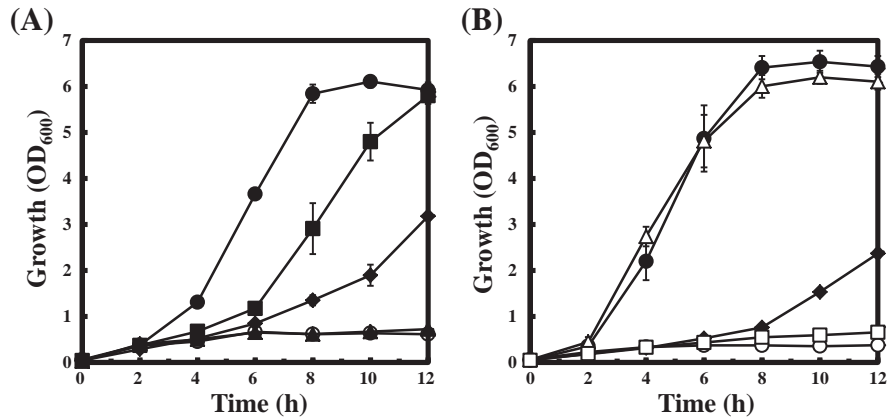


Fig. 3. Growth of the gene-deletion mutants under low-iron concentration condition. (A) The deletion mutants of the estimated gene encoding the proteins of vulnibactin-mediated iron uptake systems, as a result of the proteome analysis, were cultured in HI medium containing 10 μ g/ml EDDA and the optical densities (OD₆₀₀) were measured at the indicated time points. Data from three independent experiments are shown; standard deviations are indicated by vertical lines. ●, wild-type strain; ▲, Δ ics; ■, Δ vuub; ◆, Δ fatB; ○, Δ vuua. (B) The deletion mutants of *fatB*, *vuua*, and *vatD* genes were cultured in the same medium. ●, wild-type strain; ○, Δ fatB; Δ, Δ vuua; □, Δ vatD; ◻, Δ fatB Δ vatD.

analysis of Δ vuub because the remarkable growth impairment was not observed in this mutant compared with the other mutants. The recovery of growth by pRvuua in Δ vuua was relatively slow compared with the case in Δ fatB (Fig. 4B). A similar phenomenon was also observed by Tanabe et al., that is, when the desferrioxamine B siderophore receptor gene (*desA*) disruptant in *Vibrio furnissii* was complemented using the same plasmid, pRK415, the recovery of growth was observed 8 h after the beginning of the culture (early-stationary phase in the wild-type strain) [38]. These results demonstrated that FatB, VuuA, and VatD proteins are actually involved in the iron-acquisition system via vulnibactin.

3.3. Gene expressions of *ics*, *vuub*, *fatB*, *vuua*, and *vatD*

To investigate the gene regulation of *ics*, *vuub*, *fatB*, *vuua*, and *vatD*, RT-PCR was performed in the presence or absence of iron. As shown in Fig. 5, all transcripts could be detected as a single band in both wild-type and the Δ fur mutant. The expression level of these genes increased in wild-type under the low-iron concentration condition. On the other hand, in the Δ fur mutant, the expression of these genes under both iron-repleted and low-iron concentration conditions increased compared with the gene expression of wild-type under the iron-repleted condition. These results

demonstrated that *ics*, *vuub*, *fatB*, *vuua*, and *vatD* genes are negatively regulated by Fur. The level of *dnaA* expression in both strains was constant under the iron-repleted and low-iron concentration conditions.

4. Discussion

Iron is an essential ion for the growth of most bacteria. However, soluble iron in the human body is quite limiting because it is normally bound with high affinity to iron-chelating proteins such as transferrin and lactoferrin. Many bacteria possess specialized iron-acquisition systems to scavenge iron from the chelating molecules.

V. vulnificus acquires iron through secretion of a catecholate siderophore called vulnibactin [28]. The ferric-vulnibactin-complex is transported to the periplasm through the specific outer membrane receptor VuuA [25] and is subsequently captured by a periplasmic ferric-vulnibactin binding protein. The binding protein transfers the ligand to the cytoplasmic membrane ABC-type transporter by forming a transient electrostatic interaction with a permease component. In the present study, we demonstrated that VuuA is the only vulnibactin outer membrane receptor and FatB functions as a periplasmic binding protein in *V. vulnificus* M2799. Furthermore, proteomic analysis of *V. vulnificus* M2799 showed that

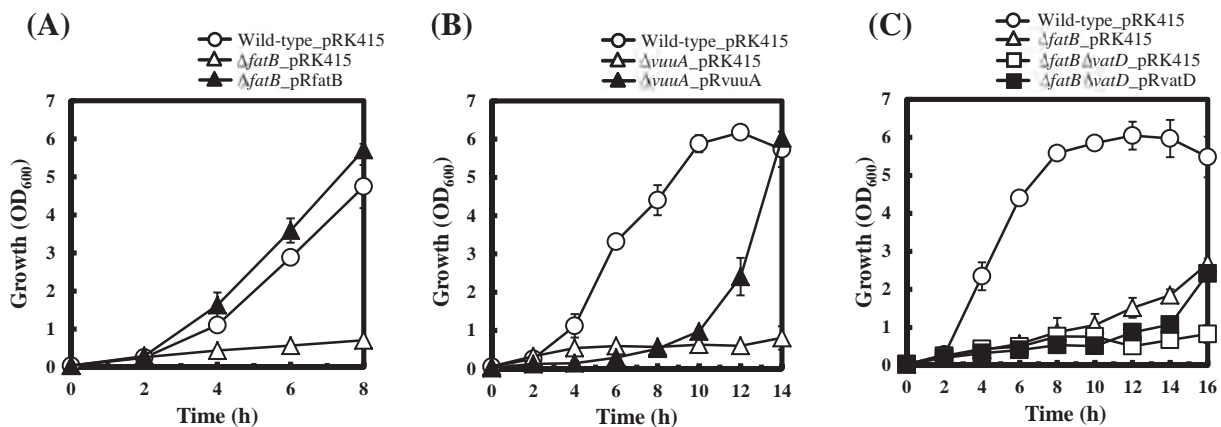


Fig. 4. Complementation analysis of the gene-deletion mutants. Plasmids pRfatB, pRvuua, and pRvatD were transferred into Δ fatB (A), Δ vuua (B), Δ fatB Δ vatD (C) mutants, respectively. The growth in HI medium in the presence of the ferric iron chelator EDDA and the measurement of OD₆₀₀ was performed at the indicated times. Data from three independent experiments are shown; standard deviations are indicated by vertical lines.

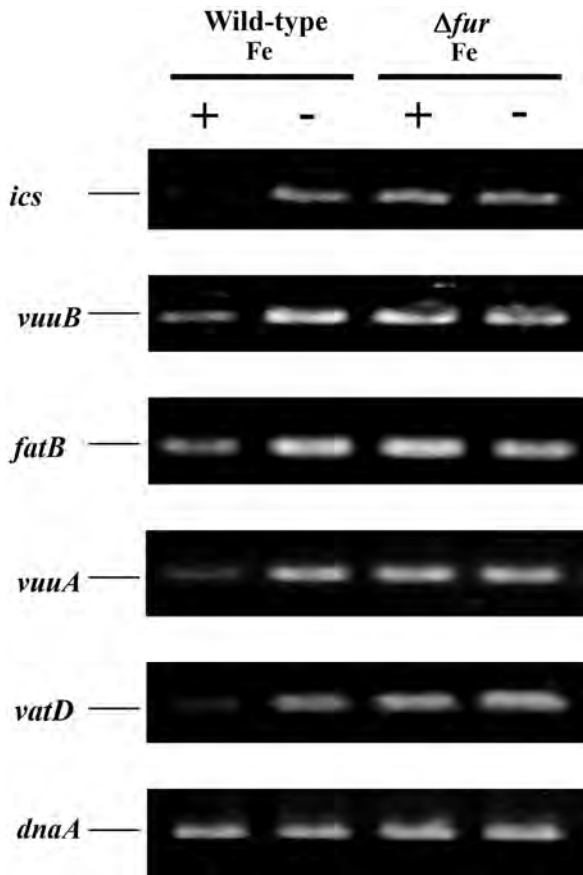


Fig. 5. Gene expression of *ics*, *vuuB*, *fatB*, *vuuA*, and *vatD*. The *V. vulnificus* M2799 (wild-type) and Δfur mutant (Δfur) were inoculated into HI medium in iron-repleted (+) and low-iron concentration (–) conditions. Total RNA was isolated and converted to the reverse transcript, which was analyzed for specific mRNA transcript levels by RT-PCR. The results for *dnaA* expression as an internal control are shown.

the expression of *FatB* was enhanced together with *VuuA* under a low-iron concentration condition [26]. The $\Delta vuuA$ mutant could not grow under the low-iron concentration condition. On the other hand, growth of $\Delta fatB$ was significantly impaired but was not completely arrested (Fig. 3A). These results indicate that *FatB* is a major periplasmic ferric-vulnibactin binding protein but that there is another periplasmic binding protein that complements defective *fatB*. *VatD* protein, which functions as a periplasmic ferric-aerobactin binding protein, was found to participate in the ferric-vulnibactin uptake system under defective *FatB* (Fig. 3B). The

growth of the single-deletion mutant of *vatD* was not defective under the low-iron concentration condition, indicating that *VatD* does not function as a ferric-vulnibactin binding protein in the presence of *FatB*. These results suggest that the affinity of *VatD* for ferric-vulnibactin is significantly lower than that of *FatB* or the amount of *VatD* in the periplasm is much lower than that of *FatB* under the conditions tested. *VatD* has been shown to function as a periplasmic binding protein of *V. vulnificus*, which transfers ferric-aerobactin to a cytoplasmic membrane ABC-type transporter [24]. Thus, the *vatCDB* cluster has been thought to contribute to siderophore piracy in *V. vulnificus* cells [24]. Furthermore, hydroxamate siderophore in the supernatant of *V. vulnificus* M2799 was not detected by the Csaky test [39] (data not shown). In the present study, we have found that *VatD* also functions as a ferric-vulnibactin binding protein in the absence of *FatB*. This is the first genetic evidence that the ferric-vulnibactin can also be transported through the periplasmic binding protein *VatD* for a different type of siderophore aerobactin. Generally, the components of ABC-type transporters are specific for the corresponding periplasmic binding protein, however, several promiscuities of the transport components have been observed in other organisms. For example, Wyckoff et al. proposed that the *V. cholerae* periplasmic binding proteins, *ViuP* and *VctP*, can deliver both vibriobactin and enterobactin siderophores to the corresponding inner membrane permease complexes for iron uptake [40]. Similarly, the *ViuPDGC* system can transport both vibriobactin and enterobactin in *E. coli*. A model for the transport of ferric-vulnibactin in *V. vulnificus* M2799 is presented in Fig. 6. In this model, ferric-vulnibactin crosses the outer membrane through *VuuA*, while aerobactin crosses via a separate outer membrane protein *IutA*, which is specific for aerobactin. Ferric-vulnibactin specifically binds to its periplasmic binding protein, *FatB*, which then delivers the ligand to the corresponding inner membrane permease complex. When the function of *FatB* is impaired, *VatD* transports the ferric-vulnibactin to the corresponding inner membrane permease complex. This is the simplest model consistent with our data, but more complex models involving additional periplasmic binding proteins and permease systems are also possible. This could be an essential survival strategy of this pathogenic bacterium under a low-iron concentration condition.

In the cytosol, Fe^{3+} is dissociated from a siderophore through cleavage of the siderophore or the action of a ferric reductase. Siderophore-interacting proteins (SIPs) are widespread among bacteria and commonly associated with iron-dependent induction and ferric reduction. One of the first SIPs was the *ViuB* protein in *V. cholerae*, which was found to be essential for ferric-vibriobactin utilization and to complement the *E. coli* *Fes* esterase [41], although no hydrolytic activity was shown for this component [42].

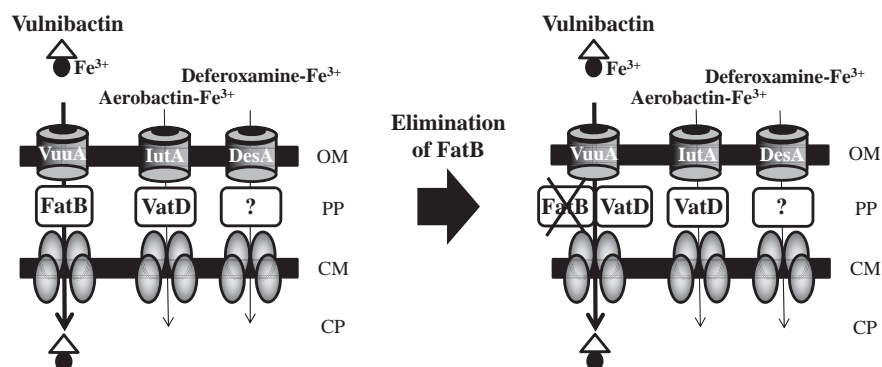


Fig. 6. Schematic representation of the vulnibactin-mediated iron-uptake system.

The VuuB mutant was unable to grow under the low-iron concentration condition. Conversely, the VuuB homolog Rv2895c was not essential for iron acquisition in *Mycobacterium tuberculosis* [43]. In *V. vulnificus* M2799, the growth of the deletion mutant of VuuB homologous to VuuB was slightly impaired (Fig. 3A). The results indicate that there must be other ferric reductases that complement the defect of the *vuuB* gene. In *E. coli*, YqjH that belongs to group II of SIPs was identified and exhibited ferric reductase activity [44]. YqjH showed the significant catalytic efficiency for hydrolyzed ferric triscatecholates and reduces ferric substrates. This group II ferric reductase activity is frequent when the enterobactin siderophore was hydrolyzed by Fes esterase in *E. coli*. *V. vulnificus* VuuB belongs to group I of SIPs as well as *V. cholerae* VuuB. Other VuuB homologous protein(s) or unidentified group II reductase (s) might exist in *V. vulnificus*. Further research is required to identify the proteins involved in the ferric reduction system in *V. vulnificus* M2799.

It has been reported that Fur, a transcriptional repressor that responds to iron utilization [18], represses the expressions of several genes such as *desA*, *vuuA*, and *vatD* under an iron-repleted condition [21,24,25]. These results were consistent with our RT-PCR data. The gene expression of *ics*, *vuuB*, *fatB*, *vuuA*, and *vatD* were remarkably upregulated under low-iron concentration conditions and, in the *fur* mutant, these genes were upregulated under both iron-repleted and low-iron concentration conditions (Fig. 5). Furthermore, in our previous proteomic analysis, the expression of ICS, VuuB, FatB, VuuA, and VatD increased under low-iron concentration conditions and the expression of these proteins increased under iron-repleted conditions in a *fur* insertion mutant [26]. Judging from the nucleotide sequences of the *ics*, *vuuB*, *fatB*, and *vuuA* genes, putative Fur boxes were identified in the upstream regions of these genes. Furthermore, a putative Fur box has been shown to be present in the upstream region of the *vatCDB* operon of this strain [24]. These results strongly indicate that the gene expression of *ics*, *vuuB*, *fatB*, *vuuA*, and *vatD* in *V. vulnificus* M2799 are regulated by Fur.

5. Conclusions

We proposed a model of a vulnibactin-mediated iron-uptake system in *V. vulnificus*, whereby ferric-vulnibactin is imported through the VuuA receptor into the periplasm and subsequently imported to the cytoplasm through the periplasmic protein FatB and unidentified ABC proteins (Fig. 6). However, the relative amount of FatB, VuuA, and VatD proteins and their associated protein–protein interactions still need to be investigated. Genetic approaches to identify the cytoplasmic membrane ABC transporter for ferric-vulnibactin are currently underway.

Acknowledgments

This study was supported in part by a Grants-in-Aid for the Strategic Research Foundation Grant-aided Project for Private Universities from the Ministry of Education, Culture, Sports, Science and Technology (MEXT), Japan, 2011–2015 (S1101031).

We thank Prof. Shin-ichi Miyoshi for supplying the *V. vulnificus* clinical isolate strain M2799.

References

- [1] Klontz KC, Lieb S, Schreiber M, Janowski HT, Baldy LM, Gunn RA. Syndromes of *Vibrio vulnificus* infections. Clinical and epidemiologic features in Florida cases, 1981–1987. *Ann Intern Med* 1988;109:318–23.
- [2] Tacket CO, Brenner F, Blake PA. Clinical features and an epidemiological study of *Vibrio vulnificus* infections. *J Infect Dis* 1984;149:558–61.

- [3] Tsuchiya T, Mitsuo E, Hayashi N, Hikita Y, Nakao H, Yamamoto S, et al. *Vibrio vulnificus* damages macrophages during the early phase of infection. *Infect Immun* 2007;75:4592–6.
- [4] Kothary MH, Kreger AS. Purification and characterization of an elastolytic protease of *Vibrio vulnificus*. *J Gen Microbiol* 1987;133:1783–91.
- [5] Miyoshi N, Shimizu C, Miyoshi S, Shinoda S. Purification and characterization of *Vibrio vulnificus* protease. *Microbiol Immunol* 1987;31:13–25.
- [6] Fan JJ, Shao CP, Ho YC, Yu CK, Hor LI. Isolation and characterization of a *Vibrio vulnificus* mutant deficient in both extracellular metalloprotease and cytolysin. *Infect Immun* 2001;69:5943–8.
- [7] Chung KJ, Cho EJ, Kim MK, Kim YR, Kim SH, Yang HY, et al. RtxA1-induced expression of the small GTPase Rac2 plays a key role in the pathogenicity of *Vibrio vulnificus*. *J Infect Dis* 2010;201:97–105.
- [8] Kim YR, Lee SE, Kook H, Yeom JA, Na HS, Kim SY, et al. *Vibrio vulnificus* RTX toxin kills host cells only after contact of the bacteria with host cells. *Cell Microbiol* 2008;10:848–62.
- [9] Kwak JS, Jeong HG, Satchell KJ. *Vibrio vulnificus* *rtxA1* gene recombination generates toxin variants with altered potency during intestinal infection. *Proc Natl Acad Sci U S A* 2011;108:1645–50.
- [10] Simpson LM, White VK, Zane SF, Oliver JD. Correlation between virulence and colony morphology in *Vibrio vulnificus*. *Infect Immun* 1987;55:269–72.
- [11] Wright AC, Powell JL, Kaper JB, Morris Jr JG. Identification of a group 1-like capsular polysaccharide operon for *Vibrio vulnificus*. *Infect Immun* 2001;69:6893–901.
- [12] Litwin CM, Rayback TW, Skinner J. Role of catechol siderophore synthesis in *Vibrio vulnificus* virulence. *Infect Immun* 1996;64:2834–8.
- [13] Wooldridge KG, Williams PH. Iron uptake mechanisms of pathogenic bacteria. *FEMS Microbiol Rev* 1993;12:325–48.
- [14] Ratledge C, Dover LG. Iron metabolism in pathogenic bacteria. *Annu Rev Microbiol* 2000;54:881–941.
- [15] Litwin CM, Byrne BL. Cloning and characterization of an outer membrane protein of *Vibrio vulnificus* required for heme utilization: regulation of expression and determination of the gene sequence. *Infect Immun* 1998;66:3134–41.
- [16] Oh MH, Lee SM, Lee DH, Choi SH. Regulation of the *Vibrio vulnificus* *hupA* gene by temperature alteration and cyclic AMP receptor protein and evaluation of its role in virulence. *Infect Immun* 2009;77:1208–15.
- [17] Kustusch RJ, Kuehl CJ, Crosa JH. The *tpc* gene is contained in two of three TonB systems in the human pathogen *Vibrio vulnificus*, but only one is active in iron transport and virulence. *J Bacteriol* 2012;194:3250–9.
- [18] Hantke K. Iron and metal regulation in bacteria. *Curr Opin Microbiol* 2001;4:172–7.
- [19] de Lorenzo V, Wee S, Herrero M, Neilands JB. Operator sequences of the aerobactin operon of plasmid ColV–K30 binding the ferric uptake regulation (*fur*) repressor. *J Bacteriol* 1987;169:2624–30.
- [20] Kim CM, Park JJ, Shin SH. A widespread deferoxamine-mediated iron-uptake system in *Vibrio vulnificus*. *J Infect Dis* 2007;196:1537–45.
- [21] Tanabe T, Takata N, Naka A, Moon YH, Nakao H, Inoue Y, et al. Identification of an AraC-like regulator gene required for induction of the 78-kDa ferrioxamine B receptor in *Vibrio vulnificus*. *FEMS Microbiol Lett* 2005;249:309–14.
- [22] Kim JS, Sung MH, Kho DH, Lee JK. Induction of manganese-containing superoxide dismutase is required for acid tolerance in *Vibrio vulnificus*. *J Bacteriol* 2005;187:5984–95.
- [23] Kimoto R, Funahashi T, Yamamoto N, Miyoshi S, Narimatsu S, Yamamoto S. Identification and characterization of the *sodA* genes encoding manganese superoxide dismutases in *Vibrio parahaemolyticus*, *Vibrio mimicus*, and *Vibrio vulnificus*. *Microbiol Immunol* 2001;45:135–42.
- [24] Tanabe T, Naka A, Aso H, Nakao H, Narimatsu S, Inoue Y, et al. A novel aerobactin utilization cluster in *Vibrio vulnificus* with a gene involved in the transcription regulation of the *iutA* homologue. *Microbiol Immunol* 2005;49:823–34.
- [25] Webster ACD, Litwin CM. Cloning and characterization of *vuuA*, a gene encoding the *Vibrio vulnificus* ferric vulnibactin receptor. *Infect Immun* 2000;68:526–34.
- [26] Miyamoto K, Kosakai K, Ikebayashi S, Tsuchiya T, Yamamoto S, Tsujibo H. Proteomic analysis of *Vibrio vulnificus* M2799 grown under iron-repleted and iron-depleted conditions. *Microb Pathog* 2009;46:171–7.
- [27] Alice AF, Naka H, Crosa JH. Global gene expression as a function of the iron status of the bacterial cell: influence of differentially expressed genes in the virulence of the human pathogen *Vibrio vulnificus*. *Infect Immun* 2008;76:4019–37.
- [28] Simpson LM, Oliver JD. Siderophore production by *Vibrio vulnificus*. *Infect Immun* 1983;41:644–9.
- [29] Griffiths GL, Sigel SP, Payne SM, Neilands JB. Vibriobactin, a siderophore from *Vibrio cholerae*. *J Biol Chem* 1984;259:383–5.
- [30] Okujo N, Saito M, Yamamoto S, Yoshida T, Miyoshi S, Shinoda S. Structure of vulnibactin, a new polyamine-containing siderophore from *Vibrio vulnificus*. *Biometals* 1994;7:109–16.
- [31] Kim CM, Park RY, Park JH, Sun HY, Bai YH, Ryu PY, et al. *Vibrio vulnificus* vulnibactin, but not metalloprotease VvpE, is essentially required for iron-uptake from human holotransferrin. *Biol Pharm Bull* 2006;29:911–8.
- [32] Kim IH, Shim JJ, Lee KE, Hwang W, Kim JJ, Choi SH, et al. Nonribosomal peptide synthase is responsible for the biosynthesis of siderophore in *Vibrio vulnificus* MO6-24/O. *J Microbiol Biotechnol* 2008;18:35–42.
- [33] Miller VL, Mekalanos JJ. A novel suicide vector and its use in construction of insertion mutations: osmoregulation of outer membrane proteins and

- virulence determinants in *Vibrio cholerae* requires toxR. J Bacteriol 1988;170:2575–83.
- [34] Milton DL, O'Toole R, Horstedt P, Wolf-Watz H. Flagellin A is essential for the virulence of *Vibrio anguillarum*. J Bacteriol 1996;178:1310–9.
- [35] Keen NT, Tamaki S, Kobayashi D, Trollinger D. Improved broad-host-range plasmids for DNA cloning in gram-negative bacteria. Gene 1988;70:191–7.
- [36] Kim YR, Lee SE, Kim CM, Kim SY, Shin EK, Shin DH, et al. Characterization and pathogenic significance of *Vibrio vulnificus* antigens preferentially expressed in septicemic patients. Infect Immun 2003;71:5461–71.
- [37] Lee HJ, Lee KH. Identification of the *fur*-binding site in regulatory region of the vulnibactin-receptor gene in *Vibrio vulnificus*. J Microbiol Biotechnol 2012;22:46–9.
- [38] Tanabe T, Funahashi T, Miyamoto K, Tsujibo H, Yamamoto S. Identification of genes, *desR* and *desA*, required for utilization of desferrioxamine B as a xenosiderophore in *Vibrio furnissii*. Biol Pharm Bull 2011;34:570–4.
- [39] Csaky TZ. On the estimation of bound hydroxylamine in biological materials. Acta Chem Scand 1948;2:450–4.
- [40] Wyckoff EE, Valle AM, Smith SL, Payne SM. A multifunctional ATP-binding cassette transporter system from *Vibrio cholerae* transports vibriobactin and enterobactin. J Bacteriol 1999;181:7588–96.
- [41] Brickman TJ, McIntosh MA. Overexpression and purification of ferric enterobactin esterase from *Escherichia coli*. Demonstration of enzymatic hydrolysis of enterobactin and its iron complex. J Biol Chem 1992;267:12350–5.
- [42] Butterton JR, Calderwood SB. Identification, cloning, and sequencing of a gene required for ferric vibriobactin utilization by *Vibrio cholerae*. J Bacteriol 1994;176:5631–8.
- [43] Santhanagopalan SM, Rodriguez GM. Examining the role of Rv2895c (ViuB) in iron acquisition in *Mycobacterium tuberculosis*. Tuberculosis 2012;92:60–2.
- [44] Miethke M, Hou J, Marahiel MA. The siderophore-interacting protein YqjH acts as a ferric reductase in different iron assimilation pathways of *Escherichia coli*. Biochemistry 2011;50:10951–64.



Application of electrolysis for inactivation of an antiviral drug that is one of possible selection pressure to drug-resistant influenza viruses



Toyohide Kobayashi^{a,b}, Jun Hirose^{a,c,1}, Hong Wu^c, Kouichi Sano^{a,c}, Takahiro Katsumata^b, Hiroshi Tsujibo^d, Takashi Nakano^{a,c,*}

^a Project Team for Medical Application of Electrolysis, Central Research Center, Osaka Medical College, 2-7 Daigaku-machi, Takatsuki-shi, Osaka 569-8686, Japan

^b Department of Pharmacy, Osaka Medical College Hospital, 2-7 Daigaku-machi, Takatsuki-shi, Osaka 569-8686, Japan

^c Department of Microbiology and Infection Control, Osaka Medical College, 2-7 Daigaku-machi, Takatsuki-shi, Osaka 569-8686, Japan

^d Department of Microbiology, Osaka University of Pharmaceutical Sciences, 4-20-1 Nasahara, Takatsuki-shi, Osaka 569-1094, Japan

A B S T R A C T

Article history:

Received 25 January 2013

Received in revised form 6 August 2013

Accepted 9 August 2013

Available online 27 August 2013

Keywords:

Tamiflu
Oseltamivir
Waterfowl
Avian influenza virus
Surface water
Available chlorine

The recent development of antiviral drugs has led to concern that the release of the chemicals in surface water due to expanded medical use could induce drug-resistant mutant viruses in zoonosis. Many researchers have noted that the appearance of an oseltamivir (Tamiflu®)-resistant avian influenza mutant virus, which may spread to humans, could be induced by oseltamivir contamination of surface water. Although past studies have reported electrolysis as a possible method for degradation of anti-neoplastics and antibacterials in water, the validity of the method for treatment of antiviral drugs is unknown. In this study, electrolysis was used to degrade an antiviral prodrug, oseltamivir, and a stable active form, oseltamivir carboxylate, and the degradation process was monitored with HPLC-UV and the neuraminidase inhibitory assay. HPLC-UV-detectable oseltamivir and oseltamivir carboxylate were decomposed by electrolysis within 60 min, and inhibitory activity of neuraminidase decreased below the detection limit of the assay used. Cytotoxic and genotoxic activity were not detected in electrolyzed fluid. These results indicate that electrolysis is a possible treatment for inactivation of the antiviral drug oseltamivir.

© 2013 Elsevier B.V. All rights reserved.

1. Introduction

Oseltamivir (Tamiflu®) is a medicine originally invented as a treatment drug of seasonal influenza (WHO, 2003; Ward et al., 2005). Oseltamivir has been used as a prophylactic drug to prevent the infection to compromised hosts. Future influenza pandemic by a novel virus strain is discussing, and the possible way of emerging pandemic strain is the mutation of avian-origin influenza virus strains (Olsen et al., 2006; Järhult et al., 2011). Oseltamivir was proved to be effective to reduce human-to-human transmission of avian influenza virus (H5N1) (Schünemann et al., 2007). Because of these advantageous properties, oseltamivir is also recommended as a primary preventive antiviral drug in the event of an influenza

pandemic (von Itzstein, 2007), and many individual nations and global organizations has stockpiled oseltamivir in the event of influenza pandemic (Harrod et al., 2006).

Orally administered oseltamivir and absorbed from the gastrointestinal tract and is immediately converted to the active metabolite oseltamivir carboxylate, a potent and selective inhibitor of influenza virus neuraminidase (Hill et al., 2002). Biotransformation from oseltamivir to oseltamivir carboxylate is illustrated in Fig. 1. The absolute bioavailability of oseltamivir is approximately 80% when 150 mg of oseltamivir is administered orally (Li et al., 1998; He et al., 1999). Oseltamivir carboxylate is entirely eliminated by renal excretion, and unabsorbed oseltamivir is excreted in feces (Li et al., 1998; He et al., 1999). Several animal species can convert oseltamivir to oseltamivir carboxylate, and excrete oseltamivir carboxylate from the urinary tract (Tamiflu® interviewform, 2009). Oseltamivir carboxylate is stable in the environment, and once the converted chemical enters the surface water, it may be consumed by waterfowl. In this way, when oseltamivir carboxylate reaches an intestinal tract of waterfowls, the virus which exists in the tract replicates and resistant mutants of the virus are induced (Singer et al., 2007). Recently, resistant mutants to oseltamivir carboxylate

* Corresponding author at: Department of Microbiology and Infection Control, Osaka Medical College, 2-7 Daigaku-machi, Takatsuki-shi, Osaka 569-8686, Japan. Tel.: +81 72 684 7367; fax: +81 72 684 6517.

E-mail address: tnakano@art.osaka-med.ac.jp (T. Nakano).

¹ Present address: HORIBA, Ltd., Miyanohigashi, Kisshoin, Minami-ku, Kyoto-shi, Kyoto Prefecture 601-8510, Japan.

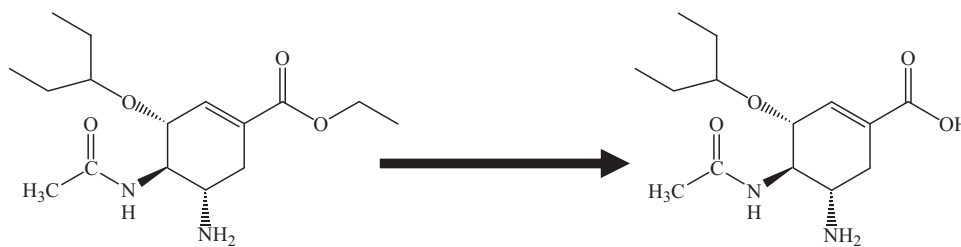


Fig. 1. Biotransformation of oseltamivir carboxylate from oseltamivir. Oseltamivir is catalyzed to the active metabolite, oseltamivir carboxylate by esterase *in vivo*. The reaction formula is shown.

in avian influenza viruses were actually isolated from wild birds (Orozovic et al., 2011).

If an oseltamivir carboxylate-resistant avian influenza virus was to spread as a pandemic in humans, vast oseltamivir phosphate stockpiles would not be helpful for medical treatment and prevention of avian-origin influenza. Therefore, detailed investigations of the persistence and degradability of oseltamivir carboxylate in the aquatic environment have been conducted (Singer et al., 2007; Bartels and von Tümpling, 2008; Saccà et al., 2009; Straub, 2009; Ghosh et al., 2010a,b). Furthermore, several studies have investigated methods for eliminating oseltamivir carboxylate before releasing sewage effluent to the surface water (Saccà et al., 2009; Ghosh et al., 2010a,b; Accinelli et al., 2010a,b; Gonçalves et al., 2011).

The potential for electrolysis methods to detoxify clinical wastewater has been evaluated. By this method, antineoplastics and antibacterials can be effectively inactivated (Hirose et al., 2005; Nakano et al., 2013). A bench-top electrolysis apparatus was shown to detoxify clinical wastewater containing antineoplastics with low energy consumption relative to another method of disposal (Kobayashi et al., 2008). Furthermore, the ability of the electrolysis method to inactivate antineoplastics in urine has been demonstrated (Kobayashi et al., 2012).

Oseltamivir and oseltamivir carboxylate solutions were electrolyzed on a small scale and whether our electrolysis method could decompose the chemicals was examined.

2. Materials and methods

2.1. Chemicals and reagents

Oseltamivir phosphate (Ro 64-0796) and D-tartrate of oseltamivir carboxylate (Ro 64-0802) were kindly provided by F. Hoffmann-La Roche (Basel, Switzerland). Sotalol hydrochloride was purchased from Tocris Bioscience (Ellisville, Missouri, USA). Ultrapure water was prepared with Yamato Millipore WQ 500 (Yamato Scientific, Tokyo, Japan) and used as the diluent.

2.2. Instruments and analytical condition

Oseltamivir and oseltamivir carboxylate concentrations before and after electrolysis were quantified with HPLC (high performance liquid chromatography)-UV (ultraviolet absorption) detection. The HPLC system (Shimadzu, Kyoto, Japan) consisted of a pump (LC-10ADvp system) and a UV detector SPD-10MAvp set at 220 nm. The analytical column, SUMIPAX ODS L-05-4615 (4.6 mm × 150 mm, 5 μm particle size) (Sumika Chemical Analysis Service, Osaka, Japan) was operated at an ambient temperature of 40 °C. The mobile phase was a 20 min linear gradient of 10% 100 mM phosphate solution to 90% acetonitrile at a flow rate of 1 mL/min. Sotalol hydrochloride was used as an internal standard (Joseph-Charles et al., 2007).

2.3. Stock and working standard solutions

Standard solutions of 320 μg/mL of oseltamivir phosphate and 303.2 μg/mL of D-tartrate of oseltamivir carboxylate were prepared. The 2 times serial dilution of each standard solution was prepared. The calibration curve was plotted with 13 point concentrations ranging from 0 to 320 μg/mL for oseltamivir phosphate, and from 0 to 303.2 μg/mL for D-tartrate of oseltamivir carboxylate, respectively. The internal standard solution (10 μg/mL of sotalol hydrochloride) was prepared. The calibration standards were freshly prepared on each day of analysis. To calculate peak area ratios, the oseltamivir and oseltamivir carboxylate peak areas were divided into the area of the internal standard. The theoretical concentration ratios were calculated as a ratio of oseltamivir or oseltamivir carboxylate concentration to the internal standard concentration. The calibration curve was generated from the peak area and theoretical concentration ratios.

2.4. Electrolysis procedure and neutralization of available chlorine

Solutions of 410.40 μg/mL of oseltamivir phosphate and 386.44 μg/mL of D-tartrate of oseltamivir carboxylate were prepared with 0.9% NaCl. These concentrations are equivalent to 1 mM oseltamivir and oseltamivir carboxylate solutions. A volume of 250 mL of oseltamivir or oseltamivir carboxylate solution was electrolyzed in a 300 mL glass beaker using a pair of electrodes (115 mm × 35 mm, placed 5 mm apart). These platinum-based iridium oxide composite electrode are advantageous for both their durability and their ability to generate available chlorine (Panizza and Cerisola, 2009). In this experiment, 1400–1530 mg/L of available chlorine was generated with 2 h of electrolysis. The electrodes were inserted into the beaker, and the solution was electrolyzed with stirring for 2 h at a constant current of 1 A. The current density was 2.48 A/dm². Samples were collected before and during electrolysis. A solution of 20% (w/v) sodium thiosulfate was used to neutralize the available chlorine that was generated by anodic oxidation during electrolysis, and the measurements were verified to ensure that the addition of 20% thiosulfate did not influence the results. The concentration of the samples was determined by analyzing 20 μL with the HPLC-UV system.

2.5. Determination of neuraminidase inhibitory activity

Inactivation of neuraminidase inhibitory activity of oseltamivir or oseltamivir carboxylate by electrolysis was measured using chemiluminescence assay (NA-Star, Influenza Neuraminidase Inhibitor Resistance Detection Kit, Life Technologies Japan, Tokyo, Japan) according to the manufacturer's instructions. For neuraminidase, human influenza virus A/Wyoming/3/2003 (H3N2) provided by Osaka Prefectural Institute of Public Health was used.

2.6. Evaluation of cytotoxicity against human cells

The cytotoxicity was evaluated using the human lymphoblastoid cell line Molt-4. A sample was diluted fourfold with RPMI-1640 medium containing 10% fetal bovine serum and the same volume of a medium containing 5×10^5 cells/mL. The mixture was then incubated in a U-bottom 96-well microplate in an atmosphere containing 5% CO₂ at 37 °C for 3 d. One hundred microliters of the cell culture was transferred to a flat-bottom 96-well microplate, mixed with 10 μ L of the solution included in the WST-8 cell counting kit (Dojin, Kumamoto, Japan), and incubated at 37 °C for 1 h. The optical density of the plate was measured using an optical densitometer (ImmunoMini NJ-2300, Microtec, Tokyo, Japan) at a wavelength of 450 nm with a reference wavelength of 620 nm. The mean and standard deviation (SD) of the optical density of the well containing culture media instead of electrolyzed solution were calculated, and disappearance of cytotoxic concentration was defined as over “mean – 2 \times SD”. The indexes of samples taken before and after electrolysis were compared.

2.7. Evaluation of genotoxicity

Whether electrolysis generates genotoxic properties in oseltamivir and oseltamivir carboxylate solutions using a kit for the *umu*-test (Protein Purify, Maebashi, Japan) (Oda et al., 1985) was examined. The kit determines *umu* gene expression using β -galactosidase activity as the index. The *umu* gene is one of the SOS genes, a group of genes induced as a result of DNA damage; the *umu* gene is directly involved in mutation. The test results are in accord with the results of the Ames test (Seino et al., 1978). When an SOS response is induced by a mutagenic substance, the “*umuC-lacZ*” fusion gene, which is under the control of the *umu* gene promoter, is expressed. β -Galactosidase activity of the gene product is used as an indicator of the degree of the SOS response; namely, the degree of genotoxicity. Assays of the oseltamivir and oseltamivir carboxylate solutions were performed according to the manufacturer's instructions.

3. Results

3.1. HPLC analysis

To determine whether oseltamivir and oseltamivir carboxylate decompose with electrolysis, qualitative analysis was performed by HPLC. A typical chromatogram of oseltamivir before and during electrolysis is shown in Fig. 2A. Before electrolysis, the retention time of the internal standard and oseltamivir were 3.79 and 10.23 min, respectively. The oseltamivir peak completely disappeared with 2 h of electrolysis. In comparison, the retention time of the internal standard and oseltamivir carboxylate were 3.79 and 7.73 min, respectively (Fig. 2B). The oseltamivir carboxylate peak also disappeared with 2 h of electrolysis. After electrolysis, both decomposed oseltamivir and oseltamivir carboxylate generate hydrophilic products with elution peaks at approximately 2.5 min retention time.

To determine the concentrations of oseltamivir and oseltamivir carboxylate, calibration curves were generated by the internal standard method. The oseltamivir and oseltamivir carboxylate calibration curves are shown in Fig. 3A; the correlation coefficient (*R*) was 0.999 for both oseltamivir and oseltamivir carboxylate. The upper limits of quantification were 243.59 μ g/mL for oseltamivir and 223.14 μ g/mL for oseltamivir carboxylate. The lower detection limit of oseltamivir and oseltamivir carboxylate was 1 μ g/mL, which was determined according to the method prescribed in Manual on analysis of investigated items (water, soil, aquatic organism)

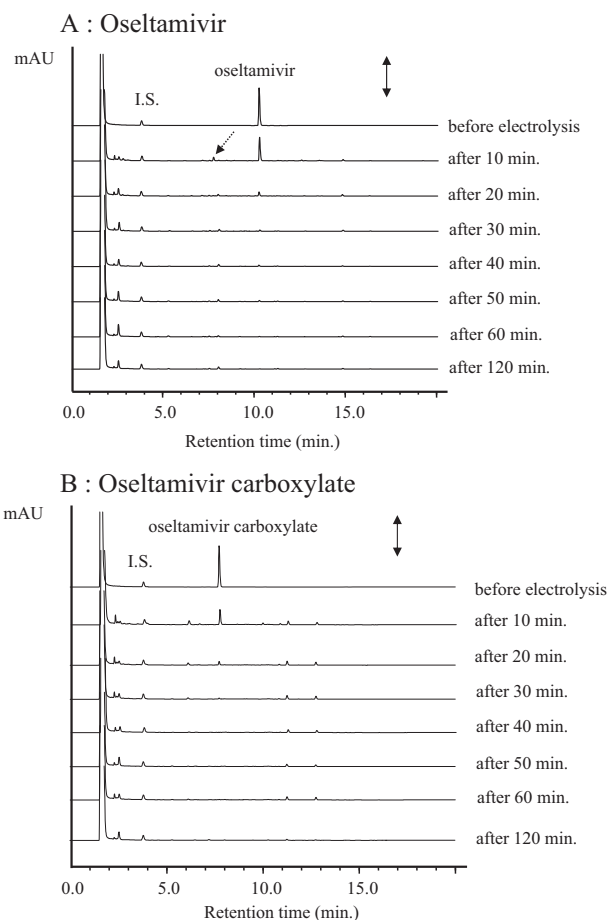


Fig. 2. The typical chromatogram of oseltamivir (A) and oseltamivir carboxylate (B) before and during electrolysis. (A) Time-dependent degradation of oseltamivir and passing appearance of oseltamivir carboxylate (break arrow) were demonstrated. (B) Time-dependent degradation of oseltamivir carboxylate was demonstrated. I.S. = internal standard. Arrows indicate 500 mAU.

(Ministry of the Environment, 2008). The lower limit of quantification was also 1 μ g/mL according to the inset of Fig. 3A. When oseltamivir or oseltamivir carboxylate concentration is beyond upper quantification limit, the concentration was determined by 2-fold dilution.

Electrolysis to perform the quantitative analysis of oseltamivir and oseltamivir carboxylate before and during electrolysis was carried out 3 times. The oseltamivir concentration was 297.60 ± 4.62 μ g/mL before electrolysis; after 60 min of electrolysis, the oseltamivir was below the detection limit. Although electrolysis generated oseltamivir carboxylate from oseltamivir in the early phase, the oseltamivir carboxylate was decomposed to below the detection limit within 30 min (Fig. 3B). In electrolysis of oseltamivir carboxylate, oseltamivir carboxylate concentration was 291.80 ± 8.99 μ g/mL before electrolysis, and fell below the detection limit after 50 min of electrolysis (Fig. 3C).

3.2. Determination of neuraminidase inhibitory activity

Neuraminidase inhibitory activity of oseltamivir carboxylate, the active form of oseltamivir, before and after electrolysis was measured. Because HPLC analysis indicated that electrolysis hydrolyzed a portion of oseltamivir to oseltamivir carboxylate, electrolysis of oseltamivir was also performed. In addition, the concentration of 50% neuraminidase inhibitory activity (IC₅₀) was determined for oseltamivir with chemiluminescence assay (Fig. 4). This assay has enough reproducibility and greater sensitivity

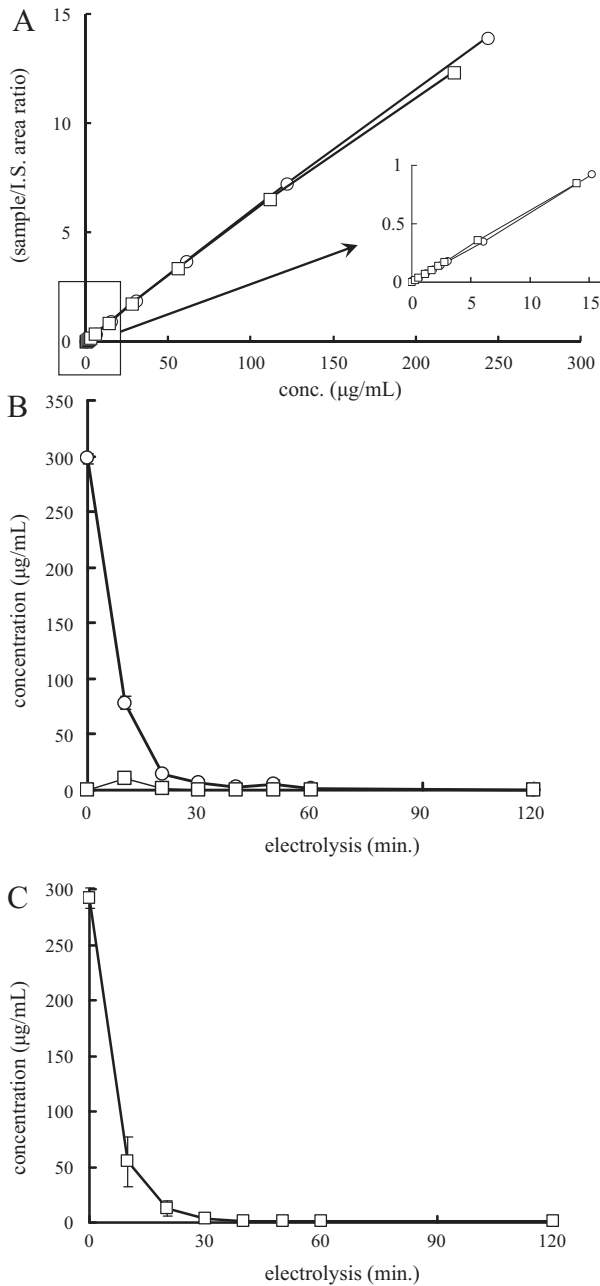


Fig. 3. (A) Calibration curves of oseltamivir and oseltamivir carboxylate. The relationship between the concentrations of oseltamivir or oseltamivir carboxylate and the relative peak area of samples compared with internal standard (I.S.) are shown. Open circles (○) represent oseltamivir, and open squares (□) represent oseltamivir carboxylate. (B) Electrolysis of oseltamivir solution, and concentrations of oseltamivir and oseltamivir carboxylate. Open circles (○) represent oseltamivir, and open squares (□) represent oseltamivir carboxylate. Measurements were made three times; and results shown are the mean \pm standard deviation. (C) Electrolysis of oseltamivir carboxylate solution and concentration of oseltamivir carboxylate. Open squares (□) represent oseltamivir carboxylate. Measurements were made three times; the results shown are the mean \pm standard deviation.

for susceptibility testing of influenza virus isolates (Wetherall et al., 2003). In their report, IC_{50} s of most of oseltamivir carboxylate sensitive strains of influenza A virus were 0.30–0.54 nM (0.085–0.154 ng/mL), and those of resistant ones were more than 76 times higher than those (median IC_{50} = 9.1 ng/mL), which is supposed that neuraminidase inhibition activity more than 9.1 ng/mL is virtually no pharmacological activities against viral neuraminidases. The IC_{50} value of oseltamivir was more than

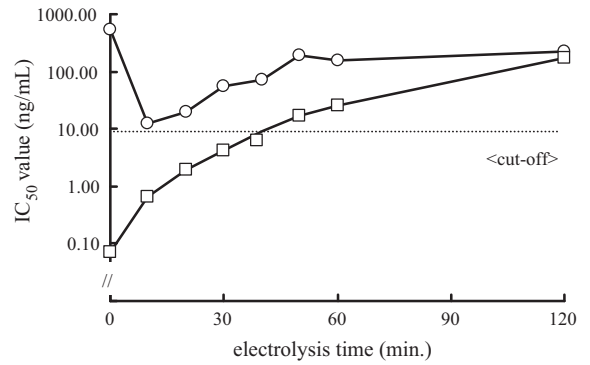


Fig. 4. Change of inhibitory activity of neuraminidase with electrolysis. Oseltamivir or oseltamivir carboxylate solutions were electrolyzed, and the neuraminidase inhibitory activities of electrolyzed products were shown. Open circles (○) represent oseltamivir, and open squares (□) represent oseltamivir carboxylate. Break line shows the cut-off value (9.1 ng/mL) of virtually no pharmacological activities against viral neuraminidases. See text in details.

9.1 ng/mL before electrolysis, and during electrolysis, it seemed to be activated after 10 min of electrolysis. After 20 min of electrolysis, the IC_{50} value increased. This result is consistent with those of HPLC analysis: Oseltamivir is partly hydrolyzed to oseltamivir carboxylate by electrolysis. In comparison, the IC_{50} value of oseltamivir carboxylate was 0.073 ng/mL before electrolysis and more than 9.1 ng/mL after 50 min of electrolysis. These data were the results when 1 mM of oseltamivir or oseltamivir carboxylate was electrolyzed, and to investigate whether oseltamivir carboxylate could be degraded at a lower concentration, 1 μ M (284.4 ng/mL) and 1 nM (284.4 pg/mL) oseltamivir carboxylate were electrolyzed. When 1 μ M oseltamivir carboxylate was electrolyzed, the IC_{50} value was 0.148 ng/mL before electrolysis and more than 9.1 ng/mL after 60 min of electrolysis. The lower concentration of oseltamivir carboxylate, 1 nM, was below the detection limit for neuraminidase inhibitory activity.

3.3. Evaluation of cytotoxicity against human cells

To examine whether new toxicity is generated in electrolyzed oseltamivir and oseltamivir carboxylate solutions, their cytotoxic activity toward human cells was measured. The detection limit of this assay for oseltamivir was 18.22 μ g/mL, and the cytotoxicity of both samples before and after 2 h of electrolysis was below the detection limit. For oseltamivir carboxylate, the cytotoxicity of samples taken before and after 2 h of electrolysis was below the detection limit, 16.58 μ g/mL. These results indicate that the cytotoxicity of oseltamivir and oseltamivir carboxylate was not changed by electrolysis; therefore, new toxic activities were not generated in electrolyzed solutions of oseltamivir or oseltamivir carboxylate.

3.4. Evaluation of genotoxicity

To evaluate whether electrolyzed oseltamivir and oseltamivir carboxylate solution acquired genotoxic properties, 1 mM oseltamivir and oseltamivir carboxylate solutions were electrolyzed and *umu* tests were performed according to the directions provided by the kit manufacturer. Genotoxic properties were determined directly from the OD_{620} value obtained from the β -galactosidase activity of the *umu-lacZ* chimeric gene product. The cut-off O.D. value for the assay was 0.231. The O.D. value for 0.3 μ g/mL of AF-2, which was used as a positive control in the absence of S-9 mix was 0.256 for 0.3 μ g/mL of 2-AA, a positive control in the presence of S-9 mix, the O.D. value was 0.247. Both O.D. values were above the cut off level, indicating that these concentrations of AF-2 and 2-AA exhibited genotoxic properties.

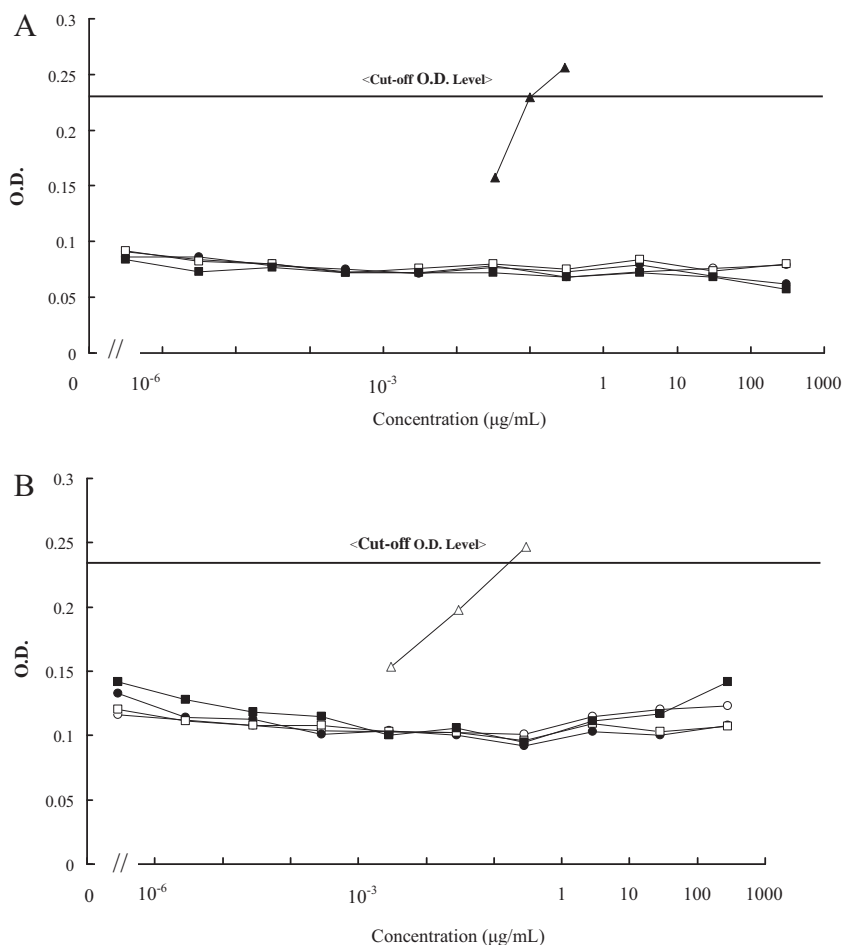


Fig. 5. (A) Evaluation of mutagenicity with *umu*-test in absence of S-9 mixture. Open and closed circles (○, ●) represent oseltamivir before and after electrolysis, respectively. Open and closed squares (□, ■) represent oseltamivir carboxylate before and after electrolysis, respectively. Closed triangles (▲) represent AF-2, which was used as a control. (B) Evaluation of mutagenicity with *umu*-test in presence of S-9 mixture. Open and closed circles (○, ●) represent oseltamivir before and after electrolysis, respectively. Open and closed squares (□, ■) represent oseltamivir carboxylate before and after electrolysis, respectively. Open triangles (△) represent 2-AA, which was used as a control.

Under the S-9-mix-absence condition, the optical density of oseltamivir solutions with concentrations between 312.4 µg/mL and 312.4 fg/mL was below the cut-off level; the optical density of electrolyzed oseltamivir solution was also below the cut-off level. The optical density was below the cut-off level for solutions with oseltamivir carboxylate concentrations between 284.4 µg/mL and 284.4 fg/mL as well as for electrolyzed oseltamivir carboxylate solution (Fig. 5A). Under the S-9-mix-presence condition, the optical density of oseltamivir, oseltamivir carboxylate, electrolyzed oseltamivir and electrolyzed oseltamivir carboxylate solutions was below the cut-off level (Fig. 5B). These results indicate that oseltamivir, oseltamivir carboxylate, electrolyzed oseltamivir and electrolyzed oseltamivir carboxylate solutions did not exhibit genotoxicity.

4. Discussion

Electrolyzed oseltamivir and oseltamivir carboxylate were measured by HPLC and neuraminidase inhibition assays in order to demonstrate that electrolysis decomposed both oseltamivir and oseltamivir carboxylate. Electrolysis significantly decomposed these chemicals, removed their pharmacological activity within 60 min, and did not generate any of the cytotoxic and genotoxic activities investigated here.

Excreted oseltamivir carboxylate is not significantly removed from sewage effluent by conventional sewage treatment methods,

which include mechanical, chemical and biological processes (Fick et al., 2007). Recently, oseltamivir carboxylate has been detected in surface water (Söderström et al., 2009; Ghosh et al., 2010a,b; Accinelli et al., 2010a). When large numbers of patients in urban areas are infected with influenza and administer oseltamivir, the potential risk of surface water contamination with oseltamivir carboxylate should be considered due to its toxicity to aquatic life and the potential for drug-resistant virus induction. Oseltamivir carboxylate does not appear to negatively affect aquatic ecology, including the growth, development and reproduction of aquatic life, under conditions of regular seasonal-use or high pandemic use of oseltamivir (Straub, 2009). In the present study, oseltamivir, oseltamivir carboxylate and their electrolyzed solutions did not demonstrate cytotoxicity or genotoxicity *in vitro*.

Surface water concentrations of oseltamivir carboxylate on the order of ng/L to µg/L are commonly estimated under seasonal-influenza and pandemic-influenza conditions (Singer et al., 2007; Bartels and von Tümpling, 2008; Saccà et al., 2009; Straub, 2009; Söderström et al., 2009; Ghosh et al., 2010a,b). As µg/L-levels of oseltamivir carboxylate are presumed in the environment, our experimental conditions correspond to a realistic scenario. Experimentally, oseltamivir carboxylate concentration which is above 1 µg/L was documented that resistance mutation H274Y was induced and developed in influenza A/H1N1 virus in mallards (Järhult et al., 2011). There is a risk of resistant gene accumulation in the influenza viruses circulating among wild birds when

oseltamivir is used extensively. By genetic reassortment or recombination, oseltamivir resistant strain can be transmitted to humans potentially causing a resistant pandemic or human-adapted highly pathogenic avian influenza (Järhult, 2012). To avoid widespread of resistant strains in the natural reservoir of viruses, oseltamivir carboxylate concentration in wastewater should be decreased before arriving at surface water.

The electrolysis method has been shown to decompose oseltamivir carboxylate by several orders of concentration partially-including the estimated environmental conditions ($\mu\text{g/L}$ to mg/L); therefore, it may have practical applications, such as eliminating the chemicals at the origin of contamination.

Potential source of oseltamivir contamination is expired Tamiflu[®] stockpiles. It was also confirmed that the oseltamivir in capsules could be decomposed with electrolysis using HPLC detection (data not shown). Because electrolysis requires less environmental load to decompose clinical wastes than other disposal methods (Kobayashi et al., 2008), it may be advantageously applied to the disposal of expired Tamiflu[®] capsules.

Recently, various methods have been reported to eliminate oseltamivir carboxylate in surface water, including bacterial degradation in sediment (Accinelli et al., 2010a), a granular bioplastic formulation entrapping (Accinelli et al., 2010b), conventional activated-sludge-based sewage treatment with ozonation (Ghosh et al., 2010a,b) and photodegradation (Gonçalves et al., 2011). A suitable method for the degradation of oseltamivir carboxylate has not yet been found. Our study is the first report that electrolysis simultaneously reduces both the concentration of chemicals and the pharmacological activity of oseltamivir carboxylate. Another advantageous property of the electrolysis method is that it can rapidly eliminate both oseltamivir and oseltamivir carboxylate with high removal efficacy. More recently, electrolysis was demonstrated to decompose an antineoplastic in urine (Kobayashi et al., 2012). It was suggested that oseltamivir carboxylate excreted in urine may also be decomposed with electrolysis. Further experiments that directly show the decomposition of oseltamivir carboxylate in surface water and urine by electrolysis are required.

5. Conclusions

The objective of this research was to determine whether electrolysis method can degrade an antiviral prodrug, oseltamivir phosphate (Tamiflu[®]) and a stable active form, oseltamivir carboxylate. The results obtained from this study revealed that HPLC-UV-detectable oseltamivir and oseltamivir carboxylate were decomposed by electrolysis within 60 min, and inhibitory activity of neuraminidase decreased below detection limit of the assay. Cytotoxic and genotoxic activity were not detected in electrolyzed fluid. The following can be concluded from the results of this research: electrolysis method is applicable to degrade both oseltamivir and oseltamivir carboxylate.

Acknowledgments

This study was supported by a Grant for Industry-University Collaborative Study from the Ministry of Education, Culture, Sports, Science and Technology, Japan. In addition, this work was supported by Grant-in-Aid for Scientific Research (KAKENHI) (C) No. 22510091. We acknowledge F. Hoffmann-La Roche, Pharma Research (Basel, Switzerland) for providing samples of oseltamivir phosphate and D-tartrate of oseltamivir carboxylate, and Osaka Prefectural Institute of Public Health for providing human influenza virus A/Wyoming/3/2003 (H3N2). We thank Ms. Hiroko Oki and Ms. Keiko Matsumura for preparation of cells and manuscripts,

respectively. Special thanks are given to Ms. Kaori Yamauchi (Sumika Chemical Analysis Service, Chiba Laboratory, Japan) for performing HPLC analyses.

References

- Accinelli, C., Saccà, M.L., Fick, J., Mencarelli, M., Lindberg, R., Olsen, B., 2010a. Dissipation and removal of oseltamivir (Tamiflu) in different aquatic environments. *Chemosphere* 79, 891–897.
- Accinelli, C., Saccà, M.L., Batisson, I., Fick, J., Mencarelli, M., Grabic, R., 2010b. Removal of oseltamivir (Tamiflu) and other selected pharmaceuticals from wastewater using a granular bioplastic formulation entrapping propagules of *phanerochaete chrysosporium*. *Chemosphere* 81, 436–443.
- Bartels, P., von Tümpling Jr., W., 2008. The environmental fate of the antiviral drug oseltamivir carboxylate in different waters. *Sci. Total Environ.* 405, 215–225.
- Fick, J., Lindberg, R.H., Tysklind, M., Haemig, P.D., Waldenström, J., Wallensten, A., Olsen, B., 2007. Antiviral oseltamivir is not removed or degraded in normal sewage water treatment: implications for development of resistance by influenza A virus. *PLoS ONE* 2 (10), e986.
- Ghosh, G.C., Nakada, N., Yamashita, N., Tanaka, H., 2010a. Oseltamivir carboxylate, the active metabolite of oseltamivir phosphate (Tamiflu), detected in sewage discharge and river water in Japan. *Environ. Health Perspect.* 118, 103–107.
- Ghosh, G.C., Nakada, N., Yamashita, N., Tanaka, H., 2010b. Occurrence and fate of oseltamivir carboxylate (Tamiflu) and amantadine in sewage treatment plants. *Chemosphere* 81, 13–17.
- Gonçalves, C., Pérez, S., Osorio, V., Petrovic, M., Alpendurada, M.F., Barceló, D., 2011. Photofate of oseltamivir (Tamiflu) and oseltamivir carboxylate under natural and simulated solar irradiation: kinetics, identification of the transformation products, and environmental occurrence. *Environ. Sci. Technol.* 45, 4307–4314.
- Harrod, M.E., Emery, S., Dwyer, D.E., 2006. Antivirals in the management of an influenza pandemic. *Med. J. Aust.* 185 (10 Suppl.), S58–S61.
- He, G., Massarella, J., Ward, P., 1999. Clinical pharmacokinetics of the prodrug oseltamivir and its active metabolite Ro 64-0802. *Clin. Pharmacokinet.* 37, 471–484.
- Hill, G., Cihlar, T., Oo, C., Ho, E.S., Prior, K., Wiltshire, H., Barrett, J., Liu, B., Ward, P., 2002. The anti-influenza drug oseltamivir exhibits low potential to induce pharmacokinetic drug interactions via renal secretion-correlation of in vivo and in vitro studies. *Drug Metab. Dispos.* 30, 13–19.
- Hirose, J., Kondo, F., Nakano, T., Kobayashi, T., Hiro, N., Ando, Y., Takenaka, H., Sano, K., 2005. Inactivation of antineoplastics in clinical wastewater by electrolysis. *Chemosphere* 60, 1018–1024.
- Järhult, J.D., Muradrasoli, S., Wahlgren, J., Söderström, H., Orozovic, G., Gunnarsson, G., Bröjer, C., Latorre-Margalef, N., Fick, J., Grabic, R., Lennerstrand, J., Waldenström, J., Lundkvist, A., Olsen, B., 2011. Environmental levels of the antiviral oseltamivir induce development of resistance mutation H274Y in influenza A/H1N1 virus in Mallards. *PLoS ONE* 6 (9), e24742.
- Järhult, J.D., 2012. Oseltamivir (Tamiflu[®]) in the environment, resistance development in influenza A viruses of dabbling ducks and the risk of transmission of an oseltamivir-resistant virus to humans – a review. *Infect. Ecol. Epidemiol.* 2, 18385.
- Joseph-Charles, J., Geneste, C., Laborde-Kummer, E., Gheyouche, R., Boudis, H., Dubost, J.P., 2007. Development and validation of a rapid HPLC method for the determination of oseltamivir phosphate in Tamiflu and genetic versions. *J. Pharm. Biomed. Anal.* 44, 1008–1013.
- Kobayashi, T., Hirose, J., Sano, K., Hiro, N., Ijiri, Y., Takiuchi, H., Tamai, H., Takenaka, H., Tanaka, K., Nakano, T., 2008. Evaluation of electrolysis apparatus for inactivating antineoplastics in clinical wastewater. *Chemosphere* 72, 659–665.
- Kobayashi, T., Hirose, J., Sano, K., Kato, R., Ijiri, Y., Takiuchi, H., Tanaka, K., Goto, E., Tamai, H., Nakano, T., 2012. Application of electrolysis for detoxification of an antineoplastic in urine. *Ecotoxicol. Environ. Saf.* 78, 123–127.
- Li, W., Escarpe, P.A., Eisenberg, E.J., Cundy, K.C., Sweet, C., Jakeman, K.J., Merson, J., Lew, W., Williams, M., Zhang, L., Kim, C.U., Bischofberger, N., Chen, M.S., Mendel, D.B., 1998. Identification of GS 4104 as an orally bioavailable prodrug of the influenza virus neuraminidase inhibitor GS 4071. *Antimicrob. Agents Chemother.* 42, 647–653.
- Manual on analysis of investigated items (water, soil, aquatic organism), 2008. Water Environment Division, Environmental Management Bureau. Ministry of the Environment, Japan.
- Nakano, T., Hirose, J., Kobayashi, T., Hiro, N., Kondo, F., Tamai, H., Tanaka, K., Sano, K., 2013. Application of electrolysis inactivation to antibacterials in clinical use. *Ecotoxicol. Environ. Saf.* 90, 98–102.
- Oda, Y., Nakamura, S., Oki, I., Kato, T., Sinagawa, H., 1985. Evaluation of the new system (Umu-test) for the detection of environmental mutagenicity and carcinogens. *Mutat. Res.* 147, 219–229.
- Olsen, B., Munster, V.J., Wallensten, A., Waldenström, J., Osterhaus, A.D., Fouchier, R.A., 2006. Global patterns of influenza A virus in wild birds. *Science* 312, 384–388.
- Orozovic, G., Orozovic, K., Lennerstrand, J., Olsen, B., 2011. Detection of resistance mutations to Antivirals oseltamivir and zanamivir in avian influenza A viruses isolated from wild birds. *PLoS ONE* 6 (1), e16028.
- Panizza, M., Cerisola, G., 2009. Direct and mediated anodic oxidation of organic pollutants. *Chem. Rev.* 109, 6541–6569.

- Saccà, M.L., Accinelli, C., Fick, J., Lindberg, R., Olsen, B., 2009. Environmental fate of the antiviral drug Tamiflu in two aquatic ecosystems. *Chemosphere* 75, 28–33.
- Schünemann, H.J., Hill, S.R., Kakad, M., Bellamy, R., Uyeki, T.M., Hayden, F.G., Yazdanpanah, Y., Beigel, J., Chotpitayasunondh, T., Del Mar, C., Farrar, J., Tran, T.H., Ozbay, B., Sugaya, N., Fukuda, K., Shindo, N., Stockman, L., Vist, G.E., Croisier, A., Nagjdaliyev, A., Roth, C., Thomson, G., Zucker, H., Oxman, A.D., 2007. WHO rapid advice guidelines for pharmacological management of sporadic human infection with avian influenza A (H5N1) virus. *Lancet Infect. Dis.* 7, 21–31.
- Seino, Y., Nagano, M., Yahagi, T., Hoshi, A., Kawachi, T., Sugimura, T., 1978. Mutagenicity of several classes of antitumor agents to *Salmonella Typhimurium* TA98, TA100 and TA92. *Cancer Res.* 38, 2148–2156.
- Singer, A.C., Nunn, M.A., Gould, E.A., Johnson, A.C., 2007. Potential risks associated with the proposed widespread use of Tamiflu. *Environ. Health Perspect.* 115, 102–106.
- Söderström, H., Järhult, J.D., Olsen, B., Lindberg, R.H., Tanaka, H., Fick, J., 2009. Detection of the antiviral drug oseltamivir in aquatic environments. *PLoS ONE* 4 (6), e6064.
- Straub, J.O., 2009. An environmental risk assessment for oseltamivir (Tamiflu) for sewage works and surface waters under seasonal-influenza- and pandemic-use conditions. *Ecotoxicol. Environ. Saf.* 72, 1625–1634.
- Tamiflu interviewform, 2009. Chugai Pharmaceutical Co. Ltd. (in Japanese).
- von Itzstein, M., 2007. The war against influenza: discovery and development of sialidase inhibitors. *Nat. Rev. Drug Discov.* 12, 967–974.
- Ward, P., Small, I., Smith, J., Suter, P., Dutkowski, R., 2005. Oseltamivir (Tamiflu) and its potential for use in the event of an influenza pandemic. *J. Antimicrob. Chemother.* 55 (Suppl. 1), i5–i21.
- Wetherall, N.T., Trivedi, T., Zeller, J., Hodges-Savola, C., McKimm-Breschkin, J.L., Zambon, M., Hayden, F.G., 2003. Evaluation of neuraminidase enzyme assays using different substrates to measure susceptibility of influenza virus clinical isolates to neuraminidase inhibitors: report of the neuraminidase inhibitor susceptibility network. *J. Clin. Microbiol.*, 742–750.
- WHO (World Health Organization), 2003. Influenza (Seasonal). Fact Sheet No. 211. Available at <http://www.who.int/mediacentre/factsheets/fs211/en/> (accessed 30.09.12).



Characterization of a Gene Encoding the Outer Membrane Receptor for Ferric Enterobactin in *Aeromonas hydrophila* ATCC 7966^T

Tatsuya FUNAHASHI,^{1,†} Tomotaka TANABE,¹ Katsushiro MIYAMOTO,² Hiroshi TSUJIBO,² Jun MAKI,¹ and Shigeo YAMAMOTO¹

¹College of Pharmaceutical Sciences, Matsuyama University, 4-2 Bunkyo-cho, Matsuyama 790-8578, Japan

²Osaka University of Pharmaceutical Sciences, 4-20-1 Nasahara, Takatsuki, Osaka 569-1094, Japan

Received October 9, 2012; Accepted November 22, 2012; Online Publication, February 7, 2013

[doi:10.1271/bbb.120774]

Aeromonas hydrophila ATCC 7966^T produces a catecholate siderophore amonabactin in response to iron starvation. In this study, we determined that this strain utilizes exogenously supplied enterobactin (Ent) for growth under iron-limiting conditions. A homology search of the *A. hydrophila* ATCC 7966^T genomic sequence revealed the existence of a candidate gene encoding a protein homologous to *Vibrio parahaemolyticus* IrgA that functions as the outer membrane receptor for ferric Ent. SDS-PAGE showed induction of IrgA under iron-limiting conditions. The growth of the double mutant of *irgA* and *entA* (one of the amonabactin biosynthetic genes) was restored when it was complemented with *irgA* in the presence of Ent. Moreover, a growth assay of three isogenic *tonB* mutants indicated that the *tonB2* system exclusively provides energy for IrgA to transport ferric Ent. Finally, reverse transcriptase-quantitative PCR revealed that the transcription of *irgA* and the *TonB2* system cluster genes is iron-regulated, consistently with the presence of a predicted Fur box in the promoter region.

Key words: *Aeromonas hydrophila*; siderophore; iron; enterobactin; TonB

Iron is an essential element for the survival and growth of nearly all bacteria, but iron bioavailability for bacteria is severely restricted, since it forms insoluble ferric hydroxide complexes under aerobic conditions at neutral pH and binds to iron-binding proteins such as transferrin and lactoferrin in a mammalian host.¹ To overcome this iron restriction, many bacteria produce low-molecular-mass high-affinity chelators, called siderophores, that specifically bind ferric ion and enable iron-bound siderophores (ferric siderophores) to be scavenged from their surroundings. In addition to their own siderophores, some bacteria have evolved the ability to utilize heterologous siderophores (termed xenosiderophores) produced by other bacterial and fungal species. In Gram-negative bacteria, ferric siderophores are internalized into the cytosol *via* siderophore-specific TonB-dependent iron-repressible outer membrane protein (IROMP) receptors and ATP-binding

cassette (ABC) transporter systems. The transport of ferric siderophores across the outer membrane receptor is also an energy-dependent process, in which the proton-motive force created by the inner membrane is transduced to outer membrane receptors by the TonB system, generally consisting of three integral inner membrane proteins, TonB, ExbB, and ExbD, thus activating the receptors to a structure that recognizes the ferric siderophores.^{1,2} Furthermore, expression of the genes involved in siderophore biosynthesis and transport of ferric complex in addition to some virulence genes are negatively regulated by a global iron-binding repressor, called the ferric uptake regulator (Fur), when the intracellular iron level rises in Gram-negative bacteria.^{3,4}

Aeromonas hydrophila is a facultative anaerobic invasive motile Gram-negative bacterium found ubiquitously in a variety of aquatic environments. It is associated with a variety of human infections, including water-borne traumatic secondary wound infections, septicemia, and gastroenteritis.^{5–7} In response to iron starvation, most isolates of *A. hydrophila* secrete and utilize a siderophore amonabactin (Amo), a group of four peptide-based catecholate compounds with two 2,3-dihydroxybenzoic acid (DHBA) moieties as ligand units.^{8,9} Recently, it was reported that a seven-gene cluster (AHA_2473–2479) (Fig. 1A) probably involved in the biosynthesis of Amo occurs in the *A. hydrophila* ATCC 7966^T genome sequence.¹⁰ It was postulated that, of these seven genes, four encode non-ribosomal peptide synthetases, and three encode enzymes with roles in the synthesis of DHBA,^{10,11} although no experimental evidence of their functions has been reported. More recently, Reith *et al.*¹² reported that no other siderophore biosynthetic genes, except for the Amo biosynthetic ones, are present in the *A. hydrophila* ATCC 7966^T genome sequence.

In the present study, first we determined that *A. hydrophila* ATCC 7966^T can utilize enterobactin (Ent) as a xenosiderophore by use of an Amo-deficient mutant. Ent is a catecholate siderophore consisting of a cyclic trimer of 2,3-dihydroxybenzoylserine that is mainly produced by certain members of the *Enterobacteriaceae*.¹³ We found, by construction of the

[†] To whom correspondence should be addressed. Fax: +81-89-926-7283; E-mail: tfunahas@cc.matsuyama-u.ac.jp

Abbreviations: ABC, ATP-binding cassette; CAS, chrome azurol S; DHBA, 2,3-dihydroxybenzoic acid; Ent, enterobactin; Fur, ferric uptake regulator; FURTA, Fur titration assay; IROMP, iron-repressible outer membrane protein; PAGE, polyacrylamide gel electrophoresis; RT-qPCR, reverse transcriptase-quantitative PCR

respective isogenic deletion mutants followed by complementation experiments, that the 66.2-kDa IROMP encoded by *irgA* functions as a ferric Ent receptor that is dependent on energy transduced by the TonB2 system.

Materials and Methods

Bacterial strains, plasmids, primers, and growth conditions. Bacterial strains and plasmids used in this study are listed in Table 1. Unless otherwise noted, *A. hydrophila* and *E. coli* were grown at 30 °C and 37 °C respectively with shaking in Luria-Bertani (LB) media, or grown on LB agar plates (1.5% agar) containing 0.5% NaCl. LB media with and without an iron chelator, ethylenediamine-di(*o*-hydroxyphenylacetic acid) (EDDA; Sigma-Aldrich, St. Louis, MO), at 250 μM were used as iron-limiting (–Fe) and iron-replete (+Fe) media respectively. As necessary, appropriate antibiotics were added to the media at the following concentrations: ampicillin (50 μg/mL), chloramphenicol (10 μg/mL), and tetracycline (10 μg/mL). The PCR primers used in this study are listed in Table 2.

DNA manipulations. Standard DNA manipulations were carried out as described by Sambrook *et al.*¹⁴ Chromosomal DNA and plasmid DNA were extracted with a Wizard® Genomic DNA Purification Kit (Promega, Madison, WI) and a High Pure Plasmid Isolation Kit (Roche Diagnostics, Mannheim, Germany) respectively. Restriction enzymes were purchased from Roche Diagnostics. A Ligation-Convenience Kit (Wako Pure Chemical Industries, Osaka, Japan) was used for DNA ligation. DNA fragments were purified from agarose gels using a MagExtractor-PCR & Gel Clean-Up DNA Fragment Purification Kit (Toyobo, Osaka, Japan). Transformation of *E. coli* was performed by electroporation with a MicroPulser™ apparatus (Bio-Rad, Benicia, CA). Oligonucleotide primers (Table 2) used in this study were designed on the basis of the *A. hydrophila* ATCC 7966^T genome sequence.¹⁰ Homology searches were performed using the BLAST program of the National Center for Biotechnology Information (NCBI; <http://blast.ncbi.nlm.nih.gov/>).

Amo production assay. Amo production was examined by chrome azurol S (CAS) plate and liquid assay.¹⁵ For the CAS plate assay, *A. hydrophila* ATCC 7966^T and its mutant defective in *entA* ($\Delta entA$) were precultured in LB medium and the cells were collected by centrifugation. After washing them twice with saline, the cell pellets were suspended in saline at an OD₆₀₀ of 0.7. An aliquot (5 μL) of the suspension was spotted on a CAS agar plate and incubated for 48 h. For the CAS liquid assay, the ATCC 7966^T and mutant strains were incubated for 30 h in a synthetic Tris-buffered succinate medium (pH 7.4)¹⁶ containing 0.1 μM ferric chloride (under iron-restricted conditions) and the culture supernatants were used after filtration with 0.22 μm cellulose acetate filters (Merck KGaA, Darmstadt, Germany).

Growth assay. The *A. hydrophila* ATCC 7966^T and mutant strains were grown overnight in LB media, and an aliquot of the preculture was inoculated into 5 mL of fresh LB medium at an OD₆₀₀ of 0.005. The culture was shaken at 70 rpm at 30 °C, and OD₆₀₀ was automatically measured every 1 h with an Advantec TVS062CA biophotorecorder (Advantec, Tokyo, Japan). When required, 20 μM of Ent (Sigma-Aldrich) was added to the iron-limiting LB medium.

IROMP analysis. *A. hydrophila* ATCC 7966^T cells cultured for 12 h in LB media under –Fe and under +Fe conditions were harvested, and according to the procedure described previously,¹⁷ the OMP-rich fractions were prepared and analyzed by SDS-polyacrylamide gel electrophoresis (PAGE). The gel developed was stained with Coomassie Brilliant Blue R-250, followed by visualizing with a Gel Doc XR system (Bio-Rad). The IROMPs were electroblotted onto a pre-wetted polyvinylidene difluoride membrane (ProBlot®; Applied Biosystems, Carlsbad, CA) with a Trans-Blot® semi-dry electrophoretic transfer cell (Bio-Rad) to determine their N-terminal amino acid sequences by the automated Edman degradation method with a Procise® Model 491 protein sequencer (Applied Biosystems).

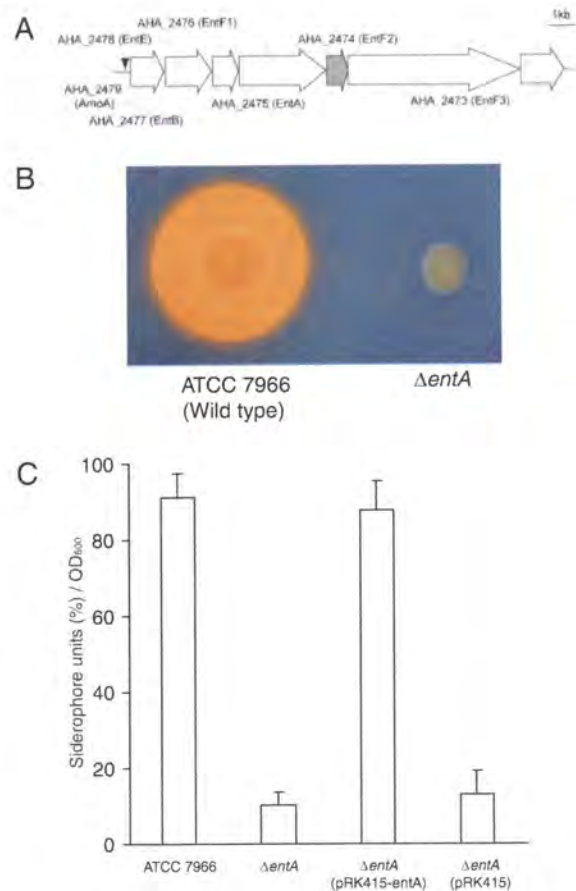


Fig. 1. Schematic Representation of the AHA₂₄₇₃₋₂₄₇₉ Gene Cluster (A), and Production of Amo by *A. hydrophila* ATCC 7966^T and $\Delta entA$ Assessed by CAS Plate Assay (B) and CAS Liquid Assay (C).

A, The gene nomenclature and definition proposed in the *A. hydrophila* ATCC 7966^T genome sequence data¹⁰ are illustrated. The position of the putative Fur box is marked by a solid arrowhead. B, Orange halo is indicative of Amo production. C, Error bars represent mean value \pm SD ($n = 3$). $\Delta entA$ /pRK415-entA and $\Delta entA$ /pRK415 were grown in the presence of tetracycline at 10 μg/mL. Siderophore units (%) were defined as $[(A_r - A_s)/A_r] \times 100$, where A_r is the absorbance at 630 nm of a reference (CAS assay solution plus 0.2 M 5-sulfosalicylic acid), and A_s is the absorbance of a sample at 630 nm.¹⁵

Fur titration assay. Fur titration assay (FURTA)¹⁸ was used to assess the presence of a potential Fur box sequence, which functions as the Fur-Fe²⁺ binding site in the promoter region of the *A. hydrophila* ATCC 7966^T *irgA* gene. PCR amplicons, including the putative Fur box of *irgA*, were prepared with primers IrgA-5 and IrgA-6 and digested with *KpnI-SalI*. The resulting 658-bp fragments were ligated into the same sites of pBluescript II KS(+) to generate pBC-irgA_{Fur}. This plasmid was electroporated into *E. coli* H1717 bearing a Fur-repressible *JhuF::lacZ* fusion (Lac⁻ phenotype under iron-replete growth conditions), and LacZ expression after incubation for 15 h was assessed by visualization of a change in colony color from white to red on MacConkey lactose agar plates (BD, Franklin Lakes, NJ) containing ampicillin and ferric chloride at 100 μM.

Construction of deletion mutants of *A. hydrophila* ATCC 7966^T. Deletion mutants were constructed by allelic exchange using R6K-ori suicide vector pXAC623 as described previously,^{19,20} with some modifications. DNA fragments with deletions in the *A. hydrophila* *entA*, *irgA*, *tonB1*, *tonB2*, and *tonB3* genes were prepared by PCR-driven overlap extension²¹ with two sets of primer pairs (EntA1-4, IrgA1-4, TonB1-1-4, TonB2-1-4, and TonB3-1-4), respectively, which were designed to partially delete the respective genes, as previously

Table 1. Bacterial Strains and Plasmids Used in This Study

Strains or plasmids	Relevant feature*	Reference or source
Strains		
<i>A. hydrophila</i>		
ATCC 7966	Wild type, type strain, an isolate from tin of milk with a fishy odor	ATCC
Δ entA	entA (amonabactin biosynthesis gene) deletion mutant from ATCC 7966	This study
Δ irgA	irgA (ferric enterobactin receptor gene) deletion mutant from ATCC 7966	This study
Δ entA Δ irgA	entA and irgA double deletion mutant from ATCC 7966	This study
Δ entA Δ tonB1	entA and tonB1 double deletion mutant from ATCC 7966	This study
Δ entA Δ tonB2	entA and tonB2 double deletion mutant from ATCC 7966	This study
Δ entA Δ tonB3	entA and tonB3 double deletion mutant from ATCC 7966	This study
<i>E. coli</i>		
β 2155	<i>thrB1004 pro thi strA hsdS Δ(lacZ)ΔM15 [F' Δ(lacZ)ΔM15 lac^R traD36 proA⁺ proB⁺] ΔdapA::erm(Em^r), pir::RP4[::kan(Km^r) from SM10]</i>	23
H1717	<i>araD139 rpsL150 Δ(argF-lac) relA1 U169 ffb5301 deoC1 ptsF25 rbsR aroB fhuF::AplacMu; host strain for FURTA</i>	18
Plasmids		
pXAC623	Suicide vector derived from pKTN701 containing <i>sacB</i> gene of <i>B. subtilis</i> ; Cm ^r	19
pBluescript II KS(+)	High-copy-number cloning vector; Ap ^r	Stratagene
pRK415	Broad-host-range plasmid (~10.5 kb); Tc ^r	24
pXAC Δ irgA	pXAC623 containing 1,162-bp <i>XbaI-XbaI</i> fragment with 1,864-bp deletion in <i>irgA</i> ; Cm ^r	This study
pXAC Δ entA	pXAC623 containing 1,085-bp <i>XbaI-XbaI</i> fragment with 682-bp deletion in <i>entA</i> ; Cm ^r	This study
pXAC Δ tonB1	pXAC623 containing 1,129-bp <i>XbaI-XbaI</i> fragment with 704-bp deletion in <i>tonB1</i> ; Cm ^r	This study
pXAC Δ tonB2	pXAC623 containing 1,094-bp <i>XbaI-XbaI</i> fragment with 606-bp deletion in <i>tonB2</i> ; Cm ^r	This study
pXAC Δ tonB3	pXAC623 containing 1,069-bp <i>XbaI-XbaI</i> fragment with 491-bp deletion in <i>tonB3</i> ; Cm ^r	This study
pRK415-irgA	pRK415 containing 2,318-bp <i>HindIII-XbaI</i> fragment with full-length <i>irgA</i> ; Tc ^r	This study
pRK415-entA	pRK415 containing 831-bp <i>BamHI-KpnI</i> fragment with full-length <i>entA</i> ; Tc ^r	This study
pBC-irgA _{fur}	pBluescript II KS(+) containing 658-bp <i>KpnI-SalI</i> fragment with <i>irgA</i> promoter region; Ap ^r	This study

*Ap^r, ampicillin resistance; Cm^r, chloramphenicol resistance; Tc^r, tetracycline resistance

described.²²) The fragments obtained after digestion with *XbaI* were ligated into *XbaI*-digested pXAC623. The resulting plasmids were transformed into *E. coli* β 2155,²³) which is a auxotroph, and then mobilized into appropriate *A. hydrophila* strains by filter mating. The resulting merodiploids were selected on LB agar plates with chloramphenicol at 10 μ g/mL without diaminopimelic acid and then incubated at room temperature for 48 h on LB agar plates containing 10% sucrose without NaCl. Sucrose-resistant and chloramphenicol-sensitive colonies were selected, and the deleted DNA regions were confirmed by PCR of their chromosomal DNAs using primer pairs (EntA-5 and -6, IrgA-5 and -6, TonB1-5 and -6, TonB2-5 and -6, and TonB3-5 and -6 in Table 2, data not shown). To complement mutants with a deletion in *entA* or *irgA*, PCR amplicons containing the full-length genes, prepared with primer pairs (EntA-comp-F and EntA-comp-R, and IrgA-comp-F and IrgA-comp-R in Table 2), were ligated into appropriately digested pRK415,²⁴) and the complementing plasmids thus obtained were electroporated into the corresponding *A. hydrophila* ATCC 7966^T mutants.

RNA isolation and reverse transcriptase-quantitative PCR (RT-qPCR). *A. hydrophila* ATCC 7966^T and Δ entA were grown in LB medium to an OD₆₀₀ of 0.3. Each culture was split into two aliquots. One was left untreated (+Fe cells) and the other was supplemented with EDDA at 250 μ M (−Fe cells). Both were further incubated until an OD₆₀₀ of 0.5 was reached. Total RNA was extracted from each cell pellet using an RNeasy[®] Protect Bacteria Mini Kit (Qiagen, Valencia, CA) and then treated, following the manufacturer's instructions, with RNase-free DNase I (Ambion, Austin, TX) to exclude the possibility of contamination with traces of chromosomal DNA. For RT-qPCR, 0.5 μ g of DNase I-treated total RNA was used to generate the cDNA product using ReverTra Ace[®] reverse transcriptase (Toyobo) and a random hexamer primer (Takara Bio, Otsu, Japan). Then qPCRs were performed with a Chromo4 Real-Time PCR detection system (Bio-Rad) with Thunderbird[®] SYBR[®] qPCR Mix (Toyobo) and the following primer pairs: for *entA*, entA-qF and entA-qR; for *irgA*, irgA-qF and irgA-qR; for *tonB2*, tonB2-qF and tonB2-qR; and for 16S rRNA, q16S1 and q16S2. The values were quantified by the comparative threshold cycle method, and were normalized to 16S rRNA.

Results and Discussion

Occurrence of a ferric Ent receptor ortholog in *A. hydrophila* ATCC 7966^T

We performed a BLAST search of the *A. hydrophila* ATCC 7966^T genome sequence using the amino acid sequences of ferric Ent receptors, IrgAs, in *V. cholerae*²⁵) and *V. parahaemolyticus*,²⁶) and found in *A. hydrophila* ATCC 7966^T an *irgA* ortholog (AHA_3963) encoding a 648-amino acid protein showing about 45% amino acid identity with IrgAs in both of these *Vibrio* species. Although in the *A. hydrophila* ATCC 7966^T genome sequence AHA_3963 has been annotated as an outer membrane receptor,¹⁰) its exact function has not been experimentally characterized. The existence of the *irgA* ortholog suggests that this strain can utilize Ent as a xenosiderophore, but the possibility has not been ruled out that the ATCC 7966^T strain can produce Ent. In order to clarify this, we examined to determine whether the spent culture filtrate of *A. hydrophila* ATCC 7966^T would stimulate the growth of Ent-deficient strain *E. coli* H1717 under iron-limiting conditions. The spent culture filtrate was prepared as follows: The ATCC 7966^T strain was grown to an OD₆₀₀ of 0.5 in −Fe medium and the spent culture was filtered through sterile membrane filter units (Sartorius Stedim, 0.2 μ m pore size). No growth was observed for *E. coli* H1717 when it was incubated in the filtered spent culture, whereas the addition of Ent, even at 1 μ M, to the spent culture filtrate promoted the growth of the *E. coli* strain (data not shown), indicating that *A. hydrophila* ATCC 7966^T cannot produce Ent as a cognate siderophore. This is consistent with a report by Reith *et al.*¹²) that this strain has no Ent biosynthetic genes. On the other hand, the *vctA* gene has been reported to encode another receptor

Table 2. PCR Primers Used in This Study

Purpose	Primer name	Sequence (5'-3')*
Construction of $\Delta entA$ fragment	EntA-1 (including <i>XbaI</i> site)	GCAAGGGTCTAGAAATCGGCAGCGTGCG
	EntA-2	atcctgcagctgccagttaaATCAAACGCC
	EntA-3	ttcactggcagctgcaggatCTGGTCGTCG
	EntA-4 (including <i>XbaI</i> site)	CCGGCGGTCTAGATAGGCCTCGCGCTCGG
Confirmation of <i>entA</i> deletion	EntA-5	AGCGGCTATCGCATCCAGCC
	EntA-6	GTGTACCCGGCTCAGATCCC
Construction of full-length <i>entA</i>	EntA-comp-F (including <i>BamHI</i> site)	GTGGTGAGGATCCAGATGACGAAGG
	EntA-comp-R (including <i>KpnI</i> site)	CCCCTGCGGTACCAGCTGTTTCAACAGC
Construction of $\Delta irgA$ fragment	IrgA-1 (including <i>XbaI</i> site)	ACGGCAGTCTAGACGTTTCGTTCACTTC
	IrgA-2	atccagcagcgagaatgagCGTGCTCAGC
	IrgA-3	ctcattctcgcgtgctggatGGTCGTCGCTAC
	IrgA-4 (including <i>XbaI</i> site)	CACCGACTCTAGAACCCGCATCTCAACCC
Confirmation of <i>irgA</i> deletion and Construction of <i>irgA</i> promoter fragment	IrgA-5	ACCGTCAAGTTCTTCAACGC
	IrgA-6	GCACATCGAGACCGTCTACC
Construction of full-length <i>irgA</i>	IrgA-comp-F (including <i>HindIII</i> site)	CCCGTATAAGCTTGTGAGAGGATAACCCG
	IrgA-comp-R (including <i>XbaI</i> site)	AAGGCCGCTAGAGTTGTGCAGGCGG
Construction of $\Delta tonB1$ fragment	TonB1-1 (including <i>XbaI</i> site)	CTCACCCACTCTAGAGAGGGTTCTGGC
	TonB1-2	tctgtttggcgcagtggtTCTCGGGCTG
	TonB1-3	ccaacactgcgccaacagAACACTGGCC
	TonB1-4 (including <i>XbaI</i> site)	GCCAATGTCTAGAGGGCGTGGTAGATGC
Confirmation of <i>tonB1</i> deletion	TonB1-5	GTTCAGATCAAGGACGAGCC
	TonB1-6	TTGTCCAGACTGCTCTGACC
Construction of $\Delta tonB2$ fragment	TonB2-1 (including <i>XbaI</i> site)	CACCATGTCTAGAAATGGTGGTCGCCG
	TonB2-2	aattgagcgccagtcaggGCTCATCAGC
	TonB2-3	ctgggactggcgctcaaatCAAAGTGGAG
	TonB2-4 (including <i>XbaI</i> site)	CAATGCGTCTAGAGCCGAGAGGCGG
Confirmation of <i>tonB2</i> deletion	TonB2-5	TTTAACCCGGAGAGCATGGC
	TonB2-6	AGCACTGCCTAGTCGAGACG
Construction of $\Delta tonB3$ fragment	TonB3-1 (including <i>XbaI</i> site)	ACAGCAGTCTAGATGAGGGCGCCATCG
	TonB3-2	tagttgaccgaggatgaagtCCGTCATGCTG
	TonB3-3	acttcatccgcgtaactaAGGAAGGTGG
	TonB3-4 (including <i>XbaI</i> site)	CGCGTTGCTAGAGCCGGTATGGCTTCCC
Confirmation of <i>tonB3</i> deletion	TonB3-5	GGGGCACAGAACAAGCAAGG
	TonB3-6	GAGCAGATACCAGGACTCCG
qPCR for <i>entA</i>	entA-qF	GTTGCCGGAGCAGTTCAAG
	entA-qR	GCCAGGAAGAGGACGGTATG
qPCR for <i>irgA</i>	irgA-qF	ACCCAGTCCGAGCAGAAGAG
	irgA-qR	GAAGTTGACCCGTGACCAGAG
qPCR for <i>tonB2</i>	tonB2-qF	CCGGGTACAGGATGTGGAAG
	tonB2-qR	ACTTGTGATCGCCTGAATGG
qPCR for 16S rRNA	q16S1	GCAACGCGAAGAACCCTTACC
	q16S2	GCGGGACTTAACCCAACATC

*Underlined sequences indicate restriction enzyme sites, and small letter sequences within primers 2 and 3 are complementary base pairs.

for ferric Ent in the two *Vibrio* species described above,^{25,26} but a BLAST search of the *A. hydrophila* ATCC 7966^T genome sequence revealed no protein with significant homology to VctA.

Construction of a mutant deficient in Amo to assess the utilization of Ent by A. hydrophila ATCC 7966^T

DHBA, a common component of catecholate siderophores, is synthesized from chorismate through the consecutive action of three enzymes, isochorismate synthase, 2,3-dihydro-2,3-dihydroxybenzoate synthase, and 2,3-dihydroxybenzoate dehydrogenase, encoded by *entC*, *entB*, and *entA* respectively, in *E. coli*.²⁷ It has been reported that a transposon insertion mutant of

amoA (corresponding to *E. coli entC*) in *A. hydrophila* 495A2 rendered it unable to produce DHBA and hence Amo.²⁸ The *amoA* product of *A. hydrophila* 495A2 showed 89% amino acid identity to AHA_2479, encoded by the first gene in the seven-gene cluster of *A. hydrophila* ATCC 7966^T (Fig. 1A). Hence we decided to construct an Amo-deficient mutant to avoid the possible effect of Amo on the growth of *A. hydrophila* ATCC 7966^T under iron-limiting conditions. Unexpectedly, a mutant with a deletion in *amoA* showed normal growth (data not shown). Since the above-mentioned transposon insertion mutant showed a polarity effect on Amo biosynthetic genes located downstream of *amoA*,²⁸ it is conceivable that inactivation of *amoA* by a deletion

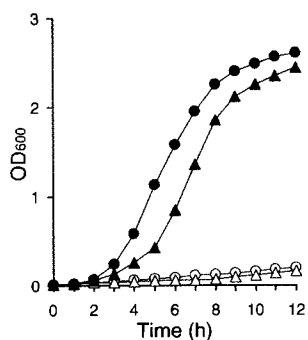


Fig. 2. Growth Profiles of $\Delta entA$ and $\Delta entA\Delta irgA$ of *A. hydrophila* ATCC 7966^T.

A. hydrophila $\Delta entA$ was grown in $-Fe$ media with (solid circle) and without (hollow circle) Ent at $20\mu M$. *A. hydrophila* $\Delta entA\Delta irgA$ (hollow triangle) and $\Delta entA\Delta irgA/pRK415-irgA$ (solid triangle) strains were grown in the $-Fe$ medium with Ent at $20\mu M$. For the growth of $\Delta entA\Delta irgA/pRK415-irgA$, tetracycline was added at $10\mu g/mL$. OD_{600} was measured every hour for 12 h. A representative of three independent experiments is indicated.

(nonpolar) mutation might be compensated for by a putative menaquinone-specific isochorismate synthase encoded by *AHA_0532*. Taking this into consideration, next we constructed a mutant with deletion in *entA*, the third gene responsible for DHBA biosynthesis, which is located in the seven-gene cluster (Fig. 1A). The $\Delta entA$ constructed failed to produce Amo (Fig. 1B and C) and did not grow in LB medium containing EDDA at $250\mu M$ (under iron-limiting conditions), unless the medium was supplemented with Ent at $20\mu M$ (Fig. 2). This suggested that *A. hydrophila* ATCC 7966^T was capable of utilizing Ent as a xenosiderophore. Moreover, the complementing strain ($\Delta entA/pRK415-entA$) harboring full-length *entA* in plasmid pRK415 produced Amo (Fig. 1C). When the agar plate was supplemented with DHBA ($20\mu M$), $\Delta entA$ produced an orange halo to an extent similar to the parental strain (data not shown), confirming that *entA* is essential to the production of Amo and that DHBA is one of the precursors of Amo.

Expression analysis of IROMPs by SDS-polyacrylamide gel electrophoresis (PAGE)

The IROMPs expressed by *A. hydrophila* ATCC 7966^T were analyzed by SDS-PAGE. At least three IROMP bands with molecular masses in a range of 66 to 80 kDa were detected (Fig. 3, lane 3), none of which was found in the parental strain or $\Delta entA$ grown under iron-replete conditions (Fig. 3, lanes 1 and 2). This suggests that one of these three IROMPs might serve as a receptor for ferric Ent. The sequence of the first 10 N-terminal amino acid residues of the 66.2-kDa IROMP was determined to be EQEVMVVT A, consistently with the amino acid sequence in the N-terminal region deduced from *A. hydrophila* *irgA* (Fig. 4B), a gene encoding the receptor for ferric Ent, as described below.

Features of *irgA* and its product IrgA in *A. hydrophila* ATCC 7966^T

A physical map of the *irgA* region and the partial nucleotide sequence of *irgA* with the deduced amino acid residues are shown in Fig. 4A and B respectively. Flanking genes (*AHA_3962* and *3964*) in the physical



Fig. 3. Detection of IrgA in *A. hydrophila* ATCC 7966^T by SDS-PAGE.

A. hydrophila ATCC 7966^T and $\Delta irgA$ were grown under iron-replete (+Fe) and iron-limiting ($-Fe$) conditions for 12 h. SDS-PAGE was carried out using 7.5% polyacrylamide in running gel (130 mm), and the gel developed was stained with Coomassie Brilliant Blue R-250. The amount of protein loaded in each lane was $25\mu g$. The figure shows only the relevant part of the SDS-PAGE gel. Arrowheads in lanes 3 and 5 indicate 66.2-kDa IROMPs. Lanes 1 and 3, *A. hydrophila* ATCC 7966^T; lanes 2 and 4, $\Delta irgA$; lane 5, $\Delta irgA/pRK415-irgA$; lane 6, $\Delta irgA/pRK415$; lane M, molecular weight marker proteins.

map encoding the predicted enzymes are thought to be unrelated to Ent utilization. *A. hydrophila* ATCC 7966^T *irgA* possesses potential promoter elements (-35 and -10) and a putative Fur box sharing 13/19 nucleotide matches with the *E. coli* consensus Fur box, which consists of 19-bp.²⁹ In accord with this, plasmid pBC-*irgA*fur containing the putative Fur box sequence in a 658-bp *KpnI-SalI* fragment conferred a Lac⁺ phenotype on *E. coli* H1717 in the FURTA.¹⁸ The IrgA protein possesses an N-terminal amino acid sequence entirely identical to that determined for the mature 66.2-kDa IROMP (Fig. 3). This also indicates that the 21 amino acid residues are to be excluded as a signal peptide from mature IrgA. The molecular mass of the mature IrgA was estimated to be 69,722-Da, larger than the 66.2-kDa estimated by electrophoretic mobility on SDS-PAGE (Fig. 3, lanes 3 and 5). The difference might be due to aberrant migration on SDS-PAGE, as frequently reported for outer membrane proteins. The putative TonB box sequence (₂₂EVMVVT A₂₉) is located close to the N-terminus of IrgA (Fig. 4B), which resembles the *E. coli* consensus sequence, D/ETXXVXA, where X is a hydrophobic amino acid residue.³⁰ It has also been reported that the last 10 amino acid residues of many OMPs of various Gram-negative bacteria are characterized by the presence of a potential amphipathic beta-sheet with hydrophobic amino acid residues at positions 1 (F), 3 (preferentially Y), 5, 7, and 9 from the C-termini of these proteins.³¹ The hydrophobic residues in the last 10 amino acid residues of *A. hydrophila* ATCC 7966^T IrgA are conserved at the proper positions, as shown in Fig. 4B.

Phenotypic analysis and complementation of the *irgA* deletion mutant

To clarify the function of *A. hydrophila* IrgA, deletion mutant $\Delta entA\Delta irgA$ was generated. In contrast to parental strain $\Delta entA$, $\Delta entA\Delta irgA$ did not grow under the $-Fe$ condition regardless of the presence of Ent (Fig. 2). Consistently with this, no band corresponding to 66.2-kDa IrgA was observed for $\Delta entA\Delta irgA$ (Fig. 3, lane 4). However, the complementing strain, $\Delta entA\Delta irgA/pRK415-irgA$, showed Ent-mediated growth promotion and the expression of IrgA as compared with vector control strain $\Delta entA\Delta irgA/$

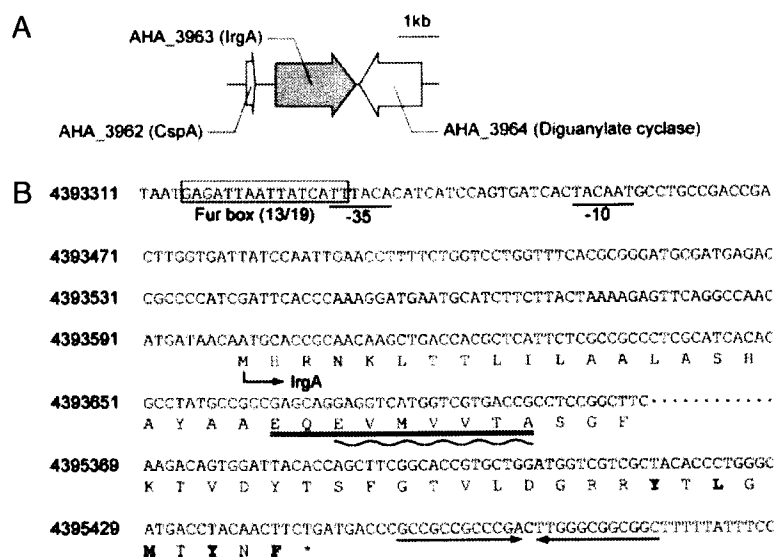


Fig. 4. Genetic Map of the *irgA* Region (A) and Partial Nucleotide Sequences of *irgA* Together with the Promoter Region and the Deduced Amino Acid Sequence (B).

A, The gene nomenclature and definition proposed in the *A. hydrophila* ATCC 7966^T genome sequence data¹⁰ are illustrated. B, The putative Fur box sequence is boxed and the promoter sequences are labeled as -10 and -35. The amino acid sequence deduced from *irgA*, which is in accord with the N-terminal amino acid sequence determined for mature IrgA, is underlined. The terminator signal is indicated by converging arrows. The putative TonB box of *irgA* is indicated by wavy underlining. The characteristic hydrophobic residues in the 10 C-terminal amino acids are shown in boldface. Nucleotide numbers correspond to nucleotide sequence positions in the *Aeromonas hydrophila* KEGG (Kyoto Encyclopedia of Genes and Genomes) Gene Database (<http://www.genome.jp/kegg-bin/show.organism?org=aha>).

pRK415 (Fig. 3, lane 6). The relatively long lag time in the growth curve observed for the complementing strain (Fig. 2) might have been due to maintenance of a large plasmid (13 kb) concomitant expression of the antibiotic resistant gene. These results indicate that IrgA is the receptor required for the uptake of ferric Ent. The growth of $\Delta irgA$ was indistinguishable from that of the parental strain in -Fe medium (data not shown), suggesting at least that IrgA does not act as a receptor for ferric Amo.

TonB specificity of IrgA

A homology search of the genome sequence of *A. hydrophila* ATCC 7966^T displayed the presence of three sets of TonB clusters, TonB1 (AHA_1987-1985), TonB2 (AHA_4251-4248), and TonB3 (AHA_3435-3438) (Fig. 5A). As in some *Vibrio* species,³² the TonB2 and TonB3 systems with the additional TtpC proteins essential to drive the uptake of multiple ferric siderophores³³ were also found in *A. hydrophila* ATCC 7966^T. To determine which TonB proteins were involved in the uptake of ferric Ent by IrgA, we constructed isogenic deletion mutants of *tonB1*, *tonB2*, and *tonB3* derived from $\Delta entA$. A growth assay was carried out for these mutants in the presence of Ent under the iron-limiting condition (Fig. 5B). No growth was observed only for the $\Delta entA\Delta tonB2$ strain, although it possesses the native *tonB1* and *tonB3* genes. In contrast, the growth of $\Delta entA\Delta tonB1$ and that of $\Delta entA\Delta tonB3$, both of which contain *tonB2*, were indistinguishable. These findings indicate that the TonB2 system can transduce the energy necessary for IrgA to transport ferric Ent. It has been reported that *V. parahaemolyticus* IrgA is supplied energy to transport ferric Ent by both the TonB1 and the TonB2 system,²⁵ whereas *V. cholerae* IrgA is energized only

by the TonB2 system.³⁴ Mey and Payne³⁴ and Tanabe *et al.*²⁵ compared the amino acid residues at the TonB box -1 positions of many siderophore receptors, and suggested that TonB1/TonB2 and TonB2 specificities are determined by hydrophilic or acidic amino acid residues and by hydrophobic amino acid residues respectively at this position. The TonB box -1 amino acid residues of *V. parahaemolyticus* IrgA and *V. cholerae* IrgA are M and D respectively, and the former is dependent on both the TonB1 and the TonB2 system, and the latter on the TonB2 system. The TonB box -1 residue of *A. hydrophila* IrgA, which depends on the TonB2 system, is hydrophilic residue Q, consistently with the above suggestion.

Analysis of the transcriptional levels of entA, irgA, and tonB2 by RT-qPCR

RT-qPCR was performed to determine the transcriptional levels of *entA*, *irgA*, and *tonB2*. The transcriptional levels of *entA* and *tonB2* in *A. hydrophila* ATCC 7966^T and *irgA* in $\Delta entA$ were much higher in the -Fe medium than in the +Fe medium. These results indicate that like *irgA*, *entA* and *tonB2* are negatively regulated through the action of Fur, consistently with the fact that the predicted Fur boxes, sharing 16/19 and 15/19 nucleotide matches with the *E. coli* consensus Fur box,²⁹ are located in the promoter regions of *amoA* (the first gene in the seven-gene operon; Fig. 1A) and *tonB2* (Fig. 5A) respectively. Transcription of *tonB1* was also activated in the -Fe medium, in accord with the predicted Fur box of *tonB1* with 14/19 nucleotide matches. No transcriptional activation of *tonB3* in the -Fe medium was observed (data not shown), consistently with the absence of a predicted Fur box. The TonB3 system has been reported to be inactive in ferric siderophore transport.³⁵ Moreover, it has been found

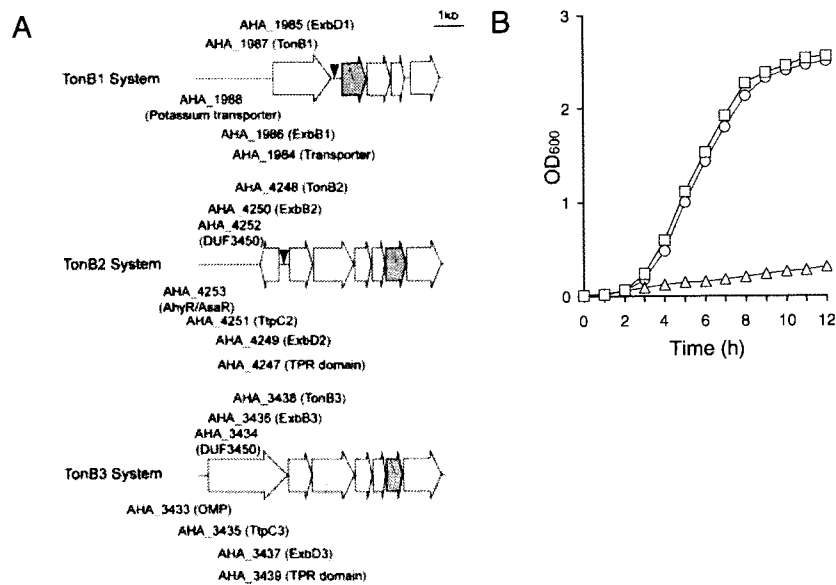


Fig. 5. Genetic Arrangement of the Three TonB System Gene Clusters (A) and Determination of the TonB Specificity of IrgA in *A. hydrophila* ATCC 7966^T by Growth Assay (B).

A, The gene nomenclature and definition proposed in the *A. hydrophila* ATCC 7966^T genome sequence data¹⁰ are illustrated. The position of the putative Fur box is marked by a solid arrowhead. B, The *A. hydrophila* $\Delta entA \Delta tonB1$ (circle), $\Delta entA \Delta tonB2$ (triangle), and $\Delta entA \Delta tonB3$ (square) strains were grown in -Fe medium containing Ent at 20 μ M. Measurement of OD₆₀₀ was performed every hour for 12 h. A representative of three independent experiments is indicated.

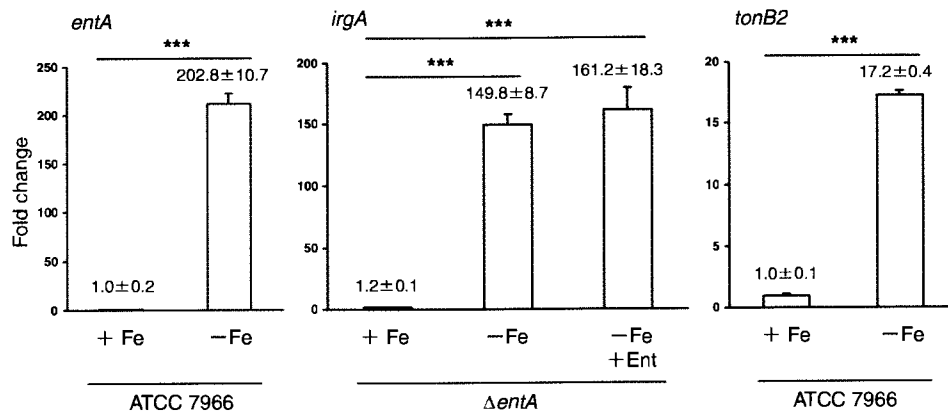


Fig. 6. RT-qPCR Analysis of *entA*, *tonB2*, and *irgA* Transcription Levels in *A. hydrophila* ATCC 7966^T and $\Delta entA$.

The amounts of *entA*, *tonB2*, and *irgA* mRNAs were assessed by RT-qPCR using the total RNA samples extracted from *A. hydrophila* ATCC 7966^T and $\Delta entA$ grown in the +Fe and -Fe media, and in -Fe medium containing 20 μ M Ent. Expression was normalized to 16S rRNA, and error bars represent mean values \pm SD (n = 5). *p*-values were estimated by Student's *t*-test (****p* < 0.001).

that transcription of *irgA* in *V. parahaemolyticus* is activated by a transcriptional activator, IrgB, which is encoded by *irgB* located immediately upstream of *irgA*, with the help of Ent under iron-limiting conditions.²⁵ However, the addition of Ent to the -Fe medium caused no induction of *irgA* transcription in $\Delta entA$ (Fig. 6). No such ortholog was detected in the *A. hydrophila* ATCC 7966^T genome sequence.

The receptor genes responsible for the utilization of Ent, mainly produced by enteric bacteria, have been characterized in some bacteria, including *Pseudomonas aeruginosa*,³⁶ *Bordetella* species,³⁷ *Neisseria* species,³⁸ *Campylobacter* species,^{39,40} and *V. anguillarum*,⁴¹ in addition to *V. cholerae*²⁵ and *V. parahaemolyticus*.²⁶ The present study also demonstrated that a distantly related bacterium, *A. hydrophila* ATCC 7966^T, possesses an IROMP, IrgA, for utilization of Ent. Ent

exhibits the highest affinity for ferric iron of any natural siderophore tested.⁴² Thus, it would be expected that this economical strategy of pirating Ent confers a distinct competitive benefit on *A. hydrophila* in its natural habitat, thereby escaping from any bacteriostatic effect caused by Ent produced by other microorganisms and increasing the chances of the survival and proliferation in a given environment. On the other hand, *A. hydrophila* IrgA shows only slight structural homology (27% amino acid identity) to *E. coli* FepA,⁴³ the receptor for native Ent, suggesting that extensive alteration of the IrgA structure can occur in this species without disrupting the stability of protein in the outer membrane or its ability to recognize and transport ferric Ent. It is notable that some amino acid residues in the TonB boxes essential to interaction with TonB are conserved, as shown in Table 3.

Table 3. Conservation of Amino Acid Sequences in the Predicted TonB Boxes from Ent Receptors of *A. hydrophila* ATCC 7966^T, *Vibrio* Species, and *E. coli*

Strain	Receptor (locus ^a)	Predicted TonB box ^b
<i>A. hydrophila</i> ATCC 7966 ^T	IrgA (AHA_3963)	E V M <u>V V T A</u>
<i>V. parahaemolyticus</i> RIMD2210633	IrgA (VP2602)	E T V <u>V V T A</u>
<i>V. cholerae</i> El Tor N16961	IrgA (VC0475)	E T M <u>V V T A</u>
<i>V. anguillarum</i> 775 (pJM1)	FetA (VAA_00188)	E K L <u>V V T A</u>
<i>E. coli</i> K-12 MG1655	FepA (b0584)	D T I <u>V V T A</u>

^aLoci are indicated according to the KEGG Database.

^bIdentical amino acid residues at the same positions in the TonB box pentapeptide are underlined. The consensus TonB box pentapeptide in TonB-dependent OMPs is proposed to be D/ETXXVXA, where X is a hydrophobic amino acid residue.³⁰

In conclusion, this study provides evidence that the 66.2-kDa IROMP, IrgA, in *A. hydrophila* ATCC 7966^T is a receptor involved in the utilization of Ent. In addition, we confirmed that the energy necessary to transport ferric Ent through the receptor is transduced by the TonB2 system. This represents another example of a bacterial species that does not produce Ent but expresses an outer membrane receptor for its ferric complex to utilize it as a xenosiderophore. Future studies are needed to elucidate the ABC transport system for ferric Ent in *A. hydrophila*.

Acknowledgments

This study was supported by a Grant-in-Aid for Young Scientists (B) from the Ministry of Education, Culture, Sports, Science, and Technology of Japan (Grant no. 20790124 to TF). We thank Ms. Y. Ido for experimental assistance.

References

- Miethke M and Marahiel MA, *Microbiol. Mol. Biol. Rev.*, **71**, 413–451 (2007).
- Krewulak KD and Vogel HJ, *Biochem. Biophys. Acta*, **1778**, 1781–1804 (2008).
- Carpenter BM, Whitmire JM, and Merrell DS, *Infect. Immun.*, **77**, 2590–2601 (2009).
- Escolar L, Pérez-Martin J, and de Lorenzo V, *J. Bacteriol.*, **181**, 6223–6229 (1999).
- Semel JD and Trenholme G, *J. Trauma*, **30**, 324–327 (1990).
- Damián RF, Zesati RV, Fernández LS, and García JL, *Infect. Dis. Obstet. Gynecol.*, **3**, 252–253 (1995).
- Janda JM and Abbott SL, *Clin. Microbiol. Rev.*, **23**, 35–73 (2010).
- Barghouthi S, Young R, Olson MOJ, Arceneaux JEL, Clem LW, and Byers BR, *J. Bacteriol.*, **171**, 1811–1816 (1989).
- Telford JR and Raymond KN, *J. Biol. Inorg. Chem.*, **2**, 750–761 (1997).
- Seshadri R, Joseph SW, Chopra AK, Sha J, Shaw J, Graf J, Haft D, Wu M, Ren Q, Posovitz MJ, Madupu R, Tallon L, Kim M, Jin S, Vuong H, Stine OC, Ali A, Horneman AJ, and Heidelberg JF, *J. Bacteriol.*, **188**, 8272–8282 (2006).
- Lemos ML and Osorio CR, "Iron Uptake and Homeostasis in Microorganisms," eds. Cornelis P and Andrews AC, Caister Academic Press, Norfolk, pp. 117–141 (2010).
- Reith ME, Singh RK, Curtis B, Boyd JM, Bouevitch A, Kimball J, Munholland J, Murphy C, Sarty D, Williams J, Nash JHE, Johnson SC, and Brown LL, *BMC Genomics*, **9**, 427 (2008).
- Payne SM and Mey AR, "Iron Transport in Bacteria," eds. Crosa JH, Mey AR, and Payne SM, ASM Press, Washington, DC, pp. 199–218 (2004).
- Sambrook J, Fritsch EF, and Maniatis T, "Molecular Cloning, a Laboratory Manual" 2nd, Cold Spring Harbor Laboratory, Cold Spring Harbor (1989).
- Schwyn B and Neilands JB, *Anal. Biochem.*, **160**, 47–56 (1987).
- Actis LA, Tolmasky ME, Crosa LM, and Crosa JH, *J. Clin. Microbiol.*, **31**, 2812–2815 (1993).
- Yamamoto S, Akiyama T, Okujo N, Matsu-ura S, and Shinoda S, *Microbiol. Immunol.*, **39**, 759–766 (1995).
- Stojiljkovic I, Bäumle AJ, and Hantke K, *J. Mol. Biol.*, **236**, 531–545 (1994).
- Kuroda T, Mizushima T, and Tsuchiya T, *Microbiol. Immunol.*, **49**, 711–719 (2005).
- Imamura T, Nitta H, Wada Y, Kobayashi H, and Okamoto K, *FEMS Microbiol. Lett.*, **284**, 35–42 (2008).
- Heckman KL and Pease LR, *Nat. Protoc.*, **2**, 924–932 (2007).
- Tanabe T, Funahashi T, Okajima N, Nakao H, Takeuchi Y, Miyamoto K, Tsujibo H, and Yamamoto S, *FEMS Microbiol. Lett.*, **284**, 35–42 (2008).
- Demarre G, Guérout AM, Matsumoto-Mashimo C, Rowe-Magnus DA, Marlière P, and Mazel D, *Res. Microbiol.*, **156**, 245–255 (2005).
- Keen NT, Tamaki S, Kobayashi D, and Trollinger D, *Gene*, **70**, 191–197 (1988).
- Mey AR, Wyckoff EE, Oglesby AG, Rab E, Taylor RK, and Payne SM, *Infect. Immun.*, **70**, 3419–3426 (2002).
- Tanabe T, Funahashi T, Shiuchi K, Okajima N, Nakao H, Miyamoto K, Tsujibo H, and Yamamoto S, *Microbiology*, **158**, 2039–2049 (2012).
- Walsh CT, Liu J, Rusnak F, and Sakaitani M, *Chem. Rev.*, **90**, 1105–1129 (1990).
- Barghouthi S, Payne SM, Arceneaux JEL, and Byers BR, *J. Bacteriol.*, **173**, 5121–5128 (1991).
- de Lorenzo V, Wee S, Herrero M, and Neilands JB, *J. Bacteriol.*, **169**, 2624–2630 (1987).
- Peacock RS, Weljie AM, Howard SP, Price FD, and Vogel HJ, *J. Mol. Biol.*, **345**, 1185–1197 (2005).
- Struyvè M, Moons M, and Tommassen J, *J. Mol. Biol.*, **218**, 141–148 (1991).
- Kuehl CJ and Crosa JH, *Future Microbiol.*, **5**, 1403–1412 (2010).
- Stork M, Otto BR, and Crosa JH, *J. Bacteriol.*, **189**, 1803–1815 (2007).
- Mey AR and Payne SM, *J. Bacteriol.*, **185**, 1195–1207 (2003).
- Kustusch RJ, Kuehl CJ, and Crosa JH, *J. Bacteriol.*, **194**, 3250–3259 (2012).
- Dean CR and Poole K, *J. Bacteriol.*, **175**, 317–324 (1993).
- Ball B and Sanden GN, *Microbiology*, **141**, 3193–3205 (1995).
- Carson SD, Klebba PE, Newton SM, and Sparling PF, *J. Bacteriol.*, **181**, 2895–2901 (1999).
- Palyada K, Threadgill D, and Stintzi A, *J. Bacteriol.*, **186**, 4714–4729 (2004).
- Xu F, Zeng X, Haigh RD, Ketley JM, and Lin J, *J. Bacteriol.*, **192**, 4425–4435 (2010).
- Naka H and Crosa JH, *Biomaterials*, **25**, 125–133 (2012).
- Thulasiraman P, Newton SM, Xu J, Raymond KN, Mai C, Hall A, Montague MA, and Klebba PE, *J. Bacteriol.*, **180**, 6689–6696 (1998).
- Lundrigan MD and Kadner RJ, *J. Biol. Chem.*, **261**, 10797–10801 (1986).

Identification and characterization of a cluster of genes involved in biosynthesis and transport of acinetoferrin, a siderophore produced by *Acinetobacter haemolyticus* ATCC 17906^T

Tatsuya Funahashi,¹ Tomotaka Tanabe,¹ Jun Maki,²
Katsushiro Miyamoto,³ Hiroshi Tsujibo³ and Shigeo Yamamoto¹

Correspondence

Tatsuya Funahashi
tfunahas@cc.matsuyama-u.ac.jp

¹Laboratory of Hygienic Chemistry, College of Pharmaceutical Sciences, Matsuyama University, 4-2 Bunkyo-cho, Matsuyama 790-8578, Japan

²Laboratory of Infectious Disease, College of Pharmaceutical Sciences, Matsuyama University, 4-2 Bunkyo-cho, Matsuyama 790-8578, Japan

³Department of Microbiology, Osaka University of Pharmaceutical Sciences, 4-20-1 Nasahara, Takatsuki, Osaka 569-1094, Japan

Acinetobacter haemolyticus ATCC 17906^T is known to produce the siderophore acinetoferrin under iron-limiting conditions. Here, we show that an operon consisting of eight consecutive genes, named *acbABCD* and *actBCAD*, participates in the biosynthesis and transport of acinetoferrin, respectively. Transcription of the operon was found to be iron-regulated by a putative Fur box located in the promoter region of the first gene, *acbA*. Homology searches suggest that *acbABCD* and *actA* encode enzyme proteins involved in acinetoferrin biosynthesis and an outer-membrane receptor for ferric acinetoferrin, respectively. Mutants defective in *acbA* and *actA* were unable to produce acinetoferrin or to express the ferric acinetoferrin receptor under iron-limiting conditions. These abilities were rescued by complementation of the mutants with native *acbA* and *actA* genes. Secondary structure analysis predicted that the products of *actC* and *actD* may be inner-membrane proteins with 12 membrane-spanning helices that belong to the major facilitator superfamily proteins. ActC showed homology to *Sinorhizobium meliloti* RhtX, which has been characterized as an inner-membrane importer for ferric rhizobactin 1021 structurally similar to acinetoferrin. Compared to the parental ATCC 17906^T strain, the *actD* mutant displayed about a 35% reduction in secretion of acinetoferrin, which was restored by complementation with *actD*, suggesting that ActD acts as an exporter of the siderophore. Finally, the *actB* product was significantly similar to hypothetical proteins in certain bacteria, in which genes encoding ActBCA homologues are arranged in the same order as in *A. haemolyticus* ATCC 17906^T. However, the function of ActB remains to be clarified.

Received 27 November 2012

Revised 7 January 2013

Accepted 25 January 2013

INTRODUCTION

Iron is a requisite nutrient for the growth and proliferation of the vast majority of microbes. However, iron bioavailability is often limited due to the insolubility of iron in aerobic environments at neutral-to-alkaline pH or to

Abbreviations: DAP, 1,3-Diaminopropane; DPD, 2,2'-dipyridyl; Fur, ferric uptake regulator; FURTA, Fur titration assay; IROMP, iron-repressible outer-membrane protein; MFS, major facilitator superfamily; OMP, outer-membrane protein.

The GenBank/EMBL/DBJ accession number for the sequence reported in this paper is AB661448.

A supplementary figure and a supplementary table are available with the online version of this paper.

sequestration of iron by high-affinity iron-binding proteins such as lactoferrin and transferrin within the host to avoid microbial infections through non-specific mechanisms (Ratledge & Dover, 2000; Bullen *et al.*, 2005; Miethke & Marahiel, 2007). Thus, to overcome this iron restriction in the competitive local environment, many microbes have evolved diverse strategies, one of the most prominent being the biosynthesis of low-molecular-mass chelators, called siderophores (Neilands, 1981; Hider & Kong, 2010). They are secreted into the local extracellular milieu, where they bind ferric iron with high specificity. In Gram-negative bacteria, iron-loaded siderophores (ferric siderophores) are transported back into the cell cytoplasm across the outer and inner membranes by iron-repressible outer-membrane protein (IROMP) receptors and ATP-binding cassette

transport systems or major facilitator superfamily (MFS) transporters, respectively. (Braun *et al.*, 1998; Andrews *et al.*, 2003; Cuív *et al.*, 2004). The receptors display relatively tight specificity for their cognate siderophores. Translocation of a ferric siderophore through the receptor into the periplasmic space is dependent on the energy-transducing TonB system, comprising two cytoplasmic membrane proteins, ExbB and ExbD, in addition to TonB, which traverses the periplasmic space (Letain & Postle, 1997). The receptors commonly possess a conserved sequence, the TonB box, which interacts with TonB to gain the energy necessary to transport the ferric siderophore into the periplasm. Most siderophores can be classified into three major groups, i.e. catecholate, hydroxamate and α -hydroxycarboxylate (Hider & Kong, 2010). The ability to synthesize and utilize siderophores has been shown to be one of the virulence determinants in numerous bacterial pathogens, since the siderophores can facilitate the acquisition of iron from iron-withholding proteins, such as transferrin and lactoferrin in animal hosts (Schaible & Kaufmann, 2004; Bullen *et al.*, 2005; Weinberg, 2009). On the other hand, high intracellular concentrations of iron may damage bacteria through the formation of undesired reactive oxygen species. In Gram-negative bacteria, maintenance of iron homeostasis is mainly regulated by the ferric uptake regulator (Fur), which functions as a transcriptional regulator (Bagg & Neilands, 1987; Escolar *et al.*, 1999). When the intracellular iron concentration is increased, Fur dimerizes with Fe^{2+} as a cofactor and binds to a 19 bp consensus sequence, termed the Fur box (de Lorenzo *et al.*, 1987; Calderwood & Mekalanos, 1988), present in the promoters of genes generally involved in iron acquisition

Acinetobacter haemolyticus has emerged as an environmental bacterium and an opportunistic, multidrug-resistant, intrahospital human pathogen, which causes septicaemia, pneumonia, meningitis, skin and wound infections, and urinary tract infection (Bergogne-Bérézin & Towner, 1996). Recently, a comparative study on the virulence potential of *Acinetobacter* species has suggested that *A. haemolyticus* and *Acinetobacter baumannii* are likely to be the most hazardous species with regard to growth ability in the mammalian environment, toxicity and intracellular infectivity (Tayabali *et al.*, 2012).

We have previously reported that, when grown under conditions of iron depletion, *A. haemolyticus* ATCC 17906^T

produces a citrate-based dihydroxamate siderophore, acinetoferrin (Fig. 1), which is characterized by 1,3-diaminopropane (DAP) moieties and monounsaturated acyl appendages (Okujo *et al.*, 1994). In this regard, acinetoferrin is very similar in chemical structure to rhizobactin 1021 (Fig. 1) produced by *Sinorhizobium meliloti* (Persmark *et al.*, 1993), in which the relevant biosynthesis gene cluster has been identified and characterized (Lynch *et al.*, 2001). This study was undertaken to obtain insight into the genetic basis of the acinetoferrin-mediated iron uptake system of *A. haemolyticus* ATCC 17906^T. The Fur titration assay (FURTA) (Stojiljkovic *et al.*, 1994) was used to identify a cluster of Fur-regulated genes involved in acinetoferrin biosynthesis and transport. We describe the identification and characterization of an operon consisting of eight ORFs, whose functions were elucidated by homology search and mutation-complementation analysis.

METHODS

Bacterial strains, plasmids, oligonucleotides and growth conditions. The bacterial strains and plasmids used in this study are listed in Table 1. Sequences of all oligonucleotides used are presented in Table S1. *A. haemolyticus* ATCC 17906^T and its mutants and *Escherichia coli* were routinely grown with shaking at 30 and 37 °C, respectively, in Luria-Bertani (LB) medium or on LB agar plates (1.5% agar) containing 0.5% NaCl. To impose iron limitation, the LB medium was supplemented with the iron chelator 2,2'-dipyridyl (DPD) at 150 μM . Media with and without DPD were named -Fe medium and +Fe medium, respectively. As necessary, appropriate antibiotics were added to the growth media at the following concentrations: ampicillin (50 $\mu\text{g ml}^{-1}$), apramycin (50 $\mu\text{g ml}^{-1}$) and tetracycline (10 $\mu\text{g ml}^{-1}$).

FURTA. The FURTA was performed as described elsewhere (Stojiljkovic *et al.*, 1994). *A. haemolyticus* ATCC 17906^T chromosomal DNA fragments (0.5–1 kb) partially digested with *Sau3AI* were ligated into the *Bam*HI site of pBluescript II KS(+), and the resulting plasmids were transformed into *E. coli* H1717. Transformants were incubated at 37 °C for 15–24 h on MacConkey lactose agar plates (Difco) containing 0.1 mM FeCl_3 and ampicillin (50 $\mu\text{g ml}^{-1}$). Red colonies (Lac⁺) denote a FURTA-positive phenotype and indicate binding of the Fur- Fe^{2+} complex to the promoter region transformed in the indicator strain. Plasmid DNA was isolated, and nucleotide sequences of the inserts were determined.

Growth assays. *A. haemolyticus* ATCC 17906^T and its mutant strains were grown overnight in LB medium, and aliquots of the preculture were inoculated into 5 ml fresh LB medium at OD₆₀₀ 0.005 and

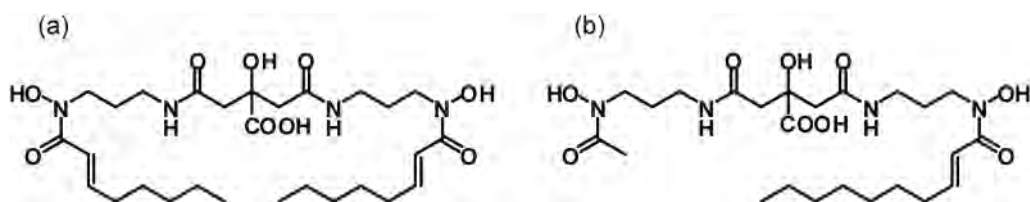


Fig. 1. Chemical structures of acinetoferrin (a) and rhizobactin 1021 (b).

Table 1. Bacterial strains and plasmids used in this study

Ap^r, Apra^r and Tc^r: resistance to ampicillin, apramycin and tetracycline, respectively.

Strain or plasmid	Relevant features	Source or reference
A. haemolyticus strains		
ATCC 17906 ^T	Clinical isolate from human sputum, type strain	ATCC
TF-acbA	ATCC 17906 ^T , <i>acbA</i> :: <i>aacC4</i> derivative; Apra ^r	This study
TF-actA	ATCC 17906 ^T , <i>actA</i> :: <i>aacC4</i> derivative; Apra ^r	This study
TF-actB	ATCC 17906 ^T , <i>actB</i> :: <i>aacC4</i> derivative; Apra ^r	This study
TF-actC	ATCC 17906 ^T , <i>actC</i> :: <i>aacC4</i> derivative; Apra ^r	This study
TF-actD	ATCC 17906 ^T , <i>actD</i> :: <i>aacC4</i> derivative; Apra ^r	This study
E. coli strains		
DH5 α	<i>endA1 hsdR17</i> (r _K ⁻ m _K ⁺) <i>supE44 thi-1 recA1 gyrA96 relA1</i> Δ (<i>argF-lacZYA</i>)U169 <i>deoR</i> [(ϕ 80d <i>lac</i> Δ (<i>lacZ</i>)M15)]	Promega
H1717	<i>araD139 rpsL150</i> Δ (<i>argF-lac</i>) <i>relA1 U169 flbB5301 deoC1 ptsF25 rbsR aroB fhuF</i> :: λ placMu; host strain for FURTA	Stojilkovic <i>et al.</i> (1994)
Plasmids		
pBluescript II KS(+)	High-copy-number cloning vector; Ap ^r	Stratagene
pRK415	Broad-host-range plasmid; Tc ^r	Keen <i>et al.</i> (1988)
pJG1011	Source of <i>aacC4</i> encoding Apra ^r	Gomez & Bishai (2000)
pFURTA-Af	Initially isolated FURTA-positive clone; pBluescript II KS(+) containing a 915 bp <i>Sau3AI-Sau3AI</i> fragment from ATCC 17906 ^T ; Ap ^r	This study
pBC-acf1	pBluescript II KS(+) containing a 2935 bp <i>PstI-PstI</i> fragment from ATCC 17906 ^T ; Ap ^r	This study
pBC-acf2	pBluescript II KS(+) containing a 3609 bp <i>XbaI-XbaI</i> fragment from ATCC 17906 ^T ; Ap ^r	This study
pRK415-acf3	pRK415 containing a 6444 bp <i>PstI-PstI</i> fragment from ATCC 17906 ^T ; Tc ^r	This study
pRK415-acf4	pRK415 containing a 6749 bp <i>EcoRI-EcoRI</i> fragment from ATCC 17906 ^T ; Tc ^r	This study
pRK415-acbA	pRK415 containing the <i>acbA</i> gene from ATCC 17906 ^T ; Tc ^r	This study
pRK415-actA	pRK415 containing the <i>actA</i> gene from ATCC 17906 ^T ; Tc ^r	This study
pRK415-actB	pRK415 containing the <i>actB</i> gene from ATCC 17906 ^T ; Tc ^r	This study
pRK415-actC	pRK415 containing the <i>actC</i> gene from ATCC 17906 ^T ; Tc ^r	This study
pRK415-actD	pRK415 containing the <i>actD</i> gene from ATCC 17906 ^T ; Tc ^r	This study

shaken at 70 r.p.m. The OD₆₀₀ was measured with an Advantec TVS062CA biophotorecorder (Advantec Toyo).

DNA manipulation, nucleotide sequencing, and protein sequence analysis. Standard DNA manipulations were carried out as described by Sambrook *et al.* (1989). Chromosomal DNA and plasmid DNA were extracted using a Wizard Genomic DNA Purification kit (Promega) and a High Pure Plasmid Isolation kit (Roche Diagnostics), respectively. Restriction enzymes were purchased from Roche Diagnostics. A Ligation-Convenience kit (Wako Pure Chemical Industries) was used for the DNA ligation reaction. DNA fragments were purified from agarose gels using a MagExtractor-PCR & Gel Clean up DNA fragment purification kit (Toyobo). Transformation of *E. coli* was performed by electroporation with a MicroPulser apparatus (Bio-Rad). The nucleotide sequence of *A. haemolyticus* ATCC 17906^T was determined in two directions with an ABI PRISM 3130XL Genetic Analyzer (Applied Biosystems) and a BigDye Terminator Cycle Sequencing kit (Applied Biosystems) according to the manufacturer's instructions. A high-fidelity KOD-Plus-DNA polymerase (Toyobo) was used when PCR fragments required minimal errors. Oligonucleotide primers (Table S1) were designed according to the determined sequence of *A. haemolyticus* ATCC 17906^T. Protein homology searches and alignments were carried out using the BLAST program on the National Center for Biotechnology Information website (<http://www.ncbi.nlm.nih.gov/>) (Altschul *et al.*, 1997). Transmembrane helices in ActC and

ActD were predicted using the HMMTOP 2.0 server (http://www.enzim.hu/hmmtop/html/adv_submit.html) (Tusnady & Simon, 2001).

RNA isolation and RT-PCR. *A. haemolyticus* ATCC 17906^T was grown in LB broth to an OD₆₀₀ of 0.3. The culture was split into two aliquots; one was left untreated to prepare +Fe cells, and the other was supplemented with DPD at 150 μ M to prepare -Fe cells. Both aliquots were further incubated until an OD₆₀₀ of 0.5 was reached. Total RNA was extracted from each cell pellet using an RNeasy Protect Bacteria Mini kit (Qiagen) and then treated, according to the manufacturer's instructions, with RNase-free DNase I (Ambion) to exclude possible contamination with traces of chromosomal DNA. RT-PCR was carried out with a ReverTra Dash RNA PCR kit (Toyobo), according to the manufacturer's directions. For first-strand cDNA synthesis, 1 μ g pretreated total RNA was incubated in a total volume of 20 μ l at 42 $^{\circ}$ C for 1 h with the primer AfRT-R complementary to the internal sequence of *actD*. Subsequent PCR was performed with 1 μ l of reverse transcriptase reaction mixture using the primer pairs designed for each gene to be tested. PCR conditions were as follows: after an initial denaturation of 2 min at 94 $^{\circ}$ C, DNA was amplified for 30 cycles, with each cycle consisting of denaturation at 94 $^{\circ}$ C for 30 s, annealing at 55 $^{\circ}$ C for 30 s and extension at 72 $^{\circ}$ C for 1 min. Total RNA without treatment with the M-MLV reverse transcriptase was used as a negative control reaction for PCR to confirm the lack of genomic DNA contamination. 16S rRNA was used as an established endogenous internal control. The

primers 16s-F and 16s-R were designed according to the nucleotide sequence of *A. haemolyticus* ATCC 17906^T 16S rRNA (accession no. Z93437). RT-PCR products were detected in a 1.5% agarose gel stained with ethidium bromide and visualized in a Gel Doc XR (Bio-Rad).

Outer-membrane protein (OMP) analysis. Cells of ATCC 17906^T and mutant strains grown for 12 h in +Fe and -Fe media were harvested by centrifugation. The OMP-rich fractions were prepared and analysed by SDS-PAGE as previously described (Yamamoto *et al.*, 1995a). Protein concentrations were determined by the method of Markwell *et al.* (1978). The developed gel was stained with Coomassie brilliant blue R-250 followed by visualizing with a Gel Doc XR system (Bio-Rad). The IROMPs were electroblotted onto a pre-wetted PVDF membrane (ProBlott; Applied Biosystems) with a Trans-Blot semi-dry electrophoretic transfer cell (Bio-Rad) for determination of their N-terminal amino acid sequences by automated Edman degradation method with a Procise model 491 protein sequencer (Applied Biosystems).

Construction of deletion/insertion mutant and complementing strains. Mutant strains of *A. haemolyticus* ATCC 17906^T, i.e. TF-*acbA*, TF-*actA*, TF-*actB*, TF-*actC* and TF-*actD*, were constructed by gene replacement as described by Aranda *et al.* (2010), and each mutant carried a partially deleted gene with a non-polar insertion cassette conferring apramycin resistance (*aacC4*). Briefly, the upstream and downstream regions (approx. 0.5 kb each) of the target gene were amplified from genomic DNA of the ATCC 17906^T

strain using primer pairs (AF and AR, and BF and BR; Table S1) for construction of amplicons A and B, respectively, of each target gene. On the other hand, the apramycin cassette was amplified using primer pairs appropriately designed to link amplicons A and B to the 5' and 3' sites of the *aacC4* cassette derived from vector pJG1011 (Gomez & Bishai, 2000) as a template. The AR and BF primers contained an extension of about 20 nt complementary to the acc-F and acc-R primers, respectively. The three PCR products purified were mixed and subjected to PCR-driven overlap extension (Heckman & Pease, 2007) with the AF and BR primers and a KOD-Plus-DNA polymerase (Toyobo). The purified PCR product containing the target gene inactivated by the *aacC4* cassette was introduced into the ATCC 17906^T strain by electroporation according to the procedure of Leahy *et al.* (1994). Recombinant mutants, whose wild-type genes were replaced by allelic exchange via double-crossover recombination, were selected on LB agar plates containing apramycin. Candidate clones were examined by PCR with the AF and BR primers to verify gene replacement (data not shown). The resulting mutants were named TF-*acbA*, -*actA*, -*actB*, -*actC* and -*actD* (Table 1), and grown in the presence of apramycin. To provide the five above-mentioned mutated genes with *in trans* complementation, the plasmids pRK415-*acbA*, pRK415-*actA*, pRK415-*actB*, pRK415-*actC* and pRK415-*actD* were constructed by PCR using *A. haemolyticus* ATCC 17906^T genomic DNA with the comp-F and comp-R primer sets (Table S1), all of which contained the corresponding entire genes. These plasmids were introduced into the respective mutant strains by electroporation (Leahy *et al.*, 1994). Empty strains containing only pRK415 were also constructed. Mutants containing pRK415 were grown in the presence

Table 2. Proteins with homology to products of the eight genes in the acinetobactin biosynthesis and transport operon of *A. haemolyticus* ATCC 17906^T

ORF (aa)	Homologous protein (aa)	Micro-organism	Identity/similarity (%) (aa overlap)	Accession no.
<i>acbA</i> (594)	Putative siderophore biosynthesis protein (517)	<i>A. baumannii</i> ATCC 17978	78/88 (517)	NC009085
	Rhizobactin biosynthesis protein, RhbC (585)	<i>S. meliloti</i> 1021	34/53 (546)	AE006469
<i>acbB</i> (493)	Putative Lys/Orn N ⁶ -monooxygenase (435)	<i>A. baumannii</i> ATCC 17978	49/63 (443)	NC009085
	Rhizobactin biosynthesis protein, RhbE (456)	<i>S. meliloti</i> 1021	41/57 (451)	AE006469
<i>acbC</i> (605)	Putative IucA/IucC (813)	<i>Anabaena variabilis</i>	39/59 (582)	NC007413
	Rhizobactin biosynthesis protein, RhbF (601)	<i>S. meliloti</i> 1021	36/55 (582)	AE006469
<i>acbD</i> (212)	Putative acetyltransferase (168)	<i>A. baumannii</i> ATCC 17978	77/88 (168)	NC009085
	Rhizobactin biosynthesis protein, RhbD (196)	<i>S. meliloti</i> 1021	37/54 (170)	AE006469
<i>actB</i> (123)	Hypothetical protein (129)	<i>P. mendocina</i> NK-01	44/61 (123)	CP002620
	Hypothetical protein (127)	<i>Pectobacterium carotovorum</i>	44/61 (123)	NC012917
	Hypothetical protein (128)	<i>Stenotrophomonas maltophilia</i> R551-3	45/55 (117)	NC011071
<i>actC</i> (411)	MFS protein (408)	<i>Pectobacterium carotovorum</i>	61/76 (403)	NC012917
	MFS protein (409)	<i>P. mendocina</i> NK-01	61/77 (383)	CP002620
	MFS protein (406)	<i>Stenotrophomonas maltophilia</i> R551-3	61/77 (392)	NC011071
	Rhizobactin transporter, RhtX (431)	<i>S. meliloti</i> 1021	34/53 (398)	AE006469
<i>actA</i> (752)	Putative iron complex outer-membrane receptor (746)	<i>A. baumannii</i> ATCC 17978	56/71 (762)	NC009085
	Putative iron complex outer-membrane receptor (746)	<i>P. mendocina</i> NK-01	54/71 (755)	CP002620
	Putative iron complex outer-membrane receptor (758)	<i>Pectobacterium carotovorum</i>	52/70 (757)	NC012917
	Putative iron complex outer-membrane receptor (751)	<i>Stenotrophomonas maltophilia</i> R551-3	47/66 (751)	NC011071
	Rhizobactin receptor precursor, RhtA (746)	<i>S. meliloti</i> 1021	33/52 (744)	AE006469
<i>actD</i> (408)	Putative arabinose efflux permease (381)	<i>Paenibacillus polymyxa</i> SC2	31/55 (394)	NC014622
	Permease of MFS (395)	<i>Paenibacillus polymyxa</i> E681	30/54 (386)	NC014483

of tetracycline and apramycin. All final constructs were sequenced to confirm that the sequences were correct.

HPLC analysis of acinetoferrin. Production of acinetoferrin was examined by HPLC with a Hitachi LaChrom Elite HPLC system equipped with an Inertsil C8-3 reversed-phase column (150 × 4.6 mm, 5 µm; GL Sciences). ATCC 17906^T and its mutant strains were grown to OD₆₀₀ 0.4 in 50 ml of a chemically defined Tris-buffered succinate medium (pH 7.4) containing 0.1 µM FeCl₃ (Okujo *et al.*, 1994), and culture supernatants filtered with 0.22 µm pore-size cellulose acetate filters were adjusted to pH 2.0 with solid citric acid. Acinetoferrin in the culture supernatants (50 ml) was adsorbed on an Amberlite XAD-7 column (120 × 10 mm ID, 20–60 mesh; Sigma-Aldrich), washed with 50 ml distilled water, and desorbed with 50 ml methanol. The methanol eluate was evaporated to dryness. The residue was resuspended in 1 ml methanol and a 10 µl aliquot was injected into the HPLC system for analysis. Forty-five per cent acetonitrile in 0.1% trifluoroacetic acid and 54% acetonitrile in 0.1% trifluoroacetic acid

were used as mobile phases. The gradient was as follows: 45% acetonitrile for 5 min and then from 45% to 54% acetonitrile within 30 min, and held at 54% acetonitrile for 10 min. Detection was at 220 nm with a flow rate of 0.5 ml min⁻¹.

RESULTS

Isolation of the DNA region encoding acinetoferrin biosynthesis and transport genes

The FURTA system (Stojiljkovic *et al.*, 1994) was successfully used to isolate Fur box-containing gene fragments from the *A. haemolyticus* ATCC 17906^T chromosome. Out of the positive clones, one clone named pFURTA-Af (Table 1, Fig. S1) was found to contain a fragment, part of which (915 bp) was predicted to encode a product that was 73% identical to

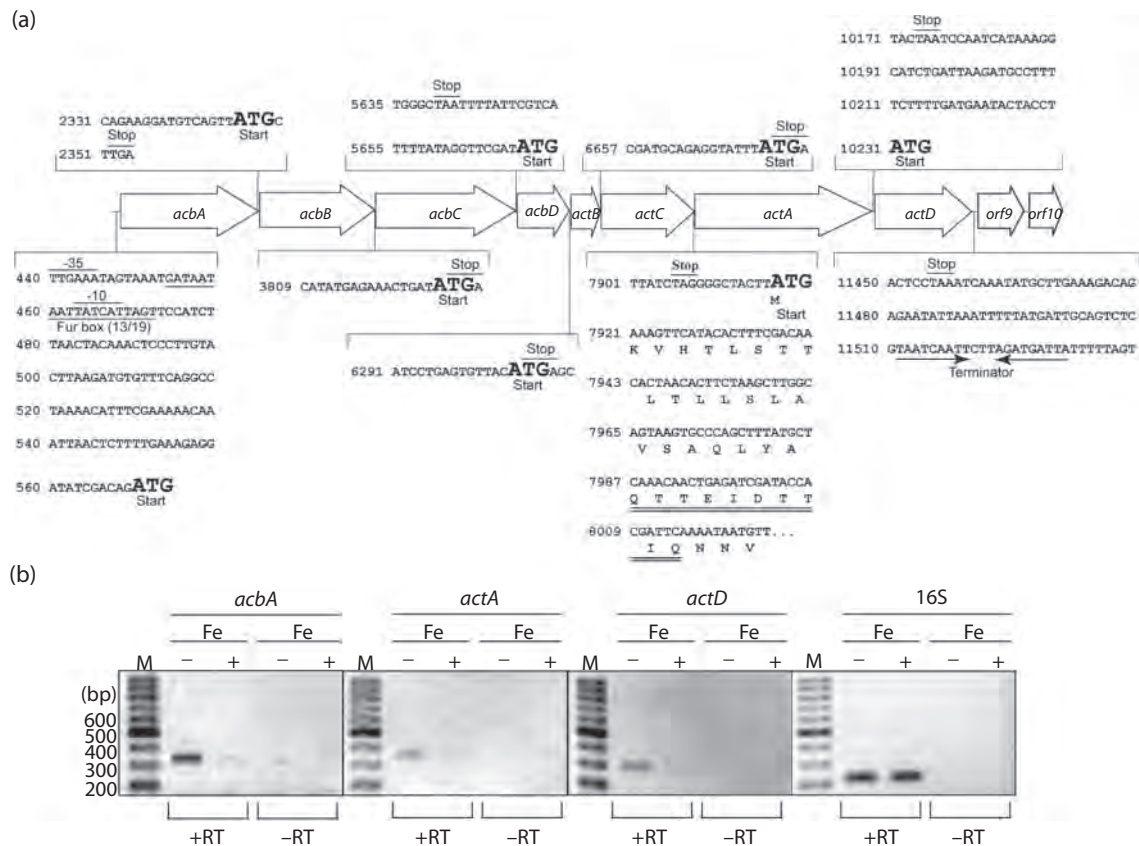


Fig. 2. Nucleotide sequences in the intergenic regions of the acinetoferrin biosynthesis and transport genes in *A. haemolyticus* ATCC 17906^T and the partial deduced amino acid sequence of ActA. Acinetoferrin cluster genes were also identified as belonging to an iron-regulated operon by RT-PCR. (a) The putative -10 and -35 promoter elements, start codons (in bold type) and stop codons are presented. The putative Fur box sequence is underlined with nucleotide matches with the 19 bp *E. coli* consensus Fur box sequence. The terminator signal is indicated by opposing arrows, and the amino acid sequence deduced from *actA*, which is compatible with the N-terminal sequence determined for the ActA protein, is indicated by double underlines. Numbers correspond to sequence positions in GenBank accession number AB661448. (b) Lanes contain RT-PCR amplicons amplified from total RNA isolated from -Fe and +Fe cells of *A. haemolyticus* ATCC 17906^T. The sizes of the amplicons derived from the representative genes are as follows: *acbA*, 334 bp; *actA*, 368 bp; and *actD*, 300 bp. As an internal control, a 225 bp fragment of the 16S rRNA gene was included. Lanes +RT and -RT represent RT-PCR products with and without reverse transcriptase, respectively; lane M, molecular size standard.

AIS_1647, one of the biosynthetic enzymes for a predicted hydroxamate siderophore produced by *A. baumannii* strains (Antunes *et al.*, 2011; Eijkelkamp *et al.*, 2011), and was 27% identical to RhbC, one of the biosynthetic enzymes for rhizobactin 1021 produced by *S. meliloti* (Lynch *et al.*, 2001). As expected, the potential Fur box, which matched 15 of 19 nt of the consensus Fur box (de Lorenzo *et al.*, 1987; Calderwood & Mekalanos, 1988), was detected in the promoter region. Then, based on these findings, the DNA sequence of the 13.1 kb region was determined, identifying eight ORFs (Fig. S1a). Cloning and sequencing of this region were performed using four plasmids (pBC-acf1, pBC-acf2, pRK-acf3 and pRK-acf4) with overlapping DNA fragments (Fig. S1b) which had been isolated by colony hybridization with DIG-labelled probes (Fig. S1c).

Predicted protein sequences

The deduced amino acid sequences of eight ORFs shared significant homology to known or predicted siderophore

biosynthetic enzymes and transporters in other bacteria (Table 2). The presence of ORFs that encode proteins homologous to putative ω -amino acid monooxygenases, acetyltransferases and TonB-dependent siderophore receptors implied a cluster associated with biosynthesis and transport of the hydroxamate siderophore, acinetoferrin. Protein products of two genes, *orf9* and *orf10*, not linked to the preceding gene, were homologous to a putative IS4 family transposase ORF1 and hypothetical protein, respectively, in *A. baumannii* strains, suggesting that they were not involved in acinetoferrin-mediated iron acquisition. On the basis of potential functions inferred from homology, the biosynthetic and transport genes were named *acbABCD* (*acb* stands for acbinetoferrin biosynthesis) and *actBCAD* (*act* stands for acinetoferrin transport) (Fig. 2a). The predicted amino acid sequences of AcbABCD shared 34–41% identity with those of the *S. meliloti* rhizobactin 1021 RhbCDEF (Lynch *et al.*, 2001), in keeping with the structural similarities between the siderophores produced by these species (Fig. 1). However, the

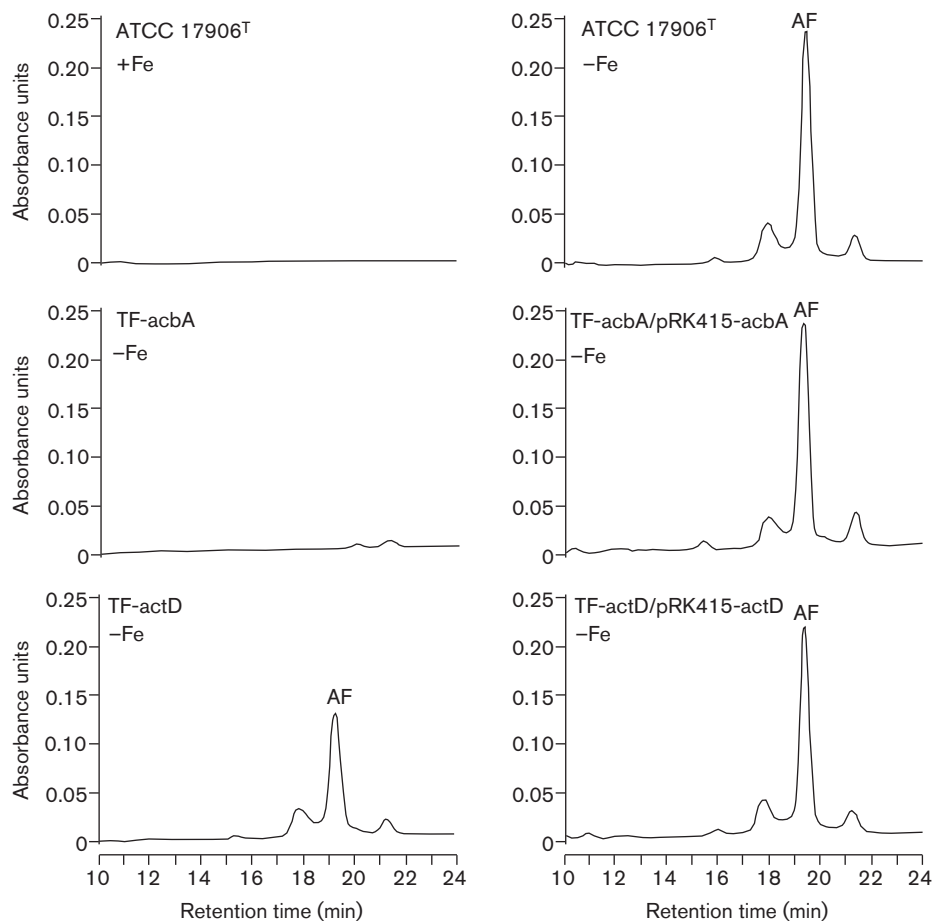


Fig. 3. HPLC profiles of acinetoferrin secreted by the wild-type *A. haemolyticus* ATCC 17906^T strain and deletion mutants into culture supernatants. The growth and HPLC conditions are described in Methods. A 10 μ l aliquot of the acinetoferrin extract (1 ml) was injected into the HPLC instrument. The peak with a retention time of 19.5 min was collected and identified as acinetoferrin by MS analysis.

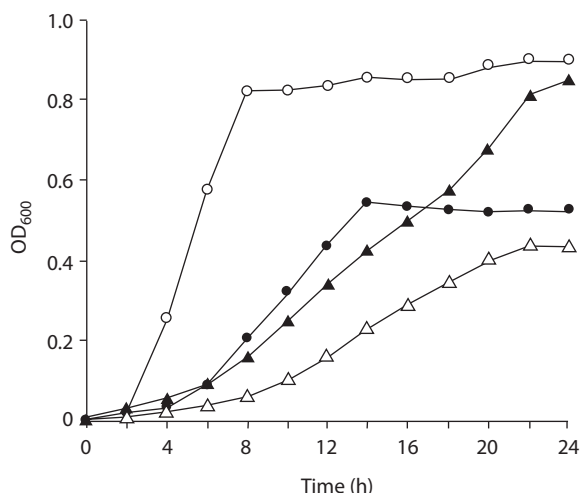


Fig. 4. Growth profiles of *A. haemolyticus* ATCC 17906^T, TF-acbA, TF-acbA/pRK415 (empty) and TF-acbA/pRK415-acbA strains. The ATCC 17906^T (○), TF-acbA (●), TF-acbA/pRK415 (△) and TF-acbA/pRK415-acbA (▲) strains were grown in -Fe medium. The OD₆₀₀ was measured every 2 h for 24 h. A representative of three independent experiments is shown.

gene order in *A. haemolyticus* was not the same as that in *S. meliloti*. Moreover, unlike in *S. meliloti*, the *A. haemolyticus* acinetoferrin cluster did not contain genes involved in DAP biosynthesis. Interestingly, *A. haemolyticus* AcbABD proteins (excluding AcbC) were highly similar (49–77% identity, 63–87% similarity) to the corresponding enzyme

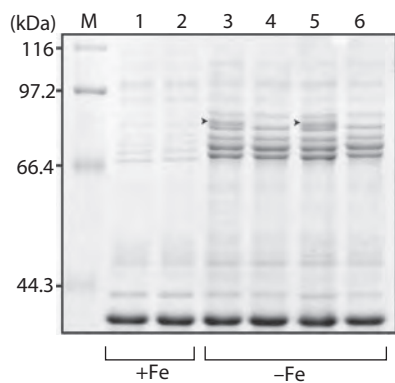


Fig. 5. OMP profiles of *A. haemolyticus* ATCC 17906^T, TF-actA, TF-actA/pRK415-actA and TF-actA/pRK415 strains. All strains were grown in +Fe and -Fe media for 12 h. SDS-PAGE was carried out using a 7.5% polyacrylamide running gel (130 mm) and the gel was stained with Coomassie brilliant blue R-250. The amount of protein loaded in each lane was 20 µg. Arrowheads in lanes 3 and 5 indicate the 79.3 kDa IROMP. Lanes 1 and 3, *A. haemolyticus* ATCC 17906^T; lanes 2 and 4, TF-actA; lane 5, TF-actA/pRK415-actA; lane 6, TF-actA/pRK415; lane M, molecular mass marker proteins.

proteins in eight fully sequenced *A. baumannii* genomes, e.g. AIS_1647, _1648, and _1657 in *A. baumannii* ATCC 17978 (Eijkelkamp *et al.*, 2011), whereas the arrangement of these genes in *A. baumannii* strains was quite different from that in the ATCC 17906^T strain. An AcbC homologue was not found in any of the whole-genome-sequenced *A. baumannii* strains.

The product of *actA* showed a significant similarity with various TonB-dependent outer-membrane receptors for ferric siderophores, including RhtA for ferric rhizobactin 1021 in *S. meliloti* (Lynch *et al.*, 2001). The amino acid sequence in the N-terminal region deduced from *actA* was identical to the first 10 N-terminal amino acids determined for the 79.3 kDa IROMP (see below). The product of *actB* showed homology to hypothetical proteins whose functions have not been ascertained for any species. The product of *actC* showed 61% identity to bacterial MFS proteins (Table 2). It was noteworthy that ActC also showed significant homology to the *S. meliloti* RhtX, an inner-membrane importer for ferric rhizobactin 1021 subsequent to outer-membrane translocation (Cuív *et al.*, 2004). HMMTOP analysis (Tusnády & Simon, 2001) placed ActC within the group of inner-membrane proteins with 12 transmembrane domains belonging to the MFS. ActD, the last gene product, showed homology to MFS efflux permeases and was divided into an inner-membrane protein with 12 transmembrane domains by HMMTOP analysis. Its subcellular location and similarity to MFS

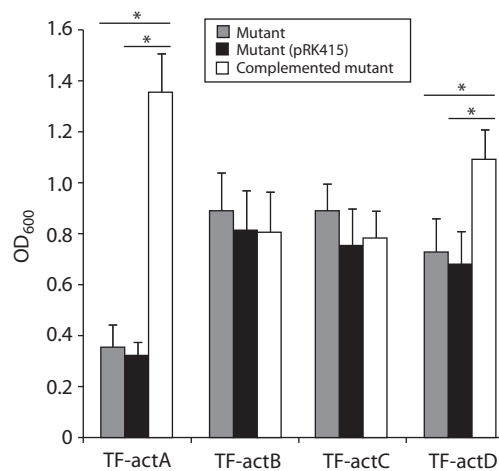


Fig. 6. Complementation of the *act* mutants with their corresponding intact genes. TF-actA, TF-actB, TF-actC and TF-actD strains and these mutants complemented with the plasmids pRK415-actA, pRK415-actB, pRK415-actC and pRK415-actD, respectively, were grown in -Fe medium, and their OD₆₀₀ values were compared after a 24 h incubation. As a control, mutants containing the empty plasmid pRK415 were grown under the same conditions. Data are the means from three independent experiments; error bars, SD. *P* values were estimated by Student's *t* test (*, *P* < 0.05).

proteins suggested that ActD could be involved in acinetoferrin secretion. Finally, although there were no proven functions for *actB* homologues in the three bacterial species cited, we note that all of them were located upstream of putative MFS importer genes followed by putative ferric siderophore outer-membrane receptor genes in the same order as *actB* in the ATCC 17906^T strain.

The *acbABCD* and *actBCAD* genes form an iron-regulated operon

The eight genes were located consecutively and oriented in the same direction with a single set of putative promoter elements in front of *acbA* and with a single rho-independent transcription terminator sequence just downstream of the stop codon of *actD*, suggesting that the eight genes are transcriptionally linked (Fig. 2a). This transcriptional organization was also suggested by the overlaps that occurred at the gene junctions as well as the presence of relatively short intervening sequences without any promoter elements. Then, in order to confirm that this gene cluster was organized as an iron-regulated operon, RT-PCR analysis was performed for *acbA*, *actA* and *actD* with three different primer combinations (Table S1) that amplified internal fragments of the corresponding genes. The primer (AfRT-R) complementary to the internal sequence of the last gene, *actD*, was used for the first-strand cDNA synthesis. Each of the reactions yielded an amplicon of the expected size without interference from DNA contamination, only when total RNA from cells grown under iron-limiting conditions was used (Fig. 2b). In addition, the level of 16S rRNA expression as a control was not affected by the iron conditions in the medium. In particular, the results of PCR for *acbA* and *actD*, the first and last genes within the eight-gene cluster, demonstrated that these genes were co-transcribed from the promoter upstream of *acbA* as a single polycistronic message under iron-limiting conditions. The presence of a potential Fur box in the promoter region of *acbA* implied that Fur was responsible for this iron-regulated transcription.

Phenotypic analysis of the *acbA* mutant

In order to characterize the acinetoferrin biosynthesis cluster, the first gene, *acbA*, was mutated using gene replacement with insertion (Aranda *et al.*, 2010). No discernible growth defect was observed for the *acbA* mutant strain when grown in +Fe medium (data not shown). As expected, *A. haemolyticus* ATCC 17906^T produced acinetoferrin when grown in the -Fe medium alone, but the TF-*acbA* mutant defective in *acbA* did not produce acinetoferrin under the same conditions (Fig. 3). In contrast, the complementing strain, TF-*acbA*/pRK415-*acbA*, produced acinetoferrin at a level similar to that of the wild-type parental strain, indicating that the *acbA* gene was one of the determinants essential for acinetoferrin biosynthesis. Nevertheless, the *acbA* mutant could grow to a modest extent with a reduced growth rate in the -Fe medium but

could not reach the same final OD₆₀₀ as the wild-type strain (Fig. 4a). The culture supernatant of the *acbA* mutant exhibited a catecholate siderophore titre similar to that of the parental strain, as determined by the Arnow colorimetric assay (Payne, 1994). It was also positive in the Chrome azurol S liquid assay, which can monitor siderophore production (Schwyn & Neilands, 1987). These results were consistent with the report that the ATCC 17906^T strain also produces a small amount of the catecholate siderophore acinetobactin, which is also produced by *A. baumannii* (Yamamoto *et al.*, 1994; Wuest *et al.*, 2009). Therefore, the modest growth observed for the *acbA* mutant may be attributable to acinetobactin. These results suggested that under iron-limiting conditions, acinetobactin could partially replace acinetoferrin in supplying iron to *A. haemolyticus* cells. However, the possibility was not ruled out that the ATCC 17906^T strain can acquire iron, although to a lesser extent, via an uncharacterized siderophore, which is different from both acinetobactin and acinetoferrin but capable of promoting growth of this strain under iron-limiting conditions. On the other hand, the complementing strain, TF-*acbA*/pRK415-*acbA*, had a reduced growth rate but eventually reached almost the same final OD₆₀₀ as the parental strain

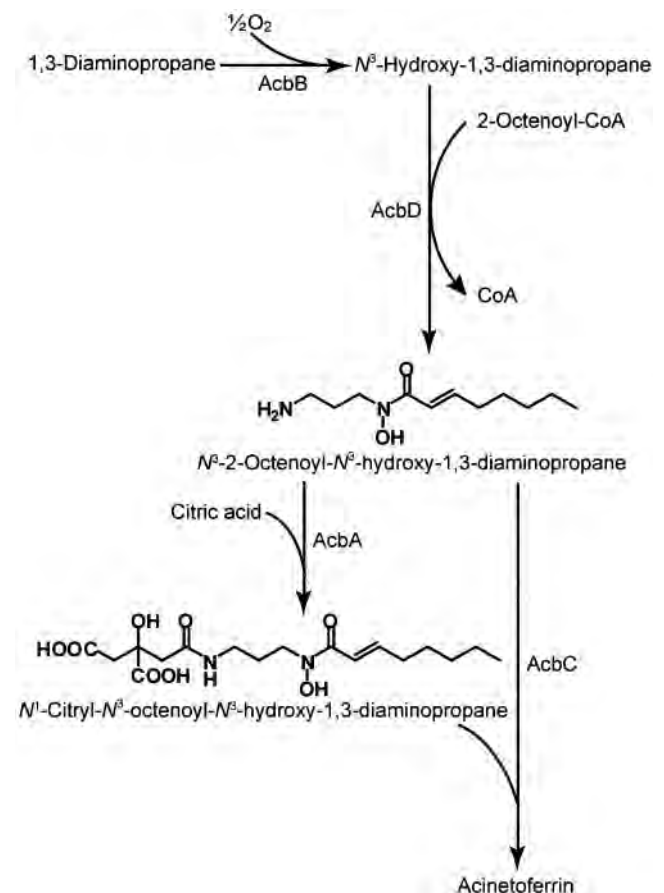


Fig. 7. Proposed biosynthetic pathway for acinetoferrin.

(Fig. 4). The strain (TF-acbA/pRK415) containing an empty plasmid also showed a more reduced growth rate than the complementing strain. However, a highly reduced growth rate was observed for TF-acbA containing pRK415 or pRK415-acbA when it was grown in -Fe medium supplemented with both tetracycline and apramycin, although the reason for this is currently unknown. The growth assay at least indicated that *acbA* participates in acinetoferrin production and that acinetoferrin was the preferred siderophore of this strain under the growth conditions used in this study. Taken together, these data indicate that *A. haemolyticus* ATCC 17906^T produced a

second siderophore, acinetobactin, but in an amount insufficient to grow at a level similar to the parental strain. Additionally, the *acbA* mutant showed normal expression of the ActA receptor protein, the seventh gene product (data not shown), confirming that the gene replacement mutation in *acbA* caused no polar effect on the downstream genes.

Phenotypic analysis of the *actA* mutant

A. haemolyticus ATCC 17906^T was grown in +Fe and -Fe media, and the profiles of total outer-membrane proteins

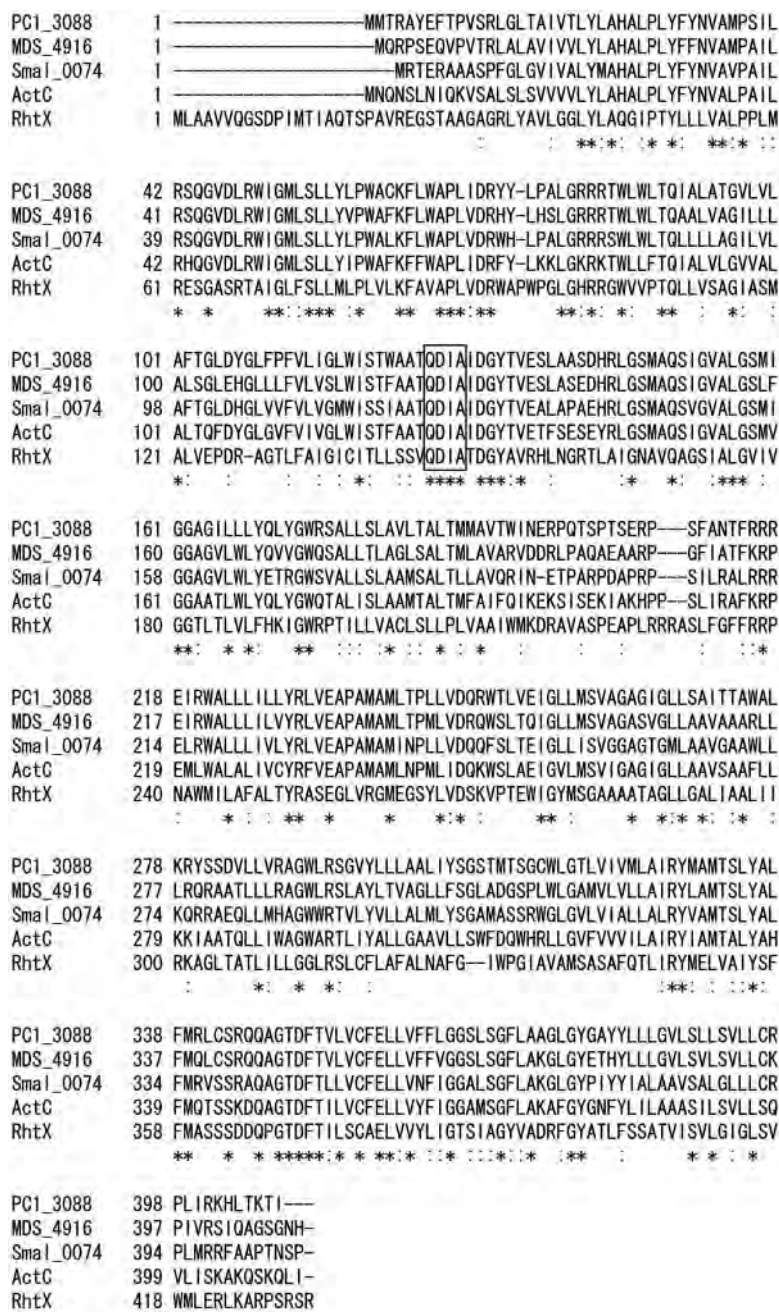


Fig. 8. Amino acid sequence alignment of *A. haemolyticus* ATCC 17906^T ActC with the three proteins showing the highest homology and *S. meliloti* RhtX. The numbers refer to amino acid positions in the unprocessed protein. Amino acids identical in the five proteins are marked by asterisks, and conserved amino acids are denoted by colons. The accession numbers of the aligned proteins are as follows: *Pectobacterium carotovorum* PC1_3088 (NC012917), *P. mendocina* NK-01 MDS_4916 (CP002620), *Stenotrophomonas maltophilia* R551-3 Sma1_0074 (NC011071) and *S. meliloti* 1021 RhtX (AE006469). The four conserved amino acid residues that are predicted to be located in a cytoplasmic loop of a novel family of MFS permeases (Cuiv *et al.*, 2004) are boxed.

(OMPs) were then compared by SDS-PAGE (Fig. 5). As a result, at least five IROMP bands were observed, only when the ATCC 17906^T strain was grown in –Fe medium (Fig. 5, lanes 1 and 3). The first 10 N-terminal amino acid sequence of the 79.3 kDa IROMP (the predicted molecular mass of the mature ActA was 79 249 kDa) was identical to that deduced from *actA* (Fig. 2a). This also indicated that the 23 amino acid residues were removed from the ActA pre-protein as a signal peptide. The *actA* mutant TF-actA was constructed to determine loss of expression of the corresponding protein. As expected, the 79.3 kDa IROMP band disappeared in this mutant (Fig. 5, lanes 2 and 4), and the corresponding band was again detected in the complementing strain, TF-actA/pRK415-actA, although it was not detected in the mutant containing the empty plasmid (Fig. 5, lanes 5 and 6). Next, we determined the effect of defective *actA* on growth in the –Fe medium. TF-actA showed an approximate 50% reduction in growth compared with the parental strain (Fig. 6), as observed for the *acbA* mutant (Fig. 4). In contrast, the *actA* mutant complemented with the *actA* gene outgrew the parental strain when incubated for 24 h under iron-limiting conditions (Fig. 6). Altogether, these data indicated that ActA could act as the outer-membrane receptor for ferric acinetoferrin.

Phenotypic analysis of the *actD* mutant

The inactivation of *actD* (TF-actD) resulted in an approximate 35% reduction in the ability to secrete acinetoferrin compared with the parental strain, whereas the introduction of pRK415-actD into the *actD* mutant (TF-actD/pRK415-actD) regained the strain's original ability to secrete acinetoferrin (Fig. 3). In addition, TF-actD/pRK415-actD outgrew the *actD* mutant (Fig. 6). These results suggested that ActD may function as an inner-membrane exporter for acinetoferrin.

Phenotypic analysis of the *actB* and *actC* mutants

When TF-actB, TF-actC and their complementing strains (TF-actB/pRK415-actB and TF-actC/pRK415-actC) were cultured in –Fe medium, no significant differences in the levels of growth after 24 h were observed (Fig. 6), and they were able to grow at levels similar to the parental strain (Fig. 4). Thus, mutational analysis failed to confirm the functions of *actB* and *actC* in ferric acinetoferrin transport. In particular, it was assumed that the additional production of acinetobactin could hamper the assessment of the function of ActC as an inner-membrane importer for ferric acinetoferrin.

DISCUSSION

The Fur box-containing DNA fragment isolated from *A. haemolyticus* ATCC 17906^T by the FURTA method facilitated cloning and sequencing of neighbouring ORFs

of related functions. Homology and mutational analyses revealed a cluster of eight ORFs encoding biosynthetic enzymes and transport components for acinetoferrin. We demonstrated that these eight ORFs were regulated by iron and were co-transcribed as a single polycistronic message. The results reported here indicate that the biosynthesis of acinetoferrin in *A. haemolyticus* ATCC 17906^T likely proceeds as shown in Fig. 7. This represents another example of the siderophore biosynthesis pathways independent of nonribosomal peptide synthetases (Oves-Costales *et al.*, 2009).

It has been reported that neighbouring genes encoding RhbA (L-2,4-diaminobutyrate:2-ketoglutarate 4-amino-transferase) and RhbB (L-2,4-diaminobutyrate decarboxylase), which are required for DAP production, are present as the first and second ORFs in the iron-regulated rhizobactin 1021 biosynthesis operon of *S. meliloti* (Lynch *et al.*, 2001). Although such genes were not present in the acinetoferrin biosynthesis operon, significant activities of these two enzymes were found in the ATCC 17906^T strain even when grown in +Fe medium (Yamamoto *et al.*, 1995b; Ikai & Yamamoto, 1997). Moreover, there was a gene located at the same direction as *acbA* immediately upstream of *acbA*, whose protein product was homologous to hypothetical proteins of *A. baumannii* strains not related to DAP production. These data support the possibility that genes involved in DAP production may be located in another chromosomal region of the strain and that the transcription of these genes may not be iron-regulated. Consistent with this, it has recently been reported that *A. baumannii*, belonging to the same genus as *A. haemolyticus*, produces DAP, which is responsible for its surface-associated motility and virulence, even under iron-replete conditions (Skiebe *et al.*, 2012). Besides rhizobactin 1021 (Persmark *et al.*, 1993) and acinetoferrin, schizokinen (Mullis *et al.*, 1971) and synechobactin (Ito & Butler, 2005) are known as hydroxamate siderophores characteristically containing DAP moieties for structural assembly. The results in this study would be useful to elucidate the genetic determinants involved in biosynthesis and transport of these siderophores.

To date, three different siderophore biosynthesis gene clusters have been described in *A. baumannii* (Antunes *et al.*, 2011; Eijkelkamp *et al.*, 2011). One gene cluster that is common to all the whole-genome-sequenced *A. baumannii* strains is proposed to function in biosynthesis of a hydroxamate siderophore of unknown structure. The *acbA*, *acbB* and *acbD* orthologues in the acinetoferrin biosynthesis cluster were found to be present in the hydroxamate siderophore cluster of *A. baumannii*. However, the genetic arrangement differs considerably between the two species, and *A. baumannii* has no *acbC* orthologue. These findings suggested that the predicted hydroxamate siderophore in *A. baumannii* may be structurally related to acinetoferrin.

The proteins *Pseudomonas aeruginosa* FptX (Cuív *et al.*, 2004) and *Legionella pneumophila* LbtC (Chatfield *et al.*, 2012), which show homology to *S. meliloti* RhtX, a member of a novel family of permeases (Cuív *et al.*, 2004), have also been reported to be encoded in the gene clusters that are involved in siderophore-mediated iron acquisition systems. The *actC* gene encoding the protein homologous to RhtX is located between *actB* and *actA* in the acinetoferrin cluster (Fig. 2a), and amino acid sequence alignment of these ActC homologues with RhtX revealed that a motif of four amino acids, QD(V/I)A, was conserved (Fig. 8), which is predicted to be located in a cytoplasmic loop in RhtX (Cuív *et al.*, 2004). These observations suggested that ActC may also be a member of a novel family of permeases and function in part as an importer of ferric acinetoferrin. Moreover, it is of interest that all of the genes encoding proteins with the highest similarity to ActC that are cited in Table 2 are preceded by genes encoding ActB homologues of unknown function. *Pseudomonas mendocina* has also been reported to produce a hydroxamate siderophore of unknown structure (Awaya & Dubois, 2008). The function of ActB in *A. haemolyticus* ATCC 17906^T, however, remains obscure.

It is of great interest to elucidate how siderophores newly synthesized under iron-limiting conditions are secreted into the extracellular milieu, since intracellular accumulation of iron-free siderophores may be toxic due to deprivation of the cellular components of essential iron cofactors. MFS efflux pumps with 12 transmembrane segments in several bacteria, e.g. in *E. coli* (EntS) (Furrer *et al.*, 2002), *Bordetella* species (AlcS) (Brickman & Armstrong, 2005), *Legionella pneumophila* (IbtB) (Allard *et al.*, 2006) and *Vibrio parahaemolyticus* (PvsC) (Tanabe *et al.*, 2006), have been identified as siderophore-specific exporters. This work indicated that *A. haemolyticus* ATCC 17906^T also secretes acinetoferrin with the help of ActD. However, it should be considered that the *actD* mutant was still able to secrete acinetoferrin in response to iron limitation, although to a lesser extent than the wild-type parental strain (Fig. 3). This may be explained by compensation by another efflux pump in this species to avoid accumulation of acinetoferrin at burdensome levels, similar to *P. aeruginosa*, in which the siderophore pyoverdine is also exported by another known multidrug efflux pump (Poole *et al.*, 1993).

Recently, we identified the gene cluster involved in biosynthesis and transport of acinetobactin in *A. haemolyticus* ATCC 17906^T (GenBank accession no. AB621369), whose gene order is very similar to that in the characterized acinetobactin gene cluster of *A. baumannii* ATCC 19606^T (Mihara *et al.*, 2004). However, genes encoding an integrase catalytic subunit and a transposase IS3/IS911 family protein intervene in the 3'-terminal region of a thioesterase gene, thereby resulting in the absence of the C-terminal 24 amino acid residues. Deletion of *angT*, encoding a thioesterase which is involved in anguibactin biosynthesis in *Vibrio anguillarum*, has been reported to

lead to a 17-fold decrease in its production (Wertheimer *et al.*, 1999). Since anguibactin is structurally similar to acinetobactin, it was assumed that *A. haemolyticus* ATCC 17906^T may also produce acinetobactin even in small amounts. For this reason, we attempted to generate a double mutant both in *acbA* and in the gene involved in acinetobactin biosynthesis. However, in spite of extensive efforts, such a mutant could not be obtained. Construction of a double mutant with regard to two different siderophore biosynthesis clusters may be necessary to clarify the advantages of possession of independent siderophore biosynthesis pathways in *A. haemolyticus*.

In conclusion, we have identified the *A. haemolyticus* ATCC 17906^T gene cluster spanning ~13 kb which participates in acinetoferrin biosynthesis and transport. This cluster includes eight ORFs which are all co-transcribed from the promoter located in front of *acbA*. The existence of the iron acquisition system mediated by acinetoferrin would give *A. haemolyticus* the opportunity to utilize different iron sources, ultimately enhancing its ability to colonize and prosper in its natural habitat and human host. Further studies will be focused on identification and characterization of genes encoding the inner-membrane active transport system for ferric acinetoferrin in connection with the function of ActC.

ACKNOWLEDGEMENTS

We thank Professor W. R. Bishai, Johns Hopkins University School of Medicine, for providing plasmid pJG1011. This study was supported by a Grant-in-Aid for Young Scientists (B) from the Ministry of Education, Culture, Sports, Science and Technology of Japan (grant no. 22790140 to T.F.).

REFERENCES

- Allard, K. A., Viswanathan, V. K. & Cianciotto, N. P. (2006). *lbtA* and *lbtB* are required for production of the *Legionella pneumophila* siderophore legiobactin. *J Bacteriol* **188**, 1351–1363.
- Altschul, S. F., Madden, T. L., Schäffer, A. A., Zhang, J., Zhang, Z., Miller, W. & Lipman, D. J. (1997). Gapped BLAST and PSI-BLAST: a new generation of protein database search programs. *Nucleic Acids Res* **25**, 3389–3402.
- Andrews, S. C., Robinson, A. K. & Rodríguez-Quiñones, F. (2003). Bacterial iron homeostasis. *FEMS Microbiol Rev* **27**, 215–237.
- Antunes, L. C. S., Imperi, F., Towner, K. J. & Visca, P. (2011). Genome-assisted identification of putative iron-utilization genes in *Acinetobacter baumannii* and their distribution among a genotypically diverse collection of clinical isolates. *Res Microbiol* **162**, 279–284.
- Aranda, J., Poza, M., Pardo, B. G., Rumbo, S., Rumbo, C., Parreira, J. R., Rodríguez-Velo, P. & Bou, G. (2010). A rapid and simple method for constructing stable mutants of *Acinetobacter baumannii*. *BMC Microbiol* **10**, 279.
- Awaya, J. D. & Dubois, J. L. (2008). Identification, isolation, and analysis of a gene cluster involved in iron acquisition by *Pseudomonas mendocina* ymp. *Biomaterials* **21**, 353–366.
- Bagg, A. & Neilands, J. B. (1987). Ferric uptake regulation protein acts as a repressor, employing iron (II) as a cofactor to bind the

- operator of an iron transport operon in *Escherichia coli*. *Biochemistry* 26, 5471–5477.
- Bergogne-Bérézin, E. & Towner, K. J. (1996).** *Acinetobacter* spp. as nosocomial pathogens: microbiological, clinical, and epidemiological features. *Clin Microbiol Rev* 9, 148–165.
- Braun, V., Hantke, K. & Köster, W. (1998).** Bacterial iron transport: mechanisms, genetics, and regulation. *Met Ions Biol Syst* 35, 67–145.
- Brickman, T. J. & Armstrong, S. K. (2005).** *Bordetella* AlcS transporter functions in alcaligin siderophore export and is central to inducer sensing in positive regulation of alcaligin system gene expression. *J Bacteriol* 187, 3650–3661.
- Bullen, J. J., Rogers, H. J., Spalding, P. B. & Ward, C. G. (2005).** Iron and infection: the heart of the matter. *FEMS Immunol Med Microbiol* 43, 325–330.
- Calderwood, S. B. & Mekalanos, J. J. (1988).** Confirmation of the Fur operator site by insertion of a synthetic oligonucleotide into an operon fusion plasmid. *J Bacteriol* 170, 1015–1017.
- Chatfield, C. H., Mulhern, B. J., Viswanathan, V. K. & Cianciotto, N. P. (2012).** The major facilitator superfamily-type protein LbtC promotes the utilization of the legiobactin siderophore by *Legionella pneumophila*. *Microbiology* 158, 721–735.
- Cuiv, P. Ó., Clarke, P., Lynch, D. & O'Connell, M. (2004).** Identification of *rhtX* and *ftfX*, novel genes encoding proteins that show homology and function in the utilization of the siderophores rhizobactin 1021 by *Sinorhizobium meliloti* and pyochelin by *Pseudomonas aeruginosa*, respectively. *J Bacteriol* 186, 2996–3005.
- de Lorenzo, V., Wee, S., Herrero, M. & Neilands, J. B. (1987).** Operator sequences of the aerobactin operon of plasmid ColV-K30 binding the ferric uptake regulation (*fur*) repressor. *J Bacteriol* 169, 2624–2630.
- Eijkkelkamp, B. A., Hassan, K. A., Paulsen, I. T. & Brown, M. H. (2011).** Investigation of the human pathogen *Acinetobacter baumannii* under iron limiting conditions. *BMC Genomics* 12, 126.
- Escolar, L., Pérez-Martín, J. & de Lorenzo, V. (1999).** Opening the iron box: transcriptional metalloregulation by the Fur protein. *J Bacteriol* 181, 6223–6229.
- Furrer, J. L., Sanders, D. N., Hook-Barnard, I. G. & McIntosh, M. A. (2002).** Export of the siderophore enterobactin in *Escherichia coli*: involvement of a 43 kDa membrane exporter. *Mol Microbiol* 44, 1225–1234.
- Gomez, J. E. & Bishai, W. R. (2000).** *whmD* is an essential mycobacterial gene required for proper septation and cell division. *Proc Natl Acad Sci U S A* 97, 8554–8559.
- Heckman, K. L. & Pease, L. R. (2007).** Gene splicing and mutagenesis by PCR-driven overlap extension. *Nat Protoc* 2, 924–932.
- Hider, R. C. & Kong, X. (2010).** Chemistry and biology of siderophores. *Nat Prod Rep* 27, 637–657.
- Ikai, H. & Yamamoto, S. (1997).** Identification and analysis of a gene encoding L-2,4-diaminobutyrate:2-ketoglutarate 4-aminotransferase involved in the 1,3-diaminopropane production pathway in *Acinetobacter baumannii*. *J Bacteriol* 179, 5118–5125.
- Ito, Y. & Butler, A. (2005).** Structure of synechobactins, new siderophores of the marine cyanobacterium *Synechococcus* sp. PCC 7002. *Limnol Oceanogr* 50, 1918–1923.
- Keen, N. T., Tamaki, S., Kobayashi, D. & Trollinger, D. (1988).** Improved broad-host-range plasmids for DNA cloning in Gram-negative bacteria. *Gene* 70, 191–197.
- Leahy, J. G., Jones-Meehan, J. M. & Colwell, R. R. (1994).** Transformation of *Acinetobacter calcoaceticus* RAG-1 by electroporation. *Can J Microbiol* 40, 233–236.
- Letain, T. E. & Postle, K. (1997).** TonB protein appears to transduce energy by shuttling between the cytoplasmic membrane and the outer membrane in *Escherichia coli*. *Mol Microbiol* 24, 271–283.
- Lynch, D., O'Brien, J., Welch, T., Clarke, P., Cuiv, P. Ó., Crosa, J. H. & O'Connell, M. (2001).** Genetic organization of the region encoding regulation, biosynthesis, and transport of rhizobactin 1021, a siderophore produced by *Sinorhizobium meliloti*. *J Bacteriol* 183, 2576–2585.
- Markwell, M. A. K., Haas, S. M., Bieber, L. L. & Tolbert, N. E. (1978).** A modification of the Lowry procedure to simplify protein determination in membrane and lipoprotein samples. *Anal Biochem* 87, 206–210.
- Miethke, M. & Marahiel, M. A. (2007).** Siderophore-based iron acquisition and pathogen control. *Microbiol Mol Biol Rev* 71, 413–451.
- Mihara, K., Tanabe, T., Yamakawa, Y., Funahashi, T., Nakao, H., Narimatsu, S. & Yamamoto, S. (2004).** Identification and transcriptional organization of a gene cluster involved in biosynthesis and transport of acinetobactin, a siderophore produced by *Acinetobacter baumannii* ATCC 19606^T. *Microbiology* 150, 2587–2597.
- Mullis, K. B., Pollack, J. R. & Neilands, J. B. (1971).** Structure of schizokinen, an iron-transport compound from *Bacillus megaterium*. *Biochemistry* 10, 4894–4898.
- Neilands, J. B. (1981).** Microbial iron compounds. *Annu Rev Biochem* 50, 715–731.
- Okujo, N., Sakakibara, Y., Yoshida, T. & Yamamoto, S. (1994).** Structure of acinetoferrin, a new citrate-based dihydroxamate siderophore from *Acinetobacter haemolyticus*. *Biometals* 7, 170–176.
- Oves-Costales, D., Kadi, N. & Challis, G. L. (2009).** The long-overlooked enzymology of a nonribosomal peptide synthetase-independent pathway for virulence-conferring siderophore biosynthesis. *Chem Commun (Camb)* (43), 6530–6541.
- Payne, S. M. (1994).** Detection, isolation, and characterization of siderophores. *Methods Enzymol* 235, 329–344.
- Persmark, M., Pittman, P., Buyer, J. S., Schwyn, P. R., Gill, P. R. & Neilands, J. B. (1993).** Isolation and structure of rhizobactin 1021, a siderophore from the alfalfa symbiont *Rhizobium meliloti* 1021. *J Am Chem Soc* 115, 3950–3956.
- Poole, K., Krebs, K., McNally, C. & Neshat, S. (1993).** Multiple antibiotic resistance in *Pseudomonas aeruginosa*: evidence for involvement of an efflux operon. *J Bacteriol* 175, 7363–7372.
- Ratledge, C. & Dover, L. G. (2000).** Iron metabolism in pathogenic bacteria. *Annu Rev Microbiol* 54, 881–941.
- Sambrook, J., Fritsch, E. F. & Maniatis, T. (1989).** *Molecular Cloning: a Laboratory Manual*, 2nd edn. Cold Spring Harbor, NY: Cold Spring Harbor Laboratory.
- Schaible, U. E. & Kaufmann, S. H. (2004).** Iron and microbial infection. *Nat Rev Microbiol* 2, 946–953.
- Schwyn, B. & Neilands, J. B. (1987).** Universal chemical assay for the detection and determination of siderophores. *Anal Biochem* 160, 47–56.
- Skiebe, E., de Berardinis, V., Morczinek, P., Kerrinnes, T., Faber, F., Lepka, D., Hammer, B., Zimmermann, O., Ziesing, S. & other authors (2012).** Surface-associated motility, a common trait of clinical isolates of *Acinetobacter baumannii*, depends on 1,3-diaminopropane. *Int J Med Microbiol* 302, 117–128.
- Stojiljkovic, I., Bäuml, A. J. & Hantke, K. (1994).** Fur regulon in Gram-negative bacteria. Identification and characterization of new iron-regulated *Escherichia coli* genes by a fur titration assay. *J Mol Biol* 236, 531–545.
- Tanabe, T., Nakao, H., Kuroda, T., Tsuchiya, T. & Yamamoto, S. (2006).** Involvement of the *Vibrio parahaemolyticus* *pvsC* gene in

export of the siderophore vibrioferrin. *Microbiol Immunol* **50**, 871–876.

Tayabali, A. F., Nguyen, K. C., Shwed, P. S., Crosthwait, J., Coleman, G. & Seligy, V. L. (2012). Comparison of the virulence potential of *Acinetobacter* strains from clinical and environmental sources. *PLoS ONE* **7**, e37024.

Tusnady, G. E. & Simon, I. (2001). The HMMTOP transmembrane topology prediction server. *Bioinformatics* **17**, 849–850.

Weinberg, E. D. (2009). Iron availability and infection. *Biochim Biophys Acta* **1790**, 600–605.

Wertheimer, A. M., Verweij, W., Chen, Q., Crosa, L. M., Nagasawa, M., Tolmasky, M. E., Actis, L. A. & Crosa, J. H. (1999). Characterization of the *angR* gene of *Vibrio anguillarum*: essential role in virulence. *Infect Immun* **67**, 6496–6509.

Wuest, W. M., Sattely, E. S. & Walsh, C. T. (2009). Three siderophores from one bacterial enzymatic assembly line. *J Am Chem Soc* **131**, 5056–5057.

Yamamoto, S., Okujo, N. & Sakakibara, Y. (1994). Isolation and structure elucidation of acinetobactin, a novel siderophore from *Acinetobacter baumannii*. *Arch Microbiol* **162**, 249–254.

Yamamoto, S., Akiyama, T., Okujo, N., Matsu-ura, S. & Shinoda, S. (1995a). Demonstration of a ferric vibrioferrin-binding protein in the outer membrane of *Vibrio parahaemolyticus*. *Microbiol Immunol* **39**, 759–766.

Yamamoto, S., Ikai, H., Uesugi, T., Horie, A. & Hirai, Y. (1995b). Occurrence and antigenic heterogeneity of L-2,4-diaminobutyrate decarboxylase in *Acinetobacter* species. *Biol Pharm Bull* **18**, 454–456.

Edited by: N. Le Brun

Characterization of *Vibrio parahaemolyticus* genes encoding the systems for utilization of enterobactin as a xenosiderophore

Tomotaka Tanabe,¹ Tatsuya Funahashi,¹ Keiichi Shiuchi,²
Noriyuki Okajima,² Hiroshi Nakao,^{2†} Katsushiro Miyamoto,³
Hiroshi Tsujibo³ and Shigeo Yamamoto¹

Correspondence

Tomotaka Tanabe
ttanabe@cc.matsuyama-u.ac.jp

¹College of Pharmaceutical Sciences, Matsuyama University, 4-2 Bunkyo-cho, Matsuyama, Ehime 790-8578, Japan

²Graduate School of Medicine, Dentistry and Pharmaceutical Sciences, Okayama University, 1-1-1 Tsushima-naka, Kita-ku, Okayama 700-8530, Japan

³Osaka University of Pharmaceutical Sciences, 4-20-1 Nasahara, Takatsuki, Osaka 569-1094, Japan

We determined the ability of *Vibrio parahaemolyticus* to utilize enterobactin (Ent) as a xenosiderophore. Homology searches of the *V. parahaemolyticus* genomic sequence revealed the presence of genes that are homologous to the *V. cholerae* ferric Ent utilization genes, which consist of the iron-repressible outer-membrane protein genes *irgA* and *vctA*, and the ATP-binding cassette transport system operon *vctPDGC*. Moreover, the *irgB* and *vctR* genes, which encode transcriptional regulators, were also found immediately upstream of *irgA* and *vctA*, respectively. Growth assays of *V. parahaemolyticus* indicated that both *irgA* and *vctA* mutants grew well in the presence of Ent under iron-limiting conditions, whereas both the *irgA/vctA* double mutant and the *vctPDGC* mutant barely grew under the same conditions. In addition, growth assays of three isogenic *tonB* mutants demonstrated that the TonB2 system, and to a lesser extent the TonB1 system, can provide energy for both IrgA and VctA to transport ferric Ent. SDS-PAGE analysis showed that expression of both IrgA and VctA was enhanced by the presence of Ent. Complementation of the *irgB* and *vctR* mutants with their respective genes resulted in the increased expression of IrgA and VctA, respectively. Finally, reverse transcriptase-quantitative PCR revealed that transcription of the Ent utilization system genes is iron-regulated, and that transcription of *irgA* and *vctA* under iron-limiting conditions is further activated by proteins encoded by *irgB* and *vctR*, respectively, together with Ent.

Received 3 April 2012
Revised 30 May 2012
Accepted 8 June 2012

INTRODUCTION

Iron is an essential element for virtually all forms of cellular life, including most bacteria, because the iron ion is a cofactor for several key enzymes required for many metabolic processes, such as redox reactions, nucleic acid synthesis and electron transfer. However, the bioavailability

of iron is extremely low, since it exists in insoluble mineral complexes under aerobic, aqueous and neutral pH conditions, or is bound to mammalian high-affinity iron-binding proteins such as transferrin, lactoferrin and ferritin. Therefore, many bacteria have developed high-affinity iron transport systems to acquire iron (Andrews *et al.*, 2003; Miethke & Marahiel, 2007). One of these strategies is based on low-molecular-mass compounds, siderophores, that specifically chelate ferric iron. Indeed, most bacteria can biosynthesize and secrete cognate siderophores in response to iron limitation. In Gram-negative bacteria, iron-bound siderophores, called ferric siderophores, are transported across the outer and inner membranes by specific iron-repressible outer-membrane proteins (IROMPs) and ATP-binding cassette (ABC) transport systems, respectively (Chu *et al.*, 2010). The transport of ferric siderophores via their specific IROMPs is dependent on the energy transferred

[†]Present address: School of Health Sciences, Faculty of Medicine, University of the Ryukyus, 207 Uehara, Nishihara, Okinawa 903-0215, Japan.

Abbreviations: ABC, ATP-binding cassette; Ent, enterobactin; Fur, ferric uptake regulator; IROMP, iron-repressible outer-membrane protein; OMP, outer-membrane protein; RT-qPCR, reverse transcriptase-quantitative PCR.

Two supplementary figures and two supplementary tables are available with the online version of this paper.

from the inner-membrane proton motive force by the TonB system, which is generally composed of TonB and its accessory proteins ExbB and ExbD (Moeck & Coulton, 1998; Noinaj *et al.*, 2010). The expression of many of the genes engaged in iron acquisition is regulated by the ferric uptake regulator (Fur), which is a global negative regulator ubiquitous in Gram-negative bacteria (Bagg & Neilands, 1987; Escolar *et al.*, 1999). When the intracellular iron concentration is increased, the Fur-ferrous iron complex binds to a consensus sequence, termed the Fur box, which overlaps the -10 and -35 elements in Fur target genes, thereby leading to repressed transcription initiation of the respective genes. In contrast to the Fur- Fe^{2+} complex, other transcriptional regulators such as the AraC-type family members (Anderson & Armstrong, 2004; Fetherston *et al.*, 1996; Heinrichs & Poole, 1993; Hollander *et al.*, 2011; Tanabe *et al.*, 2005) and LysR-type family members (Balado *et al.*, 2008; Visca *et al.*, 2002) have been shown to activate transcription initiation of siderophore synthesis genes and siderophore utilization system genes.

The halophilic Gram-negative bacterium *Vibrio parahaemolyticus* is a causative agent of watery diarrhoea that possesses multiple iron acquisition systems. We previously demonstrated that *V. parahaemolyticus* produces the cognate siderophore vibrioferrin belonging to the hydroxycarboxylate-type siderophore family (Yamamoto *et al.*, 1994), and transports ferric vibrioferrin into cells via the outer-membrane receptors PvuA1 and PvuA2, and the inner-membrane ABC transport system PvuBCDE (Tanabe *et al.*, 2003, 2011). Three sets of TonB systems, termed TonB1, TonB2 and TonB3, are present in this bacterium (Kuehl & Crosa, 2010), and the energy required for PvuA1 and PvuA2 to transport ferric vibrioferrin is provided by the TonB2 system, and both the TonB1 and TonB2 systems, respectively (Tanabe *et al.*, 2011). In addition, *V. parahaemolyticus* can utilize hydroxamate-type xenosiderophores such as desferri-ferrichrome and aerobactin (Funahashi *et al.*, 2003, 2009). Previous studies have demonstrated that several *Vibrio* species, including *Vibrio cholerae* and *Vibrio anguillarum*, can use catecholate-type siderophores, such as their cognate siderophores (Actis *et al.*, 1986; Balado *et al.*, 2009; Griffiths *et al.*, 1984) and a xenosiderophore enterobactin (Ent) mainly produced by members of the family *Enterobacteriaceae* (Carson *et al.*, 1999; Mey *et al.*, 2002; Naka & Crosa, 2012; Stork *et al.*, 2004; Wyckoff *et al.*, 2007). However, to our knowledge, the ability of *V. parahaemolyticus* to utilize catecholate-type xenosiderophores has not yet been reported.

In this study, we show that *V. parahaemolyticus* can utilize Ent as an iron source when grown in iron-limiting medium, through two newly identified receptors, namely, IrgA and VctA, and an ABC transport system encoded by *vctPDGC*. In addition, we show that both IrgA and VctA from *V. parahaemolyticus* can gain energy from the TonB1 and TonB2 systems. Finally, we demonstrate that under iron-limiting conditions in the presence of Ent, the *irgB* and *vctR* genes encoding the transcriptional regulators,

which are homologous to *V. cholerae* IrgB (Goldberg *et al.*, 1991) and VCA0231 (Mey *et al.*, 2002), are responsible for the activation of *irgA* and *vctA* expression.

METHODS

Bacterial strains, plasmids, growth conditions and primers. The bacterial strains and plasmids used in this study are listed in Tables 1 and S1 (available with the online version of this paper), respectively. The *V. parahaemolyticus* strains were routinely cultivated in Luria-Bertani (LB) medium (pH 7.0) containing 3% NaCl (+ Fe medium). The *Escherichia coli* β 2155 strain, which is a diaminopimelic acid auxotroph, was grown in LB medium containing 0.5% NaCl and 0.5 mM diaminopimelic acid. To impose iron limitation on the *V. parahaemolyticus* strains, they were cultured in $-$ Fe medium that was composed of LB medium with 25 μM ethylenediamine-di(*o*-hydroxyphenylacetic acid) (EDDA; Sigma-Aldrich). When required, the antibiotics chloramphenicol (10 $\mu\text{g ml}^{-1}$) and tetracycline (15 $\mu\text{g ml}^{-1}$) were added to the media. The PCR primers used in this study are listed in Table S2.

DNA techniques. All plasmids were extracted using a High Pure Plasmid Isolation kit (Roche). Standard DNA manipulations were performed according to the procedures of Sambrook *et al.* (1989). Oligonucleotide primers employed in this study (Table S2) were designed on the basis of the *V. parahaemolyticus* RIMD2210633 genome sequence from the Genome Information Research Center (GIRC) at Osaka University (<http://genome.gen-info.osaka-u.ac.jp/bacteria/vpara/>) (Makino *et al.*, 2003). A homology search was performed using the BLAST program of the GIRC or the National Center for Biotechnology Information (NCBI; <http://blast.ncbi.nlm.nih.gov/>). Conserved domain searches were performed using the NCBI Conserved Domain Database (<http://www.ncbi.nlm.nih.gov/Structure/cdd/wrpsb.cgi>).

Construction of *V. parahaemolyticus* deletion mutants.

Deletion mutants were created by allelic exchange using the R6K-ori suicide vector pXAC623, according to the procedure described by Kuroda *et al.* (2005). DNA fragments with deletions in the *V. parahaemolyticus* *irgA*, *vctA*, *irgB*, *vctR* and *vctPDGC* genes were prepared by PCR-driven overlap extension (Heckman & Pease, 2007) as previously described (Tanabe *et al.*, 2011), and then ligated into appropriately digested pXAC623. Each resulting plasmid was transformed into *E. coli* β 2155 (Demarre *et al.*, 2005), and mobilized into an appropriate *V. parahaemolyticus* strain by filter mating. Chloramphenicol-resistant merodiploids were spread on VDS-broth agar plates (1% polypeptone, 0.5% yeast extract, 30 mM NaCl, 55 mM KCl, 10% sucrose, 2.5% agar) at 25 °C for 30 h. Sucrose-resistant and chloramphenicol-sensitive colonies were selected, and the deleted DNA regions were confirmed by PCR using their chromosomal DNAs (Fig. S1). To complement the deletion mutants of *irgA*, *vctA*, *irgB*, *vctR* and *vctPDGC*, PCR amplicons containing the respective genes were ligated into appropriately digested pRK415 (Keen *et al.*, 1988), and the complementing plasmids thus obtained were transformed into the respective *V. parahaemolyticus* mutant strains.

Growth assay. Stationary phase *V. parahaemolyticus* cells were diluted with the $-$ Fe medium to OD₆₀₀ 0.005. When required, the $-$ Fe medium was supplemented with Ent at a final concentration of 5 μM ($-$ Fe + Ent medium). The cultures were shaken at 70 r.p.m. at 37 °C, and the OD₆₀₀ was measured every 3 h with a biophotorecorder (TVS062CA, Advantec). The siderophore Ent was purchased from EMC Microcollections GmbH and Sigma-Aldrich.

Table 1. Bacterial strains used in this study

Strain	Description	Reference or source
<i>V. parahaemolyticus</i> strains		
RIMD2210633	Clinical isolate of serotype O3:K6	Makino <i>et al.</i> (2003)
VPD5	RIMD2210633 $\Delta pvsB$	Tanabe <i>et al.</i> (2011)
VPD8	VPD5 $\Delta pvuA1 \Delta pvuA2$	Tanabe <i>et al.</i> (2011)
VPD51	VPD5 $\Delta vctA$	This study
VPD52	VPD5 $\Delta irgA$	This study
VPD54	VPD5 $\Delta vctA \Delta irgA$	This study
VPD79	VPD5 $\Delta vctA \Delta tonB1$	This study
VPD80	VPD5 $\Delta vctA \Delta tonB2$	This study
VPD81	VPD5 $\Delta vctA \Delta tonB3$	This study
VPD82	VPD5 $\Delta vctA \Delta tonB1 \Delta tonB2$	This study
VPD83	VPD5 $\Delta vctA \Delta tonB1 \Delta tonB3$	This study
VPD84	VPD5 $\Delta vctA \Delta tonB2 \Delta tonB3$	This study
VPD85	VPD5 $\Delta vctA \Delta tonB1 \Delta tonB2 \Delta tonB3$	This study
VPD86	VPD5 $\Delta irgA \Delta tonB1$	This study
VPD87	VPD5 $\Delta irgA \Delta tonB2$	This study
VPD88	VPD5 $\Delta irgA \Delta tonB3$	This study
VPD89	VPD5 $\Delta irgA \Delta tonB1 \Delta tonB2$	This study
VPD90	VPD5 $\Delta irgA \Delta tonB1 \Delta tonB3$	This study
VPD91	VPD5 $\Delta irgA \Delta tonB2 \Delta tonB3$	This study
VPD92	VPD5 $\Delta irgA \Delta tonB1 \Delta tonB2 \Delta tonB3$	This study
VPD93	VPD5 $\Delta vctA \Delta irgB$	This study
VPD94	VPD5 $\Delta irgA \Delta vctR$	This study
VPD95	VPD5 $\Delta vctPDGC$	This study
VPD98	VPD5 $\Delta pvuA1 \Delta pvuA2 \Delta vctR$	This study
VPD99	VPD5 $\Delta pvuA1 \Delta pvuA2 \Delta irgB$	This study
VPD100	VPD5 $\Delta irgB$	This study
VPD101	VPD5 $\Delta vctR$	This study
<i>E. coli</i> strain		
β 2155	<i>thrB1004 pro thi strA hsdS $\Delta(lacZ)\Delta M15$ [F' $\Delta(lacZ)M15 lac^f traD36 proA^+$ $proB^+$] $\Delta dapA::erm(Em^r)$, $pir::RP4[::kan(Km^r)$ from SM10]</i>	Demarre <i>et al.</i> (2005)

Preparation of outer-membrane protein (OMP)-rich fractions.

Stationary phase *V. parahaemolyticus* cells were inoculated at a final OD₆₀₀ of 0.005 into the +Fe and -Fe +Ent media, or OD₆₀₀ 0.01 into the -Fe medium, and the cultures were shaken at 37 °C for 12 h. The OMP-rich extracts were prepared and analysed by SDS-PAGE, as previously described (Yamamoto *et al.*, 1995). The IROMPs were electroblotted onto a wet PVDF membrane, and their N-terminal amino acid sequences were determined using the Edman degradation method with a Procise 491 HT protein sequencer (Applied Biosystems).

RNA analysis. *V. parahaemolyticus* cells were inoculated as described for the OMP-rich fractions, and the cultures were then shaken at 37 °C until they reached OD₆₀₀ 0.3–0.5. The total RNA was isolated from each cell sample by using an RNeasy Protect Bacteria Mini kit (Qiagen). Primer extension of *irgA* and *vctA* was performed with the primers *irgA*-PE and *vctA*-PE, respectively, which had been 5'-labelled with Texas red. The labelled primers were annealed with 5 µg total RNA and extended with avian myeloblastosis virus reverse transcriptase XL (Takara) for 1 h at 50 °C, and each extension product was separated, in addition to the DNA sequence ladder of the control region synthesized with the same primer, on a 6% polyacrylamide gel by using an SQ5500 DNA sequencer (Hitachi). For reverse transcriptase-quantitative PCR (RT-qPCR), the total RNA was treated with RNase-free DNase I (Ambion), and 0.5 µg DNase I-treated total RNA was then used to generate the cDNA product by

using ReverTra Ace reverse transcriptase (Toyobo) and a random hexamer primer (Takara). The PCRs were performed with Thunderbird SYBR qPCR Mix (Toyobo) in a Chromo4 Real-Time PCR detection system (Bio-Rad). The values were quantified using the comparative threshold cycle method, and the samples were normalized to 16S rRNA.

RESULTS AND DISCUSSION**Utilization of Ent by *V. parahaemolyticus***

To examine whether *V. parahaemolyticus* is capable of utilizing Ent, growth assays were performed in the -Fe media in the absence and presence of Ent. The VPD5 strain, which is defective in the vibrioferrin biosynthetic gene *pvsB*, was used to eliminate background growth resulting from vibrioferrin-mediated iron uptake in the -Fe medium. As shown in Fig. 1, the VPD5 strain was unable to grow in the -Fe medium; however, growth of VPD5 was restored to a level similar to that observed in the +Fe medium by the addition of Ent (5 µM). This demonstrates that *V. parahaemolyticus* is capable of utilizing Ent as a source of iron for growth.

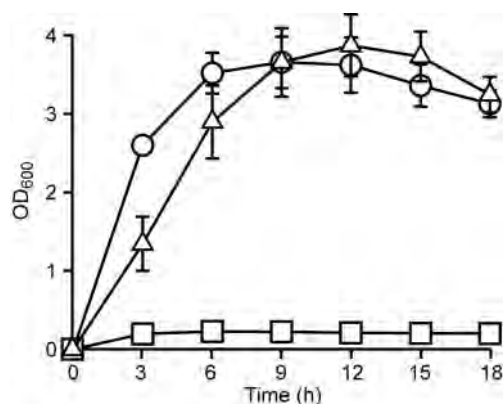


Fig. 1. Utilization of Ent in *V. parahaemolyticus*. The vibrioferrin-defective VPD5 strain was inoculated at a final OD₆₀₀ of 0.005 into +Fe (○), -Fe (□) or -Fe + Ent (△) medium. The OD₆₀₀ was measured every 3 h for 18 h. Data are the mean ± SD from three separate experiments (error bars are sometimes hidden behind symbols).

Identification of genes involved in the utilization of ferric Ent in *V. parahaemolyticus*

We performed a BLAST search of the *V. parahaemolyticus* genome with the amino acid sequences of *V. cholerae* ferric Ent receptors IrgA and VctA (Mey *et al.*, 2002). We identified potential IrgA (VP2602; 652 aa) and VctA (VPA0664; 668 aa) orthologues (Fig. 2a) that are 67 and 65% identical to IrgA and VctA in *V. cholerae*, respectively. Both IrgA and VctA in *V. parahaemolyticus* contain putative TonB box sequences (IrgA, ₃₃ETVVVTA₃₉; VctA, ₃₆EEVVVWG₄₂) close to their respective N termini (Fig. 2b) (Peacock *et al.*, 2005) and C-terminal Phe residues characteristic of TonB-dependent siderophore receptors (Struyvé *et al.*, 1991). The amino acid composition of these TonB boxes supports the notion that the TonB boxes of many TonB-dependent receptors contain primarily hydrophobic and acidic residues (Kuehl & Crosa, 2010). In addition, Fig. 2(b) demonstrates that the promoters of *V. parahaemolyticus* *irgA* and *vctA* contain potential Fur boxes sharing 17 of 19 and 14 of 19 base matches, respectively, with the *E. coli* consensus Fur box (Braun & Hantke, 1991).

To study the function of *V. parahaemolyticus* IrgA and VctA proteins, isogenic deletion mutants, namely VPD51, VPD52 and VPD54, were generated in the VPD5 background and analysed using growth assays (Fig. 3). The VPD51 and VPD52 strains, which possess the *irgA* and *vctA* genes, respectively, grew in the -Fe + Ent medium to an extent similar to that of the parental VPD5 strain; in comparison, VPD54, which is defective in both the *irgA* and *vctA* genes, showed no Ent-mediated growth. However, complementation of VPD54 with either *irgA* or *vctA* harboured in the broad-host-range plasmid pRK415 allowed the strain to regain growth to a level comparable with that of VPD5 in the -Fe + Ent medium. These results

indicate that the *V. parahaemolyticus* *irgA* and *vctA* genes encode TonB-dependent IROMPs involved in the uptake of ferric Ent.

A search of the region upstream of the *V. parahaemolyticus* *vctA* gene revealed the existence of an operon in the same gene order as that of *V. cholerae* that encodes the putative ABC transporter components VPA0657–0660 (Fig. 2a). In addition, the protein products share 56, 74, 70 and 69% identity with *V. cholerae* VctPDGC, respectively, responsible for ferric catecholate siderophore transport (Mey *et al.*, 2002). To determine whether *V. parahaemolyticus* VctPDGC also functions as the ABC transporter system for ferric Ent, a growth assay was performed with the *vctPDGC* deletion mutant VPD95 constructed from VPD5. VPD95 showed no growth in the -Fe + Ent medium, whereas the complemented strain VPD95/pRK415-*vctPDGC* regained the ability to grow in this medium (Fig. 3). Therefore we concluded that the ABC transport system encoded by *vctPDGC* in *V. parahaemolyticus* also functions in ferric Ent transport.

Involvement of *irgB* and *vctR*, together with Ent, in Ent utilization

We noted the two *V. parahaemolyticus* genes VP2603 and VPA0663, which are divergently located immediately upstream of *irgA* and *vctA*, respectively. *V. parahaemolyticus* VP2603 shares 53% identity with a LysR-type transcriptional regulator, IrgB (VC0474) (Goldberg *et al.*, 1991), and VPA0663 has 56% identity with an AraC-type transcriptional regulator, VCA0231, of unknown function (Mey *et al.*, 2002), in *V. cholerae*. Hereafter, VPA0663 was termed *vctR*. In *V. cholerae*, IrgB is well documented as a transcriptional regulator of *irgA* (Goldberg *et al.*, 1991; Watnick *et al.*, 1998). However, it is unknown whether in *V. cholerae*, Ent is also involved in the transcriptional activation of *irgA* by IrgB. The conserved domain sequences for DNA binding and co-inducer binding reported for LysR-type and AraC-type family regulator members (Gallegos *et al.*, 1997; Maddocks & Oyston, 2008) were also found in the *V. parahaemolyticus* proteins IrgB and VctR, respectively (data not shown). Furthermore, the predicted regulatory binding site consisting of a palindromic T-N₁₁-A sequence characteristic of LysR-type regulators (Maddocks & Oyston, 2008) was found upstream of the *V. parahaemolyticus* *irgA* gene (Fig. 2b).

The organization of the *irgBA* and *vctPDGC-vctR-vctA* Ent utilization system genes in *V. parahaemolyticus* is similar to that of *V. cholerae*. However, the *vctC-vctR* intergenic regions are not the same length in *V. parahaemolyticus* (641 bp) and *V. cholerae* (45 bp). In *V. parahaemolyticus*, two other annotated ORFs, namely, VPA0661 and VPA0662, intervene in this region (Fig. 2a). VPA0662 shares homology with MerR-type transcriptional regulators (Brown *et al.*, 2003) that function in response to the presence of heavy metals, whereas VPA0661 shows no convincing homology to other bacterial proteins. The functions of VPA0661 and VPA0662 are currently unknown.

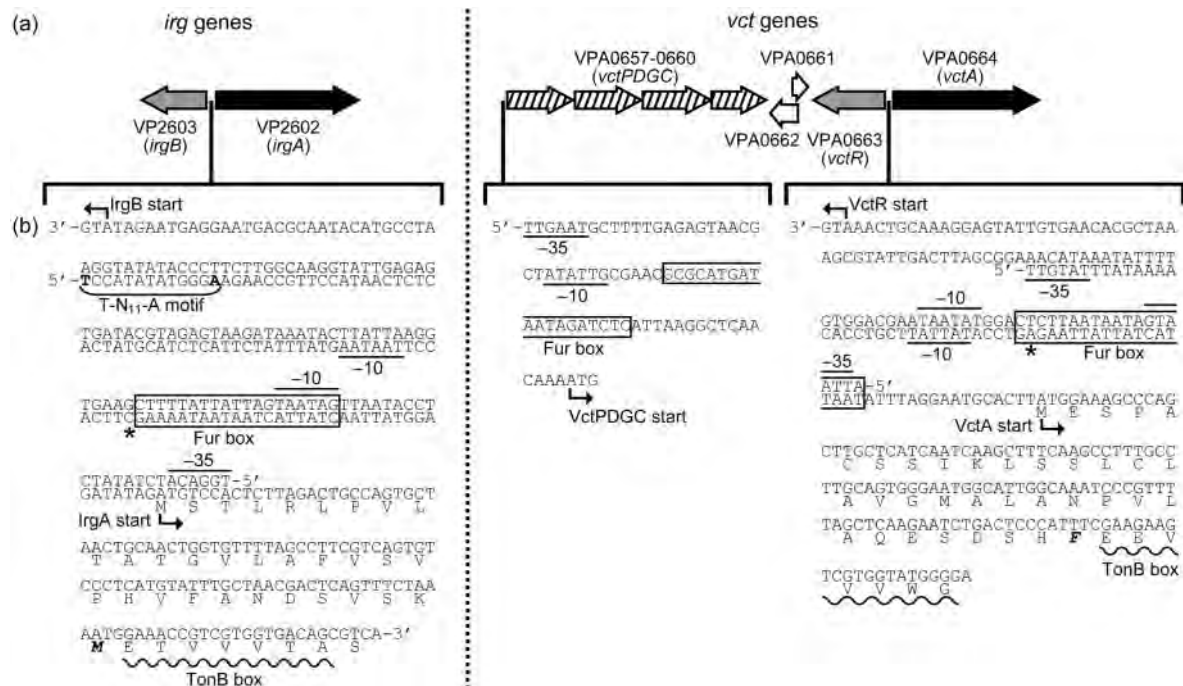


Fig. 2. Physical map and partial nucleotide sequences of the promoters and N-terminal regions with deduced amino acid residues at the *irg* and *vct* loci involved in the Ent utilization of *V. parahaemolyticus*. (a) Arrows denote the location, size and transcriptional direction of ORFs on the physical map. The functions of the small annotated VPA0661 and VPA0662 ORFs are at present unknown. The *vct* genes include a number of predicted genes, namely *vctP*, which encodes a periplasmic binding protein, *vctDG*, which encodes two integral inner-membrane permease proteins, and *vctC*, which encodes an ATP-binding protein. (b) The predicted -10 and -35 elements of each promoter are underlined or overlined and labelled; no definite -35 element was found in *irgA*. The assigned ATG start codons are indicated with bent arrows. The transcriptional start sites for the *irgA* and *vctA* genes determined by primer extension (see Fig. S2) are denoted with asterisks. Potential Fur boxes and a palindromic T-N₁₁-A motif proposed for LysR-type transcriptional regulators (Maddocks & Oyston, 2008) are indicated with boxes and a bracket, respectively. Putative TonB boxes of IrgA and VctA are indicated with wavy underlining. Hydrophobic Met and Phe residues at the TonB box -1 position of IrgA and VctA, respectively, are shown in bold italic type.

To evaluate the necessity of IrgB and VctR for Ent utilization in *V. parahaemolyticus*, we generated the *irgB* mutant VPD93 and *vctR* mutant VPD94 from VPD51 and VPD52, respectively. The Ent-mediated growth promotion that was observed in VPD51 and VPD52 was almost completely eliminated in VPD93 and VPD94, independently of the presence of *irgA* and *vctA* (Table 2). In contrast, the complementing strains VPD93/pRK415-*irgB* and VPD94/pRK415-*vctR* grew in the -Fe +Ent medium to almost the same levels as VPD51 and VPD52 (Table 2). These results suggest that both *irgB* and *vctR* encode the transcriptional factors that promote expression of the corresponding IROMPs IrgA and VctA for ferric Ent.

Necessity of *irgB* and *vctR* together with Ent for IrgA and VctA production

To identify the IrgA and VctA proteins, Sarkosyl-insoluble OMPs prepared from VPD5 cells grown in the -Fe medium were separated by SDS-PAGE, and their N-

terminal amino acid sequences were determined. Two bands, with N-terminal amino acid sequences of NDSVSKMETV and KMETVVVTAS, were derived from IrgA (Fig. 4, lane 2), whereas the band corresponding to VctA was not observed even when VPD8, which is defective in both *pvuA1* and *pvuA2* (ferric vibrioferrin receptor genes) (Tanabe *et al.*, 2011), was used to avoid overlapping with other possible IROMPs (Fig. 4, lane 3). Interestingly, when VPD8 was cultured in the -Fe +Ent medium, a fairly strong band with an N-terminal amino acid sequence of QESDSHFEEV appeared (Fig. 4, lane 4), and was determined to be VctA based on the amino acid sequence deduced from the predicted gene. Unexpectedly, the expression of the two protein bands due to IrgA was only slightly promoted in the -Fe +Ent medium when these bands were compared between lanes 3 and 4 in Fig. 4. However, the VctA band was clearly detected in the presence of Ent (Fig. 4, lane 4) but not in the absence of Ent (Fig. 4, lane 3). These data suggest that Ent produces VctA more efficiently than IrgA.

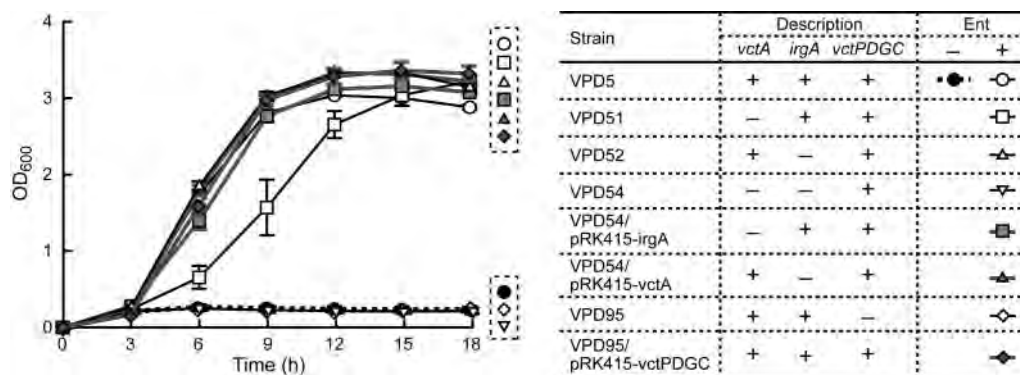


Fig. 3. Involvement of the *V. parahaemolyticus* *irgA*, *vctA* and *vctPDGC* genes in Ent utilization. The growth assay was performed as described in Fig. 1. All strains used in this experiment lack the *pvsB* gene, and therefore are unable to produce the cognate siderophore vibrioferrin. Data represent the mean \pm SD from three separate experiments.

We also examined the effects of *irgB* and *vctR* on IrgA and VctA production. SDS-PAGE analysis of IROMPs prepared from the *irgB* mutant VPD99 and *vctR* mutant VPD98 grown in the $-Fe + Ent$ medium exhibited slightly decreased production of IrgA and markedly diminished production of VctA, respectively (Fig. 4, lanes 5 and 7), compared with their parental VPD8 (Fig. 4, lane 4). However, the complementing strains VPD99/pRK415-*irgB* and VPD98/pRK415-*vctR* possessed the ability to produce IrgA and VctA, respectively (Fig. 4, lanes 6 and 8). These data suggest that the products of *irgB* and *vctR* serve as transcriptional activators with the help of Ent for their corresponding target genes *irgA* and *vctA*. In addition, the expression levels of IrgA and VctA were unaffected by the presence of *vctR* and *irgB* (Fig. 4, lanes 5–8), indicating that the Ent-mediated actions of IrgB and VctR are specific to *irgA* and *vctA*.

TonB specificity of the two ferric Ent receptors IrgA and VctA

V. parahaemolyticus possesses both the genes encoding the TonB1 and TonB2 systems in the small chromosome and the TonB3 system in the large chromosome. This is distinct from the gene distribution in *V. cholerae*, in which the genes encoding the TonB1 system are present in the small chromosome and those encoding the TonB2 system are localized to the large chromosome, and no TonB3 system is present (Kuehl & Crosa, 2010). To clarify which TonB proteins are involved in the uptake of ferric Ent through IrgA and VctA, we constructed a set of isogenic deletion mutants of *tonB1*, *tonB2* and *tonB3* from VPD51 and VPD52, which originate from VPD5. Their growth was then measured in the presence of Ent under iron-limiting conditions. The growth assays of the *tonB* mutants that

Table 2. Effect of *irgB* and *vctR* on Ent utilization

Strain*	Description†				Ent-mediated growth promotion‡
	<i>irgA</i>	<i>vctA</i>	<i>irgB</i>	<i>vctR</i>	
VPD51 (parental strain)	+	-	+	+	+
VPD93	+	-	-	+	-
VPD93/pRK415- <i>irgB</i>	+	-	+	+	+
VPD52 (parental strain)	-	+	+	+	+
VPD94	-	+	+	-	-
VPD94/pRK415- <i>vctR</i>	-	+	+	+	+

*Deletion mutants were constructed from VPD5, which is unable to produce vibrioferrin.

†The corresponding genes are present (+) and deleted (-).

‡Cells were inoculated into the $-Fe + Ent$ medium at a final OD_{600} of 0.005, and the OD_{600} was measured after incubation for 18 h. Growth curves of the parental strains VPD51 and VPD52 are shown in Fig. 3. +, Growth approximately equal to that of the parental strain; -, Ent-mediated growth promotion mostly disappeared, similar to VPD54 (Fig. 3).

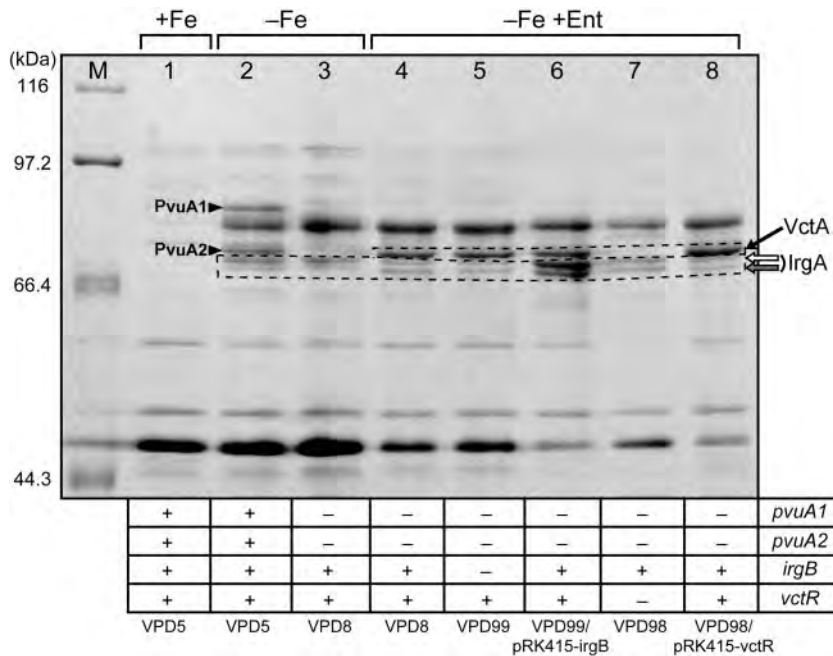


Fig. 4. SDS-PAGE analysis of Sarkosyl-insoluble OMPs. SDS-PAGE analysis was performed on VPD5, VPD8, VPD99, VPD99/pRK415-irgB, VPD98 and VPD98/pRK415-vctR strains. Each lane was loaded with 20–35 μ g of OMPs prepared from cells grown in +Fe, -Fe or -Fe +Ent medium to obtain a similar density for the individual bands between PvuA1 and PvuA2. Electrophoresis of the OMPs was performed on 7.5% SDS-polyacrylamide gels (130 mm long) at a constant current of 15 mA at 4 °C, and the gel was then stained with Coomassie brilliant blue. Only the relevant part of the gel is shown. Positions of molecular mass standards are shown to the left of the gel. Closed arrow, the VctA protein with an N-terminal sequence of QESDSHFEEV (also see Fig. 2b); open and grey arrows, the IrgA protein with N-terminal sequences of NDSVSKMETV and KMETVVVTAS (also see Fig. 2b), respectively; lane M, molecular mass marker.

possess *irgA*, but not *vctA* (Fig. 5a), and the *tonB* mutants that possess *vctA*, but not *irgA* (Fig. 5b), were analysed. The VPD79 and VPD83 strains, which possess *irgA* and *tonB2*, but not *tonB1*, as well as their parental strain, VPD51, grew in the -Fe +Ent medium; however, although the VPD80 and VPD84 strains, which contain the *irgA* and *tonB1* genes, but not *tonB2*, also grew in the same medium, their growth curves showed a delayed initial rise compared with that of VPD51. No growth was observed in the VPD82 and VPD85 strains, which possess *irgA*, but not *tonB1* and *tonB2*. Similarly, the growth curves of the *tonB* mutants generated from VPD52 resembled those of the *tonB* mutants generated from VPD51. Taken together, these findings indicate that, although both TonB1 and TonB2 can supply the energy necessary for IrgA and VctA to transport ferric Ent, TonB2 is functionally more active for both receptors than TonB1. This is distinct from the *V. cholerae* IrgA and VctA ferric Ent receptors, which are energized only by the TonB2 system (Seliger *et al.*, 2001). The results also indicate that TonB3 is not associated with the transport of ferric Ent by IrgA and VctA.

Evaluation of the transcriptional levels of the Ent utilization system genes by RT-qPCR

RT-qPCR analysis was performed to evaluate the *irgA* and *vctA* transcription levels. The transcription levels of *irgA* and *vctA* in VPD5 were higher in the -Fe medium than in the +Fe medium, and a further dramatic induction of transcription of both genes was caused by the addition of Ent to the -Fe medium (Fig. 6a). These results were consistent with those of the primer extension analysis carried out for the *irgA* and *vctA* transcripts expressed in the presence of Ent (Fig. S2). In contrast to the parental

VPD5, the transcription levels of *irgA* and *vctA* were drastically diminished in the *irgB* mutant VPD100 and *vctR* mutant VPD101, respectively, independently of the presence of Ent in the -Fe medium (Fig. 6a). These data indicate that *irgA* and *vctA* transcription in the *irgB* and *vctR* mutants was unresponsive to the Ent inducer. The presence of a potential Fur box in the promoter region of the *vctPDGC* operon (Fig. 2) prompted us to test whether the expression of this operon is also regulated by iron. The results showed that the transcription of *vctP* and *vctC* was completely derepressed in the -Fe medium, which suggests that the operon is, in fact, regulated by iron. The effect of Ent on the transcription of these genes was not significant, regardless of the presence of *vctR* (Fig. 6b). In addition, RT-qPCR analysis indicated that the *irgB* and *vctR* genes are also regulated by iron (Fig. 6c), implying that the Fur boxes predicted for *irgA* and *vctA* (Fig. 2) also function for *irgB* and *vctR*, respectively.

To effectively acquire iron in iron-restricted environments, some bacteria have evolved positive regulatory mechanisms, in which a siderophore itself serves as an extracellular stimulus or inducer, termed a ferrimone (Brickman & Armstrong, 2009), to evoke optimum expression of the corresponding outer membrane receptor gene (Crosa, 1997; Vasil & Ochsner, 1999; Visca *et al.*, 2002). The catecholate-type siderophore Ent is utilized as the iron source by several Gram-negative bacteria, including *V. cholerae* (Mey *et al.*, 2002), *V. anguillarum* (Balado *et al.*, 2009; Naka & Crosa, 2012), *Pseudomonas aeruginosa* (Dean & Poole, 1993; Ghysels *et al.*, 2005), *Neisseria gonorrhoeae* (Carson *et al.*, 1999), *Bordetella* species (Beall & Sanden, 1995) and *Campylobacter* species (Palyada *et al.*, 2004; Xu *et al.*, 2010). In this study, we also showed that *V.*

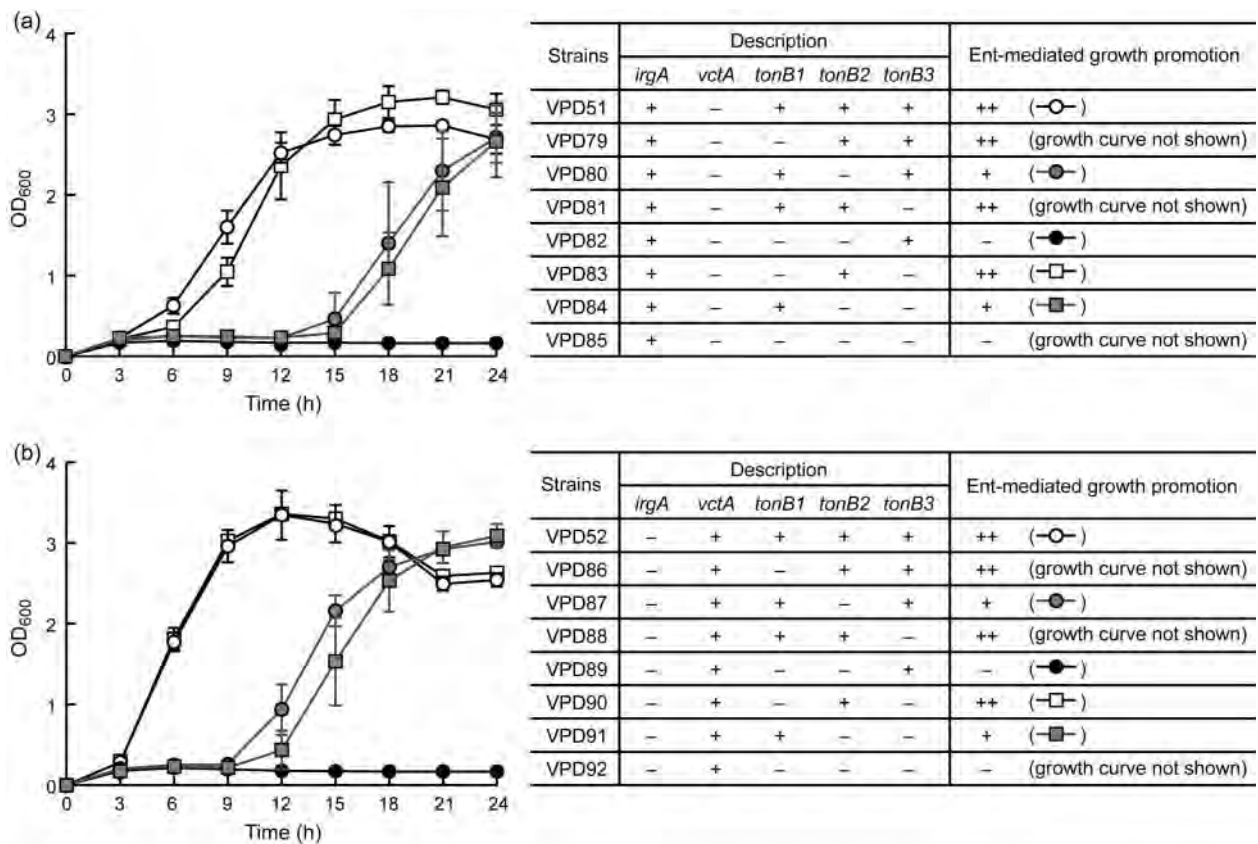


Fig. 5. TonB specificity of IrgA and VctA in *V. parahaemolyticus*. Growth assays of IrgA (a) and VctA (b) were performed as described in Fig. 1, except that the incubation time was increased to 24 h. A series of deletion mutants were constructed from VPD5, which is a mutant unable to produce vibrioferrin. The Ent-mediated growth in the strains tested was categorized: ++, growth highly similar to the parental strains VPD51 and VPD52; +, growth comparable with the parental strains, but requiring a prolonged lag time; -, no Ent-mediated growth. Data plotted are the mean \pm SD from three separate experiments. The growth curves of VPD79, VPD81, VPD85, VPD86, VPD88 and VPD92 are omitted to avoid complicating the figure, and are described as 'growth curve not shown'.

parahaemolyticus, which possesses the ferric Ent receptors IrgA and VctA, which are iron-repressible and Ent-inducible, can utilize Ent. The induction by Ent of its receptor genes has been reported in other bacteria; for example, *pfeA* in *P. aeruginosa* (Dean *et al.*, 1996) and *bfeA* in *Bordetella* species (Anderson & Armstrong, 2004). In these regulatory systems, extracellular Ent may act as a signalling molecule, possibly in its iron-loaded state. Therefore, this type of transcriptional regulation is practical in terms of cellular physiology, since responding to or sensing extracellular Ent benefits bacterial cells by permitting economical regulation of the levels of expression of the corresponding receptor protein. However, it remains unknown whether *V. parahaemolyticus* can utilize Ent in its surroundings. Alternatively, as proposed by Brickman & Armstrong (2009) for the *Bordetella* BfeA ferric Ent receptor, the authentic ligand for IrgA and VctA may also be another molecule, which is structurally similar to Ent, produced by other organisms.

We showed that the *V. parahaemolyticus* TonB1 and TonB2 systems provide energy for IrgA and VctA for the transport of ferric Ent. This distinguishes *V. parahaemolyticus* from *V. cholerae* and *V. anguillarum*, in which only the TonB2 system can energize ferric Ent transport through the IrgA and VctA receptors (Mey & Payne, 2003; Stork *et al.*, 2004). Mey & Payne (2003) proposed that a large hydrophobic amino acid residue at the TonB box -1 position allows the ferric siderophore receptors to receive energy from the TonB1 system, albeit somewhat less effectively than from TonB2. Interestingly, the TonB box -1 residues in *V. cholerae* IrgA and VctA, which depend on the TonB2 system, are the acidic residues Asp and Glu, respectively. Comparatively, *V. parahaemolyticus* IrgA and VctA, which depend on both the TonB1 and TonB2 systems, possess large hydrophobic Met and Phe residues, respectively, at this position (Fig. 2b). Similarly, in *V. parahaemolyticus*, the Met residue is found at this position of the cognate ferric vibrioferrin receptor PvuA2, which depends on both

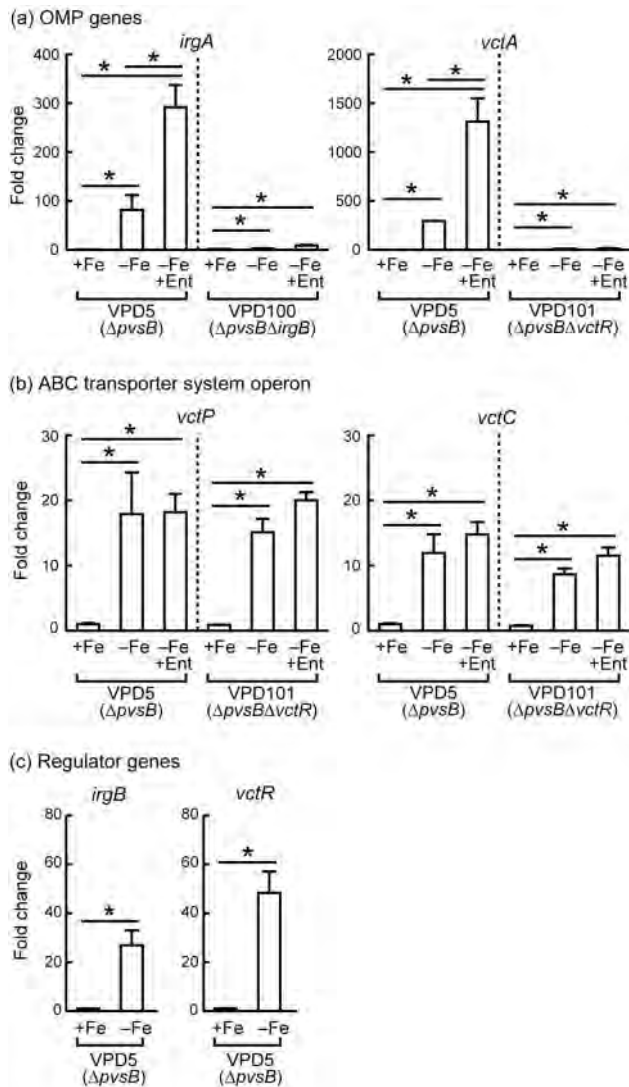


Fig. 6. RT-qPCR validation of the transcriptional activation of *V. parahaemolyticus* *irgA* and *vctA* by the presence of Ent under iron-limiting conditions. The transcriptional levels of *irgA* and *vctA* (a), an ABC transporter system operon (b), and *irgB* and *vctR* (c) were evaluated by RT-qPCR. Total RNAs were extracted from the VPD5, VPD100 and VPD101 strains grown in +Fe, -Fe and -Fe +Ent media. Error bars, SD; asterisks indicate a *P* value of <0.05.

the TonB1 and TonB2 systems; however, another ferric vibrioferrin receptor, PvuA1, that depends only on the TonB2 system possesses the hydrophilic Thr residue at this position (Tanabe *et al.*, 2011). These data also imply that the hydrophilic or acidic amino acid residues at the TonB box -1 position may determine the TonB2 specificity of ferric siderophore receptors, at least in *Vibrio* species.

In conclusion, we have demonstrated that *V. parahaemolyticus* can utilize Ent, and that the ferric Ent receptors IrgA and VctA are induced by iron-limiting conditions through the action of IrgB and VctR, respectively, with the help of

Ent. The additional iron assimilation system mediated by Ent in *V. parahaemolyticus* may reflect the importance of iron competition among resident microbes in its natural habitat. This iron assimilation system may aid in the survival and proliferation of the bacterium, and therefore increase its chances of gaining access to mammalian hosts. It will be of interest to investigate the molecular mechanisms by which Ent interacts with IrgB and VctR to activate the *irgA* and *vctA* receptor genes, respectively.

ACKNOWLEDGEMENTS

We thank Dr T. Kuroda, Okayama University, Japan, for providing *E. coli* β 2155, the suicide vector pXAC623, and helpful comments. This work was supported in part by a Grant-in-Aid for Young Scientists (B) from the Ministry of Education, Culture, Sports, Science, and Technology of Japan (23790166).

REFERENCES

- Actis, L. A., Fish, W., Crosa, J. H., Kellerman, K., Ellenberger, S. R., Hauser, F. M. & Sanders-Loehr, J. (1986). Characterization of anguibactin, a novel siderophore from *Vibrio anguillarum* 775(pJM1). *J Bacteriol* **167**, 57–65.
- Anderson, M. T. & Armstrong, S. K. (2004). The BfeR regulator mediates enterobactin-inducible expression of *Bordetella* enterobactin utilization genes. *J Bacteriol* **186**, 7302–7311.
- Andrews, S. C., Robinson, A. K. & Rodríguez-Quinones, F. (2003). Bacterial iron homeostasis. *FEMS Microbiol Rev* **27**, 215–237.
- Bagg, A. & Neilands, J. B. (1987). Ferric uptake regulation protein acts as a repressor, employing iron (II) as a cofactor to bind the operator of an iron transport operon in *Escherichia coli*. *Biochemistry* **26**, 5471–5477.
- Balado, M., Osorio, C. R. & Lemos, M. L. (2008). Biosynthetic and regulatory elements involved in the production of the siderophore vanchrobactin in *Vibrio anguillarum*. *Microbiology* **154**, 1400–1413.
- Balado, M., Osorio, C. R. & Lemos, M. L. (2009). FvtA is the receptor for the siderophore vanchrobactin in *Vibrio anguillarum*: utility as a route of entry for vanchrobactin analogues. *Appl Environ Microbiol* **75**, 2775–2783.
- Beall, B. & Sanden, G. N. (1995). A *Bordetella pertussis* *fepA* homologue required for utilization of exogenous ferric enterobactin. *Microbiology* **141**, 3193–3205.
- Braun, V. & Hantke, K. (1991). Genetics of bacterial iron transport. In *Handbook of Microbial Iron Chelates*, pp. 107–138. Edited by G. Winkelmann. Boca Raton, FL: CRC Press.
- Brickman, T. J. & Armstrong, S. K. (2009). Temporal signaling and differential expression of *Bordetella* iron transport systems: the role of ferrimones and positive regulators. *Biometals* **22**, 33–41.
- Brown, N. L., Stoyanov, J. V., Kidd, S. P. & Hobman, J. L. (2003). The MerR family of transcriptional regulators. *FEMS Microbiol Rev* **27**, 145–163.
- Carson, S. D., Klebba, P. E., Newton, S. M. & Sparling, P. F. (1999). Ferric enterobactin binding and utilization by *Neisseria gonorrhoeae*. *J Bacteriol* **181**, 2895–2901.
- Chu, B. C., Garcia-Herrero, A., Johanson, T. H., Krewulak, K. D., Lau, C. K., Peacock, R. S., Slavinskaya, Z. & Vogel, H. J. (2010). Siderophore uptake in bacteria and the battle for iron with the host; a bird's eye view. *Biometals* **23**, 601–611.

- Crosa, J. H. (1997).** Signal transduction and transcriptional and posttranscriptional control of iron-regulated genes in bacteria. *Microbiol Mol Biol Rev* **61**, 319–336.
- Dean, C. R. & Poole, K. (1993).** Cloning and characterization of the ferric enterobactin receptor gene (*pfeA*) of *Pseudomonas aeruginosa*. *J Bacteriol* **175**, 317–324.
- Dean, C. R., Neshat, S. & Poole, K. (1996).** PfeR, an enterobactin-responsive activator of ferric enterobactin receptor gene expression in *Pseudomonas aeruginosa*. *J Bacteriol* **178**, 5361–5369.
- Demarre, G., Guérout, A. M., Matsumoto-Mashimo, C., Rowe-Magnus, D. A., Marlière, P. & Mazel, D. (2005).** A new family of mobilizable suicide plasmids based on broad host range R388 plasmid (IncW) and RP4 plasmid (IncP α) conjugative machineries and their cognate *Escherichia coli* host strains. *Res Microbiol* **156**, 245–255.
- Escolar, L., Pérez-Martín, J. & de Lorenzo, V. (1999).** Opening the iron box: transcriptional metalloregulation by the Fur protein. *J Bacteriol* **181**, 6223–6229.
- Fetherston, J. D., Bearden, S. W. & Perry, R. D. (1996).** YbtA, an AraC-type regulator of the *Yersinia pestis* pesticin/yersiniabactin receptor. *Mol Microbiol* **22**, 315–325.
- Funahashi, T., Tanabe, T., Aso, H., Nakao, H., Fujii, Y., Okamoto, K., Narimatsu, S. & Yamamoto, S. (2003).** An iron-regulated gene required for utilization of aerobactin as an exogenous siderophore in *Vibrio parahaemolyticus*. *Microbiology* **149**, 1217–1225.
- Funahashi, T., Tanabe, T., Shiuchi, K., Nakao, H. & Yamamoto, S. (2009).** Identification and characterization of genes required for utilization of desferri-ferrichrome and aerobactin in *Vibrio parahaemolyticus*. *Biol Pharm Bull* **32**, 359–365.
- Gallegos, M. T., Schleif, R., Bairoch, A., Hofmann, K. & Ramos, J. L. (1997).** AraC/XylS family of transcriptional regulators. *Microbiol Mol Biol Rev* **61**, 393–410.
- Ghysels, B., Ochsner, U., Möllman, U., Heinisch, L., Vasil, M., Cornelis, P. & Matthijs, S. (2005).** The *Pseudomonas aeruginosa* *pirA* gene encodes a second receptor for ferrienterobactin and synthetic catecholate analogues. *FEMS Microbiol Lett* **246**, 167–174.
- Goldberg, M. B., Boyko, S. A. & Calderwood, S. B. (1991).** Positive transcriptional regulation of an iron-regulated virulence gene in *Vibrio cholerae*. *Proc Natl Acad Sci U S A* **88**, 1125–1129.
- Griffiths, G. L., Sigel, S. P., Payne, S. M. & Neilands, J. B. (1984).** Vibriobactin, a siderophore from *Vibrio cholerae*. *J Biol Chem* **259**, 383–385.
- Heckman, K. L. & Pease, L. R. (2007).** Gene splicing and mutagenesis by PCR-driven overlap extension. *Nat Protoc* **2**, 924–932.
- Heinrichs, D. E. & Poole, K. (1993).** Cloning and sequence analysis of a gene (*pchR*) encoding an AraC family activator of pyochelin and ferripyochelin receptor synthesis in *Pseudomonas aeruginosa*. *J Bacteriol* **175**, 5882–5889.
- Hollander, A., Mercante, A. D., Shafer, W. M. & Cornelissen, C. N. (2011).** The iron-repressed, AraC-like regulator MpeR activates expression of *fetA* in *Neisseria gonorrhoeae*. *Infect Immun* **79**, 4764–4776.
- Keen, N. T., Tamaki, S., Kobayashi, D. & Trollinger, D. (1988).** Improved broad-host-range plasmids for DNA cloning in Gram-negative bacteria. *Gene* **70**, 191–197.
- Kuehl, C. J. & Crosa, J. H. (2010).** The TonB energy transduction systems in *Vibrio* species. *Future Microbiol* **5**, 1403–1412.
- Kuroda, T., Mizushima, T. & Tsuchiya, T. (2005).** Physiological roles of three Na⁺/H⁺ antiporters in the halophilic bacterium *Vibrio parahaemolyticus*. *Microbiol Immunol* **49**, 711–719.
- Maddocks, S. E. & Oyston, P. C. (2008).** Structure and function of the LysR-type transcriptional regulator (LTTR) family proteins. *Microbiology* **154**, 3609–3623.
- Makino, K., Oshima, K., Kurokawa, K., Yokoyama, K., Uda, T., Tagomori, K., Iijima, Y., Najima, M., Nakano, M. & other authors (2003).** Genome sequence of *Vibrio parahaemolyticus*: a pathogenic mechanism distinct from that of *V. cholerae*. *Lancet* **361**, 743–749.
- Mey, A. R. & Payne, S. M. (2003).** Analysis of residues determining specificity of *Vibrio cholerae* TonB1 for its receptors. *J Bacteriol* **185**, 1195–1207.
- Mey, A. R., Wyckoff, E. E., Oglesby, A. G., Rab, E., Taylor, R. K. & Payne, S. M. (2002).** Identification of the *Vibrio cholerae* enterobactin receptors VctA and IrgA: IrgA is not required for virulence. *Infect Immun* **70**, 3419–3426.
- Miethe, M. & Marahiel, M. A. (2007).** Siderophore-based iron acquisition and pathogen control. *Microbiol Mol Biol Rev* **71**, 413–451.
- Moock, G. S. & Coulton, J. W. (1998).** TonB-dependent iron acquisition: mechanisms of siderophore-mediated active transport. *Mol Microbiol* **28**, 675–681.
- Naka, H. & Crosa, J. H. (2012).** Identification and characterization of a novel outer membrane protein receptor FetA for ferric enterobactin transport in *Vibrio anguillarum* 775 (pJM1). *Biomaterials* **25**, 125–133.
- Noinaj, N., Guillier, M., Barnard, T. J. & Buchanan, S. K. (2010).** TonB-dependent transporters: regulation, structure, and function. *Annu Rev Microbiol* **64**, 43–60.
- Palyada, K., Threadgill, D. & Stintzi, A. (2004).** Iron acquisition and regulation in *Campylobacter jejuni*. *J Bacteriol* **186**, 4714–4729.
- Peacock, R. S., Weljie, A. M., Howard, S. P., Price, F. D. & Vogel, H. J. (2005).** The solution structure of the C-terminal domain of TonB and interaction studies with TonB box peptides. *J Mol Biol* **345**, 1185–1197.
- Sambrook, J., Fritsch, E. F. & Maniatis, T. (1989).** *Molecular Cloning: a Laboratory Manual*, 2nd edn. Cold Spring Harbor, NY: Cold Spring Harbor Laboratory.
- Seliger, S. S., Mey, A. R., Valle, A. M. & Payne, S. M. (2001).** The two TonB systems of *Vibrio cholerae*: redundant and specific functions. *Mol Microbiol* **39**, 801–812.
- Stork, M., Di Lorenzo, M., Mouriño, S., Osorio, C. R., Lemos, M. L. & Crosa, J. H. (2004).** Two *tonB* systems function in iron transport in *Vibrio anguillarum*, but only one is essential for virulence. *Infect Immun* **72**, 7326–7329.
- Struyvé, M., Moons, M. & Tommassen, J. (1991).** Carboxy-terminal phenylalanine is essential for the correct assembly of a bacterial outer membrane protein. *J Mol Biol* **218**, 141–148.
- Tanabe, T., Funahashi, T., Nakao, H., Miyoshi, S., Shinoda, S. & Yamamoto, S. (2003).** Identification and characterization of genes required for biosynthesis and transport of the siderophore vibrioferrin in *Vibrio parahaemolyticus*. *J Bacteriol* **185**, 6938–6949.
- Tanabe, T., Takata, N., Naka, A., Moon, Y. H., Nakao, H., Inoue, Y., Narimatsu, S. & Yamamoto, S. (2005).** Identification of an AraC-like regulator gene required for induction of the 78-kDa ferrioxamine B receptor in *Vibrio vulnificus*. *FEMS Microbiol Lett* **249**, 309–314.
- Tanabe, T., Funahashi, T., Okajima, N., Nakao, H., Takeuchi, Y., Miyamoto, K., Tsujibo, H. & Yamamoto, S. (2011).** The *Vibrio parahaemolyticus* *pvuA1* gene (formerly termed *psuA*) encodes a second ferric vibrioferrin receptor that requires *tonB2*. *FEMS Microbiol Lett* **324**, 73–79.
- Vasil, M. L. & Ochsner, U. A. (1999).** The response of *Pseudomonas aeruginosa* to iron: genetics, biochemistry and virulence. *Mol Microbiol* **34**, 399–413.
- Visca, P., Leoni, L., Wilson, M. J. & Lamont, I. L. (2002).** Iron transport and regulation, cell signalling and genomics: lessons from *Escherichia coli* and *Pseudomonas*. *Mol Microbiol* **45**, 1177–1190.

Watnick, P. I., Butterton, J. R. & Calderwood, S. B. (1998). The interaction of the *Vibrio cholerae* transcription factors, Fur and IrgB, with the overlapping promoters of two virulence genes, *irgA* and *irgB*. *Gene* **209**, 65–70.

Wyckoff, E. E., Mey, A. R. & Payne, S. M. (2007). Iron acquisition in *Vibrio cholerae*. *Biometals* **20**, 405–416.

Xu, F., Zeng, X., Haigh, R. D., Ketley, J. M. & Lin, J. (2010). Identification and characterization of a new ferric enterobactin receptor, CfrB, in *Campylobacter*. *J Bacteriol* **192**, 4425–4435.

Yamamoto, S., Okujo, N., Yoshida, T., Matsuura, S. & Shinoda, S. (1994). Structure and iron transport activity of vibrioferrin, a new siderophore of *Vibrio parahaemolyticus*. *J Biochem* **115**, 868–874.

Yamamoto, S., Akiyama, T., Okujo, N., Matsu-ura, S. & Shinoda, S. (1995). Demonstration of a ferric vibrioferrin-binding protein in the outer membrane of *Vibrio parahaemolyticus*. *Microbiol Immunol* **39**, 759–766.

Edited by: J. Cavet

Identification and Characterization of an Outer Membrane Receptor Gene in *Acinetobacter baumannii* Required for Utilization of Desferricoprogen, Rhodotorulic Acid, and Desferrioxamine B as Xenosiderophores

Tatsuya Funahashi,^{*a} Tomotaka Tanabe,^a Kazutoshi Mihara,^b Katsushiro Miyamoto,^c Hiroshi Tsujibo,^c and Shigeo Yamamoto^a

^a College of Pharmaceutical Sciences, Matsuyama University; 4–2 Bunkyo-cho, Matsuyama 790–8578, Japan; ^b Graduate School of Medicine, Dentistry and Pharmaceutical Sciences, Okayama University; 1–1–1 Tsushima-naka, Kita-ku, Okayama 700–8530, Japan; and ^c Osaka University of Pharmaceutical Sciences; 4–20–1 Nasahara, Takatsuki, Osaka 569–1094, Japan.

Received January 16, 2012; accepted February 20, 2012; published online February 28, 2012

In this study, we found that *Acinetobacter baumannii* utilized exogenously supplied desferricoprogen, rhodotorulic acid, and desferrioxamine B for growth under iron-limiting conditions. The ferric uptake regulator (Fur) titration assay method was then successfully applied to select iron-regulated genes in *A. baumannii* genomic libraries. Part of the nucleotide sequence homologous to *Escherichia coli*, *fhuE*, obtained from one of the positive clones allowed us to clone the entire gene, which was named *fhuE*. The *fhuE* gene had an amino acid sequence consistent with the N-terminal amino acid sequence of the 76-kDa iron-repressible outer membrane proteins in *A. baumannii*. Reverse transcription-polymerase chain reaction analysis demonstrated that *fhuE* mRNA is transcribed under iron-limiting conditions, consistent with the presence of a sequence homologous to the consensus Fur box in the promoter region. Disruption of *fhuE* resulted in the loss of expression of the 76-kDa protein. In addition, the double disruptant of *fhuE* and *basD*, which encodes one of the biosynthetic genes for the cognate siderophore acinetobactin, was unable to grow in the presence of desferricoprogen, rhodotorulic acid or desferrioxamine B. However, growth of the double disruptant was restored by complementation with *fhuE*, demonstrating that *A. baumannii* FhuE functions as the receptor common to coprogen, ferric rhodotorulic acid and ferrioxamine B.

Key words *Acinetobacter baumannii*; siderophore; iron; desferricoprogen; rhodotorulic acid; desferrioxamine B

Iron is an indispensable element for survival and growth of almost all bacteria. However, the bioavailability of iron can be severely restricted because it forms insoluble ferric hydroxide complexes under aerobic environments at neutral pH value.¹⁾ In response to iron starvation, many bacteria produce siderophores that mediate high-affinity iron transport and thus, enable iron to be scavenged from their surroundings. In addition to their own siderophores, some bacteria are endowed with iron uptake systems that utilize siderophores produced by other bacterial and fungal species. In Gram-negative bacteria, these siderophores, loaded with ferric ions, are transported via the siderophore-specific TonB-dependent receptors and ATP binding cassette (ABC) transporter systems. The energy required for transport via the outer membrane receptor is provided by interaction of the receptor with the TonB-ExbB-ExbD complex, located in the inner membrane, that couples the proton motive force created by the inner membrane for energy transduction.¹⁾ Furthermore, when the intracellular iron level is raised in bacteria, the global iron-binding repressor, called the ferric uptake regulator (Fur), represses transcription initiation of iron uptake genes^{2,3)} and some virulence genes.⁴⁾

Acinetobacter baumannii, a Gram-negative, non-motile rod, is commonly found in soil, water, and sewage. In healthcare settings, it causes a wide range of infections in compromised hosts, including respiratory and urinary tract infections, secondary meningitis, and bacteremia.^{5–7)} Moreover, these

infections are often extremely difficult to treat because of their widespread resistance to the major groups of antibiotics. In response to iron starvation, *A. baumannii* ATCC19606 secretes the catecholate-type siderophore, acinetobactin,⁸⁾ whose structure has been confirmed by total synthesis.^{9,10)} The *basABCDEFGHIJ* genes are involved in biosynthesis of acinetobactin, and uptake of its ferric complex occurs via the outer membrane receptor and the ATP binding cassette transporter encoded by *bauA* and *bauBCDE*, respectively.¹¹⁾ These clusters are found in the reported genomic sequences of all of *A. baumannii* strains, except for SDF.¹²⁾ On the other hand, an ortholog of the *Escherichia coli* *fhuE* gene,¹³⁾ expected to be required for utilization of the hydroxamate-type xenosiderophores (Fig. 1), has recently been located in the genomic sequences of some *A. baumannii* isolates.^{14–17)} To date, however, none of these genes have been experimentally characterized. In the present study, we first found that *A. baumannii* utilizes desferricoprogen, rhodotorulic acid, and, to a lesser extent, desferrioxamine B as xenosiderophores (the siderophores produced by other bacterial and fungal species). We then demonstrated that the 76-kDa iron-repressible outer membrane protein (OMP), encoded by *fhuE*, functions as the receptor common to these xenosiderophores.

MATERIALS AND METHODS

Strains, Plasmids, Primers, and Media Bacterial strains and plasmids and the oligonucleotide primers used in this

The authors declare no conflict of interest.

* To whom correspondence should be addressed. e-mail: tfunahas@cc.matsuyama-u.ac.jp

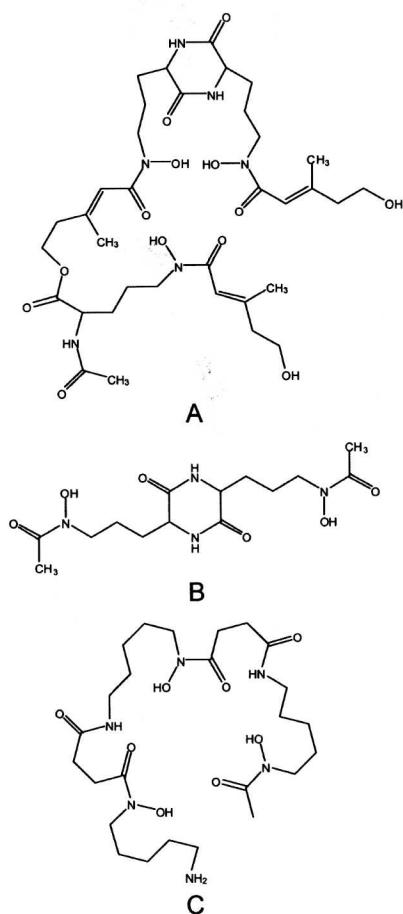


Fig. 1. Structures of Desferricoprogen (A), Rhodotorulic Acid (B), and Desferrioxamine B (C)

study are listed in Tables 1 and 2, respectively. Unless otherwise noted, *A. baumannii* and *E. coli* were routinely grown with shaking at 37°C in Luria–Bertani (LB) broth or grown on LB agar plates (1.5% agar) containing 0.5% NaCl. LB media were prepared both with and without the addition of the iron chelator, 2,2'-dipyridyl (DPD; Wako Pure Chemical Industries, Osaka, Japan), at 225 μM . DPD was used to create iron-limiting conditions. As necessary, appropriate antibiotics were added to the growth media at the following concentrations: ampicillin (50 $\mu\text{g}/\text{mL}$), apramycin (50 $\mu\text{g}/\text{mL}$), kanamycin (50 $\mu\text{g}/\text{mL}$), and ticarcillin (80 $\mu\text{g}/\text{mL}$).

Growth Assay The disruptants of *basD* and *basD/fhuE* (named ΔbasD and $\Delta\text{basD}\Delta\text{fhuE}$, respectively) were constructed from *A. baumannii* ATCC19606, as described later. Disruption of *basD*, resulting in no production of acinetobactin, avoided any cross-feeding by the siderophore in the growth assay. These disruptants were grown overnight in LB broth, and an aliquot of the preculture was inoculated into 5 mL of fresh LB broth at an optical density of 0.005 at 600 nm (OD_{600}) and shaken at 70 rpm at 37°C. The OD_{600} was automatically recorded every 1 h with an Advantec TVS-062CA biophotorecorder (Advantec Toyo Co., Ltd., Tokyo, Japan). When required, 20 μM of desferricoprogen (Biophore Research Products, Tübingen, Germany), rhodotorulic acid, or desferrioxamine B mesylate (Sigma Aldrich, St. Louis, MO, U.S.A.) was added to the iron-limiting LB broth. In

these siderophores, whose structures are shown in Fig. 1, hydroxamate groups serve as iron (Fe^{3+})-binding sites. Desferrioxamine B and rhodotorulic acid are fungal siderophores, and desferricoprogen is a bacterial siderophore. Coprogen and ferrioxamine B refer to iron complexes.

DNA Manipulations Standard DNA manipulations were carried out as described by Sambrook *et al.*¹⁸⁾ Chromosomal DNA and plasmid DNA were extracted using the Wizard[®] Genomic DNA Purification Kit (Promega, Madison, WI, U.S.A.) and the High Pure Plasmid Isolation Kit (Roche Diagnostics, Mannheim, Germany), respectively. Restriction enzymes were purchased from Roche Diagnostics. A Ligation-Convenience Kit (Wako Pure Chemical Industries) was used for the DNA ligation reaction. DNA fragments were purified from agarose gels using the MagExtractor-PCR and Gel Clean up DNA Fragment Purification Kit (Toyobo, Osaka, Japan). Transformation of *E. coli* was performed by electroporation with a MicroPulser[™] apparatus (Bio-Rad, Benicia, CA, U.S.A.). The high-fidelity KOD-Plus-DNA polymerase (Toyobo) was used when polymerase chain reaction (PCR) fragments required minimal errors. Oligonucleotide primers (Table 2) designed according to the determined sequence of *A. baumannii* ATCC19606 were synthesized by the oligonucleotide service of FASMAC Co., Ltd. (Kanagawa, Japan).

Nucleotide Sequence Determination and Sequence Analysis The nucleotide sequence of *A. baumannii* ATCC19606 was determined in two directions with an ABI PRISM[®] 3130XL Genetic Analyzer (Applied Biosystems, Carlsbad, CA, U.S.A.) and the BigDye[®] Terminator Cycle Sequencing Kit (Applied Biosystems) according to the instructions of the manufacturer. The amino acid sequences deduced from the nucleotide sequences were compared with a database using the BLAST program¹⁹⁾ at GenomeNet Database Service operated by the Institute for Chemical Research, Kyoto University (<http://www.genome.jp/>).

OMP Analysis *A. baumannii* ATCC19606 and its disruptant, ΔfhuE , were grown for 12 h in LB broth under iron-limiting or iron-replete conditions. According to the procedure previously described,²⁰⁾ the 1% sodium *N*-lauroylsarcosine (Sigma)-insoluble OMP-rich fractions were prepared from the *A. baumannii* grown in the iron-limiting or iron-replete broth. Protein concentration was determined by the Lowry method. The OMPs were separated by sodium dodecyl sulfate-polyacrylamide gel electrophoresis (SDS-PAGE) and stained with Coomassie Brilliant Blue R-250 followed by visualizing with a Gel Doc XR (Bio-Rad). In some cases, the stained OMPs were electroblotted to a pre-wetted polyvinylidene difluoride membrane (ProBlott[®]; Applied Biosystems) with a Trans-Blot[®] semi-dry electrophoretic transfer cell (Bio-Rad)²¹⁾ for determination of the N-terminal amino acid sequences by automated Edman degradation with a Procise[®] Model 491 protein sequencer (Applied Biosystems).

Isolation of Iron-Regulated Genes by Fur Titration Assay (FURTA) and Cloning of *fhuE* To isolate Fur box-containing *A. baumannii* gene fragments, FURTA was performed according to the procedures described previously.¹¹⁾ Briefly, chromosomal DNA fragments (1 to 3 kbp) of *A. baumannii* ATCC19606, partially digested with *Sau3AI*, were inserted into the unique *Bam*HI site of pUC19, and the resulting recombinant plasmids were introduced into *E. coli* H1717.²²⁾ LacZ expression was assessed by visualization of a change in

Table 1. Bacterial Strains and Plasmids Used in This Study

Strain or plasmid	Relevant feature ^{a)}	Reference or source
Strains		
<i>A. baumannii</i>		
ATCC19606	Clinical isolate, type strain	ATCC
Δ basD	ATCC19606, <i>basD</i> :: <i>aph</i> derivative; Km ^r	This study
Δ fhuE	ATCC19606, <i>fhuE</i> :: <i>aacC4</i> derivative; Apra ^r	This study
Δ basD Δ fhuE	ATCC19606, <i>basD</i> :: <i>aph</i> and <i>fhuE</i> :: <i>aacC4</i> derivative; Km ^r , Apra ^r	This study
<i>E. coli</i>		
DH5 α	<i>endA1 hsdR17</i> ($r_K^- m_K^+$) <i>supE44 thi-1 recA1 gyrA96 relA1</i> Δ (<i>argF-lacZYA</i>) <i>U169 deoR</i> [(Φ 80d <i>lac</i> Δ (<i>lacZ</i>)M15)]	Promega
H1717	<i>araD139 rpsL150</i> Δ (<i>argF-lac</i>) <i>relA1 U169 ffb5301 deoC1</i> <i>ptsF25 rbsR aroB fhuF</i> :: λ placMu; host strain for FURTA	22)
Plasmids		
pBluescript II KS(+)	High-copy-number cloning vector; Ap ^r	Stratagene
pUC19	High-copy-number cloning vector; Ap ^r	Nippon Gene
pACYC184	Low-copy-number cloning vector; Cm ^r , Tc ^r	Nippon Gene
pHSG299	Source of <i>aph</i> encoding Km ^r	Takara
pJG1011	Source of <i>aacC4</i> encoding Apra ^r	25)
pEX100T	Suicide vector carrying <i>sacB</i> ; Ap ^r	24)
pWH1266	<i>E. coli</i> - <i>A. baumannii</i> shuttle vector; Tic ^r , Tc ^r	27)
pAB5-3	Initially isolated FURTA-positive clone; pUC19 containing chromosomal ca. 2.0-kbp <i>Sau3A1</i> - <i>Sau3A1</i> fragment from ATCC19606; Ap ^r	This study
pAB2575	pACYC184 containing chromosomal 2575-bp <i>Clal</i> - <i>Clal</i> fragment from ATCC19606; Cm ^r	This study
pEXBASD	pEX100T with a 750-bp deletion and <i>aph</i> insertion within <i>basD</i>	This study
pEXFHUE	pEX100T with a 464-bp deletion and <i>aacC4</i> insertion within <i>fhuE</i>	This study
pWH1266-fhuE	pWH1266 harboring the ATCC19606 <i>fhuE</i> allele; Tic ^r	This study

a) Km^r, kanamycin resistance; Apra^r, apramycin resistance; Tc^r, tetracycline resistance; Ap^r, ampicillin resistance; Cm^r, chloramphenicol resistance; Tic^r, ticarcillin resistance.

Table 2. Oligonucleotide Primers Used in This Study

Oligonucleotide	Sequence ^{a)} (5'-3')	Used for
AbfhuE-F	AGAGCGGCCACAGCACAAAGC	DIG-probe
AbfhuE-R	CATTAGTTAACGAGTCAGCTCC	DIG-probe
AbfhuE-RT-F	GGGTCCGGTGTTCCTCTAACGCC	RT-PCR
AbfhuE-RT-R	GCGGTGTCCAACCTTGCCCAATCGG	RT-PCR
Abtsf-F	GCTGGCAACATTGCTGCTGACGG	RT-PCR
Abtsf-R	CCAGCAGCTAATGCAGCAGCAGC	RT-PCR
AbbasD-Sac-F	GAGTTTGAGCTCCGATGGCATCGCAAAC	pEXBASD construction
AbbasD-Xba-R	CCGTCATCTAGATGAGCAACTTGTGCATC	pEXBASD construction
aph-Xba-F	TGGTGATCTAGAACTTTTGCTTTGCCACGG	pEXBASD construction
aph-Eco-R	GAGCTCGAATTCACTGGCCGTCGTTTTAC	pEXBASD construction
AbbasD-Eco-F	TCCGTGGAATTCACCCTTACAGCATTTACC	pEXBASD construction
AbbasD-Kpn-R	TGTGGAGGTACCCGAGATGAGTAAAATG	pEXBASD construction
AbbasD-EcoRV-F	ATCGCAGATATCATGGCTGAGAAGGC	pEXBASD construction
AbbasD-EcoRV-R	AGTTGAGATATCCACTTCCATATTTGGCG	pEXBASD construction
AbfhuE-Bam-F	CCACCTGGATCCTTTAAGCTTACCG	pEXFHUE construction
AbfhuE-Pst-R	AGTGCACCTGCAGTTGTTGCATTAGG	pEXFHUE construction
aacC4-Pst-F	GTTTCATCTGCAGCTCCATCAGCAAAAAGG	pEXFHUE construction
aacC4-Eco-R	GCCCCAGAATTCAGCGCGACCTTGCC	pEXFHUE construction
AbfhuE-Eco-F	TGGTCAGAATTCACAGAAGCGGCCAAC	pEXFHUE construction
AbfhuE-Kpn-R	GGCTGGGGTACCATAAAAAGCCTGCCC	pEXFHUE construction
AbfhuE-EcoRV-F	CGATTTGATATCCAAAACCTCACCTATGCC	pEXFHUE construction
AbfhuE-EcoRV-R	AAGCGTGATATCATATTGACTTCATAGC	pEXFHUE construction
AbfhuE-Bam-F2	ATGGATCCATAGCATAGAGGTTTATC	pWH1266-fhuE construction
AbfhuE-Bam-R2	TTGGATCCGATATAACATGGGAAG	pWH1266-fhuE construction

a) Underlined nucleotides represent engineered restriction enzyme sites.

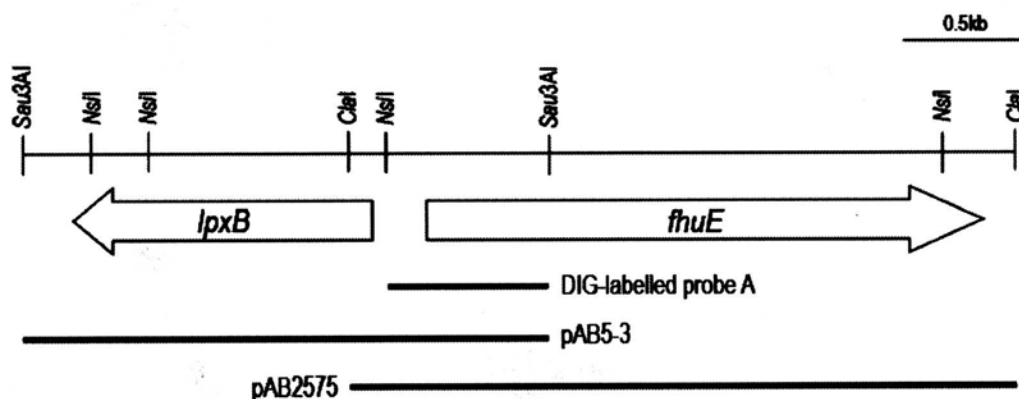


Fig. 2. Genetic Map of the *A. baumannii* ATCC19606 *fhuE* Region with the Relevant Restriction Enzyme Sites
lpxB is the putative lipid A-disaccharide synthase gene.

colony color from white to red on MacConkey lactose agar plates (BD, Franklin Lakes, NJ, U.S.A.) containing ampicillin and 25 μ M ferrous ammonium sulfate, after 15 h incubation at 37°C. More than 20 FURTA-positive clones were obtained through several rounds of screening of the pUC19 libraries, and the nucleotide sequences of their inserts were determined and their deduced amino acid sequences were used for homology search.

The chromosomal DNA from *A. baumannii* ATCC19606 was digested with various restriction enzymes and the resulting DNA fragments were analyzed by Southern blotting with the digoxigenine (DIG)-labeled probe (Fig. 2) A in order to clone the entire *fhuE*. The DIG-labeled probe A was prepared with a PCR DIG probe synthesis kit (Roche Diagnostics) using the primer pairs, AbfhuE-F and AbfhuE-R, which were designed on the basis of the nucleotide sequence for the FURTA-positive clone (pAB5-3) (Fig. 2) containing the candidate DNA fragment of *fhuE*. Hybridization followed by immunological detection of DNA was essentially performed according to the DIG system user's guide for filter hybridization (Roche Diagnostics). Finally, *ClaI*-*ClaI* fragments with a desired size were extracted and ligated into the same restriction sites of pACYC184. *E. coli* DH5 α transformants with the ligated pACYC184 on LB agar plates were transferred on a nylon membrane and screened by colony hybridization with DIG-labeled probe A to yield pAB2575. The nucleotide sequence of the insert was determined by primer walking.

Reverse Transcription (RT)-PCR *A. baumannii* ATCC19606 was grown in LB broth to an OD₆₀₀ of 0.3. The culture was split into two aliquots, and one was left untreated (iron-replete cells), and the other was supplemented with DPD at 225 μ M. Both aliquots were further incubated until an OD₆₀₀ of 0.5 was reached. Total RNA was extracted from each cell pellet using an RNeasy[®] Protect Bacteria Mini Kit (Qiagen, Valencia, CA, U.S.A.) and then treated, according to the manufacturer's instructions, with RNase-free DNase I (Ambion, Austin, TX, U.S.A.) to exclude the possibility of contamination with traces of chromosomal DNA. RT-PCR was carried out with an RNA PCR kit (TaKaRa, Shiga, Japan), following the manufacturer's directions. For first-strand cDNA synthesis, 5 μ g of pretreated total RNA was incubated in a total volume of 20 μ L at 42°C for 60 min with the primer AbfhuE-RT-R. A subsequent PCR was performed with 1 μ L of the RT reaction mixture as template and a pair of forward and reverse

primers, AbfhuE-RT-F and AbfhuE-RT-R, as follows: after an initial denaturation at 94°C for 2 min, DNA was amplified for 25 cycles, with each cycle consisting of denaturation at 94°C for 30 s, annealing at 51°C for 30 s, and extension at 72°C for 1 min. The *tsf*, encoding the elongation factor EF-Tsf,²³ was used as an established endogenous internal control. The primers, Abtsf-F and Abtsf-R, were designed according to the nucleotide sequence of *A. baumannii* ATCC19606 *tsf* (accession number EEX03313). The RT-PCR products were analyzed by 1.5% agarose gel electrophoresis, and the developed gel was stained with ethidium bromide to visualize them with the Gel Doc XR.

Construction of Disruptants Δ *basD*, Δ *fhuE*, and Δ *basD\DeltafhuE* and Complementing Plasmids** These disruptants, derived from *A. baumannii* ATCC19606, were constructed by homologous recombination and double crossover events using a suicide vector, pEX100T.²⁴ Initially, the upstream regions internal to *basD* and *fhuE* were amplified with the primer pairs, AbbasD-Sac-F and AbbasD-Xba-R, and AbfhuE-Bam-F and AbfhuE-Pst-R, respectively. The amplicons were digested with the respective restriction enzymes and the resulting fragments were inserted into pBluescript II KS(+) which was digested with the same combination of restriction enzymes. The pBluescript II KS(+) derivatives were digested with *XbaI/EcoRI* (for *basD*), and *PstI/EcoRI* (for *fhuE*). These digests were ligated with PCR products amplified with the primer pairs, aph-Xba-F and aph-Eco-R (for *basD*), and accC4-Pst-F and accC4-Eco-R (for *fhuE*), which code the pHSG299 *aph* gene (kanamycin resistance cassette) for *basD* disruption and pJG1011 *aacC4* gene²⁵ (apramycin resistance cassette) for *fhuE* disruption, respectively. The downstream regions internal to *basD* and *fhuE* were amplified with the primer pairs, AbbasD-Eco-F and AbbasD-Kpn-R, and AbfhuE-Eco-F and AbfhuE-Kpn-R, respectively, and the resulting amplicons were ligated with the pBluescript II KS(+) derivatives harboring *aph* and *aacC4* digested with *EcoRI/KpnI*. Both of the plasmids thus constructed were digested with *EcoRV*, and the resulting *EcoRV* fragments were ligated to the suicide vector, pEX100T, and digested with *SmaI* to generate pEXBASD (for *basD*) and pEXFHUE (for *fhuE*) (Table 1). These plasmids were electroporated into *A. baumannii* ATCC19606 with a MicroPulser apparatus (Bio-Rad) under the conditions of Leahy *et al.*²⁶ Apramycin- or kanamycin-resistant merodiploids, integrating the plasmid into

the chromosomal DNA by homologous recombination, were then plated on LB agar plates containing 10% sucrose without NaCl, and grown at room temperature for 48 h. Sucrose- and kanamycin-resistant colonies and sucrose- and apramycin-resistant colonies were selected for *basD* disruption and *fhuE* disruption, respectively. The chromosomal disruptants thus obtained were named $\Delta basD$ and $\Delta fhuE$. Disruption of *basD* and *fhuE* was verified by PCR amplification of the internal *basD* and *fhuE* followed by observation of the molecular mass shift due to the insertion of the *aph* and *aacC4* DNA cassettes (data not shown). The double disruptant $\Delta basD\Delta fhuE$ was also constructed from $\Delta basD$ according to the procedure for $\Delta fhuE$, as described previously.

For complementation of $\Delta fhuE$ and $\Delta basD\Delta fhuE$ with the *fhuE* gene, the *Bam*HI fragment containing the entire *fhuE* gene amplified by PCR with the primer pair AbfhuE-Bam-F2 and AbfhuE-Bam-R2 was cloned into the *E. coli*-*Acinetobacter* shuttle vector, pWH1266,²⁷ and the resulting plasmid, pWH1266-*fhuE*, was electroporated into $\Delta fhuE$ and $\Delta basD\Delta fhuE$ using a MicroPulser™ apparatus (Bio-Rad) under the conditions of Leahy *et al.*²⁶ Transformants were selected on LB plates containing ticarcillin to yield $\Delta fhuE/pWH1266$ -*fhuE* and $\Delta basD\Delta fhuE/pWH1266$ -*fhuE*.

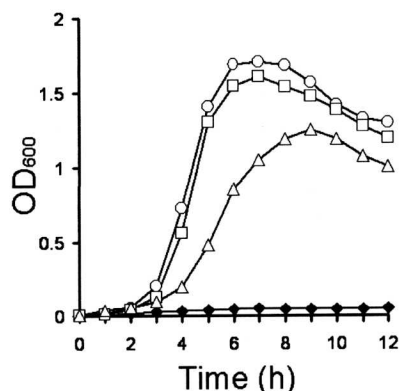


Fig. 3. Utilization of Desferricoprogen, Rhodotorulic Acid, and Desferrioxamine B as the Xenosiderophores by $\Delta basD$ of *A. baumannii* ATCC19606

Stationary-phase cells that had been grown in LB medium were inoculated at an OD₆₀₀ of 0.005 into a fresh LB medium and incubated either in the presence (●) of 225 μM DPD (iron-limiting conditions) or in the presence of both 225 μM DPD and 20 μM of a siderophore (○, Desferricoprogen; □, rhodotorulic acid; △, Desferrioxamine B). Experiments were repeated three times with similar results. Representative results are shown.

Nucleotide Sequence Accession Number Nucleotide sequence data for the *A. baumannii* ATCC19606 *fhuE* gene have been deposited in the EMBL/GenBank/DBJ databases under the accession number AB102781.

RESULTS AND DISCUSSION

Utilization of Desferricoprogen, Rhodotorulic Acid, and Desferrioxamine B by *A. baumannii* *A. baumannii* $\Delta basD$ not producing the siderophore, acinetobactin, failed to grow in LB broth containing 225 μM DPD, while the addition of 20 μM of Desferricoprogen, rhodotorulic acid, or Desferrioxamine B to the medium restored the growth (Fig. 3), indicating that the bacterium is capable of utilizing these xenosiderophores. Less efficient growth promotion was observed for Desferrioxamine B and may be due to some structural similarity of ferrioxamine B to two other ferric siderophores, as suggested by Hantke in *E. coli*.²⁸ In bacteria, the iron-repressible OMPs are known to function as receptors for ferric siderophores. SDS-PAGE of the iron-repressible OMPs in *A. baumannii* ATCC19606 exhibited at least five protein bands having molecular masses in the range of 75 to 80 kDa (Fig. 4, lane 3). The sequence of the first 10 amino acids at the N-terminal region of the 76-kDa OMP was determined to be QDAQVQA-LQT, which was consistent with the amino acid sequence in

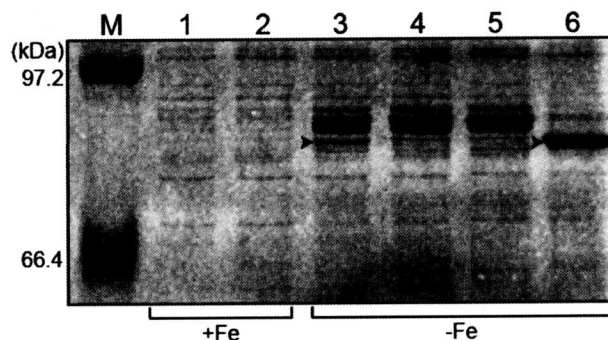


Fig. 4. OMP Profiles of *A. baumannii* ATCC19606 and its $\Delta fhuE$

All strains were grown under iron-replete (+Fe) and iron-limiting (-Fe) conditions for 12 h. SDS-PAGE was carried out using 7.5% polyacrylamide in the running gel (130 mm) and the gel developed was stained with Coomassie Brilliant Blue R-250. The amount of protein loaded in each lane was 20 μg. The figure shows only the relevant part of the SDS-PAGE gel. The arrows in lanes 3 and 6 indicate the 76-kDa iron-repressible OMPs. Lanes 1 and 3, *A. baumannii* ATCC19606; lanes 2 and 4, $\Delta fhuE$; lane 5, $\Delta fhuE$ transformed with an empty plasmid pWH1266; lane 6, $\Delta fhuE$ complemented with pWH1266-*fhuE* harboring the wild-type *fhuE* gene; lane M, molecular weight marker proteins.

```

120- TTTGAAATAATGCATTCTAGCATAGAGGTTTATCAATCTTGAACCTGATCTATATGACTTACCAAGAGCGGCCACAGCACAAGCTATCTAAAATTACACTCATTACCA
Fur box (12/19) -35

230- TCTTTTAATCTAAATTAACAATGCAATTTGAATTTAGCTTACATTTACAACAATAAAATAAATGAGAATTATTACATTATCTTTAATCTTATGAATATCCACCTCG
-10 M R I I Y I I F N L M N I P P R

340- ATCATTTAAGCTTACCGTAATCGCCTGCGGATTTGTTATGCAAACTCACCTATGCCAAGATGCACAGGTACAAGCTTTACAGACAATTCAGTT....
S F K L T V I A C A I C Y A N L T Y A Q D A Q V Q A L Q T I Q V

2410- TATGGTCCCCAGCCAACCTATACAGTTGCTGTAAGTTTAAATTAATAAGCGTAGCCAATCCCAATTTGGGGTTGGCTTCTTTTTTATTTTTTATGTGTCAGTAAAT
Y G A P A N Y T V A V K F K Y *
    
```

Fig. 5. Partial Nucleotide Sequences of *fhuE* with the Deduced Amino Acid Sequence and Its Promoter Region

The putative Fur box sequence is boxed and the promoter sequence labeled with -10 and -35. The amino acid sequence deduced from *fhuE*, which is compatible with the N-terminal amino acid sequence determined for the mature FhuE, is underlined. The predicted TonB box sequence is indicated by a wavy underline. The terminator signal is indicated by converging arrows.

the N-terminal region deduced from *A. baumannii fhuE*, as described below.

Nucleotide Sequence Analysis of the *A. baumannii fhuE* Gene

The amino acid sequence deduced from *fhuE*, whose upstream gene encodes a putative lipid A-disaccharide synthase in the reverse orientation, showed 34% identity and 55% similarity to that of *E. coli* FhuE, which was reported to be the receptor specific to coprogen, ferric rhodotorulic acid, and ferrioxamine B.¹³ Moreover, a homology search also detected *fhuE* paralogs in the genomic sequences of seven *A. baumannii* isolates reported to date. As shown in Fig. 5, the *A. baumannii* ATCC19606 *fhuE* gene possesses potential promoter elements (-35 and -10) and a putative Fur box sharing 12/19 nucleotide matches with the *E. coli* consensus Fur box.²⁹ The rather long signal sequence with 35 amino acid residues, excluded from the premature FhuE, was supported by SignalP prediction (<http://www.cbs.dtu.dk/services/SignalP/>) which displayed a most likely signal peptidase cleavage site between ³⁵A and ³⁶Q. *A. baumannii* FhuE contained an N-terminal amino acid sequence completely identical to that determined for the mature iron-repressible 76-kDa OMP. In addition, the FhuE protein was found to possess the TonB box, QTIQV, characteristic of the TonB-dependent OMPs, where the invariant amino acids threonine and valine (underlined) are present at the same positions as in *E. coli* FhuE.^{13,30}

Iron-Repressible Transcription of *fhuE* To test the function of the putative Fur box for transcription of *fhuE*, RT-PCR was performed with total RNAs isolated from *A. baumannii* ATCC19606 grown under iron-replete and iron-limiting conditions. The total RNA isolated from the iron-limiting culture provided the anticipated 226-bp product, while that from the iron-replete culture did not (Fig. 6). In addition, no band was observed when RT was omitted (data not shown), confirming that RT-PCR specifically detected mRNA. These results suggest that *fhuE* transcription is controlled by a Fur box located in front of this gene.

Phenotypic Analysis and Complementation of the Disruptants $\Delta basD\Delta fhuE$ was unable to grow under iron-limiting conditions, regardless of the presence of desferricoprogen, rhodotorulic acid, or desferrioxamine B (Fig. 7). Consistent with this, the loss of the 76-kDa FhuE protein band was observed for $\Delta fhuE$ (Fig. 4, lane 4). Moreover, $\Delta basD \Delta fhuE/pWH1266$, carrying the empty vector without expression of FhuE (Fig. 4, lane 5), showed no growth under the same conditions. However, the complementing strain, $\Delta basD\Delta fhuE/pWH1266-fhuE$, restored growth in the presence of each of the three xenosiderophores (Fig. 7), and expressed FhuE, as shown in Fig. 4, lane 6, for $\Delta fhuE/pWH1266-fhuE$. The relatively longer lag time of growth observed for the complementing strain may be due to interference from the added ticarcillin. These results demonstrate that FhuE is the receptor required for the uptake of coprogen, ferric rhodotorulic acid, and ferrioxamine B.

The finding that *A. baumannii* FhuE displays a limited degree of amino acid homology to *E. coli* FhuE, despite overlapping ligand specificities implies that structural alterations in these OMPs occur without disrupting their abilities to recognize different hydroxamate siderophore structures and transport these xenosiderophores. We considered the significance of the fact that desferrioxamine B shows little similarity in structure to desferricoprogen and rhodotorulic acid.

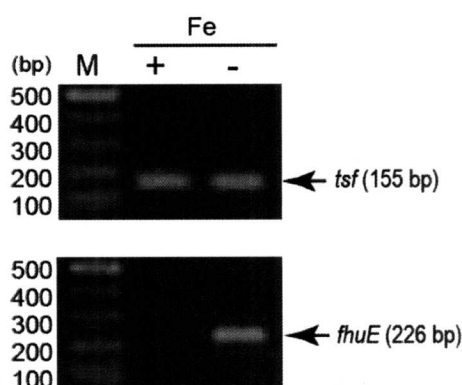


Fig. 6. Confirmation of the Iron-Regulated Transcription of *fhuE* in *A. baumannii* ATCC19606 by RT-PCR

The bacterium was grown under iron-replete conditions (+Fe) and under iron-limiting conditions (-Fe). RT-PCR conditions are described in Materials and Methods and the amplicons were analyzed by agarose gel electrophoresis. The DNA fragments were stained with ethidium bromide. The *tsf* reaction serves as an endogenous internal control. Lane M contains a 100 base-pair ladder reference.

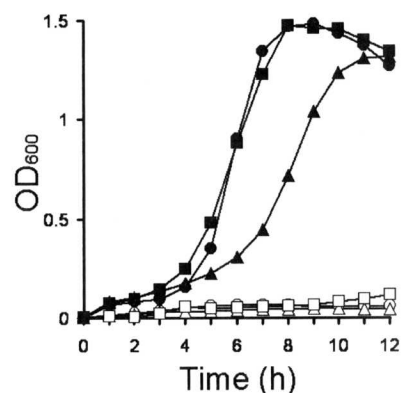


Fig. 7. Growth Complementation of $\Delta basD\Delta fhuE$ with pWH1266-*fhuE* in the Presence of Either Desferricoprogen, Rhodotorulic Acid, or Desferrioxamine B

The double disruptant, $\Delta basD\Delta fhuE$ (open symbols), and complementing strain, $\Delta basD\Delta fhuE/pWH1266-fhuE$ (closed symbols), were grown in the presence of either of desferricoprogen (○, ●), rhodotorulic acid (□, ■), or desferrioxamine B (△, ▲) at 20 μ M. The media used for the complementing strain were supplemented with ticarcillin (80 μ g/mL). Experiments were repeated three times with similar results. Representative results are shown.

However, desferricoprogen may be considered a trihydroxamate derivative of rhodotorulic acid, with a linear structure, and both contain the diketopiperazine of *N*- δ -acetyl-L-*N*- δ -hydroxyornithine.³¹ Since the iron complex of rhodotorulic acid exists in the form of $Fe_2(\text{rhodotorulic acid})_3$,³² the ferric complexes of these siderophores may resemble each other with respect to spatial structure. Similar findings are not unprecedented. For example, although the ferrichrome receptor from *Yersinia enterocolitica* is only 21% identical to the ferrichrome receptor of *E. coli*,³³ both receptors transport ferrichrome. Similarly, the ChtA receptor in *Pseudomonas aeruginosa* is able to recognize and transport citrate-containing hydroxamate-type xenosiderophores such as aerobactin, rhizobactin 1021, and schizokinen.³⁴ In any event, it should be noted that these receptors for multiple ferric siderophores contain the conserved amino acid residues in the TonB boxes involved in the interaction of these receptors with the TonB-ExbB-ExbD complex as the energy supplying system.^{13,30} In

contrast, little is known about multiple receptors specific to an inherent siderophore, with the exception of the type I ferric pyoverdine receptors, FpvA and FpvB, in *P. aeruginosa*³⁵ and the ferric vibrioferrin receptors, PvuA1 and PvuA2, in *Vibrio parahaemolyticus*.³⁶

Considering that *A. baumannii* normally inhabits soil and water surroundings, utilization of desferricoprogen, rhodotorulic acid, and desferrioxamine B may represent one of the strategies that the bacterium has adopted to compete with other neighboring microorganisms for survival and proliferation within its various niches, and promote its opportunities of gaining access to human host. In this context, it is possible that acinetobactin as the cognate siderophore in *A. baumannii* plays a larger role in acquiring iron in the human host rather than in the natural environment, because acinetobactin was reported to be able to capture iron from transferrin and lactoferrin as the main iron sources in human host.²⁰

In conclusion, we identified the *fhuE* gene in *A. baumannii* encoding the outer membrane receptor for desferricoprogen, ferric rhodotorulic acid, and desferrioxamine B. The function of the *fhuE* gene was confirmed by a growth assay using an *fhuE* disruptant and its complementing strain. Future genetic studies will be needed to elucidate the ABC transport systems for these siderophores in *A. baumannii*.

Acknowledgements We thank W. R. Bishai for providing plasmid pJG1011. This study was supported by a Grant-in-Aid for Young Scientists (B) from the Ministry of Education, Culture, Sports, Science and Technology (Grant No. 20790124 to TF) of Japan.

REFERENCES

- Miethke M, Marahiel MA. Siderophore-based iron acquisition and pathogen control. *Microbiol. Mol. Biol. Rev.*, **71**, 413–451 (2007).
- Carpenter BM, Whitmire JM, Merrell DS. This is not your mother's repressor: the complex role of *fur* in pathogenesis. *Infect. Immun.*, **77**, 2590–2601 (2009).
- Escolar L, Pérez-Martin J, de Lorenzo V. Opening the iron box: transcriptional metalloregulation by the Fur protein. *J. Bacteriol.*, **181**, 6223–6229 (1999).
- Litwin CM, Calderwood SB. Role of iron in regulation of virulence genes. *Clin. Microbiol. Rev.*, **6**, 137–149 (1993).
- Peleg AY, Seifert H, Paterson DL. *Acinetobacter baumannii*: emergence of a successful pathogen. *Clin. Microbiol. Rev.*, **21**, 538–582 (2008).
- Bergogne-Bérézin E, Towner KJ. *Acinetobacter* spp. as nosocomial pathogens: microbiological, clinical, and epidemiological features. *Clin. Microbiol. Rev.*, **9**, 148–165 (1996).
- Webster CA, Crowe M, Humphreys H, Towner KJ. Surveillance of an adult intensive care unit for long-term persistence of a multi-resistant strain of *Acinetobacter baumannii*. *Eur. J. Clin. Microbiol. Infect. Dis.*, **17**, 171–176 (1998).
- Yamamoto S, Okujo N, Sakakibara Y. Isolation and structure elucidation of acinetobactin, a novel siderophore from *Acinetobacter baumannii*. *Arch. Microbiol.*, **162**, 249–254 (1994).
- Wuest WM, Sattely ES, Walsh CT. Three siderophores from one bacterial enzymatic assembly line. *J. Am. Chem. Soc.*, **131**, 5056–5057 (2009).
- Takeuchi Y, Ozaki S, Satoh M, Mimura K, Hara S, Abe H, Nishiooka H, Harayama T. Synthesis of acinetobactin. *Chem. Pharm. Bull.*, **58**, 1552–1553 (2010).
- Mihara K, Tanabe T, Yamakawa Y, Funahashi T, Nakao H, Narimatsu S, Yamamoto S. Identification and transcriptional organization of a gene cluster involved in biosynthesis and transport of acinetobactin, a siderophore produced by *Acinetobacter baumannii* ATCC 19606T. *Microbiology*, **150**, 2587–2597 (2004).
- Eijkelkamp BA, Hassan KA, Paulsen IT, Brown MH. Investigation of the human pathogen *Acinetobacter baumannii* under iron limiting conditions. *BMC Genomics*, **12**, 126–139 (2011).
- Sauer M, Hantke K, Braun V. Sequence of the *fhuE* outer-membrane receptor gene of *Escherichia coli* K12 and properties of mutants. *Mol. Microbiol.*, **4**, 427–437 (1990).
- Smith MG, Gianoulis TA, Pukatzki S, Mekalanos JJ, Ornston LN, Gerstein M, Snyder M. New insights into *Acinetobacter baumannii* pathogenesis revealed by high-density pyrosequencing and transposon mutagenesis. *Genes Dev.*, **21**, 601–614 (2007).
- Vallenet D, Nordmann P, Barbe V, Poirel L, Mangenot S, Bataille E, Dossat C, Gas S, Kreimeyer A, Lenoble P, Oztas S, Poulain J, Segurens B, Robert C, Abergel C, Claverie JM, Raoult D, Médigue C, Weissenbach J, Cruveiller S. Comparative analysis of *Acinetobacter*: three genomes for three lifestyles. *PLoS ONE*, **3**, e1805 (2008).
- Adams MD, Goglin K, Molyneaux N, Hujer KM, Lavender H, Jamison JJ, MacDonald IJ, Martin KM, Russo T, Campagnari AA, Hujer AM, Bonomo RA, Gill SR. Comparative genome sequence analysis of multidrug-resistant *Acinetobacter baumannii*. *J. Bacteriol.*, **190**, 8053–8064 (2008).
- Nwugo CC, Gaddy JA, Zimble DL, Actis LA. Deciphering the iron response in *Acinetobacter baumannii*: A proteomics approach. *J. Proteomics*, **74**, 44–58 (2011).
- Sambrook J, Fritsch EF, Maniatis T. *Molecular Cloning: a Laboratory Manual*. 2nd, Cold Spring Harbor Laboratory, Cold Spring Harbor, 1989.
- Altschul SF, Madden TL, Schäffer AA, Zhang J, Zhang Z, Miller W, Lipman DJ. Gapped BLAST and PSI-BLAST: a new generation of protein database search programs. *Nucleic Acids Res.*, **25**, 3389–3402 (1997).
- Yamamoto S, Okujo N, Kataoka H, Narimatsu S. Siderophore-mediated utilization of transferrin- and lactoferrin-bound iron by *Acinetobacter baumannii*. *J. Health Sci.*, **45**, 297–302 (1999).
- Towbin H, Staehelin T, Gordon J. Electrophoretic transfer of proteins from polyacrylamide gels to nitrocellulose sheets: procedure and some applications. *Proc. Natl. Acad. Sci. U.S.A.*, **76**, 4350–4354 (1979).
- Stojiljkovic I, Bäumlér AJ, Hantke K. Fur regulon in gram-negative bacteria. Identification and characterization of new iron-regulated *Escherichia coli* genes by a *fur* titration assay. *J. Mol. Biol.*, **236**, 531–545 (1994).
- Gallant CV, Ponnampalam T, Spencer H, Hinton JC, Martin NL. H-NS represses *Salmonella enterica* serovar Typhimurium *dsbA* expression during exponential growth. *J. Bacteriol.*, **186**, 910–918 (2004).
- Schweizer HP, Hoang TT. An improved system for gene replacement and *xylE* fusion analysis in *Pseudomonas aeruginosa*. *Gene*, **158**, 15–22 (1995).
- Gomez JE, Bishai WR. *whmD* is an essential mycobacterial gene required for proper septation and cell division. *Proc. Natl. Acad. Sci. U.S.A.*, **97**, 8554–8559 (2000).
- Leahy JG, Jones-Meehan JM, Colwell RR. Transformation of *Acinetobacter calcoaceticus* RAG-1 by electroporation. *Can. J. Microbiol.*, **40**, 233–236 (1994).
- Hunger M, Schmucker R, Kishan V, Hillen W. Analysis and nucleotide sequence of an origin of DNA replication in *Acinetobacter calcoaceticus* and its use for *Escherichia coli* shuttle plasmids. *Gene*, **87**, 45–51 (1990).
- Hantke K. Identification of an iron uptake system specific for coprogen and rhodotorulic acid in *Escherichia coli* K12. *Mol. Gen. Genet.*, **191**, 301–306 (1983).

- 29) de Lorenzo V, Wee S, Herrero M, Neilands JB. Operator sequences of the aerobactin operon of plasmid ColV-K30 binding the ferric uptake regulation (*fur*) repressor. *J. Bacteriol.*, **169**, 2624–2630 (1987).
- 30) Sauer M, Hantke K, Braun V. Ferric-coprogen receptor FhuE of *Escherichia coli*: processing and sequence common to all TonB-dependent outer membrane receptor proteins. *J. Bacteriol.*, **169**, 2044–2049 (1987).
- 31) Howard DH. Acquisition, transport, and storage of iron by pathogenic fungi. *Clin. Microbiol. Rev.*, **12**, 394–404 (1999).
- 32) Carrano CJ, Raymond KN. Coordination chemistry of microbial iron transport compounds. 10. Characterization of the complexes of rhodotorulic acid, a dihydroxamate siderophore. *J. Am. Chem. Soc.*, **100**, 5371–5374 (1978).
- 33) Koebnik R, Hantke K, Braun V. The TonB-dependent ferrichrome receptor FcuA of *Yersinia enterocolitica*: evidence against a strict co-evolution of receptor structure and substrate specificity. *Mol. Microbiol.*, **7**, 383–393 (1993).
- 34) Cuiv PÓ, Clarke P, O'Connell M. Identification and characterization of an iron-regulated gene, *chtA*, required for the utilization of the xenosiderophores aerobactin, rhizobactin 1021 and schizokinen by *Pseudomonas aeruginosa*. *Microbiology*, **152**, 945–954 (2006).
- 35) Ghysels B, Dieu BT, Beatson SA, Pirnay JP, Ochsner UA, Vasil ML, Cornelis P. FpvB, an alternative type I ferripyoverdine receptor of *Pseudomonas aeruginosa*. *Microbiology*, **150**, 1671–1680 (2004).
- 36) Tanabe T, Funahashi T, Okajima N, Nakao H, Takeuchi Y, Miyamoto K, Tsujibo H, Yamamoto S. The *Vibrio parahaemolyticus* *pvuA1* gene (formerly termed *psuA*) encodes a second ferric vibrioferrin receptor that requires *tonB2*. *FEMS Microbiol. Lett.*, **324**, 73–79 (2011).

ORIGINAL ARTICLE

NK1.1⁺ cells regulate neutrophil migration in mice with *Acinetobacter baumannii* pneumonia

Takahiro Tsuchiya¹, Norifumi Nakao¹, Shigeo Yamamoto², Yoshikazu Hirai³, Katsushiro Miyamoto¹ and Hiroshi Tsujibo¹

¹Department of Microbiology, Osaka University of Pharmaceutical Sciences, 4-20-1 Nasahara, Takatsuki, Osaka 569-1094, ²Faculty of Pharmaceutical Sciences, Matsuyama University, 4-2 Bunkyo-cho, Matsuyama, Ehime 790-8578, and ³Division of Bacteriology, Department of Infection and Immunity, Jichi Medical University, 3311-1 Yakushiji, Shimotsuke, Tochigi 329-0498, Japan

ABSTRACT

Acinetobacter baumannii is a major cause of both community-associated and nosocomial infections worldwide. These infections are difficult to treat because the bacterium rapidly develops resistance to multiple antibiotics. However, little is known about the nature of the innate cellular response to *A. baumannii* infection. In the present study, we identified the cells infiltrating the lungs of mice with *Acinetobacter* pneumonia and analyzed their response to infection. Normal mice eradicated the *A. baumannii* infection within 3 days of inoculation. Neutrophils were rapidly recruited to the lungs, followed by macrophages and NK1.1⁺ cells. Neutrophil-depleted mice showed acute and severe symptoms, and all of the mice died within 3 days of inoculation. The majority of macrophage-depleted mice responded in a similar manner to the control mice. These results indicate that neutrophils are essential for the elimination of *A. baumannii*. Half of NK1.1⁺ cell-depleted mice died within 1 day of inoculation and the number of infiltrating neutrophils was lower than that in control mice up until 3 days post-inoculation. Moreover, the expression levels of keratinocyte chemoattractant protein (KC) decreased in NK1.1⁺ cell-depleted mice. These results indicate that NK1.1⁺ cells recruit neutrophils during the early phase of *Acinetobacter* infection by increasing KC expression.

Key words *Acinetobacter baumannii*, natural killer cell, neutrophil, pneumonia.

Acinetobacter baumannii is a ubiquitous Gram-negative bacterium that can survive for prolonged periods in water, soil, and on the skin of healthy humans. During the last decade, *A. baumannii* has emerged as a major cause of both community-associated and nosocomial infections worldwide (1–3). The urinary tract, intravenous devices, surgical sites, and decubitus are the favored sites of infection. *A. baumannii* mainly causes pneumonia, particularly in mechanically ventilated patients (4, 5). The mortality rate for ventilator-associated pneumonia caused by *A. baumannii* has been reported to be <75% (6, 7). However, little is known about the cellular and molecular

mechanisms underlying host defenses against respiratory infection by *A. baumannii* (8–10). Therefore, a deeper understanding of the innate immune system may provide new possibilities for the treatment of nosocomial pneumonia.

The innate immune system is the first line of defense against many bacterial pathogens, including *A. baumannii*. Bacterial pathogens are recognized by phagocytes, such as macrophages and neutrophils, and are rapidly eliminated from a host suffering from acute infection. CD14 and Toll-like receptor 4 play a key role in the innate sensing of *A. baumannii* via bacterial lipopolysaccharide

Correspondence

Hiroshi Tsujibo, Department of Microbiology, Osaka University of Pharmaceutical Sciences, 4-20-1 Nasahara, Takatsuki, Osaka 569-1094, Japan.
Tel: +81 72 690 1057; fax: +81 72 690 1057; email: tsujibo@gly.oups.ac.jp

Received 15 July 2011; revised 18 October 2011; accepted 26 October 2011.

List of abbreviations: Ab, antibody; BAL, bronchial alveolar lavage; HPRT, hypoxanthine phosphorybosyl transferase; IL, interleukin; i.n., intranasally; i.p., intraperitoneally; KC, keratinocyte chemoattractant protein; LPS, lipopolysaccharide; NK cells, natural killer cells.

(LPS) (9). Recently, van Faassen *et al.* reported that neutrophils play an important role in host resistance to *Acinetobacter pneumonia* (11). However, little is known about the innate cellular response and the interactions between these cells in *A. baumannii* pneumonia. Recent reports suggest that neutrophils engage in cross-talk with other leukocytes during inflammatory responses (12, 13). Immune cells (e.g. macrophages, neutrophils, NK cells, NKT cells, $\alpha\beta$ T cells, and $\gamma\delta$ T cells) play an important role in the maintenance of tissue homeostasis in the lungs. Of these, NK cells and NKT cells play a crucial role in the innate immune response to tumors, viruses, and intracellular bacteria, and also have an immunoregulatory effect on other immune cells, such as T cells, B cells, macrophages, and dendritic cells (14–20). Moreover, NK cells modulate neutrophil activation and survival by secreting various cytokines and by direct cell–cell contact (21, 22). However, because most reports are of *in vitro* studies, little is known about the role and interaction of these cells within infected tissues. The aim of the present study was to identify the cells infiltrating the lungs of mice with *Acinetobacter pneumonia* and to examine their role in host defense.

MATERIALS AND METHODS

Bacterial strains and media

Acinetobacter baumannii strain A112-II-a was isolated from a patient with chronic nephritis. The bacterium was pre-cultured in LB broth (BD Difco, Franklin Lakes, NJ, USA) at 37°C for 3 hrs. The culture was diluted 1:100 into fresh broth and then shaken at 37°C until the late logarithmic growth phase. To produce agar medium, LB broth was solidified by adding 1.5% (wt/vol) agar (Nacalai Tesque, Kyoto, Japan).

Mice

Specific pathogen-free female C57BL/6 mice were purchased from Japan SLC (Shizuoka, Japan). All experimental mice were 8–10 weeks old. The animals were housed under specific pathogen-free conditions in a small level two animal containment facility and given free access to sterile water and certified mouse chow. All experiments were carried out in accordance with the guidelines for the care and use of laboratory animals of Osaka University of Pharmaceutical Sciences.

Respiratory infection with *A. baumannii*.

Acinetobacter baumannii was grown until the late logarithmic growth phase, centrifuged at $3,500 \times g$ for 10 min, resuspended and diluted appropriately in PBS, and used immediately. Mice were anesthetized and i.n. inoculated

with approximately 10^7 or 10^8 CFU *A. baumannii* in 50 μ L PBS. The actual inoculum concentrations were determined by plating 10-fold serial dilutions onto LB agar plates. Clinical signs were monitored and scored as follows: 0, no abnormal clinical signs; 1, ruffled fur and moving slowly; 2, ruffled fur, hunched posture, and moving very slowly; 3, hunched posture, moving very slowly, and squeezed eyes; 4, dead.

Histological examination

Pulmonary lobes were harvested at the indicated time points and fixed in 10% neutral buffered formalin, which was then replaced by a sucrose solution. The lungs were then embedded in OTC (Tissue-Tec; Miles Inc., Elkhart, IN, USA) and frozen at -80°C . The tissue segments were sectioned (6 μm) on a cryostat and stained with hematoxylin and eosin (H & E).

Distribution of *A. baumannii*

Acinetobacter baumannii-inoculated mice were killed and lungs and spleen were removed. Each tissue was homogenized with PBS in a loose glass homogenizer. Cell suspensions were plated on LB agar plates and cultured at 37°C for 12 hrs.

Antibodies

Anti-M-CSFR (AFS98) was a gift from Dr S. I. Nishikawa (RIKEN, Kobe, Japan) (21). Anti-Gr1 (RB6–8C5) and anti-NK1.1 (PK136) were provided by the Cell Resource Center for Biomedical Research Institute of Development, Aging and Cancer Tohoku University. Anti-CD11b (M1/70), CD45 (30-F11), CD3 (145–2C11) and CD49 (DX5) were purchased from BD Pharmingen (San Jose, CA, USA).

Antibody treatment

To deplete neutrophils, NK/NKT cells, and macrophages, mice were injected i.p. with 250 μg anti-mouse monoclonal antibodies, RB6–8C5, PK136, and AFS98 (23–25), respectively, on Days 5, 3, and 1 before and Days 1 and 3 post-inoculation with *A. baumannii*.

Analysis of infiltrating cells

Pulmonary lobes were removed, minced in Hanks' Balanced Salt Solution (HBSS; Invitrogen, Carlsbad, CA, USA) and incubated with 150 U/mL collagenase (Sigma, St Louis, MO, USA) and 0.1 mg/mL DNase I (Wako Pure Chemicals, Osaka, Japan) for 30 min at 37°C. Spleens were homogenized in PBS using a loose glass homogenizer, centrifuged for 5 min, resuspended in PBS, and passed through nylon mesh (70 μm).

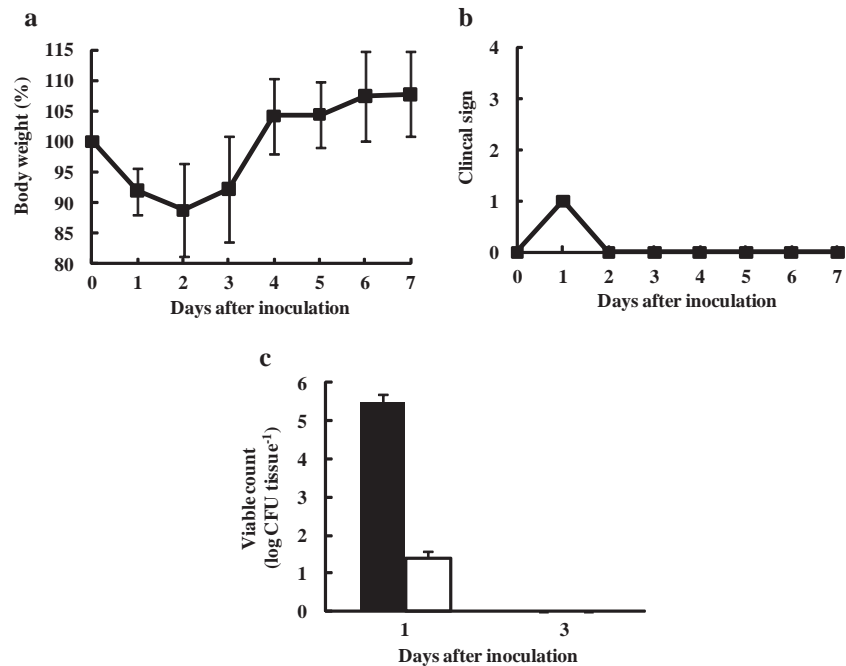


Fig. 1. Bodyweight, clinical scores, and bacterial burden in mice after intranasal inoculation with *A. baumannii*. C57BL/6 female mice were inoculated with 3.0×10^7 CFU *A. baumannii*. (a) Bodyweight changes and (b) clinical scores were monitored for 7 days. (c) Bacterial burden in the lungs (solid bars) and spleen (open bars) was measured on day 1 and day 3. Detection limits for the bacterial burden were 2 log CFU/lung and 0.7 log CFU/spleen. Error bars indicate the mean \pm standard deviation.

Flow cytometry analysis

Fluorescein isothiocyanate (FITC)-conjugated rat anti-mouse Gr1 mAb (BD Pharmingen), R-PE-conjugated rat anti-mouse CD11b mAb (BD Pharmingen), R-PE-conjugated mouse anti-mouse CD49 mAb (BD Pharmingen), and FITC-conjugated armenian hamster anti-mouse CD3 were used as the primary antibodies. Flow cytometric profiles were analyzed using a FACScan analyzer and CellQuest software (Becton Dickinson, Mountain View, CA, USA).

RT-PCR

Mice were anesthetized and inoculated i.n. with approximately 10^7 CFU of *A. baumannii* and the lungs harvested on Days 1 and 3 post-infection. Total RNA was isolated from lung tissue using an RNeasy Mini Kit (Qiagen, Tokyo, Japan), and treated with DNaseI (Qiagen). RNA was transcribed to cDNA using M-MLV reverse transcriptase (Promega, Madison, WI, USA) and the cDNA was amplified with AmpliTaq gold (Applied Biosystems, Foster City, CA, USA). The primer pairs used to amplify keratinocyte chemoattractant protein, KC (CXCL1) and hypoxanthine phosphoribosyl transferase (HPRT) were: KC, 5'-TAT CGC CAA TGA GCT GCG C-3' and 5'-AAG CCA GCG TTC ACC AGA C-3; and HPRT, 5'-CTG TAG ATT TTA TCA GAC TGA AGA G-3' and 5'-GTC AAG GGC ATA TCC AAC AAC AAA-3'.

Measurement of KC levels

Groups of five PK136 or rIgG-treated C57BL/6 mice were killed 1 and 3 days after i.n. inoculation with 10^7 CFU *A. baumannii*. The trachea were exposed through a mid-line incision and cannulated with a plastic catheter. Lungs were lavaged twice with 400 μ L PBS and the lavage fluid centrifuged at $440 \times g$ for 5 min. The supernatant was collected and stored at -80°C for ELISA. The levels of KC in the BAL fluid were determined using mouse CXCL1/KC Quantikine Kits (R & D Systems, Minneapolis, MN, USA).

Statistical analysis

The significance of the differences was calculated using one-way analysis of variance. A *P* value of <0.05 was considered to be significant.

RESULTS

Acinetobacter pneumonia in normal mice

We first examined the host immune responses to *Acinetobacter* pneumonia. Because *A. baumannii* was easily eradicated within 3 days by healthy animals, we focused on the innate immune responses and analyzed the physiological mechanisms involved in the exclusion of *A. baumannii*. First, the effective dose of *A. baumannii* required for the development of experimental pneumonia in normal

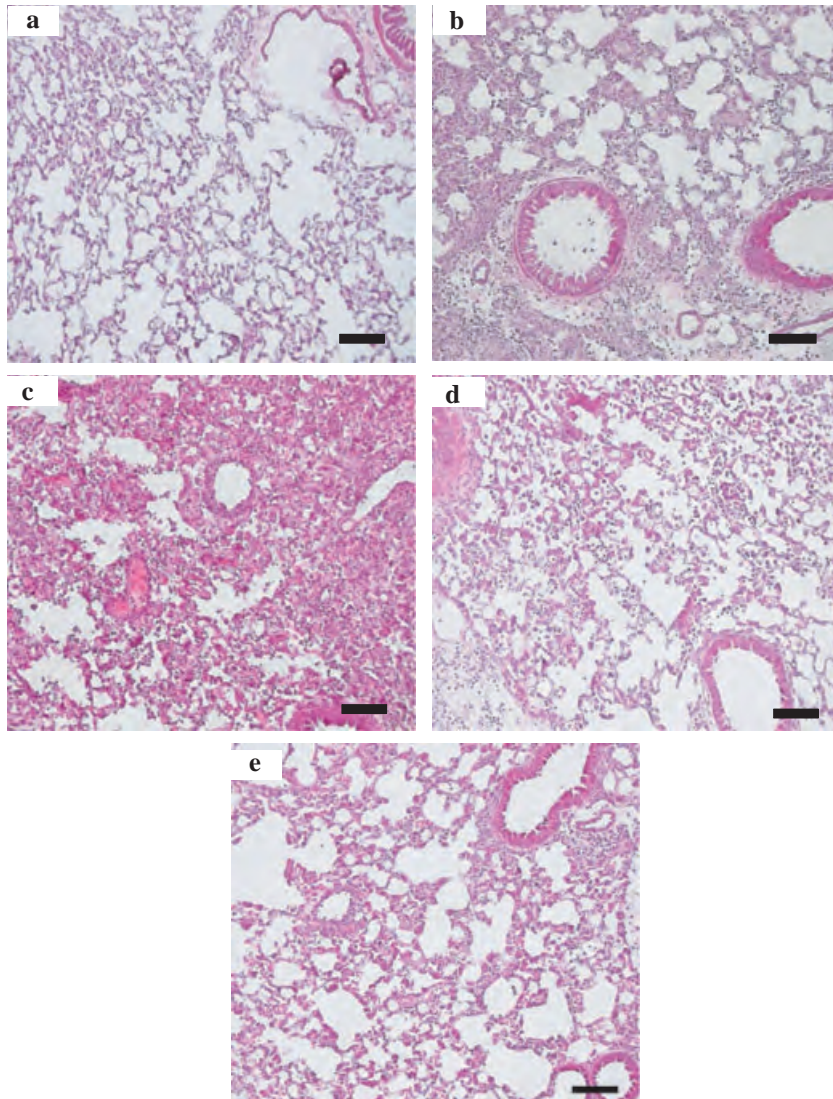


Fig. 2. Histopathological analysis of the lungs from C57BL/6 mice killed at (a) Day 0, (b) Day 1, (c) Day 3, (d) Day 5 and (e) Day 7 post-inoculation with 3.0×10^7 CFU *A. baumannii*. Scale bar = 100 μm .

C57BL/6 mice was determined. When mice were inoculated with $<10^8$ CFU, all the mice survived; however, when a dose of 10^9 CFU was used, the survival rate was 83% (5/6 mice) after 7 days (data not shown). Therefore, 10^7 or 10^8 CFU of *A. baumannii* was chosen for the pneumonia model. Although all mice inoculated with 10^7 CFU lost weight up until Day 3 and showed mild clinical signs on Day 1, all recovered completely by Day 4 post-inoculation (Fig. 1A, B). The viable bacterial counts in the lungs and spleens were 10^5 CFU and 10^1 CFU, respectively, on Day 1, and no viable bacteria were detected by Day 3 (Fig. 1C). Histological examination of the lungs harvested from mice with pneumonia was undertaken on Days 0, 1, 3, 5, and 7 post-infection (Fig. 2). Many leukocytes had infiltrated the alveoli on Day 1, reaching maximum numbers on Day 3 (Fig. 2A–C). The

number of leukocytes decreased on Day 5, and the alveoli had fully recovered by Day 7 (Fig. 2D, E). We next examined the profile of these infiltrating leukocytes using flow cytometry. $\text{Mac1}^+/\text{Gr1}^{\text{high}}$ cells, $\text{Mac1}^+/\text{Gr1}^{\text{low/-}}$ cells, $\text{NK1.1}^+/\text{CD3}^-$ cells, and $\text{NK1.1}^+/\text{CD3}^+$ cells were identified as neutrophils, macrophages, NK cells, and NKT cells, respectively. The number of neutrophils in the alveoli increased up until Day 3 post-inoculation, and then returned to normal levels by Day 5 (Fig. 3A). Macrophages and NK cells also infiltrated the alveoli, reaching maximum levels on Day 3, before returning to normal by Day 7 (Fig. 3B, C). NKT cells were hardly detected in the alveoli, the number of these cells did not show significant change through seven days (Fig. 3D). These results were in agreement with those obtained from the histological analysis (Fig. 2).

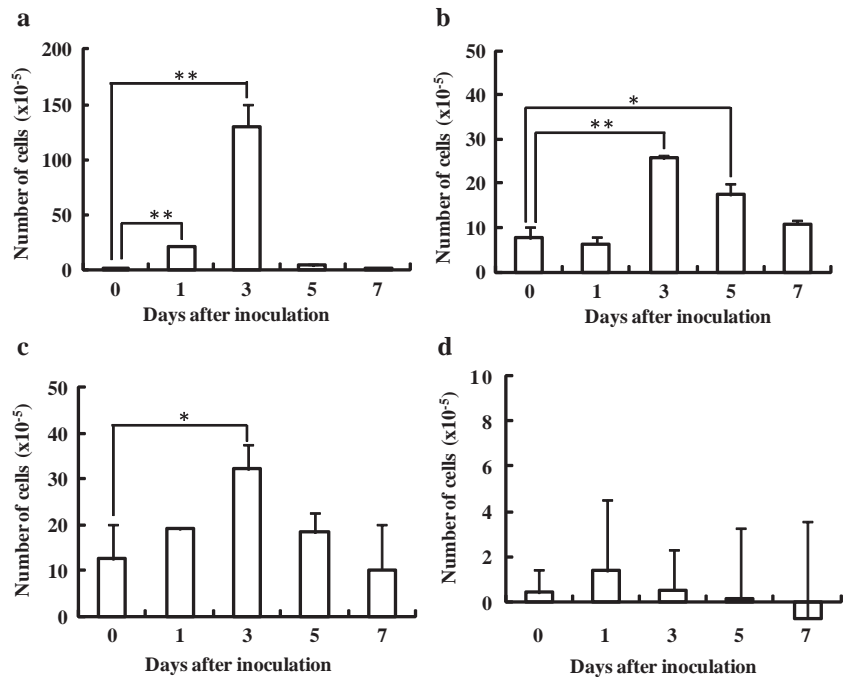


Fig. 3. Flow cytometry analysis of cells infiltrating the lungs. Female C57BL/6 mice were inoculated i.n. with 3.0×10^7 CFU *A. baumannii* and the cells infiltrating the lungs were collected and analyzed by flow cytometry ($n = 3$). (a) Neutrophils: Mac1⁺/Gr1^{hi}, (b) macrophages: Mac1⁺/Gr1^{low/-}, (c) NK cells: NK1.1⁺/CD3⁻, and (d) NKT cells: NK1.1⁺/CD3⁺. * $P < 0.05$; ** $P < 0.01$. Error bars indicate the mean \pm standard deviation.

Survival rates for pneumonia mice cell depleted of specific cell types

We next assessed the contribution made by neutrophils, macrophages and NK1.1⁺ cells to the elimination of *A. baumannii* by depleting each of the cell types using monoclonal antibodies. As described in Materials and Methods, mice were inoculated i.n. with 10^8 CFU *A. baumannii*. The survival rate of mice injected with the control Ab was 100%, whereas that of mice injected with anti-Gr1 Ab, anti-NK1.1 Ab, and anti-M-CSFR Ab was 0%, 50%, and 83%, respectively (Fig. 4). These results suggest that neutrophils are essential for the elimination of *A. baumannii*. They also suggest that NK1.1⁺ cells play an active protective role in host immune responses against *A. baumannii*. However, the contribution made by macrophages appears to be very small (Fig. 4). Therefore, we next examined the specific role of neutrophils and NK1.1⁺ cells in the elimination of *A. baumannii*.

Lung inflammation in neutrophil- and NK1.1⁺ cell-depleted mice

To examine the effects of neutrophils on the elimination of *A. baumannii*, neutrophil-depleted mice were inoculated i.n. with 10^7 CFU *A. baumannii*. The viable bacterial count in the lungs of the control mice was 5×10^5 CFU on Day 1, although no bacteria were detected on Day 3 (Fig. 5A). However, in mice injected with anti-Gr1 Ab (neutrophil-depleted), the viable bacterial count

was 6×10^7 CFU on Day 1 and 7×10^3 CFU on Day 3. The viable bacterial count in NK1.1⁺ cell-depleted mice was similar to that in control mice on Day 1, and the count was still 1×10^2 CFU on Day 3 (Fig. 5B). We then examined the profile of leukocytes infiltrating the lungs of cell-depleted mice with pneumonia. Neutrophils were not detected in mice injected with the anti-Gr1 Ab until Day 5 (Fig. 6A). The number of macrophages infiltrating into alveoli was higher than that in control mice up until Day 3, but decreased to similar levels by Day 5 (Fig. 6B). The number of NK cells continued to increase up until Day 7 in both pneumonia and control mice (Fig. 6C). Interestingly, the number of infiltrating neutrophils was less than that in control mice up until Day 3 (Fig. 7A). These results indicate that neutrophils are essential for the elimination of *A. baumannii*, and that NK1.1⁺ cells play a role in the migration of neutrophils into the alveoli of *Acinetobacter* pneumonia mice. The number of infiltrating macrophages was similar to that in the control mice (Fig. 7B). Small numbers of NK cells were observed up until Day 7 in mice injected with the anti-NK1.1 Ab (Fig. 7C).

Chemokine expression in NK1.1⁺ cell-depleted mice with pneumonia

To elucidate the role played by NK1.1⁺ cells in the migration of neutrophils, the expression level of chemokines was measured in the lung tissues of anti-NK1.1 Ab-injected

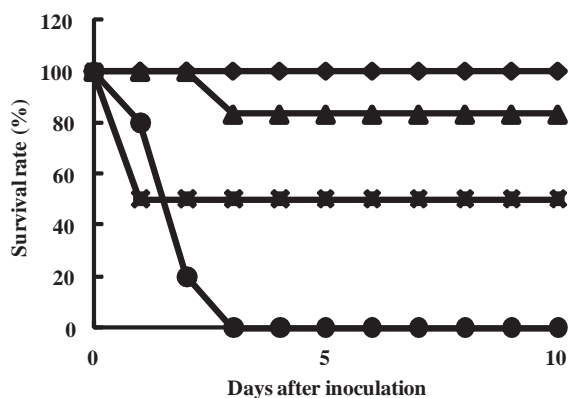


Fig. 4. Effect of antibody treatment on the survival of mice after i.n. inoculation with 5.0×10^8 CFU *A. baumannii*. Groups of C57BL/6 female mice ($n = 6$) were injected i.p. with 250 μ g control IgG (diamonds), anti-M-CSFR Ab (triangles), anti-NK1.1 Ab (crosses), or anti-Gr1 Ab (circles) on Days 5, 3, and 1 before and on Days 1 and 3 post-inoculation. Survival was recorded for 10 days.

mice with pneumonia. RT-PCR was used to detect CXC chemokine mRNAs in lung tissues, as CXC chemokines are chemotactic for neutrophils. As shown in Figure 8A, lung tissues from control mice constantly expressed KC (CXCL1) mRNA, even after *Acinetobacter* infection; however, the KC levels in mice injected with anti-NK1.1 Ab were lower than those in the control mice on Days 1 and 3.

In addition to KC mRNA levels, the amount of KC protein in the BAL fluid was measured by ELISA (Fig. 8B). There was no significant difference in the level of KC in the BAL fluid between anti-NK1.1 Ab-injected mice and control Ab-injected mice on Day 0. The level of KC in the BAL fluid of the control Ab-injected and anti-NK1.1 Ab-injected mice increased substantially following *Acinetobacter* challenge, reaching maximum levels in control mice on Day 1, before returning to normal on Day 5. However, KC levels in anti-NK1.1 Ab-injected mice were maximal on Day 3, although they remained lower than those in control mice from Day 1 to Day 5.

DISCUSSION

Nosocomial infection with *A. baumannii* pneumonia is an increasing threat because of high mortality rates and antibiotic resistance (6, 26–28). However, little is known about host defense against respiratory infection by this pathogen (9, 11, 29, 30). To investigate the pathology and the responses of immunocompetent cells to *A. baumannii*, we analyzed the cells infiltrating the lungs of mice with *A. baumannii* pneumonia and examined their role in the immune response. Normal healthy C57BL/6 mice inoculated i.n. with $<10^8$ CFU *A. baumannii* completely elimi-

nated the pathogen within 3 days, and the inflamed lungs recovered within 7 days (Figs 1, 2). However, large numbers of neutrophils infiltrated the alveoli of mice with *Acinetobacter* pneumonia (Fig. 3). Increased numbers of macrophages, NK cells, $\alpha\beta$ T cells, and $\gamma\delta$ T cells were also observed up until 3 days post-inoculation, decreasing to normal levels thereafter (Fig. 3 and data not shown). Few NKT cells were detected in the alveoli, and the numbers of these cells were constant after *A. baumannii* infection (Fig. 3D). These results are consistent with earlier observations (11).

Next, we examined the effects of neutrophils on the elimination of *A. baumannii* using mice depleted of neutrophils by i.p. injection of an anti-Gr1 Ab. Neutrophils play an important role in host defense against bacterial pathogens (31, 32). *A. baumannii* caused severe pneumonia in mice injected with anti-Gr1 Ab, and the viable bacterial count in the lungs was 100-fold higher than that in control mice (6, and Fig. 5). Furthermore, all of the anti-Gr1 Ab-injected mice died within 3 days of

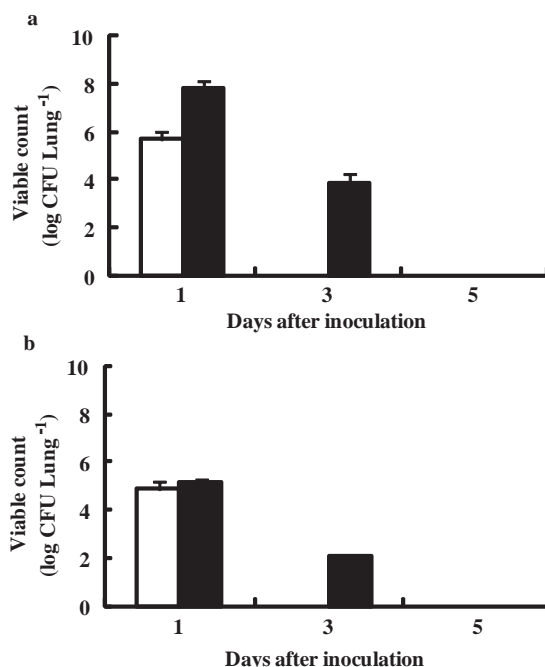


Fig. 5. Effect of antibody treatment on the bacterial burden in the lungs of C57BL/6 mice inoculated with 3.0×10^7 CFU *A. baumannii* ($n = 3$). (A) C57BL/6 mice were injected i.p. with 250 μ g anti-Gr1 Ab (solid bar) or an equivalent amount of control IgG (open bar) on Days 5, 3, and 1 before and on Days 1 and 3 post-inoculation. (B) C57BL/6 mice were injected i.p. with 250 μ g anti-NK1.1 Ab (solid bar), or an equivalent amount of control IgG (open bar) on Days 5, 3, and 1 before and on Days 1 and 3 post-inoculation. Detection limits were 2 log CFU/lung and 0.7 log CFU/spleen. Error bars indicate the mean \pm standard deviation.

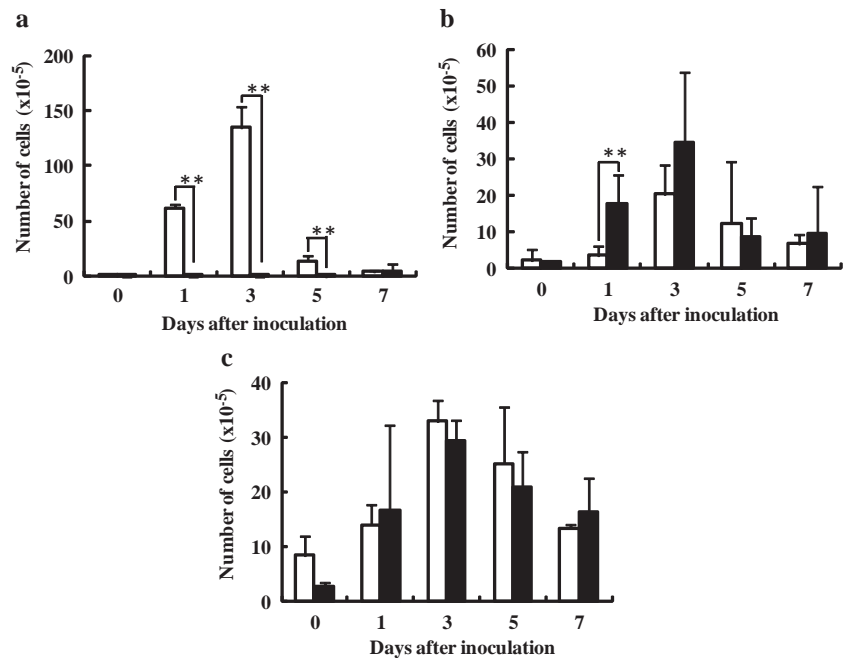


Fig. 6. Effect of anti-Gr1 Ab treatment on cells infiltrating the lungs after inoculation with *A. baumannii*. C57BL/6 mice were injected i.p. with 250 μ g anti-Gr1 Ab (solid bars) or an equivalent amount of control IgG (open bars) on Days 5, 3, and 1 before and on Days 1 and 3 post-inoculation with 3.3×10^7 CFU *A. baumannii*. Infiltrating cells were collected and analyzed by flow cytometry ($n = 3$). (a) Neutrophils: Mac1⁺/Gr1^{hi}, (b) macrophages: Mac1⁺/Gr1^{low/-} and (c) NK cells: NK1.1⁺/CD3⁻. Results are representative of three separate experiments. * $P < 0.05$; ** $P < 0.01$. Error bars indicate the mean \pm standard deviation.

inoculation (Fig. 4). However, 83% of mice injected with the anti-M-CSFR Ab survived (Fig. 4). These results indicate that host innate immune defenses in the respiratory tract of normal mice are mediated by neutrophils rather than by macrophages, which suppress bacterial growth and prevent the development of severe disease. The number of infiltrating NK cells in the lungs of both anti-Gr1 Ab-injected and control mice also increased from Day 1 post-inoculation (Fig. 6C); therefore, we next examined the effect of NK1.1⁺ cells on the elimination of *A. baumannii*.

Although NK cells play a key role in the immune response to tumors, viruses, and intracellular bacteria (33–36), little is known about their role in the response to extracellular bacterial infection (37). There are no published reports assessing the contribution of NK cells to the response against *A. baumannii* pneumonia. The functional role of the NK1.1⁺ cells was examined by injecting mice with an anti-NK1.1 Ab. As observed for the anti-Gr1 Ab-injected mice, mice injected with anti-NK1.1 Ab showed a reduced ability to eliminate the bacteria, and the overall survival rates were less than those in control mice (Figs 4, 5B). These results indicate that NK1.1⁺ cells play a crucial role in host defense against respiratory infection by *A. baumannii*. In anti-NK1.1 Ab-injected mice, the number of infiltrating neutrophils decreased compared with those in control mice up until Day 3 post-inoculation, and the viable bacterial count in the lungs was 100-fold higher than that in control mice by Day 3 (Figs 5B, 7A).

Moreover, as shown in Fig. 8, the expression levels of KC in anti-NK1.1 Ab-injected mice were significantly lower than those in control mice. These results suggest that NK1.1⁺ cells induce the recruitment of neutrophils by increasing the expression of KC during the early phase of *Acinetobacter* infection. NK1.1 is expressed on NK cells and NKT cells, so anti-NK1.1 Ab treatment depleted NK cells and NKT cells. In this experiment, these results may be caused by NK cells and/or NKT cells. However, it is likely that NK cells rather than NKT cells play an important role in the recruitment of neutrophils during *A. baumannii* infection, because the numbers of NKT cells were not significantly increased in the lung during infection. NK cells, along with CD8⁺ T cells, function as key effector cells during Th1-type immune responses, and secrete inflammatory cytokines such as IFN- γ and TNF- α . A recent study shows that A/J mice are much more sensitive to *Acinetobacter baumannii* infection than C57BL/6 mice, due to delayed neutrophil recruitment during the early phase of infection (38). C57BL/6 and A/J mice exhibit predominantly Th1-type and Th2-type immune responses, respectively, and Th1-type cytokines, such as IFN- γ and IL-12, induce early neutrophil-mediated host defenses (39, 40). Judging from these reports, the neutrophil recruitment essential for the elimination of *A. baumannii* may be induced by Th1-type immune responses, and these Th1-type cytokines may be secreted by NK1.1⁺ cells. NKT cells can make both the Th1-type cytokine IFN- γ and the Th2-type cytokines IL-4 and IL-13. These cells appear to play an important role

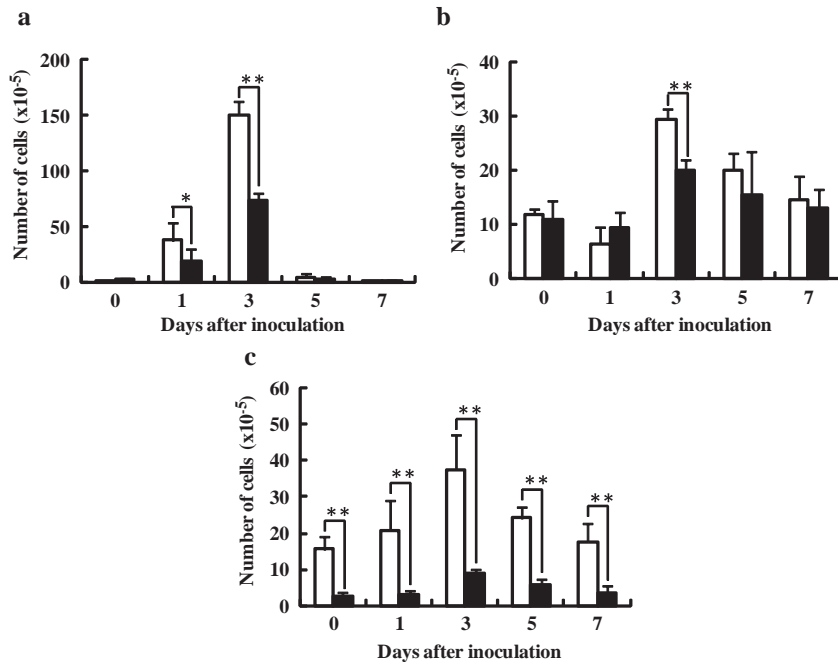


Fig. 7. Effect of anti-NK1.1 Ab treatment on cells infiltrating the lungs of mice after inoculation with *A. baumannii*. C57BL/6 mice were injected i.p. with 250 μ g anti-NK1.1 Ab (solid bars) or an equivalent amount of control IgG (open bars) on Days 5, 3, and 1 day before and on Days 1 and 3 post-inoculation with 2.7×10^7 CFU *A. baumannii*. Infiltrating cells were collected and analyzed by flow cytometry ($n = 3$). (a) Neutrophils: Mac1⁺/Gr1^{hi}, (b) Macrophages: Mac1⁺/Gr1^{low/-} and (c) NK cells: NK1.1⁺/CD3⁻. Results are representative of three separate experiments. * $P < 0.05$; ** $P < 0.01$. Error bars indicate the mean \pm standard deviation.

in allergy, autoimmunity, and tumor control. Moreover, NKT cells play an important protective role in bacterial infection (19, 20). However, Bourgeois *et al.* reported that NKT cells suppressed neutrophil migration into the lung via Th1-type cytokines IFN- γ and IL-12 (41). It is neces-

ary to clarify whether NK cells or NKT cells are important in the migration of neutrophils.

IL-17A is thought to participate in host defense against various pathogens and induce the production of TNF- α and CXC chemokines in the lung (42–45). In the present study, the expression level of IL-17A increased in lung tissues at 1 day after inoculation of *A. baumannii*, and up-regulation of IL-17A was delayed by anti-NK1.1 Ab treatment (data not shown). IL-17A and IL-17F may increase the expression level of neutrophil chemotactic factors, including KC (in mouse), MIP-2 (in mouse and humans), and IL-8 (in humans) and may be driven by lung epithelial cells (46). Also, the IL-17A-producing cells in bacterially infected lungs appear to be $\gamma\delta$ T cells rather than CD4⁺ Th17 cells (47–49). In the present study, $\gamma\delta$ T cells were detected in the lungs of mice with *Acinetobacter* pneumonia, and their numbers rapidly increased up until Day 3 post-inoculation (data not shown). Thus, $\gamma\delta$ T cells may be involved in neutrophil recruitment and may directly or indirectly interact with NK1.1⁺ cells. The detailed molecular mechanisms underlying the role of $\gamma\delta$ T cells on *Acinetobacter* pneumonia remain to be elucidated.

In conclusion, the results of the present study show that NK1.1⁺ cells induce neutrophil recruitment by increasing the expression levels of KC during the early phase of *Acinetobacter* infection. Further understanding of the molecular mechanisms underlying NK1.1⁺ cell-mediated immune regulation may lead to improved control of *A. baumannii* infections.

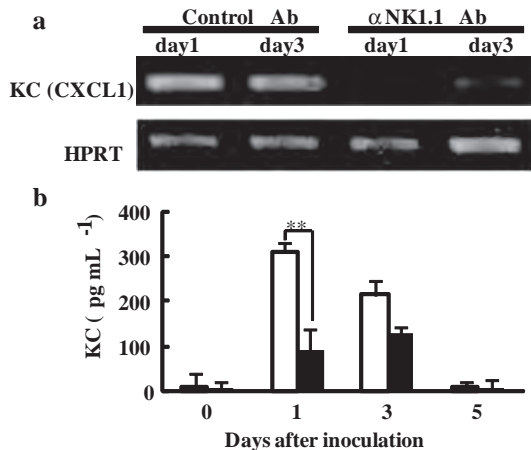


Fig. 8. (a) Effect of anti-NK1.1 Ab treatment on chemokine mRNA expression levels and (b) the concentration of KC in BAL fluid from mice inoculated with *A. baumannii*. C57BL/6 mice were injected i.p. with 250 μ g anti-NK1.1 Ab (solid bars) or an equivalent amount of control IgG (open bars) on Days 5, 3, and 1 before and on Days 1 and 3 post-inoculation with 2.9×10^7 CFU *A. baumannii*. Results are representative of four separate experiments. * $P < 0.05$. Error bars indicate the mean \pm standard deviation.

ACKNOWLEDGMENTS

This study was supported in part by a Grant-in-Aid for High Technology Research from the Ministry of Education, Culture, Sports, Science and Technology, Japan. We are grateful to Professor Shin-Ichi Nishikawa for supplying the anti-M-CSF monoclonal antibody, AFS98.

DISCLOSURE

The authors who have taken part in this study declare that they do not have anything to disclose regarding funding or conflict of interest with respect to this manuscript.

REFERENCES

- Dijkshoorn L., van Aken E., Shunburne L., van der Reijden T.J., Bernards A.T., Nemeč A., Towner K.J. (2005) Prevalence of *Acinetobacter baumannii* and other *Acinetobacter* spp. in faecal samples from non-hospitalised individuals. *Clin Microbiol Infect* **11**: 329–32.
- Gaynes R., Edwards J. R. (2005) Overview of nosocomial infections caused by gram-negative bacilli. *Clin Infect Dis* **41**: 848–54.
- Joly-Guillou M.L. (2005) Clinical impact and pathogenicity of *Acinetobacter*. *Clin. Microbiol Infect* **11**: 868–73.
- Garnacho J., Sole-Violan J., Sa-Borges M., Diaz E., Rello J. (2003) Clinical impact of pneumonia caused by *Acinetobacter baumannii* in intubated patients: a matched cohort study. *Crit Care Med* **31**: 2478–82.
- Lortholary O., Fagon J.Y., Hoi A.B., Slama M.A., Pierre J., Giral P., Rosenzweig R., Gutmann L., Safar M., Acar J. (1995) Nosocomial acquisition of multiresistant *Acinetobacter baumannii*: risk factors and prognosis. *Clin Infect Dis* **20**: 790–6.
- Fagon J.Y., Chastre J., Domart Y., Trouillet J.L., Pierre J., Darne C., Gibert C. (1989) Nosocomial pneumonia in patients receiving continuous mechanical ventilation. Prospective analysis of 52 episodes with use of a protected specimen brush and quantitative culture techniques. *Am Rev Respir Dis* **139**: 877–84.
- Fagon J.Y., Chastre J., Domart Y., Trouillet J. L., Gibert C. (1996) Mortality due to ventilator-associated pneumonia or colonization with *Pseudomonas* or *Acinetobacter* species: assessment by quantitative culture of samples obtained by a protected specimen brush. *Clin Infect Dis* **23**: 538–42.
- Fournier P.E., Richet H. (2006) The epidemiology and control of *Acinetobacter baumannii* in health care facilities. *Clin Infect Dis* **42**: 692–9.
- Knapp S., Wieland C. W., Florquin S., Pantophlet R., Dijkshoorn L., Tshimbalanga N., Akira S., van der Poll T. (2006) Differential roles of CD14 and toll-like receptors 4 and 2 in murine *Acinetobacter* pneumonia. *Am J Respir Crit Care Med* **173**: 122–9.
- Lee J.S., Lee J.C., Lee G.M., Jung I.D., Jeong Y.I., Seong E.Y., Chung H.Y., Park Y.M. (2007) Outer membrane protein A of *Acinetobacter baumannii* induces differentiation of CD4⁺ T cells toward a Th1 polarizing phenotype through the activation of dendritic cells. *Biochem Pharmacol* **74**: 86–97.
- van Faassen H., KuoLee R., Harris G., Zhao X., Conlan J.W., Chen W. (2007) Neutrophils play an important role in host resistance to respiratory infection with *Acinetobacter baumannii* in mice. *Infect Immun* **75**: 5597–608.
- Novais F.O., Santiago R.C., Báfica A., Khouri R., Afonso L., Borges V.M., Brodskyn C., Barral-Netto M., Barral A., de Oliveira C.I. (2009) Neutrophils and macrophages cooperate in host resistance against *Leishmania braziliensis* infection. *J Immunol* **183**: 8088–98.
- Silva M.T. (2010) Neutrophils and macrophages work in concert as inducers and effectors of adaptive immunity against extracellular and intracellular microbial pathogens. *J Leukoc Biol* **87**: 805–13.
- Blanca I.R., Bere E.W., Young H.A., Ortaldo J.R. (2001) Human B cell activation by autologous NK cells is regulated by CD40–CD40 ligand interaction: role of memory B cells and CD5⁺ B cells. *J Immunol* **167**: 6132–9.
- Cooper M.A., Fehniger T.A., Fuchs A., Colonna M., Caligiuri M.A. (2004) NK cell and DC interactions. *Trends Immunol* **25**: 47–52.
- Dalbeth N., Gundle R., Davies R.J., Lee Y.C., McMichael A.J., Callan M.F. (2004) CD56bright NK cells are enriched at inflammatory sites and can engage with monocytes in a reciprocal program of activation. *J Immunol* **173**: 6418–26.
- Zingoni A., Sornasse T., Cocks B. G., Tanaka Y., Santoni A., Lanier L. L. (2004) Cross-talk between activated human NK cells and CD4⁺ T cells via OX40–OX40 ligand interactions. *J Immunol* **173**: 3716–24.
- Zingoni A., Sornasse T., Cocks B.G., Tanaka Y., Santoni A., Lanier L.L. (2005) NK cell regulation of T cell-mediated responses. *Mol Immunol* **42**: 451–4.
- Joyce A.G., Qiu H., Fan Y., Wang S., Yang X. (2008) Natural killer T cells are critical for dendritic cells to induce immunity in *Chlamydial* pneumonia. *Am J Respir Crit Care Med* **178**: 745–56.
- Kawakami K., Yamamoto N., Kinjo Y., Miyagi K., Nakasone C., Uezu K., Kinjo T., Nakayama T., Taniguchi M., Saito A. (2003) Critical role of Valpha14⁺ natural killer T cells in the innate phase of host protection against *Streptococcus pneumoniae* infection. *Eur J Immunol* **33**: 3322–30.
- Bhatnagar N., Hong H.S., Krishnaswamy J.K., Haghikia A., Behrens G.M., Schmidt R.E., Jacobs R. (2010) Cytokine-activated NK cells inhibit PMN apoptosis and preserve their functional capacity. *Blood* **116**: 1308–16.
- Costantini C., Micheletti A., Calzetti F., Perbellini O., Pizzolo G., Cassatella M.A. (2010) Neutrophil activation and survival are modulated by interaction with NK cells. *Int Immunol* **22**: 827–38.
- Sudo T., Nishikawa S., Ogawa M., Kataoka H., Ohno N., Izawa A., Hayashi S., Nishikawa S. (1995) Functional hierarchy of *c-kit* and *c-fms* in intramarrow production of CFU-M. *Oncogene* **11**: 2469–76.
- Conlan J.W., North R.J. (1994) Neutrophils are essential for early anti-*Listeria* defense in the liver, but not in the spleen or peritoneal cavity, as revealed by a granulocyte-depleting monoclonal antibody. *J Exp Med* **179**: 259–68.
- Zhang B., Yamamura T., Kondo T., Fujiwara M., Tabira T. (1997) Regulation of experimental autoimmune encephalomyelitis by natural killer (NK) cells. *J Exp Med* **186**: 1677–87.
- Bergogne-Berezin E., Towner K.J. (1996) *Acinetobacter* spp. as nosocomial pathogens: microbiological, clinical, and epidemiological features. *Clin Microbiol Rev* **9**: 148–65.
- Karageorgopoulos D.E., Falagas M.E. (2008) Current control and treatment of multidrug-resistant *Acinetobacter baumannii* infections. *Lancet Infect Dis* **8**: 751–62.
- Peleg A.Y., Seifert H., Paterson D. L. (2008) *Acinetobacter baumannii*: emergence of a successful pathogen. *Clin Microbiol Rev* **21**: 538–82.
- Eveillard M., Soltner C., Kempf M., Saint-Andre J.P., Lemarie C., Randrianarivelo C., Seifert H., Wolff M., Joly-Guillou M.L. (2010) The virulence variability of different *Acinetobacter baumannii* strains in experimental pneumonia. *J Infect* **60**: 154–61.

30. Renckens R., Roelofs J. J., Knapp S., de Vos A.F., Florquin S., van der Poll T. (2006) The acute-phase response and serum amyloid A inhibit the inflammatory response to *Acinetobacter baumannii* Pneumonia. *J Infect Dis* **193**: 187–95.
31. Leendertse M., Willems R.J., Giebelen I.A., Roelofs J.J., Bonten M.J., van der Poll T. (2009) Neutrophils are essential for rapid clearance of *Enterococcus faecium* in mice. *Infect Immun* **77**: 485–91.
32. Pedrosa J., Saunders B.M., Appelberg R., Orme I.M., Silva M.T., Cooper A.M. (2000) Neutrophils play a protective nonphagocytic role in systemic *Mycobacterium tuberculosis* infection of mice. *Infect Immun* **68**: 577–83.
33. Ashkar A., Reid A.S., Verdu E.F., Zhang K., Coombes B. K. (2009) Interleukin-15 and NK1.1+ cells provide innate protection against acute *Salmonella enterica* serovar Typhimurium infection in the gut and in systemic tissues. *Infect Immun* **77**: 214–222.
34. Feng C.G., Kaviratne M., Rothfuchs A.G., Cheever A., Hieny S., Young H.A., Wynn T.A., Sher A. (2006) NK cell-derived IFN-gamma differentially regulates innate resistance and neutrophil response in T cell-deficient hosts infected with *Mycobacterium tuberculosis*. *J Immunol* **177**: 7086–93.
35. Humann J., Lenz L.L. (2010) Activation of naive NK cells in response to *Listeria monocytogenes* requires IL-18 and contact with infected dendritic cells. *J Immunol* **184**: 5172–8.
36. Miyazaki S., Ishikawa F., Shimizu K., Ubagai T., Edelstein P.H., Yamaguchi K. (2007) Gr-1-high polymorphonuclear leukocytes and NK cells act via IL-15 to clear intracellular *Haemophilus influenzae* in experimental murine peritonitis and pneumonia. *J Immunol* **179**: 5407–14.
37. Small C.L., McCormick S., Gill N., Kugathasan K., Santosuosso M., Donaldson N., Heinrichs D. E., Ashkar A., Xing Z. (2008) NK cells play a critical protective role in host defense against acute extracellular *Staphylococcus aureus* bacterial infection in the lung. *J Immunol* **180**: 5558–68.
38. Qiu H., KuoLee R., Harris G., Chen W. (2009) High susceptibility to respiratory *Acinetobacter baumannii* infection in A/J mice is associated with a delay in early pulmonary recruitment of neutrophils. *Microbes Infect* **11**: 946–55.
39. Sun K., Salmon S.L., Lotz S.A., Metzger D.W. (2007) Interleukin-12 promotes gamma interferon-dependent neutrophil recruitment in the lung and improves protection against respiratory *Streptococcus pneumoniae* infection. *Infect Immun* **75**: 1196–202.
40. Yamamoto N., Kawakami K., Kinjo Y., Miyagi K., Kinjo T., Uezu K., Nakasone C., Nakamatsu M., Saito A. (2004) Essential role for the p40 subunit of interleukin-12 in neutrophil-mediated early host defense against pulmonary infection with *Streptococcus pneumoniae*: involvement of interferon-gamma. *Microbes Infect* **6**: 1241–1249.
41. Bourgeois E.A., Levescot A., Diem S., Chauvineau A., Bergès H., Milpied P., Lehuen A., Damotte D., Gombert J.M., Schneider E., Girard J.P., Gourdy P., Herbelin A. (2011) A natural protective function of invariant NKT cells in a mouse model of innate-cell-driven lung inflammation. *Eur J Immunol* **41**: 299–305.
42. Jovanovic D.V., Di Battista J.A., Martel-Pelletier J., Jolicoeur F.C., He Y., Zhang M., Mineau F., Pelletier J.P. (1998) IL-17 stimulates the production and expression of proinflammatory cytokines, IL-beta and TNF-alpha, by human macrophages. *J Immunol* **160**: 3513–21.
43. Laan M., Cui Z.H., Hoshino H., Lötvalld J., Sjöstrand M., Gruenert D.C., Skoogh B.E., Lindén A. (1999) Neutrophil recruitment by human IL-17 via C-X-C chemokine release in the airways. *J Immunol* **162**: 2347–52.
44. Liu Y., Mei J., Gonzales L., Yang G., Dai N., Wang P., Zhang P., Favara M., Malcolm K.C., Guttentag S., Worthen G.S. (2011) IL-17A and TNF-alpha exert synergistic effects on expression of CXCL5 by alveolar type II cells in vivo and in vitro. *J Immunol* **186**: 3197–205.
45. Ye P., Rodriguez F.H., Kanaly S., Stocking K.L., Schurr J., Schwarzenberger P., Oliver P., Huang W., Zhang P., Zhang J., Shellito J.E., Bagby G.J., Nelson S., Charrier K., Peschon J.J., Kolls J.K. (2001) Requirement of interleukin 17 receptor signaling for lung CXC chemokine and granulocyte colony-stimulating factor expression, neutrophil recruitment, and host defense. *J Exp Med* **194**: 519–27.
46. Alcorn J.F., Crowe C.R., Kolls J.K. (2010) TH17 cells in asthma and COPD. *Annu Rev Physiol* **72**: 495–516.
47. Hamada S., Umemura M., Shiono T., Tanaka K., Yahagi A., Begum M.D., Oshiro K., Okamoto Y., Watanabe H., Kawakami K., Roark C., Born W.K., O'Brien R., Ikuta, K., Ishikawa H., Nakae S., Iwakura Y., Ohta T., Matsuzaki G. (2008) IL-17A produced by gammadelta T cells plays a critical role in innate immunity against *Listeria monocytogenes* infection in the liver. *J Immunol* **181**: 3456–63.
48. Shibata K., Yamada H., Hara H., Kishihara K., Yoshikai Y. (2007) Resident Vdelta1+ gammadelta T cells control early infiltration of neutrophils after *Escherichia coli* infection via IL-17 production. *J Immunol* **178**: 4466–72.
49. Umemura M., Yahagi A., Hamada S., Begum M.D., Watanabe H., Kawakami K., Suda T., Sudo K., Nakae S., Iwakura Y., Matsuzaki G. (2007) IL-17-mediated regulation of innate and acquired immune response against pulmonary *Mycobacterium bovis* bacille Calmette-Guerin infection. *J Immunol* **178**: 3786–96.

Identification of Genes, *desR* and *desA*, Required for Utilization of Desferrioxamine B as a Xenosiderophore in *Vibrio furnissii*

Tomotaka TANABE,*^a Tatsuya FUNAHASHI,^a Katsushiro MIYAMOTO,^b Hiroshi TSUJIBO,^b and Shigeo YAMAMOTO^a

^a College of Pharmaceutical Sciences, Matsuyama University; 4–2 Bunkyo-cho, Matsuyama, Ehime 790–8578, Japan; and

^b Osaka University of Pharmaceutical Sciences; 4–20–1 Nasahara, Takatsuki, Osaka 569–1094, Japan.

Received December 17, 2010; accepted January 4, 2011; published online January 27, 2011

We found that *Vibrio (V.) furnissii* ATCC35016 can gain iron through a xenosiderophore desferrioxamine B (DFOB) for its growth under iron-limiting conditions, concurrent with the expression of the 79-kDa iron-repressible outer membrane protein (IROMP) in response to the presence of DFOB. Based on the sequence of the ferrioxamine B (an iron-bound form of DFOB) receptor gene in *V. vulnificus*, two *V. furnissii* genes, termed *desA* and *desR*, encoding the 79-kDa IROMP and AraC-type transcriptional regulator, respectively, were identified and cloned. Nucleotide sequences located in the promoter regions of both *desR* and *desA* predicted the presence of consensus ferric uptake regulation (Fur)-binding sequences. The transcription of both genes was negatively regulated by exogenous iron levels. Deletion of the *desA* gene abolished the ability of *V. furnissii* to utilize DFOB, and neither *desA* mRNA nor DesA was detected in the deletion mutant of *desR* regardless of the presence of DFOB. The functions of DesA and DesR as the ferrioxamine B receptor and transcriptional activator for *desA*, respectively, were confirmed by complementation of *desA* and *desR* deletion mutants.

Key words ferrioxamine B receptor gene; AraC-type regulator gene; xenosiderophore; iron utilization system; *Vibrio furnissii*

Iron is an essential element for bacterial survival and proliferation. However, the availability of iron is extremely limited because it is insoluble in water under aerobic environments and neutral pH or is sequestered in the vertebrate host by the use of high-affinity iron-binding molecules, such as transferrin, lactoferrin, and heme in hemoglobin.¹⁾ Most bacteria have accordingly evolved specialized iron acquisition systems to overcome the conditions of its restriction. One of the common strategies for iron acquisition is the use of siderophores, high-affinity ferric iron-chelating molecules.²⁾ In response to conditions of iron depletion, many bacteria are able not only to biosynthesize and secrete cognate siderophores, but also to pirate siderophores produced by other microbial species (termed xenosiderophores).²⁾ In Gram-negative bacteria, ferric ion trapped with such a siderophore is taken up into cells *via* the siderophore-specific TonB-dependent outer membrane receptor and ATP binding cassette (ABC) transporter system.³⁾ However, under iron-replete conditions, most of the genes involved in iron acquisition systems are negatively regulated by a ferric uptake regulation (Fur) protein with ferrous iron as a corepressor.⁴⁾

Vibrio (V.) furnissii, first described as a gas-producing biogroup of *V. fluvialis*, was classified by DNA relatedness as a species separate from *V. fluvialis*.⁵⁾ *V. furnissii*, like other pathogenic *Vibrio* species, is a halophilic Gram-negative bacterium and is thought to cause acute gastroenteritis and diarrhea through eating seafood contaminated with the bacterium.⁶⁾ We previously observed that *V. furnissii* produces the siderophore fluvibactin, which is produced by *V. fluvialis*,⁷⁾ to capture insoluble ferric iron. However, although the ability to use xenosiderophores has been elucidated in some *Vibrio* species, such as *V. vulnificus*,^{8,9)} *V. parahaemolyticus*,^{10,11)} and *V. cholerae*,¹²⁾ little is known about that of other *Vibrio* species including *V. furnissii*. In this study, we found that *V. furnissii* can use a fungal siderophore, desferrioxamine B (DFOB), as the iron source. This prompted us to investigate genes involved in the utilization

of DFOB by the bacterium. As a result, *V. furnissii* was found to possess not only a gene (called *desA*) encoding a TonB-dependent outer membrane receptor protein with an amino acid sequence homologous to the ferrioxamine B (FOB, an iron-bound form of DFOB) receptor derived from the *V. vulnificus desA* gene,⁸⁾ but also a gene (called *desR*), located just upstream of *desA*, encoding a putative AraC-type transcriptional regulator. The functions of *desA* and *desR* that encode the receptor of FOB and the transcriptional activator of *desA*, respectively, were confirmed by phenotypic analyses of the respective gene-deletion mutants constructed from *V. furnissii* followed by complementation experiments.

MATERIALS AND METHODS

Bacterial Strains and Media *V. furnissii* ATCC35016 (type strain) isolated from human feces was used in this study. *V. furnissii* and *Escherichia coli* strains were routinely cultivated in Luria–Bertani (LB) media containing 2.0% and 0.5% NaCl, respectively. *E. coli* β 2155,¹³⁾ a diamminopimelate (DAP) auxotroph, was cultured in LB medium with 0.5 mM DAP. LB media with and without 2,2'-dipyridyl (DPD; Wako Pure Chemical Industries, Osaka, Japan) at 200 μ M were used for growth as iron-limiting (–Fe) and -replete (+Fe) media, respectively. DFOB mesylate (Sigma, St. Louis, MO, U.S.A.) was added into the –Fe medium at a final concentration of 20 μ M as needed. Appropriate antibiotics were added to media at the following concentrations: ampicillin at 100 μ g/ml; chloramphenicol at 30 μ g/ml; and tetracycline at 10 μ g/ml.

Growth Assay Stationary-phase *V. furnissii* cells were diluted to an optical density of 0.005 at 600 nm (OD₆₀₀) with the –Fe medium with or without DFOB. Cultures were shaken at 70 rpm at 37 °C, and OD₆₀₀ was measured at every hour for 20 h.

DNA Manipulations Isolation of plasmids and chromosomal DNAs, restriction enzyme digestion, gel electrophore-

* To whom correspondence should be addressed. e-mail: ttanabe@cc.matsuyama-u.ac.jp

sis, recovery of DNA from agarose gel, and DNA ligation were carried out following the methods of Sambrook *et al.*¹⁴⁾ Digoxigenin (DIG)-labeled probes A and B were prepared with a polymerase chain reaction (PCR) DIG probe synthesis kit (Roche, Basel, Switzerland) using *V. furnissii* ATCC35016 chromosomal DNA as a template and the following primers: for probe A, *desA*-1 (5'-CAAAGCTATTACGATGGTTT-3') and *desA*-2 (5'-TCACGCTCAAAGGTATCCA-3') (designed according to the *desA* gene sequence of *V. vulnificus* M2799); and for probe B, *desR*-1 (5'-CGTGATGGGTTTGAATTGG-3') and *desR*-2 (5'-GTCACGGTTTCTGTGTCTGC-3'). To clone the *desA* gene, chromosomal DNA from *V. furnissii* ATCC35016 was digested with *Hind*III, and ca. 5-kb DNA fragments were ligated into pACYC184 (Nippon Gene, Tokyo, Japan). Candidate colonies were selected by colony hybridization with probe A, and a positive clone including a *Hind*III insert of 5389 bp was designated as pDES_Vfur1. Clone pDES_Vfur7, which has a *Sal*I insert of 1982 bp containing the *desR* gene, was isolated with probe B in a manner similar to that described for the construction of pDES_Vfur1. The nucleotide sequences of pDES_Vfur1 and pDES_Vfur7 were determined using dideoxy-chain termination methods using an ABI PRISM 3130XL sequencer (Applied Biosystems, Foster City, CA, U.S.A.).

Construction of Deletion Mutants from *V. furnissii* ATCC35016 Each deletion fragment of *V. furnissii desA* and *desR* genes was prepared by PCR-driven overlap extension, as described previously.^{15,16)} The following primers were used for construction of the deletion fragments: for the *desA* deletion, A1 (5'-CTGATTTTCTAGAGCAGGTGCCAAGTGTGTG-3'), A2 (5'-accacagtgtgtcagctgttCTGTGTCTGC-3'), A3 (5'-aaacctgacacactgtgtTACTTGTCTG-3'), and A4 (5'-TTGGGCATCTAGAGATCGAGCACAATCACGTCG-3'); and for the *desR* deletion, R1 (5'-CGTTTGCATCTAGATGATCAACACTTCGTGG-3'), R2 (5'-tccatctcgcaaatcatccAGCGACAACG-3'), R3 (5'-ggatattgcccagatggaTTATTGGTTGC-3'), and R4 (5'-TGGGCCTTCTAGACCTCCAGTTGCTGCATC-3') (the underlined sequences are *Xba*I sites, and the lowercase letter sequences are each complementary). Each deletion fragment was digested with *Xba*I and ligated into the same site of the R6K-ori suicide vector pCVD442.¹⁷⁾ The resulting plasmids were transformed into *E. coli* β 2155, a DAP auxotroph conjugal donor, and mobilized into *V. furnissii* ATCC35016 by filter mating. Ampicillin-resistant merodiploids were grown overnight in LB medium with 10% sucrose and 1% NaCl and then spread on agar plates of the same composition. Sucrose-resistant and ampicillin-sensitive colonies were selected, and $\Delta desA$ and $\Delta desR$ strains that contained a 1844-bp deletion in *desA* and a 739-bp deletion in *desR*, respectively (Fig. 1A), were confirmed by PCR of the chromosomal DNA with the following primer pairs designed to show the size of the deletion: for PCR of *desA*, A5 (5'-CCGAAGCTCTGATTCATGGT-3') and A6 (5'-TGGCTAAAGCCTTGCAGTTT-3'); and for PCR of *desR*, R5 (5'-TCGACATGACCTTTGAGCAG-3') and R6 (5'-GGTGGTATCGAGCGTCACTT-3').

RNA Analysis RNA was extracted from *V. furnissii* ATCC35016 and $\Delta desR$ strains grown in the -Fe or +Fe media using an RNeasy Protect Bacteria mini kit (Qiagen, Valencia, CA, U.S.A.) and then treated with RNase-free

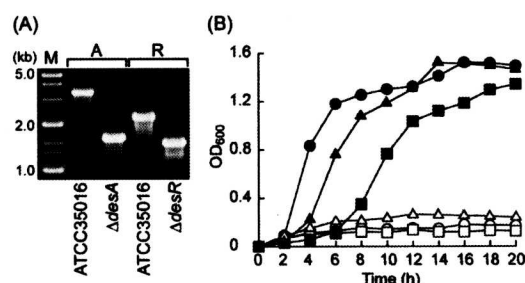


Fig. 1. Confirmation of the Deletion in *V. furnissii* ATCC35016 Deletion Mutants of the *desA* and *desR* Genes by PCR (A), and Utilization of DFOB by the Wild-Type and These Mutant Strains (B)

(A) The chromosomal DNAs isolated from *V. furnissii* ATCC35016, $\Delta desA$, and $\Delta desR$ strains were used for PCR. A, PCR products obtained with the primer pair A5 and A6; R, PCR products obtained with the primer pair R5 and R6; M, 1-kb ladder marker. (B) Growth rate of *V. furnissii* ATCC35016 strain was assessed in the -Fe medium with (closed circle) or without (open circle) DFOB at 20 μ M. Meanwhile, the growth rates of *V. furnissii* $\Delta desA$ (open square), $\Delta desA/pRK415-desA$ (closed square), $\Delta desR$ (open triangle), and $\Delta desR/pRK415-desR$ (closed triangle) strains were evaluated in the -Fe medium with DFOB at 20 μ M. The measurement of OD₆₀₀ was performed at every hour for 20 h. A representative of three independent experiments is indicated.

DNase I (Ambion, Austin, TX, U.S.A.). Quantitative real-time PCR (qPCR) was performed using cDNA generated from 1 μ g of DNase I-treated RNA with PrimeScript reverse transcriptase (Takara, Shiga, Japan). qPCR primers used were following: for *desR*, qR1 (5'-CAGTTCTGAAATCAGCTTTAGCC-3') and qR2 (5'-AGTGTGGCGACC-AAGCTTAC-3'); for the *desRA* intergenic region, qRA1 (5'-GGATTATTGGTTGCCGATTG-3') and qRA2 (5'-GGCATCAAAAGTGCCAAGAT-3'); for *desA*, qA1 (5'-GCGATCTTGGCACTTTTGTAT-3') and qA2 (5'-GTGTCTGCGCTTGTGGACT-3'); and for 16S rRNA, q16s1 (5'-GTTGTGAGGTAAGGGCTCA-3') and q16s2 (5'-GCTGATCATCCTCTCAGACCA-3'). qPCR reactions were carried out using SYBR Premix Ex Taq (Takara) in a Chromo 4 Real-Time PCR detection system (Bio-Rad, Hercules, CA, U.S.A.). Values were quantified with the comparative threshold cycle method, and the expression of *desR* and *desA* was normalized to that of 16S rRNA.

Construction of Complementation Strains To perform *desA* and *desR* complementation experiments, each PCR fragment containing the full *desA* or *desR* gene was ligated into a broad host-range plasmid pRK415.¹⁸⁾ The primers used were: for *desA* complementation, the primer pair A1 and A4 containing *Xba*I sites; and for *desR* complementation, compR1 (5'-GCGGCGGAATTCATAACATGCAC-TAAACAAC-3') and compR2 (5'-AGCATGTTCTA-GACTCAGCGATCTCAATCGGC-3') (the underlined sequences were *Eco*RI and *Xba*I sites, respectively). The plasmids pRK415-*desA* and pRK415-*desR* containing an *Xba*I insert of 3055 bp and an *Eco*RI-*Xba*I insert of 1097 bp, respectively, were introduced into *E. coli* β 2155 and mobilized into the $\Delta desA$ and $\Delta desR$ strain, respectively, by filter mating. Tetracycline-resistant colonies were selected, and the transfer of pRK415-*desA* and pRK415-*desR* to the respective mutant strains was verified by PCR and restriction enzyme analysis of each of the extracted plasmids (data not shown).

Preparation of Outer Membrane Protein (OMP)-Rich Fractions and Determination of the N-Terminal Amino Acid Sequences of Iron-Repressible OMPs OMP-rich fractions were prepared from *V. furnissii* ATCC35016,

$\Delta desA$, $\Delta desR$, $\Delta desA/pRK415-desA$, and $\Delta desR/pRK415-desR$ strains grown in the +Fe or -Fe medium, as previously described.¹⁹⁾ The N-terminal amino acid sequences of the iron-repressible OMPs (IROMPs) were determined using the Edman degradation method with a Procise 491 HT protein sequencer (Applied Biosystems) with an online phenylthiohydantoin derivative analyzer.

Nucleotide Sequence Accession Number Nucleotide sequences of the *V. furnissii* *desR* and *desA* genes have been deposited in the EMBL/GenBank/DDBJ databases under the accession number AB550609.

RESULTS AND DISCUSSION

Utilization of DFOB by *V. furnissii* The growth of *V. furnissii* ATCC35016 was suppressed in the -Fe medium, while the addition of 20 μ M DFOB to the same medium restored the growth (Fig. 1B), indicating that the bacterium can use DFOB as a xenosiderophore. To examine OMP profiles of *V. furnissii* ATCC35016 grown both in the +Fe medium and -Fe medium with or without DFOB, sarcosyl-insoluble outer membrane fractions were prepared,¹⁹⁾ and the proteins were then separated by sodium dodecyl sulfate-polyacrylamide gel electrophoresis (SDS-PAGE). In the -Fe medium, one major and three minor IROMPs were strongly expressed, although they were undetectable in the +Fe medium (Fig. 2, lanes 1, 2). Moreover, when the bacterium was grown in the -Fe medium supplemented with DFOB, expression of 79-kDa IROMP, of which the N-terminal amino sequence was determined to be ADESTSADTE, was markedly increased (Fig. 2, lane 3 arrowhead), suggesting that DFOB may serve as a coactivator for this event.

Determination of Nucleotide Sequences of *desA* and *desR* The *V. furnissii* *desA* gene was amplified by PCR with the primer pair *desA*-1 and *desA*-2 designed according to the gene sequence of *V. vulnificus* *desA*⁸⁾ (data not shown). The *V. furnissii* *desA* gene was then cloned, and the colonies were hybridized with probe A to obtain a recombinant plasmid, called pDES_vfur1 (Fig. 3A). In a similar way as above, the

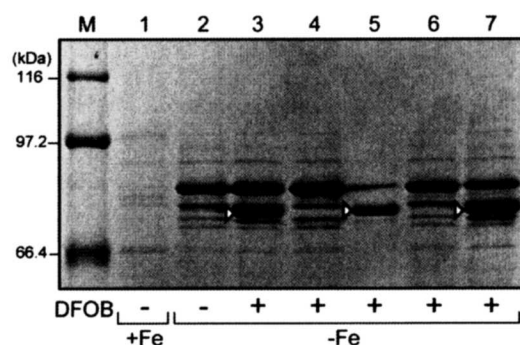


Fig. 2. IROMP Profiles of *V. furnissii* and Its *desA* and *desR* Mutant Strains

The OMP fraction of *V. furnissii* ATCC35016 was prepared from cells grown in the +Fe (lane 1), -Fe (lane 2), or -Fe with 20 μ M DFOB (lane 3) medium. Meanwhile, the OMP fractions of $\Delta desA$ (lane 4), $\Delta desA/pRK415-desA$ (lane 5), $\Delta desR$ (lane 6), and $\Delta desR/pRK415-desR$ (lane 7) were prepared from the cells grown in the -Fe medium with 20 μ M DFOB. SDS-PAGE was performed using 7.5% SDS-polyacrylamide gel (130 mm long) at a constant current of 15 mA at 4°C, and the gel was stained with Coomassie blue. The amounts of protein loaded per lane were 25 μ g (lanes 1 to 4, 6, and 7) and 2.5 μ g (lane 5). This figure shows only the relevant part of the SDS-PAGE gel. Lane M, molecular weight marker proteins; open arrowheads, 79-kDa DesA protein.

upstream region of the *V. furnissii* *desA* gene was cloned with probe B, and the resulting recombinant plasmid was called pDES_vfur7 (Fig. 3A). The nucleotide sequence of the 6389-bp region cloned was determined by primer walking. The amino acid sequence deduced from *desA* showed 59% identity to that of *V. vulnificus* DesA, a receptor for FOB,⁸⁾ and the protein product of an upstream gene adjacent to *V. furnissii* *desA*, called DesR, showed 47% identity to *V. vulnificus* DesR, an AraC-type transcriptional activator (Table 1). Moreover, database searches revealed the orthologous proteins in *V. harveyi*, *V. splendidus*, and *V. fischeri*, which show more than 40% identity and 60% similarity with the *V. furnissii* DesR and DesA proteins, respectively (Table 1). However, no obvious protein with a significant homology to DesR or DesA was found in the genomic sequences of *V. cholerae* and *V. parahaemolyticus*. As shown in Fig. 3B and C, each of the *V. furnissii* *desR* and *desA* genes possesses potential promoter elements (-35 and -10) and a putative Fur box sharing 13/19 nucleotide matches with the *E. coli* consensus Fur box.²⁰⁾ In addition, *V. furnissii* DesA was found to contain an N-terminal amino acid sequence completely identical to that determined for the DFOB-inducible 79-kDa IROMP (Fig. 3C).

Iron-Repressible Transcription of *desR* and *desA* To test the effects of the putative Fur boxes of *desR* and *desA* on their transcription, qPCR was carried out in total RNA from *V. furnissii* ATCC35016 cells grown in the +Fe and -Fe media. The degree of *desR* transcription was slightly elevated

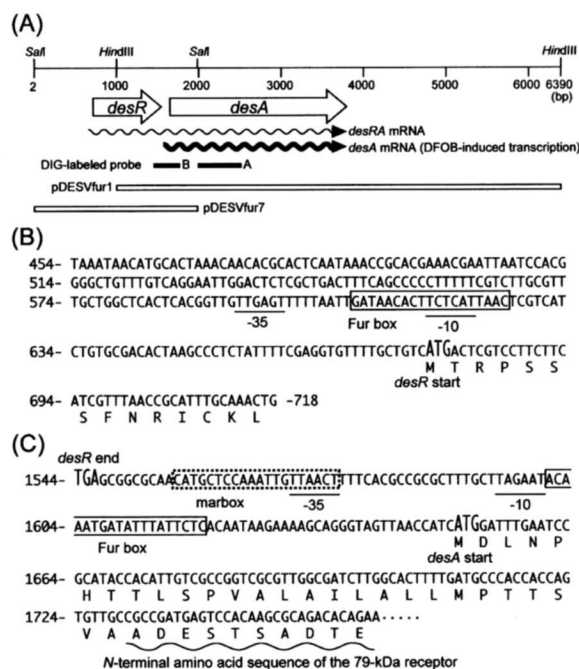
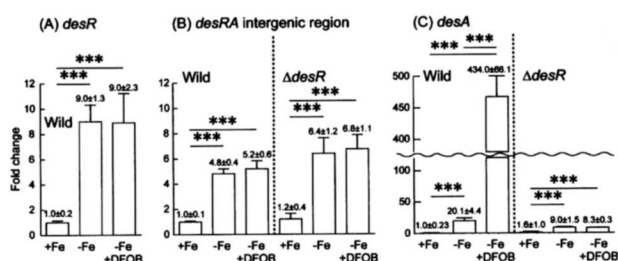


Fig. 3. Genetic Map of Open Reading Frames in the Cloned *V. furnissii* ATCC35016 *desRA* Region with the Relevant Restriction Enzyme Sites (A) and Nucleotide Sequences of the Promoter Regions of *desR* (B) and *desA* (C)

(A) Arrows indicate the full-length open reading frames with their transcriptional direction. Closed bar, constructed DIG-labeled probes; open bar, relevant plasmids. (B and C) The putative promoter elements are underlined. Potential Fur boxes and marbox are boxed with solid and dashed lines, respectively. The amino acid sequence coinciding with that of the N-terminus of the *V. furnissii* ATCC35016 79-kDa IROMP is indicated with a wavy line.

Table 1. Proteins in Other *Vibrio* Species Homologous to *V. furnissii* DesR and DesA

<i>V. furnissii</i> Protein	Homologue			Identity (%)	Similarity (%)
	Protein	Source	GenBank		
DesR	DesR	<i>V. vulnificus</i>	AB208775	48	66
	VS_II0500	<i>V. splendidus</i>	FM954973	51	67
	VIBHAR_06300	<i>V. harveyi</i>	CP000790	49	65
	VF_A0785	<i>V. fischeri</i>	CP000021	40	61
DesA	DesA	<i>V. vulnificus</i>	AB208775	59	74
	VIBHAR_06299	<i>V. harveyi</i>	CP000790	61	75
	VF_A0784	<i>V. fischeri</i>	CP000021	60	76
	VS_II0501	<i>V. splendidus</i>	FM954973	52	69

Fig. 4. qPCR Analysis of *desR* (A), *desR-desA* Intergenic Region (B), and *desA* (C) in *V. furnissii* ATCC35016 and Δ *desR* Strains

The amounts of mRNA for *desR*, the *desR-desA* intergenic region, and *desA* were assessed with qPCR using the total RNA samples extracted from *V. furnissii* ATCC35016 and Δ *desR* strains grown in the +Fe and -Fe media, and -Fe medium with 20 μ M DFOB. Expression was normalized to that of 16S ribosomal RNA, and each bar represents the mean value \pm S.D. ($n=3$). p -Values were estimated using Student's t -test (***) $p < 0.001$.

in the -Fe medium compared with that in the +Fe medium (Fig. 4A). Moreover, the transcription of the intergenic region between *desR* and *desA* showed a similar induction pattern to that of *desR* (Fig. 4B). These results suggest that in response to iron limitation, the *desR* and *desA* genes are co-transcribed as a polycistronic mRNA (Fig. 3A). In addition, it was observed that the degree of *desA* transcription in the -Fe medium increased more than two-fold compared with that of *desR* or the *desRA* intergenic region in the same medium (Fig. 4). This suggests that *desA* is also transcribed as a monocistronic mRNA.

Effects of DFOB on *desA* Transcription The addition of DFOB to the -Fe medium led to a marked induction of *desA* gene expression (Fig. 4C), but not of *desR* (Fig. 4A) and the *desRA* intergenic region (Fig. 4B). This suggests that transcription of the *desA* gene as a monocistronic mRNA is exclusively promoted by the presence of DFOB. Moreover, the promoter region of *V. furnissii desA* was found to possess a potential marbox (Fig. 3C),²¹ a 20-bp DNA consensus sequence to which an AraC-type transcriptional activator binds, suggesting that *desA* is activated by an AraC-type activator DesR encoded by a gene just upstream. To confirm this, qPCR was performed with total RNA from Δ *desR* cells grown in the +Fe, -Fe, and -Fe with DFOB media. In contrast to the wild-type strain, the *desA* transcription level in Δ *desR* was dramatically decreased even in the -Fe medium with DFOB (Fig. 4C). These results clearly indicate that *desA* transcription as a monocistronic message is regulated by DesR and its coactivator, presumably FOB, but not DFOB.

IROMP Profiles and Growth Assay of *desR* and *desA* Deletion Mutants

The profile of IROMPs from the Δ *desA* strain demonstrated the disappearance of the 79-kDa DesA protein band induced by DFOB (Fig. 2, lane 4). The Δ *desA* strain in the -Fe medium was unable to restore the growth in spite of the presence of DFOB (Fig. 1B). In addition, genetic complementation of the Δ *desA* strain with pRK415-*desA* in *trans* restored the enhanced expression of DesA (Fig. 2, lane 5) and growth in the -Fe medium with DFOB (Fig. 1B). These results indicate that DesA is the receptor involved in the uptake of FOB. On the other hand, the DesA expression enhanced by DFOB was abolished in the Δ *desR* strain (Fig. 2, lane 6), coincident with the result of qPCR analysis showing the loss of the *desA* message in the Δ *desR* strain (Fig. 4C). Moreover, although the Δ *desR* strain exhibited no growth even in the presence of DFOB (Fig. 1B), the complement strain Δ *desR*/pRK415-*desR* regained the abilities to produce DesA (Fig. 2, lane 7) and to grow in the -Fe medium containing DFOB (Fig. 1B). These results also support the hypothesis that DesR functions as a transcriptional activator of *desA*, and that FOB is an inducer that binds DesR to activate it.

In conclusion, we identified the *desA* and *desR* genes in *V. furnissii* encoding the outer membrane receptor for FOB and the AraC-type transcriptional activator of *desA*, respectively. The function of the *desA* gene was confirmed in a growth assay using the *desA* deletion mutant and its complement strain. On the other hand, the IROMP expression profile and qPCR analysis of the *desR* deletion mutant revealed that activation of *desA* expression under iron-limiting conditions requires DesR and the presence of DFOB itself, acting both as an inducer and as an iron source. Moreover, the putative *desRA* orthologues were detected in some other *Vibrio* species. Considering that *V. furnissii* mainly inhabits estuarine and brackish environments, acquisition of the DFOB-utilization system may represent one of the strategies that it employs to compete with other neighboring microorganisms for survival and growth within its various niches. It has been reported that hydroxamate-type siderophores, including ferrioxamine species, and microbes that produce such siderophores are widely distributed in aquatic and terrestrial environments.^{22–25} In addition, the expression of a specific IROMP stimulated by the presence of a xenosiderophore as an iron source would represent a common energy-saving strategy adopted by natural inhabitants of microbes. Future studies will be needed to elucidate the ABC transporter system genes for FOB in *V. furnissii* and molecular mechanisms

of the transcriptional activation of *desA* by DesR along with FOB.

Acknowledgment We thank T. Kuroda for providing *E. coli* β 2155 and for his helpful comments.

REFERENCES

- 1) Ratledge C., Dover L. G., *Annu. Rev. Microbiol.*, **54**, 881—941 (2000).
- 2) Miethke M., Marahiel M. A., *Microbiol. Mol. Biol. Rev.*, **71**, 413—451 (2007).
- 3) Krewulak K. D., Vogel H. J., *Biochim. Biophys. Acta*, **1778**, 1781—1804 (2008).
- 4) Bagg A., Neilands J. B., *Biochemistry*, **26**, 5471—5477 (1987).
- 5) Brenner D. J., Hickman-Brenner F. W., Lee J. V., Steigerwalt A. G., Fanning G. R., Hollis D. G., Farmer J. J., Weaver R. E., Joseph S. W., Seidler R. J., *J. Clin. Microbiol.*, **18**, 816—824 (1983).
- 6) Dalsgaard A., Glerup P., Høybye L. L., Paarup A. M., Meza R., Bernal M., Shimada T., Taylor D. N., *Epidemiol. Infect.*, **119**, 143—149 (1997).
- 7) Yamamoto S., Okujo N., Fujita Y., Saito M., Yoshida T., Shinoda S., *J. Biochem.*, **113**, 538—544 (1993).
- 8) Tanabe T., Takata N., Naka A., Moon Y. H., Nakao H., Inoue Y., Narimatsu S., Yamamoto S., *FEMS Microbiol. Lett.*, **249**, 309—314 (2005).
- 9) Tanabe T., Naka A., Aso H., Nakao H., Narimatsu S., Inoue Y., Ono T., Yamamoto S., *Microbiol. Immunol.*, **49**, 823—834 (2005).
- 10) Funahashi T., Tanabe T., Aso H., Nakao H., Fujii Y., Okamoto K., Narimatsu S., Yamamoto S., *Microbiology*, **149**, 1217—1225 (2003).
- 11) Funahashi T., Tanabe T., Shiuchi K., Nakao H., Yamamoto S., *Biol. Pharm. Bull.*, **32**, 359—365 (2009).
- 12) Wyckoff E. E., Mey A. R., Payne S. M., *BioMetals*, **20**, 405—416 (2007).
- 13) Demarre G., Guérout A. M., Matsumoto-Mashimo C., Rowe-Magnus D. A., Marlière P., Mazel D., *Res. Microbiol.*, **156**, 245—255 (2005).
- 14) Sambrook J., Fritsch E. F., Maniatis T., "Molecular Cloning: A Laboratory Manual," 2nd ed., Cold Spring Harbor Laboratory Press, New York, 1989.
- 15) Heckman K. L., Pease L. R., *Nat. Protoc.*, **2**, 924—932 (2007).
- 16) Tanabe T., Funahashi T., Moon Y. H., Tamai E., Yamamoto S., *Microbiol. Immunol.*, **54**, 606—617 (2010).
- 17) Donnenberg M. S., Kaper J. B., *Infect. Immun.*, **59**, 4310—4317 (1991).
- 18) Keen N. T., Tamaki S., Kobayashi D., Trollinger D., *Gene*, **70**, 191—197 (1988).
- 19) Yamamoto S., Akiyama T., Okujo N., Matsu-ura S., Shinoda S., *Microbiol. Immunol.*, **39**, 759—766 (1995).
- 20) de Lorenzo V., Wee S., Herrero M., Neilands J. B., *J. Bacteriol.*, **169**, 2624—2630 (1987).
- 21) Martin R. G., Gillette W. K., Rhee S., Rosner J. L., *Mol. Microbiol.*, **34**, 431—441 (1999).
- 22) Essén S. A., Bylund D., Holmström S. J., Moberg M., Lundström U. S., *BioMetals*, **19**, 269—282 (2006).
- 23) Mawji E., Gledhill M., Milton J. A., Tarran G. A., Ussher S., Thompson A., Wolff G. A., Worsfold P. J., Achterberg E. P., *Environ. Sci. Technol.*, **42**, 8675—8680 (2008).
- 24) Tortell P. D., Maldonado M. T., Granger J., Price N. M., *FEMS Microbiol. Ecol.*, **29**, 1—11 (1999).
- 25) Winkelmann G., "Iron Transport in Bacteria," ed. by Crosa J. H., Mey A. R., Payne S. M., ASM Press, Washington, D.C., 2004, pp. 437—450.

The *Vibrio parahaemolyticus* *pvuA1* gene (formerly termed *psuA*) encodes a second ferric vibrioferrin receptor that requires *tonB2*

Tomotaka Tanabe¹, Tatsuya Funahashi¹, Noriyuki Okajima², Hiroshi Nakao², Yasuo Takeuchi², Katsushiro Miyamoto³, Hiroshi Tsujibo³ & Shigeo Yamamoto¹

¹College of Pharmaceutical Sciences, Matsuyama University, Matsuyama, Ehime, Japan; ²Graduate School of Medicine, Dentistry and Pharmaceutical Sciences, Okayama University, Okayama, Japan; and ³Osaka University of Pharmaceutical Sciences, Takatsuki, Osaka, Japan

Correspondence: Tomotaka Tanabe, College of Pharmaceutical Sciences, Matsuyama University, 4-2 Bunkyo-cho, Matsuyama, Ehime 790-8578, Japan. Tel.: +81 89 925 7111 (ext 869); fax: +81 89 926 7162; e-mail: ttanabe@cc.matsuyama-u.ac.jp

Received 8 June 2011; revised 15 August 2011; accepted 15 August 2011.
Final version published online 13 September 2011.

DOI: 10.1111/j.1574-6968.2011.02389.x

Editor: Arnoud van Vliet

Keywords

Vibrio parahaemolyticus; TonB-dependent outer-membrane receptor; siderophore; vibrioferrin-utilization gene cluster; ferric vibrioferrin receptor.

Introduction

Most microorganisms absolutely require iron to survive and grow. However, iron bioavailability is often limited owing to its insolubility in aerobic environments at neutral pH. To overcome this iron restriction, many microorganisms biosynthesize and secrete high-affinity iron-chelating molecules, termed siderophores, which serve to solubilize insoluble ferric iron and deliver the ferric siderophore complex into microbial cells (Andrews *et al.*, 2003; Wandersman & Delepelaire, 2004). Most Gram-negative bacteria have developed a sophisticated strategy for ferric siderophore transport that involves an outer membrane receptor, a periplasmic binding protein, and an inner-membrane ATP-binding cassette (ABC) transport system (Miethke & Marahiel, 2007). Transport of the ferric siderophore complexes across the outer

Abstract

We previously reported that the *Vibrio parahaemolyticus* *pvsABCDE* and *psuA-pvuABCDE* operons are involved in the biosynthesis and transport of its own siderophore, vibrioferrin (VF). Of these, *psuA* and *pvuA* encode TonB-dependent outer-membrane proteins (OMPs). Although *pvuA* was characterized as the ferric vibrioferrin receptor gene, the role of the *psuA* product remains unknown. In this study, a growth assay of isogenic *psuA*, *pvuA*, and *psuA-pvuA* double-deletion mutants followed by complementation of the double-deletion mutant with *psuA* or *pvuA* was used to identify *psuA* as a gene encoding an OMP involved in the uptake of ferric VF. Thus, *psuA* and *pvuA* were renamed *pvuA1* and *pvuA2*, respectively. Moreover, we clarified the TonB specificities of PvuA1 and PvuA2, because *V. parahaemolyticus* has three sets of the TonB systems. The triple deletion of *pvuA1*, *tonB1*, and *tonB2*, and the double deletion of *pvuA2* and *tonB2* resulted in the complete loss of growth promotion by VF. This finding indicates that the energy required for PvuA1 and PvuA2 to transport ferric VF across the outer membrane is provided by the TonB2 system and by both the TonB1 and TonB2 systems, respectively.

membrane via the receptors depends on the proton motive force supplied by an inner-membrane complex comprising TonB, ExbB, and ExbD (TonB system) (Noinaj *et al.*, 2010).

Vibrio parahaemolyticus, a halophilic Gram-negative bacterium that inhabits warm brackish waters and river causes watery diarrhea and is transmitted by eating raw or uncooked contaminated seafood (Daniels *et al.*, 2000). We previously reported that *V. parahaemolyticus* possesses multiple iron-acquisition systems, including the utilization of its own siderophore, vibrioferrin (VF) (Funahashi *et al.*, 2002), as well as exogenous siderophores, aerobactin (Funahashi *et al.*, 2003) and ferrichrome (Funahashi *et al.*, 2009). The cluster of genes involved in VF biosynthesis, and secretion and the transport of ferric VF consists of two divergent operons: *pvsABCDE* and *psuA-pvuABCDE* (Tanabe *et al.*, 2003) (Fig. 1a). Although

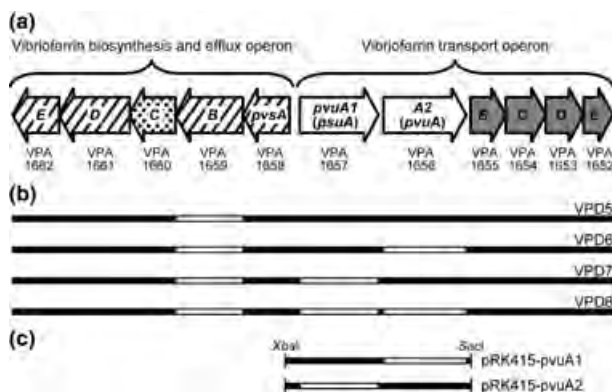


Fig. 1. (a) Genetic organization of the VF utilization gene cluster on *V. parahaemolyticus* chromosome 2 (VPA1652 to VPA1662). The *pvs* and *pvu* operons are involved in the biosynthesis and secretion of VF, and the transport of ferric VF, respectively. Arrows indicate transcriptional directions of the genes. Open arrows, TonB-dependent outer-membrane receptor genes; gray arrows, inner-membrane ABC transporter system genes; hatched arrows, VF biosynthesis genes; dotted arrow, VF secretion gene. (b, c) Schematic representation of the regions deleted from the VF utilization gene cluster in the VPD5, VPD6, VPD7, and VPD8 strains (b) and the DNA inserts in the complementary plasmids, pRK415-pvuA1 and pRK415-pvuA2 (c). Open bars, regions deleted; closed bars, regions not deleted.

both *psuA* and *pvuA* are suggested to encode TonB-dependent outer-membrane proteins (OMPs) on the basis of homology searches, only *pvuA* has been identified as the ferric VF receptor gene. In addition, a BLASTP search revealed that PvuA is homologous to many ferrichrome

receptors, including the *V. parahaemolyticus* FhuA (Funahashi *et al.*, 2009) (25% identity, 42% similarity), rather than *PsuA*. However, we found that a nonpolar deletion mutant of *pvuA* constructed in this study could still use VF as an iron source, suggesting that *V. parahaemolyticus* possesses another ferric VF receptor gene. On the other hand, database searches of the *V. parahaemolyticus* genomic sequences (Makino *et al.*, 2003) and a recent review of the TonB systems in *Vibrio* species (Kuehl & Crosa, 2010) revealed that this bacterium possesses three sets of *tonB* genes in its chromosomes: *tonB1* (VPA0426), *tonB2* (VPA0155), and *tonB3* (VP0163). However, it is unknown which TonB proteins contribute to the energy-coupled transport of ferric VF across the outer membrane. Here, we report that *psuA* encodes another ferric VF receptor protein that exclusively depends on TonB2. Hereafter, the formerly termed *psuA* and *pvuA* genes are renamed *pvuA1* and *pvuA2*, respectively, because both genes encode the ferric VF receptors; *pvu* stands for *V. parahaemolyticus* vibrioferrin utilization.

Materials and methods

Strains, plasmids, and growth conditions

Vibrio parahaemolyticus strains, and *Escherichia coli* strain and plasmids used in this study are listed in Table 1, and Table S1, respectively. *Vibrio parahaemolyticus* VPD5, which carries a deletion in *pvsB* that results in no VF production, was used as a parental strain for the construction

<i>V. parahaemolyticus</i> strains	Description	Reference or source
RIMD2210633	Clinical isolate of serotype O3:K6	Makino <i>et al.</i> (2003)
VPD5	RIMD2210633 $\Delta pvsB$ (vibrioferrin-nonproducer mutant)	Present study
VPD6	VPD5 $\Delta pvuA2$	Present study
VPD7	VPD5 $\Delta pvuA1$	Present study
VPD8	VPD5 $\Delta pvuA1 \Delta pvuA2$	Present study
VPD23	VPD5 $\Delta pvuA2 \Delta tonB1$	Present study
VPD24	VPD5 $\Delta pvuA2 \Delta tonB2$	Present study
VPD25	VPD5 $\Delta pvuA2 \Delta tonB3$	Present study
VPD26	VPD5 $\Delta pvuA2 \Delta tonB1 \Delta tonB2$	Present study
VPD27	VPD5 $\Delta pvuA2 \Delta tonB1 \Delta tonB3$	Present study
VPD28	VPD5 $\Delta pvuA2 \Delta tonB2 \Delta tonB3$	Present study
VPD29	VPD5 $\Delta pvuA2 \Delta tonB1 \Delta tonB2 \Delta tonB3$	Present study
VPD30	VPD5 $\Delta pvuA1 \Delta tonB1$	Present study
VPD31	VPD5 $\Delta pvuA1 \Delta tonB2$	Present study
VPD32	VPD5 $\Delta pvuA1 \Delta tonB3$	Present study
VPD33	VPD5 $\Delta pvuA1 \Delta tonB1 \Delta tonB2$	Present study
VPD34	VPD5 $\Delta pvuA1 \Delta tonB1 \Delta tonB3$	Present study
VPD35	VPD5 $\Delta pvuA1 \Delta tonB2 \Delta tonB3$	Present study
VPD36	VPD5 $\Delta pvuA1 \Delta tonB1 \Delta tonB2 \Delta tonB3$	Present study

Table 1. *Vibrio parahaemolyticus* strains used in the present study

of various mutants to avoid any effects of VF produced by the wild-type strain. *Escherichia coli* β 2155 (Demarre *et al.*, 2005), a diaminopimelic acid (DAP) auxotroph, was grown in Luria–Bertani (LB) medium containing 0.5% NaCl and 0.5 mM DAP. *Vibrio parahaemolyticus* was routinely cultured in LB medium containing 3.0% NaCl (+Fe medium). Appropriate antibiotics were added to the medium at the following concentrations: 10 $\mu\text{g mL}^{-1}$ chloramphenicol, and 15 $\mu\text{g mL}^{-1}$ tetracycline. When required, *V. parahaemolyticus* was grown in LB medium containing 3.0% NaCl supplemented with 25 μM ethylenediamine di-*o*-hydroxyphenylacetic acid (EDDA; Sigma, St. Louis, MO) (–Fe medium) to impose iron limitation (Miles & Khimji, 1975).

Nucleotide and amino acid sequence analyses

The genomic sequence information of *V. parahaemolyticus* RIMD2210633 (Makino *et al.*, 2003) was obtained from the Genome Information Research Center (GIRC) at Osaka University (<http://genome.bio.titech.ac.jp/bacteria/vpara/>). A homology search was carried out using the BLAST program on GIRC or National Center for Biotechnology Information (<http://blast.ncbi.nlm.nih.gov/>) (Altschul *et al.*, 1997).

Growth analysis

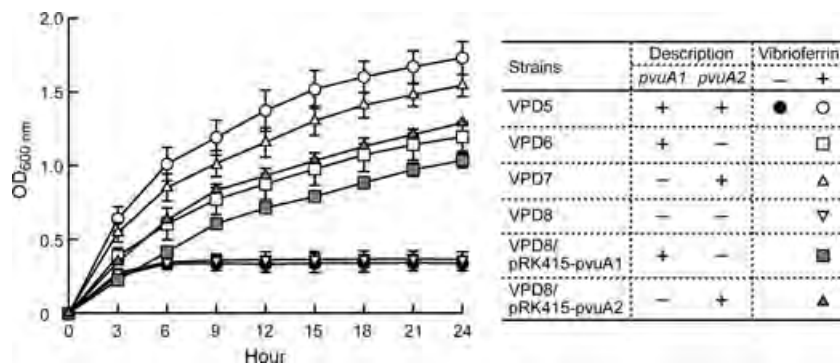
The *V. parahaemolyticus* cultures grown overnight in the +Fe medium were inoculated into the +Fe and –Fe media at an optimal density of 0.005 at 600 nm ($\text{OD}_{600\text{ nm}}$). When required, the –Fe medium was supplemented with VF (Yamamoto *et al.*, 1994) at a final concentration of 20 μM (–Fe + VF medium). The cultures were then shaken at 70 rpm at 37 °C, and the $\text{OD}_{600\text{ nm}}$ was measured every 3 h for 24 h with a biophotorecorder TVS062CA (Advantec, Tokyo, Japan). Although it was reported that EDDA is a strong chelator of ferric iron and the association constant of ferric EDDA (*c.* 10^{34})

(Miles & Khimji, 1975) is higher than that of ferric VF (*c.* 10^{23}) (Amin *et al.*, 2009), growth of VF-nonproducer mutant VPD5 (i.e. $\Delta pvsB$) repressed in the –Fe medium was restored in the –Fe + VF medium (Fig. 2). This indicates that a very small amount of ferric VF required for the growth of *V. parahaemolyticus* could be supplied successively by equilibrium, although almost all ferric iron would be ferric EDDA in the –Fe + VF medium. Thus, the medium prepared was successfully used to estimate growth promotion of the mutants by VF.

Construction of nonpolar gene-deletion mutants

The primers used to construct the gene-deletion fragments and confirm gene deletions in various mutants are listed in Table S2. PCR amplicons with the respective deletions in the *V. parahaemolyticus* *pvsB*, *pvuA1*, *pvuA2*, *tonB1*, *tonB2*, and *tonB3* genes were prepared by PCR-driven overlap extension as described previously (Heckman & Pease, 2007; Tanabe *et al.*, 2010). Briefly, the upstream and downstream regions of the respective genes were amplified in a reaction with corresponding primer pairs #1 and #2, and #3 and #4 shown in Table S2, respectively. The upstream and downstream amplicons were then used as templates in a second PCR using primer #1 and #4 to construct the gene-deletion fragments. Each gene-deletion fragment was ligated into an R6K-ori suicide vector pXAC623 (Kuroda *et al.*, 2005). The resultant plasmids were each transformed into *E. coli* β 2155 and mobilized into an appropriate *V. parahaemolyticus* strain by filter mating. The resultant merodiploids were selected on LB agar plates with chloramphenicol at 10 $\mu\text{g mL}^{-1}$ without DAP. The merodiploids were then cultured on VDS-broth agar plates (1% polypepton, 0.5% yeast extract, 30 mM NaCl, 55 mM KCl, 10% sucrose, and 2.5% agar) (Kuroda *et al.*, 2005) at 25 °C for 30 h. Sucrose-resistant and chloramphenicol-sensitive colonies were selected, and the deleted DNA regions were confirmed by PCR analysis

Fig. 2. VF-mediated growth promotion in VPD5 (parental $\Delta pvsB$), VPD6 ($\Delta pvuA2$), VPD7 ($\Delta pvuA1$), VPD8 ($\Delta pvuA1\Delta pvuA2$), VPD8/pRK415-*pvuA1*, and VPD8/pRK415-*pvuA2*. Cells pre-cultured overnight in the +Fe medium were inoculated at a final $\text{OD}_{600\text{ nm}}$ of 0.005 into the –Fe medium with or without VF at 20 μM . The $\text{OD}_{600\text{ nm}}$ was measured every 3 h for 24 h. Data are shown as means \pm SD from three separate experiments.



of their chromosomal DNAs (Fig. S1), and a lack of VF productivity was tested by a chrome azurol S liquid assay (Schwyn & Neilands, 1987) (data not shown).

Construction of *trans*-complementation strains

The primers used to construct PCR amplicons for complementary experiments are listed in Table S2. To perform complementation experiments for *pvuA1* and *pvuA2*, each PCR amplicon containing the full-length *pvuA1* or *pvuA2* gene, which was amplified with the chromosomal DNA from the VPD6 or VPD7 strain (Fig. 1b), respectively, was ligated into a broad host-range plasmid, pRK415 (Keen *et al.*, 1988). The resultant plasmids, pRK415-*pvuA1* and pRK415-*pvuA2* (Fig. 1c), were each mobilized into VPD8 (Fig. 1b) to construct VPD8/pRK415-*pvuA1* and VPD8/pRK415-*pvuA2*, respectively, as described previously (Tanabe *et al.*, 2010).

Preparation of OMP-enriched fractions

The OMP-enriched fractions were prepared from the VPD5, VPD6, VPD7, VPD8, VPD8/pRK415-*pvuA1*, and VPD8/pRK415-*pvuA2* strains (see Fig. 1b,c for a schematic representation) grown in the +Fe or -Fe medium, as described previously (Yamamoto *et al.*, 1995). Five residues of the N-terminal amino acid sequences of the iron-repressible OMPs (IROMPs) from the relevant strains were determined using a Procise 491 HT protein sequencer (Applied Biosystems, Foster City, CA) with an online phenylthiohydantoin derivative analyzer.

Results and discussion

Growth assay of the *pvuA2* deletion mutant for VF utilization

The gene responsible for the 78-kDa IROMP was identified as *pvuA2*, whose insertion mutant generated by Campbell-type recombination resulted in the loss of the capability to utilize VF (Funahashi *et al.*, 2002). However, because the *pvuA1-pvuA2-pvuBCDE* genes are linked as a single operon (Tanabe *et al.*, 2003) (Fig. 1), a foreign DNA insertion within *pvuA2* is expected to exert a polar effect on the expression of *pvuBCDE* encoding the periplasmic binding protein-dependent ABC transporter for ferric VF. Therefore, to obtain highly precise information regarding the function of *pvuA2*, the VPD6 strain (a non-polar *pvuA2* deletion mutant) was generated from the parental VPD5 strain (*pvsB* deletion mutant unable to produce VF), which failed to grow in the -Fe medium that did not contain VF (Fig. 2). SDS-PAGE analysis showed that the 78-kDa IROMP, which has the N-termi-

nal amino acid sequence APAAK – identical to that deduced from *pvuA2* – was not found in the OMP-enriched fractions prepared from the *pvuA2* deletion mutant VPD6 (Fig. 3, lane 3). However, it is intriguing that VPD6 still exhibited more than 50% growth after 24 h incubation, as compared with the growth of VPD5, in the -Fe + VF medium (Fig. 2). This indicates that at least one more outer-membrane receptor for ferric VF must be present in *V. parahaemolyticus*.

Identification of *pvuA1*, another ferric VF receptor gene

We previously showed that *V. parahaemolyticus* possesses *pvuA1* located in tandem with *pvuA2* on chromosome 2; however, we were unable to elucidate the function of *pvuA1* (Funahashi *et al.*, 2002). Bacterial genes involved in iron uptake as well as the biosynthesis and secretion of siderophores are often clustered within a genome. This suggests that *pvuA1* in the VF-utilization cluster encodes another ferric VF receptor. To clarify this, VPD7 and VPD8 were generated from VPD5 and VPD6, respectively (see Fig. 1b for a schematic presentation). Comparison of the IROMP profiles obtained from VPD7 and VPD8 clearly showed the disappearance of the 83-kDa PvuA1 band, which has the N-terminal amino acid sequence SEETN; this sequence is identical to that deduced from *pvuA1*, which was expressed in VPD5 and VPD6 when

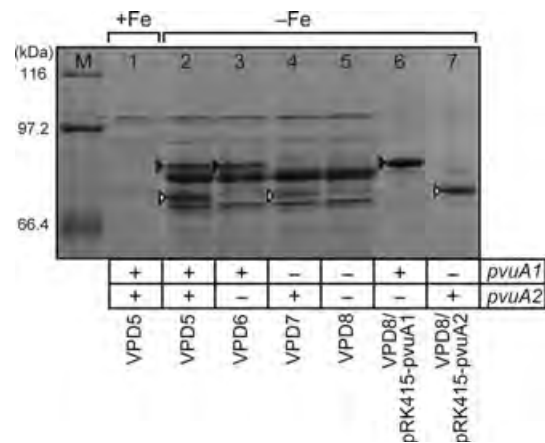


Fig. 3. SDS-PAGE analysis of IROMPs from VPD5 (parental $\Delta pvsB$), VPD6 ($\Delta pvuA2$), VPD7 ($\Delta pvuA1$), VPD8 ($\Delta pvuA1\Delta pvuA2$), VPD8/pRK415-*pvuA1*, and VPD8/pRK415-*pvuA2* strains. The OMP fractions were prepared from cells grown in the +Fe or -Fe medium. SDS-PAGE was carried out in a 7.5% SDS-polyacrylamide gel (length, 130 mm) with a constant current of 15 mA at 4 °C; the gel was stained with Coomassie Brilliant Blue. Lanes 1–5 and 6–7 were loaded with 30 and 3 μ g IROMPs, respectively. This figure shows only the relevant portions of the gel. Lane M, molecular weight marker proteins; open arrowheads, 78-kDa PvuA2 protein; closed arrowheads, 83-kDa PvuA1 protein.

grown in the $-Fe + VF$ medium (Fig. 3, lanes 2–5). As shown in Fig. 2, the growth of VPD7 after 24-h incubation in the $-Fe + VF$ medium was reduced by 10% compared with that of the parental VPD5 in the same medium; meanwhile, VPD8, in which both *pvuA1* and *pvuA2* were defective, was completely impaired by VF-mediated growth promotion. In addition, VPD8 restored the expressions of PvuA1 and PvuA2 when it was complemented with pRK415-pvuA1 and pRK415-pvuA2, respectively (Fig. 3, lanes 6 and 7), indicating the ability to utilize VF (Fig. 2).

It has recently been reported that VF-Fe is converted to the photoproduct (VF*) and ferrous iron (immediately converted to ferric iron) by photolysis in an aqueous solution containing 0.7 M KNO_3 and 50 mM of the appropriate buffer (Amin *et al.*, 2009). It was of great interest to determine whether VF* is also involved in transport of iron. We then prepared VF* according to the method of Amin *et al.* (2009). However, the addition of VF* at 20 μM to the $-Fe$ medium could not promote the growth of VPD5, at least indicating that both of PvuA1 and PvuA2 do not function as the receptors for VF*-Fe even if it is produced under the medium conditions used in this study. In addition, no difference between light and dark conditions was observed in the

growth rate of VPD5 in the $-Fe + VF$ medium. VPD5, VPD6, and VPD7 could also grow in the $-Fe + VF$ medium illuminated prior to use as well as in the $-Fe + VF$ medium not illuminated, but not VPD8. These results indicate that *V. parahaemolyticus* is unable to utilize VF* as the iron source, and that photolysis of VF-Fe to VF* may be hard to occur in the $-Fe + VF$ medium (red-brown-colored). Therefore, we concluded that both of *pvuA1* and *pvuA2* encode the IROMP receptors for ferric VF, although the amino acid sequences deduced from these genes exhibited no significant homology to each other.

Moreover, VPD8 as well as VPD5 was able to grow in the $-Fe$ medium containing hydroxamate siderophores such as ferrichrome and ferrioxamine at 20 μM , at least indicating that PvuA1 and PvuA2 do not function as the receptors for these hydroxamates. On the other hand, our previous finding that the growth of the TNB4 strain (a *pvuB*-disrupted mutant with defective periplasmic binding protein) under iron-limiting conditions is completely repressed even in the presence of VF (Tanabe *et al.*, 2003) supports the notion that the PvuBCDE inner-membrane transport system contributes to the function of PvuA1 the same way as it does to the function of PvuA2.

Table 2. TonB specificity of PvuA1 and PvuA2 in VF utilization

Strains*	Description†					VF-mediated growth promotion‡
	<i>pvuA1</i>	<i>pvuA2</i>	<i>tonB1</i>	<i>tonB2</i>	<i>tonB3</i>	
(a) A series of gene-deletion mutants of <i>tonB</i> genes generated from VPD6						
VPD6	+	–	+	+	+	+
VPD23	+	–	–	+	+	+
VPD24	+	–	+	–	+	–
VPD25	+	–	+	+	–	+
VPD26	+	–	–	–	+	–
VPD27	+	–	–	+	–	+
VPD28	+	–	+	–	–	–
VPD29	+	–	–	–	–	–
(b) A series of gene-deletion mutants of <i>tonB</i> genes generated from VPD7						
VPD7	–	+	+	+	+	+
VPD30	–	+	–	+	+	+
VPD31	–	+	+	–	+	+
VPD32	–	+	+	+	–	+
VPD33	–	+	–	–	+	–
VPD34	–	+	–	+	–	+
VPD35	–	+	+	–	–	+
VPD36	–	+	–	–	–	–

*A series of deletion mutants were constructed from VPD5, a mutant unable to produce VF. VPD23 to VPD29 and VPD30 to VPD36 are derivatives of VPD6 and VPD7, respectively.

†+, Gene present; –, gene deleted.

‡Cells were inoculated at a final $OD_{600\text{ nm}}$ of 0.005 into the $-Fe$ medium supplemented with VF at 20 μM , and the $OD_{600\text{ nm}}$ was measured after incubation for 24 h. The growth curves of parental VPD6 and VPD7 strains are shown in Fig. 2. + indicates the growth is approximately equal to the parental strain; – indicates that no VF-mediated growth promotion was observed. Experiments were repeated twice with the same results.

TonB specificities of the two ferric VF receptors

In Gram-negative bacteria, the TonB system is essential for providing energy for ferric siderophore transport via an outer-membrane receptor (Postle & Larsen, 2007). The genomic sequence of *V. parahaemolyticus* RIMD2210633 was predicted to possess three sets of paralogous genes of the TonB systems on chromosomes 1 (TonB3) and 2 (TonB1 and TonB2). To determine which TonB systems contribute to the transport of ferric VF via PvuA1 and PvuA2, a series of deletion mutants of these *tonB* genes were constructed from VPD6 and VPD7, and used to examine the TonB specificities toward PvuA1 and PvuA2. The growth of VPD23, VPD25, and VPD27 – all of which have the native *pvuA1* and *tonB2*, but not *pvuA2* – was promoted in the –Fe + VF medium to an extent similar to that of VPD6; in contrast, VPD24, VPD26, VPD28, and VPD29 – all of which have the native *pvuA1*, but not *pvuA2* and *tonB2* – failed to grow in the same medium (Table 2a). Meanwhile, the single-deletion mutants of the *tonB* genes, VPD30, VPD31, and VPD32 generated from VPD7 – all of which have the native *pvuA2* in addition to either *tonB1* or *tonB2* or both – grew well in the –Fe + VF medium, similar to VPD7 (Table 2b). In contrast, VPD34 and VPD35, which have *pvuA2* in addition to either *tonB1* or *tonB2*, were also able to grow in the same medium; however, VPD33, which has *pvuA2* and *tonB3* but neither *tonB1* nor *tonB2*, showed a complete loss of VF-mediated growth promotion (Table 2b). These findings indicate that TonB2 but not TonB1 functions in the transport of ferric VF via PvuA1, whereas both TonB1 and TonB2 proteins operate in the transport of ferric VF via PvuA2. In addition, TonB3 may not be involved at least in the transport of ferric VF.

In conclusion, we showed that PvuA1 serves as a ferric VF receptor together with PvuA2, although these proteins showed no significant amino acid sequence similarity. Several bacteria are reported to possess multiple outer-membrane receptors to recruit exogenous siderophores such as the ferric enterobactin receptors CfrA and CfrB in *Campylobacter* (Xu *et al.*, 2010) and VctA and IrgA in *Vibrio cholerae* (Mey *et al.*, 2002). However, little is known about multiple receptors for a cognate siderophore with the exception of the type I ferric pyoverdine receptors FpvA and FpvB in *Pseudomonas aeruginosa* (Ghysels *et al.*, 2004). Because *fpvA* and *fpvB* are located on separate replicons and both proteins exhibit 54% amino acid sequence similarity, our study presents the first examples of two IROMPs encoded by different tandem genes in the same operon functioning as the receptors for the same cognate siderophore. This strategy may provide an alternative backup system – that is, protection against mutational loss – for VF-mediated iron

acquisition in *V. parahaemolyticus*. However, the coexistence of *pvuA1* and *pvuA2* in the VF-utilization cluster raise the possibility that either *pvuA1* or *pvuA2* actually preferentially binds and transports an unknown siderophore ligand that is structurally related to VF.

We also determined the specificities of the ferric VF receptors on three sets of TonB systems for ferric VF. It is noteworthy that TonB2 is exclusively required for the PvuA1-mediated transport of ferric VF; meanwhile, the PvuA2-mediated transport of ferric VF is supported by both TonB1 and TonB2. Further studies are needed to understand the specificities of TonB for other *V. parahaemolyticus* receptors for the uptake of heme/hemoglobin as well as exogenous siderophores such as aerobactin (Funahashi *et al.*, 2003) and ferrichrome (Funahashi *et al.*, 2009).

Acknowledgements

We thank T. Kuroda for providing *E. coli* β 2155 and a suicide vector pXAC623 and for his helpful comments. This work was supported in part by a grant from the Cooperative and Collaboration Agreement between Ehime University and Matsuyama University.

References

- Altschul SF, Madden TL, Schaffer AA, Zhang J, Zhang Z, Miller W & Lipman DJ (1997) Gapped BLAST and PSI-BLAST: a new generation of protein database search programs. *Nucleic Acids Res* **25**: 3389–3402.
- Amin SA, Green DH, Kupper FC & Carrano CJ (2009) Vibrioferrin, an unusual marine siderophore: iron binding, photochemistry, and biological implications. *Inorg Chem* **48**: 11451–11458.
- Andrews SC, Robinson AK & Rodriguez-Quinones F (2003) Bacterial iron homeostasis. *FEMS Microbiol Rev* **27**: 215–237.
- Daniels NA, MacKinnon L, Bishop R *et al.* (2000) *Vibrio parahaemolyticus* infections in the United States, 1973–1998. *J Infect Dis* **181**: 1661–1666.
- Demarre G, Guerout AM, Matsumoto-Mashimo C, Rowe-Magnus DA, Marliere P & Mazel D (2005) A new family of mobilizable suicide plasmids based on broad host range R388 plasmid (IncW) and RP4 plasmid (IncAlpha) conjugative machineries and their cognate *Escherichia coli* host strains. *Res Microbiol* **156**: 245–255.
- Funahashi T, Moriya K, Uemura S, Miyoshi S, Shinoda S, Narimatsu S & Yamamoto S (2002) Identification and characterization of *pvuA*, a gene encoding the ferric vibrioferrin receptor protein in *Vibrio parahaemolyticus*. *J Bacteriol* **184**: 936–946.
- Funahashi T, Tanabe T, Aso H, Nakao H, Fujii Y, Okamoto K, Narimatsu S & Yamamoto S (2003) An iron-regulated gene

- required for utilization of aerobactin as an exogenous siderophore in *Vibrio parahaemolyticus*. *Microbiology* **149**: 1217–1225.
- Funahashi T, Tanabe T, Shiuchi K, Nakao H & Yamamoto S (2009) Identification and characterization of genes required for utilization of desferri-ferrichrome and aerobactin in *Vibrio parahaemolyticus*. *Biol Pharm Bull* **32**: 359–365.
- Ghysels B, Dieu BT, Beatson SA, Pirnay JP, Ochsner UA, Vasil ML & Cornelis P (2004) FpvB, an alternative type I ferrityoverdine receptor of *Pseudomonas aeruginosa*. *Microbiology* **150**: 1671–1680.
- Heckman KL & Pease LR (2007) Gene splicing and mutagenesis by PCR-driven overlap extension. *Nat Protoc* **2**: 924–932.
- Keen NT, Tamaki S, Kobayashi D & Trollinger D (1988) Improved broad-host-range plasmids for DNA cloning in gram-negative bacteria. *Gene* **70**: 191–197.
- Kuehl CJ & Crosa JH (2010) The TonB energy transduction systems in *Vibrio* species. *Future Microbiol* **5**: 1403–1412.
- Kuroda T, Mizushima T & Tsuchiya T (2005) Physiological roles of three Na⁺/H⁺ antiporters in the halophilic bacterium *Vibrio parahaemolyticus*. *Microbiol Immunol* **49**: 711–719.
- Makino K, Oshima K, Kurokawa K *et al.* (2003) Genome sequence of *Vibrio parahaemolyticus*: a pathogenic mechanism distinct from that of *V. cholerae*. *Lancet* **361**: 743–749.
- Mey AR, Wyckoff EE, Oglesby AG, Rab E, Taylor RK & Payne SM (2002) Identification of the *Vibrio cholerae* enterobactin receptors VctA and IrgA: IrgA is not required for virulence. *Infect Immun* **70**: 3419–3426.
- Miethke M & Marahiel MA (2007) Siderophore-based iron acquisition and pathogen control. *Microbiol Mol Biol Rev* **71**: 413–451.
- Miles AA & Khimji PL (1975) Enterobacterial chelators of iron: their occurrence, detection, and relation to pathogenicity. *J Med Microbiol* **8**: 477–490.
- Noinaj N, Guillier M, Barnard TJ & Buchanan SK (2010) TonB-dependent transporters: regulation, structure, and function. *Annu Rev Microbiol* **64**: 43–60.
- Postle K & Larsen RA (2007) TonB-dependent energy transduction between outer and cytoplasmic membranes. *Biometals* **20**: 453–465.
- Schwyn B & Neilands JB (1987) Universal chemical assay for the detection and determination of siderophores. *Anal Biochem* **160**: 47–56.
- Tanabe T, Funahashi T, Nakao H, Miyoshi S, Shinoda S & Yamamoto S (2003) Identification and characterization of genes required for biosynthesis and transport of the siderophore vibrioferrin in *Vibrio parahaemolyticus*. *J Bacteriol* **185**: 6938–6949.
- Tanabe T, Funahashi T, Moon YH, Tamai E & Yamamoto S (2010) Identification and characterization of a *Vibrio mimicus* gene encoding the heme/hemoglobin receptor. *Microbiol Immunol* **54**: 606–617.
- Wandersman C & Delepelaire P (2004) Bacterial iron sources: from siderophores to hemophores. *Annu Rev Microbiol* **58**: 611–647.
- Xu F, Zeng X, Haigh RD, Ketley JM & Lin J (2010) Identification and characterization of a new ferric enterobactin receptor, CfrB, in *Campylobacter*. *J Bacteriol* **192**: 4425–4435.
- Yamamoto S, Okujo N, Yoshida T, Matsuura S & Shinoda S (1994) Structure and iron transport activity of vibrioferrin, a new siderophore of *Vibrio parahaemolyticus*. *J Biochem* **115**: 868–874.
- Yamamoto S, Akiyama T, Okujo N, Matsu-ura S & Shinoda S (1995) Demonstration of a ferric vibrioferrin-binding protein in the outer membrane of *Vibrio parahaemolyticus*. *Microbiol Immunol* **39**: 759–766.

Supporting information

Additional Supporting Information may be found in the online version of this article:

Fig. S1. PCR confirmation of the deletions of *pvuA1* and *pvuA2* (a), and *tonB1*, *tonB2*, and *tonB3* (b) on *V. parahaemolyticus* chromosomes.

Table S1. *E. coli* strain and plasmids used in this study.

Table S2. PCR primers used in this study.

Please note: Wiley-Blackwell is not responsible for the content or functionality of any supporting materials supplied by the authors. Any queries (other than missing material) should be directed to the corresponding author for the article.

SHORT
COMMUNICATIONIdentification of key amino acids responsible
for the distinct aggregation properties of
microtubule-associated protein 2 and tauCe Xie,^{*,†} Yoshiyuki Soeda,[‡] Yuki Shinzaki,[†] Yasuko In,[§] Koji Tomoo,[§]
Yasuo Ihara[†] and Tomohiro Miyasaka[†]^{*}Key Laboratory for Cellular and Molecular Biology of Liaoning Province, College of Basic Medical
Sciences, Dalian Medical University, Dalian, Liaoning, China[†]Department of Neuropathology, Faculty of Life and Medical Sciences, Doshisha University,
Kyotanabe, Kyoto, Japan[‡]Department of Aging Neurobiology, Center for Development of Advanced Medicine for Dementia,
National Center for Geriatrics and Gerontology, Obu, Aichi, Japan[§]Department of Physical Chemistry, Osaka University of Pharmaceutical Sciences, Takatsuki, Osaka,
Japan**Abstract**

The carboxyl-terminal sequence of tau composes the framework for its intracellular inclusions that appear in diverse neurodegenerative disorders known as tauopathies. However, microtubule-associated protein 2 (MAP2), which contains a homologous carboxyl-terminal sequence of tau, is undetectable in the mature tau inclusions. The mechanisms underlying this phenomenon have remained largely unknown. Here, we show that tau and MAP2 have different aggregation properties: tau aggregates to form filaments but MAP2

remains to be granules. Exchanging ²²¹YKPV²²⁴ of tau (ON3R) near the PHF6 motif for ³⁴⁰TKKI³⁴³ of MAP2c profoundly changed aggregation properties, suggesting that the YKPV motif is important for filament formation, whereas the TKKI motif is for granule formation. Thus, these minimal sequences may determine the different fates of tau and MAP2 in the formation of inclusions in tauopathies.

Keywords: aggregation, inclusion, MAP2, microtubule-associated protein 2, tau, tauopathies.

J. Neurochem. (2015) **135**, 19–26.

Abnormal protein aggregation is observed in a variety of diseases such as Huntington's disease, Creutzfeldt–Jakob disease, Parkinson's disease, and tauopathies. The aggregations of these distinct proteins appear to represent the major pathological process (Ross and Poirier 2004). The intracellular neurofibrillary tangles (NFTs) comprising aggregates of tau in the central nervous system are the major pathological hallmarks of tauopathies including Alzheimer's disease (AD), frontotemporal dementia, and Parkinsonism linked to chromosome 17 (FTDP-17) (Lee *et al.* 2001; Mandelkow and Mandelkow 2012).

The microtubule-associated protein tau has the microtubule-binding domains (MTBDs) consisting of three or four imperfect repeats, which are called 3 repeat (3R)-tau or 4 repeat (4R)-tau, respectively, and are located in the carboxyl-terminal region. Neurons contain a tau homolog, named

microtubule-associated protein 2 (MAP2). MAP2 also has MTBDs, which are typically of three imperfect repeats. Thus, both tau and MAP2 have homologous carboxyl-terminal regions and are considered to evolve from the same ancient protein (Dehmelt and Halpain 2004). Previous studies have indicated that the core of NFTs is made up of the carboxyl-terminal sequence of tau (Kondo *et al.* 1988; Wischik *et al.* 1988). This raises the possibility that MAP2 is also involved in NFT formation. In recent studies, we examined the

Received May 29, 2015; accepted June 19, 2015.

Address correspondence and reprint requests to Tomohiro Miyasaka, Department of Neuropathology, Faculty of Life and Medical Sciences, Doshisha University, 1-3 Tatara Miyakodani, Kyotanabe, Kyoto 610-0394, Japan. E-mail: tomiyasa@mail.doshisha.ac.jp

Abbreviations used: AD, Alzheimer's disease; MAP2, microtubule-associated protein 2; NFTs, neurofibrillary tangles; ThT, thioflavin T.

relationship between the carboxyl-terminal sequences of tau and MAP2 and their roles in the inclusion formation in AD brains. Our results showed that the carboxyl-terminal sequence of tau is involved in the mature inclusions, whereas the homologous carboxyl-terminal sequence of MAP2 is not detected (Xie *et al.* 2014). These findings led us to investigate what causes the different fates of tau and MAP2 in tauopathies.

Here, we compared the aggregation properties of full-length tau and MAP2 containing wild-type or mutant sequences. We found that the aggregation properties of tau and MAP2 are determined solely by their homologous carboxyl-terminal sequences. Tau aggregated to form filaments, whereas MAP2 aggregated to granules. According to the previous study, the motif PHF6 comprising six-amino acid sequence VQIVYK is required for tau fibril formation (von Bergen *et al.* 2001). Therefore, we compared the corresponding amino acid sequences of tau and MAP2 around the PHF6 motif, and found a similar sequence of 11 amino acids (VQIVXKXXDLS) in tau and MAP2. To our surprise, the different aggregation properties of tau and MAP2 could be changed by exchanging a few amino acids in the 11 amino acids. This finding indicated that these amino acids are the key to determine the aggregation properties of the two microtubule-associated proteins.

Experimental procedures

Chemicals and proteins

Heparin sodium was obtained from ACROS Organics (Geel, Belgium). Thioflavin T (ThT) was purchased from Waldeck GmbH & Co. KG (Münster, Germany). Human tau cDNA cloned in the pRK172 vector was a gift from Dr M. Goedert. Human MAP2c cDNA was amplified and cloned into *Nde*I- and *Eco*RI-digested sites of the pRK172 vector. Site-directed mutagenesis of constructs was performed by PCR and confirmed by DNA sequencing. Proteins were purified as described in a previous study (Xie *et al.* 2014). Briefly, the recombinant proteins expressed in *Escherichia coli* strain BL21(DE3) were applied to a phosphocellulose column and eluted with a gradient of 0.1–0.3 M NaCl. Protein-containing fractions were purified further by ammonium sulfate precipitation. Finally, the heat-stable supernatant was fractionated by reversed-phase HPLC (Cosmosyl Protein-R; Nacalai Tesque, Inc., Kyoto, Japan). The purified proteins were quantified by sodium dodecyl sulfate–polyacrylamide gel electrophoresis followed by Coomassie brilliant blue staining.

Aggregation assay

The aggregation of recombinant proteins was induced with heparin as described previously (Xie *et al.* 2014). Briefly, 10 μ M recombinant proteins were mixed with 60 μ g/mL heparin sodium, 100 mM NaCl, 10 μ M ThT, and 10 mM HEPES (pH 7.4). ThT fluorescence of the mixture was measured at the indicated time points at 465 ± 35 nm (excitation) and 535 ± 25 nm (emission).

Atomic force microscopy

Morphology of the aggregated proteins was viewed using a modification of a previously described protocol (Maeda *et al.* 2007). After the aggregation assay, samples that included the aggregates were loaded onto mica and incubated at room temperature (22–26°C) for 30 min in a moist box. The mica was washed with Milli-Q water, and the aggregates were imaged by atomic force microscope (SPM9700; Shimadzu Corp., Kyoto, Japan). Two or three images ($2 \times 2 \mu$ m) were obtained from the surface of the mica coated with the aggregates.

Molecular dynamic analysis

Molecular dynamics (MD) of peptides were performed by CHARMM (Brooks *et al.* 1983) in DS modeling program package (Accelrys Software Inc., San Diego, CA, USA). The simulation was performed in vacuum using the CHARMM force field. Two methods, Steepest Descents and Conjugate Gradients, were used in the energy minimization. The total calculation number was 2000 with 1 fs for one calculation. The equilibration dynamics of the experimental temperature were calculated 10 000 times with 1 fs for one calculation. Finally, the dynamics of 100 productions were saved for each system.

Results

The carboxyl-terminal sequences of tau and MAP2 determine their aggregation properties

Because MAP2 typically contains 3R MTBDs and the shortest isoform MAP2c has a similar molecular weight as tau, we compared MAP2c and 3R-tau in this study. Our previous studies suggested that tau and MAP2 have different aggregation properties (Xie *et al.* 2014). However, it was unknown which regions of tau and MAP2 determine the different aggregation properties. Thus, we asked whether the homologous carboxyl-terminal sequence of tau and MAP2 is important for their aggregation properties. To address this issue, we expressed and purified recombinant full-length 3R-tau and MAP2c from *E. coli*. The homologous 160-amino acid carboxyl-terminal sequences of tau and MAP2 were exchanged with each other to obtain two chimeric proteins, which were named tauN–MAP2C and MAP2N–tauC (Fig. 1a). Aggregations of the following proteins, tau, MAP2, tauN–MAP2C, and MAP2N–tauC were induced with heparin and monitored by the ThT fluorescence, which reflects the amount of β -pleated sheet structure (Fig. 1b). The ThT fluorescence value of tau increased constantly to a plateau in 24 h, whereas that of MAP2 stayed at a lower level. This suggested that tau and MAP2 have different aggregation properties, which is also consistent with the finding in our previous studies (Xie *et al.* 2014).

To identify which region, the amino-terminal or the carboxyl-terminal sequence, is the key that determines the aggregation properties, the two chimeric proteins were incubated with heparin. The aggregation properties of MAP2N–tauC were similar to that of tau, whereas the

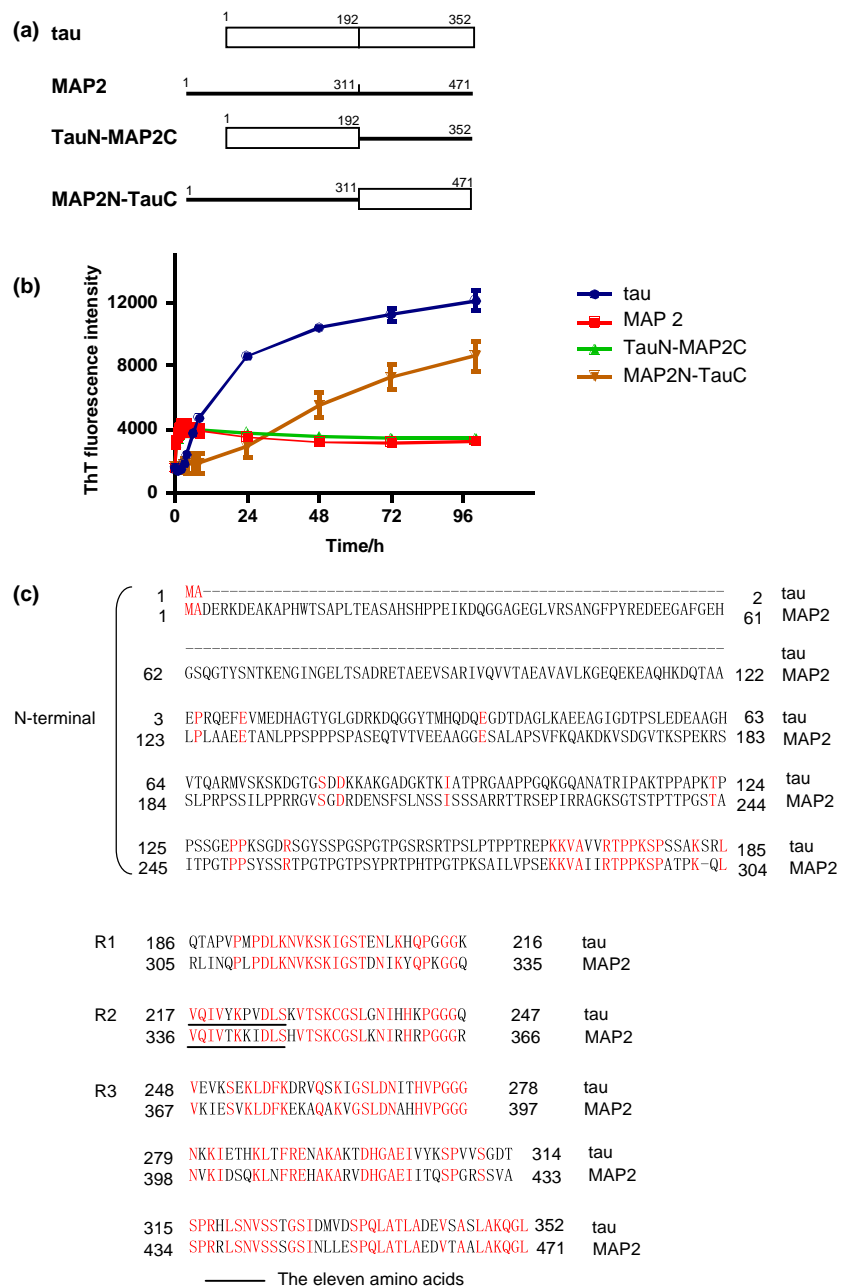


Fig. 1 The aggregation properties of tau and MAP2 are determined by the homologous carboxyl-terminal sequences. (a) Bar diagrams of tau (0N3R), MAP2c, and their chimeric proteins. The numbers shown above indicate the position of amino acids. (b) Thioflavin T (ThT) fluorescence of tau, MAP2, and chimeric protein aggregations was measured at the indicated time (h). Error bars represent SD; $n = 3$. (c) Comparison of the amino acid sequences of tau (0N3R) and MAP2c. The identical amino acids are shown in red. R, repeat; (d) ThT fluorescence of tau, MAP2, tau-TKKI, and MAP2-YKPV aggregations was measured at the indicated time points. Error bars represent SD; $n = 4$. (e) (AFM) imaging of tau, MAP2, tau-TKKI, and MAP2-YKPV aggregations. Arrows indicate the filaments that are formed from MAP2-YKPV. Bars = 400 nm. Note that exchanging the corresponding amino acids between tau and MAP2 (T and Y, K and P, and I and V) reversed their aggregation properties and that MAP2-YKPV aggregated to filaments but tau-TKKI remained granules.

aggregation properties of tauN-MAP2C were similar to that of MAP2. This suggested that the aggregation properties of tau and MAP2 depend on the homologous carboxyl-terminal sequence (Fig. 1b).

Exchanging three amino acids between tau and MAP2 remarkably alters their aggregation properties

The carboxyl-terminal sequences of tau and MAP2 are very similar and about 70% of the amino acids match completely (Fig. 1c). We next asked which amino acids in the carboxyl terminus are important for the different aggregation properties. Because the PHF6 motif (VQIVYK) is required for tau

fibril formation (von Bergen *et al.* 2001), we compared the corresponding amino acid sequences of tau and MAP2 around the PHF6 motif and found a particular sequence of 11 amino acids (VQIVXKXXDLS) in tau and MAP2, as shown in Fig. 1(c). In the 11-amino acid sequence, only three amino acids differed between tau and MAP2; that is, the corresponding sequence of ²²¹YKPV²²⁴ in tau (0N3R) was replaced by ³⁴⁰TKKI³⁴³ in MAP2c.

To examine whether the small changes regulate the different aggregation properties of tau and MAP2, we constructed, expressed, and purified site-directed mutant proteins in which YKPV of tau and TKKI of MAP2 were

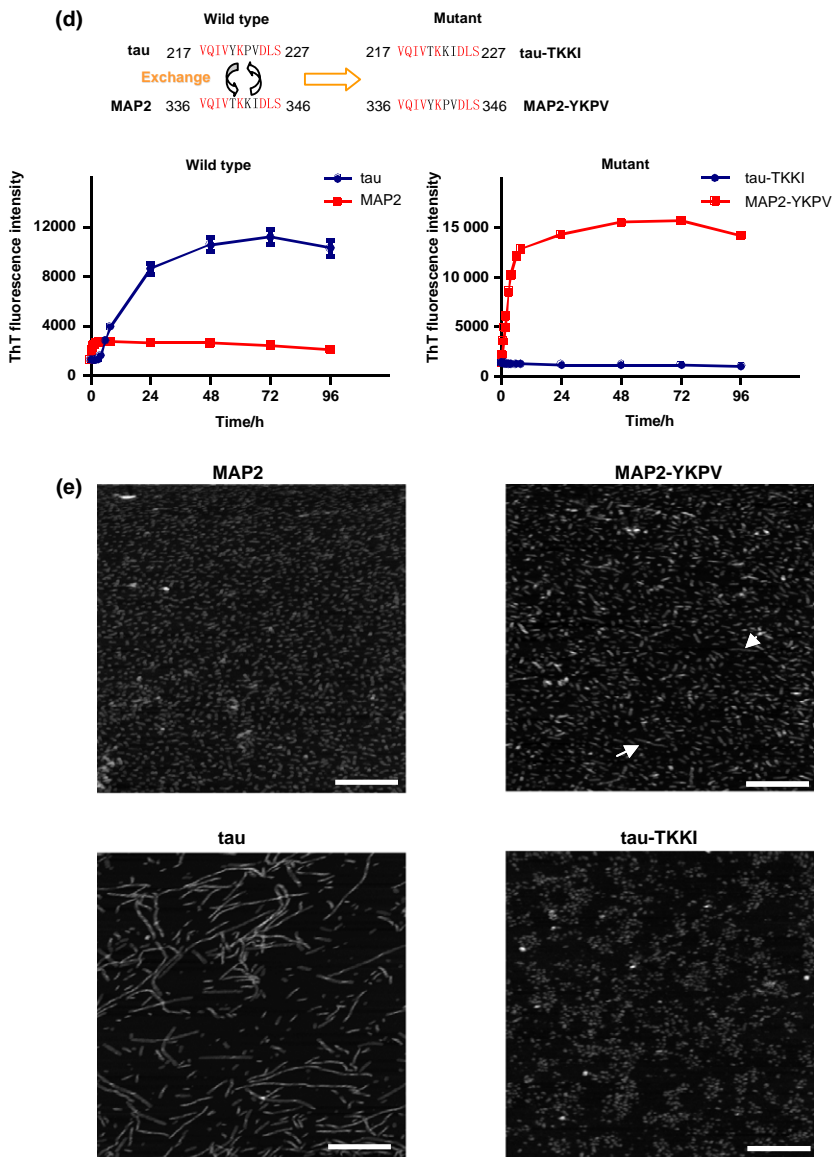


Fig. 1 Continued.

exchanged to obtain two mutant proteins, tau-TKKI and MAP2-YKPV (Fig. 1d, upper). To our surprise, the aggregation properties of tau and MAP2 monitored by ThT fluorescence were greatly altered by exchanging just the three amino acids (Fig. 1d, lower). The aggregation products after 7-day incubation were imaged by atomic force microscopy. As shown in Fig. 1(e), for the wild-type proteins, tau clearly aggregated to form filaments, whereas MAP2 formed only granules. For mutants, tau-TKKI, which contained three amino acids of MAP2, showed MAP2-like aggregation properties in that only granules were formed. By contrast, MAP2-YKPV, which contained three amino acids of tau, led to filament formation, although the filaments were shorter than those formed by tau (Fig. 1e). These results clarified that the small difference between YKPV and TKKI

determined the different aggregation properties of tau and MAP2 whether or not forming filaments.

Tyrosine and proline together are sufficient for the full filament formation

We next examined which amino acid is important for filament formation. Tyrosine 221 (Y221) has been proven to be essential for fibril formation (Nishiura *et al.* 2010; Sogawa *et al.* 2012). Mutating Y221 to another amino acid such as alanine abolished the aggregation of tau. However, it remained unclear whether the difference between Y221 of tau and threonine 340 (T340) of MAP2 is important to the regulation of the aggregation properties. We exchanged Y221 and T340 to obtain two site-directed mutant proteins, tau-TKPV and MAP2-YKKI, and examined their

aggregation properties by monitoring ThT fluorescence, as described in the method section. The ThT fluorescence value of tau-TKPV stayed at the baseline level, suggesting that tau-TKPV lost the ability to form filaments. Similarly, MAP2-YKKI did not aggregate to filaments either, which suggests that Y is essential but not sufficient for filament formation (Fig. 2a). Therefore, the other two amino acids, proline 223 (P223) and/or valine 224 (V224) of tau may be necessary for filament formation. We constructed and purified the other two mutant proteins MAP2-YKPI and MAP2-YKKV in which Y, and P or V were received from the tau sequence. The aggregation properties of MAP2-YKPI and MAP2-YKKV were examined. The fluorescence value of MAP2-YKPI increased constantly to a plateau

comparable to that of tau, indicating the filament formation. By contrast, this increase in the fluorescence was not observed in MAP2-YKKV (Fig. 2b). Moreover, the MAP2-TKPI mutant with only P substitution showed weaker filament formation ability, suggesting that only P is not sufficient for the full filament formation like MAP2-YKPI. Taken together, these results indicated that Y and P together are sufficient for the full filament formation.

Molecular characteristics of the sequences

Because the two motifs YKPV and TKKI determined the aggregation properties, we speculate that the sequences containing YKPV and TKKI motifs may have completely different molecular conformations. To test this speculation,

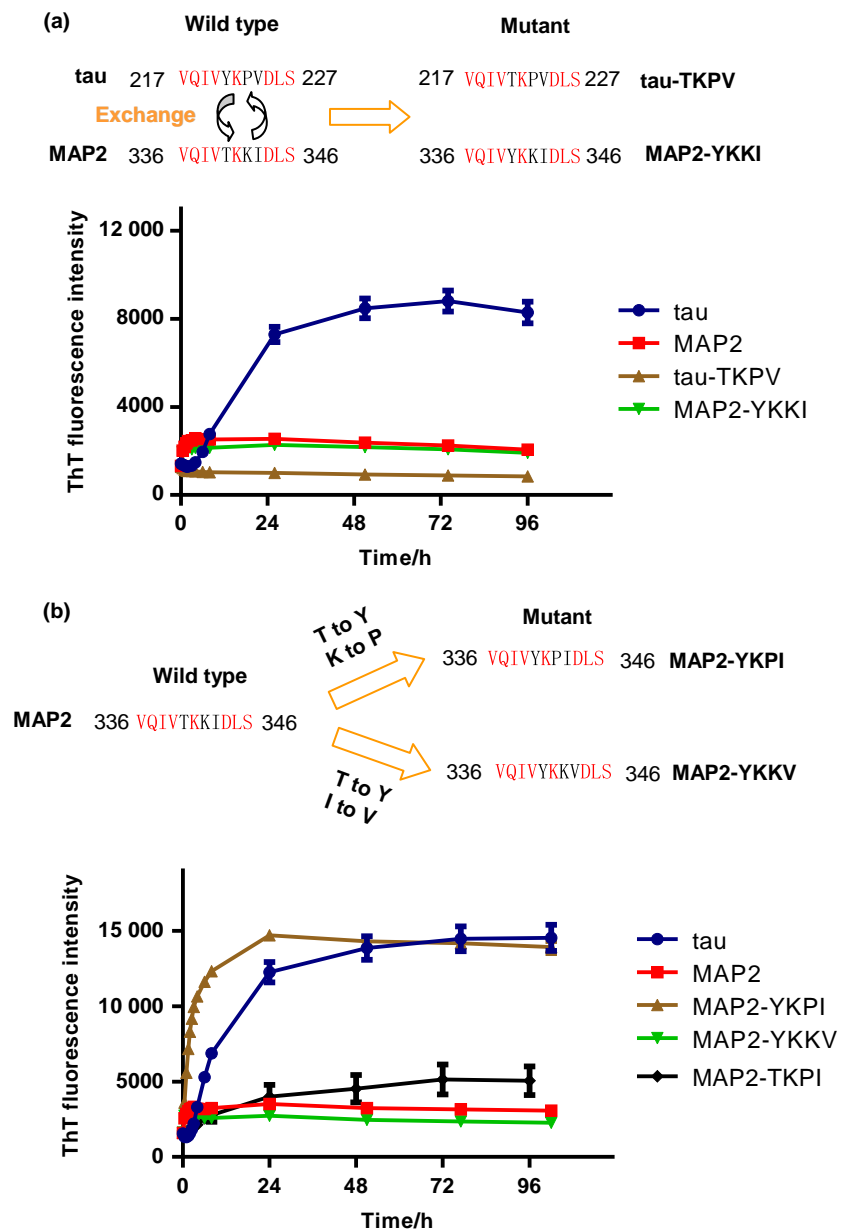


Fig. 2 Key amino acids are responsible for the filament formation of tau and MAP2. Thioflavin T (ThT) fluorescence of tau, MAP2, tau-TKPV, MAP2-YKKI, MAP2-YKPI, MAP2-YKKV and MAP2-TKPI were measured at the indicated time points. Error bars represent SD; $n = 3$. (a) Tyrosine 221 (Y) is essential but not sufficient for the filament formation. (b) Tyrosine 221 (Y) and proline 223 (P) together were sufficient for the full filament formation.

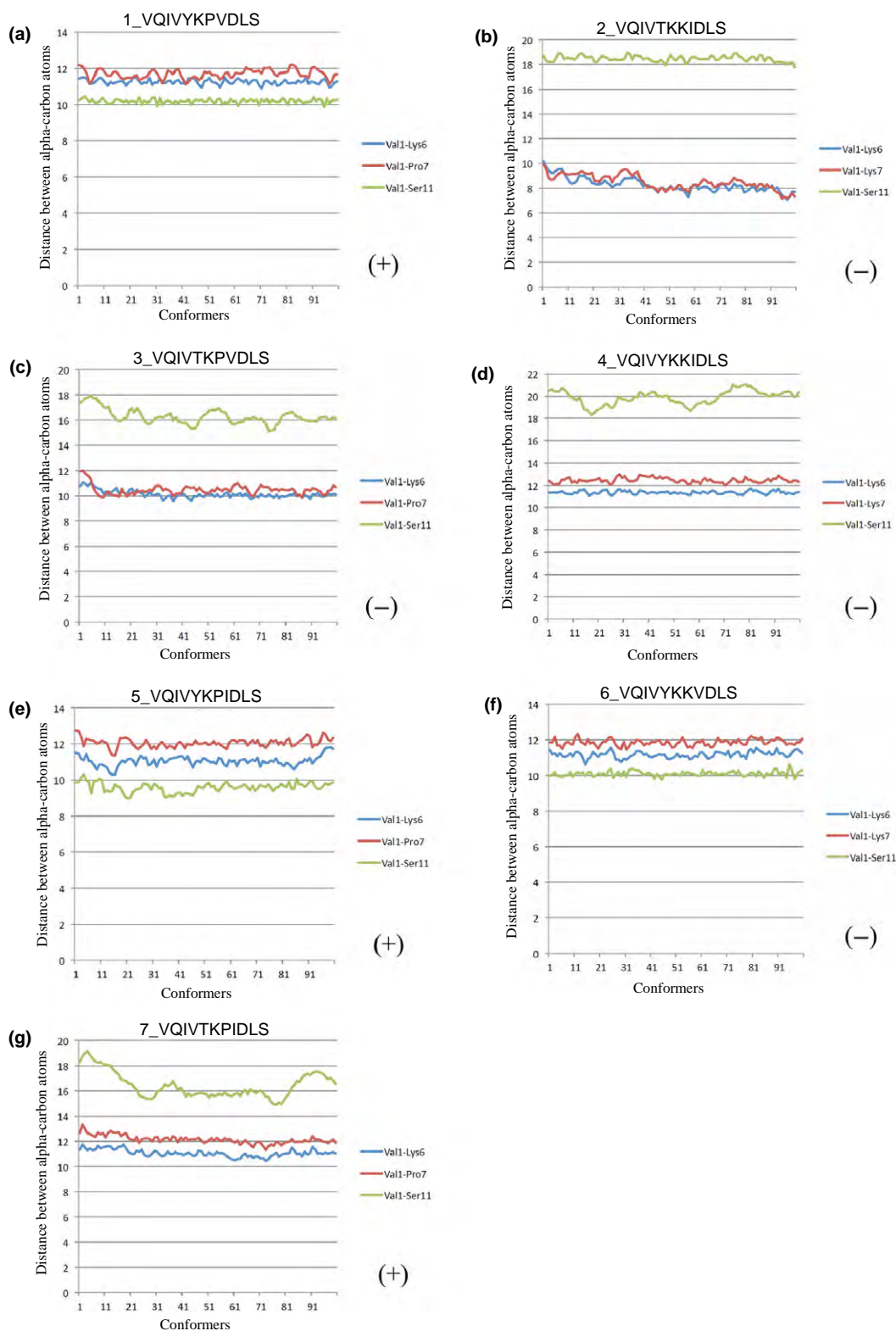


Fig. 3 Molecular characteristics analysis of the sequences. The horizontal axes indicate conformers and the vertical axes indicate the distance between alpha carbon atoms (in Å) at 37°C. (+) indicates

that the peptide have filament formation ability and (-) indicates no. The peptides (a, e, and f) showed non-extended conformation and the peptides (b, c, d, and g) showed extended conformation.

molecular dynamics simulation was performed to calculate the structural changes of two peptides, ²¹⁷VQI-VYKPV²²⁷ of tau (0N3R) and ³³⁶VQIVTKKIDLS³⁴⁶ of MAP2c. The distance between the alpha carbon atoms was calculated at 37°C (Fig. 3a and b). In Fig. 3(a) for the peptide ¹VQIVYKPV¹¹, all conformers showed a shorter distance between alpha carbon atoms of V1 and S11 than the distance between V1 and K6 or P7 suggested that the peptide has a relatively non-extended conformation. On the other hand, in Fig. 3(b) for the peptide ¹VQIVTKKIDLS¹¹, all conformers showed a longer distance between alpha carbon atoms of V1 and S11 than the distance between V1 and K6 or K7, suggesting that the peptide has an extended conformation.

To examine the relationship between molecular conformation and aggregation properties, we further analyzed the other sequences used in this study by molecular dynamics simulation. The peptides A, E, and G have filament formation ability, tended to show non-extended conformation except for the peptide G, which showed an extended conformation. And the peptides that have no filament formation ability, including B, C, D, and F tended to show extended conformation except for the peptide F, which showed a non-extended conformation (Fig. 3). It seems that there are no rules in the relationship between molecular conformation and aggregation properties here; however, our data give an insight into the conformations of these peptides and suggest that the filaments formation may be easier when the non-extended molecular conformation exists and may be prevented relatively by the extended molecular conformation.

Discussion

We focused on MAP2 because it has a homologous carboxyl-terminal sequence to that of tau. The carboxyl-terminal region of tau is characterized by the localization of most mutations causing the hereditary tauopathy FTDP-17 and forming the core of NFTs, suggesting a close relationship between the sequences and tauopathies. However, little is known about the relationship between MAP2 and tauopathies. Our previous study showed that tau and MAP2 have different fates in the formation of inclusions and prompted us to investigate the cause of this phenomenon (Xie *et al.* 2014). Tau and MAP2 are the two major microtubule-associated proteins and, therefore, the different fates of both in NFT formation may be considered as one pathological hallmark of tauopathies. Moreover, the homologous sequence between tau and MAP2 suggests that MAP2 may be considered as a mutation of tau that is not involved in the inclusion-forming process. Therefore, comparing the properties of MAP2 and tau may lead us to a better understanding of tauopathies.

The most important properties of tau inclusions found in AD brains are the β -pleated sheet-rich filaments. In Fig. 1, despite the MAP2-YKPV and wild-type tau forming different filaments and showing distinct aggregation kinetics, both formed β -pleated sheet-rich filaments, as judged by atomic force microscopy and ThT fluorescence. This suggests that the major properties of tau inclusions solely depend on the short YKPV motif.

Thus far, increasing evidence suggests that the mechanisms responsible for neuronal degeneration may not be limited to the formation of inclusions, which is the final step of the pathology (Gomez-Isla *et al.* 1997; Miyasaka *et al.* 2005; Santacruz *et al.* 2005). Many studies showed that soluble species of tau such as oligomers were toxic to neurons (Cowan and Mudher 2013). Although MAP2 is incapable of forming filaments, our previous studies have reported that soluble MAP2 is neurotoxic, which raises the possibility that MAP2 may also be involved in the mechanism of neurodegeneration (Xie *et al.* 2014).

Acknowledgments and conflict of interest disclosure

This work was supported in part by Grant-in-Aid for Scientific Research (KAKENHI; Grant-in-Aid for Young Scientists (B); 20700324; T.M. and 24700368; C.X. and Grant-in-Aid for Challenging Exploratory Research; 22650074; T.M.), Core Research for Evolutional Science and Technology (CREST; T.M., C.X., and Y. Ihara), the Japan Science and Technology Agency (JST), the Japan Society for the Promotion of Science (JSPS) and Grant-in-Aid for Scientific Research on Innovative Areas (Brain Protein Aging and Dementia Control; T.M. 26117004).

All experiments were conducted in compliance with the ARRIVE guidelines. The authors have no conflict of interest to declare.

Author Contribution

C.X. and T.M. designed the study; C.X., T.M., and Y. Shinzaki performed the research; Y. Soeda performed the atomic force microscopic observation; Y. In and K.T. performed the molecular dynamics simulation; C.X., T.M., and Y. Ihara wrote the manuscript.

References

- von Bergen M., Barghorn S., Li L., Marx A., Biernat J., Mandelkow E. M. and Mandelkow E. (2001) Mutations of tau protein in frontotemporal dementia promote aggregation of paired helical filaments by enhancing local beta-structure. *J. Biol. Chem.* **276**, 48165–48174.
- Brooks B. R., Brucoleri R. E., Olafson B. D., States D. J., Swaminathan S. and Karplus M. (1983) A program for macromolecular energy,

- minimization, and dynamics calculations. *J. Comput. Chem.* **4**, 187–217.
- Cowan C. M. and Mudher A. (2013) Are tau aggregates toxic or protective in tauopathies? *Front. Neurol.* **4**, 114.
- Dehmelt L. and Halpain S. (2004) The MAP2/Tau family of microtubule-associated proteins. *Genome Biol.* **6**, 204.
- Gomez-Isla T., Hollister R., West H., Mui S., Growdon J. H., Petersen R. C., Parisi J. E. and Hyman B. T. (1997) Neuronal loss correlates with but exceeds neurofibrillary tangles in Alzheimer's disease. *Ann. Neurol.* **41**, 17–24.
- Kondo J., Honda T., Mori H., Hamada Y., Miura R., Ogawara M. and Ihara Y. (1988) The carboxyl third of tau is tightly bound to paired helical filaments. *Neuron* **1**, 827–834.
- Lee V. M., Goedert M. and Trojanowski J. Q. (2001) Neurodegenerative tauopathies. *Annu. Rev. Neurosci.* **24**, 1121–1159.
- Maeda S., Sahara N., Saito Y., Murayama M., Yoshiike Y., Kim H., Miyasaka T., Murayama S., Ikai A., Takashima A. (2007) Granular tau oligomers as intermediates of tau filaments. *Biochemistry* **46**, 3856–3861.
- Mandelkow E. M. and Mandelkow E. (2012) Biochemistry and cell biology of tau protein in neurofibrillary degeneration. *Cold Spring Harb. Perspect Med.* **2**, a006247.
- Miyasaka T., Ding Z., Gengyo-Ando K., Oue M., Yamaguchi H., Mitani S. and Ihara Y. (2005) Progressive neurodegeneration in *C. elegans* model of tauopathy. *Neurobiol. Dis.* **20**, 372–383.
- Nishiura C., Takeuchi K., Minoura K., Sumida M., Taniguchi T., Tomoo K. and Ishida T. (2010) Importance of Tyr310 residue in the third repeat of microtubule binding domain for filament formation of tau protein. *J. Biochem.* **147**, 405–414.
- Ross C. A. and Poirier M. A. (2004) Protein aggregation and neurodegenerative disease. *Nat. Med.* **10**(Suppl), S10–S17.
- Santacruz K., Lewis J., Spirets T. *et al.* (2005) Tau suppression in a neurodegenerative mouse model improves memory function. *Science* **309**, 476–481.
- Sogawa K., Okuda R., In Y., Ishida T., Taniguchi T., Minoura K. and Tomoo K. (2012) C-H. π interplay between Ile308 and Tyr310 residues in the third repeat of microtubule binding domain is indispensable for self-assembly of three- and four-repeat tau. *J. Biochem.* **152**, 221–229.
- Wischik C. M., Novak M., Thøgersen H. C., Edwards P. C., Runswick M. J., Jakes R., Walker J. E., Milstein C., Roth M. and Klug A. (1988) Isolation of a fragment of tau derived from the core of the paired helical filament of Alzheimer disease. *Proc. Natl Acad. Sci. USA* **85**, 4506–4510.
- Xie C., Miyasaka T., Yoshimura S., Hatsuta H., Yoshina S., Kage-Nakadai E., Mitani S., Murayama S. and Ihara Y. (2014) The homologous carboxyl-terminal domains of microtubule-associated protein 2 and TAU induce neuronal dysfunction and have differential fates in the evolution of neurofibrillary tangles. *PLoS ONE* **9**, e89796.

Eringiactal A, 5,6-*seco*-(5*S*,6*R*,7*R*,9*S*)-5,6:5,7:6,9-Triepoxyergosta-8(14),22-diene-3 β ,7 β -diol, an Unusual Ergostane Sterol from the Fruiting Bodies of *Pleurotus eryngii*

Takashi Kikuchi,^[a] Yuki Masumoto,^[a] Yasuko In,^[a] Koji Tomoo,^[a] Takeshi Yamada,^[a] and Reiko Tanaka*^[a]

Keywords: Natural products / *Pleurotus eryngii* / Steroids / Structure elucidation

A new rearranged ergostane-type steroid, named eringiactal A (**1**), together with known compound **2**, were isolated from the fruiting bodies of *Pleurotus eryngii* (Pleurotaceae). Its structure was fully elucidated by NMR spectroscopy and X-ray crystallography. Eringiactal A (**1**) features an unprecedented 5,6-*seco*-(5*S*,6*R*,7*R*,9*S*)-5,6:5,7:6,9-triepoxysteroid. This is the first report of a 5,6-*seco*-ergostane-type steroid. A plausible biogenetic pathway

of **1** from **2** is also described. Furthermore, isolated compounds were evaluated for inhibitory effects on nitric oxide (NO) production induced by lipopolysaccharide in macrophages. Compound **1** exhibited inhibitory activity on NO production ($IC_{50} = 19.9 \mu M$) accompanied by modest cytotoxicity ($IC_{50} = 25.6 \mu M$). Compound **2** did not have inhibitory effects on NO production or cytotoxicity ($IC_{50} > 100 \mu M$ each).

Introduction

The cultivation of *Pleurotus eryngii*, also referred as Boletus of the Steppes, King Trumpet Mushroom and Trumpet Royale, has been rapidly expanding in South East Asia for the past decade. Other countries that grow this mushroom commercially include Japan, Italy, Australia, South Africa, South Korea, and the USA. *P. eryngii* is an edible mushroom with a pleasant aroma, and its storage life is longer than that of other oyster mushroom varieties. *P. eryngii* ranks third in the amount produced among mushrooms grown worldwide for food. It contains a generous amount of nutrients, which include carbohydrates, proteins, vitamins, minerals, and fiber. Stajic et al. reviewed the biology of *P. eryngii* and its role in biotechnological processes.^[1] Manzi et al. reported the nutritional quality and effect of cooking of commercial mushrooms, which included *P. eryngii*.^[2] Li et al. reported antioxidant and antibacterial activities of polysaccharides from *P. eryngii*.^[3] Alam et al. reported antioxidant and tyrosinase inhibitory effects of phenolic compounds from *P. eryngii*.^[4] Lee et al. reported that *P. eryngii* stalk residue improved meat quality in broiler chickens,^[5] and Yang et al. reported antitumor activity of a polysaccharide from *P. eryngii*.^[6] Jeong et al. reported antitumor and immunomodulating activities of *endo*-biopolymers obtained from a submerged culture of *P.*

eryngii.^[7] Chen et al. reviewed hepatoprotective and hypolipidemic effects of polysaccharidic extracts of *P. eryngii*.^[8] Eringioliolide,^[9] preurone, nicotinic acid,^[10] and known ergostane-type steroids^[11] have been isolated from the fruiting body of *P. eryngii*; however, the steroids of *P. eryngii* have not yet been examined in detail. Therefore, we herein investigated the steroid compartment of the fruiting bodies of *P. eryngii*.

Results and Discussion

The fruiting bodies of *P. eryngii* were extracted with MeOH, and the extract was partitioned between EtOAc and H₂O. The EtOAc-soluble portion was separated by silica gel column chromatography, medium-pressure liquid chromatography, and reverse-phase HPLC to give new steroid **1** and known steroid **2** (Figure 1).

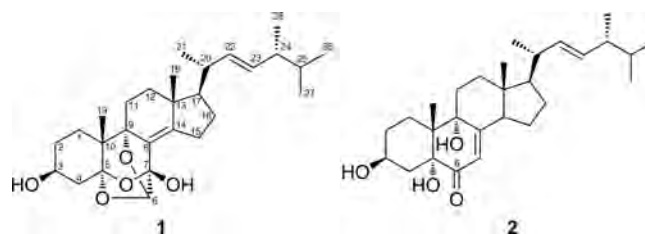


Figure 1. Structures of **1** and **2** from *P. eryngii*.

Eringiactal A (**1**) was obtained as colorless crystals. Its molecular formula was determined to be C₂₈H₄₂O₅ ($m/z = 458.3024 [M]^+$, calcd. 458.3033) based on HRMS and to contain 8 degrees of unsaturation. The IR absorption bands

[a] Osaka University of Pharmaceutical Sciences, 4-20-1 Nasahara, Takatsuki, Osaka 569-1094, Japan
E-mail: tanakar@gly.oups.ac.jp
http://www.oups.ac.jp/

Supporting information for this article is available on the WWW under <http://dx.doi.org/10.1002/ejoc.201500382>.

indicated the existence of hydroxy groups ($\tilde{\nu}_{\max} = 3424 \text{ cm}^{-1}$). The ^{13}C NMR spectrum of **1** suggested that 2 out of the 8 degrees of unsaturation came from two carbon-carbon double bonds; thus, the remaining 6 degrees of unsaturation indicated that **1** was hexacyclic. ^1H and ^{13}C NMR spectra (Table 1) revealed the presence of two annular methyl groups [$\delta_{\text{H}} = 0.90$ (s, 3 H), 1.00 (s, 3 H) ppm], four secondary methyl groups [$\delta_{\text{H}} = 0.83$ (d, $J = 6.7$ Hz, 3 H), 0.84 (d, $J = 6.7$ Hz, 3 H), 0.93 (d, $J = 6.8$ Hz, 3 H), 1.05 (d, $J = 6.8$ Hz, 3 H) ppm], seven methylene groups, six sp^3 methine groups, which include two oxymethine groups [$\delta_{\text{H}} = 4.05$ (tt), 5.13 (s) ppm; $\delta_{\text{C}} = 67.9$ (d), 103.6 (d) ppm], a disubstituted olefin [$\delta_{\text{H}} = 5.22$ (dd), 5.24 (dd) ppm], five sp^3 quaternary carbon atoms, which include three oxycarbon atoms [$\delta_{\text{C}} = 85.2$ (s), 108.5 (s), and 111.3 (s) ppm], and a tetrasubstituted olefin [$\delta_{\text{C}} = 126.0$ (s), 143.7 (s) ppm]. Among the 28 carbon atoms, three [$\delta_{\text{C}} = 103.6$ (d), 108.5 (s), 111.3 (s) ppm] appeared to be acetal carbon atoms from their chemical shift values. In addition, a tertiary hydroxy group [$\delta_{\text{H}} = 3.19$ (s) ppm; signal disappeared with D_2O] was connected to a carbon atom ($\delta_{\text{C}} = 108.5$ ppm).

An analysis of the ^1H - ^1H COSY spectrum (H_2 -1- H_2 -2- H -3- H_2 -4; H_2 -11- H_2 -12; H_2 -15- H_2 -16- H -17) revealed that

a secondary hydroxy group was attached to the usual C-3 β [$\delta_{\text{H}} = 4.05$ (tt, $J = 5.3$ and 9.2 Hz) ppm]; therefore, the A-ring was confirmed to be a cyclohexanol structure by analysis of the ^1H - ^1H COSY and HMBC spectra. This result indicated that the four other oxygen atoms did not appear to bind to C-1, C-2, C-4, C-11, C-12, C-15, C-16, or C-17. The order of the side chain (C-20-C-28) was seen to be the same as common ergost-22-ene by using ^1H - ^1H COSY and HMBC spectra (Figure 2). These results suggested that the four remaining oxygen atoms were concentrated in the B-ring. Most of the scaffolds of the B-ring were mainly established by a comprehensive analysis of the HMBC spectrum.

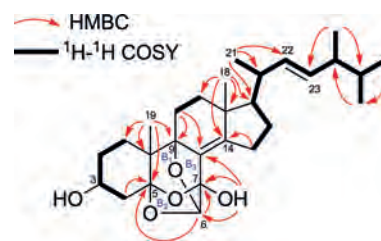


Figure 2. Key ^1H - ^1H COSY and key HMBC correlations in **1**.

Table 1. NMR spectroscopic data (CDCl_3) for eringiactal A (**1**).

Position	δ_{H} [ppm] ^[a]	J [Hz]	^1H - ^1H COSY	NOE	δ_{C} [ppm]	HMBC (C) ^[b]	
1 α	2.10	m	1 β , 2 α , 2 β	3	25.1	t	2, 10, 19
1 β	1.36	dt (2.9, 13.5)	1 α , 2 α , 2 β				5
2 α	1.95	m	1 α , 1 β , 2 β , 3 α		30.0	t	3
2 β	1.49	m	1 α , 1 β , 2 α , 3 α	19			1, 3
3	4.05	tt (5.3, 9.2)	2 α , 2 β , 4 α , 4 β	1 α	67.9	d	
4 α	2.01	m	3 α , 4 β		37.8	t	2, 3, 5, 10
4 β	1.94	m	3 α , 4 α	19			2, 3, 5
5					111.3	s	
6	5.13	s			103.6	d	5, 7, 9
7					108.5	s	
8					126.0	s	
9					85.2	s	
10					43.1	s	
11 α	1.67	ddd (2.4, 4.7, 15.5)	11 β , 12 α , 12 β		22.2	t	8, 9, 12, 13
11 β	1.75	br. dd (4.4, 14.4)	11 α , 12 β	18, 19			10, 12
12 α	1.29	br. dd (5.0, 13.5)	11 α , 11 β , 12 β	17	33.2	t	11, 13, 17, 18
12 β	1.88	m	11 α , 11 β , 12 α	21			9, 14
13					44.0	s	
14					143.7	s	
15 α	2.66	ddd (9.4, 9.4, 18.8)	15 β , 16 α , 16 β	16 α	25.3	t	8, 14
15 β	2.46	dd (9.4, 18.8)	15 α , 16 α , 16 β	16 β			8, 14
16 α	1.81	br. dd (7.3, 13.5)	15 α , 15 β , 16 β , 17 α	15 α	28.2	t	13, 14, 17
16 β	1.45	m	15 α , 15 β , 16 α , 17 α	15 β , 18			17, 20
17	1.25	ddd (6.8, 8.5, 12.3)	16 α , 16 β , 20	12 α	56.3	d	12, 13, 16, 18, 20, 21, 22
18	0.90	s		11 β , 16 β , 19, 21	16.8	q	12, 13, 14, 17
19	1.00	s		2 β , 4 β , 11 β , 18	17.67	q	1, 5, 9, 10
20	2.14	m		18	38.6	d	17, 22, 23
21	1.05	d (6.8)	17 α , 21, 22	12 β	21.5	q	17, 20, 22
22	5.22	dd (7.3, 15.2)	21, 23		135.1	d	20, 23, 24
23	5.24	dd (6.8, 15.2)	22, 24		132.5	d	22, 24
24	1.87	m	23, 25, 28		42.8	d	22, 23, 25, 26, 27, 28
25	1.48	m	24, 26, 27		33.0	d	23, 26, 27, 28
26	0.84	d (6.7)	25		19.9	q	24, 25, 27
27	0.83	d (6.7)	25		19.6	q	24, 25, 26
28	0.93	d (6.8)	24		17.64	q	23, 24, 25
7-OH	3.19	s					6, 7, 8

[a] ^1H chemical shift values (δ [ppm] from SiMe_4) followed by multiplicity and coupling constants. [b] Long-range ^1H - ^{13}C correlation from H to C observed in the HMBC experiment.

One of the three acetal carbon atoms [$\delta_C = 111.3$ (s) ppm] was located at C-5, because correlations were observed between Me-19 [$\delta_H = 1.00$ (s) ppm], H₂-4 [$\delta_H = 1.94$ (m), 2.01 (m) ppm], H-6 [$\delta_H = 5.13$ (s) ppm], and C-5 in the HMBC spectrum. Therefore, the C-5–C-6 linkage was not presumed to be connected directly. The next acetal carbon atom was a methine group [$\delta_C = 103.6$ (d) ppm; $\delta_H = 5.13$ (s) ppm], and this methine proton [$\delta_H = 5.13$ (s) ppm] correlated with the following three carbon atoms: C-5 [$\delta_C = 111.3$ (s) ppm], a new acetal carbon atom [$\delta_C = 108.5$ (s) ppm], and an oxygenated quaternary carbon atom [$\delta_C = 85.2$ (s) ppm]; therefore, the second acetal carbon atom was suggested to be C-6. A hydroxy proton [$\delta_H = 3.19$ (s) ppm] correlated with two acetal carbon atoms: C-6 and the remaining acetal carbon atom [$\delta_C = 108.5$ (s) ppm], and an sp² quaternary carbon atom [$\delta_C = 126.0$ (s) ppm] in the HMBC spectrum; therefore, this hydroxy group was assumed to bind to C-7. Thus, this remaining acetal carbon atom [$\delta_C = 108.5$ (s) ppm] may be C-7. Based on these re-

sults, we estimated that three acetal carbon atoms were situated in the C-5, C-6, and C-7 positions, respectively. In brief, the structure of **1** was assumed to have the 5,6-*seco*-5,6:5,7:6,9-triepoxy-3 β ,7-dihydroxyergostane framework given the combination style of the three acetal carbon atoms. Accordingly, the B-ring appeared to have a basket-type structure comprised of three rings of B1, B2, and B3 that involved three oxygen atoms. Furthermore, a tetrasubstituted olefin was at the $\Delta^{8(14)}$ position as deduced by correlation between Me-18 [$\delta_H = 0.89$ (s) ppm] and C-14 [$\delta_C = 143.7$ (s) ppm], and between OH [$\delta_H = 3.19$ ppm] and C-8 [$\delta_C = 126.0$ (s) ppm] in the HMBC spectrum.

The relative configuration of **1** was determined by a NOESY experiment (Figure 3). Key NOE interactions were observed for H-3/H-1 α , Me-18/H-11 β , H-16 β , Me-19, and Me-21; Me-19/H-2 β , H-4 β , H-11 β , and Me-18; these results indicated 3-OH, Me-18, and Me-19 were all in a β -orientation, whereas H-12 α /H-17 α showed that H-17 was in an α -axial orientation. However, the NOESY spectrum was not

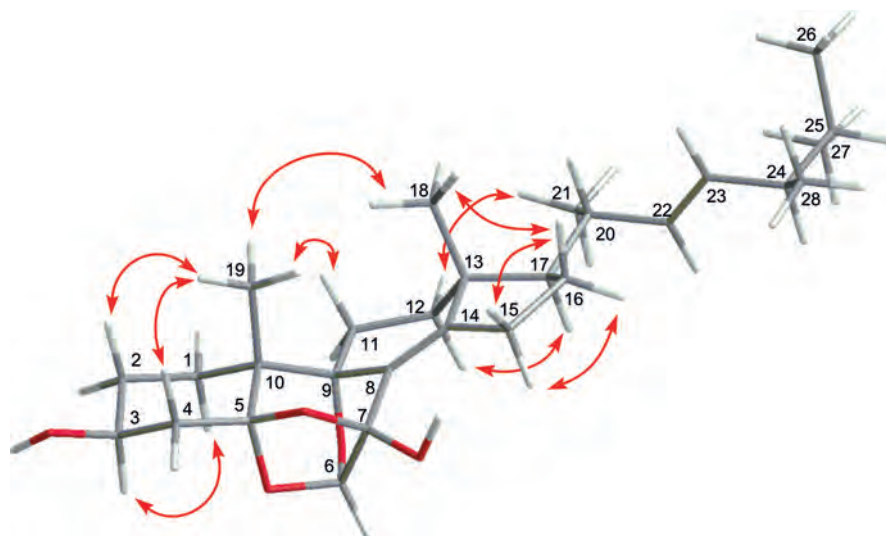


Figure 3. Key NOEs for **1**.

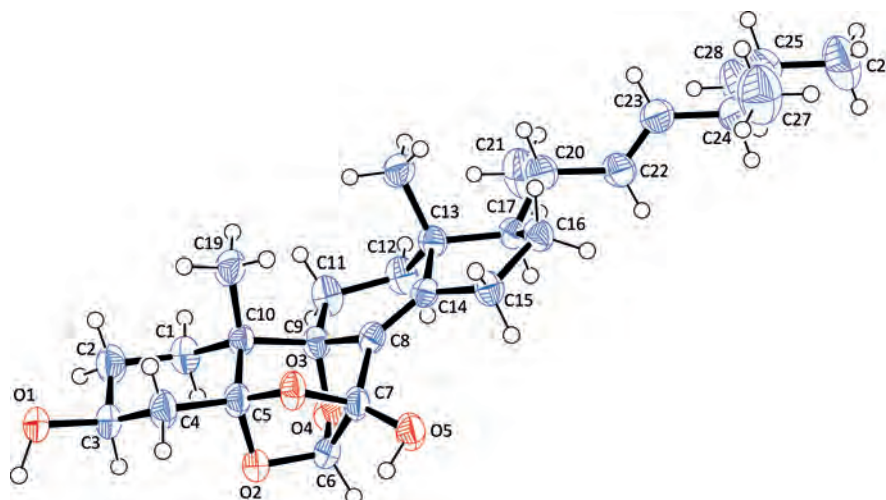
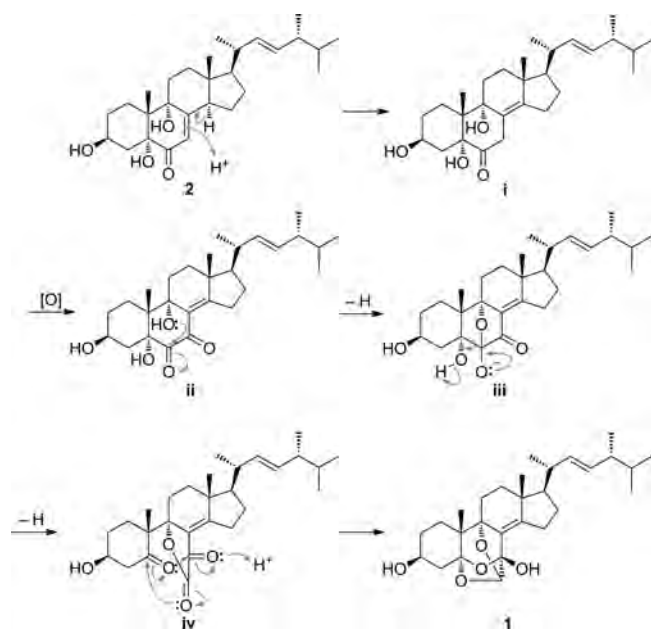


Figure 4. Single-crystal X-ray structure of **1**.

effective in the outskirts of the B-ring. A correlation was not found from H-6, which was the only hydrogen atom of the B ring.

A single crystal of **1** obtained from MeOH/CH₂Cl₂ was mounted on an X-ray diffractometer equipped with graphite-monochromated Mo-*K*_α radiation ($\lambda = 0.71069 \text{ \AA}$) at 240 K. An X-ray diffraction analysis was conducted to confirm the proposed structure, and it also allowed for the unambiguous assignment of the stereostructure of **1** (Figure 4). As expected, the B-ring had a basket-type structure (B1, B2, B3) among three oxygen atoms. The chiral centers of the B-ring of **1** were determined to be (5*S*), (6*R*), (7*R*), and (9*S*), respectively. A 5,6-*seco*-ergostane-type steroid has not yet been isolated.

Eringiacetal A (**1**) exhibited features of an unprecedented basket-type steroid that appeared to be biosynthesized from known steroid 3 β ,5 α ,9 α -trihydroxyergosta-7,22-dien-6-one (**2**). An allylic shift in **2**, followed by oxidation of **i** gave **ii**. Nucleophilic addition by 9-OH on the carbonyl group of C-7 induced cleavage of the C-5–C-6 bond to give **iv**. Eringiacetal A (**1**) was prepared from **iv** by the formation of an O–C bond [5-O–C-7, 6-O–C-5 (Scheme 1)].



Scheme 1. Plausible biosynthetic pathway of **1**.

Compounds **1**, **2** and the positive control, *N*^G-monomethyl-L-arginine acetate (L-NMMA), were examined for their inhibitory effects on nitric oxide (NO) production induced by LPS in macrophages. Their cytotoxicities were also evaluated by the 3-(4,5-dimethyl-2-thiazolyl)-2,5-diphenyl-2*H*-tetrazolium bromide (MTT) assay. Compound **1** exhibited a stronger inhibitory effect on NO production ($IC_{50} = 19.9 \mu\text{M}$) than L-NMMA ($IC_{50} = 53.7 \mu\text{M}$). However, the inhibitory effect of **1** on NO production was attributed to cytotoxicity ($IC_{50} = 25.6 \mu\text{M}$). Compound **2** did not have inhibitory effects on NO production or cytotoxicity ($IC_{50} > 100 \mu\text{M}$ each).

Conclusions

A new ergostane-type steroid that has a cage-shaped structure, named eringiacetal A (**1**), was isolated from the fruiting bodies of *Pleurotus eryngii*. Its structure was fully elucidated by NMR spectroscopy and X-ray crystallography. This is the first report of a 5,6-*seco* ergostane-type steroid. Compound **1**, the biogenetic pathway of which contained the cleavage of C-5–C-6 bond, and formation of three O–C bonds, could be derived from **2**. Compound **1** exhibited inhibitory activity on NO production accompanied by modest cytotoxicity.

Experimental Section

General: Chemicals and reagents were purchased as follows: fetal bovine serum (FBS) from Invitrogen Co. (Carlsbad, CA, U.S.A.), MTT from Sigma–Aldrich Japan Co. (Tokyo, Japan), Dulbecco's modified Eagle's medium (D-MEM), antibiotics, LPS from *Escherichia coli* O157, from Nacalai Tesque, Inc. (Kyoto, Japan). Sulfanilamide and *N*-(1-naphthyl)ethylenediamine dihydrochloride from Tokyo Chemical Industry Co., Ltd. (Tokyo, Japan), L-NMMA from Dojindo Molecular Technologies, Inc. (Kumamoto, Japan). All other chemicals and reagents were of analytical grade. Melting points were determined with a Yanagimoto micro-melting point apparatus. Optical rotations were measured with a JASCO DIP-1000 digital polarimeter. IR spectra were recorded with a Perkin–Elmer 1720X FTIR spectrophotometer. ¹H (600 MHz) and ¹³C (150 MHz) NMR spectra were recorded with an Agilent vnmr600 instrument in CDCl₃ with tetramethylsilane as the internal standard. The EIMS data were recorded with a Hitachi 4000H double-focusing mass spectrometer (70 eV). Silica gel (70–230 mesh, Merck) and silica gel 60 (230–400 mesh, Nacalai Tesque, Inc., Kyoto, Japan), and octadecyl silica gel (ODS; Chromatorex-ODS, 100–200 mesh; Fuji Silysia Chemical, Ltd., Aichi, Japan) were used for column chromatography. HPLC was carried out on an SiO₂ column [Cosmosil 5SL-II column (Nacalai Tesque, Inc., Kyoto, Japan), 25 cm × 20 mm i.d.] with hexane/EtOAc [1:1 (HPLC system I)], and on ODS column [Cosmosil 5C₁₈-PAQ column (Nacalai Tesque, Inc., Kyoto, Japan) (25 cm × 20 mm i.d.) with MeOH/H₂O (95:5; HPLC system II), Cosmosil 5C₁₈-MS-II column (Nacalai Tesque, Inc., Kyoto, Japan) (25 cm × 20 mm i.d.) with MeOH/H₂O (85:15; HPLC system III)] at 35 °C with a flow rate of 4.0 mL/min.

Material: The fruiting body of *Pleurotus eryngii*, produced in Japan (Kagawa prefecture), were purchased from HOKUTO corporation in 2014. A voucher specimen was deposited in the Herbarium of the Laboratory of Medicinal Chemistry, Osaka University of Pharmaceutical Sciences.

Extraction and Isolation: The fruiting bodies of *Pleurotus eryngii* (fresh weight 11.03 kg) were subjected to extraction with MeOH at reflux temperatures (3 d, 4 times). The MeOH extract (2625 g) was partitioned between EtOAc and H₂O (10 L/10 L, 4 times). The EtOAc-soluble fraction (240 g) was subjected to SiO₂ column chromatography [CC; SiO₂ (2.8 kg); CHCl₃/EtOAc (1:0, 5:1, 1:1, and 0:1), and MeOH in increasing order of polarity] that resulted in 37 fractions (Fr. A–Z, a–k). In following operations, fractions that contained ergostane-type steroids were selected based on their ¹H NMR spectra. Fr. T (2874.46 mg), eluted with CHCl₃/EtOAc (1:1), was subjected to SiO₂ CC to yield 8 fractions, T1–T8. Fr. T5 (118.92 mg), eluted with hexane/EtOAc (1:1), was subjected to SiO₂ CC to yield 5 fractions, T5-1–T5-5, followed by T5-2 (101.02 mg),

eluted with hexane/EtOAc (1:1), was subjected to re-SiO₂ CC to give 9 fractions, T5-2-1-9. Preparative HPLC (HPLC system I) of Fr. T5-2-4 (55.05 mg) gave 9 fractions, T5-2-4-1-9. Purification of T5-2-4-6 (4.16 mg; $t_R = 51.5$ min) with HPLC (HPLC system II) gave compound **1** (2.53 mg; $t_R = 23.4$ min). Fr. W (2626.15 mg), eluted with CHCl₃/EtOAc (1:1), was subjected to SiO₂ CC to yield 11 fractions (Fr. W1–W11). Fr. W6 (533.51 mg), eluted with EtOAc, was subjected to ODS CC to yield 7 fractions (Fr. W6-1–W6-7. Preparative HPLC (HPLC system III) of Fr. W6-3 (132.93 mg), eluted with MeOH, gave compound **2** (21.78 mg; $t_R = 152$ min).

Eringiacetal A (1): Colorless crystals (MeOH/CH₂Cl₂). M.p. 215–218 °C. $[\alpha]_D^{25} = 12.9$ ($c = 0.074$, EtOH). IR (KBr): $\tilde{\nu}_{\max} = 3424, 3171, 2961, 2868, 1462, 1317, 1062, 1052, 993, 977, 968, 879, 866$ cm⁻¹. ¹H and ¹³C NMR: see Table 1. MS (EI): m/z (%) = 458 (8) [M]⁺, 412 (21) [M – H₂O]⁺, 331 (100), 207 (44), 128 (14), 125 (15). HRMS (EI): calcd. for C₂₈H₄₂O₅ [M]⁺ 458.3033; found 458.3024.

X-ray Crystallographic Analysis of 1: C₂₈H₄₂O₅ (458.62), orthorhombic, space group *P*₂₁, $a = 8.488$ (3) Å, $b = 6.327$ (2) Å, $c = 24.135$ (8) Å, $\beta = 97.085$ (5)°, $V = 1286.2$ (7) Å³, $D_x = 1.184$ g cm⁻³, $Z = 2$, $F(000) = 500$, $\mu(\text{Mo-K}\alpha) = 0.079$ mm⁻¹, 6131 measured independent reflections, 3661 reflections used for refinement [$I > 2\sigma(I)$], 297 parameters used for refinement, final $R = 0.0497$ [for $I > 2\sigma(I)$] and $wR = 0.1281$ (for all data), $(\delta/\sigma)_{\max} = 0.000$, $\Delta\rho_{\max} = 0.244$ e Å⁻³, and $\Delta\rho_{\min} = -0.241$ e Å⁻³. X-ray diffraction data were collected with a Bruker AXS SMART APEX CCD camera. The crystal structure was solved by using a direct method with the SHELXS-97 program. Atomic scattering factors were taken from the International Tables for X-ray Crystallography. Positional parameters of non-H-atoms were refined by a full-matrix least-squares method with anisotropic thermal parameters by using the SHELXL-97 program. CCDC-1022875 (for **1**) contains the supplementary crystallographic data for this paper. These data can be obtained free of charge from The Cambridge Crystallographic Data Centre via www.ccdc.cam.ac.uk/data_request/cif.

Cell Cultures: The cell lines RAW264.7 [mouse macrophage; obtained from DS Pharma Biomedical Co., Ltd. (Osaka, Japan)] were grown in D-MEM. The medium was supplemented with FBS (10%) and antibiotics (100 units/mL penicillin and 100 µg/mL streptomycin). The cells were incubated at 37 °C in a CO₂ (5%) humidified incubator.

Determination of RAW264.7 Cells Proliferation: RAW264.7 cells proliferation was examined according to a method reported previously.^[12] Briefly, RAW264.7 cells (5×10^4 cells in 100 µL) were seeded onto a 96-well microplate and incubated for 24 h. D-MEM (100 µL) that contained test samples (final concentration of 100, 30, 10, or 3 µM) dissolved in dimethyl sulfoxide (DMSO; final concentration 0.2%) was added. After treatment for 24 h, MTT solu-

tion was added. After 3 h of incubation, sodium dodecyl sulfate (20%) in HCl (0.1 M) was added to dissolve the formazan produced in the cells. The absorbance of each well was measured at 570 nm with a microplate reader. The optical density of vehicle control cells was assumed to be 100%.

Inhibitory Assay of NO Production: Inhibitory assay of nitric oxide production was examined according to a method reported previously^[13] with a few modifications. Briefly, RAW264.7 cells (5×10^4 cells in 100 µL) were seeded onto a 96-well microplate, and incubated for 24 h. D-MEM (100 µL) that contained test samples (final concentration of 30, 10, 3, or 1 µM) dissolved in DMSO (final concentration 0.2%), and LPS (final concentration of 5 µg/mL), was added. After treatment for 24 h, *N*-(1-naphthyl)ethylenediamine (50 µL of 0.1%) in H₂O and sulfanilamide (1%) in phosphoric acid (5%) were added. After incubation for 30 min, the absorbance of each well was measured at 570 nm with a microplate reader. The optical density of vehicle control cells was assumed to be 100%.

Acknowledgments

We thank Dr. Katsuhiko Minoura and Dr. Mihoyo Fujitake (Osaka University of Pharmaceutical Sciences) for the NMR and MS measurements.

- [1] M. Stajic, J. Vukojevic, S. Duletic-Lausevic, *Crit. Rev. Biotechnol.* **2009**, *29*, 55–66.
- [2] P. Manzi, S. Marconi, A. Aguzzi, L. Pizzoferrato, *Food Chem.* **2004**, *84*, 201–206.
- [3] S. Li, N. P. Shah, *Food Chem.* **2014**, *165*, 262–270.
- [4] N. Alam, K. N. Yoon, K. R. Lee, J. S. Lee, T. S. Lee, *Adv. Environ. Biol.* **2011**, *5*, 1104–1113.
- [5] T. T. Lee, J. Y. Ciou, C. J. Chiang, Y. P. Chao, B. Yu, *J. Agric. Food Chem.* **2012**, *60*, 11157–11163.
- [6] Z. Yang, J. Xu, Q. Fu, X. Fu, T. Shu, Y. Bi, B. Song, *Carbohydr. Polym.* **2013**, *95*, 615–620.
- [7] Y. T. Jeong, S. C. Jeong, Y. A. Gu, R. Islam, C. H. Song, *Food Sci. Biotechnol.* **2010**, *19*, 399–404.
- [8] J. Chen, D. Mao, Y. Yong, J. Li, H. Wei, L. Lu, *Food Chem.* **2012**, *130*, 687–694.
- [9] S. Wang, Y. Li, L. Bao, J. Han, X. Yang, H. Li, Y. Wang, S. Li, H. Liu, *Org. Lett.* **2012**, *14*, 3672–3675.
- [10] I. S. Lee, I. J. Ryoo, K. Y. Kwon, J. S. Ahn, I. D. Yoo, *J. Antibiot.* **2011**, *64*, 587–589.
- [11] Y. Yaoita, R. Kohata, R. Kakuda, K. Machida, M. Kikuchi, *Chem. Pharm. Bull.* **2002**, *50*, 681–684.
- [12] T. Yamada, Y. Muroga, M. Jinno, T. Kajimoto, Y. Usami, A. Numata, R. Tanaka, *Bioorg. Med. Chem.* **2011**, *19*, 4106–4113.
- [13] Y. Matsui, T. Kikuchi, T. Inoue, O. Muraoka, T. Yamada, R. Tanaka, *Molecules* **2014**, *19*, 17130–17140.

Received: March 23, 2015

Published Online: June 10, 2015



Carapanolides M–S from seeds of andiroba (*Carapa guianensis*, Meliaceae) and triglyceride metabolism-promoting activity in high glucose-pretreated HepG2 cells



Takanobu Inoue^a, Yuuki Matsui^a, Takashi Kikuchi^a, Takeshi Yamada^a, Yasuko In^b, Osamu Muraoka^c, Chie Sakai^d, Kiyofumi Ninomiya^d, Toshio Morikawa^d, Reiko Tanaka^{a,*}

^a Laboratory of Medicinal Chemistry, Osaka University of Pharmaceutical Sciences, 4-20-1 Nasahara, Takatsuki, Osaka 569-1094, Japan

^b Laboratory of Physical Chemistry, Osaka University of Pharmaceutical Sciences, 4-20-1 Nasahara, Takatsuki, Osaka 569-1094, Japan

^c Laboratory of Pharmaceutical Organic Chemistry, Faculty of Pharmacy, Kinki University, 3-4-1 Kowakae, Higashi-osaka, Osaka 577-8502, Japan

^d Pharmaceutical Research and Technology Institute, Kinki University, 3-4-1 Kowakae, Higashi-osaka, Osaka 577-8502, Japan

ARTICLE INFO

Article history:

Received 2 February 2015

Received in revised form 2 March 2015

Accepted 3 March 2015

Available online 7 March 2015

Keywords:

Carapa guianensis

Meliaceae

Seed oil

Limonoid

Carapanolides M–S

Triglyceride metabolism promoter

ABSTRACT

Five novel phragmalin-type limonoids, carapanolides M–Q (**1–5**), together with two mexicanolide-type limonoids, carapanolides R–S (**6–7**), were isolated from the oil of *Carapa guianensis* AUBLET (Meliaceae) seeds, a traditional medicine in Brazil and Latin American countries. Their structures were elucidated on the basis of spectroscopic analyses using 1D and 2D NMR techniques and a single-crystal X-ray diffraction analysis. Compounds **1–7** along with 12 known limonoids, **8–19**, isolated from the flower and seed oil of *C. guianensis* were assayed to determine their triglyceride metabolism-promoting activities in the high glucose-pretreated human hepatocellular carcinoma cell line, HepG2. Gedunin-type limonoid: **14** (% of control at 10 μ M: 35.4 \pm 3.9), **13** (55.0 \pm 3.6 at 10 μ M), and **18** (75.4 \pm 4.2 at 10 μ M) significantly reduced TG levels in hepatocytes.

© 2015 Elsevier Ltd. All rights reserved.

1. Introduction

Meliaceae plants are distributed in tropical regions throughout the world. As natural products of the Meliaceae, limonoids established both chemical and biological properties.¹ *Carapa guianensis* AUBLET (Meliaceae) is a popular medicinal plant known as 'Andiroba' in Brazil, and is in the same family as mahogany. It is widely distributed in the tropical rainforests of the Amazon or other regions in Brazil. Andiroba is a large and towering tree that grows to over 300 feet (90 m) and has been used not only for its commercial value, but also as a herbal medicine or remedy by the indigenous people of Brazil and the Amazon basin. The andiroba tree produces a brown, ligneous, quadrilateral nut, which is approximately 3–4 inches in diameter and has appearance of

a chestnut. The nut from andiroba contains several oil-rich kernels and seeds, which are composed of approximately 60% pale yellow oil. The seed oil of andiroba was previously reported to exhibit highly efficient analgesic,² anti-bacterial,³ anti-inflammatory,⁴ anti-cancerous,⁵ anti-tumor and anti-fungal,⁶ and anti-allergic properties,⁷ and was also effective against wounds, bruises, herpes ulcers, rheumatism, ear infections, and insect bites as a repellent,⁸ and have growth-inhibiting properties.⁹ We recently identified carapanolides A and B,¹⁰ guianolide A and B,¹¹ carapanolides C–I,¹² and carapanolides J–L¹³ in the seed oil of andiroba. Our continuing research on the seed oil of andiroba revealed the structures of five novel phragmalin-type limonoids, referred to as carapanolides M (**1**), N (**2**), O (**3**), P (**4**), and Q (**5**), and two novel mexicanolide-type limonoids, carapanolides R (**6**) and S (**7**). We herein described the isolation and structural elucidation of the new limonoids as well as the TG metabolism-promoting activities of the limonoid constituents in high glucose-pretreated HepG2 cells.¹⁴

* Corresponding author. Tel./fax: +81 72 690 1084; e-mail address: tanakar@gly.oups.ac.jp (R. Tanaka).

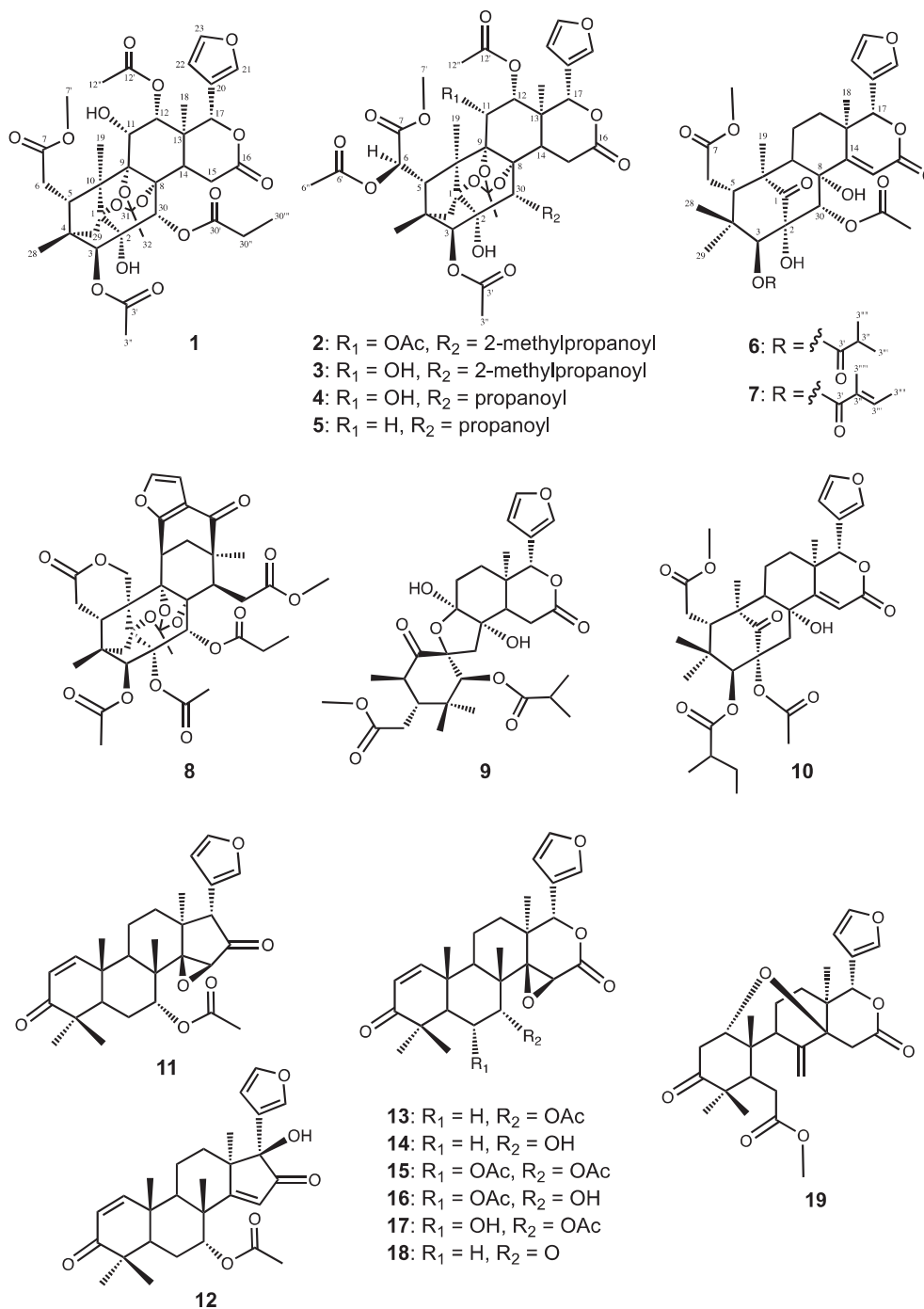


Fig. 1. Structures of compounds isolated from *C. guianensis*.

The above results confirmed that **1** was a phragmalin-1,8,9-orthoacetate closely related to Andriolides E and F.¹⁵ The configurations of H-11 and H-12 were both α because of the significant NOEs between H-11 and H-5 β , H-6 β , H-12, Me-19, and Me-12''; between H-12 and H-5 β , H-11, H-17 β , and H-30 β , and the coupling constants of H-11 [δ_{H} 4.32 (d, $J_{11,12}$ =2.3 Hz)], and H-12 [δ_{H} 4.50 (d, $J_{11,12}$ =2.3 Hz)]; therefore the relative structure was confirmed, as shown in Fig. 1.

Carapanolide N (**2**), a colorless crystal, had a molecular formula of C₄₁H₅₀O₁₉ (m/z 847.3024 [M+H]⁺, calcd 847.3025) by HRFABMS. The IR spectrum showed the presence of a hydroxy group (ν_{max} 3510 cm⁻¹) and carbonyl groups (ν_{max} 1747 cm⁻¹). The UV absorption band showed a furan ring at λ_{max} =208 nm (log ϵ 3.52). ¹H

and ¹³C NMR spectra (Table 1) exhibited signals assignable to three tertiary methyl groups [δ_{H} 1.08, 1.29, 1.37 (each s)]; four acetyl groups [δ_{H} 1.65, 2.10, 2.17, 2.23 (each 3H, s), δ_{C} 168.8, 169.0, 169.1, 170.6 (each s)]; a 2-methylpropanoyl [δ_{H} 1.10, 1.19 (each 3H, d), 2.57 (1H, sept); δ_{C} 175.0 (s)], a methyl ester [δ_{H} 3.81 (3H, s); δ_{C} 53.0 (q), 169.6 (s)]; a 1,8,9-orthoacetate [δ_{H} 1.69 (3H, s), δ_{C} 21.1 (q), 85.0 (s), 85.7 (s), 85.8 (s), 119.3 (s)]; a sp³ methylene, eight sp³ methines including six oxymethines [δ_{H} 4.57 (d), 4.65 (s), 5.67 (s), 5.67 (d), 6.02 (s), 6.07 (br s)]; seven sp³ quaternary carbons including four oxycarbons [δ_{C} 79.9, 85.0, 85.7, 85.8 (each s)] and a furan ring [δ_{H} 6.44 (dd), 7.39 (t), 7.50 (br s)]. In ¹H–¹H COSY spectrum, the cross-peaks were observed between H-5–H-6, H-11–H-12, H-14–H-15 and H-22–H-23, as shown in bold face in Fig. 3. In the HMBC

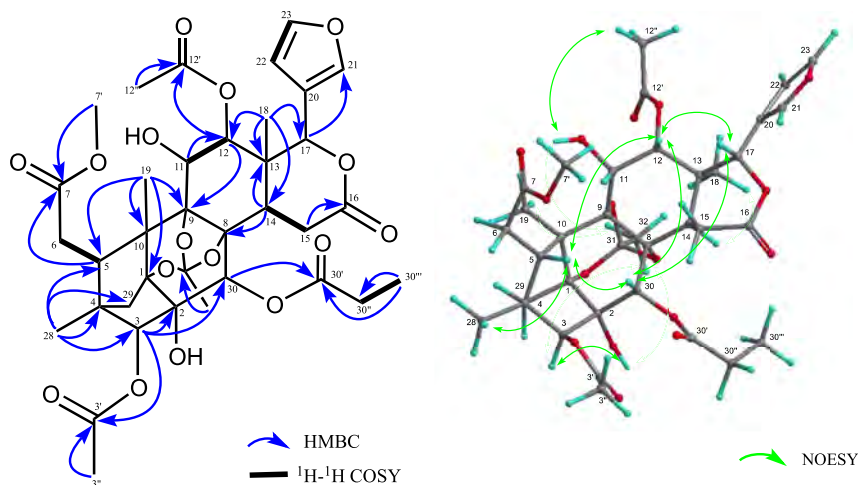


Fig. 2. Key ^1H – ^1H COSY, HMBC, and NOESY correlations of carapanolide M (**1**).

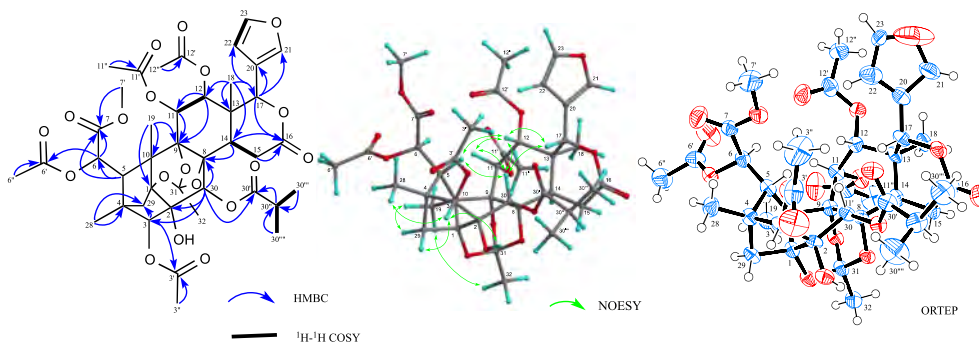


Fig. 3. Key ^1H – ^1H COSY, HMBC, and NOESY correlations and ORTEP drawing of carapanolide N (**2**).

spectrum (Fig. 3), cross-peaks were observed from H-3 [δ_{H} 4.65 (s)]/C-2 [δ_{C} 79.9 (s)], C-4, C-5, C-3' [δ_{C} 170.6 (s)]; H-6 [δ_{H} 6.07 (br s)]/C-4, C-5, C-7 [δ_{C} 169.6 (s)]; H-11 [δ_{H} 5.67 (d)]/C-8 [δ_{C} 85.8 (s)], C-9 [δ_{C} 85.7 (s)], C-10, C-12 [δ_{C} 69.8 (d)], C-13, C-11' [δ_{C} 168.8 (s)]; H-12 [δ_{H} 4.57 (d)]/C-13, C-17 [δ_{C} 76.5 (s)], C-18, C-12' [δ_{C} 169.0 (s)]; H-14 [δ_{H} 2.64 (d)]/C-8, C-13, C-15, C-16 [δ_{C} 169.5 (s)], C-17, C-18, C-30 [δ_{C} 69.8 (d)]; H-17 [δ_{H} 5.67 (s)]/C-13, C-14, C-20 [δ_{C} 120.7 (s)], C-21 [δ_{C} 143.1 (d)], C-22 [δ_{C} 109.7 (d)]; Me-18 [δ_{H} 1.37 (s)]/C-12, C-13, C-14, C-17; Me-19 [δ_{H} 1.29 (s)]/C-1 [δ_{C} 85.0 (s)], C-5, C-9 [δ_{C} 85.7 (s)], C-10; Me-28 [δ_{H} 1.08 (s)]/C-3 [δ_{C} 83.2 (d)], C-4, C-5, C-29; 2-OH [δ_{H} 2.65 (s)]/C-2, C-3, H-6 [δ_{H} 6.07 (br s)]/C-4, C-5, C-7 [δ_{C} 169.6 (s)], C-10; Me-6'' [δ_{H} 2.17 (s)]/C-6' [δ_{C} 169.1 (s)]; Me-7' [δ_{H} 3.81 (s)]/C-7. The relative configuration of **2** was determined on the basis of NOESY correlations (Fig. 3). Intense NOESY correlation between H-3 and Me-28, H-29_{pro-S}; between H-5 β and H-6, H-12, H-30 β , and Me-28; between H-11 and H-6 and H-30 β ; between H-12 and H-5 β , H-17 β , and H-30 β ; between Me-19 and H-6, H-29_{pro-R}, and Me-32; between Me-32 and Me-19 and 2-OH revealed an acetyl group at C-3 in a β orientation, C-11 and C-12 in an α orientation, the hydroxyl group at C-2 in an α orientation, and the 2-methylpropanoyl group at C-30 in an α orientation. In addition, significant NOEs were observed between H-6 [δ_{H} 6.07 (br s)] and H-11 β , H-12 β and H-17 β , and also between H-6'' and Me-28; therefore C-6, was presumed to be in an *R*-configuration. However, C-6R¹⁶ and C-6S¹⁷ were both present naturally. A single-crystal X-ray diffraction analysis was successfully conducted to confirm the proposed structure of C-6R, and the configurations of C-11 and C-12 were determined as *R* and *R*, respectively. In addition, two conformations were identical; however, a large number of differences were not observed, and an ORTEP view was shown in Fig. 3.

The molecular formula of carapanolide O (**3**) was assigned as $\text{C}_{39}\text{H}_{48}\text{O}_{18}$ ($[\text{M}+\text{H}]^+$; m/z 805.2919, calcd for 805.2919) based on HRFABMS. The IR spectrum of **3** showed the presence of a hydroxy group at 3457 cm^{-1} and ester groups at 1743 cm^{-1} . According to the structure of **3**, its IR, ^1H and ^{13}C NMR spectra (Table 1) were very similar to those of **2**, except for the absence of an acetyl group and presence of a hydroxyl group. In the ^1H – ^1H COSY spectrum of **3**, cross-peaks were observed between H-11 [δ_{H} 4.47 (br s)] and H-12 [δ_{H} 4.48 (br s)]. In the HMBC spectrum, cross-peaks were observed between Me-18 [δ_{H} 1.43 (s)] and C-12 [δ_{C} 71.5 (d)], C-13, C-14, and C-17 [δ_{C} 76.6 (d)]; and between H-12 and C-9, C-13, C-17, C-18, and C-12' [δ_{C} 169.7 (s)]. In the NOESY spectrum, significant NOEs were observed between H-11 and H-5 β , H-6, H-17 β , and H-30 β ; between H-12 and H-5 β , H-6, H-17 β , H-21, H-22, and H-30 β ; between H-6 and H-5 β , H-11 β , H-12 β , Me-19, and H-6''; between H-6'' and Me-19 and Me-28; therefore, an acetyl group was attached at C-12 while a hydroxyl group was attached at C-11, and the configurations of H-11 and H-12 were both α while that of C-6 was presumed to be *R*, which was the same as that of carapanolide N (**2**).

Carapanolide P (**4**), obtained from an amorphous powder, had the molecular formula $\text{C}_{38}\text{H}_{48}\text{O}_{18}$ ($[\text{M}+\text{H}]^+$; m/z 791.2762, calcd for 791.2760) as determined by HRFABMS. The IR spectrum showed hydroxy and ester groups at 3526 and 1744 cm^{-1} . The IR, ^1H , and ^{13}C NMR spectra (Table 1) were very similar to those of **3**, except for the absence of a 2-methylpropanoyl group at C-30 and presence of a propanoyl group [δ_{H} 1.09 (3H, t, $J=7.3$ Hz), 2.38 and 2.39 (each 1H, q, $J=7.3$ Hz), 6.00 (1H, s); δ_{C} 69.8 (d)] in **3**. In the NOESY experiments, cross-peaks between H-6 [δ_{H} 5.97 (1H, br s)] and H-5 β , H-11 β , H-12 β , Me-19, and H-6'' indicated that the relative stereochemistry of **4** to had the same configuration as **2** and **3**.

The molecular formula of carapanolide **Q** (**5**) was assigned as $C_{38}H_{46}O_{17}$ ($[M+H]^+$; m/z 775.2814, calcd for 775.2811) based on HRFABMS. The IR spectrum showed hydroxy and ester groups at 3495 and 1740 cm^{-1} . The IR, and 1H and ^{13}C NMR spectra (Table 1) of **5** were very similar to those of **4**, except for the absence of a hydroxy group at C-11. Therefore, the relative structure of **5** was established, as shown in Fig. 1.

Carapanolide **R** (**6**), an amorphous powder, had the molecular formula $C_{33}H_{42}O_{12}$ ($[M+H]^+$; m/z 631.2754, calcd for 631.2755) as determined by HRFABMS. The IR and UV spectra showed a hydroxyl group at ν_{max} 3478, ester groups at ν_{max} 1709 cm^{-1} , and an α,β -unsaturated δ -lactone at ν_{max} 1634 cm^{-1} and λ_{max} 224.5 nm ($\log \epsilon$ 3.78). The 1H and ^{13}C NMR spectra (Table 2) indicated the presence of four tertiary methyls [δ_H 0.82, 0.91, 1.10, 1.29], an acetyl methyl [δ_H 2.12 (3H, s)], a methyl ester [δ_H 3.71 (3H, s)], a 2-methylpropanoyl group [δ_H 1.20 and 1.27 (each 3H, d), 2.83 (1H, sept.), δ_C 175.4 (s)], three methylenes, five sp^3 methines including three oxymethines [δ_H 5.18 (s), 5.45 (s), 6.49 (s)], five sp^3 quaternary carbons including two oxycarbons [δ_C 80.4 (s), 86.2 (s)], a furan ring [δ_H 6.47 (dd), 7.44 (t), 7.45 (br s)], a six-membered ring ketone [δ_C 204.1 (s)], and an α,β -unsaturated δ -lactone [δ_H 5.45 (s), 6.29 (s), δ_C 164.9 (s)] (Table 2). After assignments of HMQC, 1H – 1H COSY, and HMBC spectra (Fig. 4), it became clear that **6** was a mexicanolide-type limonoid with an acetyl at C-30, a 2-methylpropanoyl group at C-3, and hydroxy groups at C-2 and C-8.¹⁸ The relative structure of **6** was confirmed from the NOESY as shown in Fig. 1.

The molecular formula of carapanolide **S** (**7**) was assigned as $C_{34}H_{42}O_{12}$ ($[M+H]^+$; m/z 643.2755, calcd for 643.2755) based on HRFABMS. The UV and IR spectra of **7** showed hydroxy, α,β -unsaturated δ -lactone, and ester groups. According to the structure of **7**, its UV, IR, 1H , and ^{13}C NMR spectra were very similar to those of **6**, except for the absence of a 2-methylpropanoyl group at C-3 and presence of a tigloyl group [δ_H 1.90 (3H, d, $J=7.1$ Hz), 1.92 (3H, s), 6.89 (1H, q, $J=7.1$ Hz)] in **7** (Table 2).¹⁹ Therefore, the relative structure of **7** was established, as shown in Fig. 1.

2.2. Effects of carapanolides (1–19) on TG contents in high glucose-pretreated HepG2 cells

Fatty liver is recognized as a significant risk factor for serious liver diseases.^{20,21} A strong causal linkage has been identified between fatty liver diseases and hyperinsulinemic insulin resistance.^{22,23} Thus, fatty liver is considered to be closely associated with obesity and type 2 diabetes.²³ During an exploratory study of the bioactive functions of natural products, we examined the

Table 2
 1H NMR and ^{13}C NMR data for compounds **6** and **7**

Position	6		7	
	$^1H^a$ (J, Hz)	$^{13}C^b$	$^1H^a$ (J, Hz)	$^{13}C^b$
1		204.1 (s)		204.2 (s)
2		86.2 (s)		86.1 (s)
3	5.18 s	79.7 (d)	5.45 s	80.3 (d)
4		43.4 (s)		43.6 (s)
5	2.62 br d (6.7)	38.6 (d)	2.69 br d (6.5)	38.8 (d)
6	A 2.35 dd (6.7, 17.1)	32.9 (t)	2.36 dd (18.1, 6.5)	32.9 (t)
	B 2.47 d (17.1)		2.46 d (18.1)	
7		173.8 (s)		173.9 (s)
8		80.4 (s)		80.3 (s)
9	2.45 dd (6.1, 13.0)	65.4 (d)	2.45 t (1.5)	65.3 (d)
10		55.2 (s)		55.5 (s)
11	α 1.72 m	19.9 (t)	1.71 m	20.0 (t)
	β 1.49 m		1.48 m	
12	α 1.58 td (12.9, 0.8)	30.1 (t)	1.56 m	30.1 (t)
	β 1.76 ddd (12.9, 6.0, 0.8)		1.77 m	
13		39.4 (s)		39.3 (s)
14		165.8 (s)		166.0 (s)
15	6.29 s	115.5 (d)	6.16 s	115.4 (d)
16		164.9 (s)		164.9 (s)
17	5.45 s	78.9 (d)	5.17 s	79.0 (d)
18	1.29 s	21.3 (q)	1.28 s	21.3 (q)
19	1.10 s	18.8 (q)	1.10 s	18.9 (q)
20		120.2 (s)		120.2 (s)
21	7.45 br s	141.7 (d)	7.46 dd (0.1, 0.3)	141.7 (d)
22	6.47 dd (0.8, 1.8)	110.4 (d)	6.48 d (0.1)	110.4 (d)
23	7.44 t (1.8)	143.0 (d)	7.45 d (0.3)	143.1 (d)
28	0.82 s	21.3 (q)	0.85 s	25.4 (q)
29	0.91 s	24.9 (q)	0.91 s	21.3 (q)
30	6.49 s	74.5 (d)	6.36 s	74.8 (d)
3'		175.4 (s)		166.2 (s)
3''	2.83 sept (6.8)	34.3 (d)		128.6 (s)
3'''	1.20 d (6.8)	18.1 (q)	6.89 q (7.1)	138.5 (d)
3''''	1.27 d (6.8)	19.7 (q)	1.90 d (7.1)	12.4 (q)
			1.92 s	14.7 (q)
7'	3.71 s	52.3 (q)	3.71 s	52.3 (q)
30'		168.8 (s)		168.5 (s)
30''	2.12 s	20.6 (q)	2.08 s	20.6 (q)
2-OH	4.10 s		4.12 s	
8-OH	2.85 s		2.83 s	

^a Measured at 600 MHz in $CDCl_3$.

^b Measured at 150 MHz in $CDCl_3$.

inhibitory effects of the limonoids from *C. guianensis* on TG levels in high glucose-pretreated HepG2 cells.^{24,25} The test compounds were carapanolides M–S (**1–7**) and known limonoids (**8–19**). The known limonoids were isolated from the flower or seed oil of *C. guianensis*: guianolide A (**8**),¹¹ carapanolide A (**9**),¹⁰ Carapanolide C (**10**),¹²

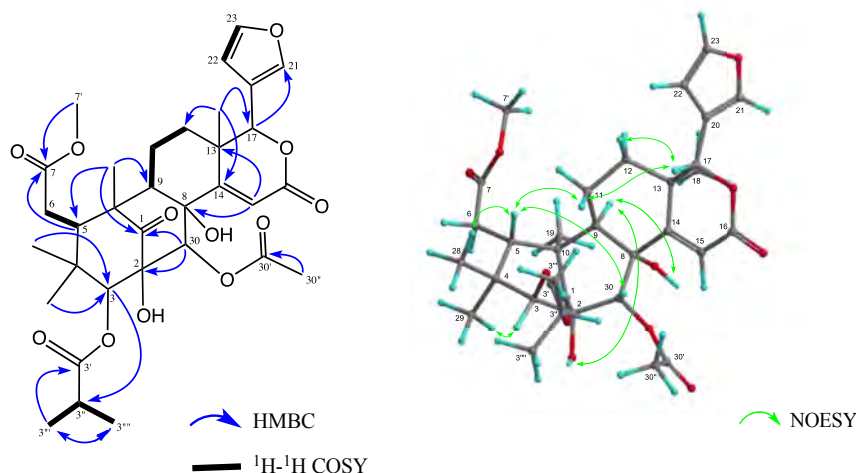


Fig. 4. Key 1H – 1H COSY, HMBC, and NOESY correlations of carapanolide **R** (**6**).

gedunin-type limonoids (**11**)²⁶ and (**12**)²⁷ from the seed oil of *C. guianensis*, and gedunin-type limonoids (**13**),¹⁵ (**14**),²⁸ (**15**),¹⁵ (**16**),¹⁸ (**17**),¹⁵ and (**18**)¹⁵ and an andirobin-type limonoid (**19**) from the flower oil of *C. guianensis*. As shown in Table 3, 7-deacetoxy-7-hydroxygedunin (**14**) (% of control at 10 μ M: 35.4 \pm 3.9), gedunin (**13**) (55.0 \pm 3.6 at 10 μ M), and 7-deacetoxy-7-oxogedunin (**18**) (75.4 \pm 4.2 at 10 μ M) significantly reduced TG levels in hepatocytes and these reductions were equal or stronger than those obtained using the hypoglycemic medicine, metformin (89.3 \pm 3.1 at 10 μ M).^{29,30} On the other hand, **11** (% of control at 30 μ M: 65.0 \pm 7.7), **12** (69.8 \pm 3.1 at 30 μ M), **16** (70.2 \pm 5.0 at 30 μ M), **17** (79.8 \pm 4.1 at 30 μ M), and **15** (85.5 \pm 3.7 at 30 μ M) demonstrated moderate activities. Gedunin-type limonoids (**14**, **13**, **18**), which had no substituent at C-6 exhibited stronger activities than those of **15**, **16**, and **17**, which have a hydroxyl or acetyl group at C-6. The strongest gedunin-type limonoid was **14**, having H₂ at C-6 and α -OH at C-7, followed by **13**, having H₂ at C-6 and α -OAc at C-7. In addition, gedunin-type limonoids having an α , β -epoxy cyclopentanone ring (**11**) or α , β -unsaturated cyclopentanone moiety (**12**) in the D ring, exhibited lower activity than those having α , β -epoxy- δ -lactone (**13**–**18**) in the D ring. On the other hand, other types of limonoids, such as phragmalin (**1**–**5**), mexicanolide (**6**, **7**, **10**), andirobin (**19**), migrated phragmalin 1,8,9-orthoacetate (**8**), 9,10-*seco*-mexicanolide (**9**) did not exhibit marked activity. Thus, these gedunin-type limonoids (**14**, **13**, and **18**) were responsible for the fatty liver preventive effects of *C. guianensis*.

Table 3
Effects on TG/protein content in the homogenate

Treatment	TG/protein content in the homogenate (% of control)				
	Concn (μ M)	0	3	10	30
3		100.0 \pm 2.6	79.5 \pm 5.4**	90.1 \pm 3.9	85.4 \pm 4.6*
4		100.0 \pm 5.0	91.3 \pm 4.2	88.8 \pm 4.4	80.7 \pm 4.8*
8		100.0 \pm 2.5	87.6 \pm 3.2	88.0 \pm 4.8	83.4 \pm 2.6*
10		100.0 \pm 2.1	104.5 \pm 2.5	113.3 \pm 1.6*	111.8 \pm 1.7*
11		100.0 \pm 4.6	96.4 \pm 9.4	86.9 \pm 8.2	65.0 \pm 7.7**
12		100.0 \pm 3.0	96.7 \pm 5.5	93.0 \pm 3.8	69.8 \pm 3.1**
13		100.0 \pm 2.0	74.3 \pm 2.2**	55.0 \pm 3.6**	49.9 \pm 2.5**
14		100.0 \pm 3.9	71.9 \pm 1.0**	35.4 \pm 3.9**	32.0 \pm 3.0**
15		100.0 \pm 3.1	89.5 \pm 2.6*	96.8 \pm 3.1	85.5 \pm 3.7**
16		100.0 \pm 3.2	88.8 \pm 3.5	86.0 \pm 1.9*	70.2 \pm 5.0**
17		100.0 \pm 2.9	93.6 \pm 2.7	107.3 \pm 8.3	79.8 \pm 4.1**
18		100.0 \pm 2.7	82.5 \pm 1.2**	75.4 \pm 4.2**	79.6 \pm 3.0**
Metformin		100.0 \pm 1.6	81.9 \pm 2.7**	85.4 \pm 1.5**	78.1 \pm 2.8**

Each value represents the mean \pm S.E.M. (N=4). Asterisks denote significant differences from the control, * p <0.05, ** p <0.01.

Compounds **1**, **2**, **5**–**7**, **9**, and **19** did not show the effects.

3. Conclusion

The present study demonstrated that andiroba is a unique source of limonoids, similar to *Azadirachta indica*¹ and *Chukrasia tabularis*.³¹ The structure of compound **2** was confirmed by the configurations of C-6R, C-11R, and C-12R, respectively, from 2D NMR and single-crystal X-ray diffraction analyses. The biological activities of gedunin-type limonoids, 7-deacetoxy-7-hydroxygedunin (**14**), gedunin (**13**), and 7-deacetoxy-7-oxogedunin (**18**) significantly reduced TG levels in hepatocytes. These compounds may become fatty liver preventive agents.

4. Experimental

4.1. General experimental procedures

Melting points were determined on a Yanagimoto micromelting point apparatus and were uncorrected. Optical rotations were measured with a JASCO DIP-1000 digital polarimeter. IR spectra

were recorded on a Perkin–Elmer 1720X FTIR spectrophotometer. UV spectra were measured on a HITACHI U-2000 spectrometer using acetonitrile as a solvent. ¹H and ¹³C NMR spectra were recorded on a Varian INOVA 500 spectrometer with standard pulse sequences, operating at 600 and 150 MHz, respectively. CDCl₃ was used as the solvent and TMS as the internal standard. FABMS was recorded on a JEOL JMS-7000 mass spectrometer. CD spectra were measured on a JASCO J-820 spectrometer. Column chromatography (silica gel, 70–230 mesh; Merck) and medium-pressure liquid chromatography (MPLC; silica gel, 230–400 mesh; Merck) were conducted. HPLC was run on a JASCO PU-1586 instrument equipped with a differential refractometer (RI 1531). Fractions obtained from column chromatography were monitored by TLC (silica gel 60F₂₅₄; Merck).

4.2. Plant material

The oil of the seeds of *C. guianensis* AUBLET (Meliaceae), was collected in the Amazon, Brazil, in March, 2011. A voucher specimen (CG-01-1) was deposited in the Herbarium of the Laboratory of Medicinal Chemistry, Osaka University of Pharmaceutical Sciences.

4.3. Isolation of compounds 1–7

Preliminary silica gel column chromatography was performed to separate the seed oil (1.1 kg) of the *C. guianensis* AUBLET into 8 fractions: Fraction A (Fr. No. 1–76, 900 g) eluted with CHCl₃, B (Fr. No. 77–110, 12.0 g) eluted with CHCl₃, C (Fr. No. 111–125, 21.0 g) eluted with CHCl₃/EtOAc=5:1, D (Fr. No. 126–155, 10.9 g) eluted with CHCl₃/EtOAc=5:1, E (Fr. No. 156–170, 1.4 g) eluted with CHCl₃/EtOAc=2:1, F (Fr. No. 171–180, 2.4 g) eluted with EtOAc, G (Fr. No. 181–195, 2.9 g) eluted with EtOAc, and H (Fr. No. 196–208, 0.7 g) eluted with EtOAc/MeOH=5:1. Fraction C (21 g) was rechromatographed on a silica gel (70–230 mesh, 500 g) column using *n*-hexane/EtOAc=1:1 to give the residue C15 (660 mg). Residue C15 (660 mg) was rechromatographed on a silica gel (70–230 mesh, 500 g) column using *n*-hexane/EtOAc=2:1 to give residues C16 (89 mg), C17 (281 mg), and C-18 (25 mg). Residue C16 was separated by HPLC (ODS, 70% MeOH) to give carapanolide N (**1**) (1.5 mg). Residue C17 was separated by HPLC (ODS, 60% CH₃CN) to give carapanolide Q (**5**) (2.8 mg). Residue C18 was separated by HPLC (ODS, 70% MeOH) to give carapanolide R (**6**) (1.5 mg). Fraction D (11 g) was rechromatographed on a silica gel (70–230 mesh, 500 g) column using *n*-hexane/EtOAc=1:1 to give residues D1 (2.9 g) and D2 (1.4 g). Residue D1 was rechromatographed on a silica gel (70–230 mesh, 600 g) column using *n*-hexane/EtOAc=2:1 to give residue D5 (Fr. No. 156–160, 367.5 mg). Residue D5 was rechromatographed on a silica gel (230–400 mesh, 40 g) column using *n*-hexane/EtOAc=2:1 to give residue D6 (94.3 mg). Residue D6 was separated by HPLC (ODS, 70% MeOH) to give carapanolide S (**7**) (6.9 mg). Residue D2 (1.4 g) was rechromatographed on a silica gel (70–230 mesh, 500 g) column using *n*-hexane/EtOAc=2:1 to give residue D7 (Fr. No. 81–90, 79.8.8 mg). Residue D7 was separated by HPLC (ODS, 50% CH₃CN) to give carapanolides M (**1**) (3.3 mg), O (**3**) (3.2 mg), and P (**4**) (4.7 mg).

4.3.1. Carapanolide M (1). Colorless solid; mp 128–130 °C; [α]_D²² –70.8 (c 0.1, CHCl₃); UV λ_{\max} (CH₃CN)/nm: 213.5 (log ϵ 3.73); HRFABMS m/z : 775.2814 [M+H]⁺ (C₃₈H₄₇O₁₇, calcd for 775.2811); IR ν_{\max} (KBr) cm⁻¹: 3489, 2952, 1743, 1371; FABMS m/z (rel int.): 773 ([M+H]⁺, 50%), 43 (100); CD λ nm ($\Delta\epsilon$) [c 4.0 \times 10⁻⁴ M, CH₃CN]: 217 (1.87), 340 (0); ¹H and ¹³C NMR data: see Table 1.

4.3.2. Carapanolide N (2). Colorless crystal mp 168–169° (MeOH/CHCl₃); [α]_D²² –34.8 (c 0.1, CHCl₃); UV λ_{\max} (CH₃CN)/nm: 208 (log ϵ

3.52); HRFABMS m/z : 847.3024 $[M+H]^+$ ($C_{41}H_{51}O_{19}$, calcd for 847.3025); IR ν_{\max} (KBr) cm^{-1} : 3510, 2936, 1747, 1638, 1505; FABMS m/z (rel int.): 847 ($[M+H]^+$, 56%), 43 (100); CD λ nm ($\Delta\epsilon$) [c 4.0×10^{-4} M, CH_3CN]: 218 (7.58), 260 (0); 1H and ^{13}C NMR data: see Table 1.

4.3.3. *Carapanolide O* (3). Colorless solid; mp 126–128 °C; $[\alpha]_D^{22}$ –7.4 (c 0.1, $CHCl_3$); UV λ_{\max} (CH_3CN)/nm: 216.5 ($\log \epsilon$ 3.76); HRFABMS m/z : 805.2919 $[M+H]^+$ ($C_{39}H_{49}O_{18}$, calcd for 805.2919); IR ν_{\max} (KBr) cm^{-1} : 3457, 2938, 1743, 1470; FABMS m/z (rel int.): 805 ($[M+H]^+$, 35%), 43 (100); CD λ nm ($\Delta\epsilon$) [c 4.0×10^{-4} M, CH_3CN]: 212 (0), 221 (1.0), 235 (0.3), 262 (1.4), 300 (0.5), 316 (0.6), 324 (0.5), 331 (0.6), 355 (0); 1H and ^{13}C NMR data: see Table 1.

4.3.4. *Carapanolide P* (4). Colorless solid; mp 153–155 °C. $[\alpha]_D^{22}$ –59.6 (c 0.1, $CHCl_3$); UV λ_{\max} (CH_3CN)/nm: 218 ($\log \epsilon$ 3.74); HRFABMS m/z : 791.2762 $[M+H]^+$ ($C_{38}H_{47}O_{18}$, calcd for 791.2760); IR ν_{\max} (KBr) cm^{-1} : 3526, 2952, 1744, 1370; FABMS m/z (rel int.): 791 ($[M+H]^+$, 64%), 43 (100); CD λ nm ($\Delta\epsilon$) [c 4.0×10^{-4} M, CH_3CN]: 209 (0), 222 (11.5), 353 (0); 1H and ^{13}C NMR data: see Table 1.

4.3.5. *Carapanolide Q* (5). Colorless solid, mp 126–128 °C. $[\alpha]_D^{22}$ –64 (c 0.1, $CHCl_3$); UV λ_{\max} (CH_3CN)/nm: 216 ($\log \epsilon$ 3.75); HRFABMS m/z : 775.2814 $[M+H]^+$ ($C_{38}H_{47}O_{17}$, calcd for 775.2811); IR ν_{\max} (KBr) cm^{-1} : 3495, 2925, 2854, 1740, 1465; FABMS m/z (rel int.): 775 ($[M+H]^+$, 100%), 43 (75); CD λ nm ($\Delta\epsilon$) [c 4.0×10^{-4} M, CH_3CN]: 218 (2.1), 248 (0), 260 (–0.3), 288 (0); 1H and ^{13}C NMR data: see Table 1.

4.3.6. *Carapanolide R* (6). Colorless amorphous. $[\alpha]_D^{22}$ –27.8 (c 0.1, $CHCl_3$); UV λ_{\max} (CH_3CN)/nm: 224.5 ($\log \epsilon$ 3.78); HRFABMS m/z : 631.2754 $[M+H]^+$ ($C_{33}H_{43}O_{12}$, calcd for 631.2755); IR ν_{\max} (KBr) cm^{-1} : 3478, 2975, 1709, 1634; FABMS m/z (rel int.): 631 ($[M+H]^+$, 24%), 95 (31), 43 (100); CD λ nm ($\Delta\epsilon$) [c 4.0×10^{-4} M, CH_3CN]: 218 (10.1), 232 (0), 240 (–3.4), 252 (0), 266 (3.3), 284 (0), 309 (–4.0), 360 (0); 1H and ^{13}C NMR data: see Table 2.

4.3.7. *Carapanolide S* (7). Colorless amorphous. $[\alpha]_D^{22}$ +35.8 (c 0.1, $CHCl_3$); UV λ_{\max} (CH_3CN)/nm: 233 ($\log \epsilon$ 3.82); HRFABMS m/z : 643.2755 $[M+H]^+$ ($C_{34}H_{43}O_{12}$, calcd for 643.2755); IR ν_{\max} (KBr) cm^{-1} : 3506, 2925, 1726, 1463; FABMS m/z (rel int.): 643 ($[M+H]^+$, 10%), 83 (100); CD λ nm ($\Delta\epsilon$) [c 4.0×10^{-4} M, CH_3CN]: 230 (20.0), 246 (1.2), 266 (4.8), 287 (0), 310 (–4.0), 356 (0); 1H and ^{13}C NMR data: see Table 1.

4.4. Crystal data of 2

$C_{82}H_{100}O_{38}$, M_r 1693.62, orthorhombic, space group: $P2_12_12_1$, $a=11.062$ (5) Å, $b=19.419$ (8) Å, $c=38.519$ (16) Å, $\alpha=\beta=\gamma=90.00^\circ$, $V=8274$ (6) Å³, $D_x=1.360$ g/cm^{–3}, $Z=4$, $F(000)=3584$, $\mu(Mo\ K\alpha)=0.108$ mm^{–1}, measured independent reflections=19,798, number of reflections used for refinement=9108 ($I>2\sigma(I)$), parameters used for refinement=1081, final $R=0.0719$ (for $I>2\sigma(I)$) and $wR=0.1692$ (for all data), $(\delta/\sigma)_{\max}=0.000$, $\Delta\rho_{\max}=0.250$ e Å^{–3}, and $\Delta\rho_{\min}=-0.305$ e Å^{–3}. X-ray diffraction data were collected with a Bruker AXS SMART APEX CCD camera. Crystal structures were solved by a direct method using the SHELXS-97 program. Atomic scattering factors were taken from International Tables for X-ray Crystallography. Positional parameters of non-H-atoms were refined by a full-matrix least-squares method with anisotropic thermal parameters using the SHELXL-97 program. Structural data were deposited with the following designation: 7: CCDC-1034402. These can be obtained free of charge at www.ccdc.cam.ac.uk/conts/retrieving.html (or from the Cambridge Crystallographic Data Centre, 12 Union Road, Cambridge CB21EZ, U.K.; fax: (+44) 1223 336 033; e-mail: deposit@ccdc.cam.ac.uk).

4.5. Effects on TG content in high glucose-pretreated HepG2 cells

HepG2 cells (RIKEN) were maintained in Minimum Essential Medium Eagle (MEM, Sigma–Aldrich) containing 10% fetal bovine serum, 1% MEM non-essential amino acids (Invitrogen), penicillin G (100 units/mL), and streptomycin (100 mg/mL) at 37 °C under a 5% CO₂ atmosphere. Cells were inoculated into 48-well tissue culture plates [105 cells/well in 200 mL/well in MEM]. After 20 h, the medium was replaced with 200 mL/well of Dulbecco's Modified Eagle's Medium (DMEM) containing high glucose (4500 mg/L) and cultured for 6 days. Medium was replaced with fresh medium one every 2 days. After lipid accumulation, the medium was exchanged to 200 mL/well of DMEM containing low glucose (1000 mg/L) and a test sample, and the cells were cultured. After 20 h, TG and protein contents in the cells were determined in the same manner as described above. An antidiabetic agent, metformin, was used as a reference compound.³²

Acknowledgements

We thank Mr. Akira Yoshino for collecting and identifying the plant material. We also thank Dr. Katsuhiko Minoura and Dr. Mihoyo Fujitake (this University) for NMR and MS measurements.

Supplementary data

Supplementary data related to this article can be found at <http://dx.doi.org/10.1016/j.tet.2015.03.017>.

References and notes

- Tan, Q.-G.; Xiao-Dong, L. *Chem. Rev.* **2011**, *111*, 7437–7522.
- Penido, C.; Costa, K. A.; Pennaforte, R. J.; Costa, M. F. S.; Pereira, J. F. G.; Siani, A. C.; Henriques, M. G. M. O. *Inflamm. Res.* **2005**, *54*, 295–303.
- Pereira da Silva, V. P.; Oliveira, R. R.; Figueiredo, M. R. *Phytochem. Anal. PCA* **2009**, *20*, 77–81.
- Penido, C.; Conte, F. P.; Chagas, M. S.; Rodrigues, C. A.; Pereira, J. F.; Henriques, M. G. *Inflamm. Res.* **2006**, *55*, 457–464.
- Nakanishi, K. *Chem. Pharm. Bull.* **1965**, *13*, 882–890.
- Waterman, A. M. *Trop. Woods* **1946**, *88*, 1–11.
- Ferraris Fausto, K.; Rodrigues, R.; da Silva, V. P.; Figueiredo, R.; Penido, C.; Henriques, M. G. M. O. *Int. Immunopharmacol.* **2011**, *11*, 1–11.
- Miranda, J.; Raimundo, N. C.; Dolabela, M. F.; da Silva, M. N.; Povoa, M. M.; Maia, J. G. S. *J. Ethnopharmacol.* **2012**, *142*, 679–683.
- Prophiro Josiane, S.; da Silva Mario, A. N.; Kanis Luiz, A.; da Silva, B. M.; Jonny, E.; da Silva Onilda, S. *Parasitol. Res.* **2012**, *110*, 713–719.
- Inoue, T.; Nagai, Y.; Mitooka, A.; Ujiie, R.; Muraoka, O.; Yamada, T.; Tanaka, R. *Tetrahedron Lett.* **2012**, *53*, 6685–6688.
- Inoue, T.; Matsui, Y.; Kikuchi, T.; In, Y.; Yamada, T.; Muraoka, O.; Matsunaga, S.; Tanaka, R. *Org. Lett.* **2013**, *15*, 3018–3021.
- Inoue, T.; Matsui, Y.; Kikuchi, T.; In, Y.; Muraoka, O.; Yamada, T.; Tanaka, R. *Ri-toterapia* **2014**, *96*, 56–64.
- Matsui, Y.; Kikuchi, T.; Inoue, T.; Muraoka, O.; Yamada, T.; Tanaka, R. *Molecules* **2014**, *17*, 17130–17140.
- Morikawa, T.; Ninomiya, K.; Xu, F.; Okumura, N.; Matsuda, H.; Muraoka, O.; Hayakawa, T.; Yoshikawa, M. *Phytochem. Lett.* **2013**, *6*, 198–204.
- Tanaka, Y.; Yamada, T.; In, Y.; Muraoka, O.; Kajimoto, T.; Tanaka, R. *Tetrahedron* **2011**, *67*, 782–792.
- Abdelgaleil, S. A.; Okamura, H.; Iwanaga, T.; Sato, A.; Miyahara, I.; Doe, M. *Tetrahedron* **2001**, *57*, 119–126.
- Zhang, H.; VanDerveer, D.; Wang, X.; Chen, F.; Androulakis, X. M.; Wargovich, M. J. *J. Chem. Crystallogr.* **2007**, *37*, 463–467.
- Tanaka, Y.; Sakamoto, A.; Inoue, T.; Yamada, T.; Kikuchi, T.; Kajimoto, T.; Muraoka, O.; Sato, A.; Wataya, Y.; Kim, H.-S.; Tanaka, R. *Tetrahedron* **2012**, *68*, 3669–3677.
- Kulkarni, K. S.; Paknikar, S. K.; Bhattacharyya, S. C. *Tetrahedron* **1964**, *20*, 1289–1300.
- Bellentani, S.; Tiribelli, C.; Saccoccio, G.; Sodde, M.; Fratti, N.; De Martin, C.; Cristia-nini, G. *Hepatogly* **1994**, *20*, 1442–1449.
- El-Hassan, A. Y.; Ibrahim, E. M.; Al-Mulhim, F. A.; Nabhan, A. A.; Chammas, M. Y. *Br. J. Radiol.* **1992**, *65*, 774–778.
- Marceau, P.; Biron, S.; Hould, F. S.; Marceau, S.; Simard, S.; Thung, S. N.; Kral, J. G. *J. Clin. Endocrinol. Metab.* **1999**, *84*, 1513–1517.
- Marchesini, G.; Brizi, M.; Morselli-Labate, A. M.; Bianchi, G.; Bugianesi, E.; McCul-lough, A. J.; Forlani, G.; Melchionda, N. *Am. J. Med.* **1999**, *107*, 450–455.

24. Morikawa, T.; Xu, F.; Kashima, Y.; Matsuda, H.; Ninomiya, K.; Yoshikawa, M. *Org. Lett.* **2004**, *6*, 869–872.
25. Morikawa, T.; Xu, F.; Ninomiya, K.; Matsuda, H.; Yoshikawa, M. *Chem. Pharm. Bull.* **2004**, *52*, 494–497.
26. Kraus, W.; Cramer, R.; Sawitzki, G. *Phytochemistry* **1981**, *20*, 117–120.
27. Mallavarapu, G.; Gopal, R.; Murslikrishna, E. *Phytochemistry* **1985**, *24*, 305–307.
28. Gary, E. L. B.; Matthew, D. S.; Thomas, E. P.; Brian, S. J. B. *J. Med. Chem.* **2008**, *51*, 6495–6502.
29. Liu, J.; Jin, X.; Yu, C.-H.; Chen, S.-H.; Li, W.-P.; Li, Y.-M. *J. Gastroenterology Hepatology* **2010**, *25*, 613–618.
30. Zhou, G.; Myers, R.; Li, Y.; Chen, Y.; Shen, X.; Fenyk-Melody, J.; Wu, M.; Ventre, J.; Doebber, T.; Fujii, N.; Musi, N.; Hirshman, M.-F.; Goodyear, L.-J.; Moller, D.-E. *J. Clin. Invest.* **2001**, *108*, 1167–1174.
31. Kaur, R.; Arora, S. *J. Med. Plants Res.* **2009**, *3*, 196–216.
32. Muraoka, O.; Morikawa, T.; Zhang, Y.; Ninomiya, K.; Nakamura, S.; Matsuda, H.; Yoshikawa, M. *Tetrahedron* **2009**, *65*, 4142–4148.

CH– π Interaction in VQIVYK Sequence Elucidated by NMR Spectroscopy is Essential for PHF Formation of Tau

Koushirou Sogawa,¹ Katsuhiko Minoura,¹ Yasuko In,¹ Toshimasa Ishida,¹ Taizo Taniguchi,² Koji Tomoo¹

¹Department of Physical Chemistry, Osaka University of Pharmaceutical Sciences, Osaka 569-1094, Japan

²Department of Pharmaceutical Health Care, Faculty of Pharmaceutical Sciences, Himeji Dokkyo University, Hyogo 670-8524, Japan

Received 30 January 2014; accepted 27 March 2014

Published online 29 March 2014 in Wiley Online Library (wileyonlinelibrary.com). DOI 10.1002/bip.22489

ABSTRACT:

One of the histopathological features of Alzheimer's disease (AD) is higher order neurofibrillary tangles formed by abnormally aggregated tau protein. Investigation of the mechanism of tau aggregation is important for the clarifying the cause of AD and the development of therapeutic drugs. The microtubule-binding domain, which consists of repeats of similar amino acids (R1–R4) is thought to form the core component of paired helical filament (PHF). The hexapeptide³⁰⁶VQIVYK³¹¹ of R3 has been shown to take a key role of promoting tau aggregation and assumed that its CH– π interaction between the side chains of Ile308 and Tyr310 would contribute in stabilizing the filament.

In this work, we investigated a short isoform of tau (4RTau), R3, VQIVYK peptide and their mutants by thioflavin S (ThS) fluorescence, and NMR measurements, and proved for the first time that this CH– π interaction stabilizes the filament at the atomic level. In addition, by molecular modeling, we revealed that this interaction further supports an extended amphipathic structure for molecular self-association during the process of PHF formation of tau protein. The present work indicates new approach that inhibits the CH– π interaction for develop-

ing a therapeutic agent for AD. © 2014 Wiley Periodicals, Inc. *Biopolymers (Pept Sci)* 102: 288–295, 2014.

Keywords: tau protein; CH– π interaction; NMR spectroscopy

This article was originally published online as an accepted preprint. The “Published Online” date corresponds to the preprint version. You can request a copy of the preprint by emailing the Biopolymers editorial office at biopolymers@wiley.com

INTRODUCTION

Alzheimer's disease (AD) is a neurodegenerative disease accompanied by accumulation of misfolded proteins. AD pathology is characterized by the extracellular amyloid plaques and the neurofibrillary tangles (NFTs).^{1,2} NFTs consist of paired helical filament (PHF), and abnormally phosphorylated tau is known to form the PHF.^{3–8} Therefore, investigation of mechanism of PHF formation by tau protein is important for the pathogenic mechanism and the development of therapeutic drugs for AD.

Six tau isoforms are expressed ranging in size from 352 to 441 amino acids in the central nervous system of the adult human brain (Figure 1A).^{9–11} Tau contains a microtubule binding domain (MBD) consisting of three or four repeats of 31 or 32 similar amino acid sequences in the C-terminal half. The MBD is not only important for binding of tau to microtubule but also have a key role for abnormal self-aggregation of tau.^{12–14} Even though the sequence of repeat peptides are similar to each other, the abilities of self-aggregation of these repeat peptides (R1–R4) are quite different. R1 and R4 have no ability

Correspondence to: Koji Tomoo; Department of Physical Chemistry, Osaka University of Pharmaceutical Sciences, 4-20-1 Nasahara, Takatsuki, Osaka 569-1094, Japan; e-mail: tomoo@gly.oups.ac.jp

© 2014 Wiley Periodicals, Inc.

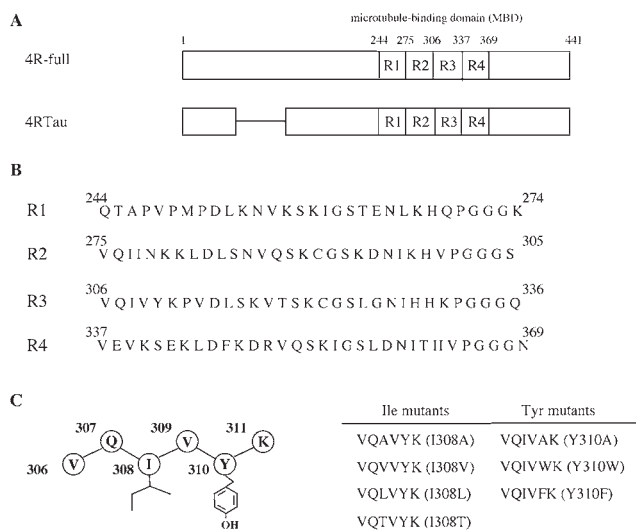


FIGURE 1 Schematic representations of (A) the full-length tau (4R-full) and its isoform 4RTau, (B) amino acid sequences of four single-repeat peptides of MBD, and (C) VQIVYK and mutant peptides used in this work. 4RTau which is deleted N-terminal inserts from 4R-full consists of 383 residues. Residual numbering is adapted to that of 4R-full (441 residues).

of filament formation. On the other hand, both R2 and R3 make a filament. Especially, R3 has the most active function *in vitro* filament formation.¹⁵ We have shown that R3 with 31 amino acid residues in a TFE solution takes a well refined extended structure in Val1–Lys6 region and an α -helical structure with amphipathic distribution of the respective side chains in Leu10–Leu20 region.¹⁶ The results of our investigations on these repeat peptides (R1–R4) and the series of mutant peptides of R3 have revealed that Ile308 and Tyr310 in the sequence of ³⁰⁶VQIVYK³¹¹ of R3, are indispensable for the filament formation of tau.^{17,18}

In order to clarify the reason why these repeat peptides (R1–R4) are so different in conformational propensity even though the amino acid sequences are similar to each other and to investigate the role of these two residues, Ile308 and Tyr310, we investigated the interactions between the side chains of VQIVYK peptide and the R3 mutants by ¹H-NMR measurements and elucidated the relationship between the structural properties and ability of filament formation of tau protein.

MATERIALS AND METHODS

Chemical Synthesis of Peptides

All of the hexapeptides and R3-I308A (mutant from Ile to Ala at position 308) were synthesized using a conventional solid-phase synthesizer. The peptides obtained in lyophilized form were characterized

by mass spectrometry and determined to be >95.0% pure by reverse-phase HPLC. Heparin (average molecular weight = 6000) and thioflavin S (ThS) were purchased from Sigma. The other commercially available materials used were of reagent grade or higher.

Preparation of 4RTau Mutants

The gene of 4RTau-Y310F, 4RTau-I308L, and 4RTau-I308T prepared from 4RTau-wild DNA using mutagenized primers and the Quick Change site-directed mutagenesis kit from Stratagene. The gene expression in *Escherichia coli* and the purification of His-tagged 4RTau mutants were performed as described in a previous paper.¹⁹ The purity of each mutant was confirmed on the basis of a single band by SDS-PAGE. The concentration of each sample was determined by measuring UV absorption at 280 nm ($\epsilon = 1280 \text{ mol}^{-1} \text{ L cm}^{-1}$ for Tyr residue) and by Bradford protein assay.²⁰

ThS Fluorescence Measurement

A 25 μM solution of each sample was prepared using 50 mM Tris-HCl buffer (pH 7.6) with 10 μM ThS added to each solution. Fluorescence intensity was measured using a JASCO FP-6500 instrument with a 2 mm quartz cell maintained at 25°C using a circulating water bath. After adding 6.25 μM heparin (an optimal concentration for aggregation) to each solution, the aggregation profile of each sample was monitored by plotting the time course of fluorescence intensity with an excitation at 440 nm and an emission at 500 nm. The background fluorescence of each sample solution was subtracted when necessary. The same measurement was repeated at least three times using the newly prepared sample to confirm reproducibility, and the average was used for the data presentation.

EM Measurement

A 25 μM solution of each sample was mixed with 6.25 μM heparin in 50 mM Tris-HCl buffer (pH 7.6) and then incubated at 37°C for 48 h. Copper grids (600 mesh) were used for negative-staining EM. One drop of each protein solution and one drop of 2% uranyl acetate were placed on the grid. After 1 min, excess fluid was removed from the grids. Negative staining EM was performed using an electron microscope (Hitachi H-600) operated at 75 kV.

¹H-NMR Analyses

¹H-NMR spectra were recorded on an Agilent NMR system 600-DD2-600 spectrometer with a variable temperature-control unit. ¹H chemical shifts were referenced to 0 ppm for TSP. The 2D DQF-COSY, TOCSY, NOESY of R3-I308A were acquired almost same the following conditions as the case of R3 (wild type)¹⁶ and R3-Y310A¹⁷ using standard programs available in the Varian software library. The TOCSY spectra were recorded at mixing times of 70 and 120 ms. The NOESY spectra were measured at mixing times of 200, 300, and 400 ms and the ROESY spectra were measured at mixing times of 200 and 300 ms. The solvent used for R3-I308A peptide was TFE-*d*₂ and the concentration was 1 mM. For VQIVYK and their substituted peptides, the solvent was *d*-Tris-HCl pH 7.6 and the concentration was 2 mM. Proton peak assignments were performed by combination of the connectivity information via scalar coupling in phase-sensitive TOCSY experiments and the sequential NOE and ROE networks along the peptide backbone protons.

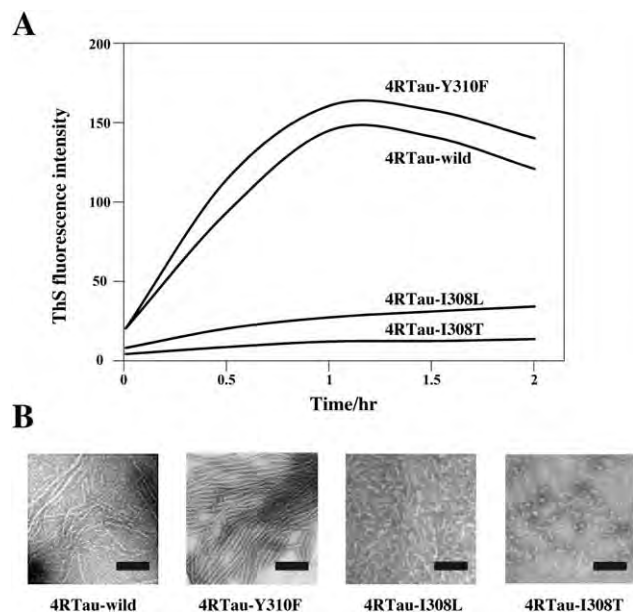


FIGURE 2 (A) Time-dependent ThS fluorescence intensity profiles and (B) negative-staining EM images of 4RTau-wild and its mutants at the position 308 and 310. The length of the bar in (B) corresponds to 500 nm.

Computational Molecular Modeling for R3-I308A

Various 3D structures that satisfy the NOE distance and J torsion angle constraints of intramolecular proton pairs were constructed by dynamic SA (simulated annealing) calculations using the CNS program.²¹ After randomizing the peptide into extended strands, corresponding to each disjointed molecular entity, the initial structures were constructed by referring to the data structures and statistical analysis of the average property. The constructed structure was then annealed for 15 ps at 50,000 K and cooled to 300 K (at a rate of 250 K/step) for 10 ps, and the minimization of more than 5000 steps was continued. The constraints for distances and torsion angles were used as the harmonic potential function. Assuming the same correlation time for all the protons, the offset dependence of the NOESY cross peaks was used for the estimation of proton-proton distances. The NOE intensities were classified into three groups (strong, medium and weak). On the other hand, the vicinal coupling constants obtained from DQF-COSY measurements were used to estimate possible torsion angles:

${}^3J_{\text{HNC}\alpha\text{H}} = 1.9 - 1.4 \cos \theta + 6.4 \cos 2\theta$, where $\varphi = |\theta - 60^\circ|$ for φ torsion angle around $C'_{i-1} - N_i - C\alpha_i - C'_i$ bond sequence. Ramachandran plots and RMSD analyses of energy minimized structures were carried out using the program MOLMOL.²²

RESULTS

Different Behaviors Among 4RTau Mutants of Ile308 and Tyr310 Residues for Filament Formation

In previous study, we have investigated aggregation behaviors of 4RTau and its mutant by the ThS fluorescence intensity and electron microscopy. The results showed that the aggregation path-

way to filament formation depends on properties of the amino acid residues at 308 and 310 position.¹⁹ In order to make this relation clearer, three mutants of 4RTau, 4RTau-Y310F, 4RTau-I308L, and 4RTau-I308T were synthesized and investigated. The results are shown in Figure 2, and summarized in Table I.

The aggregation behavior of 4RTau-Y310F is almost the same as that of 4RTau-wild. The fluorescence intensity of 4RTau-Y310F increased with time course. The EM figure of 4RTau-Y310F showed long filaments as the same as 4RTau-wild. By referring to the previous results, it indicates that aromatic residues at the position of 310 are necessary for filament formation of 4RTau.

From the result of the mutation at 308 from Ile to Leu, both of which are belonged in aliphatic amino acids, the fluorescence intensity of 4RTau-I308L decreased by approximately 35% when compared with the wild type. In addition, its EM figure was quite different from that of 4RTau-wild. The shape of filament of 4RTau-I308L was shorter than that of 4RTau-wild. A similar result was obtained in the case of Val mutant at 308 in our previous study.¹⁹ Furthermore, the polar mutation from Ile to Thr markedly decreased or almost lost the fluorescence intensity of 4RTau-I308T. Its EM figure was a granule, not a filament. These results showed that the mutation of Ile308 governs the elongation of filament and suggest that the requirement of position 308 is not only the aliphatic residues, but also the filament formation is deeply dependent on the type of side chain.

As the detail is to be discussed later, the filament formation which would be accompanied by fixing the hexapeptide regions of R3 should be triggered by CH- π interaction.

Ile308 and Tyr310 are Related to the Conformational Stability of VQIVYK Region in R3 Domain

We have reported that the abilities of self-aggregation of the repeat domains (R1–R4) are quite different from each other,

Table I Comparison of ThS Fluorescences and EM Morphologies of 4RTau and their Mutants (25 μM)

Wild/mutant	Relative fluorescence intensity (%) ^a	EM picture ^b
4RTau-wild	100	filament
4RTau-Y310F	100	filament
4RTau-I308L	35	short filament
4RTau-I308T	10	granule

^a The fluorescence intensities of mutants correspond to the values relative to those of 4RTau-wild at 1 hr after initiating aggregation by addition of heparin.

^b EM morphology at 48hr after initiating aggregation by addition of heparin.



FIGURE 3 Diagram of NOE connectivity between neighboring ($d_{\alpha N(i, i+1)}$, $d_{NN(i, i+1)}$, $d_{\alpha N(i, i+3)}$, and $d_{\alpha\beta(i, i+3)}$) protons and J -coupling constants ($^3J_{\text{HNC}\alpha\text{H}}$). The strength of the observed NOE is represented by the thickness of respective bars. Residues with $^3J_{\text{HNC}\alpha\text{H}} < 6$ Hz are indicated by arrows.

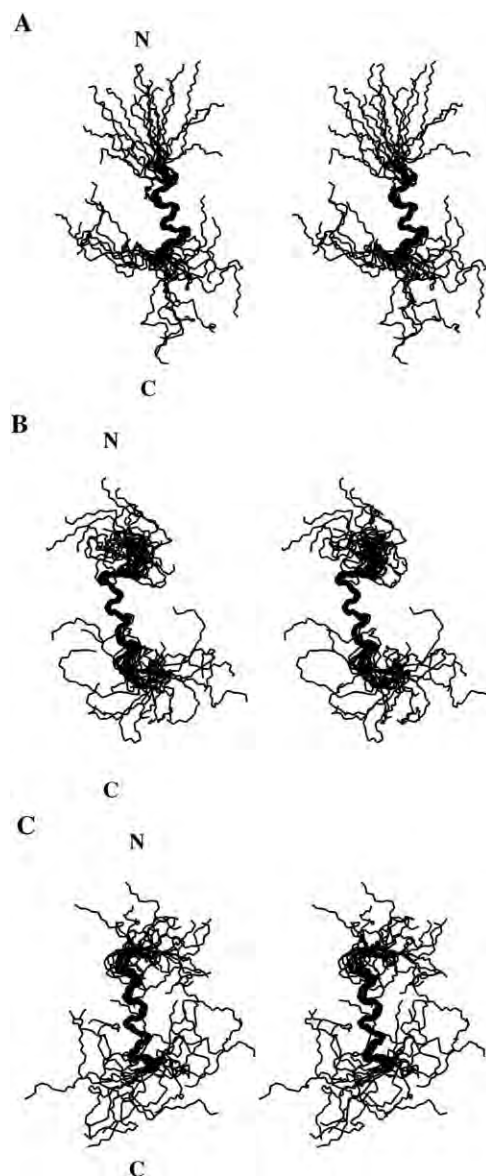


FIGURE 4 Stereoscopic superposition of the most 20 stable conformers of (A) R3, (B) R3-Y310A, and (C) R3-I308A. Each conformer is projected in order to superimpose on the Leu10–Leu20 sequence. The upper and lower sides of conformers correspond to N- and C-terminal regions, respectively.

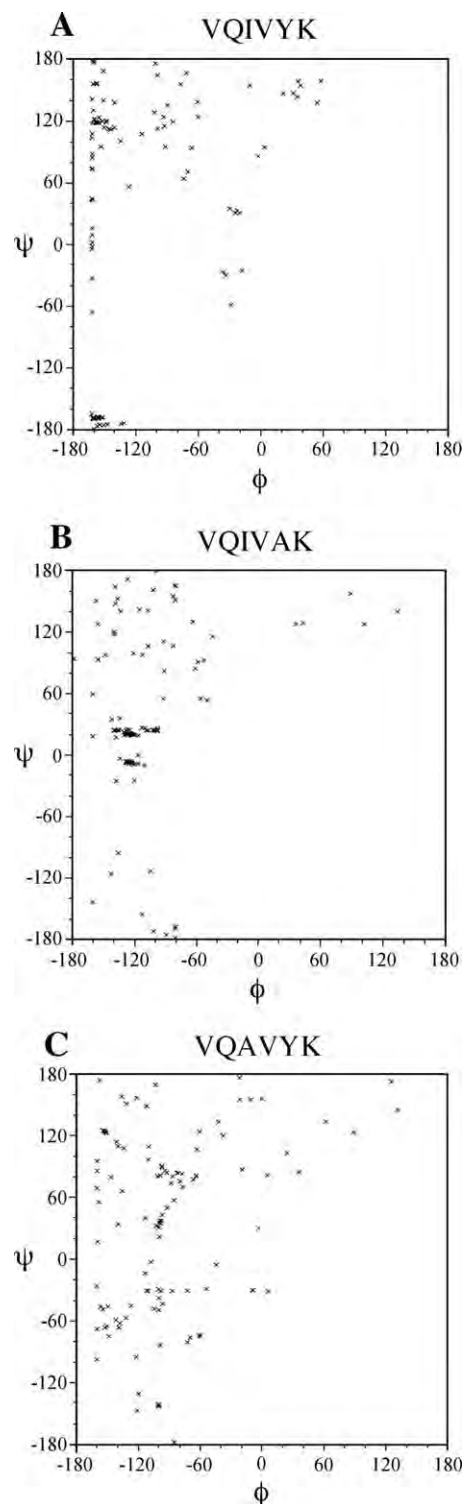


FIGURE 5 Ramachandran plots of the 20 most stable N-terminal partial conformers of (A) R3, (B) R3-Y310A, and (C) R3-I308A in TFE solution.

and R3 domain has the most active function *in vitro* filament formation. Furthermore, we elucidated the difference of ability of filament formation was dependent upon the structural

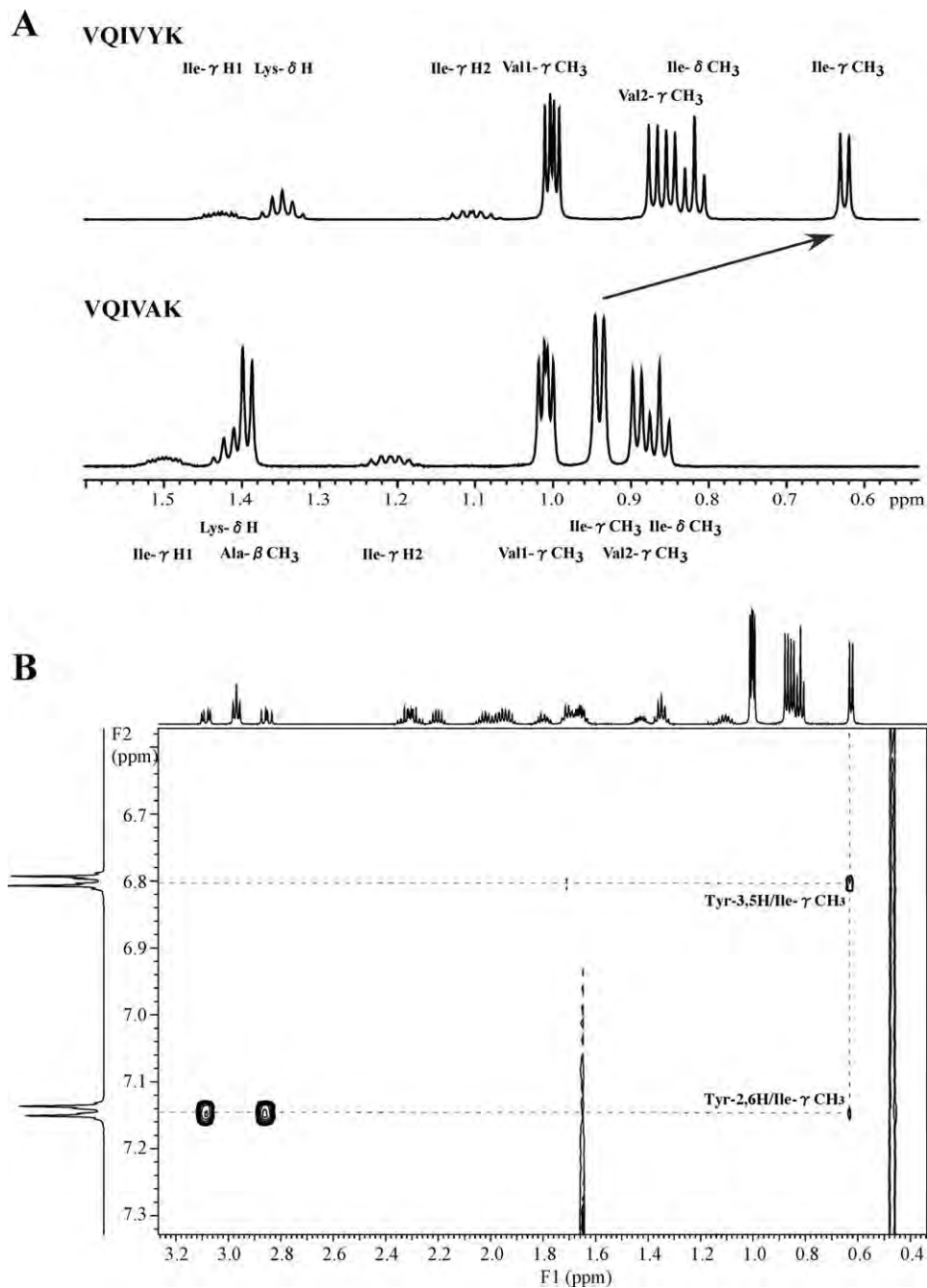


FIGURE 6 (A) Comparison of chemical shifts of the ^1H -NMR spectra for VQIVYK and VQIVAK (Y310A) peptides in d -Tris-DCl (pH 7.6). (B) ROESY spectrum (mixing time 300 ms) for VQIVYK peptide in d -Tris-DCl (pH 7.6).

flexibility of each repeat domains by ^1H -NMR. The measurement with TFE condition by NMR is useful for the analysis of structural flexibility because the peptides tend to have helical structure in TFE solution. A previous study by NMR analysis showed that the R1, R2 and R4 repeat peptides took helical structures in TFE. However, the N-terminal VQIVYK region of

R3 showed extended structure in TFE even though the other regions of R3 showed helical structure.¹⁶ In addition, we reported that the conformational feature of R3 N-terminal region shifted from an extended to a random structure in R3-Y310A in TFE.¹⁷ In this study, we analyzed the role of Ile308 on the structural feature of VQIVYK using R3-I308A in TFE

Table II Upfield Chemical Shift Changes of VQIVYK and their Mutant Peptides Compared to these Ala-Mutants^a

Peptide	Residue	Position	Chemical shift (ppm)		
			δ_{H}	$\delta_{\text{H(Ala-mutant)}}^{\text{a}}$	$\Delta\delta_{\text{H}}$ (ppm) ^b
VQIVYK (wild)	Ile308	γ CH ₃	0.625	0.892	0.267
VQIVWK (Y310W)	Ile308	γ CH ₃	0.579	0.892	0.313
VQIVFK (Y310F)	Ile308	γ CH ₃	0.719	0.892	0.173
VQAVYK (I308A)	Ala308	β CH ₃	1.312	1.392	0.080
VQVVYK (I308V)	Val308	γ CH ₃	0.721	0.925	0.204
VQLVYK (I308L)	Leu308	β CH ₂	1.421	1.637	0.216
VQTVYK (I308T)	Thr308	γ CH ₃	1.045	1.210	0.165

^a $\delta_{\text{H(Ala-mutant)}}$ Values show the chemical shifts (ppm) of side chains in the basic amino acids (VQIVAK, VQAVAK, VQVVAK, VQLVAK, VQTVAK).

^b $\Delta\delta_{\text{H}} (= \delta_{\text{H(Ala-mutant)}} - \delta_{\text{H}})$ indicate upfield chemical shift changes.

by ¹H-NMR spectroscopy and molecular modeling calculations. The construction of possible conformers was attempted by dynamic SA calculation by using 235 NOE constraints for proton-proton distances and 23 ³J_{HNC α H} constraints for ϕ torsion angles as summarized in Figure 3. One hundred 3D structures of R3-I308A were constructed and the 20 most stable conformers were evaluated.

In Figure 4, the result of the analysis are shown with previous results of R3-Y310A and R3 itself. It shows that the N-terminal regions of both mutants are more flexible than that of R3. Interestingly, the constriction of N-terminal structure of R3-Y310A was better than that of R3-I308A.

To evaluate the conformational flexibility of N-terminal region, we compared ϕ and ψ torsion angle of peptide bond between R3 and the mutants by Ramachandran plots (Figure 5). The ϕ and ψ angles of R3 were nearly located in the β -strand region. On the other hand, plot of R3-Y310A angles, which was disrupted the CH- π interaction, were concentrated

in the α -helix region. The difference of these two plots showed that R3-Y310A is more flexible than R3. The conformational flexibility of R3-Y310A reflected the disruption of CH- π interaction. Furthermore, R3-I308A mutant showed another interesting structural feature. The conformation of R3-I308A is even more random than that of R3-Y310A in TFE solution. The flexibility of R3-I308A is at a moderate level among R3 and mutant peptides. The present results suggested that the existence of Tyr310 could restrict the conformational flexibility around the N-terminal region of R3.

Demonstration of CH- π Interaction in VQIVYK Motif Mutant Peptides Using NMR

We have shown by NMR analysis that the ³⁰⁶VQIVYK³¹¹ region in the R3 domain takes an extended structural feature in TFE¹⁶ and both Ile308 and Tyr310 are essential for the

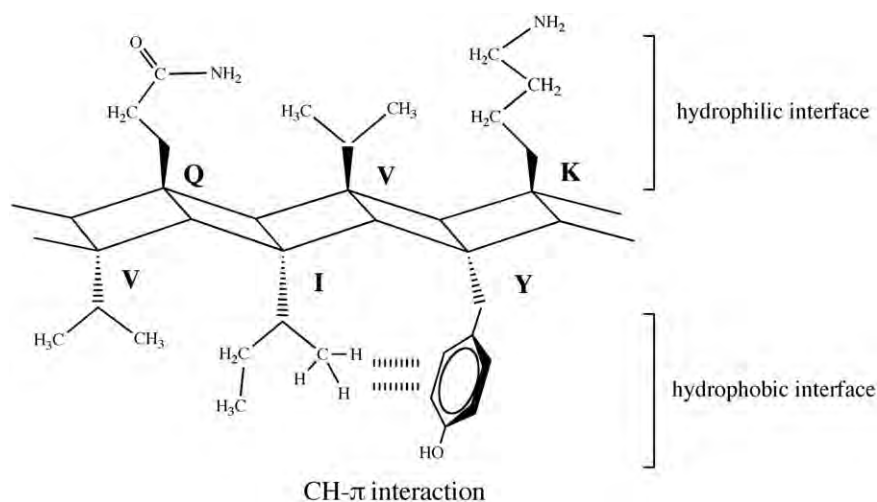


FIGURE 7 The extended amphipathic structure formed by CH- π interaction between Ile308 and Tyr310 in VQIVYK.

stabilization of extended structure. We have been interested in what kind of interaction formed between these two residues. In the $^1\text{H-NMR}$ spectra, the chemical shift of Ile- γCH_3 was shifted to upfield by 0.267 ppm to that of VQIVAK (Figure 6A). This marked upfield shift clearly means that a close contact exists between Ile308- γCH_3 and the aromatic ring of Tyr310 in VQIVYK. This close contact was also observed between these two residues from the ROESY spectrum (Figure 6B).

The similar upfield shifts were obtained from other mutant peptides containing the pair of hydrophobic and aromatic residues at position of 308 and 310 (Table II). However, the extent of upfield shifts of Ile- γCH_3 in VQIVFK and VQIVWK were different from that of VQIVYK. The upfield shift of VQIVFK was less than that of VQIVYK. In contrast, chemical shifts of VQIVWK were greater than that of VQIVYK. The changes of chemical shifts would be caused by difference in π electron density of aromatic residue such as Phe, Trp, and Tyr. The upfield shift of Val308 in VQVVYK were observed in only one side of γCH_3 even though Val at position 308 have two γCH_3 groups. This implies the interaction reduced free rotation of the side chain of Ile to stabilize the conformation of VQIVYK. In addition, it is noteworthy the effects of concentration of peptides and hydrophobicity of solvent were very little on ROESY spectra. Based on these observations, it was concluded that the interaction between Ile- γCH_3 and aromatic ring of Tyr residue was actually an intramolecular CH- π interaction and not a hydrogen bond or a hydrophobic interaction.^{23–26}

DISCUSSION

The sequence of VQIVYK is known to be important for filament formation not only in short peptides and MBD but also in full-length tau.^{27–29} However, the filament formation profile of VQIVYK was not elucidated before. We have reported that Ile308 and Tyr310 in VQIVYK peptide would play an important role in filament formation. In this report, we observed for the first time the CH- π interaction between γCH_3 of Ile308 and aromatic ring of Tyr310 in VQIVYK by NMR spectroscopy at an atomic level. Therefore, this new finding is likely to be important for elucidation of the PHF formation mechanism by tau protein.

We have reported the filament formation of tau protein progresses through two steps of nucleation and elongation from the results of the dynamic light scattering (DLS) data.³⁰ The early step of filament formation is nucleation that is composed of tau oligomer. Subsequently, the seeds of filament progress to PHF at elongation step. Therefore, the elongation of filament depends on the shape of seed. In our previous study, the conformation of VQIVYK region in R3 domain is rigid

even though the other repeats domains are flexible. The CH- π interaction between Ile and Tyr certainly plays a key role in the structural feature of R3 that is necessary for good shape of seed. We analyzed the influence of CH- π interaction on filament formation by using several mutants of tau protein. Both mutants of R3-I308A and R3-Y310A that disrupted CH- π interaction lost the ability of filament formation. On the other hand, all mutants that kept the CH- π interaction formed filaments even though the shape of filaments was different. The ability of filament formation is related to the conformational flexibility of peptides. The CH- π interaction contributed to keeping the planer conformation, which is favored for filament formation. The VQIVYK region in R3 domain is an amphipathic sequence, and this amphipathic structural character is also favored for filament formation (Figure 7). The planer conformation with the CH- π interaction may contribute to the stabilized amphipathic condition. Although the filament formation profile of tau is not clear, these results present important information for the development of therapeutic drugs for AD.

REFERENCES

1. Delacourte, A.; Buee, L. *Int Rev Cytometry* 1997, 171, 167–224.
2. Ballatore, C.; Brunden, K. R.; Trojanowski, J. Q.; Lee, V. M. Y.; Smith, A. B. III.; Huryn, D. M. *Curr Top Med Chem* 2011, 11, 317–330.
3. Goedert, M.; Spillantini, M. G. *Biochim Biophys Acta* 2000, 1502, 110–121.
4. Gendron, T. F.; Petrucelli, L. *Mol Neurodegen* 2009, 4, 13.
5. Gendron, T. F.; Petrucelli, L. *Mol Neurodegen* 2009, 4, 13.
6. Braak, H.; Braak, E. *Acta Neurol Pathol* 1991, 82, 239–259.
7. Bandyopadhyay, B.; Li, G.; Yin, H.; Kuret, J. *J Biol Chem* 2007, 282, 16454–16464.
8. Maeda, S.; Sahara, N.; Saito, Y.; Murayama, S.; Ikai, A.; Takashima, A. *Neurosci Res* 2006, 54, 197–201.
9. Goedert, M.; Spillantini, M. G.; Portier, M. C.; Ulrich, J.; Crowther, R. A. *EMBO J* 1989, 8, 393–399.
10. Goedert, M.; Spillantini, M. G.; Jakes, R.; Rutherford, D.; Crowther, R. A. *Neuron* 1989, 3, 519–526.
11. Goedert, M.; Jakes, R. *EMBO J* 1990, 9, 225–4230.
12. Lee, G.; Neve, R. L.; Kosik, K. S. *Neuron* 1989, 2, 1615–1624.
13. Butner, K. A.; Kirschner, M. W. *J Cell Biol* 1991, 115, 717–730.
14. Goode, B. L.; Feinstein, S. C. *J Cell Biol* 1994, 124, 769–782.
15. Okuyama, K.; Nishiura, C.; Mizushima, F.; Minoura, K.; Sumida, M.; Taniguchi, T.; Tomoo, K.; Ishida, T. *FEBS J* 2008, 275, 1529–1539.
16. Minoura, K.; Mizushima, F.; Tokimasa, M.; Hiraoka, S.; Tomoo, K.; Sumida, M.; Taniguchi, T.; Ishida, T. *Biochem Biophys Res Commun* 2005, 327, 1100–1104.
17. Nishiura, C.; Takeuchi, K.; Minoura, K.; Sumida, M.; Taniguchi, T.; Tomoo, K.; Ishida, T. *J Biochem* 2010, 147, 405–414.
18. Naruto, K.; Minoura, K.; Okuda, R.; Taniguchi, T.; In, Y.; Ishida, T.; Tomoo, K. *FEBS Lett* 2010, 584, 4233–4236.

19. Sogawa, K.; Okuda, R.; In, Y.; Ishida, T.; Taniguchi, T.; Tomoo, K. *J Biochem* 2012, 152, 3, 221–229.
20. Bradford, M. M. *Anal Biochem* 1976, 72, 248–254.
21. Brunger, A. T.; Adams, P. D.; Clore, G. M.; DeLano, W. L.; Gros, P.; Grosse-Kunstleve, R. W.; Jiang, J. S.; Kuszewski, J.; Nilges, M.; Pannu, N. S.; Read, R. J.; Rice, L. M.; Simonson, T.; Warren, G. L. *Acta Crystallogr* 1998, D54, 905–921.
22. Koradi, R.; Billeter, M.; Wuthrich, K. *J Mol Graphics* 1996, 14, 51–55.
23. Nishio, M.; Umezawa, Y.; Hirota, M.; Takeuchi, Y. *Tetrahedron* 1995, 51, 8665–8701.
24. Suezawa, H.; Hashimoto, T.; Tuchinaga, K.; Yoshida, T.; Yuzuri, T.; Sakakibara, K.; Hirota, M.; Nishio, M. *Perkin Trans* 2000, 12, 243–1249.
25. Kobayashi, K.; Asakawa, Y.; Kikuchi, Y.; Toi, H.; Aoyama, Y. *J Am Chem Soc* 1993, 115, 2648–2654.
26. Maeda, I.; Shimohigashi, Y.; Nakamura, I.; Sakamoto, H.; Kawano, K.; Ohno, M. *Biochem Biophys Res Commun* 1993, 193, 428–433.
27. Von Bergen, M.; Friedhoff, P.; Biernat, J.; Heberle, J.; Mandelkow, E. M.; Mandelkow, E. *Proc Natl Acad Sci USA* 2000, 97, 5129–5134.
28. Von Bergen, M.; Barghorn, S.; Li, L.; Marx, A.; Biernt, J.; Mandelkow, E. M.; Mandelkow, E. *J Biol Chem* 2001, 276, 48165–48174.
29. Sawaya, M. R.; Sambashivan, S.; Nelson, R.; Ivanova, M. I.; Sievers, S. A.; Apostol, M. I.; Thompson, M. J.; Balbirnie, M.; Wiltzius, J. J. W.; McFarlane, H. T.; Madsen, A. O.; Riek, C.; Eisenberg, D. *Nature* 2007, 447, 453–457.
30. Sugino, E.; Nishiura, C.; Minoura, K.; In, Y.; Sumida, M.; Taniguchi, T.; Tomoo, K.; Ishida, T. *Biochem Biophys Res Commun* 2009, 385, 236–240.



Carapanolides C–I from the seeds of andiroba (*Carapa guianensis*, Meliaceae)



Takanobu Inoue^a, Yuuki Matsui^a, Takashi Kikuchi^a, Yasuko In^a, Osamu Muraoka^b, Takeshi Yamada^a, Reiko Tanaka^{a,*}

^a Laboratory of Medicinal Chemistry, Osaka University of Pharmaceutical Sciences, 4-20-1 Nasahara, Takatsuki, Osaka 569-1094, Japan

^b Department of Organic Chemistry, Faculty of Pharmaceutical Sciences, Kinki University, 3-4-1 Kowakae, Higashiosaka, Osaka 577-8502, Japan

ARTICLE INFO

Article history:

Received 28 January 2014

Accepted in revised form 4 April 2014

Available online 15 April 2014

Keywords:

Carapanolides C–I

Carapa guianensis

Seed

Meliaceae

Limonoid

ABSTRACT

Five new mexicanolide-type limonoids, carapanolides C–G (**1–5**), together with two new phragmalin-type limonoids, carapanolides H–I (**6, 7**), were isolated from the oil of *Carapa guianensis* AUBLET (Meliaceae) seeds. Their structures were elucidated on the basis of spectroscopic analyses using 1D and 2D NMR spectra and FABMS. Carapanolides C (**1**), E (**3**), and I (**7**) exhibited moderate activity in the P388 (IC₅₀ 17.9 μM in **1**, 15.8 μM in **3**) and L1210 cell lines (IC₅₀ 13.3 μM in **1**, 18.1 μM in **3**, 16.9 μM in **7**). On the other hand, Carapanolide D (**2**) exhibited a strong inhibitory effect in the HL-60 cell line (IC₅₀ 11.0 μM), Carapanolides F (**4**) showed inhibitory activity in the L1210 cell line (IC₅₀ 15.9 μM), and the cytotoxic activity of Carapanolides I (**7**) was moderate in all cell lines.

© 2014 Elsevier B.V. All rights reserved.

1. Introduction

Limonoids, a series of structurally diverse and highly oxygenated tetranortriterpenes, are mainly found in the Meliaceae family, and have been attracting attention from biogenetic and synthetic perspectives [1–3]. *Carapa guianensis* AUBLET (Andiroba, Meliaceae) is a tall tropical tree with fragrant flowers, that sometimes reaches up to 50 m in height. Andiroba is one of the largest leafed trees in the rain forests of South America. Its woody four cornered nut has four cells, each of which contains two to three seeds with oil-rich kernels. Extracts from its bark, flowers, and seeds have been used for centuries by the Amazonian people and exhibit various repellent [4], analgesic [5], anti-malarial [6], anti-inflammatory [7], anti-allergic [8], and anti-plasmodial [9] activities, and also acute and subacute toxicities [10]. Our recent study on the components of the flower of *Carapa guianensis* revealed the absolute structures of Andiroloides A–G [11], structures of Andiroloides H–P and anti-malarial activity [12], and structures of Andiroloides Q–V and

cytotoxic activity [13]. We recently isolated and elucidated the structures of two new unusual 9,10-*seco*-mexicanolide-type limonoids, named Carapanolides A and B [14], and two novel carbon skeletal limonoids, named Guianolides A and B [15], from the seeds of *Carapa guianensis*. The present study describe the isolation and structural determination of seven novel limonoids, named carapanolides C–I (**1–7**), and their cytotoxic activities against the murine P388, human HL-60, and murine L1210 leukemia cell lines.

2. Experimental

2.1. Materials and methods

2.1.1. General procedures

Melting points were determined on a Yanagimoto micro-melting point apparatus and were uncorrected. Optical rotations were measured with a JASCO DIP-1000 digital polarimeter. IR spectra were recorded on a Perkin-Elmer 1720X FTIR spectrophotometer. UV spectra were measured on a HITACHI U-2000 spectrometer using acetonitrile as a solvent. ¹H and ¹³C NMR spectra were recorded on an Agilent vnmrs 600 spectrometer

* Corresponding author. Tel./fax: +81 72 690 1084.
E-mail address: tanakar@gly.oups.ac.jp (R. Tanaka).

Table 1
¹H NMR and ¹³C NMR spectroscopic data for compounds 1–3.

Position	1		2		3		δ_c^b
	δ_H (J in Hz) ^a		δ_H (J in Hz) ^a		δ_H (J in Hz) ^a		
1							208.1 (s)
2							83.5 (s)
3	5.21 s		5.23 s				81.6 (s)
4							40.2 (s)
5	3.09 t	5.2 (6 α , 6 β)	2.59 d	6.7 (6 β)			41.6 (d)
6	α 2.33 s		α 2.45 d	16.1 (6 β)			33.3 (t)
	β 2.33 s		β 2.34 dd	6.7 (5), 16.1 (6 α)			
7							173.2 (s)
8							72.1 (s)
9	2.16 dd	13 (11 β), 4.8 (11 α)	2.46 dd	6.2 (11a), 12.9 (11b)			64.7 (d)
10							50.4 (s)
11	α 2.17 d	4.8 (9)	α 1.70 m				21.0 (t)
	β 1.69 m		β 1.47 m				
12	α 1.55 m		α 1.57 m				30.2 (t)
	β 1.82 m		β 1.75 m				
13							39.6 (s)
14							166.8 (s)
15	6.21 s		6.26 s				115.6 (d)
16							165.2 (s)
17	5.33 s		5.45 s				79.1 (d)
18	1.31 s		1.28 s				21.5 (q)
19	1.17 s		1.08 s				17.4 (q)
20							120.2 (s)
21	7.49 t	0.7 (22, 23)	7.45 br d	0.9 (22)			141.8 (d)
22	6.51 dd	0.7 (21), 1.6 (23)	6.47 dd	0.9 (21), 1.8 (23)			110.6 (d)
23	7.44 t	1.6 (21, 22)	7.44 t	1.8 (22)			142.9 (d)
28	0.91 s		0.91 s				23.4 (q)
29	0.73 s		0.82 s				22.6 (q)
30	α 2.36 d	17.4 (30 β)	6.45 s				44.8 (t)
	β 4.21 d	17.4 (30 α)					
2'							171.1 (s)
2''	2.15 s						21.6 (q)
3'							175.2 (s)
3''	2.55 q	6.9 (3''''')	2.66 q	5.8 (3''''')			41.8 (d)
3'''	A 1.56 m		A 1.54 m				26.6 (t)
	B 1.74 dt	7.4 (3'''''), 13.8 (3''''A)	B 1.79 m				
3''''	0.96 t	7.4 (3''''A, 3''''B)	0.95 t	7.3 (3''''A, 3''''B)			11.7 (q)
3'''''	1.24 d	6.9 (3''')	1.17 d	5.8 (3''')			17.0 (q)
7'	3.67 s		3.70 s				52.2 (q)
30'							52.3 (q)
30''			2.12 s				168.8 (s)
2-OH			4.10 s				20.6 (q)
8-OH	5.14 s		2.83 s				

^a Measured at 600 MHz in CDCl₃.

^b Measured at 150 MHz in CDCl₃.

with standard pulse sequences, operating at 600 and 150 MHz, respectively. CDCl₃ was used as the solvent and TMS as the internal standard. FABMS was recorded on a JEOL JMS-7000 mass spectrometer. CD spectra were measured on a JASCO J-820 spectrometer. Column chromatography was performed on silica gel (70–230, 230–400 mesh; Merck). HPLC was run on a JASCO PU-1586 equipped with a differential refractometer (RI 1531). Fractions obtained from column chromatography were monitored by TLC (silica gel 60 F₂₅₄; Merck).

2.1.2. Plant material

The oil of the seeds (1.1 kg) of *C. guianensis* AUBLET (Meliaceae) was collected in the Amazon, Brazil, in March, 2011. A voucher specimen (CGS-01-1) was deposited in the Herbarium of the Laboratory of Medicinal Chemistry, Osaka University of Pharmaceutical Sciences.

2.1.3. Isolation of compounds 1–7

Preliminary silica gel CC was performed to separate the seed oil of *C. guianensis* AUBLET (Meliaceae) (1.1 kg) into 8 fractions: Fraction A (Fr. No. 1–76, 900 g) eluted with CHCl₃, B (Fr. No. 77–110, 12.0 g) eluted with CHCl₃, C (Fr. No. 111–125, 21.0 g) eluted with CHCl₃:EtOAc 5:1, D (Fr. No. 126–155, 10.9 g) eluted with CHCl₃:EtOAc 5:1, E (Fr. No. 156–170, 1.4 g) eluted with CHCl₃:EtOAc 2:1, F (Fr. No. 171–180, 2.4 g) eluted with EtOAc, G (Fr. No. 181–195, 2.9 g) eluting with EtOAc, and H (Fr. No. 196–208, 0.7 g) eluted with EtOAc: MeOH 5:1. Fraction C (21.0 g) was rechromatographed over a silica gel column (CC) (70–230 mesh, 600 g) eluted with *n*-hexane-AcOEt (10:1 → 0:100) to give 13 fractions (Residue C(1) (Fr. No. 1–83, 2.7 g), C2 (Fr. No. 84–116, 5.3 g), C(3) (Fr. No. 117–123, 331 mg), C(4) (Fr. No. 124–130, 783 mg), C(5) (Fr. No. 131–135, 324 mg), C(6) (Fr. No. 136–139,

Table 2
¹H NMR and ¹³C NMR spectroscopic data for compounds **4** and **5**.

Position	4			5		
	δ_{H} (J in Hz) ^a		δ_{C} ^b	δ_{H} (J in Hz) ^a		δ_{C} ^b
1			108.5 (s)			108.2 (s)
2			81.2 (s)			81.1 (s)
3		4.92 s	82.5 (d)		4.85 s	82.9 (d)
4			38.7 (s)			38.6 (s)
5		2.74 brd	40.3 (d)		2.74 dd	40.3 (d)
6	α	2.36 dd	16.7 (6 β), 8.9 (5)	α	2.19 dd	16.3 (6 β), 10.1 (5)
	β	2.19 brd		β	2.38 dd	16.3 (6 α), 1.6 (5)
7			173.8 (s)			173.8 (s)
8			80.3 (s)			80.2 (s)
9		2.24 d	51.5 (d)		2.23 dd	51.5 (d)
10			42.2 (s)			42.2 (s)
11	α	1.87 m	15.0 (t)	α	1.81 m	14.9 (t)
	β	2.39 m		β	2.35 m	
12	α	1.41 m	25.1 (t)	α	1.39 m	25.1 (t)
	β	2.07 m		β	2.09 m	
13			38.9 (s)			38.9 (s)
14			158.2 (s)			154.4 (s)
15		6.12 s	118.4 (d)		6.02 s	118.3 (d)
16			163.1 (s)			163.1 (s)
17		4.91 s	81.2 (d)		4.87 s	81.3 (d)
18		1.21 s	19.5 (q)		1.21 s	19.5 (q)
19		1.15 s	20.6 (q)		1.15 s	20.6 (q)
20			120.0 (s)			119.9 (s)
21		7.48 br d	141.2 (d)		7.48 dd	141.2 (d)
22		6.42 d	109.9 (d)		6.42 dd	109.9 (d)
23		7.41 t	142.8 (d)		7.41 t	142.7 (d)
28		1.32 s	24.4 (q)		0.81 s	24.5 (q)
29		0.79 s	21.6 (q)		1.32 s	21.7 (q)
30		5.61 s	75.3 (d)		5.57 s	75.2 (d)
3'			167.9 (s)			168.2 (s)
3''			127.6 (s)			127.5 (s)
3'''		6.87 m	139.5 (d)		6.87 m	139.6 (d)
3''''		1.82 s	14.6 (q)		1.81 s	14.6 (q)
3'''''		1.80 s	12.0 (q)		1.81 s	12.1 (q)
7'		3.69 s	51.9 (q)		3.70 s	173.8 (s)
30'			174.7 (s)			175.2 (s)
30''		2.30 q	7.2 (30''''')		2.47 sept	34.1 (d)
30'''	A	1.60 m	25.9 (t)		1.06 d	18.9 (q)
	B	1.31 m				
30''''		0.84 t	11.4 (q)		1.05 d	18.8 (q)
30'''''		1.02 d	16.0 (q)			
1-OH		4.36 s			4.54 s	
2-OH		4.77 s			4.24 s	

^a Measured at 600 MHz in CDCl₃.

^b Measured at 150 MHz in CDCl₃.

670 mg), C(7) (Fr. No. 140–160, 1220 mg), C(8) (Fr. No. 161–174, 280 mg), C(9) (Fr. No. 175–179, 280 mg), C(10) (Fr. No. 180–187, 1207 mg), C(11) (Fr. No. 188–191, 660 mg), C(12) (Fr. No. 192–194, 1292 mg), and C(13) (Fr. No. 195–218, 5.9 g). Fraction C(4) was subjected to CC (230–400 mesh, 50 g) using *n*-hexane–EtOAc (7:2) to give the fraction 27–28 (200 mg), which was separated by HPLC (ODS, 70% MeOH) to give compounds **1** (32.0 mg) and **4** (35.0 mg). Fraction C(5) was subjected to CC (230–400 mesh, 50 g) eluted with *n*-hexane–EtOAc (3:1) to give an amorphous solid that was purified by HPLC (ODS, 70% MeOH) to give compound **5** (7.5 mg). Fraction C(8) was subjected to CC (230–400 mesh, 70 g) eluted with *n*-hexane–EtOAc (2:1) to give an amorphous solid, which was separated by HPLC (ODS, 60% CH₃CN) to give compounds **3** (7.6 mg) and **7** (7.3 mg). Fraction C(9) was rechromatographed over a silica gel column (230–400 mesh, 40 g) eluted with

n-hexane–EtOAc (2:1) followed by HPLC (ODS, 70% MeOH) to give compound **6** (2.4 mg).

2.1.3.1. Carapanolide C (1). White powder; mp 110–112 °C (MeOH–CHCl₃); $[\alpha]_{\text{D}}^{22} - 53.8^{\circ}$ (c 0.10, CHCl₃); UV (CH₃CN) λ_{max} (log ϵ): 228 (4.8) nm; CD (c 4.0 × 10⁻⁴ M, CH₃CN): $\Delta\epsilon_{224}$ (18.2), $\Delta\epsilon_{238}$ 0, $\Delta\epsilon_{242} - 1.2$, $\Delta\epsilon_{248}$ (0), $\Delta\epsilon_{260}$ (3.4), $\Delta\epsilon_{272}$ (0), $\Delta\epsilon_{297}$ (-9.6), $\Delta\epsilon_{331}$ (0); IR (KBr) ν_{max} : 3448, 2971, 1731, 1506, 1459, 1374 cm⁻¹; ¹H and ¹³C NMR data, see Table 1; FABMS *m/z* (rel. int.): 629 ([M + H]⁺, 91), 467 (64), 57 (100); HRFABMS *m/z*: 629.2962 [M + H]⁺ (calcd for C₃₄H₄₅O₁₁, 629.2962).

2.1.3.2. Carapanolide D (2). White powder; mp 91–93 °C (MeOH–CHCl₃); $[\alpha]_{\text{D}}^{22} - 27.8^{\circ}$ (c 0.10, CHCl₃); UV (CH₃CN) λ_{max} (log ϵ): 222 (4.8) nm; CD (c 4.0 × 10⁻⁴ M, CH₃CN):

Table 3

¹H NMR and ¹³C NMR spectroscopic data for compounds 6 and 7.

Position	6			7		
	δ_{H} (J in Hz) ^a		δ_{C} ^b	δ_{H} (J in Hz) ^a		δ_{C} ^b
1			84.3 (s)			84.9 (s)
2			75.2 (s)			78.4 (s)
3		5.26 s	84.9 (d)	4.65 s		83.9 (d)
4			44.6 (s)			45.6 (s)
5		2.33 m	40.4 (d)	3.01 dd	9.4 (6 β), 3.2 (6 α)	36.9 (d)
6	α	2.35 m	33.9 (t)	2.40 dd	16.7 (6 β), 3.2 (5)	34.4 (t)
	β	2.40 m		2.49 dd	16.7 (6 α), 9.4 (5)	
7			173.3 (s)			172.8 (s)
8			83.9 (s)			83.4 (s)
9			87.4 (s)			84.9 (s)
10			47.3 (s)			47.2 (s)
11	α	1.94 dt	15.4 (11 β , 12 β), 4.1 (12 α)	2.04 m		25.2 (t)
	β	2.12 dt	15.4 (11 β , 12 α), 3.6 (12 β)	2.04 m		
12	α	1.19 m		29.1 (t)	1.37 dt	13.0 (12 β), 4.58 (11 α , 11 β)
	β	1.19 m			1.62 m	26.1 (t)
13			38.1 (s)			37.8 (s)
14			154.4 (s)			161.1 (s)
15		6.45 s	121.9 (d)	6.06 s		119.9 (d)
16			163.7 (s)			163.3 (s)
17		5.84 s	80.3 (d)	5.17 s		80.3 (d)
18		1.40 s	19.7 (q)	1.13 s		18.7 (q)
19		1.27 s	15.7 (q)	1.17 s		16.2 (q)
20			119.5 (s)			119.6 (s)
21		7.44 d	0.6 (22)	141.9 (d)	7.54 d	0.68 (22, 23)
22		6.43 dd	1.6 (23), 0.55 (21)	109.9 (d)	6.46 dd	1.83 (23), 0.68 (21)
23		7.41 t	1.6 (21, 22)	143.0 (d)	7.42 t	1.83 (21, 22)
28		0.76 s		14.5 (q)	0.93 s	14.7 (q)
29	α	1.78 d	11.3 (29 β)	39.1 (t)	1.80 d	10.8 (29 β)
	β	1.82 d	11.3 (29 α)		1.92 d	10.8 (29 α)
30		4.57 s		78.0 (d)	5.70 s	69.7 (d)
31				119.6 (s)		119.6 (s)
32		1.70 s		16.6 (q)	1.66 s	21.2 (q)
3'				176.7 (s)		176.6 (s)
3''		2.49 sept	6.86 (3''', 3''''')	34.1 (d)	2.56 sept	7.1 (3''', 3''''')
3'''		1.16 d	6.86 (3'')	18.2 (q)	1.11 d	7.1 (3'')
3''''		1.14 d	6.86 (3'')	20.3 (q)	1.21 d	7.1 (3'')
7'		3.67 s		52.2 (q)	3.69 s	52.0 (q)
30'						170.5 (s)
30''					2.09 s	21.2 (q)
1-OH		3.55 br s				
2-OH		3.55 br s			3.03 s	

^a Measured at 600 MHz in CDCl₃.^b Measured at 150 MHz in CDCl₃.

$\Delta\epsilon_{220}$ (7.6), $\Delta\epsilon_{232}$ (0), $\Delta\epsilon_{240}$ (−2.5), $\Delta\epsilon_{250}$ (0), $\Delta\epsilon_{267}$ (2.6), $\Delta\epsilon_{284}$ (0), $\Delta\epsilon_{308}$ (−3.1), $\Delta\epsilon_{375}$ (0); IR (KBr) ν_{max} : 3567, 3438, 3148, 3072, 2974, 2885, 2324, 1723, 1650, 1504 cm^{−1}; ¹H and ¹³C NMR data, see Table 1; FABMS m/z (rel. int.): 645 ([M + H]⁺, 11), 149 (100), 43 (38); HRFABMS m/z : 645.2911 [M + H]⁺ (calcd for C₃₄H₄₅O₁₂, 645.2911).

2.1.3.3. Carapanolide E (3). White powder; mp 113–115 °C (MeOH–CHCl₃); $[\alpha]_{\text{D}}^{22}$ − 71.2° (c 0.10, CHCl₃); UV (CH₃CN) λ_{max} (log ϵ): 224.5 (6.8) nm; CD (c 4.0 × 10^{−4} M, CH₃CN): $\Delta\epsilon_{223}$ (17.8), $\Delta\epsilon_{245}$ (0), $\Delta\epsilon_{263}$ 2.6, $\Delta\epsilon_{276}$ (0), $\Delta\epsilon_{299}$ (−5.8), $\Delta\epsilon_{335}$ (0); IR (KBr) ν_{max} : 3456, 2075, 2880, 1731, 1636, 1505, 1459 cm^{−1}; ¹H and ¹³C NMR data, see Table 1; FABMS m/z (rel. int.): 557 ([M + H]⁺, 100), 71 (33); HRFABMS m/z : 557.2750 [M + H]⁺ (calcd for C₃₁H₄₁O₉, 557.2750).

2.1.3.4. Carapanolide F (4). White powder; mp 180–182 °C (MeOH–CHCl₃); $[\alpha]_{\text{D}}^{22}$ + 50.0° (c 0.10, CHCl₃); UV (CH₃CN) λ_{max} (log ϵ): 234.0 (4.8) nm; CD (c 4.0 × 10^{−4} M, CH₃CN):

$\Delta\epsilon_{233}$ (15.9), $\Delta\epsilon_{248}$ (5.0), $\Delta\epsilon_{266}$ (8.1), $\Delta\epsilon_{307}$ (0); IR (KBr) ν_{max} : 3567, 3367, 2974, 2938, 2884, 1714, 1653, 1653, 1599, 1504 cm^{−1}; ¹H and ¹³C NMR data, see Table 2; FABMS m/z (rel. int.): 685 ([M + H]⁺, 29), 247 (17), 83 (100); HRFABMS m/z : 685.3224 [M + H]⁺ (calcd for C₃₇H₄₉O₁₂, 685.3224).

2.1.3.5. Carapanolide G (5). White powder; mp 203–205 °C (MeOH–CHCl₃); $[\alpha]_{\text{D}}^{22}$ + 13.6° (c 0.10, CHCl₃); UV (CH₃CN) λ_{max} (log ϵ): 234.0 (7.8) nm; CD (c 4.0 × 10^{−4} M, CH₃CN): $\Delta\epsilon_{230}$ (15.4), $\Delta\epsilon_{248}$ (3.6), $\Delta\epsilon_{267}$ (6.4), $\Delta\epsilon_{304}$ (0); IR (KBr) ν_{max} : 3567, 3438, 3148, 3072, 2974, 2885, 2324, 1723, 1650, 1504 cm^{−1}; ¹H and ¹³C NMR data, see Table 2; FABMS m/z (rel. int.): 671 ([M + H]⁺, 18), 83 (100); HRFABMS m/z : 671.3068 [M + H]⁺ (calcd for C₃₆H₄₇O₁₂, 671.3068).

2.1.3.6. Carapanolide H (6). Colorless amorphous; $[\alpha]_{\text{D}}^{22}$ + 105.6° (c 0.1, CHCl₃); UV (CH₃CN) λ_{max} (log ϵ): 225.5 (3.8) nm; CD (c 4.0 × 10^{−4} M, CH₃CN): $\Delta\epsilon_{222}$ (14.3), $\Delta\epsilon_{247}$ (3.5), $\Delta\epsilon_{263}$ (6.4), $\Delta\epsilon_{310}$ (0); IR (KBr) ν_{max} : 3523, 2929, 1727, 1458 cm^{−1};

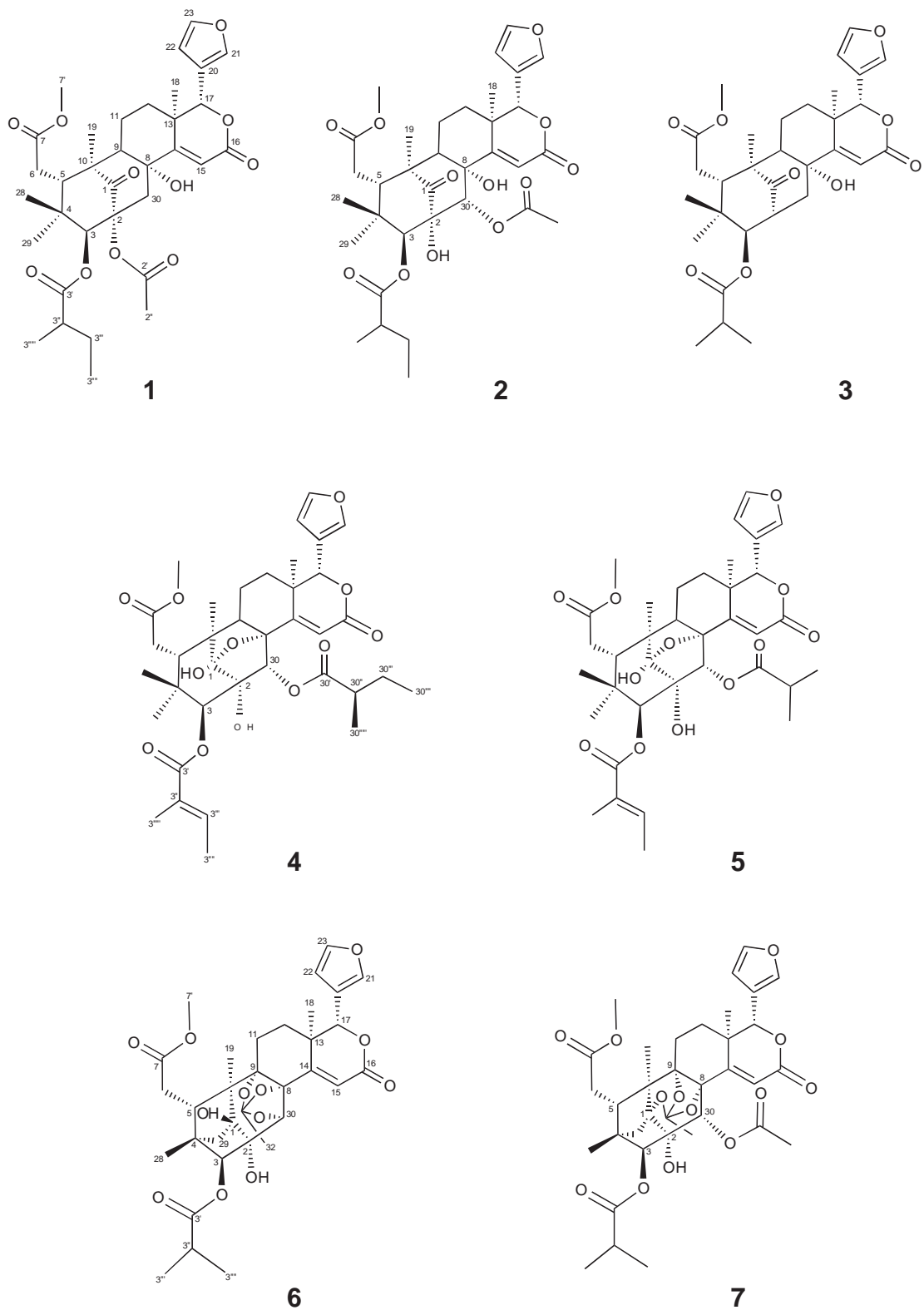


Fig. 1. Structures of compounds 1–7 from the seeds of *C. guianensis*.

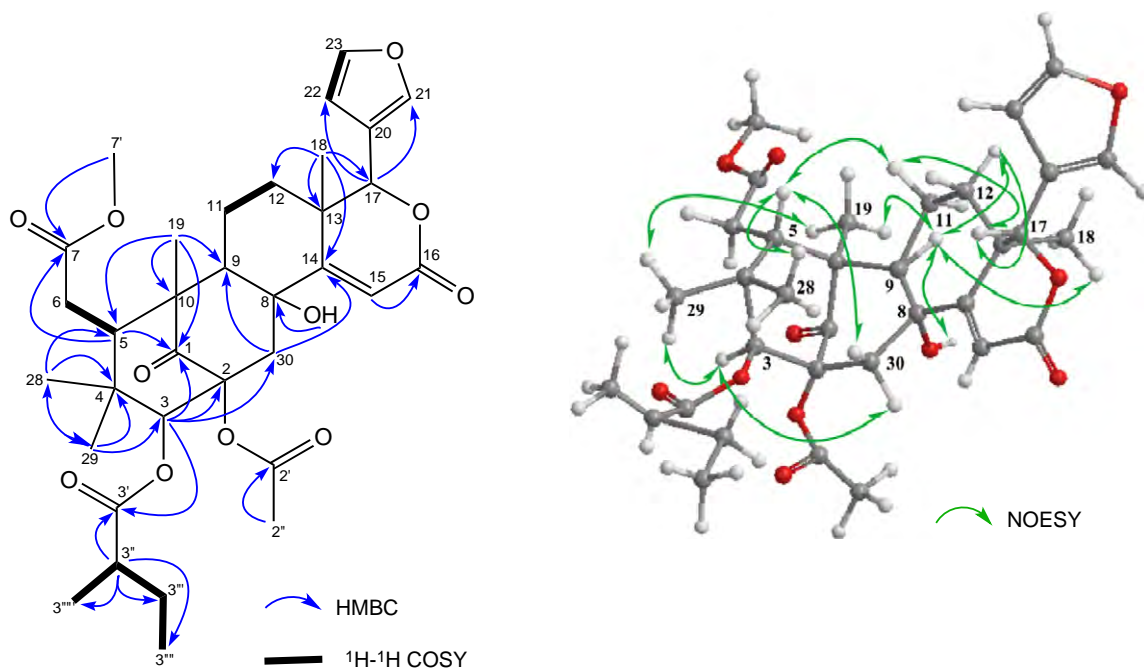


Fig. 2. Key HMBC, COSY and NOESY correlations for compound 1.

^1H and ^{13}C NMR data, see Table 3; FABMS m/z (rel. int.): 629 ($[\text{M} + \text{H}]^+$, 100), 43 (80); HRFABMS m/z : 629.2598 $[\text{M} + \text{H}]^+$ (calcd for $\text{C}_{33}\text{H}_{41}\text{O}_{12}$, 629.2598).

2.1.3.7. Carapanolide I (7). Colorless powder; mp 103–105 °C (MeOH- CHCl_3); $[\alpha]_D^{25} - 22.2^\circ$ (c 0.1, CHCl_3); UV (CH_3CN) λ_{max} (log ϵ): 223.5 (3.8) nm; CD (c 4.0×10^{-4} M, CH_3CN): $\Delta\epsilon_{221}$ (4.2), $\Delta\epsilon_{242}$ (0), $\Delta\epsilon_{245}$ (−0.1), $\Delta\epsilon_{247}$ (0), $\Delta\epsilon_{270}$ (3.8), $\Delta\epsilon_{303}$ (0), $\Delta\epsilon_{312}$ (−0.2), $\Delta\epsilon_{320}$ (0); IR (KBr) ν_{max} : 3626, 3572, 3146, 2974, 2879, 1731, 1629, 1504 cm^{-1} ; ^1H and ^{13}C NMR data, see Table 3; FABMS m/z (rel. int.): 671 ($[\text{M} + \text{H}]^+$, 100), 43 (54); HRFABMS m/z : 671.2702 $[\text{M} + \text{H}]^+$ (calcd for $\text{C}_{35}\text{H}_{43}\text{O}_{13}$, 671.2702).

2.1.3.8. Crystal data of 4. Space group: $P2_12_12_1$, $a = 12.097$ (5), $b = 12.578$ (6), $c = 23.309$ (10), $a = b = c = 90.00$, $V = 3547$ (3), $Z = 4$. Parameters used for refinement, $R_1 = 0.063$. The X-ray diffraction data were collected with a Bruker AXS SMART APEX CCD camera. Crystal structure was solved by a direct method using the SHELXS-97 program. Atomic scattering factors were taken from International Tables for X-Ray Crystallography. Positional parameters of non-H atoms were refined by a full-matrix least-squares method with anisotropic thermal parameters using the SHELXL-97 program. The structural data were deposited with the following designation: **7**: CCDC-992541. These can be obtained free of charge at www.ccdc.cam.ac.uk/conts/retrieving.html (or from the Cambridge Crystallographic Data Centre, 12 Union Road, Cambridge CB21EZ, U.K.; fax: (+44) 1223-336-033; e-mail: deposit@ccdc.cam.ac.uk).

2.1.4. Assay for cytotoxicity in P-388 and HL-60 cells

Cytotoxic activities of carapanolides C-I (**1–7**) were examined using the 3-(4,5-dimethyl-2-thiazoyl)-2,5-diphenyl-2H-

tetrazolium bromide (MTT) method. P-388 and HL-60 cells were cultured in RPMI-1640 (10% fetal calf serum) at 37 °C in 5% CO_2 . The test material was dissolved in dimethyl sulfoxide (DMSO) to a concentration of 10 mM, and the solution was diluted with medium to yield concentrations of 200, 20, and 2 μM . Each solution was combined with the cell suspension (1×10^5 cells mL^{-1}) in the medium. After incubating at 37 °C for 72 h in 5% CO_2 , the cells that grew labeled with 4 mg mL^{-1} MTT in phosphate-buffered saline (PBS), and the absorbance of formazan dissolved in 20% sodium dodecyl sulfate (SDS) in 0.1 N HCl was measured at 540 nm using a microplate reader (Model 450) (Bio-Rad Laboratories, Inc., Tokyo, Japan). Each absorbance value was expressed as a percentage relative to that of the control cell suspension prepared without the test substance using the same procedure. All assays were performed three times, semilogarithmic plots were constructed from the averaged data, and the effective dose of the substance required to inhibit cell growth by 50% (IC_{50}) was determined. Compounds **1–7** had a purity of over 99%. 5-Fluorouracil (5-FU) [Sigma-Aldrich Japan Co. (Tokyo, Japan) (purity > 98.5%)] was used as α positive control.

3. Results and discussion

The oil of *C. guianensis* seeds was dissolved in CHCl_3 , and the extract was separated by silica gel column chromatography, medium-pressure liquid chromatography (MPLC), and reversed phase HPLC to obtain seven new limonoids named carapanolides C-I (**1–7**) (Fig. 1).

Carapanolide C (**1**) was isolated as a colorless amorphous and shown to have the molecular formula $\text{C}_{34}\text{H}_{44}\text{O}_{11}$ ($[\text{M} + \text{H}]^+$; m/z 629.2962, calcd for 629.2962) by HRFABMS, indicating 13 degrees of unsaturation. The IR and UV spectra revealed

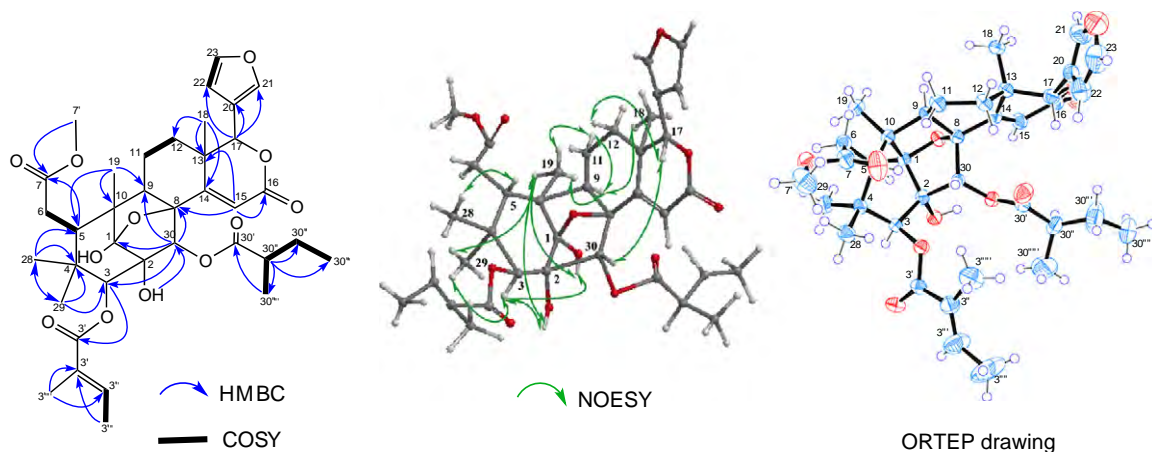


Fig. 3. Key HMBC, COSY and NOESY correlations and ORTEP drawing of compound 4.

the presence of a hydroxyl group and several ester groups at ν_{\max} 3448, 1731 cm^{-1} and λ_{\max} at 228 nm ($\log \epsilon$ 4.81). The ^1H and ^{13}C NMR spectra of **1** (Table 1) indicated the presence of four tertiary methyl groups [δ_{H} 0.73, 0.91, 1.17, 1.31 (each 3H, s)], an acetyl methyl group [δ_{H} 2.15 (s)], a methyl ester [δ_{H} 3.67 (s)], five methylene groups, five sp^3 methine groups including two oxymethine groups [δ_{H} 5.21 (s), δ_{H} 5.33 (s)], a trisubstituted olefin [δ_{H} 6.21 (s), δ_{C} 115.6 (d), 166.8 (s)], a furan ring [δ_{H} 6.51 (dd), 7.44 (t), 7.49 (t)], five sp^3 quaternary carbons including two oxycarbonyls [δ_{C} 72.1, 83.5 (each s)], three ester carbonyls [δ_{C} 171.1 (s), 173.2 (s), 175.2 (s)], a lactone carbonyl [δ_{C} 165.2 (s)], and a ketone [δ_{C} 208.1 (s)]. Cross-peaks were observed in the HMBC spectrum (Fig. 2), from Me-18 [δ_{H} 1.31 (s)]/C-12, C-13, C-14 [δ_{C} 166.8 (s)], C-17 [δ_{C} 79.1 (d)]; Me-19 [δ_{H} 1.17 (s)]/C-1 [δ_{C} 208.1 (s)], C-5, C-9, C-10; Me-28 [δ_{H} 0.91 (s)]/C-3 [δ_{C} 81.6 (d)], C-4, C-5, C-29; Me-29 [δ_{H} 0.73 (s)]/C-3, C-4, C-5, C-28; H-3 [δ_{H} 5.21 (s)]/C-1, C-2 [δ_{C} 83.5 (s)], C-4, C-5, C-28, C-29, C-30, C-3' [δ_{C} 175.2 (s)]; H-5 [δ_{H} 3.09 (t)]/C-1, C-3, C-4, C-6, C-7 [δ_{C} 173.2 (s)], C-10, C-28, C-29; H-15 [δ_{H} 6.21 (s)]/C-8 [δ_{C} 72.1 (s)], C-13, C-14, C-16 [δ_{C} 165.2 (s)]; H-30 α [δ_{H} 2.36 (d)] and H-30 β [δ_{H} 4.21 (d)]/C-1, C-2, C-8, C-9, C-14; H-3'' [δ_{H} 2.55 (q)]/C-3' [δ_{C} 175.2 (s)], C-3''', C-3'''' [δ_{C} 11.7 (q)], C-3''''' [δ_{C} 17.0 (q)]. An analysis of ^1H - ^1H COSY correlations were shown in bold face in Fig. 2. The above results confirmed that **1** was a mexicanolide-type limonoids with a tertiary hydroxyl group at C-8, 2-methylbutanoyl group at C-3, acetyl group at C-2, and methyl ester group at C-7. The relative configuration of **1** was deduced from an analysis of correlation of the NOESY spectrum (Fig. 2), and significant NOEs were observed between H-3/Me-29, H-30 α ; H-9/Me-18, Me-19, H-12 α , and 8-OH, which indicated that these protons were all α -oriented. However, the NOESY correlations of H-5/H-11 β , H-30 β , Me-28; H-17/H-11 β , H-12 β , revealed that a β -orientation in the corresponding protons. Therefore, the relative structure of compound **1** was established, as shown in Fig. 1, except for the stereostructure of 2-methylbutanoyl group at C-3.

Carapanolides D (**2**) and E (**3**) were determined as analogs of **1** and had the molecular formula $\text{C}_{34}\text{H}_{44}\text{O}_{12}$ in **2** (m/z : 645.2911 [$\text{M} + \text{H}]^+$; calcd for $\text{C}_{34}\text{H}_{45}\text{O}_{12}$, 645.2911) and $\text{C}_{31}\text{H}_{40}\text{O}_9$ in **3** (m/z : 557.2750 [$\text{M} + \text{H}]^+$; calcd for $\text{C}_{31}\text{H}_{41}\text{O}_9$, 557.2750) based

on HRFABMS. An analysis of the ^1H and ^{13}C NMR spectra (Table 1) of **2** and **3** revealed that **2** was devoid of an acetyl group, but had a hydroxyl group at C-2 and substituted an acetyl group at C-30, **3** was removed a 2-methylbutanoyl group at C-3 in **1**, and attached a 2-methylpropanoyl group at C-3, and lacked an acetyl group at C-2 in **1**. The location of these substituents was confirmed by the HMBC spectrum, cross-peaks were observed from H-3 [δ_{H} 5.23 (s)] and H-30 [δ_{H} 6.45 (s)] to C-2 [δ_{C} 86.1 (s)], from OCOCH_3 at C-30'' [δ_{H} 2.12 (s)] to C-30' [δ_{C} 168.8 (s)] in **2**. Therefore, hydroxyl and acetyl groups were attached at the C-2, and C-30 positions in **2**. On the other hand, cross peaks were observed in the HMBC spectrum of **3**, from H-3 [δ_{H} 4.87 (d)] to C-2 [δ_{C} 44.6 (d)], C-4 [δ_{C} 39.8 (s)], C-5 [δ_{C} 41.4 (d)], C-30 [δ_{C} 35.6 (t)], from H-3'' [δ_{H} 2.65 (sept)] to C-3''' [δ_{C} 19.1 (q)] and C-3'''' [δ_{C} 19.2 (q)]. Therefore, a 2-methylpropanoyl group was attached at C-3 in **3**. NOEs were observed in the NOESY spectrum, between H-3 and Me-29 in **2** and **3**, and between H-30 and H-5 β in **2**. Therefore, **2** and **3** were confirmed to have the same relative configuration as **1**, shown in Fig. 1.

Carapanolide F (**4**) was obtained as an amorphous solid, and its molecular formula was established as $\text{C}_{37}\text{H}_{48}\text{O}_{12}$ ($[\text{M} + \text{H}]^+$; m/z 685.3224, calcd. for 685.3224) by HRFABMS, implying 14 degrees of unsaturation. The ^1H and ^{13}C NMR spectra indicated that eight of the 14 units of unsaturation came from four carbon-carbon double bonds and four ester carbonyls. Therefore, the remaining degrees of unsaturation required **4** to have a hexacyclic. The IR and UV spectra revealed the presence of a hydroxyl group and several ester groups at ν_{\max} 3367, 1714 cm^{-1} , and λ_{\max} at 234 nm ($\log \epsilon$ 4.83). The ^1H and ^{13}C NMR spectra of **4** (Table 2) indicated the presence of four tertiary methyl groups [δ_{H} 0.79, 1.15, 1.21, 1.32 (each s)], a tigroyl group [δ_{H} 1.80 (s), 1.82 (s), 6.87 (m); δ_{C} 12.0 (q), 14.6 (q), 127.6 (s), 139.5 (d), 167.9 (s)], a 2-methylbutanoyl group [δ_{H} 0.84 (3H, t), 1.02 (3H, d), 1.31 (1H, m), 1.60 (1H, m), 2.30 (1H, q); δ_{C} 11.4 (q), 16.0 (q), 25.9 (t), 40.9 (d), 174.7 (s)], methyl ester [δ_{H} 3.69 (3H, s); δ_{C} 51.9 (q), 173.8 (s)], four methylene groups, six sp^3 methine groups including three oxymethine group [δ_{H} 4.91 (s), 4.92 (s), 5.61 (s)], a trisubstituted olefin [δ_{H} 6.12 (s), δ_{C} 118.4 (d), 158.2 (s)], a furan ring [δ_{H} 6.42 (d), 7.41 (t), 7.48 (brd)], six sp^3 quaternary carbons including an oxycarbon [δ_{C} 80.3 (s)]

and a tertiary hydroxyl group [δ_C 81.2 (s)], an acetal carbon [δ_C 108.5 (s)], three ester carbonyls [δ_C 167.9 (s), 173.8 (s), 174.7 (s)], and a lactone carbonyl [δ_C 163.1 (s)]. An analysis of the ^1H – ^1H COSY spectrum of **4** revealed the partial structure shown in bold face in Fig. 3. Cross-peaks were observed in the HMBC spectrum (Fig. 3), from Me-19 [δ_H 1.15 (s)] to C-1 (δ_C 108.5), C-5, C-9, and C-10; from H-30 [δ_H 5.61 (s)] to C-1, C-2 [δ_C 81.2 (s)], C-3 [δ_C 82.5 (d)], C-8 [δ_C 80.3 (s)], and C-9. Because a quaternary carbon at δ_C 108.5 was assignable to C-1, a hemiketal group was related to that found in xylogranatins B–D [16]. The singlet oxymethine proton at δ 4.92 was assigned to C-3 through HMBC correlations to C-1, C-2, C-5, C-29, C-30 [δ_C 75.3 (d)], and C-3' [δ_C 167.9 (s)], while another singlet proton at δ_H 5.61, showing HMBC correlations to C-1, C-8, C-9, and C-30' [δ_C 174.7 (s)], was assigned to C-30. An OH group was located at C-2, as confirmed by HMBC correlations from 2-OH [δ_H 4.77 (s)] to C-1, C-2, and C-10. Additionally, the HMBC cross-peaks from H-3 to another tigloyl carbonyl at δ_C 167.9 (C-3'), and from H-30 to another 2-methylbutanoyl carbon at δ_C 174.7 [C-30' (s)]. The relative configuration of **4** was established on the basis of NOE interactions. Significant NOE interactions (Fig. 3) were observed from H-5 [δ_H 2.74 (brd)]/Me-28 [δ_H 1.32 (s)]; Me-29 [δ_H 0.79 (s)]/H-3 [δ_H 4.92 (s)]; H-9 [δ_H 2.24 (d)]/H-11 α [δ_H 1.87 (m)], Me-18 [δ_H 1.21 (s)], Me-19 [δ_H 1.15 (s)]; H-30 [δ_H 5.61 (s)]/H-17 [δ_H 4.91 (s)]; H-17/H-12 β [δ_H 2.07 (m)]; which indicated the α -orientation of H-3, H-9, Me-18, and Me-19, and β -orientation of H-5, H-17, and H-30. Fortunately, a single-crystal X-ray diffraction analysis was successfully conducted to confirm 2*R* at 2-methylbutanoyl group attached at C-30 position. Therefore, the structure of **4** was established as shown in Fig. 1, which was an analog of Andirolide U [13].

Carapanolide G (**5**) was isolated as a colorless amorphous and demonstrated to have the molecular formula $\text{C}_{36}\text{H}_{46}\text{O}_{12}$ ($[\text{M} + \text{H}]^+$; m/z 671.3068, calcd. for 671.3068) by HRFABMS, which was smaller than that of **4** by a CH_2 unit. The ^1H and ^{13}C NMR spectra of **5** (Table 2) were very similar to those of **4** except for the absence of a 2-methylbutanoyl group at C-30 and the presence of a 2-methylpropanoyl group [δ_H 1.05 (3H, d), 1.06

(3H, d), 2.47 (1H, sept); δ_C 18.8 (q), 18.9 (q), 34.1 (d), 175.2 (s)]. The ^1H – ^1H COSY correlation between H-30', H-30''', and H-30'''' revealed the presence of a 2-methylpropanoyl group at C-30.

Carapanolide H (**6**), isolated as colorless amorphous, had the molecular formula $\text{C}_{33}\text{H}_{40}\text{O}_{12}$ ($[\text{M}]^+ + \text{H}$; m/z 629.2598, calcd. for 629.2598) as determined by HRFABMS. The IR spectrum showed the presence of a hydroxyl at ν_{max} 3523 cm^{-1} , and ester groups at ν_{max} 1727 cm^{-1} . The ^1H and ^{13}C NMR spectra (Table 3) indicated the presence of three angular methyls [δ_H 0.76, 1.27, 1.40 (each 3H, s)], a 2-methylpropanoyl group [δ_H 1.14, 1.16 (each 3H, d), 2.49 (1H, sept)], a methoxycarbonyl group [δ_H 3.67 (3H, s), δ_C 52.2 (q), 173.3 (s)], an α,β -unsaturated δ -lactone group [δ_H 6.45 (1H, s), δ_C 121.9 (d), 163.7 (s)], an orthoacetate [δ_H 1.70 (3H, s), δ_C 16.6 (q), 119.6 (s)], two tertiary hydroxyl groups [δ_C 75.2 (s), 84.3 (s)], and a furan ring [δ_H 6.43 (dd), 7.41 (t), 7.44 (d)]. In the HMBC spectrum, cross-peaks were observed from Me-18 [δ_H 1.40 (s)]/C-12, C-13, C-14 [δ_C 154.5 (s)], C-17 [δ_C 80.3 (d)]; Me-19 [δ_H 1.27 (s)]/C-1 [δ_C 84.3 (s)], C-5, C-9 [δ_C 87.4 (s)], C-10; Me-28 [δ_H 0.76 (s)]/C-3 [δ_C 84.9 (d)], C-4, C-5, C-29; H-3 [δ_H 5.26 (s)]/C-2 [δ_C 75.2 (s)], C-4, C-5, C-6, C-28, C-29, C-30, C-3'; H-5 [δ_H 2.33 (s)]/C-1, C-2, C-3, C-4, C-6, C-7, C-10, C-19, C-29; H-15 [δ_H 6.45 (s)]/C-8, C-13, C-14, C-16 [δ_C 163.7 (s)], C-18; H-30 [δ_H 4.57 (s)]/C-1, C-2, C-8, C-9, C-14, C-30' [δ_C 170.5 (s)]; 1-OH and 2-OH [δ_H 3.55 (2H, brs)]/C-3, C-10. The positions of the two hydroxyl, a 2-methylpropanoyl, a methoxycarbonyl, and an orthoacetate were located by detailed ^1H – ^1H COSY and HMBC correlations (Fig. 4). In the NOESY spectrum, significant NOEs (Fig. 4) were observed between H-3/1-OH and 2-OH; between H-5/Me-28 and H-30; between Me-18/H-11 α and H-12 α ; between Me-19/H-11 α ; between Me-32/1-OH, therefore, the hydroxyl groups at C-1 and C-2 were both in an α orientation and the 2-methylpropanoyl group at C-3 was a β orientation. The relative structure was established to be the same as Andirolides G, which was isolated from the flower oil of *C. guianensis* [11].

Carapanolide I (**7**), isolated as colorless amorphous solid, had the molecular formula $\text{C}_{35}\text{H}_{42}\text{O}_{13}$ ($[\text{M}]^+ + \text{H}$; m/z 671.2702, calcd. for 671.2702) as determined by HRFABMS. The IR spectrum showed the presence of a hydroxyl at ν_{max} 3572 cm^{-1} , and ester groups at ν_{max} 1731 cm^{-1} . The ^1H and

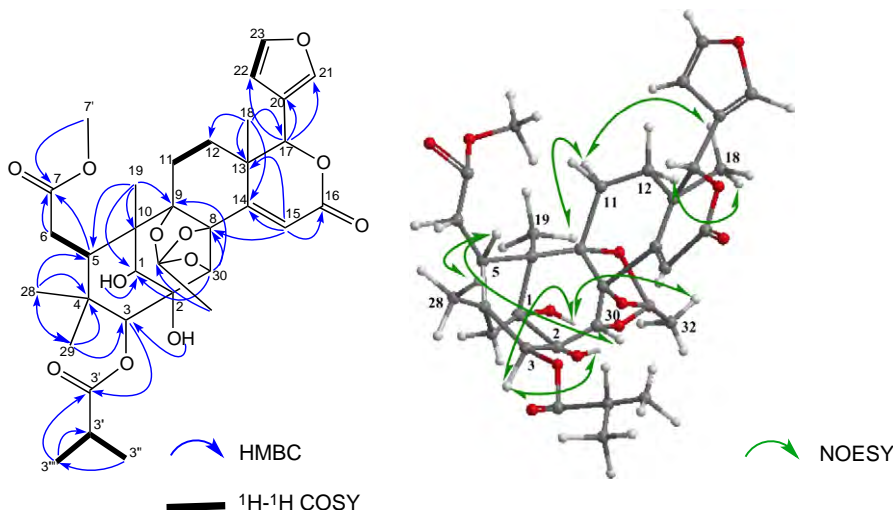


Fig. 4. Key HMBC, COSY, and NOESY correlations for compound **6**.

Table 4
Cytotoxic activity of Carapanolides C (1)–I (7).

Compound	IC ₅₀ (μM)		
	P388	HL-60	L1210
	(Murine leukemia)	(Human leukemia)	(Murine leukemia)
1	17.9	52.3	13.3
2	27.1	11.0	>100
3	15.8	45.0	18.1
4	>100	63.7	15.9
5	81.2	39.7	14.2
6	89.8	90.8	24.3
7	22.2	21.2	16.9
5-Fluorouracil	2.3	1.9	2.3

¹³C NMR spectra indicated the presence of three tertiary methyls [δ_{H} 0.93, 1.13, 1.17 (each 3H, s)], an acetyl methyl [δ_{H} 2.09 (3H, s)], a 2-methylpropanoyl group [δ_{H} 1.11 and 1.21 (each 3H, d), 2.56 (1H, sept)], an orthoacetyl methyl [δ_{H} 1.66 (3H, s)], four methylenes, six *sp*³ methines including three oxymethines [δ_{H} 4.65 (s), 5.17 (s), 5.70 (s)], eight *sp*³ quaternary carbons including a tertiary hydroxyl group [δ_{C} 78.4 (s)] and an orthoacetal carbon [δ_{C} 119.6 (s)], a furan ring [δ_{H} 6.46 (d), 7.42 (t), 7.54 (s)] and an α,β -unsaturated δ -lactone [δ_{H} 6.06 (s); 163.3 (s)] (Table 3). In the HMBC spectrum, cross-peaks were observed from Me-18 [δ_{H} 1.13 (s)]/C-12, C-13, C-14 [δ_{C} 161.1 (s)], C-17 [δ_{C} 80.3 (d)]; Me-19 [δ_{H} 1.17 (s)]/C-1 [δ_{C} 84.9 (s)], C-5, C-9 [δ_{C} 84.9 (s)], C-10; H-30 [δ_{H} 5.70 (s)]/C-2 [δ_{C} 78.4 (s)], C-8 [δ_{C} 83.4 (s)], C-9, C-30 [δ_{C} 69.7 (d)]; Me-28 [δ_{H} 0.93 (s)]/C-3 [δ_{C} 83.9 (s)], C-4, C-5, C-29; H-3 [δ_{H} 4.65 (s)]/C-2, C-4, C-5, C-28, C-29, C-30, C-3' [δ_{C} 176.6 (s)]; H-5 [δ_{H} 3.01 (dd)]/C-1, C-3, C-4, C-6, C-7, C-10, C-19, C-29; H-15 [δ_{H} 6.06 (s)]/C-8, C-13, C-14 [δ_{C} 161.1 (s)], C-16 [δ_{C} 163.3 (s)]; H-17 [δ_{H} 5.17 (s)]/C-12, C-13, C-14, C-18, C-20 [δ_{C} 119.6 (s)], C-21 [δ_{C} 141.5 (d)], C-22 [δ_{C} 109.8 (d)]; 2-OH [δ_{H} 3.03 (s)]/C-1, C-2, C-3, therefore, the planar structure of **7** was established as phragmalin-1,8,9-orthoacetate [11], and the positions of a 2-methylpropanoyl group was attached at C-3, an acetyl group at C-30, a methyl ester at C-7 and an orthoacetate was formed at C-1, C-8 and C-9. In the NOESY spectrum, significant NOEs were observed between H-3/2-OH; H-5 β /Me-28; H-17/H-12 β ; Me-18/H-11 α , H-12 α ; Me-19/H-11 α , Me-32; H-30/H-5 β , H-12 β . Therefore the relative structure of **7** was confirmed as shown in Fig. 1.

As a primary screen for the inhibition of cancer cell growth, Carapanolides C–J (**1**–**7**) were examined using the murine P388, murine L1210, and human HL-60 leukemia cell lines (Table 4) [17]. Carapanolides C (**1**), E (**3**), and I (**7**) exhibited moderate activity in the P388 (IC₅₀ 17.9 μM in **1**, 15.8 μM in **3**) and L1210 cell lines (IC₅₀ 13.3 μM in **1**, 18.1 μM in **3**, 16.9 μM in **7**). On the other hand, Carapanolide D (**2**) exhibited a strong inhibitory effect in the HL-60 cell line (IC₅₀ 11.0 μM), and Carapanolides F (**4**) showed inhibitory activity

in L1210 cell line (IC₅₀ 15.9 μM). The cytotoxic activity of Carapanolides I (**7**) was moderate in all cell lines.

Acknowledgments

We thank Mr. Akira Yoshino for collecting and identifying the plant material. We also thank Dr. Katsuhiko Minoura and Dr. Mihoyo Fujitake (this university) for NMR and MS measurements.

References

- [1] Liao SG, Chen H-D, Yue JM. Plant orthoesters. *Chem Rev* 2009;109:1092–140.
- [2] Fang X, Di YT, Hao XJ. The advances in the limonoid chemistry of the Meliaceae family. *Curr Org Chem* 2011;15:1363–91.
- [3] Tan QG, Luo XD. Meliaceous limonoids: chemistry and biological activities. *Chem Rev* 2011;111:7437–522.
- [4] Prophiro JS, da Silva Mario AN, Kanis LA, da Rocha LCBP, Duque-Luna JE, da Silva OS. First report on susceptibility of wild *Aedes aegypti* (Diptera: Culicidae) using *Carapa guianensis* (Meliaceae) and *Copaifera* sp. (Leguminosae). *Parasitol Res* 2012;110:699–705.
- [5] Penido C, Costa KA, Pennaforte RJ, Costa MFS, Pereira JFG, Siani AC, et al. Anti-allergic effects of natural tetranortriterpenoids isolated from *Carapa guianensis* Aublet on allergen-induced vascular permeability and hyperalgesia. *Inflamm Res* 2005;54:295–303.
- [6] Bickii J, Njifutie N, Foyere JA, Basco LK, Ringwald PJ. In vitro antimalarial activity of limonoids from *Khaya grandifoliola* C.D.C. (Meliaceae). *J Ethnopharmacol* 2000;69:27–33.
- [7] Penido C, Conte FP, Chagas MSS, Rodrigue CAB, Pereira JFG, Henriques MGMO. Antiinflammatory effects of natural tetranortriterpenoids isolated from *Carapa guianensis* Aublet on zymosan-induced arthritis in mice. *Inflamm Res* 2006;55:457–64.
- [8] Ferraris Fausto K, Rodrigues R, da Silva VP, Figueiredo R, Penido C, Henriques MGMO. Modulation of T lymphocyte and eosinophil functions in vitro by natural tetranortriterpenoids isolated from *Carapa guianensis* Aublet. *Int Immunopharmacol* 2011;11:1–11.
- [9] Miranda Junior RNC, Dolabela MF, da Silva MN, Povoá MM, Maia JGS. Antiplasmodial activity of the andiroba (*Carapa guianensis* Aublet, Meliaceae) oil and its limonoid-rich fraction. *J Ethnopharmacol* 2012;142:679–83.
- [10] Costa-Silva H, Lima CR, Silva EJR, Araujo AV, Fraga MCCR, Ribeiro E, et al. Acute and subacute toxicity of the *Carapa guianensis* Aublet (Meliaceae) seed oil. *J Ethnopharmacol* 2008;116:495–500.
- [11] Tanaka Y, Yamada T, In Y, Muraoka O, Kajimoto T, Tanaka R. Absolute stereostructure of Andriolides A–G from the flower of *Carapa guianensis* (Meliaceae). *Tetrahedron* 2011;67:782–92.
- [12] Tanaka Y, Sakamoto A, Inoue T, Yamada T, Kikuchi T, Kajimoto T, et al. Andriolides H–P from the flower of *Carapa guianensis* (Meliaceae). *Tetrahedron* 2012;68:3669–77.
- [13] Sakamoto A, Tanaka Y, Inoue T, Kikuchi T, Kajimoto T, Muraoka Yamada T, et al. Andriolides Q–V from the flower of andiroba (*Carapa guianensis*, Meliaceae). *Fitoterapia* 2013;90:20–9.
- [14] Inoue T, Nagai Y, Mitooka A, Ujike R, Muraoka O, Yamada T, et al. Carapanolides A and B: unusual 9,10-seco-mexicanolides having a 2R,9S-oxygen bridge from the seeds of *Carapa guianensis*. *Tetrahedron Lett* 2012;53:6685–8.
- [15] Inoue T, Matsui Y, Kikuchi T, In Y, Yamada T, Muraoka O, et al. Guianolides A and B, new carbon skeletal limonoids from the seeds of *Carapa guianensis*. *Org Lett* 2013;15:3018–21.
- [16] Wu J, Zhang S, Li M, Zhou Y, Xiao Q. Xylogranatins A–D, New Mexicanolides from the fruit of a Chinese Mangrove *Xylocarpus granatum*. *Chem Pharm Bull* 2006;54:1582–5.
- [17] Muroga Y, Yamada T, Numata A, Tanaka R. Chaetomugilins I–O, new potent cytotoxic metabolites from a marine-fish-derived Chaetomium species. Stereochemistry and biological activities. *Tetrahedron* 2009;65:7580–6.

Biosynthetic Origin of Alchivemycin A, a New Polyketide from *Streptomyces* and Absolute Configuration of Alchivemycin B

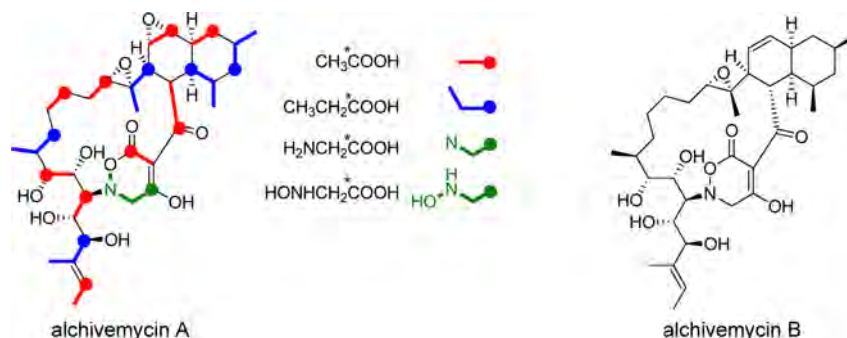
Youngju Kim,^{†,§} Yasuko In,[‡] Toshimasa Ishida,[‡] Hiroyasu Onaka,^{†,||} and
Yasuhiro Igarashi^{*†}

Biotechnology Research Center, Toyama Prefectural University, 5180 Kurokawa,
Imizu, Toyama 939-0398, Japan, and Department of Physical Chemistry,
Osaka University of Pharmaceutical Sciences, 4-20-1 Nasahara, Takatsuki,
Osaka 569-1041, Japan

yas@pu-toyama.ac.jp

Received April 18, 2013

ABSTRACT



Biosynthetic origin of 2*H*-tetrahydro-4,6-dioxo-1,2-oxazine, an unprecedented structural unit first discovered in alchivemycin A (1), was investigated by feeding ¹³C-labeled precursors. Incorporations of both [¹⁻¹³C]glycine and [¹⁻¹³C]-*N*-hydroxyglycine into the carbon at the 4-position of this six-membered ring indicate that the hydrooxazine ring is assembled through a PKS-NRPS hybrid pathway. Additionally, alchivemycin B (2), a deoxygenated analog of 1, was isolated and its relative and absolute configurations were determined by spectroscopic analysis including NMR and CD and X-ray crystallography.

Polyketides are one of the largest classes of secondary metabolites, distributed in a wide range of organisms including bacteria, fungi, and plants. These compounds have served as an invaluable source for drug discovery due to their desirable medicinal properties as well as high structural diversity.¹ Polyketide synthases (PKSs) are multifunctional enzymes responsible for the biosynthesis of polyketides. According to the variation of the chain

elongation system, PKSs are largely divided into type I that gives rise to aliphatic compounds such as macrolides and types II and III that essentially afford aromatic compounds such as anthraquinones and flavonoids.² Bacterial type I PKSs are multifunctional multienzymes containing all the active sites required for each step of the chain extension, and thus are much larger than fungal type I PKSs in which a single module for chain elongation works repetitively.³ This difference makes the bacterial type I PKS-derived products larger, more complex with more chiral centers than the fungal counterparts. Nonribosomal peptide synthetases (NRPSs) use a similar strategy to type I PKS for the assembly of amino acid components.⁴ Fusion

[†] Toyama Prefectural University.

^{*} Osaka University of Pharmaceutical Sciences.

[§] Present address: Molecular Design and Synthesis, Department of Chemistry, Katholieke Universiteit Leuven (KU Leuven), Celestijnenlaan 200F, Leuven 3001, Belgium.

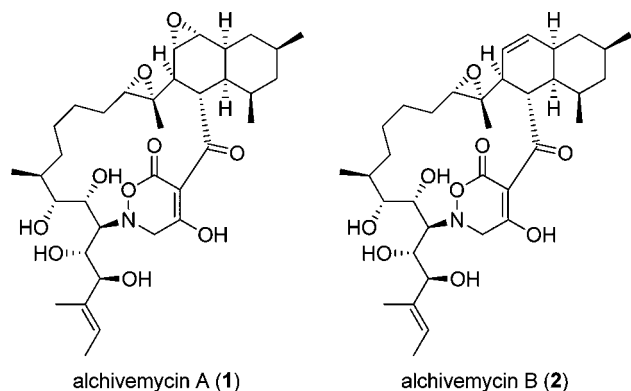
^{||} Present address: Department of Biotechnology, Graduate School of Agricultural and Life Sciences, The University of Tokyo, 1-1-1 Yayoi, Bunkyo, Tokyo 113-8657, Japan.

(1) (a) Hertweck, C. *Angew. Chem., Int. Ed.* **2009**, *48*, 4688–4716. (b) Nett, M.; Ikeda, H.; Moore, B. S. *Nat. Prod. Rep.* **2009**, *26*, 1362–1384.

(2) (a) Shen, B. *Curr. Opin. Chem. Biol.* **2003**, *7*, 285–295. (b) Staunton, J.; Weissman, K. *J. Nat. Prod. Rep.* **2001**, *18*, 380–416.

(3) Stefano, D.; Paolo, M.; Margherita, S. *Nat. Prod. Rep.* **2007**, *24*, 1073–1109.

of type I PKS and NRPS enables incorporation of nitrogen atom(s) into the polyketide backbone,⁵ providing additional structural variations as exemplified by an immunosuppressant FK506⁶ and an antitumor agent epothilone.⁷



Alchivemycin A (**1**) is a polycyclic polyketide discovered from an extract of *Streptomyces* through our LC/UV-based chemical screening targeted at bacterial type I PKS products.⁸ **1** exhibits selective antimicrobial activity against *Micrococcus luteus* with an MIC value of 0.03 $\mu\text{g/mL}$ and inhibits the invasion of murine colon carcinoma 26-L5 cells into Matrigel with an IC_{50} of 0.34 μM without showing cytotoxic effects. Further chemical analysis of the extract of this strain led to the isolation and characterization of alchivemycin B (**2**), a deoxy analog of **1** with more potent antimicrobial activity against *M. luteus* (MIC = 0.004 $\mu\text{g/mL}$) and a comparable inhibitory effect on tumor cell invasion (IC_{50} = 1.9 μM).

The most intriguing structural feature present in alchivemycins is the 2*H*-tetrahydro-4,6-dioxo-1,2-oxazine ring that is unprecedented in nature. This nitrogen- and oxygen-containing six-membered ring apparently looks like a hybrid of tetramic acid and tetronic acid. In polyketides, the tetramic acid ring is assembled by condensation of a polyketide unit and an α -amino acid and the following Dieckman cyclization,⁹ while a three-carbon unit, probably 1,3-bisphosphoglyceric acid derived from the glycolytic pathway, is proposed to be a precursor for the tetronic acid ring assembly.¹⁰ According to the structural analogy

to tetramic acid, we hypothesized that the tetrahydrooxazine is constructed by condensation of a polyketide chain and *N*-hydroxyglycine which could be derived from the oxidation of glycine. To explore the validity of this hypothesis, incorporation experiments with plausible ¹³C-labeled precursors were carried out. Herein, we describe the results from the ¹³C-labeling experiments of alchivemycin A (**1**) and the isolation and structure determination of alchivemycin B (**2**).

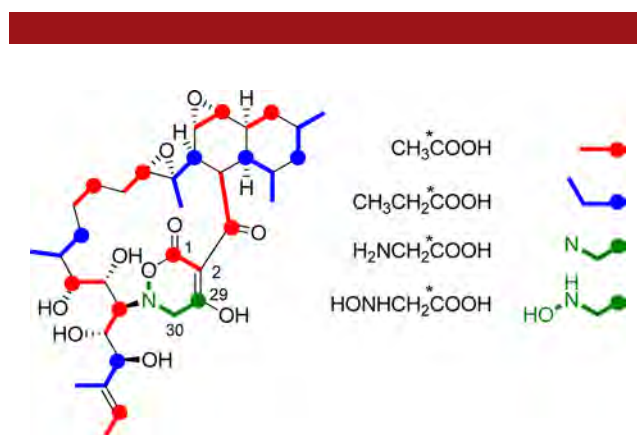


Figure 1. Incorporation of ¹³C-labeled precursors into **1**.

In order to elucidate the biosynthetic origin of the tetrahydrooxazine ring, incorporation of plausible ¹³C-labeled precursors into **1** was investigated (Figure 1). First, [1-¹³C]acetate and [1-¹³C]propionate were fed to the cultures to confirm the extender units of the polyketide backbone (Table 1). High levels of enrichments were observed at C-1, C-3, C-9, C-11, C-15, C-17, C-21, C-23, and C-27 in [1-¹³C]acetate-labeled **1**, while C-5, C-7, C-13, C-19, and C-25 were equally enriched in [1-¹³C]propionate-labeled **1**. Two carbons C-29 and C-30 in the tetrahydrooxazine ring were not labeled by these precursors, indicating that these carbons are not derived from the malonate pathway. As expected, [1-¹³C]glycine was incorporated into **1** with high efficiency to give enrichment only at C-29. Next, we examined the incorporation of [1-¹³C]-*N*-hydroxyglycine which was prepared by the treatment of [1-¹³C]bromoacetic acid with *N*-hydroxylamine in methanol.¹¹ C-29 was again enriched by [1-¹³C]-*N*-hydroxyglycine at a significant incorporation level. These results provided the convincing evidence that the tetrahydrooxazine ring was assembled from a polyketide and an amino acid component.

Based on the labeling experiments, we propose the biosynthetic route to the tetrahydrooxazine ring through a PKS-NRPS hybrid pathway as illustrated in Figure 2. Glycine might be a direct substrate for NRPS giving an enzyme-bound glycine which would be hydroxylated later and condensed with the polyketide moiety. Alternatively,

(4) (a) Chen, H.; O'Connor, S.; Cane, D. E.; Walsh, C. T. *Chem. Biol.* **2001**, *6*, 899–912. (b) Mootz, H. D.; Schwarzer, D.; Marahiel, M. A. *ChemBioChem* **2002**, *3*, 490–504.

(5) Wenzel, S. C.; Müller, R. *Curr. Opin. Chem. Biol.* **2005**, *9*, 447–458.

(6) Iwasaki, K.; Shiraga, T.; Nagase, K.; Tozuka, Z.; Noda, K.; Sakuma, S.; Fujitsu, T.; Shimatani, K.; Sato, A.; Fujioka, M. *Drug Metab. Dispos.* **1993**, *21*, 971–977.

(7) Gerth, K.; Bedorf, N.; Höfle, G.; Irschik, H.; Reichenbach, H. *J. Antibiot.* **1996**, *49*, 560–563.

(8) Igarashi, Y.; Kim, Y.; In, Y.; Ishida, T.; Kan, Y.; Fujita, T.; Iwashita, T.; Tabata, H.; Onaka, H.; Furumai, T. *Org. Lett.* **2010**, *12*, 3402–3405.

(9) (a) Royles, B. J. L. *Chem. Rev.* **1995**, *95*, 1981–2001. (b) Halo, L. M.; Marshall, J. W.; Yakasai, A. A.; Song, Z.; Butts, C. P.; Crump, M. P.; Heneghan, M.; Bailey, A. M.; Simpson, T. J.; Lazarus, C. M.; Cox, R. J. *ChemBioChem* **2008**, *9*, 585–594.

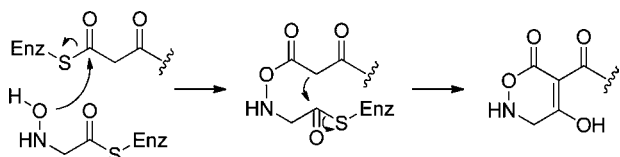
(10) (a) Walton, L. J.; Corre, C.; Challis, G. L. *J. Ind. Microbiol. Biotechnol.* **2006**, *33*, 105–120. (b) Sun, Y. H.; Hong, H.; Gillies, F.; Spencer, J. B.; Leadlay, P. F. *ChemBioChem* **2008**, *9*, 150–156. (c) Schobert, R.; Schlenk, A. *Bioorg. Med. Chem.* **2008**, *16*, 4203–4221.

(11) (a) Cao, X.; Iqbal, A.; Patel, A.; Gretz, P.; Huang, G.; Crowder, M.; Day, R. A. *Biochem. Biophys. Res. Commun.* **2003**, *311*, 267–271. (b) Goto, G.; Kawakita, K.; Okutani, T.; Miki, T. *Chem. Pharm. Bull.* **1986**, *34*, 3202–3207. (c) Zhang, J.; Kjonaas, R.; Flurkey, W. H. *Phytochemistry* **1999**, *775*–783.

Table 1. Incorporation of ^{13}C -Labeled Precursors into **1**

	δ_{C}	relative enrichments ^a			
		[^{13}C]-acetate	[^{13}C]-propionate	[^{13}C]-glycine	[^{13}C]- <i>N</i> -hydroxy-glycine
1	176.3	2.26	0.85	0.68	0.86
2	104.8	0.79	0.58	1.05	1.00
3	201.6	3.69	0.96	1.24	1.19
4	38.0	0.92	0.67	1.07	1.00
5	43.0	1.45	7.47	1.11	1.04
6	39.3	0.93	0.87	1.04	0.99
7	39.5	1.17	7.59	0.94	1.15
8	34.5	1.72	1.83	1.28	0.87
9	39.4	2.81	1.04	1.17	1.05
10	40.8	0.88	0.85	0.96	0.85
11	134.4	2.74	0.90	1.00	1.00
12	126.0	0.96	0.88	0.94	1.04
13	54.3	1.52	7.58	1.14	1.11
14	61.5	0.88	0.82	1.11	1.02
15	64.4	3.03	0.87	1.12	1.05
16	25.2	0.88	0.87	1.01	1.00
17	27.2	2.88	0.85	1.16	1.08
18	27.4	1.56	1.02	1.25	1.26
19	34.3	0.95	6.40	1.03	0.89
20	36.1	0.81	0.64	0.85	0.91
21	79.7	3.00	1.09	1.41	1.19
22	74.8	1.10	1.02	1.22	1.18
23	62.2	3.00	0.63	1.00	1.03
24	71.3	1.01	0.95	1.17	1.12
25	79.9	1.14	6.41	1.04	0.90
26	136.9	0.97	1.02	1.04	1.07
27	123.6	2.46	0.71	0.84	0.83
28	13.3	1.00	1.03	1.08	1.05
29	192.1	1.03	0.95	13.35	2.41
30	63.5	0.72	0.84	1.00	1.00
31	21.6	0.98	0.80	1.07	0.96
32	22.8	1.00	1.00	1.16	1.12
33	13.8	1.15	0.94	1.23	1.34
34	11.9	1.00	0.90	1.00	1.09
35	11.7	0.94	0.88	1.00	1.01

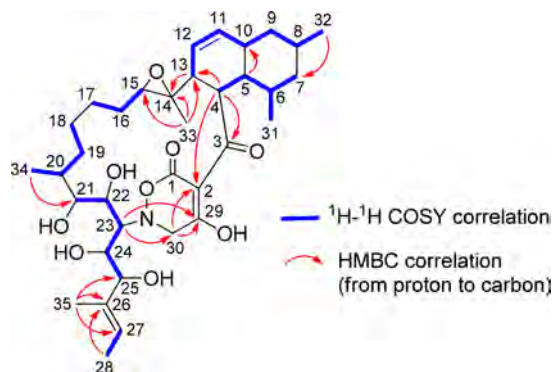
^a ^{13}C signal intensity of each peak in the labeled alchivemycin A divided by that of the corresponding signal in the unlabeled, normalized to give an enrichment ratio of alchivemycin A for enriched peak (C-28 for [^{13}C]acetate, C-32 for [^{13}C]propionate, and C-30 for [^{13}C]glycine labeling). The numbers in bold type indicate ^{13}C -enriched atoms from ^{13}C -labeled precursors.

**Figure 2.** Proposed biosynthetic pathway for tetrahydrooxazine ring.

glycine could be hydroxylated early to give *N*-hydroxy-glycine which is then utilized as a substrate for NRPS.

An extremely high incorporation ratio of glycine into **1** likely suggests that glycine is the direct substrate for NRPS; while it is possible that NRPS could accept both glycine and *N*-hydroxyglycine as substrates, glycine is preferred.¹²

In the course of this study, a minor peak showing a UV spectrum (λ_{max} 224, 285 nm) almost identical to that of **1** was detected. The 1-butanol extract of the whole culture broth was successively subjected to silica gel and ODS column chromatographies and reversed-phase HPLC purification using an ODS column to yield alchivemycin B (**2**) as optically active colorless needles. The IR spectrum of **2** displayed absorption bands for the hydroxy and carbonyl groups at 3417 and 1647 cm^{-1} , respectively. The molecular formula of **2** was determined as $\text{C}_{35}\text{H}_{53}\text{NO}_9$ (obsd $[\text{M}-\text{H}]^-$ at m/z 630.3641, calcd $[\text{M}-\text{H}]^-$ at m/z 630.3642) on the basis of the high-resolution ESITOFMS data, corresponding to the loss of one oxygen atom from **1**.

**Figure 3.** 2D NMR correlations for **2**.**Figure 4.** ORTEP drawing of crystal structure of **2**.

1D- and 2D-NMR analysis revealed that most of the proton and carbon chemical shifts of **2** showed high similarity to **1** except for the resonances at C-11 and

(12) Shiman, R. *J. Biol. Chem.* **1980**, *255*, 10029–10032.

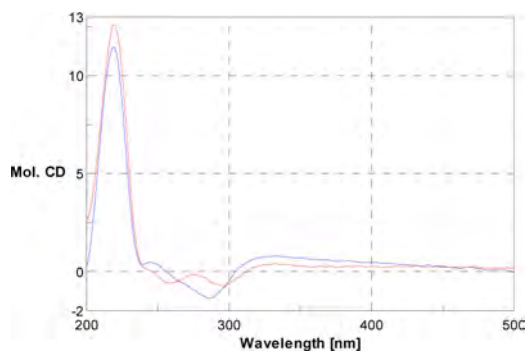


Figure 5. CD spectra of alchivemycins in MeOH (blue: **1**; red: **2**).

C-12. ^1H NMR signals of H-11 (δ 5.86) and H-12 (δ 5.39) of **2** were resonated downfield relative to those of **1** (H-11, δ 3.11; H-12, δ 3.05), suggesting that **2** had a double bond between C-11 and C-12 instead of an epoxy functionality. This was consistent with the olefinic ^{13}C NMR resonances for C-11 (δ 134.4) and C-12 (δ 126.0). The remaining part of the planar structure of **2** was readily assigned by comparing the NMR data with **1** (Figure 3, Table S1).

Recrystallization of **2** from a mixture of dichloromethane and methanol afforded colorless prisms suitable for X-ray crystallographic analysis (CCDC accession No. 739981, Figure 4). Relative configurations of all the chiral centers present in **2** were identical with those in **1**. Although

(13) Chemical derivatization with chiral anisotropic reagents (e.g., MTPA, MPA) failed, giving complex mixture of esters difficult to be separated.

2 showed positive optical rotation ($[\alpha]_{\text{D}}^{22} +35$ (c 1.0, MeOH)), opposite to that of **1** ($[\alpha]_{\text{D}}^{23} -17$ (c 1.0, MeOH)), circular dichroism (CD) spectra of **1** and **2** displayed nearly identical CD curves with a strong positive Cotton effect around 218 nm (Figure 5). In view of the biosynthetic relationship, it is most likely that **1** and **2** possess the same absolute configuration.¹³

In summary, we have proposed a biosynthetic pathway for tetrahydrooxazine ring formation in alchivemycins on the basis of ^{13}C -labeling experiments. Future investigations will be focus on biosynthetic gene analysis to identify the enzymatic reactions responsible for tetrahydrooxazine ring formation. Concomitantly, alchivemycin B (**2**), a new minor congener of alchivemycin A (**1**), was isolated and its absolute configuration was elucidated by spectroscopic and X-ray crystallographic analyses.

Acknowledgment. We acknowledge Drs. I. Saiki and S. Miyayaga at Toyama University for assistance with the antiinvasion assay. Dr. N. Oku and Mr. T. Fukuda at Toyama Prefectural University are also thanked for assistance with NMR measurements. This research was supported by a Grant-in-aid for Scientific Research from the Ministry of Education, Culture, Sports, and Technology of Japan to Y.I.

Supporting Information Available. Experimental details; NMR data, 1D/2D NMR spectra, UV and IR spectra of **2**; ^{13}C NMR spectra of **1** derived from ^{13}C -labeled precursors. This material is available free of charge via the Internet at <http://pubs.acs.org>.

The authors declare no competing financial interest.

Guianolides A and B, New Carbon Skeletal Limonoids from the Seeds of *Carapa guianensis*

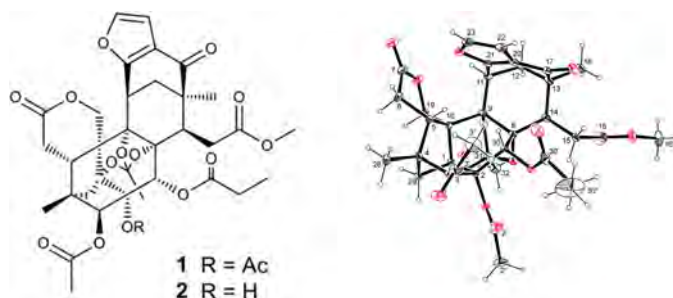
Takanobu Inoue,[†] Yuuki Matsui,[†] Takashi Kikuchi,[†] Yasuko In,[†] Takeshi Yamada,[†] Osamu Muraoka,[‡] Shunyo Matsunaga,[†] and Reiko Tanaka^{*,†}

Osaka University of Pharmaceutical Sciences, 4-20-1 Nasahara, Takatsuki, Osaka 569-1094, Japan, and Faculty of Pharmaceutical Sciences, Kinki University, 3-4-1 Kowakae, Higashiosaka, Osaka 577-8502, Japan

tanakar@gly.oups.ac.jp

Received April 30, 2013

ABSTRACT



Two novel limonoids, named guianolides A (1) and B (2), were isolated from the seeds of *Carapa guianensis* AUBLET (Meliaceae). Their structures were established by spectroscopic analyses and X-ray crystallography. Guianolides A (1) and B (2) featured an unprecedented carbon skeleton via the formation of a C-11–C-21 bond.

Limonoids, a series of structurally diverse and highly oxygenated tetranortriterpenes, are mainly found in the Meliaceae family and have been attracting attention from biogenetic and synthetic perspectives.¹ In recent years, a number of limonoids have been isolated by several research groups, such as phyllanthoids A and B,² aphanamixoid A,³ walsucochinoids A and B,⁴ chukrasone A,⁵

Tabulvelutin A,⁶ cipaferens A–D,⁷ and walsogynes B–G.⁸ Andiroba (*Carapa guianensis*, Meliaceae) is a tall tropical tree with fragment flowers, sometimes reaching up to 50 m tall. Andiroba is one of the largest leafed trees in the rain forests of South America. The woody four cornered nut has four cells, with each cell containing two to three seeds with oil-rich kernels. Seed oil from *C. guianensis* is used as

[†] Osaka University of Pharmaceutical Sciences.

[‡] Kinki University.

(1) (a) Liao, S.-G.; Chen, H.-D.; Yue, J.-M. *Chem. Rev.* **2009**, *109*, 1092–1140. (b) Tan, Q.-G.; Luo, X.-D. *Chem. Rev.* **2011**, *111*, 7437–7522. (c) Fang, X.; Di, Y. T.; Hao, X. J. *Curr. Org. Chem.* **2011**, *15*, 1363–1391.

(2) Zhao, J.-Q.; Wang, Y.-M.; He, H.-P.; Li, S.-H.; Li, X.-N.; Yang, C.-R.; Wang, D.; Zhu, H.-T.; Xu, M.; Zhang, Y.-J. *Org. Lett.* **2013**, *15*, 2414–2417.

(3) Cai, J.-Y.; Zhang, Y.; Shi-Hong Luo, S.-H.; Chen, D.-Z.; Tang, G.-H.; Yuan, C.-M.; Di, Y.-T.; Li, S.-H.; Hao, X.-J.; He, H.-P. *Org. Lett.* **2012**, *14*, 2524–2527.

(4) Han, M.-L.; Zhang, H.; Yang, S.-P.; Yue, J.-M. *Org. Lett.* **2012**, *14*, 486–489.

(5) Liu, H.-B.; Zhang, H.; Li, P.; Gao, Z.-B.; Yue, J.-M. *Org. Lett.* **2012**, *14*, 4438–4441.

(6) Yin, J.-L.; Di, Y.-T.; Fang, X.; Liu, E.-D.; Liu, H.-Y.; He, H.-P.; Li, S.-L.; Li, S.-F.; Hao, X.-J. *Tetrahedron Lett.* **2011**, *52*, 3083–3085.

(7) Bandi Siva, B.; G. Suresh, G.; Poornima, B.; Venkanna, A.; Babu, K. S.; Prasad, K. R.; Reddy, L. P. A.; Sreedhar, A. S.; Rao, C. V. *Tetrahedron Lett.* **2013**, *54*, 2934–2937.

(8) Nugroho, A. E.; Okuda, M.; Yamamoto, Y.; Hirasawa, Y.; Wong, C.-P.; Kaneda, T.; Shirota, O.; Hadi, A. H. A.; Morita, M. *Tetrahedron* **2013**, *69*, 4139–4145.

(9) (a) Miranda, J.; Raimundo, N. C.; Dolabela, M. F.; da Silva, M. N.; Povoia, M. M.; Maia, J. G. S. *J. Ethnopharmacol.* **2012**, *142*, 679–683. (b) Ferreira, M. R. A.; Santiago, R. R.; Souza, T. P.; Egito, E. S. T.; Oliveira, E. E.; Soares, L. A. L. *AAPS PharmSciTech* **2010**, *11*, 1383–1390. (c) Ferrari, M.; Oliveira, M. S. C.; Nakano, A. K.; Rocha-Filho, P. A. *Revista Brasileira de Farmacognosia* **2007**, *17*, 626–630. (d) Prophiro, J. S.; da Silva, M. A. N.; Kanis, L. A.; da Rocha, L. C. B. P.; Duque-Luna, J. E.; da Silva, O. S. *Parasitology Res.* **2012**, *110*, 699–705. (e) Prophiro, J. S.; da Silva, M. A. N.; Kanis, L. A.; da Silva, B. M.; Duque-Luna, J. E.; da Silva, O. S. *Parasitology Res.* **2012**, *110*, 713–719. (f) Ferreira, M. R. A.; Santiago, R. R.; de Souza, T. P.; Egito, E. S. T.; Oliveira, E. E.; Soares, L. A. L. *PharmSciTech* **2010**, *11*, 1383–1390.

a repellent⁹ and has analgesic,¹⁰ antibacterial,¹¹ anti-inflammatory,¹² anticancerous,¹³ and antiallergic¹⁴ activities. It is also effective against arthritis and rheumatism.¹⁵

We recently reported the isolation and structure elucidation of carapanolides A and B, two novel 9,10-*seco*-2*R*,9*S*-epoxymexicanolide-type limonoids from the seeds of *C. guianensis*.¹⁶ In the current study, two new carbon skeletal limonoids, named guianolides A (**1**) and B (**2**), were isolated from the seed oil of *C. guianensis*. Guianolides A (**1**) and B (**2**) featured an unprecedented carbon skeleton via the formation of the C-11–C-21 bond in phragmalin-1,8,9-orthoacetate. We describe herein the structures and cytotoxic activities of **1** and **2** against three tumor cell lines, P388, L1210, and HL-60.

Medium-pressure liquid chromatography (MPLC) and reverse phase HPLC were used to obtain the two new limonoids, **1** and **2**.



Guianolide A (**1**)¹⁷ was obtained as a colorless crystal. Its molecular formula was determined to be C₃₆H₄₀O₁₅ (*m/z* 713.2445 [M+H]⁺, calcd 713.2445) based on HRFABMS due to 17 degrees of unsaturation. The IR absorption bands indicated the existence of several carbonyl groups (ν_{\max} 1749 cm⁻¹) and an α,β -unsaturated six-membered ring ketone (ν_{\max} 1682 cm⁻¹). The UV spectrum of **1** showed λ_{\max} 210 and 260 nm. The ¹³C NMR spectrum of **1** suggested

(10) Penido, C.; Costa, K. A.; Pennaforte, R. J.; Costa, M. F. S.; Pereira, J. F. G.; Siani, A. C.; Henriques, M. G. M. O. *Inflamm. Res.* **2005**, *54*, 295–303.

(11) Nayak, B. S.; Kanhai, J.; Milne, D. M.; Pereira, L. P.; Swanston, W. H. *Evid. Based Complement Alternat. Med.* **2011**, *2011*, 419612.

(12) Penido, C.; Conte, E. P.; Chagas, M. S. S.; Rodrigues, C. A. B.; Pereira, J. F. G.; Henriques, M. G. M. O. *Inflammation Res.* **2006**, *55*, 457–464.

(13) Nakanishi, K. *Chem. Pharm. Bull.* **1965**, *13*, 882–890.

(14) Ferraris Fausto, K.; Rodrigues, R.; da Silva, V. P.; Figueiredo, R.; Penido, C.; Henriques, M. G. M. O. *Int. Immunopharmacol.* **2011**, *11*, 1–11.

(15) Costa-Silva, J. H.; Lima, C. R.; Silva, E. J. R.; Araujo, A. V.; Fraga, M. C. C. A.; Ribeiro, E.; Ribeiro, A.; Arruda, A. C.; Lafayette, S. S. L.; Wanderley, A. G. *J. Ethnopharmacol.* **2008**, *116*, 495–500.

(16) Inoue, T.; Nagai, Y.; Mitooka, A.; Ujike, R.; Muraoka, O.; Yamada, T.; Tanaka, R. *Tetrahedron Lett.* **2012**, *53*, 6685–6688.

(17) Guianolide A (**1**): Colorless crystals (in *n*-hexane/CHCl₃); mp 143–145 °C; HRFABMS at *m/z*: 713.2445 [M+H]⁺ (calcd for 713.2445, C₃₆H₄₁O₁₅); $[\alpha]_D^{22} +106.2^\circ$ (*c* 0.100, CHCl₃); UV (CH₃CN) λ_{\max} (log ϵ) 260 (3.36), 210 (3.72); CD [0.000400 M, CH₃CN] λ_{\max} ($\Delta\epsilon$): 228 (0), 262 (43.07), 289 (11.5), 330 (30.3), 358 (0); IR ν_{\max} (KBr) cm⁻¹: 3608, 2951, 2359, 1749, 1682, 1439; ¹H and ¹³C NMR data, see Table 1.

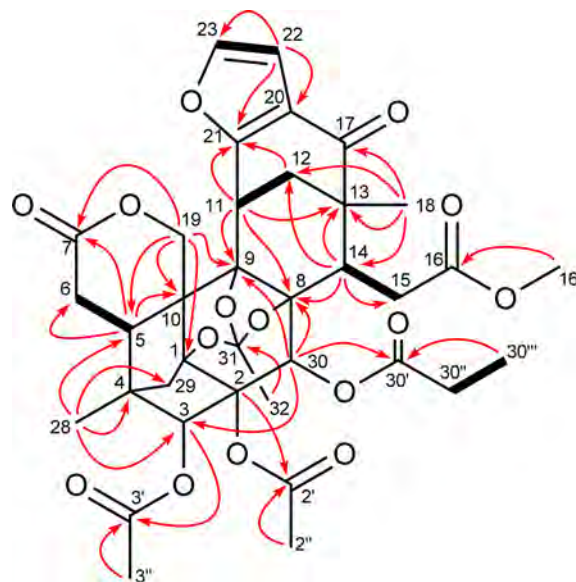


Figure 1. Key ¹H–¹H COSY (bold \rightarrow) and HMBC (\rightarrow (red)) correlations of **1**.

that 8 out of 17 degrees of unsaturation came from two carbon–carbon double bonds and six carbonyls; thus, the remaining 9 degrees of unsaturation indicated **1** to be nonacyclic. The ¹H and ¹³C NMR spectra (Table 1) showed the presence of two acetyls [δ_H 1.89, 2.08 (each 3H, s)], a propanoyl [δ_H 1.10 (3H, t), 2.18 (2H, m); δ_C 170.6], a methyl ester [δ_H 3.71 (3H, s); δ_C 51.9 (q), 174.2 (s)], a δ -lactone [δ_H 4.82, 4.89 (each 1H, d); δ_C 172.3 (s)], a ketone [δ_C 193.2 (s)], an orthoacetate [δ_H 1.81 (3H, s); δ_C 21.4 (q), 86.0 (s), 87.1 (s), 87.6 (s), 120.6 (s)], a tertiary methyl [δ_H 1.05 (3H, s)], five methylenes, five sp³ methines including two oxymethines [δ_H 5.13 (s); δ_C 80.5 (d); δ_H 5.40 (s); δ_C 68.9 (d)], seven sp³ quaternary carbons including four oxycarbons, a disubstituted olefin [δ_H 6.98 (d), 7.43 (d); δ_C 109.0 (d), 142.1 (d)], and a tetrasubstituted olefin [δ_C 123.6, 161.9 (each s)]. When **1** was compared with usual phragmalin-type limonoids, it lacked a methylene and one more methine in the DEPT and HSQC spectra. Analysis of the ¹H–¹H COSY spectrum (H-5–H₂-6; H-11–H₂-12; H-14–H₂-15; H-22–H-23; H₂-30'''–H₃-30''') of **1** revealed the partial structures shown in boldface in Figure 1.

The planar structure of **1** was constructed by the detailed analysis of 1D and 2D NMR data, especially the HMBC spectrum. The A, B, and F rings were readily established as phragmalin-1,8,9-orthoacetate when compared with those of andirolides E, F, O, and P,^{18,19} which were isolated from the flowers of *C. guianensis*, and the linkage of the substituents was confirmed by the HMBC spectrum (Figure 1). In the HMBC spectrum, two acetyl groups were attached to

(18) Tanaka, Y.; Yamada, T.; In, Y.; Muraoka, O.; Kajimoto, T.; Tanaka, R. *Tetrahedron* **2011**, *67*, 782–792.

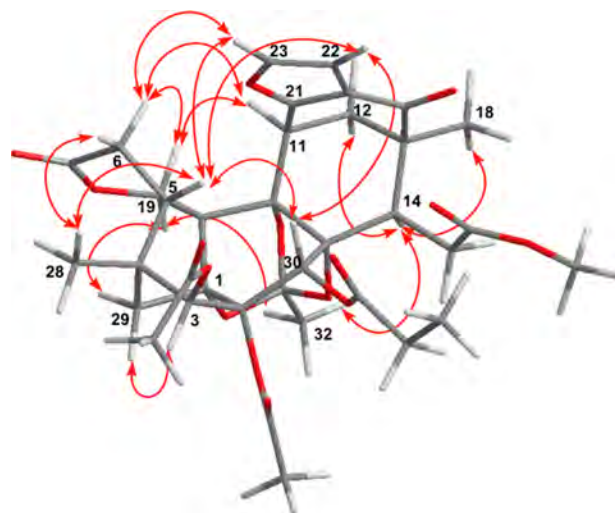
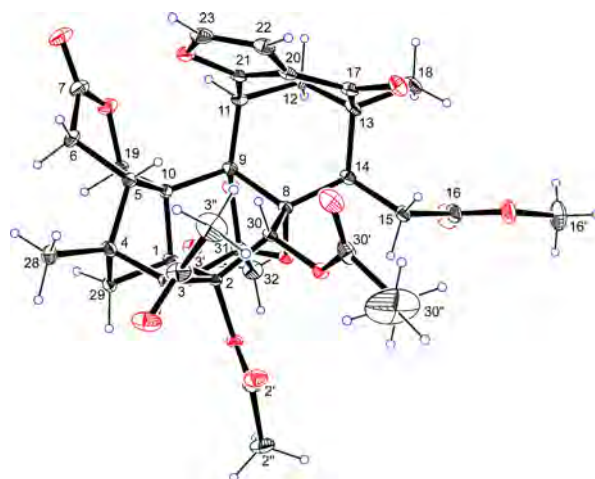
(19) Tanaka, Y.; Sakamoto, A.; Inoue, T.; Kikuchi, T.; Kajimoto, T.; Muraoka, O.; Sata, A.; Wataya, Y.; Kim, H. S.; Tanaka, R. *Tetrahedron* **2012**, *68*, 3669–3677.

Table 1. ^1H and ^{13}C NMR Data for **1** and **2** in CDCl_3

	1		2	
	δ_{C}^a	δ_{H} (mult; J , Hz) a	δ_{C}^a	δ_{H} (mult; J , Hz) a
1	86.0 (s)		86.2 (s)	
2	86.8 (s)		80.8 (s)	
3	80.5 (d)	5.13 s	83.2 (d)	4.48 s
4	45.5 (s)		44.8 (s)	
5	35.1 (d)	1.66 (t, 5.6)	36.4 (d)	1.78 (t, 5.6)
6 α	31.3 (t)	2.41 (dd, 16.5, 5.6)	31.5 (t)	2.41 (dd, 16.4, 5.6)
6 β		3.14 (dd, 16.5, 5.6)		2.98 (dd, 16.4, 5.6)
7	172.3 (s)		172.2 (s)	
8	87.6 (s)		89.0 (s)	
9	87.1 (s)		87.8 (s)	
10	47.5 (s)		47.2 (s)	
11	34.3 (d)	4.00 (t, 3.2)	34.4 (d)	4.04 (t, 3.2)
12 α	41.2 (t)	2.35 (dd, 13.1, 3.2)	40.9 (t)	2.33 (dd, 13.2, 3.2)
12 β		2.14 (dd, 13.1, 3.2)		2.14 (dd, 13.2, 3.2)
13	45.9 (s)		45.9 (s)	
14	51.5 (d)	2.92 (m)	51.0 (d)	2.91 (m)
15A	30.1 (t)	2.34 (m)	29.7 (t)	2.36 (m)
15B		2.93 (m)		2.89 (m)
16	174.2 (s)		174.1 (s)	
17	193.2 (s)		193.2 (s)	
18	21.9 (q)	1.05 s	21.9 (q)	1.04 s
19 α	68.8 (t)	4.82 (d, 13.2)	68.8 (t)	4.66 (d, 13.2)
19 β		4.89 (d, 13.2)		5.05 (d, 13.2)
20	123.6 (s)		123.8 (s)	
21	161.9 (s)		161.8 (s)	
22	109.0 (d)	6.98 (d, 1.7)	109.0 (d)	6.95 (d, 1.7)
23	142.1 (d)	7.43 (d, 1.7)	142.1 (d)	7.43 (d, 1.7)
28	14.7 (q)	0.93 s	14.5 (q)	0.94 s
29 $_{\text{pro-R}}$	38.2 (t)	2.38 (d, 11.7)	37.2 (t)	2.16 (d, 11.5)
29 $_{\text{pro-S}}$		1.66 (d, 11.7)		1.75 (d, 11.5)
30	68.9 (d)	5.40 s	69.0 (d)	5.01 s
31	120.6 (s)		120.7 (s)	
32	21.4 (q)	1.81 s	21.5 (q)	1.82 s
2'	169.9 (s)			
2''	21.9 (q)	2.08 s		
3'	169.1 (s)		169.9 (s)	
3''	20.7 (q)	1.89 s	20.9 (q)	1.86 s
16'	51.9 (q)	3.71 s	52.1 (q)	3.70 s
30'	170.6 (s)		171.4 (s)	
30'A	27.4 (t)	2.18 m	27.9 (t)	2.29 m
30'B		2.18 m		2.29 m
30'''	8.4 (q)	1.10 (t, 7.0)	8.7 (q)	1.12 (t, 7.4)
2-OH				2.88 s

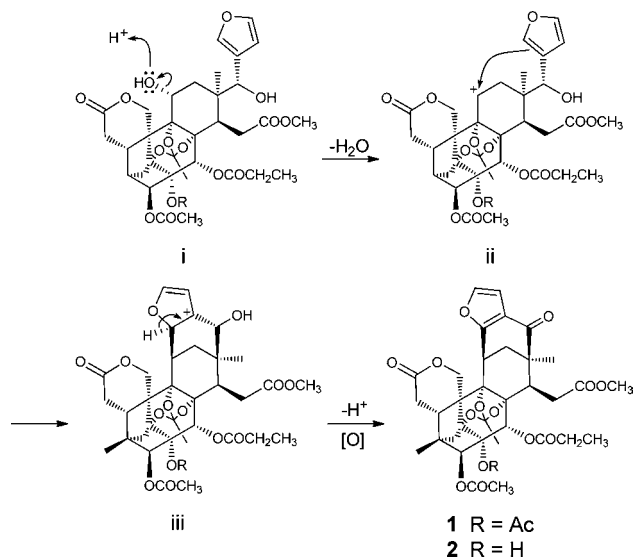
a ^1H NMR spectra were recorded at 600 MHz and ^{13}C NMR spectrum at 150 MHz.

C-2 and C-3 by the correlation between H-3 (δ_{H} 5.13) and the carbonyl of the acetyl group at C-3' (δ_{C} 169.1) and a quaternary oxygenated carbon at C-2 (δ_{C} 86.8); between Me-28 (δ_{H} 0.93) and C-3 (δ_{C} 80.5), C-4, C-5, and C-29; between an acetyl Me at C-2'' (δ_{H} 2.08) and the carbonyl of the acetyl group at C-2' (δ_{C} 169.9); and between H₂-29 (δ_{H} 1.66, 2.38) and C-1 (δ_{C} 86.0), C-2, C-3, C-4, C-5, and C-10, and a propanoyl ester group was attached to C-30 (δ_{C} 68.9) by the correlation between H-30 and the carbonyl of the propanoyl group at C-30' (δ_{C} 170.6). An 1,8,9-orthoacetate was confirmed by the HMBC spectrum, between H₂-19 (δ_{H} 4.82, 4.89) and C-1, C-5, C-7 (δ_{C} 172.3), C-9 (δ_{C} 87.1), and C-10; between H-14 (δ_{H} 2.92) and C-8 (δ_{C} 87.6); and between orthoacetyl Me (δ_{H} 1.81) and C-31 (δ_{C} 120.6). Most of the scaffolds of C–E rings were mainly established

**Figure 2.** Key NOE correlations (↔) of **1**.**Figure 3.** Single-crystal X-ray structure of **1**.

by comprehensive analysis of the HMBC spectrum, by the correlation between H₂-12 [(δ_{H} 2.14, 2.35 (each 1H, dd)] and the methine signal (δ_{C} 34.3) at C-11, C-13, C-14, and C-21 (δ_{C} 161.9); between H-11 (δ_{H} 4.00, 1H, t) and C-8, C-12, C-13, and C-21; between H-22 (δ_{H} 6.98) and C-20 (δ_{C} 123.6, s), C-21, and C-23 (δ_{C} 142.1, d); and between Me-18 (δ_{H} 1.05, s) and C-12, C-13, C-14, and C-17 (δ_{C} 193.2). Thus, the above-mentioned results indicated a unique linkage between C-11 and C-21; therefore, the C–E rings were revealed as an uncommon connected ring system.

The relative stereostructure of **1** was determined by the NOESY spectrum (Figure 2). The NOESY cross-peaks of Me-32/H-14, H-19 α ; H-14/H-12 α , Me-18 indicated that H-14, Me-18, and Me-32 presented an α -orientation. The NOESY correlation of H-11/H-6 β , H-19 β ; H-6 β /H-23 indicated that H-11 was also in the α -direction. On the

Scheme 1. Plausible Biogenetic Pathway for 1 and 2

other hand, the cross-peaks of Me-28/H-5; H-5/H-22, H-23, and H-30; H-22/H-30 indicated that H-5, Me-28, and H-30 adopted a β -orientation. In addition, H-29_{pro-R}/H-19 α ; H-29_{pro-S}/H-3 indicated that H-3 adopted an α -orientation. Therefore, the C and D rings presented a *cis* form and were bent at a 90° angle, and the E ring was in the same plane as the D ring. Thus, the E-ring was located spatially on the upper part of the B-ring. Fortunately, single-crystal X-ray diffraction analysis was successfully conducted to confirm

(20) Guianolide B (**2**): Colorless amorphous; HRFABMS at m/z : 671.2339 [M+H]⁺ (calcd for 671.2339, C₃₄H₃₈O₁₄); [α]_D²² +53.8° (*c* 0.100, CHCl₃); UV (CH₃CN) λ_{\max} (log ϵ) 261 (3.52), 215 (3.75); CD [0.000400 M, CH₃CN] λ_{\max} ($\Delta\epsilon$): 226 (0), 261 (53.4), 287 (15.3), 317 (43.3), 324 (34.5), 330 (41.7), 339 (21.6), 359 (0); IR ν_{\max} (KBr) cm⁻¹: 3435, 2923, 1754, 1731, 1678, 1510; ¹H and ¹³C NMR data, see Table 1.

(21) Chen, K.-M.; Semple, J. E.; Joullie, M. *J. Org. Chem.* **1985**, *50*, 3997–4005.

(22) Czeskis, B. A.; Beackstrom, P.; Moiseenkov, A. M.; Norin, T. *Seriya Khimicheskaya* **1989**, *1*, 131–134.

the proposed structure. In addition, **1** included the two molecules of CHCl₃ as a crystal solvent and, therefore, allowed unambiguous assignment of the absolute configuration of **1** (Figure 3).

Guianolide B (**2**)²⁰ was assigned the molecular formula C₃₄H₃₈O₁₄ (m/z 671.2339 [M+H]⁺, calcd 671.2339) by HRFABMS. The ¹H and ¹³C NMR spectra (Table 1) of **2** were very similar to those of **1**, except for the absence of an acetyl group at C-2 and the presence of an OH group [δ_{H} 2.88 (1H, s), δ_{C} 80.8 (s)]. HMBC correlations were observed at 2-OH/C-3 and C-32. The NOESY experiment revealed that the relative structure of **2** had the same conformation as **1**.

Guianolides A (**1**) and B (**2**) featured an unprecedented carbon skeleton via the formation of the C-11–C-21 bond of phragmalin-1,8,9-orthoacetate. A possible biosynthetic pathway of **1** and **2** was postulated in Scheme 1. The biosynthetic precursor of **1** and **2** has been proposed to be 11-hydroxy-phragmalin-1,8,9-orthoacetate **i**, which was dehydroxylated enzymatically to give **ii**. **ii** then underwent an intermolecular Friedel–Crafts type reaction, followed by oxidation into **1** and **2** (Scheme 1).^{21,22}

As a primary screen for cancer cell growth inhibition, compounds **1** and **2** were examined using the murine P388 and L1210, and human HL-60 leukemia cell lines. Compound **1** showed weak activity against the P388 cell line (IC₅₀ 33.7 μ M), but **2** was inactive against all cell lines.

Acknowledgment. We thank Mr. Akira Yoshino (NGO Green Heart) for the collection and identification of the plant material. We also thank Dr. Katsuhiko Minoura and Dr. Mihoyo Fujitake (Osaka University of Pharmaceutical Sciences) for NMR and MS measurements.

Supporting Information Available. Experimental procedures and physical and spectroscopic data of guianolides A (**1**) and B (**2**). This material is available free of charge via the Internet at <http://pubs.acs.org>.

The authors declare no competing financial interest.



Officinatrione: an unusual (17S)-17,18-seco-lupane skeleton, and four novel lupane-type triterpenoids from the roots of *Taraxacum officinale*



Daisuke Saeki^a, Takeshi Yamada^a, Yasuko In^a, Tetsuya Kajimoto^a, Reiko Tanaka^{a,*}, Yota Iizuka^b, Takahisa Nakane^b, Akihito Takano^b, Kazuo Masuda^{b,*}

^a Osaka University of Pharmaceutical Sciences, 4-20-1 Nasahara, Takatsuki Osaka 569-1094, Japan

^b Showa Pharmaceutical University, 3-3165 Higashi Tamagawa Gakuen, Machida, Tokyo 194-8543, Japan

ARTICLE INFO

Article history:

Received 30 August 2012

Received in revised form 30 November 2012

Accepted 2 December 2012

Available online 19 December 2012

Keywords:

Officinatrione

(17S)-17,18-seco-Lup-19(21)-ene-3,18,22-trione

3β-Acetoxy-18α,19α-epoxylupan-21β-ol

18α,19α-Epoxy-21β-hydroxylupan-3-one

Lup-18-ene-3,21-dione

Lupa-18,21-dien-3β-yl acetate

triterpene

Root

Taraxacum officinale

L1210 cell line

ABSTRACT

Novel 5 lupane-type of triterpenoids, i.e., 3β-acetoxy-18α,19α-epoxylupan-21β-ol (**1**), 18α,19α-epoxy-21β-hydroxylupan-3-one (**2**), lup-18-ene-3,21-dione (**3**), lupa-18,21-dien-3β-yl acetate (**4**), and (17S)-17,18-seco-lup-19(21)-ene-3,18,22-trione (**5**), named officinatrione, as well as 16 known compounds from the roots of *Taraxacum officinale* collected in Takatsuki city, Osaka, Japan. Of the above compounds, **5** was the first lupane-type triterpene, of which the D-ring was open to form a nine-membered ring. Compounds **2** and **5** exhibited moderate cytotoxic activities against L1210 cell line (IC₅₀ 10.5 and 10.1 μM).

© 2012 Elsevier Ltd. All rights reserved.

1. Introduction

Dandelion is a general name of around 2000 species of plants, which belong to *Taraxacum* genus (Compositae). Most of species grow in the Eurasia continent and the dried roots of *Taraxacum officinale* have been used as a traditional Chinese drug from ancient time to cure dropsy and as an antidote agent. Moreover, the traditional medicine has been used to treat sterility since some components of the plant showed an activity like female hormones. On the basis of these backgrounds, a number of studies on the components of the roots of *T. officinale* have been reported to date. Kromayer isolated taraxacerin from milky liquid of the roots in 1861,¹ of which the structure was determined by Power and Browning in 1912,^{2,3} and confirmed by Zellner in 1925.⁴ Stigmasterol, sitosterol, β-amyrin, taraxol, taraxerol (skimmiol), ψ-taraxasterol as well as taraxasterol were isolated from the roots of

dandelion by Burrow in 1938.⁵ Arnidiol was also isolated by Zimmerman in 1941.⁶ The presence of β-sitosterol, β-amyrin, and methyl sterol was reported by Axel in 1967.⁷ In addition, neolupeol and tarolupeol and their acetates were isolated by Ageta from *Taraxacum japonica* in 1981⁸ and 3β-hydroxylup-18(19)-en-21-one was reported by Kisiel in 2000.⁹ Recently, Masuda revised the structure of tarolupenyl acetate to be lup-19(21)-en-3β-yl acetate.¹⁰

Since, in recent, Ebizuka obtained cDNA of synthetic enzyme of triterpenes from *T. officinale* and mentioned molecular revolution of the enzymes, which are responsible to annelation reaction of oxido-squares,¹¹ there could still exist novel triterpenes in the plants of *Taraxacum* species. Thus, we embarked on the chemical study of the components of the roots of dandelion collected in Takatsuki city in 2010 and could isolate 5 novel triterpenes as well as 16 known compounds, for example, neolupenyl acetate, tarolupenyl acetate, tarolupenone, lupenyl acetate, lupenone, butyrospermoyl acetate, taraxasteryl acetate, taraxasterone, α-amyrin acetate, α-amyrone, β-amyrin acetate, β-amyrone, ψ-taraxasteryl acetate, ψ-taraxasterone, dammaradienyl acetate, and dammaradienone. Herein, we report the details of the structure determination of the novel triterpenes (**1–5**).

* Corresponding authors. Tel./fax: +81 72 690 1084 (R.T.); Tel.: +81 427 21 1511 (K.M.); e-mail addresses: tanakar@gly.oups.ac.jp (R. Tanaka), masuda@ac.shoyaku.ac.jp (K. Masuda).

2. Results and discussion

Methanol extract (730 g) of the roots of *T. officinale* (10 kg) was partitioned between Et₂O and water. The organic layer was condensed in vacuo to give yellowish residue (249 g) and separated by silica gel chromatography followed by HPLC [ODS, MeOH/H₂O (95:5)] to afford five novel lupane-type triterpenes and sixteen known compounds (Fig. 1).

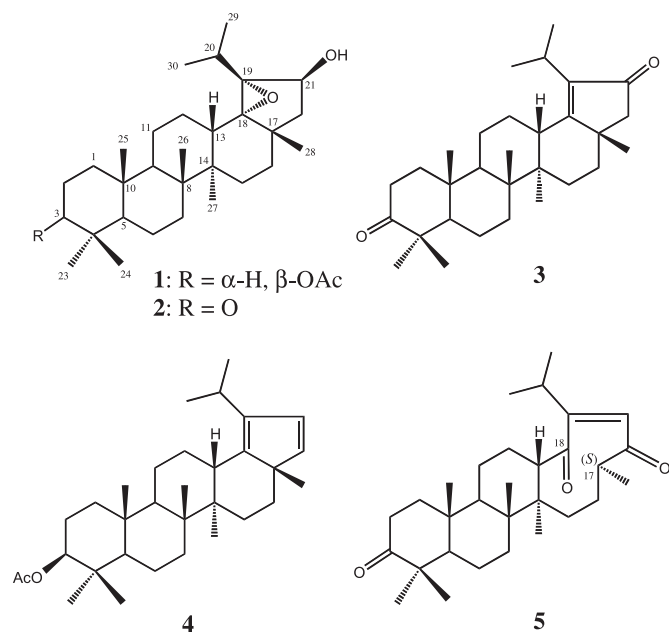


Fig. 1. Chemical structures of compounds 1–5 from *Taraxacum officinale*.

Compound **1** was obtained as colorless needles, of which the molecular ion peak at m/z 500.3871 in HREIMS showed the molecular formula C₃₂H₅₂O₄ (calcd for 500.3866). Its IR spectrum showed the presence of hydroxyl and ester groups at 3440, 1741, and 1245 cm⁻¹, respectively. Detail assignments of ¹H and ¹³C NMR spectra (Table 1) using HSQC and DEPT methods revealed the presence of six tertiary methyl groups, two secondary methyl groups [δ_{H} 1.18 and 1.20 (each d, $J=7.0$ Hz)], an acetyl methyl group [δ_{H} 2.04 (s)], nine methylenes, six methines including two oxymethines [δ_{H} 4.38 (dd, $J=6.2, 3.9$ Hz), δ_{C} 74.1 (d); δ_{H} 4.47 (dd, $J=11.2, 5.3$ Hz), δ_{C} 80.9 (d)], two oxygenated sp³ quaternary carbon [δ_{C} 72.3 (s), 77.3 (s)], and eight quaternary carbons including an acetyl C=O group [δ_{C} 170.9 (s)]. The EIMS showed the fragment ion peaks characteristic for the cleavage of the C-ring at m/z 249 (C₁₆H₂₅O₂) and 189 (249–HOAc), which revealed the presence of the acetyl group at the C-3 position.¹² In the HMBC spectrum, which showed the long-range correlation between ¹H and ¹³C atoms, confirmed the planar structure of **1** as shown in Fig. 2. Namely, correlations were observed between Me-23, 24 (δ_{H} 0.85, 0.84, respectively) and C-3 (δ_{C} 80.9), C-4, and C-5; between Me-25 (δ_{H} 0.88) and C-1, C-5, C-9, and C-10; between Me-26 (δ_{H} 1.09) and C-7, C-8, C-9, and C-14; between Me-27 (δ_{H} 1.06) and C-8, C-13, C-14, and C-15; between Me-28 (δ_{H} 1.17) and C-16, C-17, C-18 (δ_{C} 77.3), and C-22; between Me-29, 30 (δ_{H} 1.18 and 1.20, respectively) and C-19 (δ_{C} 72.3), and C-20 (δ_{C} 29.2); between H-13 (δ_{H} 2.52) and C-11, C-12, C-14, C-15, C-17, C-18, C-19, and C-27; and between H-21 (δ_{H} 4.38) and C-17, C-18, C-19, C-20, and C-22. In the ¹H–¹H COSY spectrum, cross-peak was seen between the hydroxyl proton (δ_{H} 1.24) and H-21; between H-21 and geminal protons at H₂-22 (δ_{H} 1.14, 1.53), and another cross

peak was shown by bold-faced line in Fig. 2. Therefore, the plain structure of **1** should be 3 β -acetoxy-18,19-epoxylupan-21-ol or 3 β -acetoxy-19,21-epoxylupan-18-ol. To clarify a location of a hydroxyl group at C-18 or C-21, mild acetylation of **1** by Ac₂O/Py afforded a diacetate (**1b**). ¹H NMR of **1b** showed an acetoxy methine proton signal at δ 5.26 (d, $J=6.6$ Hz) indicating secondary hydroxyl group was at C-21. Therefore the structure of **1** was determined to be 3 β -acetoxy-18,19-epoxylupan-21-ol. The proton signal of Me-26 appeared at lower magnetic field (δ 1.09), because 18,19-epoxy group was α -oriented (Fig. 3). Dihedral angle between H-21 α and H-22 β is almost 90° by the view of Dreiding model, therefore the ¹H NMR signal of H-21 α appeared as 4.38 (dd, $J_{21\alpha,22\alpha}=6.2$ Hz, $J_{21\alpha,21\text{-OH}}=3.9$ Hz). Relative configuration was established by NOESY spectrum (Fig. 3); between H-3 α (δ_{H} 4.47) and H-5 α (δ_{H} 0.81), Me-23 (δ_{H} 0.85); between Me-26 (δ_{H} 1.09), Me-28 (δ_{H} 1.17) and H-13 β (δ_{H} 2.52); between Me-29, Me-30 and H-13 β ; between 21-OH and Me-28. However, the cross-peak between Me-28 and H-21 (δ_{H} 4.38) was not observed. Therefore, 18-19-epoxy group of **1** was α -oriented and the secondary hydroxyl group at C-21 adopted β configuration and the structure of **1** was determined as 3 β -acetoxy-18 α ,19 α -epoxylupan-21 β -ol.

Compound **2** was obtained as colorless needles, of which the molecular ion peak at m/z 456.3601 in HREIMS showed the molecular formula C₃₀H₄₈O₃ (calcd for 456.3604). Its IR spectrum showed the presence of hydroxyl and carbonyl groups at 3465 and 1698 cm⁻¹, respectively. Precise assignments of ¹H and ¹³C NMR spectra (Table 1) revealed the presence of six tertiary methyl groups, two secondary methyl groups [δ_{H} 1.19, 1.20 (each d, $J=7.3$ Hz)], nine methylenes, six methines including an oxymethine [δ_{H} 4.38 (dd, $J=6.2, 4.3$ Hz), δ_{C} 74.0 (d)], two oxygenated sp³ quaternary carbon [δ_{C} 72.3 (s), 77.2 (s)], and eight quaternary carbons including a ketone group [δ_{C} 218.1 (s)]. The ¹H and ¹³C NMR spectra were similar to those of **1** except for the absence of signals assignable to an acetoxy group and presence of a ketone. A fragment ion peak at m/z 205 in the EIMS revealed the presence of a ketone group at the C-3 position.¹² The HMBC spectrum showed the long-range correlation between Me-23, 24 (δ_{H} 1.08, 1.04, respectively) and C-3 (δ_{C} 218.1); between Me-25 (δ_{H} 0.95) and C-1, C-5, C-9, and C-10; between Me-26 (δ_{H} 1.13) and C-7, C-8, C-9, and C-14; between Me-27 (δ_{H} 1.08) and C-8, C-13, C-14, and C-15; between Me-28 (δ_{H} 1.18) and C-16, C-17, C-18 (δ_{C} 77.2), and C-22; between H₂-2 (δ_{H} 2.44, 2.49) and H-5 α (δ_{H} 1.36) and C-3 (δ_{C} 218.1); between H-20 (δ_{H} 1.96) and C-18, C-19 (δ_{C} 72.3), C-21 (δ_{C} 74.0), C-29, and C-30; between H-21 (δ_{H} 4.38) and C-17, C-18, C-19, C-20, and C-22. In the ¹H–¹H COSY spectrum, a cross-peak was observed between the hydroxyl proton (δ_{H} 1.26) and H-21, between H-21 and H₂-22 (δ_{H} 1.16, 1.54). In the NOESY spectrum of **2**, correlations were observed between Me-29, Me-30 (δ_{H} 1.96) and H-13 β (δ_{H} 2.55); between 21-OH and Me-28, but no NOESY correlation was observed between H-21 and Me-28 as well as **1**. Thus, the relative structure of **2** was concluded to be 18 α ,19 α -epoxy-21 β -hydroxylupan-3-one.

Compound **3** was isolated as colorless needles, of which the molecular ion peak at m/z 438.3494 in HREIMS showed the molecular formula C₃₀H₄₆O₂ (calcd for 438.3498). Its UV and IR spectra suggested the presence of α,β -unsaturated five-membered cyclic ketone [λ_{max} 239.5 nm (log ϵ 3.9), ν_{max} 1697 cm⁻¹] and six-membered ring ketone (ν_{max} 1697 cm⁻¹). Analysis of ¹H and ¹³C NMR spectra using DEPT method exhibited the presence of six tertiary methyl groups, two secondary methyl groups (δ_{H} 1.18, 1.20, each d, $J=7.1$ Hz), nine methylenes, four methines, a tetra-substituted olefin (δ_{C} 143.8, 177.5, each s), nine quaternary carbons including two ketones (δ_{C} 208.6, 217.8) (Table 1). HMBC correlations (Fig. 4) were observed between Me-23, 24 (δ_{H} 1.09, 1.04) and C-3 (δ_{C} 217.8), C-4, and C-5; between Me-25 (δ_{H} 0.99) and C-1, C-5, C-9, and C-10; between Me-26 (δ_{H} 1.19) and C-7, C-8, C-9, and C-14; between Me-27 (δ_{H} 0.92) and C-8, C-13, C-14, and C-15;

Table 1
 ^1H NMR and ^{13}C NMR spectroscopic data of compounds **1**, **2** and **3**

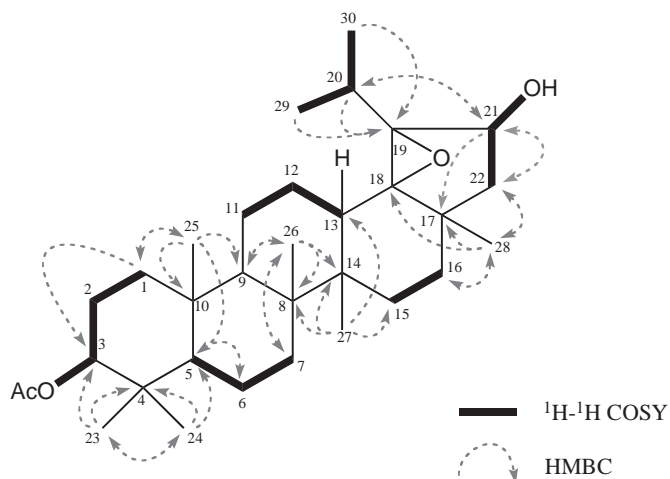
Position	1		2		3	
	$^1\text{H}^a$ (J,Hz)	$^{13}\text{C}^b$	$^1\text{H}^a$ (J,Hz)	$^{13}\text{C}^b$	$^1\text{H}^a$ (J,Hz)	$^{13}\text{C}^b$
1 α	1.02 m	38.3 (t) ^b	1.42 m	39.5 (t) ^b	1.48 m	39.7 (t) ^b
1 β	1.78 dt 13.1, 3.5		1.91 ddd	12.6, 7.6, 4.8	1.98 ddd 18.5, 7.2, 5.5	
2 α	1.64 m	23.7 (t)	2.44 ddd 15.6, 9.0, 4.8	34.1 (t)	2.59 m	33.9 (t)
2 β	1.64 m		2.49 ddd 15.6, 9.4, 7.6			
3	4.47 dd 11.2, 5.3	80.9 (d)		218.1 (s)		217.8 (s)
4		37.8 (s)		47.2 (s)		47.2 (s)
5 α	0.81 m	55.2 (d)	1.36 m	54.6 (d)	1.39 dd 8.3, 5.7	54.6 (d)
6 α	1.54 m	18.2 (t)	1.48 m	19.7 (t)	1.49 m	19.6 (t)
6 β	1.42 m		1.48 m		1.42 m	34.1 (t)
7	1.42 m	33.8 (t)	1.46 m	33.1 (t)	1.55 ddd 13.5, 4.8, 2.1	
8		41.0 (s)		40.9 (s)		41.2 (s)
9 α	1.37 m	49.7 (d)	1.46 m	49.2 (d)	1.44 m	50.4 (d)
10		37.0 (s)		36.1 (s)		36.9 (s)
11 α	1.52 m	20.5 (t)	1.52 m	21.1 (t)	1.62 ddd 12.6, 6.0, 3.3	21.9 (t)
11 β	1.33 m		1.40 m		1.34 ddd 16.3, 12.6, 3.9	
12 α	1.45 m	22.9 (t)	1.43 m	23.0 (t)	1.90 m	27.8 (t)
12 β	1.45 m		1.48 m		1.95 m	
13 β	2.52 dd 11.2, 4.3	33.8 (d)	2.55 dd 11.4, 4.1	34.0 (d)	2.90 dd 12.6, 3.7	41.9 (d)
14		44.5 (s)		44.6 (s)		45.9 (s)
15 α	1.10 m	26.5 (t)	1.14 m	26.6 (t)	1.21 m	27.5 (t)
15 β	1.80 td 13.7, 4.6		1.81 m		1.90 m	
16 α	1.58 m	31.4 (t)	1.59 td 13.2, 4.0	31.3 (t)	1.45 m	37.1 (t)
16 β	1.43 m		1.45 m		1.72 ddd 13.3, 4.3, 2.5	
17		41.0 (s)		41.0 (s)		41.7 (s)
18		77.3 (s)		77.2 (s)		177.5 (s)
19		72.3 (s)		72.3 (s)		143.8 (s)
20	1.97 hept 7.0	29.2 (d)	1.96 hept 7.3	29.3 (d)	3.13 hept 7.1	24.9 (d)
21	4.38 dd 6.2, 3.9	74.1 (d)	4.38 dd 6.2, 4.3	74.0 (d)		208.6 (s)
22 α	1.14 m	45.9 (t)	1.16 m	45.9 (t)	2.10 d 18.8	52.1 (t)
22 β	1.53 m		1.54 m		2.16 d 18.8	
23	0.85 s	27.9 (q)	1.08 s	26.8 (q)	1.09 s	26.9 (q)
24	0.84 s	16.5 (q)	1.04 s	21.0 (q)	1.04 s	20.9 (q)
25	0.88 s	16.2 (q)	0.95 s	16.1 (q)	0.99 s	16.7 (q)
26	1.09 s	16.0 (q)	1.13 s	15.8 (q)	1.19 s	16.6 (q)
27	1.06 s	14.7 (q)	1.08 s	14.6 (q)	0.92 s	15.6 (q)
28	1.17 s	24.1 (q)	1.18 s	24.1 (q)	1.20 s	25.0 (q)
29	1.18 d 7.0	21.3 (q)	1.19 d 7.3	21.0 (q)	1.18 d 7.1	20.4 (q)
30	1.20 d 7.0	18.5 (q)	1.20 d 7.3	18.5 (q)	1.20 d 7.1	20.2 (q)
3'		170.9 (s)				
3''	2.04 s	21.0 (q)				
21-OH	1.24 d 3.9		1.26 d 4.3			

^a Measured at 500 MHz in CDCl_3 .^b Measured at 125 MHz in CDCl_3 .

between Me-28 (δ_{H} 1.20) and C-16, C-17, C-18 (δ_{C} 177.5), and C-22; between Me-29, 30 (δ_{H} 1.18, 1.20) and C-19 (δ_{C} 143.8), and C-20; between H₂-22 (δ_{H} 2.10 and 2.16, each d) and C-16, C-17, C-18 (δ_{H} 177.5), C-21 (δ_{C} 208.6), and C-28. The ^1H – ^1H COSY correlations

revealed the partial structure as shown by bold-faced lines in Fig. 4. On the basis of the NOESY correlations, which were observed between H-13 β (δ_{H} 2.90, dd, $J=12.6, 3.7$ Hz) and H-11 β (δ_{H} 1.34), H-15 β (δ_{H} 1.90), Me-26 and Me-28 (δ_{H} 1.19 and 1.20, respectively), into the consideration, the structure of **3** was determined to be lup-18-ene-3,21-dione.

Compound **4** isolated as colorless needles showed the molecular ion peak at m/z 466.3806 in HREIMS, which indicated the molecular formula $\text{C}_{32}\text{H}_{50}\text{O}_2$ (calcd for 466.3811). UV spectrum (λ_{max} 254.5 nm, $\log \epsilon$ 3.50) suggested the presence of conjugated diene and IR spectrum showed the presence of ester group at 1731 and 1250 cm^{-1} . Analysis of ^1H and ^{13}C NMR spectra using DEPT method exhibited the presence of an acetyl group (δ_{H} 2.05), six tertiary methyl groups, two secondary methyl groups (δ_{H} 1.05 and 1.08, each d, $J=6.6$ Hz), five methine groups including one oxygen bearing methine (δ_{H} 4.49, dd, $J=11.0, 5.7$ Hz; δ_{C} 80.9, d), five methylenes, five quaternary carbons, a disubstituted olefin (δ_{H} 6.21 and 6.31, each d, $J=5.4$ Hz), a tetra-substituted olefin (δ_{C} 141.2 and 145.6), and an acetyl group (δ_{C} 171.0). In the ^1H – ^1H COSY spectrum, cross-peaks were observed between H₂-1 (δ_{H} 1.06, 1.78) and H₂-2 [δ_{H} 1.67 (2H)]; H₂-6 (δ_{H} 1.40, 1.50) and H-5 α (δ_{H} 0.82), and H₂-7 (δ_{H} 1.40, 1.50); H₂-11 (δ_{H} 1.31, 1.57) and H-9 α (δ_{H} 1.38), and H₂-12 (δ_{H} 1.81, 1.95); H₂-15 (δ_{H} 1.06, 1.79) and H₂-16 (δ_{H} 1.04, 1.64); H-21 (δ_{H} 6.31) and H-22 (δ_{H} 6.21). HMBC correlations, which were observed

**Fig. 2.** Selected ^1H – ^1H COSY and HMBC correlations of **1**.

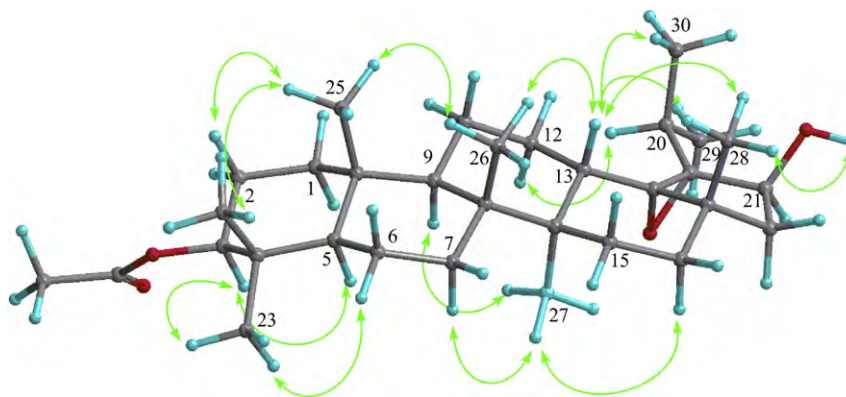


Fig. 3. Key NOESY correlations for **1**.

between Me-28 (δ_{H} 0.97) and C-16, C-17, C-18 (δ_{C} 145.6), and C-22 (δ_{C} 144.3); between H-20 (δ_{H} 3.01) and C-18, C-19 (δ_{C} 141.2), C-21 (δ_{C} 128.3), C-29, and C-30. The above data showed the presence of the conjugated double bond on the E-ring, i.e., from the C-18 to the C-22. Moreover, NOE correlations were seen between the H-13 β (δ_{H} 2.57) and H-11 β , H-15 β , Me-26, Me-28, Me-29 and Me-30. Thus, the structure of **4** was determined to be lup-18,21-dien-3 β -yl acetate.

Compound **5**, named officinatrione, isolated as colorless needles showed the molecular ion peak at m/z 454.3447 in HREIMS, which indicated the molecular formula $\text{C}_{30}\text{H}_{46}\text{O}_3$ (calcd for 454.3447). UV spectrum (λ_{max} 238.0 nm, $\log \epsilon$ 3.94) suggested the presence of enedione and IR spectrum showed the presence of conjugated ketones at 1662 and 1687 cm^{-1} as well as a six-membered ring ketone at 1705 cm^{-1} . Analysis of ^1H and ^{13}C NMR spectra using DEPT method exhibited the presence of five tertiary methyl groups, three secondary methyl groups (δ_{H} 0.97, 1.11, 1.21, each d), eight methylenes, five sp^3 -methine carbons, one sp^2 -methine (δ_{H} 5.79, d, $J=1.1$ Hz), eight quaternary carbons including three ketones (δ_{C} 205.9, 214.1, 217.7). Based on the presence of these functional groups and the unsaturated number derived from the molecular formula, compound **5** was attributed to a four cyclic triterpene. HMBC correlations (Fig. 5) were observed between H-13 (δ_{H} 3.07, dd) and C-12, C-14, C-18 (δ_{C} 214.1), C-19 (δ_{C} 166.1), and C-27 (δ_{C} 11.7); between H-20 (δ_{H} 2.46, hept) and C-18, C-19, and C-21 (δ_{C} 123.7); between H-21 (δ_{H} 5.79, d) and C-17, C-18, C-19, C-20, and C-22 (δ_{C} 205.9); between Me-28 (δ_{H} 0.97, d) and C-16, C-17, and C-22; between Me-29, C-30 (δ_{H} 1.11 and 1.21, each d) and C-19 and C-20.

Meanwhile, correlations between Me-28 and C-18; H-13 and C-17 were not seen in the HMBC spectrum. These results revealed the planar structure of **5** as a novel type of triterpene having 17,18-*seco*-lupane skeleton. Because of flexible conformation of nine-membered ring, the relative configuration of **5** was not unambiguously determined by NOESY spectrum. Fortunately, a suitable single crystal was obtained for X-ray diffraction, so the results of which established the relative configuration of the chiral center at C-17S (Fig. 6). As shown in Fig. 6, **5** was a triterpenoid having a new carbon skeletal system of 6–6–6–9 four membered ring as we predicted. The NOESY spectra were resolved, because the structure of **5** was determined for an X-ray crystallographic analysis. In the NOESY experiments, NOE correlations were observed between H-13 β and H-11 β , H-20, Me-26, Me-29, Me-30; between Me-28 and H-16, H-21, and Me-27 (δ_{H} 1.10) (Fig. 7). Therefore, the structure of **5** was unambiguously determined to be (17S)-17,18-*seco*-lup-19(21)-ene-3,18,22-trione.

Herein, we speculated that the officinatrione (**5**) could be plausibly biosynthesized from compound **4** by a series of reactions initiated with [4+2] cycloaddition of the cyclopentadiene moiety (the E-ring) of **5** and oxygen molecule to afford a peroxide intermediate **6**. The oxygen–oxygen bond would be subsequently cleaved to give enedione **7**, which was then deacetylated and oxidized to yield **5**. The methyl group at the C-28 might be orientated to the α -face as the result of thermodynamic control of keto–enol tautomerization occurring during the biosynthesis of **5** from **4** (Scheme 1).

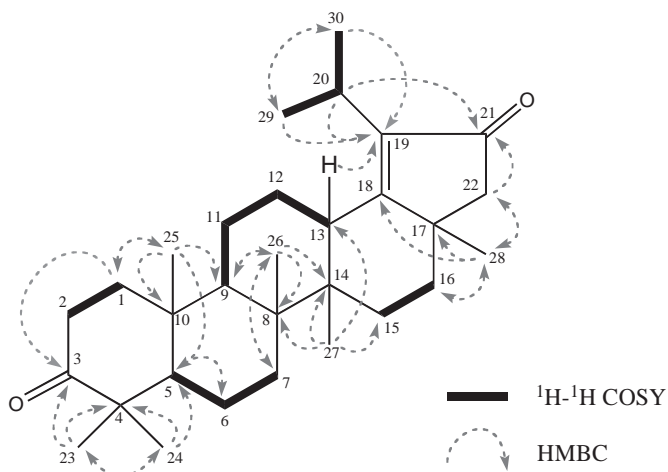


Fig. 4. Selected ^1H – ^1H COSY and HMBC correlations of **3**.

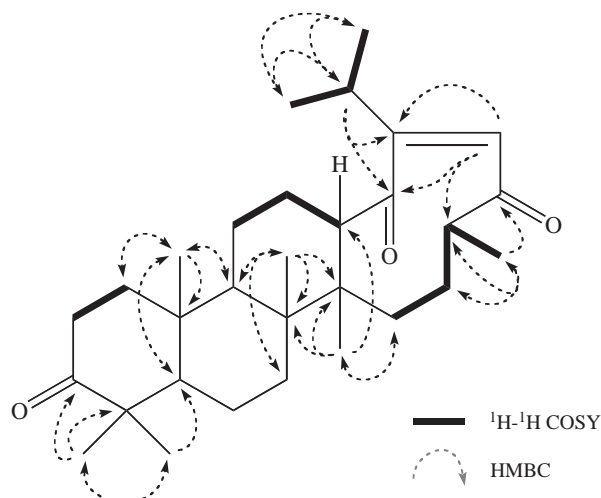
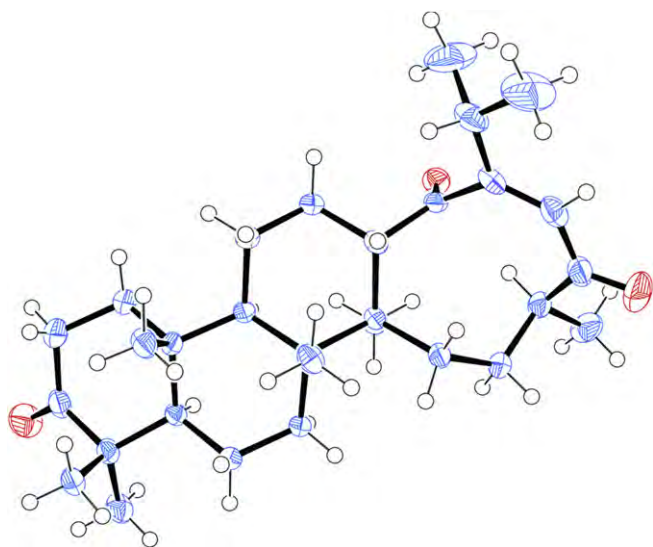
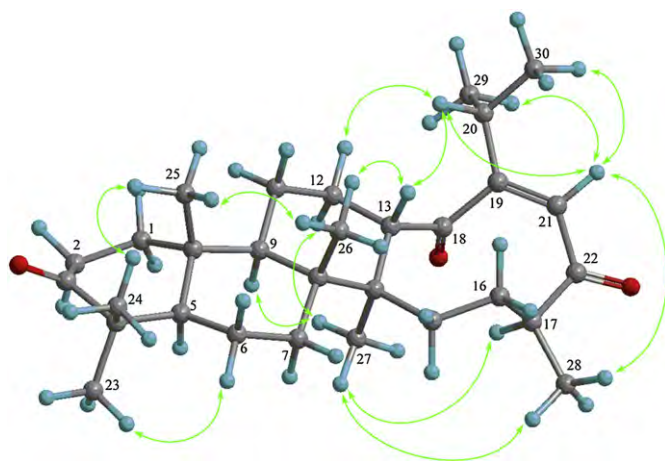


Fig. 5. Selected ^1H – ^1H COSY and HMBC correlations of **5**.

Fig. 6. ORTEP drawing of **5**.Fig. 7. Key NOESY correlations for **5**.

Searching for the possibility as anti-tumor agents, cytotoxicities of compounds **2–5** were tested against P388, L1210, HL-60, and KB cell lines. Minor product **1** could not be assayed because not enough material was available. As a result, compound **2** bearing epoxy alcohol and compound **5** having an enedione group on the *seco*-lupane skeleton exhibited moderate cytotoxicities against the cell lines, especially toward L1210 (Table 3).¹³

3. Conclusion

In conclusion, we could isolate five novel lupane-type of triterpenoids from the root of dandelion, *T. officinale*. Among them, officinatrione (**5**) would attract the interest of natural product chemists in terms of having a new skeleton of triterpene, i.e., (17*S*)-17,18-*seco*-lupane skeleton, of which the structure was confirmed by using X-ray diffraction analysis. Moreover, it was shown that compounds **2** and **5** possess moderate cytotoxic activity against L1210.

4. Experimental

4.1. General procedures

Melting points were determined on a Yanagimoto micro-melting point apparatus and are uncorrected. Optical rotations were measured with a JASCO DIP-1000 digital polarimeter. IR spectra were recorded on a Perkin–Elmer 1720X FTIR spectrophotometer. UV spectra were recorded on a Hitachi U-2000 spectrophotometer. ¹H and ¹³C NMR spectra were recorded on a Varian INOVA 500 spectrometer with standard pulse sequences, operating at 500 and 125 MHz, respectively. CDCl₃ was used as the solvent and TMS as the internal standard. EIMS was recorded on a Hitachi 4000H double-focusing mass spectrometer (70 eV). Column chromatography (silica gel, 70–230 mesh; Merck) and medium-pressure liquid chromatography (MPLC; silica gel, 230–400 mesh; Merck) were conducted. HPLC was run on a JASCO PU-1586 instrument equipped with a differential refractometer (RI 1531). Fractions obtained from column chromatography were monitored by TLC (silica gel 60 F₂₅₄; Merck). Preparative TLC was carried out on Merck silica gel F₂₅₄ plates (20×20 cm, 0.5 mm thick).

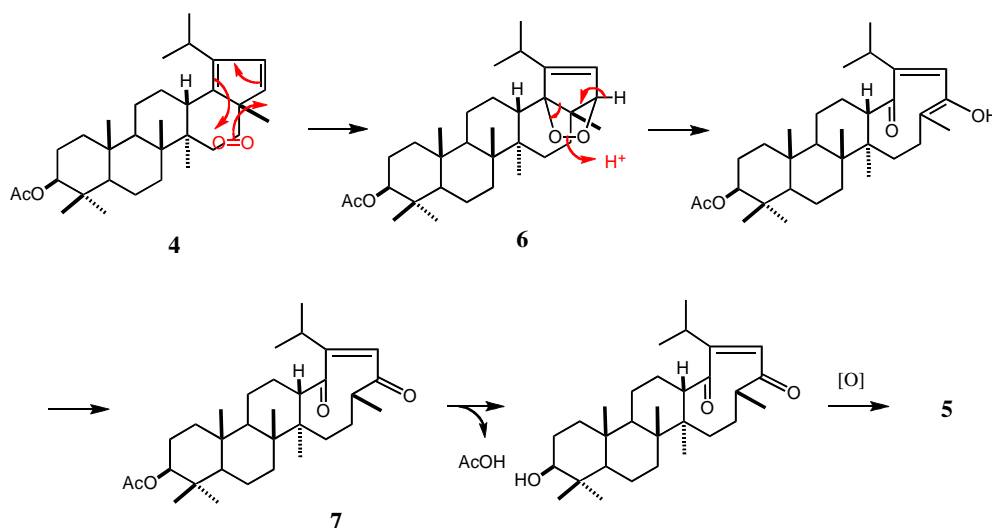
Scheme 1. Alternative biosynthetic pathway from compound **4** to **5**.

Table 2
¹H NMR and ¹³C NMR spectroscopic data of compounds **4** and **5**

Position	4		5		
	¹ H ^a (J,Hz)		¹³ C ^b	¹ H ^a (J,Hz)	¹³ C ^b
1 α	1.06 m		38.6 (t) ^b	1.50 m	39.6 (t) ^b
1 β	1.78 m			1.94 dt	13.2, 6.4
2	1.67 m		23.7 (t)	2.48 dd	8.7, 6.4
3 α	4.49 dd	11.0, 5.7	80.9 (d)		33.9 (t)
4			37.8 (s)		217.7 (s)
5 α	0.82 dd	11.2, 1.8	55.5 (d)	1.38 m	47.1 (s)
6 α	1.50 m		18.2 (t)	1.50 m	54.6 (d)
6 β	1.40 m			1.50 m	19.6 (t)
7 α	1.40 m		35.5 (t)	1.31 m	
7 β	1.50 m			1.56 m	32.3 (t)
8			41.0 (s)		42.8 (s)
9 α	1.38 m		51.3 (d)	1.48 m	50.0 (d)
10			37.2 (s)		37.1 (s)
11 α	1.57 m		21.6 (t)	1.61 m	20.7 (t)
11 β	1.31 ddd	24.5, 11.9, 3.4		1.38 m	
12 α	1.81 m		27.7 (t)	1.92 ddd	26.0, 14.5, 4.7
12 β	1.95 m			1.50 m	
13 β	2.57 dd	13.0, 3.4	40.2 (d)	3.07 dd	13.0, 3.3
14			45.8 (s)		56.2 (d)
15 α	1.06 m		27.7 (t)	1.41 m	44.2 (s)
15 β	1.79 m			1.68 m	30.6 (t)
16 α	1.04 m		32.3 (t)	1.47 m	
16 β	1.64 m			1.47 m	33.6 (t)
17 α			54.3 (s)	3.02 m	40.3 (d)
18			145.6 (s)		214.1 (s)
19			141.2 (s)		166.1 (s)
20	3.01 hept	6.6	25.7 (d)	2.46 hept	7.1
21	6.31 d	5.4	128.3 (s)	5.79 d	1.1
22	6.21 d	5.4	144.3 (s)		
23	0.85 s		27.9 (q)	1.09 s	
24	0.85 s		16.5 (q)	1.03 s	
25	0.93 s		16.7 (q)	0.92 s	
26	1.16 s		16.8 (q)	0.97 s	
27	0.72 s		15.3 (q)	1.10 s	
28	0.97 s		19.4 (q)	0.97 d	6.2
29	1.05 d	6.6	23.0 (q)	1.11 d	7.1
30	1.08 d	6.6	23.0 (q)	1.21 d	7.1
3'			171.0 (s)		21.1 (q)
3''	2.05 s		21.3 (q)		

^a Measured at 500 MHz in CDCl₃.

^b Measured at 125 MHz in CDCl₃.

4.2. Materials

The roots of *T. officinale* (Compositae) were collected in Nasahara area in Takatsuki city, Osaka, Japan in April, 2010. A voucher specimen (CG-01-1) was deposited in the Herbarium of the Laboratory of Medicinal Chemistry, Osaka University of Pharmaceutical Sciences.

4.3. Isolation of compounds 1–4

The root of *T. officinale* (10 kg) was extracted with MeOH at 60 °C for 20 days, of which the dried extract (730 g) was partitioned between Et₂O and water. The organic layer (249 g) was condensed

Table 3
 Cytotoxicity of compounds **2–5**, against the P388, HL-60, L1210, and KB cell lines

Compounds	Cell lines			
	P388 IC ₅₀ ^a (μM)	HL-60 IC ₅₀ ^a (μM)	L1210 IC ₅₀ ^a (μM)	KB IC ₅₀ ^a (μM)
2	79.0	36.8	10.5	62.9
3	>200	>200	>200	>200
4	>200	>200	>200	>200
5	51.1	94.7	10.1	79.3
5-FU ^b	2.3	2.2	2.1	7.7

^a DMSO was used for vehicle.

^b Positive control.

in vacuo and subjected to column chromatography (silica gel (7 kg); CHCl₃) affording yellow residues F1 (Fr. No. 9, 2.05 g) and F2 (Fr. No. 40–53, 1.06 g). F1 was partially subjected to HPLC (ODS, 95% acetone) to afford compounds **1** (1.4 mg) and **3** (2.8 mg). F2 was rechromatographed over silica gel containing 10% silver nitrate (2 kg; CHCl₃) giving amorphous solids (Fr. No. 198–202, 23.1 mg, residue A), (Fr. No. 203, 204, 20.6 mg, residue B) and (Fr. No. 206–208, 62.3 mg, residue C). Residues A and B were subjected to HPLC (ODS, 95% MeOH) to afford compounds **4** (5.2 mg) and **5** (4.6 mg). Residue C was subjected to medium-pressure column chromatography using *n*-hexane/AcOEt 10:1 to afford the residue (Fr. No. 74–76, 7.86 mg). The residue was further purified by HPLC (ODS, 95% MeOH) to give compound **2** (2.2 mg).

4.3.1. Compound 1. Colorless needles; mp 268–270 °C; [α]_D²³+70.5 (c 0.07, CHCl₃); HREIMS *m/z*: 500.3871 [M]⁺ (C₃₂H₅₂O₄, calcd for 500.3866); EIMS *m/z* (rel int.): 500 ([M]⁺, 95%), 485 (100), 425 (15), 402 (71), 249 (14), 221 (20), 189 (70); IR ν_{\max} (KBr, cm⁻¹): 3440 (OH), 2938, 2358, 1741 (C=O), 1446, 1382, 1245, 1028, 980, 928. ¹H and ¹³C NMR data, see Table 1.

4.3.2. Acetylation of compound 1. Compound **1** (3 mg) newly isolated from *Taraxacum venustum* (Ezotanpopo in Japanese) was acetylated by pyridine/acetic anhydride (3:1) at room temperature for 24 h to afford 1.5 mg of 3 β ,21 β -diacetoxy-18 α ,19 α -epoxylupane (**1b**). Compound **1b**. ¹H NMR (600 MHz, CDCl₃): H₂-1 (δ 1.02, 1.68),

H₂-2 (δ 1.64, 1.64), H-3 (δ 4.47, dd, $J=11.7, 5.4$ Hz), H-5 α (δ 0.81), H₂-6 (δ 1.12, 1.53), H₂-7 (δ 1.41, 1.41), H-9 α (δ 1.37), H₂-11 (δ 1.34, 1.52), H₂-12 (δ 1.43, 1.43), H-13 (δ 2.52 dd, $J=11.2, 4.3$ Hz), H₂-15 (δ 1.21, 1.79), H₂-16 (δ 1.43, 1.59), H-20 (δ 1.97, hept., $J=7.2$ Hz), H-21 α (δ 5.26, dd, $J=6.6, 3.1$ Hz), H₃-23 (δ 0.85), H₃-24 (δ 0.84), H₃-25 (δ 0.88), H₃-26 (δ 1.09), H₃-27 (δ 1.06), H₃-27 (δ 1.09), H₃-29 (δ 1.11d, $J=7.2$ Hz), H₃-30 (δ 1.06d, $J=7.2$ Hz), –OCOCH₃ (C-3, δ 2.04), –OCOCH₃ (C-21, δ 2.05). ¹³C NMR (150 MHz, CDCl₃): C-1 (δ 38.3), C-2 (δ 23.6), C-3 (δ 80.8), C-4 (δ 37.7), C-5 (δ 55.2), C-6 (δ 18.2), C-7 (δ 33.7), C-8 (δ 49.7), C-10 (δ 37.0), C-11 (δ 20.5), C-12 (δ 22.9), C-13 (δ 33.6), C-14 (δ 44.4), C-15 (δ 26.5), C-16 (δ 31.2), C-17 (δ 42.0), C-18 (δ 77.5), C-19 (δ 71.1), C-20 (δ 29.0), C-21 (δ 75.3), C-22 (δ 42.7), C-23 (δ 27.9), C-24 (δ 16.5), C-25 (δ 16.3), C-26 (δ 16.0), C-27 (δ 14.6), C-28 (δ 23.3), C-29 (δ 20.6), C-30.

4.3.3. Compound 2. Colorless needles; mp 280–281 °C; $[\alpha]_D^{23}+83.8$ (c 0.11, CHCl₃); HREIMS m/z : 456.3601 [M]⁺ (C₃₀H₄₈O₃, calcd for 456.3601); EIMS m/z (rel int.): 456 ([M]⁺, 100%), 441 (7), 358 (28), 237 (4), 205 (11), 163 (4), 121 (15); IR ν_{\max} (KBr, cm⁻¹): 3465 (OH), 2960, 1698 (C=O), 1460, 1384, 1315, 1082, 853. ¹H and ¹³C NMR data, see Table 1.

4.3.4. Compound 3. Colorless needles; mp 238–241 °C; $[\alpha]_D^{23}-53.0$ (c 0.26, CHCl₃); UV λ_{\max} at 239.5 nm (log ϵ 3.93); HREIMS m/z : 438.3494 [M-2]⁺ (C₃₀H₄₆O₂, calcd for 438.3498); EIMS m/z (rel int.): 438 ([M]⁺, 91%), 423 (13), 395 (7), 339 (12), 232 (7), 219 (100), 205 (5); IR ν_{\max} (KBr, cm⁻¹): 2937, 1697 (C=O), 1605, 1459, 1378, 1313, 1239, 1113, 975. ¹H and ¹³C NMR data, see Table 1.

4.3.5. Compound 4. Colorless needles; mp 241–244 °C; $[\alpha]_D^{23}-103.5$ (c 0.14, CHCl₃); UV λ_{\max} at 254.5 nm (log ϵ 3.50); HREIMS m/z : 466.3806 [M+H]⁺ (C₃₂H₅₀O₂, calcd for 466.3811); EIMS m/z (rel int.): 466 ([M+H]⁺, 100%), 451 (6), 423 (5), 289 (4), 249 (2), 203 (21), 189 (13), 134 (83), 122 (47); IR ν_{\max} (KBr, cm⁻¹): 2925, 2358, 1732 (C=O), 1465, 1366, 1378, 1250, 1023, 982. ¹H and ¹³C NMR data, see Table 2.

4.3.6. Officinatrione (5). Colorless powder; mp 213–215 °C; $[\alpha]_D^{23}+347.0$ (c 0.10, CHCl₃); UV λ_{\max} at 238.0 nm (log ϵ 3.94); HREIMS m/z : 454.3447 [M]⁺ (C₃₀H₄₆O₃, calcd for 454.3447); EIMS m/z (rel int.): 454 ([M]⁺, 100%), 436 (11), 426 (13), 411 (12), 369 (8), 223 (40), 205 (65); ν_{\max} (KBr, cm⁻¹): 2964, 1705, 1687, 1662, 1457, 1385, 1219, 919. ¹H and ¹³C NMR data, see Table 2.

4.3.7. Crystal data of 5. C₃₀H₄₆O₃, Mw 454.67, orthorhombic, space group: P2₁2₁2₁, $a=10.829$ (9), $b=15.093$ (12), $c=15.548$ (17), $\alpha=\beta=\gamma=90.00$, $V=2541.3$ (4), $Z=4$. Parameters used for refinement, $R_1=0.054$. The X-ray diffraction data were collected with a Bruker AXS SMART APEX CCD camera. Crystal structure was solved by a direct method using the SHELXS-97 program.¹⁴ Atomic scattering factors were taken from International Tables for X-ray Crystallography.¹⁵ Positional parameters of non-H-atoms were refined by a full-matrix least-squares method with anisotropic thermal parameters using the SHELXL-97 program.¹⁴ The structural data were deposited with the following designation: **5**: CCDC-850152. These can be obtained free of charge at www.ccdc.cam.ac.uk/conts/retrieving.html (or from The Cambridge Crystallographic Data Centre, 12 Union Road,

Cambridge CB21EZ, UK; fax: +44 1223 336 033; e-mail: deposit@ccdc.cam.ac.uk).

4.4. Cytotoxic assay against P388, HL-60, L1210, and KB cell lines

Cytotoxic activities of compounds **2–5** were examined by the 3-(4,5-dimethyl-2-thiazolyl)-2,5-diphenyl-2H-tetrazolium bromide (MTT) method. P388, HL-60, L1210, and KB cells were cultured in Eagle's Minimum Essential Medium (10% fetal calf serum) at 37 °C in 5% CO₂. The test material was dissolved in dimethyl sulfoxide (DMSO) to give a concentration of 10 mM, and the solution was diluted with the Essential Medium to give the concentrations of 200, 20 and 2 μ mol, respectively. Each solution was combined with each cell suspension (1×10^5 cells/ml) in the medium, respectively. After incubation at 37 °C for 72 h in 5% CO₂, the grown cells were labeled with 5 μ g/ml MTT in phosphate-buffered saline (PBS), and then the absorbance of formazan dissolved by 20% sodium dodecyl sulfate (SDS) in 0.1 N HCl was measured at 540 nm using a microplate reader (Model 450, BIO-RAD). Each absorbance value was expressed as a percentage, relative to the control cell suspension which was prepared without the test substance by the same procedure as described above. All assays were performed three times, semilogarithmic plots were constructed from the averaged data, and the effective dose of the substance required to inhibit cell growth by 50% (IC₅₀) was determined.

Acknowledgements

We thank Dr. Katsuhiko Minoura and Mrs. Mihoyo Fujitake (in Osaka University of Pharmaceutical Sciences) for NMR and MS measurements.

Supplementary data

Supplementary data associated with this article can be found in the online version, at <http://dx.doi.org/10.1016/j.tet.2012.12.001>.

References and notes

- Simonsen, J.; Ross, W. C. J. *The TERPENES*, Cambridge University Press: Cambridge, 1957; Vol. IV, pp 155–167.
- Power, F. B.; Browning, H. J. *J. Chem. Soc.* **1912**, 101, 2411–2429.
- Power, F. B.; Browning, H. J. *J. Chem. Soc.* **1914**, 105, 1829–1845.
- Stern, A.; Zellner, B. *Monatsh. Chem.* **1925**, 46, 459.
- Burrows, S.; Simpson, J. C. E. *J. Chem. Soc.* **1938**, 2042–2047.
- Zimmerman, J. *Helv. Chim. Acta* **1941**, 24, 393–395.
- Axel, R. T.; Evans, S.; Kelley, M. T.; Nicholas, H. J. *Phytochemistry* **1967**, 6, 511–524.
- Ageta, H.; Shiojima, K.; Masuda, K.; Lin, T. *Tetrahedron Lett.* **1981**, 22, 2289–2290.
- Kisiel, W.; Barszcz, B.; Szneler, E. *Pol. J. Chem.* **2000**, 74, 281–283.
- Shibuya, M.; Zhang, H.; Endo, A.; Shishikura, K.; Kushiro, T.; Ebizuka, Y. *Eur. J. Biochem.* **1999**, 266, 302–307.
- Shinozaki, J.; Nakane, T.; Onodera, N.; Takano, A.; Masuda, K. *Chem. Pharm. Bull.* **2011**, 59, 767–769.
- Budzikiewicz, H.; Wilson, J. M.; Djerassi, C. *J. Am. Chem. Soc.* **1963**, 85, 3688–3699.
- Miki, I.; Ishihara, N.; Otoshi, M.; Kase, H. *J. Immunol. Methods* **1993**, 164, 155–164.
- Sheldrick, G. M. *SHELXL-97*; University of Gottingen: Gottingen, 1997.
- Hahn, T., Ed. *International Tables for X-ray Crystallography*, Kluwer Academic Publishers: Dordrecht, 1992; Vol. C.

DOI: 10.1002/chem.201204423

Substituent Effect of Bis(pyridines)iodonium Complexes as Iodinating Reagents: Control of the Iodocyclization/Oxidation Process

Takashi Okitsu,^[a] Saki Yumitate,^[a] Kana Sato,^[a] Yasuko In,^[b] and Akimori Wada*^[a]

Iodonium-mediated electrophilic cyclization, namely iodocyclization, is one of the most powerful methods for the construction of functionalized cyclic compounds.^[1] This reaction creates simultaneously both a ring system and an iodo component from an acyclic substrate, and the latter can be transformed to another functionality.^[2]

For an iodinating reagent, the use of the iodonium complex of pyridine in organic synthesis was first demonstrated by Barluenga and co-workers.^[3] Bis(pyridine)iodonium(I) tetrafluoroborate (IPy₂BF₄), termed Barluenga's reagent,^[4] and its variants, such as bis(2,4,6-collidine)iodonium(I) hexafluorophosphate [I(coll)₂PF₆],^[5] are widely used (Figure 1). However, the relative reactivities of different aromatic amines have not been systematically examined yet.^[6]

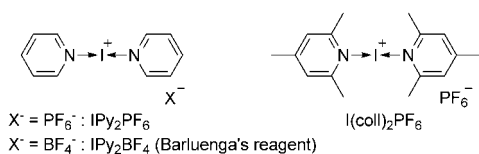
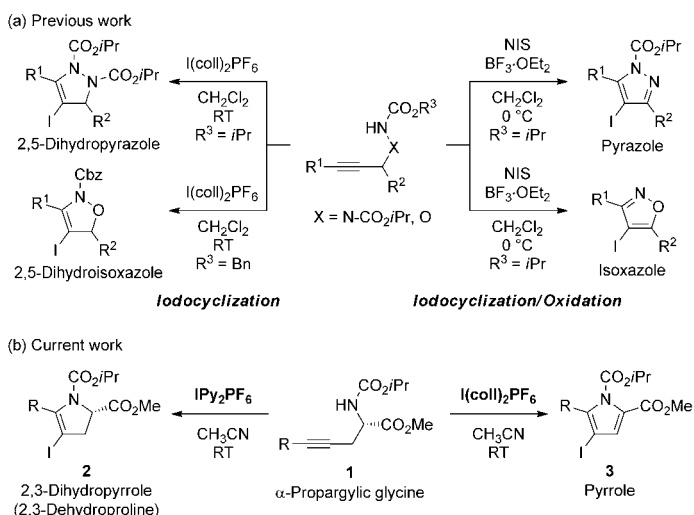


Figure 1. Structures of iodonium complexes of pyridines.

Recently, we successfully achieved a product switch through reagent-controlled iodocyclization (Scheme 1a).^[7] This strategy takes advantage of the dual nature of iodine reagents as both iodinating and oxidizing agents and enables the divergent synthesis of pyrazoles, isoxazoles, and their 2,5-dihydro products. During the course of our studies on iodocyclization of α -propargylic glycine derivatives **1**,^[8] we found that switchable access to 2,3-dihydropyrroles **2** and pyrroles **3** could be achieved by the choice of the iodonium



Scheme 1. Product switch in iodocyclization.

complexes of pyridines, IPy₂PF₆ and I(coll)₂PF₆ (Scheme 1b).^[9] This was the first report of a product switch controlled by the nature of the iodonium complexes of pyridines. Furthermore, pyrrole skeletons, such as **2** and **3**, are important components of proline-based organic catalysts,^[10] pharmaceuticals, and natural alkaloids,^[11] making divergent approaches toward functionalized proline derivatives especially attractive. Herein, our initial studies on these unique reactions are described.

The reaction conditions were screened with racemic substrate **1a** (Table 1). With common iodine reagents, pyrrole **3a** was obtained in low yields (Table 1, entries 1–2). In contrast, the use of I(coll)₂PF₆ improved the yields of **3a** (Table 1, entries 3–6) and the use of acetonitrile as a solvent gave the best result (Table 1, entry 5). To our great surprise, treatment with IPy₂PF₆, which changed the aromatic amine of the iodine reagent from 2,4,6-collidine to pyridine, gave 2,3-dihydropyrrole (2,3-dehydropyrrole) (**2a**) as the sole product (Table 1, entries 7–10). In this case, acetonitrile again performed well as the solvent (Table 1, entry 8). Of the carbamate groups used as N-protecting groups, isopropoxycarbonyl was the most suitable for both iodocyclization conditions (data not shown).

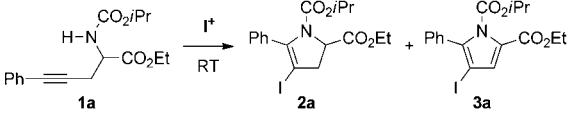
With the optimized reaction conditions established, the scope of IPy₂PF₆ mediated iodocyclization was next examined by using various optically active substrates **1b–n** (Scheme 2). With respect to the substituents on alkynes, var-

[a] Dr. T. Okitsu, S. Yumitate, K. Sato, Prof. Dr. A. Wada
Department of Organic Chemistry for Life Science
Kobe Pharmaceutical University
4-19-1, Motoyamakita-machi
Higashinada-ku, Kobe 658-8558 (Japan)
Fax: (+81) 78-441-7562
E-mail: a-wada@kobepharmaceutical-u.ac.jp

[b] Dr. Y. In
Department of Physical Chemistry
Osaka University of Pharmaceutical Sciences
4-20-1, Nasahara, Takatsuki, Osaka 569-1094 (Japan)

Supporting information for this article is available on the WWW under <http://dx.doi.org/10.1002/chem.201204423>.

Table 1. Optimization for the iodocyclization of **1a**.^[a]



Entry	Reagents (equiv)	Solvent	<i>t</i> [h]	Yield of 2a [%]	Yield of 3a [%]
1 ^[b]	NIS (3), BF ₃ ·OEt ₂ (3)	CH ₂ Cl ₂	1	0	26
2	I ₂ (3), K ₂ CO ₃ (3)	CH ₃ CN	17	0	14
3	I(coll) ₂ PF ₆ (2)	CH ₂ Cl ₂	1	0	42
4	I(coll) ₂ PF ₆ (2)	CH ₃ CN	1	0	64
5	I(coll) ₂ PF ₆ (3)	CH ₃ CN	1	0	93
6	I(coll) ₂ PF ₆ (3)	CH ₃ NO ₂	1.5	0	29
7	IPy ₂ PF ₆ (2)	CH ₃ CN	1	56	0
8	IPy ₂ PF ₆ (3)	CH ₃ CN	1	84	0
9	IPy ₂ PF ₆ (3)	CH ₃ NO ₂	0.5	67	0
10	IPy ₂ PF ₆ (3)	CH ₂ Cl ₂	1	71	0

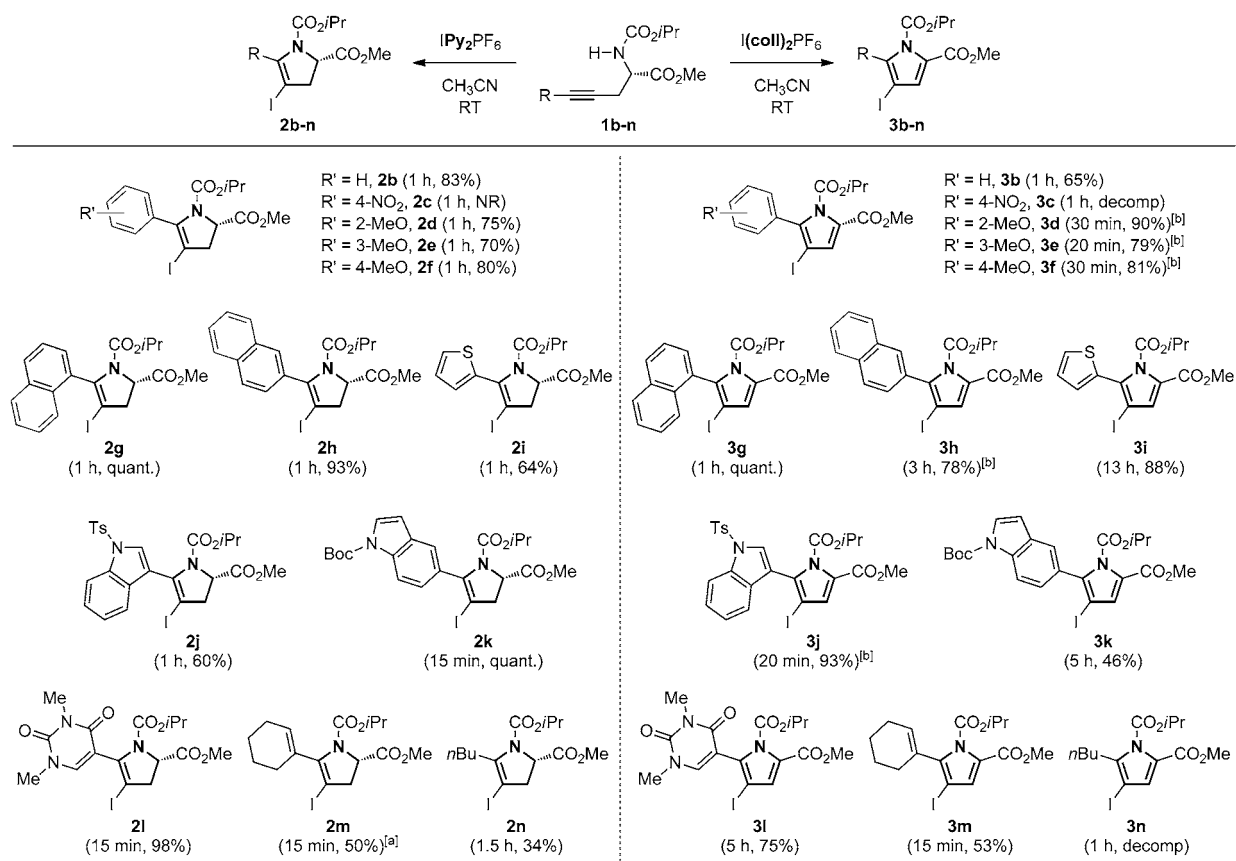
[a] Reaction was performed under argon atmosphere. Yields are given for isolated products after column chromatography. [b] Reaction was performed at 0 °C.

ious aryl and heteroaryl groups successfully gave **2d–l**, whereas the 4-nitrophenyl group **1c** was not suitable as a substrate. IPy₂PF₆ did not influence the vinylic group on the alkyne **1m** by diminishing the reagent to give **2m** in moder-

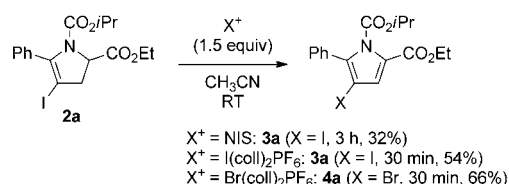
ate yield. Alkyl-substituted alkyne **1n** was also applicable to this reaction, although the yield of **2n** was low. It is noteworthy that iodocyclization of **1b** (>99.5% enantiomeric excess, *ee*) resulted in no loss of enantiomeric excess of 2,3-dehydropyrrole **2b** (>99.5% *ee*). In addition, the *N*-tosyl and *N*-Boc groups remained intact under these reaction conditions. These results imply that the reaction conditions are very mild, and that our reaction can be applied to the asymmetric synthesis of proline analogues.

The transformation of **1b–n** to pyrroles **3b–n** by I(coll)₂PF₆ also proceeded in a similar manner (Scheme 2). Thus, various substrates were applicable under these reaction conditions, whereas 4-nitrophenyl- and *n*-butyl-substituted alkynes **1c** and **1n** were gradually decomposed. Although pyrroles **3d–f**, **3h**, and **3j** were not sufficiently produced, the use of BF₃·OEt₂ as an activator of I(coll)₂PF₆ significantly improved their yields.

For a clear understanding of the reaction mechanism, 2,3-dihydropyrrole (**2a**) was treated with *N*-iodosuccinimide (NIS) or I(coll)₂PF₆ to give pyrrole **3a** in 32 and 54% yields, respectively (Scheme 3). Complex **2a** was also exposed to



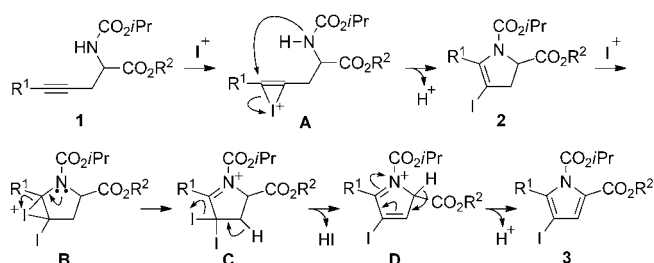
Scheme 2. Iodocyclization of **1**. Unless noted otherwise, reactions were carried out with **1** (1 equiv) and IPy₂PF₆ or I(coll)₂PF₆ (3 equiv) in CH₃CN (0.1 M) at room temperature under Ar. Yields are given for isolated products after column chromatography. [a] IPy₂PF₆ (1.1 equiv) was used. [b] The reaction included BF₃·OEt₂ (3 equiv) as an additive.



Scheme 3. Halonium-mediated oxidation of **2a**.

$\text{Br(coll)}_2\text{PF}_6$ ^[5b] to give bromopyrrole **4a** in 66% yield. Compound **4a** was individually prepared from the reaction of **1a** with $\text{Br(coll)}_2\text{PF}_6$ in 54% yield. On the other hand, **2a** was intact toward 2,4,6-collidine and silica gel. These results indicated that the pyrrole **3** was produced via electrophilic addition of halonium ion to 2,3-dihydropyrzole (**2**).

Based on the outcomes of these reactions, a plausible mechanism for the iodocyclization of **1** to give **2** and **3** was proposed (Scheme 4). The 5-*endo* cyclization of iodonium ion **A** gives 2,3-dihydropyrzole **2**. When a more reactive I^+



Scheme 4. Plausible reaction mechanism.

source, $\text{I(coll)}_2\text{PF}_6$, is employed, further iodination of the ene carbamate group of **2** might be caused to produce iodonium ion **B**. The ring opening of **B** followed by the elimination of HI from acyl iminium ion **C** would give **D**. Finally, pyrrole **3** is obtained through the deprotonation of **D**.

The structures of IPy_2PF_6 and $\text{I(coll)}_2\text{PF}_6$ were determined by single-crystal X-ray diffraction to clarify their differences in reactivity (Figures 2 and 3). The N-I-N bond patterns of both the iodonium cations are nearly linear. The iodous halogen bonds of IPy_2PF_6 show symmetry and the I-N bond length is 2.259 Å, whereas those of $\text{I(coll)}_2\text{PF}_6$ are asymmetric and the I-N bond length are 2.272 and 2.304 Å. Another difference is the dihedral angle that consisted of the least-squares planes of the two pyridine rings: IPy_2PF_6 is 1.2 and $\text{I(coll)}_2\text{PF}_6$ is 18.5°. Brayer and James analyzed the X-ray structure of $\text{I(coll)}_2\text{ClO}_4$ and their result almost agreed with bis(2,4,6-collidine)iodonium cation of $\text{I(coll)}_2\text{PF}_6$.^[12] They mentioned that the significant twisted conformation would be caused by the steric hindrance between the methyl groups at the 2,6-position of the pyridine ring and the iodine atom. Due to its asymmetric, longer I-N bond length and twisted conformation, $\text{I(coll)}_2\text{PF}_6$ is a more highly reactive I^+ source than IPy_2PF_6 .

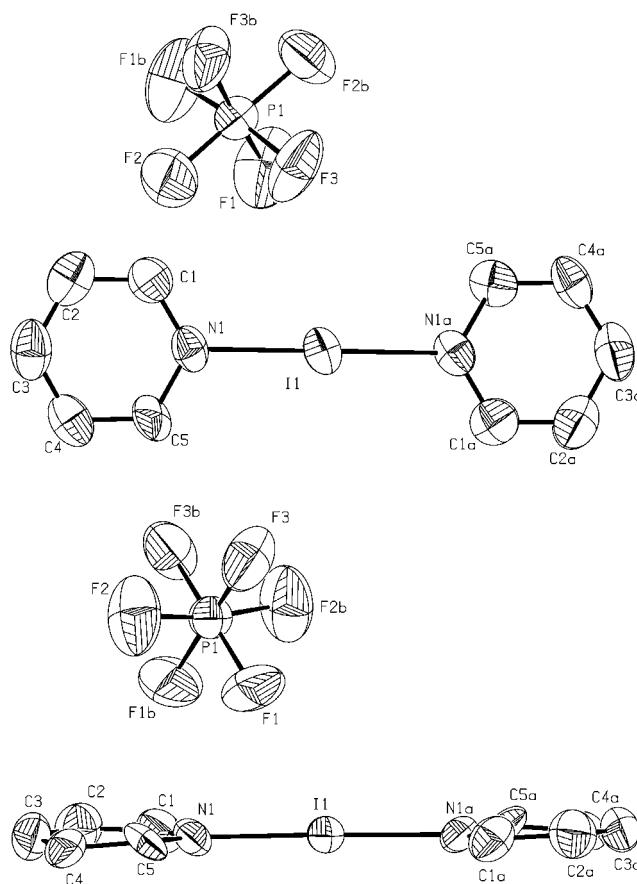
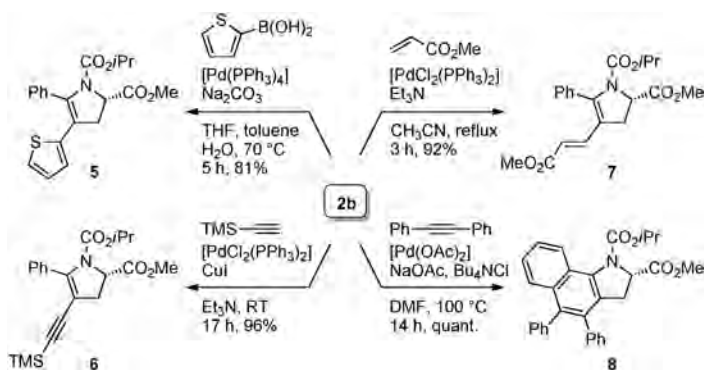


Figure 2. ORTEP representation of IPy_2PF_6 ; thermal ellipsoids are set at 50% probability. Hydrogen atoms are omitted for clarity. Selected bond lengths [Å] and angles [°]: I1-N1 2.259, I1-N1a 2.259; N1-I1-N1a 179.0.

The iodo component produced by iodocyclization can be further transformed by Pd-catalyzed cross-coupling reactions. Because of the importance of generating a library of proline scaffolds, 2,3-dehydropyrzole (**2b**) was preliminarily elaborated with Suzuki-Miyaura cross-coupling,^[13] Sonogashira cross-coupling,^[14] Heck reaction,^[15] and Larock carbocyclization^[16] to get a variety of C-C bond formations in high yields (Scheme 5). Thus, our methodology could provide access to a wide variety of 2,3-dehydropyrzole derivatives.



Scheme 5. Transformations of **2b**.

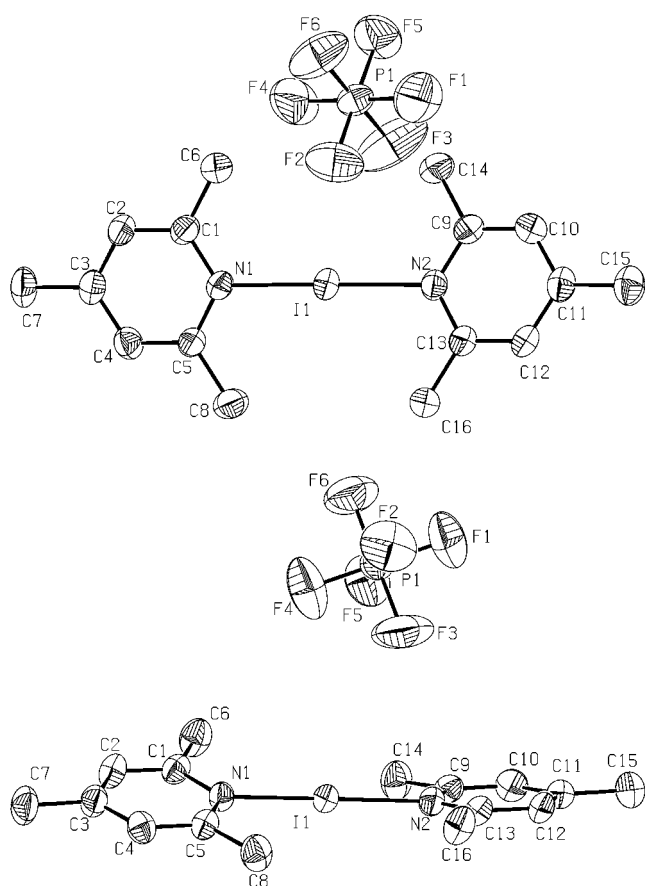


Figure 3. ORTEP representation of $I(coll)_2PF_6$; thermal ellipsoids are set at 50% probability. Hydrogen atoms are omitted for clarity. Selected bond lengths [Å] and angles [°]: I1–N1 2.272, I1–N2 2.304; N1–I1–N2 178.9.

In conclusion, a switchable access to 2,3-dihydropyrroles (2,3-dehydroprolines) and pyrroles from common α -proparglycines has been investigated. Our studies revealed that the iodocyclization/oxidation sequence was controllable by the slight differences in the iodonium complexes of pyridines. This information would be valuable for tuning the electrophilicity of iodonium complexes. In addition, our flexible synthetic strategy may assist the development of proline-based organic catalysts and provide a powerful tool for drug discovery. Investigation of new iodonium complexes of pyridines and the scope of substrates is ongoing.

Experimental Section

Synthesis of IPy_2PF_6 : Based on a literature procedure for the preparation of $I(coll)_2PF_6$ ^[5b] to a solution of $AgNO_3$ (50.96 g, 0.300 mol) and KPF_6 (55.77 g, 0.303 mol) in distilled water (510 mL), pyridine (68.9 mL, 0.852 mol) was added over 15 min while stirring at RT. A slightly exothermic reaction was observed, corresponding to the formation of a white solid. After the mixture was stirred for 75 min at RT, the solid was suction filtered, and the residue was washed with distilled water (600 mL). The residue was repeatedly dried by filter paper and was further dried in the dark in a desiccator under high vacuum over P_2O_5 for

one week to give bis(pyridine)silver(I) hexafluorophosphate ($AgPy_2PF_6$, 120.8 g, 98%) as a colorless solid. M.p. 182.5–185°C; 1H NMR (300 MHz, CD_3CN): δ = 8.57–8.55 (br m, 4H), 7.91 (br s, 2H), 7.50 ppm (br s, 4H); ^{13}C NMR (75 MHz, $CDCl_3$): δ = 151.9, 126.0, 116.5 ppm; elemental analysis calcd (%) for $C_{10}H_{10}AgF_6N_2P$: C 29.22; H 2.45; N 6.82; found: C 29.14; H 2.48; N 6.83.

To a mixture of $AgPy_2PF_6$ (11.6 g, 28.3 mmol) in dry CH_2Cl_2 (87 mL), iodine (7.11 g, 28.0 mmol) was added at RT over 5 min. The vessel was filled with argon and stirred at RT in the dark for 1 h. The mixture was filtered, washed with dry CH_2Cl_2 , and the filtrate was evaporated to give IPy_2PF_6 (11.5 g, 95%) as a colorless solid. M.p. 152–153°C; 1H NMR (300 MHz, CD_3CN): δ = 8.77 (d, J = 5.1 Hz, 4H), 8.25 (t, J = 7.8 Hz, 2H), 7.65–7.60 ppm (m, 4H); ^{13}C NMR (75 MHz, CD_3CN): δ = 150.7, 143.3, 128.9 ppm; elemental analysis calcd (%) for $C_{10}H_{10}F_6IN_2P$: C 27.93; H 2.34; N 6.51; found: C 27.89; H 2.33; N 6.46.

General procedure for iodocyclization: To a solution of **1** (1 equiv) in dry CH_3CN (0.1 M), IPy_2PF_6 or $I(coll)_2PF_6$ (3 equiv) was added, and the reaction mixture was stirred at RT for 1 h under argon. The reaction mixture was quenched with a saturated aqueous solution of $Na_2S_2O_3$ and was extracted with AcOEt. The organic layer was dried over Na_2SO_4 , filtered, and evaporated in vacuo. The residue was purified by flash-column chromatography on silica gel by using hexane/AcOEt (5:1 to 2:1) as an eluent to give **2** or **3**.

CCDC-907268 (IPy_2PF_6) and CCDC-907267 ($I(coll)_2PF_6$) contain the supplementary crystallographic data for this paper. These data can be obtained free of charge from The Cambridge Crystallographic Data Centre via www.ccdc.cam.ac.uk/data_request/cif.

Acknowledgements

This work was supported by a Grant-in-Aid for Young Scientists (B) from MEXT. T.O. also acknowledges support from the Society of Iodine Science.

Keywords: cyclization • iodine • oxidation • substituent effects • synthetic methods

- [1] For reviews, see: a) A. N. French, S. Bissmire, T. Wirth, *Chem. Soc. Rev.* **2004**, *33*, 354–362; b) R. C. Larock, *Acetylene Chem.* **2005**, 51–99; c) H. Togo, S. Iida, *Synlett* **2006**, 2159–2175; d) M. J. Mphahlele, *Molecules* **2009**, *14*, 4814–4837.
- [2] For selected papers on the iodocyclizations of alkynes, see: a) D. Fischer, H. Tomeba, N. K. Pahadi, N. T. Patil, Y. Yamamoto, *Angew. Chem.* **2007**, *119*, 4848–4850; *Angew. Chem. Int. Ed.* **2007**, *46*, 4764–4766; b) S. A. Worlikar, T. Kesharwani, T. Yao, R. C. Larock, *J. Org. Chem.* **2007**, *72*, 1347–1353; c) R. H. Halim, P. J. Scammells, B. L. Flynn, *Org. Lett.* **2008**, *10*, 1967–1970; d) J. Barluenga, D. Palomas, E. Rubio, J. M. González, *Org. Lett.* **2007**, *9*, 2823–2826; e) D. R. Garud, M. Koketsu, *Org. Lett.* **2008**, *10*, 3319–3322; f) H.-P. Bi, L.-N. Guo, X.-H. Duan, F.-R. Gou, S.-H. Huang, X.-Y. Liu, Y.-M. Liang, *Org. Lett.* **2007**, *9*, 397–400; g) D. Yue, T. Yao, R. C. Larock, *J. Org. Chem.* **2005**, *70*, 10292–10296; h) D. Yue, T. Yao, R. C. Larock, *J. Org. Chem.* **2006**, *71*, 62–69; i) T. Yao, R. C. Larock, *J. Org. Chem.* **2005**, *70*, 1432–1437; j) T. Yao, M. A. Campo, R. C. Larock, *J. Org. Chem.* **2005**, *70*, 3511–3517; k) Z. A. Khan, T. Wirth, *Org. Lett.* **2009**, *11*, 229–231; l) X. Zhang, R. C. Larock, *J. Am. Chem. Soc.* **2005**, *127*, 12230–12231; m) S. Mehta, J. P. Waldo, R. C. Larock, *J. Org. Chem.* **2009**, *74*, 1141–1147; n) A. Arcadi, S. Cacchi, S. D. Giuseppe, G. Fabrizi, F. Marinelli, *Org. Lett.* **2004**, *6*, 2409–2412; o) K. O. Hessian, B. L. Flynn, *Org. Lett.* **2003**, *5*, 4377–4380; p) A.-Y. Peng, Y.-X. Ding, *Org. Lett.* **2004**, *6*, 1119–1121; q) A. Sniady, K. A. Wheeler, R. Dembinski, *Org. Lett.* **2005**, *7*,

- 1769–1772; r) Y. Liu, F. Song, L. Cong, *J. Org. Chem.* **2005**, *70*, 6999–7002.
- [3] J. Barluenga, J. M. González, P. J. Campos, G. Asensio, *Angew. Chem.* **1985**, *97*, 341–342; *Angew. Chem. Int. Ed. Engl.* **1985**, *24*, 319–320.
- [4] a) J. Barluenga, M. A. Rodríguez, P. J. Campos, *J. Org. Chem.* **1990**, *55*, 3104–3106; b) J. Barluenga, P. J. Campos, J. M. González, J. L. Suárez, *J. Org. Chem.* **1991**, *56*, 2234–2237; c) J. Barluenga, M. Trincado, E. Rubio, J. M. González, *Angew. Chem.* **2003**, *115*, 2508–2511; *Angew. Chem. Int. Ed.* **2003**, *42*, 2406–2409; d) J. Barluenga, H. Vázquez-Villa, A. Ballesteros, J. M. González, *J. Am. Chem. Soc.* **2003**, *125*, 9028–9029; e) J. Barluenga, M. Trincado, E. Rubio, J. M. González, *J. Am. Chem. Soc.* **2004**, *126*, 3416–3417; f) J. Barluenga, F. González-Bobes, M. C. Murguía, S. R. Ananthoju, J. M. González, *Chem. Eur. J.* **2004**, *10*, 4206–4213; g) J. Barluenga, M. Trincado, M. Marco-Arias, A. Ballesteros, E. Rubio, J. M. González, *Chem. Commun.* **2005**, 2008–2010; h) J. Barluenga, M. Trincado, E. Rubio, J. M. González, *Angew. Chem.* **2006**, *118*, 3212–3215; *Angew. Chem. Int. Ed.* **2006**, *45*, 3140–3143; i) J. Barluenga, H. Vázquez-Villa, I. Merino, A. Ballesteros, J. M. González, *Chem. Eur. J.* **2006**, *12*, 5790–5805; j) J. Barluenga, E. Campos-Gómez, A. Minatti, D. Rodríguez, J. M. González, *Chem. Eur. J.* **2009**, *15*, 8946–8950; k) B. Crone, S. F. Kirsch, K.-D. Umland, *Angew. Chem.* **2010**, *122*, 4765–4768; *Angew. Chem. Int. Ed.* **2010**, *49*, 4661–4664.
- [5] a) H. Fujioka, H. Kitagawa, Y. Nagatomi, Y. Kita, *J. Org. Chem.* **1996**, *61*, 7309–7315; b) F. Homsí, S. Robin, G. Rousseau, *Org. Synth.* **2000**, *77*, 206–211; c) T. Okitsu, D. Nakazawa, R. Taniguchi, A. Wada, *Org. Lett.* **2008**, *10*, 4967–4970; d) T. Okitsu, D. Nakazawa, A. Kobayashi, M. Mizohata, Y. In, T. Ishida, A. Wada, *Synlett* **2010**, 203–206.
- [6] Only one report about the iodo-lactonization toward medium membered lactones is known: B. Simonot, G. Rousseau, *J. Org. Chem.* **1994**, *59*, 5912–5919.
- [7] a) T. Okitsu, K. Sato, A. Wada, *Org. Lett.* **2010**, *12*, 3506–3509; b) T. Okitsu, K. Sato, T. M. Potewar, A. Wada, *J. Org. Chem.* **2011**, *76*, 3438–3449.
- [8] Knight and co-workers reported an elegant approach for synthesis of 2,3-dehydropyrrolines (2,3-dihydropyrroles) by iodocyclization of racemic *N*-tosyl- α -propargylic glycine derivatives, see: a) D. W. Knight, A. L. Redfern, J. Gilmore, *Chem. Commun.* **1998**, 2207–2208; b) D. W. Knight, A. L. Redfern, J. Gilmore, *J. Chem. Soc. Perkin Trans. 1* **2001**, 2874–2883; c) D. W. Knight, H. C. Rost, C. M. Sharland, J. Singkhonrat, *Tetrahedron Lett.* **2007**, *48*, 7906–7910.
- [9] Yoshida and co-workers reported a synthesis of substituted 3-iodopyrroles by cycloisomerization of propargylic aziridines with iodine, see: M. Yoshida, S. Easmin, M. Al-Amin, Y. Hirai, K. Shishido, *Tetrahedron* **2011**, *67*, 3194–3200.
- [10] For reviews, see: a) B. List, *Tetrahedron* **2002**, *58*, 5573–5590; b) W. Notz, F. Tanaka, C. F. Barbas III, *Acc. Chem. Res.* **2004**, *37*, 580–591; c) H. Pellissier, *Tetrahedron* **2007**, *63*, 9267–9331; d) M. Bhanushali, C.-G. Zhao, *Synthesis* **2011**, 1815–1830.
- [11] a) M. I. Calaza, C. Cativiela, *Eur. J. Org. Chem.* **2008**, 3427–3448; b) C. Nájera, J. M. Sansano, *Angew. Chem.* **2005**, *117*, 6428–6432; *Angew. Chem. Int. Ed.* **2005**, *44*, 6272–6276.
- [12] G. D. Brayer, M. N. G. James, *Acta Crystallogr.* **1982**, *B38*, 654–657.
- [13] N. Miyaura, A. Suzuki, *Chem. Rev.* **1995**, *95*, 2457–2483.
- [14] K. Sonogashira, *J. Organomet. Chem.* **2002**, *653*, 46–49.
- [15] R. F. Heck, *Org. React.* **1982**, *27*, 345–390.
- [16] R. C. Larock, M. J. Doty, Q. Tian, J. M. Zenner, *J. Org. Chem.* **1997**, *62*, 7536–7537.

Received: December 12, 2012

Revised: January 28, 2013

Published online: March 1, 2013

A conserved motif within the flexible C-terminus of the translational regulator 4E-BP is required for tight binding to the mRNA cap-binding protein eIF4E

Keum Soon PAKU, Yu UMENAGA, Tsunego USUI, Ai FUKUYO, Atsuo MIZUNO, Yasuko IN, Toshimasa ISHIDA and Koji TOMOO¹

Department of Physical Chemistry, Osaka University of Pharmaceutical Sciences, 4-20-1 Nasahara, Takatsuki, Osaka 569-1094, Japan

Although the central α -helical $Y(X)_4L\Phi$ motif (X, variable amino acid; Φ , hydrophobic amino acid) of the translational regulator 4E-BP [eIF (eukaryotic initiation factor) 4E-binding protein] is the core binding region for the mRNA cap-binding protein eIF4E, the functions of its N- and C-terminal flexible regions for interaction with eIF4E remain to be elucidated. To identify the role for the C-terminal region in such an interaction, the binding features of full-length and sequential C-terminal deletion mutants of 4E-BPn ($n=1-3$) subtypes were investigated by SPR (surface plasmon resonance) analysis and ITC (isothermal titration calorimetry). Consequently, the conserved PGVTS/T motif within the C-terminal region was shown to act as the second binding region and to play an important role in the tight binding to eIF4E. The 4E-BP subtypes increased the association constant with eIF4E by approximately 1000-fold in the presence of this conserved region compared with that in the absence of this region. The sequential deletion of this conserved region in 4E-

BP1 showed that deletion of Val⁸¹ leads to a considerable decrease in the binding ability of 4E-BP. Molecular dynamics simulation suggested that the conserved PGVTS/T region functions as a kind of paste, adhering the root of both the eIF4E N-terminal and 4E-BP C-terminal flexible regions through a hydrophobic interaction, where valine is located at the crossing position of both flexible regions. It is concluded that the conserved PGVTS/T motif within the flexible C-terminus of 4E-BP plays an auxiliary, but indispensable, role in strengthening the binding of eIF4E to the core $Y(X)_4L\Phi$ motif.

Key words: eukaryotic initiation factor 4E-binding protein (4E-BP), eukaryotic initiation factor 4E (eIF4E), interaction, isothermal titration calorimetry, molecular dynamics simulation, surface plasmon resonance.

INTRODUCTION

The control of mRNA translation at the level of initiation is critical for gene expression in mammalian cells [1]. Eukaryotic initiation is performed by many eIFs (eukaryotic initiation factors) and regulated through changes in the phosphorylation states of eIFs and endogenous regulator proteins [2]. One of the main regulatory steps in translation initiation involves the formation of the eIF4F complex, which is a supramolecular complex of three subunits, i.e. eIF4E, eIF4A and eIF4G, and is required to recruit ribosomal subunits to mRNA during cap-dependent initiation [3]. In the first initiation step in cap-dependent translation, the m⁷G (*N*⁷-methylguanine) cap structure covalently attached to the 5' terminus of mRNA must be selectively recognized by eIF4E. Thus eIF4E serves as a master switch that controls eukaryotic translation, and its function in initiation is regulated by the association/dissociation of endogenous 4E-BP (eIF4E-binding protein) [2,4,5].

4E-BP regulates the function of eIF4E via competitive binding with eIF4G to a common region of eIF4E [6–8] and thus plays a critical role in the proper control of protein biosynthesis. Three subtypes of 4E-BP (4E-BP1–4E-BP3) are known [2,4] and they bind to eIF4E through a common $Y(X)_4L\Phi$ motif (X, variable amino acid; Φ , hydrophobic amino acid; see Figure 1) [7,8]. The hyperphosphorylation of threonine and serine residues in response to growth factors and mitogens results in the release of 4E-BP from eIF4E [5,9]. 4E-BP itself has no secondary structure, but its $Y(X)_4L\Phi$ motif region forms a helical structure when bound to

the conserved surface on the dorsal side of the eIF4E cap-binding pocket (Figure 2) [10,11].

We previously identified the 4E-BP-binding pocket of eIF4E in the mRNA cap-bound state using X-ray crystal structure analysis of the m⁷GpppA–eIF4E–4E-BP peptide (Thr³⁶–Thr⁷⁰ fragment of human 4E-BP1) ternary complex [11]. However, the structural scaffold for the regulatory function of eIF4E by 4E-BP remains to be elucidated at the atomic level, because the N- and C-terminal sequences of 4E-BP are both structurally flexible and thus could not be observed in the crystal structure. The importance of such conformational flexibility for the proper functioning of proteins has received much attention [12–15]. For example, the N-terminal region of eIF4E actively participates in the conformational coupling between eIF4E and eIF4G, thus enhancing ribosome loading on to the mRNA cap, although its structure is flexible and scarcely contributes to the ternary structural formation of eIF4E [12]. Therefore we have been investigating the function of the N- and C-terminal flexible regions of 4E-BP in their interaction with eIF4E; the N- and C-terminal regions are regions upstream and downstream of the central $Y(X)_4L\Phi$ motif respectively (see Figure 1).

Previously we determined the kinetic parameters of the interaction of 4E-BP2 with m⁷GTP-bound eIF4E by SPR (surface plasmon resonance) analysis using sequential N- and/or C-terminal deletion mutants. As a result, the flexible N-terminal 1–45 amino acids scarcely participated in the interaction with eIF4E [16]. In contrast, the C-terminal His⁷⁴–Glu⁸⁹ sequence of 4E-BP2 showed a marked contribution to the binding of eIF4E.

Abbreviations used: 4E-BP, eIF4E-binding protein; eIF, eukaryotic initiation factor; GST, glutathione transferase; ITC, isothermal titration calorimetry; MD, molecular dynamics; m⁷G, *N*⁷-methylguanine; SPR, surface plasmon resonance.

¹ To whom correspondence should be addressed (e-mail tomoo@gly.oups.ac.jp).

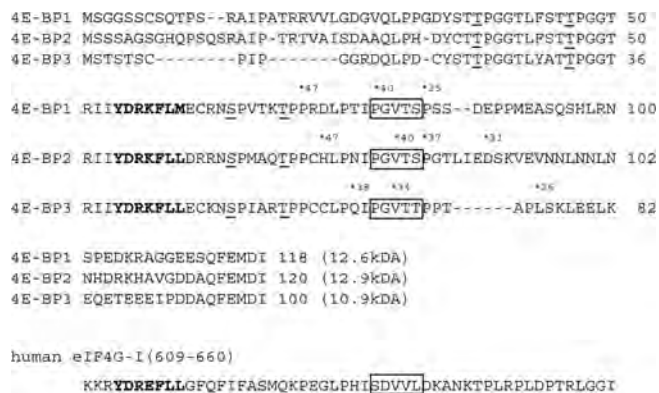


Figure 1 Amino acid sequences of 4E-BP1–4E-BP3 subtypes

The sequences of 4E-BPs are aligned on the basis of their functional similarities. The eIF4E-binding sequence [Y(X)₄LΦ] is shown in bold. The Pro⁷⁹–Ser⁸³ of 4E-BP2 and the corresponding sequences of 4E-BP1 and 4E-BP3 are boxed. The phosphorylation residues are underlined. The asterisk and number above the sequence represent the deletion point and number from the C-terminal end respectively. The sequence from amino acid 609 to 660 of human eIF4G-I is shown for comparison.

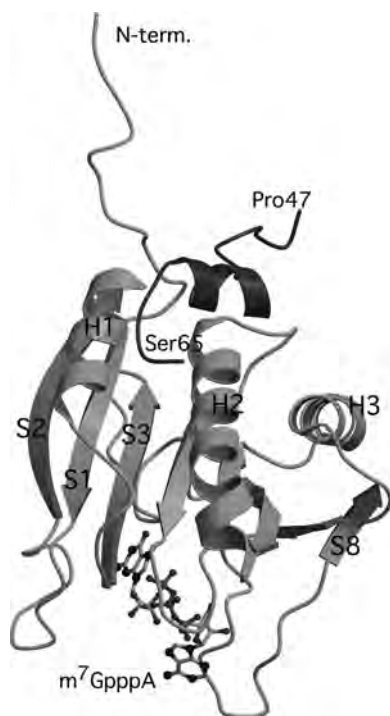


Figure 2 Overall structure of the m⁷GpppA–eIF4E–4E-BP1 peptide (Pro⁴⁷–Ser⁶⁵) ternary complex [11]

The eIF4E and the 4E-BP1 peptide are shown using the ribbon model, and m⁷GpppA is depicted using the stick-bond model. H1–H3, S1–S3 and S8 represent the number of α-helices (H) and β-strands (S) of eIF4E respectively.

As this second eIF4E-binding region of 4E-BP2 appears to be important for understanding the functional regulation of eIF4E by 4E-BP, in the present study, we analysed in detail the C-terminal sequences of 4E-BP1–4E-BP3 subtypes to clarify the critical residues and their structural function in the interaction with eIF4E using full-length and sequential C-terminal deletion mutants. Clarification of the role of the 4E-BP flexible region in the interaction with eIF4E would help us to understand the

functional difference between 4E-BP and eIF4G via binding to the common region of eIF4E.

EXPERIMENTAL

Preparation of full-length 4E-BP1–4E-BP3 and their N- or C-terminal deletion mutants

Gene expression in *Escherichia coli* and the isolation of the N-terminal GST (glutathione transferase)-fused human full-length 4E-BP1–4E-BP3 and their purification by glutathione–Sepharose 4B affinity and anion-exchange chromatography were performed as reported previously [17,18]. For sample preparation 50 mM Tris/HCl (pH 8.0) supplemented with 1 mM EDTA and 100 mM NaCl was used as the buffer. GST was removed using a PreScission Protease kit (Amersham Biosciences), and the resulting GST-free 4E-BP was separated by gel chromatography.

The gene encoding the sequential N- or C-terminal deletion of 4E-BP (abbreviated as Ndx- or Cddy-4E-BP respectively) was constructed by TA cloning. Each gene was amplified by PCR using a primer designed to produce each deleted gene and rTaq polymerase. After purification, the gene was inserted into the pGEM T-Easy vector and transformed in the DHα strain. After purifying the plasmid, the respective deleted genes were excised using restriction enzymes; these genes were verified by forward and reverse dideoxy sequencing. Transformation into the pET23b vector, gene expression in the BL21(DE3) strain and purification of the expressed protein was then performed in the same manner as that for full-length 4E-BP. The N- and C-terminal-deleted mutants of 4E-BP were also prepared using the same method.

Preparation of m⁷GTP-free or m⁷GTP-bound full-length or N-terminal-residue-deleted eIF4Es

The gene construction, expression and purification of full-length or N-terminal-residue-deleted eIF4E in *E. coli* was performed as described previously [19]. A supernatant containing the recombinant protein was applied to the m⁷GTP–Sepharose 4B affinity column equilibrated with 20 mM Hepes/KOH (pH 7.5) buffer containing 1 mM DTT (dithiothreitol), 0.1 mM EDTA and 100 mM KCl. m⁷GTP-free or m⁷GTP-bound full-length or N-terminal-residue-deleted eIF4Es were prepared by elution with the same buffer supplemented with 1 M KCl and 100 μM m⁷GTP, respectively; m⁷GTP-free eIF4E was further purified by gel filtration. The eluate was concentrated using Centricon 10 filters (Amicon) to the desired concentration, which was determined using the Bradford method [19a]. The purity of the sample was confirmed on the basis of a single band detected by SDS/PAGE.

SPR analysis

A binding assay was performed using BIAcore X as described in our previous study [16]. The ligand, full-length 4E-BP or its deletion mutant was immobilized on a CM5 sensor chip using the amine-coupling method, according to the manufacturer's protocol; that is, 10 μg/ml protein was reacted with the sensor chip in 10 mM sodium acetate buffer (pH 4.5) and the concentration of the immobilized protein was adjusted to approximately 150 RU (resonance units) within the range recommended for the accurate measurement of the kinetic parameters [20]. As the analyte, m⁷GTP-free or m⁷GTP-bound full-length eIF4E or its N-terminal deletion mutant was then injected as a function of concentration. Each cycle consisted of the injection of the indicated amount (15–25 μl) of eIF4E into the BIAcore running buffer [10 mM

Hepes/NaOH (pH 7.4), 150 mM NaCl, 3 mM EDTA and 0.05 % surfactant P20]. The chip was regenerated after each cycle by washing three times with 10–20 μ l of 2 M NaCl and five times with 15 μ l of running buffer. The measurement was performed at a flow rate of 5 μ l/min at 25 °C. The response from the non-immobilized chip measured as a reference was subtracted from the sample response to obtain the sensorgram for a specific interaction and then the sensorgram obtained was evaluated using the BIAevaluation software package. The respective values were checked for consistency using local fitting for each analyte concentration. The kinetic parameters of the association rate k_a , the dissociation rate k_d and the equilibrium dissociation constant K_d ($= k_d/k_a$) were estimated by the Langmuir (1:1) binding model for the k_a/k_d -dependent bow-shaped SPR profile and by the steady affinity (Scatchard) model (only K_d) for the trapezoidal SPR profile. The respective model fittings yielded reasonable χ^2 values (<10) and distributions of residual plots.

ITC (isothermal titration calorimetry)

ITC was performed to obtain the thermodynamic parameters of the interaction using the VP-ITC titration calorimetric system (Microcal). The 5 μ M eIF4E solution in the calorimetric cell was titrated with 50 μ M 4E-BP solution dissolved in the same buffer [20 mM $\text{NaH}_2\text{PO}_4/\text{NaOH}$ (pH 7.4) and 100 mM NaCl] in the titration cell. Before the measurement, both samples were properly degassed and carefully loaded into their respective cells to avoid bubble formation during stirring, and the heat due to the interaction of both molecules was measured as the difference between the heat of reaction and the corresponding heat of dilution. ITC measurement was performed on the m⁷GTP-free and m⁷GTP-bound eIF4Es to investigate the effect of the mRNA cap structure on the interaction, and the thermodynamic parameters were estimated using a one-site or two-site model.

MD (molecular dynamics) simulation

To estimate a possible binding region of the C-terminal sequence of 4E-BP2 on the molecular surface of eIF4E, we previously performed an MD calculation of the eIF4E–4E-BP2 fragment (Pro⁴⁷–Asp⁹⁰) complex for 3 ns [16]. Consequently, the stable binding of the Cys⁷³–Glu⁸⁹ sequence of 4EBP2 at the root (Ile³⁵–Pro³⁸) of the N-terminal flexible region of eIF4E through relatively weak hydrophobic interactions was suggested. To confirm the extent of the stability of this hydrophobic interaction in the dynamic state, in the present study, the MD simulation of this complex was performed for 10 ns, assuming a neutral state in an aqueous solution. The atomic co-ordinates for MD simulation were constructed from the X-ray crystal structure of the m⁷GpppA–eIF4E–4E-BP1 fragment ternary complex [11] (PDB code 1WKW) and by referring to the NMR data published by Gross et al. [12] (PDB code 1RF8). Each solute (i.e. eIF4E, 4E-BP2 fragment peptide and chloride ions) was placed in a rectangular box [89 \times 58 \times 70 \AA^3 (1 \AA = 0.1 nm)] filled with TIP3P water molecules [21]. An AMBER all-atom-force-field parameter [22] was used for these solutes. The MD simulation was performed using the AMBER 7 program (<http://ambermd.org/>), with the parameters the same as those used in our previous study [11].

RESULTS

SPR analysis

Previous SPR analysis showed the notable contribution of the C-terminal side, but not the N-terminal side, of 4E-BP2 to the binding to eIF4E, in addition to the Y(X)₄L Φ -binding sequence (first binding region) of the central region [16], suggesting the second eIF4E-binding site in the C-terminal region of 4E-BP. As the regulatory mechanism of eIF4E by 4E-BP has not yet been fully elucidated, a detailed structural and functional analysis of this second region is very important. In the present study, we performed SPR analysis of 4E-BP1–4E-BP3 subtypes to determine the critical residue or sequence of the second binding region for the interaction with eIF4E and to clarify its structural function.

The k_a , k_d and K_d values of a series of C-terminal deletion mutants of 4E-BP1–4E-BP3 are given in Table 1. The SPR profiles of m⁷GTP-bound eIF4E–4E-BP1 complexes are shown in Figure 3. The sensorgram for the interaction with eIF4E showed a considerable difference depending on the C-terminal deletion length of 4E-BP1. Such differences were also observed for 4E-BP2 and 4E-BP3.

4E-BP1–4E-BP3 subtypes have a common eIF4E-binding site in the C-terminal region

It was reconfirmed that the N-terminal flexible 1–45 amino acid region of 4E-BP2 has no notable contribution to the interaction with eIF4E. The k_a (10^5) and k_d (10^{-3}) values were of similar orders, and the K_d values of the 12 residues from the N-terminal deletion mutant of 4E-BP2 (Nd12-4E-BP2), 32 residues from the N-terminal deletion mutant of 4E-BP2 (Nd32-4E-BP2) and 45 residues from the N-terminal deletion mutant of 4E-BP2 (Nd45-4E-BP2) with m⁷GTP-bound eIF4E were almost of the same order as that of full-length 4EBP2 (Table 1). As 4E-BP2 has the longest N-terminal sequence among the three 4E-BP subtypes (Figure 1), the N-terminal flexible regions of 4E-BP1 and 4E-BP3 are assumed to exert a similar behaviour for the interaction with eIF4E.

In contrast, the sequential deletion analysis of the C-terminal flexible region showed a remarkable contribution to the interaction with eIF4E. Note that the SPR profile between the 35 and 40 residues from C-terminal deletion mutants of 4E-BP1 (Cd35- and Cd40-4E-BP1 respectively) showed a marked difference for the interaction with eIF4E (Figure 3), whereas the SPR profiles between Cd35-4E-BP1 and full-length 4E-BP1, and between Cd40-4E-BP1 and Cd47-4E-BP1 gave respective similar kinetic parameters. The association and dissociation rates of Cd40- and Cd47-4E-BP1s are characteristically too high to be accurately estimated using the Langmuir (1:1) binding model. This means that the deficit of the C-terminal 36–40 amino acid region markedly changes the interaction mode with eIF4E, and that the essential binding region with eIF4E is in the Pro-Gly-Val-Thr-Ser (amino acids 79–83) sequence (Figure 1). The K_d values estimated using the Langmuir (1:1) binding or the Scatchard affinity model (Table 1) show that the deletion of more than 40 residues at the C-terminus of 4E-BP1 weakens the interaction with eIF4E by approximately two orders of magnitude, compared with that in the case of full-length 4E-BP, whereas the deletion of less than 35 residues scarcely affects the kinetic parameters. On the other hand, the SPR profiles of 4E-BP1 and its deletion mutants scarcely differed between m⁷GTP-free eIF4E and m⁷GTP-bound eIF4E, indicating that the binding of 4E-BP1 to eIF4E is not directly affected by mRNA cap binding to the pocket located at the C-terminus of eIF4E (Figure 2).

Table 1 SPR kinetic parameters of 4E-BP subtypes and their deletion mutants or fragment peptides with m⁷GTP-free or -bound eIF4E at 25 °C, together with the data previously published in [16]

n.d., not detected.

Pair		k_a (1/M · s)	k_d (1/s)	K_d (M)
Molecule 1	Molecule 2			
m ⁷ GTP-free eIF4E	Full-length 4E-BP1	5.76×10^5	3.42×10^{-3}	5.93×10^{-9}
m ⁷ GTP-bound eIF4E	Full-length 4E-BP1	3.65×10^5	3.42×10^{-3}	2.14×10^{-9}
m ⁷ GTP-free eIF4E	Cd35-4E-BP1	4.40×10^5	3.25×10^{-3}	7.38×10^{-9}
m ⁷ GTP-bound eIF4E	Cd35-4E-BP1	4.36×10^5	4.33×10^{-3}	9.94×10^{-9}
m ⁷ GTP-free eIF4E	Cd40-4E-BP1	–	–	3.72×10^{-7}
m ⁷ GTP-bound eIF4E	Cd40-4E-BP1	–	–	2.63×10^{-7}
m ⁷ GTP-free eIF4E	Cd47-4E-BP1	–	–	3.33×10^{-7}
m ⁷ GTP-bound eIF4E	Cd47-4E-BP1	–	–	2.32×10^{-7}
m ⁷ GTP-free eIF4E	Full-length 4E-BP2	4.94×10^5	4.26×10^{-4}	8.61×10^{-9}
m ⁷ GTP-bound eIF4E	Full-length 4E-BP2	5.47×10^5	4.28×10^{-4}	7.83×10^{-9}
m ⁷ GTP-free eIF4E	Cd31-4E-BP2	1.15×10^5	3.75×10^{-4}	3.26×10^{-9}
m ⁷ GTP-bound eIF4E	Cd31-4E-BP2	1.57×10^5	4.85×10^{-4}	3.10×10^{-9}
m ⁷ GTP-free eIF4E	Cd37-4E-BP2	1.08×10^5	3.12×10^{-4}	2.88×10^{-9}
m ⁷ GTP-bound eIF4E	Cd37-4E-BP2	2.42×10^5	6.63×10^{-4}	2.22×10^{-9}
m ⁷ GTP-free eIF4E	Cd40-4E-BP2	–	–	3.72×10^{-7}
m ⁷ GTP-bound eIF4E	Cd40-4E-BP2	–	–	8.01×10^{-7}
m ⁷ GTP-free eIF4E	Cd47-4E-BP2	–	–	2.65×10^{-6}
m ⁷ GTP-bound eIF4E	Cd47-4E-BP2	–	–	1.88×10^{-6}
m ⁷ GTP-free eIF4E	Full-length 4E-BP1	4.07×10^5	2.70×10^{-3}	6.65×10^{-9}
m ⁷ GTP-bound eIF4E	Full-length 4E-BP1	6.46×10^5	7.84×10^{-4}	1.16×10^{-9}
m ⁷ GTP-free eIF4E	Cd26-4E-BP3	2.52×10^5	2.96×10^{-3}	1.17×10^{-9}
m ⁷ GTP-bound eIF4E	Cd26-4E-BP3	5.08×10^5	1.26×10^{-3}	2.49×10^{-9}
m ⁷ GTP-free eIF4E	Cd34-4E-BP3	–	–	1.82×10^{-6}
m ⁷ GTP-bound eIF4E	Cd34-4E-BP3	–	–	1.17×10^{-6}
m ⁷ GTP-free eIF4E	Cd38-4E-BP3	–	–	3.67×10^{-6}
m ⁷ GTP-bound eIF4E	Cd38-4E-BP3	–	–	1.65×10^{-6}
m ⁷ GTP-bound eIF4E	Full-length 4E-BP2	5.47×10^5	4.28×10^{-4}	7.83×10^{-9}
m ⁷ GTP-bound eIF4E	Nd12-4E-BP2	3.18×10^5	3.38×10^{-3}	1.20×10^{-9}
m ⁷ GTP-bound eIF4E	Nd32-4E-BP2	1.63×10^5	5.43×10^{-3}	3.33×10^{-9}
m ⁷ GTP-bound eIF4E	Nd45-4E-BP2	1.70×10^5	7.61×10^{-3}	4.48×10^{-9}
m ⁷ GTP-bound eIF4E	Nd45/Cd31-4E-BP2	1.55×10^5	8.79×10^{-3}	5.65×10^{-9}
m ⁷ GTP-bound eIF4E	4E-BP2 peptide I (Thr ⁴⁶ –Thr ⁷⁰)	–	–	2.21×10^{-6}
m ⁷ GTP-bound eIF4E	4E-BP2 peptide II (His ⁷⁴ –Glu ⁸⁹)	n.d.	n.d.	n.d.

Similar marked differences were also observed for the SPR profiles of 4E-BP2 and 4E-BP3, and a difference of approximately three orders of magnitude was observed between the K_d values of the Cd31-4E-BP2 and Cd47-4E-BP2 mutants, and between those of the Cd26-4E-BP3 and Cd38-4E-BP3 mutants (Table 1). These results clearly show that 4E-BP1–4E-BP3 have a common eIF4E-binding site (second binding region) in their C-terminal conserved Pro-Gly-Val-Thr-Ser/Thr (PGVTS/T) sequence (Figure 1).

Val⁸¹ is an essential residue in the second eIF4E-binding region of 4E-BP1

To determine which residue or sequence is most essential in the second binding region of 4E-BP1, a sequential deletion analysis of the PGVTS sequence was performed. As seen in Table 2 (compare row 5 with row 6) the association constant was significantly decreased by the deletion from the C-terminal to Val⁸¹ compared with the Cd37- and Cd38-4E-BP1 mutants: a difference in K_d of more than one order of magnitude was observed between the presence and absence of this residue. The importance of Val⁸¹ for the interaction with eIF4E was supported by the V81A mutant of Cd36 and Cd37-4E-BP1: the mutation of C-terminal Iso-Pro-Gly-Ala decreased the association constant by approximately one-fifth, compared with that of Cd37-4E-BP1 (C-terminal Iso-Pro-Gly-Val), and this was mainly due to the increased k_d value and the unchanged k_a value (Table 2, compare row 5 with row 10).

In contrast, Ser⁸³ appeared to not significantly contribute to the interaction with eIF4E, because its K_d value was almost within the same range as that of Cd35-4E-BP1 (Table 2, compare row 3 with row 4). The 4E-BP1 mutants with a deletion of less than 36 or more than 38 residues from the C-terminus exhibited nearly the same K_d values on the order of $\sim 9 \times 10^{-9}$ and $\sim 2 \times 10^{-7}$ respectively. Thus Val⁸¹ is concluded to be the major residue in the second eIF4E-binding site of 4E-BP1. Although such sequential deletion experiments have not yet been performed on 4E-BP2 and 4E-BP3, the same conclusion could be assumed because of their similar sequences (Figure 1); the K_d values of Cd40-4E-BP2 and Cd34-4E-BP3 in the interaction with m⁷GTP-free or -bound eIF4E are almost in the same range as that of 4E-BP1 lacking the second binding region (Table 1).

The N-terminal flexible region of eIF4E controls the binding of 4E-BP through the interaction with the second binding region

The crystal structure of the m⁷GpppA–eIF4E–4E-BP1 peptide ternary complex [11] showed possible overlapping of the second binding region of 4E-BP with the H1 (Thr⁶⁸–His⁷⁹) and/or H2 (Gln¹²⁰–Asp¹⁴⁰) helices of eIF4E (Figure 2). As the N-terminal region of eIF4E is flexible enough to interact with the C-terminal domain of 4E-BP, we investigated the effect of both flexible regions on the interaction (Table 3). The N-terminal 33 residues

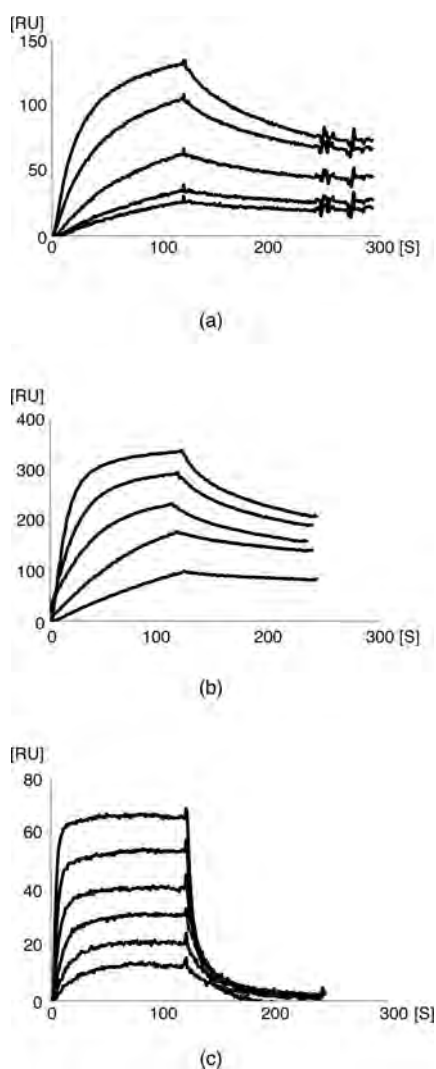


Figure 3 SPR sensorgram of the binding of (a) full-length 4E-BP1, (b) Cd35-4E-BP1 and (c) Cd40-4E-BP1 to m^7 GTP-bound eIF4E

Each SPR signal shows the time response of the addition of the 4E-BP1 mutant to eIF4E as a function of the concentration (nM) (indicated in each sensorgram). The phases of eIF4E injection (right) and the exposure of the chip to eIF4E-free buffer (left) are indicated.

of eIF4E correspond to the flexible region and form no secondary structure; this region was not observed in the crystal structure owing to its high thermal motion.

4E-BP1–4E-BP3, including the C-terminal second binding region, exhibit similar binding affinities to eIF4E despite the presence or absence of their N-terminal flexible region. In contrast, 4E-BP1–4E-BP3 lacking their second binding region showed higher association constants by approximately one order of magnitude for the interaction with the N-terminal-residue-deleted eIF4E than the full-length eIF4E. As the N-terminal region of 4E-BP had no contribution to the interaction with eIF4E (Table 1) [16], this result indicates that the N-terminal flexible region of eIF4E controls the binding of 4E-BP by suppressing the interaction with the second binding region.

ITC

To determine how strongly the second binding region of 4E-BP interacts with eIF4E compared with the first $Y(X)_4L\Phi$ -binding

region, we previously measured the kinetic parameters of two 4E-BP2 fragment peptides, i.e. peptide I (Thr⁴⁶–Thr⁷⁰ including the first binding site) and peptide II (His⁷⁴–Glu⁸⁹ including the second binding site), by SPR analysis (Table 1). The dissociation constant of peptide I was of the order of $\sim 10^{-6}$, three orders of magnitude less than that of full-length 4E-BP1, and no notable SPR signal was observed for peptide II. In contrast, the K_d of both N- and C-termini deleted Nd45/Cd31-4E-BP2 (including the first and second binding sites) was approximately 3-fold larger than that of peptide I and is within the range of that of full-length 4E-BP2. This clearly indicates that both peptide sequences, Thr⁴⁶–Thr⁷⁰ and His⁷⁴–Glu⁸⁹, are indispensable for revealing the intact interaction of 4E-BP2 with eIF4E, where the second binding region plays an auxiliary, but important, role in the interaction with eIF4E. To confirm this insight thermodynamically, ITC analysis was performed using peptides I, II and III (Ile⁵²–Glu⁸⁹ including the first and second binding sites). The results are given in Table 4, together with the data for full-length eIF4E and 4E-BP subtypes and their deleted mutants; the thermodynamic parameters were estimated using a one-site model; however, for peptide III the two-site model was used. The interactions were all exothermic and enthalpy-driven.

Synergistic collaboration between the first and second binding sites for binding to eIF4E is observed using peptides, but is screened by the existence of the flexible region

The ITC profiles of 4E-BP2 fragment peptides I and III for the interaction with m^7 GTP-bound eIF4E are shown in Figures 4(a) and 4(b) respectively; the results of peptide II are not shown because of a monotonically increasing profile, indicating no specific interaction. The ITC results obtained using the 4E-BP2 fragment peptides supported the result of SPR analysis concerning the function of the second binding site for the binding to eIF4E. Peptide I, which includes only the first binding region [$Y(X)_4L\Phi$ motif], showed a one-step binding profile with thermal parameters similar to those of Cd40-4E-BP1 and Cd40-4E-BP2. In contrast, peptide II, which includes only the second binding region, gave no notable binding profile, indicating that the His⁷⁴–Glu⁸⁹ sequence alone is too weak to detect the interaction with eIF4E by ITC; such a weak interaction was also shown by SPR analysis (Table 1) [16].

On the other hand, peptide III showed a two-step binding profile, in which two types of sigmoid curve were observed in 0–1.0 and 1.0–2.0 molar ratios. This shows the two-step interaction of 4E-BP2 with eIF4E via the first and second binding sites. Although not yet verified experimentally, this ITC profile would indicate that the interaction of the first binding region with eIF4E is reinforced by the synergistic collaboration with the second binding region in the range $[\text{peptide III}]/[\text{eIF4E}] < 1$ ($K_a = 1.42 \times 10^{11}$ at $n = 0.57$), whereas the binding in the range of $[\text{peptide III}]/[\text{eIF4E}] > 1$ is dependent on the first binding region. In other words, the large K_a and negative ΔG at $n = 0.57$ imply that the docking of 4E-BP to eIF4E through the first binding region is ensured by the synergistic function of the second binding region.

To investigate the effect of the 4E-BP C-terminal flexible region on the interaction with eIF4E, the thermodynamic parameters of the 4E-BP mutants were estimated (Table 4). The ITC profiles of the full-length 4E-BP2 and Cd40-4E-BP2 mutant for the interaction with m^7 GTP-bound full-length eIF4E are shown in Figures 4(c) and 4(d). Notably, these show similar one-site binding profiles despite the length of the deleted C-terminal residues, although their K_a values were approximately one order of magnitude larger in the presence of the second binding domain than in its absence. Similar one-site binding profiles were also

Table 2 SPR kinetic parameters of the 4E-BP1 mutant sequentially deleted at its C-terminal IPGVTSPPSSD sequence with m⁷GTP-bound eIF4E at 25 °C, together with those of V81A mutants

4E-BP1 mutant	C-terminal sequence	k_a (1/M · s)	k_d (1/s)	K_d (M)
Cd31-4E-BP1	-IPGVTSPPSSD	4.05×10^4	3.31×10^{-4}	8.18×10^{-9}
Cd35-4E-BP1	-IPGVTS	4.36×10^5	4.33×10^{-3}	9.94×10^{-9}
Cd36-4E-BP1	-IPGV	4.25×10^5	3.83×10^{-3}	9.02×10^{-9}
Cd37-4E-BP1	-IPGV	1.15×10^5	2.05×10^{-3}	1.79×10^{-8}
Cd38-4E-BP1	-IPG			1.41×10^{-7}
Cd40-4E-BP1	-I			2.63×10^{-7}
Cd47-4E-BP1				2.32×10^{-7}
Cd36V81A-4E-BP1	-IPGAT	6.25×10^4	2.83×10^{-3}	4.53×10^{-8}
Cd37V81A-4E-BP1	-IPGA	1.39×10^5	1.29×10^{-2}	9.24×10^{-8}

Table 3 SPR kinetic parameters of 4E-BP subtypes and deletion mutants with m⁷GTP-bound full-length eIF4E or its deletion mutant at 25 °C

eIF4E	4E-BP	k_a (1/M · s)	k_d (1/s)	K_d (M)
Nd33-eIF4E	Full-length 4E-BP1	5.27×10^5	1.21×10^{-4}	2.29×10^{-9}
Nd33-eIF4E	Cd35-4E-BP1	5.41×10^5	2.34×10^{-3}	4.33×10^{-9}
Nd33-eIF4E	Cd40-4E-BP1	2.60×10^6	2.62×10^{-2}	1.01×10^{-8}
Full-length eIF4E	Cd40-4E-BP1	–	–	2.63×10^{-7}
Nd33-eIF4E	Full-length 4E-BP2	1.19×10^6	5.68×10^{-4}	4.97×10^{-10}
Nd33-eIF4E	Cd35-4E-BP2	8.15×10^5	2.02×10^{-3}	2.48×10^{-9}
Nd33-eIF4E	Cd40-4E-BP2	6.56×10^5	3.32×10^{-2}	5.06×10^{-8}
Full-length eIF4E	Cd40-4E-BP2	–	–	8.01×10^{-7}
Nd33-eIF4E	Full-length 4E-BP3	7.93×10^5	1.63×10^{-3}	2.05×10^{-9}
Nd33-eIF4E	Cd35-4E-BP3	5.33×10^5	1.51×10^{-3}	2.84×10^{-9}
Nd33-eIF4E	Cd40-4E-BP3	1.02×10^5	1.30×10^{-2}	1.27×10^{-7}
Full-length eIF4E	Cd40-4E-BP3	–	–	1.17×10^{-6}

Table 4 Thermodynamic parameters of full-length 4E-BP subtypes and their deletion mutants or fragment peptides with m⁷GTP-bound full-length eIF4E or its N-terminal-deleted mutant at 25 °C

n.d., not detected.

eIF4E	4E-BP	ΔG (kcal/mol)	ΔH (kcal/mol)	$-T\Delta S$ (kcal/mol)	n	K_a (M ⁻¹)
Full-length	4E-BP2 peptide I (46–70)	– 10.61	– 15.05	4.41	1.03	5.89×10^7
Full-length	4E-BP2 peptide II (74–89)	n.d.	n.d.	n.d.	n.d.	n.d.
Full-length	4E-BP2 peptide III (52–89)	– 15.21	– 13.11	– 2.13	0.57	1.42×10^{11}
		– 9.44	– 11.61	2.13	1.41	8.22×10^6
Full-length	Full-length 4E-BP2	– 11.56	– 10.07	– 1.49	0.92	2.97×10^8
Full-length	Cd31-4E-BP2	– 12.02	– 10.12	– 1.9	0.97	6.55×10^8
Full-length	Cd40-4E-BP2	– 10.55	– 9.12	– 1.43	0.93	5.46×10^7
Full-length	Nd45-4E-BP2	– 10.96	– 9.38	– 1.58	0.94	1.08×10^7
Full-length	Full-length 4E-BP1	– 12.49	– 17.59	6.56	0.99	1.24×10^8
Full-length	Cd31-4E-BP1	– 10.65	– 15.18	4.53	0.91	1.51×10^8
Full-length	Cd40-4E-BP1	– 10.46	– 17.70	7.24	0.98	5.03×10^7
Full-length	Nd45-4E-BP1	– 10.05	– 13.23	3.18	0.95	2.33×10^7
Nd33	Full-length 4E-BP1	– 11.59	– 19.22	7.62	0.75	1.91×10^8
Nd33	Cd35-4E-BP1	– 10.63	– 18.73	8.10	0.75	5.84×10^8
Nd33	Cd40-4E-BP1	– 10.72	– 16.17	5.50	0.80	5.57×10^7

observed for the interaction of the Nd45-4E-BP2 and Nd45-4E-BP1 mutants with eIF4E. Thus this ITC result shows that the N- and C-terminal flexible regions of 4E-BP behave so as to cover the inherent two-step binding via the first and second binding regions, i.e. the collaborative interaction between the first and second binding regions, as was observed for peptide III.

The N-terminal flexible region of eIF4E scarcely affects the interaction with 4E-BP

The crystal structure of the m⁷GpppA–eIF4E–4E-BP1 fragment ternary complex [11] suggested an interaction between the N-terminal flexible region of eIF4E and both terminal regions of

4E-BP, although none of these regions were observed because of their high thermal motions. Therefore we investigated the effect of the N-terminal flexible region of eIF4E on the interaction with 4E-BP1, using Nd33-eIF4E (Table 4). Consequently, a one-site binding profile was obtained, regardless of full-length 4E-BP1 or its deletion mutant, and it was shown that the N-terminal flexible region of eIF4E scarcely affected the interaction with 4E-BP1.

Different interaction behaviour observed by the ITC and SPR analyses

The ITC analysis showed different results from the SPR analysis in the following respects: (i) the ITC analysis showed that the

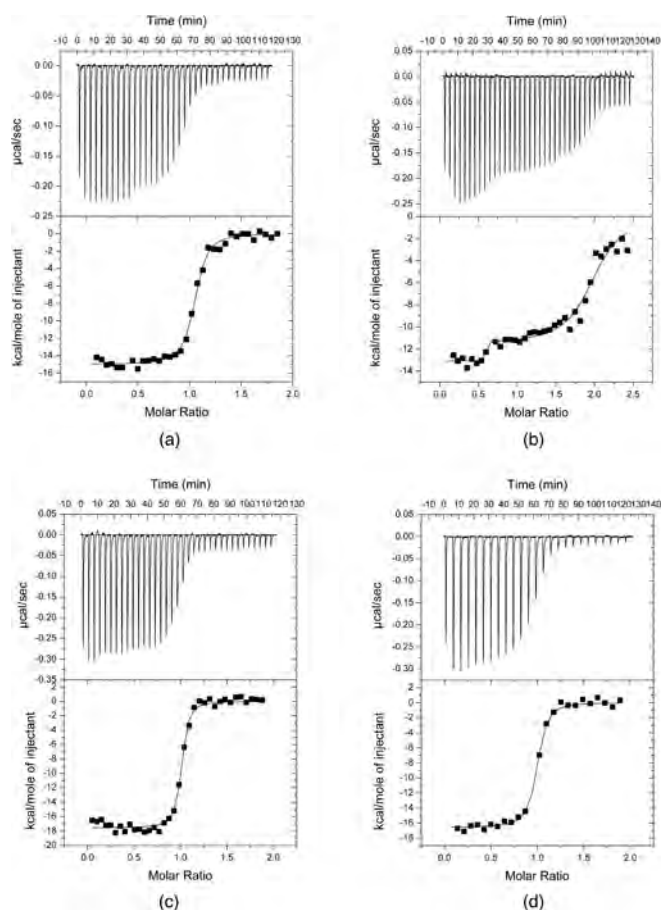


Figure 4 ITC profiles of (a) 4E-BP2 peptide I (Thr⁴⁶–Thr⁷⁰), (b) 4E-BP2 peptide III (Ile⁵²–Glu⁸⁹), (c) full-length 4E-BP2 and (d) Cd40-4E-BP2 for binding to m⁷GTP-bound eIF4E

The raw data (top panels) and their integrated data (bottom panels) of heat changes are shown. The best-fitted curve by a one-site (a, c and d) or two-site (b) binding model is shown on the integrated data. The binding isotherms correspond to the heat effect associated with 4E-BP2 (5 μ l per injection at a 50 μ M concentration) injected into the calorimetric cell (1.4 ml) containing 5 μ M m⁷GTP-bound full-length eIF4E. The experiments were performed in 20 mM NaH₂PO₄/NaOH (pH 7.4) buffer containing 100 mM NaCl at 25 °C.

presence of the 4E-BP N-terminal domain increases the K_a value by approximately one order of magnitude (Table 4), whereas no notable contribution of the N-terminal region of 4E-BP to the interaction with eIF4E was observed by SPR analysis (Table 1), and (ii) ITC showed no notable affect of the eIF4E N-terminal flexible region on the interaction with 4E-BP1 (Table 4), whereas the SPR analysis showed that the N-terminal flexible region of eIF4E disrupts the interaction of the second binding region with 4E-BP (Table 3).

Although this discrepancy remains unclear, it may be partly due to the different observations of the molecular interaction, i.e. the SPR analysis reflecting a dynamic interaction and the ITC analysis reflecting a static interaction. The interaction between the flexible regions in aqueous solution may not be sensitively detected by the static ITC analysis compared with the dynamic SPR analysis.

Possible binding mode of 4E-BP to eIF4E by MD calculation

We previously performed MD simulation for 3 ns to estimate the possible interaction between the eIF4E and 4E-BP2 Pro⁴⁷–

Asp⁹⁰ fragment in an aqueous solution [16]. The result suggested that the second binding region (Cys⁷³–Glu⁸⁹) is located at the root of the N-terminal flexible region of eIF4E through relatively weak hydrophobic interactions [16]. This result appears to be important for elucidating the regulatory mechanism of eIF4E by 4E-BP, because a similar binding mode was reported for the interaction of eIF4G with eIF4E [12]. Therefore, in the present study, we performed MD simulation for 10 ns to more accurately simulate the structural features and stability of this non-specific hydrophobic interaction.

The MD snapshot at 10 ns (Figure 5a) showed the possible interaction mode between the Pro⁴⁷–Asp⁹⁰ fragment of 4E-BP2 and the N-terminal flexible region of eIF4E. The simulation suggested that the 4E-BP2 fragment forms a right-handed ring so as to wrap around the root (Ile³⁵–Pro³⁸) of the N-terminal flexible region of eIF4E, and its spatial orientation to eIF4E was retained during the MD simulation. The helical Asp⁵⁵–Arg⁶³ region, including the first binding region, was stabilized by three hydrogen bonds throughout the MD simulation after reaching the stationary state of the system (Figure 5b): the average distances of Tyr⁵⁴ O η H ··· O Pro³⁸, Arg⁵⁶ N ϵ H ··· O ϵ 2 Glu¹³², Arg⁵⁶ N η 2H ··· O ϵ 1 Glu¹³² and Leu⁵⁹ O ··· N ϵ 1H Trp⁷³ atomic pairs were 2.7 ± 0.2 , 3.0 ± 0.2 , 2.8 ± 0.1 and 2.9 ± 0.1 Å respectively. On the other hand, the C-terminal Cys⁷³–Asp⁹⁰ region, including the second binding region, was located at the periphery of the N-terminal flexible, H1 helix and S2 sheet regions of eIF4E (Figure 5b). In contrast with the large structural fluctuation of the C-terminal moiety of 4E-BP2, the Thr⁷⁰–Ile⁷⁸ moiety showed a relatively stable spatial orientation to the H1 and S2 secondary structures during the MD simulation (Figure 5c). Hydrophobic interactions were observed between the side chains of 4E-BP (Leu⁷⁵ and Ile⁷⁸) and eIF4E (Lys⁶⁵ and Lys⁹⁶) (Figure 6a), in addition to the electrostatic interactions between Thr⁷⁰ O γ 1 ··· N η H Lys³⁶ and His⁷⁴ N δ 1H ··· O γ Ser⁶⁴ after ~ 4 ns of MD simulation (Figure 6b). Although Val⁸¹ of 4E-BP2 exhibited a relatively large structural fluctuation at 3–6 ns, the hydrophobic interactions with the Pro³⁸ and Lys³⁶ side chains of eIF4E were observed after 6 ns (Figure 6c). Notably, Val⁸¹ was exactly located at the crossing position between the 4E-BP C-terminal and eIF4E N-terminal flexible regions (Figure 5c). That the deletion of Val⁸¹ leads to a considerable decrease in the association constant with eIF4E (Table 2) emphasizes the importance of Val⁸¹ at this position for maintaining the stable interaction with eIF4E through the first binding region. The importance of Val⁸¹ via its hydrophobic interaction with eIF4E was also supported by the V81A mutation (Table 2). Thus the second binding region plays an important role in the clipping between the eIF4E N-terminal and 4E-BP C-terminal flexible regions.

It is interesting to note that the N- and C-terminal regions of the 4E-BP2 fragment approach each other as the MD simulation progresses, forming a ring structure through the electrostatic interactions between Arg⁵¹ and Gly⁸⁵/Asp⁹⁰ residues after 4 ns (Figures 5b and 6d). Although MD simulation for such a flexible region is largely dependent on the starting structure and thus could not effectively provide its exact conformation, this ring formation may be one reason why the N- and C-terminal flexible regions of 4E-BP form a molecular bracelet that wraps around the N-terminus of eIF4E.

DISCUSSION

Although the central α -helical Y(X)_nL Φ motif (X, variable amino acids; Φ , hydrophobic amino acids) of the translational regulator 4E-BP is the core binding region for the mRNA cap-binding

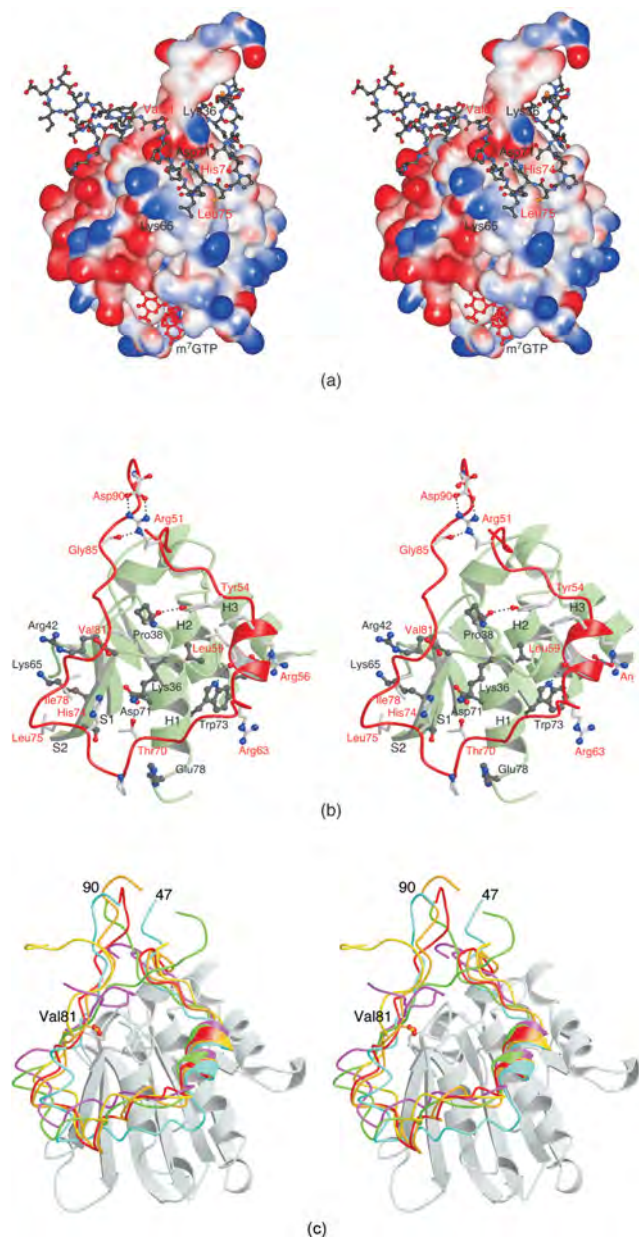


Figure 5 MD-simulated stereoscopic snapshots over 10 ns of (a) 4E-BP2 Pro⁴⁷–Asp⁹⁰ fragment (ball-and-stick) around the root of the N-terminal flexible region of eIF4E (space-fill) shown in wrapping mode, (b) overall structure of 4E-BP2 fragment (red) viewed from the N-terminal region of eIF4E (green), and (c) 4E-BP2 fragments at 0 (cyan), 1 (green), 2 (magenta), 3 (yellow), 6 (orange) and 10 (red) ps superimposed on to eIF4E at 10 ps

(a) eIF4E is represented using the molecular surface model, where positively and negatively charged regions are shown in blue and red respectively. (b) The N-terminal-extended (His³⁷–Gln⁴⁰, green wire), H1 (Trp⁷³–Asn⁷⁷), H2 (Gln¹²⁰–Asp¹⁴⁰) and S2 (Asn⁵⁹–Phe⁶⁶) regions (green ribbons) of eIF4E participate in binding with the first Y(X)₄LΦ and second binding regions of 4E-BP. Dotted lines represent possible hydrogen bonds.

protein eIF4E, the functions of its N- and C-terminal flexible regions remain to be elucidated. As the importance of such conformational flexibility for the proper functioning of proteins has received much attention in recent years, we have been investigating the function of the N- and C-terminal flexible regions of 4E-BP1–4E-BP3 subtypes in their interactions with eIF4E. Previous SPR analysis using sequential N-terminal deletion mutants of 4E-BP2 showed no notable contribution of the N-

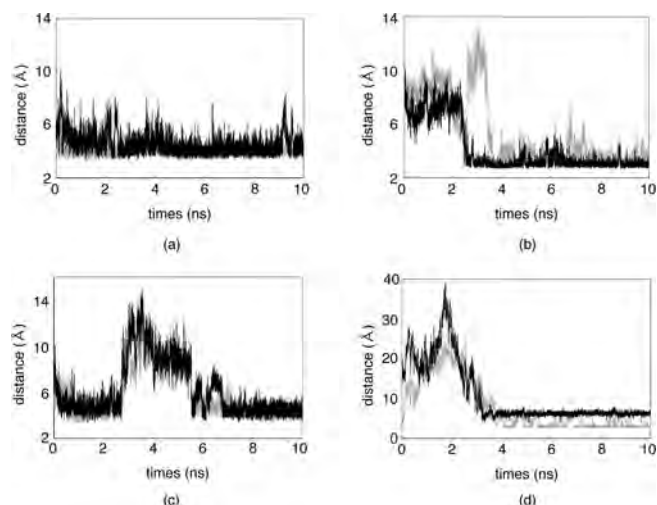


Figure 6 Time-distance profiles of three 4E-BP2...eIF4E (a–c) and two 4E-BP2...4E-BP2 (d) atomic pairs

(a) Leu⁷⁵ Cδ1...Cγ Lys⁶⁵ (black) and Ile⁷⁸ Cδ1...Cβ Lys⁹⁶ (grey). (b) His⁷⁴ Nδ1 H...Oγ Ser⁶⁴ (black) and Thr⁷⁰ Oγ1...Nγ Lys³⁶ (grey). (c) Val⁸¹ Cγ1...Cβ Lys³⁶ (black) and Val⁸¹ Cγ2...Cγ Pro³⁸ (grey). (d) Arg⁵¹ Nη2H...Oδ1 Asp⁹⁰ (black) and Arg⁵¹ NeH...O Gly⁸⁵ (grey).

terminal flexible region (1–45 amino acid sequence) to the interaction with eIF4E [16]. Therefore, in the present study, we mainly investigated the functions of the C-terminal flexible regions of 4E-BP1–4E-BP3 in the interaction with eIF4E using their sequential C-terminal deletion mutants. Consequently, the SPR analyses confirmed the presence of the second eIF4E-binding site in the C-terminal conserved sequence (Pro-Gly-Gly-Val-Thr-Ser/Thr) of 4E-BP and identified valine as the most essential residue for the binding. We also clarified that, although the central α-helical Y(X)₄LΦ motif of 4E-BP is the first binding region for eIF4E, its intact association with eIF4E requires the auxiliary, but synergistic, function of the second binding region and that the N-terminal flexible region of eIF4E acts as a regulator for the binding to 4E-BP through its suppressive interaction with the second binding site.

On the other hand, the ITC analysis showed that the interaction between 4E-BP and eIF4E is enthalpy-driven and that the association constant is approximately one order of magnitude larger in the presence than in the absence of the second binding region. The ITC profiles using the fragment peptides of 4E-BP showed the synergistic association between the first and second binding sites of 4E-BP for the interaction with eIF4E. However, the presence of flexible regions of eIF4E and/or 4E-BP act so as to cover the inherent interaction feature, where the two-site binding profile based on each different binding region is integrated into a one-site binding profile.

The MD simulation for 10 ns suggested that the second binding region plays a role in the clipping between the eIF4E N-terminal and 4E-BP2 C-terminal flexible regions, where Val⁸¹ in the conserved sequence is located at a crossing position between the 4E-BP2 C-terminal and eIF4E N-terminal flexible regions through hydrophobic interactions. This situation clearly explains the dynamic SPR results. The binding of the 4E-BP subtype to eIF4E via the hydrogen bonds of the first binding region and the hydrophobic interactions of the second binding region would stabilize the complex and lead to a high resistance for the release of 4E-BP from the complex. This may explain why

hyperphosphorylation, but not hypophosphorylation, of 4E-BP is required for dissociation from eIF4E [23].

As 4E-BP regulates the biological function of eIF4E via competitive binding with eIF4G to the same surface of eIF4E [7], investigation of the difference between their binding features is useful. The sequential difference between 4E-BP and eIF4G in the eIF4E-binding region is shown in Figure 1. The S⁶³⁷DVVL⁶⁴¹ sequence of eIF4G-I corresponds to the second binding region of the 4E-BP subtype. Because the fragment peptide (Gly⁶³²–Thr⁶⁴⁷) of eIF4G-I afforded no SPR signal for the interaction with eIF4E [16], its binding ability may not be as strong as that of its core Y(X)₄LΦ-binding region, as similarly observed for the second binding region of 4E-BP. However, the second binding sequence sandwiched between two proline residues of 4E-BP (Pro⁷⁹ and Pro⁸⁴ for 4E-BP2), which is further characterized by the presence of two phosphorylation residues [23] (Ser⁶⁵ and Thr⁷⁰ for 4E-BP2) between the first and second binding regions, may afford a different function from that conferred by the S⁶³⁷DVVL⁶⁴¹ sequence of eIF4GI for the interaction with eIF4E.

AUTHOR CONTRIBUTION

Keum Soon Paku, Yu Umenaga, Tsunego Usui, Ai Fukuyo and Atsuo Mizuno performed the expression and purification of recombinant proteins, and performed SPR and ITC measurements. Yasuko In performed molecular dynamics calculations. Toshimasa Ishida supervised the project. Koji Tomoo analysed the data. The paper was written by Koji Tomoo and Toshimasa Ishida.

FUNDING

This work was supported by Grants-in-Aid for High Technology Research and Scientific Research from the Ministry of Education, Culture, Sports, Science and Technology of Japan.

REFERENCES

- Dever, T. E. (2002) Gene-specific regulation by general translation factors. *Cell* **108**, 545–556
- Sonenberg, N. and Dever, T. E. (2003) Eukaryotic translation initiation factors and regulators. *Curr. Opin. Struct. Biol.* **13**, 56–63
- Sonenberg, N. and Hinnebusch, A. G. (2009) Regulation of translation initiation in eukaryotes: mechanisms and biological targets. *Cell* **136**, 731–745
- Pause, A., Belsham, G. J., Gingras, A. C., Donze, O., Lin, A. A., Laurence, Jr, J. C. and Sonenberg, N. (1994) Insulin-dependent stimulation of protein synthesis by phosphorylation of a regulator of 5'-cap function. *Nature* **371**, 762–767
- Sonenberg, N. and Gingras, A. C. (1998) The mRNA 5'-cap binding protein eIF4E and control of cell growth. *Curr. Opin. Cell Biol.* **10**, 268–275
- Haghighat, A., Mader, S., Pause, A. and Sonenberg, N. (1995) Repression of cap-dependent translation by 4E-binding protein 1: competition with p220 for binding to eukaryotic initiation factor -4E. *EMBO J.* **14**, 5701–5709
- Mader, S., Lee, H., Pause, A. and Sonenberg, N. (1997) The translation initiation factor eIF4E binds to a common motif shared by the translation factor eIF4-γ and the translational repressor 4E-binding proteins. *Mol. Cell. Biol.* **17**, 6940–6947
- Altmann, M., Schmitz, N., Berset, N. and Trachsel, H. (1997) A novel inhibitor of cap-dependent translation initiation in yeast-p20 competes with eIF4G for binding to eIF4E. *EMBO J.* **16**, 1114–1121
- Gingras, A. C., Gygi, S. P., Raught, B., Polakiewicz, R. D., Abraham, R. T., Hoekstra, M. F., Aebersold, R. and Sonenberg, N. (1999) Regulation of 4E-BP1 phosphorylation: a novel two-step mechanism. *Genes Dev.* **13**, 1422–1437
- Marcotrigiano, J., Gingras, A.-C., Sonenberg, N. and Burley, S. K. (1999) Cap-dependent translation initiation in *Eukaryotes* is regulated by a molecular mimic of eIF4G. *Mol. Cell* **3**, 707–716
- Tomoo, K., Matsushita, Y., Fujisaki, H., Abiko, F., Shen, X., Taniguchi, T., Miyagawa, H., Kitamura, K., Miura, K. and Ishida, T. (2005) Structural basis for mRNA cap-binding regulation of eukaryotic initiation factor 4E by 4E-binding protein, studied by spectroscopic, X-ray crystal structural, and molecular dynamics simulation methods. *Biochim. Biophys. Acta* **1753**, 191–208
- Gross, J. D., Moerke, N. J., von der Haar, T., Lugovskoy, A. A., Sachs, A. B., McCarthy, J. E. G. and Wagner, G. (2003) Ribosome loading onto the mRNA cap is driven by conformational coupling between eIF4G and eIF4E. *Cell* **115**, 739–750
- Chang, S.-Y., Chen, Y.-K., Wang, A. H.-J. and Liang, P.-H. (2003) Identification of the active conformation and the importance of length of the flexible loop 72–83 in regulating the conformational change of undecaprenyl pyrophosphate synthase. *Biochemistry* **42**, 14452–14459
- Bhalla, J., Storchan, G. B., MacCarthy, C. M., Uversky, V. N. and Tcherkasskaya, O. (2006) Local flexibility in molecular function paradigm. *Mol. Cell. Proteomics* **5**, 1212–1223
- Amaro, R. E., Minh, D. D., Cheng, L. S., Lindstrom, Jr, W. M., Olson, A. J., Lin, J. H., Li, W. W. and McCammon, J. A. (2007) Remarkable loop flexibility in avian influenza N1 and its implications for antiviral drug design. *J. Am. Chem. Soc.* **129**, 7764–7765
- Mizuno, A., In, Y., Fujita, Y., Abiko, F., Miyagawa, H., Kitamura, K., Tomoo, K. and Ishida, T. (2008) Importance of C-terminal flexible region of 4E-binding protein in binding with eukaryotic initiation factor 4E. *FEBS Lett.* **582**, 2439–3444
- Abiko, F., Tomoo, K., Mizuno, A., Morino, S., Imataka, H. and Ishida, T. (2007) Binding preference of eIF4E for 4E-binding protein isoform and function of eIF4E N-terminal flexible region for interaction, studied by SPR analysis. *Biochem. Biophys. Res. Commun.* **355**, 667–672
- Nishi, N., Morino, S., Tomoo, K., Yutani, T. and Ishida, T. (1998) Expression of a synthetic gene for initiation factor 4E-binding protein 1 in *Escherichia coli* and its interaction with eIF4E and eIF4E.m⁷GTP complex. *J. Biochem.* **123**, 157–161
- Morino, S., Hazama, H., Ozaki, M., Teraoka, Y., Shibata, S., Doi, M., Ueda, H., Ishida, T. and Uesugi, S. (1996) Analysis of the mRNA cap-binding ability of human eukaryotic initiation factor-4E by use of recombinant wild-type and mutant forms. *Eur. J. Biochem.* **239**, 597–601
- Bradford, M. M. (1976) A rapid and sensitive method for the quantitation of microgram quantities of protein utilizing the principle of protein-dye binding. *Anal. Biochem.* **72**, 248–254
- Nagata, K. and Handa, H. (1998) *Real Time Analysis of Biomolecular Interactions*, Springer-Verlag, Tokyo
- Jorgensen, W. L., Chandrasekhar, J., Madura, J. D., Impey, R. W. and Klein, M. L. (1983) Comparison of simple potential functions for simulating liquid water. *J. Chem. Phys.* **79**, 926–935
- Cornell, W. D., Cieplak, P., Bayly, C. I., Gould, I. R., Merz, Jr, K. M., Ferguson, D. M., Spellmeyer, D. C., Fox, T., Caldwell, J. W. and Kollman, P. A. (1995) A second generation force field for the simulation of proteins, nucleic acids, and organic molecules. *J. Am. Chem. Soc.* **117**, 5179–5197
- Gingras, A., Raught, B., Gygi, S.P., Niedzwiecka, A., Miron, M., Burley, S. K., Polakiewicz, R. D., Wyslouch-Cieszyńska, A., Aebersold, R. and Sonenberg, N. (2001) Hierarchical phosphorylation of the translation inhibitor 4E-BP1. *Genes Dev.* **15**, 2852–2864

Received 13 September 2010/30 August 2011; accepted 13 September 2011
Published as BJ Immediate Publication 13 September 2011, doi:10.1042/BJ20101481

C–H... π interplay between Ile308 and Tyr310 residues in the third repeat of microtubule binding domain is indispensable for self-assembly of three- and four-repeat tau

Received February 14, 2012; accepted May 1, 2012; published online June 1, 2012

Koushirou Sogawa^{1,*}, Ryouhei Okuda^{1,*},
Yasuko In¹, Toshimasa Ishida¹,
Taizo Taniguchi², Katsuhiko Minoura^{1,†} and
Koji Tomoo^{1,‡}

¹Department of Physical Chemistry, Osaka University of Pharmaceutical Sciences, 4-20-1 Nasahara, Takatsuki, Osaka 569-11 and ²Department of Pharmaceutical Health Care, Faculty of Pharmaceutical Sciences, Himeji Dokkyo University, 7-2-1 Kamiohno, Himeji, Hyogo 670-8524, Japan

[†]Katsuhiko Minoura, Research Center, Osaka University of Pharmaceutical Sciences, 4-20-1 Nasahara, Takatsuki, Osaka 569-1094, Japan. Fax: +81 726 90 1039, Tel: +81 726 90 1068, e-mail: minoura@gly.oups.ac.jp.

[‡]Koji Tomoo, Department of Physical Chemistry, Osaka University of Pharmaceutical Sciences, 4-20-1 Nasahara, Takatsuki, Osaka 569-1094, Japan. Fax/Tel: +81 726 90 1068. e-mail: tomoo@gly.oups.ac.jp.

*These authors contributed equally to this work.

Information on the structural scaffold for tau aggregation is important in developing a method of preventing Alzheimer's disease (AD). Tau contains a microtubule binding domain (MBD) consisting of three or four repeats of 31 and 32 similar residues in its C-terminal half. Although the key event in tau aggregation has been considered to be the formation of β -sheet structures from a short hexapeptide ³⁰⁶VQIVYK³¹¹ in the third repeat of MBD, its aggregation pathway to filament formation differs between the three- and four-repeated MBDs, owing to the intermolecular and intramolecular disulphide bond formations, respectively. Therefore, the elucidation of a common structural element necessary for the self-assembly of three-/four-repeated full-length tau is an important research subject. Expanding the previous results on the aggregation mechanism of MBD, in this paper, we report that the C–H... π interaction between the Ile308 and Tyr310 side chains in the third repeat of MBD is indispensable for the self-assembly of three-/four-repeated full-length tau, where the interaction provides a conformational seed for triggering the molecular association. On the basis of the aggregation behaviours of a series of MBD and full-length tau mutants, a possible self-association model of tau is proposed and the relationship between the aggregation form (filament or granule) and the association pathway is discussed.

Keywords: C–H... π interaction/isoleucine residue/microtubule binding domain/tau protein/tyrosine residue.

Abbreviations: AD, Alzheimer's disease; CD, circular dichroism; DTT, dithiothreitol; EM, electron

microscopy; His, histidine; MBD, microtubule binding domain; MT, microtubule; PHF, paired helical filament; ThS, thioflavin S; 3Rtau, three repeat full-length tau; 4Rtau, four repeat full-length tau; 3RMBD, three-repeated MBD; 4RMBD, four-repeated MBD.

Tau is a major microtubule (MT)-associated protein that is also the main component of the aberrant filaments like the neurofibrillary tangles (1, 2), found in the brain of Alzheimer's disease (AD) patients. Tau is highly soluble and adopts a natively unfolded structure in solution. However, in the brains of AD patients, tau dissociates from axonal MTs through extensive phosphorylation and aggregates to form an insoluble paired helical filament (PHF) called the neurofibrillary tangle (3–9). Information on the mechanism of PHF formation of tau is important for elucidating the mechanisms and the development of therapeutic drugs for AD.

In the central nervous system of the adult human brain, six tau isoforms are expressed ranging in size from 352 to 441 amino acids (Fig. 1) (10–12). Tau contains a microtubule binding domain (MBD) consisting of three or four repeats of 31 and 32 similar amino acid sequences in the C-terminal half, and binds to and stabilizes microtubules (13–15). Generally, the key event in tau polymerization is the formation of a β -strand structure from the short hexapeptide ³⁰⁶VQIVYK³¹¹ in the third repeat of MBD (16, 17), where the residual number corresponds to the longest isoform. An X-ray crystal analysis of this peptide showed that it adopts a β -strand conformation and forms β -sheets with neighbouring peptides that combine in a face-to-face interdigitating 'steric zipper' structure (18).

Tauopathies can be characterized on the basis of the isoform composition of their filaments (19, 20). For example, filaments in Pick disease contain three repeats (3R: R1–R3–R4), whereas those in progressive supranuclear palsy and corticobasal degeneration contain four repeats (4R: R1–R2–R3–R4). Filaments in AD incorporate three- and four-repeated tau. On the other hand, we previously reported that the association pathway of four-repeated MBD (4RMBD) is different from that of three-repeated MBD (3RMBD) in the

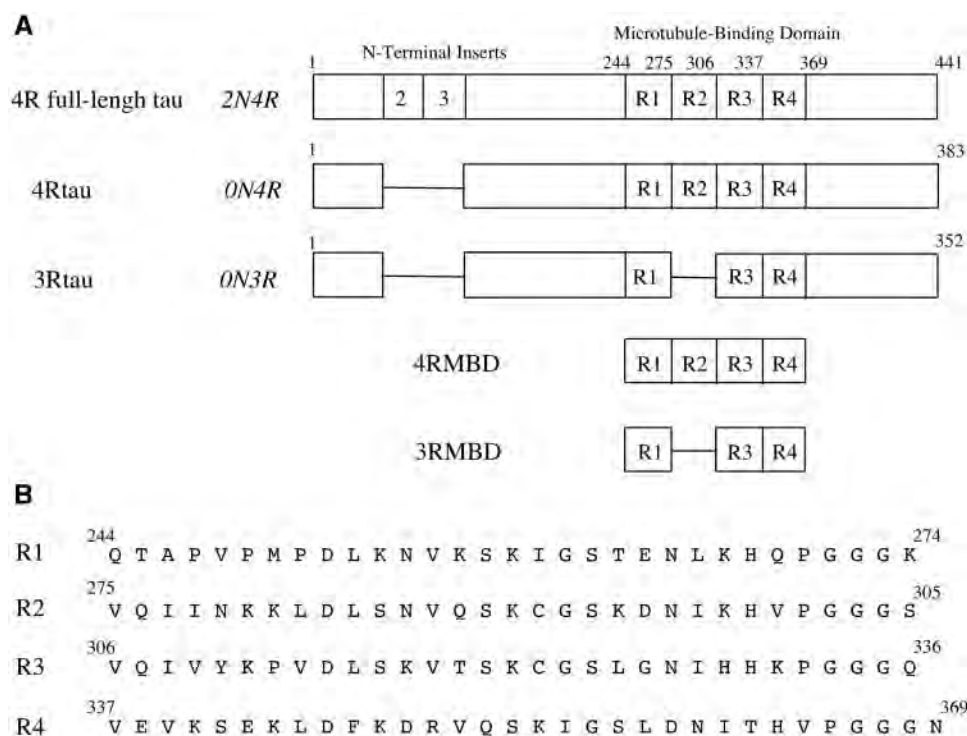


Fig. 1 Schematic representations of (A) longest 4R-tau isoform including two N-terminal inserts (*2N4R*) among six different tau isoforms, together with three- and four-repeat isoforms of 4Rtau (*0N4R*), 3Rtau (*0N3R*), 4RMBD and 3RMBD used in this work and (B) amino acid sequences of first to fourth repeats (R1–R4). Residual numbering is adapted to that of the longest isoform 4Rtau (441 residues).

following points: (i) the elemental unit for the association is an intermolecular Cys–Cys disulphide-bonded dimer between the neighbouring third repeats (R3) for 3RMBD and an intramolecular disulphide-bonded monomer between the second (R2) and third (R3) repeats for 4RMBD (21, 22), and (ii) the presence of dithiothreitol (DTT), a reducing agent, decreases the filament formation ability of 3RMBD, but it increases that of 4RMBD (23). Therefore, information on the common structural element that enables the initial self-association of three- and four-repeated MBD (3R/4RMBD) or tau (3R/4Rtau) is crucial for developing AD inhibitors. Recently, we reported the importance of Tyr located at position 310 (24) and of its interplay with Ile308 in the progress of the filament formation of 4RMBD (25). Thus, it is important upon confirming the universal role of this interplay in the initial association to examine whether the interplay between these Ile and Tyr residues is similarly indispensable for the filament formation of 3RMBD and 3R/4Rtau. In this article, we report that the interplay of Ile308 and Tyr310 residues is the least indispensable structural element for initiating the molecular association of 3R/4Rtau as well as of 3R/4RMBD, and the C–H... π interaction formed between their side chains functions as a conformational seed for triggering molecular self-association. Although the mechanism of tau PHF formation is not yet completely elucidated, the present result provides important information on key residues and structural scaffolds essential for initiating the molecular association, which is useful for designing AD inhibitors.

Experimental procedures

Chemicals

General laboratory chemicals and molecular biology reagents [heparin with a mean molecular weight around 6,000, and thioflavin S (ThS)] were purchased from (Sigma Co, MO, U.S.A.).

Preparation of VQIVYK residue-substituted MBD and tau mutants

A cDNA (clone T9) encoding the human brain tau gene (*2N4R*, *0N4R* and *0N3R*) was provided by Professor H. Mori (Osaka City University). Wild-type four repeat full-length tau (4Rtau), three repeat full-length tau (3Rtau) 4RMBD, and 3RMBD constructs (Fig. 1) were prepared by polymerase chain reaction amplification, using clone T9 as the template, as previously reported (24). The gene expression in *Escherichia coli* and the purification of histidine (His)-tagged 4R/3RMBD and 4R/3Rtau were performed as described in a previous article (21), and the purity of the recombinant protein was confirmed on the basis of a single band by SDS–PAGE.

A series of VQIVYK residue-substituted genes or Cys-substituted genes of His-tagged 4R/3RMBD and 4Rtau/3Rtau were obtained using several wild-type tau DNA, mutagenized primers and the QuikChange site-directed mutagenesis kit from (Stratagene, CA, U.S.A.). The gene expression and purification of a His-tagged mutant were performed in the same manner as that of the wild protein. The purity of each mutant was confirmed on the basis of a single band by SDS–PAGE. The sample concentration was determined by Bradford protein assay, measuring 280 nm UV absorption ($\epsilon = 1280 \text{ mol}^{-1} \text{ cm}^{-1}$ for Tyr residue).

ThS fluorescence measurement

A solution of each sample at 25 μM were prepared using 50 mM Tris–HCl buffer (pH 7.6), and 10 μM ThS was added. After adding 6.25 μM heparin, fluorescence intensity was measured with a JASCO FP-6500 instrument at 25°C, with an excitation at 440 nm and an emission at 500 nm. The background fluorescence of each sample solution was subtracted when needed. The averaged value of three times measurements was used for the data presentation.

Circular dichroism measurement

A solution of each sample at 25 μ M were prepared using 20-mM phosphate buffer (pH 7.6). After adding 6.25 μ M heparin, the circular dichroism (CD) spectral change was measured with a JASCO J-820 spectrometer at 25°C. For each experiment, eight spectra were summed up, and the molar ellipticity was determined after normalizing for the protein concentrations.

Electron microscopy measurement

A solution of each sample at 25 μ M was mixed with 6.25 μ M heparin in 50 mM Tris–HCl buffer (pH 7.6) and then incubated at 37°C for 48 h. Sample solutions (10 μ l) were placed on 600-mesh copper grids and negatively stained with 2% uranyl acetate for 1 min. The specimens were examined with an electron microscope (Hitachi Co., Tokyo, Japan) operated at 75 kV.

Results**Interplay between Ile and Tyr residues in the R3 repeat is essential for the aggregation of 3RMBD as well as of 4RMBD**

The aggregation behaviours of a series of 3RMBD mutants, in which the residue of the ³⁰⁶VQIVYK³¹¹ sequence was substituted with Ala or Tyr, were investigated by ThS fluorescence measurement, CD spectroscopy and EM. The results are summarized in Table I, in which some results of 4RMBD mutants (25) are given for comparison. Selected examples are shown in Fig. 2. The ThS fluorescence intensity of the monosubstituted mutant by Ala showed that the mutation of I308 or Y310 residue causes the complete disappearance of the filament formation, although the Ala mutation of other residues still has aggregation ability with a detectable extent (data not shown). To investigate the importance of Tyr at position 310 in the aggregation of 3RMBD, the aggregation behaviours of a series of Y310A-fixed and Tyr-scanned mutants of the ³⁰⁶VQIVYK³¹¹ sequence were investigated. Consequently, the following two important results

were observed. First, the aggregation ability of 3RMBD is considerably lost only by Y310A regardless of the Tyr substitution for other residues in the ³⁰⁶VQIVYK³¹¹ sequence, except Q307Y/Y310A. These mutants inhibited filament formation, although a small number of granulated aggregates were formed. In particular, the complete loss of aggregates was induced by I308Y/Y310A. Such a remarkable loss of aggregation ability by Y310A was also observed for 4RMBD, indicating that Tyr310 in the third repeat of MBD is essential for the filament formation despite the number of repeats. Second, Q307Y/Y310A shows a high aggregation ability and has a similar filament morphology to 3RMBD. This suggests that the self-association mechanism of Q307Y/Y310A is essentially the same as that of 3RMBD (discussed later).

The complete loss of the aggregation abilities of I308A, Y310A and I308Y/Y310A indicates clearly that the interplay between I308 and Y310 residues is essential for the molecular aggregation of 3RMBD. It is clear from Table I that these aggregation behaviours are almost the same as those of 4RMBD. Previously, we reported that the building units for molecular aggregation are different between 3RMBD and 4RMBD (22), that is, the intermolecular R3–R3 disulphide-bonded dimer for 3RMBD and the intramolecular R2–R3 disulphide-bonded monomer for 4RMBD. However, the present result indicates that the interplay between I308 and Y310 residues in the R3 repeat is a common structural element indispensable for initiating the molecular association of both MBDs.

Interplay between I308 and Y310 residues is based on the C–H... π interaction

The comparison between the aggregation abilities of wild MBD and its I308A or Y310A mutant (Table I)

Table I. Comparison of ThS fluorescences, CD amplitudes and EM morphologies of 3RMBD/4RMBD and their mutants (25 μ M)^{a,b}.

Wild/Mutant	Without DTT			With DTT	
	Relative fluorescence intensity (%)	Relative change (%) of molar ellipticity at 200 nm	EM morphology	Relative fluorescence intensity (%)	EM morphology
3RMBD	100	100	Filament	25	Short filament
Y310A	0	0	No granule and no filament	0	No granule and no filament
I308A	0	0	No granule and no filament	0	No granule and no filament
I308V	60	50	Short filament	20	Short filament
I308Y/Y310A	0	0	No granule and no filament	0	No granule and no filament
I308Y/Y310I	0	0	No granule and no filament	0	No granule and no filament
Q307Y	250	150	Filament + granule(+2)	300	Granule(+2)
Q307Y/Y310A	70	40	Short filament	20	Short filament
Q307Y/V309A/Y310A	0	0	No granule and no filament	0	No granule and no filament
4RMBD	100	100	Filament	120	Filament
Y310A	0	0	No granule and no filament	0	No granule and no filament
I308A	0	0	No granule and no filament	0	No granule and no filament
I308V	90	90	Filament	120	Filament
I308Y/Y310I	0	0	No granule and no filament	0	No granule and no filament
Q307Y	300	150	Filament + granule(+2)	300	Filament + granule(+2)
Q307Y/Y310A	100	90	Filament	120	Filament
Q307Y/V309A/Y310A	0	0	No granule and no filament	0	No granule and no filament

^aThe fluorescence intensities and CD amplitudes of mutants correspond to values relative to those of wild 3RMBD and 4RMBD without DTT at 1 h after initiating aggregation by addition of heparin.

^bEM morphology at 48 h after initiating aggregation by addition of heparin.

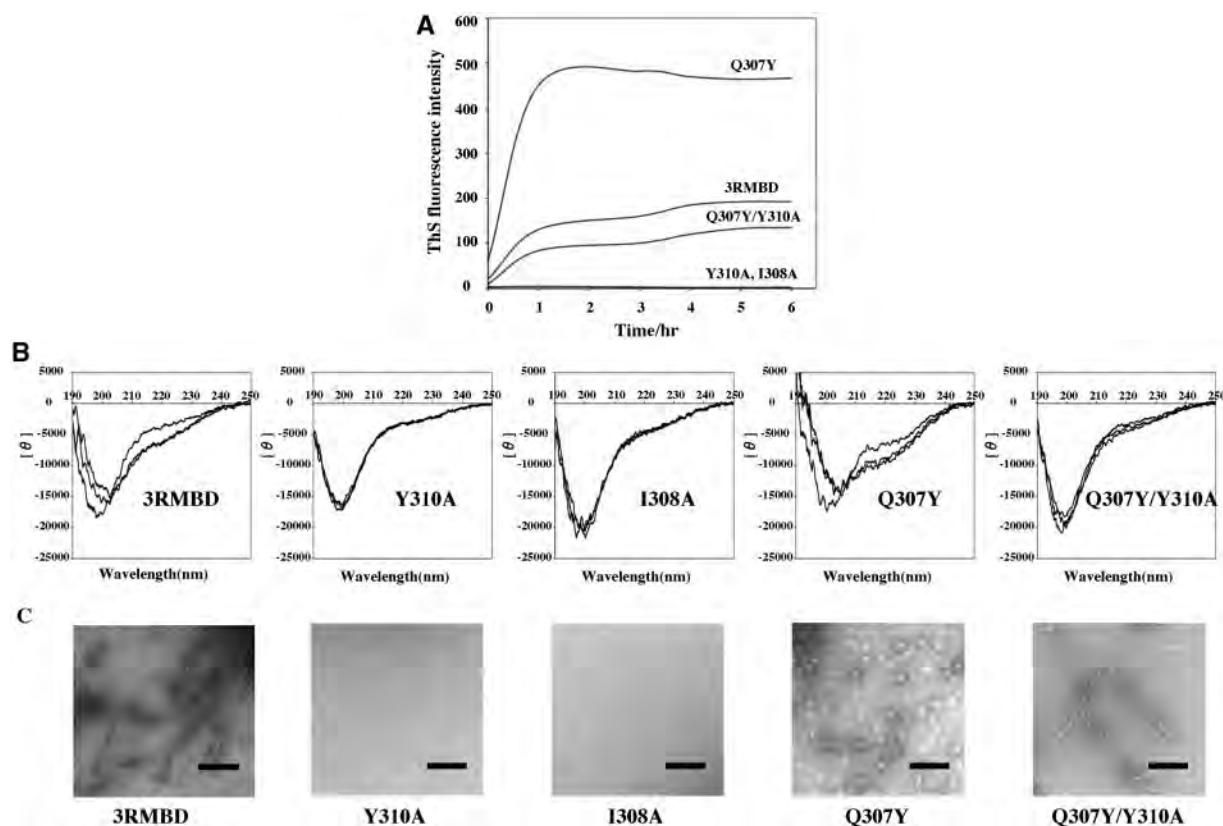


Fig. 2 (A) Time-dependent ThS fluorescence intensity profiles, (B) time-dependent CD spectral changes and (C) negative-staining EM images of 3RMBD and its Y310A, I308A, Q307Y and Q307Y/Y310A mutants. The Q307Y/V309A/Y310A mutant shows essentially the same results as I308A. The respective CD spectra from bottom to top at the 200 nm correspond to those obtained at 0 min, 3, 6 and 24 h after adding heparin to the solution. The length of the bar in (C) corresponds to 500 nm.

indicates that the interplay between I308 and Y310 is based on the C–H... π interaction between their residues, where the C–H group of the Ile side chain interacts with the π electron of the Tyr phenyl ring. This is supported by the suppressed aggregation ability of I308V compared with that of the wild type because Val has a lower hydrophobicity than Ile. It is important to note that the filament formation *via* the C–H... π interaction is dependent on the positional relationship between Ile and Tyr residues because I308Y/Y310I showed a complete loss of their molecular aggregation ability, similarly to the case of I308Y/Y301A. This clearly indicates that Ile should be located on the N-terminal side compared with Tyr, that is, the C–H... π interaction should be formed along the N side \rightarrow C side direction of the sequence.

As could be deduced from the aggregation behaviours of the Q307Y, Q307Y/Y310A and Q307Y/V309A/Y310A of 3R/4RMBD, a structural requirement for filament formation *via* the C–H... π interaction is a planar backbone of the $^{306}\text{VQIVYK}^{311}$ sequence. The $^{306}\text{VQIVYK}^{311}$ sequence in the R3 repeat was previously showed to be planar by NMR analysis in both aqueous and 2,2,2-trifluoroethanol solutions (26) and X-ray crystal structure (18). The planar conformation of $^{306}\text{VYIVYK}^{311}$ sequence in the Q307Y enables an intramolecular C–H... π interaction between I308 and Y310 residues on one side of

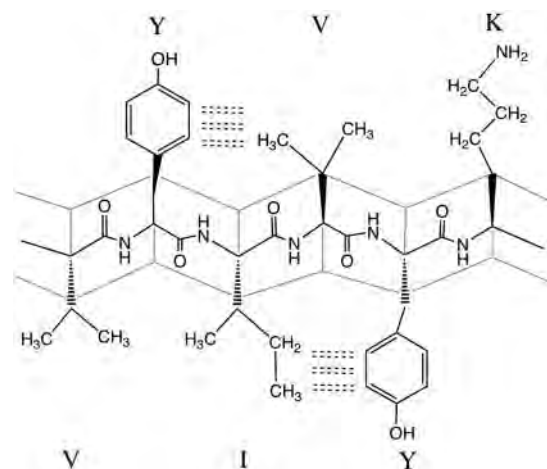


Fig. 3 Double C–H... π interactions of Q307Y–V309 and I308–Y310 pairs on both sides of planar VYIVYK backbone of R3 repeat in Q307Y mutant.

the plane and a similar C–H... π interaction between the Y307 and V309 residues on the opposite side (Fig. 3). These C–H... π interactions on both sides could almost be related with a 2-fold symmetry running along the centre of a pleated peptide plane of the VYIVYK sequence. This would be the reason Q307Y markedly increased aggregation rate, which became 3-fold higher than that of wild MBD. The similar

aggregation ability of Q307Y/Y310A to that of wild MBD and the complete lack of the aggregation ability of Q307Y/V309A/Y310A also support the C–H... π interaction between the V309 and Y307 side chains.

C–H... π interaction between Ile and Tyr residues in R3 repeat is essential for the molecular aggregation of 3R/4Rtau

To determine whether the common structural element indispensable for starting the molecular association of 3R/4RMBD is also applicable to that of full-length tau, a series of ³⁰⁶VQIVYK³¹¹ residue-substituted mutants of 3R/4Rtau were prepared and examined for their aggregation behaviours. The results are given in Table II, and some examples are shown in Fig. 4.

The CD spectra of 3R/4Rtau and their mutants showed no notable conformational change for >6 h after starting aggregation. This may result from that the flexible sequences bound to both sides of MBD affect the aggregation behaviour of tau in such a way that the structural change accompanied by the MBD aggregation is not smoothly propagated toward the whole structure. However, it is clear that the C–H... π interaction between I308 and Y310 residues is indispensable to the filament formation of 3R/4Rtau. The I308A and Y310A of 3R/4Rtau completely lost their aggregation ability. In contrast, I308V or Y310W showed similar aggregation ability to 4Rtau. A marked increase in the aggregation rate of Q307Y, probably due to double C–H... π interactions of Y307–V309 and I308–Y310 pairs, was also observed for 3R/4Rtau. These results clearly confirm the importance of the C–H... π interaction between the I308 and Y310 residues for the filament formation of tau as well as of its MBD.

On the other hand, the difference between the aggregation behaviours of tau and MBD was observed in the ThS fluorescence intensity and electron microscopy (EM) morphology of their Q307Y/Y310A mutants.

The Q307Y/Y310A of 3R/4Rtau no longer showed notable aggregation behaviour such as that of 3R/4RMBD, indicating that the single C–H... π interaction from the back side on the planar hexapeptide in the R3 repeat is not passable for the molecular aggregation of tau. This would be due to the effect of the N- and C-terminal flexible regions bound to both sides of MBD, because the N- and C-terminal regions remain largely disordered, form a fuzzy coat and fold back onto the repeats (27) to form transient intramolecular contact (28). In such a situation, it would be reasonable to consider that the filament formation of 3R/4Rtau proceeds via the C–H... π interaction between Ile308 and Tyr310 residues on one side of the R3 repeat, although no such a structural restriction is required up to the granule formation stage, as observed for Q307Y.

Different effect of reducing agent on molecular aggregations of MBD and tau

Our previous study clarified that the building units for 3RMBD and 4RMBD are intermolecular R3–R3 disulphide-bonded dimers and intramolecular R2–R3 disulphide-bonded monomers, respectively (22), and this difference results in the marked suppression and enhancement of the molecular aggregations of 3RMBD and 4RMBD, respectively, by the addition of DTT, a reducing agent (23). To confirm the effect of DTT on the molecular aggregations of 3R/4Rtau, the aggregation behaviours of the respective wild-type and mutants with and without DTT were compared in terms of the ThS fluorescence intensity and EM morphology; the results are given in Table II.

As previously reported, DTT enhanced the molecular aggregation of both wild and mutant 4RMBDs including a single C–H... π interaction, whereas the molecular aggregations of 3RMBD and its mutant via a single C–H... π interaction were considerably suppressed by DTT. DTT increased the fluorescence

Table II. Comparison of ThS fluorescences and EM morphologies of 3Rtau/4Rtau and their mutants (25 μ M)^{a,b}.

Wild/Mutant	Without DTT		With DTT	
	Relative fluorescence intensity (%)	EM morphology	Relative fluorescence intensity (%)	EM morphology
3Rtau	100	Filament	10	Granule(+1)
I308A	0	No granule and no filament	0	No granule and no filament
Y310A	0	No granule and no filament	0	No granule and no filament
Q307Y	300	Granule(+2)	300	Granule
Q307Y/Y310A	10	Granule(+1)	0	No granule and no filament
4Rtau	100	Filament	10	Granule(+1)
I308A	0	No granule and no filament	0	No granule and no filament
I308V	40	Short filament	5	No granule and no filament
Y310A	0	No granule and no filament	0	No granule and no filament
Y310W	100	Filament	150	Filament
I308Y/Y310I	0	No granule and no filament	0	No granule and no filament
Q307Y	300	Granule(+2)	300	Granule(+2)
Q307Y/Y310A	10	No granule and no filament	5	No granule and no filament
Q307Y/V309A/Y310A	0	No granule and no filament	0	No granule and no filament

^aThe fluorescence intensities of mutants correspond to the values relative to those of wild 3Rtau and 4Rtau without DTT at 1 h after initiating aggregation by addition of heparin.

^bEM morphology at 48 h after initiating aggregation by addition of heparin.

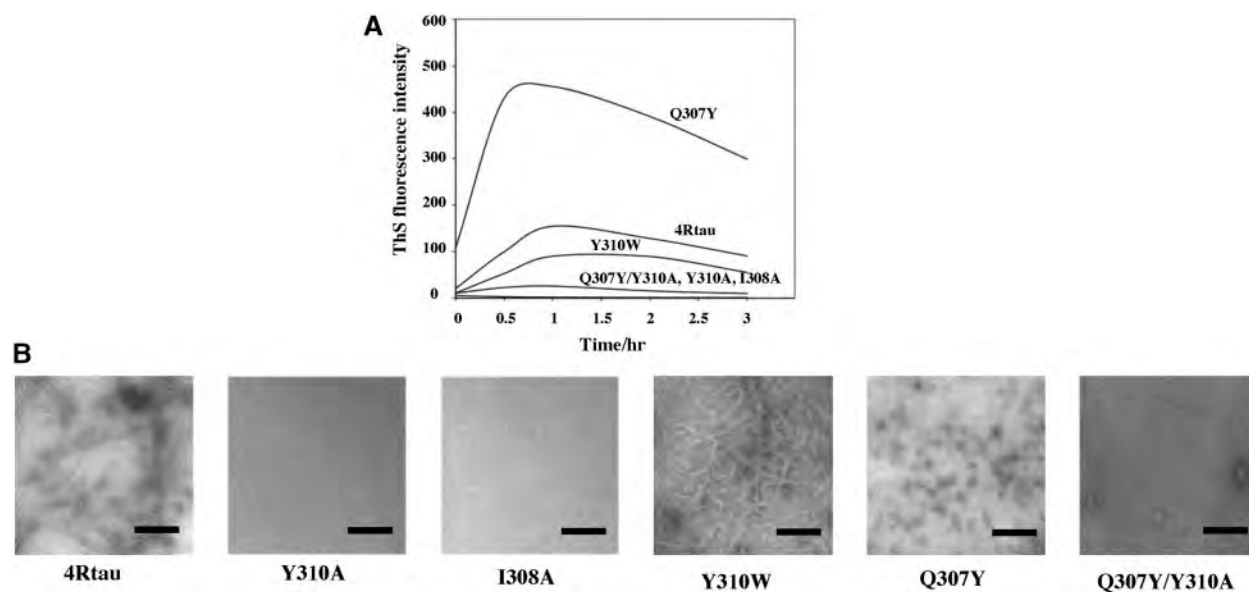


Fig. 4 (A) Time-dependent ThS fluorescence intensity profiles and (B) negative-staining EM images of 4Rtau and its Y310A, I308A, Y310W, Q307Y and Q307Y/Y310A mutants. The Q307Y/V309A/Y310A mutant shows essentially the same results as those of I308A. The length of the bar in (B) corresponds to 500 nm.

intensity of 4RMBD to nearly the same extent as that of 3RMBD without DTT, and this would indicate that the folded structure of the intramolecular R2–R3 disulphide-bonded 4RMBD is disadvantageous for the aggregation and the DTT-induced open structure confers 4RMBD similar aggregation ability to that of 3RMBD dimers, because we clarified that 4RMBD under a reduced solution is composed of the intermolecular associated dimers (21). In contrast, the DTT-induced transition of the intermolecular R3–R3 disulphide-bonded dimer of 3RMBD to the monomer lost its original aggregation ability.

On the other hand, the 3R/4Rtau showed a different behaviour from 3R/4RMBD. The ThS intensities of 3R/4Rtau were both decreased by the DTT addition, and this is in contrast to the cases of 3RMBD and 4RMBD, in which the DTT-dependent molecular aggregation process is dependent on, respectively, intermolecular and intramolecular disulphide bond formation. This discrepancy would mean that such disulphide bond formation is insufficient to control the overall aggregation behaviour of 3R/4Rtau, probably owing to the presence of flexible sequences attached to both the N- and C-terminal sides of MBD. However, the aggregation ability of the Q307Y mutant of 3R/4Rtau, as well as of 3R/4RMBD, having double C–H... π interactions within the R3 repeat was hardly affected by the addition of DTT. This would mean that the double C–H... π interactions on the R3 core moiety precede the disulphide bond formation for the molecular association, and the interaction provides the platform that is indispensable for starting molecular association, although it does not proceed to the mature filament formation.

To investigate the roles of the Cys291 and Cys322 residues of tau in the filament formation, Ala-substituted mutants of 4R/3RMBD and 3R/4Rtau

Table III. Comparison of ThS fluorescences and EM morphologies of C291A and/or C322A mutants of 4R/3RMBD and 4R/3Rtau (25 μ M)^{a,b}.

Wild/Mutant	Relative fluorescence intensity (%)	EM morphology
4RMBD	100	Filament
C291A	100	Filament
C322A	80	Filament
C291A/C322A	120	Filament
3RMBD	100	Filament
C322A	20	Short filament
4Rtau	100	Filament
C291A/C322A	20	Granule(+1)
3Rtau	100	Filament
C322A	10	Granule(+1)

^aThe fluorescence intensities of mutants correspond to values relative to those of wild-types at 1 h after initiating aggregation by addition of heparin.

^bEM morphology at 48 h after initiating aggregation by addition of heparin.

were prepared. Their ThS fluorescence intensities and EM morphologies are given in Table III. The results showed the different role between the Cys residues of 3RMBD and 4RMBD in their filament formations; the results were about in accord with those of DTT effect on the intra/intermolecular disulphide bond formation in their molecular aggregations. In contrast, no notable difference was observed for 3R/4Rtau and these Ala-substituted mutants similarly decreased the ThS fluorescence intensities and transformed the filamentous morphology to small granules, similar to the case of DTT addition to wild 3R/4Rtau. This clearly indicates the participation of Cys residues in the second and third repeats in mature filament formation of tau. Therefore, we could state that intermolecular/intramolecular disulphide-bonded formation formed in 3R/4RMBD participates importantly in the filament

formation of 3R/4Rtau, although DTT-dependent aggregation behaviour is different between MBD and tau.

Discussion

The filament formation of tau protein is based on short hexapeptide motif (VQIVYK) in the R3 repeat domain of MBD. This short motif has a planar conformation even though tau protein has a random structure. The VQIVYK sequence, in addition to its structural character, has a partially hydrophobic character and tend to make a cross β -structure, which is the core of PHF.

The crystal structure of the VQIVYK peptide reported by Sawaya *et al.* (18) provides a molecular view of the structural organization of the spine of tau fibrils. In the crystal structure, the peptide adopts a planar conformation and forms an anti-parallel β -sheet with a neighbouring peptide that combines in a face-to-face interdigitating dry 'steric zipper' structure, where the back surface of this β -sheet constitutes a wet interface linked through water molecules.

The planar backbone conformation of VQIVYK peptide enables the direct interactions between the Ile and Tyr side chains on the same side of the peptide plane and between the Gln and Lys side chains on the other side. Therefore, it would be reasonable in a polar environment such as an aqueous solution to consider that the C–H... π interaction between the side chains of the Ile and Tyr residues under the hydrophobic environment provides a conformational seed to form an anti-parallel β -sheet with the VQIVYK sequence of the other R3 repeat. As determined from the results given in Tables I and II, it could say that this C–H... π interaction is the common structural element for initiating the molecular association of 3R/4RMBD and 3R/4Rtau irrespective of their difference in aggregation pathway.

Generally, the filament formation of tau can be divided into the following stages: activation \rightarrow nucleation \rightarrow extension \rightarrow PHF formation. The EM figures showed either a filament or a granule as the aggregation form of wild or mutant tau. Herein, we discuss the possible relation between the aggregation form (filament or granule) and its association stage. From the relationship between the dynamic light scattering (DLS) data and EM pictures, we previously reported that the granule forms of MBD correspond to the nucleation state, which does not further proceed to the extension stage, whereas the filament form proceeds to the stage of PHF formation (23). It is clear that wild 3R/4RMBD and 3R/4Rtau proceed to the PHF stage through continuous molecular piling irrespective of the number of repeats. Thus, as a possible reason why some mutants stop at the granular nucleation stage, it could say that such systematic piling is impossible because of the structural disorder probably due to an unsystematic molecular association, although the aggregation is allowed up to the nucleation stage to some extent. In the case of the Q307Y mutant, the double C–H... π interactions of Val309–Tyr307 and Ile308–Tyr310 pairs would enable the rapid aggregation progress up to the nucleation stage, but not up to the filament

formation stage, and this would be further due to the disturbance of alternative hydrophobic/hydrophilic stacking layer of the molecules. The presence of N- and C-terminal flexible regions bound to both terminals of MBD affect the aggregation behaviour of full-length tau concerning the time dependence of CD spectral change and the effect of DTT on the aggregation, which are considerably different from those of MBD.

On the basis of previous results that the building units for molecular aggregations of 4RMBD and 3RMBD are intramolecular R2–R3 disulphide-bonded monomer and intermolecular R3–R3 disulphide-bonded dimer, respectively, possible aggregation pathway is proposed in Fig. 5A and B. The four-repeat tau forms an intramolecular Cys291–Cys322 disulphide bond between the second and third repeats under a physiological condition (Fig. 5A). This conformational restriction and the presence of Pro301 and Pro312 residues would enable the formation of a U-shaped structure at the R2–R3 linkage of 4RMBD, where these Pro residues are located at both corners. This model shows that the anti-parallelly arranged MBDs pile up through the alternate hydrophobic and hydrophilic interactions among the neighbouring SVQIVYK β -strands along the fiber direction. In this model, the double C–H... π formation by the Q307Y mutation would change the hydrophilic interaction into the hydrophobic one, thus resulting in a rapid aggregation to the granule form in an aqueous solution. On the other hand, three-repeat tau would form a parallel dimer by the intermolecular disulphide bond of Cys322 residue in the third repeat (Fig. 5B). The parallel dimer would be stabilized by the hydrophilic interaction between the polar residues of SVQIVYK β -strands, where the VQIVYK plane in the Gly302–Lys311 sequence is rotatable around the ω torsion angles of Pro301–Gly302 and Lys311–Pro312 bonds because of the lack of a notable energy barrier between the *trans* and *cis* isomers at the Pro–Gly and Lys–Pro peptide bonds and of the lack of an intramolecular disulphide bond within MBD, different from the case of 4RMBD. The neighbouring parallel dimers would be stacked in an anti-parallel manner and piled up along the fiber direction through alternative hydrophobic/hydrophilic interactions among the KVQIVYK β -strands. The double C–H... π formation by Q307Y mutation would increase aggregation rate by the same reason as that for 4Rtau.

In conclusion, the present results indicated that two factors are important for molecular aggregation of tau: one is that the C–H... π interaction between Ile308 and Tyr310 side chains is an essential structural factor that enables the initial self-association of 3R/4Rtau as well as 3R/4RMBD and the other is that the intermolecular/intramolecular disulphide bond formation in 3R/4RMBD participates importantly in the filament formation of 3R/4Rtau. Although the mechanism of tau PHF formation remains to be elucidated, the present work provides important information on key residues and structural scaffolds essential for initiating the molecular association, which is important for designing AD inhibitors.

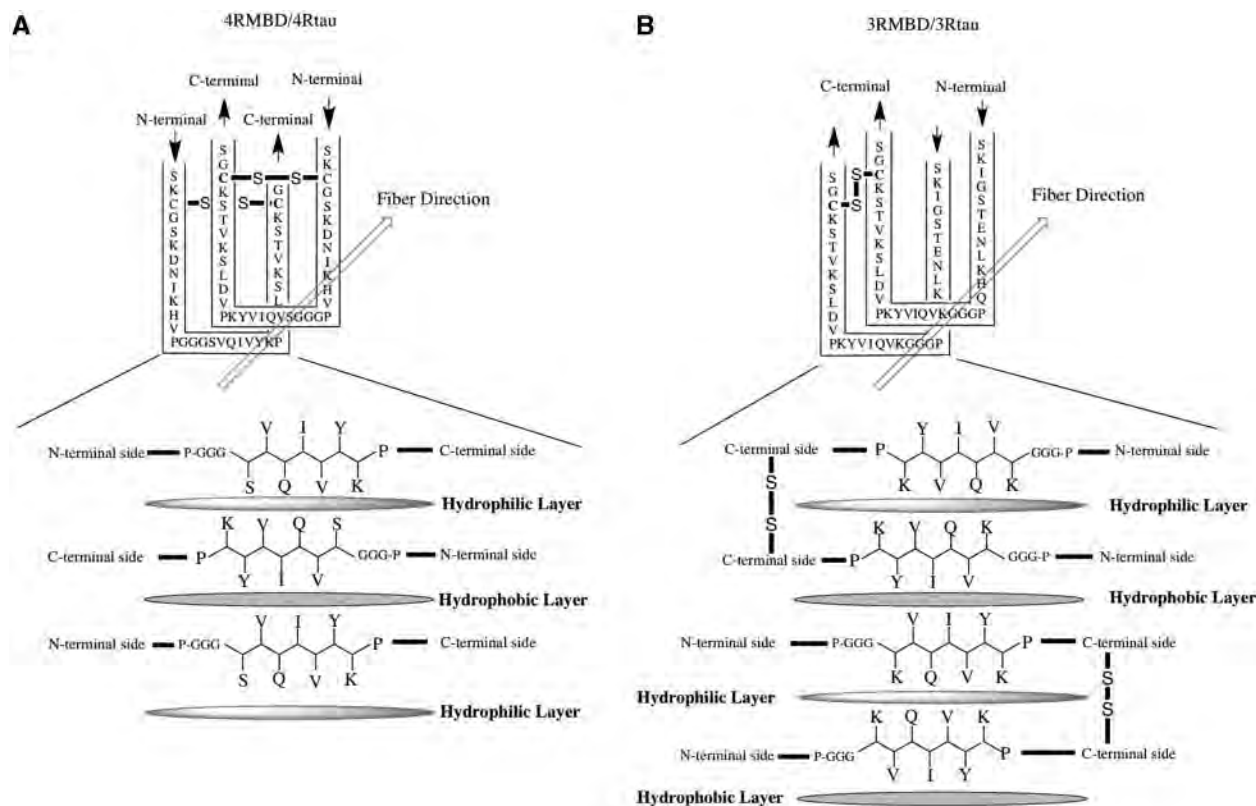


Fig. 5 Schematic aggregation models of (A) 4RMBD/4Rtau and (B) 3RMBD/3Rtau. The overall structure of 4R/3RMBD and its piling direction are shown on the upper side, and the alternate hydrophobic and hydrophilic interaction modes between neighbouring VQIVYK β -strands are shown on the lower side.

Funding

Grant-in-Aid for High Technology Research from the Ministry of Education, Culture, Sports, Science and Technology, Japan.

Conflict of interest

None declared.

References

- Delacourte, A. and Buee, L. (1997) Normal and pathological tau proteins as factors for microtubule assembly. *Int. Rev. Cytol.* **171**, 167–224
- Ballatore, C., Brunden, K.R., Trojanowski, J.Q., Lee, V.M.Y., Smith, A.B. III, and Huryn, D.M. (2011) Modulation of protein-protein interactions as a therapeutic strategy for the treatment of neurodegenerative tauopathies. *Curr. Top. Med. Chem.* **11**, 317–330
- Goedert, M. and Spillantini, M.G. (2000) Tau mutations in frontotemporal dementia FTDP-17 and their relevance for Alzheimer's disease. *Biochim. Biophys. Acta.* **1502**, 110–121
- Gendron, T.F. and Petrucelli, L. (2009) The role of tau in neurodegeneration. *Mol. Neurodegen.* **4**, 13
- Braak, H. and Braak, E. (1991) Neuropathological staging of Alzheimer-related changes. *Acta. Neuro. Pathol.* **82**, 239–259
- Bandyopadhyay, B., Li, G., Yin, H., and Kuret, J. (2007) Tau aggregation and toxicity in a cell culture model of tauopathy. *J. Biol. Chem.* **282**, 16454–16464
- Maeda, S., Sahara, N., Saito, Y., Murayama, M., Yoshiike, Y., Kim, H., Miyasaka, T., Murayama, S., Ikai, A., and Takashima, A. (2007) Granular tau oligomers as intermediates of tau filaments. *Biochemistry* **46**, 3856–3861
- Maeda, S., Sahara, N., Saito, Y., Murayama, S., Ikai, A., and Takashima, A. (2006) Increased levels of granular tau oligomers: an early sign of brain aging and Alzheimer's disease. *Neurosci. Res.* **54**, 197–201
- Lasagna-Reeves, C.A., Castillo-Carranza, D.L., Guerrero-Munoz, M.J., Jackson, G.R., and Kaye, R. (2010) Preparation and characterization of neurotoxic tau oligomers. *Biochemistry* **49**, 10039–10041
- Goedert, M., Spillantini, M.G., Portier, M.C., Ulrich, J., and Crowther, R.A. (1989) Cloning and sequencing of the cDNA encoding an isoform of microtubule-associated protein tau containing four tandem repeats: differential expression of tau protein mRNAs in human brain. *EMBO J.* **8**, 393–399
- Goedert, M., Spillantini, M.G., Jakes, R., Rutherford, D., and Crowther, R.A. (1989) Multiple isoforms of human microtubule-associated protein tau: sequences and localization in neurofibrillary tangles of Alzheimer's disease. *Neuron* **3**, 519–526
- Goedert, M. and Jakes, R. (1990) Expression of separate isoforms of human tau protein: correlation with the tau pattern in brain and effects on tubulin polymerization. *EMBO J.* **9**, 4225–4230
- Lee, G., Neve, R.L., and Kosik, K.S. (1989) The microtubule-binding domain of tau protein. *Neuron* **2**, 1615–1624
- Butner, K.A. and Kirschner, M.W. (1991) Tau protein binds to microtubules through a flexible array of distributed weak sites. *J. Cell. Biol.* **115**, 717–730

15. Goode, B.L. and Feinstein, S.C. (1994) Identification of a novel microtubule binding and assembly domain in the developmentally regulated inter-repeat region of tau. *J. Cell. Biol.* **124**, 769–782
16. Von Bergen, M., Friedhoff, P., Biernat, J., Heberle, J., Mandelkow, E.M., and Mandelkow, E. (2000) Assembly of tau protein into Alzheimer paired helical filaments depends on a local sequence motif ((306)VQIVYK(311)) forming beta structure. *Proc. Natl. Acad. Sci. USA* **97**, 5129–5134
17. Von Bergen, M., Barghorn, S., Li, L., Marx, A., Biernt, J., Mandelkow, E.M., and Mandelkow, E. (2001) Mutations of tau protein in front temporal dementia promote aggregation of paired helical filaments by enhancing local beta-structure. *J. Biol. Chem.* **276**, 48165–48174
18. Sawaya, M.R., Sambashivan, S., Nelson, R., Ivanova, M.I., Sievers, S.A., Apostol, M.I., Thompson, M.J., Balbirnie, M., Wiltzius, J.J.W., McFarlane, H.T., Madsen, A.O., Riek, C., and Eisenberg, D. (2007) Atomic structures of amyloid cross- β spines reveal varied steric zipper. *Nature* **447**, 453–457
19. Hong, M., Zukareva, V., Vogelsberg-Ragaglia, V., Wszolek, Z., Reed, L., Miller, B., Geschwind, D.H., Bird, T.D., McKeel, D., Goate, A., Morris, J.C., Wilhelmsen, K.C., Schellenberg, G.D., Trojanowski, J.Q., and Lee, V.M.Y. (1998) Mutation-specific functional impairments in distinct tau isomers of hereditary FTDP-17. *Science* **282**, 1914–1917
20. Lu, M. and Kosik, K.S. (2001) Competition for microtubule-binding domain with dual expression of tau missense and splice isoforms. *Mol. Biol. Cell.* **12**, 171–184
21. Yao, T.M., Tomoo, K., Ishida, T., Hasegawa, H., Sasaki, M., and Taniguchi, T. (2003) Aggregation analysis of the microtubule-binding domain in tau protein by spectroscopic methods. *J. Biochem.* **134**, 91–99
22. Okuyama, K., Nishiura, C., Mizushima, F., Minoura, K., Sumida, M., Taniguchi, T., Tomoo, K., and Ishida, T. (2008) Linkage-dependent contribution of repeat peptides to self-aggregation of three- or four-repeat microtubule-binding domains in tau protein. *FEBS J.* **275**, 1529–1539
23. Sugino, E., Nishiura, C., Minoura, K., In, Y., Sumida, M., Taniguchi, T., Tomoo, K., and Ishida, T. (2009) Three-/four repeat-dependent aggregation profile of tau microtubule-binding domain clarified by dynamic light scattering analysis. *Biochem. Biophys. Res. Commun.* **385**, 236–240
24. Nishiura, C., Takeuchi, K., Minoura, K., Sumida, M., Taniguchi, T., Tomoo, K., and Ishida, T. (2010) Importance of Tyr310 residue in the third repeat of microtubule binding domain for filament formation of tau protein. *J. Biochem.* **147**, 405–414
25. Naruto, K., Minoura, K., Okuda, R., Taniguchi, T., In, Y., Ishida, T., and Tomoo, K. (2010) Interplay between I308 and Y310 residues in the third repeat of microtubule-binding domain is essential for tau filament formation. *FEBS Lett.* **584**, 4233–4236
26. Minoura, K., Tomoo, K., Ishida, T., Hasegawa, H., Sasaki, M., and Taniguchi, T. (2003) Solvent-dependent conformation of the third repeat fragment in the microtubule-binding domain of tau protein, analyzed by $^1\text{H-NMR}$ spectroscopy and molecular modeling calculation. *Bull. Chem. Soc. Jpn* **76**, 1617–1624
27. Jeganathan, S., Von Bergen, M., Brutlach, H., Steinhoff, H.J., and Mandelkow, E. (2006) Global hairpin folding of tau in solution. *Biochemistry* **45**, 2283–2293
28. Mukrasch, M.D., Bibow, S., Korukottu, J., Jeganathan, S., Biernat, J., Griesinger, C., Mandelkow, E., and Zweckstetter, M. (2009) Structural polymorphism of 441-residue tau at single residue resolution. *PLoS Biol.* **7**, e34

生体分子の立体構造と分子間相互作用の研究を振り返って

石田 寿昌

Overview of Structural Study on Conformations and Intermolecular Interactions of Biomolecules

Toshimasa Ishida

*Laboratory of Physical Chemistry, Osaka University of Pharmaceutical Sciences;
4-20-1 Nasahara, Takatsuki, Osaka 569-1094, Japan.*

(Received March 20, 2012)

Information on the conformational feature and specific intermolecular interaction of biomolecules is important to understand the biological function and to develop device for treating disorder caused by the abnormal function. Thus the 3D structures of the biologically active molecules and the specific interactions with their target molecules at the atomic level have been investigated by various physicochemical approaches. Herein, the following five subjects are reviewed: (1) function-linked conformations of biomolecules including natural annular products, opioid peptides and neuropeptides; (2) π - π stacking interactions of tryptophan derivatives with coenzymes and nucleic acid bases; (3) mRNA cap recognition of eukaryotic initiation factor 4E and its regulation by 4E-binding protein; (4) conformational feature of histamine H2 receptor antagonists and design of cathepsin B inhibitors; (5) self-aggregation mechanism of tau protein and its inhibition.

Key words—conformation; biomolecule; mRNA cap recognition; initiation factor 4E; inhibitor; tau aggregation

1. はじめに

昭和45年4月、生薬などの天然医薬品の構造-活性相関の研究をされていた井上正敏先生（大阪薬科大学）の薬品物理化学教室助手として採用され、粉末X線回折法や熱分析法による「グリセロリン酸カルシウムの構造と物性」に関する研究を開始した。その後、研究を進展させる上でX線結晶構造解析法を習得する必要性から、大阪大学大学院薬学研究科修士課程（富田研一先生の薬品物理化学講座）に進学した。幸い、3年後の昭和51年4月に本学の同研究室助手として再採用が認められ現在に至っている。以来、一貫して生体分子の立体構造とその分子間相互作用に関する構造化学的研究を行ってきた。すなわち、X線結晶解析法を始め各種物理化学的手法を駆使し、生理活性分子の立体構造と活性の相関について、また、補酵素、核酸やタンパク質

構成分子とその標的分子との特異的相互作用（認識機構）の解明について研究を進めてきた。本稿では(1)生理活性分子の立体構造と活性に関する研究、(2)トリプトファンと補酵素及び核酸塩基とのスタッキング相互作用に関する研究、(3)タンパク質生合成開始因子eIF4EによるmRNAキャップ認識機構と4E-結合タンパク質によるその制御機構に関する研究、(4)ヒスタミンH2受容体拮抗剤の構造特徴とカテプシンB阻害剤の開発に関する研究、そして(5)認知症原因タンパク質タウの自己重合機構とその阻害剤に関する研究について概説する。

2. 生理活性分子の立体構造と活性相関

生体あるいは天然由来の生理活性分子の構造活性相関に関する研究は新規医薬品の開発において重要である。多くの生理活性分子の機能発現には特定の立体構造あるいは活性コンフォメーションをとると考えられる。それゆえ、活性が異なる一連の類似分子の立体構造情報は、活性分子の構造活性相関を考える上で重要である。

2-1. グリセロリン酸カルシウム グリセロリン酸カルシウム (CaG) は生体中のカルシウムイオ

The author declares no conflict of interest.

大阪薬科大学（〒569-1094 高槻市奈佐原4丁目20番1号）

e-mail: t-ishida@diary.ocn.ne.jp

本総説は、平成23年度退職にあたり在職中の業績を中心に記述されたものである。

ンやリン酸基の供給源として用いられている。グリセロリン酸は生体膜の構成分子であることから、CaG の構造研究はカルシウムイオンの膜輸送機構を考える上で重要である。CaG には α -CaG と β -CaG の 2 種類があり α -CaG は無水物、1 水和物、2 水和物の 3 種類、 β -CaG には無水物と 1 水和物の 2 種類の結晶形を有していることを明らかにした。それぞれの結晶形をエネルギー計算、粉末 X 線回折法、熱分析法により解析し、CaG の安定コンフォメーション及び水分子に対する結合安定性と結合様式との関係を明らかにした。^{1,2)} また、 β -CaG 無水物の X 線結晶構造解析はカルシウムイオンとグリセロリン脂質との結合様式を明らかにした (Fig. 1).³⁾

2-2. 環状化合物 これまで解析した主な天然由来の環状化合物のコンフォメーションの特徴と活性との関係について述べる。

2-2-1. アシジアサイクラマイド類 海洋生物

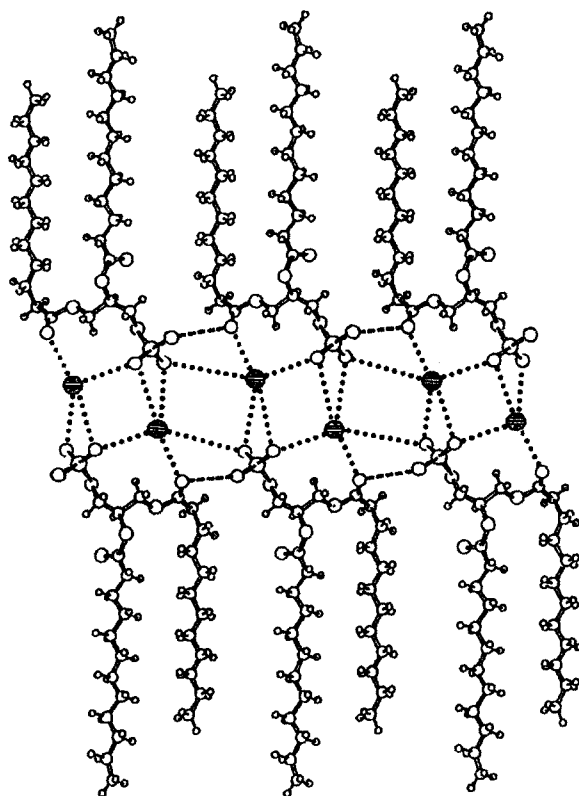


Fig. 1. Binding Mode of Calcium Ion to Phospholipid Based on the Crystal Structure of Calcium Glycerophosphate
Shaded circles and broken and dotted lines represent calcium ions, hydrogen bonds and coordination bonds, respectively.

ホヤから単離された一連の環状ペプチド類 (Fig. 2) は強い抗腫瘍・殺細胞活性を示す。^{4,5)} いずれもチアゾール環とオキサゾリン環の異常アミノ酸をともに含み、分子内 2 回回転対称の環状構造を有しているのが特徴である。アシジアサイクラマイド、^{6,7)} ユリチアサイクラマイド⁸⁾ そしてパテラマイド⁹⁻¹¹⁾ の溶液あるいは結晶構造解析から、これら環状ペプチドは Type II と Type III の 2 種類のコンフォメーションが可能で、Type I の構造を介して可逆的構造変換が行われることを明らかにした (Fig. 3)。アシジアサイクラマイド及びユリチアサイクラマイドは Type II が、パテラマイド B-D は Type III が優位コンフォメーションであることから、分子内 2 回対称からの構造ずれが Type II から Type III へのコンフォメーション変換のトリガーになっている。アシジアサイクラマイドとパテラマイドは同程度の抗腫瘍・殺細胞活性を示す⁴⁾ ことからアシジアサイクラマイド類の活性コンフォメーションとして Type II と III のいずれであるかは断定できないが、最も活性の高いユリチアサイクラマイドが Type II であることから、Type II のコンフォメーション (Fig. 4) が活性型であると考えられる。このコンフォメーションから明らかのように、活性発現に関係する構造特徴としては、(i) 分子内 2 回対称の環形成、(ii) チアゾール環とオキサゾリン環による円筒状に折れ曲がった (2.6-2.9 Å の曲率半径) 馬の鞍型構造、(iii) 環状構造の内側に向けた NH 基の水素結合を介した極性分子の補足と環状構造から突き出した非極性側鎖間の疎水結合による溶媒分子の補足などが挙げられる。

2-2-2. スウィンホライド 海綿の脂溶性画分から単離されるスウィンホライド類 (Fig. 5) は強い抗腫瘍活性を示す二量体マクロライドで、44 員環ラクトン構造を有している。¹²⁾ 一方、ラクトン環の巻き方が異なるイソスウィンホライド A にはそのような活性がみられないことから、この二量体マクロライドの立体構造と活性との相関に興味を持たれる。

スウィンホライド A のブロム誘導体の X-線構造解析から、Fig. 5 に示す絶対構造とそのコンフォメーション (Fig. 6) を明らかにした。構造特徴として、(i) 環状構造は平面から大きく反り返った馬の鞍型構造、(ii) 2 回回転対称が保持された 44 員環構

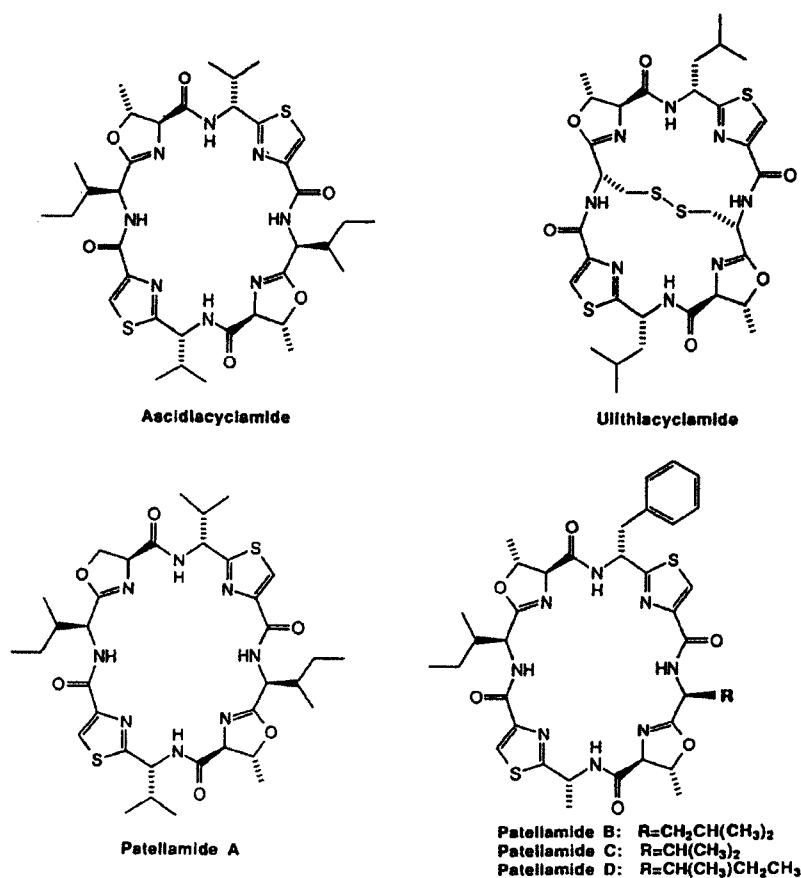


Fig. 2. Chemical Structures of Several Cytotoxic Cyclic Peptides Isolated from Ascidian

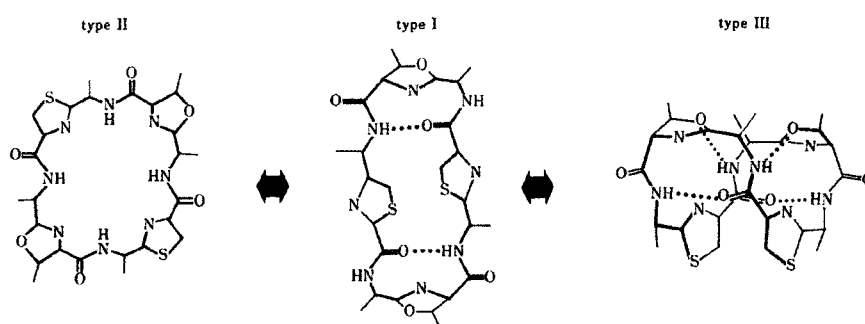


Fig. 3. Conformational Transition among Types I-III
Dotted lines represent intramolecular hydrogen bonds.

造, (iii)分子内水素結合形成の欠如とファンデルワールス接触による環構造の安定化, (iv)水酸基及びエーテル様酸素の環内への配向等がみられる. 活性を示さないイソスウィンホライド A の分子動力学 (MD) 計算によるコンフォメーション比較から, スウィンホライドの活性発現にこれらの構造特徴の重要性が示唆された.^{13,14)}

2-2-3. オーレオバシジン E 微生物 *Aureobasidium pullulans* の代謝産物であるオーレオバシジン類 (A-R) は低毒性の抗真菌抗生物質である.¹⁵⁾ オーレオバシジン E の構造式を Fig. 7 に示す. いずれも 8 個のアミノ酸ユニットと 1 つの水酸基ユニット (Hmp) から構成されていて, Hmp と β -HOMeVal 間でのエステル結合による 27 員環構

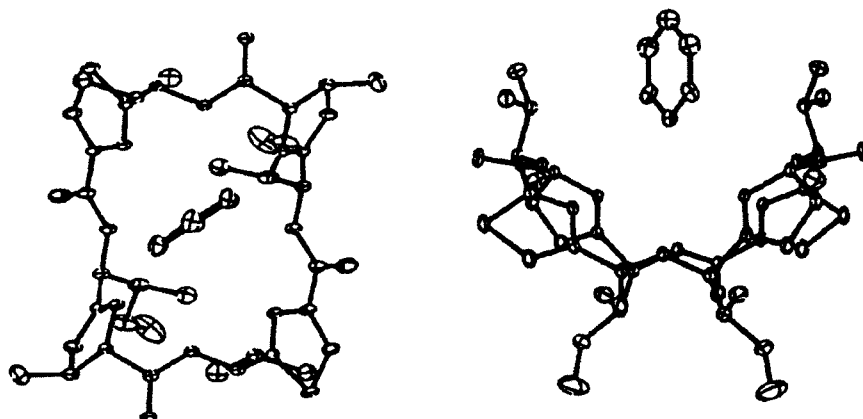


Fig. 4. Molecular Conformation of Benzene Including Ascidiacyclamide (type II), Viewed along the C_2 -Symmetry Axis (left) and Perpendicular to the Axis (right)

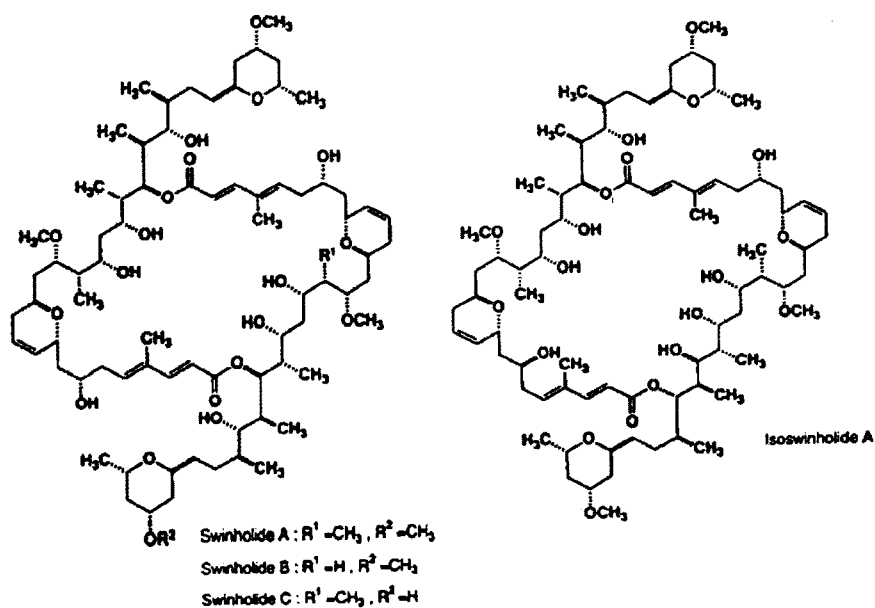


Fig. 5. Chemical Structure of Swinholide Family

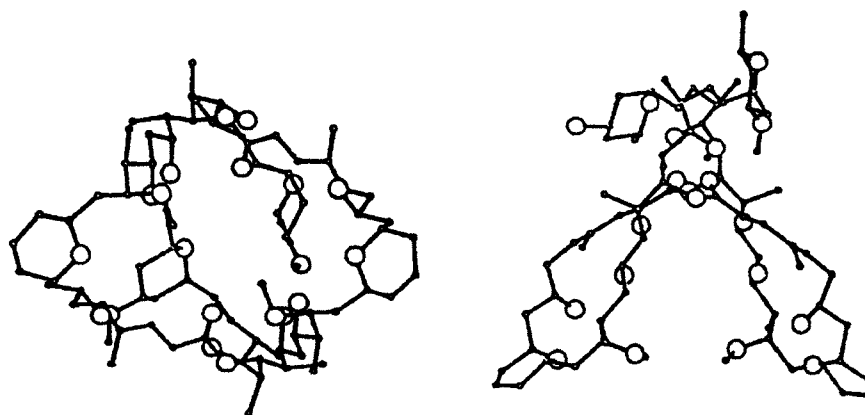


Fig. 6. Molecular Conformation of Swinholide A, Viewed along the Pseudo C_2 -Symmetry Axis (left) and Perpendicular to the Axis (right)

Oxygen atoms are shown by open circles.

造が形成されている。Figure 8は構造解析によって得られたオーレオバシジン E の立体コンフォメーションを示している。¹⁶⁻¹⁸⁾ 27 員環構造は 3 本の分子内水素結合によって安定化され、全体として“やじり”様の五角形構造をとっている。 β -HOMeVal がその先端部分に配座し、その水酸基は隣接する Hmp 及び β -HOMeVal のカルボニル酸素との二股の水素結合によって固定されている。この構造特徴は 7 個のアミド基のうちの 4 個はメチル化されているため、残り 3 組のペアによる分子内水素結合が環内で優先的に形成されることである。したがって、

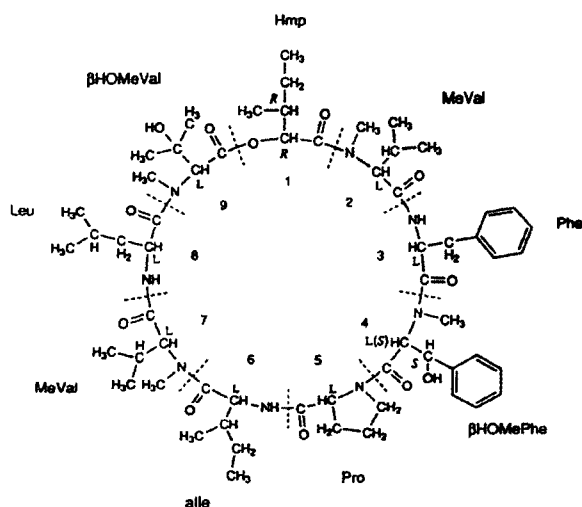


Fig. 7. Chemical Structure of Aureobasidin E

解析によって明らかになった“やじり”様の五角形構造がオーレオバシジン類の活性コンフォメーションを反映していると考えられる。DMSO 中での NMR 解析と MD 計算からも同様な結論が得られている。¹⁷⁾

これ以外の大環状化合物としては微生物 *Alkalophilic actinomycete* から単離され、細胞毒性、駆虫活性を有する 28 員環マクロライド抗生物質 IKD-8344¹⁹⁾ の立体構造を解析した。²⁰⁾

2-3. オピオイドペプチド モルヒネ様活性を有する内因性オピオイドとして発見されたエンケファリン (ENK) は 5 つのアミノ酸からなるペプチドで、生体内ではメチオニンエンケファリン (MENK) とロイシンエンケファリン (LENK) が存在する。²¹⁾ 一方、ENK と結合するレセプターとしては μ , δ , κ , σ 等の複数のサブクラスが存在するが、主に μ 及び δ レセプターへの結合を介して ENK が機能していると考えられている。²²⁾

これまでに Table 1 に示す LENK, MENK,²³⁻³⁰⁾ dermorphin (DER),³¹⁾ deltorphin (DEL), deltorphin-I (DEL-I), deltorphin-II (DEL-II),^{32,33)} endomorphin-1 (EM-1), endomorphin-2 (EM-2)³⁴⁻³⁶⁾ 及びその関連ペプチドを用い、そのコンフォメーションを X 線結晶構造解析や溶液中での NMR 解析により明らかにしてきた。しかし、直鎖ペプチドのコンフォメーションは一様でなく、用いる溶媒に依

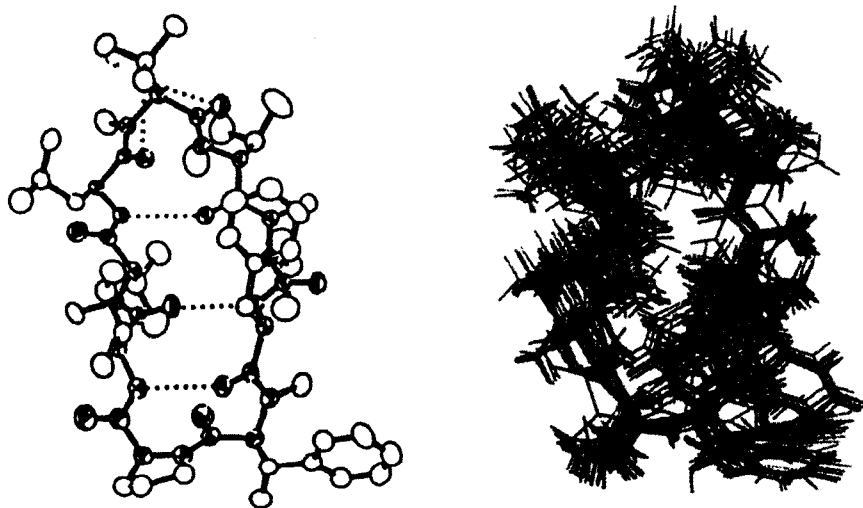


Fig. 8. Molecular Conformation of Aureobasidin E in Crystal (left) and Superposition of the 40 Converged Structures in Solution (right)

Backbone chain is shown by filled bond. Intramolecular hydrogen bonds are shown by dotted lines.

Table 1. Abbreviation, Sequence and μ/δ -binding Ratio of Opioid Peptide

Abbreviation	Sequence	Ratio (μ/δ)*
Morphine		5.6
LENK	Tyr-Gly-Gly-Phe-Leu	0.021
MENK	Tyr-Gly-Gly-Phe-Met	0.065
DEL	Tyr-D-Met-Phe-His-Leu-Met-Asp-NH ₂	6.6×10^{-4}
DEL-I	Tyr-D-Ala-Phe-Asp-Val-Val-Gly-NH ₂	1.5×10^{-4}
DEL-II	Tyr-D-Ala-Phe-Glu-Val-Val-Gly-NH ₂	1.6×10^{-4}
DER	Tyr-D-Ala-Phe-Gly-Tyr-Pro-Ser-NH ₂	12.56
EM-1	Tyr-Pro-Trp-Phe-NH ₂	3.6
EM-2	Tyr-Pro-Phe-Phe-NH ₂	59.4

* Ratio of binding assay (IC₅₀, nM) of opioid to guinea pig ileum (μ -opioid receptor) and mouse vas deferens (δ -opioid receptor).

Table 2. Molecular Conformation of Enkephalin Analogue

Peptide	Conformation
Tyr-Gly-Gly-Phe-Leu 2H ₂ O	β -turn
Tyr-Gly-Gly-Phe-Leu 2H ₂ O 2DMF	extend
Tyr-Gly-Gly-(4-Br)Phe-Leu 2.5H ₂ O	β -turn
Boc-Tyr-Gly-Gly-(4-Br)Phe-Met 2H ₂ O	extend
Tyr-Gly-Gly-(4-Br)Phe-Met 4.5H ₂ O	extend
Tyr-Gly-Gly-Phe-Met 5H ₂ O	extend
Tyr-Gly-Gly-Phe-Leu H ₂ O	extend
Tyr-D-Nle-Gly-Phe-Nle 2.5H ₂ O CH ₃ OH	β -turn
Tyr-Gly-Gly-Phe-Leu 0.5H ₂ O	extend
Tyr-Gly-Gly-Phe-Met 5.3H ₂ O	extend
Tyr-Gly-Gly-Phe-Met 3H ₂ O	extend
Tyr-Gly-Gly-Phe-Leu 3H ₂ O	S-shaped fold

存してその優位コンフォメーションは平面 (extend) 構造とフォールド (fold) 構造に大別される。Table 2 は X 線解析で明らかになったエンケファリン類似体のコンフォメーションを示している。ENK の活性コンフォメーションとしては、 μ 選択性モルヒネとの構造比較より (Fig. 9), フォールド構造が μ レセプターとの結合に平面構造は δ レセプターとの結合に適した構造と考えられる。一方、ENK の μ/δ レセプター選択性は他のオピオイドペプチドと比べて低いこと、また ENK は溶媒環境によってフォールドと平面の両構造をとることから、両構造と μ/δ レセプター選択性との関連を検討した。その結果、平面構造の 2 量体は互いに背中合わせになった 2 分子のフォールド構造と関係づけられる可能性のあることを示した (Fig. 10).³⁷⁾ そしてこれを確認するため、モルヒネ分子の 2 量体 (Fig. 11) を合成し、その μ, δ レセプター活性を測定し

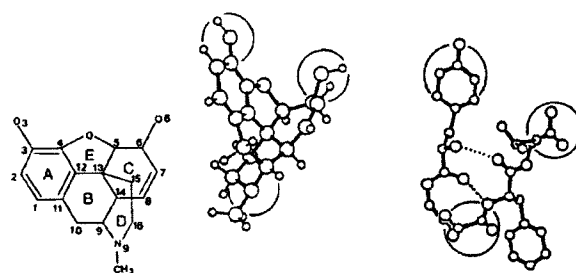


Fig. 9. Conformational Similarity between Morphine (left) and Enkephalin Folded Form (right)
Open circles represent similar positions between both molecules.

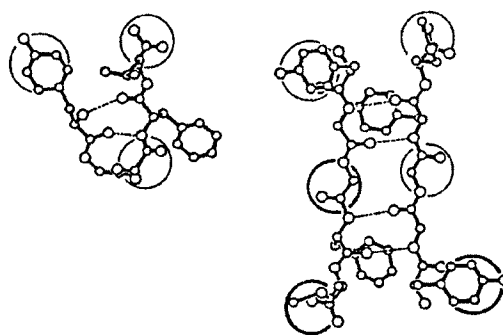


Fig. 10. Three-Dimensional Similarity between β -Turn Folded Form (left) and Dimeric Antiparallel Extended Structure (right) of Enkephalin

The spatial dispositions of Tyr1, Gly3 and Met5/Leu5 residues, marked by open circles, show the similarity between both conformations. The two halves of the extended dimer structure are almost related by a C_2 -symmetry, as are shown by the thin and thick open circles.

た結果、 μ 選択的なモルヒネは NOR2 で δ 選択性に移行することを明らかにした。³⁸⁾ このことは、フォールド構造は μ レセプター結合に、平面構造は δ レセプター結合に適した構造であることを示している。

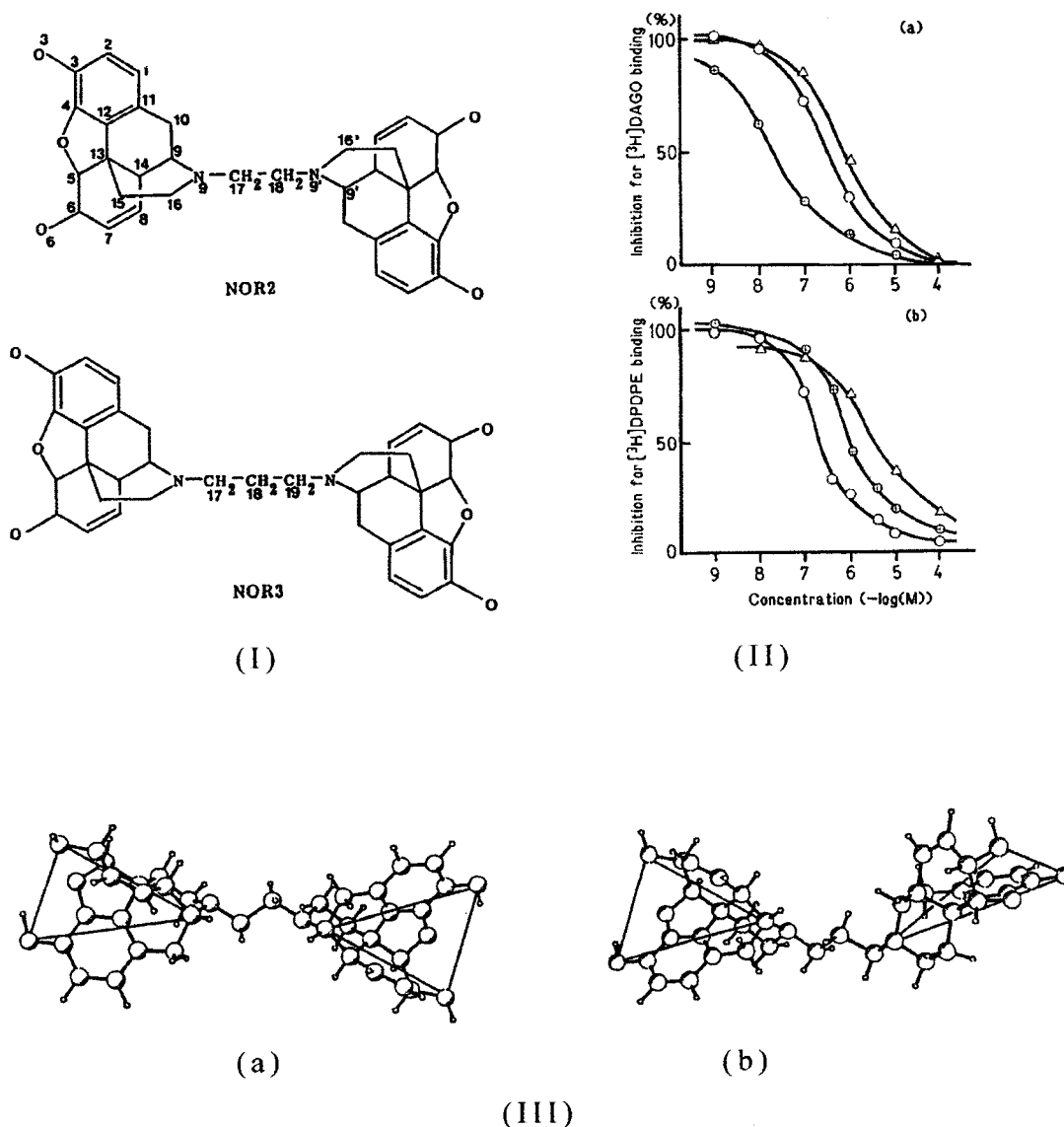


Fig. 11. (I) Chemical Structures of NOR2 and NOR3, (II) Their Competitive Curves in Rat Membrane Preparation [(a) μ -binding assay, (b) δ -binding assay] and (III) Most Energetically Stable Conformers of NOR2 (a) and NOR3 (b)
The symbols \oplus , \circ , and Δ in (II) represent morphine, NOR2 and NOR3, respectively.

一方、ENKより長いペプチドで高い μ/δ 選択性を示すDER, DEL, DEL-I, DEL-IIは溶液中で両構造が混在した種々なコンフォーマー³¹⁻³³をとることから、その構造と活性の相関を解釈するうえSchwyzerによって提唱されたメッセージアドレス仮説の有効性が示された。³⁹すなわち、N-末端3-4残基は μ/δ -レセプター選択性に関する情報を、C-末端2-3残基はレセプター親和性に関する情報を反映している仮説である。われわれは、この仮説に基づき、高い μ 選択性を示すEM-2について、膜環境を考慮したDPC (dodecylphosphocholine) ミセ

ル中でのコンフォメーション解析を行い、その結果得られた優位コンフォメーションを用いた μ -レセプターへの結合モデルを提示した (Fig. 12)。³⁵このモデルでは、オピオイドペプチドとの結合に重要とされるレセプター中のアミノ酸残基はすべてフォールド構造のEM-2との結合に関与していた。オピオイドペプチドのレセプター選択特異的コンフォメーションの解明にはそのレセプターとの複合体の結晶構造解析が不可欠であり、現在、その構造解析に取り組んでいる。

2.4. ニューロペプチド 軟体動物アフリカマ

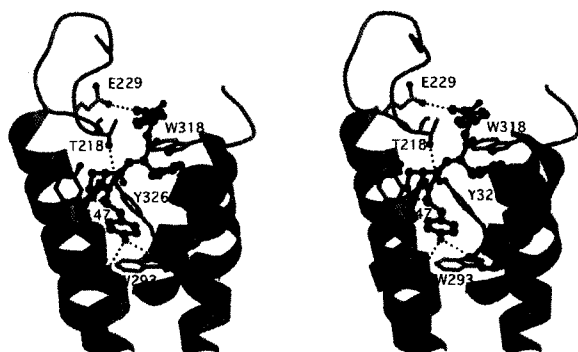


Fig. 12. Stereoscopic Docking Model of EM-2 Folded Conformer (ball and stick) on Agonist Binding Site of μ -Opioid Receptor (ribbon)

Dotted lined represent possible hydrogen bonds or electrostatic interactions.

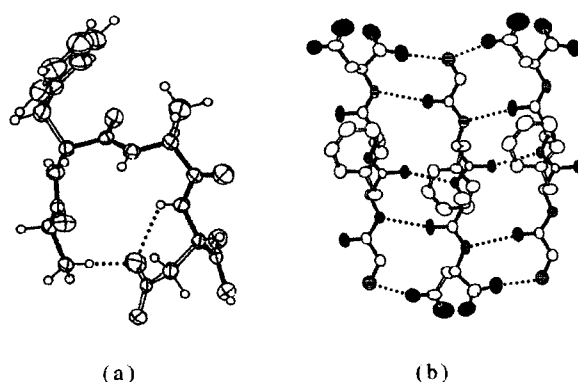


Fig. 13. Molecular Conformations of Achatin-I (a) and Achatin-II (b)

Dotted lines represent hydrogen bonds. Oxygen, nitrogen and carbon atoms in (b) are shown with filled, shaded and open ellipsoids, respectively, and the backbone chains of achatin-I and II are marked by thick lines.

イマイより神経伝達物質として単離されたアカチン-I (Gly-D-Phe-Ala-Asp) とアカチン-II (Gly-Phe-Ala-Asp) において、前者は顕著な神経興奮作用を示すのに対し、後者にはその活性はみられない。^{40,41)} 両者は D/L-Phe のみが異なることから、その立体構造に対する D/L-Phe の影響が機能発現に関係していることは明らかである。Figure 13 に示すように、アカチン-II は 5 組の分子間水素結合で安定化された β シート構造を形成しているのに対して、アカチン-I は分子内水素結合で安定化された Type-II' 様の β ターン構造をとっている。この構造形成には D-Phe 残基の寄与が大きいことから、活性コンフォメーションと考えられる。⁴²⁻⁴⁴⁾

その他のニューロペプチドとしてドーモイ酸、カ

イニン酸及びイソドーモイ酸の立体構造解析を行い、活性とコンフォメーションの関係を報告した。^{45,46)}

3. トリプトファンの生体構成分子とのスタッキング相互作用

高等動物の生体内では自ら作り出すことのできない必須アミノ酸の 1 つであるトリプトファン (Trp) は、その代謝産物とともに生命維持に不可欠な生理作用を発現しているのみならず、タンパク質の構成分子としてその機能発現に重要な役割を演じている。これは、Trp のインドール環は他の芳香族アミノ酸のうちで最も π -電子供与能に優れていることにある。⁴⁷⁾ これまでに π -電子欠損の芳香環との間で形成される選択特異的な π - π 電荷移動型相互作用を構造化学的に明らかにしてきた。

3-1. 補酵素との相互作用 酵素中の Trp 残基がピリジン、フラビン、チアミン、PQQ 補酵素との結合に果たす役割を明らかにする目的で、一連のモデル化合物あるいは複合体の構造解析により、その相互作用様式を原子レベルで明らかにしてきた。

3-1-1. ピリジン補酵素との相互作用⁴⁸⁻⁵²⁾ 生体内酸化還元反応を触媒する NAD や NADP は補酵素として関与している。アポ酵素がいかにかこの補酵素を捕らえるかを明らかにする目的で、Fig. 14 に示す化合物や複合体の構造解析を行った。その結果、1 及び 4 の場合とは対照的に、2 及び 3 の両芳香環においては顕著な重なり構造を形成することを明らかにした。両者に共通な構造特徴は、3.4-3.5 Å の平均面間隔でインドール環とニコチンアミド環が平行に重なることである (Table 3)。一方、1 におけるピリジン環の場合、このようなスタッキング相互作用が形成されないことから、ピリジン環の窒素 4 級化 (プロトネーション) がインドール環との顕著なスタッキング相互作用を誘起させる要因であると考えられる。分子軌道計算の結果は、ピリジン環がピリジニウム環になることにより、その最低空軌道 (LUMO) のエネルギーレベルがインドール環の最高占有軌道 (HOMO) のエネルギーレベルに接近するため、インドール環からピリジン環への π -電荷移動が容易になることを示した。しかし、4 の場合では両芳香環の重なり構造がみられなかったことから、2 及び 3 でみられた顕著な重なり構造の形成にはピリジン環窒素 4 級化に加えてアミド基

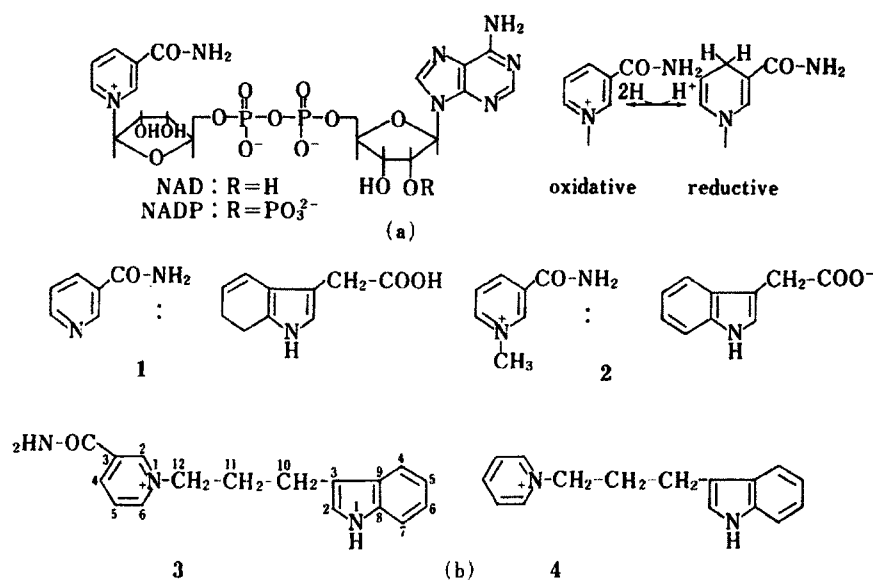
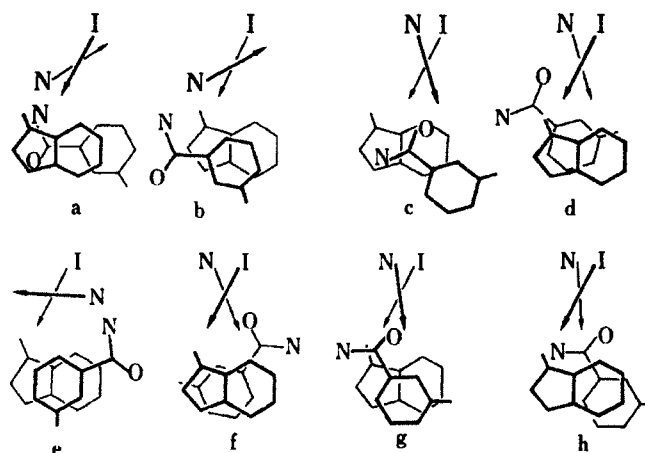


Fig. 14. Chemical Structure of Pyridine Coenzyme (a) and Its Model Compounds or Complexes Used for the Interaction with Indole Ring

Table 3. Stacking Parameters for Indole-Nicotinamide Ring Interactions

Compound	Donor	Acceptor	Molar ratio	Overlapping mode	Interplanar spacing (Å)	Dihedral angle (°)	Angle between dipole moment (°)
[1-(Indole-3-ethyl)-3-carbamoyl-pyridinium]	Indole	NA	1 : 1	Fig. a	3.359	8.6	155
				Fig. b	3.407	8.6	155
AcTrp-1-MNA complex	AcTrp	1-MNA	1 : 1	Fig. c	3.598	9.7	43
				Fig. d	3.440	9.7	43
2	IAA	1-MNA	1 : 1	Fig. e	3.356	3.1	65
				Fig. f	3.394	1.9	47
3	Indole	NA	1 : 1	Fig. g	3.505	3.2	31
				Fig. h	3.402	3.2	31

Abbreviations: NA, 3-carbamoylpyridinium; 1-MNA, 1-methylnicotinamide; AcTrp, *N*-acetyl-L-tryptophan; IAA, Indole-3-acetic acid.



Arrows of N and I represent the directions and strengths of dipole moments of nicotinamide and indole rings, respectively.

の存在が重要であることを示している。これらのスタッキング結合においてはピリジン環の還元原子である C4 原子はインドール環平面に対して 3.4 Å 以下の距離で接触している。これは、インドール環が電荷移動によりこれら原子のプロトン受容能を高める機能を果たしていることを示している。すなわち、Trp 残基はピリジン補酵素の固定化に加えて、還元作用を促進させる役割も演じていることを意味している。

3-1-2. フラビン補酵素との相互作用⁵³⁻⁵⁸⁾ フラビン補酵素もピリジン補酵素と同様、生体内酸化還元反応の触媒作用に不可欠であり、フラビン補酵素の固定化にはホロ酵素中の Trp 残基が重要であると考えられている。そこで、そのことを構造化学的に検証する目的でモデル化合物及び複合体 (Fig. 15) を解析した。その結果、5 及び 6 では、ピリジン補酵素の場合と同様、インドール環とフラビン環は平行に重なり、その平均面間隔は 3.4–3.5 Å の共通の構造特徴がみられた (Table 4)。同様なスタック

キング相互作用は 7 の複合体においても観測された。これらのスタッキング結合においては、ピリジン補酵素の場合と同様、フラビン環の還元原子である N1 及び N5 原子はインドール環平面に対して 3.4 Å 以下の距離で接触している。これは、インドール環が π -電荷移動によりこの還元原子のプロトン受容能を高める結果、Trp 残基はフラビン補酵素の固定化に加えて、還元作用を促進させる役割も果たしていることを示している。一方、化合物 9 では両芳香環に顕著な相互作用は観測されなかった。これは、ピリジン補酵素モデルである 4 と同様、スタッキング相互作用よりも結晶化に伴う分子パッキング力の影響が反映されたと考えられ、ピリジン補酵素のモデル分子 3 とは対照的な結果である。このことは明確なプロトネーション状態をとらないイソアロキサチン環は、インドール環に対する π 電子受容能に対して、窒素 4 級化したニコチンアミド環よりも弱いことを示している。

複合体 8 の解析結果はフラビン環とアデニン塩基

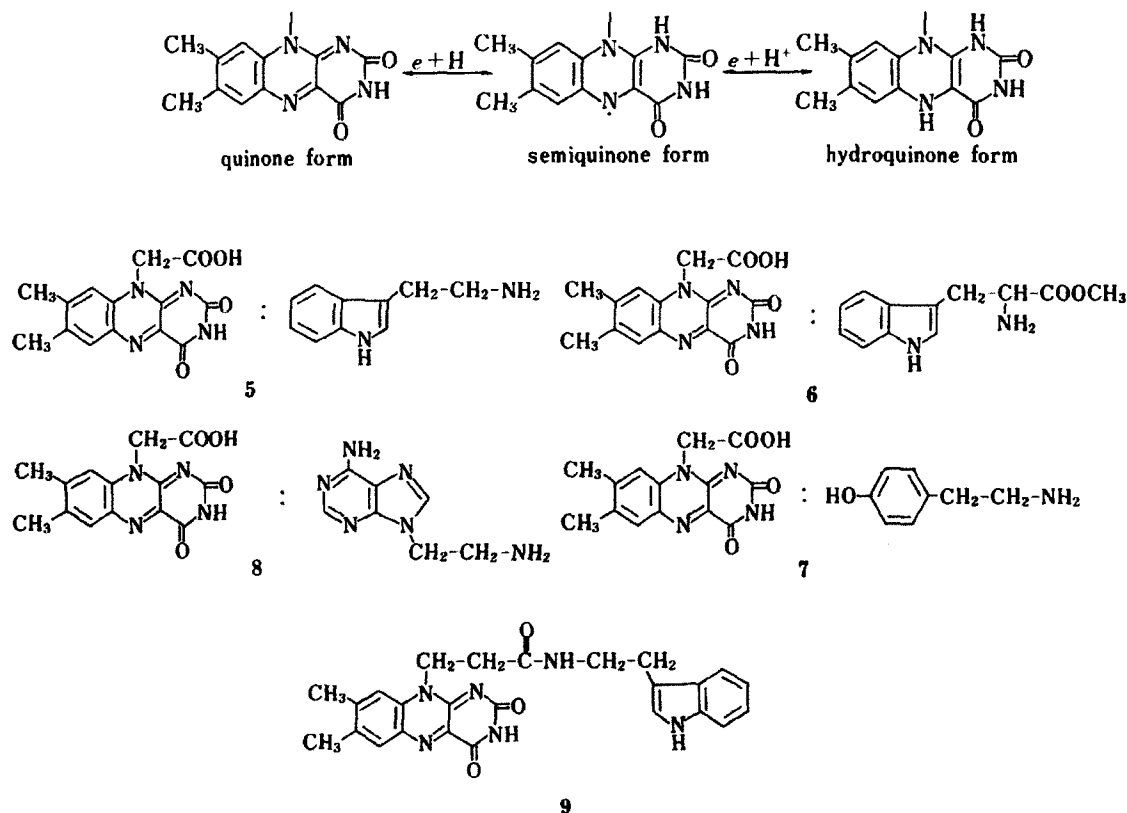
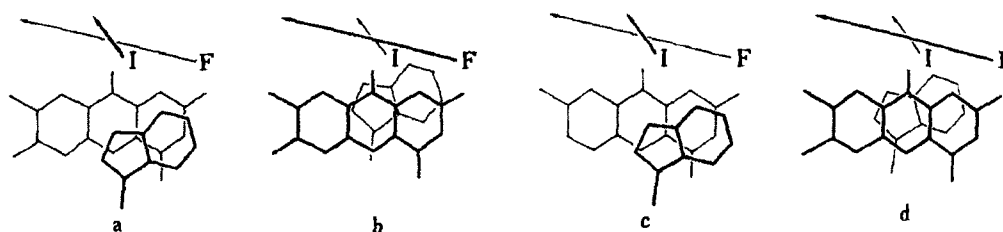


Fig. 15. Oxidative and Reductive Forms of Flavin Coenzyme (upper) and Its Model Compounds or Complexes Used for the Interaction with Indole Ring (lower)

Table 4. Stacking Parameters for Indole-Isoalloxazine Ring Interactions

Compound	Donor	Acceptor	Molar ratio	Overlapping mode	Interplanar spacing (Å)	Dihedral angle (°)	Electrostatic energy ^{a)} (kcal/mol)	Stabilization energy ^{b)} (kcal/mol)
5	TPA	DIA	1 : 1	Fig. a	3.179	3.0	-25.114	-71.977
				Fig. b	3.401	3.0	-24.733	-69.902
6	TrpOMe	DIA	1 : 1	Fig. c	3.316	4.4	-25.560	-72.726
				Fig. d	3.377	4.4	-23.495	-68.647

^{a)} Electrostatic energy was calculated by equation, $332.0 \times \sum_i \sum_j q_i q_j / r_{ij}$, where r_{ij} is the distance (in Å) between atom i in 3-methylindole and atom j in lumiflavin, and q_i is the Coulombic charge on atom i , calculated by CNDO/2 method. ^{b)} Stabilization energy was calculated by using the following equation and the total energy (E) calculated by CNDO/2 method. Stabilization energy = $E_{\text{stacked pair}} - (E_{3\text{-methylindole}} + E_{\text{lumiflavin}})$.



Arrows of F and I represent the directions and strengths of dipole moments of isoalloxazine and indole rings, respectively.

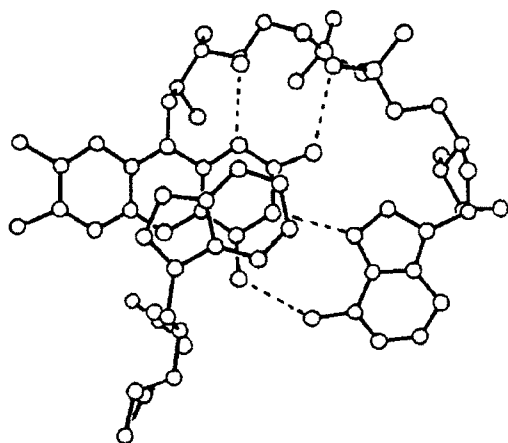


Fig. 16. Binding Model between FAD and Tryptophan, Built from Model Complexes of 6 and 8
Hydrogen bonds are shown with broken lines.

の結合様式を反映していることから、複合体 6 の結果と合わせると、FAD に対する Trp の可能な結合様式として Fig. 16 を示すことができる。

3-1-3. チアミン補酵素との相互作用⁵⁹⁻⁶¹⁾ チアミン (ビタミン B1) のピロリン酸エステル (TPP) はピルビン酸などの脱炭酸反応の補酵素として作用している。アポ酵素との結合には Mg^{2+} などの金属イオンのほかに Trp 残基が重要な働きをしていることから、その作用機構を明らかにする目的でモデル分子及び複合体の構造解析を行った

(Fig. 17).

11 及び 12 の解析結果はインドール環とピリジニウム環及びチアゾリウム環とのスタッキング結合様式を示した (Table 5)。一方, 10 ではチアミンは F- 型の安定コンフォメーションをとっており [Fig. 18(a)], インドール環はチアゾリウム環とは相互作用せず, ピリミジン環との間でスタッキング相互作用を介した 2 量体構造を形成していた。

分子軌道計算では, インドール環はピリミジン環よりもプラス電荷を帯びたチアゾリウム環に対してより強く結合することを示したが, この結果は, 両芳香環がメチレン基で結合したチアミン分子では, 特に結晶場のような分子運動が制限される環境下においては, Fig. 18(a) のような結合が安定であることを示している。この結合様式は, Trp 残基によるチアミン補酵素の固定化に対して Fig. 18(b) のような形態で行われることを示唆している。一方, 溶液中におけるインドール環は TPP のチアゾリウム環とピリミジン環の両芳香環に跨るスタッキング相互作用を介してチアミン分子を活性型の V-型コンフォメーション [Fig. 18(c)] に移行させ, さらにチアゾリウム環の C2 プロトンの H-D 交換速度を促進させることを明らかにした。⁶¹⁾ このことは, Trp 残基はチアミン補酵素の触媒活性にも寄与することを示している。

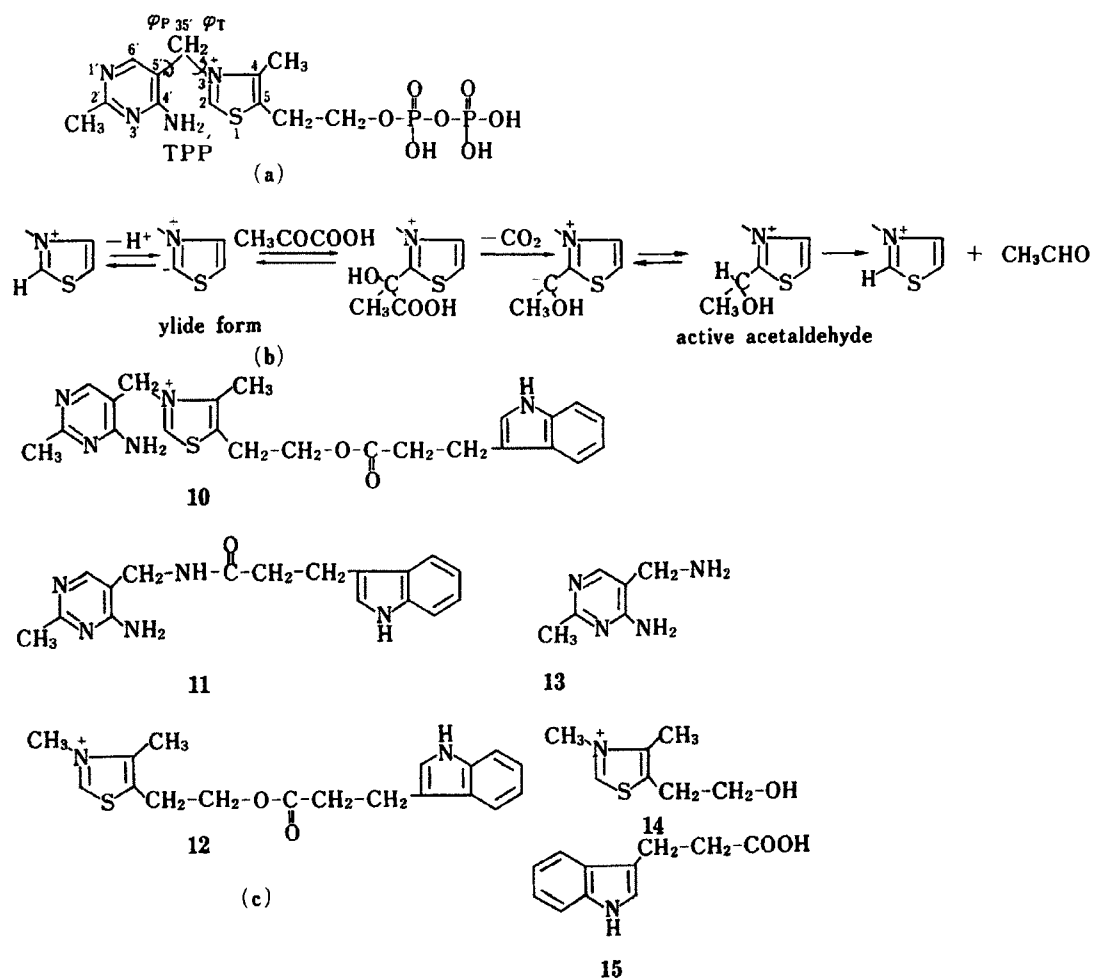
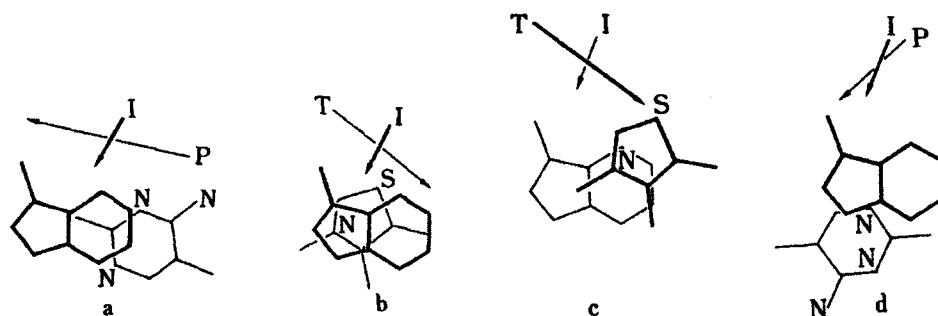


Fig. 17. Chemical Structure (a) and Decarboxylation Mechanism (b) of Thiamine Pyrophosphate (TPP), and Its Model Compounds or Complexes (c) Used for the Interaction with Indole Ring

Table 5. Stacking Parameters for Indole-Thiamine Ring Interactions

Compound	Donor	Acceptor	Overlapping mode	Interplanar spacing (Å)	Dihedral angle (°)	Electrostatic energy (kcal/mol)	Stabilization energy (kcal/mol)
10	Indole	Pyrimidinium	Fig. a	3.338	9.2	12.24	-33.51
12	Indole	Thiazolium	Fig. b	3.498	3.4	15.64	-34.20
			Fig. c	3.759	3.4	15.60	-30.12
11	Indole	Pyrimidinium	Fig. d	3.578	11.7	-2.89	-31.37



Arrows of P, T and I represent the directions and strengths of dipole moments of pyrimidine, thiazolium, and indole rings, respectively.

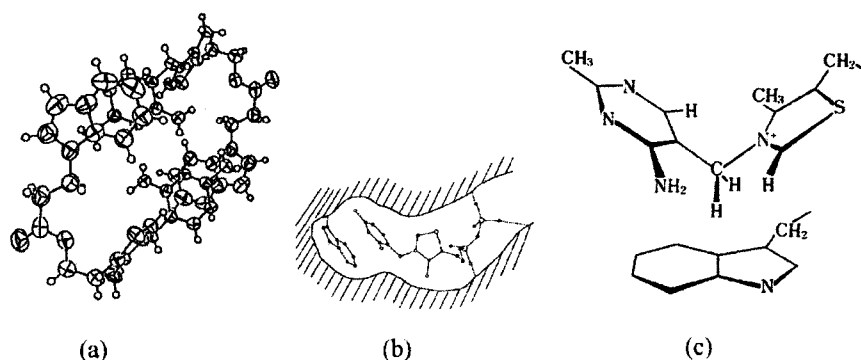


Fig. 18. Stacking Dimer Observed in Crystal Structure of **10** (a) and Interaction Model between TPP and Trp Residue in Enzyme (b) and Solution (c)

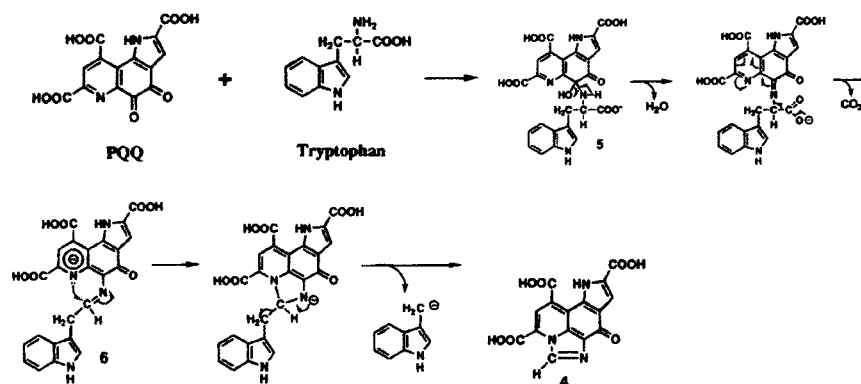


Fig. 19. Reaction Mechanism for Tryptophan Conversion by PQQ under Aerobic Condition

3-1-4. ピロロキノリノキノン (PQQ) との相互作用⁶²⁻⁶⁵⁾ キノタンパク質の補綴分子である PQQ は、微生物の成長促進作用に加え、生体分子とシッフ塩基形成を介して、非酵素反応の触媒として機能している。^{66,67)} Trp と PQQ の相互作用については、両分子の混合により顕著な色調変化が観測されることから、電荷移動錯体の形成は明らかであるが、両分子間の相互作用様式を原子レベルで明らかにされていない。それは、これまでの補酵素の場合とは異なり、その複合体構造は不安定でさらに反応が進行するためである。嫌気条件下における PQQ の還元作用を介した Trp との反応機構を明らかにした (Fig. 19)。

以上、Trp は π -電子供与能に優れたインドール環を有し、他の生化学的に重要な芳香族化合物との間で電荷移動を含む π - π スタッキング相互作用の形成を介して生体内での機能発現に重要な役割を果たしていると結論づけられる。

3-2. 核酸塩基との相互作用 タンパク質による特定の核酸塩基あるいは塩基配列の認識は生命維持にとって極めて重要である。これを可能にするには核酸との結合に必要なタンパク質の立体構造要件に加え、各塩基を選択特異的に認識するアミノ酸残基の構造要件を解明することが不可欠である。後者における両分子間の基本的な結合様式として、(i)塩基性アミノ酸とヌクレオチドリン酸との静電気相互作用、(ii)極性アミノ酸とヌクレオチドの塩基、リポース、リン酸基との水素結合、(iii)芳香族アミノ酸と核酸塩基とのスタッキング相互作用、(iv)非極性アミノ酸側鎖と核酸塩基との疎水結合が考えられる。筆者は(iii)の相互作用を介して核酸塩基を認識する Trp 残基の役割について研究した。

3-2-1. 中性の核酸塩基との相互作用⁶⁸⁻⁷²⁾ 電荷を持たない中性の核酸塩基と芳香族アミノ酸とのスタッキング相互作用の多くは溶液中で観測されているが、結晶場での顕著な形成は一般に観測されて

いない。結晶構造解析で観測される場合でも、一般にその重なり程度は小さく、周囲の環境に大きく依存している。このことは、スタッキング結合は水素結合と比べその結合力は弱く、結晶化に伴うパッキング力の影響により、溶液中で観測される重なり状態は結晶場でかならずしも保持されないことを示している。

3-2-2. 核酸塩基の窒素4級化（プロトネーション）によるスタッキング相互作用⁷³⁻⁸⁴ 中性の塩基とは対照的に、核酸塩基の窒素原子をメチル化すると、Trpを始め芳香族アミノ酸残基との顕著なスタッキング相互作用が結晶場においても観測される。インドール酢酸と7-メチルグアノシン複合体⁷⁵の例を Fig. 20 に示す。顕著なスタッキング相互作用がみられる根拠としては、既にピリジン補酵素の項で述べたように、核酸塩基の窒素原子4級化（プロトネーション）により、塩基の LUMO 軌道

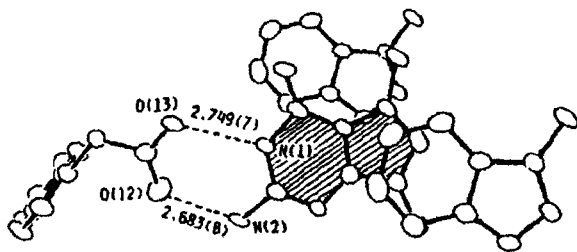


Fig. 20. Stacking Interaction between Indole Ring and N7-protonated Guanine Base Observed in Crystal Structure of Indole-3-acetic Acid-N7-methylguanine (1:1) Complex

Shaded ring shows the N7-methylated guanine base. The carboxyl group of indole-3-cetic acid forms hydrogen bonding pair with the N(1)H and N(2)H of guanine base.

エネルギーが低下し, Trp インドール環の HOMO 軌道エネルギーに接近する結果, インドール環から核酸塩基への π 電荷移動がより容易になるためである (Fig. 21). その結果, 両芳香環の平均間距離は 3.3–3.5 Å の範囲内でほぼ並行に重なる。アデニン, グアニン, シトシンの芳香環窒素原子 4 級化による芳香族アミノ酸とのスタッキング例をまとめて Table 6 に示している。

アデニン, グアニン, シトシンの pK_a 値はそれぞれ 4.2, 3.3, 4.6 であることから, 生理条件下では通常プロトネーションは起こらないと思われるが, タンパク質中の酸性アミノ酸残基近傍に存在する核酸塩基ではプロトネーションは十分考えられ, 近くに Trp などの芳香族アミノ酸残基が存在すれば, スタッキング結合を介した標的塩基の認識は可能である。また, DNA のアルキル化剤等による DNA 損傷部位の認識においても, この相互作用形成を介して Trp は重要な役割を果たしていると思われる。

3-2-3. スタッキング相互作用と水素結合による N7-メチルグアニン塩基 (m7G) の選択特異的結合⁸⁵⁻⁹⁰ アミノ酸による特定の核酸塩基との選択的な結合力としては, 水素結合とスタッキング結合は他の結合よりも優れている。したがって, 極性アミノ酸と芳香族アミノ酸を含有するペプチドは両結合の同時形成を介して特定塩基を選択的に認識することが可能と考えられる。一方, インドール酢酸と7-メチルグアノシン複合体構造 (Fig. 20) では, グアニン塩基はインドール酢酸のカルボキシル基と水素結合対を, インドール環とスタッキング結合を同

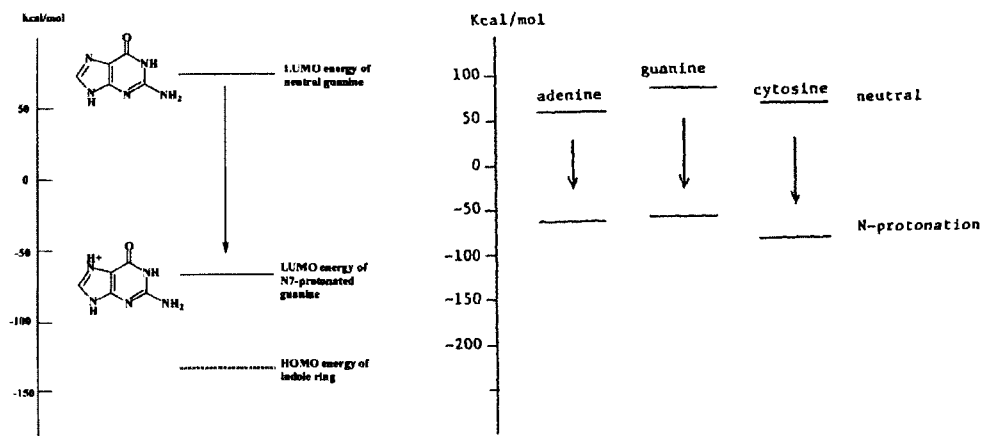
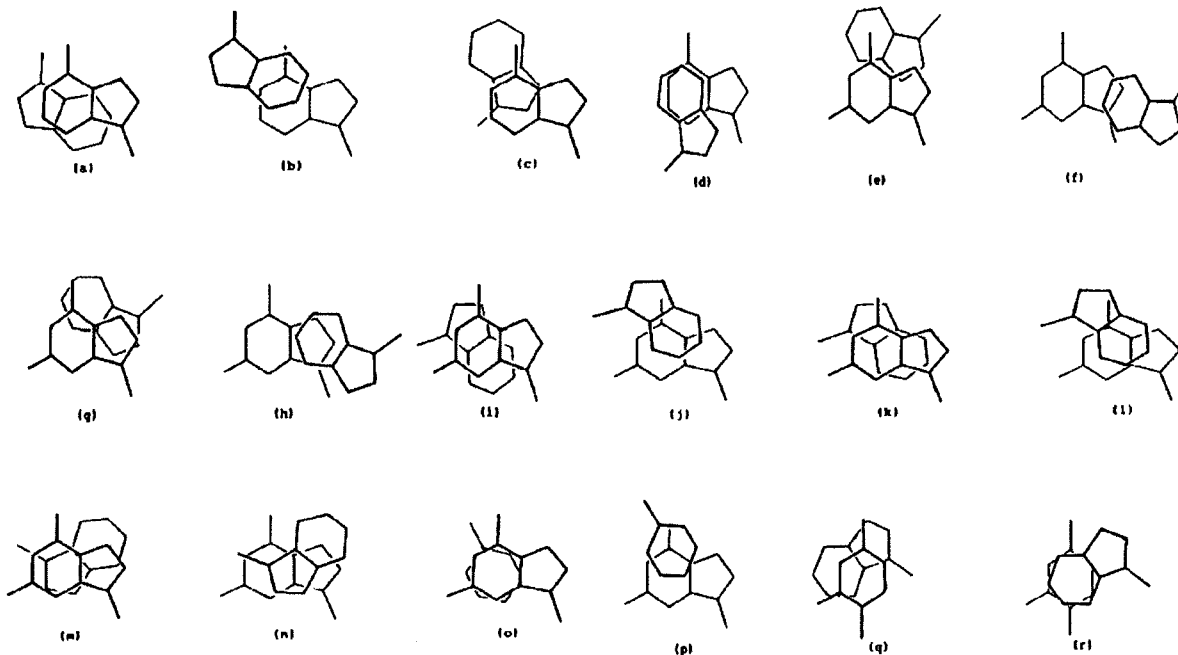


Fig. 21. LUMO Energy Level of Neutral and N-Protonated Nucleic Acid Base, Together with HOMO Energy Level of Indole Ring

Table 6. Structural Parameters for Stacking Interaction between N-Quarternized Nucleic Acid Base and Aromatic Ring of Amino Acid

Compounds	Base	Aromatic ring	Ratio	No. of waters per complex pair	Overlapping mode	Averaged interplanar spacing (Å)	Dihedral angle (°)	Angle between dipole moments (°)	Notation ^{a)}
1,9-Dimethyladenine: indole-3-acetic acid	Adenine	Indole	1 : 1	3	Fig. (a)	3.497	2.8	71	A1-I1
					(b)	3.351	2.8	71	A1-I11
9-(3-Indol-3-ylpropyl)-1-methyladenine	Adenine	Indole	1 : 1	2	(c)	3.431	2.1	152	A1-I1
					(d)	3.476	2.1	152	A1-I11
					(e)	3.554	13.0	115	G7-I1
					(f)	3.435	13.0	115	G7-I11
7-Methyl-9-ethylguanine: indole-3-acetic acid	Guanine	Indole	2 : 2	0	(g)	3.568	10.4	113	G72-I2
					(h)	3.475	10.4	113	G72-I22
					(i)	3.41	4.2	39	G7-I1
					(j)	3.32	4.2	39	G7-I11
7-Methylguanosine: indole-3-acetic acid	Guanine	Indole	2 : 2	4	(k)	3.46	2.7	45	G72-I2
					(l)	3.33	2.7	45	G72-I22
					(m)	3.356	3.8	111	G7-I1
					(n)	3.380	3.8	111	G7-I11
7-Methylguanosine-5'-phosphate: tryptamide	Guanine	Indole	1 : 1	3	(o)	3.39	33.0	87	G7-B1
					(p)	3.67	33.0	87	G7-B11
7-Methylguanosine-5'-phosphate: phenylalanine	Guanine	Benzene	1 : 1	6	(q)	3.393	2.7	4	C3-I1
					(r)	3.428	2.7	4	C3-I11

^{a)} A1, G7, C3, I1, and B1 represent the 1-methyladenine, 7-methylguanine, 3-methylcytosine, indole, and benzene rings for 1 : 1 complex pair, respectively. For 2 : 2 complex pairs of the guanine-indole system, the notations of G7-I1 and G72-I2 pairs were used. The I11, I22, or B11 shows the indole or benzene ring related by the one-unit cell translation operation of I1, I2, or B1, respectively.



時に形成していた。⁷⁵⁾そこで、m7G塩基を選択特異的に認識できるような酸性アミノ酸とTrp含有オリゴペプチドの設計を試みた。その結果、(i) m7G塩基に対してTrp-GluのGluはワトソン・クリック型の水素結合対を、Trpはスタッキング結合を同時形成できる最短ペプチドであること (Fig.

22),⁸⁶⁾ (ii)-Trp-(Gly)m-Asp/Glu-(Gly)n-Trp-(m=0-2, n=0-2)は水素結合とスタッキング結合の同時形成によるm7Gの選択特異的認識に最も適した配列であることを明らかにした。⁸⁹⁾

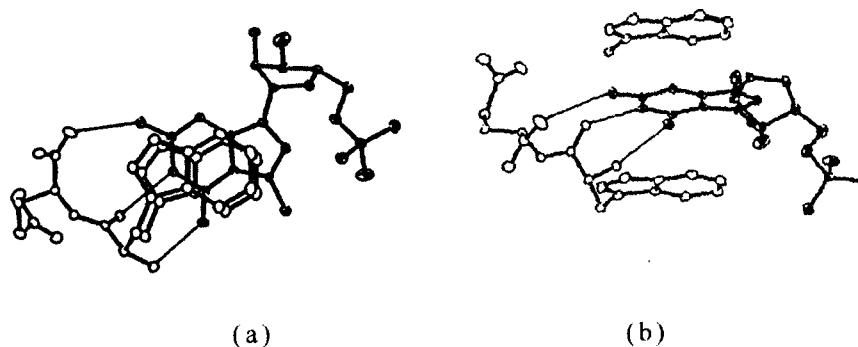


Fig. 22. Simultaneous Formation of Stacking and Hydrogen Bond Pairing Interactions between m7GMP and Trp-Glu Dipeptide, Viewed Perpendicular (a) and Parallel (b) to the Base
m7GMP is shown by thick bond. Hydrogen bond is shown by thin line.

4. タンパク質合成開始因子 eIF4E の mRNA キャップ認識機構の解明

真核生物における翻訳開始反応は多くの開始因子によって行われている。その最初のステップは mRNA のリボゾームサブユニットへの結合で、現在、Fig. 23 に示すような開始機構が確立されている。⁹¹⁾ 真核生物の mRNA はその 5'-末端にキャップ構造と呼ばれる m7G 塩基を有しており、開始因子の 1 つである eIF4E はこの構造を選択特異的に認識することでタンパク質合成の反応が開始される。筆者は eIF4E による mRNA キャップ認識機構について研究を進めた。

まずこの研究を開始した背景について述べたい。前章で述べたように筆者は Trp と生体構成分子との相互作用様式について研究してきた。核酸塩基に関しては、塩基中の窒素原子がプロトネートすると Trp インドール環との間で電荷移動を含む顕著な π - π 型スタッキング相互作用を形成することを明らかにした。さらに Trp-Glu ジペプチド-m7GMP 複合体の結晶構造 (Fig. 22) で示されたように、酸性アミノ酸と Trp 含有ペプチドは m7G 塩基を選択特異的に認識できることを明らかにした。それ故、この認識機構が現実の生体内反応において利用されているかを調べることは、これまでの分子間相互作用研究が単なるモデル研究に留まらず、構造生物学的にも重要な研究であることを証明する上で、筆者にとって極めて重要な課題であった。そこで、当時、その構造科学的な研究は全くなされていなかったものの、タンパク質合成開始因子の 1 つである eIF4E は mRNA の 5'-末端が m7G トリリン酸で修

飾されたキャップ構造の認識に関与していることが報告されていたことから、この認識様式を解明するため eIF4E-mRNA キャップ複合体の結晶構造解析に取り組んだ。

当初、eIF4E を天然から大量に取り出すことは困難であったため、大腸菌が用いるコドンに置き換えたヒト eIF4E の遺伝子を化学合成し、大腸菌からの組換え体として得ることを計画した。組換え技術が十分確立していなかった時期で、m7G 結合能を有するタンパク質の発現に手間取ったが、最終的には大腸菌からの直接発現による可溶性画分から単離、精製に成功し、⁹²⁻⁹⁵⁾ 得られた組換え体は天然型 eIF4E と同一の立体構造をとっていること、同程度のキャップ構造認識能を有すること、一連の変換体を用いた実験からキャップ結合には Trp 残基が重要に係わっていること等を明らかにした。⁹⁶⁻⁹⁸⁾ 次に、mRNA キャップ構造のモデル分子として m7GpppA を用い、それとの複合体結晶の調製に取り組んだ。構造解析に適した結晶を得るためにかなり時間を要したが、最終的に X 線回折強度データを収集し、⁹⁸⁾ その X 線結晶構造解析にも成功した (Fig. 24)。⁹⁸⁻¹⁰¹⁾

構造解析の結果は、m7GpppA の m7G 塩基は、eIF4E の Trp56 と Trp102 のインドール環のスタッキング結合による上下からの挟み込みと、Glu103 の側鎖カルボキシル基による m7G 塩基の N1 原子及び N2H 基との水素結合対形成により強固に固定されていることを示した。すなわち、eIF4E はこのスタッキング相互作用と水素結合対の同時形成により、mRNA のキャップ構造を選択特異的に認識し

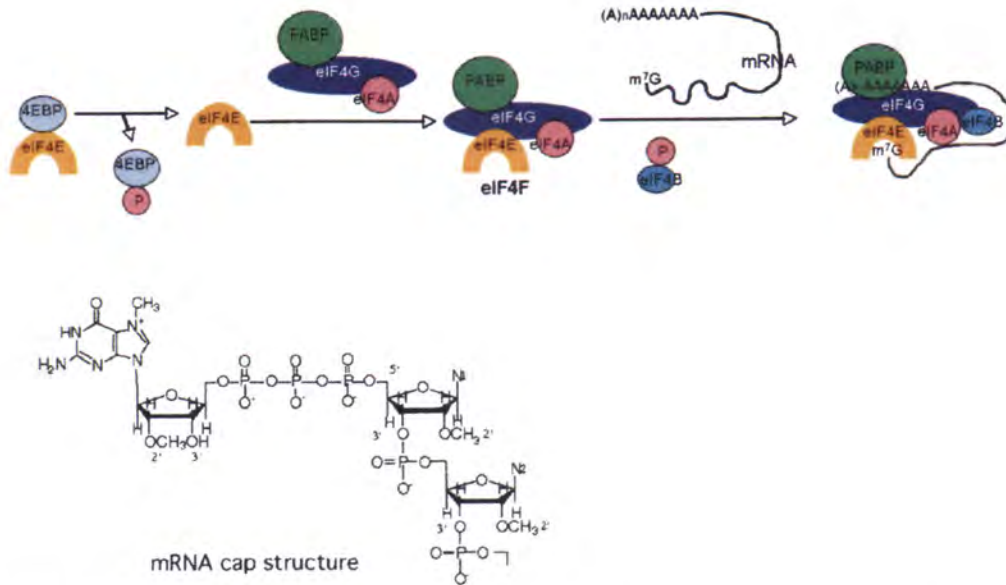


Fig. 23. Scheme of Eukaryotic Cap-Dependent Translation Initiation Pathway
 mRNA is activated by the binding of eIF4F (eIF4E, eIF4G, eIF4A) to the cap at the 5'-terminal and poly A-binding protein (PABP) to the poly A tail at the 3'-terminal. The eIF4F assembly is blocked by 4EBP binding to eIF4E. Phosphorylation of 4EBP dissociates 4EBP from eIF4E, leading to association of eIF4F.

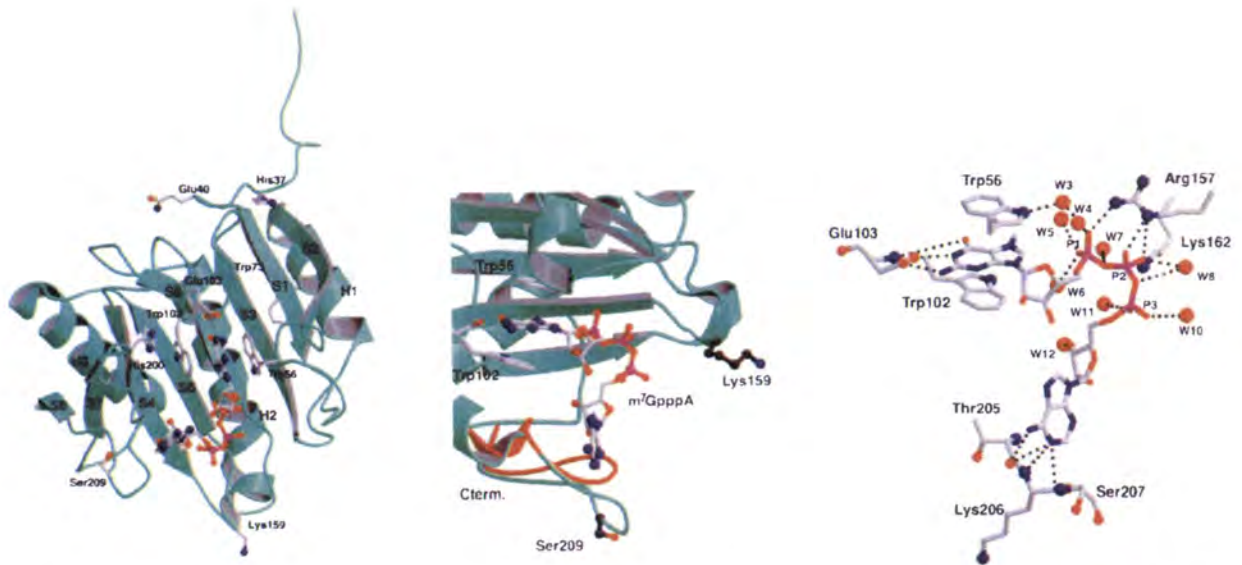


Fig. 24. (a) Overall Structure of eIF4E-m7GpppA Complex, (b) Expanded Cap-Binding Pocket of eIF4E, and (c) Its Binding Mode of m7GpppA

eIF4E and m7GpppA are depicted with ribbon and stick-bond models, respectively. Hydrogen bonds and short contacts in (c) are shown by dotted line. Blue and red circles represent nitrogen and oxygen atoms, respectively.

ていることを原子レベルで初めて明らかにした。この認識機構は Trp-Glu : m⁷GTP 複合体の構造解析で示された分子間相互作用様式 (Fig. 22) と本質的に一致している。この事実は、筆者がこれまで行ってきた分子間相互作用研究は生体内反応における

特異的相互認識機構の本質を解明する上で極めて重要な情報を提供することを証明するものである。

5. 内因性タンパク質 4EBP による eIF4E の機能制御機構

タンパク合成の休止期では、eIF4E は 3 種類の

isoform を持つ内因性タンパク質 4EBP (Table 7) と複合体を形成して eIF4E の機能が制御されている (Fig. 23). タンパク合成の開始シグナルにより 4EBP がリン酸化されると eIF4E から離れ, eIF4E は代わりに合成開始因子 eIF4G と会合して一連の生合成反応が開始される.

4EBP による eIF4E の制御機構を解明する目的で, ヒト 4EBP 組換え体と eIF4E との相互作用を分光学的に解析するとともに,¹⁰²⁻¹⁰⁵ その複合体の X 線結晶構造解析に取り組んだ. eIF4E との結合に必須な 4EBP1 の Thr36-Thr70 断片ペプチドを用い, eIF4E-m7GpppA 複合体との三元複合体結晶の構造

解析を行いその結合様式を明らかにした (Fig. 25).^{106,107} その結果, eIF4E の 4EBP 結合領域は mRNA キャップ結合領域の背面側の N-末端側に存在し, 54 番目から 60 番目の YDRKFLM 配列 (Table 7 の太字部分) が eIF4E との結合に重要であることを明らかにした. さらに生理環境下での分子動力学計算に基づき, 両分子間相互作用に対する mRNA キャップ構造の影響や, 4EBP の eIF4E への結合による制御スイッチの on, 4EBP リン酸化による off 機構について構造化学に考察した.

一方, 4EBP の 54 番目-60 番目 (eIF4E との結合に必須) を中心として, その N-末端側及び C-末端

Table 7. Amino Acid Sequence of 4EBP1-3 Isoform

4EBP1	MSGGSSCSQTPS--RAIPATRRVVLGDGVOLPPGDYSTTPGGTLFSTTPGGT	50
4EBP2	MSSSAGSGHQPSQSRAIP-TRTVAISDAAQLPH-DYCTTPGGTLFSTTPGGT	50
4EBP3	MSTSTSC-----PIP-----GGRDQLPD-CYSTTPGGTLYATTPGGT	36
4EBP1	RIIYDRKFLME CRNSPVTKTPPR DLPTIPGVTSPSS--DE PPMEASQSHLRN	100
4EBP2	RIIYDRKFL LLDRRNSPMAQT PPCHLPNIPGVTSPGTLIE DSKVEVNNLNNLN	102
4EBP3	RIIYDRKFL LECKNSPIART PPCCLPQIPGVTTPPT -----APLSKLEELK	82
4EBP1	SPEDKRAGGEESQFEMDI	118 (12.6 kDA)
4EBP2	NHDRKHAVGDDAQFEMDI	120 (12.9 kDA)
4EBP3	EQTEEEEIPDDAQFEMDI	100 (10.9 kDA)
human eIF4GI (609-660)		
	KKRY DR E FL LG FQ FI FAS M Q K PE GL PHI SD V VL DK ANK T PL R PL D PT R LO OI	

The first and second eIF4E-binding regions of 4EBP isoform are shown by bold letter and rectangular box, respectively. The 609-660 sequence of human eIF4GI is shown for comparison.

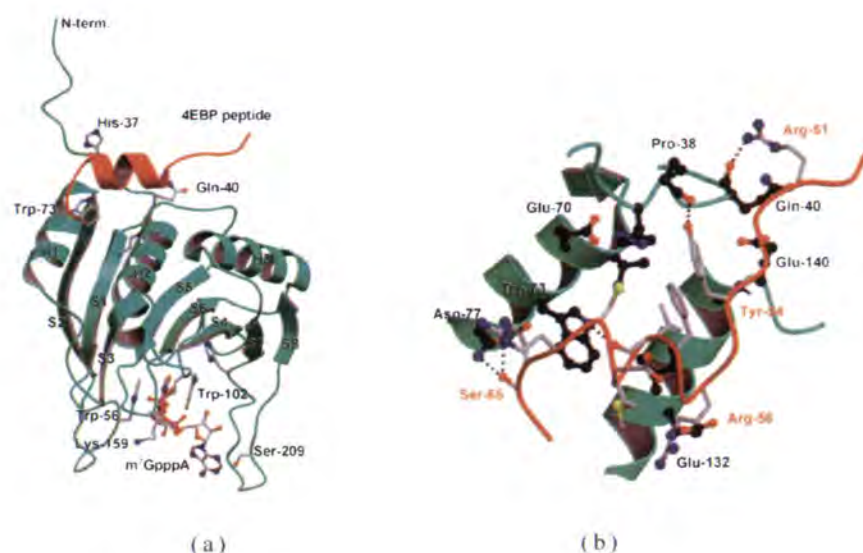


Fig. 25. (a) Overall View of 4EBP1 Peptide Fragment (red ribbon)—eIF4E (green ribbon)—m7GpppA (ball and stick) Ternary Complex and (b) Detailed Binding Mode of 4EBP1 Peptide Fragment (red wire) to eIF4E N-terminal Region

側のアミノ酸配列を切断した一連の変換体を調製し、eIF4E との会合定数を分光学的に測定した結果、C-末端領域 (Table 7 の囲い部分) には第2の eIF4E 結合領域が存在すること、その結合には特に Val80 が関与する eIF4E との疎水相互作用が重要であることを明らかにした。¹⁰⁸⁻¹¹⁰⁾ さらに興味深いことには、これに対応する eIF4G 領域 (Table 7) にはそのような機能が存在しないことを明らかにした。¹¹¹⁾ このことは eIF4E に対する 4EBP の制御機能と eIF4G の合成促進機能の差異を反映しており、詳細な研究を進めている。

6. 酵素阻害剤の開発

標的とする酵素に対する選択特異的な阻害剤の開発はその酵素の生理機能の解明のみならず、酵素機能の異常によって引き起こされる疾病の治療薬としても重要である。われわれはこれまで、一連のアンジオテンシン変換酵素阻害剤,^{112,113)} メチルトランスフェラーゼ阻害剤,^{114,115)} トリプシン阻害剤,¹¹⁶⁻¹¹⁸⁾ アルドース還元酵素阻害剤,¹¹⁹⁻¹²²⁾ フォスホリパーゼ A₂ 阻害剤¹²³⁻¹³⁰⁾ の分子構造あるいはその酵素複合体の立体構造を解析し、その立体構造情報に基づく阻害剤の構造と活性相関について研究してきた。本節では H2-レセプター拮抗剤とカテプシン B 阻害剤について述べる。

6-1. H2-レセプターアンタゴニストの構造活性相関 シメチジンを始めとする一連の H2-レセプターアンタゴニストの立体構造を解析し、阻害活性の発現に必要な立体構造の特徴について研究してきた。¹³¹⁻¹³⁶⁾ シメチジンは結晶化条件により4種類の異なる結晶形 (Form A, B, C, D) を与え,¹³²⁾ 溶解速度並びに抗潰瘍抑制効果に対するこれら剤形のバイオアベイラビリティーが異なることを明らかにした (Table 8)。¹³³⁾ そのうち X 線構造解析が行われた Form A, C, D (Fig. 26) で最も高活性なコンフォメーションは分子内で折れたたまった1水和物の Form C である。

Table 9 のうちで構造解析がなされた化合物の立体構造に基づきイミダゾール環に対す側鎖の NH 基の立体配座を比較すると、Fig. 27 に示すように活性を示す化合物の NH 基はイミダゾール N 原子に対して一定の空間範囲(破線)内に位置しており、イミダゾール N 原子と側鎖 NH 基との分子内水素結合による折れ曲がり構造が活性型であることが示

Table 8. Effects of Four Crystalline Forms of Cimetidine for Stress Ulceration in Rat

Dose, mg/kg	Mean Area of Ulcer, mm ²	Inhibition Rate, %
Control	22.3±4.3	
Form A		
12.5	6.9±2.1	69.3
25.0	5.9±2.4	73.7
50.0	3.4±2.3	84.4
Form B		
12.5	8.7±4.8	60.8
25.0	3.2±1.1	85.5
50.0	3.6±2.2	84.0
Form C		
12.5	2.8±1.7	87.4 ^a
25.0	3.2±1.1	85.8
50.0	2.2±0.9	90.4
Form D		
12.5	8.0±2.6	64.1

^a $p < 0.05$ relative to the same dose of form A or B.

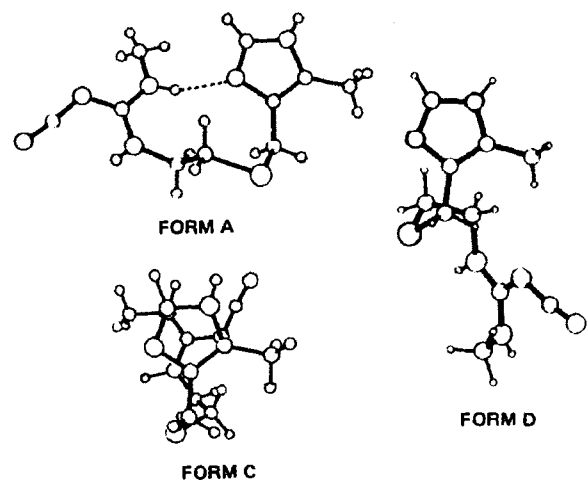


Fig. 26. Molecular Conformations of Cimetidine Forms A, C, and D

Dotted line of Form A represents an intramolecular hydrogen bond.

された。このことはまた、H2-レセプターには基質との結合に一定のポケットが存在すること、そのポケットの形状は基質ヒスタミンの折れ曲がり構造を受容するのに適した構造であるとともに、その窒素原子に対して側鎖アミノ基の空間配座の位置は水素結合可能なように分子設計することがアンタゴニスト活性を高める上で重要であることを示している。

6-2. カテプシン B 選択阻害剤の開発 システインプロテアーゼはシステイン (Cys) 残基が活性

Table 9. Chemical Structures, Drug Names and Relative Activities of H₂-Receptor Antagonists

No.	Chemical structure	Name	Activity
7		Cimetidine	2
8		Metiamide	2
9		Thiaburimamide	1
10		Burimamide	1
11		Ranitidine	3
12		RANTS	0
13		RANET	0

中心としてタンパク質分解を触媒する酵素群の総称で、植物細胞中ではパピインやアクチニジンが、動物細胞中ではカテプシン B, H, L 等がある。システインプロテアーゼは生体内で産生される前駆体タンパク質の活性型へのプロセシングや機能を失ったタンパク質の分解処理など生命維持にとって重要な役割を果たしている。一方、これら酵素機能の異常亢進は筋ジストロフィー症、骨粗鬆症、肺気腫、腫瘍細胞転移などの疾病との関係が示唆されている。それゆえ、各システインプロテアーゼに選択的な阻害剤の開発は重要である。

内因性システインプロテアーゼインヒビターとしてシスタチンファミリーが存在し、酵素機能を制御している。一方、外因性の低分子量インヒビターとしてはロイペプチン、アンチパイン、E64 等が知られている。筆者は微生物 *Aspergillus japonicus* から単離された代表的なシステインプロテアーゼインヒビター E64¹³⁷⁾ から開発された低分子量インヒビター E64c (Fig. 28) をリード化合物としてカテプシン B 選択的阻害剤の開発を試みた。

実験開始当初、カテプシン B の結晶構造解析には成功していなかったため、パピインと E64c の複合体の結晶構造を解析し、その結合様式を明らかにした (Fig. 29).¹³⁸⁻¹⁴⁵⁾ その結果、E64c のエポキシサクシニル基がパピインの活性中心である Cys25 の SH 基と共有結合を形成する共有結合型阻害剤であることを明らかにするとともに、この環開裂による OH 基の生成並びに E64c の他の構造部分のパピイン S1-S3 ポケットへの結合様式を明らかにした。ついで、その複合体の立体構造情報を基に、分子動力学計算によるカテプシン B の立体構造予測を行った。¹⁴⁶⁾ その結果、カテプシン B の基質結合ポケットの特徴はパピインとは反対側の S1'-S3' サイドにあり、それに対応する E64c 阻害剤の側鎖としては P1'-P3' に対応する部位での構造改変が示唆された。すなわち、E64c のエポキシ環に結合している側鎖がパピインの場合とは逆サイドへ結合することを予測し、カテプシン B の基質結合ポケットの構造特徴を考慮して設計した。^{147,148)} Table 10(a) は各サイトへの最適ドッキングを期待して設計した

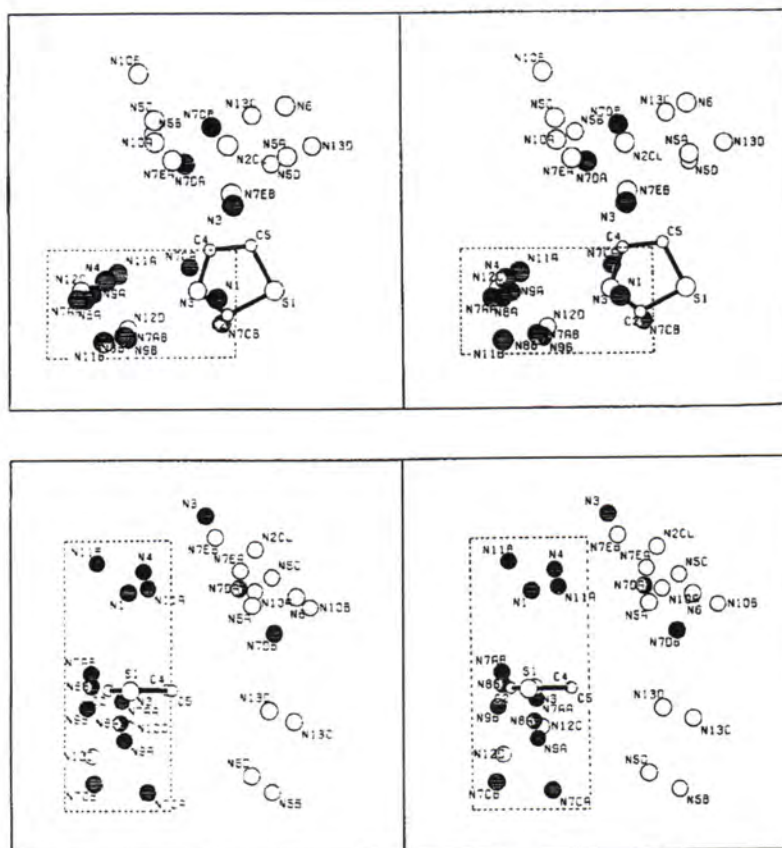


Fig. 27. Stereoscopic View of Spatial Position of Side Chain NH Group to the N Atom on Thiazole, Imidazole or Furan Ring, Viewed Perpendicular (upper) and Along (lower) to the Imidazole Ring Plane

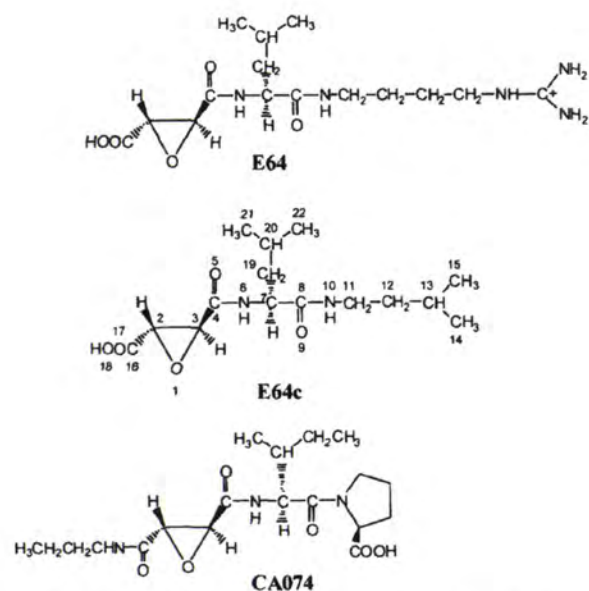


Fig. 28. Chemical Structures of E64, E64c and CA074

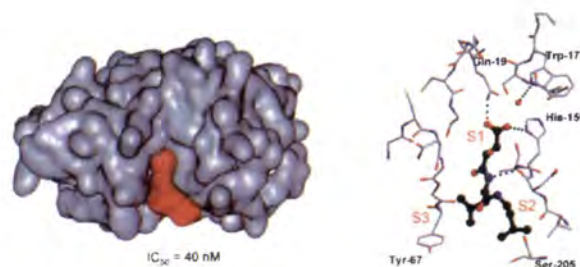


Fig. 29. Docking of E64c (red space-fill) to Active Site Cleft of Papain (black space-fill, left) and Interaction Mode of Epoxysuccinyl, Leucyl, and Isoamylamide Groups of E64c (right)

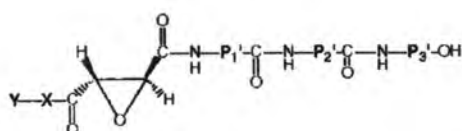
Red circles and dotted lines in right side represent oxygen atoms and hydrogen bonds, respectively.

側鎖とその阻害活性を示している。その結果、P1'を Ile 残基、P2'を Pro 残基の場合、カテプシン B に対する選択性と阻害活性が著しく向上した。なお、カテプシン B にはオクルディンググループと呼ばれる他のシステインプロテアーゼ群には存在しな

Table 10. Structure-Activity Relationship of E64c Analogues at (a) Sn' and (b) Sn Subsites

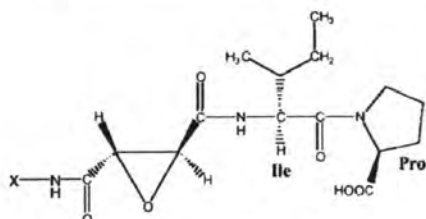
(a)

Compound			Cathepsin B (nM)	Papain (nM)
P1'	P2'	P3'		
Ile			24000	132000
Gly	Pro		15300	95400
Pro	Pro		50	>100000
Ile	Ala		23	5800
Ile	Pro		3	16000
Ile	Pro	OBzl	930	2000



(b)

Compound X	Cathepsin B (nM)	Papain (nM)
CH ₃ CH ₂	7	53000
(CH ₃) ₂ CH	5	55000
CH ₃ CH ₂ CH ₂ CA074	2	57400
(CH ₃) ₂ CH ₂ CH ₂	2	60000
Cyclo-(C ₆ H ₁₂)	2	14200



いアミノ酸配列を有し (Fig. 30), それが S3' サイト近傍に存在することが示唆されたことから, P3' 以上の構造付加はカテプシン B に対する阻害活性の向上に有効でないと予測された. 一方, Table 10 (b) に示すように, カテプシン B の S サイトには基質特異性を示すポケットは存在せず, いずれの側鎖においても優れた差はみられなかった. そのうち, 側鎖にプロピル基を有する CA074 は他のカテプシン群には顕著な阻害活性は示さないことから, カテプシン B に対する選択的特異的な共有結合型阻害剤として, 現在, 広く用いられている. 後年, E64c¹⁴⁹⁾ 及び一連の CA074 誘導体¹⁵⁰⁾ とカテプシン B との複合体の結晶構造を解析し, CA074 の阻害機構を明らかにした. その結果, 分子動力学計算により予測されたカテプシン B の基質特異性に関する構造特徴は, 詳細な点は異なるものの, 全体とし

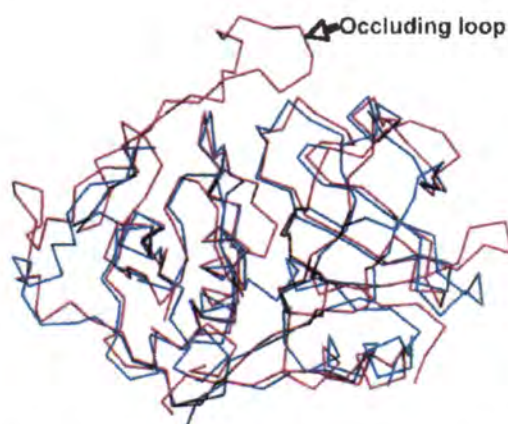


Fig. 30. Superimposition of C α Backbones of Tertiary Structures of Cathepsin B (red) and Papain (blue)

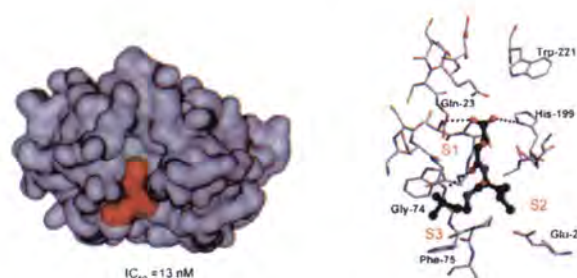


Fig. 31. Docking of CA074 to Active Site Cleft of Cathepsin B (space fill, left) and Interaction Mode of CA074 (thick bond) at Cathepsin B Binding Pocket (right)

て正しいことが確認できた (Fig. 31).

7. 認知症原因タンパク質タウの自己重合機構の解明と重合阻害剤分子の開発

7-1. タウタンパク質の自己重合機構の解析

微小管結合タンパク質タウは神経細胞の骨組みを作り細胞内の物質輸送を担う微小管に結合して, その重合促進と安定化に寄与している. アルツハイマー型認知症 (AD; Alzheimer's disease) 患者の脳内では, 異常にリン酸化されたタウは微小管への結合が抑制され, それに伴って自己重合を起し, PHF (paired helical filament) と呼ばれる不溶性線維 (タングル) の束を形成して神経細胞内に蓄積している.¹⁵¹⁾ これは神経原線維変化と呼ばれ, 認知症の重症度と高い相関を示し, アルツハイマー型認知症の病理学的変化を特徴づける病理構造物の1つとされている. タウ分子中の微小管結合部位 MBD (Microtubule Binding Domain) は, 相同性の高い約 30 残基のアミノ酸配列が 3 回 (3RMBD) 若し

くは4回(4RMBD)繰り返した特徴的な配列を有しており、タウの微小管結合能の発現領域であると同時に、自己重合にも大きく関与していると考えられている。^{152,153)} また、MBDを構成する4種のリピートペプチド(R1-R4)においても、その自己重合能に差異のあることが認められている。¹⁵⁴⁾ よって、MBDや各リピートペプチドの自己重合機構の解明とその重合を阻害する化合物の開発は、ADの治療や予防に有効であると考えられる。そこで、種々の物理化学的手法を駆使し、タウタンパク及びその構成分子(MBDと各リピートペプチド)(Fig. 32)の凝集機構の解明について研究を進めた。¹⁵⁵⁻¹⁶⁹⁾ その結果、(i)MBDを構成する各繰り返しペプチドの自己重合能は $R3 \gg R2 > R1 = R4$ の順であること、

(ii)とりわけMBDの自己会合にはR3のN-末端6残基(VQIVYK)の β シート様構造が凝集のための核形成に重要であること、(iii)R2-R3配列が重合に最も促進的であること、(iv)R2-R3の強い自己会合能は配列内に存在するLys, Pro, Tyr残基に大きく影響していること、(v)R1, R4の自己重合能は抑制的であるがMBD全体の重合度を成熟させるのに必要なこと等を明らかにしてきた。

一方、MBDの全体構造に関しては、重合していない正常なMBDは可溶性のランダム構造をとっているが、リン酸化等の環境変化によりR3のN-末端6残基は β シート構造に、R2-R3領域の残りの部分は両親媒性の α -ヘリックス構造に変換され、それが起点となってMBD全体の自己重合が開始さ

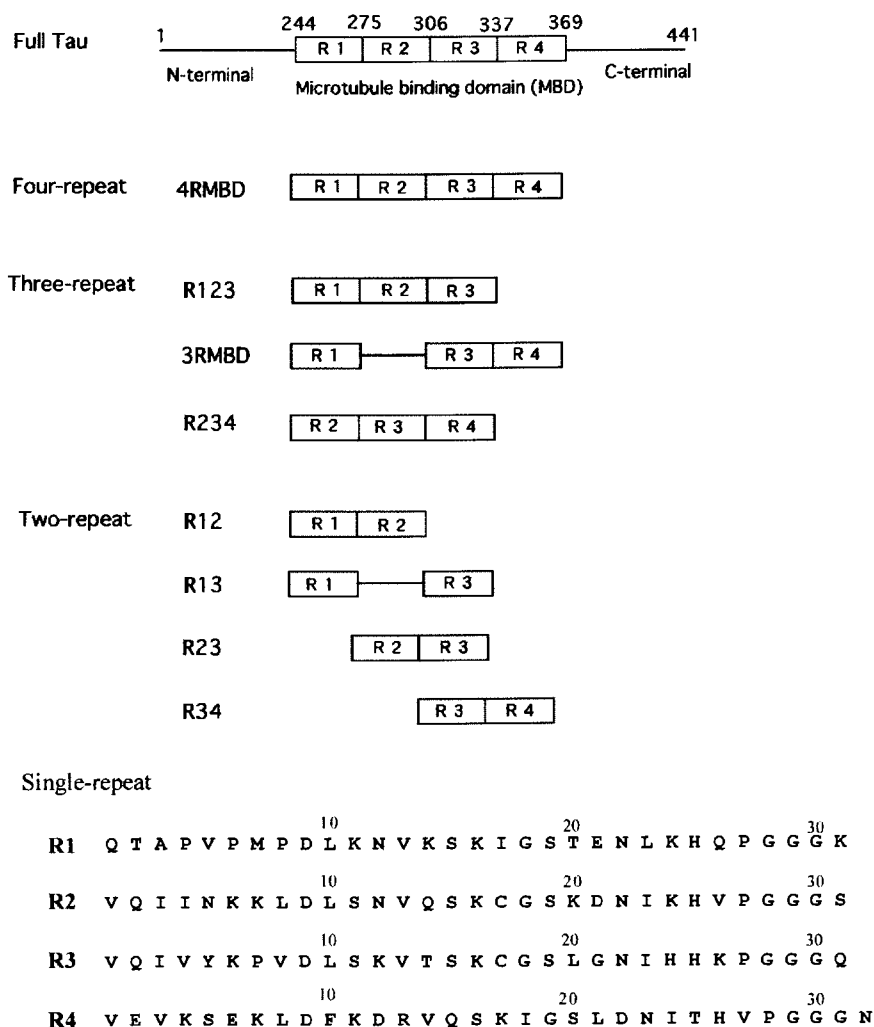


Fig. 32. Schematic Diagram of Full-length Tau, Three- and Four-repeated MBDs (3RMBD and 4RMBD) and Various Combinations of Their Constituents

れ、最終的に β シート様構造が形成される機構を提案した。¹⁶²⁾ また、441 アミノ酸残基からなる完全長タウのタンゲル形成には MBD の自己凝集の性質が大きく影響することを明らかにするとともに、一連のタウ変換体の自己凝集能測定から、Tyr310 残基はタウのフィラメント形成の中核をなしていることを初めて明らかにした。¹⁶⁹⁾ さらに、Tyr310 残基は Ile308 残基側鎖間で形成される CH $\cdots\pi$ 相互作用がフィラメント形成に不可欠であること、その構造要因として ³⁰⁶VQIVYK³¹¹ 配列の平面構造の Ile308 と Tyr310 の C-H $\cdots\pi$ 相互作用を介した安定化に起因していることを明らかにした (Table 11).¹⁶⁸⁾

そして、これまでの研究成果を基に、C-H $\cdots\pi$ 相互作用を介したタウタンパク質のタンゲル形成機構モデルを提唱した (Fig. 33).¹⁷⁰⁾

7-2. タウタンパク質の重合阻害分子

7-2-1. 食品中からの阻害物質の探索¹⁷¹⁾

食生活環境によって認知症の進行を抑えることができるという疫学的知見を参考に、種々な食品からタウ凝

集阻害物質を探索した。その結果、ワインなどに多く含まれるポリフェノール成分に強い抑制効果が認められた。ポリフェノール類 (Fig. 34) の構造活性相関から、シアニジン (Cy) のような完全な平面構造は阻害効果を示すのに対し、カテキン (CH) やエピカテキン (EC) のような平面構造からずれる置換基を有する化合物は阻害効果を示さないことを明らかにした。さらに、同様な平面構造のフェノチアジン骨格を有する化合物についても検討した結果、メチレンブルー (MB) やチオニン¹⁷²⁾ は強い凝集阻害効果を示すのに対し、同じ平面骨格を有するものの置換基が導入され平面性を失うクロルプロマジン (CP) は全く阻害効果を示さないことから、化合物の平面構造が重合阻害効果に不可欠な構造要素であることを明らかにした。

7-2-2. タウタンパク質の凝集阻害抗体

タウのタンゲル形成に重要な MBD 領域、なかでも R2 と R3 リピート領域の自己凝集能は極めて高いことから、この領域を選択的に認識する抗体はタウのタ

Table 11. Comparison of ThS Fluorescence Intensities and Electron Microscopy Morphologies of Full-length Three/Four-Repeated (3R/4R) Tau and Their Mutants (25 μ M)^{a,b}

Wild/Mutant	Without DTT		With DTT	
	Relative fluorescence intensity (%)	EM morphology	Relative fluorescence intensity (%)	EM morphology
3Rtau	100	filament	10	granule(+1)
I308A	0	no granule and no filament	0	no granule and no filament
Y310A	0	no granule and no filament	0	no granule and no filament
Q307Y	300	granule(+2)	300	granule
Q307Y/Y310A	10	granule(+1)	0	no granule and no filament
4Rtau	100	filament	10	granule(+1)
I308A	0	no granule and no filament	0	no granule and no filament
I308V	40	short filament	5	no granule and no filament
Y310A	0	no granule and no filament	0	no granule and no filament
Y310W	100	filament	150	filament
I308Y/Y310I	0	no granule and no filament	0	no granule and no filament
Q307Y	300	granule(+2)	300	granule(+2)
Q307Y/Y310A	10	no granule and no filament	5	no granule and no filament
Q307Y/V309A/Y310A	0	no granule and no filament	0	no granule and no filament

^a The fluorescence intensities of mutants correspond to the values relative to those of wild 3Rtau and 4Rtau without DTT at 1 h after initiating aggregation by addition of heparin. ^b EM morphology at 48 h after initiating aggregation by addition of heparin.

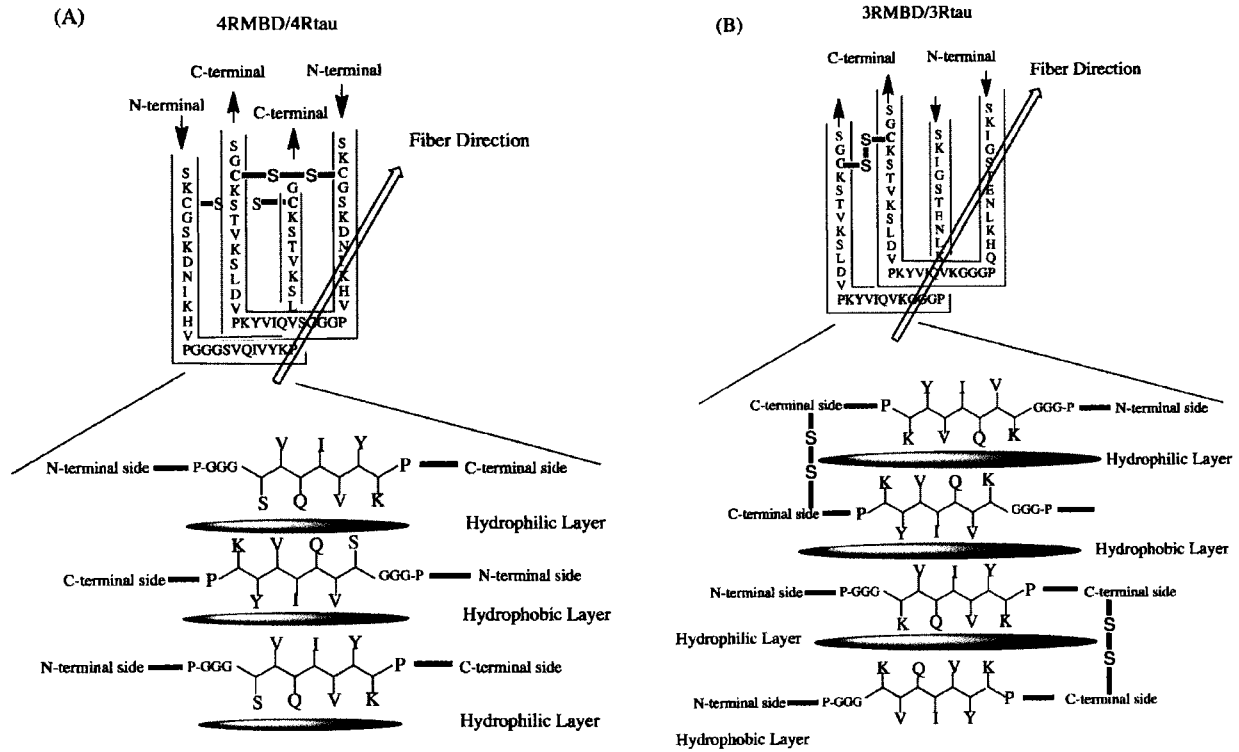


Fig. 33. Schematic Aggregation Model of Four-repeated (A) and Three-repeated (B) MBD or Full-length Tau
 The overall structure of tau and its piling direction are shown at the upper side, and the alternate hydrophobic and hydrophilic interaction modes between neighboring VQIVYK β -strands are shown at the lower side.

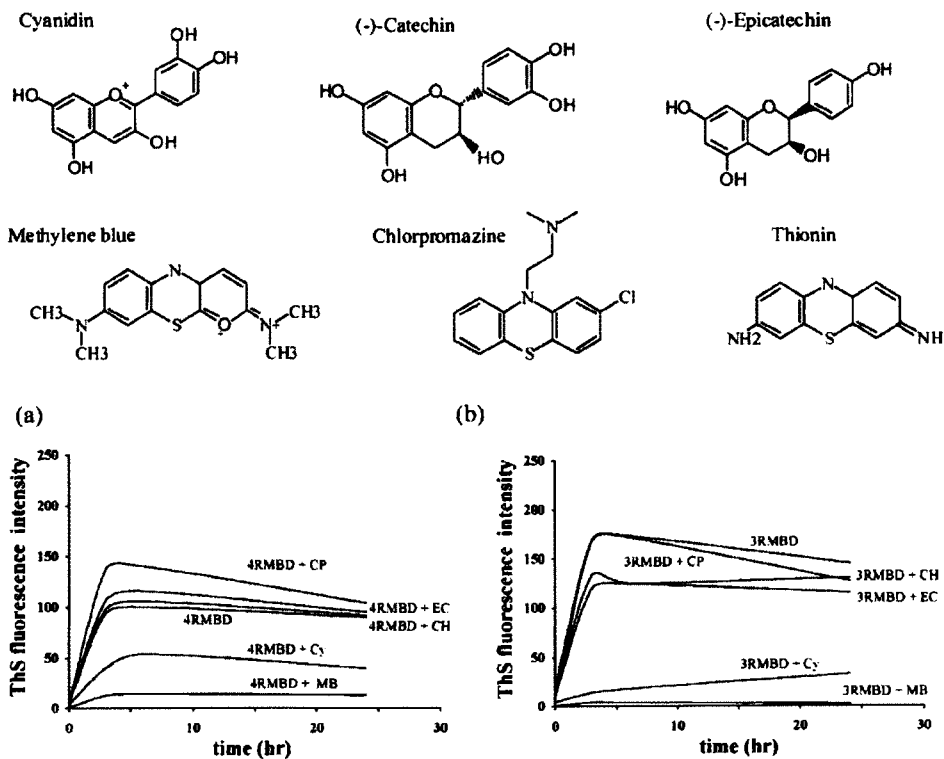


Fig. 34. Chemical Structures of Cyanidin, Methylene Blue, and Their Analogues (upper) and ThS Fluorescence Intensity Changes in 50 mM Tris-HCl Buffer (pH 7.6, lower)

ングル形成阻害に極めて有効であることが期待できる。そこで、種々の MBD リピート領域認識抗体の作成を試みた結果、R1 の C-末端から R2 の N-末端領域に存在する $^{272}\text{GGKVQIINKKLDL}^{283}$ 配列 (Fig. 32) を認識する Tau2r3 抗体をマウスハイブリドーマ細胞から単離精製することに成功した。この Tau2r3 抗体は抗原である R23 及び 4RMBD の自己重合を完全に阻害すること (Fig. 35), 3RMBD 及び R1 の重合はある程度抑制すること, R3, R4 リピートペプチドの重合は全く抑制しないことを確認した。このことは Tau2r3 抗体がタウの $^{272}\text{GGKVQIINKKLDL}^{283}$ 配列を正確に認識していることを示している。¹⁷²⁾

その認識様式を原子レベルで解析するため、Tau2r3 抗体のパパイン処理によって得られる Fab フラグメント (Fab2r3) とエпитープ断片である VQIINK ペプチドとの複合体の結晶構造解析に取り組んだ。解析によって得られた Fab2r3-VQIINK の全体構造を Fig. 36 に示している。また、VQIINK の Fab2r3 の超可変領域への結合様式は Fig. 37 に示している。VQIINK の Glu (Q) と Lys (K) の両極性基が抗体の超可変領域 (CDR 領域) との結合認識に大きく関与していた。前者は Fab2r3 L 鎖の Tyr30, Thr31, Gly94 とのスタッキング相互作用及び水素結合により、後者は H 鎖の 99-104 番目の極性アミノ酸残基との水素結合により安定に保持されている。現在、R3 リピート領域を認識する抗体の作成に取り組んでいて、認知症治療の抗体医薬品の開発を目指している。

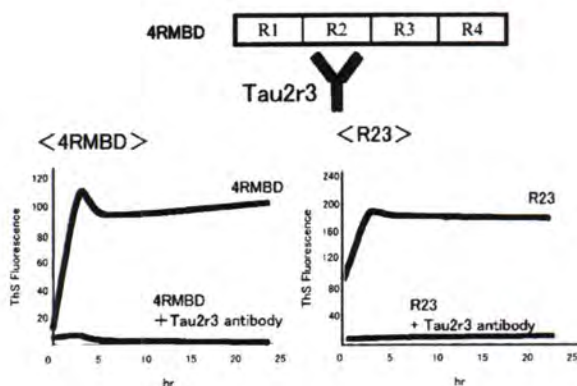


Fig. 35. Inhibition of Tau2r3 Antibody for Aggregation of 4RMBD and R23

8. おわりに

40 年近い研究活動のうちの主なものについてその概要を述べてきた。しかし、それ以外にも、興味深い多くの天然物や合成分子あるいはその標的分子との複合体の結晶構造解析による構造-活性相関な

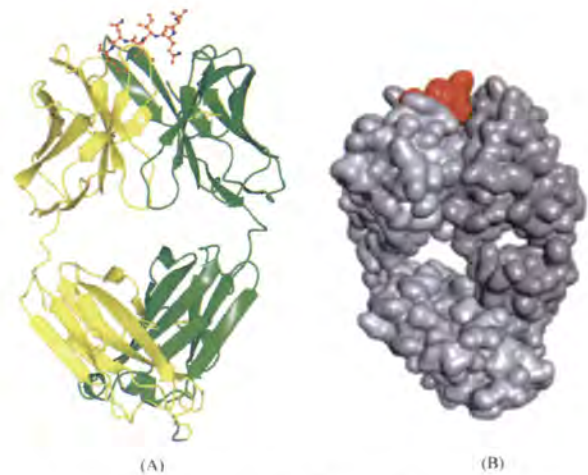


Fig. 36. Overall Structure of Fab2r3-VQIINK Complex, Shown by Ribbon (A) and Space-Fill (B) Models

Heavy and light chains of Fab2r3 in (A) are shown with yellow and green ribbons, respectively, and VQIINK peptide (red) is shown by ball-and-stick model.

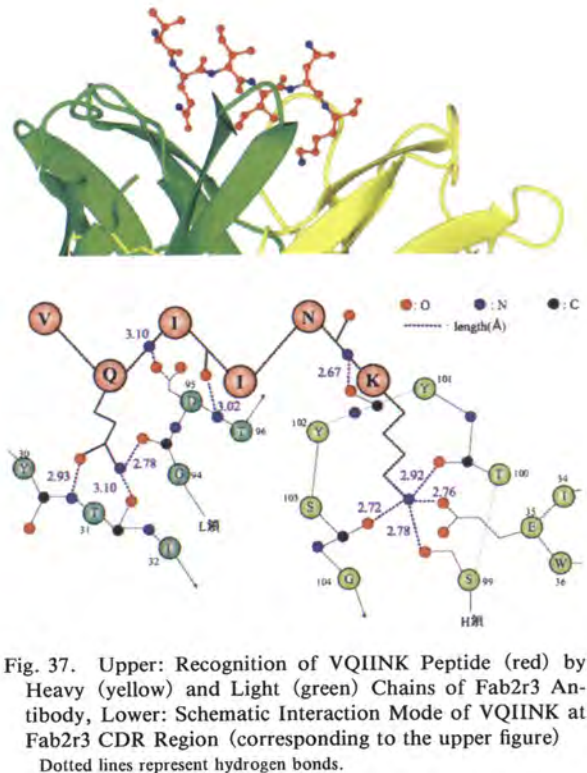


Fig. 37. Upper: Recognition of VQIINK Peptide (red) by Heavy (yellow) and Light (green) Chains of Fab2r3 Antibody, Lower: Schematic Interaction Mode of VQIINK at Fab2r3 CDR Region (corresponding to the upper figure) Dotted lines represent hydrogen bonds.

ど、その研究分野で活躍されている先生との共同研究により有意義な研究を行うことができたことに感謝している。

本学は私立薬科大学の中で、充実した結晶構造解析のための測定機器を備えている。それは、これまで数度にわたる私立大学大型研究機器購入助成金を獲得して最新の超強力 X 線回折装置（低分子・高分子用）を導入することができたことにある。これは学内の多くの先生方が構造解析の重要性を理解して頂き、機器導入に協力して頂いた賜物であり、ここに感謝申し上げたい。これまでに数多くの研究成果を報告できたのもこの機器によるところが極めて大きい。

ここに紹介した研究は長年にわたり友尾幸司准教授と尹 康子准教授とともに進めてきた薬品物理化学研究室の成果である。また、これらの研究を精力的に行ってくれた多くの大学院生、学部学生の努力の賜物であり、改めて各位に感謝を申し上げる。

なお、eIF4E の mRNA キャップ構造認識機構の研究は上田仁司博士（バイエル薬品）、森野重信博士（アステラス製薬）そして上杉晴一名誉教授（横浜国大）、カテプシン B 阻害剤の研究は山本大助准教授（大阪医大）、山元 淳博士（田辺三菱製薬）並びに大正製薬（北村一泰博士、村田充男博士、松本慶太博士）、タウタンパク質の自己重合機構の研究は箕浦克彦講師（大阪薬大）、角田美穂博士（行動医学研究所）そして谷口泰造教授（姫路獨協大・薬）との共同研究であり、この場を借りて感謝申し上げます。

REFERENCES

- 1) Nakagaki M., Inoue M., Mitoguchi S., Ishida T., *Chem. Pharm. Bull.*, **27**, 1887-1892 (1979).
- 2) Inoue M., Inoue A., Mino Y., Ishida T., Nakagaki M., *Chem. Pharm. Bull.*, **28**, 1491-1496 (1980).
- 3) Inoue M., In Y., Ishida T., *J. Lipid Res.*, **33**, 985-994 (1992).
- 4) Ireland C. M., Durso A. R. Jr., Newman R. A., Hacker M. P., *J. Org. Chem.*, **47**, 1807-1811 (1982).
- 5) Hamamoto Y., Endo M., Kanagawa M., Nakanishi T., Mizukawa K., *J. Chem. Soc., Chem. Commun.*, 323-324 (1983).
- 6) Ishida T., Inoue M., Hamada Y., Kato S., Shioiri T., *J. Chem. Soc., Chem. Commun.*, 370-371 (1987).
- 7) Ishida T., Tanaka M., Nabae M., Inoue M., Kato S., Hamada Y., Shioiri T., *J. Org. Chem.*, **53**, 107-112 (1988).
- 8) Ishida T., Ohishi H., Inoue M., Kamigauchi M., Sugiura M., Takao N., Kato S., Hamada Y., Shioiri T., *J. Org. Chem.*, **54**, 5337-5343 (1989).
- 9) In Y., Doi M., Inoue M., Ishida T., Hamada Y., Shioiri T., *Chem. Pharm. Bull.*, **41**, 1686-1690 (1993).
- 10) In Y., Doi M., Inoue M., Ishida T., Hamada Y., Shioiri T., *Acta Crystallogr., Sect. C*, **50**, 432-434 (1994).
- 11) Ishida T., In Y., Shinozaki F., Doi M., Yamamoto D., Hamada Y., Shioiri T., Kamigauchi M., Sugiura M., *J. Org. Chem.*, **60**, 3944-3952 (1995).
- 12) Kobayashi M., Tanaka J., Katori T., Matsuura M., Kitagawa I., *Tetrahedron Lett.*, **30**, 2963-2966 (1989).
- 13) Kitagawa I., Kobayashi M., Katori T., Yamashita M., Tanaka J., Doi M., Ishida T., *J. Am. Chem. Soc.*, **112**, 3710-3712 (1990).
- 14) Doi M., Ishida T., Kobayashi M., Kitagawa I., *J. Org. Chem.*, **56**, 3629-3632 (1991).
- 15) Takesako K., Ikai K., Haruna F., Endo M., Shimanaka K., Sono E., Nakamura T., Kato I., *J. Antibiot.*, **44**, 919-924 (1991).
- 16) Ishida T., In Y., Fujikawa A., Urata H., Inoue M., Ikai K., Takesako K., Kato I., *J. Chem. Soc., Chem. Commun.*, 1231-1233 (1992).
- 17) Fujikawa A., In Y., Inoue M., Ishida T., Nemoto N., Kobayashi Y., Kataoka R., Ikai K., Takesako K., Kato I., *J. Org. Chem.*, **59**, 570-578 (1994).
- 18) In Y., Ishida T., Takesako K., *J. Pept. Res.*, **53**, 492-500 (1999).
- 19) Minami Y., Yoshida K., Azuma R., Nishii M., Inagaki J., Nohara F., *Tetrahedron Lett.*, **33**, 7373-7376 (1992).
- 20) Ishida T., In Y., Nishi M., Minami Y., *Chem. Lett.*, 1321-1322 (1994).
- 21) Hughes J., Smith T. W., Kosterlitz H. W., Fothergill L., Morgan B. A., Morris H. R.,

- Nature*, **258**, 577–579 (1975).
- 22) Paterson S. J., Robson L. E., Kosterlitz H. W., “The Peptides, Analysis, Synthesis, Biology,” Vol. 6, eds. by Udenfriend S., Meienhofer J., Academic Press Inc., New York, 1984, pp. 147–189.
 - 23) Ishida T., Kenmotsu M., Mino Y., Inoue M., Fujiwara T., Tomita K., Kimura T., Sakakibara S., *Biochem. J.*, **218**, 677–689 (1984).
 - 24) Doi M., Ishida T., Inoue M., Fujiwara T., Tomita K., Kimura T., Sakakibara S., *FEBS Lett.*, **170**, 229–231 (1984).
 - 25) Doi M., Tanaka M., Ishida T., Inoue M., Fujiwara T., Tomita K., Kimura T., Sakakibara S., Sheldrick G. M., *J. Biochem.*, **101**, 485–490 (1987).
 - 26) Ishida T., Yoneda S., Doi M., Inoue M., Kitamura K., *Biochem. J.*, **255**, 621–628 (1988).
 - 27) Yoneda S., Kitamura K., Doi M., Inoue M., Ishida T., *FEBS Lett.*, **239**, 271–275 (1988).
 - 28) Doi M., Takehara S., Ishida T., Inoue M., *Int. J. Pept. Protein Res.*, **34**, 369–373 (1989).
 - 29) Doi M., Ishida T., *Curr. Topics Mol. Pharmacol.*, **1**, 23–31 (1993).
 - 30) Doi M., Ishibe A., Shinozaki H., Urata H., Inoue M., Ishida T., *Int. J. Pept. Protein Res.*, **43**, 325–331 (1994).
 - 31) Segawa M., Ohno Y., Doi M., Inoue M., Ishida T., Iwashita T., *Int. J. Pept. Protein Res.*, **44**, 295–304 (1994).
 - 32) Segawa M., Ohno Y., Doi M., Ishida T., Iwashita T., *Int. J. Pept. Protein Res.*, **46**, 37–46 (1995).
 - 33) Ohno Y., Segawa M., Ohishi H., Doi M., Kitamura K., Ishida T., Inoue M., Iwashita T., *Eur. J. Biochem.*, **212**, 185–191 (1993).
 - 34) In Y., Minoura K., Ohishi H., Minakata H., Kamigauchi M., Sugiura M., Ishida T., *J. Pept. Res.*, **58**, 399–412 (2001).
 - 35) In Y., Minoura K., Tomoo K., Sasaki Y., Lazarus L. H., Okada Y., Ishida T., *FEBS J.*, **272**, 5079–5097 (2005).
 - 36) Tsuda Y., Miyazaki A., Yamada T., Isozaki K., Shimohigashi Y., Ambo A., Sasaki Y., Minoura K., In Y., Ishida T., Okada Y., *Pept. Sci.*, **2008**, 227–228 (2009).
 - 37) Doi M., Tanaka M., Ishida T., Inoue M., *FEBS Lett.*, **213**, 265–268 (1987).
 - 38) Yara H., Katagawa Y., Doi M., Ishida T., Inoue M., Yasuda M., Baba A., Iwata H., Kitamura K., Sadatome T., *Eur. J. Pharmacol.*, **188**, 359–368 (1990).
 - 39) Schwyzer R., *Biochemistry*, **25**, 6335–6342 (1986).
 - 40) Kim K. H., Takeuchi H., Kamatani Y., Minakata H., Nomoto K., *Eur. J. Pharmacol.*, **194**, 99–106 (1991).
 - 41) Kim K. L., Takeuchi H., Kamatani Y., Minakata H., Nomoto K., *Life Sci.*, **48**, PL91–PL96 (1991).
 - 42) Kamatani Y., Minakata H., Iwashita T., Nomoto K., In Y., Doi M., Ishida T., *FEBS Lett.*, **276**, 95–97 (1991).
 - 43) Ishida T., In Y., Doi M., Inoue M., Yasuda Y., Minakata H., Iwashita T., Nomoto K., *Int. J. Pept. Protein Res.*, **39**, 258–264 (1992).
 - 44) Ishida T., In Y., Inoue M., Yasuda Y., Minakata H., Iwashita T., Nomoto K., *FEBS Lett.*, **307**, 253–256 (1992).
 - 45) Maeda M., Kodama T., Tanaka T., Yoshizumi H., Takemoto T., Nomoto K., Fujita T., *Chem. Pharm. Bull.*, **34**, 4892–4895 (1986).
 - 46) Nomoto K., Takemoto T., Maeda M., In Y., Doi M., Inoue M., Ishida T., *Biochem. Biophys. Res. Commun.*, **187**, 325–331 (1992).
 - 47) Pullman B., Pullman A., *Proc. Natl. Acad. Sci. USA*, **44**, 1197–1202 (1958).
 - 48) Ishida T., Inoue M., Senda S., Tomita K., *Biochem. Biophys. Res. Commun.*, **83**, 21–26 (1978).
 - 49) Inoue M., Ishida T., Fujiwara T., Tomita K., *Bull. Chem. Soc. Jpn.*, **51**, 1118–1122 (1978).
 - 50) Miyamoto Y., Ishida T., Inoue M., *Chem. Pharm. Bull.*, **29**, 3427–3432 (1981).
 - 51) Ishida T., Miyamoto Y., Nakamura A., Inoue M., *Acta Crystallogr., Sect. B*, **38**, 192–195 (1982).
 - 52) Ishida T., Ibe S., Inoue M., *J. Chem. Soc., Perkin Trans. 2*, 297–304 (1984).
 - 53) Ishida T., Inoue M., Fujiwara T., Tomita K., *J. Chem. Soc., Chem. Commun.*, 358–360 (1979).
 - 54) Inoue M., Shibata M., Ishida T., *Biochem. Biophys. Res. Commun.*, **93**, 415–419 (1980).
 - 55) Ishida T., Yanagitani T., Nakagawa Y., Inoue M., *Biochem. Biophys. Res. Commun.*, **99**, 1179–1184 (1981).

- 56) Inoue M., Shibata M., Kondo Y., Ishida T., *Biochemistry*, **20**, 2936–2945 (1981).
- 57) Inoue M., Okuda Y., Ishida T., Nakagaki M., *Arch. Biochem. Biophys.*, **227**, 52–70 (1983).
- 58) Ishida T., Itoh M., Horiuchi M., Yanashita S., Doi M., Inoue M., Mizunoya Y., Tona Y., Okada A., *Chem. Pharm. Bull.*, **34**, 1853–1864 (1986).
- 59) Inoue M., Hirano H., Sugiyama K., Ishida T., Nakagaki M., *Biochem. Biophys. Res. Commun.*, **108**, 604–609 (1982).
- 60) Ishida T., Matsui M., Inoue M., Hirano H., Yamashita M., Sugiyama K., *Biochem. Biophys. Res. Commun.*, **116**, 486–491 (1983).
- 61) Ishida T., Matsui M., Inoue M., Hirano H., Yamashita M., Sugiyama K., Sugiura M., Tomita K., *J. Am. Chem. Soc.*, **107**, 3305–3314 (1985).
- 62) Ishida T., Doi M., Tomita K., Hayashi H., Inoue M., Urakami T., *J. Am. Chem. Soc.*, **111**, 6822–6828 (1989).
- 63) Ishida T., Kawamoto E., In Y., Amano T., Kanayama J., Doi M., Iwashita T., Nomoto K., *J. Am. Chem. Soc.*, **117**, 3278–3279 (1995).
- 64) Ishida T., In Y., Kawamoto E., Amano T., Kanayama J., Doi M., Iwashita T., Nomoto K., *Chem. Pharm. Bull.*, **44**, 1387–1390 (1996).
- 65) Kawamoto E., Amano T., Kanayama J., In Y., Doi M., Ishida T., Iwashita T., Nomoto K., *J. Chem. Soc., Perkin Trans. 2*, 1331–1336 (1996).
- 66) Gallop P. M., Paz M. A., Fluckiger R., Kagan H. M., *Trends Biochem. Sci.*, **14**, 343–346 (1989).
- 67) Duine J. S., Frank J., Jongejan J. A., *Adv. Enzymol.*, **59**, 169–212 (1986).
- 68) Ishida T., Inoue M., Tomita K., *Acta Crystallogr., Sect. B*, **35**, 1642–1648 (1979).
- 69) Ishida T., Inoue M., Senda S., Tomita K., *Bull. Chem. Soc. Jpn.*, **52**, 2953–2958 (1979).
- 70) Ishida T., Doi M., Okuno T., Inoue M., *Chem. Pharm. Bull.*, **30**, 4249–4257 (1982).
- 71) Ishida T., Yamamoto K., Inoue M., *Bull. Chem. Soc. Jpn.*, **56**, 955–956 (1983).
- 72) Ishida T., Tokura Y., Shimamoto M., Doi M., Inoue M., *Chem. Pharm. Bull.*, **35**, 1691–1701 (1987).
- 73) Ishida T., Inoue M., *Biochem. Biophys. Res. Commun.*, **99**, 149–154 (1981).
- 74) Ishida T., Usami H., Inoue M., Yamagata Y., Tomita K., *Biochem. Biophys. Res. Commun.*, **107**, 746–751 (1982).
- 75) Ishida T., Katsuta M., Inoue M., Yanagata Y., Tomita K., *Biochem. Biophys. Res. Commun.*, **115**, 849–854 (1983).
- 76) Ishida T., Shibata M., Fujii K., Inoue M., *Biochemistry*, **22**, 3571–3581 (1983).
- 77) Ishida T., Usami H., Inoue M., *Chem. Pharm. Bull.*, **31**, 4220–4229 (1983).
- 78) Ishida T., Kamiichi K., Kuwahara A., Doi M., Inoue M., *Biochem. Biophys. Res. Commun.*, **136**, 294–299 (1986).
- 79) Kamiichi K., Danshita M., Minamino N., Doi M., Ishida T., Inoue M., *FEBS Lett.*, **195**, 57–60 (1986).
- 80) Kamigauchi M., Doi M., Nabae M., Ishida T., Inoue M., *J. Chem. Soc., Perkin Trans. 1*, 1739–1745 (1987).
- 81) Ishida T., Doi M., Ueda H., Inoue M., Scheldrick G. M., *J. Am. Chem. Soc.*, **110**, 2286–2294 (1988).
- 82) Ueda H., Segawa K., Doi M., Inoue M., Ishida T., *Nucleic Acid Res.*, **21**, 59–60 (1989).
- 83) Ishida T., Ohnishi K., Doi M., Inoue M., *Chem. Pharm. Bull.*, **37**, 1–4 (1989).
- 84) Ishida T., Tarui M., In Y., Ogiyama M., Doi M., Inoue M., *FEBS Lett.*, **333**, 214–216 (1993).
- 85) Ishida T., Iyo H., Ueda H., Doi M., Inoue M., *J. Chem. Soc., Chem. Commun.*, 217–218 (1990).
- 86) Ishida T., Iyo H., Ueda H., Doi M., Inoue M., Nishimura S., Kitamura K., *J. Chem. Soc., Perkin Trans 1*, 1847–1853 (1991).
- 87) Iyo H., Ueda H., Usami Y., Kafuku Y., Doi M., Inoue M., Ishida T., *Chem. Pharm. Bull.*, **39**, 2483–2486 (1991).
- 88) Tarui M., Furumura H., Kafuku Y., Ishida T., Inoue M., *Biochem. Biophys. Res. Commun.*, **183**, 577–583 (1992).
- 89) Kafuku Y., Ohnishi J., Doi M., Inoue M., Ishida T., *Chem. Pharm. Bull.*, **41**, 231–234 (1993).
- 90) Ishida T., Toda Y., Tarui M., Doi M., Inoue M., *Chem. Pharm. Bull.*, **42**, 674–676 (1994).
- 91) Sonenberg N., Hinnebusch A. G., *Cell*, **136**,

- 731–745 (2009).
- 92) Ueda H., Maruyama H., Doi M., Inoue M., Ishida T., Morioka H., Tanaka T., Nishikawa S., Uesugi S., *J. Biochem.*, **109**, 882–889 (1991).
- 93) Morino S., Yasui M., Doi M., Inoue M., Ishida T., Ueda H., Uesugi S., *J. Biochem.*, **116**, 687–693 (1994).
- 94) Morino S., Teraoka Y., Doi M., Ishida T., Ueda H., Uesugi S., *Biol. Pharm. Bull.*, **18**, 372–376 (1995).
- 95) Morino S., Ueda H., Doi M., Ishida T., *Yakugaku Zasshi*, **115**, 401–419 (1995).
- 96) Morino S., Hazama H., Ozaki M., Teraoka Y., Shibata S., Doi M., Ueda H., Ishida T., Uesugi S., *Eur. J. Biochem.*, **239**, 597–601 (1996).
- 97) Teraoka Y., Morino S., Tomoo K., Ishida T., *Biochem. Biophys. Res. Commun.*, **228**, 704–708 (1996).
- 98) Morino S., Tomoo K., Nishi N., Okabe K., Doi M., Ishida T., Kitamura K., *J. Biochem.*, **119**, 224–225 (1996).
- 99) Tomoo K., Shen X., Okabe K., Nozoe Y., Fukuhara S., Morino S., Ishida T., Taniguchi T., Hasegawa H., Terashima A., Sasaki M., Katsuya Y., Kitamura K., Miyoshi H., Ishikawa M., Miura K., *Biochem. J.*, **362**, 539–544 (2002).
- 100) Tomoo K., Shen X., Okabe K., Nozoe K., Fukuhara S., Morino S., Ishida T., Taniguchi T., Sasaki M., Katsuya Y., Kitamura K., Miyoshi H., Ishikawa M., Miura K., *Acta Crystallogr., Sect. A*, **58**, C278 (2002).
- 101) Tomoo K., Shen X., Okabe K., Nozoe Y., Fukuhara S., Morino S., Sasaki M., Taniguchi T., Miyagawa H., Kitamura K., Miura K., Ishida T., *J. Mol. Biol.*, **328**, 365–383 (2003).
- 102) Nishi N., Morino S., Tomoo K., Youtani T., Ishida T., *J. Biochem.*, **123**, 157–161 (1998).
- 103) Miyoshi H., Youtani T., Ide H., Hori H., Okamoto K., Ishikawa M., Wakiyama M., Nishino T., Ishida T., Miura K., *J. Biochem.*, **126**, 897–904 (1999).
- 104) Youtani T., Tomoo K., Ishida T., Miyoshi H., Miura K., *IUBMB Life*, **49**, 27–31 (2000).
- 105) Shen X., Tomoo K., Uchiyama S., Kobayashi Y., Ishida T., *Chem. Pharm. Bull.*, **49**, 1299–1303 (2001).
- 106) Tomoo K., Matsushita Y., Fujisaki H., Abiko F., Shen X., Taniguchi T., Miyagawa H., Kitamura K., Miura K., Ishida T., *Biochim. Biophys. Acta*, **1753**, 191–208 (2005).
- 107) Fukuyo A., In Y., Ishida T., Tomoo K., *J. Pept. Sci.*, **17**, 650–657 (2011).
- 108) Abiko F., Tomoo K., Mizuno A., Morino S., Imataka H., Ishida T., *Biochem. Biophys. Res. Commun.*, **355**, 667–672 (2007).
- 109) Mizuno A., In Y., Fujita Y., Abiko F., Miyagawa H., Kitamura K., Tomoo K., Ishida T., *FEBS Lett.*, **582**, 3439–3444 (2008).
- 110) Paku K. S., Umenaga Y., Usui T., Fukuyo A., Mizuno A., In Y., Ishida T., Tomoo K., *Biochem. J.*, **441**, 237–245 (2012).
- 111) Umenaga Y., Paku K. S., In Y., Ishida T., Tomoo K., *Biochem. Biophys. Res. Commun.*, **414**, 462–467 (2011).
- 112) In Y., Shibata M., Doi M., Ishida T., Inoue M., Sasaki Y., Morimoto S., *J. Chem. Soc., Chem. Commun.*, 473–474 (1986).
- 113) Doi M., In Y., Inoue M., Ishida T., Iizuka K., Akahane K., Harada H., Umeyama H., Kiso Y., *J. Chem. Soc., Perkin Trans. 2*, 1153–1158 (1991).
- 114) Ishida T., Morimoto H., Inoue M., Fujiwara T., Tomita K., *J. Chem. Soc., Chem. Commun.*, 671–673 (1981).
- 115) Ishida T., Tanaka A., Inoue M., Fujiwara T., Tomita K., *J. Am. Chem. Soc.*, **104**, 7239–7248 (1982).
- 116) Nakamura M., Tomoo K., Ishida T., Taguchi H., Tsuda Y., Okada Y., Okunomiya A., Wanaka K., Okamoto S., *Biochem. Biophys. Res. Commun.*, **213**, 583–587 (1995).
- 117) Odagaki Y., Nakai H., Senokuchi K., Kawamura M., Hamanaka N., Nakamura M., Tomoo K., Ishida T., *Biochemistry*, **34**, 12849–12853 (1995).
- 118) Tomoo K., Satoh K., Tsuda Y., Wanaka K., Okamoto S., Hijikata-Okunomiya A., Okada Y., Ishida T., *J. Biochem.*, **129**, 455–460 (2001).
- 119) Ishida T., In Y., Ohishi H., Yamamoto D., Inoue M., Tanaka C., Ueno Y., Ohmomo Y., Kanda N., Tanaka A., Tanimoto T., *Mol. Pharmacol.*, **34**, 377–387 (1988).
- 120) Ishida T., In Y., Inoue M., Ueno Y., Tanaka C., Hamanaka N., *Tetrahedron Lett.*, **30**, 959

- 962 (1989).
- 121) Ishida T., In Y., Inoue M., Tanaka C., Hamanaka N., *J. Chem. Soc., Perkin Trans. 2*, 1085-1091 (1990).
- 122) Ishida T., In Y., Tanaka C., Inoue M., *Acta Crystallogr., Sect. B.*, **47**, 806-813 (1991).
- 123) Tomoo K., Ohishi H., Ishida T., Inoue M., Ikeda K., Aoki Y., Samejima Y., *J. Biol. Chem.*, **264**, 3636-3638 (1989).
- 124) Fujiyoshi T., Yoneda S., Kitamura K., Amisaki T., Inoue M., Ishida T., *Protein Eng.*, **4**, 443-450 (1991).
- 125) Tomoo K., Ohishi H., Doi M., Ishida T., Inoue M., Ikeda K., Hata Y., Samejima Y., *Biochem. Biophys. Res. Commun.*, **184**, 37-143 (1992).
- 126) Tomoo K., Ohishi H., Doi M., Ishida T., Inoue M., Ikeda K., Mizuno H., *Biochem. Biophys. Res. Commun.*, **187**, 821-827 (1992).
- 127) Ohishi H., Fujii S., Tomoo K., Ishida T., Ikeda K., Tanabe K., Kitamura K., *J. Biochem.*, **114**, 210-214 (1993).
- 128) Tomoo K., Fujii S., Ishida T., Inoue M., Ikeda K., Samejima Y., Iwata S., Katsunuma S., *J. Biochem.*, **113**, 411-412 (1993).
- 129) Tomoo K., Ohishi H., Ishida T., Inoue M., Ikeda K., Sumiya S., Kitamura K., *Protein Struct. Funct. Genet.*, **19**, 330-339 (1994).
- 130) Tomoo K., Yamane A., Ishida T., Fujii S., Ikeda K., Iwama S., Katsumura S., Sumiya S., Miyagawa H., Kitamura K., *Biochim. Biophys. Acta*, **1340**, 178-186 (1997).
- 131) Shibata M., Kagawa M., Morisaka K., Ishida T., Inoue M., *Acta Crystallogr., Sect. C*, **39**, 1255-1257 (1983).
- 132) Shibata M., Kokubo H., Morimoto K., Morisaka K., Ishida T., Inoue M., *J. Pharm. Sci.*, **72**, 1436-1442 (1983).
- 133) Kokubo H., Morimoto K., Ishida T., Inoue M., Morisaka K., *Int. Pharm.*, **35**, 181-183 (1987).
- 134) Ishida T., In Y., Shibata M., Doi M., Inoue M., Yanagisawa I., *Mol. Pharmacol.*, **31**, 410-416 (1987).
- 135) In Y., Ishida T., Doi M., Inoue M., Shibata K., *Chem. Pharm. Bull.*, **36**, 2295-2302 (1988).
- 136) Ishida T., In Y., Doi M., Inoue M., Yanagisawa I., *Acta Crystallogr., Sect. B*, **45**, 505-512 (1989).
- 137) Hanada K., Tamai M., Yamagishi S., Ohmura S., Sawada J., Tanaka I., *Agric. Biol. Chem.*, **42**, 523-528 (1978).
- 138) Matsumoto K., Yamamoto D., Ohishi H., Tomoo K., Ishida T., Inoue M., Sadatome T., Kitamura K., Mizuno H., *FEBS Lett.*, **245**, 177-180 (1989).
- 139) Yamamoto D., Matsumoto K., Ohishi H., Ishida T., Inoue M., Kitamura K., Hanada K., *FEBS Lett.*, **263**, 134-136 (1990).
- 140) Yamamoto D., Ishida T., Inoue M., *Biochem. Biophys. Res. Commun.*, **171**, 711-716 (1990).
- 141) Yamamoto D., Ohishi H., Ishida T., Inoue M., Sumiya S., Kitamura K., *Chem. Pharm. Bull.*, **38**, 2339-2343 (1990).
- 142) Yamamoto D., Matsumoto K., Ohishi H., Ishida T., Inoue M., Kitamura K., Mizuno H., *J. Biol. Chem.*, **266**, 14771-14777 (1991).
- 143) Kim M. J., Yamamoto D., Matsumoto K., Inoue M., Ishida T., Mizuno H., Sumiya S., Kitamura K., *Biochem. J.*, **287**, 797-803 (1992).
- 144) Yamamoto A., Tomoo K., Doi M., Ohishi H., Inoue M., Ishida T., Yamamoto D., Tsunoi S., Okamoto H., Okada Y., *Biochemistry*, **31**, 11305-11309 (1992).
- 145) Matsumoto K., Murata M., Sumiya S., Kitamura K., Ishida T., *Biochim. Biophys. Acta*, **1208**, 268-276 (1994).
- 146) Fujiyoshi T., Yoneda S., Kitamura K., Amisaki T., Inoue M., Ishida T., *Protein Eng.*, **4**, 443-450 (1991).
- 147) Sumiya S., Yoneda T., Kitamura K., Murata M., Yokoo C., Tamai M., Yamamoto A., Inoue M., Ishida T., *Chem. Pharm. Bull.*, **40**, 299-303 (1992).
- 148) Ishida T., Yamamoto A., Tomoo K., Matsumoto K., Murata M., Kitamura K., *Peptide Science-Present and Future*, 631-633 (1999).
- 149) Yamamoto A., Tomoo K., Matsugi K., Hara T., In Y., Murata M., Kitamura K., Ishida T., *Biochim. Biophys. Acta*, **1597**, 244-251 (2002).
- 150) Watanabe D., Yamamoto A., Tomoo K., Matsumoto K., Murata M., Kitamura K., Ishida T., *J. Mol. Biol.*, **362**, 979-993 (2006).
- 151) Braak H., Braak E., *Neurobiol. Aging*, **18**,

- 351–357 (1997).
- 152) Lee G., Neve R. L., Kosik K. S., *Neuron*, **2**, 1615–1624 (1989).
- 153) Goedert M., Spillantini M. G., *Biochim Biophys. Acta*, **1502**, 110–121 (2000).
- 154) Von Bergen M., Friedhoff P., Biernat J., Heberle J., Mandelkow E. M., Mandelkow E., *Proc. Natl. Acad. Sci. USA*, **97**, 5129–5134 (2000).
- 155) Minoura K., Tomoo K., Ishida T., Hasegawa H., Sasaki M., Taniguchi T., *Biochem. Biophys. Res. Commun.*, **294**, 210–214 (2002).
- 156) Minoura K., Tomoo K., Ishida T., Hasegawa H., Sasaki M., Taniguchi T., *Bull. Chem. Soc. Jpn.*, **76**, 1617–1624 (2003).
- 157) Yao T. M., Tomoo K., Ishida T., Hasegawa H., Sasaki M., Taniguchi T., *J. Biochem.*, **134**, 91–99 (2003).
- 158) Hiraoka S., Yao T. M., Minoura K., Tomoo K., Sumida M., Taniguchi T., Ishida T., *Biochem. Biophys. Res. Commun.*, **315**, 659–663 (2004).
- 159) Minoura K., Yao T. M., Tomoo K., Sumida M., Sasaki M., Taniguchi T., Ishida T., *Eur. J. Biochem.*, **271**, 545–552 (2004).
- 160) Minoura K., Mizushima F., Tokimasa M., Hiraoka S., Tomoo K., Sumida M., Taniguchi T., Ishida T., *Biochem. Biophys. Res. Commun.*, **327**, 1100–1104 (2005).
- 161) Tokimasa M., Minoura K., Hiraoka S., Tomoo K., Sumida M., Taniguchi T., Ishida T., *FEBS Lett.*, **579**, 3481–3486 (2005).
- 162) Tomoo K., Yao T. M., Minoura K., Hiraoka S., Sumida M., Taniguchi T., Ishida T., *J. Biochem.*, **138**, 413–423 (2005).
- 163) Mizushima F., Minoura K., Tomoo K., Sumida M., Taniguchi T., Ishida T., *Biochem. Biophys. Res. Commun.*, **343**, 712–718 (2006).
- 164) Mizushima F., Minoura K., Tomoo K., Sumida M., Taniguchi T., Ishida T., *J. Biochem.*, **142**, 49–54 (2007).
- 165) Hikosou R., Kurabayashi Y., Doumoto M., Hoshitoku K., Mizushima F., Minoura K., Tomoo K., Ishida T., *Chem. Pharm. Bull.*, **55**, 1030–1033 (2007).
- 166) Okuyama K., Nishiura C., Mizushima F., Minoura K., Sumida M., Taniguchi T., Tomoo K., Ishida T., *FEBS J.*, **275**, 1529–1539 (2008).
- 167) Sugino E., Nishiura C., Minoura K., In Y., Sumida M., Taniguchi T., Tomoo K., Ishida T., *Biochem. Biophys. Res. Commun.*, **385**, 236–240 (2009).
- 168) Naruto K., Minoura K., Okuda R., Taniguchi T., In Y., Ishida T., Tomoo K., *FEBS Lett.*, **584**, 4233–4236 (2010).
- 169) Nishiura C., Takeuchi K., Minoura K., Sumida M., Taniguchi T., Tomoo K., Ishida T., *J. Biochem.*, **147**, 405–414 (2010).
- 170) Sogawa K., Okuda R., In Y., Ishida T., Taniguchi T., Minoura K., Tomoo K., *J. Biochem.* (in press)
- 171) Hattori M., Sugino E., Minoura K., In Y., Sumida M., Taniguchi T., Tomoo K., Ishida T., *Biochem. Biophys. Res. Commun.*, **374**, 158–163 (2008).
- 172) Taniguchi T., Sumida M., Hiraoka S., Tomoo K., Kakehi T., Minoura K., Sugiyama S., Inaka K., Ishida T., Saito N., Tanaka C., *FEBS Lett.*, **579**, 1399–1404 (2005).

分子識別能を有するトリプトファンの構造に魅せられて

石田寿昌

Toshimasa ISHIDA

大阪薬科大学教授

1 はじめに

私は、40年近く、大阪薬科大学で教育と研究に従事してきた。その間、大勢の方にお世話になった。感謝に堪えない。本年3月末で定年を迎えた。そんな折、ファルマシア編集部から「挑戦者からのメッセージ」執筆の依頼があった。このコラムの主旨は「薬学分野で素晴らしい成果を出された先生からの、後進への糧となる、わくわくするような読み物」と記されている。私は、そのような素晴らしい研究成果を挙げたとは思っておらず、この点では執筆の資格に疑問符が付く。が、後進への糧という点に強く引かれた。後輩へ言い残せるものは何であろうか？と考えさせられた。研究者は、長期的視野に立って、自身の興味(科学的でない困るが)をできる限り追求するものだと思っている。実際、私は学生時代に興味を持った分子間相互作用の研究を一貫して続けてきた。一度決めた研究テーマを続け得る幸運に恵まれたともいえるが、私なりに挑戦者になっていたかもしれない。

以下に、後輩の参考になればとの期待から、恐縮ではあるが、自身の研究をいかに展開してきたかについて述べてみたい。

2 研究を始めるに当たって思ったこと

私は、以前より生体内で生じている分子間の相互作用の不思議さに興味を持っていた。相互作用の一つ一つが生体のメカニズムそのものであり、それゆえに、新薬を生み出す際の必要不可欠な情報であると思ったからである。一方、生体分子間の相互作用は生物学的現象であるが、その原理は分子を構成する構造特徴にあり、それを知るには、分子の3D構造を明らかにする必要がある。

3D構造を精度よく知る手段は、今も昔もX線結

晶構造解析法しかない。しかしながら、私が研究を開始した1970年代後半当時の結晶構造解析の適応範囲は限定的で、生体高分子の3D構造、ましてや高分子複合体の3D構造を明らかにすることは極めて困難なことであった。しかし、分子サイズの制限はX線回折の理論にあるのではなく、位相決定のための方法論とコンピュータの処理能力にあり、それらの進歩と共に分子サイズの制限は緩和されるはずと考え、その時代に適合した分子サイズのレベルで、生体分子間相互作用の研究(3D構造の解明)をしようと考えた。

必須アミノ酸のトリプトファン(Trp)の構造特徴は π -電子に富むインドール環にある。Trpはセロトニンやインドール酢酸などの代謝産物とともに、生命維持に不可欠な生理機能を発現している。これは、インドール環と特異的に相互作用する複数の生体分子が存在することを意味している。それゆえ、生体構成分子との特異な相互作用様式を原子レベルで解明することを目的として研究を開始し、以下に述べる成果を得ることができた。

3 補酵素との相互作用¹⁾

当時、Trpはピリジンやフラビン補酵素と電荷移動相互作用をすることは分光学的に示されていたが、原子レベルでの詳細な結合様式は不明であった。そこで、一連の補酵素の構成分子とTrp誘導体との複合体の結晶構造を解析し、インドール環に対するこれら補酵素の相互作用様式を原子レベルで解明した。そして、インドール環はピリジン、フラビン、チアミン補酵素の芳香環に対して3.3~3.5Å前後の面間隔で並行に重なる共通した構造特徴と、それを可能にする分子間力を明らかにした。すなわち、 π -電子供与能に富むインドール環の最高占有軌道(highest occupied molecular orbital; HOMO)

と補酵素中の芳香環の π 電子受容能に富む最低空軌道 (lowest unoccupied molecular orbital ; LUMO) との軌道間相互作用が分子間力の本質であることを明らかにした。このことは、酵素中の Trp 残基が π 電子移動を介して補酵素の固定と触媒活性に重要な役割を果たしていることを示している。

4 核酸塩基との特異的相互作用²⁾

核酸塩基と Trp との相互作用は、一般に強くない。しかし上記の研究は、核酸塩基の窒素四級化によって、その LUMO エネルギーは Trp の HOMO エネルギーに接近し、両者間のスタッキング相互作用を強めることを示唆した。事実、一連の *N*-メチル核酸塩基と Trp 誘導体との複合体の結晶構造解析により、両者は芳香環間の電荷移動を含む顕著なスタッキングを形成することが明らかとなった。

タンパク質による特定の核酸塩基あるいは塩基配列の認識は、生命維持にとって不可欠である。Trp 残基の役割としては、核酸塩基とのスタッキング相互作用が考えられる。塩基は生理条件下ではプロトネート状態にはないが、酸性環境下 Trp 残基が存在すれば、スタッキング相互作用を介したこれらの塩基に対する選択的結合は可能である。また、アルキル化等による DNA 損傷において、その損傷部位の認識に Trp 残基は重要な役割を果たすと考えられる。

一方、核酸の塩基対で示されるように、水素結合は塩基識別力に優れていることから、極性アミノ酸と Trp を含有するペプチドは、水素結合対とスタッキング結合の同時形成を介した特定の核酸塩基認識が可能と考えられた。そこで、*N*7-メチルグアニン (m7G) 塩基を選択特異的に認識するような両アミノ酸含有オリゴペプチドの設計を試みた結果、①Trp-Glu と m7GMP 複合体の結晶構造は、m7G 塩基に対して Glu はワトソン・クリック型の水素結合対を、Trp はスタッキング結合を同時形成できる最短のジペプチド(図1)であること、②-Trp-(Gly)*m*-Asp/Glu-(Gly)*n*-Trp-(*m*=0~2, *n*=0~2) は水素結合とスタッキング結合の同時形成による m7G の選択特異的認識に最も適した配列であることが明らかとなった。

この認識様式が現実の生体メカニズムにおいても

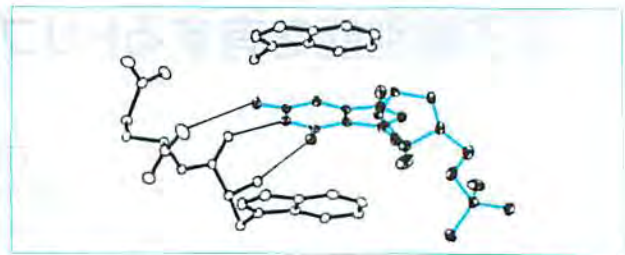


図1 Trp-Gluとm7GMP(太線;水色)との相互作用様式
細線は水素結合を示す。

用いられているかを調べることは、私にとって極めて興味深い重要な課題となった。なぜなら、これまでの分子間相互作用研究は単にモデル研究にとどまらず、構造生物学的にも重要であることを証明する絶好の機会を提供しているからである。そこで、タンパク質生合成開始因子の1つである eukaryotic initiation factor (eIF)4E に着目した。このタンパク質は、その構造に関する研究は全く報告されていなかったものの、真核生物の mRNA 5' 末端が m7G で修飾されたキャップ構造の認識を介してタンパク質合成の開始に不可欠であることが報告されていたことから、eIF4E によるキャップ認識機構の解明に取り組んだ。

5 eIF4E の mRNA キャップ認識機構³⁾

真核生物における翻訳開始反応には多くの開始因子が関与しているが、その最初のステップは mRNA のリボゾームへの結合であり、eIF4E による mRNA キャップ構造の認識を介して反応は開始される。

eIF4E を天然から大量に取り出すことは困難であったため、大腸菌からの組み換え体として得ることを計画した。開始当初、組み換え技術は十分には確立しておらず失敗を繰り返したが、阪大薬学部・上杉晴一助教授(当時)指導の下、大腸菌が採用しているコドンに置き換えたヒト *eIF4E* 遺伝子(全長 660 塩基対)の化学合成、プラスミドの構築、大腸菌からの直接発現、可溶性画分からの単離・精製に成功した。得られた組み換え体は天然型 eIF4E と同一の物性と立体構造をとること、同程度のキャップ結合能を有することを分光学的に確認した。

次に、mRNA キャップ構造のモデル分子として m7GpppA を用い、eIF4E との複合体の結晶化に取り組んだが、X 線回折測定に適した結晶を得るま

でに数年間を要した。結晶構造解析には位相問題の解決が不可欠であり、通常、この位相決定には重原子同型置換法が用いられる。このタンパク質の場合、良質な同型結晶を得ることは困難であり、また他の位相決定法を種々試みたものの、構造解析に成功しない状態が数年続くこととなった。その間、N-末端 27 残基を削除したマウス eIF 4 E の m7GDP 複合体の結晶構造が Sonenberg (eIF 4 E の発見者) らによって *Cell* に報告された。世界の数グループが関連複合体の構造解析に取り組んでいることは承知していたが、長年の努力が報われない結果となり、競争の厳しさと実力不足を痛感した。しかし気を取り直して解析を続け、完全長ヒト eIF 4 E と m7GpppA 複合体の結晶構造解析に成功した。^{4,5)}

図2から明らかのように、eIF 4 E の Trp 56 と Trp 102 のインドール環はスタッキング結合により m7G 塩基を上下から挟み込み、Glu 103 の側鎖カルボキシル基は m7G 塩基の N1 原子および N2 H 基との間で水素結合対を形成して塩基を固定していた。このスタッキング相互作用と水素結合対形成による eIF 4 E の mRNA キャップ構造認識様式は、その低分子モデルである Trp-Glu : m7GTP 複合体の構造解析において得られた分子間相互作用様式 (図1) と本質的に一致するものであった。このことは、これまで行ってきた分子間相互作用研究が生体内反応における特異的相互認識の本質を解明する上

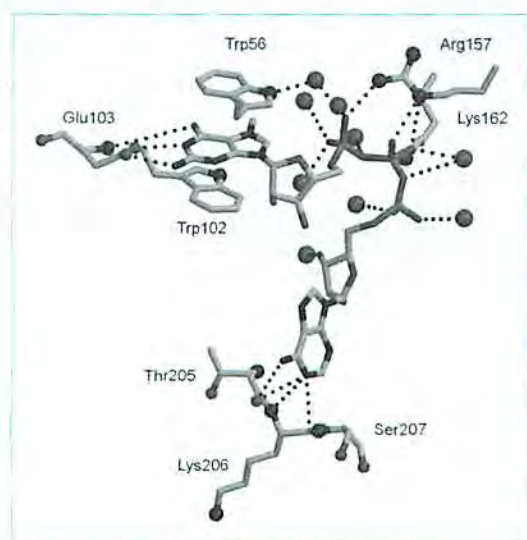


図2 eIF 4 E の m7G キャップ構造認識様式

●は水分子を示す。



図3 自動四軸 X 線回折装置と筆者 (1979 年)

で極めて重要であることを証明している。

6 おわりに

ここで紹介した研究は 1980~2000 年までの約 20 年間、コンピュータや測定機器の進歩に沿って、それらを利用して行ってきたものである (図3)。低分子モデルから始まったこれまでの研究成果により、eIF 4 E の mRNA キャップ認識に不可欠な分子構造の本質的な姿を明らかにしてきた。現在、上記の研究は内因性の制御タンパク質 4 EBP による eIF 4 E の機能制御機構の解明、翻訳開始に関与する eIF 4 A や eIF 4 G の構造解析等、翻訳開始機構の研究に進展している。

また、ここでは触れなかったが、酵素と阻害剤の相互作用に基づいた薬物設計や、認知症原因タンパク質タウの自己重合メカニズムとその制御分子の研究についても精力的に進めてきた。これらの分子間相互作用研究に対して、日本薬学会奨励賞 (1988 年)、⁴⁾ 日本薬学会学術貢献賞 (2009 年)⁶⁾ を受賞した。関係者各位に感謝する次第である。なお、上記の研究は完了したわけではない。しかし、今後の展開は後進に譲ることにして、私の役目を終えたいと思っている。

最後に、これから研究を開始する人達に伝えたいことは、いかなる研究環境においても自分の興味、すなわち研究を続けること、その意思が、自分が納得できる研究結果へと導くということである。

参考文献

- 1) 石田寿昌, *Yakugaku Zasshi*, 108, 506-527 (1988).
- 2) 石田寿昌, "薬学研究の進歩 研究成果報告集 8," 東京, 1992, pp. 55-82.
- 3) 森野重信ほか, *Yakugaku Zasshi*, 115, 401-419 (1995).
- 4) Tomoo K. et al., *Biochem. J.*, 362, 539-544 (2002).
- 5) Tomoo K. et al., *J. Mol. Biol.*, 328, 365-383 (2003).
- 6) Ishida T., *Chem. Pharm. Bull.*, 57, 1309-1334 (2009).

CH- π Interaction between I308 and Y310 Residues is Required for Self Assembly of Full Length Tau

Koushirou Sogawa¹, Ryouhei Okuda¹, Katsuhiko Minoura¹, Yasuko In¹,
Toshimasa Ishida¹, Taizo Taniguchi², and Koji Tomoo¹

¹Osaka University of Pharmaceutical Sciences, 4-20-1 Nasahara, Takatsuki, Osaka 569-1094, and ²Department of Pharmaceutical Health Care, Faculty of Pharmaceutical Sciences, Himeji Dokkyo University, 7-2-1 Kamiohno, Himeji, Hyogo 670-8524, Japan

e-mail: minoura@gly.oups.ac.jp

To determine whether the common structural element indispensable for starting the molecular association of 4MBD is also applicable to that of 3RMBD and full-length tau, a series of ³⁰⁶VQIVYK³¹¹ residue-substituted mutants of 3RMBD and 3R/4Rtau were prepared and examined of their aggregation profiles. The results clearly confirm the importance of the C-H... π interaction between the I308 and Y310 residues for the filament formation of 3R/4Rtau as well as of its MBD.

Keywords: C-H... π interaction, filament formation, isoleucine residue, tau, tyrosine residue

Introduction

Investigation of the mechanism of tau polymerization is indispensable for finding inhibitory conditions or identifying compounds preventing the formation of paired helical filaments (PHFs) or oligomers. Tau contains a microtubule binding domain (MBD) consisting of three or four repeats in its C-terminal half. It has been considered that the key event in tau polymerization is the formation of a β -sheet structure arising from a short hexapeptide ³⁰⁶VQIVYK³¹¹ in the third repeat of tau. To investigate the function of the Tyr310 residue in MBD filament formation, we have, recently, investigated the aggregation behavior of a series of Tyr-substituted, deleted or inserted MBD mutants and clarified the importance of the interplay between Ile308 and Tyr310 residues for 4RMBD filament formation [1, 2]. In this study, we report that the C-H... π interaction between the side chains of Ile308 and Tyr310 residues is the least indispensable structural element for initiating the molecular association of 3RMBD and full length tau (3R/4Rtau) as well as of 4RMBD, which functions as a conformational seed for triggering molecular self-association.

Results and Discussion

The aggregation behavior of a series of 3RMBD mutants were investigated by ThS fluorescence measurement, CD, and EM. Selected examples are shown in Fig. 2. The ThS fluorescence intensity of the mutant monosubstituted by Ala showed that the

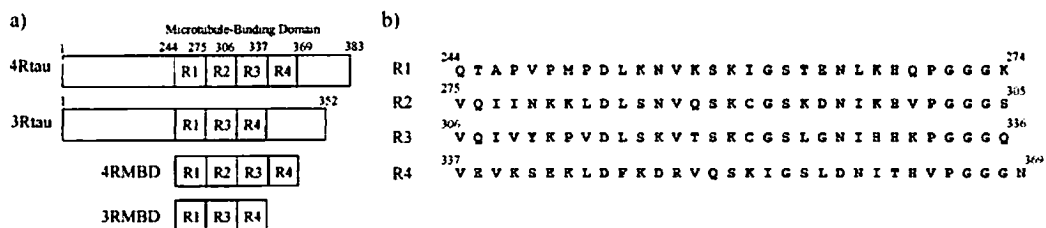


Fig. 1. Schematic representations of (a) three- and four-repeat isomers of 4Rtau, 3Rtau, 4RMBD, and 3RMBD used in this work, and (b) amino acid sequences of first to fourth repeats (R1 ~ R4).

mutation of the I308 or Y310 residue causes the complete disappearance of the filament formation. To investigate the importance of Tyr at position 310 in the aggregation of 3RMBD, then, the aggregation behaviors of a series of Y310A-fixed and Tyr-scanned mutants of the ³⁰⁶VQIVYK³¹¹ sequence were investigated. Consequently, the following two important results were observed. First is that the aggregation ability of 3RMBD is considerably lost only by Y310A regardless of the Tyr substitution for other residues in the ³⁰⁶VQIVYK³¹¹ sequence, except Q307Y/Y310A. These mutants inhibited filament formation. Such a remarkable loss of aggregation ability by Y310A was also observed for 4RMBD, indicating that Tyr310 in the third repeat of MBD is essential for the filament formation despite the number of repeats. Second is that Q307Y/Y310A shows a high aggregation ability and has a similar filament morphology to 3RMBD. This means that the self-association mechanism of Q307Y/Y310A is essentially the same as that of 3RMBD. The complete loss of the aggregation abilities of I308A, Y310A and I308Y/Y310A indicates clearly that the interplay between I308 and Y310 residues is essential for the molecular aggregation of 3RMBD. It is clear from Table 1 that these aggregation behaviors are almost the same as those of 4RMBD. Previously, we reported that the building units for molecular aggregation are different between 3RMBD and 4RMBD, *i.e.*, the intermolecular R3–R3 disulfide-bonded dimer for 3RMBD and the intramolecular R2–R3 disulfide-bonded monomer for 4RMBD. However, the present result indicates that the interplay between I308 and Y310 residues in the R3 repeat is a common structural element indispensable for initiating the molecular association of both MBDs.

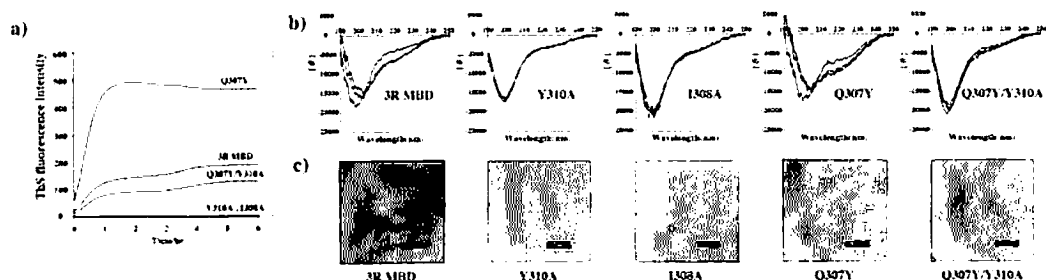


Fig. 2. (a) Time-dependent ThS fluorescence intensity profiles, (b) time-dependent CD spectra, and (c) negative-staining EM images of 3RMBD and its mutants. The Q307Y/Y309A/Y310A mutant shows essentially the same results as I308A. The respective CD spectra correspond to those obtained 0 min, 3, 6, and 24 hr after adding heparin to the solution. The length of the bar in (c) corresponds to 500 nm.

Table 1. Comparison of ThS fluorescences and EM morphologies.

Wild/Mutant	Without DTT		With DTT		Wild/Mutant	Without DTT		With DTT	
	Relative fluorescence intensity (%)	EM morphology	Relative fluorescence intensity (%)	EM morphology		Relative fluorescence intensity (%)	EM morphology	Relative fluorescence intensity (%)	EM morphology
3RMBD	100	filament	25	short filament	3Rtau	100	filament	10	granule
Y310A, I308A I308Y/Y310A, I308Y/Y310A, Q307Y/V309A/Y310A	0	no granule and no filament	0	no granule and no filament	Y310A, I308A	0	no granule and no filament	0	no granule and no filament
Q307Y/Y310A	70	short filament	20	short filament	Q307Y/Y310A	10	granule	0	no granule and no filament
Q307Y	250	filament+granule	300	granule	Q307Y	300	granule	300	granule
I308V	80	short filament	20	short filament					
4RMBD	100	filament	120	filament	4Rtau	100	filament	10	granule
Y310A, I308A I308Y/Y310I, I308Y/V309A/Y310A	0	no granule and no filament	0	no granule and no filament	Y310A, I308A I308Y/Y310I, Q307Y/V309A/Y310A	0	no granule and no filament	0	no granule and no filament
I308V	90	filament	120	filament	I308V	40	short filament	5	no granule and no filament
Q307Y	300	filament+granule	300	filament+granule	Q307Y	300	granule	300	granule
Q307Y/Y310A	100	filament	120	filament	Q307Y/Y310A	10	no granule and no filament	5	no granule and no filament
					Y310W	100	filament	150	filament

*The fluorescence intensities of mutants correspond to values relative to those of wild 3RMBD, 4RMBD, 3Rtau, and 4Rtau without DTT. †EM morphology at 48 hr after initiating starting aggregation by addition of heparin.

The comparison between the aggregation abilities of wild MBD and its I308A or Y310A mutants indicates that the interplay between I308 and Y310 is based on the C-H... π interaction between their residues, where the C-H group of the Ile side chain interacts with the π electron of the Tyr phenyl ring. This is supported by the suppressed aggregation ability of I308V compared with that of the wild type, because Val has a lower hydrophobicity than Ile. It is important to note that the filament formation *via* the C-H... π interaction is dependent on the positional relationship between Ile and Tyr residues, because I308Y/Y310I as well as I308Y/Y301A showed a complete loss of their molecular aggregation ability. This clearly indicates that Ile should be located on the N-terminal side compared with Tyr, that is, the C-H... π interaction should be formed along the N side \rightarrow C side direction of the sequence.

To determine whether the common structural element indispensable for starting the molecular association of MBD is also applicable to that of full-length tau, a series of ³⁰⁶VQIVYK³¹¹ residue-substituted mutants of 3R/4Rtau were prepared and examined of their aggregation profiles (Fig. 3). It is clear that the C-H... π interaction between I308 and Y310 residues is also indispensable to the filament formation of 3R/4Rtau. The I308A and Y310A of 3R/4Rtau completely lost their aggregation ability. In contrast, I308V and Y310W showed similar aggregation ability to 4Rtau. A marked increase in the aggregation rate of Q307Y, probably due to double C-H... π interactions of Y307-V309 and I308-Y310 pairs, was also observed for 3R/4Rtau. These results confirm the importance of the C-H... π interaction between the I308 and Y310 residues for the filament formation of full-length tau as well as of its MBD.

On the other hand, the difference between the aggregation behaviors of full-length tau and MBD could be observed in the ThS fluorescence intensity and EM morphology of their Q307Y/Y310A mutants. The Q307Y/Y310A of 3R/4Rtau no longer showed notable aggregation behavior such as that of 3R/4RMBD, indicating that the side selection on the planar hexapeptide in the R3 repeat is required for the molecular aggregation of full-length tau via the C-H... π interaction. This is clearly due to the effect of the N- and C-terminal flexible regions of MBD, because the N- and C-terminal regions remain largely disordered, form a fuzzy coat, and fold back onto the repeats to form transient intramolecular contact. Thus, it is reasonable to consider that the molecular aggregation of 3R/4Rtau proceeds via the C-H... π interaction on only one side of the R3 hexapeptide, although no such a structural restriction is required up to the granule formation stage, as observed for Q307Y.

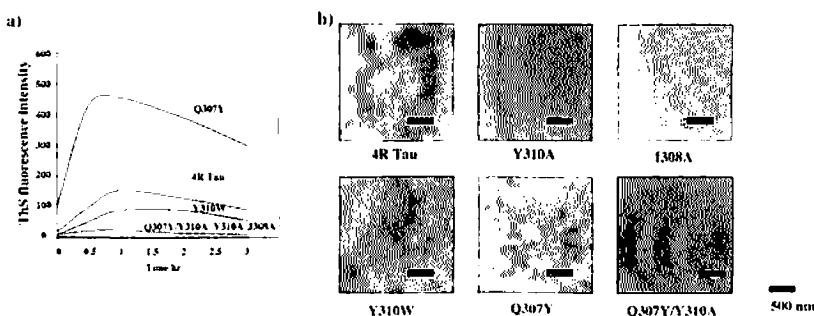


Fig. 3. (a) Time-dependent ThS fluorescence intensity profiles and (b) negative-staining EM images. The Q307Y/V309A/Y310A mutant shows essentially the same results as those of I308A.

Our previous study clarified that the building units for 3RMBD and 4RMBD are intermolecular R3-R3 disulfide-bonded dimers and intramolecular R2-R3 disulfide-bonded monomers, respectively, and this difference results in the marked suppression and enhancement of the molecular aggregations of 3RMBD and 4RMBD with the addition of DTT, respectively. To confirm the effect of DTT on the molecular aggregations of 3R/4RMBD and 3R/4Rtau, the aggregation behaviors of the respective wild type and mutants with and without DTT were compared in terms of the ThS fluorescence intensity and EM morphology; the results are given in Table 1. DTT increases the fluorescence intensity of 4RMBD to nearly the same extent as that of oxidative 3RMBD. This result indicates that the folded structure of the intramolecular disulfide bonded 4RMBD is disadvantageous for the aggregation and the DTT-induced open structure confers 4RMBD similar aggregation ability to that of 3RMBD dimers.

On the other hand, the 3R/4Rtau shows a different behavior from 3R/4RMBD as regards the effect of DTT on the molecular aggregation of MBD. The ThS intensities of 3R/4Rtau were both decreased by the DTT addition, and this is in contrast to the cases of 3R/4RMBD, in which the DTT-dependent molecular aggregation process is dependent on intermolecular/intramolecular disulfide bond formation, respectively. This discrepancy means that such disulfide bond formation is insufficient to control the overall aggregation behavior of 3R/4Rtau, probably owing to the presence of flexible sequences on both the N- and C-terminal sides of MBD. However, the aggregation ability of the Q307Y mutant of 3R/4Rtau, as well as of 3R/4RMBD, having double C-H... π interactions within the R3 repeat was hardly affected by DTT. This suggests that the formation of the double C-H... π interactions on the planar structure of the R3 core moiety provides the platform that is indispensable for starting molecular association, although it does not proceed to the filament formation. The present results clarified that two factors are important for molecular aggregation of tau: conformational fixation by C-H... π interaction and molecular fixation by intermolecular dimer formation.

The present work provides important information on key residues and structural scaffolds essential for initiating the molecular association, which is important for designing AD inhibitors.

References

1. Nishiura, C., Takeuchi, K., Minoura, K., Sumida, M., Taniguchi, T., Tomoo, K., and Ishida, T. (2010) *J. Biochem.*, **147**, 405-414.
2. Naruto, K., Minoura, K., Okuda, R., Taniguchi, T., In, Y., Ishida, T., and Tomoo, K. (2010) *FEBS Lett.*, **584**, 4233-4236.



Identification and function of the second eIF4E-binding region in N-terminal domain of eIF4G: Comparison with eIF4E-binding protein

Yu Umenaga, Keum Soon Paku, Yasuko In, Toshimasa Ishida, Koji Tomoo*

Department of Physical Chemistry, Osaka University of Pharmaceutical Sciences, 4-20-1 Nasahara, Takatsuki, Osaka 569-1094, Japan

ARTICLE INFO

Article history:

Received 7 September 2011

Available online 21 September 2011

Keywords:

Initiation factor 4E

Initiation factor 4G

4E-Binding protein

Surface plasmon resonance

Isothermal titration calorimetry

ABSTRACT

The eukaryotic initiation factor 4E (eIF4E) serves as a master switch that controls mRNA translation through the promotive binding to eIF4G and the regulative binding with the endogenous inhibitor 4E-BP. Although the bindings of eIF4G and 4E-BP to eIF4E proceed through the common eIF4E recognition Y(X)₄Lφ motif (X: variable, φ: hydrophobic) (first binding site), the relationship between their eIF4E binding mode and the functional difference is hardly known. Recently, we have clarified the existence and function of the second eIF4E binding site in 4E-BP. Surface plasmon resonance (SPR) analysis based on the sequential comparison between 4E-BP and eIF4GI clarified that eIF4G has the second binding site at the periphery of the ⁵⁹⁷SDVVL⁶⁰¹ sequence and that it plays an auxiliary but indispensable function in stabilizing the binding of the first binding sequence ⁵⁷²YDREFLL⁵⁷⁸. The kinetic parameters of the interactions of the eIF4GI and 4E-BP2 fragment peptides with eIF4E showed that the association (*ka*) and dissociation (*kd*) rates of the former peptide are about three and two orders of magnitude lower than those of the latter peptide, respectively. This means that eIF4G has a potent resistive property for release from eIF4E, although its rate of binding to eIF4E is not as high as that of 4E-BP, that is, 4E-BP is apt to bind to and be released from eIF4E, as compared with eIF4G. Isothermal titration calorimetry (ITC) showed the opposite behavior between the second binding sites of eIF4GI and 4E-BP for the interaction with eIF4E. This clearly indicates the importance of the second binding region for the difference in function between eIF4G and 4E-BP for eIF4E translation.

© 2011 Elsevier Inc. All rights reserved.

1. Introduction

The control of mRNA translation at the initiation level is critical for gene expression in mammalian cells [1]. Eukaryotic initiation is performed by many eukaryotic initiation factors (eIFs) and is regulated through changes in the phosphorylation states of eIFs and endogenous regulator proteins [2]. One of the main regulatory steps in translation initiation is the formation of the eukaryotic initiation factor 4F (eIF4F) complex. eIF4F is a supermolecular complex of three subunits, i.e., eIF4E, eIF4A and eIF4G, that is required to recruit ribosomal subunits to mRNA during cap-dependent initiation. In the first initiation step in the cap-dependent translation of mRNA, the selective recognition of the 7-methylated

Abbreviations: 4E-BP, eIF4E-binding protein; CD, circular dichroism; DTT, dithiothreitol; eIF4E, eukaryotic initiation factor 4E; HEPES, 2-[4-(2-hydroxyethyl)-1-piperazinyl] ethanesulfonic acid; ITC, isothermal titration calorimetry; MD, molecular dynamics; m⁷GTP, 7-methylguanosine 5'-triphosphate; m⁷GpppA, P¹-7-methylguanosine-P³-adenosine-5',5'-triphosphate; P-20, poly(oxyethylene)sorbitan monolaurate (Tween-20); RU, resonance unit; SPR, surface plasmon resonance.

* Corresponding author. Fax: +81 72 690 1068.

E-mail address: tomoo@gly.oups.ac.jp (K. Tomoo).

guanine (m⁷G) cap structure covalently attached to the 5' terminus of mRNA by eIF4E is required. During cap-dependent translation, eIF4G brings the 5' end of the mRNA close to the helicase eIF4A through interactions with eIF4E. Since the initiation function of eIF4E is controlled via the association with the endogenous 4E-binding protein (4E-BP) [3], eIF4E serves as a master switch that controls eukaryotic translation.

The regulation of the eIF4E function by 4E-BP is performed by the competitive interaction with eIF4G in the overlapped region of eIF4E [4,5] and is thus critical for the proper control of protein biosynthesis. The crystal structures of the m⁷GDP-eIF4E-eIF4GII fragment peptide (Lys621–Ala637) [6] and m⁷GpppA-eIF4E-4EBP1 fragment peptide (Thr36–Thr70) [7] complexes show that both 4E-BP and eIF4GII interact with the invariant portion of the convex surface of eIF4E through the conserved eIF4E recognition Y(X)₄Lφ motif (X: variable, φ: hydrophobic). However, the structural difference between the eIF4G translational and 4E-BP regulatory functions for eIF4E has not yet been satisfactorily elucidated, although it is known that the functional regulation of eIF4E by 4E-BP is released by dissociation through the phosphorylation of the Thr and Ser residues in 4E-BP [8].

To examine the functions of the N- and C-terminal sides from the eIF4E recognition motif (⁵⁴YDRKFL⁶⁰: first binding site) of

4E-BP in the interaction with eIF4E, we have recently investigated the binding features of full-length 4E-BP and its sequentially N- and/or C-terminal residue-deleted 4E-BP mutants and clarified that, although the N-terminal flexible region hardly affects the binding to eIF4E, the ⁷⁹PGVTS/⁸³ sequence of the C-terminal side plays an important role as the second binding site in the tight binding with eIF4E [9,10]. This result led us to investigate the eIF4E binding behavior of eIF4G and the difference of eIF4G from 4E-BP. In this work, we investigated the feature of the binding of eIF4G to m⁷GTP-bound eIF4E by the surface plasmon resonance (SPR) method and isothermal titration calorimetry (ITC), in which the eIF4G1 fragment peptides including the eIF4E recognition Y(X)₄L ϕ motif (first binding site) and/or the peptide corresponding to the second eIF4E binding site of 4E-BP were used (Fig. 1). The comparison with the corresponding fragment peptides of 4E-BP2 clarified the different behavior of the second binding site for interaction with eIF4E. This report on the second binding site of eIF4G is important to understand the functional difference between eIF4G and 4E-BP for eIF4E translation.

2. Materials and methods

2.1. Peptides

The respective fragment peptides of eIF4G1 and 4E-BP2 were synthesized using a solid-phase peptide synthesizer, characterized by mass spectrometry, and found to be of >99.0% purity, as assessed by reverse-phase HPLC.

2.2. Preparation of m⁷GTP-bound eIF4E

The gene construction, expression, and purification of full-length eIF4E were performed in accordance with previous reports [11]. The supernatant containing the recombinant protein was applied to an m⁷GTP-Sepharose 4B affinity column equilibrated with 20 mM HEPES–KOH (pH 7.5) buffer containing 1 mM DTT, 0.1 mM EDTA, and 100 mM KCl. m⁷GTP-bound eIF4E was prepared by elution with the same buffer supplemented with 100 μ M m⁷GTP. The eluate was concentrated by Centricon 10 (Amicon Co.) to the desired concentration, which was determined by the Bradford method. The purity of the sample was confirmed by SDS–PAGE.

2.3. SPR analysis

A binding assay was performed using BIAcore X (GE Healthcare). As the ligand, m⁷GTP-bound eIF4E was immobilized on a CM5 sensor chip by the amine-coupling method, according to the manufacturer's instructions, in which 10 μ g/ml protein was reacted in 10 mM sodium acetate buffer (pH 4.5) and the concentration of the immobilized protein was adjusted within the range recommended for the accurate measurement of the kinetic param-

eters [12]. As the analyte, the peptide of eIF4G1 or 4E-BP2 was then injected as a function of the peptide concentration. Each cycle consisted of the injection of the indicated amount (15–25 μ L) of the peptide into the BIAcore running buffer (10 mM HEPES–NaOH (pH 7.5), 225 mM NaCl, 3 mM EDTA, and 0.01% Surfactant P-20). The chip was regenerated after each cycle by washing it three times with 10–20 μ L of 2 M NaCl and five times with 15 μ L of the running buffer. The measurement was performed at a flow rate of 5 μ L/min at 25 °C. The obtained sensorgram was evaluated using the BIA evaluation software package, through which the response from the unimmobilized flow cell as the reference was subtracted from the sample response to obtain the sensorgram for a specific interaction. The constants for association rate, k_{on} , and dissociation rate, k_{off} , and the equilibrium constant for dissociation, KD ($=k_{off}/k_{on}$), were estimated from the respective sensorgrams depending on the SPR profiles and curve-fitting patterns, i.e., the Langmuir (1:1) binding model for the ka/kd -dependent bow-shaped profiles and the steady affinity (Scatchard) model (only KD) for the trapezoidal ones. The respective model fittings yielded reasonable χ^2 values (<10) and distributions of residual plots.

2.4. ITC analysis

ITC analysis was performed to obtain the thermodynamic parameters of the interaction using the VP-ITC titration calorimetric system (Microcal Inc.). The solution (5 μ M) of m⁷GTP-bound eIF4E in the calorimetric cell was titrated with eIF4G1 or 4E-BP2 peptide solution (50 μ M) dissolved in the same buffer (20 mM NaH₂PO₄–NaOH (pH 7.4), 100 mM NaCl) in a titration cell. Before the measurement, both samples were properly degassed and carefully loaded into their respective cells to avoid bubble formation during stirring, and the heat due to the interaction between both molecules was measured as the difference between the heat of reaction and the corresponding heat of dilution. The thermodynamic parameters were estimated using a one- or two-site model.

2.5. MD simulation

To estimate where and how the 4G-I peptide binds to the molecular surface of eIF4E, MD simulation was performed for an aqueous solution system of the m⁷GpppA-bound eIF4E–4G-I peptide complex; the structure of the complex was built from the X-ray crystal structure of the m⁷GpppA–eIF4E–4E-BP1 peptide (PDB file: 1WKW) and the atomic coordinate of the undetermined sequence was constructed manually on a graphics computer, by referring to the solution structure of the yeast m⁷GDP-bound eIF4E–eIF4G fragment (393–490) complex (PDB file: 1RF8) [13]. Assuming a neutral pH (7.0) of the system, MD simulation was performed for 3 ns in the same manner as that in our previous paper [9] using the AMBER 6 program [14].

3. Results

3.1. SPR analysis

The SPR sensorgrams of the 4G-I, 4G-II, BP2-I, and BP2-II peptides for the interaction with eIF4E are shown in Fig. 2. The k_{on} , k_{off} and KD values estimated by SPR analysis are given in Table 1. No notable SPR signals were observed for 4G-III or BP2-III, indicating that the binding abilities of these sequences alone with eIF4E are considerably weak.

The SPR sensorgrams of 4G-I and 4G-II clarified the characteristic difference between these peptides for the interaction with eIF4E. The association and dissociation rates of 4G-II with eIF4E were too high to estimate accurately by 1:1 (Langmuir) binding

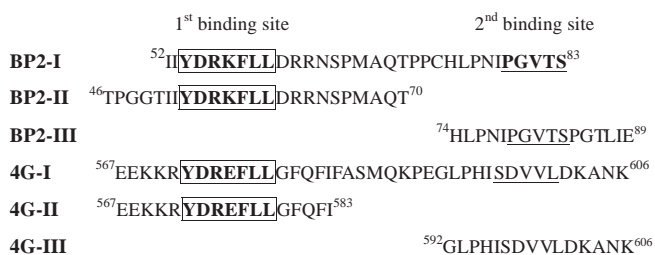


Fig. 1. Fragment peptides of first and second eIF4E binding site of 4E-BP and eIF4G1 used in this work. Bold letters enclosed with a box shows the first eIF4E binding sequences of eIF4G1 and 4E-BP2, and the second binding sequence of 4E-BP2 is underlined. The corresponding sequence of eIF4G1 is also underlined.

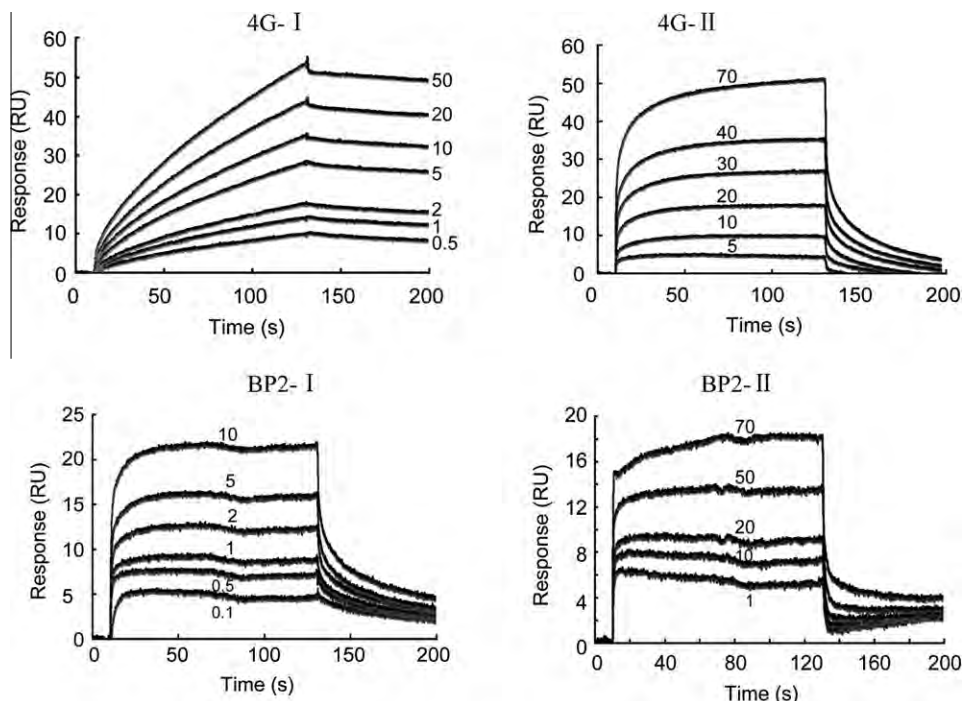


Fig. 2. SPR sensorgrams of 4G-I, 4G-II, BP2-I and BP2-II peptides for interaction with m^7 GTP-bound eIF4E. Each SPR signal shows the time response to eIF4E as a function of the concentration (μ M) of the peptide (indicated in each sensorgram). The right and left parts of each sensorgram indicate the phases of the injection of the peptide and the exposure of the chip to a peptide-free buffer, respectively.

Table 1

SPR kinetic parameters of the interactions of eIF4G and 4E-BP2 peptides with m^7 GTP-bound eIF4E at 25 °C.^a 4G-I: Glu567–Thr607, 4G-II: Glu567–Pro590, 4G-III: Glu591–Thr607. BP2-I: Thr46–Glu89, BP2-II: Thr46–Thr70, BP2-III: His74–Glu89.

Peptide	k_a (1/M s)	k_d (1/s)	K_D (M)
4G-I	$1.82 \pm 0.85 \times 10^3$	$2.01 \pm 0.92 \times 10^{-4}$	$1.10 \pm 2.03 \times 10^{-7}$
4G-II	–	–	$4.30 \pm 1.71 \times 10^{-5}$
4G-III	n.d.	n.d.	n.d.
BP2-I	$1.44 \pm 0.42 \times 10^6$	$1.22 \pm 0.84 \times 10^{-2}$	$8.48 \pm 2.04 \times 10^{-9}$
BP2-II	–	–	$4.30 \pm 1.21 \times 10^{-5}$
BP2-III	n.d.	n.d.	n.d.

^a The kinetic parameters of 4G-I and BP2-I were estimated using the 1:1 (Langmuir) binding model. The K_D (M) values of 4G-II and BP2-II were estimated using static Scatchard affinity model.

analysis, indicating that the deficit of this C-terminal region changes the mode of interaction with eIF4E significantly, compared with the presence of this region. Thus, the K_D values estimated by Scatchard affinity analysis show that the deletion of the C-terminal 18 residues of 4G-I weakens the interaction with eIF4E significantly, because the dissociation constants of 4G-I and 4G-II peptides from eIF4E were on the orders of $\sim 10^{-7}$ and 10^{-5} , respectively. This clearly suggests that eIF4GI has the second eIF4E-binding site in the Glu591–Lys606 region of eIF4GI (Fig. 1).

Although the Glu591–Thr607 region of eIF4GI was shown to be important for interaction with eIF4E, 4G-III alone showed no notable SPR signal for the interaction with eIF4E, showing that the binding ability of the second binding sequence itself is considerably low. Therefore, the SPR results of 4G-I, 4G-II, and 4G-III show the supportive but indispensable role of the second binding site in the intact binding of the first binding site to eIF4E, where the auxiliary effect of the Gly592–Lys606 sequence is sufficiently effective for activating the interaction up to K_D of $\sim 10^{-7}$.

Previously, we clarified [10] that the PGVTS/T sequence (Fig. 1) of the 4E-BP C-terminal side plays an important role in the tight binding with eIF4E, where the association constant is about 10^3 -

fold larger than that of its sequence-deleted 4E-BP mutant. In this work, the interaction with eIF4E was detected for the BP2-II peptide containing only the first binding site ($K_D = \sim 10^{-5}$ M) but not for the BP2-III peptide. However, the BP2-I peptide interacted with eIF4E on nearly the same order as the full-length 4E-BP2 ($K_D = \sim 10^{-9}$ M) [9,10], reconfirming that the PGVTS/T sequence of 4E-BP constitutes the second binding site and plays an auxiliary but indispensable role in strengthening the first binding site for the interaction with eIF4E. A similar function is possible for the Gly592–Lys606 region of eIF4GI. Although we have to wait for detailed analysis before we can draw a conclusion, it is reasonable to consider that the ⁵⁹⁷SDVVL⁶⁰¹ sequence of eIF4GI corresponds to the PGVTS sequence of 4E-BP2 (Fig. 1).

On the other hand, a notable difference was observed between the kinetic parameters of 4G-I and BP2-I (Table 1). The association and dissociation rates of BP2-I are about three and two orders of magnitude higher than those of 4G-I, respectively. This means that eIF4G has a potent resistive property for the release from eIF4E, although its rate of binding to eIF4E is not as high as that of 4E-BP, that is, 4E-BP is apt to bind to and be released from eIF4E compared with eIF4G. Because there is no notable difference between the kinetic parameters of 4G-II and BP2-II, this is due to the difference in function between the second binding sequences in eIF4G and 4E-BP on the interaction with eIF4E.

3.2. ITC analysis

To investigate the thermodynamic feature of the interaction of eIF4GI with eIF4E and compare it with that of 4E-BP, ITC analysis was performed on 4G-I, 4G-II, BP2-I, and BP2-II. The ITC profiles of 4G-I, 4G-II, and BP2-I for the interactions with m^7 GTP-bound eIF4E are shown in Fig. 3. The thermodynamic parameters are given in Table 2; the respective values were estimated using a one- or two-site model depending on their ITC profile patterns.

The ITC results supported the results of the SPR analysis of peptides II and III, i.e., BP2-II showed almost the same thermal param-

eters as 4G-II, and no notable ITC responses were observed for 4G-III or BP2-III, indicating that the eIF4E binding abilities of the second binding sequences alone are both weak. Interestingly, a remarkable difference was observed between the ITC profiles of 4G-I and BP2-I peptides. As was expected, BP2-I showed a two-site binding profile, in which two types of binding site exist in the ranges of 0–1.0 and 1.0–2.0 M ratios, suggesting the two-step interaction of 4E-BP2 with eIF4E via the first and second binding sites. This ITC profile appears to show that the second binding site reinforces the binding via the first binding site, thus leading to the collaborative binding of $K_a = 6.91 \times 10^9 \text{ (M}^{-1}\text{)}$ at a molar ratio of n ([BP2-I peptide]/[eIF4E]) < 1, although the binding via the first

binding site is dominant at a molar ratio of $n > 1$. In contrast, 4G-I showed no notable ITC response, which suggests the disturbance of the second binding site for the interaction of the first binding site with eIF4E. Although we have no reliable answer yet for the discrepancy between the SPR and ITC results, it may be partly due to the different points of observation for the molecular interaction. SPR measurement determines the dynamic binding of the peptide to eIF4E, the peptide takes the open conformers; thus, both binding sites could interact with eIF4E independently. In contrast, the ITC measurement determines the static interaction of the peptide with eIF4E in the cell, in which the peptide is in an equilibrium state between the open and folded conformers. In such a situation,

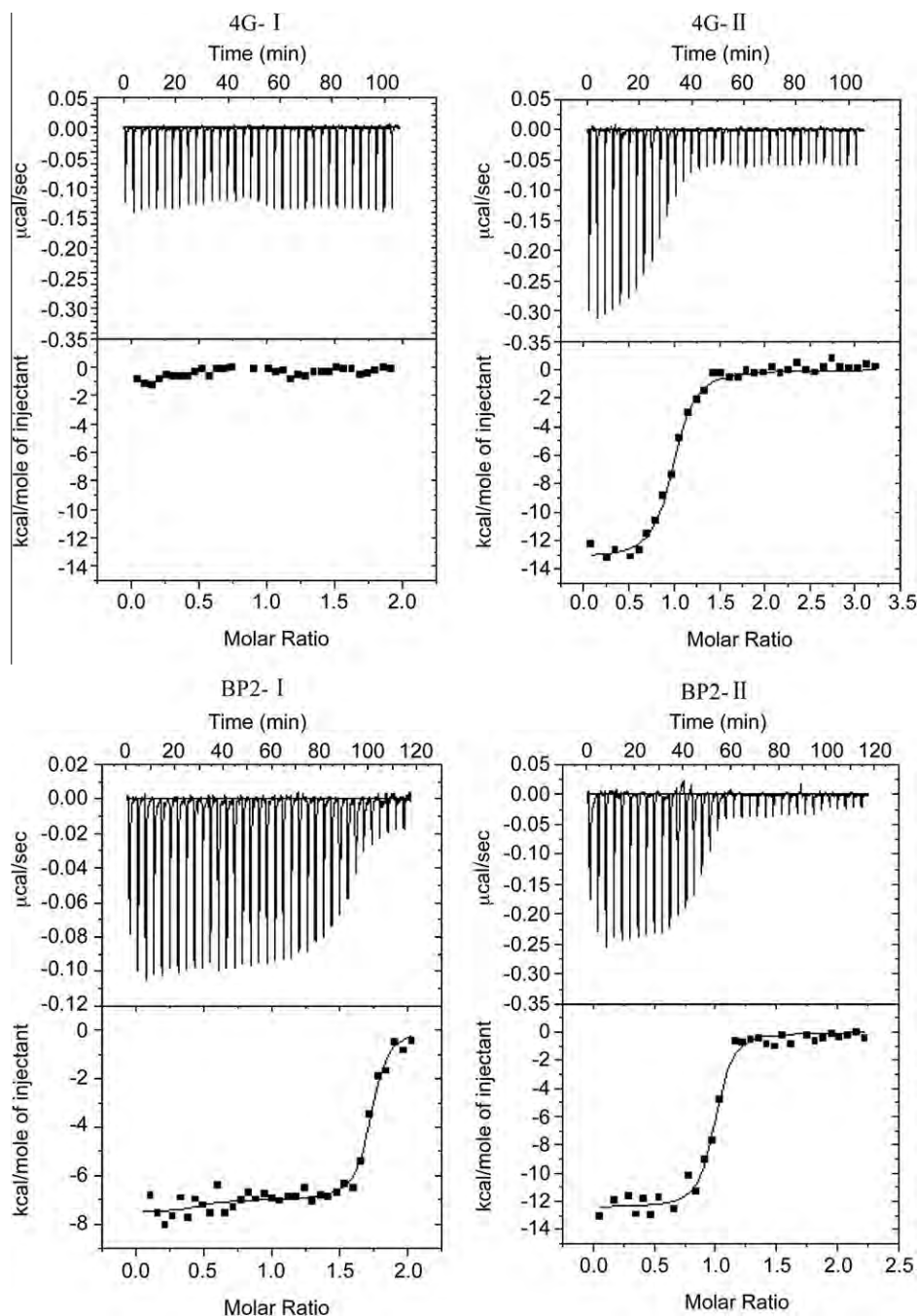


Fig. 3. ITC profiles of 4G-I, 4G-II, BP2-I, and BP2-II peptides for interaction with $m^7\text{GTP}$ -bound eIF4E. The top and bottom panels show the raw data and integrated heat changes with the curve best fitted using a one-site or two-site binding model, respectively. The binding isotherms show the heat effects associated with the injection of each 4G/BP2 peptide (5 μL per injection of a 50 μM concentration) into the calorimetric cell (1.4 mL) of 5 μM $m^7\text{GTP}$ -bound full-length eIF4E.

Table 2
Thermodynamic parameters of eIF4E binding peptides of eIF4G and 4E-BP2 with m⁷GTP-bound eIF4E at 25 °C. 4G-I: Glu567–Thr607, 4G-II: Glu567–Pro590, 4G-III: Glu591–Thr607. BP2-I: Thr46–Glu89, BP2-II: Thr46–Thr70, BP2-III: His74–Glu89.

Peptide	ΔG (kcal/M)	ΔH (kcal/M)	$-\Delta S$ (kcal/M)	n	K_A (M ⁻¹)
4G-I	n.d.	n.d.	n.d.		
4G-II	-9.87	-13.24 ± 0.19	3.37	0.965 ± 0.08	1.73 ± 0.23 × 10 ⁷
4G-III	n.d.	n.d.	n.d.		
BP2-I	-13.43	-7.50 ± 0.28	-5.93	0.46 ± 0.18	6.91 ± 0.34 × 10 ⁹
	-10.63	-7.06 ± 0.13	-3.57	1.25 ± 0.18	7.81 ± 0.31 × 10 ⁷
BP2-II	-10.35	-12.46 ± 0.11	2.11	0.976 ± 0.02	3.85 ± 0.15 × 10 ⁷
BP2-III	n.d.	n.d.	n.d.		

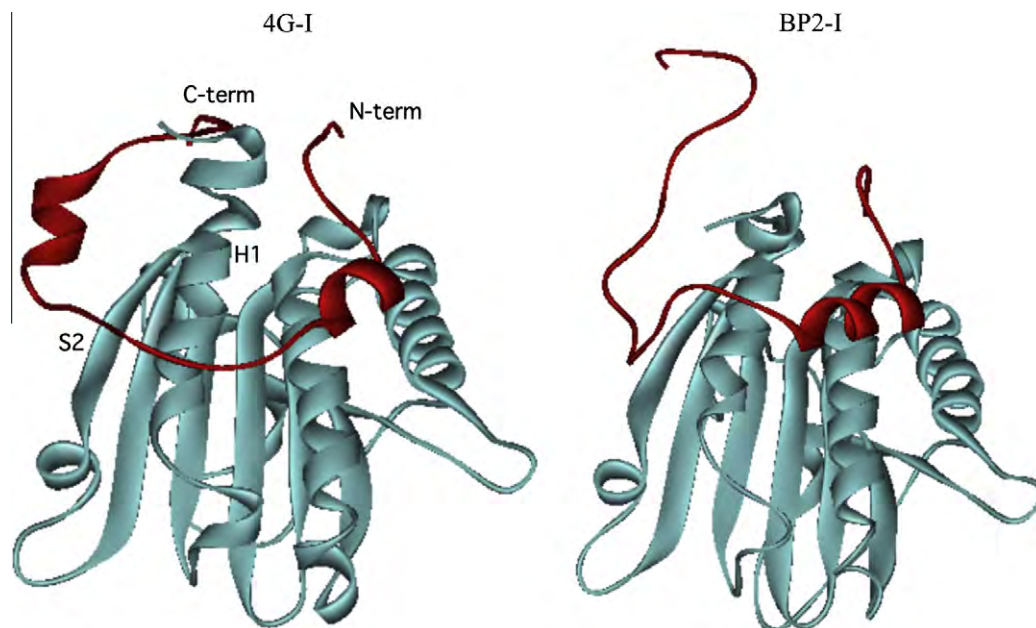


Fig. 4. MD snapshots of interactions of 4G-I and BP2-I peptides (red) with eIF4E (blue) at 3 ns. H1 and S2 on eIF4E denote the S2-sheet and H1-helix secondary structures, respectively. N- and C-term indicate the N- and C-terminal sides of eIF4E, respectively. (For interpretation of the references to color in this figure legend, the reader is referred to the web version of this article.)

the transition of the first binding sequence from a random conformation to an α -helical form, which is necessary for the binding to eIF4E, is disrupted by the free contact with the second binding sequence.

In any event, it is clear from the present results that the second eIF4E binding sequence is crucial to the difference in behavior between eIF4G and 4E-BP for their interaction with eIF4E, because the interactions of the first binding sequence site with eIF4E are almost the same for both molecules.

4. Discussion

On the basis of our previous studies of the existence and function of the second eIF4E binding region in 4E-BP [9,10], we studied the difference between the eIF4E binding behaviors of eIF4G and 4E-BP using the fragment peptides of these proteins by SPR analysis. Consequently, we clarified the existence of a second eIF4E binding site at the periphery of the ⁵⁹⁷SDVVL⁶⁰¹ sequence in eIF4G and its auxiliary but indispensable function in stabilizing the eIF4E binding at the first binding site, ⁵⁷²YDREFL⁵⁷⁸.

Although similar features were already observed for the first and second binding regions of 4E-BP, the kinetic parameters of these regions showed a characteristic difference. In particular, the association and dissociation rates of BP2-I were about three or two orders of magnitude higher than those of 4G-I. This suggests

that although its rate of binding to eIF4E is not as high as that to 4E-BP, eIF4G has a resistive property for the release from its complex with eIF4E, reflecting well the regulative and promotive roles of 4E-BP and eIF4G in the translational function of eIF4E, respectively. Because no notable difference was observed between the kinetic parameters of 4G-II and BP2-II, this difference is clearly due to the effect of their second binding regions on the interaction of the first binding region with eIF4E and indicates the importance of the second binding site for the eIF4G/4E-BP-inherent function.

It is interesting to consider the possible mode of interaction of 4G-I with eIF4E and compare it with that of BP2-I. Previously, we performed MD simulation for the BP2-I–eIF4E complex in a neutral aqueous solution [9]. Because Gross et al. [13] determined the solution structure of the m⁷GDP-bound yeast eIF4E–eIF4GII fragment peptide complex by NMR analysis and this fragment peptide corresponds to the 517–606 sequence of human eIF4G, the structure of the eIF4E–4G-I peptide complex was constructed from the solution structure and subjected to MD simulation for comparison. The snapshots of both complexes at 3 ns are shown in Fig. 4, in which the helical conformations formed at the Asp575–Phe584 and Gly592–Asp598 sequences in 4G-I correspond to a part of the first and second eIF4E binding regions, respectively.

The MD snapshot of 4G-I appears to reflect the binding feature observed in the SPR analysis. The peptide forms a right-handed ring so as to wrap around the root (Ile35–Pro38) of the N-terminal flexible region of eIF4E. A similar model of the binding of BP2-I to

eIF4E was also simulated by the MD calculation of its eIF4E complex. Therefore, it is conceivable from the present SPR results that such a spatial binding of both binding sequences to the N-terminal root of eIF4E is important for the functional performance of eIF4G and 4E-BP.

On the other hand, the notable difference between 4G-I and BP2-I is that the helical conformation of 4G-I (Gly592–Asp598) used as an MD starting structure, which is in part overlapped with the ⁵⁹⁷SDVVL⁶⁰¹ sequence, is maintained during the MD simulation for 3 ns, whereas the corresponding sequence of BP2-I (His74–Val81) shifts to a random structure with the progress of MD simulation and forms a relatively stable spatial orientation with the H1 helical and S2 sheet structures of eIF4E through hydrophobic interactions.

The N-terminal side from the first binding site of eIF4G has a much longer sequence than that of 4E-BP. According to the solution structure of eIF4GII fragment peptide bound to eIF4E, the second binding region of 4GII peptide was close contact with the N-terminal side from the first binding site of 4GII peptide [13]. Thus, it is reasonable to consider that the dissociation of eIF4G from eIF4E is much more protective than that of 4E-BP. In any event, the presence of the long N-terminal sequence in eIF4G would be responsible for its inherent function. The present results provide important information on the difference in eIF4E binding function between eIF4G and 4E-BP.

References

- [1] T.E. Dever, Gene-specific regulation by general translation factors, *Cell* 108 (2002) 545–556.
- [2] N. Sonenberg, A.G. Hinnebusch, Regulation of translation initiation in eukaryotes: mechanisms and biological targets, *Cell* 136 (2009) 731–745.
- [3] N. Sonenberg, T.E. Dever, Eukaryotic translation initiation factors and regulators, *Curr. Opin. Struct. Biol.* (2003) 56–63.
- [4] S. Mader, H. Lee, A. Pause, N. Sonenberg, The translation initiation factor eIF4E binds to a common motif shared by the translation factor eIF4- γ and the translational repressor 4E-binding proteins, *Mol. Cell. Biol.* 17 (1997) 6940–6947.
- [5] M. Altmann, N. Schmitz, N. Berset, H. Trachsel, A novel inhibitor of cap-dependent translation initiation in yeast–p20 competes with eIF4G for binding to eIF4E, *EMBO J.* 16 (1997) 1114–1121.
- [6] J. Marcotrigiano, A.C. Gingras, N. Sonenberg, S.K. Burley, Cap-dependent translation initiation in *Eukaryotes* is regulated by a molecular mimic of eIF4G, *Mol. Cell* 3 (1999) 707–716.
- [7] K. Tomoo, Y. Matsushita, H. Fujisaki, F. Abiko, X. Shen, T. Taniguchi, H. Miyagawa, K. Kitamura, K. Miura, T. Ishida, Structural basis for mRNA cap-binding regulation of eukaryotic initiation factor 4E by 4E-binding protein, studied by spectroscopic, X-ray crystal structural, and molecular dynamics simulation methods, *Biochim. Biophys. Acta* 1753 (2005) 191–208.
- [8] A.C. Gingras, B. Raught, S.P. Gygi, A. Niedzwiecka, M. Miron, S.K. Burley, R.D. Polakiewicz, A. Wyslouch-Cieszynska, A. Aebersold, N. Sonenberg, Hierarchical phosphorylation of the translation inhibitor 4E-BP1, *Genes Dev.* 15 (2001) 2852–2864.
- [9] A. Mizuno, Y. In, Y. Fujita, F. Abiko, H. Miyagawa, K. Kitamura, K. Tomoo, T. Ishida, Importance of C-terminal flexible region of 4E-binding protein in binding with eukaryotic initiation factor 4E, *FEBS Lett.* 582 (2008) 2439–2444.
- [10] K.S. Park, Y. Umenaga, A. Fukuyo, A. Mizuno, Y. In, T. Ishida, K. Tomoo, 130 Ann. Meeting of Pharm. Soc. of Japan, Poster No. 30P-am067, Okayama, 2010.
- [11] S. Morino, H. Hazama, M. Ozaki, Y. Teraoka, S. Shibata, M. Doi, H. Ueda, T. Ishida, S. Uesugi, Analysis of the mRNA cap-binding ability of human eukaryotic initiation factor–4E by use of recombinant wild-type and mutant forms, *Eur. J. Biochem.* 239 (1996) 597–601.
- [12] K. Nagata, H. Handa, *Real Time Analysis of Biomolecular Interactions*, Springer, Verlag, Tokyo, 1998.
- [13] J.D. Gross, N.J. Moerke, T. Von der Haar, A.A. Lugovskoy, A.B. Sachs, J.E.G. McCarthy, G. Wagner, Ribosome loading onto the mRNA cap is driven by conformational coupling between eIF4G and eIF4E, *Cell* 115 (2003) 739–750.
- [14] D.A. Case, D.A. Pearlman, J.W. Caldwell, T.E. Cheatham III, J. Wang, W.S. Ross, C.L. Simmerling, T.A. Darden, K.M. Merz, R.V. Stanton, A.L. Cheng, J.J. Vincent, M. Crowley, V. Tsui, H. Gohlke, R.J. Radmer, Y. Duan, J. Pitera, L. Massova, G.L. Seibel, U.C. Singh, P.K. Weiner, P.A. Kollman, *AMBER7*, University of California, San Francisco, 2002.

Structural scaffold for eIF4E binding selectivity of 4E-BP isoforms: crystal structure of eIF4E binding region of 4E-BP2 and its comparison with that of 4E-BP1

Ai Fukuyo, Yasuko In, Toshimasa Ishida and Koji Tomoo*

To clarify the higher eukaryotic initiation factor 4E (eIF4E) binding selectivity of 4E-binding protein 2 (4E-BP2) than of 4E-BP1, as determined by Trp fluorescence analysis, the crystal structure of the eIF4E binding region of 4E-BP2 in complex with m⁷GTP-bound human eIF4E has been determined by X-ray diffraction analysis and compared with that of 4E-BP1. The crystal structure revealed that the Pro47-Ser65 moiety of 4E-BP2 adopts a L-shaped conformation involving extended and α -helical structures and extends over the N-terminal loop and two different helix regions of eIF4E through hydrogen bonds, and electrostatic and hydrophobic interactions; these features were similarly observed for 4E-BP1. Although the pattern of the overall interaction of 4E-BP2 with eIF4E was similar to that of 4E-BP1, a notable difference was observed for the 60–63 sequence in relation to the conformation and binding selectivity of the 4E-BP isoform, i.e. Met-Glu-Cys-Arg for 4E-BP1 and Leu-Asp-Arg-Arg for 4E-BP2. In this paper, we report that the structural scaffold of the eIF4E binding preference for 4E-BP2 over 4E-BP1 is based on the stacking of the Arg63 planar side chain on the Trp73 indole ring of eIF4E and the construction of a compact hydrophobic space around the Trp73 indole ring by the Leu59-Leu60 sequence of 4E-BP2. Copyright © 2011 European Peptide Society and John Wiley & Sons, Ltd.

Keywords: 4E-BP1; 4E-BP2; eIF4E; ternary complex; X-ray crystal structure; binding preference

Introduction

Eukaryotic translation initiation is performed by many eukaryotic initiation factors (eIFs) and regulated through structural changes in the phosphorylation states of eIFs and endogenous regulator proteins [1]. In the cap-dependent translation of mRNA, an interaction is required between the cap structure and the eukaryotic initiation factor 4F, a supramolecular complex of three subunits, eIF4E, eIF4A and eIF4G, for the efficient translation of mRNA. The first step in the translation process is the binding of eIF4E, the smallest subunit in eIF4F, to the mRNA cap structure. Because this is the rate-limiting step in translation initiation, eIF4E serves as a master switch that controls eukaryotic translation and a pivot molecule for translational control [2]. As the initiation function of eIF4E is controlled by the association/dissociation with the endogenous 4E-binding protein (4E-BP) [1,3,4], the study on the interaction of eIF4E with 4E-BP is therefore important in understanding the regulation mechanism of such a process.

At present, three isoforms of 4E-BP, namely, 4E-BP1–4E-BP3, are known [1,3] and their sequences are shown in Figure 1. Concerning the function of the 4E-BP, it is known that (i) these isoforms bind to eIF4E through a sequence of the Y(X)₄L ϕ motif (X: variable, ϕ : hydrophobic, see Figure 1) [5,6], (ii) the hyperphosphorylations of their Thr and Ser residues in response to growth factors and mitogens result in their release from eIF4E [4,7], and (iii) although 4E-BP1 and 4E-BP2 themselves show a random structure, their eIF4E binding regions form a helical structure upon binding to a conserved surface on the dorsal side of the eIF4E cap-binding pocket [3,4]. In contrast, the functional difference of these isoforms upon binding to eIF4E is poorly understood.

For more insight, we previously measured the interactions of these 4E-BP isoforms with eIF4E by the Trp fluorescence titration method [8] and observed the binding preference of eIF4E for 4E-BP2 over 4E-BP1 and 4E-BP3 under a physiological condition, where the association constant of 4E-BP2 was two- to threefold larger than that of 4E-BP1. However, it became clear by surface plasmon resonance measurement that the association constants of eIF4E with 4E-BP1–3 isoforms are almost within the same range (unpublished data). This disagreement indicates obviously that the local interaction mode at the binding site is meaningfully different, although the overall interaction model of eIF4E with 4E-BP is nearly same. Thus, it is reasonable to consider that the binding preference shown by the Trp fluorescence titration results from the difference between 4E-BP1 and 4E-BP2 in the mode of interaction of the Trp73 residue of eIF4E, especially the 4E-BP1-specific Met-Glu-Cys and 4E-BP2-specific Lys-Asp-Arg (60–62) sequences, because the direct participation of the Trp73 residue of eIF4E in the binding with 4E-BP isoform is shown by the X-ray crystal structure of the eIF4E–4E-BP1 fragment complex [9].

Previously, we reported the crystal structure of the ternary complex of m⁷GpppA–eIF4E–4E-BP1 fragment (Thr36–Thr70) [8]. Therefore, to clarify the difference in the microscopic situation at

* Correspondence to: Koji Tomoo, Laboratory of Physical Chemistry, Osaka University of Pharmaceutical Sciences, 4-20-1 Nasahara, Takatsuki, Osaka 569-1094, Japan. E-mail: tomo@gly.oups.ac.jp

Laboratory of Physical Chemistry, Osaka University of Pharmaceutical Sciences, 4-20-1 Nasahara, Takatsuki, Osaka 569-1094, Japan

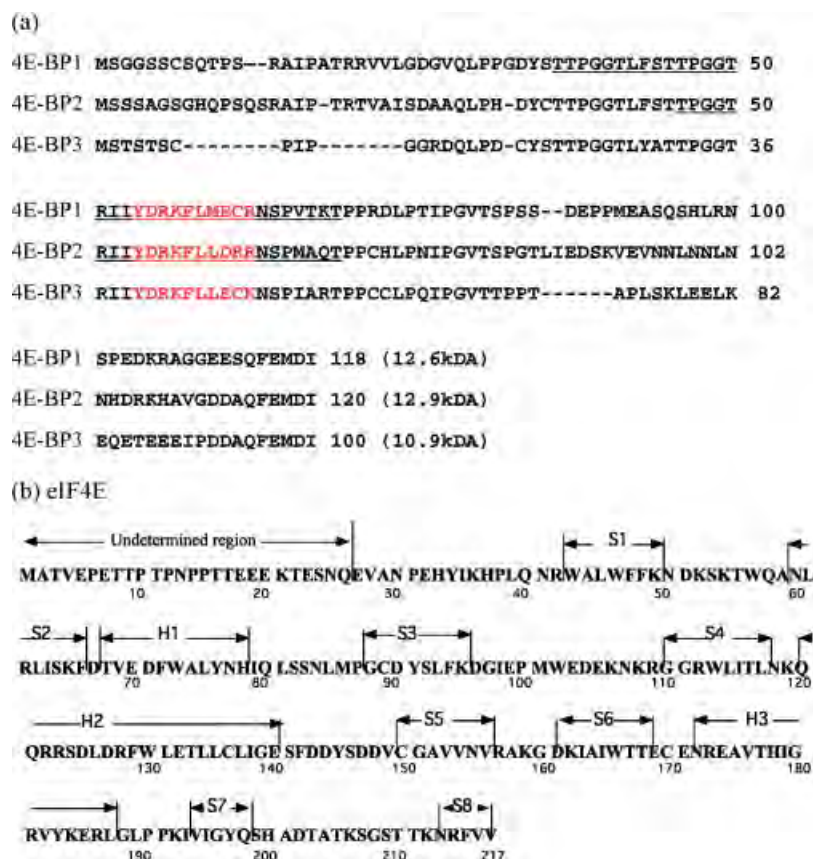


Figure 1. Amino acid sequences of (a) 4E-BP1–3 isoforms and (b) eIF4E. The sequences of (a) are aligned on the basis of their functional similarities. The eIF4E α -helical binding region of the 4E-BP isoforms is shown in bold. The sequences of the 4E-BP1 and 4E-BP2 peptides used for the complex formation are underlined. The secondary structural elements of eIF4E (b) elucidated by X-ray crystal analysis are indicated by H1–H3 and S1–S8, which correspond to the helices and strand structures in Figure 3, respectively.

eIF4E binding site between 4E-BP1 and 4E-BP2 at the atomic level, we determined the crystal structure of the complex of m⁷GTP-bound eIF4E with the 4E-BP2 fragment peptide (Thr46–Thr70), in which m⁷GTP was used as a model of the mRNA cap structure, and compared with the X-ray result of the m⁷GpppA–eIF4E–4E-BP1 peptide ternary complex. In this paper, we report these results and the structural scaffold for the eIF4E binding preference for 4E-BP2 over 4E-BP1.

Materials and Methods

Peptide Synthesis

The commercially available materials used were of reagent grade or higher purity. The Thr46–Thr70 fragment of 4E-BP2 used for the crystallization was synthesized using a solid-phase peptide synthesizer. The peptide (including TFA as the counter ion) was obtained in the form of lyophilized powder. The peptide was characterized by mass spectrometry and had a purity >95.0%, as determined by RP HPLC.

Preparation of Full-Length Human eIF4E

The commercially available reagents used for preparing recombinant proteins were purchased from either Sigma Chemical, Takara Shuzo, New England Biolabs Inc., Toyobo Co., Novagen Co., or GE Healthcare Co. The gene expression of human full-length eIF4E in

Escherichia coli and the isolation and purification of the expressed protein were carried out according to a previous method [10]. The supernatant containing recombinant eIF4E was applied to an m⁷GTP-Sepharose 4B affinity column equilibrated with buffer A (50 mM HEPES–NaOH (pH 7.5), 1 mM EDTA, 100 mM NaCl). The m⁷GTP-bound eIF4E was prepared by elution with buffer B (buffer A + 100 μ M m⁷GTP). The solution was concentrated with Centricon 10 (Amicon Co.) to the desired concentration. The m⁷GTP-bound eIF4E in buffer A was then incubated with an equimolar amount of the 4E-BP2 peptide and concentrated to a protein concentration of 5 mg/ml. Droplets of 2 μ l initial volume were equilibrated at 18 °C against the reservoir solution (2 μ l) of 100 mM MES (2-(*N*-morpholino)ethanesulfonic acid) buffer (pH 5.6) containing 0.2 M ammonium sulfate and 15–25% PEG-MME (monomethyl ether) 2000 (Hampton Res.).

X-ray Crystal Analysis

Needle-shaped crystals of the m⁷GTP-eIF4E–4E-BP2 peptide ternary complex were obtained after 1 week by the hanging drop vapor diffusion method at 15 °C, growing up to dimensions of 0.05 mm \times 0.05 mm \times 0.5 mm. X-ray diffraction data at 100 K were collected using CuK α radiation from an FR-E rotating anode X-ray generator (Rigaku Corp) equipped with a confocal mirror (Osmic Inc.) and an R-AXIS VII detector. The crystal was cryoprotected using the cryosolvent prepared by adding 15–20% glycerol to the reservoir solution. Data processing was performed with the

Table 1. Crystallographic data and refinement statistics

Crystallographic data	
Cell dimensions (Å)	$a = b = 87.84, c = 37.75$
Space group	$P4_3$
Z	4
V_m (Å ³ /Da)	3.08
Temperature (K)	100
X-ray source (Å)	1.54
Resolution (Å)	44–2.1
Unique reflection	16 431
Completeness (%)	95.4
R_{merge} (%)	10.1
Refinement statistics	
Resolution (Å)	30–2.2
Reflection	14 502
R-factor (%)	22.8
R_{free} (%) ³	26.5
Number of atoms	
Protein	1735
m ⁷ GTP	51
Water	94
Overall B protein (Å ²)	36
Estimated maximum coordinate error (Å)	0.26
RMS deviation	
Bond (Å)	0.007
Angle (°)	1.30
Improper	0.66

program CrystalClear [11]. The crystal diffracted up to a 2.1 Å resolution and the data were processed in a tetragonal lattice system.

The space group and cell constants were essentially the same as those of the m⁷GpppA–eIF4E–4E-BP1 peptide ternary complex [8]. Thus, the initial structure of the present crystal was determined with the CNS program [12] using the atomic coordinates of the eIF4E (PDB code 1WKW). An atomic model of the complex was constructed using the TURBO-FRODO graphics program [13], and the structure was refined using the CNS program package. After several cycles of refinement, the difference electron density maps gave densities sufficient for constructing the entire m⁷GTP structure and the Pro47–Ser65 moiety of the 4E-BP2 peptide, although the terminal sides of the peptide showed low densities due to the high temperature factors. Further refinement of the complex structure and the addition of clearly identifiable water molecules improved the R-factor. Data collection and refinement statistics are presented in Table 1. The final atomic coordinates have been deposited in the RCSB Brookhaven Protein Data Bank (the accession code is 3AM7).

Results and Discussion

Overall Structure of Ternary Complex

An overview of the ternary complex of m⁷GTP–eIF4E–4E-BP2 peptide is shown in Figure 2, together with the electron density map of 4E-BP2 peptide moiety; the amino acid sequence and secondary structural elements of eIF4E are shown in Figure 1. The electron density from the N-terminal to Gln26 of eIF4E was not

assigned because of the high thermal motion, and this structural flexibility in the N-terminal region was the same as that in the eIF4E–m⁷GpppA binary complex [14] and the ternary complex with the 4E-BP1 fragment peptide [8]. Because the overall structure of eIF4E complexed with 4E-BP2 was essentially the same as that with 4E-BP1 complex (the rms deviation between their whole atomic coordinates was 0.08 Å), it could say that the interactions of eIF4E with 4E-BP1 and 4E-BP2 are essentially unaffected by the difference between m⁷GpppA and m⁷GTP used as a model of mRNA cap structure in the respective complexes. The entire structure of 4E-BP2 peptide (Thr46–Thr70) was not observed, and the electron density was detected for the Pro47–Ser65 moiety (Figure 2); this was the same as the 4E-BP1 peptide. The rms deviation between the whole atomic coordinates of 4E-BP2 and 4E-BP1 peptides was 2.48 Å.

The 4E-BP2 peptide was localized at the dorsal N-terminal root surface of the eIF4E cap-binding pocket and adopted a L-shaped open form, where the Asp55–Arg63 moiety formed an α -helical secondary structure and the Pro47–Tyr54 and Asn64–Ser65 sequences were in an extended conformation, without adopting any defined secondary structure; similar L-shaped conformation was observed for 4E-BP1 peptide. As the CD spectra of full-length 4E-BP1 \sim 3 and their fragment peptides including the Y(X)₄L ϕ sequence show a random conformation in the isolated state, it is evident that the eIF4E binding region is induced to adopt an α -helical structure by interacting with eIF4E. The peptide is mainly fixed by hydrogen bonds, and electrostatic and hydrophobic interactions with three structural parts of eIF4E, i.e. the N-terminal loop (His37–Gln40), H1 helix (Val69–Asn77) and H2 helix (Glu132–Glu140) regions. The present result confirmed the importance of Tyr54, Leu59 and Leu60 in the Y(X)₄L ϕ sequence for the interaction with eIF4E (to be discussed later).

Conformations of 4E-BP Isoforms

The molecular conformation of 4E-BP2 is shown in Figure 3, together with that of 4E-BP1 for comparison. Possible intramolecular hydrogen bonds and selected electrostatic short contacts are given in Table 2. The conformation of 4E-BP2 is affected not only by the interaction at the eIF4E binding pocket, but also by the crystal packing, because the interatomic short contacts of 4E-BP2 are formed between the neighboring eIF4E in the crystal; similar affect was also observed for the conformation of 4E-BP1. The overall structures of both peptides are similar in such a way that the sequences of the N- and C-terminal sides adopt the extended (Pro47–Tyr54) and α -helical (Asp55–Arg63) conformations, respectively. However, notable differences are observed between the structurally rigid α -helical moieties. In addition to the difference in hydrogen bonding pattern between the 60 and 64 sequences of both peptides (Table 2), one remarkable feature of 4E-BP2 is the intramolecular π – π stacking interaction between the Phe58 benzene ring and the Arg62 guanidyl group (average spacing = 3.6 Å and dihedral angle = 35°). This stacking structure is stabilized by bifurcated Arg62 N ϵ H/N η H \cdots O Phe58 hydrogen bonds (2.93 and 2.92 Å), thus contributing to the stabilization of the α -helical structure. In the case of 4E-BP1, the Cys62 SH group undergoes a S–H \cdots π interaction with the Phe58 benzene ring, although the extent of this interaction is rather limited because of the deviation in the Cys62 SH position from the center of the benzene ring. Another difference is in the orientation of the C-terminal backbone chain. In the conformation of 4E-BP2, the *trans*-oriented Arg63 side chain with respect to Arg62 directs the orientation of the

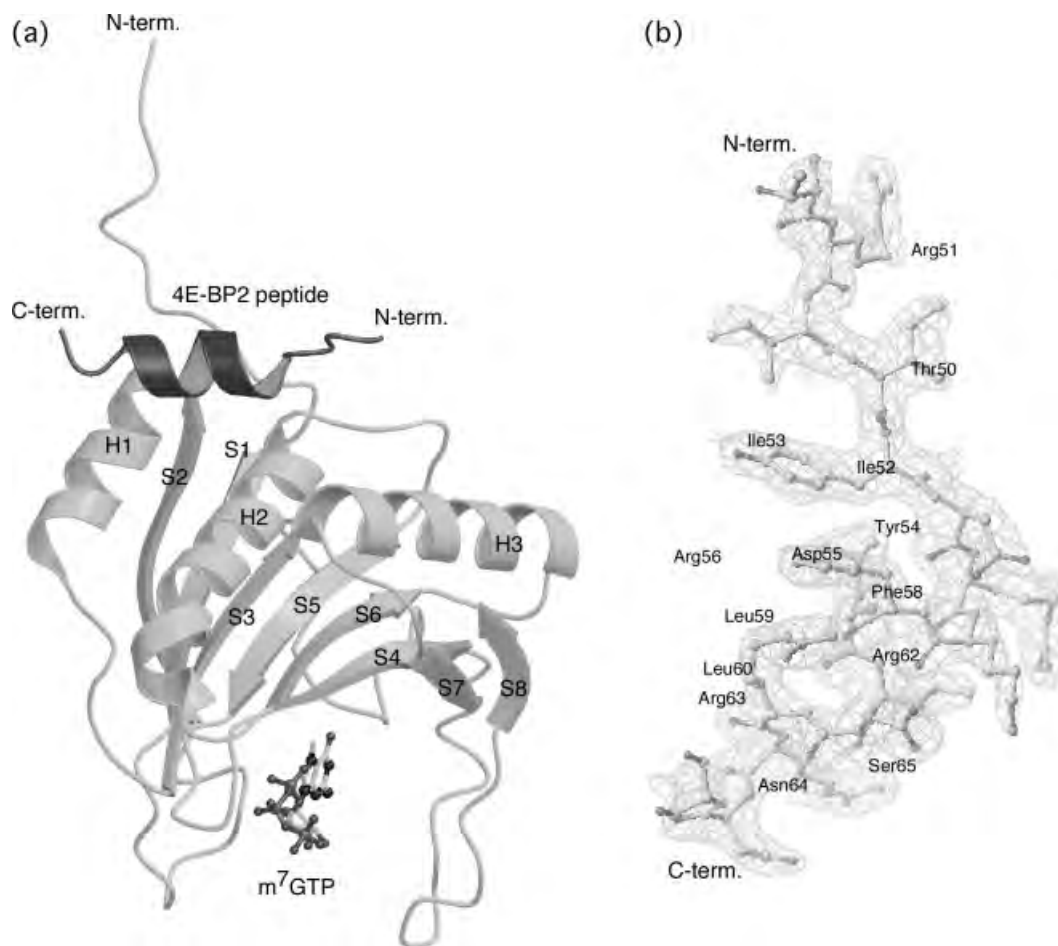


Figure 2. Overall structure of ternary complex of m⁷GTP-eIF4E-4E-BP2 peptide and 2Fo-Fc omit map of 4E-BP2 peptide. eIF4E (gray) and the 4E-BP2 peptide [Pro47-Ser65] (black) are shown using the ribbon model, and m⁷GTP is depicted using the stick-bond model. Three α -helices and eight sheets of eIF4E are labeled by H1-H3 and S1-S8, respectively, and the N-terminal moiety of eIF4E is shown by the N-term. The contour of electron density is depicted at the 3 σ level.

Asn63-Ser64 sequence toward the direction opposite to 4E-BP1. Consequently, the Ser65 of 4E-BP2 does not participate in the hydrogen bonding with the Asn77 N δ 2H of eIF4E (to be discussed later); however, such a hydrogen bond is formed for 4E-BP1.

The molecular conformation of 4E-BP3 is not yet available. However, the conformation of its eIF4E binding sequence would be similar to that of 4E-BP1, because the influence of the Glu47-Cys48-Lys49 sequence on the conformation of 4E-BP3 could be nearly the same as that of the Glu61-Cys62-Arg63 sequence of 4E-BP1, rather than the Asp62-Arg63-Arg64 sequence of 4E-BP2.

4E-BP Isoform-specific Binding with eIF4E

The binding mode between 4E-BP2 peptide and eIF4E is shown in Figure 4(a) and the difference in the binding mode between 4E-BP1 and 4E-BP2 is shown in Figure 4(b). Hydrogen bonds and selected electrostatic short contacts between both molecules are given in Table 3. Concerning the eIF4E residues associated with the 4E-BP binding selectivity or specificity, Leu39, Trp73, Val69, and Gly139 residues are identified in spectroscopic studies [15]. It is evident from Table 3 that Trp73 and Gly139 participate in the interaction of both 4E-BPs. Furthermore, in the case of 4E-BP2, the planar propyl side chain of Arg63 is stacked on the Trp73 indole ring through hydrophobic interaction (average spacing = 4.0 Å);

Table 2. Comparison of some intramolecular hydrogen bonds and electrostatic short contacts of 4E-BP1 and 4E-BP2 characterizing the conformational features

Donor	Acceptor	Distance (Å)	
		4E-BP1	4E-BP2
Lys57NH	O δ Asp55	3.11	2.62
Phe58NH	O δ Asp55	2.87	2.72
Phe58NH	O Asp55	3.33	2.90
Leu59NH	O Asp55	3.24	3.26
Met60NH	O Arg56	2.94	
Leu60NH	O Arg56		2.84
Glu61NH	O Lys57	2.56	
Glu61NH	O Phe58	3.00	
Asp61NH	O Lys57		2.94
Cys62NH	O Phe58	2.81	
Arg62N ϵ H	O Phe58		2.93
Arg62N η H	O Phe58		2.92
Arg62NH	O Leu59		3.26
Arg63NH	O Met60	2.65	
Arg63NH	O Glu61	2.41	
Arg63NH	O Leu60		3.19

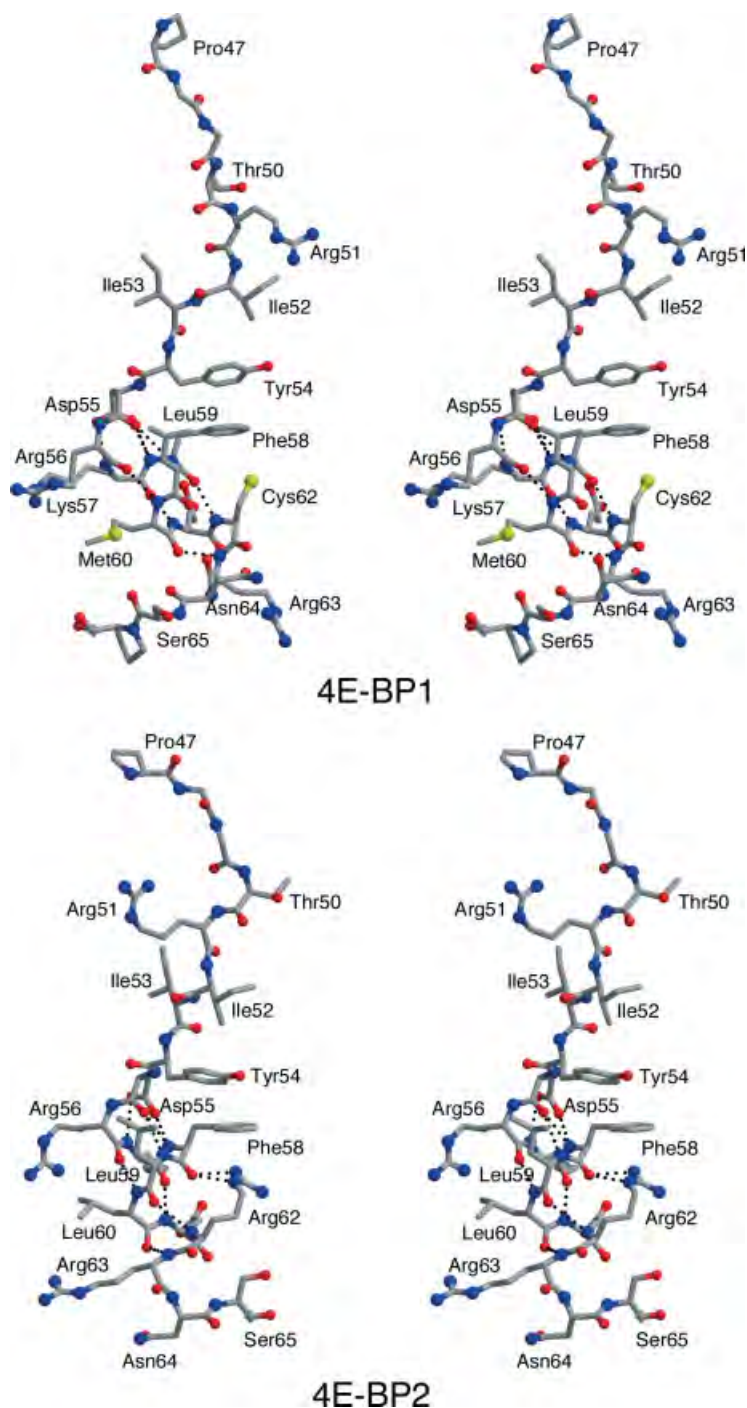


Figure 3. Molecular conformations (in stereo) of 4E-BP1 and 4E-BP2. Dotted lines represent intramolecular hydrogen bonds. Each amino acid residue is shown with a three-code label. The red and blue circles represent oxygen and nitrogen atoms, respectively. Dotted lines represent intramolecular hydrogen bonds reflecting the difference between both molecules.

such an interaction is not induced for 4E-BP1 (Figure 5(a)). This is probably due to the *trans* orientation of the Arg63 side chain with respect to the Arg62 for 4E-BP2, and such conformational constraint is not imposed for the Arg63 residue of 4E-BP1 because of the Cys62 residue (Figure 3). On the other hand, the Leu39 and Val69 residues of eIF4E constitute a compact hydrophobic core in collaboration with the Tyr54, Phe58 and Leu59 residues of 4E-BP2. However, a similar hydrophobic core is also formed by interaction with 4E-BP1. Thus, the binding of Leu39 and Val69 residues of

eIF4E appear not to be strong enough to account for the binding selectivity of 4E-BP isoforms (Figure 4).

On the other hand, it is reasonable to consider that the difference in eIF4E binding specificity between 4E-BP1 and 4E-BP2 results mainly from the difference in their 60–62 sequences, i.e. Met-Glu-Cys for 4E-BP1 and Leu-Asp-Arg for 4E-BP2. Ptushkina *et al.* [15] reported that this sequential difference between 4E-BP1 and 4E-BP2 affects the hydrophobic interaction of Met60/Leu60 with the Trp73 indole ring (eIF4E) and the electrostatic interaction of

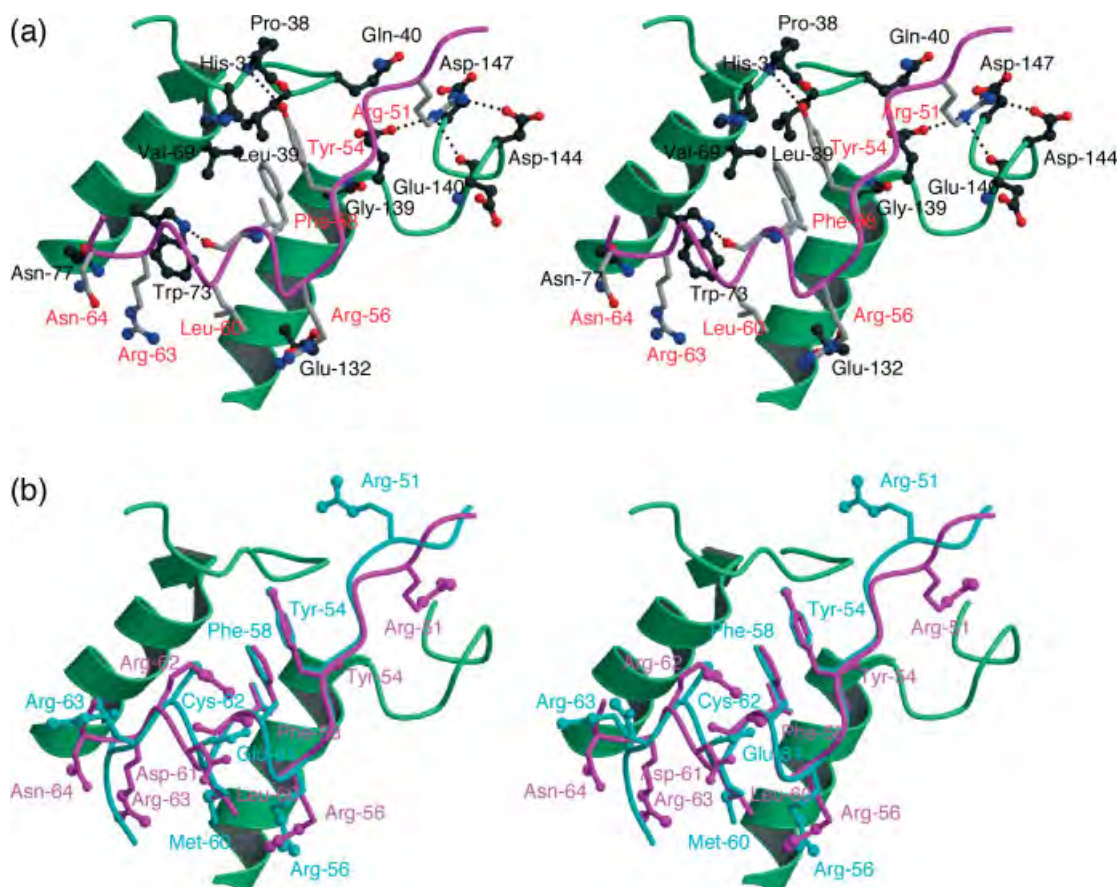


Figure 4. (a) Binding mode (in stereo) of 4E-BP2 peptide (magenta wire) at 4E-BP binding pocket of eIF4E (green) and (b) its superimposition with 4E-BP1 (cyan wire). The N-terminal extended (His37–Gln40, wire), and H1 (Trp73–Asn77) and H2 (Glu132–Gly139) helical (ribbons) regions of eIF4E form the 4E-BP binding pocket. Dotted lines in (a) represent hydrogen bonds between eIF4E and 4E-BP2 peptide.

Table 3. Hydrogen bonds and selected C–H/C=O... π interactions between eIF4E and 4E-BP1/4E-BP2 peptides

4E-BP	Structure ^a	eIF4E	Binding region ^b	Distance(Å)	Interaction type
4E-BP1					
Arg51 N ϵ H	Extend	Gln40 O ϵ 1	N-term	2.67	H-bond
Arg51 N η 2H	Extend	Gln40 O	N-term	2.89	H-bond
Tyr54 NH	Extend	Gly139 O	H2	2.97	H-bond
Tyr54 O η H	Extend	Pro38 O	N-term	2.53	H-bond
Arg56 N ϵ H	Helix	Glu132 O ϵ 1	H2	2.81	H-bond
Phe58 benzene	Helix	His37 imidazole	N-term	~3.7 to 4.0	C–H... π ^c
Leu59 O	Helix	Trp73 N ϵ 1H	H1	2.90	H-bond
Arg63 O	Extend	Trp73 indole	H1	~3.2	C=O... π ^c
Asn64 N δ 2H	Extend	Asn77 O δ 1	H1	3.19	H-bond
Ser65 O γ H	Extend	Asn77 N δ 2	H1	2.53	H-bond
4E-BP2					
Arg51 N ϵ H	Extend	Asp143 O	H2	3.39	H-bond
Arg51 N η 1H	Extend	Asp144 O δ 1	H2	3.04	H-bond
Ile52 NH	Extend	Gln40 O ϵ 1	N-term	2.76	H-bond
Tyr54 NH	Extend	Gly139 O	H2	3.00	H-bond
Arg56 N ϵ H	Helix	Glu132 O ϵ 2	H2	2.93	H-bond
Arg56 N η H	Helix	Glu132 O ϵ 2	H2	2.81	H-bond
Phe58 benzene	Helix	His37 imidazole	N-term	~3.7 to 4.0	C–H... π ^c
Leu59 O	Helix	Trp73 N ϵ 1 H	H1	2.85	H-bond

^a Extend and helix represent the distorted extend and α -helical structure moieties of the 4E-BP peptide, respectively.

^b N-term, H1 and H2 denote the N-terminal, H1 and H2 helix regions of the eIF4E molecule shown in Figure 3, respectively.

^c These interactions are of edge-to-face type.

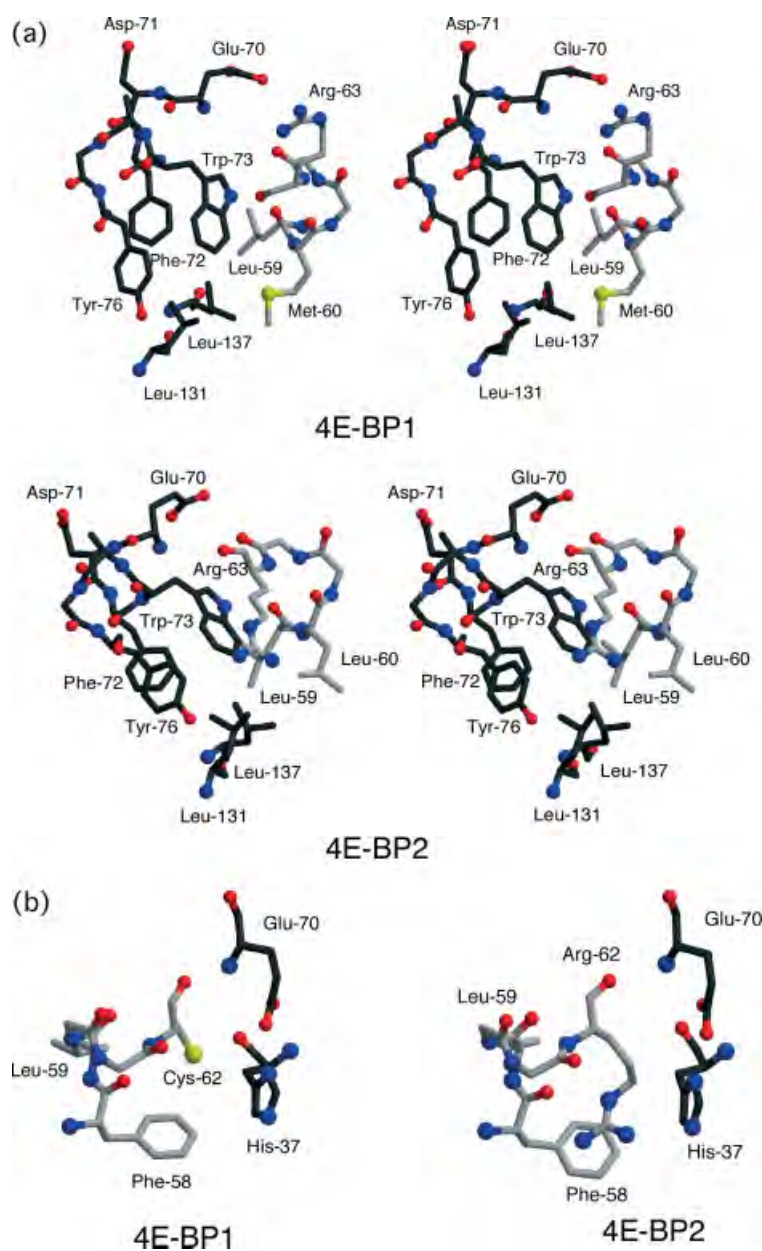


Figure 5. Different interaction mode between 4E-BP1 and 4E-BP2 (gray bond) with eIF4E (dark bond): (a) Leu59/Met60-Trp73 and Leu59/Leu60-Trp73 (in stereo) and (b) Cys62/Phe58-His37/Glu70 and Arg62/Phe58-His37/Glu70.

Cys62/Arg62 with the His37 imidazole ring and Glu70 carboxyl group of eIF4E. To confirm the structural differences between these regions, the crystal structures of the respective complexes were compared in detail. It was clarified that (i) the Trp73 indole ring of eIF4E is significantly affected by the Arg63 side chain of 4E-BP2 through hydrophobic interaction, and this is in contrast to that in the case of 4E-BP1, where the interaction of Trp73 with the Met60 of 4E-BP1 is negligible (Figure 5(a)), and (ii) the guanidyl group of Arg62 orients itself so as to interact with the Phe58 benzene ring of 4E-BP2 and localizes apart from the site of interaction with the His37 imidazole ring and Glu70 carboxyl group of eIF4E (Arg62 N ϵ H \cdots His37 N ϵ 2 and Glu70 O ϵ = 3.35 and 2.98 Å, respectively), whereas the Cys62 of 4E-BP1 localizes in the range within electrostatic interaction with these residues (Figure 5(b)). Thus, the notable interactions of the Arg62 side chain with the

Trp73 indole ring (eIF4E) for 4E-BP2 and of the Cys62 SH group with the His37/Glu70 side chains for 4E-BP1 could be a structural scaffold for differentiating the eIF4E-binding specificity between 4E-BP1 and 4E-BP2. Another notable difference could be observed between the Met60 of 4E-BP1 and the Leu60 of 4E-BP2. The Leu59-Leu60 sequence of 4E-BP2, together with the Leu131 and Leu137 of eIF4E, provides a more compact hydrophobic space around the Trp73 indole ring than the Leu59-Met60 of 4E-BP1 (Figure 5(a)); this could induce the quenching effect of Trp fluorescence intensity more efficiently for the interaction with 4E-BP2 than that with 4E-BP1.

Different Binding Orientation of 4E-BP Terminal Sequence

A difference in binding with eIF4E was also observed between the C-terminal sequences of 4E-BP1 and 4E-BP2 peptides. The Asn64

N δ 2H and Ser65 O of 4E-BP1 form hydrogen bonds with Asn77 O δ 1 and N δ 2H of eIF4E, thus directing the C-terminal sequence toward the C-terminal side of eIF4E. In contrast, the *trans*-oriented Arg63 side chain of 4E-BP2 with respect to the Arg62 side chain (Figure 3), which results from the interaction between the Arg62 guanidyl group of 4E-BP2 and the Phe58 benzene ring of eIF4E, directs the orientation of the Asn64-Ser65 sequence toward the opposite side from the case of 4E-BP1, thus turning the sequence toward the N-terminal side of eIF4E.

Conclusion

This work was performed to clarify the structural basis of the difference in eIF4E binding specificity between 4E-BP1 and 4E-BP2. The X-ray crystal structure of the m⁷GTP–eIF4E–4E-BP2 peptide ternary complex clarified the molecular conformation of the 4E-BP2 peptide and its interaction mode with eIF4E, which was located at the root of the handle of the temple-bell-shaped eIF4E through hydrophilic and hydrophobic interactions. The comparison with the previously determined X-ray result of the m⁷GpppA–eIF4E–4E-BP1 peptide complex afforded the structural scaffold for the eIF4E binding preference for 4E-BP2 over 4E-BP1, i.e. (i) the stacking of the Arg63 planar side chain on the Trp73 indole ring of eIF4E and (ii) the construction of a compact hydrophobic space around the Trp73 indole ring using the Leu59–Leu60 sequence of 4E-BP2, together with the Leu131 and Leu135 of eIF4E. These structural features explain the eIF4E binding preference for 4E-BP2 over 4E-BP1, determined by the quenching titration of Trp fluorescence, because the masking of the Trp73 indole ring by the hydrophobic groups leads to a large quenching of fluorescence intensity.

References

- 1 Sonenberg N, Dever TE. Eukaryotic translation initiation factors and regulators. *Curr. Opin. Struct. Biol.* 2003; **13**: 56–63.
- 2 Sonenberg N, Hinnebusch AG. Regulation of translation initiation in eukaryotes: mechanisms and biological targets. *Cell* 2009; **136**: 731–745.
- 3 Pause A, Belsham GJ, Gingras AC, Donze O, Lin AA, Laurence JC Jr, Sonenberg N. Insulin-dependent stimulation of protein synthesis by phosphorylation of a regulator of 5'-cap function. *Nature* 1994; **371**: 762–767.
- 4 Sonenberg N, Gingras AC. The mRNA 5'-cap binding protein eIF4E and control of cell growth. *Curr. Opin. Cell Biol.* 1998; **10**: 268–275.
- 5 Mader S, Lee H, Pause A, Sonenberg N. The translation initiation factor eIF4E binds to a common motif shared by the translation factor eIF4- γ and the translational repressor 4E-binding proteins. *Mol. Cell. Biol.* 1997; **17**: 6940–6947.
- 6 Altmann M, Schmitz N, Berset N, Trachsel H. A novel inhibitor of cap-dependent translation initiation in yeast – p20 competes with eIF4G for binding to eIF4E. *EMBO J.* 1997; **16**: 1114–1121.
- 7 Gingras AC, Gygi SP, Raught B, Polakiewicz RD, Abraham RT, Hoekstra MF, Aebersold R, Sonenberg N. Regulation of 4E-BP1 phosphorylation: a novel two-step mechanism. *Genes Dev.* 1999; **13**: 1422–1437.
- 8 Tomoo K, Matsushita Y, Fujisaki H, Abiko F, Shen X, Taniguchi T, Miyagawa H, Kitamura K, Miura K, Ishida T. Structural basis for mRNA cap-binding regulation of eukaryotic initiation factor 4E by 4E-binding protein, studied by spectroscopic, X-ray crystal structural, and molecular dynamics simulation methods. *Biochim. Biophys. Acta* 2005; **1753**: 191–208.
- 9 Marcotrigiano J, Gingras AC, Sonenberg N, Burley, SK. Cap-dependent translation initiation in *Eukaryotes* is regulated by a molecular mimic of eIF4G. *Mol. Cell* 1999; **3**: 707–716.
- 10 Morino S, Hazama H, Ozaki M, Teraoka Y, Shibata S, Doi M, Ueda H, Ishida T, Uesugi S. Analysis of the mRNA cap-binding ability of human eukaryotic initiation factor-4E by use of recombinant wild-type and mutant forms. *Eur. J. Biochem.* 1996; **239**: 597–601.
- 11 Pflugrath JW. The finer things in X-ray diffraction data collection. *Acta Crystal.* 1999; **D55**: 1718–1725.
- 12 Brunger AT, Adams PD, Clore GM, DeLano WL, Gros P, Grosse-Kunstleve RW, Jiang JS, Kuszewski J, Nilges M, Pannu NS, Read RJ, Rice LM, Simonson T, Warren GL. Crystallography & NMR system: A new software suite for macromolecular structure determination. *Acta Crystal.* 1998; **D54**: 905–921.
- 13 Jones TA. A graphics model building and refinement system for macromolecules. *J. Appl. Cryst.* 1987; **15**: 23–31.
- 14 Tomoo K, Shen X, Okabe K, Nozoe Y, Fukuhara S, Morino S, Sasaki M, Taniguchi T, Miyagawa H, Kitamura K, Miura K, Ishida T. Structural features of human initiation factor 4E, studied by X-ray crystal analyses and molecular dynamics simulations. *J. Mol. Biol.* 2003; **328**: 365–383.
- 15 Ptushkina M, von der Haar T, Karim MM, Hughes JMX, McCarthy JE. Repressor binding to a dorsal regulatory site traps human eIF4E in a high cap-affinity state. *EMBO J.* 1999; **18**: 4068–4075.



Absolute stereostructure of Andiolides A–G from the flower of *Carapa guianensis* (Meliaceae)

Yuji Tanaka^a, Takeshi Yamada^a, Yasuko In^a, Osamu Muraoka^b, Tetsuya Kajimoto^a, Reiko Tanaka^{a,*}

^aOsaka University of Pharmaceutical Sciences, 4-20-1 Nasahara, Takatsuki, Osaka 569-1094, Japan

^bFaculty of Pharmaceutical Sciences, Kinki University, 3-4-1 Kowakae, Higashiosaka, Osaka 577-8502, Japan

ARTICLE INFO

Article history:

Received 30 August 2010

Received in revised form 5 November 2010

Accepted 5 November 2010

Available online 13 November 2010

Keywords:

Carapa guianensis

Limonoid

Andiolides A–G

CD spectrum

X-ray analysis

ABSTRACT

A new gedunin, three new mexicanolides and three new phragmalin-type limonoids named Andiolides A (**1**), B (**2**), C (**3**), D (**4**), E (**5**), F (**6**), and G (**7**) were isolated from oil of the flower of *Carapa guianensis* Aublet (Meliaceae). Their absolute stereostructures were determined by 2D NMR and CD spectra, and single-crystal X-ray analysis, and all compounds were confirmed to have the C-17βH configuration. Considering the similarity in CD spectra between Andiolide G (**7**) and the xylocensins reported by Wu, we concluded that the structures of xylocensins should be revised so as to have the absolute configuration of 17R.

© 2010 Elsevier Ltd. All rights reserved.

1. Introduction

Carapa guianensis AUBLET (Meliaceae), referred to andiroba or Brazilian mahogany in Brazil and Colombia, is a towering tree, which grows up to 40 m high in the tropical rainforests of South America. The tree has been used not only as timber but also as material for herbal medicines by indigenous people in the Amazon. In particular, the oil collected from the seeds is used as an insect repellent and as a standing medicine for the treatment of wounds and bruises. Interestingly, gedunin-type limonoids bearing the 4,4,8-trimethyl-17-furanylsteroid (tetra-*nor*-triterpene) skeleton, such as andirobin,¹ 7-deacetoxy-7-oxogedunin,² 11β-acetoxygedunin and 6α,11β-diacetoxygedunin,³ 6α-acetoxy-epoxyazadiradione, 6α-acetoxygedunin and 6α-hydroxygedunin,⁴ 6β,11β-diacetoxygedunin and 6α-acetoxygedunin,⁵ and 1,2-dihydro-3β-hydroxy-7-deacetoxy-7-oxogedunin,⁶ were isolated from the seeds or wood; however, the presence of mexicanolide- or phragmalin-type limonoids, which are biosynthesized via gedunin-type limonoids, have not been reported to date. As our initial hypothesis, the flower moiety, the most highly differentiated organ in the plant body, could contain novel metabolites produced downstream of the biosynthetic pathways. Thus, we investigated the components of the flower oil of *C. guianensis* as a part of our study

on bioactive limonoids from Meliaceae plants. As expected, three new mexicanolide and three new phragmalin-type of limonoids named Andiolide B (**2**), C (**3**), D (**4**), E (**5**), F (**6**), and G (**7**), respectively, were obtained as well as a novel gedunin-type Andiolide A (**1**). In the present paper, we report the details of their isolation, structure determination, and cytotoxic activities against P388, KB, L1210, and HL-60 cell lines. Moreover, we discuss the absolute structures of these compounds and propose the necessity of reexamining those of xylocensins Q–V in the literature.^{7,8}

2. Results and discussion

Flower oil of *C. guianensis* was dissolved in CHCl₃, the extract of which was separated by silica gel column chromatography, medium-pressure liquid chromatography (MPLC), and reverse phased HPLC to obtain seven new limonoids (**1–7**) along with the known 7-deacetoxy-7-oxogedunin (**8**)⁹ and 6α-acetoxygedunin (**9**).^{4,10}

Andiolide A (**1**) was isolated as colorless needles and demonstrated to have the molecular formula C₃₀H₃₆O₉ ([M]⁺+H; *m/z* 541.2442, calcd for 541.2437) by HRFABMS. The ¹H and ¹³C NMR spectra, which were characteristic of a gedunin limonoid such as 6α-acetoxygedunin (**9**),^{4,10} indicated the presence of five tertiary methyls [δ_{H} 1.16, 1.20, 1.24, 1.27, and 1.47], two acetyl methyls [δ_{H} 2.02, 2.07], two methylenes, four sp³ methines including two oxymethines [δ_{H} 5.47 (dd), 5.50 (d)], an α,β-unsaturated ketone [δ_{H} 5.94 (d), 7.06 (d), δ_{C} 204.0 (s)], a β-substituted furan ring [δ_{H} 6.47 (dd), 7.43 (t), 7.57 (dd)], five sp³ quaternary carbons including an

* Corresponding author. E-mail address: tanakar@gly.oups.ac.jp (R. Tanaka).

acetal or hemiacetal carbon [δ_C 104.0 (s)], and an α,β -unsaturated lactone [δ_C 111.3 (d), 163.2 (s), 169.3 (s)] (Table 1). The IR spectrum showed the presence of a hydroxyl group at ν_{\max} 3448 cm^{-1} . In addition, a combination of the IR absorption at ν_{\max} 1672 cm^{-1} and the UV absorption λ_{\max} at 236 nm ($\log \epsilon$ 3.49) supported the

Table 1
 ^1H NMR and ^{13}C NMR spectroscopic data of compound **1**

Position	1		$^{13}\text{C}^b$	
	$^1\text{H}^a$ (J, Hz)			
1	7.06	d 10.2 (2)	155.8	
2	5.94	d 10.2 (1)	126.7	
3			204.0	
4			44.8	
5	2.51	d 12.2 (6)	47.5	
6	5.47	dd 12.2 (5) 2.4 (7)	69.6	
7	5.50	d 2.4 (6)	73.1	
8			45.0	
9	2.24	dd 11.7 (11 β), 8.6 (11 α)	36.2	
10			41.2	
11	α	1.99	m	15.3
	β	1.83	m	
12	α	1.60	m	23.4
	β	2.28	m	
13			42.1	
14			169.3	
15	5.67	s	111.3	
16			163.2	
17			104.0	
18	1.16	s	23.7	
19	1.24	s	20.7	
20			125.2	
21	7.57	dd 2.2 (23), 1.2 (22)	141.8	
22	6.47	dd 2.2 (23), 1.2 (21)	109.9	
23	7.43	t 2.2 (22, 21)	143.2	
28	1.27	s	31.6	
29	1.20	s	20.5	
30	1.47	s	23.7	
6'			170.3	
6''	2.07	s	21.3	
7'			170.0	
7''	2.02	s	20.7	

^a Measured at 500 MHz in CDCl_3 .

^b Measured at 125 MHz in CDCl_3 .

presence of α,β -unsaturated carbonyl groups. Next, the results of the ^1H – ^1H COSY analysis of **1** revealed the partial structures shown by bold-faced lines in Fig. 2. Herein, it should be particularly noted that H-6 (δ_{H} 5.47) was correlated with H-5 (δ_{H} 2.51) and H-7 (δ_{H} 5.50). In the HMBC spectrum, cross-peaks were observed from Me-18/C-12, C-13, C-14, and C-17 [δ_C 104.0 (s)]; Me-19/C-1, C-5, C-9, and C-10; H-5/C-4, C-6 [δ_C 69.6 (d)], and C-7 [δ_C 73.1 (d)]; H-6/C-5, C-6' [δ_C 170.3 (s)], C-7 [δ_C 73.1 (d)], and C-8; H-15/C-13, and C-16 [δ_C 163.2 (s)] (Fig. 2). Furthermore, two methyl groups at δ_{H} 2.02 (3H, s) and 2.07 (3H, s) showed HMBC correlations with carbonyl groups δ_C 170.0 (s) and 170.3 (s), respectively, indicating the presence of the two-acetyl groups. Finally, the hydroxyl group was attached at C-17 to satisfy its molecular formula ($\text{C}_{30}\text{H}_{36}\text{O}_9$) and the presence of a hemiacetal carbon at δ_C 104.0 (s). Regarding the relative configuration of chiral centers, the hydroxyl group at C-17 was assigned as β , because NOEs were observed between Me-18 and H-9 α , H-12 α and H-21 (Fig. 3). The relative configuration at C-6 was determined to be α because of the significant NOEs between H-6 and Me-19, Me-29 and Me-30, and the coupling constants of H-6 [δ_{H} 5.47 (dd, $J_{6\beta,5\alpha}=12.2$ Hz, $J_{6\beta,7\beta}=2.4$ Hz)]. The configuration of C-7 was α due to the significant NOEs between H-7 and H-15 and Me-30, and the coupling constants of H-7 [δ_{H} 5.50 (d, $J_{7\beta,6\beta}=2.4$ Hz)], the same as **9**.^{4,10} HMBC and NOESY spectra showing the relative structure of **1** are shown in Figs. 2 and 3.

Andirolide B (**2**), isolated as colorless needles, had the molecular formula $\text{C}_{31}\text{H}_{38}\text{O}_{11}$ ($[\text{M}]^+ + \text{H}$; m/z 587.2493, calcd for 587.2492) as

determined by HRFABMS. The ^1H and ^{13}C NMR spectra, which were characteristic of mexicanolide,^{11–13} indicated the presence of four tertiary methyls [δ_{H} 0.74, 0.90, 1.18, 1.32], two acetyl methyls (δ_{H} 2.18, 2.22), a methyl ester group (δ_{H} 3.67), four methylenes, four sp^3 methines including two oxymethines [δ_{H} 5.24 (s), 5.32 (s)], five sp^3 quaternary carbons including two oxycarbons [δ_C 72.1 (s), 83.5 (s)], four sp^2 methines including a furan ring [δ_{H} 6.50 (dd), 7.44 (t), 7.49 (br s)], and seven sp^2 quaternary carbons including two acetyl C=O [δ_C 169.8 (s), 171.2 (s)], a COOCH_3 [δ_C 173.3 (s)], and an α,β -unsaturated δ -lactone [δ_C 165.3 (s)] (Table 2). The IR absorption at ν_{\max} 3448 cm^{-1} showed the presence of a hydroxyl group. The combination of IR absorption at ν_{\max} 1672 cm^{-1} and UV absorption λ_{\max} at 236 nm ($\log \epsilon$ 3.49) supported the presence of α,β -unsaturated carbonyl groups. After assignments of HMQC, ^1H – ^1H COSY and HMBC spectra (Fig. 4), it became clear that **2** was a common mexicanolide.^{11–13} In the NOESY spectrum, significant NOEs were observed between H-5 β and H-11 β and H-30 β ; between H-9 α and H-12 α ; between H-11 α and Me-19; between H-12 β and H-17 β ; between H-15 and H-30 α . The relative structure was confirmed from the NOESY spectrum (Fig. 5).

The molecular formula of Andirolide C (**3**) and Andirolide D (**4**) was assigned as $\text{C}_{33}\text{H}_{42}\text{O}_{11}$ ($[\text{M}]^+ + \text{H}$; m/z 615.2800, calcd for 615.2805) and $\text{C}_{34}\text{H}_{42}\text{O}_{11}$ ($[\text{M}]^+ + \text{H}$; m/z 627.2798, calcd for 627.2805), respectively, based on HRFABMS. The UV and IR spectra of **3** and **4** showed the presence of a hydroxyl (ν_{\max} 3445 cm^{-1} in **3**; ν_{\max} 3439 cm^{-1} in **4**), an α,β -unsaturated δ -lactone (ν_{\max} 1680 cm^{-1} ; λ_{\max} 224.6 nm in **3**; λ_{\max} 227.5 nm in **4**) and ester groups (ν_{\max} 1259 cm^{-1}). According to the structures of **3** and **4**, their UV, IR, and ^1H and ^{13}C NMR spectra were very similar to those of **2** except for the absence of an acetyl group at C-3 and the presence of a 2-methylpropanoyl group [δ_{H} 1.25 and 1.26 (each 3H, d, $J=6.9$ Hz); 2.73 (1H, sept, $J=6.9$ Hz); 5.21 (1H, s)] in **3**, and the presence of a tigloyl group [δ_{H} 1.89 (3H, d, $J=7.0$ Hz), 1.94 (3H, s), 6.97 (1H, qd, $J=7.0, 1.4$ Hz)] in **4** (Table 2).¹⁴ In the HMBC spectrum of **3**, cross-peaks were observed from H-3/C-3' and isopropyl methyl/C-3', and cross-peaks were observed from H-3/C-3', tigloyl group/C-3' in compound **4**; therefore, the relative structures of **3** and **4** were established as shown in Fig. 1.

Andirolide E (**5**), isolated as colorless prisms, had the molecular formula $\text{C}_{35}\text{H}_{40}\text{O}_{14}$ ($[\text{M}]^+ + \text{H}$; m/z 685.2493, calcd for 685.2496) as determined by HRFABMS. The ^1H and ^{13}C NMR spectra indicated the presence of two angular methyls [δ_{H} 0.98, 1.13 (each 3H, s)], two acetyl methyls [δ_{H} 2.15 and 2.24 (each 3H, s)], a primary methyl group [δ_{H} 1.05 (3H, t)], another methyl group [δ_{H} 1.69 (3H, s)], δ_C 21.6 (q)], seven methylenes including an oxymethylene [δ_{H} 4.38 and 4.77 (each d, $J=13.8$ Hz)], five sp^3 methines including three oxymethines [δ_{H} 5.16 (s), 5.35 (s), 6.10 (s)], eight sp^3 quaternary carbons, a furan ring [δ_{H} 6.41 (d), 7.44 (t), 7.49 (s)], and two lactones [δ_C 169.8 (s), 171.0 (s)] (Table 3), which were characteristic of phragmalin limonoids.^{7,8,15} Alkaline hydrolysis of **5** with KOH/MeOH yielded a triol (**5a**), in which the two carbinolic methine proton signals were considerably up-field shifted at [δ_{H} 3.61 and 4.49 (each s)]. In the HMBC spectrum, cross-peaks were observed from Me-18/C-12, C-13, C-14, and C-17; H-3/C-1, C-4, and C-3'; H-14/C-8, and C-16; H-17/C-13, C-20, C-21, and C-22; H-30/C-9, C-30, and C-30' (Fig. 6). Two methyl groups at δ_{H} 2.15 and 2.24 (each 3H, s) showed HMBC correlations with carbonyl groups δ_C 170.2 (s) and 169.5 (s), respectively, indicating the presence of the two-acetyl groups. In addition, the COSY correlation between a primary methyl [δ_{H} 1.05 (3H, t)] and methylene signals [δ_{H} 2.44 (1H, dq), 2.46 (1H, dq)], correlated with the carbonyl carbon [δ_C 172.1 (s)], indicated the presence of a propanoyl group.

A quaternary carbon at δ_C 119.4 (C-31) showing an HMBC correlation with H-32 [δ_{H} 1.69 (s)], suggested the presence of an orthoacetyl group. A pair of geminal doublets at δ_{H} 1.73 (d, $J=11.8$ Hz) and 2.33 (d, $J=11.8$ Hz) was assigned to H-29 in A-ring.

Table 2
¹H NMR and ¹³C NMR spectroscopic data of compounds 2–4

Position	2		3		4	
	¹ H ^a (J, Hz)	¹³ C ^b	¹ H ^a (J, Hz)	¹³ C ^b	¹ H ^a (J, Hz)	¹³ C ^b
1		208.3		208.2		208.4
2		83.5		83.6		83.7
3	5.24 s	81.8	5.21 s	81.6	5.31 s	81.8
4		40.3		40.3		40.6
5	3.08 t 5.7 (6)	41.4	3.10 t 5.5 (6)	41.5	3.14 t 5.9 (6)	41.4
6	2.34 d 5.7 (5)	33.3	2.34 d 5.5 (5)	33.3	2.34 d 5.9 (5)	33.3
7		173.3		173.3		173.3
8		72.1		72.0		72.0
9	2.15 dd 13.0 (11β), 4.6 (11α)	64.6	2.16 dd 13.0 (11β), 4.6 (11α)	64.6	2.16 dd 13.1(11β), 4.1(11α)	64.6
10		50.2		50.3		50.2
11	α 1.70 dtd 13.0 (11β), 4.6 (9, 12β), 2.0 (12α)	21.0	1.70 dtd 13.0 (11β), 4.6 (9, 12β), 2.0 (12α)	30.3	1.70 dtd 13.1 (11β), 4.1 (9, 12β), 2.2 (12α)	21.0
	β 1.42 qd 13.0 (9, 11α, 12α), 2.0 (12β)		1.42 qd 13.0 (9, 11α, 12α), 2.0 (12β)		1.43 dq 13.1(9, 11α, 12α), 2.2 (11α)	
12	α 1.53 td 13.0 (11β, 12β), 2.0 (12β)	30.4	1.54 td 13.0 (11β, 12β), 2.0 (11α)	21.0	1.53 td 13.1 (11β, 12β), 2.2 (11α)	30.5
	β 1.83 ddd 13.0 (12α), 4.6 (11α), 2.0 (11β)		1.83 ddd 13.0 (12α), 4.6 (11α), 2.0 (11β)		1.83 ddd 13.1 (12α), 4.1 (11α), 2.2 (11β)	
13		39.5		39.6		39.6
14		166.8		166.8		167.0
15	6.26 s	115.7	6.22 s	115.6	6.19 s	115.6
16		165.3		165.2		165.1
17	5.32 s	79.2	5.33 s	79.1	5.33 s	79.1
18	1.32 s	21.6	1.30 s	21.5	1.31 s	21.6
19	1.18 s	17.2	1.17 s	17.1	1.18 s	17.2
20		120.1		120.1		120.1
21	7.49 br s	141.8	7.49 br s	141.8	7.49 br s	141.8
22	6.50 dd 1.8 (23), 0.9 (21)	110.6	6.50 dd 1.8 (23), 0.7 (21)	110.6	6.50 dd 1.6 (23), 0.7 (21)	110.6
23	7.44 t 1.8 (21, 22)	143.0	7.44 t 1.8 (21, 22)	143.0	7.44 t 1.6 (21, 22)	143.1
28	0.74 s	22.3	0.72 s	22.4	0.73 s	23.1
29	0.90 s	23.3	0.91 s	23.3	0.93 s	22.5
30	α 2.39 d 17.1 (30β)	44.6	2.38 d 17.2 (30β)	44.7	2.42 d 17.2 (30β)	44.6
	β 4.14 d 17.1 (30α)		4.19 d 17.2 (30α)		4.22 d 17.2 (30α)	
2'		171.2		171.2		171.3
2''	2.18 s	21.7	2.16 s	21.6	2.17 s	21.7
3'		169.8		175.8		166.6
3''	2.22 s	20.9	2.73 sept. 6.9 (3''', 3''''')	34.3		127.8
3'''			1.26 d 6.9 (3''')	18.9	1.94 s	12.4
3''''			1.25 d 6.9 (3''''')	19.4	6.97 qd 7.0 (3''''') 1.4	139.3
3'''''				1.89 d 7.0 (3''''')		14.7
7'	3.67 s	52.2	3.68 s	52.2	3.67 s	52.2
8-OH	5.03 s		5.08 s		5.03 s	

^a Measured at 500 MHz in CDCl₃.

^b Measured at 125 MHz in CDCl₃.

The IR spectrum showed broad ester bands at ν_{\max} 1751, 1723, and 1243 cm⁻¹, which could be assigned to two acetyl and a propanoyl esters. Thus, the planar structure of **5** was established as phragmalin-1,8,9-orthoacetate,¹⁶ and the positions of a propanoyl group, two acetyl groups, and two δ -lactones were determined from HMBC and ¹H–¹H COSY correlations (Fig. 6). The location of an orthoacetate and the relative structure of **5** were determined from the NOESY spectrum (Fig. 7) and by single-crystal X-ray diffraction (Fig. 8). In the NOESY spectrum, significant NOEs were observed between H-5 β and H-12 β , H-30 β and Me-28; between H-15 β and H-30 β ; between H-17 β and H-12 β , H-22 and H-30 β ; and between H-30 β and H-12 β , H-15 β , and H-17 β ; therefore, the C-ring adopted a boat-like conformation similar to switenialide D.¹⁷

Andirolide F (**6**), obtained from colorless needles, had the molecular formula C₃₅H₃₈O₁₄ ([M]⁺+H; m/z 683.2335, calcd for 683.2340) as determined by HRFABMS. The UV and IR spectra showed α,β -unsaturated δ -lactone and ester groups. The IR, ¹H, and ¹³C NMR spectra were very similar to those of **5** except for a double bond at C-14:15 [δ_{H} 6.05 (s), δ_{C} 121.0 (d), 159.6 (s)] (Table 3). NOESY experiments revealed the relative stereochemistry of **6** to have the same conformation as **5**.

Andirolide G (**7**), isolated as colorless needles, had the molecular formula C₃₄H₄₀O₁₄ ([M]⁺+H; m/z 673.2505, calcd for 673.2495) as determined by HRFABMS. The IR spectrum showed the presence of a hydroxyl at ν_{\max} 3568 cm⁻¹, and ester groups at ν_{\max} 1729 cm⁻¹. The ¹H and ¹³C NMR spectra indicated the presence of two angular

methyls [δ_{H} 1.32, 1.48 (each 3H, s)], an acetyl methyl [δ_{H} 2.09 (3H, s)], a propanoyl group [δ_{H} 1.16 (3H, t), 2.44 (1H, dq), 2.46 (1H, dq)], a methyl ester group [δ_{H} 3.71 (3H, s), δ_{C} 173.8 (s)], an α,β -unsaturated lactone group [δ_{H} 6.62 (1H, s), δ_{C} 163.5 (s)], an orthoacetate [δ_{H} 1.70 (3H, s), δ_{C} 16.5 (q), 119.7 (s)], a secondary hydroxyl group [δ_{H} 3.87 (ddd)], a tertiary hydroxyl group [δ_{C} 84.1 (s)] and a furan ring [δ_{H} 6.61 (dd), 7.53 (t), 7.64 (br s)] (Table 3). In the HMBC spectrum, cross-peaks were observed from H-3 [δ_{H} 5.22 (s)]/C-4, C-28, C-30 [δ_{C} 74.3 (d)], and C-3' [δ_{C} 169.1 (s)]; H-5/C-3 [δ_{C} 85.0 (s)], C-4, C-6, C-7 [δ_{C} 173.8 (s)], C-9 [δ_{C} 86.1 (s)] and C-29; 1-OH [δ_{H} 3.40 (s)]/C-1 and C-29; H-30 [δ_{H} 5.35 (s)]/C-1, C-2, C-3 [δ_{C} 85.0 (s)], C-8 [δ_{C} 83.6 (s)], C-9, C-14 [δ_{C} 153.8 (s)], and C-31 [δ_{C} 119.7 (s)]. The positions of an acetoxy, a propanoyl, a hydroxyl, a carbomethoxyl, and an orthoacetate were located by detailed ¹H–¹H COSY and HMBC correlations (Fig. 9). In particular, the location of the orthoacetate was confirmed by the HMBC correlation between H-30 and C-31, in addition to the correlation between the hydroxyl proton at C-1 and C-29. In the NOESY spectrum, significant NOEs (Fig. 10) were observed between H-11 α and Me-18; between H-11 β and Me-19; between H-12 β and H-5 β , H-17 β and H-21, therefore, the C-12 hydroxyl group [δ_{H} 3.87 (1H, dd, $J=13.0$ (11 α), 4.5 (11 β))] was attached at the α equatorial. The relative structure was established as a phragmalin 8,9,30-orthoacetate analog, which was once isolated from *Xylocarpus granatum*.^{7,8,15}

Next, Andirolide G (**7**) showed two positive Cotton effects at 213 nm ($\Delta\epsilon=+8.5$) and 264 nm ($\Delta\epsilon=+2.8$), as did xylocensin Q.

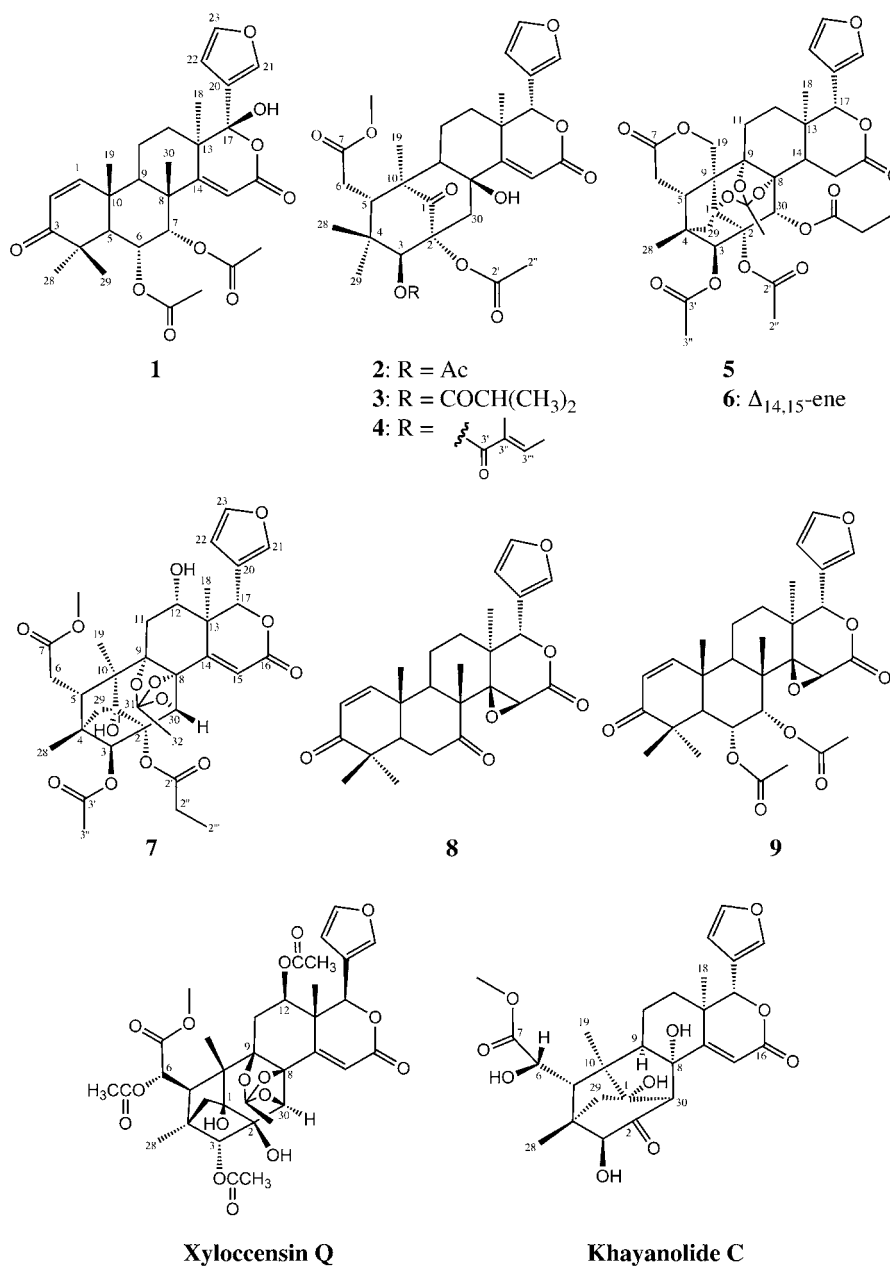


Fig. 1. Structures of compounds 1–9 isolated from *C. guianensis*, xylocensins Q, and Khayanolide C.

Although both compounds should have the same absolute structure having the configuration of C-17R, as claimed by Wu, limonoids are known to be biosynthesized via euphane-type triterpenoid intermediates with 17βH; thus, it was necessary to reconfirm the absolute configuration of xylocensins. Herein, CD spectra of compounds 1–4 and 6–7 were measured, which afforded the following results; compound **1** [235 (Δε=+9.4), 264 (Δε=+1.4), 299 (Δε=−1.4), 340 (Δε=−2.0)]; **2** [220 (Δε=+13.5), 261 (Δε=+1.8), 297 (Δε=−4.4)]; **3** [219 (Δε=+11.3), 260 (Δε=+1.6), 297 (Δε=−3.5)]; **4** [223 (Δε=+13.7), 260 (Δε=+1.2), 297 (Δε=−3.8)]; **6** [224 (Δε=+7.6), 270 (Δε=+6.1)]; **7** [213 (Δε=+8.5), 268 (Δε=+2.8)] (Fig. 11).

Since compound **1** had an α,β-unsaturated ketone on a six-membered ring and compounds 2–4 had a ketone on a six-membered ring in each molecule, some interactions between the ketones and the α,β-unsaturated lactone on C-17 would cause negative Cotton effects at 299 nm (Δε=−1.4) and 340 nm (Δε=−2.0) in **1** and at 297 nm in 2–4 (Δε=−4.4, −3.5, and −3.8, respectively). This assumption was

supported by the finding that compounds 6–7, which have no functional groups to affect the CD spectra, showed no Cotton effects in the region of wavelengths longer than 300 nm (Fig. 12). Moreover, X-ray diffraction analysis of the 16-*p*-bromobenzoate **8d** derived from the most abundant limonoid, 7-deacetoxy-7-oxogedunin (**8**) (Scheme 1), revealed the structure to have the absolute configuration as shown in Fig. 13. As a result, the absolute stereochemistry of Andriolides A–G (1–7) and **8** was determined as shown in Fig. 1.

Wu may have mistaken the stereochemistry of xylocensins because the presence of the C-2 ketone was not considered, which could affect the Cotton spectrum of Khayanolide C. In conclusion, we estimated that the Cotton effects could be potentially affected by the interactions of a chromophore and a carbonyl group. Namely, the carbonyl groups of the α,β-unsaturated δ-lactone and the C-2 ketone were orientated in the same direction in Khayanolide C, while the carbonyl groups of the α,β-unsaturated lactone and ketone at the C-1 or C-3 position in compounds 1–4 faced in different directions (Fig. 12). Thus, the

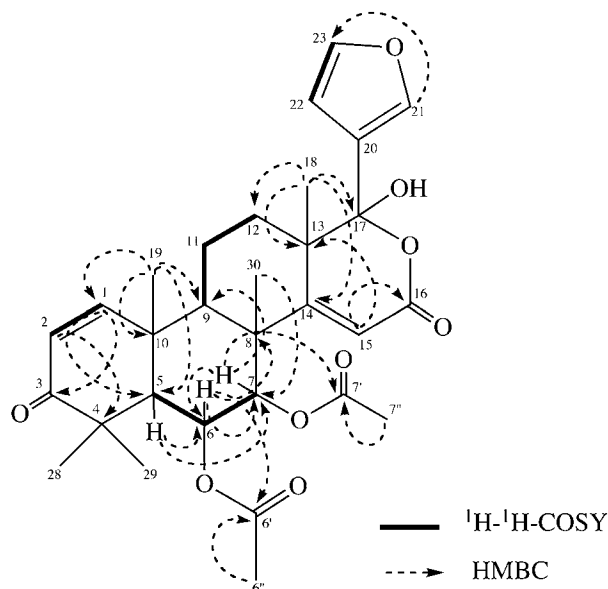


Fig. 2. Selected ^1H – ^1H COSY and HMBC correlations in Andiroliide A (1).

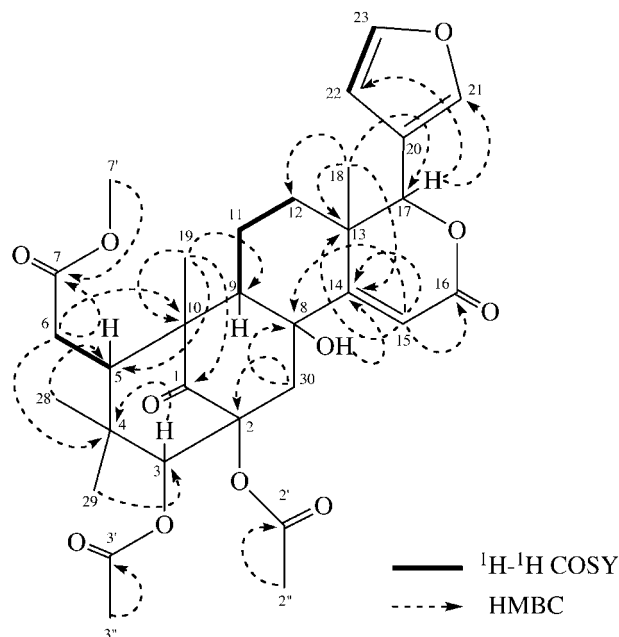


Fig. 4. Selected ^1H – ^1H COSY and HMBC correlations in Andiroliide B (2).

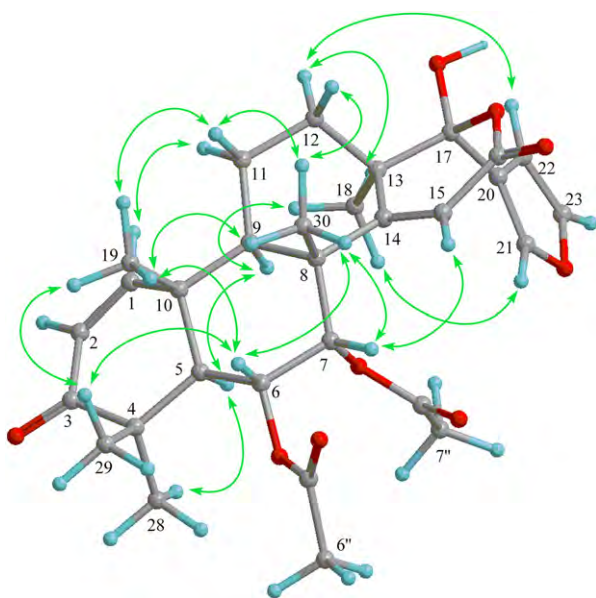


Fig. 3. Key NOESY correlations for Andiroliide A (1).

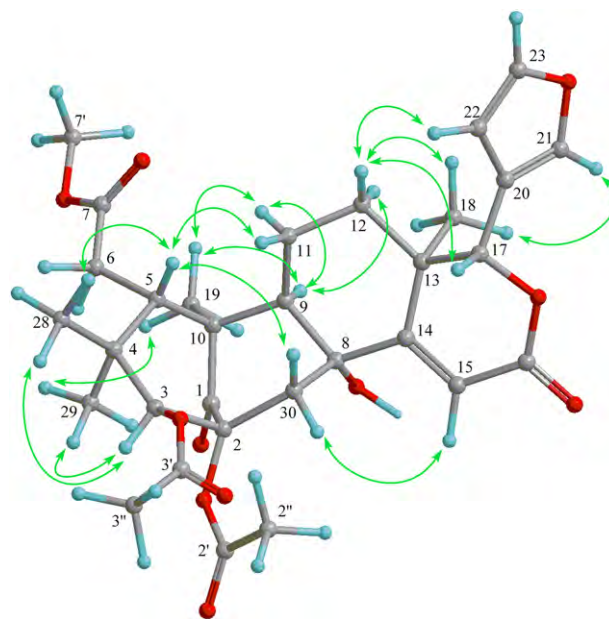


Fig. 5. Key NOESY correlations for Andiroliide B (2).

negative Cotton effect at 245 nm ($\Delta\epsilon = -4.3$) in the CD spectrum of Khayanolide C would be caused by the interaction between parallel orientated carbonyl groups. Moreover, the first Cotton effect for the furan ring chromophore at 225 nm should have had a negative Cotton effect, if xylocensins were enantiomers.

Wu took the reversed sign of $\Delta\delta$ values in applying the Mosher method using (*R*)-(-)- and (*S*)-(+)-MTPACl to determine the absolute structure of xylocensin Q, i.e., (*R*)-MTPACl should afford (*S*)-esters; however, it was stated that the (*R*)-ester was generated.^{18,19} The isolated compounds 1–7 were subjected to assays of growth inhibition using various cancer cell lines. As a primary screening for antitumor activities, the cell growth inhibitory properties of compounds 1–7 were examined using the murine P388 leukemia cell line, the human HL-60 leukemia cell line, the murine L1210 leukemia cell line and the human KB epidermoid carcinoma cell line. Compound 1 exhibited significant cytotoxic activity against all cell lines (Table 4).²⁰ Compound 6 also showed moderate cytotoxic activity.

3. Experimental

3.1. General procedures

Melting points were determined on a Yanagimoto micro-melting point apparatus and are uncorrected. Optical rotations were measured with a JASCO DIP-1000 digital polarimeter. IR spectra were recorded on a Perkin–Elmer 1720X FTIR spectrophotometer. ^1H and ^{13}C NMR spectra were recorded on a Varian INOVA 500 spectrometer with standard pulse sequences, operating at 500 and 125 MHz, respectively. CDCl_3 was used as the solvent and TMS as the internal standard. FAB/MS was recorded on a JEOL JMS-700 mass spectrometer. Column chromatography (silica gel, 70–230 mesh; Merck) and medium-pressure liquid chromatography (MPLC; silica gel,

Table 3
¹H NMR and ¹³C NMR data for compounds 5–7

Position	5			6			7			
	¹ H ^a (J, Hz)		¹³ C ^b	¹ H ^a (J, Hz)		¹³ C ^b	¹ H ^a (J, Hz)		¹³ C ^b	
1			85.9			83.9			84.1	
2			85.2			84.6			83.4	
3	5.16	s	81.3	5.27	s	81.3	5.22	s	85.0	
4			46.2			46.4			44.6	
5	2.62	dd 6.2 (6β), 4.0 (6α)	33.0	2.72	m	33.7	2.12	brd 10.5 (6)	39.9	
6	α	2.63	dd 18.5 (6β), 4.0 (5)	30.8	2.58	m	31.4	2.35	m	33.7
	β	2.45	dd 18.5 (6α), 6.2 (5)		2.62	m				
7			171.0			170.9			173.8	
8			85.7			84.2			83.6	
9			85.1			82.6			86.1	
10			45.1			46.9			48.1	
11	α	1.88	m	25.7	2.16	m	25.6	1.98	dd 17.0 (11β), 13.0 (12)	34.6
	β	2.26	m		2.34	m		2.22	dd 17.0 (11α), 4.5 (12)	
12	α	1.49	m	29.1	1.49	m	26.5	3.87	ddd 13.0 (11α), 4.5 (11β), 2.0 (12-OH)	66.6
	β	1.42	m		1.64	m				
13			34.4			37.6			44.8	
14		2.04	dd 10.5 (15α), 1.6 (15β)	42.8		159.6			153.8	
15	α	2.72	dd 18.9 (15β), 10.5 (14)	26.5	6.05	s	121.0	6.62	s	123.7
	β	3.22	br s 18.9 (15α)							
16			169.8			163.0			163.5	
17		5.35	s	78.6	5.10	s	80.4	5.90	s	78.8
18		1.13	s	20.7	1.14	s	18.6	1.48	s	13.0
19	α	4.77	d 13.8 (19β)	68.8	4.87	d 13.7 (19α)	68.6	1.32	s	15.4
	β	4.38	d 13.8 (19α)		4.36	d 13.7 (19β)				
20			120.9			119.4			121.4	
21		7.49	s	140.9	7.52	br s	141.4	7.64	br s	142.4
22		6.41	d 1.6 (23)	109.6	6.44	dd 1.9 (23) 0.7 (21)	109.7	6.61	dd 1.6 (23) 0.7 (21)	109.6
23		7.44	t 1.6 (21, 22)	143.4	7.44	t 1.9 (21, 22)	143.3	7.53	t 1.6 (21, 22)	144.8
28		0.98	s	13.7	1.02	s	14.1	0.74	s	14.4
29	pro-R	1.73	d 11.8 (29β)	39.0	1.78	d 11.4 (29β)	39.2	1.72	d 10.7 (29β)	39.8
	pro-S	2.33	d 11.8 (29α)		2.38	d 11.4 (29α)		1.96	d 10.7 (29α)	
30		6.10	s	68.5	5.78	s	68.1	5.35	s	74.3
31			119.4			121.0			119.7	
32		1.69	s	21.6	1.68	s	20.9	1.70	s	16.5
2'			170.2			170.0			173.9	
2''	A	2.15	s	20.9	2.17	s	21.8	2.44	dq 13.8 (2''B), 7.6 (2''')	28.1
	B						2.46	dq 13.8 (2''A), 7.6 (2''')		
2'''							1.16	t 7.6 (2''')	8.9	
3'			169.5			169.1			169.1	
3''		2.24	s	21.2	2.03	s	20.8	2.09	s	21.7
7'							3.71	s	52.3	
30'			172.1			173.3				
30''	A	2.19	dq 11.2 (30''B), 7.3 (30''')	27.7	2.24	m	27.4			
	B	2.21	dq 11.2 (30''A), 7.3 (30''')		2.34	m				
30'''		1.05	t 7.3 (30''')	8.3	1.07	t 7.4 (30''')	8.5			
1-OH							3.40	s		
12-OH							1.23	d 2.0 (12)		

^a Measured at 500 MHz in CDCl₃.^b Measured at 125 MHz in CDCl₃.

230–400 mesh; Merck) were conducted. HPLC was run on a JASCO PU-1586 instrument equipped with a differential refractometer (RI 1531). Fractions obtained from column chromatography were monitored by TLC (silica gel 60 F₂₅₄; Merck). Preparative TLC was carried out on Merck silica gel F₂₅₄ plates (20×20 cm, 0.5 mm thick).

3.2. Materials

The oil of the flower of *C. guianensis* Aublet (Meliaceae), was collected in Amazon, Brazil, in March, 2006. A voucher specimen (CG-01-1) was deposited in the Herbarium of the Laboratory of Medicinal Chemistry, Osaka University of Pharmaceutical Sciences.

3.3. Isolation of compounds 1–8

The flower oil of *C. guianensis* Aublet (Meliaceae) (500 g) was dissolved in CHCl₃, and the CHCl₃ solution was subjected to CC (silica gel (7 kg); CHCl₃) affording a yellow oil (Fr. No. 17–21, 164.9 g), and a crystalline solid (Fr. No. 29–30, 31.3 g). The crystalline solid was

repeatedly recrystallized from MeOH/CHCl₃ to give 7-deacetoxy-7-oxogedunin (**8**) (10.1 g). The yellow oil was rechromatographed over silica gel (2 kg) giving an amorphous solid (Fr. No. 19–31, 6.0 g), which was subjected to CC using *n*-hexane/AcOEt 5:1 to afford the residue F1 (Fr. No. 43–51, 900 mg), subjected to CC with *n*-hexane/AcOEt 3:1 giving the residue F2 (Fr. No. 65–76, 433 mg), subjected to CC with *n*-hexane/AcOEt 2:1 affording the residues F3 (Fr. No. 80–86, 1.0 g) and F4 (Fr. No. 87–100, 900 mg), and subjected to CC with *n*-hexane/AcOEt 1:1 to give F5 (Fr. No. 101–112, 380 mg). Residue F1 was subjected to CC (silica gel (230–400 mesh, 100 g); *n*-hexane/AcOEt 5:1) giving a crystalline solid (40 mg, Fr. No. 51–60), which was separated by HPLC (ODS, 60% CH₃CN) to afford compounds **3** (12 mg) and **4** (13 mg). Residue F2 was subjected to CC (silica gel (230–400 mesh, 100 g); *n*-hexane/AcOEt, 5:1–3:1) giving an amorphous solid (93 mg, Fr. No. 19–51), which was purified by HPLC (ODS, 60% MeOH) to afford compound **1** (15 mg). Residue F3 was subjected to CC (silica gel (230–400 mesh, 100 g); *n*-hexane/AcOEt, 5:1) to give a crystalline solid (1.0 g, Fr. No. 80–86), which was twice subjected to CC (silica gel (230–400 mesh, 100 g); *n*-hexane/

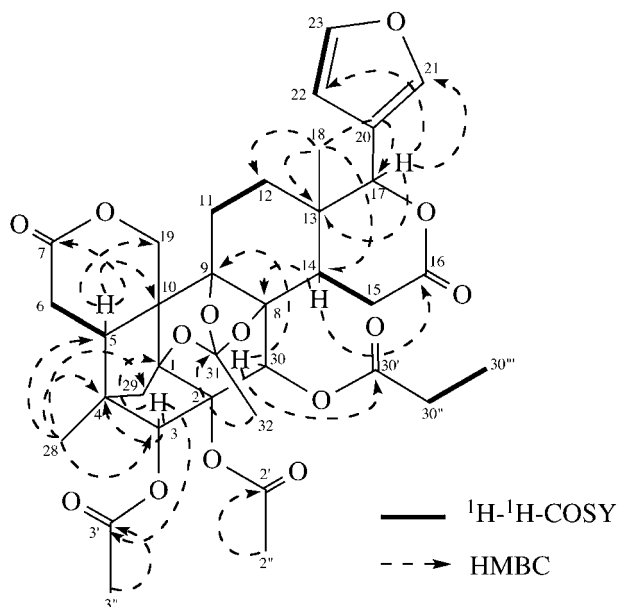


Fig. 6. Selected ^1H – ^1H COSY and HMBC correlations in Andirolide E (5).

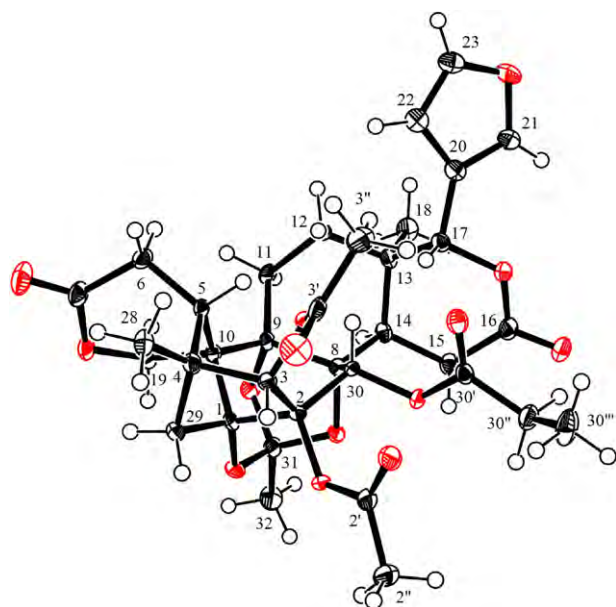


Fig. 8. ORTEP drawing of Andirolide E (5).

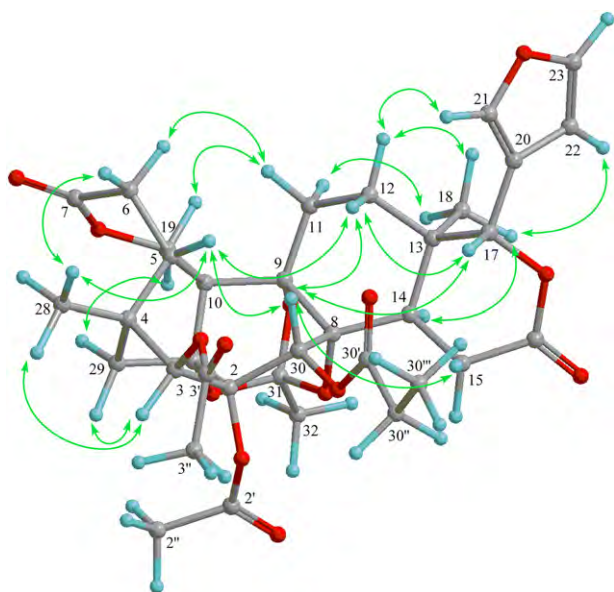


Fig. 7. Key NOESY correlations for Andirolide E (5).

AcOEt, 5:1) to give a colorless solid (240 mg, Fr. No. 97–109), which in turn was separated by HPLC (ODS, 50% CH_3CN) to afford compounds **2** (10 mg) and **6** (12 mg). Residue F4 was subjected to CC (silica gel (230–400 mesh, 100 g); *n*-hexane/AcOEt 2:1) to give an amorphous solid (250 mg, Fr. No. 65–72), which was purified by HPLC (ODS, 60% MeOH) to afford compound **5** (100 mg). Residue F5 was subjected to CC (silica gel (230–400 mesh, 100 g); *n*-hexane/AcOEt, 2:1) to give an amorphous solid (78 mg, Fr. No. 86–120), which was purified by HPLC (silica gel, $\text{CHCl}_3/\text{MeOH}$, 50:1) to afford compound **7** (15 mg).

3.3.1. Andirolide A (1). Colorless needles; mp 151–153°C (MeOH/ CHCl_3); $[\alpha]_D^{23} +3.1$ (c 0.20, CHCl_3); HRFABMS m/z : 541.2442 $[\text{M}+\text{H}]^+$ ($\text{C}_{30}\text{H}_{37}\text{O}_9$, calcd for 541.2437); FABMS m/z (rel.int.): 541 ($[\text{M}+\text{H}]^+$, 64), 523 (36), 481 (7), 463 (6), 421 (25), 403 (7); UV λ_{max} nm (log ϵ): 236 (3.49); IR ν_{max} cm^{-1} : 3448 (OH), 2979, 1742, 1723, 1672, 1459,

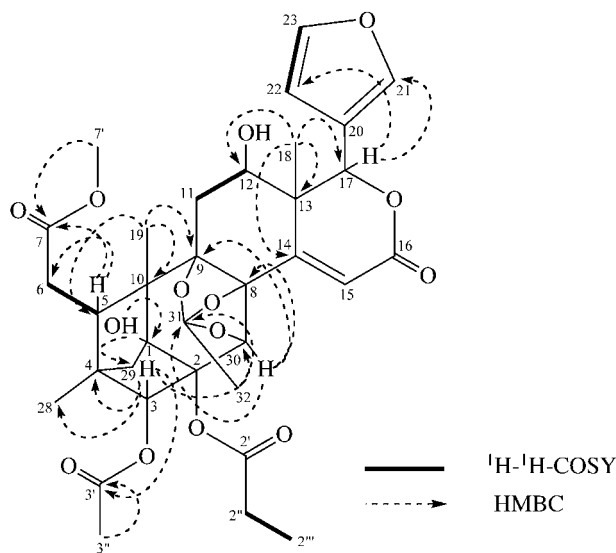


Fig. 9. Selected ^1H – ^1H COSY and HMBC correlations in Andirolide G (7).

1370, 1246, 1031, 973, 875; CD λ nm ($\Delta\epsilon$)[c 7.39×10^{-4} M, CH_3CN]: 235 (9.4), 251 (0.7), 264 (1.4), 281 (0), 299 (–1.4), 340 (–2.0), 393 (0). ^1H and ^{13}C NMR data, see Table 1.

3.3.2. Andirolide B (2). Colorless needles; mp 138–140°C (MeOH/ CHCl_3); $[\alpha]_D^{23} -16.5$ (c 0.13, CHCl_3); HRFABMS m/z : 587.2493 $[\text{M}+\text{H}]^+$ ($\text{C}_{31}\text{H}_{39}\text{O}_{11}$, calcd for 587.2492); FABMS m/z (rel.int.): 587 ($[\text{M}+\text{H}]^+$, 100), 569 (12), 527 (9), 509 (8), 467 (56), 449 (11); UV λ_{max} nm (log ϵ): 223 (3.73); IR ν_{max} cm^{-1} : 3448 (OH), 2926, 1734, 1680, 1458, 1375, 1240, 1030, 875; CD λ nm ($\Delta\epsilon$)[c 4.37×10^{-4} M, CH_3CN]: 220 (13.5), 238 (0), 243 (–0.7), 249 (0), 261 (1.8), 273 (0), 297 (–4.4), 319 (0). ^1H and ^{13}C NMR data, see Table 2.

3.3.3. Andirolide C (3). Colorless needles; mp 138–140°C (MeOH/ CHCl_3); $[\alpha]_D^{23} -37.3$ (c 0.08, CHCl_3); HRFABMS m/z : 615.2800 $[\text{M}+\text{H}]^+$ ($\text{C}_{33}\text{H}_{43}\text{O}_{11}$, calcd for 615.2805); FABMS m/z (rel.int.): 615 ($[\text{M}+\text{H}]^+$, 87%), 597 (19), 555 (5), 537 (5), 527 (6), 467 (68), 449 (17); UV ν_{max} nm (log ϵ): 224.6 (3.94); IR ν_{max} cm^{-1} : 3445 (OH),

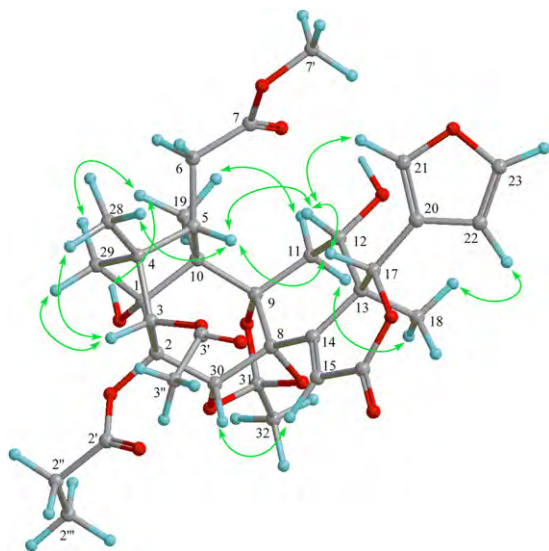


Fig. 10. Key NOESY correlations for Andiroside G (7).

2973, 1727, 1680, 1459, 1374, 1259, 1026, 875; CD λ nm ($\Delta\epsilon$)[c 4.15×10^{-4} M, CH₃CN]: 219 (11.3), 243 (−0.2), 260 (1.6), 274 (0), 297 (−3.5), 320 (0); ¹H and ¹³C NMR data, see Table 2.

3.3.4. *Andiroside D (4)*. Colorless needles; mp 131–133°C (MeOH/CHCl₃); $[\alpha]_D^{23}$ −48.6 (c 0.08, CHCl₃); HRFABMS m/z : 627.2798 [M+H]⁺ (C₃₄H₄₃O₁₁, calcd for 627.2805); FABMS m/z (rel int.): 627 [M+H]⁺, (25), 609 (5), 567 (2), 549 (3), 527 (3), 509 (1), 467 (13), 449 (4); UV ν_{\max} nm (log ϵ): 227.5 (4.12); IR ν_{\max} cm^{−1}: 3439 (OH), 2952, 1727, 1680, 1459, 1374, 1259, 1027, 876; CD λ nm ($\Delta\epsilon$)[c 5.44×10^{-4} M, CH₃CN]: 223 (13.7), 245 (−0.1), 260 (1.2), 272 (0), 297 (−3.8), 323 (0); ¹H and ¹³C NMR data, see Table 2.

3.3.5. *Andiroside E (5)*. Colorless prisms; mp 180–182°C (MeOH/CHCl₃); $[\alpha]_D^{23}$ −24.3 (c 0.10, CHCl₃); HRFABMS m/z : 685.2493 [M+H]⁺ (C₃₅H₄₁O₁₄, calcd for 685.2496); FABMS m/z (rel int.): 685 [M+H]⁺, (69), 625 (6), 551 (3), 491 (12), 449 (34); IR ν_{\max} cm^{−1}: 2979, 1751 (δ -lactone), 1723, 1638, 1374, 1243, 1146, 1083, 1048, 1022, 874; ¹H and ¹³C NMR data, see Table 2.

3.3.6. *Crystal data of 5*. C₃₅H₄₂O₁₄, M_r 686.69, orthorhombic, space group: *P*2₁2₁2₁, $a=9.844$ (6) Å, $b=15.145$ (10) Å, $c=21.469$ (13) Å, $\alpha=90.00^\circ$, $\beta=90.00^\circ$, $\gamma=90.00^\circ$, $V=3200.7$ (3) Å³, $D_x=1.425$ g/cm^{−3},

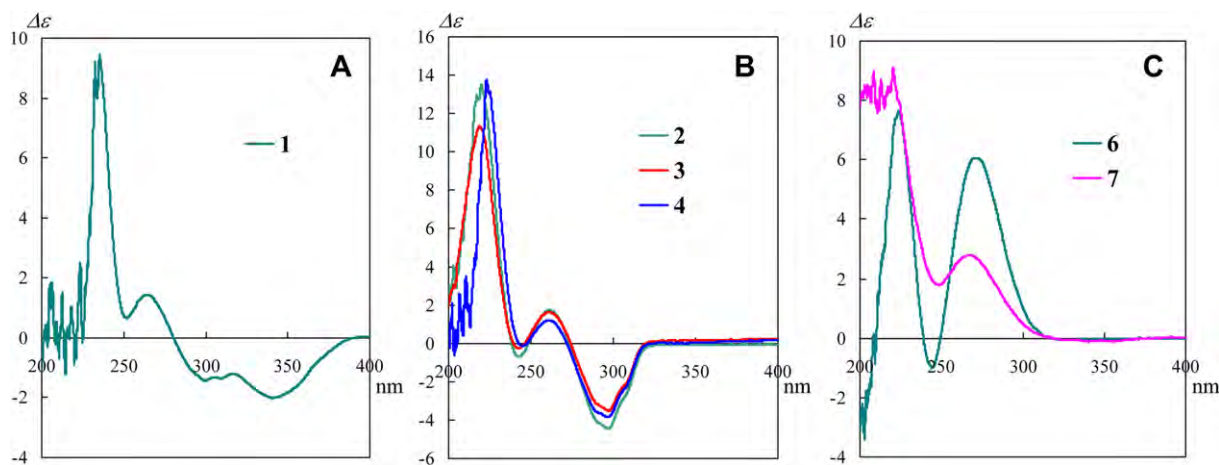
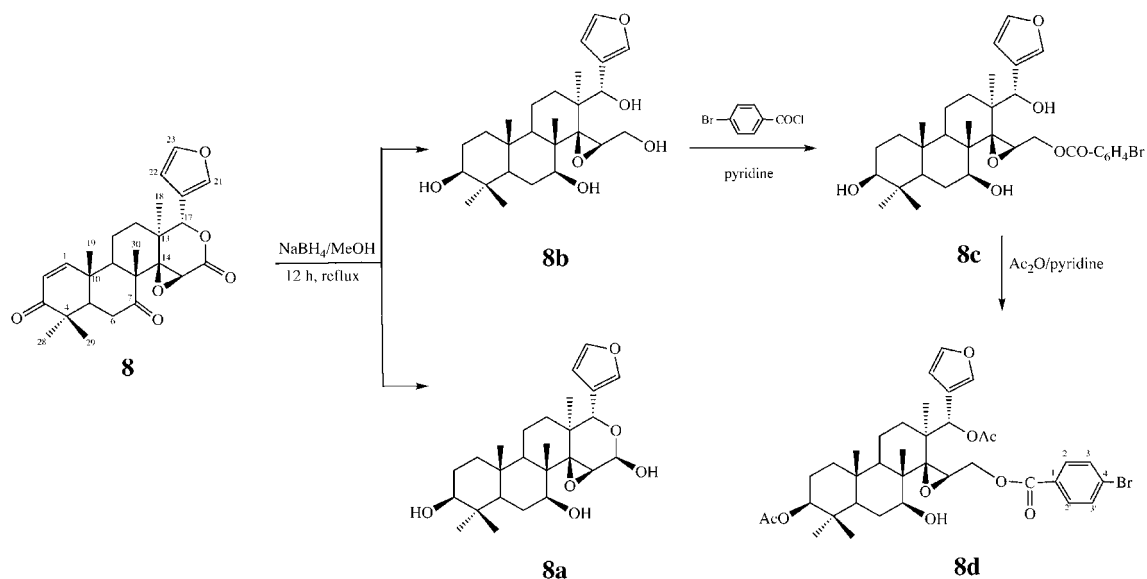


Fig. 11. (A) CD spectrum of Andiroside A (1). (B) CD spectra of Andiroside B (2), C (3), D (4). (C) CD spectra of Andiroside F (6), G (7).



Scheme 1. Synthesis of **8d** from 7-deacetoxy-7-oxogedunin (**8**).

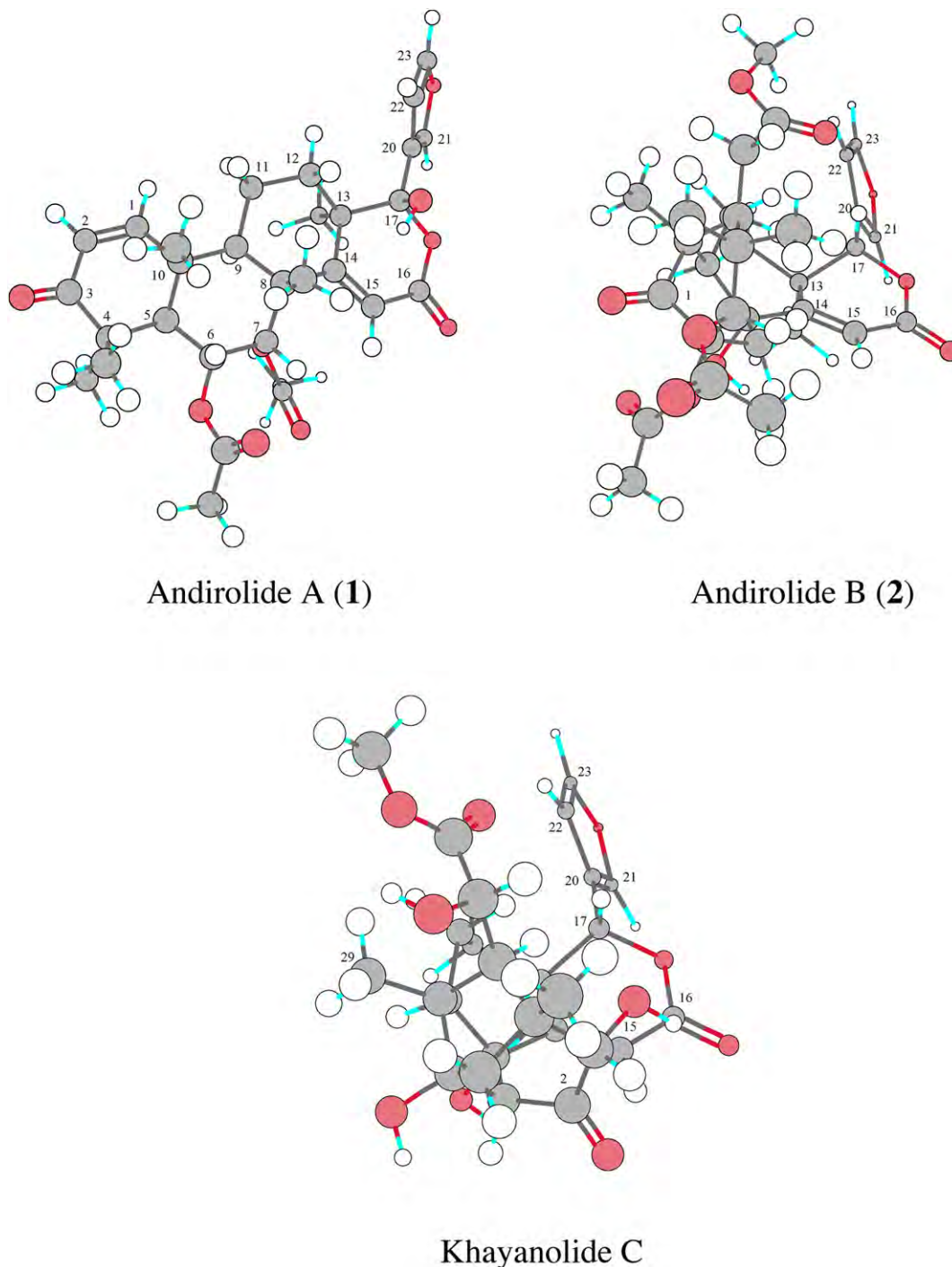


Fig. 12. The stable conformations of Andiolides A (1), B (2), and Khayanolide C calculated on Chem 3D.

$Z=4$. $F(000)=1456$, $\mu(\text{Mo K}\alpha)=0.110\text{ mm}^{-1}$, measured independent reflections 7679, reflections 7329 ($I>2\sigma(I)$), parameters used for refinement 442, $R_1=0.0598$ (for $I>2\sigma(I)$), $wR_2=0.1398$ (for all data). X-ray diffraction data were collected with a Bruker AXS SMART APEX CCD camera using graphite-monochromated Mo $K\alpha$ radiation ($\lambda=0.71069$) at 120 K for **5**. The crystal structures were solved by a direct method using the SHELXS-97 program.²¹ Atomic scattering factors were taken from the International Tables for X-ray Crystallography.²² Positional parameters of non-H-atoms were refined by a full-matrix least-squares method with anisotropic thermal parameters using the SHELXL-97 program.²¹ The structural data were deposited with the following designation: **5**: CCDC-773260.

These can be obtained free of charge at www.ccdc.cam.ac.uk/conts/retrieving.html (or from the Cambridge Crystallographic Data Centre, 12 Union Road, Cambridge CB21EZ, U.K.; fax: +44 1223 336 033; e-mail: deposit@ccdc.cam.ac.uk). The H-atoms were calculated assuming idealized geometries but were not refined.

3.3.7. *Alkaline hydrolysis of Andiolide E (5)*. Compound **5** (7.6 mg) was refluxed with a solution of 0.03 mol dm^{-3} KOH in MeOH over a steam bath for 6 h. Evaporation of the solvent under reduced pressure afforded a residue, which was subjected to HPLC [ODS, MeOH/H₂O (60:40)] to afford compound **5a** (4.6 mg): HRFABMS m/z : 545.2030 $[\text{M}+\text{H}]^+$ ($\text{C}_{28}\text{H}_{33}\text{O}_{11}$, calcd for 545.2023); FABMS m/z

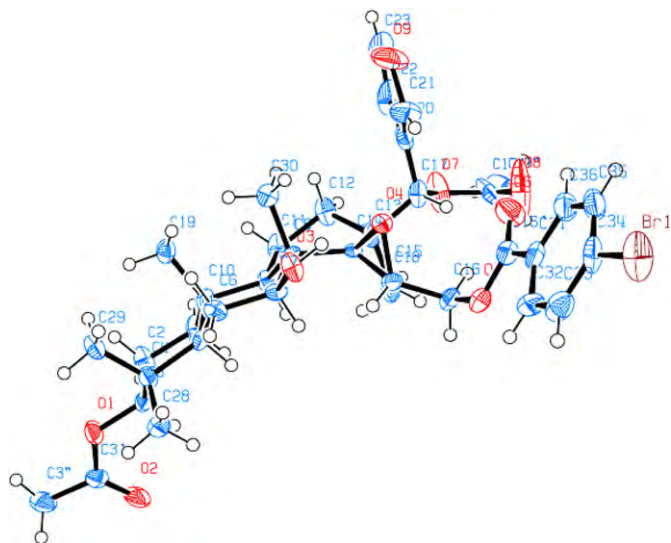
Fig. 13. ORTEP drawing of **8d**.

Table 4

Cytotoxicity of Andiroloides A–G (1–7) against the P388, HL-60, L1210 and KB cell lines

Compounds	Cell line P388 IC50 (mM) ^a	Cell line HL-60 IC50 (mM) ^a	Cell line L1210 IC50 (mM) ^a	Cell line KB IC50 (mM) ^a
1	3.3	19.4	16.7	11.4
2	>100	>100	>100	>100
3	>100	>100	>100	>100
4	>100	79.9	>100	>100
5	>100	>100	>100	>100
6	14.4	16.1	27.0	29.3
7	50.6	>100	>100	68.5
5-Fluoro uracil ^b	0.8	0.9	0.4	7.7

^a DMSO was used as vehicle.^b Positive control.

(rel int.): 545 [M+H]⁺ (100), 527 (2), 509 (1), 485 (4), 425 (11); ¹H NMR δ ppm (CDCl₃): 1.08 (3H, s, H₃-28), 1.10 (3H, s, H₃-18), 1.42 (1H, m, H-12 β), 1.49 (1H, m, H-12 α), 1.62 (3H, s, H₃-32), 1.63 [1H, d, J =11.0 Hz, H-29 *pro-R*], 1.77 (1H, m, H-11 α), 1.93 [1H, dd, J =9.8 Hz (15 α), 1.4 Hz (15 β), H-14], 2.18 [1H, d, J =11.0 Hz, H-29 *pro-S*], 2.24 (1H, m, H-11 β), 2.42 [1H, dd, J =16.7 Hz (6 α), 5.1 Hz (5), H-6 β], 2.61 [1H, dd, J =16.7 Hz (6 β), 4.0 Hz (5), H-6 α], 2.62 [1H, dd, J =19.0 Hz (15 β), 9.8 Hz (14), H-15 α], 2.76 [1H, dd, J =5.1 Hz (6 β), 4.0 Hz (6 α), H-5], 2.98 (1H, s, 2-OH), 3.22 [1H, dd, J =19.0 Hz (15 α), 1.4 Hz (14), H-15 β], 3.61 (1H, s), 3.64 [1H, d, J =7.6 Hz (30), 30-OH], 4.36 [1H, d, J =13.7 Hz (19 α), H-19 β], 4.49 [1H, d, J =7.6 Hz (30-OH), H-30], 4.76 [1H, d, J =13.7 Hz (19 β), H-19 α], 5.45 (1H, s, H-17), 6.38 [1H, d, J =1.7 Hz (23), H-22], 7.36 [1H, t, J =1.7 Hz (21, 22), H-23], 7.44 [1H, d, J =1.7 Hz (23), H-21].

3.3.8. Andiroloide F (6). Colorless needles; mp 188–190°C (MeOH/CHCl₃); [α]_D²³ +15.4 (c 0.06, CHCl₃); HRFABMS m/z : 683.2335 [M+H]⁺ (C₃₅H₃₉O₁₄, calcd for 683.2340); FABMS m/z (rel int.): 683 [M+H]⁺ (100), 623 (4), 507 (10), 447 (7); UV λ_{\max} nm (log ϵ): 225 (3.94); IR ν_{\max} cm⁻¹: 3445 (OH), 2973, 1727, 1680, 1459, 1374, 1259, 1026, 875; CD λ nm ($\Delta\epsilon$): [c 3.59 \times 10⁻⁴ M, CH₃CN]: 224 (7.6), 239 (0), 244 (-1.0), 249 (0), 270 (6.1), 317 (0); ¹H and ¹³C NMR data, see Table 3.

3.3.9. Andiroloide G (7). Colorless needles; mp 145–147°C (MeOH/CHCl₃); [α]_D²³ +3.2 (c 0.17, CHCl₃); HRFABMS m/z : 673.2505 [M+H]⁺ (C₃₄H₄₁O₁₄, calcd for 673.2495); FABMS m/z (rel.int.): 673 [M+H]⁺ (17), 655 (5), 613 (6), 599 (69), 479 (7); UV λ_{\max} nm (log ϵ): 229

(3.68); IR ν_{\max} cm⁻¹: 3568 (OH), 2929, 1729, 1459, 1236, 1160, 1022, 875; CD λ nm ($\Delta\epsilon$): [c 4.46 \times 10⁻⁴ M, CH₃CN]: 213 (8.5), 249 (1.8), 268 (2.8), 323 (0); ¹H and ¹³C NMR data, see Table 3.

3.3.10. 7-Deacetoxy-7-oxogedunin (8). Colorless prisms; mp 264–266°C (MeOH/CHCl₃); [α]_D²³ -38.8 (c 0.178, CHCl₃). Compound **8** was identified from published data.²

3.3.11. NABH₄ reduction of 8. To a solution of **8** (104.0 mg) in MeOH (20 ml), NaBH₄ (95 mg) was added and the mixture was refluxed for 12 h. The addition of AcOEt and H₂O was followed by the usual work-up. Evaporation of the solvent under reduced pressure afforded a residue (83.0 mg), which was subjected to HPLC (ODS, MeOH/H₂O, 60:40) to give **8a** (55.2 mg) and **8b** (19.0 mg). Compound **8a**: HRFABMS m/z : 429.2637 [M-OH]⁺ (C₂₆H₃₇O₅, calcd for 429.2641); FABMS m/z (rel int.): 429 ([M-OH], 12%), 411 (3). Compound **8b**: HRFABMS m/z : 431.2796 [M-OH]⁺ (C₂₆H₃₉O₅, calcd for 431.2798); FABMS m/z (rel int.): 431 ([M-OH], 87%), 413 (41), 395 (2); ¹H NMR δ ppm (CDCl₃): 0.79 (3H, s, H₃-29), 0.86 [1H, dd, J =12.3 Hz (6 β), 2.1 Hz (6 α), H-5], 0.90 (3H, s, H₃-19), 0.94 (1H, m, H-1 α), 1.00 (3H, s, H₃-28), 1.05 (3H, s, H₃-18), 1.15 (3H, s, H₃-30), 1.18 (1H, m, H-9), 1.20 (1H, m, H-12 α), 1.50 (1H, m, H-6 α), 1.52 (1H, m, H-11 β), 1.56 (1H, m, H-2 α), 1.60 (1H, m, H-11 α), 1.64 (1H, m, H-1 β), 1.65 (1H, m, H-6 β), 1.66 (1H, m, H-2 β), 1.91 (1H, m, H-12 β), 3.20 [1H, dd, J =11.4 Hz (2 β), 4.3 Hz (2 α), H-3], 3.67 [1H, dd, J =10.7 Hz (6 β), 4.3 Hz (6 α), H-7], 3.91 [1H, dd, J =7.8 Hz (16 β), 2.8 Hz (16 α), H-15], 4.11 [1H, dd, J =12.4 Hz (16 β), 2.8 Hz (15), H-16 α], 4.25 [1H, dd, J =12.4 Hz (16 α), 7.8 Hz (15), H-16 β], 4.99 (1H, s, H-17), 6.42 [1H, dd, J =1.6 Hz (23), 0.7 Hz (21), H-22], 7.36 [1H, t, J =1.6 Hz (22, 21)], 7.42 (1H, br s, H-21).

3.3.12. Formation of mono-*p*-bromobenzoate of 8b. *p*-Bromobenzoylchloride (39 mg) and DMAP (3 mg) were added to a pyridine solution (2 ml) of **8b** (19.0 mg), and the reaction mixture was refluxed for 2 h. AcOEt and H₂O were added and a standard work-up followed. The solvent was evaporated under reduced pressure, and the residue (83.0 mg) was purified by HPLC (ODS, MeOH/H₂O, 80:20) to give **8c** (5.6 mg). Compound **8c**: HRFABMS m/z : 630.4590 [M+H]⁺ (C₃₃H₄₄⁷⁹BrO₇, calcd for 630.4591).

3.3.13. Acetylation of 8c. To a solution of **8c** (5.6 mg) in pyridine (0.5 ml) was added Ac₂O (1.0 ml), and the reaction mixture was left at room temperature overnight. The mixture was concentrated dry under reduced pressure, and the residue was purified by HPLC (ODS, MeOH/H₂O, 85:15) to give **8d** (3.8 mg).

Compound **8d**: Colorless prisms; mp 241–243°C (MeOH/CHCl₃); [α]_D²³ +4.1 (c 0.03, CHCl₃); HRFABMS m/z : 715.2484 [M+H]⁺ (C₃₇H₄₈⁷⁹BrO₉, calcd for 715.2481); FABMS m/z (rel int.): 715 [M+H]⁺ (10), 657 (19), 655 (19), 639 (5), 637 (4), 455 (12), 395 (6), 377 (7). ¹H NMR δ ppm (CDCl₃): 0.81 (3H, s, H₃-30), 0.84 (3H, s, H₃-29), 0.86 (3H, s, H₃-28), 0.90 (3H, s, H₃-19), 0.94 [1H, dd, J =13.0 Hz (6 β), 2.0 Hz (6 α), H-5], 1.03 (1H, m, H-1 α), 1.17 (3H, s, H₃-18), 1.28 (1H, m, H-12 α), 1.42 (1H, m, 6 α), 1.52 (1H, m, H-12 β), 1.54 (1H, m, H-2 α), 1.55 (1H, m, H-11 α), 1.61 (1H, m, 1 β), 1.65 (1H, m, 6 β), 1.68 (1H, m, 2 β), 1.70 (1H, m, 11 β), 2.04 (3H, s, Ac), 2.07 (3H, s, Ac), 3.59 [1H, dd, J =10.8 Hz (6 β), 4.6 Hz (6 α), H-7], 3.92 [1H, dd, J =8.7 Hz (16 β), 2.6 Hz (16 α), H-15], 4.45 [1H, dd, J =11.6 Hz (2 β), 4.6 Hz (2 α), H-3], 4.84 [1H, dd, J =12.3 Hz (16 α), J =8.7 Hz (15), H-16 β], 4.96 [1H, dd, J =12.3 Hz (16 β), 2.6 Hz (15), H-16 α], 6.13 (1H, s, H-17), 6.50 [1H, dd, J =1.8 Hz (23), 0.7 Hz (21), H-22], 7.35 [1H, t, J =1.8 Hz (22, 21), H-23], 7.55 (1H, br s, H-21), 7.62 [each 1H, d, J =8.7 Hz, H-2, 2'], 7.98 [each 1H, d, J =8.7 Hz, H-3, 3'].

3.3.14. Crystal data of 8d. C₃₇H₄₇BrO₉, M_r 715.66, monoclinic, space group: $P2_1$, a =7.1529 (12) Å, b =27.995 (5) Å, c =9.411 (17) Å, α =90.00°, β =112.017 (3)°, γ =90.00°, V =1747.0 (5) Å³, D_x =1.360 g/cm³, Z =2. $F(000)$ =752, μ (Mo $K\alpha$)=1.230 mm⁻¹, measured independent reflections 6241, reflections 3635 (I >2 σ (I)), parameters

used for refinement 423, $R_1=0.0645$ (for $I>2\sigma(I)$), $wR_2=0.1507$ (for all data), Flack χ parameter=0.025(12). X-ray diffraction data were collected with a Bruker AXS SMART APEX CCD camera using graphite-monochromated Mo K α radiation ($\lambda=0.71069$) at 293 K for **8d**. The crystal structures were solved by a direct method using the SHELXS-97 program.¹⁶ Atomic scattering factors were taken from the International Tables for X-ray Crystallography.¹⁷ Positional parameters of non-H-atoms were refined by a full-matrix least-squares method with anisotropic thermal parameters using the SHELXL-97 program.¹⁸ The structural data were deposited with the following designation: **8d**: CCDC-773261. These can be obtained free of charge at www.ccdc.cam.ac.uk/conts/retrieving.html (or from the Cambridge Crystallographic Data Centre, 12 Union Road, Cambridge CB21EZ, U.K.; fax: +44 1223 336 033; e-mail: deposit@ccdc.cam.ac.uk). The H-atoms were calculated assuming idealized geometries but were not refined.

3.3.15. Cytotoxic assay against P388, HL-60, L1210, and KB cell lines. Cytotoxic activities of compounds **1–6** were examined by the 3-(4,5-dimethyl-2-thiazolyl)-2, 5-diphenyl-2H-tetrazolium bromide (MTT) method. P388, HL-60, L1210, and KB cells were cultured in Eagle's Minimum Essential Medium (10% fetal calf serum) at 37°C in 5% CO₂. The test material was dissolved in dimethyl sulfoxide (DMSO) to give a concentration of 10 mM, and the solution was diluted with Essential Medium to give concentrations of 200, 20, and 2 μ mol, respectively. Each solution was combined with each cell suspension (1×10^5 cells/ml) in the medium, respectively. After incubation at 37°C for 72 h in 5% CO₂, the grown cells were labeled with 5 mg/ml MTT in phosphate-buffered saline (PBS), and then the absorbance of formazan dissolved by 20% sodium dodecyl sulfate (SDS) in 0.1 N HCl was measured at 540 nm using a microplate reader (Model 450; BIO-RAD). Each absorbance value was expressed as a percentage relative to the control cell suspension, which was prepared without the test substance by the same procedure as described above. All assays were performed three times, semi-logarithmic plots were constructed from the averaged data, and the effective dose of the substance required to inhibit cell growth by 50% (IC₅₀) was determined.

Acknowledgements

We thank Dr. Katsuhiko Minoura and Mrs. Mihoyo Fujitake (this university) for NMR and MS measurements. This work was

supported by a Grant-in-Aid for High Technology from the Ministry of Education, Sciences, Sports and Culture, Japan.

Supplementary data

Supplementary data related to this article can be found online version, at doi:10.1016/j.tet.2010.11.028.

References and notes

- Ollis, W. D.; Ward, A. D.; Zelnik, R. *Tetrahedron Lett.* **1964**, 2607–2614.
- Ollis, W. D.; Ward, A. D.; Oliveira, H. M. D.; Zelnik, R. *Tetrahedron* **1970**, *26*, 1637–1645.
- Connolly, J. D.; McCrindle, R.; Overton, K. H.; Feeney, J. *Tetrahedron* **1966**, *22*, 891–896.
- Lavie, D.; Levy, E. C.; Zelnik, R. *Bioorg. Chem.* **1972**, *2*, 59–64.
- Marcelle, G. B.; Mootoo, B. S. *Phytochemistry* **1975**, *14*, 2717–2718.
- Ambrozin, A. R. P.; Leite, A. C.; Bueno, F. C.; Vieira, P. C.; Fernandes, J. B.; Bueno, O. C.; Fernandes da Silva, M. F. G.; Pagnocca, F. C.; Hebling, M. J. A.; Bacci, M., Jr. *J. Braz. Chem. Soc.* **2006**, *17*, 542–547.
- Wu, J.; Xiao, Q.; Zhang, S.; Li, X.; Xiao, Z.; Ding, H.; Li, Q. *Tetrahedron* **2005**, *61*, 8382–8389.
- Wu, J.; Xiao, Q.; Huang, J. S.; Xiao, Z.; Ding, H.; Li, Q. *Org. Lett.* **2004**, *6*, 1841–1844.
- Ekong, D. E. U.; Olagbemi, E. O. *Tetrahedron Lett.* **1967**, *36*, 3525–3527.
- Kadota, S.; Marpaung, L.; Kikuchi, T.; Ekimoto, H. *Chem. Pharm. Bull.* **1990**, *38*, 639–651.
- Okorie, D. A.; Taylor, D. A. H. *Phytochemistry* **1968**, *7*, 1683–1686.
- Wu, J.; Zhang, S.; Xiao, Q.; Li, Q. X.; Huang, J. S.; Xiao, Z. H.; Long, L. J. *Z. Naturforsch.* **2003**, *58*, 1216–1219.
- Wu, J.; Zhang, S.; Li, M.; Zhou, Y.; Xiao, Q. *Chem. Pharm. Bull.* **2006**, *54*, 1582–1585.
- Gan, L. S.; Wang, X.-N.; Wu, Y.; Yue, J.-M. *J. Nat. Prod.* **2007**, *70*, 1344–1347.
- Cui, J.; Deng, Z.; Li, J.; Fu, H.; Proksch, P.; Lin, W. *Phytochemistry* **2005**, *66*, 2334–2339.
- Nakatani, M.; Abdelgaleil, S. A. M.; Saad, M. M. G.; Huang, R. C.; Doe, M.; Iwagawa, T. *Phytochemistry* **2004**, *65*, 2833–2841.
- Saad, M. M. G.; Iwagawa, T.; Doe, M.; Nakatani, M. *Tetrahedron* **2003**, *59*, 8027–8033.
- Kanokmedhakul, S.; Kanokmedhakul, K.; Nasomjai, P.; Louangsysouphanh, S.; Soyong, K.; Isobe, M.; Kongsaeere, P.; Prabpai, S.; Suksamrarn, A. *J. Nat. Prod.* **2006**, *69*, 891–895.
- Jongrungruangchok, S.; Kittakoop, P.; Yongsmith, B.; Bavovada, R.; Tanasupawat, S.; Larpornmatulee, N.; Thebtaranonth, Y. *Phytochemistry* **2004**, *65*, 2569–2575.
- Muroga, Y.; Yamada, T.; Numata, A.; Tanaka, R. *Tetrahedron* **2009**, *65*, 7580–7586.
- Sheldrick, G. M. *SHELXL-97, Program for Structure Determination by Direct Method of Crystal Structure*; University of Gottingen: Gottingen, 1997.
- International Tables for X-ray Crystallography*; Hahn, T., Ed.; Kluwer Academic: Dordrecht, 1996; Vol. A.

Synthesis and Conformational Analysis of Dcp-Containing Homo-Oligopeptides

Yasuko In¹, Katsuhiko Minoura¹, Toshimasa Ishida¹, Shio Fujioka²,
Misai Takeda², Takashi Murashima² and Takashi Yamada²

¹Department of Physical Chemistry, Osaka University of Pharmaceutical Sciences,
4-20-1 Nasahara, Takatsuki, Osaka 569-1094, Japan, ²Department of Chemistry,
Faculty of Science and Engineering, Konan University, 8-9-1 Okamoto,
Higashinada-ku, Kobe 658-8501, Japan
e-mail: yoon@gly.oups.ac.jp

In order to clarify in more detail the effect of α,α -dicyclopropylglycine (Dcp) on the homo-oligopeptide conformation, we investigated the conformations of a series of Dcp-containing homo-oligopeptides (Z -(Dcp)_n-OMe, n=3~5) by X-ray crystal and NMR solution analyses. Consequently, it was shown that these tri-, tetra- and pentapeptides adopted 3_{10} -helical structure stabilized by one, two and three intramolecular hydrogen bonds of Dcp-NH protons in both the crystal and solution states, respectively, suggesting the importance of Dcp as a helical constrained building block.

Keywords: 3_{10} -helical structure, α,α -dicyclopropylglycine, conformational analysis, crystal structure, solution structure

Introduction

Various α,α -disubstituted amino acids have an influence on the peptide conformation, and the incorporation of these amino acids into the oligopeptides restricts their conformational freedom. For example, it is well known that α,α -dimethylglycine (Aib) makes the folded 3_{10} -helical or α -helical structure more stable than the extended structure, whereas α,α -diethylglycine (Deg) or α,α -dipropylglycine (Dpg) leads to the extended C_5 -conformation rather than the helical structure [1]. Therefore, α,α -disubstituted glycine could be a useful tool to restrict the peptide backbone conformation to a well-defined secondary structure [2].

We have investigated the effect of α,α -dicyclopropylglycine (Dcp, Fig. 1(a)) on the molecular conformation of homo-oligopeptide. In this study, we performed the conformational analyses of Dcp-containing homo-oligopeptides (Z -(Dcp)_n-OMe, n=3~5, Fig. 1(b)) by X-ray and NMR structural analyses and clarified their 3_{10} -helical conformations in both the solid and solution states; the conformational features of (Z -(Dcp)_n-OMe, n=4,5) were already reported in the last peptide symposium. Based on the conformational analyses of three peptides, we discuss the universal effect of Dcp on the Dcp-containing homo-oligopeptide conformation (Fig. 1 (b)).

Results and Discussion

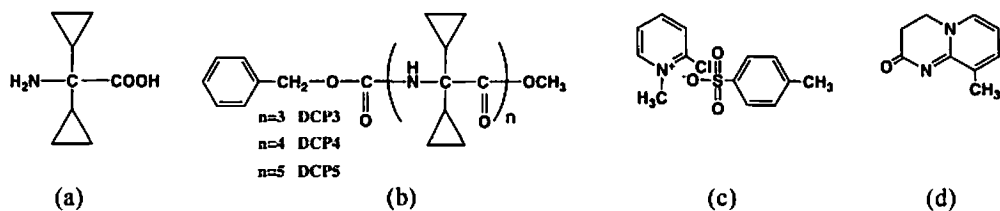


Fig. 1. Chemical structures of (a) Dcp, (b) Z-(Dcp)_n-OMe, (c) CMPT, and (d) AC9M.

Table 1. Summary of crystal data and structure refinement of Z-(Dcp)_n-OMe (n=3~5)

	DCP3(n=3)	DCP4(n=4)	DCP5(n=5)
Crystal data			
Formula / Formula weight	C ₃₃ H ₄₃ N ₃ O ₆ / 577.7	C ₄₁ H ₅₄ N ₄ O ₇ / 714.9	C ₄₉ H ₆₅ N ₅ O ₈ / 852.06
Space Group / Crystal System	P2 ₁ / monoclinic	P2 ₁ /h / monoclinic	P-1 / triclinic
Cell constant			
a(Å), α(°)	a=10.222(1)	a=20.427(5)	a=18.966(2), α=104.674(1)
b(Å), β(°)	b=20.326(2), β=105.187(2)	b=18.531(5), β=100.492(5)	b=11.667(1), β=93.183(2)
c(Å), γ(°)	c=15.334(2)	c=20.446(5)	c=10.725(1), γ=75.470(2)
V(Å ³) / Z	3074.7(6) / 4	7610(3) / 8	2222.2(4) / 2
F(000) / μ (Mo Kα)/mm ⁻¹	1240 / 0.086	3072 / 0.085	916 / 0.087
Refinement			
Refinement method		Full-matrix least squares of F ²	
Final R-indices [I>2σ]	R1=0.0613, wR2=0.1336	R1=0.1044, wR2=0.2289	R1=0.0624, wR2=0.1588
R-indices (all data)	R1=0.0685, wR2=0.1375	R1=0.1598, wR2=0.2588	R1=0.0787, wR2=0.1734
Δρ _{max} and Δρ _{min}	0.407 and -0.210	1.876 and -0.436	0.407 and -0.210
Goodness-of-fit on F ²	1.105	1.069	0.933
Data collections			
Wavelength / Temperature		0.7107 / 120K	
number of reflections used for refinement (I>2σ)	9741	11058	7797

Synthesis of Dcp-containing homo-oligopeptide

Dcp-dipeptide (Z-Dcp-Dcp-OMe) was synthesized by various coupling methods such as EDC-HOAt, EEDQ and CMPT (2-chloro-1-methylpyridinium *p*-toluenesulfonate)-AC9M (9-methyl-3,4-dihydro-2H-pyrido[1,2-*a*]pyrimidin-2-one) methods and gave the desired dipeptide in moderate yields (47%, 54%, 68%, respectively). The tri-, tetra- and pentapeptides of Dcp (Z-(Dcp)_n-OMe, n=3~5), were also synthesized by using the CMPT-AC9M/DIEA/DMF method (41%, 9%, 11%, respectively). (Fig. 1 (c) and (d))

Crystal structure analysis

Crystals of Z-(Dcp)_n-OMe, (n=3~5) were mounted on a nylon loop with 30%-glycerol and then flash-frozen under a nitrogen stream (120K). Data collection was performed on a CCD diffractometer (Bruker AXS SMART APEX).

The crystal structure was solved by direct methods using the SIR97 program. The positional parameters of non-H atoms were refined by a full-matrix least-squares method with anisotropic thermal parameters using the SHELXL-97 program. The positions of Dcp-NH protons were determined from a difference Fourier map, while those of the other H atoms were calculated on the basis of their stereochemical

requirement. The crystallographic data summarized in Table 1. The crystals of these peptides, except DCP5, consist of two independent molecules (A and B) per

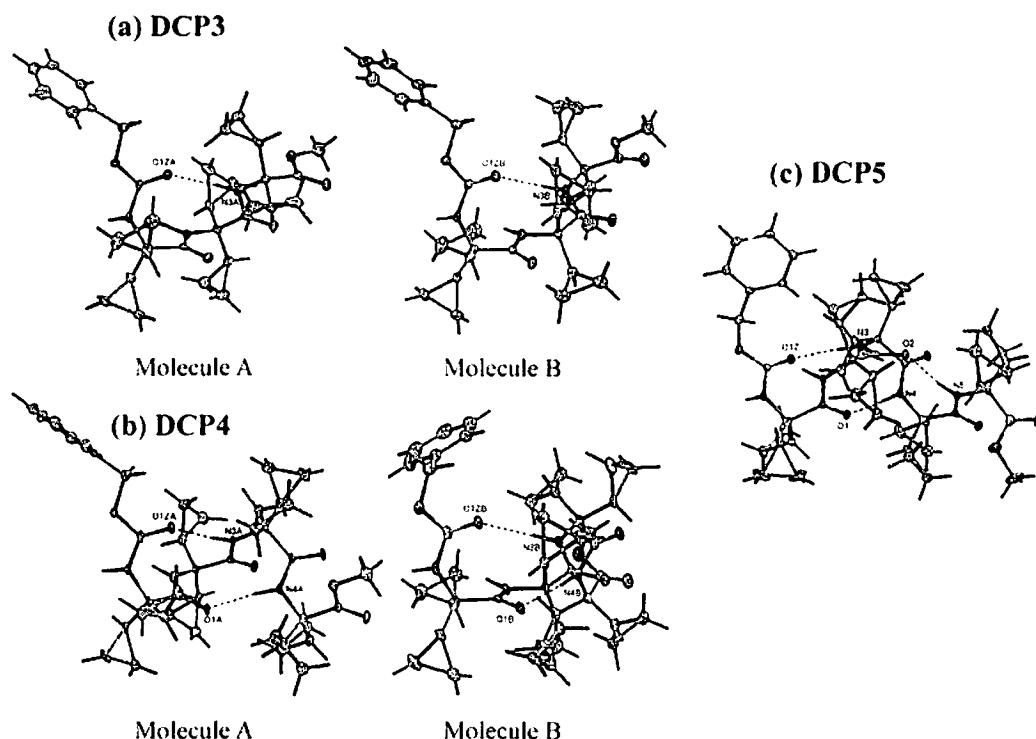


Fig. 2. Crystal structure of $Z\text{-(Dcp)}_n\text{-OMe}$ ($n=3$: DCP3, $n=4$: DCP4, $n=5$: DCP5). Dotted lines indicate intramolecular hydrogen bond.

Table 2. Intra- and Intermolecular H-bond parameters of $Z\text{-(Dcp)}_n\text{-OMe}$.

DCP3 (n=3)				DCP4 (n=4)			
Donor	Acceptor	Distance(Å)	Angle(°)	Donor	Acceptor	Distance(Å)	Angle(°)
D—H	A	D...A	D—H...A	D—H	A	D...A	D—H...A
molecule A				molecule A			
N1A	O2B	2.821(3)	159.0(2)	N1A	O3B	2.922(4)	144.1(2)
N2A	O3B	3.160(3)	142.2(2)	N2A	O4B	3.271(4)	136.2(2)
N3A	O1ZA	2.936(3)	169.6(1)	N3A	O1ZA	3.015(4)	175.8(2)
molecule B				molecule B			
N1B	O2A	2.868(3)	154.6(2)	N1B	O3A	2.831(4)	155.6(2)
N2B	O3A	3.108(3)	153.0(2)	N2B	O4A	3.053(4)	152.2(2)
N3B	O1ZB	2.874(3)	159.7(2)	N3B	O1ZB	3.005(4)	166.9(2)
DCP5 (n=5)				DCP5 (n=5)			
N1	O4	2.869(2)	161.5(1)	N4B	O1B	2.930(4)	173.4(2)
N3	O1Z	3.040(2)	175.3(1)				
N4	O1	2.934(2)	176.7(1)				
N5	O2	2.880(2)	174.1(1)				

asymmetric unit: DCP3 for $Z\text{-(Dcp)}_3\text{-OMe}$, DCP4 for $Z\text{-(Dcp)}_4\text{-OMe}$, DCP5 for $Z\text{-(Dcp)}_5\text{-OMe}$.

These crystal structures are shown in Fig. 2. Intra- and intermolecular H-bond

parameters and backbone torsion angles of Z-(Dcp)_n-OMe (n=3~5) are given in Table 2 and 3. The results of X-ray analysis revealed that DCP3, DCP4 and DCP5 adopted 3₁₀-helical structures stabilized by one, two and three intramolecular hydrogen bonds

Table 3. Backbone torsion angles of Z-(Dcp)_n-OMe.

	Angles	Dcp ¹	Dcp ²	Dcp ³	Dcp ⁴	Dcp ⁵	
DCP3 (n=3)							
molecule A	φ (°)	-43.8 (3)	-39.6 (3)	46.1 (3)			<i>right-handed 3₁₀-helices</i>
	ψ (°)	-38.8 (3)	-42.1 (3)	51.2 (3)			
	ω (°)	177.4 (2)	174.9 (2)	175.7 (2)			
molecule B	φ (°)	40.6 (3)	60.4 (3)	-40.2 (3)			<i>left-handed 3₁₀-helices</i>
	ψ (°)	39.0 (3)	27.6 (3)	-50.5 (3)			
	ω (°)	175.9 (2)	175.1 (2)	-174.6 (3)			
DCP4 (n=4)							
molecule A	φ (°)	-46.2 (5)	-42.6 (4)	-55.4 (4)	34.7 (5)		<i>right-handed 3₁₀-helices</i>
	ψ (°)	-40.3 (4)	-36.3 (4)	-36.3 (4)	52.3 (4)		
	ω (°)	-178.6 (3)	-175.3 (3)	-172.5 (3)	174.8 (3)		
molecule B	φ (°)	43.0 (5)	43.0 (4)	64.1 (4)	-35.2 (4)		<i>left-handed 3₁₀-helices</i>
	ψ (°)	45.0 (4)	36.4 (4)	23.9 (4)	-58.5 (4)		
	ω (°)	176.2 (3)	172.1 (3)	179.9 (3)	-177.9 (3)		
DCP5 (n=5)							
	φ (°)	42.1 (2)	36.0 (3)	44.7 (2)	61.1 (2)	-35.4 (2)	<i>left-handed 3₁₀-helices</i>
	ψ (°)	42.9 (2)	43.5 (2)	32.7 (2)	28.1 (2)	-54.1 (2)	
	ω (°)	-179.7 (2)	177.7 (2)	176.5 (2)	175.4 (2)	-177.2 (2)	

φ, ψ and ω are the C_{i-1}-N_i-Cα_i-C_i, N_i-Cα_i-C_i-N_{i+1}, and Cα_i-C_i-N_{i+1}-Cα_{i+1} torsion angles, respectively.

of Dcp-NH protons (DCP3: Dcp³-NH, DCP4: Dcp^{3,4}-NH, DCP5: Dcp^{3,4,5}-NH), respectively. And as these peptides lack any chiral amino acid, the right-handed and left-handed 3₁₀-helical structures having the opposite conformation to each other were both presented in the solid state (Fig. 2).

Furthermore all NH-protons of these peptides participated in an intra- and inter-molecular hydrogen bonds except Dcp²-NH proton of DCP5 (Table 2).

NMR analysis

In NMR analysis, assignments of all signals of ¹H and ¹³C-NMR spectra for all peptides were made clearly by COSY, DEPT, HMQC and HMBC techniques. On chemical shifts of Dcp³-NH, Dcp⁴-NH and Dcp⁵-NH in the DCP3, DCP4 and DCP5 the large lower-field shifts were observed (δ 7.00-7.63). The solvent dependence of NH chemical shifts in these peptides showed that the chemical shifts of Dcp³-NH, Dcp⁴-NH and Dcp⁵-NH are insensitive to the addition of DMSO-*d*₆ into the CDCl₃ solution. Therefore, these amide protons probably participate in an intramolecular hydrogen bond. This means that the preferred conformation of the peptides, DCP3, DCP4 and DCP5 in CDCl₃ solution are 3₁₀-helical structure, consistent with the crystal structures (Fig. 2).

In conclusion the solution- and solid-state analyses of Z-(Dcp)_n-OMe (n=3~5) showed that the Dcp residue prefers stable folded 3₁₀-helical structure rather than the extended structure. Moreover, the Dcp residue has moderate reactivity, and thus it may be promising one of the conformationally constrained building blocks.

References

1. Benedetti, E. (1996) *Biopolymers*, **40**, 3-44.
2. Toniolo, C. and Benedetti, E. (1991) *Macromolecules*, **24**, 4004-4009.

Article

Carapanolides T–X from *Carapa guianensis* (Andiroba) Seeds

Teppey Miyake¹, Sari Ishimoto¹, Naoko Ishimatsu¹, Keiichiro Higuchi¹, Katsuhiko Minoura¹, Takashi Kikuchi¹, Takeshi Yamada¹, Osamu Muraoka² and Reiko Tanaka^{1,*}

Received: 29 October 2015; Accepted: 16 November 2015; Published: 24 November 2015

Academic Editor: Isabel C. F. R. Ferreira

¹ Laboratory of Medicinal Chemistry, Osaka University of Pharmaceutical Sciences, 4-20-1 Nasahara, Takatsuki, Osaka 569-1094, Japan; teppei-727@ezweb.ne.jp (T.M.); saridon55@yahoo.co.jp (S.I.); mini-mini.naoko@hotmail.co.jp (N.I.); rikiaifuni815@yahoo.co.jp (K.H.); minoura@gly.oups.ac.jp (K.M.); t.kikuchi@gly.oups.ac.jp (T.K.); yamada@gly.oups.ac.jp (T.Y.)

² Laboratory of Pharmaceutical Organic Chemistry, Faculty of Pharmacy Kinki University, 3-4-1 Kowakae, Higashi-osaka, Osaka 577-8502, Japan; muraoka@phar.kindai.ac.jp

* Correspondence: tanakar@gly.oups.ac.jp; Tel./Fax: +81-72-690-1084

Abstract: Two new mexicanolide-type limonoids, carapanolides T–U (1–2), and three new phragmalin-type limonoids, carapanolides V–X (3–5), were isolated from the seeds of *Carapa guianensis* (andiroba). Their structures were determined on the basis of 1D- and 2D-NMR spectroscopy.

Keywords: *Carapa guianensis*; Meliaceae; andiroba; seeds; limonoid; mexicanolide; phragmalin; NO production

1. Introduction

Limonoids, a series of structurally-diverse and highly-oxygenated tetranortriterpenes, are mainly found in the Meliaceae family and have been attracting attention from biogenetic and synthetic perspectives [1–3]. *Carapa guianensis* Aublet (Meliaceae), known locally as andiroba, is a tall tropical tree that is widely distributed in the Amazonas State of Brazil, and its wood is extensively used as commercial timber. The towering tree of andiroba grows up to 40 m in height. Extracts from its bark, flowers and seeds have been used for centuries by the Amazonian people and exhibit various repellent [4], analgesic [5], anti-bacterial [6], anti-inflammatory [7], wound healing [8], anti-malarial [9], anti-allergic [10] and anti-plasmoidal [11] activities, in addition to acute and subacute toxicities [12]. Our previous study on the components of the seed oil of *Carapa guianensis* revealed the structures of two new unusual 9,10-*seco*-mexicanolide-type limonoids, carapanolides A and B [13], two novel carbon skeletal limonoids, guianolides A and B [14], and carapanolides C–I [15], carapanolides J–L [16] and carapanolides M–S [17]. We herein describe the isolation and structural determination of five novel limonoids, carapanolides T–X (1–5). The structures of 1–5 were determined on the basis of NMR spectroscopy, including 1D and 2D (¹H, ¹H-COSY, NOESY, HSQC, HMBC) NMR and HRFABMS.

2. Results and Discussion

Carapanolide T (1) (Figure 1) was obtained as a colorless amorphous solid, and its molecular formula was established as C₃₁H₄₀O₁₀ ([M + H]⁺; *m/z* 573.2704, calcd. for 573.2697) by HRFABMS, implying 12 on the degrees of unsaturation. IR and UV spectra showed the presence of hydroxyl groups at ν_{\max} 3462 cm⁻¹, ester groups at ν_{\max} 1727 cm⁻¹ and $\alpha\beta$ -unsaturated δ -lactone at λ_{\max} 230 nm (log ϵ 3.85). ¹H- and ¹³C-NMR data indicated that eight out of the 12 units of

unsaturation came from three carbon-carbon double bonds and three ester carbonyls, including a lactone carbonyl and ketone.

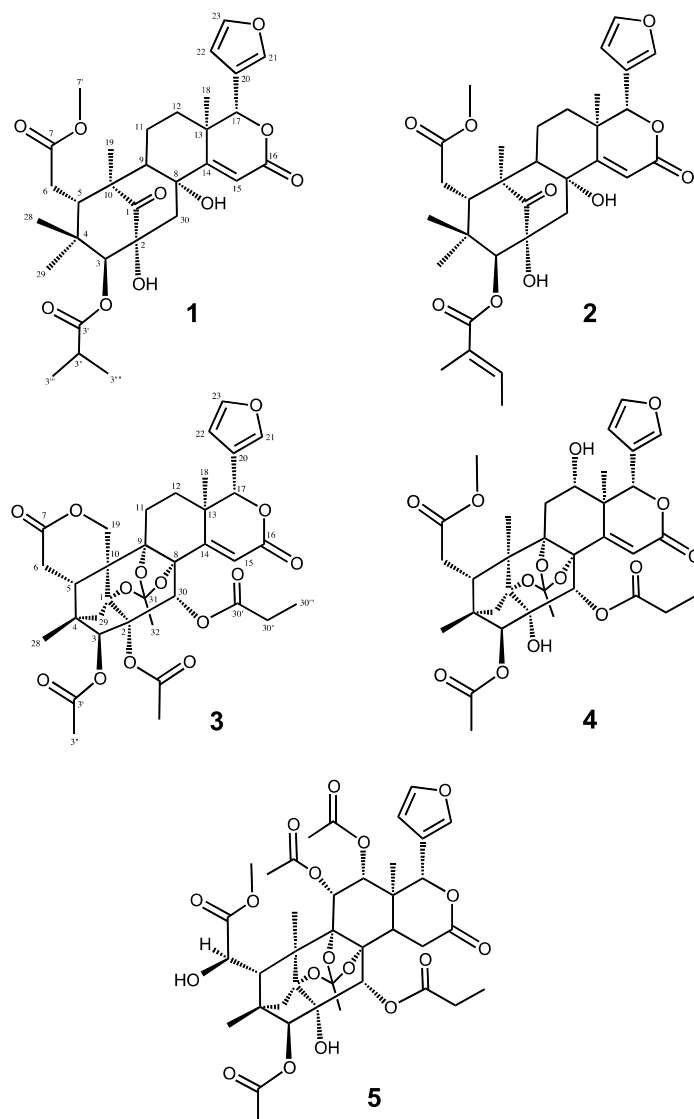


Figure 1. Chemical structures of Compounds 1–5.

Therefore, the remaining degrees of unsaturation required **1** to be pentacyclic. The ^1H - and ^{13}C -NMR spectra of **1** (Table 1) indicated the presence of four tertiary methyls (δ_{H} 0.69, 0.86, 1.23, 1.27 (each s)), a 2-methyl propanoyl (δ_{H} 1.25 and 1.27 (each 3H, d), 2.71 (1H, sept); δ_{C} 19.1 and 19.2 (each q), 34.3 (d), 176.2 (s)), methyl ester (δ_{H} 3.71 (s); δ_{C} 52.2 (q), 173.6 (s)), four methylenes (δ_{C} 20.7 (t), 32.9 (t), 33.7 (t), 45.0 (t)), four sp^3 methines, including two oxymethines (δ_{H} 4.80 (s), 5.16 (s)), a furan ring (δ_{H} 6.49 (dd), 7.44 (t), and 7.51 (brs)), an α,β -unsaturated δ -lactone (δ_{H} 5.16 (s), 6.18 (s); δ_{C} 78.8 (d), 116.3 (d), 167.5 (s)), five sp^3 quaternary carbons, including two oxycarbons (δ_{C} 72.8 (s), 76.7 (s)), and a ketone (δ_{C} 216.8 (s)). An analysis of the ^1H - ^1H COSY spectrum of **1** revealed the partial structures shown in bold face in Figure 2.

In the HMBC spectrum (Figure 2), cross-peaks were observed from Me-18 (δ_{H} 1.27 (s)) to C-12, C-13, C-14 (δ_{C} 164.7 (s)) and C-17 (δ_{C} 78.8 (d)), from Me-19 (δ_{H} 1.23 (s)) to C-1 (δ_{C} 216.8 (s)), C-5, C-9, and C-10, from H-5 (δ_{H} 3.36 (dd)) to C-4, C-6, C-7 (δ_{C} 173.6 (s)) and C-10, from H₂-30 (δ_{H} 2.51 and 3.55 (each d)) to C-1, C-2 (δ_{C} 76.7 (s)), C-3 (δ_{C} 85.5 (d)), C-8 (δ_{C} 72.8 (s)) and C-9 and from H-15 (δ_{H} 6.18 (s)) to C-8, C-13, C-14 (δ_{C} 164.7 (s)) and C-17. In the ^1H - ^1H COSY spectrum, (H-5–H₂-6; H-9–H₂-11–H₂-12;

H-22–H-23; H-3''–H-3''' and H-3''''') revealed the partial structure shown in Figure 2. Significant NOE interactions (Figure 2) were observed from H-3 (δ_{H} 4.80 (s))/Me-28, Me-29; H-5 (δ_{H} 3.36 (dd))/H-11 β , Me-28, H-30 β ; 2-OH (δ_{H} 4.05 (s))/H-12 α , Me-19; 8-OH (δ_{H} 2.81 (s))/H-9, H-12 α , Me-18; H-17 (δ_{H} 5.16 (s))/H-5, H-11 β , H-12 β and H-30 β , which indicated the α -orientation of H-3, H-9, Me-18, Me-19, 2-OH and 8-OH and the β -orientation of H-5 and H-17. Therefore, the relative structure of **1** was established as shown in Figure 1.

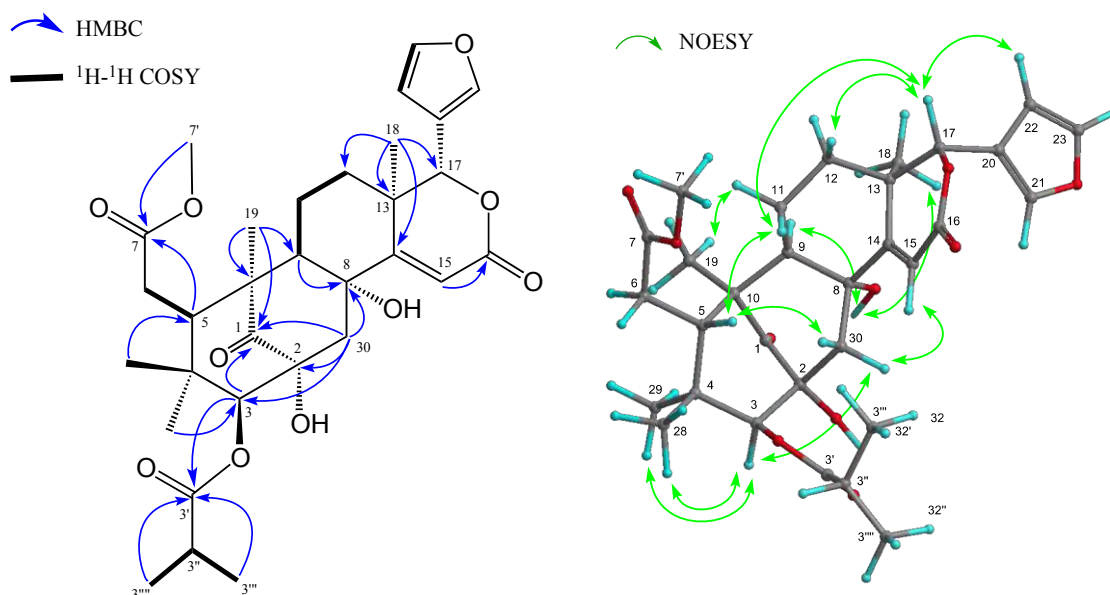


Figure 2. Key HMBC, COSY and NOESY correlations for carapanolide T (**1**).

Carapanolide U (**2**) was isolated as colorless needles and shown to have the molecular formula $\text{C}_{32}\text{H}_{40}\text{O}_{10}$ (m/z : 585.2701 [$\text{M} + \text{H}$] $^+$ (calcd for 585.2700) by HRFABMS. IR and UV spectra revealed the presence of hydroxy and ester groups and an $\alpha\beta$ -unsaturated δ -lactone at ν_{max} 3537, 1748 and 1719 cm^{-1} , and λ_{max} at 230 nm ($\log \epsilon$ 4.11). The ^1H - and ^{13}C -NMR spectra of **2** (Table 1) were very similar to those of **1**, except for the absence of the 2-methylpropanoyl group at C-3 and the presence of the tigroyl group at C-3. The relative structure of **2** was determined as shown in Figure 1.

Carapanolide L (**3**) was obtained as colorless crystals, and its molecular formula was established as $\text{C}_{35}\text{H}_{38}\text{O}_{14}$ ($[\text{M} + \text{H}]^+$; m/z 683.2335, calcd. for 683.2340) by HRFABMS, implying 17 on the index of hydrogen deficiency. IR and UV spectra revealed the presence of ester groups and an $\alpha\beta$ -unsaturated δ -lactone at ν_{max} 1748 and 1719 cm^{-1} and λ_{max} at 226 nm ($\log \epsilon$ 3.73). ^1H - and ^{13}C -NMR data indicated that eight out of the 17 units of unsaturation came from three carbon-carbon double bonds and five ester carbonyls, including two lactone carbonyls. Therefore, the remaining degrees of unsaturation required **3** to be non-acyclic. The ^1H - and ^{13}C -NMR spectra of **3** (Table 2) indicated the presence of two tertiary methyls (δ_{H} 1.02, 1.14 (each s)), two acetyls (δ_{H} 2.04 (s), 2.17 (s); δ_{C} 20.8 (q), 21.8 (q), 169.1 (s), 170.1 (s)), an *n*-propanoyl group (δ_{H} 1.07 (3H, t), 2.25 (1H, m), 2.29 (1H, m); δ_{C} 8.5 (q), 27.4 (t), 173.3 (s)), an orthoacetyl group (δ_{H} 1.68 (3H, s); δ_{C} 20.9 (q), 120.1 (s)), four methylenes, including an oxymethylene (δ_{H} 4.34 and 4.86 (each 1H, d), four sp^3 methines, including three oxymethines (δ_{H} 5.10 (s), 5.27 (s) and 5.78 (s)), a furan ring (δ_{H} 6.44 (dd), .44 (t) and 7.52 (brs)), seven sp^3 quaternary carbons, including four oxycarbonyls (δ_{C} 82.6, 83.9, 84.2, 84.6 (each s)), and two lactone carbonyl groups (δ_{C} 163.0 and 171.0 (each s)). An analysis of the ^1H - ^1H COSY spectrum of **3** revealed the partial structures shown in bold face in Figure 3. In the HMBC spectrum (Figure 3), cross-peaks were observed from Me-18 (δ_{H} 1.14 (s)) to C-12, C-13, C-14 (δ_{C} 159.6) and C-17 (δ_{C} 80.4), from Me-28 (δ_{H} 1.02 (s)) to C-3 (δ_{C} 81.3), C-4, C-5 and C-29, from H-30 (δ_{H} 5.78 (s)) to C-1 (δ_{C} 84.6 (s)), C-2 (δ_{C} 84.2 (s)), C-3, C-8 (δ_{C} 82.6 (s)) and C-9 (δ_{C} 83.9 (s)) and from H-15 (δ_{H} 6.05 (s))

to C-8, C-13, C-14 and C-16 (δ_C 163.0 (s)). Therefore, the planar structure of **3** was established as phragmalin-1,8,9-orthoacetate [13], and the positions of the two acetyls and an *n*-propyl group were located at C-2, C-3 and C-30, respectively, by detailed ^1H - ^1H COSY and HMBC correlations (Figure 3). In the NOESY spectrum, significant NOEs (Figure 3) were observed between H-3 and H-29 *pro-S*, H-30 and Me-28, between H-5 β (δ_H 2.72 (dd)) and H-12 β , Me-28 and H-30 between H-15 (δ_H 6.05 (s)) and H-17 β and H-30, between H-17 β (δ_H 5.10 (s)) and H-12 β , H-15, H-22 and H-30 β and between Me-18 (δ_H 1.14 (s)) and H-11 α , H-12 α and Me-32. Therefore, the relative structure of **3** was established as shown in Figure 1.

Table 1. ^1H - (600 MHz) and ^{13}C - (150 MHz) NMR spectroscopic data of compounds **1** and **2**.

Position	1		2				
	$^1\text{H}^a$ (J, Hz)	$^{13}\text{C}^b$	$^1\text{H}^a$ (J, Hz)	$^{13}\text{C}^b$			
1		216.8		216.7			
2		76.7		77.0			
3	4.80	s	85.5	4.88	s	85.8	
4			39.7			40.0	
5	3.36	dd (9.4, 1.5)	41.8	3.39	dd (7.9, 1.1)	41.8	
6	α	2.34	dd (17.3, 1.5)	32.9	2.37	m	32.9
	β	2.38	dd (17.3, 9.4)		2.34	m	
7			173.6			173.6	
8			72.8			72.9	
9	1.85	dd (13.3, 6.0)	60.2	1.87	t (5.6)	60.1	
10			47.9			47.8	
11	α	1.48	m	20.7	1.67	m	20.7
	β	1.52	m		1.53	m	
12	α	1.28	m	33.7	1.34	m	33.8
	β	2.00	ddd (14.1, 6.8, 3.6)		2.02	m	
13			38.5			38.5	
14			164.7			164.6	
15	6.18	s	116.3	6.16	s	116.3	
16			167.5			167.6	
17	5.16	s	78.8	5.18	s	79.8	
18	1.27	s	23.2	1.28	s	23.2	
19	1.23	s	18.3	1.24	s	18.4	
20			119.8			119.8	
21	7.51	brs	141.7	7.51	br s	141.7	
22	6.49	dd (2.1, 0.9)	110.4	6.49	m	110.4	
23	7.44	t (2.1)	143.1	7.44	t (1.4)	143.1	
28	0.69	s	22.3	0.70	s	22.4	
29	0.86	s	22.6	0.88	s	22.6	
30	α	2.51	d (16.0)	45.0	2.52	dd (14.9, 1.2)	45.0
	β	3.55	d (16.0)		3.58	d (14.9)	
3'			176.2			167.2	
3''	2.71	sept (6.7)	34.3			128.1	
3'''	1.25	d (6.7)	19.1	6.96	q (7.1)	138.8	
3''''	1.27	d (6.7)	19.2	1.88	d (7.1)	14.7	
3'''''				1.92	s	12.4	
7'	3.71	s	52.2	3.70	s	52.1	
2-OH	4.05	s					
8-OH	2.81	s					

^a Measured at 600 MHz in CDCl_3 . ^b Measured at 150 MHz in CDCl_3 .

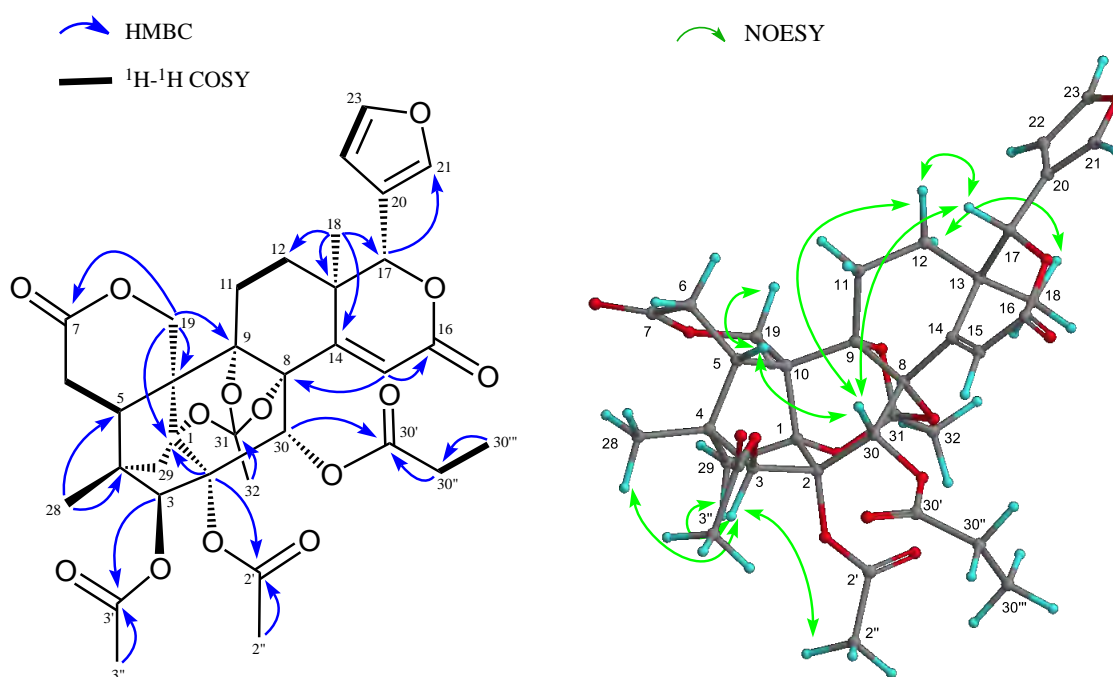


Figure 3. Key HMBC, COSY and NOESY correlations for carapanolide V (**3**).

Carapanolide W (**4**) was obtained as colorless crystals, and its molecular formula was established as $C_{34}H_{40}O_{14}$ ($[M + H]^+$; m/z 673.2492, calcd. for 673.2496) by HRFABMS. IR and UV spectra revealed the presence of hydroxy groups and ester groups and an α -unsaturated δ -lactone at ν_{\max} 3657, 1728 and 1698 cm^{-1} and λ_{\max} at 230 nm ($\log \epsilon$ 3.73). The ^1H - and ^{13}C -NMR spectra of **4** (Table 2) indicated the presence of three tertiary methyl groups (δ_{H} 0.74, 1.32, 1.48 (each s)), an acetyl (δ_{H} 2.09 (s); δ_{C} 21.7 (q), 169.1 (s)), an *n*-propanoyl group (δ_{H} 1.16 (3H, t), 2.45 (2H, m); δ_{C} 8.9 (q), 28.1 (t), 173.8 (s)), methyl ester (δ_{H} 3.71 (3H, s); δ_{C} 52.3 (q), 173.9 (s)), three methylene groups, five sp^3 methine groups, including four oxymethine groups (δ_{H} 3.86 (dd), 5.22 (s), 5.35 (s), 5.90 (s)), a furan ring (δ_{H} 6.61 (dd), 7.53 (br s), 7.64 (t)), seven sp^3 quaternary carbons, including four oxycarbons (δ_{C} 83.5 (s), 83.7 (s), 84.2 (s), 86.1 (s)), three ester carbonyls (δ_{C} 169.1 (s), 173.8 (s), 173.9 (s)) and an $\alpha\beta$ -unsaturated δ lactone (δ_{H} 6.62 (s), δ_{C} 123.7 (d), 163.5 (s)). Cross-peaks were observed in the HMBC spectrum, from Me-18 (δ_{H} 1.48 (s)) to C-12 (δ_{C} 66.6 (d)), C-13, C-14 (δ_{C} 153.8 (s)) and C-17 (δ_{C} 78.8 (d)), from Me-19 (δ_{H} 1.32 (s)) to C-1 (δ_{C} 84.2 (s)), C-5, C-9 (δ_{C} 86.1 (s)) and C-10, from H-15 (δ_{H} 6.62 (s)) to C-8 (δ_{C} 83.7 (s)), C-13, C-14 and C-16 (δ_{C} 163.5 (s)) and from H-30 (δ_{H} 5.35 (s)) to C-1 (δ_{C} 84.2 (s)), C-2 (δ_{C} 83.5 (s)), C-3 (δ_{C} 85.0 (d)), C-8 and C-9. The singlet oxymethine proton at δ_{H} 5.22 was assigned to C-3 through HMBC correlations to C-1, C-2, C-5, C-28, C-29, C-30 (δ_{C} 74.3 (d)) and C-3' (δ_{C} 169.1 (s)), while another singlet proton at δ_{H} 5.35, showing HMBC correlations to C-1, C-2, C-8, C-9, C-14 (δ_{C} 153.8 (s)) and C-30' (δ_{C} 173.8 (s)), was assigned to C-30. An oxymethine proton at δ_{H} 5.22 (dd) was assigned to C-12 through HMBC correlations to C-9, C-11, C-13, C-14, C-17 (δ_{C} 78.8 (d)) and C-18. In an analysis of the ^1H - ^1H COSY spectrum of **4**, H-5–H₂-6; H₂-11–H-12; H-22–H-23; H-30''–H-30''') revealed the partial structure. The relative configuration of **4** was established on the basis of NOE interactions. Significant NOE interactions were observed from H-5 (δ_{H} 2.11 (m))/H-11 β , H-30, Me-28; H-30 (δ_{H} 5.35 (s))/H-3, H-5, H-15; H-17 (δ_{H} 5.90 (s))/H-5, H-12 β , H-15, H-21, H-22, which indicated the α -orientation of H-3, Me-18 and Me-19 and the β -orientation of H-5, H-12, H-17 and H-30. Therefore, the relative structure of **4** was established as shown in Figure 1.

Table 2. ^1H - (600 MHz) and ^{13}C - (150 MHz) NMR spectroscopic data of compounds 3–5.

Position	3			4			5			
	$^1\text{H}^a$ (J, Hz)		$^{13}\text{C}^b$	$^1\text{H}^a$ (J, Hz)		$^{13}\text{C}^b$	$^1\text{H}^a$ (J, Hz) ^a		δ_{C}^b	
1			84.6			84.2			85.1	
2			84.2			83.5			79.6	
3	5.27	s	81.3	5.22	s	85.0	4.59	s	83.7	
4			46.4			44.6			45.5	
5	2.72	dd (4.7, 3.2)	33.8	2.11	m	39.9	3.30	brs	40.1	
6	α	2.64	dd (17.0, 3.2)	68.6	2.34	m	33.7	5.98	brs	71.5
	β	2.59	dd (17.0, 4.7)		2.36	m				
7			171.0			173.9			169.4	
8			82.6			83.7			84.8	
9			83.9			86.1			86.0	
10			46.9			48.1			46.2	
11	α	2.19	m	25.6	1.97	m	34.6	4.49	d (2.3)	69.4
	β	2.33	m		2.21	dd (14.7, 4.1)				
12	α	1.50	m	26.5	3.86	dd (13.5, 4.1)	66.6	4.48	d (2.3)	71.7
	β	1.64	m							
13			37.6			44.8			38.4	
14			159.6			153.8	2.79	dd (10.4, 0.6)	42.3	
15	6.05	s	121.0	6.62	s	123.7	2.90	dd (18.7, 10.4)	26.9	
							3.22	dd (18.7, 0.6)		
16			163.0			163.5			170.8	
17	5.10	s	80.4	5.90	s	78.8	5.98	s	76.9	
18	1.14	s	18.7	1.48	s	13.0	1.43	s	15.8	
19	α	4.86	d (14.0)	31.4	1.32	s	15.5	1.23	s	13.8
	β	4.34	d (14.0)							
20			119.4			121.4			120.9	
21	7.52	br s	141.4	7.53	br s	144.8	7.48	brs	141.0	
22	6.44	dd (1.7, 0.6)	109.7	6.61	dd (1.7, 0.9)	109.6	6.46	dd (1.8, 1.5)	110.9	
23	7.44	t (1.7)	143.3	7.64	t (1.7)	142.4	7.00	t (1.8)	143.1	
28	1.02	s	14.2	0.74	s	14.5	1.10	s	15.4	
29	<i>pro-R</i>	1.78	d (11.6)	39.2	1.72	d (11.5)	39.8	1.81	d (10.9))	39.9
	<i>pro-S</i>	2.38	d (11.6)		1.96	d (11.5)		2.06	d (10.9)	
30		5.78	s	68.1	5.35	s	74.3	6.01	s	69.8
31			120.1			119.7			119.3	
32	1.68	s	20.9	1.70	s	16.5	1.76	s	21.1	
2'			170.1							
2''	2.17	s	21.8							
3'			169.1			169.1			169.6	
3''	2.04	s	20.8	2.09	s	21.7	2.18	s	21.2	
7'				3.71	s	52.3	3.69	s	53.1	
11'									169.7	
11''							2.22	s	21.4	
12'									169.6	
12''							1.70	s	20.1	
30'			173.3			173.8			172.5	
30''	A	2.25	m	27.4	2.45	m	28.1	2.38	dq (11.2, 7.3)	27.9
	B	2.29	m					2.38	dq (11.2, 7.3)	
30'''		1.07	t (7.6)	8.5	1.16	t (7.7)	8.9	1.09	t (7.3)	8.6

^a Measured at 600 MHz in CDCl_3 . ^b Measured at 150 MHz in CDCl_3 .

Carapanolide X (**5**) was isolated as a colorless amorphous solid and had the molecular formula $\text{C}_{38}\text{H}_{46}\text{O}_{18}$ ($[\text{M} + \text{H}]^+$; m/z 791.2765, calcd. for 791.2763) as determined by HRFABMS. The IR spectrum showed the presence of a hydroxyl at ν_{max} 3352 cm^{-1} and ester groups at ν_{max} 1742 cm^{-1} . ^1H - and ^{13}C -NMR spectra (Table 2) indicated the presence of three methyls (δ_{H} 1.10, 1.23, 1.43 (each 3H, s)), three acetyl groups (δ_{H} 1.70, 2.18, 2.22 (each 3H, s)), a propanoyl group (δ_{H} 1.09 (3H, t), 2.38 (2H, dq), δ_{C} 172.5 (s)), a methoxycarbonyl group ((δ_{H} 3.69 (3H, s), δ_{C} 53.1 (q), 169.4 (s)), sp^3 methylene ((δ_{C} 26.9 (t)), δ -lactone (δ_{H} 5.98 (1H, s), δ_{C} 76.9 (d), 170.8 (s)), a tertiary hydroxyl group (δ_{C} 79.6 (s)), seven sp^3 methines, including five oxymethines (δ_{H} 4.48 (d), 4.49 (d), 4.59 (s), 5.98 (s)), seven sp^3 quaternary carbons, including four oxycarbons (δ_{C} 79.6 (s), 84.8 (s), 85.1 (s), 86.0 (s)), and a furan ring (δ_{H} 6.46 (dd), 7.00 (t), 7.48 (brs)). In the HMBC spectrum, cross-peaks were observed between Me-18 (δ_{H} 1.43 (s)) and C-12 (δ_{C} 71.7 (d)), C-13, C-14 and C-17 (δ_{C} 76.9 (d)), between Me-19

(δ_{H} 1.23 (s)) and C-1 (δ_{C} 85.1 (s)), C-5, C-9 (δ_{C} 86.0 (s)) and C-10, between Me-28 (δ_{H} 1.10 (s)) and C-3 (δ_{C} 83.7 (d)), C-4, C-5 and C-29 and between H-3 (δ_{H} 4.59 (s)) and C-1 and C-2 (δ_{C} 79.6 (s)), C-4, C-5, C-28, C-29, C-30 (δ_{C} 69.8 (d)) and C-3' (δ_{C} 169.6 (s)), between H-5 (δ_{H} 3.30 (brs)) and C-1, C-3, C-4, C-6 (δ_{C} 71.5 (d)), C-7 (δ_{C} 169.4 (s)), C-10, C-19, C-28 and C-29, between H-6 (δ_{H} 5.98 (brs)) and C-4, C-5, C-7 and C-10 and between H-30 (δ_{H} 6.01 (s)) and C-1, C-2, C-3, C-8 (δ_{C} 84.8 (s)), C-9 and C-30' (δ_{C} 172.5 (s)). In the ^1H - ^1H COSY spectrum, (H-5–H-6; H-11–H-12; H-14–H-15; H-22–H-23 and H-30''–H-30''') was observed. Therefore, the positions of two hydroxyls, a propanoyl and a methoxycarbonyl were located at C-2, C-6, C-30 and C-7, while three acetyl groups were located at C-3, C-11 and C-12, respectively (Figure 4). In the NOESY experiments, cross peaks (Figure 4) were observed between H-3 (δ_{H} 4.59 (s)) and H-29 *pro-S*, H-30 and Me-28, between H-5 (δ_{H} 3.30 (brs)) and Me-28 and H-30, between H-6 (δ_{H} 5.98 (brs)) and H-5 β and H-11, between H-11 (δ_{H} 4.49 (d)) and H-5 β and H-12, between H-12 (δ_{H} 4.48 (d)) and H-5 β , H-11 and H-17 β , between H-30 β (δ_{H} 6.01 (s)) and H-11 and H-12 and between Me-19 and H-6 and Me-32. Therefore, the propanoyl group at C-30 and acetoxy groups at C-11 and C-12 were all α , while the acetoxy group at C-3 had a β orientation. The configuration of C-6 was presumed to be *R*, which was the same as that of carapanolide N [17].

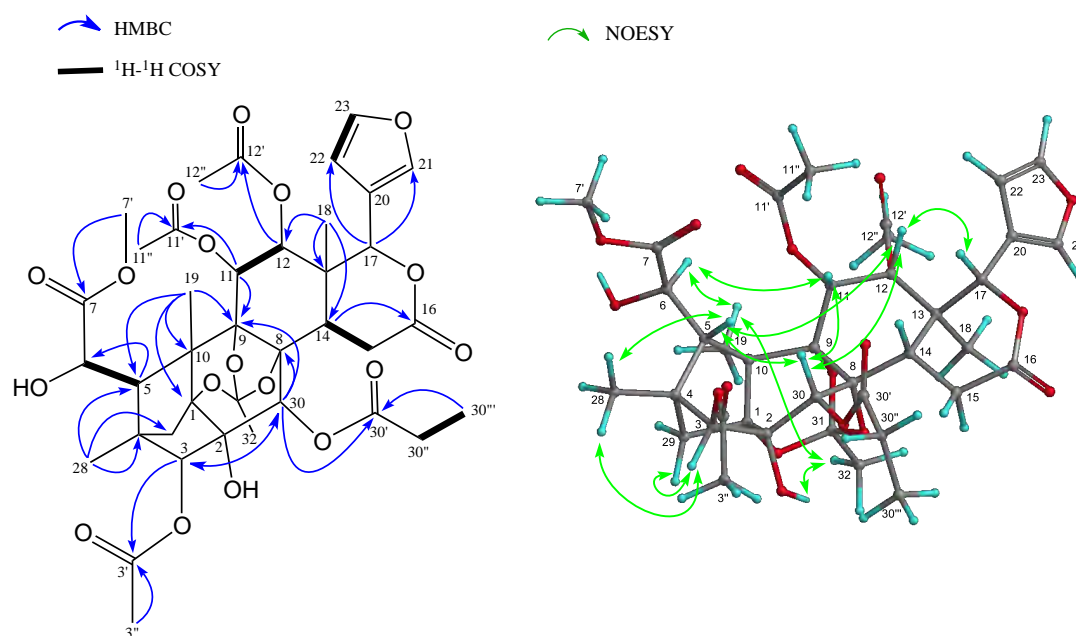


Figure 4. Key HMBC, COSY and NOESY correlations for carapanolide X (5).

Macrophages may be a potential therapeutic target for inflammatory diseases [18]. Activated macrophages release pro-inflammatory mediators, such as NO, reactive oxygen, interleukin-1 beta, tumor necrosis factor-alpha and other inflammatory mediators, which play important roles in biological defense. However, the overexpression of these mediators had been implicated in diseases, such as osteoarthritis, rheumatoid arthritis and diabetes, because the increased production of pro-inflammatory mediators has been shown to induce severe or chronic inflammation [18]. In the present study, four limonoids and *N*^G-monomethyl-L-arginine acetate (L-NMMA), an inducible nitric oxide synthase (iNOS) inhibitor, were evaluated for their inhibitory effects on NO production in LPS-stimulated RAW264.7 cells (Figure 5). To determine safe concentrations, the cytotoxicities of these limonoids against RAW 264.7 were assessed by the MTT assay. In the NO inhibitory assay, Compounds 1 and 2 exhibited comparable NO inhibitory activities (IC_{50} 1: 22.0 μM ; 2: 23.3 μM) to L-NMMA (IC_{50} 23.9 μM). Of these, 2 did not show cytotoxicities at 1–30 μM . Compound 1 exhibited low cytotoxicity at 30 μM , but not at the effective concentration, namely 10 μM . Compounds 3–5 did not exhibit inhibitory effects on macrophage activation (IC_{50} >30 μM). These

results suggested that Compounds 1 and 2 have potential as anti-inflammatory disease agents. In a previous study, we revealed inhibitory activities on NO production of a phragmalin-type limonoid, such as carapanolide J (IC_{50} 37.4 μ M) [16], and gedunin-type limonoids, such as 7-deacetoxy-7-oxogedunin (IC_{50} 12.8 μ M), 6 α -acetoxygedunin (IC_{50} 7.9 μ M), 6 α -hydroxygedunin (IC_{50} 19.1 μ M), 6 α -acetoxy-7 α -deacetoxy-7 α -hydroxygedunin (IC_{50} 9.4 μ M), gedunin (IC_{50} 4.6 μ M) and 7-deacetoxy-7-hydroxygedunin (IC_{50} 8.4 μ M), [19]. Compounds 1 and 2 exhibited stronger inhibitory activities on NO production than carapanolide J, however weaker than the gedunin-type limonoids. These data suggest that gedunin-type limonoids are more effective for the inhibition of NO production than phragmalin-type ones in general.

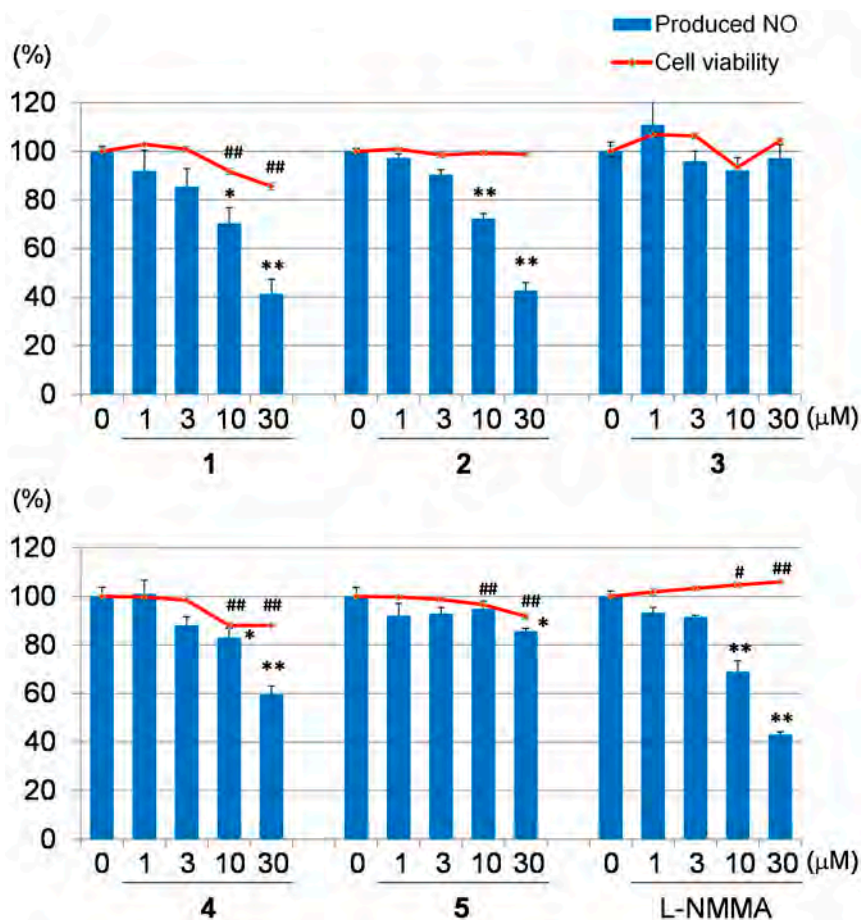


Figure 5. Inhibitory activities on NO production and cytotoxicities of Compounds 1–5 and L-NMMA. Each value represents the mean \pm the standard error (S.E.) of four determinations. Significant differences from the vehicle control (0 μ M) group shown as * $p < 0.05$ and ** $p < 0.01$ in the NO inhibitory assay and # $p < 0.05$ and ## $p < 0.01$ in the cytotoxicity assay.

3. Experimental Section

3.1. General Procedures

Melting points were determined on a Yanagimoto micro-melting point apparatus and were uncorrected. Optical rotations were measured using a JASCO DIP-1000 digital polarimeter. IR spectra were recorded using a Perkin-Elmer 1720X FTIR spectrophotometer (Perkin-Elmer Inc., Wellesley, MA, USA). ^1H - and ^{13}C -NMR spectra were obtained on an Agilent vnmrs 600 spectrometer (Agilent Technologies, Santa Clara, CA, USA) with standard pulse sequences, operating at 600 and 150 MHz, respectively. CDCl_3 was used as the solvent and TMS as the internal standard. FABMS

were recorded on a JEOL-7000 mass spectrometer (JEOL, Tokyo, Japan). Column chromatography was performed over silica gel (70–230 mesh, Merck, Darmstadt, Germany), while medium pressure liquid chromatography (MPLC) was conducted with silica gel (230–400 mesh, Merck). HPLC was run on a JASCO PU-1586 instrument (JASCO, Tokyo, Japan) equipped with a differential refractometer (RI 1531). Fractions obtained from column chromatography were monitored by TLC (silica gel 60 F₂₅₄, Merck).

3.2. Plant Material

The oil of (2.03 kg) *Carapa guianensis* AUBLET (Meliaceae) was collected in the Amazon, Brazil, in March 2013, and was kindly provided by Mr. Akira Yoshino (who is a representative of the “NGO Green Heart Love Amazon Project”). A voucher specimen (CGS-01-2) was deposited in the Herbarium of the Laboratory of Medicinal Chemistry, Osaka University of Pharmaceutical Sciences.

3.3. Isolation of Compounds 1–5

The seed oil of *Carapa guianensis* AUBLET (Meliaceae) (2.03 kg) was dissolved in CHCl₃, and the CHCl₃ solution was subjected to CC (silica gel 14 kg), affording 7 fractions: Fraction A (fraction (Fr.) No. 1–85, 1.512 kg) was eluted with *n*-hexane-CHCl₃ = 1:1; B (Fr. No. 86–179, 229.1 g) was eluted with CHCl₃; C (Fr. No. 180–20, 29.3 g) was eluted with CHCl₃-EtOAc = 5:1; D (Fr. No. 221–225, 13.2 g) was eluted with CHCl₃-EtOAc = 2:1; E (Fr. No. 226–265, 84.5 g) was eluted with CHCl₃-EtOAc = 2:1; F (Fr. No. 266–290, 25.3 g) was eluted with EtOAc; G (Fr. No. 291–315, 72.8 g) was eluted with EtOAc:MeOH = 5:1; and H (Fr. No. 316–333, 45.4 g) was eluted with MeOH. Residue D was rechromatographed over a silica gel column (CC) (230–400 mesh, 300 g) eluted with *n*-hexane-EtOAc (1:1) to give 13 fractions: D1 (Fr. No. 1–35, 1.52 g), D2 (Fr. No. 36–49, 0.81 g), D(3) (Fr. No. 50–88, 0.70 g), D(4) (Fr. No. 89–115, 0.53 g), D(5) (Fr. No. 116–130, 0.60 g), D(6) (Fr. No. 131–140, 0.52 g), D(7) (Fr. No. 141–205, 0.47 g), D(8) (Fr. No. 206–215, 0.51 g), D(9) (Fr. No. 216–220, 0.42 g), D(10) (Fr. No. 221–240, 0.40 g), D(11) (Fr. No. 241–250, 1.11 g) and D(12) (Fr. No. 251–313, 1.36 g). Fraction D(6) was subjected to CC (230–400 mesh, 40 g) eluted with *n*-hexane-EtOAc (3:1) to give an amorphous solid (24.1 mg) that was separated by HPLC (ODS, 75% MeOH, at 25 °C, flow rate 4.0 mL min⁻¹, UV = 220 nm, column 250 × 20 mm i.d., 5 μm) to give Compounds 2 (6.2 mg) and 3 (1.8 mg). Fraction D(8) was subjected to CC (230–400 mesh, 40 g) eluted with *n*-hexane-EtOAc (3:1) to give an amorphous solid (34.0 mg), which was subsequently subjected to CC (230–400 mesh, 40 g) eluted with *n*-hexane-EtOAc (3:1) to give an amorphous solid that was purified by HPLC (ODS, 75% MeOH, at 25 °C, flow rate 4.0 mL·min⁻¹, UV = 220 nm, column 250 × 20 mm i.d., 5 μm) to give Compounds 1 (7.50 mg) and 4 (3.8 mg). Fraction D(9) was subjected to CC (230–400 mesh, 30 g) eluted with *n*-hexane-EtOAc (3:1) to give an amorphous solid (25.5 mg), which was subsequently separated by HPLC (ODS, 70% MeOH, at 25 °C, flow rate 4.0 mL·min⁻¹, UV = 220 nm, column 250 × 20 mm i.d., 5 μm) to give Compound 5 (6.3 mg).

3.4. Analytical Data

Compound 1: Colorless crystals; mp 83–85 °C; $[\alpha]_D^{25} +16.6^\circ$ (*c* 0.1, CHCl₃); HRFABMS *m/z*: 573.2719 [M + H]⁺ (C₃₁H₄₁O₁₀, calcd for 573.2720); UV (EtOH) λ_{max} nm (log ε): 230 (3.85); IR (KBr) ν_{max} cm⁻¹: 3462 (OH), 2970, 1727 (O=C=O), 1649 (C=C-C=O), 1461; ¹H- and ¹³C-NMR, see Table 1. FABMS *m/z* (relative intensity (rel. int.)): 573 ([M + H]⁺, 100), 555 (11), 485 (20).

Compound 2: Colorless crystals; mp 133–136 °C; $[\alpha]_D^{25} -18.1^\circ$ (*c* 0.1, EtOH); HRFABMS *m/z*: 585.2701 [M + H]⁺ (C₃₂H₄₁O₁₀, calcd for 585.2700); UV λ_{max} (EtOH) nm (log ε): 230 (4.11); IR (KBr) ν_{max} cm⁻¹: 3537 (OH), 1748, 1719; ¹H- and ¹³C-NMR, see Table 1. FABMS *m/z* (rel. int.): 607 (3) [M + Na]⁺, 585 (6), [M + H]⁺, 567 (6), 485 (7), 83 (100).

Compound 3: Colorless crystals; mp 181–184 °C; $[\alpha]_D^{25} -74^\circ$ (*c* 0.4, EtOH); HRFABMS *m/z*: 683.2335 [M + H]⁺ (C₃₅H₃₈O₁₄, calcd for 683.2340); UV λ_{max} (EtOH) nm (log ε): 226 (3.73); IR (KBr) ν_{max} cm⁻¹:

1748, 1719; ^1H - and ^{13}C -NMR, see Table 1. FABMS m/z (rel. int.): 683 (100) $[\text{M} + \text{H}]^+$, 641 (5), 586 (7), 507 (7), 95 (21).

Compound 4: Colorless crystals; mp 144–146 °C; $[\alpha]_D^{25} +43.3^\circ$ (c 0.1, CHCl_3); HRFABMS m/z : 673.2492 $[\text{M} + \text{H}]^+$ ($\text{C}_{34}\text{H}_{41}\text{O}_{14}$, calcd for 673.2496); UV λ_{max} (EtOH) nm (log ϵ): 230 (3.73); IR (KBr) ν_{max} cm^{-1} : 3657 (OH), 1728, 1698; ^1H - and ^{13}C -NMR, see Table 1. FABMS m/z (rel. int.): 695 (6) $[\text{M} + \text{Na}]^+$, 673 (47) $[\text{M} + \text{H}]^+$, 613 (10), 599 (100).

Compound 5: Colorless amorphous; $[\alpha]_D^{25} -46.8^\circ$ (c 0.1, CHCl_3); HRFABMS m/z : 791.2765 $[\text{M} + \text{H}]^+$ ($\text{C}_{38}\text{H}_{47}\text{O}_{18}$, calcd for 791.2763); UV λ_{max} (EtOH) nm (log ϵ): 208 (1.26), IR (KBr) ν_{max} cm^{-1} : 3352 (OH), 1742 (O=C=O); ^1H - and ^{13}C -NMR, see Table 2. FABMS m/z (rel. int.): 791 $[\text{M} + \text{H}]^+$ (55), 735 (5), 95 (54), 43 (100), 329 (14), 176 (47).

3.5. Determination of RAW264.7 Cell Proliferation

RAW264.7 cell proliferation was examined according to a method reported previously [20] with few modifications. Briefly, RAW264.7 cells (5×10^4 cells in 100 μL) were seeded onto 96-well microplates and incubated for 24 h. D-MEM (100 μL) containing test samples (final concentration of 100, 30, 10 or 3 μM) dissolved in DMSO (final concentration 0.2%) was added. After the cells had been treated for 24 h, the MTT solution was added. After 3 h of incubation, 20% sodium dodecyl sulfate (SDS) in 0.1 M HCl was added to dissolve the formazan produced by the cells. The absorbance of each well was read at 570 nm using a microplate reader. The optical density of vehicle control cells was assumed to be 100%.

3.6. Inhibitory Assay of NO Production

An inhibitory assay of nitric oxide production was performed according to a method reported previously [16] with slight modifications. Briefly, RAW264.7 cells (5×10^4 cells in 100 μL) were seeded onto 96-well microplates and incubated for 24 h. D-MEM (100 μL) containing test samples (final concentration of 100, 30, 10 or 3 μM) dissolved in DMSO (final concentration 0.2%) and LPS (final concentration of 5 $\mu\text{g}/\text{mL}$) were added. After cells had been treated for 24 h, 50 μL of 0.1% *N*-(1-naphthyl)ethylenediamine in H_2O and 50 μL of 1% sulfanilamide in 5% phosphoric acid were added. After being incubated for 30 min, the absorbance of each well was read at 570 nm using a microplate reader. The optical density of vehicle control cells was assumed to be 100%.

4. Conclusions

Two novel mexicanolide-type limonoids, carapanolides T–U (1–2), as well as three novel phragmalin-type limonoids, carapanolides V–X (3–5), were isolated from the seeds of *Carapa guianensis* (andiroba). Their structures were determined by spectroscopic analyses. Compounds 1 and 2 were mexicanolide-type limonoids that had OH in C-2 and C-8. Compounds 3–5 were phragmalin-type limonoids that were highly oxidized.

In the NO inhibitory assay, Compounds 1 and 2 exhibited similar NO inhibitory activities (IC_{50} 1: 22.0 μM ; 2: 23.3 μM) against L-NMMA (IC_{50} 23.9 μM). Compound 1 did not exhibit cytotoxicity at 1–30 μM , while Compound 2 exhibited low cytotoxicity at 30 μM , but not at an effective concentration at 10 μM . These results suggest that Compounds 1 and 2 have potential as anti-inflammatory disease agents.

Acknowledgments: We thank Mihoyo Fujitake (this university) for MS measurements.

Author Contributions: R. Tanaka prepared the manuscript. T. Miyake, S. Ishimoto, N. Ishimatsu and K. Higuchi contributed to the isolation and structure elucidation. K. Minoura conducted NMR measurement. T. Kikuchi performed evaluation of bioactivities. T. Yamada and O. Muraoka supervised whole research project.

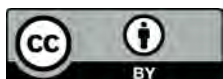
Conflicts of Interest: The authors declare no conflict of interest.

References

1. Tan, Q.G.; Luo, X.D. Meliaceous limonoids: Chemistry and biological activities. *Chem. Rev.* **2011**, *111*, 7437–7522. [[CrossRef](#)] [[PubMed](#)]
2. Fang, X.; Di, Y.T.; Hao, X.J. The advances in the limonoid chemistry of the Meliaceae family. *Curr. Org. Chem.* **2011**, *15*, 1363–1391.
3. Liao, S.G.; Chen, H.D.; Yue, J.M. Plant orthoesters. *Chem. Rev.* **2009**, *109*, 1092–1140. [[CrossRef](#)] [[PubMed](#)]
4. Prophiro, J.S.; da Silva Mario, A.N.; Kanis, L.A.; da Rocha, L.C.B.P.; Duque-Luna, J.E.; da Silva, O.S. First report on susceptibility of wild *Aedes aegypti* (Diptera: Culicidae) using *Carapa guianensis* (Meliaceae) and *Copaifera* sp. (Leguminosae). *Parasitol. Res.* **2012**, *110*, 699–705. [[CrossRef](#)] [[PubMed](#)]
5. Penido, C.; Costa, K.A.; Pennaforte, R.J.; Costa, M.F.S.; Pereira, J.F.G.; Siani, A.C.; Henriques, M.G.M.O. Anti-allergic effects of natural tetranortriterpenoids isolated from *Carapa guianensis* Aublet on allergen-induced vascular permeability and hyperalgesia. *Inflamm. Res.* **2005**, *54*, 295–303. [[CrossRef](#)] [[PubMed](#)]
6. Nayak, B.S.; Kanhai, J.; Milne, D.M.; Pereira, L.P.; Swanston, W.H. Experimental Evaluation of Ethanolic Extract of *Carapa guianensis* L. Leaf for Its Wound Healing Activity Using Three Wound Models. *Evid. Based Complement. Altern. Med.* **2011**, *2011*. [[CrossRef](#)] [[PubMed](#)]
7. Penido, C.; Conte, F.P.; Chagas, M.S.S.; Rodrigue, C.A.B.; Pereira, J.F.G.; Henriques, M.G.M.O. Antiinflammatory effects of natural tetranortriterpenoids isolated from *Carapa guianensis* Aublet on zymosan-induced arthritis in mice. *Inflamm. Res.* **2006**, *55*, 457–464. [[CrossRef](#)] [[PubMed](#)]
8. Nayak, B.S.; Kanhai, J.; Milne, D.M.; Swanston, W.H.; Mayers, S.; Eversley, M.; Rao, A.V. Investigation of the wound healing activity of *Carapa guianensis* L. (Meliaceae) bark extract in rats using excision, incision, and dead space wound models. *J. Med. Food.* **2010**, *13*, 141–146. [[CrossRef](#)] [[PubMed](#)]
9. Bickii, J.; Njifutie, N.; Foyere, J.A.; Basco, L.K.; Ringwald, P.J. *In vitro* antimalarial activity of limonoids from *Khaya grandifoliola* C.D.C. (Meliaceae). *J. Ethnopharmacol.* **2000**, *69*, 27–33. [[CrossRef](#)]
10. Ferraris, F.K.; Rodrigues, R.; da Silva, V.P.; Figueiredo, R.; Penido, C.; Henriques, M.G.M.O. Modulation of T lymphocyte and eosinophil functions *in vitro* by natural tetranortriterpenoids isolated from *Carapa guianensis* Aublet. *Int. Immunopharmacol.* **2011**, *11*. [[CrossRef](#)] [[PubMed](#)]
11. Miranda, J.R.N.C.; Dolabela, M.F.; da Silva, M.N.; Povoá, M.M.; Maia, J.G.S. Antiplasmodial activity of the andiroba (*Carapa guianensis* Aublet., Meliaceae) oil and its limonoid-rich fraction. *J. Ethnopharmacol.* **2012**, *142*, 679–683. [[CrossRef](#)] [[PubMed](#)]
12. Costa-Silva, H.; Lima, C.R.; Silva, E.J.R.; Araujo, A.V.; Fraga, M.C.C.R.; Ribeiro, E.; Ribwiro, A.; Arruda, A.C.; Lafayette, S.S.L.; Wanderley, J. Acute and subacute toxicity of the *Carapa guianensis* Aublet (Meliaceae) seed oil. *J. Ethnopharmacol.* **2008**, *116*, 495–500. [[CrossRef](#)] [[PubMed](#)]
13. Inoue, T.; Nagai, Y.; Mitooka, A.; Ujike, R.; Muraoka, O.; Yamada, T.; Tanaka, R. Carapanolides A and B: Unusual 9,10-*seco*-mexicanolides having a 2R,9S-oxygen bridge From the seeds of *Carapa guianensis*. *Tetrahedron Lett.* **2012**, *53*, 6685–6688. [[CrossRef](#)]
14. Inoue, T.; Matsui, Y.; Kikuchi, T.; In, Y.; Yamada, T.; Muraoka, O.; Matsunaga, S.; Tanaka, R. Guianolides A and B, New Carbon Skeletal Limonoids from the seeds of *Carapa guianensis*. *Org. Lett.* **2013**, *15*, 3018–3021. [[CrossRef](#)] [[PubMed](#)]
15. Inoue, T.; Matsui, Y.; Kikuchi, T.; In, Y.; Muraoka, O.; Yamada, T.; Tanaka, R. Carapanolides C–I from the seeds of andiroba (*Carapa guianensis*, Meliaceae). *Fitoterapia* **2014**, *96*, 56–64. [[CrossRef](#)] [[PubMed](#)]
16. Matsui, Y.; Kikuchi, T.; Inoue, T.; Muraoka, O.; Yamada, T.; Tanaka, R. Carapanolides J–L from the Seeds of *Carapa guianensis* (Andiroba) and Their Effects on LPS-Activated NO Production. *Molecules* **2014**, *19*, 17130–17140. [[CrossRef](#)] [[PubMed](#)]
17. Inoue, T.; Matsui, Y.; Kikuchi, T.; Yamada, T.; In, Y.; Muraoka, O.; Sakai, C.; Ninomiya, K.; Morikawa, T.; Tanaka, R. Carapanolides M–S from seeds of andiroba (*Carapa guianensis*, Meliaceae) and triglyceride metabolism-promoting activity in high glucose-pretreated HepG2 cells. *Tetrahedron* **2015**, *71*, 2753–2760. [[CrossRef](#)]
18. Zhang, Y.; Liu, C.; Dong, B.; Ma, X.; Hou, L.; Cao, X.; Wang, C. Anti-inflammatory Activity and Mechanism of Surfactin in Lipopolysaccharide-Activated Macrophages. *Inflammation* **2015**, *38*, 756–764. [[CrossRef](#)] [[PubMed](#)]

19. Sakamoto, A.; Tanaka, Y.; Yamada, T.; Kikuchi, T.; Muraoka, O.; Ninomiya, K.; Morikawa, T.; Tanaka, R. Andriolides W-Y from the Flower Oil of Andiroba (*Carapa guianensis*, Meliaceae). *Fitoterapia* **2015**, *100*, 81–87. [[CrossRef](#)] [[PubMed](#)]
20. Yamada, T.; Muroga, Y.; Jinno, M.; Kajimoto, T.; Usami, Y.; Numata, A.; Tanaka, R. New class azaphilone produced by a marine fish-derived *Chaetomium globosum*. The stereochemistry and biological activities. *Bioorg. Med. Chem.* **2011**, *19*, 4106–4113. [[CrossRef](#)] [[PubMed](#)]

Sample Availability: Samples of the compounds are not available from the authors.



© 2015 by the authors; licensee MDPI, Basel, Switzerland. This article is an open access article distributed under the terms and conditions of the Creative Commons by Attribution (CC-BY) license (<http://creativecommons.org/licenses/by/4.0/>).



Anthcolorins A–F, novel cytotoxic metabolites from a sea urchin-derived *Aspergillus versicolor*



Kyoko Nakanishi^a, Mitsunobu Doi^a, Yoshihide Usami^a, Taro Amagata^b,
Katsuhiko Minoura^a, Reiko Tanaka^a, Atsushi Numata^{a,†}, Takeshi Yamada^{a,*}

^a Osaka University of Pharmaceutical Sciences, 4-20-1 Nasahara, Takatsuki, Osaka 569-1094, Japan

^b Department of Chemistry and Biochemistry, San Francisco State University, San Francisco, CA 94132, USA

ARTICLE INFO

Article history:

Received 11 March 2013

Received in revised form 1 April 2013

Accepted 2 April 2013

Available online 8 April 2013

Keywords:

Anthcolorins

Aspergillus versicolor

Growth inhibition

Sea urchin

An X-ray crystal-structure analysis

Marine organisms

ABSTRACT

Anthcolorins A–F were isolated from a strain of *Aspergillus versicolor* originally isolated from the sea urchin *Anthocidaris crassispana*, and their absolute stereostructures were elucidated on the basis of spectroscopic analyses, including 1D and 2D NMR techniques, an X-ray crystal-structure analysis and CD spectra. These compounds were unique tetrahydropyrane diterpene type metabolites with oxoindoline at C-3, and some of them exhibited significant growth inhibition against cultured P388 cells.

© 2013 Elsevier Ltd. All rights reserved.

1. Introduction

Marine microorganisms are potentially prolific sources of highly bioactive secondary metabolites that might serve as useful leads in the development of new pharmaceutical agents. Based on the fact that some of the bioactive materials isolated from marine animals have been produced by bacteria, we have focused our attention on new antitumor agents from microorganisms separated from marine organisms.^{1–6} As part of this study, we have examined metabolites from the fungus *Aspergillus versicolor* OUPS-N136 originally obtained from the sea urchin *Anthocidaris crassispana*, and isolated six new compounds having a tetrahydropyrane diterpene core. These compounds were designated anthcolorins A–F (1–6).⁷ Diterpene with indole isolated from fungal strain has structural variations and unique bioactivities, and the examination of the biosynthesis is proceeded.^{8–10} As a difference point from indole diterpenes reported previously, 1–6 isolated in this study have an *N*-substituted oxoindoline. In addition, some of them exhibited significant cytotoxic activity against the murine P388

leukemia cell line. We describe herein the elucidation of the absolute stereostructure and biological activities of these compounds.

2. Results and discussion

A microorganism from the sea urchin *A. crassispana* was cultured at 27 °C for 6 weeks in a medium (40 L) containing 2% D-glucose, 1% peptone and 0.5% yeast extract in artificial seawater adjusted to pH 7.5. After incubation, the MeOH extract of the fungal strain was purified by bioassay-directed fractionation (cytotoxicities to P388 cell line) employing a stepwise combination of Sephadex LH-20, silica gel column chromatography, and reverse-phase HPLC to afford anthcolorins A–F (1–6) (Fig. 1).

Anthcolorin A (1) had the molecular formula C₃₃H₄₇NO₃ as established by the [M]⁺ peak in high-resolution electron impact mass spectrometry (HREIMS). Its IR spectrum exhibited bands at 3436, 1703, 1611, and 1596 cm⁻¹, which are characteristic of hydroxy groups, amido groups, and aromatic rings. The UV spectrum showed absorption for the oxoindoline at 207 (log ε 4.37), 252 (3.84), and 282 (3.11) nm. Close inspection of the ¹H and ¹³C NMR spectra (Table 1) in DEPT and HMQC experiments revealed the presence of six tertiary methyls (C-15–C-18, C-33, and C-34), seven sp³-hybridized methylenes (C-1, C-2, C-6, C-7, C-11, C-12, and C-20), five sp³-methines (C-3, C-8, C-10, C-13, and C-21) including two oxygen-bearing carbons (C-8, and C-18), four quaternary sp³-

* Corresponding author. Tel.: +81 72 690 1085; fax: +81 72 690 1084; e-mail address: yamada@gly.oups.ac.jp (T. Yamada).

† Deceased.

carbons (C-5, C-9, C-14, and C-30) including one oxygen-bearing carbon (C-14) and one nitrogen-bearing carbon (C-30), two terminal methylenes (C-4, C-19, C-31, and C-32), one amido carbonyl (C-22), and a 1,2-substituted benzene (C-24–C-29). ^1H – ^1H COSY analysis of **1** yielded five partial structural units as shown by boldfaced lines in Fig. 2. The connection of these units and the remaining functional groups were determined on the basis of the key HMBC data summarized in Fig. 2. The fragmentation in EIMS {214 [a] $^+$, 201 [b+H] $^+$ and 145 [c] $^+$ } supported the structure of the oxindoline moiety; i.e., the connection of a vinyl isopropyl group (Fig. 2). Thus, the planar structure of **1** was elucidated, as shown in Fig. 1.

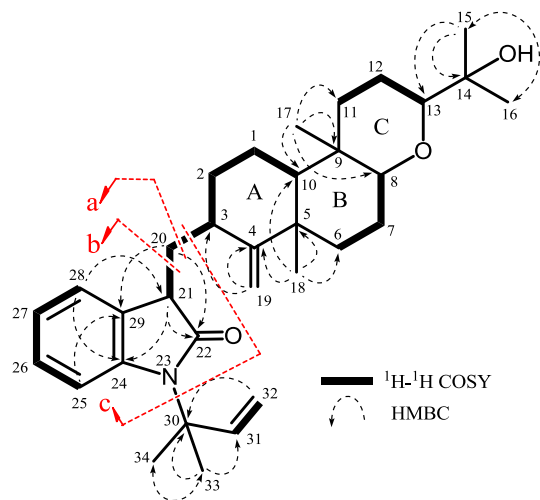


Fig. 2. Selected ^1H – ^1H COSY and HMBC correlations of **1**.

In the NOESY experiment, NOE correlations for the 1,3-diaxial arrangement (H-8/H-6 α , H-10, H-11 α , and H-13; H-17/H-7 β , H-12 β , and H-18) revealed that the ring juncture for the B and C rings was trans, and both rings existed in a chair conformation (Fig. 3). On the other hand, NOE correlations in the A ring (H-18/H-1 β , H-3, H-7 β , and H-17; H-10/H-2 α , and H-8) implied that the ring juncture for the A and B rings was trans, and the A ring existed in a half-chair conformation. The above evidence indicated the relative configuration for the tetrahydropyrene diterpene core (Fig. 3). In addition, the stereochemistry for C-21, the chiral center in the indoline moiety, was established by an X-ray crystal-structure analysis for a single crystal of **1** (obtained by recrystallization from $\text{CH}_2\text{Cl}_2/\text{MeOH}$) (Fig. 4). The result supported the conformation and relative configuration for **1**, revealed by NOE correlations. As described later, the comparison between **1** and **5** in CD spectra allowed assignment of the absolute configuration of all the asymmetric centers (3S, 8S, 9S, 10R, 13S, and 21R) in **1** (Fig. 5); i.e., negative ($\Delta\epsilon_{282} -1.2$ and $\Delta\epsilon_{252} -3.6$) Cotton effects observed in **1** indicated 21R configuration.

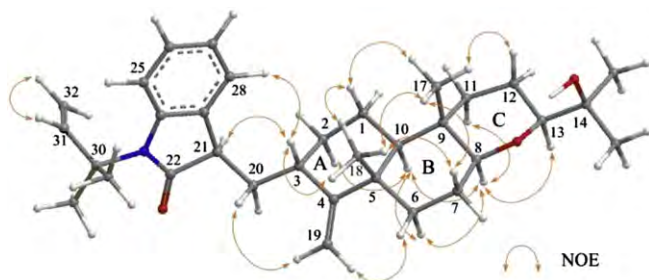


Fig. 3. Key NOE correlations of **1**.

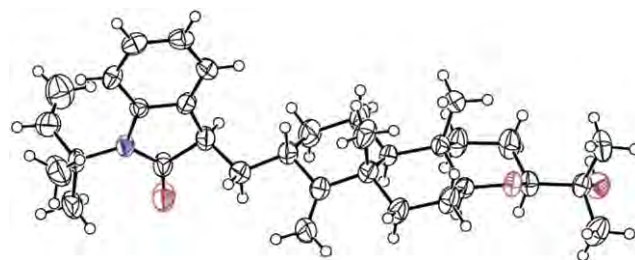


Fig. 4. ORTEP drawing of the X-ray structure for **1**.

Antholorin B (**2**) was assigned the same molecular formula as **1** based on HREIMS data. The general features of its UV, IR, and NMR spectra (Table 1) closely resembled those of **1** except for some of the ^1H and ^{13}C NMR signals [H-2 β ($\Delta\delta_{\text{H}}$ 0.15), H-3 ($\Delta\delta_{\text{H}}$ 0.09), H-19A ($\Delta\delta_{\text{H}}$ 0.12), H-20A ($\Delta\delta_{\text{H}}$ 0.22), H-20B ($\Delta\delta_{\text{H}}$ 0.33), C-2 ($\Delta\delta_{\text{C}}$ 0.8), C-4 ($\Delta\delta_{\text{C}}$ 0.5), and C-19 ($\Delta\delta_{\text{C}}$ 0.5)]. ^1H – ^1H COSY and HMBC experiments led to the elucidation of the planar structure of **2**, which was the same as that of **1**. We inferred from the differences in NMR chemical shifts from those of **1** that **2** was the stereoisomer at C-3 of **1**, however, NOE correlations (H-3/H-18 and H-3/H-1 β) excluded this possibility. A detailed examination of NOESY led to the finding that the relative configuration for the tetrahydropyrene diterpene core was the same as that of **1**, and NOE correlations (H-28/H-2 β and H-28/H-19A) observed in **1** had disappeared in **2**. The above evidence suggested that **2** was the epimer at C-21 of **1**, while explained the differences in NMR chemical shifts and NOE correlations between **1** and **2**, and so we established the absolute stereostructure of **2** as 3S, 8S, 9S, 10R, 13S, and 21S. In the CD spectra of **2**, positive ($\Delta\epsilon_{280} +1.2$) and negative ($\Delta\epsilon_{250} -1.8$) Cotton effects were observed, which showed S configuration at C-21 (Fig. 5).

Antholorins C (**3**) and D (**4**) were assigned the molecular formula $\text{C}_{33}\text{H}_{47}\text{NO}_3$, which had the same molecular formula as **1** and **2**. The general spectral features of **3** closely resembled those of **1** except for the NMR signals for the C ring and the hydroxy isopropyl group [H-8 ($\Delta\delta_{\text{H}}$ 0.53), H-11 α ($\Delta\delta_{\text{H}}$ 0.39), H-11 β ($\Delta\delta_{\text{H}}$ 0.29), H-12 α ($\Delta\delta_{\text{H}}$ 0.37), H-12 β ($\Delta\delta_{\text{H}}$ 0.09), H-13 ($\Delta\delta_{\text{H}}$ 0.45), C-8 ($\Delta\delta_{\text{C}}$ 8.0), C-9 ($\Delta\delta_{\text{C}}$ 0.6), C-10 ($\Delta\delta_{\text{C}}$ 0.9), C-11 ($\Delta\delta_{\text{C}}$ 2.1), C-12 ($\Delta\delta_{\text{C}}$ 2.0), C-13 ($\Delta\delta_{\text{C}}$ 7.1), C-14 ($\Delta\delta_{\text{C}}$ 1.7), C-15 ($\Delta\delta_{\text{C}}$ 1.3), and C-17 ($\Delta\delta_{\text{C}}$ 4.0)], while the same differences were found in the comparison of the NMR chemical shifts between **4** and **2** (Table 1). The analyses of ^1H – ^1H COSY and HMBC connectivities demonstrated that the planar structure of **3** and **4** was the same as that of **1** and **2**, respectively, therefore, we examined the NOESY spectra of **3** and **4**. NOE correlations (H-1 β /H-3, H-17, and H-18; H-10/H-6 α , and H-8) in **3** showed that the A and B rings existed in a chair conformation with H-1 β , H-3 β , H-17, and H-18 in coaxial arrangements. NOE correlations (H-17/H-13, H-8/H-11 α , H-12 α , H-15, and H-16) suggested that the C ring existed in a boat conformation with the hydroxy isopropyl group in the α -orientation. These features for NOE correlations in **3** were also observed in **4**. This evidence implied that **3** and **4** were epimers at C-13 of **1** and **2**, respectively.

The absolute configuration for **3** and **4** was deduced from the comparison of CD spectra with **5** and **6**, respectively. The negative Cotton effects ($\Delta\epsilon_{281} -0.9$ and $\Delta\epsilon_{252} -3.7$) in the CD spectrum of **3**, identical with those of **5**, showed the R configuration at the C-21 position in **3** (Fig. 5). This evidence together with NOE correlations (H-28/H-2 β and H-28/H-19A) revealed the absolute configuration for the stereogenic centers in **3** to be 3S, 8S, 9S, 10R, 13R, 21R. On the other hand, the CD Cotton effects of **4** ($\Delta\epsilon_{281} +1.1$ and $\Delta\epsilon_{251} -1.6$), the 21-epimer of **3**, were identical with those of **6** as expected (Fig. 5), and the absolute configuration for **4** was deduced as 3S, 8S, 9S, 10R, 13R, 21S.

Antholorins E (**5**) and F (**6**), $\text{C}_{33}\text{H}_{49}\text{NO}_4$, had one oxygen and two hydrogen atoms more than the above metabolites **1**–**4**. In ^1H

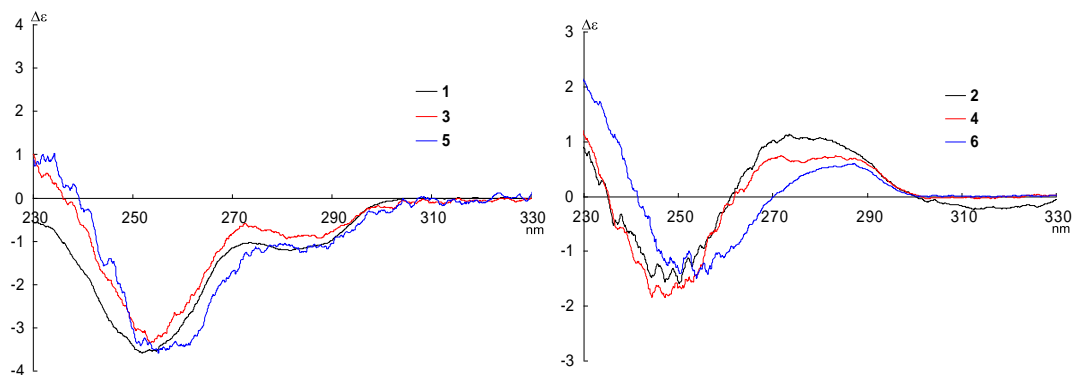


Fig. 5. CD spectra of 1–6.

and ^{13}C NMR spectra of **5** (Table 2), the signals for around the C ring were notably different from those of **1** [H-7 α , H-7 β , H-8 ($\Delta\delta_{\text{H}}$ 0.49), H-10, H-11, H-12, H-13, C-7 ($\Delta\delta_{\text{C}}$ 3.1), C-8 ($\Delta\delta_{\text{C}}$ 11.9), C-9 ($\Delta\delta_{\text{C}}$ 4.7), C-10 ($\Delta\delta_{\text{C}}$ 5.9), C-11 ($\Delta\delta_{\text{C}}$ 3.0), C-12 ($\Delta\delta_{\text{C}}$ 2.7), C-13 ($\Delta\delta_{\text{C}}$ 5.3), and C-17 ($\Delta\delta_{\text{C}}$ 3.7)]. 2D NMR spectral analyses together with the molecular formula implied that **5** had a planar structure opening the ether

linkage of the C ring, which is present in **1–4**. This was supported by the derivatization to 2-methoxy-2-phenyl-2-(trifluoro-methyl) acetic acid (MTPA) esters as described later; i.e., two ester groups changed from the hydroxyl groups appeared.

In NOESY experiments, the observed NOE correlations (H-17/H-1 β , and H-18; H-10/H-6 α , and H-8; H-18/H-1 β , and H-3; H-28/H-2 β ,

Table 2
NMR data for **5** and **6** in CDCl_3 .

Position	5				6				
		$^1\text{H}^{\text{a}}$ (J, Hz)		$^{13}\text{C}^{\text{b}}$	$^1\text{H}^{\text{a}}$ (J, Hz)		$^{13}\text{C}^{\text{b}}$		
1	α	1.66	m	21.5	(t) ^b	1.62	m	21.5	(t) ^b
	β	1.60	m			1.54	m		
2	α	1.00	qd	12.6, 4.8	34.4	(t)	1.00	qd	12.4, 4.8
	β	2.08	dq	12.6, 3.4		1.98	dq	12.4, 3.0	
3		2.81	dtd	12.6, 7.0, 3.1	35.4	(d)	2.73	dtd	12.4, 6.9, 3.0
4				161.9	(s)			161.5	(s)
5				40.1	(s)			40.1	(s)
6	α	1.61	m	35.6	(t)	1.62	m	35.6	(t)
	β	1.61	m			1.62	m		
7	α	1.78	m	27.9	(t)	1.78	m	27.9	(t)
	β	1.78	m			1.78	m		
8		3.46	dd	11.0, 5.0	73.6	(d)	3.46	dd	11.0, 5.0
9				41.5	(s)			41.5	(s)
10		1.06	dd	11.8, 3.8	48.1	(d)	1.06	dd	12.0, 3.3
11	A	1.53	m	34.3	(t)	1.55	m	34.3	(t)
	B	1.61	m			1.60	m		
12	A	1.07	m	24.6	(t)	1.07	m	24.6	(t)
	B	1.42	m			1.42	m		
13		3.31	dd	9.8, 2.1	79.3	(d)	3.30	dd	10.0, 2.1
14				73.3	(s)			73.3	(s)
15		1.16	s	23.6	(q)	1.16	s	23.6	(q)
16		1.21	s	26.6	(q)	1.21	s	26.6	(q)
17		0.89	s	16.8	(q)	0.87	s	16.8	(q)
18		1.10	s	21.2	(q)	1.12	s	21.2	(q)
19	A	4.63	s	100.6	(t)	4.73	s	101.1	(t)
	B	4.72	s			4.75	s		
20	A	1.87	dt	14.0, 7.0	35.4	(t)	1.64	dt	13.7, 6.9
	B	1.92	dt	14.0, 7.0		2.22	dt	13.7, 6.9	
21		3.42	t	7.0	43.7	(d)	3.48	t	6.9
22				179.6	(s)			179.2	(s)
24				143.9	(s)			143.8	(s)
25		7.16	dd	7.3, 1.4	113.8	(d)	7.17	dd	7.3, 1.4
26		7.13	t	7.3	126.8	(d)	7.13	t	7.3
27		6.99	td	7.3, 1.4	121.5	(d)	6.99	td	7.3, 1.4
28		7.20	d	7.3	123.5	(d)	7.16	d	7.3
29				130.4	(s)			130.7	(s)
30				60.3	(s)			60.3	(s)
31		6.13	dd	17.4, 10.8	145.0	(d)	6.13	dd	17.6, 10.8
32	A	5.17	d	10.8	112.5	(t)	5.16	d	10.8
	B	5.18	d	17.4		5.18	d	17.6	
33		1.79	s	27.0	(q)	1.79	s	26.9	(q)
34		1.78	s	26.7	(q)	1.78	s	26.7	(q)

^a Measured at 500 MHz in CDCl_3 .

^b Measured at 125 MHz in CDCl_3 .

and H-19A) demonstrated the relative stereostructure of **5** except for C-13 in the side chain (C-11–C-16). On the other hand, the differences in NMR signals between **5** with **6** were clearly identified with those between **1** and **2**; i.e., **6** was the epimer at C-21 of **5** (Table 2). In order to determine the absolute configuration at C-8 and C-13, the modified Mosher's method¹¹ was applied to **5**, which had two secondary hydroxyl groups at C-8 and C-13. The ¹H chemical shift differences between the (*R*)- and (*S*)-MTPA esters **5a** and **5b** are shown in Fig. 6. The results revealed an *S* configuration at C-8 and C-13 in **5**, respectively, and led to the elucidation of the absolute stereostructure for **5**. Therefore, the absolute configuration of **6** could be established as 3*S*, 8*S*, 9*S*, 10*R*, 13*S*, and 21*S*. In the CD spectra, while negative ($\Delta\epsilon_{284} -1.3$ and $\Delta\epsilon_{254} -3.6$) Cotton effects were observed in **5**, positive ($\Delta\epsilon_{286} +0.6$) and negative ($\Delta\epsilon_{254} -1.5$) Cotton effects were observed in **6** (Fig. 5). We found that the signs of $\Delta\epsilon$ values at around 280 nm indicate the absolute configuration at C-21, and applied this rule to the determination of the absolute stereostructure for **1–4** as described above.

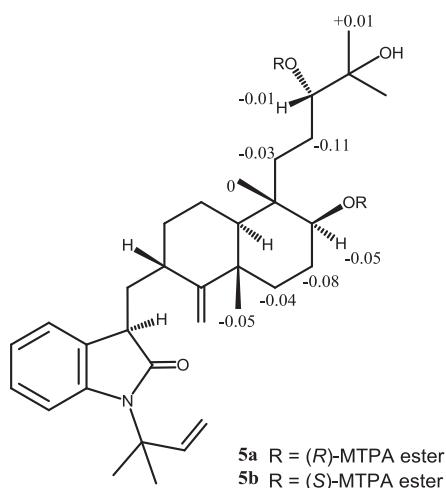


Fig. 6. ¹H chemical shift differences ($\Delta\delta = \delta_S - \delta_R$) between the (*R*)- and (*S*)-MTPA esters **5a** and **5b**, respectively.

For the possibility of the epimerization at C-21 of **1–6**, the conditions during the purification such as silica gel column chromatography, and the leaving in MeOH at room temperature did not lead them to a mixture of the two epimers. In addition, the isomerization from **5** and **6** to the other related compounds; i.e., the C ring formation and the epimerization of 13hydroxy groups, was not observed. So we thought that **1–6** were not artifact produced after extraction.

In this investigation, we could organize the influence of the absolute configuration at C-21 on NMR (the chemical shifts and NOE correlations) and CD spectra for anthcolorins A–F (**1–6**); i.e., NMR chemical shifts at C-2, C-3, C-4, C-19, and C-20 positions, the presence of NOE correlations between H-28 and H-2 β , H-19A, and the signs of a Cotton effect at around 280 nm in CD spectra.

As a primary screen for antitumor activity, cancer cell growth inhibitory properties of anthcolorins A–F (**1–6**) were examined using the murine P388 leukemia cell line. Compounds **2**, **3**, and **4** exhibited significant cytotoxic activity against the cancer cell line (Table 3). Notably, **3** and **4** showed potent cytotoxic affects equal to 5-fluorouracil, the positive control. This result suggested that the strong activity required the presence of the C ring existing in a boat conformation. In addition, **1** was examined using a disease-oriented panel of 39 human cell lines (HCC panel).^{12,13} The effective concentration (MG-MID), the delta value, and the range value for **1** did not show significantly selective cytotoxic activity (effective value: MG-MID < -5, delta ≥ 0.5 , and range ≥ 1.0) (Table 4).

Table 3
Cytotoxicity of the metabolites against P388 cell line

Compounds	Cell line P388	
	IC ₅₀ ^a (μ M)	
Anthcolorin	A (1)	17.4
	B (2)	8.5
	C (3)	2.2
	D (4)	5.5
	E (5)	22.1
	F (6)	26.7
5-Fluorouracil ^b		1.2

^a DMSO was used for vehicle.

^b Positive control.

Table 4
Cytotoxicity of **1** against a panel of 39 human cancer cell lines

Origin of cancer	Cell line	Log GI ₅₀ ^a (M)
		1
Breast	HBC-4	-4.41
	BSY-1	-4.59
	HBC-5	-4.54
	MCF-7	-4.47
	MDA-MB-231	-4.51
	U-251	-4.57
Central nervous system	SF-268	-4.04
	SF-295	-4.47
	SF-539	-4.60
	SNB-75	-4.62
	SNB-78	-4.51
	HCC2998	-4.47
Colon	KM-12	-4.41
	HT-29	-4.49
	HCT-15	-4.44
	HCT-116	-4.49
	NCI-H23	-4.60
	NCI-H226	-4.70
Lung	NCI-H522	-4.72
	NCI-H460	-4.49
	A549	-4.44
	DMS273	-4.70
	DMS114	-4.70
	LOX-IMVI	-4.60
Melanoma	OVCAR-3	-4.44
	OVCAR-4	-4.40
	OVCAR-5	-4.54
	OVCAR-8	-4.35
	SK-OV-3	-4.00
	RXF-631L	-4.00
Kidney	ACHN	-4.47
	St-4	-4.26
	MKN1	-4.52
	MKN7	-4.60
	MKN28	-4.46
	MKN45	-4.47
Stomach	MKN74	-4.66
	DU-145	-4.54
	PC-3	-4.57
	MG-MID ^b	-4.48
	Delta ^c	0.24
	Range ^d	0.72

^a Log concentration of compounds for inhibition of cell growth at 50% compared to control.

^b Mean value of log GI₅₀ over all cell lines tested.

^c The difference in log GI₅₀ value of the most sensitive cell and MG-MID value.

^d The difference in log GI₅₀ value of the most sensitive cell and the least sensitive cell.

3. Experimental section

3.1. General procedure

Mps were determined on a Yanagimoto micro-melting point apparatus and are uncorrected. UV spectra were recorded on

a Hitachi U-2000 spectrophotometer and IR spectra, on a JASCO FT/IR-680 plus. NMR spectra were recorded at 27 °C on Varian UNITY INOVA-500 and MERCURY spectrometers with tetramethylsilane (TMS) as internal reference. FABMS was determined using a JEOL JMS-700 (Ver. 2) mass spectrometer. Optical rotations were recorded on a JASCO J-820 polarimeter. Liquid chromatography over silica gel (mesh 230–400) was performed at medium pressure. HPLC was run on a Waters ALC-200 instrument equipped with a differential refractometer (R 401) and Shim-pack PREP-ODS (25 cm×20 mm i. d.). Analytical TLC was performed on precoated Merck aluminum sheets (DC-Alufolien Kieselgel 60 F254, 0.2 mm) with the solvent system CH₂Cl₂/MeOH (19:1), and compounds were viewed under an UV lamp and sprayed with 10% H₂SO₄, followed by heating.

3.2. Culture and isolation of metabolites

A strain of *A. versicolor* was initially isolated from the sea urchin *A. crassispina* collected in Tanabe Bay in Wakayama, Japan. The gastrointestinal tract of the sea urchin was applied to the surface of nutrient agar layered in a Petri dish on a clean bench. Serial transfers of one of the resulting colonies yielded a pure strain of *A. versicolor*. The fungal strain was cultured at 27 °C for 6 weeks in a liquid medium (40 L) containing D-glucose 2%, pepton 1%, and yeast extract 0.5% in artificial seawater adjusted to pH 7.5. The culture was filtered under suction and the mycelia collected were extracted thrice with MeOH. The combined extracts were evaporated in vacuo to give a mixture of crude metabolites (30.9 g), which exhibited cytotoxicity against the P388 cell line (IC₅₀ 17.6 μg/mL). The CH₂Cl₂/MeOH (1:1) soluble fraction of the MeOH extract (11.8 g) was passed through Sephadex LH-20 using CH₂Cl₂/MeOH (1:1) as the eluent. The second fraction (5.1 g) in which the activity was concentrated was chromatographed on a silica gel column with a CH₂Cl₂/MeOH gradient as the eluent. The MeOH/CH₂Cl₂ (1:99) eluate (193.9 mg) was purified by HPLC using acetone/H₂O (80:20) as the eluent to afford **1** (10.9 mg, 0.09%), **2** (7.4 mg, 0.06%), **3** (7.2 mg, 0.06%), and **4** (8.2 mg, 0.07%). The MeOH/CH₂Cl₂ (2:98) eluate (152.2 mg) was purified by HPLC using acetone/H₂O (75:25) as the eluent to afford **5** (5.0 mg, 0.04%), and **6** (4.7 mg, 0.04%).

3.2.1. Anthcolorin A (1). Colorless plate (CH₂Cl₂/MeOH); mp 181–183 °C; $[\alpha]_D^{22}$ –132.0 (c 0.34, CHCl₃); IR (KBr) ν_{\max} 3436, 1703, 1638, 1611, 1596 cm⁻¹; UV (EtOH) λ_{\max} (log ϵ) 252 (3.84), 282 (3.11) nm; NMR data, see Table 1; EIMS m/z (rel int. %) 505 ([M]⁺, 67), 214 ([a]⁺, 35), 201 ([b+H]⁺, 100), 145 ([c]⁺, 98); HREIMS m/z 505.3551 [M]⁺ (calcd for C₃₃H₄₇NO₃: 505.3556).

3.2.2. Anthcolorin B (2). Colorless oil; $[\alpha]_D^{22}$ –70.8 (c 0.24, CHCl₃); IR (liquid) ν_{\max} 3429, 1714, 1634, 1607, 1599 cm⁻¹; UV (EtOH) λ_{\max} (log ϵ) 253 (3.86), 286 (3.04) nm; NMR data, see Table 1; EIMS m/z (rel int. %) 505 ([M]⁺, 67), 214 ([a]⁺, 26), 201 ([b+H]⁺, 73), 145 ([c]⁺, 100); HREIMS m/z 505.3551 [M]⁺ (calcd for C₃₃H₄₇NO₃: 505.3556).

3.2.3. Anthcolorin C (3). Colorless oil; $[\alpha]_D^{22}$ –108.0 (c 0.40, CHCl₃); IR (liquid) ν_{\max} 3448, 1716, 1638, 1607, 1602, 1585 cm⁻¹; UV (EtOH) λ_{\max} (log ϵ) 253 (3.82), 286 (3.10) nm; NMR data, see Table 1; EIMS m/z (rel int. %) 505 ([M]⁺, 90), 214 ([a]⁺, 43), 201 ([b+H]⁺, 73), 145 ([c]⁺, 100); HREIMS m/z 505.3552 [M]⁺ (calcd for C₃₃H₄₇NO₃: 505.3556).

3.2.4. Anthcolorin D (4). Colorless oil; $[\alpha]_D^{22}$ –74.8 (c 0.44, CHCl₃); IR (liquid) ν_{\max} 3407, 1726, 1638, 1606, 1603, 1589 cm⁻¹; UV (EtOH) λ_{\max} (log ϵ) 252 (3.74), 286 (3.05) nm; NMR data, see Table 1; EIMS m/z (rel int. %) 505 ([M]⁺, 65), 214 ([a]⁺, 46), 201 ([b+H]⁺, 86), 145 ([c]⁺, 91); HREIMS m/z 505.3550 [M]⁺ (calcd for C₃₃H₄₇NO₃: 505.3556).

3.2.5. Anthcolorin E (5). Colorless oil; $[\alpha]_D^{22}$ –68.5 (c 0.22, CHCl₃); IR (liquid) ν_{\max} 3409, 1710, 1634, 1607, 1603 cm⁻¹; UV (EtOH) λ_{\max}

(log ϵ) 252 (3.81), 285 (3.15) nm; NMR data, see Table 2; EIMS m/z (rel int. %) 523 ([M]⁺, 25), 505 ([M–H₂O]⁺, 4), 214 ([a]⁺, 38), 201 ([b+H]⁺, 100), 145 ([c]⁺, 83); HREIMS m/z 523.3657 [M]⁺ (calcd for C₃₃H₄₉NO₄: 523.3662).

3.2.6. Anthcolorin F (6). Colorless oil; $[\alpha]_D^{22}$ –55.2 (c 0.29, CHCl₃); IR (liquid) ν_{\max} 3409, 1710, 1634, 1607, 1603 cm⁻¹; UV (EtOH) λ_{\max} (log ϵ) 252 (3.76), 283 (3.06) nm; NMR data, see Table 2; EIMS m/z (rel int. %) 523 ([M]⁺, 24), 505 ([M–H₂O]⁺, 4), 214 ([a]⁺, 29), 201 ([b+H]⁺, 100), 145 ([c]⁺, 78); HREIMS m/z 523.3659 [M]⁺ (calcd for C₃₃H₄₉NO₄: 523.3662).

3.2.7. Crystal data for 1. C₃₃H₄₇NO₃, $M=505.72$, orthorhombic, $P2_12_12_1$, $a=16.062(3)$ Å, $b=26.583(7)$ Å, $c=6.835(2)$ Å, $V=2918.4$ (12) Å³, $Z=4$, $D_x=1.151$ g cm⁻³, $F(000)=1104$, $\mu(\text{Cu K}\alpha)=0.56$ mm⁻¹. Data collection was performed by Rigaku AFC5R using graphite-monochromated radiation ($\lambda=1.5418$ Å); 4648 reflections were collected until $\theta_{\max}=70.19^\circ$, in which 3829 reflections ($R_{\text{int}}=0.0446$) were observed ($I>2\sigma(I)$). The crystal structure was solved by the direct method using SHELXS-97.9.¹⁴ The structure was refined by the full matrix least-squares method on F^2 using SHELXL-97.9.¹⁴ For the structural refinements, non-hydrogen atoms were refined with anisotropic temperature factors. Hydrogen atoms were calculated on the geometrically ideal positions by the 'ride on' method, and were included in the calculation of structural factors with isotropic temperature factors. At the final stage, $R1=0.0761$, $Rw=0.2091$ were obtained. CCDC 919704.

3.3. Formation of the (R)- and (S)-MTPA esters 5a and 5b from anthcolorin E (5)

(R)-MTPA (1.5 mg), dicyclohexylcarbodiimide (DCC) (1.3 mg), and 4-(dimethylamino)-pyridine (DMAP) (0.5 mg) were added to a CH₂Cl₂ solution (0.2 mL) of **5** (1.3 mg), and the reaction mixture was left at room temperature for 3 h. The solvent was evaporated off under reduced pressure, and the residue was purified by HPLC using MeOH/H₂O (90:10) as the eluent to afford (R)-MTPA ester **5a** (0.5 mg, 21.1%) as a colorless powder. The same reaction with **5** (2.1 mg) using (S)-MTPA (2.9 mg) gave ester **5b** (0.6 mg, 25.3%) as a colorless powder.

3.3.1. Ester 5a. EIMS m/z (rel int. %) 955 ([M]⁺, 11); HREIMS m/z 955.4438 [M]⁺ (calcd for C₅₃H₆₃F₆NO₈: 955.4441); δ_{H} (CDCl₃) 0.73 (3H, s, H-17), 0.90 (1H, m, H-2 α), 0.97 (1H, m, H-12A), 1.04 (1H, dd, $J=11.8, 3.8$ Hz, H-10), 1.10 (3H, s, H-18), 1.15 (3H, s, H-15), 1.19 (3H, s, H-16), 1.20 (1H, m, H-11A), 1.25 (1H, m, H-12B), 1.32 (1H, m, H-1 β), 1.44 (1H, m, H-1 α), 1.66 (1H, m, H-11B), 1.68 (2H, m, H-6), 1.79 (6H, s, H-33 and H-34), 1.83 (1H, dt, $J=14.0, 7.0$ Hz, H-20A), 1.85 (1H, m, H-2 β), 1.92 (2H, m, H-7), 1.93 (1H, m, H-20B), 2.79 (1H, dtd, $J=12.6, 7.0, 3.1$ Hz, H-3), 3.40 (1H, t, $J=7.0$ Hz, H-21), 3.49 (3H, s, OCH₃), 3.59 (3H, s, OCH₃), 4.65 (1H, s, H-19A), 4.73 (1H, s, H-19B), 4.76 (1H, dd, $J=10.0, 1.8$ Hz, H-13), 4.98 (1H, dd, $J=11.0, 5.0$ Hz, H-8), 5.16 (1H, d, $J=10.8$ Hz, H-32A), 5.18 (1H, d, $J=17.4$ Hz, H-32B), 6.13 (1H, dd, $J=17.4, 10.8$ Hz, H-31), 6.99 (1H, dt, $J=7.3, 1.4$ Hz, H-27), 7.14 (1H, t, $J=7.3$ Hz, H-26), 7.16 (1H, dd, $J=7.3, 1.4$ Hz, H-25), 7.19 (1H, d, $J=7.3$ Hz, H-28), 7.42 (6H, m, Ar–H), and 7.55 (4H, m, Ar–H).

3.3.2. Ester 5b. EIMS m/z (rel int. %) 955 ([M]⁺, 9); HREIMS m/z 955.4437 [M]⁺ (calcd for C₅₃H₆₃F₆NO₈: 955.4441); δ_{H} (CDCl₃) 0.73 (3H, s, H-17), 0.85 (1H, m, H-2 α), 0.86 (1H, m, H-12A), 0.98 (1H, dd, $J=11.8, 3.8$ Hz, H-10), 1.05 (3H, s, H-18), 1.15 (3H, s, H-15), 1.17 (1H, m, H-11A), 1.20 (3H, s, H-16), 1.22 (1H, m, H-12B), 1.22 (1H, m, H-1 β), 1.32 (1H, m, H-1 α), 1.63 (1H, m, H-11B), 1.64 (2H, m, H-6), 1.79 (6H, s, H-33 and H-34), 1.80 (1H, m, H-2 β), 1.80 (2H, m, H-7), 1.83 (1H, dt, $J=14.0, 7.0$ Hz, H-20A), 1.93 (1H, m, H-20B), 2.75 (1H, dtd, $J=12.6, 7.0, 3.1$ Hz, H-3), 3.39 (1H, t, $J=7.0$ Hz, H-21), 3.51 (3H, s, OCH₃), 3.59 (3H, s, OCH₃), 4.62 (1H, s, H-19A), 4.70 (1H, s, H-19B),

4.75 (1H, dd, $J=10.0, 1.8$ Hz, H-13), 4.93 (1H, dd, $J=11.0, 5.0$ Hz, H-8), 5.17 (1H, d, $J=10.8$ Hz, H-32A), 5.18 (1H, d, $J=17.4$ Hz, H-32B), 6.13 (1H, dd, $J=17.4, 10.8$ Hz, H-31), 6.99 (1H, dt, $J=7.3, 1.4$ Hz, H-27), 7.14 (1H, t, $J=7.3$ Hz, H-26), 7.16 (1H, dd, $J=7.3, 1.4$ Hz, H-25), 7.18 (1H, d, $J=7.3$ Hz, H-28), 7.33–7.49 (6H, m, Ar. H), and 7.55 (4H, m, Ar. H).

3.4. Assay for cytotoxicity

Cytotoxic activities of Anthcolorins A–F (**1–6**) were examined with the 3-(4,5-dimethyl-2-thiazolyl)-2,5-diphenyl-2H-tetrazolium bromide (MTT) method. P388 cells were cultured in Eagle's minimum essential medium (10% fetal calf serum) at 37 °C in 5% CO₂. The test material was dissolved in dimethyl sulfoxide (DMSO) to give a concentration of 10 mM, and the solution was diluted with the essential medium to yield concentrations of 200, 20, and 2 μM, respectively. Each solution was combined with each cell suspension (1×10^5 cells/mL) in the medium, respectively. After incubating at 37 °C for 72 h in 5% CO₂, grown cells were labeled with 5 mg/mL MTT in phosphate-buffered saline (PBS), and the absorbance of formazan dissolved in 20% sodium dodecyl sulfate (SDS) in 0.1 N HCl was measured at 540 nm with a microplate reader (Model 450, BIO-RAD). Each absorbance value was expressed as percentage relative to that of the control cell suspension that was prepared without the test substance using the same procedure as that described above. All assays were performed three times, semilogarithmic plots were constructed from the averaged data, and the effective dose of the substance required to inhibit cell growth by 50% (IC₅₀) was determined.

Acknowledgements

We thank Dr. T. Yamori (Screening Committee of Anticancer Drugs supported by a Grant-in-Aid for Scientific Research on

Priority Area 'Cancer' from the Ministry of Education, Culture, Sports, Science and Technology, Japan) for performing the assay for cytotoxicity using a panel of 39 human cell lines. We are grateful to Ms. M. Fujitake of this university for MS measurements. This study was supported by a Grant-in-Aid for Scientific Research from the Japan Society for the Promotion of Science.

References and notes

1. Yamada, T.; Iritani, M.; Doi, M.; Minoura, K.; Ito, T.; Numata, A. *J. Chem. Soc., Perkin Trans. 1* **2001**, 3046–3053.
2. Yamada, T.; Iritani, M.; Minoura, K.; Kawai, K.; Numata, A. *Org. Biomol. Chem.* **2004**, 2131–2135.
3. Yamada, T.; Imai, E.; Nakatani, K.; Numata, A.; Tanaka, R. *Tetrahedron Lett.* **2007**, 48, 6294–6296.
4. Muroga, Y.; Yamada, T.; Numata, A.; Tanaka, R. *Tetrahedron* **2009**, 65, 7580–7586.
5. Yamada, T.; Kitada, H.; Kajimoto, T.; Numata, A.; Tanaka, R. *J. Org. Chem.* **2010**, 75, 4146–4153.
6. Kitano, M.; Yamada, T.; Amagata, T.; Minoura, K.; Tanaka, R.; Numata, A. *Tetrahedron Lett.* **2012**, 53, 4192–4194 and references cited therein.
7. A part of this work has been presented orally: Yamada, K.; Doi, M.; Minoura, K.; Numata, A. 42nd Symposium on the Chemistry of Natural Products, Okinawa, 2000; Symposium Papers, p 397–402.
8. Kimura, Y.; Nishibe, M.; Nakajima, H.; Hamasaki, T.; Shigemitsu, N.; Sugawara, F.; Stout, T.; Clandry, J. *Tetrahedron Lett.* **1992**, 33, 6987–6990.
9. Fueki, S.; Tokiwano, T.; Toshima, H.; Oikawa, H. *Org. Lett.* **2004**, 16, 2697–2700 and references cited therein.
10. Tagami, K.; Liu, C.; Minami, A.; Noike, M.; Isaka, T.; Fueki, S.; Shichijo, Y.; Toshima, H.; Gomi, K.; Dairi, T.; Oikawa, H. *J. Am. Chem. Soc.* **2013**, 135, 1260–1263 and references cited therein.
11. Ohtani, I.; Kusumi, T.; Kashman, Y.; Kakizawa, H. *J. Am. Chem. Soc.* **1991**, 113, 4092–4096.
12. Yamori, T.; Matsunaga, A.; Sato, S.; Yamazaki, K.; Komi, A.; Ishizu, K.; Mita, I.; Edatsugi, H.; Matsuba, Y.; Takezawa, K.; Nakanishi, O.; Kohno, H.; Nakajima, Y.; Komatsu, H.; Andoh, T.; Tsuruo, T. *Cancer Res.* **1999**, 59, 4042–4049.
13. Yamori, T. *Cancer Chemother. Pharmacol.* **2003**, 52, S74–S79.
14. Sheldrick, G. M. *Acta Crystallogr.* **2008**, A64, 112–122.



Published in final edited form as:

J Nat Prod. 2012 December 28; 75(12): 2193–2199. doi:10.1021/np300640g.

Creation of an HDAC-Based Yeast Screening Method for Evaluation of Marine-Derived Actinomycetes: Discovery of Streptosetin A[‡]

Taro Amagata^{†,*}, Jing Xiao[†], Yi-Pei Chen[†], Nicholas Holsopple[†], Allen G. Oliver[‡], Trevor Gokey[†], Anton B. Guliaev[†], and Katsuhiko Minoura[§]

[†]Department of Chemistry and Biochemistry, San Francisco State University, San Francisco, CA 94132

[‡]Department Chemistry and Biochemistry, University of Notre Dame, Notre Dame, 46556

[§]Osaka University of Pharmaceutical Sciences, Takatsuki, Osaka 569–1094, Japan

Abstract

A histone deacetylase (HDAC)-based yeast assay employing a URA3 reporter gene was applied as a primary screen to evaluate a marine-derived actinomycete extract library and identify human class III HDAC (SIRT) inhibitors. Based on the bioassay-guided purification, a new compound designated as streptosetin A (**1**) was obtained from one of the active strains identified through the yeast assay. The gross structure of the new compound was elucidated from the 1D and 2D NMR data. The absolute stereostructure of **1** was determined based on X-ray crystal structure analysis and simulation of ECD spectra using time-dependent density functional theory (TD-DFT) calculations. This compound showed weak inhibitory activity against yeast Sir2p, and human SIRT1 and SIRT2.

Class III HDACs (SIRT1-7) are NAD-dependent epigenetic enzymes unlike classical zinc-dependent class I, II and IV HDACs, and are known to be insensitive to zinc-dependent HDAC inhibitors such as trichostatin A.¹ Among SIRT isoforms, SIRT1 and SIRT2 have received increased attention as targets for anticancer molecules because the former is overexpressed in cancer cells² and the latter is involved in the cell cycle.³ More importantly, SIRT1 and SIRT2 interact with the same non-histone substrates as those regulated by classical HDACs, which include the tumor suppressor protein p53,⁴ and α -tubulin.⁵ In addition, the synthetic SIRT1/SIRT2 inhibitor sirtinol demonstrated apoptotic and autophagic cell death in an MCF-7 breast cancer cell line.⁶ Given the evidence listed above and the FDA approvals of two classical HDAC inhibitors, SAHA (vorinostat, 2006) and FR901228 (istodax, 2009), for the treatment of cutaneous T-cell lymphoma (CTCL), as well as LBH589 (panobinostat) currently being evaluated in phase I/II/III clinical trials,⁷ class III HDAC (SIRT) inhibitors are anticipated to be anticancer drug candidates. Crucial SIRT inhibitors have not been discovered from natural sources yet, except for a few mild SIRT1/SIRT2 inhibitors including tanikolide dimer,⁸ (+)-guttiferone G⁹ and amurensin G.¹⁰ On the

[‡]Dedicated to the memory of the late Dr. Atsushi Numata of Osaka University of Pharmaceutical Sciences for his effort on discovering anticancer lead compounds.

*Corresponding author. Tel.: 415-338-7713. Fax: 415-338-2384. amagata@sfsu.edu.

Supporting Information Available.

Sequence data of the *Streptomyces* sp. CP13-10, 1D and 2D NMR data (¹H, ¹³C NMR, COSY, HSQC, HMBC and NOESY), and crystal data for **1**. This information is free of charge via the Internet at <http://pubs.acs.org>.

other hand, a number of synthetic SIRT inhibitors including a potent SIRT1 selective inhibitor EX-527,¹¹ have been developed in the past decade.

The SIRT family is evolutionally conserved from bacteria to mammals.¹² Among the human SIRT enzymes, SIRT1 is the closest homolog of the yeast silent information regulator 2 protein (Sir2p).¹³ Furthermore, the seven human isoforms possess close sequence identity, where their catalytic and NAD⁺ binding domains are also conserved.¹ Consequently, Sir2p inhibitors are likely to inhibit human SIRT enzymes. In fact, sirtinol¹⁴ and splitomicin,¹⁵ the most common molecular probes for SIRT1 and SIRT2, have been independently identified as Sir2p inhibitors from a synthetic chemical library using a genetically modified yeast strain as a screening tool. As described in the article previously reported by the Schreiber group,¹⁴ this yeast screening employs a URA3¹⁶ reporter gene embedded in the telomere region of the yeast chromosome, which is activated by Sir2p inhibitors. Selective Sir2p inhibitory activity is visually observed by adding 5-fluoroorotic acid (5-FOA) in the culture medium. The reporter gene activated by a Sir2p inhibitor converts 5-FOA into the cytotoxic compound 5-fluorouracil (5-FU), which leads to the death of yeast cells, whereas yeast cells survive the Sir2p inhibitor in the absence of 5-FOA. We have begun a program to further apply such a yeast screen to evaluate natural products libraries and isolate SIRT inhibitors. Reported below are outcomes based on the evaluation of extract libraries created from marine-derived actinomycetes. The yeast screening has led to the discovery of a new compound designated as streptosetin A (**1**).

Results and Discussion

Prior to screening our chemical library, we first verified the sensitivity of the two yeast strains DMY2843¹⁷ and UCC1001¹⁵ with a URA3 reporter gene in the telomere region using the known Sir2p inhibitor splitomicin. The DMY2843 strain showed more pronounced activity at 20 μ M than those observed in the UCC1001 strain (Figure S3). Thus, the yeast strain, DMY2843, was chosen for further screening in this study. A mini-library composed of 506 extracts created from the same number of marine-derived actinomycetes was tested against the DMY2843 strain at 20 μ g/mL as the final concentration. This screening identified a total of 53 active strains, which were divided into two groups: (1) selective activity (19 strains, 3.8%), and (2) non-selective activity (34 strains, 6.7%). In the former group, yeast growth was inhibited only in the presence of 5-FOA based on Sir2p inhibition, while yeast cell death was observed both in the presence and absence of 5-FOA in the latter group. The non-selective activity originates either from potent Sir2p inhibitory activity or from different modes of action. Among the selective active strains, *Streptomyces* sp. CP13-10 was selected for further study. A peak library created from the extract (30 mg) of this strain was subjected to the same yeast screening to pinpoint compounds responsible for the selective activity. The screening result indicated that the compound eluting at 15 min showed Sir2p inhibitory activity. To characterize the active compound, this strain was cultured in liquid medium (6 L) containing starch (1%), yeast extract (0.4%), peptone (0.2%), CaCO₃ (0.1%), Fe₂SO₄ · 7H₂O (0.004%) in artificial seawater (6 L) for 7 days at 30 °C, shaking at 200 rpm. The bacterial pellet and culture broth were independently extracted with MeOH. The combined MeOH extract was then partitioned between EtOAc and H₂O. The organic layer was dried under reduced pressure to afford an extract. The active compound designated as streptosetin A (**1**) was purified from the extract using reversed phase HPLC.

The molecular formula of streptosetin A (**1**) was established as C₁₉H₂₅NO₅ from the HRESIMS data. The initial ¹³C NMR spectrum showed only 17 carbon signals (Table 1), which were classified into the following five groups from DEPT and HSQC experiments: (1) three carbonyl groups (C-3, C-11, C-18), (2) a trisubstituted double bond carbons (C-7,

C-8), (3) four sp^3 methines (C-5, C-9, C-10, C-13) including one oxygen bearing methine (δ_{H-9} 70.1, δ_{H-9} 4.44), (4) four sp^3 methylenes (C-6, C-12, C-14, C-19) including one nitrogen bearing methylene (δ_{H-19} 51.2, δ_{H-19} 3.79), and (5) three methyl groups (C-15, C-16, C-17) including one vinyl methyl (δ_{H-17} 19.4, δ_{H-17} 1.71). The COSY analysis provided two spin systems (C-7-C-6-C-5-C-10-C-9 and C-12-C-15) as indicated in boldfaced lines in Figure 2. An analysis of the HMBC data led to the two substructures (Figure 2). The former spin system was incorporated into a cyclohexene with an oxygen atom at the allylic position based on the HMBC correlations from H-7 to C-9/C-17, from H-9 to C-7/C-8, and from H-17 to C-7/C-8/C-9. This cyclohexene and the latter spin system were further connected via C-4 and C-11 to form a decalin system, substructure A, based on the HMBC correlations from H-5 to C-4, from H-9 to C-11, from H-10 to C-11, and from H-12 to C-4/C-11. Finally, substructure A incorporated a methyl group (C-16) and a ketone (C-3) at C-4 due to HMBC correlations from H-5 to C-3/C-16, and from H-16 to C-3/C-4/C-5/C-13. In addition, it was expected that C-9 possessed an alcohol group as no other carbons bearing an oxygen atom were observed in the ^{13}C NMR spectrum. A second substructure B with a nitrogen atom was defined by the HMBC correlation from the nitromethylene H₂-19 to C-18. At this point the unaccounted atoms consisted of C₂H₂O, which were invisible in the both the 1H and ^{13}C NMR spectra. Subsequently, as shown in Table 1 these carbons were visualized by a ^{13}C NMR spectrum acquired at 75 MHz and were eventually assigned to C-1 (δ_C 180.1) and C-2 (δ_C 100.6), as discussed further below. The two hydrogens were assigned as exchange protons since they were not detected in the 1H NMR spectrum measured in CD₃OD. Thus, substructure C with C₂O was proposed.

The relative configuration and conformation of substructure A were further determined by detailed analysis of vicinal coupling constants and NOESY correlations (Figure 3). The large coupling constant between H-5 and H-10 ($^3J_{5,10} = 12.7$ Hz) suggested a *trans*-fused decalin. NOE correlations between H-10 and H-12ax, H-10 and H₃-16, H-12ax and H₃-16 and H-13 and H₃-16 denoted a chair conformation for the cyclohexane ring with H-10, H-12ax and 16-CH₃ in axial positions and H-13 in an equatorial arrangement. NOEs between H-12eq and H₃-15 and H-5 and H₂-14a implied that H-5 and 13-C₂H₅ are arranged *trans* to 16-CH₃ with both axial arrangement. The cyclohexene ring was deduced to exist in a twist-chair conformation due to relatively large coupling constants between H-5 and H-6ax ($^3J_{5,6ax} = 10.7$ Hz) and H-9 and H-10 ($^3J_{9,10} = 8.6$ Hz) and NOEs between H-5 and H-9 and H-6ax and H-10. These observations suggested that 9-OH is pseudoequatorial, and oriented *cis* to H-6ax, H-10 and 16-CH₃, and *trans* to H-5 and 13-C₂H₅.

Our attention shifted next to elucidating the total structure of streptosetin A (**1**). The two carbons in substructure C were concluded to be sp^2 quaternary carbons (a tetrasubstituted double bond) as no reasonable working structures with sp and sp^3 quaternary carbons were generated. Finally, two working structures **1a** and **1b** with a conjugated diketo-enol motif were proposed (Figure 4). These working structures possessed a dynamic tautomerism system through the carbons, C-1, C-2, C-3 and C-18. Thus, the carbon signals C-1 and C-2 were not detected in the ^{13}C NMR spectrum due to signal broadening. Based on biogenetic assumptions, working structure **1a** appeared to be more reasonable because it was categorized as a relatively common tetramic acid derivative. It was extremely difficult to observe all the carbon signals in the tetramic acid moiety at 125.7 MHz at room temperature (25°C) due to tautomerism. This appears to be a common issue with tetramic acid derivatives,¹⁸ which could be solved by measuring the ^{13}C NMR at low temperature as reported in the articles regarding this class of secondary metabolites.^{19,20} However, attempts to observe the carbon signals for C-1 and C-2 at -25 °C were unsuccessful. Interestingly, these two carbons were detected as broad signals at δ_C 100.6 (C-2) and 180.1 (C-1) at lower frequency (75.4 MHz). The latter carbon signal (C-1) was confirmed by the HMBC spectrum, in which a cross-peak was observed between H-19 and C-1.

An X-ray single crystal structure analysis was carried out for the final structure determination because NMR techniques could not distinguish between the working structures. The X-ray crystal structure²¹ was identical with **1a**, which justified the configuration and conformational assignments for the decalin system obtained from the NMR data (Figure 5). In the X-ray structure, intramolecular hydrogen bonding was observed between the hydroxy group at C-1 and the carbonyl group at C-3. In addition, the absolute configurations of the stereogenic centers were determined to be *4R,5R,9R,10S,13R* based on the comparison of intensities of Friedel pairs of reflections [Flack *x* parameter = 0.06(6),²² Hooft *y* parameter = 0.060(9)²³; values of zero indicate the correct enantiomorph]. To confirm the absolute stereostructure of **1** suggested from analysis of the X-ray structure, the modified Mosher's method²⁴ was initially chosen as this molecule possessed an equatorial secondary alcohol at C-9. However this reaction yielded a complex mixture of products, in which the desired Mosher's ester was not detected. This could be attributed to the β -hydroxyketone moiety in the decalin system, which could assist the dehydration between C-9 and C-10 and/or retro-aldol type reaction rather than esterification. Absolute configurations of the asymmetric centers in **1** were finally confirmed using *ab initio* electronic circular dichroism (ECD) spectral calculations.^{25,26} ECD spectra for a set of enantiomers of **1** obtained by geometry optimization were generated using time-dependent density functional theory (TD-DFT) calculations at B3LYP/AUG-cc-pVDZ level. The general features of the experimental ECD spectrum of **1** agreed well with that calculated for the *4R,5R,9R,10S,13R* isomer though the simulated ECD spectra, but were blue-shifted by 35 nm (Figure 6). These absolute configurations were identical to those obtained from the X-ray crystal structure described above. Consequently, the absolute configurations in **1** were firmly determined as *4R,5R,9R,10S,13R*.

On the other hand, three possible tautomers (**I**, **II** and **III**) based on the conjugated diketoenol moiety were considered in solution state, though tautomer **I** was originally assigned as the structure of **1** using NMR techniques as well as X-ray crystal structure analysis (Figure 7). A literature search for this class of compounds implied that the type **III** tautomer was the most favored form among the three tautomers. However, analysis of the published carbon chemical shift values for the four conjugated sp^2 carbons in each tautomeric form indicated that it was impossible to assign an appropriate form using these carbon chemical shifts because the ranges of these chemical shifts in the three tautomers overlapped one another. (Table S1). Consequently, the structure of **1** in solution remains undetermined.

Enzyme inhibitory activities of streptosein A (**1**) were assessed using the yeast screening described above and SIRT1/SIRT2 fluorescent assays. In these assays, sirtinol was selected as a positive control. In the yeast screening, compound **1** showed weak cytotoxicity at 10 mM and a minimum inhibitory concentration (MIC) at 2.5 mM based on Sir2p inhibition whereas sirtinol showed an MIC at 12.5 μ M (Figure S4). The yeast assay results for **1** and sirtinol mirrored human SIRT inhibitory activities. Compound **1** showed IC_{50} values of 3.7 mM (SIRT1) and 4.5 mM (SIRT2), while sirtinol inhibited SIRT1 and SIRT2 with IC_{50} values of 40.1 μ M and 45.8 μ M, respectively (Figure S5).

Conclusions

The genetically modified yeast strain used in this study proved to be a useful screening tool for identifying SIRT inhibitors from an actinomycete-derived chemical library. Though the new compound streptosein A (**1**) obtained through this yeast screening turned out to be a weak SIRT inhibitor, this compound showed clear dose-response curves in the SIRT1 and SIRT2 enzyme assays (Figure S5). In addition, MIC values defined by the yeast assay appear to be parallel to the IC_{50} values determined by SIRT1 and SIRT2 enzyme assays. Structurally, streptosein A (**1**) is categorized as a polyketide tetramic acid derivative

produced by an NRPS-PKS hybrid pathway, as reported for equisetin (**2**) isolated from a *Fusarium equiseti*.²⁷ The structure elucidation of this class of compounds appears to be challenging due to proton and/or carbon signal broadening caused by the dynamic tautomeric system. It is even more challenging to assign the correct tautomer for this class of compounds, which is often overlooked in the process of structure elucidation. More importantly, this compound may be applied to a chemical epigenetic approach to alter the chemical profile for microorganisms as epigenetic enzyme inhibitors like SAHA (class I HDAC inhibitor) and 5-AZT (DNA methyl transferase inhibitor) are known to induce new compounds based on activating silent biosynthetic genes in fungi.^{28,29} We will continue to search for new and/or potent SIRT inhibitors from other active strains identified through this study.

Experimental Section

General Experimental Procedures

Melting points were recorded on a Barnstead International Mel-Temp Electrothermal melting point apparatus 1101D, and are uncorrected. Optical rotations were obtained on a JASCO P-2000 polarimeter. The UV spectrum was measured on an Agilent 8453 UV/vis diode array spectrophotometer. The CD spectrum was collected with a JASCO J-820 CD spectrometer. 1D and 2D NMR spectra were recorded on a Varian Inova spectrometer operated at 500 MHz (¹H) and 125.7 MHz (¹³C) and a Bruker Avance spectrometer operated at 300 MHz (¹H) and 75.4 MHz (¹³C). The chemical shifts were calibrated using the internal solvent peak (δ_{H} 3.31 and δ_{C} 49.0). High resolution MS data were obtained on a Marinar ESI-TOFMS. HPLC was performed on an Agilent 1200 LC system equipped with a diode array detector.

Isolation of Actinomycete Strains

A total of 506 actinobacteria were separated from marine samples collected from various locations; Santa Monica basin, CA [sediments (–900 m), July 2008], Hawaii, HI [sands (various depths, –10 – –300 m), November 2008], San Francisco Bay, CA [sediments (–1 m), August 2008], Moss Landing, CA [sediments (–1 m), August 2009] and Baja, Mexico [sands, (–15 – –30 m), May 2009]. These marine samples were stored at –20 °C until processed. Each marine sample (1 cm^{–3}) was thoroughly dried at 50 °C, and then aseptically diluted in 9 mL of phosphate buffered saline (PBS). This suspension was heated at 60 °C for 30 min to afford a 10-fold diluted suspension, which was further diluted to a 100-fold suspension with PBS. These two suspensions (100 μ L) were individually plated on starch-nitrate agar and ISP3 agar plates. These two agar plates were prepared using artificial seawater [NaCl (1%), KCl (0.2%), MgSO₄ · 7H₂O (0.4%) and CaCl₂ · 2H₂O (0.03%)]. The plates were incubated at 28 °C for two months. Each actinomycete colony on the plates was transferred onto a seawater-based ISP2 agar plate, and was passaged repeatedly until a pure strain was obtained.

Building the Extract Library

All of the separated strains were cultured in a seed medium (25 mL) composed of soluble starch (2%), D-glucose (1%), yeast extract (0.5%), peptone (0.5%) and CaCO₃ (0.5%) in artificial seawater as described above with a trace element mix (25 μ L) at 30 °C for 5 days at 200 rpm. The trace element mix is composed of the following inorganic salts: FeSO₄ · 7H₂O (4 g), MnSO₄ · H₂O (5 g), ZnSO₄ · 7H₂O (2.5 g), Na₂B₄O₇ · 10H₂O (1.4 g), CoCl₂ · 6H₂O (0.2 g), CuSO₄ · 5H₂O (0.5 g), Na₂MoO₄ (0.2 g) in ultrapure H₂O (1 L). When the trace element mix was prepared, the pH was adjusted between 1 and 2, and then each ingredient was added in the order listed. The seed culture (1 mL) was inoculated into a production media (100 mL) at 30 °C for 7 days at 200 rpm. The composition of the

production media was the same as that of the seed media described above with HP20 resin (5 mL). The bacterial pellet and HP-20 separated from the production culture were extracted with MeOH (50 mL) twice and the combined MeOH solution was dried to obtain a MeOH extract. The MeOH extract was dissolved in EtOAc (100 mL) and rinsed with H₂O (50 mL) twice to remove salts and media components. The EtOAc solution was dried under reduced pressure to provide an organic extract. A library of the extracts was generated with a concentration of 10 mg/mL in DMSO in 96 deep-well plates. This library of extracts was stored at -20 °C before being screened for bioactivity against the strain.

Yeast Strains and URA3 Reporter Gene Screening

Two genetically modified *Saccharomyces cerevisiae* strains (DMY2843 and UCC1001) with a URA3 reporter gene embedded in the telomere region were used for screening. The genotypes of the two strains are as followed: DMY2843 (*MATa ade2-1 ura3-1 his3-11 trp1-1 leu2-3 leu2-112 can1-100 TEL-VIII::URA3*) and UCC1001 (*MATa ura3-52 lys-801 ade2-101 trpΔ63 his3D200 leu2-Δ1 TEL VIII adh4::URA3*). A loopful (10 μL) of a fresh yeast colony from a YPD agar plate was incubated in YPD media (40 mL) overnight at 27 °C and 180 rpm to furnish the yeast culture for screening. Yeast screening was performed in two different screening solutions (solutions A and B) using flat bottom clear 96-well plates.¹⁴ The master mix of solution A was composed of fresh YPD media (9.765 mL), 15% 5-FOA in DMSO (0.135 mL) and yeast culture (0.1 mL), while the master mix of solution B was composed of fresh YPD media (9.9 mL) and yeast culture (0.1 mL). The chemical library samples (2 μL) adjusted as 10 mg/mL in DMSO were mixed separately with each master mix (98 μL) in the well. DMSO and splitomicin (50 μM as final concentration) were used as negative and positive standard compounds, respectively. The screening results were evaluated within 24 to 36 h when the negative control well was saturated with yeast growth, which was determined by visual inspection. Active samples resulted in a visibly clear well due to the death of yeast cells whereas inactive samples resulted in a visibly cloudy well due to the growth of yeast cells. Sir2p inhibitory activity was defined as selective when the screened sample resulted in the death of yeast cells only in the presence of 5-FOA. Cytotoxic or non-selective activity was determined as the death of yeast cells in both the screening solutions A and B.

Bacterial Identification

The actinomycete strain (CP13-10) was separated from a sediment sample collected at the depth of 1m in San Francisco Bay in August 2008. The genomic DNA of this strain was extracted using a DNA release kit (MicroLysis, Gel Company). The 16s rRNA (ca. 1400 bp) was amplified using a hot start TAQ PCR mix (MegaMix Royal, Gel Company) employing two universal primers, 27F and 1492R.³⁰ The PCR was performed under the following thermal condition: 95 °C for 5 min, 35 cycles of denaturation at 94 °C for 1 min, annealing at 64 °C for 1 min, extension at 72 °C for 1.5 min and additional extension at 72 °C for 10 min. The PCR product was purified with a purification kit (MicroElute DNA clean up kit, Omega Bio-tek). The purified PCR product was sequenced at Saga Gene, Inc. using the same primers described above and four additional universal primers including 514F, 530R, 936R, and 1114F.³⁰ This strain was identified as a *Streptomyces* sp. on the basis of 100% sequence similarity to *Streptomyces violaceusniger* Tu 4113 (GenBank accession number CP002994). The 16s rRNA sequence of the CP13-10 strain has been deposited to GenBank with the accession number JX235443.

Isolation of Streptostatin A (1)

The seed culture (10 mL) of the strain CP13-10 prepared as described above was inoculated to the production media (1L × 6). The production media was cultured at 30 °C for 7 days at 200 rpm. The culture was centrifuged (6000g, 30 min) to separate the culture broth from the

actinomycete pellet. To the culture broth, HP-20 resin (50 mL/L) was added and the suspension was stirred for 30 min. This resin was filtered and rinsed thoroughly with H₂O. Then, organic materials were extracted from the HP-20 resin using MeOH. The pellet was soaked in MeOH overnight three times. The combined MeOH solution from the HP-20 resin and pellet was dried under reduced pressure. The residue that dissolved in EtOAc (200 mL) was rinsed with H₂O (200 mL) three times and the organic layer was dried under reduced pressure to provide an extract (261 mg). This extract was subjected to reversed-phase HPLC using a linear gradient system (10% – 100% CH₃CN in H₂O over 20 min). The semipure fraction obtained around 15 min was further purified using another gradient system (40% to 70% CH₃CN in H₂O over 20 min) to afford **1** (6.5 mg).

Streptosetin A (**1**)

Colorless crystals; mp 99–100°C; [α]_D²⁴ -115 (*c* 1.0 MeOH); UV (MeOH) λ_{\max} (log ϵ) 243 nm (2.53), 283 nm (3.12); CD (EtOH) $\Delta\epsilon$ (nm) 228 (-1.70), 250 (-0.27), 285 (-4.24), 317 (+2.22); ¹H and ¹³C NMR data, see Table 1; HRESI-TOFMS *m/z* 370.1622 [M+Na]⁺ (calcd for C₁₉H₂₅NO₅Na, 370.1625).

X-Ray Crystallography of **1**

Suitable crystals were grown at 4 °C by vapor diffusion of pentane into a CHCl₃ solution of **1**. A representative crystal (0.51 × 0.22 × 0.13 mm) was selected and mounted on a Bruker APEX diffractometer³¹ under a cold nitrogen stream at 100(2) K. An arbitrary hemisphere of data was recorded (3600 frames, 0.5° per frame with a combination of ω - and ϕ -scans, exposure time 20s/frame, $2\theta_{\max} = 135.92^\circ$) with graphite monochromated Cu-K α radiation (1.54178 Å). Data were integrated with Bruker SAINT v7.66A³¹ yielding 19805 reflections, of which 4334 were independent ($R_{\text{int}} = 3.53\%$) and 3843 with $I > 2\sigma(I)$. Data were corrected for absorption, Lorentz and polarization effects with SADABS³² ($T_{\min}/T_{\max} = 0.4396/0.8361$). The structure was solved by direct methods (SHELXS) and refined by full-matrix least-square techniques on F^2 (SHELXL³²). All non-hydrogen atoms, except the disordered water of crystallization, were refined with anisotropic thermal displacement parameters. Hydrogen atoms on the molecule of interest and chloroform of crystallization were included in geometrically calculated positions. Hydrogen atoms on the waters of crystallization could not be reliably located and were not included in the model but were included in the chemical formula. The structure refined to $R_1 = 9.42\%$ and $wR_2 = 0.2665$ for all 3846 data $I > 2\sigma(I)$ and $R_1 = 10.32\%$ and $wR_2 = 27.93\%$ for all 4334 data (GooF = 1.023) for 297 parameters. The absolute configuration was determined based on a Flack *x* parameter of 0.06(6) and a Hooft *y* parameter of 0.060(9).

Crystal Data for **1**

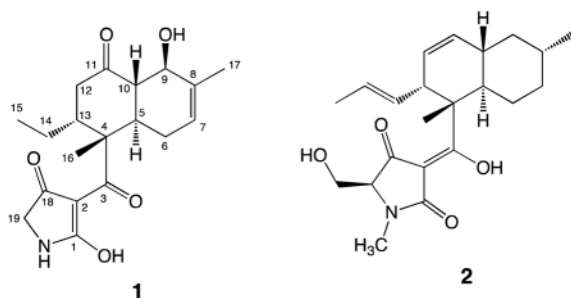
C₁₉H₂₅NO₅ · CHCl₃ · H₂O; $M_r = 484.78$; trigonal; space group P3₂21; $a = 11.1313(3)$ Å; $b = 11.1313(3)$ Å; $c = 33.9045(9)$ Å; $\alpha = 90^\circ$; $\beta = 90^\circ$; $\gamma = 120^\circ$; $V = 3638.14(17)$ Å³; $Z = 6$; $T = 100(2)$ K; λ (Cu-K α) = 1.54178 Å; μ (Cu-K α) = 3.716 mm⁻¹; $d_{\text{calc}} = 1.328$ g·cm⁻³.

ECD Calculations for **1**

All the DFT calculations were performed using Gaussian 09.³³ Geometry optimization employing the B3LYP function (AUG-cc-pVDZ level) was performed in the gas phase for **1**. A set of enantiomers of **1** generated from geometry optimization was subjected to the TD-DFT method with the B3LYP/AUG-cc-pVDZ basis set using SCRF (self-consistent reaction field) to calculate the excitation energies and oscillator and rotational strengths of the lowest 50 electronic excitations. These calculation results were simulated into ECD spectra with a Gaussian function (a half-bandwidth of 0.3 eV) using GaussView 5.0.9.

SIRT1 and SIRT2 Inhibition Assays

SIRT1 and SIRT2 inhibitory activities were measured using SIRT1 and SIRT2 Direct Fluorescent Screening Assay kits (Cayman Chemical Company). The assays were performed in a 96-well plate based on the supplier's protocol. To the 50 mM Tris-HCl buffer (25 μ L), human recombinant SIRT or SIRT2 (5 μ L), the substrate [Arg-His-Lys-Lys(ϵ -acetyl)-AMC] (15 μ L, 125 μ M), and various concentrations of the samples (5 μ L in DMSO) were added and the assay plate was incubated on a shaker at room temperature for 45 min (SIRT1) or 37 $^{\circ}$ C for 45 min (SIRT2). Then, to each well, the stop/developer solution containing nicotinamide (50 μ L) was added to stop deacetylation. Thirty minutes after adding this stop/developer solution, the fluorescence was measured using a fluorometric reader (Molecular Device, SpectraMax M2) at 350 nm for excitation and 450 nm for emission. The values of % inhibition against SIRT1 and SIRT2 were calculated from the fluorescence readings of the sample wells relative to those of 100% initial activity wells [50 mM Tris-HCl (25 μ L), SIRT1/SIRT2 (5 μ L), DMSO (5 μ L), the substrate (15 μ L) and the stop/developer solution (50 μ L)]. The IC₅₀ values of the samples were determined using IDBS XL fit5.



Supplementary Material

Refer to Web version on PubMed Central for supplementary material.

Acknowledgments

This work was supported by Grant Number SC2GM088057 from the National Institute of General Medical Sciences. The Cell and Molecular Image Center (CMIC) of the College of Science and Engineering, SF State University was funded by Grant Number P20MD000544 from the National Center on Minority Health and Health Disparities. We are grateful for the gift of yeast strains from Dr. D. Moazed (Harvard Medical School) and Dr. D. E. Gottschling (Fred Hutchinson Cancer Research Center). We thank Dr. A. Chan (SFSU, CMIC) for assistance with microscopy, Dr. T. Komada (SFSU) for providing sediment samples, and Dr. T. Yamada (OUPS) for experimental ECD measurement.

References and Notes

1. Yamamoto H, Schoonjans K, Auwerx J. *Mol Endocrinol*. 2007; 21:1745–1755. [PubMed: 17456799]
2. Jung-Hynes B, Nihal M, Zhong W, Ahmad N. *J Biol Chem*. 2009; 284:3823–3832. [PubMed: 19075016]
3. Inoue T, Hiratsuka M, Osaki M, Oshimura M. *Cell Cycle*. 2007; 6:1011–1018. [PubMed: 17457050]
4. Yi J, Luo J. *Biochim Biophys Acta*. 2010; 1804:1684–1689. [PubMed: 20471503]
5. North BJ, Marshall BL, Borra MT, Denu JM, Verdin E. *Mol Cell*. 2003; 11:437–444. [PubMed: 12620231]
6. Wang J, Kim TH, Ahn MY, Lee J, Jung JH, Choi WS, Lee BM, Yoon KS, Yoon S, Kim HS. *Int J Oncol*. 2012; 41:1101–1109. [PubMed: 22751989]

7. Hymes KB. Clin Lymphoma Myeloma Leuk. 2010; 10:98–109. [PubMed: 20371442]
8. Gutierrez M, Andrianasolo EH, Shin WK, Goeger DE, Yokochi A, Schemies J, Jung M, France D, Cornell-Kennon S, Lee E, Gerwick WH. J Org Chem. 2009; 74:5267–5275. [PubMed: 19572575]
9. Gey C, Kyrylenko S, Hennig L, Nguyen LH, Buttner A, Pham HD, Giannis A. Angew Chem Int Ed Engl. 2007; 46:5219–5222. [PubMed: 17516596]
10. Oh WK, Cho KB, Hien TT, Kim TH, Kim HS, Dao TT, Han HK, Kwon SM, Ahn SG, Yoon JH, Kim TH, Kim YG, Kang KW. Mol Pharmacol. 2010; 78:855–864. [PubMed: 20713551]
11. Napper AD, Hixon J, McDonagh T, Keavey K, Pons JF, Barker J, Yau WT, Amouzegh P, Flegg A, Hamelin E, Thomas RJ, Kates M, Jones S, Navia MA, Saunders JO, DiStefano PS, Curtis R. J Med Chem. 2005; 48:8045–8054. [PubMed: 16335928]
12. Brachmann CB, Sherman JM, Devine SE, Cameron EE, Pillus L, Boeke JD. Genes Dev. 1995; 9:2888–2902. [PubMed: 7498786]
13. Frye RA. Biochem Biophys Res Commun. 2000; 273:793–798. [PubMed: 10873683]
14. Grozinger CM, Chao ED, Blackwell HE, Moazed D, Schreiber SL. J Biol Chem. 2001; 276:38837–38843. [PubMed: 11483616]
15. Bedalov A, Gatabont T, Irvine WP, Gottschling DE, Simon JA. Proc Natl Acad Sci U S A. 2001; 98:15113–15118. [PubMed: 11752457]
16. Silar P, Thiele DJ. Genes Dev. 1991; 104:99–102.
17. Tanny JC, Kirkpatrick DS, Gerber SA, Gygi SP, Moazed D. Mol Cell Biol. 2004; 24:6931–6946. [PubMed: 15282295]
18. Ondeyka J, Harris G, Zink D, Basilio A, Vicente F, Bills G, Platas G, Collado J, Gonzalez A, de la Cruz M, Martin J, Kahn JN, Galuska S, Giacobbe R, Abruzzo G, Hickey E, Liberator P, Jiang B, Xu D, Roemer T, Singh SB. J Nat Prod. 2009; 72:136–141. [PubMed: 19115836]
19. Phillips NJ, Goodwin JT, Fraiman A, Cole RJ, Lynn DG. J Am Chem Soc. 1989; 111:8223–8231.
20. Lang G, Blunt JW, Cummings NJ, Cole ALJ, Munro MHG. J Nat Prod. 2005; 68:810–811. [PubMed: 15921439]
21. Crystallographic data for streptocytin A (**1**) have been deposited at the Cambridge Crystallographic Data Center (deposition number: CCDC894421). Copies of the data can be obtained, free of charge, on application to the Director, CCDC, 12 Union Road, Cambridge CB21EZ, UK [fax: +44-(0)1223–33603.3 or e-mail: deposit@ccdc.cam.ac.uk or <http://www.ccdc.cam.ac.uk>].
22. Flack HD. Acta Crystallogr Sect A. 1983; 39:876–881.
23. Hoofst RW, Straver LH, Spek AL. J Appl Crystallogr. 2008; 41:96–103. [PubMed: 19461838]
24. Ohtani I, Kusumi T, Kashman Y, Kakisawa H. J Am Chem Soc. 1991; 113:4092–4096.
25. Li XC, Ferreira D, Ding Y. Curr Org Chem. 2010; 14:1678–1697.
26. Li L, Si YK. J Pharm Biomed Anal. 2011; 56:465–470. [PubMed: 21794998]
27. Sims JW, Fillmore JP, Warner DD, Schmidt EW. Chem Commun. 2005:186–188.
28. Henrikson JC, Hoover AR, Joyner PM, Cichewicz RH. Org Biomol Chem. 2009; 7:435–438. [PubMed: 19156306]
29. Wang XR, Sena JG, Hoover AR, King JB, Ellis TK, Powell DR, Cichewicz RH. J Nat Prod. 2010; 73:942–948. [PubMed: 20450206]
30. Mincer TJ, Fenical W, Jensen PR. Appl Environ Microbiol. 2005; 71:7019–7028. [PubMed: 16269737]
31. Bruker APEX-II v2010-7 (SAINT v7.66A). Bruker AXS Inc; Madison WI: 2010.
32. Sheldrick GM. Acta Crystallogr, Sect A. 2008; 64:112–122. [PubMed: 18156677]
33. Frisch, MJ.; Trucks, GW.; Schlegel, HB.; Scuseria, GE.; Robb, MA.; Cheeseman, JR.; Scalmani, G.; Barone, V.; Mennucci, B.; Petersson, GA.; Nakatsuji, H.; Caricato, M.; Li, X.; Hratchian, HP.; Izmaylov, AF.; Bloino, J.; Zheng, G.; Sonnenberg, JL.; Hada, M.; Ehara, M.; Toyota, K.; Fukuda, R.; Hasegawa, J.; Ishida, M.; Nakajima, T.; Honda, Y.; Kitao, O.; Nakai, H.; Vreven, T.; Montgomery, JA., Jr; Peralta, JE.; Ogliaro, F.; Bearpark, M.; Heyd, JJ.; Brothers, E.; Kudin, KN.; Staroverov, VN.; Kobayashi, R.; Normand, J.; Raghavachari, K.; Rendell, A.; Burant, JC.; Iyengar, SS.; Tomasi, J.; Cossi, M.; Rega, N.; Millam, JM.; Klene, M.; Knox, JE.; Cross, JB.; Bakken, V.; Adamo, C.; Jaramillo, J.; Gomperts, R.; Stratmann, RE.; Yazyev, O.; Austin, AJ.; Cammi, R.; Pomelli, C.; Ochterski, JW.; Martin, RL.; Morokuma, K.; Zakrzewski, VG.; Voth,

GA.; Salvador, P.; Dannenberg, JJ.; Dapprich, S.; Daniels, AD.; Farkas, Ö.; Foresman, JB.; Ortiz, JV.; Cioslowski, J.; Fox, DJ. Gaussian 09, Revision A.1. Gaussian, Inc; Wallingford CT: 2009.

\$watermark-text

\$watermark-text

\$watermark-text

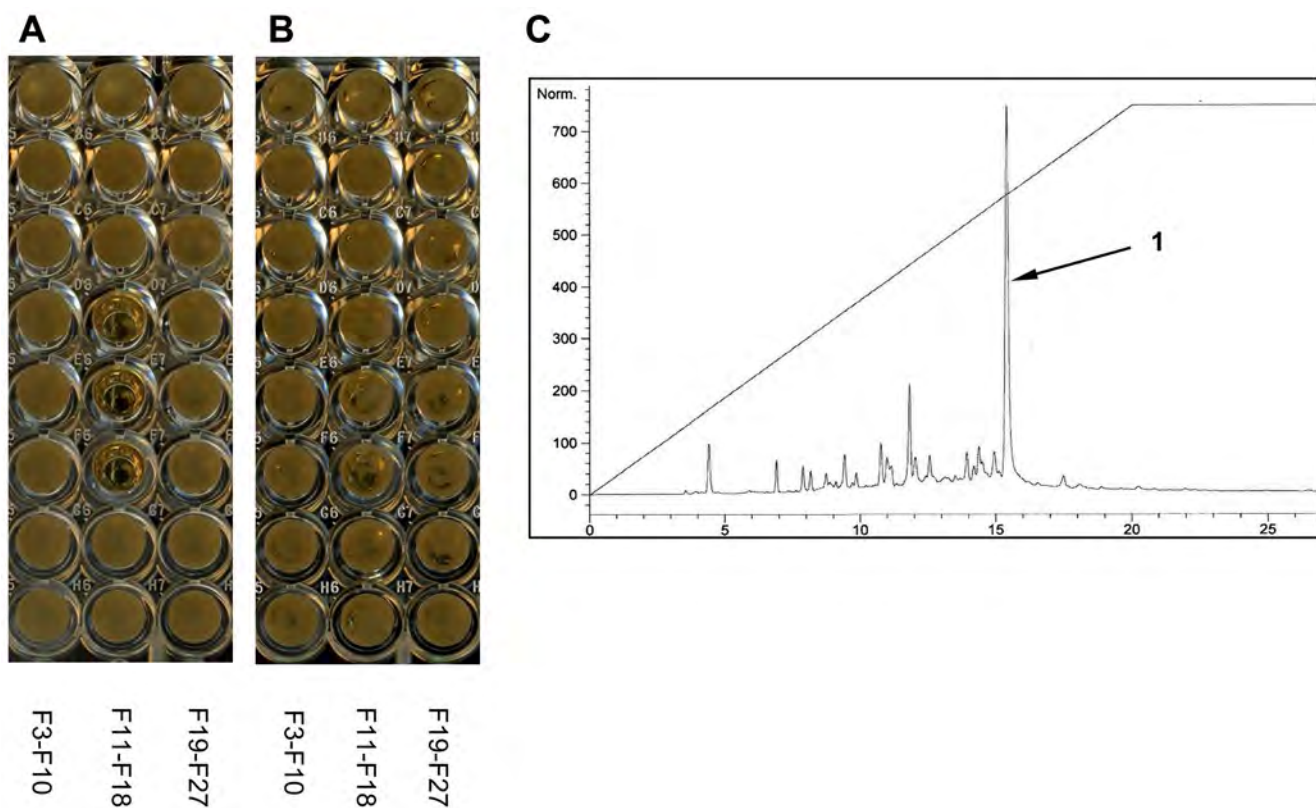


Figure 1.

Yeast screening result (24 h) for the peak library of the CP13-10 strain; (A) YPD media with 5-FOA, (B) YPD media, (C) HPLC chromatogram (UV at 280 nm) of the extract peak library (10% to 100% CH₃CN in H₂O, linear gradient over 20 min). The number of fractions in A and B corresponds to the retention time in the HPLC chromatogram. Selective activity was observed for fractions: F14 (14 min), F15 (15 min) and F16 (16 min).

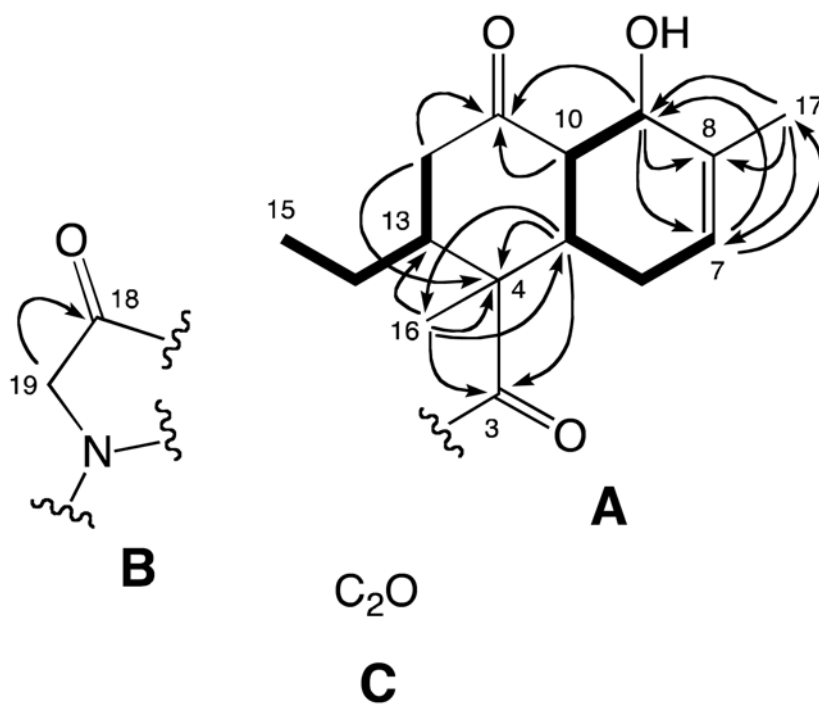


Figure 2. Substructures and significant 2D NMR correlations for **1**. Arrows indicate HMBC correlations. Bold lines show COSY spin systems.

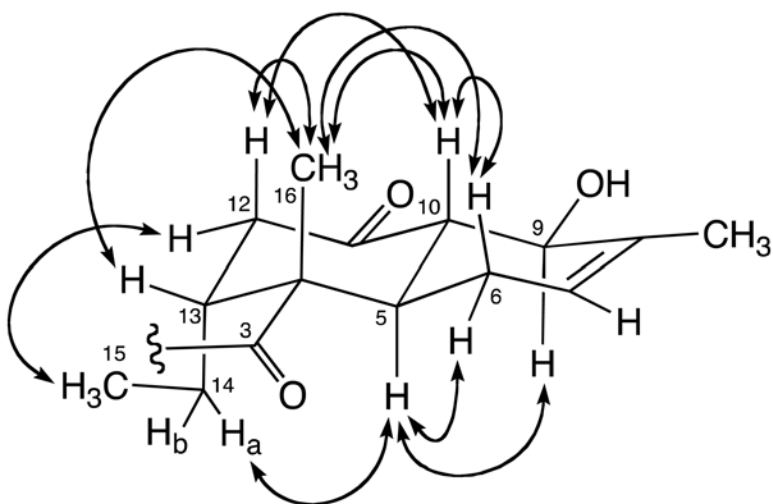


Figure 3.
Key NOESY correlations for **1**.

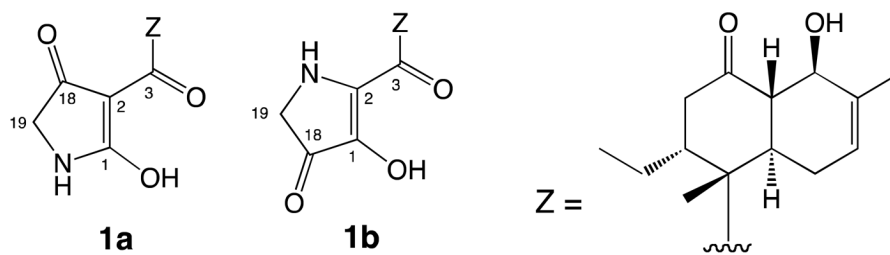


Figure 4.
Working structures for **1**.

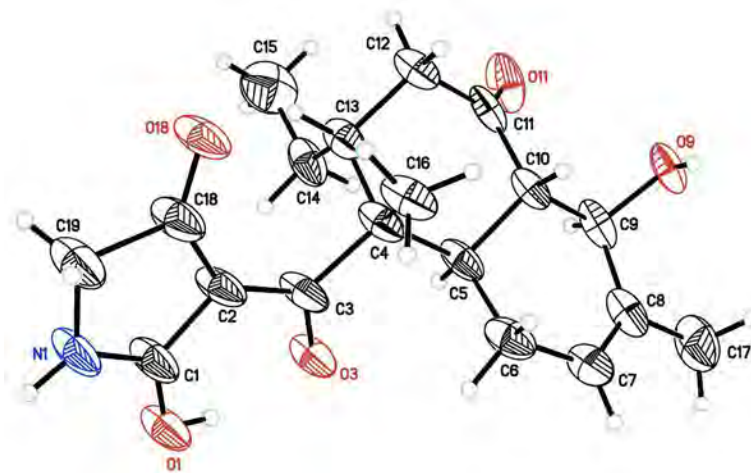


Figure 5.
X-ray crystal structure for **1**. Thermal displacement ellipsoids depicted at 50% probability with chloroform and the water of crystallization omitted for clarity.

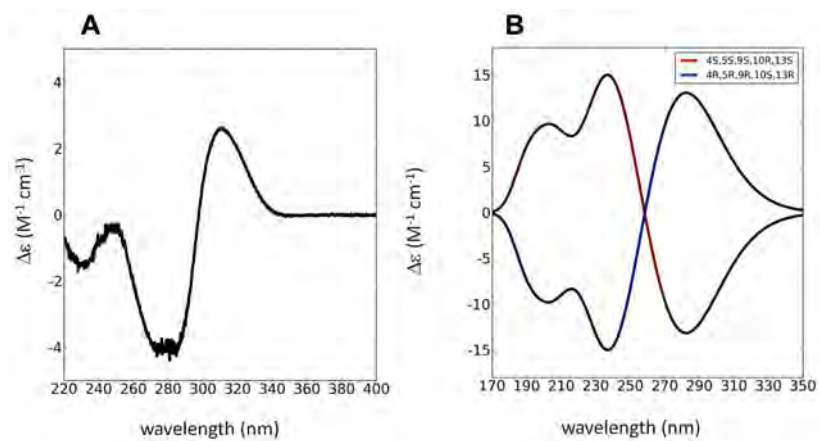


Figure 6. Experimental (A) and calculated (B) ECD spectra of **1**.

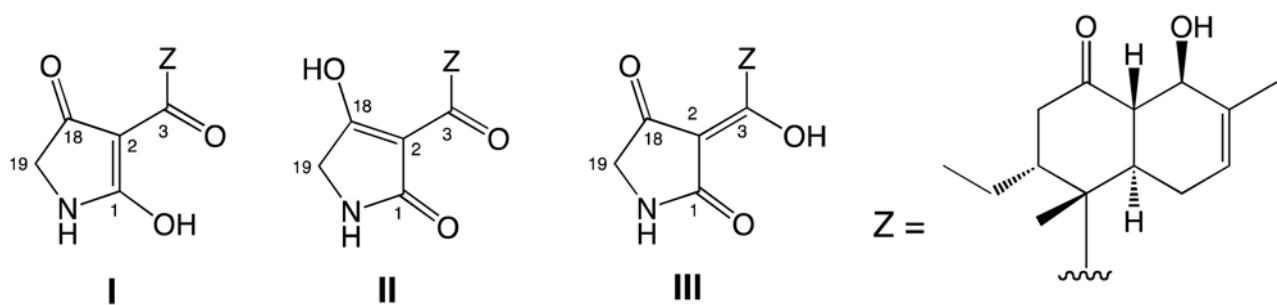


Figure 7.
Three possible tautomers for **1**.

Table 1

NMR Data of **1** in CD₃OD (500 MHz for ¹H, 125 MHz for ¹³C)

position	δ_c , type	δ_H , mult (<i>J</i> in Hz)	COSY	HMBC	NOESY
1	180.1, ^a C				
2	100.6, ^a C				
3	202.4, C				
4	51.6, C				
5	40.9, CH	2.61, ddd (12.7, 10.7, 3.8)	6ax, 10	3, 4, 6, 7, 9, 10, 16	6eq, 9, 14a
6ax	29.0, CH ₂	2.01, m	5, 6eq, 9, 17		6eq, 7, 10
6eq		2.20, br. d (16.7)	6ax, 7	5, 7, 8, 10	5, 6ax, 7
7	124.8, CH	5.48, dq (6.1, 2.3)	6eq, 17	5, 6, 9, 17	6ax, 6eq, 17
8	135.6, C				
9	70.1, CH	4.44, br. d (8.6)	6ax, 10, 17	5, 7, 8, 10, 11	5, 10, 17
10	55.2, CH	2.48, dd (12.7, 8.6)	5, 9	5, 6, 9, 11	6ax, 9, 12ax, 16
11	213.9, C				
12ax	40.2, CH ₂	2.88, dd (13.7, 4.8)	12eq, 13	4, 11, 13, 14	10, 12eq, 13, 16
12eq		2.37, dd (13.7, 3.1)	12ax	4, 10, 11, 13, 14	12ax, 13, 15
13	44.3, CH	3.07, br. d (9.8)	12ax, 14a		12ax, 12eq, 14b, 15, 16
14a	23.5, CH ₂	0.98, ddq (14.0, 11.6, 7.1)	13, 14b, 15	12, 13, 15	5, 14b, 15
14b		1.15, m	14a, 15	4, 12, 13, 15	13, 14a, 15
15	12.3, CH ₃	0.79, t (7.2)	14a, 14b	13, 14	12eq, 13, 14a, 14b
16	16.0, CH ₃	1.79, s		3, 4, 5, 13	6ax, 10, 12ax, 13
17	19.4, CH ₃	1.71, br. dd (2.3, 1.2)	7, 6ax, 9	7, 8, 9	7, 9
18	192.4, C				
19	51.2, CH ₂	3.79 (2H), m		1, 18	

^aDetected at 75 MHz



Novel pyridino- α -pyrone sesquiterpene type pileotin produced by a sea urchin-derived *Aspergillus* sp.

Mayumi Kitano^a, Takeshi Yamada^{a,*}, Taro Amagata^b, Katsuhiko Minoura^a, Reiko Tanaka^a, Atsushi Numata^a

^a Osaka University of Pharmaceutical Sciences, 4-20-1 Nasahara, Takatsuki, Osaka 569-1094, Japan

^b Department of Chemistry and Biochemistry, San Francisco State University, San Francisco, CA 94132, USA

ARTICLE INFO

Article history:

Received 16 April 2012

Revised 28 May 2012

Accepted 30 May 2012

Available online 7 June 2012

Keywords:

Sea urchin

Toxopneustes pileolus

Pileotin

Marine-derived microorganisms

Aspergillus fumigatus

Oxalicine B

Cytotoxic activity

ABSTRACT

A new metabolite, pileotin A, was isolated from a strain of *Aspergillus fumigatus* originally obtained from the sea urchin *Toxopneustes pileolus* together with the known compound oxalicine B. The relative stereostructure of pileotin A was elucidated based on spectroscopic analyses, including 1D and 2D NMR techniques. This unique pyridino- α -pyrone sesquiterpene type metabolite has spiro- δ -lactone at C-4.

© 2012 Elsevier Ltd. All rights reserved.

We have focused on potential new antitumor materials from marine-derived microorganisms as marine products include a number of compounds with unique structures, some of which

may exhibit unusual bioactivities. As a part of this study, we have examined metabolites from the fungus *Aspergillus fumigatus* OUPS-N138 originally obtained from the sea urchin *Toxopneustes pileolus*,

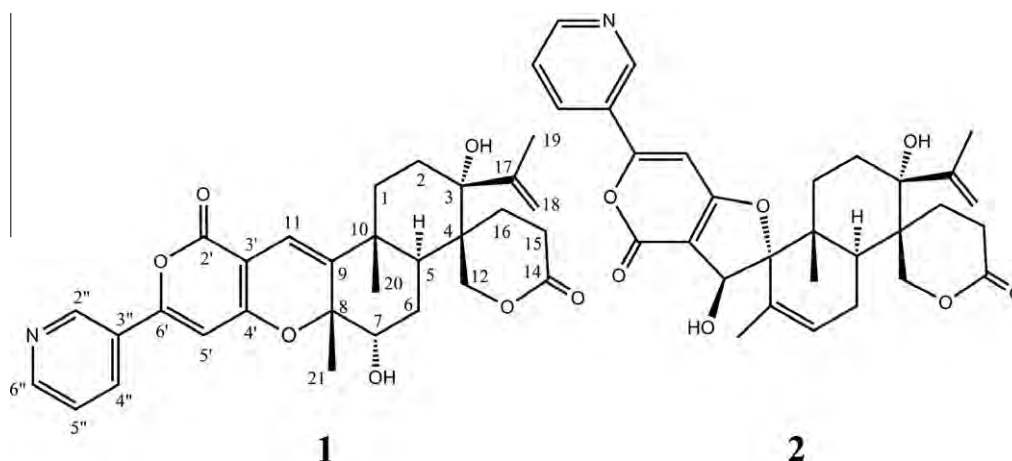


Figure 1. Structures of metabolites from *A. fumigatus*.

* Corresponding author.

E-mail address: yamada@gly.oups.ac.jp (T. Yamada).

Table 1
NMR spectroscopic data (CDCl₃) for pileotin A (**1**)

Position		$\delta_{\text{H}}^{\text{a}}$		J/Hz	$^1\text{H}-^1\text{H}$ COSY	NOE	$\delta_{\text{C}}^{\text{c}}$	HMBC (c) ^b	
1	α	2.11	td	13.2 (1 β , 2 β), 3.2 (2 α)	1 β , 2 α , 2 β	1 β , 2 α , 5, 11	31.9 (t)		
	β	1.89	m		1 α , 2 α , 2 β	1 α , 11, 20			
	α	1.60	dt		15.3 (2 β), 3.2 (1 α , 1 β)	1 α , 1 β , 2 β		1 α , 2 β , 18B	30.0 (t)
	β	2.42	m		1 α , 1 β , 2 α	2 α , 12 α , 19, 20			
3						76.5 (s)			
4						44.7 (s)			
5		2.74	dd	12.8 (6 β), 2.0 (6 α)	6 α , 6 β	1 α , 6 α , 16 α	40.4 (d)	12	
	α	2.04	ddd		12.8 (6 β), 3.2 (7), 2.0 (5)	5, 6 β , 7			5, 6 β , 7, 15 α , 16 β
6	β	1.94	td	12.8 (5, 6 α), 2.0 (7)	5, 6 α , 7	6 α , 7, 12 α , 20, 21	26.4 (t)		
		4.09	dd		3.2 (6 α), 2.0(6 β)	6 α , 6 β		6 α , 6 β , 21, 7-OH	
7							72.3 (d)		
8							84.1 (s)		
9							145.1 (s)		
10							38.7 (s)		
11		6.45	s			1 α , 1 β	111.5 (d)	8, 10, 2', 4'	
	α	4.42	d	12.7 (12 β)	12 β	2 β , 12 β , 19, 20			
12	β	4.14	d	12.7 (12 α)	12 α	6 β , 12 α , 20	68.3 (t)	3	
							173.2 (s)	3, 4, 14, 16	
14							30.0 (t)		
	α	2.46	m		15 α , 16 α , 16 β	15 β , 16 α , 16 β			
15	β	2.38	m		15 β , 16 α , 16 β	6 α , 15 α , 16 β			
	α	2.53	m		15 α , 15 β , 16 β	15 α , 16 β , 18B	25.0 (t)		
16	β	1.66	ddd	13.8 (16 α), 5.2 (15 α), 2.3 (15 β)	15 α , 15 β , 16 α	5, 6 α , 15 α , 15 β , 16 α			
							150.2 (s)		
17							115.1 (t)	3, 19	
	A	5.09	s		19	18B, 19			
18	B	5.21	s		19	2 α , 16 α , 18A, 3-OH		3, 19	
		1.92	s		18A, 18B	2 β , 12 α , 18A	21.7 (q)	3, 17, 18	
19		1.20	s			1 β , 2 β , 6 β , 11, 12 α , 12 β , 21	23.6 (q)	1, 5, 9, 10	
20		1.54	s			6 β , 7, 20	25.6 (q)	7, 8, 9	
21							161.2 (s)		
2'							101.7 (s)		
3'							160.8 (s)		
4'		6.58	s			2'', 4''	98.3 (d)	3', 4', 6', 3''	
5'							157.3 (s)		
6'							146.3 (d)		
2''		9.02	br s			5'	127.8 (s)		
3''							132.9 (d)		
4''		8.13	d	8.0 (5'')	5''	5', 5''	123.7 (d)		
5''		7.42	dd	8.0 (4''), 4.6 (6'')	4'', 6''	4'', 6''	151.5 (d)		
6''		8.69	br d	4.6 (5'')	5''	5''			
3-OH		1.09	s			18B			
7-OH		2.75	br s			7			

^a ^1H chemical shift values (d ppm from SiMe₄) followed by multiplicity and then the coupling constants (J/Hz). Figures in parentheses indicate the proton coupling with that position.

^b Long range $^1\text{H}-^{13}\text{C}$ correlations from H to C observed in the HMBC experiment.

and isolated new compounds together with a known compound, which have a pyridino- α -pyrone sesquiterpene core. The new compound was designated as pileotin A (**1**). On the other hand, the known compound was identified with oxalicine B by comparison with the spectral data reported in previous literature.¹ Pyripyropenes^{2–4} isolated from the same class of fungus, and oxalicines^{5–8} and decaturins^{5–7} isolated from *Penicillium* fungus had been reported previously as metabolites having a pyridino- α -pyrone sesquiterpene skeleton. We describe herein the elucidation of the relative stereostructure for **1** and the biological activity of **2**.

A microorganism from the sea urchin *T. pileolus* was cultured at 27 °C for 4 weeks in a medium (80 L) containing 1% soluble starch and 0.1% casein in 50% artificial seawater adjusted to pH 7.5. The culture was filtered under suction, and the culture filtrate was extracted three times with EtOAc. The combined extracts were evaporated in vacuo to afford a mixture of crude metabolites that exhibited cytotoxicity against P388 cell line (IC₅₀ 2.5 $\mu\text{g}/\text{mL}$). The EtOAc extract was purified employing Sephadex LH-20, silica gel column chromatography, and reverse phased HPLC to afford pileotin A (**1**, 1.3 mg) and oxalicine B (**2**, 3.8 mg) (Fig. 1).

Pileotin A (**1**)⁹ was assigned the molecular formula C₃₀H₃₃NO₇ based on the [M]⁺ peak in HREIMS. Its IR spectrum exhibited bands at 3446, 1733, and 1716 cm⁻¹, characteristic of a hydroxy group and lactones. A close inspection of the ^1H and ^{13}C NMR spectra (Table 1) of **1** in DEPT and HMQC experiments revealed the

presence of two tertiary methyls (C-20, C-21), one olefin methyl (C-19), six sp³-hybridized methylenes (C-1, C-2, C-6, C-12, C-15, and C-16) including an oxygen-bearing carbon (C-12), two sp³-methines (C-5 and C-7) including an oxygen-bearing carbon (C-7), a terminal methylene (C-18), six sp²-methines (C-11, C-5', C-2'', C-4'', C-5'', and C-6''), four quaternary sp³-carbons (C-3, C-4, C-8, and C-10) including two oxygen-bearing carbons (C-3 and C-8), six quaternary sp²-carbons (C-9, C-17, C-3', C-4', C-6', and C-3'') including two oxygen-bearing carbons (C-4' and C-6'), and two ester carbonyls (C-14 and C-2'). First $^1\text{H}-^1\text{H}$ COSY correlations

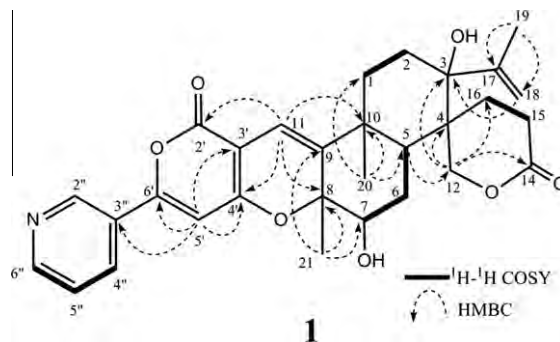


Figure 2. $^1\text{H}-^1\text{H}$ COSY and key HMBC correlations in **1**.

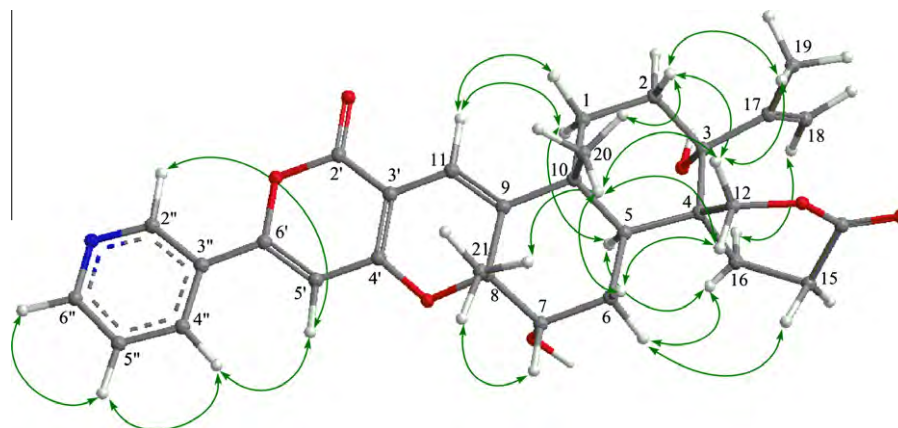


Figure 3. Key NOEs for **1**.

shown by bold-faced lines and the key HMBC correlations summarized in Figure 2 revealed the sesquiterpene moiety to have a δ -spiro lactone at C-4. In the ^1H NMR spectrum, signals observed in low field (H-2'', H-4'', H-5'' and H-6'') together with their ^1H - ^1H COSY and HMBC correlations (Fig. 2) suggested the presence of a pyridine ring having a substituent at C-3''. In addition, HMBC correlations from H-5' to C-3', C-4', C-6' and C-3'', and from H-11 to C-2' and C-4' demonstrated the presence of a 3,4-disubstituted 6-(3-pyridyl)- α -pyrone. The connection between the two units (the sesquiterpene core and α -pyrone moiety) was deduced on the basis of HMBC correlations [H-11/C-8, C-10, C-2' and C-4'], and carbon signals in a lower field than usual [C-4' (δ_{C} 170.7)] to establish a planar structure of **1** as shown in Figure 2.

The relative stereochemistry of **1** was deduced from NOESY experiments (Fig. 3). NOE correlations (H-1 α /H-5, H-2 β /H-20, and H-12 β /H-20) implied that the A ring existed in a chair conformation with H-1 α , 3-OH, and H-5 in coaxial arrangements. In the spiro δ -lactone ring at C-4, NOEs (H-12 α /H-2 β , H-12 α /H-19, H-12 β /H-6 β , H-16 α /H-18B, H-16 β /H-5, and H-15 β /H-6 α) showed a half boat conformation. The NOE correlations (H-20/H-6 β , H-21) together with the large coupling constant ($J_{5,6\beta} = 12.8$ Hz) implied that the B ring existed in a half chair conformation with 8-CH₃, H-6 β , and 10-CH₃ in coaxial arrangements. This evidence and the vicinal proton coupling constant ($J_{6\alpha,7} = 3.2$ Hz and $J_{6\beta,7} = 2.0$ Hz) showed that 7-OH was oriented *trans* to 8-CH₃ in an axial arrangement, allowing for the relative stereostructure of **1**. In future, following the supplement of **1** by repeating the incubation, we will determine its absolute stereostructure.

Oxalicine B (**2**) was assigned the same molecular formula as **1** based on the deduction made from HREIMS data. The general features of the ^1H and ^{13}C NMR spectra of **2** (vide info) revealed the presence of a pyridine ring having a substituent, an α -pyrone, an isopropenyl group, a δ -lactone, and a sesquiterpene core, which were the same partial structures as **1**. In comparison with **1** for the ^1H and ^{13}C NMR spectra, the signals for the A ring except for C-1, δ -lactone, and the pyridine ring closely resembled those of **1**. The signals for α -pyrone showed some differences from **1**. Following the analyses of the ^1H - ^1H COSY and HMBC correlations, **2** was identified with oxalicine B by the verification of the spectral data against that reported in the previous literature.¹

As a primary screen for antitumor activity, cancer cell growth inhibitory properties of oxalicine B (**2**) were examined using the

murine P388 leukemia cell line. **2** exhibited moderate cytotoxic activity (55.9 μM). The activity of 5-fluorouracil as positive standard was 0.6 μM . This time, the assay for **1** was impracticable because of insufficient quantity. Henceforth, we will supplement **1** with enough culture volume, and examine using a disease-oriented panel of 39 human cell lines^{10,11} to reveal their selective cytotoxic activity and mode of action.

Acknowledgments

We thank Dr. T. Ito (the National Institute of Technology and Evaluation, Biological Resource Center) for identification of the fungal strain. We are grateful to Ms. M. Fujitake for MS measurements. This study was supported by a Grant-in-aid for High Technology from the Ministry of Education, Culture, Sports, Science, and Technology, Japan.

Supplementary data

Supplementary data associated with this article can be found, in the online version, at <http://dx.doi.org/10.1016/j.tetlet.2012.05.144>.

References and notes

- Ubillas, R. P. "Chemical Studies on *Penicillium oxalicum*," Ph. D. thesis, University of Missouri-Columbia, 1990, pp. 61–74.
- Kim, Y. K.; Tomoda, H.; Omura, S. *J. Antibiot.* **1994**, *47*, 154–162.
- Tomoda, H.; Tabata, N.; Yang, D.-J.; Takayanagi, H.; Nishida, H.; Omura, S. *J. Antibiot.* **1995**, *48*, 495–498.
- Tomoda, H.; Tabata, N.; Yang, D.-J.; Namatae, I.; Tanaka, H.; Omura, S. *J. Antibiot.* **1996**, *49*, 292–298.
- Li, C.; Gloer, J. B.; Wicklow, D. T.; Dowd, P. F. *J. Nat. Prod.* **2005**, *68*, 319–322.
- Zhang, Y.; Li, C.; Swenson, D. C.; Gloer, J. B.; Wicklow, D. T.; Dowd, P. F. *Org. Lett.* **2003**, *5*, 773–776.
- Abe, M.; Imai, T.; Ishii, N.; Usui, M.; Okuda, T.; Oki, T. *J. Pestic. Sci.* **2007**, *32*, 124–127.
- Ubillas, R. P.; Barnes, C. L.; Gracz, H.; Rottinghaus, G. E.; Tempesta, M. S. *J. Chem. Soc., Chem. Commun.* **1989**, 1618–1619.
- Pileotin A (**1**): Pale yellow oil; $[\alpha]_{\text{D}}^{25} -4.1$ (c 0.11, EtOH); UV λ_{max} (EtOH) nm (log ϵ) 204 (4.3), 254 (4.1), 293 (3.7), 381 (3.9); IR ν_{max} (liquid) cm^{-1} 3446, 1733, 1716, 1558; 519.2251 [M]⁺ (calcd for C₃₀H₃₃NO₇, 519.2247). ^1H and ^{13}C NMR data are listed in Table 1.
- Yamori, T.; Matsunaga, A.; Sato, S.; Yamazaki, K.; Komi, A.; Ishizu, K.; Mita, I.; Edatsugi, H.; Matsuba, Y.; Takezawa, K.; Nakanishi, O.; Kohno, H.; Nakajima, Y.; Komatsu, H.; Andoh, T.; Tsuruo, T. *Cancer Res.* **1999**, *59*, 4042–4049.
- Yamori, T. *Cancer Chemother. Pharmacol.* **2003**, *52*, S74–S79.

ORIGINAL ARTICLE

Mnk1 is a novel acinar cell-specific kinase required for exocrine pancreatic secretion and response to pancreatitis in mice

Jaroslav Cendrowski,¹ Víctor J Sánchez-Arévalo Lobo,¹ Matthias Sendler,² Antonio Salas,³ Jens-Peter Kühn,⁴ Xavier Molero,⁵ Rikiro Fukunaga,⁶ Julia Mayerle,² Markus M Lerch,² Francisco X Real^{1,7}

► Additional material is published online only. To view please visit the journal online (<http://dx.doi.org/10.1136/gutjnl-2013-306068>).

For numbered affiliations see end of article.

Correspondence to

Dr Francisco X Real, Cancer Cell Biology Programme, Centro Nacional de Investigaciones Oncológicas (CNIO), Melchor Fernández Almagro, 3, Madrid 28029, Spain; preal@cnio.es

Received 11 September 2013

Revised 1 June 2014

Accepted 25 June 2014

Published Online First

18 July 2014

ABSTRACT

Objective Pancreatic acinar cell maturation is dependent on the activity of the pancreas transcription factor 1 (PTF1) complex. Induction of pancreatitis leads to MAP kinase activation and transient suppression of the acinar differentiation programme. We investigated the role of MAP kinase-interacting kinase 1 (Mnk1) in mouse exocrine pancreas development and in the response to secretagogue-induced pancreatitis.

Design Mnk1 expression was analysed using immunohistochemistry, RT-qPCR and western blotting. Ptf1a binding to *Mnk1* was assessed by chromatin immunoprecipitation and qPCR. Acute pancreatitis was induced in wild type and *Mnk1*^{-/-} mice by 7 h intraperitoneal injections of caerulein. In vitro amylase secretion and trypsinogen activation were assessed using freshly isolated acinar cells. In vivo secretion was quantified by secretin-stimulated MRI.

Results Mnk1 is expressed at the highest levels in pancreatic acinar cells and is a direct PTF1 target. Mnk1 is activated upon induction of pancreatitis and is indispensable for eIF4E phosphorylation. The pancreas of *Mnk1*^{-/-} mice is histologically normal. Digestive enzyme content is significantly increased and c-Myc and *Ccnd1* levels are reduced in *Mnk1*^{-/-} mice. Upon induction of acute pancreatitis, *Mnk1*^{-/-} mice show impaired eIF4E phosphorylation, activation of c-Myc and downregulation of zymogen content. Acinar cells show defective localisation of digestive enzymes, polarity defects and impaired secretory response in vitro and in vivo.

Conclusions Mnk1 is a novel pancreatic acinar cell-specific stress response kinase that regulates digestive enzyme abundance and eIF4E phosphorylation. It is required for the physiological secretory response of acinar cells and for the homeostatic response to caerulein administration during acute pancreatitis.

INTRODUCTION

Pancreatic acinar cells originate from multipotent progenitor cells (MPCs) in a pancreas transcription factor 1 (PTF1) complex-dependent manner.¹ Ptf1a, a pancreas-specific PTF1 component, is expressed in MPCs at E9.5–E13 and thereafter becomes restricted to acinar precursors and mature cells where it is required for differentiation.¹ Acinar cells are dedicated to high-level production of digestive enzymes and regulated secretion.² To prevent self-digestion, they have evolved several

Significance of this study

What is already known on this subject?

- Acinar cells are specialised to produce, store and secrete high amounts of digestive enzymes.
- The acinar differentiation programme is strictly dependent on pancreas transcription factor 1 (PTF1) transcriptional activity.
- In mice, acute caerulein-induced pancreatitis leads to intracellular digestive enzyme activation followed by tissue damage and enzyme leakage to plasma.
- Upon pancreatitis, MAP kinases are activated but their exact role has not been unravelled.

What are the new findings?

- The stress kinase Mnk1 is highly expressed in mouse pancreatic acinar cells being a transcription target of PTF1.
- *Mnk1*^{-/-} mice develop normally but display an increase in pancreatic digestive enzyme content and a decrease in c-Myc and *Ccnd1*, proteins known to be regulated by Mnk1-eIF4E pathway.
- Mnk1 is activated upon caerulein-induced acute pancreatitis. In its absence, the physiological downregulation of digestive enzymes and upregulation of c-Myc levels are impaired.
- Upon secretagogue stimulation, pancreatic acinar cells of *Mnk1*^{-/-} mice display polarity defects in vivo and suboptimal secretory capacity in vitro.
- *Mnk1*^{-/-} mice show a defect in pancreatic secretion upon secretin stimulation in vivo.

How might it impact on clinical practice in the foreseeable future?

- Pharmacological modulation of the Mnk1/MAPK pathway may contribute to the treatment of pancreatitis.
- MNK1 may participate in the pathogenesis of pancreatitis and pancreatic ductal adenocarcinoma.

protective mechanisms including the synthesis of proteases as proenzymes, their storage in zymogen granules, production of protease inhibitors and shutdown of enzyme production in response to stress.³



CrossMark

To cite: Cendrowski J, Sánchez-Arévalo Lobo VJ, Sendler M, et al. *Gut* 2015;64:937–947.

Acute pancreatitis leads to local tissue damage and enzyme leakage. In mice, it can be modelled by administration of supra-physiological doses of caerulein, a cholecystokinin (CCK) analogue.⁴ Initial events include impaired exocytosis and intracellular activation of trypsinogen; cathepsin B has been proposed to play a crucial role in this process.⁵ Acute caerulein-induced pancreatic damage leads to the transient downregulation of the acinar transcription programme.^{6–7} Persistent stress leads to sustained suppression of acinar differentiation favouring acino-ductal metaplasia, a preneoplastic lesion in models of pancreatic ductal adenocarcinoma.^{8–9}

The response to extracellular signals and stress is largely coordinated by the JNK, ERK and p38 MAP kinase signalling pathways.¹⁰ These pathways are activated during pancreatitis but their role in damage response or in the ensuing regeneration has not been fully unravelled.^{11–12} The MAP kinase-interacting kinases Mnk1 and Mnk2 integrate signals from Erk1/2 and p38 α / β .^{13–14} Upon direct and simultaneous phosphorylation by them, Mnks are activated and regulate protein synthesis through phosphorylation of the translation initiation factor eIF4E, among other mechanisms.¹⁵ eIF4E is involved in the general regulation of translation initiation; its phosphorylation leads to preferential translation of a subset of mRNAs coding for important proteins such as c-Myc and Ccnd1.^{16–17} Mice lacking Mnk1, Mnk2 or both kinases develop normally and display no overt phenotype. However, Mnk1/2 null embryonic fibroblasts lack basal and stress-induced eIF4E phosphorylation.¹⁸ The role of Mnk and eIF4E phosphorylation in the pancreas has not been studied.

Here, we show that Mnk1 is expressed at very high levels in pancreatic acinar cells, is a PTF1 target and is involved in the control of digestive enzyme content. We use *Mnk1*^{-/-} mice to assess its role in acinar physiology as well as in the response to acute damage and the ensuing regeneration. Most notably, Mnk1 is required for physiological exocrine pancreatic secretion.

MATERIALS AND METHODS

Mice

Mnk1^{-/-} mice were generated in a 129 genetic background.¹⁸ Wild type (WT) and *Mnk1*^{-/-} mice were bred to a predominant C57Bl/6J background and maintained under sterile and pathogen-free conditions. Unless otherwise indicated, experiments were conducted with 10–14-week-old mice. Procedures were approved by the Animal Ethical Committee of Instituto de Salud Carlos III and performed following guidelines for Ethical Conduct in the Care and Use of Animals as stated in The International Guiding Principles for Biomedical Research involving Animals, developed by the Council for International Organizations of Medical Sciences.

Caerulein-induced acute pancreatitis

Acute pancreatitis was induced by 7 hourly injections of caerulein (50 μ g/kg; Sigma-Aldrich) as described.⁴ Mice were sacrificed 0.5, 4, 8 h, 1, 2 and 7 days after the first injection. Control mice were not treated.

Histopathology, immunohistochemistry and immunofluorescence

Tissues were fixed in 4% PBS-buffered formaldehyde, paraffin-embedded and serially sectioned. For histology, sections were stained with H&E. Immunoperoxidase and immunofluorescence stainings were performed as reported.¹⁹ Primary antibodies used are listed as online supplementary information. Peroxidase-conjugated

secondary antibodies were from Dako; nuclei were counterstained with haematoxylin. For double-immunofluorescence, species-specific Alexa- and Cyanine-conjugated antibodies were used (Invitrogen and Jackson Laboratories). Nuclei were counterstained with 4',6-diamidino-2-phenylindole (DAPI). Images were captured using a Leica TCS SP5 MP confocal microscope and pseudo-coloured using Leica Application Suite (Leica Microsystems).

mRNA expression analyses

Total RNA was extracted using guanidine thiocyanate buffer, followed by acid phenol-chloroform. RNA was treated with DNase I (Ambion DNA-free kit, Invitrogen) and converted to cDNA using TaqMan reverse transcription reagents (Applied Biosystems). Quantitative RT-PCR (RT-qPCR) was performed using SYBR-green mastermix in a Prism7900HT instrument (Applied Biosystems). Reactions were done in triplicate. Gene expression was normalised to endogenous Hprt mRNA, using the $\Delta\Delta$ Ct method. Primers (see online supplementary table S1) were designed using Primer3Plus.

Protein analyses

Extracts were prepared in RIPA buffer (50 mM Tris-HCl pH 7.4, 150 mM NaCl, 1 mM ethylenediaminetetraacetic acid (EDTA), 1% Triton X-100, 1% sodium deoxycholate, 0.1% SDS) supplemented with protease and phosphatase inhibitors and sonicated. Primary antibodies used are listed in online supplementary information.

Chromatin immunoprecipitation

Chromatin immunoprecipitation (ChIP) was performed using pancreas from 8- to 12-week-old mice, as described,³ followed by qPCR (primers listed in online supplementary table S2).

Biochemical assays

Pancreatic lysates were prepared as described.⁷ Acini were isolated with collagenase (NB8 Broad Range, SERVA).²⁰ Tissue amylase activity was measured using Reflotron Pancreatic Amylase tests (Roche). Trypsin and cathepsin B activities were measured by fluorometric enzyme kinetics.²¹ Amylase release assays were performed as reported.²⁰

MR cholangiopancreatography

MRI was used to measure pancreatic exocrine function. MR cholangiopancreatography (MRCP) imaging (MRI) was performed using a 7.1 Tesla animal MR system (Bruker, Ettlingen, Germany) and a mouse whole body coil. Animals were allowed free access to pineapple juice, instead of water, 24 h before the MRI examination. Images were acquired before, 5 and 10 min after retro-orbital intravenous secretin injection (ChiroStim, ChiRhoClin, Burtonville, Maryland, USA) (10 IU units/kg) using a T2-weighted turbo-spin-echo sequence. Sequences were acquired using the following parameters: TR/TE 4400/83 ms; flip angle: 180°; matrix 256 \times 256; field of view 40 \times 40 mm; bandwidth 315 hz/pixel; slice thickness 1 mm; 20 slices. An expert GI radiologist analysed the images. Fluid secretion into the small intestine was segmented in each slice using Osirix (V5; Pixameo, Bernex, Switzerland). A fluid zone was defined by the high signal intensity in T2-weighted images. Care was taken to avoid artefacts caused by respiratory, bowel motion and field heterogeneity. The volume of intraluminal small intestinal fluid was assessed before and after injection of secretin. To evaluate the total excreted volume (TEV), measurements after secretin injection were normalised to measurements before secretin injection.

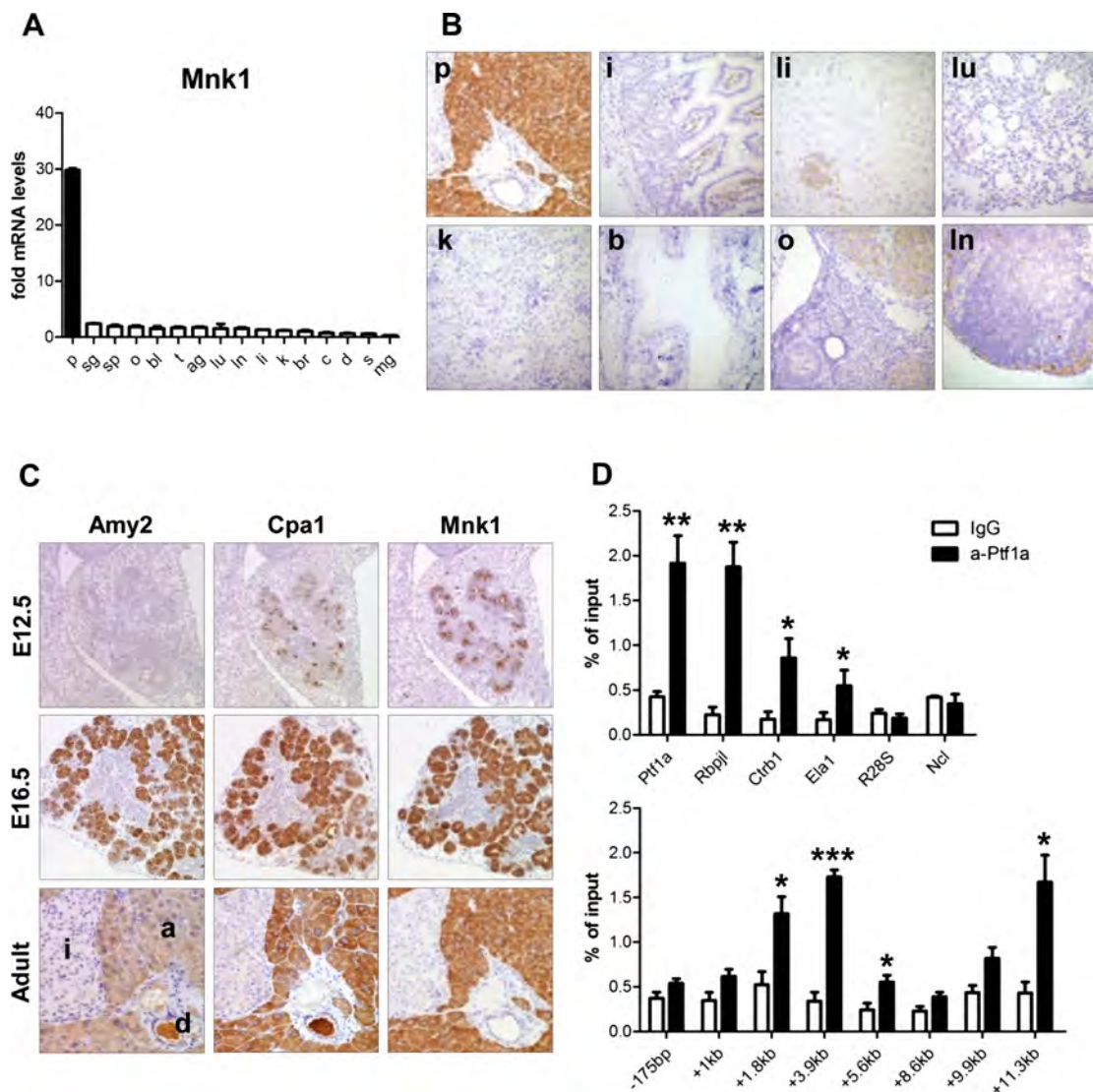


Figure 1 *Mnk1* is a novel Ptf1a target highly expressed in pancreatic acinar cells. (A and B) *Mnk1* mRNA (A) and protein (B) expression in adult mouse tissues (p, pancreas; sg, salivary gland; sp, spleen; o, ovary; bl, bladder; t, thymus; ag, adrenal gland; lu, lung; ln, lymph node; li, liver; k, kidney; br, brain; c, colon; d, duodenum; s, stomach; mg, mammary gland) detected by RT-qPCR (brain tissue used as reference) and immunohistochemistry. (C) Expression of *Amy2*, *Cpa1* and *Mnk1* in embryonic (E12.5 and E16.5) and adult mouse pancreas (a, acinar cells; d, duct; i, islets). (D) Ptf1a binding to known PTF1 target genes (upper) and *Mnk1* assessed by ChIP-qPCR (*R28S* and *Ncl*, negative controls) (n=3/group). Results shown as mean±SEM; *p<0.05, **p<0.01, ***p<0.001.

Statistical analyses

Data are provided as mean±SEM. Statistical analysis was performed using unpaired two-tailed Student t test (p<0.05 was considered significant) using Graph Pad Prism software.

RESULTS

Mnk1 is a Ptf1a target gene that is highly expressed in pancreatic acinar cells

Manual curation of Genepaint in situ hybridisation images (<http://www.genepaint.org>) showed that *Mnk1* is highly expressed in mouse embryonic pancreas (see online supplementary figure S1A). This was confirmed at the protein level by immunohistochemistry: the pancreas is the embryonic tissue with highest *Mnk1* immunoreactivity (see online supplementary figure S1A). In the adult, mRNA expression of *Mnk1*—but not *Mnk2*—was 20–30-fold higher in the pancreas than in any other tissue analysed (figure 1A and online supplementary

figure S1C). Accordingly, the protein was also most abundant in the adult mouse pancreas (figure 1B).

Mnk1 was detected in pancreatic MPCs at E12.5 (*CpA1*^{low} and *Amy2*⁻); at E16.5, expression was restricted to acinar precursors (*CpA1*^{high} and *Amy2*^{high}). In the adult pancreas, *Mnk1* was detected exclusively in acinar cells (figure 1C). *Mnk1* mRNA, but not *Mnk2*, expression increased progressively during development following a pattern that was highly similar to that of digestive enzymes (see online supplementary figure S1B,C).

The acinar-specific expression and developmental regulation suggested that *Mnk1* might be a PTF1 target. Mining a Ptf1a ChIP-seq dataset (R MacDonald, personal communication) revealed seven high-scoring putative PTF1 binding sites in *Mnk1* (+1, +1.8, +3.9, +5.6, +8.6, +9.9 and +11.3 kb from the transcription start site (TSS)). Ptf1a occupancy of these sites was confirmed by ChIP-qPCR (figure 1D). The three sites with the strongest signal correspond to the three top-scoring

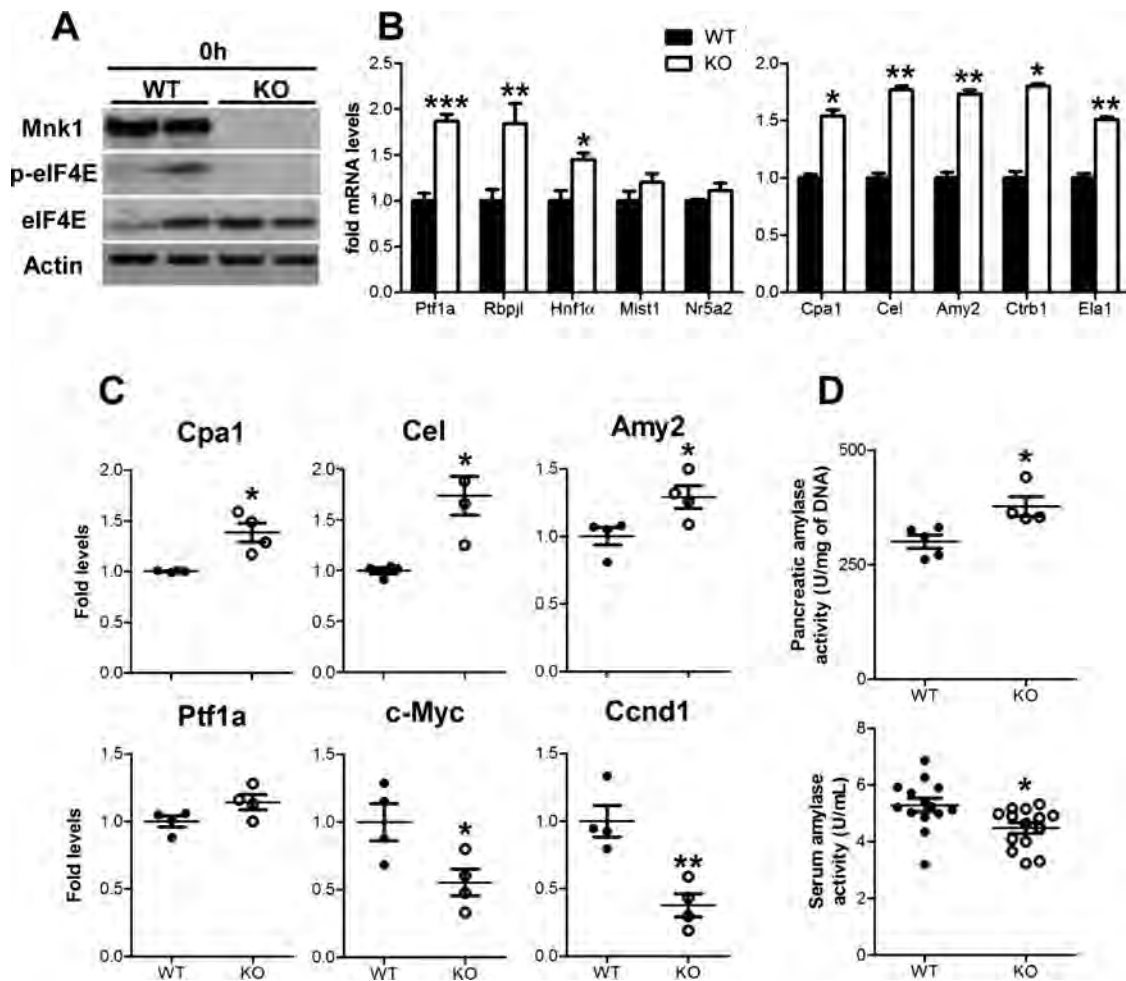


Figure 2 Increased enzymatic content and reduced expression of p-eIF4E target proteins in *Mnk1*^{-/-} pancreata. (A) Western blotting of pancreatic lysates from *Mnk1*^{+/+} (wild type; WT) and *Mnk1*^{-/-} (knockout; KO) mice. (B) mRNA levels of acinar transcription factors (left) and digestive enzymes (right) in WT and KO pancreata detected by RT-qPCR (n=6). (C) Protein levels in WT and KO pancreata quantified by western blotting densitometry (see online supplementary figure S2). (D) Pancreatic and serum amylase activity in WT and KO mice. Results shown as mean±SEM; *p<0.05, **p<0.01, ***p<0.001.

ChIP-seq peaks. Therefore, Mnk1 is an acinar-restricted kinase whose expression in the pancreas is embedded in the PTF1 transcriptional programme.

Mnk1^{-/-} mice display altered expression of digestive enzymes and p-eIF4E target proteins in the pancreas

We used *Mnk1*^{-/-} mice to assess the role of this kinase in the pancreas. Lack of Mnk1 was confirmed using immunohistochemistry (see online supplementary figure S2A) and western blotting (figure 2A). *Mnk1*^{-/-} pancreata developed normally and were histologically indistinguishable from WT counterparts (see online supplementary figure S2A). However, mRNAs coding for the acinar-specific transcription factors Ptf1a and Rbpjl, and those for Hnf1α and Amy2, Cpa1, Cel, Ela1 and Ctrb1, were 1.5–2-fold higher in *Mnk1*^{-/-} pancreata (figure 2B). By contrast, mRNA levels of Mist1 and Nr5a2—required for the complete differentiation of acinar cells—were unchanged. Expression of selected proteins was assessed by western blotting and densitometry (figure 2C, see online supplementary figure S2B). Ptf1a was expressed at similar levels in both mouse strains but the levels of three digestive enzymes analysed were higher in *Mnk1*^{-/-} mice: Cel (75%, p=0.031), Cpa1 (40%, p=0.027) and Amy2 (25%, p=0.034) (n=4 mice/group); trypsinogen levels were not

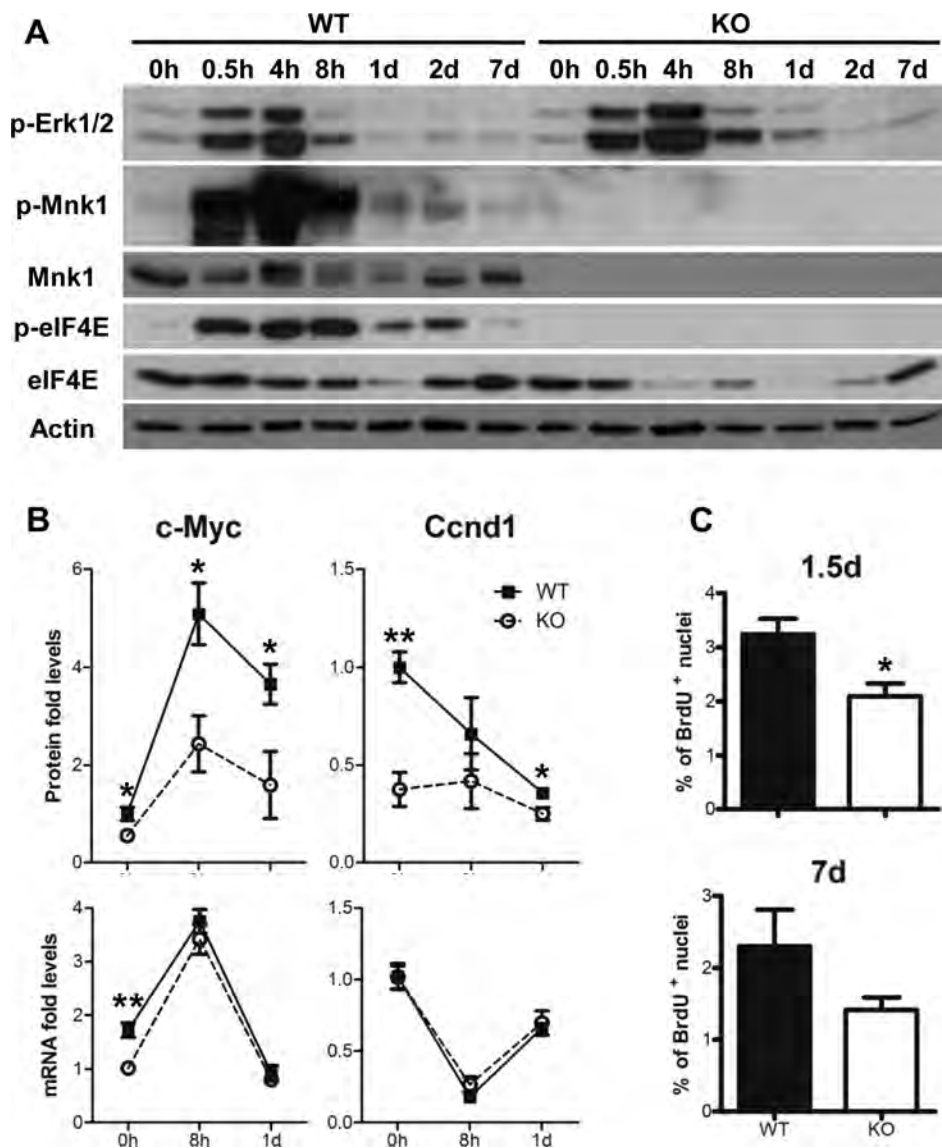
significantly higher in *Mnk1*^{-/-} pancreata. Tissue amylase activity was 26% higher (p=0.017) in an independent group of *Mnk1*^{-/-} mice (figure 2D). In contrast, serum amylase activity, a measure of acinar cell damage, was lower in *Mnk1*^{-/-} mice (15.9%, p=0.014) (figure 2D).

eIF4E is the best characterised Mnk1 substrate.¹⁵ Total eIF4E levels were similar in both mouse strains but basal p-eIF4E levels were lower in *Mnk1*^{-/-} mice (figure 2A). Levels of c-Myc and Ccnd1, two known p-eIF4E-regulated proteins, were 45% (p=0.045) and 62% (p=0.008) lower in *Mnk1*^{-/-} mice, respectively (figure 2C and online supplementary figure S2B), while their transcripts were not (see online supplementary figure S2C), supporting the involvement of a post-translational mechanism. These results show that inactivation of Mnk1 differentially affects abundance of digestive enzymes and p-eIF4E-regulated proteins.

Mnk1 is activated and downregulated upon caerulein-induced acute pancreatitis

We analysed Mnk1 expression and activation during acute caerulein-induced pancreatitis. Consistent with published data,⁶ Ptf1a mRNA levels were downregulated 8 h after the first caerulein administration and gradually restored during the recovery

Figure 3 Mnk1 is necessary for eIF4e phosphorylation, proper c-Myc upregulation and acinar proliferation during caerulein-induced acute pancreatitis. (A) Western blotting of wild type (WT) and knockout (KO) pancreatic lysates during acute pancreatitis. (B) c-Myc and Ccnd1 expression in WT and KO pancreata upon acute pancreatitis assessed by western blotting densitometry and RT-qPCR (n=4). (C) Quantification of immunohistochemical staining for BrdU in WT and KO mouse pancreata (n>5). Results shown as mean±SEM; *p<0.05, **p<0.01.



period (see online supplementary figure S3A), as were the mRNA levels of *Amy2* and *Cpa1*. *Mnk1* mRNA expression dynamics followed the same pattern as digestive enzyme transcripts, consistent with it being a PTF1 target (see online supplementary figure S3A). *Mnk1* protein was gradually downregulated, reaching the lowest levels by day 1, and then restored by day 7 (figure 3A). The MAPK-Mnk1-eIF4E pathway was rapidly activated in response to caerulein: an increase in p-Erk1/2, p-Mnk1 and p-eIF4E was observed as early as 30 min after the first caerulein injection. Phosphorylation of these proteins was highest at 4 h; p-Erk1/2 returned to basal levels by day 1 whereas p-Mnk1 and p-eIF4E were persistently elevated (figure 3A). As *Mnk1*, eIF4E was rapidly downregulated and then restored during the recovery phase. *Mnk1* protein kinetics followed mRNA downregulation; however, eIF4E transcript levels remained unchanged during acute pancreatitis (not shown).

Caerulein administration also led to the subcellular redistribution of *Mnk1* (see online supplementary figure S3B). In basal conditions, *Mnk1* displayed a uniform cytoplasmic localisation. By contrast, 4 h after caerulein administration, *Mnk1* predominantly localised to the basolateral region of acinar cells. Subsequently, a broad cytoplasmic distribution of the protein was recovered (see online supplementary figure S3B). Thus, *Mnk1* is activated

downstream of MAP kinase activation during acute pancreatitis as part of the acinar stress response programme.

Mnk1 is required for eIF4E phosphorylation and involved in c-Myc protein induction during acute pancreatitis

In *Mnk1*^{-/-} mice, pancreatitis-induced eIF4E phosphorylation was completely abrogated (figure 3A). Therefore, we analysed expression of c-Myc and Ccnd1 during acute pancreatitis. As shown above (figure 2C), their levels were significantly lower in untreated *Mnk1*^{-/-} mice. In WT pancreata, c-Myc levels increased fivefold (p=0.008) and fourfold (p=0.009) at 8 h and day 1, respectively. By contrast, Ccnd1 protein expression was progressively downregulated until day 1 (figure 3B and online supplementary figure S4). In *Mnk1*^{-/-} mice, c-Myc upregulation was impaired reaching only 24% (at 8 h) and 43% (at day 1) of the induction observed in WT mice (p=0.01 and p=0.05, respectively). Ccnd1 levels also remained lower in *Mnk1*^{-/-} than in WT mice during the study period (figure 3B and online supplementary figure S4). Lower c-Myc and Ccnd1 levels in *Mnk1*^{-/-} mice during the early stages of pancreatitis are likely due to post-transcriptional regulation as mRNA levels were similar in both mouse strains (figure 3B).

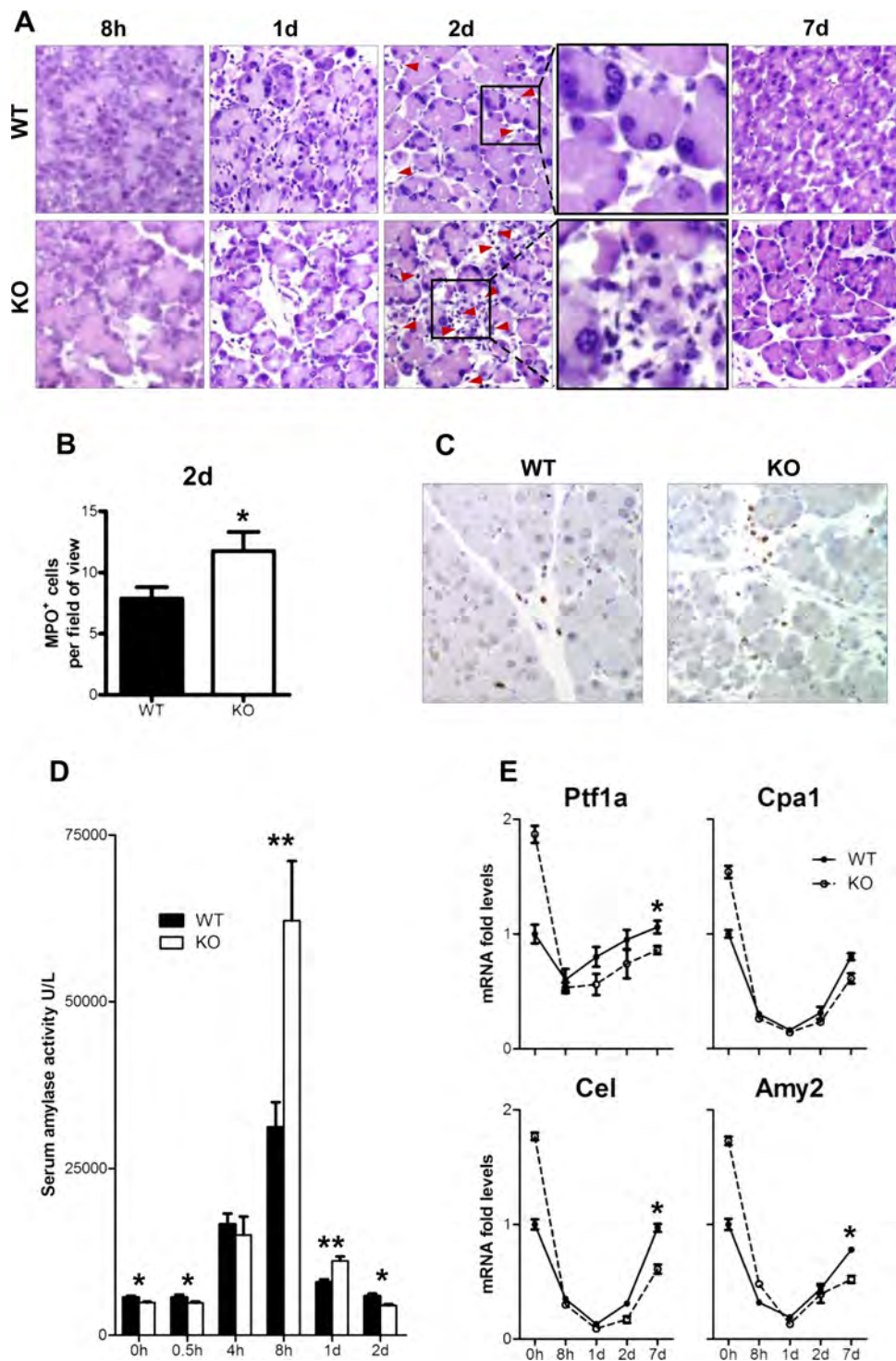


Figure 4 Increased severity of caerulein-induced acute pancreatitis in *Mnk1*^{-/-} mice. (A) Histology of wild type (WT) and knockout (KO) pancreata during acute pancreatitis (inflammatory cell infiltration 2 days after pancreatitis induction is indicated by arrowheads and shown in higher magnification insets). (B) Number of MPO⁺ cells/field (100×) in sections of WT and KO pancreata 2 days after pancreatitis induction (n>5). (C) Immunohistochemical staining of MPO⁺ cells in WT and KO pancreata 2 days after pancreatitis induction. (D) Serum amylase activity in WT and KO mice during acute pancreatitis. (E) mRNA expression dynamics of acinar genes in WT and KO pancreata upon acute pancreatitis detected by RT-qPCR (n>3); *p<0.05, **p<0.01.

Acute pancreatic damage results in the proliferation of a small fraction of acinar cells.²² Acinar BrdU uptake was reduced in *Mnk1*^{-/-} mice at day 1.5 (2.1% vs 3.2%, p=0.015) and day 7 (1.4% vs 2.2%, p=0.14) (figure 3C), in agreement with the reduced c-Myc and Ccnd1 levels. Thus, *Mnk1* is required for the induction of cell cycle regulators and proliferation upon acute pancreatic damage.

Mnk1^{-/-} mice display a more severe acute caerulein-induced pancreatitis

Next, we determined the effect of *Mnk1* inactivation on the response to pancreatic injury during caerulein-induced pancreatitis. At the histological level, inflammation, oedema and cell death were similar in *Mnk1*^{+/+} and *Mnk1*^{-/-} mice (figure 4A).

However, at day 2 a significant increase in inflammatory cell infiltration (predominantly neutrophils) was detected in the absence of Mnk1 (histological score, $p=0.03$) (figure 4A and online supplementary figure S5A). These results were confirmed by immunostaining and quantification of myeloperoxidase⁺ cells (11.8 vs 7.9 cells/field, $p=0.05$) (figure 4B, C). Serum amylase activity increased similarly during the first 4 h but it was significantly higher in *Mnk1*^{-/-} mice at 8 h (twofold) and at day 1 (figure 4D). By day 2, serum amylase levels had normalised in both mouse strains.

As described above, basal levels of *Ptf1a*, *Rbpil*, *Hnf1a*, *Amy2*, *Ela1*, *CpA*, *Ctrb1* and *Cel* transcripts were higher in *Mnk1*^{-/-} mice (figure 2B). However, in *Mnk1*^{-/-} mice, a more dramatic downregulation of these transcripts was observed at 8 h and the subsequent recovery was more sluggish. Most of these differences were statistically significant (figure 4E and online supplementary figure S5B). These effects did not result from lower levels of *Ptf1a* (see online supplementary figure S5C).

Hence, Mnk1 inactivation leads to a modest increase in severity in the late phase of caerulein-induced pancreatitis.

Mnk1 is not required for the heat shock response associated with pancreatitis

The severity of pancreatitis is modulated by heat shock proteins.^{23–24} Mnk1 being a stress kinase, its effects might be mediated through a modulation of the heat shock response.²⁵ Therefore, we analysed Hsp expression during pancreatitis in *Mnk1*^{-/-} mice. As expected,^{26–27} protein levels of Hsp27 and Hsp70 were upregulated in WT mice; a similar response was observed in *Mnk1*^{-/-} mice. The expression of Hsp48 and Hsp90 was unaffected in both mouse strains (see online supplementary figure S6).

Impaired enzymatic protein downregulation and subcellular distribution upon acute pancreatitis in *Mnk1*^{-/-} mice

Caerulein administration leads to rapid downregulation of pancreatic amylase.⁷ *Amy2*, *CpA* and *Cel* (0, 8 h and day 1) were decreased by 30%–40% in *Mnk1*^{+/+} mice (figure 5A and online supplementary figure S7A). Similarly, pancreatic amylase activity was reduced (0 and 8 h) (figure 5B). This downregulation was impaired in *Mnk1*^{-/-} mice at 8 h and confirmed by a higher protein to DNA ratio in *Mnk1*^{-/-} mice as compared with controls (figure 5C). At day 1, both WT and *Mnk1*^{-/-} mice showed highly reduced pancreatic enzyme content (figure 5A and online supplementary figure S7A). Next, we analysed whether the delayed reduction of enzymes in the absence of Mnk1 had an impact on zymogen activation. Trypsinogen activation upon pancreatitis followed similar kinetics in both mouse strains (figure 5D). Levels of cCpa1—the trypsin-mediated 35 kDa product of procarboxypeptidase A1 (*Cpa1*)—also reflect zymogen activation.²⁸ In WT mice, the levels of cCpa1 increased 30 min after the first administration of caerulein and then progressively decreased (figure 5E and online supplementary figure S7B). By contrast, persistent elevation of cCpa1 levels was observed in *Mnk1*^{-/-} mice (figure 5E and online supplementary figure S7B). By day 1 pancreatic cCpa1 levels reached baseline in both *Mnk1*^{+/+} and *Mnk1*^{-/-} mice (data not shown).

As shown above, caerulein administration leads to the redistribution of Mnk1 to the basolateral region of acinar cells. Concomitantly, *Cpa1* (at 4 and 8 h) (figure 6A and online supplementary figure S8A) and *Try* (at 8 h) (see online supplementary figure S8A) relocalised towards the apical pole yielding a

mutually exclusive pattern with Mnk1. The redistribution of digestive enzymes did not occur in *Mnk1*^{-/-} mice (figure 6B and online supplementary figure S8A).

Muc1 and E-cad showed the expected apical and basolateral localisation, respectively, in untreated mice of both strains. In response to caerulein, *Muc1* underwent a broader redistribution to intracellular compartments—including partial colocalisation with E-cadherin—in WT mice but this response was less prominent and delayed in *Mnk1*^{-/-} mice (figure 6C). Importantly, at 8 h *Muc1* expression pattern was more disorganised and partially associated with basolateral membranes marked by E-cadherin. By 24 h, *Muc1* displayed an apical distribution in both mouse strains (see online supplementary figure S8B). These findings indicate that Mnk1 participates in the changes in polarity and traffic associated with the response to caerulein during acute pancreatic damage.

Mnk1^{-/-} acinar cells are defective in the response to secretagogues in vitro

The increased enzymatic content and decreased amylase serum levels observed in untreated *Mnk1*^{-/-} mice, together with the alterations in polarised proteins described above, suggested a secretion defect. We isolated acini and assessed the response to secretagogues. Upon isolation, control acinar cells showed hyperphosphorylation of Mnk1 and eIF4E (figure 7A), both being absent in *Mnk1*^{-/-} cells. In WT cells, caerulein treatment induced a typical biphasic dose-response with basal amylase release of approximately 3.5%/30 min, optimal release at 100 pM (8%/30 min) and a fall of amylase secretion at supra-maximal concentrations (1 and 10 nM) (figure 7B). *Mnk1*^{-/-} cells released significantly less amylase in basal (2.9%/30 min, $p=0.03$) and optimal (by 6.6%/30 min, $p=0.02$) conditions. In addition, *Mnk1*^{-/-} acinar cells displayed reduced CCK-induced intracellular trypsinogen activation ($p<0.05$) (figure 7C) while cathepsin B activation and cell death rate were similar (see online supplementary figure S9A,B). These findings indicate that Mnk1 is required for a physiological secretagogue response as well as for intracellular protease activation in vitro.

Mnk1^{-/-} mice are defective in the response to secretagogues in vivo

To determine whether lack of Mnk1 also affects pancreatic secretion in vivo, we assessed the TEV over time, an accepted approach to assess pancreatic exocrine function.²⁹ We compared secretin-induced TEV into the duodenum in WT and *Mnk1*^{-/-} littermates using MRCP. WT mice secreted 61 ± 8 μ L over 5 min upon intravenous secretin stimulation; by contrast, *Mnk1*^{-/-} mice did not show a significant increase in secretion (3.5 μ L ± 0.1 , $p<0.05$) (figure 8A, B). These findings indicate that *Mnk1*^{-/-} mice also display a pancreatic secretion defect in vivo.

DISCUSSION

The activation of stress response mechanisms is essential for organismal homeostasis. Many of these processes are shared across cell/tissue types and few cell type-restricted kinases have been described. Here, we identify Mnk1 as a kinase regulated within the acinar cell differentiation programme that is part of an acinar cell-specific homeostatic loop.

Mnk1 is an acinar-specific stress response kinase required for acinar cell homeostasis

Stress response pathways have been shown to participate in acinar cell responses to injury but their exact role is not completely understood. Here, we find that Mnk1 is ubiquitously

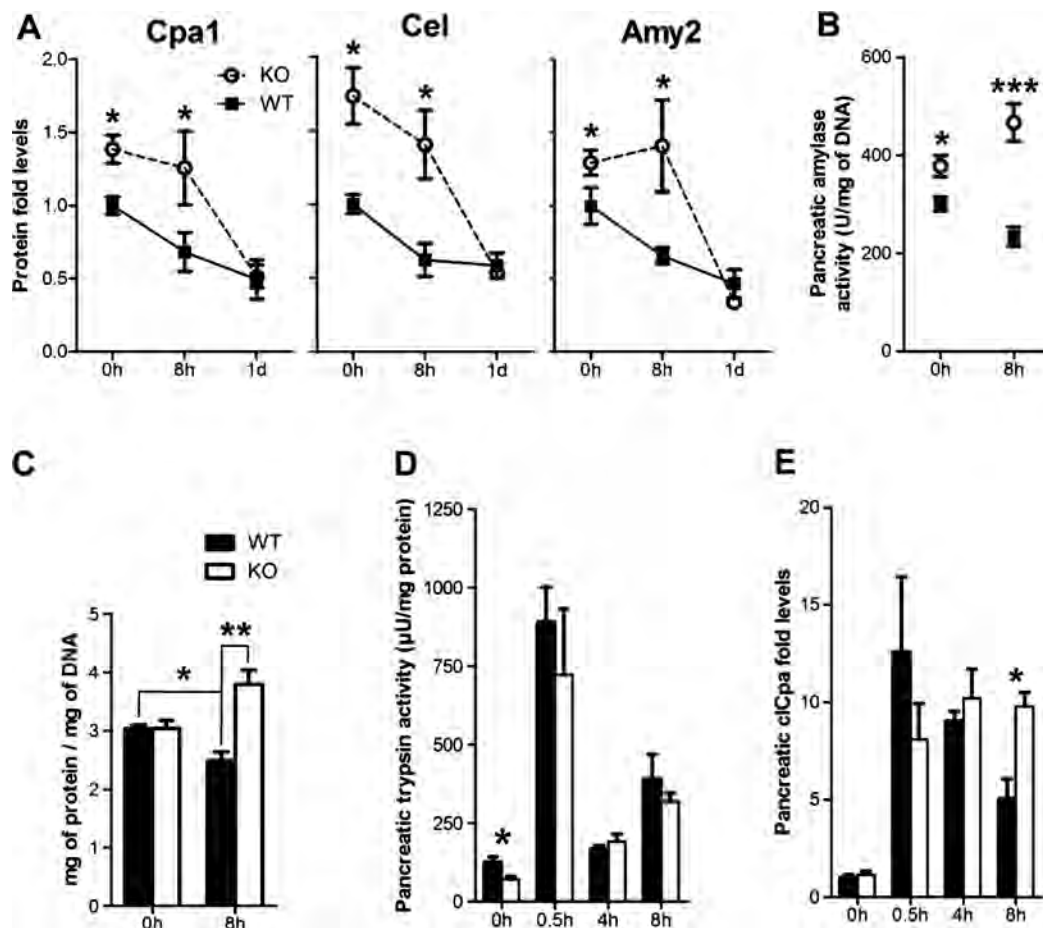


Figure 5 Delayed downregulation of enzymes upon acute pancreatitis in *Mnk1*^{-/-} mice. (A) Digestive enzyme levels in wild type (WT) and knockout (KO) pancreata during acute pancreatitis assessed by western blotting (see online supplementary figure S7A) densitometry. (B and C) Amylase activity (B) and total pancreatic protein (C) in untreated (0 h) and caerulein-treated (8 h) WT and KO pancreata. (D) Trypsin activity in WT and KO pancreata upon acute pancreatitis (n>3). (E) cCpa1 levels in WT and KO pancreata upon acute pancreatitis assessed by western blotting (see online supplementary figure S9B) densitometry (n=4); *p<0.05, **p<0.01, ***p<0.001.

expressed at low levels but is expressed at very high levels selectively in pancreatic acinar cells. This results from the fact that *Mnk1* is embedded within the acinar transcription programme, being a direct PTF1 target. *Mnk1* is already detectable in MPCs, its expression being driven by the Rbpj-containing PTF1-J complex.³⁰ Unlike in the case of digestive enzymes,³ PTF1 binds *Mnk1* predominantly downstream of the TSS, in the first intron. The significance of this finding remains unknown but genome-wide ChIP coupled with massive parallel sequencing has unveiled that PTF1 often occupies binding sites downstream of the TSS of known target genes (unpublished). *Mnk1* also contains a putative PTF1 binding site around 175bp upstream of TSS but binding of Ptf1a to this region has neither been detected by ChIP-seq nor by ChIP-qPCR.

Consistent with these findings, *Mnk1* is coregulated with digestive enzymes upon injury in mice and—in areas of acinoductal metaplasia—is downregulated in cells showing ductal morphology, both in murine and human tissues (see online supplementary figure S3B).

Mnk1 is dispensable for normal mouse pancreas development^{15 18} but subtle molecular alterations in acinar physiology were detected in *Mnk1*^{-/-} mice. We found increased levels of digestive enzymes and decreased levels of c-Myc and *Cnd1*, whose IRES-dependent translation¹⁶ and mRNA nuclear export,¹⁷ respectively, are positively regulated by p-eIF4E.

The accumulation of digestive enzymes might result from higher mRNA levels or from impaired secretion of digestive enzymes. *Mnk1* is known to affect mRNA stability through proteins that bind AU-rich elements.³¹ However, digestive enzyme transcripts lack such sequences in their 3' UTRs. Our results indicate that *Mnk1* is unique among the acinar proteins involved in the regulation of their differentiation: it is part of such a programme but has a suppressive, rather than promotive, role as evidenced by the upregulation of enzyme transcripts in *Mnk1*^{-/-} mice. The precise mechanisms involved need to be identified.

***Mnk1* regulates acinar proliferation upon caerulein-induced acute pancreatitis, possibly through p-eIF4E-dependent translation**

Mnk1 is the first acinar-specific kinase reported, mediating stress responses and leading to a rapid, robust and selective phosphorylation of eIF4E. This role is not shared by *Mnk2* that, consistent with published data, is responsible only for basal eIF4E phosphorylation.¹⁸ eIF4E has been reported to be phosphorylated in the mouse pancreas upon caerulein-induced pancreatitis but the physiological significance of this biochemical event is not fully understood.³² We show that lack of eIF4E phosphorylation in *Mnk1*^{-/-} pancreata upon acute pancreatitis is associated with lower induction of c-Myc. The lack of *Mnk1* did not lead

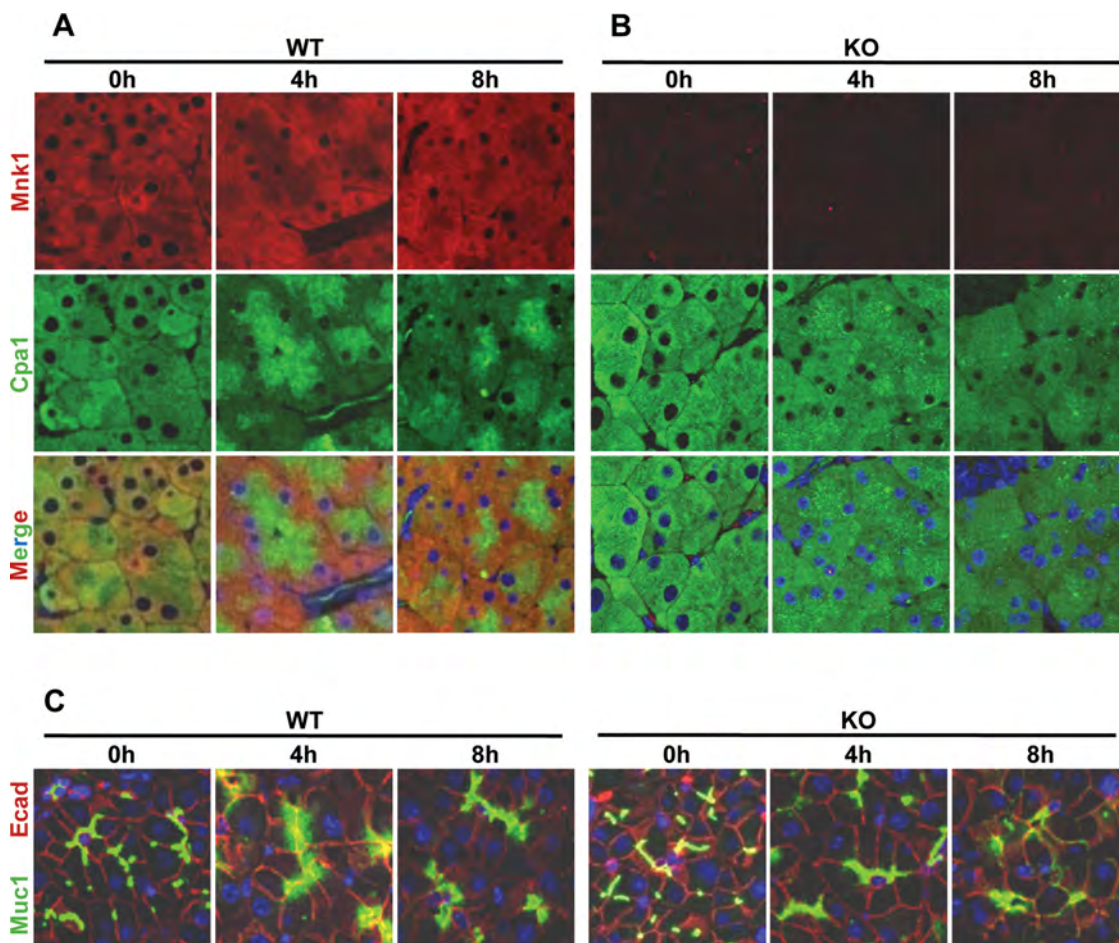


Figure 6 Impaired subcellular redistribution of enzymes in *Mnk1*^{-/-} mice during acute pancreatitis. (A and B) Double immunofluorescence analysis of Mnk1/Cpa1 in wild type (WT) (A) and knockout (KO) (B) pancreata upon caerulein administration (0, 4, 8 h). (C) Ecad/Muc1 double staining in acinar cells of WT and KO pancreata upon caerulein administration (0, 4, 8 h).

to reduced *Ccnd1* levels but was associated with lower acinar proliferation during recovery from damage. These results support an important role of c-Myc in this process.

Mnk1 has a protective role in acute experimental pancreatitis

In agreement with proteomic studies assessing the effects of caerulein administration,³³ we found reduced digestive enzymes using both western blotting and enzyme activity in WT mice. *Mnk1* inactivation led to altered caerulein-associated downregulation of digestive enzymes and total protein content. This may underlie the modest increase in severity of pancreatitis, shown both at the tissue level and by elevated serum amylase activity.

Mnk1 is required for normal trypsin activation *in vitro* but this protease appears to play a minor role in the severity of secretagogue-induced pancreatitis in *Mnk1*^{-/-} mice. As opposed to other zymogens analysed, levels of total pancreatic trypsinogen were not significantly elevated in *Mnk1*^{-/-} mice (see online supplementary figure S9C). Accordingly, we did not find increased levels of trypsin activity *in vivo* and, as shown previously, the degree of trypsinogen activation does not necessarily parallel the severity of the disease in animals.^{34 35} In contrast, we observed persistent elevation of cleaved carboxypeptidase (cCpa1). Cpa1 cleavage is an early event in the response to caerulein and coincides with activation of trypsinogen. The higher levels of cCpa1 in *Mnk1*^{-/-} mice may result from

increased Cpa1, prolonged procarboxypeptidase conversion or inappropriate release of the cleaved form from acinar cells (see below). CpA cleavage has been shown to be associated with cellular damage *in vitro*²⁸ and a recent study found that genetic variants in *CPA1* are associated with early onset chronic pancreatitis, possibly associated with misfolding-induced endoplasmic reticulum stress.³⁶

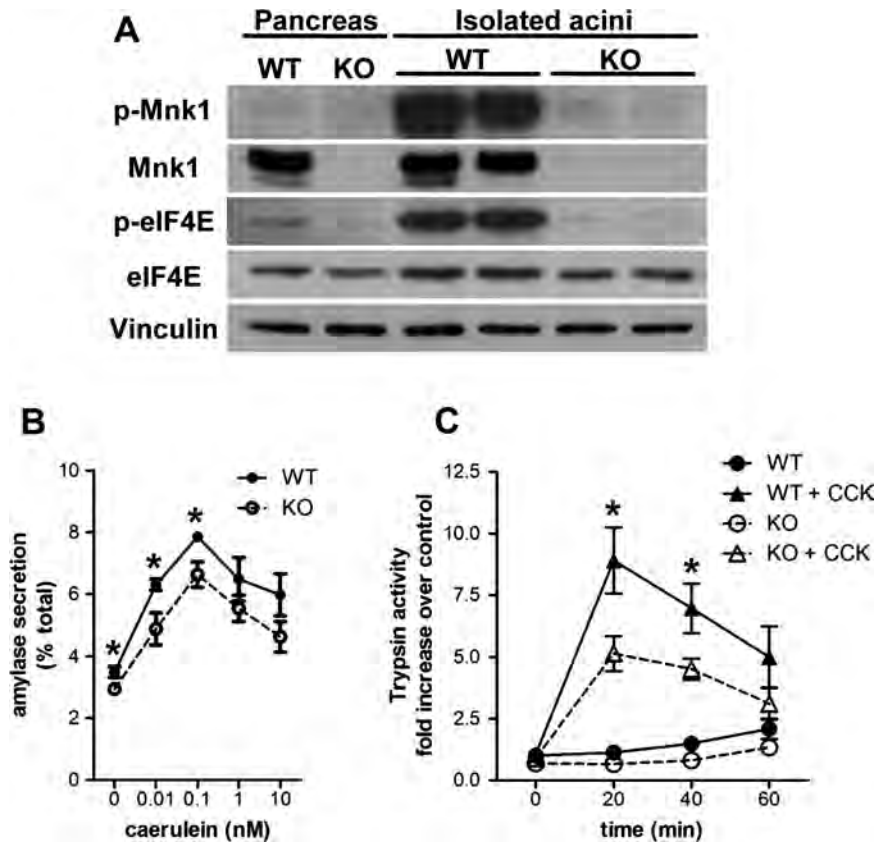
Mnk1 is also known to regulate the translation of cytokine mRNAs in response to stress and the inflammatory cell response.^{31 37 38} The changes in inflammatory infiltrates found in *Mnk1*^{-/-} mice were mild and occurred relative late, suggesting that they are secondary events. *Mnk1* inactivation in haematopoietic cells may also contribute to the phenotype rather than being a consequence of the acinar defects. The use of conditional tissue-specific *Mnk1* knockout mice should elucidate the contribution of epithelial versus non-epithelial cells.

Mnk1 is required for the physiological exocrine secretory response

Several results shown above suggest an involvement of *Mnk1* in acinar cell transport and secretion, including the higher amounts of digestive enzymes in *Mnk1*^{-/-} pancreata, lower amylase serum activity and abnormal subcellular distribution of polarised proteins upon pancreatitis. However, the strongest evidence comes from the suboptimal amylase secretion in freshly isolated acini and the reduced secretory response upon secretagogue administration in

Pancreas

Figure 7 Impaired response to secretagogues by *Mnk1*^{-/-} acini. (A) Western blotting analysis of isolated acini from wild type (WT) and knockout (KO) pancreata. (B) Caerulein-induced amylase release by isolated WT and KO acini. (C) Cholecystikinin (CCK)-induced changes in trypsin activity in isolated WT and KO acini. Data shown as mean±SEM (n=5); *p<0.05.

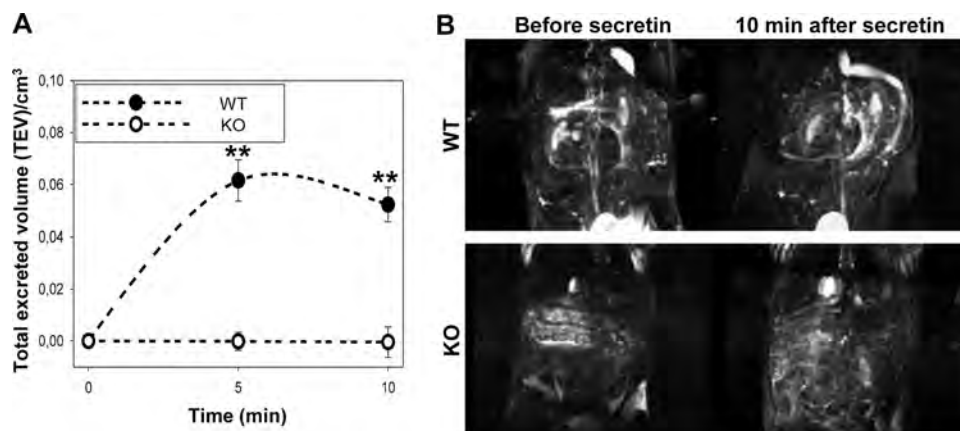


Mnk1^{-/-} mice. Defective secretion could also contribute to the delay in zymogen downregulation in acinar cells from *Mnk1*^{-/-} pancreata upon serial caerulein injection, in agreement with the altered intracellular zymogen localisation upon caerulein administration in *Mnk1*^{-/-} acinar cells. The lack of demonstrable differences between WT and *Mnk1*^{-/-} mice in a non-secretagogue model of acute pancreatitis (ie, L-arginine pancreatitis, see online supplementary information and supplementary figure S10) strengthens the relevance of the secretory defect in *Mnk1*^{-/-} mice.

The mechanisms involved in this secretory defect need to be unravelled. We have not observed differences in Erk or p38 phosphorylation (not shown), suggesting that downstream effectors/substrates are involved. LK6, the *Drosophila melanogaster* Mnk1 homologue, has been found to be associated with microtubules³⁹ and cytoskeletal proteins might be responsible for the secretory abnormalities.⁴⁰

Mnk1 adds to a growing list of proteins that have a protective role during acute pancreatitis, including Nupr1 (p8)⁴¹ or Itmap1.⁴² The phenotype of *Mnk1*^{-/-} mice is relatively mild, suggesting that adaptive mechanisms compensate for the constitutive lack of Mnk1 in the pancreas. The detailed comparison of the pancreas of WT and *Mnk1*^{-/-} at the transcriptomic and proteomic levels and the analysis of pancreas-specific *Mnk1*^{-/-} mice may provide further clues as to the regulatory processes in which Mnk1 participates in acinar cell pathophysiology. Additional experiments are required to elucidate whether Mnk1 contributes to tissue regeneration in chronic pancreatitis. Furthermore, the fact that Mnk1 has been described to be involved in cancer biology^{16 17 43} and that acinar cells participate in the development of pancreatic ductal adenocarcinoma⁴⁴ call for an analysis of the role of this kinase in tumour development/progression.

Figure 8 Defective pancreatic secretion in response to secretin in *Mnk1*^{-/-} mice. (A) Quantification of pancreatic fluid secretion in wild type (WT) (n=5) and knockout (KO) (n=4) mice, assessed by MRI. (B) MR cholangiopancreatography images of WT and KO mice showing fluid secretion into the duodenum. Data shown as mean±SEM; **p<0.05, paired t test.



Author affiliations

- ¹Epithelial Carcinogenesis Group, Spanish National Cancer Research Center-CNIO, Madrid, Spain
²Department of Medicine A, University Medicine, Ernst-Moritz-Arndt University, Greifswald, Germany
³Servei d'Anatomia Patològica, Hospital Mútua Terrassa, Barcelona, Spain
⁴Institute of Radiology, University Medicine, Ernst-Moritz-University, Greifswald, Germany
⁵Exocrine Pancreas Research Unit, Hospital Universitari Vall d'Hebron, Institut de Recerca (VHIR), Universitat Autònoma de Barcelona, CIBEREHD, Barcelona, Spain
⁶Osaka University of Pharmaceutical Sciences, Osaka, Japan
⁷Departament de Ciències Experimentals i de la Salut, Universitat Pompeu Fabra, Barcelona, Spain

Acknowledgements We thank B Bréant for providing antibodies against Ptf1a and R MacDonald for sharing unpublished Ptf1a ChIP-Seq information, E Purich (ChiRhoClin) for providing ChiroStim, S Hadlich for help with the rodent MRI experiments, and C Proud, M Buxadé, M Olszewski and A Nebreda for valuable contributions.

Contributors JC, VJS-AL, MS, J-PK and XM designed, performed and analysed experiments. AS performed pathological analysis of samples. RF provided essential reagents. JM, MML and FXR designed experiments and supervised research. JC and FXR wrote the manuscript with contributions from all authors. MML and FXR obtained financial support.

Funding This work was supported, in part, by grants from Ministerio de Economía y Competitividad (SAF2007-60860, SAF2011-29530 and ONCOBIO Consolidar), Fondo de Investigación Sanitaria (PI11/01542) (Madrid, Spain), Deutsche Krebshilfe/Dr Mildred-Scheel-Stiftung (109102), Deutsche Forschungsgemeinschaft (DFG GRK840-D2/E3/E4, MA 4115/1-2/3), Federal Ministry of Education and Research (BMBF GANI-MED 03IS2061A and BMBF 0314107, 01ZZ9603, 01ZZ0103, 01ZZ0403, 03ZIK012), and the European Union (EPC-TM-Net and EU-FP7-REGPOT-2010-1). JC was supported by a "La Caixa" International PhD Programme Fellowship.

Competing interests None.

Provenance and peer review Not commissioned; externally peer reviewed.

Data sharing statement We will gladly supply any related information on request.

REFERENCES

- Beres TM, Masui T, Swift GH, *et al.* PTF1 is an organ-specific and Notch-independent basic helix-loop-helix complex containing the mammalian Suppressor of Hairless (RBP-J) or its paralogue, RBP-L. *Mol Cell Biol* 2006;26:117–30.
- Case RM. Synthesis, intracellular transport and discharge of exportable proteins in the pancreatic acinar cell and other cells. *Biol Rev Camb Philos Soc* 1978;53:211–354.
- Pandolfi SJ. *The Exocrine Pancreas*. San Rafael, CA: Morgan & Claypool Life Sciences, 2010.
- Mayerle J, Schnenburger J, Kruger B, *et al.* Extracellular cleavage of E-cadherin by leukocyte elastase during acute experimental pancreatitis in rats. *Gastroenterology* 2005;129:1251–67.
- Saluja AK, Lerch MM, Phillips PA, *et al.* Why does pancreatic overstimulation cause pancreatitis? *Annu Rev Physiol* 2007;69:249–69.
- Molero X, Adell T, Skoudy A, *et al.* Pancreas transcription factor 1alpha expression is regulated in pancreatitis. *Eur J Clin Invest* 2007;37:791–801.
- Molero X, Vaquero EC, Flandez M, *et al.* Gene expression dynamics after murine pancreatitis unveils novel roles for Hnf1alpha in acinar cell homeostasis. *Gut* 2012;61:1187–96.
- Houbracken I, de Waele E, Lardon J, *et al.* Lineage tracing evidence for transdifferentiation of acinar to duct cells and plasticity of human pancreas. *Gastroenterology* 2011;141:731–41.
- Guerra C, Schuhmacher AJ, Canamero M, *et al.* Chronic pancreatitis is essential for induction of pancreatic ductal adenocarcinoma by K-Ras oncogenes in adult mice. *Cancer Cell* 2007;11:291–302.
- Schramek H. MAP kinases: from intracellular signals to physiology and disease. *News Physiol Sci* 2002;17:62–7.
- Grady T, Dabrowski A, Williams JA, *et al.* Stress-activated protein kinase activation is the earliest direct correlate to the induction of secretagogue-induced pancreatitis in rats. *Biochem Biophys Res Commun* 1996;227:1–7.
- Wagner AC, Metzler W, Hofken T, *et al.* p38 map kinase is expressed in the pancreas and is immediately activated following cerulein hyperstimulation. *Digestion* 1999;60:41–7.
- Fukunaga R, Hunter T. MNK1, a new MAP kinase-activated protein kinase, isolated by a novel expression screening method for identifying protein kinase substrates. *EMBO J* 1997;16:1921–33.
- Waskiewicz AJ, Flynn A, Proud CG, *et al.* Mitogen-activated protein kinases activate the serine/threonine kinases Mnk1 and Mnk2. *EMBO J* 1997;16:1909–20.
- Buxade M, Parra-Palau JL, Proud CG. The Mnks: MAP kinase-interacting kinases (MAP kinase signal-integrating kinases). *Front Biosci* 2008;13:5359–73.
- Shi Y, Frost P, Hoang B, *et al.* MNK kinases facilitate c-myc IRES activity in rapamycin-treated multiple myeloma cells. *Oncogene* 2012;32:190–7.
- Wheater MJ, Johnson PW, Blaydes JP. The role of MNK proteins and eIF4E phosphorylation in breast cancer cell proliferation and survival. *Cancer Biol Ther* 2010;10:728–35.
- Ueda T, Watanabe-Fukunaga R, Fukuyama H, *et al.* Mnk2 and Mnk1 are essential for constitutive and inducible phosphorylation of eukaryotic initiation factor 4E but not for cell growth or development. *Mol Cell Biol* 2004;24:6539–49.
- Flandez M, Cendrowski J, Canamero M, *et al.* Nr5a2 heterozygosity sensitises to, and cooperates with, inflammation in KRasG12V-driven pancreatic tumorigenesis. *Gut* 2014;63:647–55.
- Williams JA. *Isolation of rodent pancreatic acinar cells and acini by collagenase digestion*. The Pancreas: Exocrine Pancreas Knowledge Base, 2010.
- Sendler M, Dummer A, Weiss FU, *et al.* Tumour necrosis factor alpha secretion induces protease activation and acinar cell necrosis in acute experimental pancreatitis in mice. *Gut* 2013;62:430–9.
- Lechene de la Porte P, Iovanna J, Odaïra C, *et al.* Involvement of tubular complexes in pancreatic regeneration after acute necrohemorrhagic pancreatitis. *Pancreas* 1991;6:298–306.
- Weber CK, Gress T, Müller-Pillasch F, *et al.* Supramaximal secretagogue stimulation enhances heat shock protein expression in the rat pancreas. *Pancreas* 1995;10:360–7.
- Bhagat L, Singh VP, Hietaranta AJ, *et al.* Heat shock protein 70 prevents secretagogue-induced cell injury in the pancreas by preventing intracellular trypsinogen activation. *J Clin Invest* 2000;106:81–9.
- Schäfer C, Williams JA. Stress kinases and heat shock proteins in the pancreas: possible roles in normal function and disease. *J Gastroenterol* 2000;35:1–9.
- Ethridge RT, Ehlers RA, Hellmich MR, *et al.* Acute pancreatitis results in induction of heat shock proteins 70 and 27 and heat shock factor-1. *Pancreas* 2000;21:248–56.
- Tashiro M, Schäfer C, Yao H, *et al.* Arginine induced acute pancreatitis alters the actin cytoskeleton and increases heat shock protein expression in rat pancreatic acinar cells. *Gut* 2001;49:241–50.
- Grady T, Mah'Moud M, Otani T, *et al.* Zymogen proteolysis within the pancreatic acinar cell is associated with cellular injury. *Am J Physiol* 1998;275:G1010–1017.
- Mensel B, Messner P, Mayerle J, *et al.* Secretin-stimulated MRCP in volunteers: assessment of safety, duct visualization, and pancreatic exocrine function. *AJR Am J Roentgenol* 2014;202:102–8.
- Masui T, Long Q, Beres TM, *et al.* Early pancreatic development requires the vertebrate Suppressor of Hairless (RBPJ) in the PTF1 bHLH complex. *Genes Dev* 2007;21:2629–43.
- Buxade M, Parra JL, Rousseau S, *et al.* The Mnks are novel components in the control of TNF alpha biosynthesis and phosphorylate and regulate hnRNP A1. *Immunity* 2005;23:177–89.
- Sans MD, Williams JA. Translational control of protein synthesis in pancreatic acinar cells. *Int J Gastrointest Cancer* 2002;31:107–15.
- Williams JA. Proteomics as a systems approach to pancreatitis. *Pancreas* 2013;42:905–91128.
- Krüger B, Lerch MM, Tessenow W. Direct detection of premature protease activation in living pancreatic acinar cells. *Lab Invest* 1998;78:763–4.
- Halangk W, Krüger B, Ruthenbürger M, *et al.* Trypsin activity is not involved in premature, intrapancreatic trypsinogen activation. *Am J Physiol Gastrointest Liver Physiol* 2002;282:G367–374.
- Witt H, Beer S, Rosendahl J, *et al.* Variants in CPA1 are strongly associated with early onset chronic pancreatitis. *Nat Genet* 2013;45:1216–20.
- Joshi S, Sharma B, Kaur S, *et al.* Essential role for Mnk kinases in type II interferon (IFNgamma) signaling and its suppressive effects on normal hematopoiesis. *J Biol Chem* 2011;286:6017–26.
- Rowlett RM, Chrestensen CA, Nyce M, *et al.* MNK kinases regulate multiple TLR pathways and innate proinflammatory cytokines in macrophages. *Am J Physiol Gastrointest Liver Physiol* 2008;294:G452–459.
- Kidd D, Raff JW. LK6, a short lived protein kinase in Drosophila that can associate with microtubules and centrosomes. *J Cell Sci* 1997;110(Pt 2):209–19.
- Schnenburger J, Weber IA, Hahn D, *et al.* The role of kinesin, dynein and microtubules in pancreatic secretion. *Cell Mol Life Sci* 2009;66:2525–37.
- Vasseur S, Folch-Puy E, Hlouschek V, *et al.* p8 improves pancreatic response to acute pancreatitis by enhancing the expression of the anti-inflammatory protein pancreatitis-associated protein I. *J Biol Chem* 2004;279:7199–207.
- Imamura T, Asada M, Vogt SK, *et al.* Protection from pancreatitis by the zymogen granule membrane protein integral membrane-associated protein-1. *J Biol Chem* 2002;277:50725–33.
- Ueda T, Sasaki M, Elia AJ, *et al.* Combined deficiency for MAP kinase-interacting kinase 1 and 2 (Mnk1 and Mnk2) delays tumor development. *Proc Natl Acad Sci U S A* 2010;107:13984–90.
- Rooman I, Real FX. Pancreatic ductal adenocarcinoma and acinar cells: a matter of differentiation and development? *Gut* 2012;61:449–58.



Mnk1 is a novel acinar cell-specific kinase required for exocrine pancreatic secretion and response to pancreatitis in mice

Jaroslaw Cendrowski, Víctor J Sánchez-Arévalo Lobo, Matthias Sendler, Antonio Salas, Jens-Peter Kühn, Xavier Molero, Rikiro Fukunaga, Julia Mayerle, Markus M Lerch and Francisco X Real

Gut 2015 64: 937-947 originally published online July 18, 2014
doi: 10.1136/gutjnl-2013-306068

Updated information and services can be found at:
<http://gut.bmj.com/content/64/6/937>

These include:

Supplementary Material

Supplementary material can be found at:
<http://gut.bmj.com/content/suppl/2014/07/19/gutjnl-2013-306068.DC1.html>

References

This article cites 42 articles, 19 of which you can access for free at:
<http://gut.bmj.com/content/64/6/937#BIBL>

Email alerting service

Receive free email alerts when new articles cite this article. Sign up in the box at the top right corner of the online article.

Topic Collections

Articles on similar topics can be found in the following collections

[Pancreas and biliary tract](#) (1926)
[Pancreatitis](#) (529)

Notes

To request permissions go to:
<http://group.bmj.com/group/rights-licensing/permissions>

To order reprints go to:
<http://journals.bmj.com/cgi/reprintform>

To subscribe to BMJ go to:
<http://group.bmj.com/subscribe/>

Interplay between chromatin-modifying enzymes controls colon cancer progression through Wnt signaling

Martine Chevillard-Briet^{1,2,†}, Muriel Quaranta^{1,2,†}, Aude Grézy^{1,2}, Lise Mattera^{1,2}, Céline Courilleau^{1,2}, Magali Philippe^{1,3}, Pascale Mercier^{1,3}, Denis Corpet⁴, John Lough⁵, Takeshi Ueda⁶, Rikiro Fukunaga⁷, Didier Trouche^{1,2,†} and Fabrice Escaffit^{1,2,†,*}

¹Université de Toulouse, UPS, F-31062 Toulouse, France, ²CNRS; LBCMCP, F-31062 Toulouse, France, ³CNRS; IPBS; Anexplo-Service de transgénèse, F-31077 Toulouse, France, ⁴Université de Toulouse; INP-ENVT INRA-ToxAlim, F-31076 Toulouse, France, ⁵Department of Cell Biology, Neurobiology and Anatomy, Medical College of Wisconsin, Milwaukee, WI, USA, ⁶Research Institute for Radiation Biology and Medicine, Hiroshima University, Hiroshima, Japan and ⁷Osaka University of Pharmaceutical Sciences, Laboratory of Biochemistry, Osaka, Japan

Received October 14, 2013; Revised and Accepted November 25, 2013

Cancer progression is associated with epigenetic alterations, such as changes in DNA methylation, histone modifications or variants incorporation. The p400 ATPase, which can incorporate the H2A.Z variant, and the Tip60 histone acetyltransferase are interacting chromatin-modifying proteins crucial for the control of cell proliferation. We demonstrate here that Tip60 acts as a tumor suppressor in colon, since mice heterozygous for Tip60 are more susceptible to chemically induced preneoplastic lesions and adenomas. Strikingly, heterozygosity for p400 reverses the Tip60-dependent formation of preneoplastic lesions, uncovering for the first time pro-oncogenic functions for p400. By genome-wide analysis and using a specific inhibitor *in vivo*, we demonstrated that these effects are dependent on Wnt signaling which is antagonistically impacted by p400 and Tip60: p400 directly favors the expression of a subset of Wnt-target genes and regulators, whereas Tip60 prevents β -catenin acetylation and activation. Taken together, our data underline the physiopathological importance of interplays between chromatin-modifying enzymes in the control of cancer-related signaling pathways.

INTRODUCTION

Cancer progression is accompanied by alterations that allow the activation of pro-oncogenic pathways and inactivate anti-cancer barriers. These alterations can be genetic, such as point mutations, allele amplification or loss, translocations, but also epigenetics. These epigenetic modifications include DNA methylation on specific promoters/enhancers (1), which is known for long to induce the transcriptional silencing of tumor suppressors encoding genes, and also modifications of chromatin structure such as histone posttranslational modifications or histone variants incorporation (for review, see (2–4)). Consequently, chromatin-modifying enzymes that set up these modifications are frequently mutated or aberrantly expressed in cancer (for review, see (4)).

The histone acetyltransferase Tip60 has been shown to act as a haplo-insufficient tumor suppressor, since heterozygous Tip60^{+/-} mice are more sensitive to lymphoma genesis upon c-Myc activation (5). Tip60 is required for the efficient activation of the DNA damage response (DDR) pathways (5,6) and its roles in ATM (7,8) and p53 (9–11) acetylation have been described as crucial events for DDR signaling and anti-proliferative cell fate, respectively.

Tip60 belongs to a multimolecular complex containing several other chromatin modifying enzymes, such as the p400 ATPase, which mediates the incorporation of the histone variant H2A.Z (12). We and others (6,13,14) have shown that Tip60 and p400 can have antagonistic functions in some situations (14,15). This relationship has a critical impact on the

*To whom correspondence should be addressed at: LBCMCP-UMR5088-CNRS, 118 Route de Narbonne, 31062 Toulouse Cedex 9, France. Tel: +33 561558184; Fax: +33 561556507; Email: fabrice.escaffit@univ-tlse3.fr

[†]Equal contributions.

proliferation of colon tumor cell lines in culture (6) and the p400/Tip60 ratio is systematically altered in human colorectal tumors, in favor of p400, independently of the grade and the stage of the tumor. This imbalance greatly alters the sensitivity of cancer cell lines to apoptosis *in vitro*.

Colorectal carcinogenesis is a complex multistep process that includes changes in histomorphological appearance of the colonic mucosa and deregulations at molecular level. Some critical mutations impacting key regulatory pathways have been identified in the tumorigenesis of both inherited and sporadic colorectal cancers (for review, see (16)). APC, KRAS and p53 genes are the major mutated oncogenes or tumor-suppressor genes, impairing the function of Wnt/ β -catenin, tyrosine kinase receptors and DDR signaling pathways, respectively. In addition, several other mutations have also been uncovered that affect important mechanisms such as DNA repair (MLH1, MSH2, etc.), TGF- β response (DCC, SMADs, etc.) or apoptosis (PTEN, BAX, etc.) ((16) and references therein).

In regard to their histopathological features as well as their biological, histochemical, genetic and epigenetic deregulations, Aberrant Crypt Foci (ACF) are now considered as the earliest preneoplastic lesions that can be seen in the colonic mucosa (for review, see (17,18)). ACF were first described on examination of methylene-blue-stained colonic mucosa of azoxymethane (AOM)-treated mice under light microscopy. The carcinogen AOM has been extensively used to study colonic carcinogenesis and chemoprevention (19,20). The AOM-induced colon tumors recapitulate many features associated with the progression of human sporadic colorectal cancers (21,22). Indeed, AOM initiates mutations in crucial genes controlling cell proliferation, such as *KRAS* or *CTNNB*, thereby activating colon cancer-related pathways (23). Finally, long-term feeding of rats with various fat diets modulates the AOM-induced colon carcinogenesis through Wnt/ β -catenin signaling. Thus, such *in vivo* model is of functional relevance to study early steps of colon tumorigenesis.

The activation of Wnt pathway is not sufficient to induce tumorigenesis, if barriers against malignant transformation remain active (24). Indeed, upon repression of Casein kinase α , a critical partner of the β -catenin-destruction complex, a massive activation of Wnt signaling is observed without causing malignant transformation since the p53 pathway is able to counteract the pro-tumorigenic effects of Wnt activation by increasing DDR (24) and thus, promoting subsequent anti-proliferative effects (25). Considering the crucial role of Tip60 in the p53 pathway and in the DDR activation (7, 10), we intended here to characterize the impact of the Tip60/p400 imbalance on the Wnt-involving colon tumorigenesis. Thus, our study brings important new insights to the continuously growing field of epigenetics and cancer (2).

RESULTS

P400 and Tip60 antagonistically control colon cancer progression

We previously showed that the p400/Tip60 ratio is modified in colon cancer (6), antagonistically impacting the viability of colon cancer cells, at least in culture conditions. To test whether such deregulations could be causal for cancer

progression, we intended to characterize the impact of the Tip60/p400 imbalance on early steps of colon tumorigenesis *in vivo*. To that goal, we used mutant mice models harboring Tip60 (5, 26) or p400 (27) heterozygosities (the homozygous genotype being lethal in both cases) and we crossed them to generate double heterozygous mice (Supplementary Material, Fig. S1). Importantly, we did not observe any Tip60 $-/-$ or p400 Δ/Δ homozygotes indicating that, although Tip60 and p400 have antagonistic functions, the depletion of one of them does not rescue the lethality observed upon inactivation of the other one.

We first analyzed the susceptibility of heterozygous mice to the formation of ACF, which are well-known preneoplastic lesions (18); we tested the appearance of such lesions upon administration of AOM (28), a compound commonly used to evaluate the susceptibility to preneoplastic lesions formation and early colon tumorigenesis (20, 29). In the Tip60 $+/-$ and/or p400 $+/\Delta$ mice strains, no spontaneous tumor-associated phenotype is observed, neither in the colon or elsewhere. Moreover, no ACF is found in young (6 weeks) or old (18 months) mice, indicating that heterozygosity for Tip60 and/or p400 does not induce spontaneous hyperplasia. However, after carcinogen injection, Tip60 $+/-$ mice harbor a significantly higher number of ACF than wild-type ones (Fig. 1A). This indicates that the reduction of the Tip60 expression induces an increase of susceptibility to AOM-induced ACF formation.

In order to characterize the impact of the Tip60 heterozygosity at later steps of tumorigenesis, we analyzed the formation of adenomas after AOM injection in the presence of a proinflammatory treatment (Fig. 1B). As for early preneoplastic lesions, we observed a significant increase in the number of adenoma in Tip60 $+/-$ mice, as compared with wild-type ones (Mann-Whitney P -value < 0.02). These results demonstrate that the increased ACF formation upon defective Tip60 function translates into increased adenoma occurrence, indicating that Tip60 is a tumor suppressor in colon, as already shown for *MYC*-induced lymphoma (5).

We next assayed the sensitivity of p400 $+/\Delta$ and double heterozygous mice to AOM-induced ACF formation. We found that p400 $+/\Delta$ mice exhibit a susceptibility to AOM comparable with control mice (Fig. 1A). However, the disruption of one p400 allele almost abolishes the increase in ACF number observed in Tip60 $+/-$ mice (compare Tip60 $+/-$ with Tip60 $+/-$ and p400 $+/\Delta$). This observation indicates that p400 and Tip60 exert antagonistic effects on early stages of colon tumorigenesis *in vivo*. Interestingly, this also shows that p400 favors hyperplasia, at least in a Tip60 $+/-$ background. To our knowledge, these data are the first demonstration of *in vivo* oncogenic activities of p400. We failed to test adenoma formation for p400 $+/\Delta$ mice, because these mice are more prone to die following proinflammatory treatment, probably due to the previously published (25) higher sensitivity to stresses upon p400 reduction.

Tip60 and p400 antagonistically control colon cancer initiation through the Wnt pathway

To gain insights into the mechanisms by which p400 and Tip60 antagonistically control colon cancer initiation *in vivo*, we analyzed their roles on critical pathways involved in cancer progression. We performed transcriptomic experiments in colon

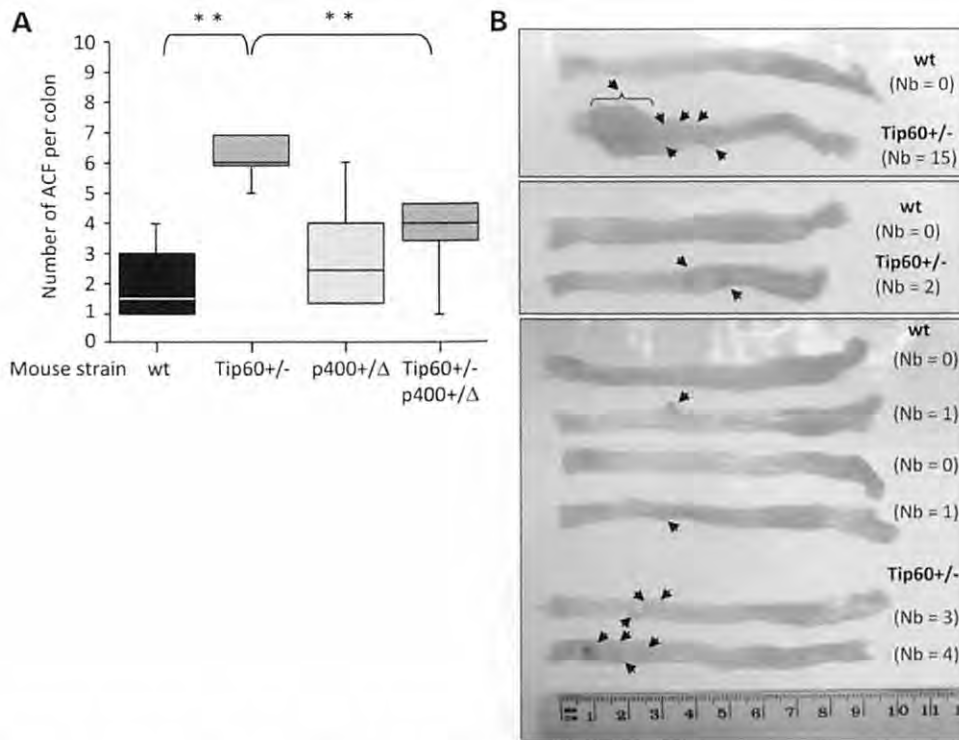


Figure 1. The Tip60/p400 ratio controls the sensitivity to AOM. (A) Fifteen mice per indicated genotypes were injected with azoxymethane as indicated in Materials and Methods, sacrificed and colons were analyzed. Box plots (box: 25–75%, whisker: 2–98%) indicate the median of the ACF number per colon in the population. Statistical analysis was done using Mann–Whitney *t*-test (** $P < 0.02$). (B) Colon adenoma induction in wild-type and Tip60^{+/-} mice. Mice were injected with AOM and then treated using DSS in the drinking water for 1 week immediately after AOM injection. Ten weeks later, colons were dissected and fixed as described in Materials and Methods. Shown are the results of three independent experiments. The number of observed adenomas (arrows) is mentioned for each colon.

carcinoma HCT116 cells by transfecting cells in duplicate using two independent controls, Tip60 or p400 siRNAs (leading to four control, four p400-depleted and four Tip60-depleted samples). The efficiency of siRNA-mediated knockdown is shown in Supplementary Material, Figure S2A. Total RNAs were then prepared and hybridized to microarrays containing most human genes (Fig. 2A). We observed that the two p400 siRNA have very similar knockdown efficiencies (see Supplementary Material, Fig. S2A and B). We therefore considered a RefSeq as regulated by p400 when its expression is significantly deregulated in the four p400-depleted samples compared with the four control samples. Such an analysis leads to a list of 2718 p400-regulated RefSeqs (Supplementary Material, Table S1). In contrast, the efficiencies of the two siRNAs against Tip60 are very different (see Supplementary Material, Fig. S2A and B), precluding such an analysis. For each RefSeq, we thus compared the values of the two Tip60 siRNAs samples relative to the two control samples, leading to 4-fold change values. We considered a RefSeq as deregulated upon Tip60 knockdown when three out of four of these values are >1.25 (or <0.8 for repressed genes). Such an analysis led to the identification of 2412 Tip60-regulated RefSeqs (Supplementary Material, Table S2). Importantly, microarrays results were validated on selected genes for both Tip60 and p400 (Supplementary Material, Fig. S2C). In addition, 731 RefSeqs are regulated by both p400 and Tip60, which is a highly significant overlap (expected 146,

χ^2 independence test P -value $< 10^{-100}$), in agreement with the fact that they are present within the same complex and that many genes are known to be regulated, either similarly or antagonistically, by both Tip60 and p400. Strikingly, a gene ontology analysis (Fig. 2A) indicated that genes linked to the Wnt pathway are significantly deregulated upon Tip60 (P -value = 0.0431686) and p400 depletion (P -value = 0.00078871).

Given the critical role of this pathway in colon cancer initiation and progression, we next tested whether it participates in the consequences of p400 and Tip60 depletion on colon cancer initiation. To that goal, we used a recently developed inhibitor of Wnt signaling, the C59 compound, which exhibits a good *in vivo* bioavailability and thus can be used in mice (30). This inhibitor targets the membrane-bound *O*-acyltransferase porcupine (PORCN), an important Wnt-positive regulator (31). We induced ACF formation using AOM in wild-type and Tip60^{+/-} mice, and treated them, or not, with C59 (Fig. 2B). This inhibitor does not significantly affect the number of ACF observed in wild-type mice, in agreement with the fact that AOM mainly targets other pathways, such as *KRAS*-dependent ones. However, treatment with this inhibitor completely blocks the increase in ACF formation observed in Tip60 heterozygous mice, indicating that Tip60 is a tumor suppressor in colon by repressing Wnt signaling. In addition, the inactivation of one p400 allele (see Fig. 1A) mimics the inhibition of the Wnt pathway, since it affects ACF formation only in the Tip60

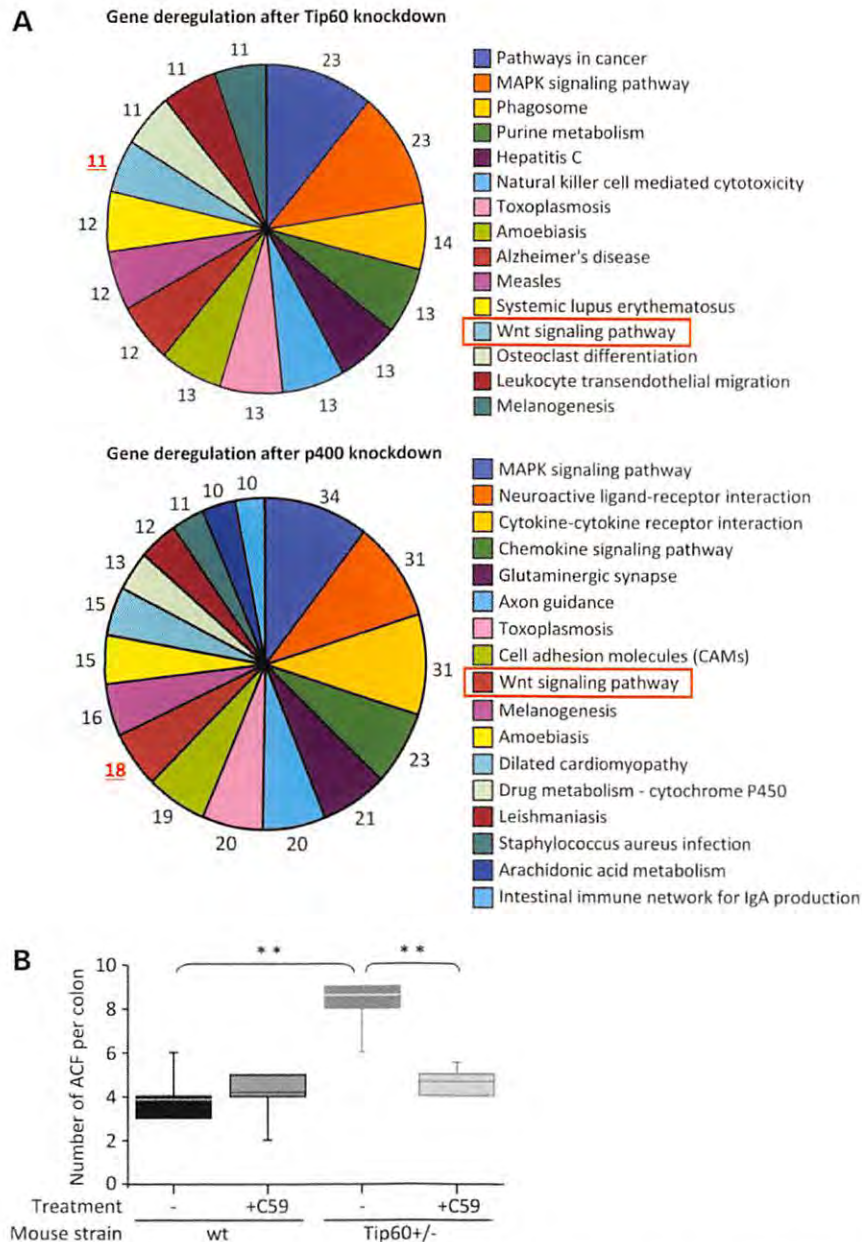


Figure 2. Involvement of the Wnt pathway in the Tip60/p400 control of colon cancer initiation. (A) Gene ontology analysis of pathways dysregulated upon Tip60 or p400 knockdown in HCT116 cells. (B) Ten mice per indicated genotypes were injected with azoxymethane and then treated or not using 5 mg/kg per day of the Wnt inhibitor C59 in the drinking water. three weeks later, colons were dissected, fixed in formalin and analyzed for ACF detection. Box plots (box: 25–75%, whisker: 2–98%) indicate the median of the ACF number per colon in the population. Statistical analysis was done using Mann–Whitney *t*-test (***P* < 0.02).

heterozygous context, indicating that p400 participates in ACF formation by favoring Wnt signaling.

Tip60 and p400 control the proliferation of normal and colorectal cancer-derived cells through the Wnt pathway

In order to provide insights into the molecular mechanisms involved, we next investigated whether the effects of the Tip60/p400 balance on the Wnt signaling can be observed in

cultured cells. We found that, in tumoral HCT116 cells, Tip60 down-regulation using a specific siRNA increased the transactivating abilities of the Wnt-dependent Tcf/Lef transcription factors (measured using a luciferase-based reporter vector), whereas p400 knockdown decreased it (Fig. 3A, see Supplementary Material, Fig. S3A for siRNA efficiencies). Similar results were obtained upon activation of the Wnt pathway by the Wnt3a ligand. Moreover, they were also confirmed using an independent siRNA, ruling out off-target effects (Supplementary

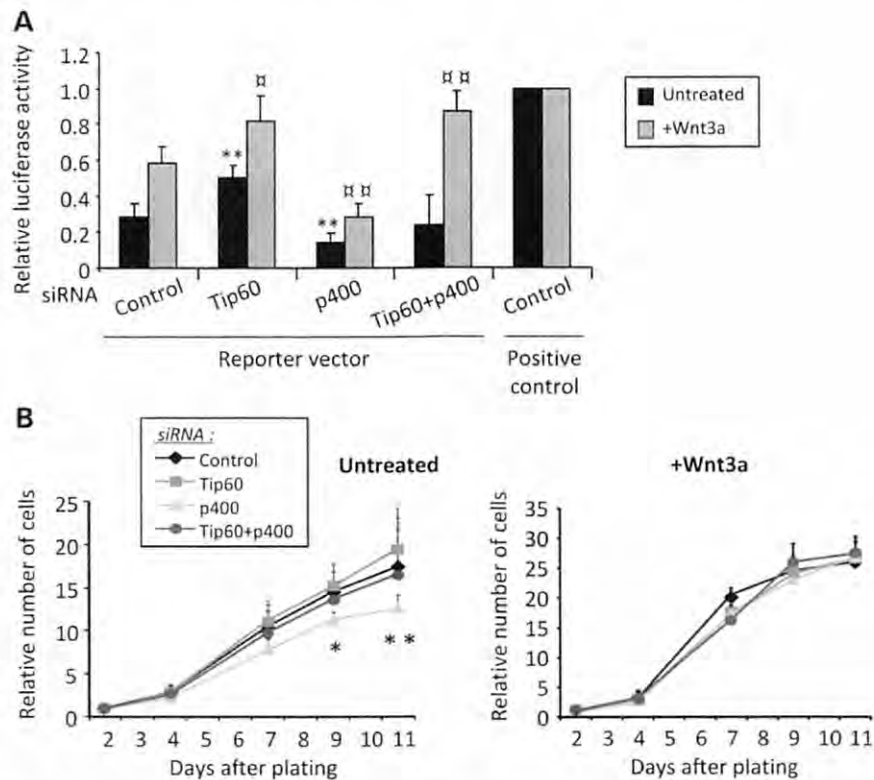


Figure 3. p400 prevents Tip60-dependent effects on the Wnt activity and the proliferation of cancer cells. (A) HCT116 cells were transfected with the indicated siRNAs and the reporter Tcf/Lef-Firefly or positive control vectors. Twenty-four hours later, cells were treated or not with 150 ng/ml Wnt3a for 24 h before harvesting and measure of luciferase. The mean and standard deviation from four-independent experiments are shown. Results are shown relative to 1 for the positive control (** $P < 0.02$ versus untreated control siRNA; \square , $P < 0.05$ and $\square\square$, $P < 0.02$ versus untreated corresponding siRNA). (B) HCT116 cells were transfected using the indicated siRNAs and treated or not, 24 h following transfection, with 150 ng/ml Wnt3a. Cell number was measured at indicated times (* $P < 0.05$; ** $P < 0.02$ versus control siRNA). The mean and standard deviation from three-independent experiments are shown.

Material, Fig. S3B and C). Thus, in colon cancer cells, Tip60 represses the Wnt pathway, whereas p400 expression favors it, even upon overactivation by exogenous ligand. Strikingly, close examination of our microarrays results confirmed this finding for endogenous genes: we observed that Wnt-target genes affected by Tip60 knockdown are globally activated (mean fold change = 1.17), whereas Wnt-target genes, whose expression changes upon p400 knockdown, are mainly repressed (mean fold change = 0.91).

To study whether such changes in Wnt pathway activity can translate into changes in cell proliferation, we transfected HCT116 cells with siRNAs and assayed their proliferation abilities (Fig. 3B). No effect of Tip60 knockdown could be observed (left graph), as expected since these cells already have a largely defective Tip60 function, due to the change in the Tip60/p400 ratio (6). However, p400 knockdown significantly slows the proliferation rate. This is due to changes in the Tip60/p400 ratio, since it is reversed by the concomitant knockdown of Tip60. P400 knockdown is known in other cell types to lead to a cell proliferation arrest by inducing the expression of the cell cycle inhibitor p21 (13,14). However, in HCT116 cells, we do not observe any change in p21 mRNA expression (data not shown), consistent with our previously published data in HCT116 (6) showing that effects of Tip60/p400 ratio on cell

growth are mediated through p53-independent pathway. Rather, we observed that these effects are mediated through the Wnt pathway, since the anti-proliferative effects of p400 knockdown were no longer observed in the presence of the Wnt3a ligand (Fig. 3B, right), which restores normal Wnt pathway activity in p400-depleted cells (see Fig. 3A). Thus, p400 promotes colon cancer cells proliferation by favoring the activity of the Wnt pathway.

Since the Wnt pathway and cell proliferation are strongly affected by cell transformation, and given that the consequences of Tip60 or p400 depletion *in vivo* are observed at early stages of colon cancer progression, we also analyzed the effects of Tip60 and p400 on the Wnt pathway activity and proliferation in non-transformed cells. Using a siRNA-based strategy, we found that Tip60 and p400 antagonistically control Tcf/Lef transcriptional activity in MEFs (Fig. 4A, left; see Supplementary Material, Fig. S4A for siRNA efficiencies), both in presence or in absence of the Wnt3a ligand, as already observed in HCT116 human cancer cells (see Fig. 3A).

To investigate the impact of such Wnt signaling regulation on the proliferation of normal cells, we generated MEFs from mice heterozygous for Tip60 and/or p400. We found, as expected, a 2-fold reduction in Tip60 and wild-type p400 (Supplementary Material, Fig. S1B and C). Importantly, p400 heterozygosity

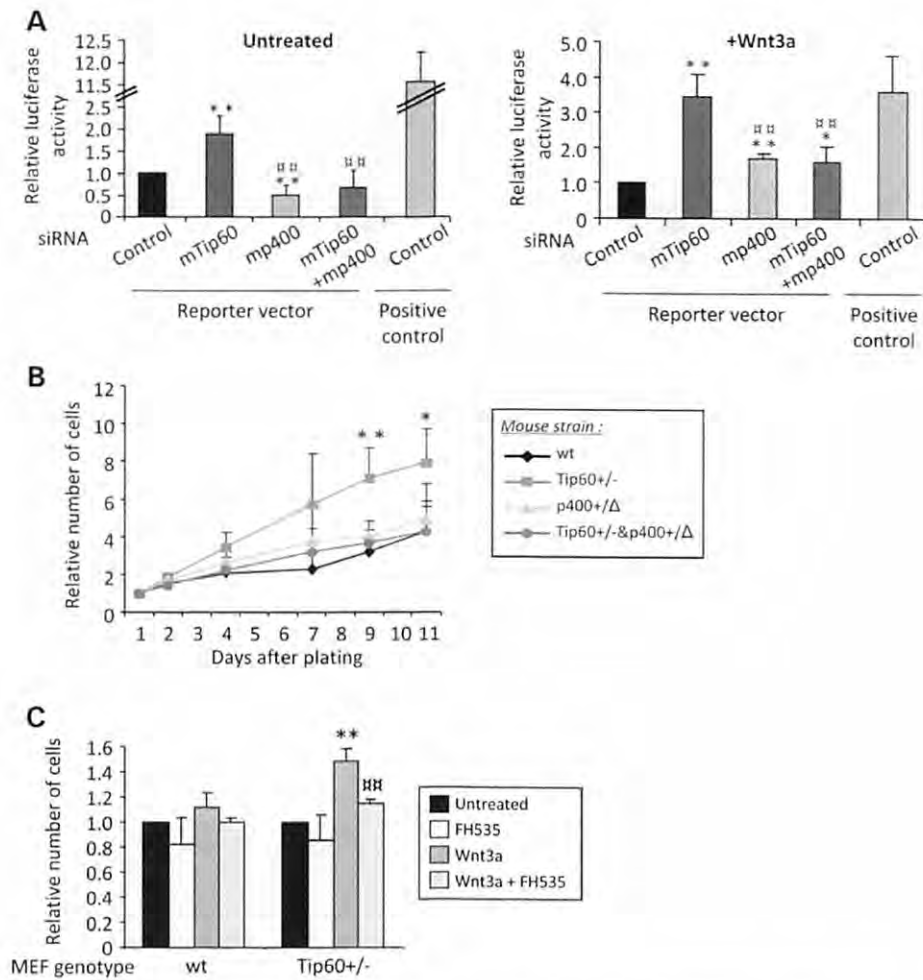


Figure 4. The regulation of cancer cell proliferation by Tip60/p400 is Wnt dependent also in normal cells. (A) Wild-type MEFs were transfected using the indicated siRNAs and the Tcf/Lef-Firefly reporter. Twenty-four hours later, cells were treated or not with 150 ng/ml Wnt3a for 24 h before collection and measure of luciferase. Results are shown relative to 1 for control siRNA (* $P < 0.05$; ** $P < 0.02$ versus control siRNA; ^{###} $P < 0.02$ versus Tip60 siRNA). The mean and standard deviation from three-independent experiments are shown. (B) The cell number of MEFs derived from four-independent embryos of indicated genotypes was measured at indicated times after plating (* $P < 0.05$; ** $P < 0.02$ versus wild-type cells). The mean and standard deviation from three-independent experiments are shown. (C) Wild-type or Tip60^{+/-} MEFs were treated or not, 24 h after plating, with 200 nM FH535, 150 ng/ml Wnt3a or both for 3 days. Cell number was measured and represented relative to 1 for untreated MEFs (** $P < 0.02$ versus untreated samples; ^{##} $P < 0.02$ versus Wnt3a-treated corresponding genotype). The mean and standard deviation from three-independent experiments are shown.

has no impact on Tip60 expression, and reciprocally. We observed that Tip60^{+/-} MEFs grow faster than the wild-type ones (Fig. 4B), providing evidence that a two-fold decrease in Tip60 expression is sufficient to increase the growth rate of these normal cells. Strikingly, p400 heterozygosity completely reverses the increase of proliferation observed in Tip60^{+/-} MEFs (compare Tip60^{+/-} with Tip60^{+/-} and p400^{+Δ}), underlining the importance of a correct p400/Tip60 ratio for the appropriate control of normal cell proliferation. To test whether these changes in normal cell proliferation are dependent on the Wnt pathway, we analyzed the impact of the Wnt3a ligand and the FH535 agent, an inhibitor blocking the β -catenin/Tcf transactivation (32,33), on the proliferation of wild-type or Tip60^{+/-} MEFs (Fig. 4C). We found that Wnt3a stimulates more efficiently the proliferation of normal cells in a Tip60-reduced context.

Importantly, this facilitating effect of the Tip60 heterozygosity is almost totally abolished by inhibiting the β -catenin/Tcf activity using FH535. Taken together, Figures 3 and 4 results indicate that Tip60 and p400 antagonistically controls the proliferation of normal and colon cancer-derived cells through the Wnt pathway, in perfect agreement with their Wnt-dependent role in colon cancer initiation *in vivo*.

Tip60 counteracts β -catenin acetylation and accumulation

We next intended to characterize the mechanism by which p400 and Tip60 participate in Wnt signaling. First, we analyzed the expression of key players of this pathway. We found that depletion of Tip60, either in siRNA-treated or heterozygous MEFs, consistently increases β -catenin protein expression (Fig. 5A and B

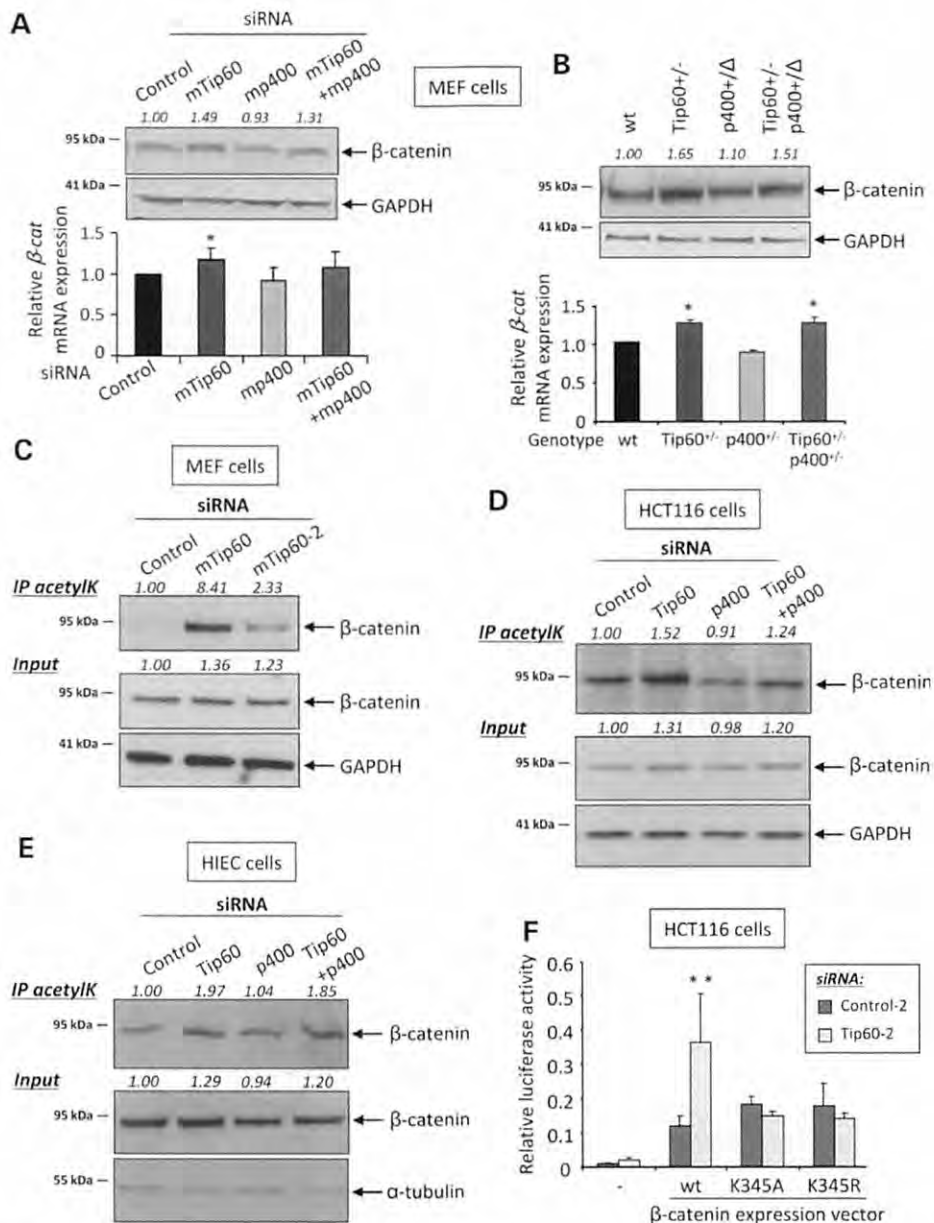


Figure 5. Tip60 regulates β -catenin accumulation and acetylation. (A) Wild-type MEFs were transfected using indicated the siRNA and total protein or mRNA were extracted 48 h later, and subjected to β -catenin and GAPDH analysis by western-blot or qPCR, respectively. Quantification of β -catenin was normalized to GAPDH and shown above the western-blot panels or in qPCR graph ($*P < 0.05$ versus control siRNA). The mean and standard deviation from three-independent qPCR experiments are shown. (B) Same as in (A) for MEFs harboring indicated genotypes. (C) Protein extracts from wild-type MEFs cells transfected using the indicated siRNAs were subjected to IP experiments using an anti-acetyl-lysine antibody. The acetylated β -catenin was then analyzed and quantified, as well as the β -catenin amounts in the total extracts. (D) Same as in (C) for HCT116 cells. (E) Same as in (C) for HIEC cells. (F) HCT116 cells were transfected with the indicated siRNAs and expression vectors, in addition to the reporter Tcf/Lef-Firefly vector. Forty-eight hours later, cells were harvested and the luciferase was measured ($**P < 0.02$ versus control siRNA). The mean and standard deviation from three-independent experiments are shown.

and Supplementary Material, Fig. S4B). Interestingly, β -catenin mRNA levels are only weakly, if anything, affected by Tip60 depletion, indicating that Tip60 mainly acts at a posttranscriptional level. Similar increase of β -catenin amount is also observed in human colon carcinoma HCT116 cells (Fig. 5D, Inputs panels) or in the normal Human Intestinal Crypt Cells HIEC cells (34)

(Fig. 5E, inputs panels; Supplementary Material, Fig. S4C for silencing efficiency). Thus, Tip60 negatively controls β -catenin accumulation.

Since Tip60 is an acetyltransferase, and given that acetylation of a protein can modulate its stability, we tested whether β -catenin can be a substrate of Tip60. Surprisingly, Tip60

depletion increases β -catenin acetylation in MEFs (using two-independent Tip60 siRNAs, Fig. 5C), but also in human tumoral HCT116 (Fig. 5D), or normal HIEC (Fig. 5E) cells, indicating that Tip60 negatively regulates β -catenin acetylation. Acetylation of β -catenin by CBP/p300 or PCAF is known to lead to its stabilization and to the stimulation of its transactivating abilities (35–37). These findings led us to test whether Tip60 could prevent Wnt signaling by inhibiting β -catenin acetylation. To that goal, we made use of unacetylatable K345A/R mutants of β -catenin (35). Both mutants activate the Tcf/Lef reporter promoter as efficiently as the wild-type β -catenin (Fig. 5F). However, they are not able to sustain the extra-activation observed upon Tip60 knockdown, in a striking contrast to the wild type. Thus, we conclude from Figure 5 experiments that the major mechanism by which Tip60 negatively regulates the Wnt pathway is by counteracting β -catenin acetylation and consequently its accumulation and transactivating abilities. Since the mutated site is a known target for CBP/p300, this suggests that Tip60 regulates Wnt activity by antagonizing CBP/p300 activating role on β -catenin.

P400 favors the expression of a subset of Wnt-target genes

In Figure 5 experiments, depleting p400 has no significant effect on β -catenin accumulation or acetylation, indicating that p400 modulates Wnt pathway activity independently of controlling β -catenin acetylation. Interestingly, p400 depletion in MEFs affects the expression of some of the Wnt/ β -catenin-target genes, such as *Itf2* (Supplementary Material, Fig. S5A) that encodes a transcription factor promoting the neoplastic transformation (38) and colon cancers (39). We also observed, by ChIP analysis, that the *Itf2* promoter is enriched in p400 immunoprecipitates (Supplementary Material, Fig. S5B). This enrichment is specific, since no signal can be detected in the no antibody control and since the *Itf2* promoter is more present in the p400 ChIP than the control *RPLP0* gene. Moreover, the binding of p400 to the *Itf2* promoter is similar to that observed on the *CDKN1A^{p21}* promoter, to which p400 binding is well established (13). Thus, the Wnt-target *Itf2* gene is directly regulated by p400. Interestingly, treating MEF cells with Wnt3a (which activates *Itf2* transcription, Supplementary Material, Fig. S5C) leads to a drastic increase in the p400 ChIP efficiency of the *Itf2* promoter (Supplementary Material, Fig. S5B), indicating that the binding of p400 to the *Itf2* promoter increases upon the activation of the Wnt pathway. These data thus suggest that p400 participates in the Wnt-dependent transcriptional activation, at least on some Wnt-target genes.

To test whether such a finding can be generalized, we intended to globally characterize genes bound by p400 in colon-derived cells (Fig. 6A). Two-independent p400 ChIP from HCT116 cells were hybridized to Human ChIP-chip Promoter Arrays. Data analysis lead to the identification of 8809 RefSeqs (Supplementary Material, Table S3), corresponding to 3010 p400-bound genes. As expected, the *CDKN1A^{p21}* promoter is identified in this analysis, and we validated other p400 target genes by conventional ChIP qPCR (Supplementary Material, Fig. S5D).

The overlapping between p400-bound and p400-regulated genes is not very good (231 out of 2150 (1/9) p400-regulated genes are bound by p400), nor with Tip60-regulated genes (128 out of 2002 (1/15) Tip60-regulated genes), underlining

the importance of indirect effects in genes regulation by p400 and Tip60. Strikingly, however, we found, by gene ontology analysis (Fig. 6A), that genes from the Wnt pathway are highly significantly enriched among p400-bound promoters (P -value = $2.88903e-06$). In addition, when we compared with β -catenin-target genes, previously identified by ChIP-Seq experiments (40), we found that 158 out of 988 (1/6) β -catenin-target genes are also bound by p400, indicating that p400 binds to a subset of Wnt-target genes. Importantly, these 158 genes are mostly repressed upon p400 knockdown (mean of the log₂ (fold change) = -0.06 , P -value = 0.001316), indicating that, on these genes, p400 has mainly an activating role. Thus, this genome-wide experiment confirmed that p400 binds to and participate in the activation of a subset of Wnt-target genes.

In addition, some genes encoding key Wnt pathway modulators were apparently bound by p400 (see Supplementary Material, Table S3), such as the Wnt-positive regulator *PORCN*, which is the target of the inhibitor we used *in vivo*. Careful analysis, by conventional ChIP followed by qPCR, of genes encoding several important Wnt modulators (Fig. 6B) indeed confirmed that genes encoding *PORCN* and another positive regulator, *FZD2*, as well as the gene encoding *CAMKIID*, an indirect repressor of the canonical Wnt pathway (41), are bound by p400. The binding of p400 on these genes is similar to that observed on *SART3* and *CDKN1A^{p21}* (positive genes in ChIP-chips experiments) and significantly higher than on negative genes *RPLP0* and *PTGER3*. Interestingly, the knockdown of p400 using specific siRNAs decreased the expression of *FZD2* and *PORCN* mRNA, and increased the expression of *CAMKIID* mRNA (Fig. 6C). All these effects result in a decreased activation of the Wnt pathway, probably explaining the effect of p400 depletion on Tcf/Lef luciferase reporter gene (Fig. 3A). Thus, taken together, these experiments indicate that p400 directly participates in the activation of a subset of β -catenin-target genes, and favors Wnt signaling by controlling the expression of key modulators of this pathway.

DISCUSSION

Here, we found that, by modifying the expression of Tip60 and p400, one can modulate the sensitivity to colon cancer initiation and progression, and that this function is linked to the antagonistic regulation of Wnt pathway activity by the two enzymes (Fig. 7). The role of Tip60 as a negative regulator of Wnt signaling, that we show here, was suspected (42), but never demonstrated. We show here that it is largely, if not only, dependent on its ability to counteract β -catenin acetylation and accumulation. This is an important and surprising finding, since it shows that a HAT (Tip60) can act antagonistically to other HATs (CBP/p300, PCAF, etc.), which acetylate β -catenin, leading to its stabilization and activation (35–37). Such an interference mechanism between HATs had not previously been shown, to our knowledge. Whether it is restricted to the Wnt pathway or can be generalized is an issue deserving further consideration.

In contrast, p400 acts as a positive regulator of the Wnt pathway. This is likely to be mediated by a different mechanism, since no effect of p400 on β -catenin accumulation could be found. Our ChIP-chips data allow us to propose that p400 binds to and favors the expression of a subset of Wnt-target

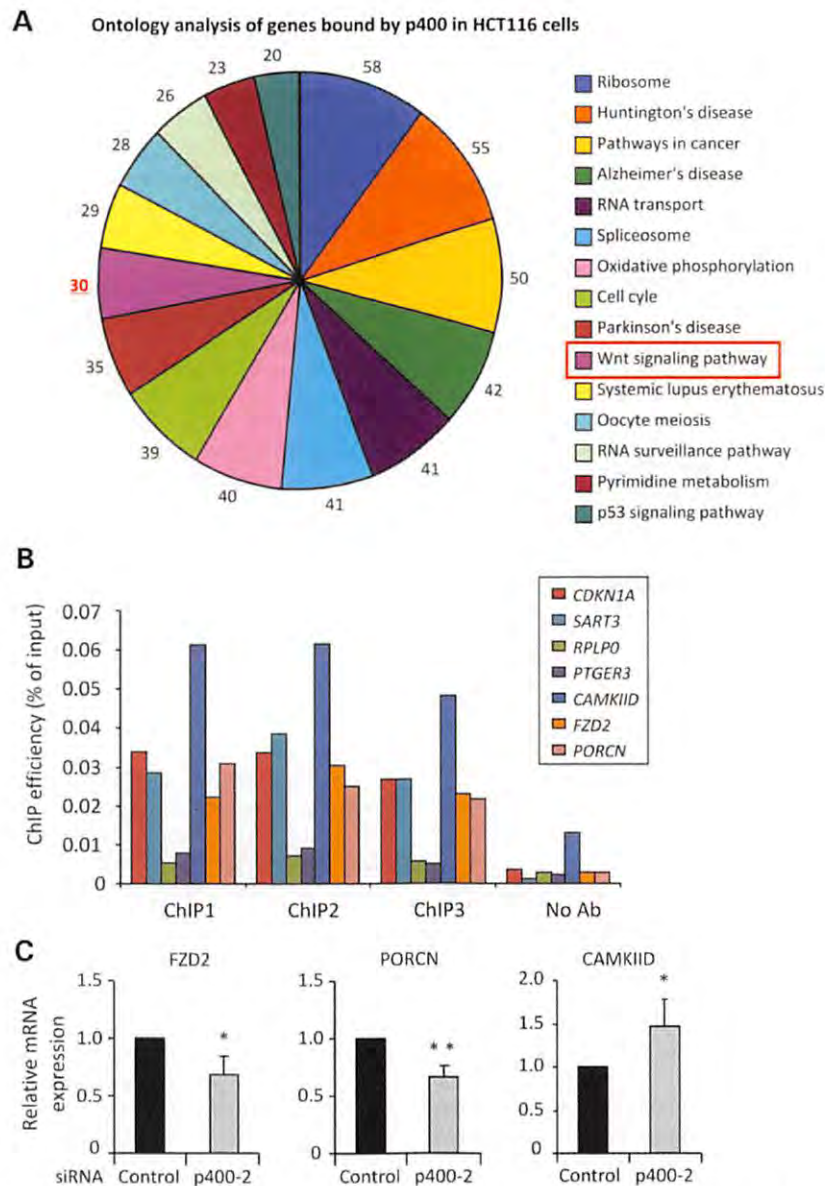


Figure 6. p400 regulation of Wnt-related genes. (A) Gene ontology analysis of pathways represented in p400-bound genes in HCT116 cells. (B) Three-independent samples of p400 ChIPs, similar to those used in (A), were subjected to qPCR analysis of selected promoters. We found the binding of p400 on three ChIP-chips positive promoters (*CDKN1A*, *SART3* or *PORCN*), as well as the low specific enrichment of two negative promoters (*RPLP0* and *PTGER3*) compared with no antibody (No Ab) control. We also identify the specific binding of p400 on *CAMKIID* and *FZD2* genes. (C) HCT116 cells were transfected with the indicated siRNAs. Forty-eight hours later, total RNA were extracted and analyzed by qPCR using specific primers. Results were normalized to GAPDH and represented relative to 1 for control siRNA-transfected cells (* $P < 0.05$; ** $P < 0.02$). The mean and standard deviation from four-independent experiments are shown.

genes in human cells (such as *Itf2* in MEFs), as it has been shown for Tip49a (43). Although some genes bound by p400 are not (or only weakly) affected by p400 depletion in HCT116 cells (such as *MYC* for example), these genes may be very important in other cellular contexts. For example, *CDKN1A*^{p21} expression is not affected by p400 depletion in HCT116 cells (microarrays results in Supplementary Material, Table S1), although it is very important to mediate the cell cycle arrest and senescence induction upon p400 depletion in other cell types (14,44). The direct control of Wnt-target genes is probably not the only

mechanism by which p400 participates in the Wnt pathway (Fig. 7): indeed, we also observed that p400 negatively controls the expression of genes involved in the repression of the canonical Wnt/ β -catenin pathway (such as *Wif1* and *sFrp1* in MEFs, or *DKK1* and *CAMKIID* in human cells, Supplementary Material, Fig. S6 and Fig. 6C). Moreover, p400 is also responsible for direct-positive regulations of important Wnt pathway components such as *FZD2* and *PORCN* (Fig. 6B and C). All these data indicate that the transcriptional modulations depending on p400 affect different levels of the Wnt pathway and participate

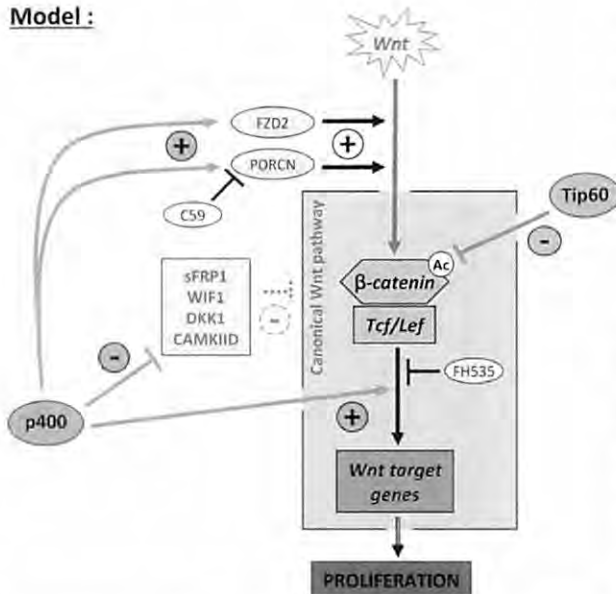
Model :

Figure 7. Model of fine-tuning of the Wnt pathway by Tip60/p400. Tip60 negatively controls the Wnt signaling via the decrease of β -catenin accumulation and acetylation, resulting in a weaker Wnt activity. Conversely, p400 stimulates the Wnt activity by acting as a co-activator for a subset of Wnt-target genes, as well as for some Wnt-positive modulators (such as *PORCN* or *FZD2*), but also possibly by other mechanisms, such as by repressing the expression of inhibitors (*sFRP1*, *WIF1*, *DKK1*, *CAMKIID*, etc.). As a consequence, Tip60 and p400 antagonistically regulate Wnt pathway activity, normal and cancer cells proliferation and early steps of colon tumorigenesis.

to its activation (Fig. 7). The importance of such direct regulations is indicated by our findings that inhibiting p400 mimics the effects of targeting *PORCN* for ACF formation *in vivo*. Our data thus uncover p400 as an important new player in the Wnt signaling.

Our results also indicate that, although Tip60 and p400 physically interact, they probably affect Wnt signaling by independent mechanisms. This is reminiscent to what has been described on the *CDKN1A^{p21}* promoter that p400 represses by incorporating H2A.Z and that Tip60 activates, once the p400-induced repression has been relieved, through histone acetylation (13). It is tempting to speculate that p400 and Tip60 have acquired, during evolution, antagonistic functions on many different processes, some of which being mediated by their physical interaction and the direct repressive effect of p400 on Tip60 histone acetyltransferase activity (15), others through independent mechanisms. Strikingly, in most cases (regulation of p21 expression (14), senescence induction (44, 45), DDR activation (6) and Wnt signaling (this study)), p400 has a proproliferation role, whereas Tip60 has an anti-proliferative role.

Importantly, our data indicate that the status of Tip60 and of p400 are crucial *in vivo* elements controlling the sensitivity to preneoplastic lesions in a Wnt-dependent manner. Our results allow us to propose that the Tip60/p400 ratio exerts a fine-tuning control on the Wnt pathway activity (Fig. 7), impacting early steps of colon tumorigenesis and cancer cells proliferation. We observed changes in colon cancer initiation through the modulation of the Wnt pathway in heterozygous animals, i.e. when

Tip60 or p400 expression levels are modified by 2-fold. Strikingly, we previously uncovered an approximate 2-fold difference in the Tip60/p400 ratio in a collection of colon cancers as compared with normal adjacent tissues (6). Our results thus show that the imbalance found in human cancers is probably sufficient to affect Wnt signaling and, as a consequence, could participate in colon cancer progression in humans.

Tip60 has already been shown to be a tumor suppressor for myc-induced lymphoma. In this case, depleting Tip60 was shown to prevent the activation of the oncogene-induced DNA damage response (ODDR) pathway (5). Our data thus demonstrate that Tip60 can also prevent cancer progression by an alternate mechanism, i.e. by repressing Wnt signaling. Interestingly, Tip60 is involved in many other anti-proliferative processes, such as p53 activation (46,47), apoptosis (12,14) or senescence induction (44). Since Tip60 is known to be underexpressed in a variety of human cancers (5,48), the consequence of this underexpression is probably both an activation of the pro-cancer Wnt pathway and an inhibition of various anti-cancer barriers, including the p53 pathway, the ODDR and senescence. Our data thus underline the importance of the Tip60 function and of the Tip60/p400 imbalance for cancer initiation and progression.

Strikingly, we show for the first time that p400 possesses some oncogenic properties, at least in a Tip60-reduced context, i.e. when cancer progression is dependent on the Wnt pathway. Given the importance of the Wnt pathway in many different cancers, p400 expression and activity is probably important for the progression not only of colon cancer, but also of other cancers. Importantly, since p400 directly regulates a subset of Wnt-target genes and some genes encoding key Wnt modulators, it probably participates in setting up epigenetic modifications, such as the presence of H2AZ, on these promoters. In this respect, our data highlight the importance of the epigenetic control of Wnt signaling. Given that epigenetic modifications are reversible, one can imagine that epigenetic drugs, in particular drugs that target p400, may reverse these epigenetic modifications and decrease the activation of Wnt signaling. Our results thus underline the importance of developing and testing epigenetic drugs targeting this new Wnt pathway modulator.

In addition, our findings showing that Tip60/p400 balance affects the proliferation of normal cells in a Wnt pathway-dependent manner provide evidence that the Tip60/p400 status can also influence the cell physiology prior to tumorigenesis. Thus, any alteration of the ratio could impact critical physiological roles of the Wnt/ β -catenin pathway, such as the transcriptional control of pluripotency genes, the self-renewal of stem cells and many differentiation processes (49). It could also be involved in other important pathologies involving the Wnt signaling (diabetes, osteoporosis, obesity, coronary diseases, etc., for review, see (50)). The contribution of Tip60 and p400 in normal development or pathologies, through Wnt signaling, clearly deserves further investigation.

MATERIALS AND METHODS

All microarrays data from this publication have been submitted to the GEO public functional genomics data repository (GSE45616). Statistical significance was calculated using Student's *t*-test, χ^2 independence test or Mann-Whitney test. For

protocol complements, see Supplementary Material, Experimental Procedures.

Ethics statement

The experiments involved with animals were conducted accordingly to French governmental norms and the protocol was approved by the IPBS-CNRS Ethic Committee (Approval #20090326/62).

Animals

Mice heterozygous for Tip60 (26) were obtained from Dr B. Amati and back-crossed with C57Bl/6J females (Charles-River, L'Arbresle, France). Frozen embryos of the p400 strain (27) were purchased from RIKEN-BRC (Ibaraki, Japan) and reviviscence was done using C57Bl/6J mice.

Induction of preneoplastic lesions

Six- to 8-week-old animals received, twice at 1 week apart, an intraperitoneal injection of AOM (Sigma-Aldrich, St-Quentin-Fallavier, France) in saline solution at 15 mg/kg of body weight or vehicle alone. Mice were then treated or not using 5 mg/kg per day of the Wnt inhibitor C59 (BioVision Inc, Milpitas, CA, USA) in the drinking water immediately after the first AOM injection. Three weeks after the second injection, animals were sacrificed and colons were slit opened longitudinally and examined for ACF, after fixation in formalin and staining with 0.05% methylene-blue solution (Sigma-Aldrich).

To accelerate the appearance of advanced lesions, mice were also treated with 1% DSS (MP Biomedicals, Illkirch, France), a proinflammatory molecule, for 1 week in the drinking water immediately after AOM injection. Ten weeks later, colons were dissected, fixed in formalin and photographed.

Analysis of microarrays results

Analysis of large-scale gene expression in HCT116 cells previously transfected with siRNAs (see Supplementary Material, Fig. S2A for efficiencies and Experimental Procedures for details) were done using Nimblegen (Roche Nimblegen, Madison, WI, USA) DNA microarrays (Human Gene Expression 12x135K Arrays).

Chromatin immunoprecipitation and ChIP-chips experiments

ChIP experiments were performed as described (14) and analyzed by qPCR using specific primers.

ChIP-chips experiments were done using two-independent p400-immunoprecipitated chromatin samples from HCT116 cells. After the p400-ChIP, samples were amplified using the WGA kit (Sigma-Aldrich). DNA labeling and hybridization on Human ChIP-chip 385K RefSeq Promoter Arrays (Roche Nimblegen) were performed. Bioinformatic analysis allowing identification of peaks was done using the NimbleScan software. A promoter was recorded as bound by p400 if binding peaks ($P < 0.01$) were identified in the two experiments at < 500 pb distance, which corresponds to the ChIP resolution. Clustering

of bound genes was done using GeneCoDis3 online software (<http://genecodis.cnb.csic.es>) (51).

SUPPLEMENTARY MATERIAL

Supplementary Material is available at *HMG* online.

ACKNOWLEDGEMENTS

We thank Dr B. Amati for providing us Tip60^{+/-} mice from Dr J. Lough's lab. We greatly thank Dr C. Neuvet for providing us all β -catenin expression vectors and Dr J.-F. Beaulieu for the gift of HIEC cells. We thank N. Naud for her help with ACF analysis. We used the INSA-GeT-Biopuces and the LBCMCP Toulouse Genotoul TRI cytometry platforms as well as the luminometry facility of the LBME (UMR5099, Toulouse).

Conflict of Interest statement: None declared.

FUNDING

This work was supported by the Ligue Nationale Contre le Cancer as an 'Équipe labellisée' (Grant #VP7537) and from the Fondation of the Association pour la Recherche contre le Cancer. L.M. and F.E. were awarded by the Fondation de France for this work.

REFERENCES

- Aran, D. and Hellman, A. (2013) DNA methylation of transcriptional enhancers and cancer predisposition. *Cell*, **154**, 11–13.
- Bojang, P. Jr and Ramos, K.S. (2013) The promise and failures of epigenetic therapies for cancer treatment. *Cancer Treat. Rev.*, **40**, 153–169.
- Skene, P.J. and Henikoff, S. (2013) Histone variants in pluripotency and disease. *Development*, **140**, 2513–2524.
- Fullgrabe, J., Kavanagh, E. and Joseph, B. (2011) Histone onco-modifications. *Oncogene*, **30**, 3391–3403.
- Gorrini, C., Squatrito, M., Luise, C., Syed, N., Perma, D., Wark, L., Martinato, F., Sardella, D., Verrecchia, A., Bennett, S. *et al.* (2007) Tip60 is a haplo-insufficient tumour suppressor required for an oncogene-induced DNA damage response. *Nature*, **448**, 1063–1067.
- Mattera, L., Escafit, F., Pillaire, M.J., Selves, J., Teyca, S., Hoffmann, J.S., Gourraud, P.A., Chevillard-Briet, M., Cazaux, C. and Trouche, D. (2009) The p400/Tip60 ratio is critical for colorectal cancer cell proliferation through DNA damage response pathways. *Oncogene*, **28**, 1506–1517.
- Kaidi, A. and Jackson, S.P. (2013) KAT5 tyrosine phosphorylation couples chromatin sensing to ATM signalling. *Nature*, **498**, 70–74.
- Sun, Y., Jiang, X., Chen, S., Fernandes, N. and Price, B.D. (2005) A role for the Tip60 histone acetyltransferase in the acetylation and activation of ATM. *Proc. Natl. Acad. Sci. USA*, **102**, 13182–13187.
- Tang, Y., Luo, J., Zhang, W. and Gu, W. (2006) Tip60-dependent acetylation of p53 modulates the decision between cell-cycle arrest and apoptosis. *Mol. Cell*, **24**, 827–839.
- Dar, A., Shibata, E. and Dutta, A. (2013) Deubiquitination of Tip60 by USP7 determines the activity of the p53-dependent apoptotic pathway. *Mol. Cell Biol.*, **33**, 3309–3320.
- Sykes, S.M., Mellert, H.S., Holbert, M.A., Li, K., Marmorstein, R., Lane, W.S. and McMahon, S.B. (2006) Acetylation of the p53 DNA-binding domain regulates apoptosis induction. *Mol. Cell*, **24**, 841–851.
- Ikura, T., Ogryzko, V.V., Grigoriev, M., Groisman, R., Wang, J., Horikoshi, M., Scully, R., Qin, J. and Nakatani, Y. (2000) Involvement of the TIP60 histone acetylase complex in DNA repair and apoptosis. *Cell*, **102**, 463–473.
- Gevry, N., Chan, H.M., Laflamme, L., Livingston, D.M. and Gaudreau, L. (2007) p21 transcription is regulated by differential localization of histone H2A.Z. *Genes Dev.*, **21**, 1869–1881.

14. Tyteca, S., Vandromme, M., Legube, G., Chevillard-Briet, M. and Trouche, D. (2006) Tip60 and p400 are both required for UV-induced apoptosis but play antagonistic roles in cell cycle progression. *EMBO J.*, **25**, 1680–1689.
15. Park, J.H., Sun, X.J. and Roeder, R.G. (2010) The SANT domain of p400 ATPase represses acetyltransferase activity and coactivator function of TIP60 in basal p21 gene expression. *Mol. Cell Biol.*, **30**, 2750–2761.
16. Fearon, E.R. (2011) Molecular genetics of colorectal cancer. *Annu. Rev. Pathol.*, **6**, 479–507.
17. Cheng, L. and Lai, M.D. (2003) Aberrant crypt foci as microscopic precursors of colorectal cancer. *World J. Gastroenterol.*, **9**, 2642–2649.
18. Lopez-Ceron, M. and Pellise, M. (2012) Biology and diagnosis of aberrant crypt foci. *Colorectal Dis.*, **14**, e157–e164.
19. Pamaud, G., Tache, S., Peiffer, G. and Corpet, D.E. (1999) Polyethylene-glycol suppresses colon cancer and causes dose-dependent regression of azoxymethane-induced aberrant crypt foci in rats. *Cancer Res.*, **59**, 5143–5147.
20. Pierre, F.H., Santarelli, R.L., Allam, O., Tache, S., Naud, N., Gueraud, F. and Corpet, D.E. (2010) Freeze-dried ham promotes azoxymethane-induced mucin-depleted foci and aberrant crypt foci in rat colon. *Nutr. Cancer*, **62**, 567–573.
21. Boivin, G.P., Washington, K., Yang, K., Ward, J.M., Pretlow, T.P., Russell, R., Besselsen, D.G., Godfrey, V.L., Doetschman, T., Dove, W.F. *et al.* (2003) Pathology of mouse models of intestinal cancer: consensus report and recommendations. *Gastroenterology*, **124**, 762–777.
22. Guda, K., Upender, M.B., Belinsky, G., Flynn, C., Nakanishi, M., Marino, J.N., Ried, T. and Rosenberg, D.W. (2004) Carcinogen-induced colon tumors in mice are chromosomally stable and are characterized by low-level microsatellite instability. *Oncogene*, **23**, 3813–3821.
23. Takahashi, M. and Wakabayashi, K. (2004) Gene mutations and altered gene expression in azoxymethane-induced colon carcinogenesis in rodents. *Cancer Sci.*, **95**, 475–480.
24. Elyada, E., Pribluda, A., Goldstein, R.E., Morgenstem, Y., Brachya, G., Cojocaru, G., Snir-Alkalay, I., Burstain, I., Haffner-Krausz, R., Jung, S. *et al.* (2011) CK1alpha ablation highlights a critical role for p53 in invasiveness control. *Nature*, **470**, 409–413.
25. Matterna, L., Courilleau, C., Legube, G., Ueda, T., Fukunaga, R., Chevillard-Briet, M., Canitrot, Y., Escaffit, F. and Trouche, D. (2010) The E1A-associated p400 protein modulates cell fate decisions by the regulation of ROS homeostasis. *PLoS Genetics*, **6**, e1000983.
26. Hu, Y., Fisher, J.B., Koprowski, S., McAllister, D., Kim, M.S. and Lough, J. (2009) Homozygous disruption of the Tip60 gene causes early embryonic lethality. *Dev. Dyn.*, **238**, 2912–2921.
27. Ueda, T., Watanabe-Fukunaga, R., Ogawa, H., Fukuyama, H., Higashi, Y., Nagata, S. and Fukunaga, R. (2007) Critical role of the p400/mDomino chromatin-remodeling ATPase in embryonic hematopoiesis. *Genes Cells*, **12**, 581–592.
28. De Robertis, M., Massi, E., Poeta, M.L., Carotti, S., Morini, S., Cecchetelli, L., Signori, E. and Fazio, V.M. (2011) The AOM/DSS murine model for the study of colon carcinogenesis: From pathways to diagnosis and therapy studies. *J. Carcinog.*, **10**, 9.
29. Lu, Q., Jiang, B., Lin, C. and Shan, T. (2008) Dark Aberrant Crypt Foci with activated Wnt pathway are related to tumorigenesis in the colon of AOM-treated rat. *J. Exp. Clin. Cancer Res.*, **27**, 26.
30. Proffitt, K.D., Madan, B., Ke, Z., Pendharkar, V., Ding, L., Lee, M.A., Hannoush, R.N. and Virshup, D.M. (2012) Pharmacological inhibition of the Wnt acyltransferase PORCN prevents growth of WNT-driven mammary cancer. *Cancer Res.*, **73**, 502–507.
31. Proffitt, K.D. and Virshup, D.M. (2012) Precise regulation of porcupine activity is required for physiological Wnt signaling. *J. Biol. Chem.*, **287**, 34167–34178.
32. Handeli, S. and Simon, J.A. (2008) A small-molecule inhibitor of Tcf/beta-catenin signaling down-regulates PPARgamma and PPARdelta activities. *Mol. Cancer Ther.*, **7**, 521–529.
33. Iida, J., Dorchak, J., Lehman, J.R., Clancy, R., Luo, C., Chen, Y., Somiari, S., Ellsworth, R.E., Hu, H., Mural, R.J. *et al.* (2012) FH535 inhibited migration and growth of breast cancer cells. *PLoS ONE*, **7**, e44418.
34. Beaulieu, J.F. and Menard, D. (2012) Isolation, characterization, and culture of normal human intestinal crypt and villus cells. *Methods Mol. Biol.*, **806**, 157–173.
35. Levy, L., Wei, Y., Labalette, C., Wu, Y., Renard, C.A., Buendia, M.A. and Neuveut, C. (2004) Acetylation of beta-catenin by p300 regulates beta-catenin-Tcf4 interaction. *Mol. Cell Biol.*, **24**, 3404–3414.
36. Wolf, D., Rodova, M., Miska, E.A., Calvet, J.P. and Kouzarides, T. (2002) Acetylation of beta-catenin by CREB-binding protein (CBP). *J. Biol. Chem.*, **277**, 25562–25567.
37. Ge, X., Jin, Q., Zhang, F., Yan, T. and Zhai, Q. (2009) PCAF acetylates [beta]-catenin and improves its stability. *Mol. Biol. Cell*, **20**, 419–427.
38. Kolligs, F.T., Nieman, M.T., Winer, I., Hu, G., Van Mater, D., Feng, Y., Smith, I.M., Wu, R., Zhai, Y., Cho, K.R. *et al.* (2002) ITF-2, a downstream target of the Wnt/TCF pathway, is activated in human cancers with beta-catenin defects and promotes neoplastic transformation. *Cancer Cell*, **1**, 145–155.
39. Mologni, L., Dekhil, H., Ceccon, M., Purgante, S., Lan, C., Cleris, L., Magistroni, V., Formelli, F. and Gambacorti-Passerini, C.B. (2010) Colorectal tumors are effectively eradicated by combined inhibition of [beta]-catenin, KRAS, and the oncogenic transcription factor ITF2. *Cancer Res.*, **70**, 7253–7263.
40. Bottomly, D., Kyler, S.L., McWeeney, S.K. and Yochum, G.S. (2010) Identification of [beta]-catenin binding regions in colon cancer cells using ChIP-Seq. *Nucleic Acids Res.*, **38**, 5735–5745.
41. Ishitani, T., Kishida, S., Hyodo-Miura, J., Ueno, N., Yasuda, J., Waterman, M., Shibuya, H., Moon, R.T., Ninomiya-Tsuji, J. and Matsumoto, K. (2003) The TAK1-NLK mitogen-activated protein kinase cascade functions in the Wnt-5a/Ca(2+) pathway to antagonize Wnt/beta-catenin signaling. *Mol. Cell Biol.*, **23**, 131–139.
42. Baek, S.H., Ohgi, K.A., Rose, D.W., Koo, E.H., Glass, C.K. and Rosenfeld, M.G. (2002) Exchange of N-CoR corepressor and Tip60 coactivator complexes links gene expression by NF-kappaB and beta-amyloid precursor protein. *Cell*, **110**, 55–67.
43. Feng, Y., Lee, N. and Fearon, E.R. (2003) TIP49 regulates beta-catenin-mediated neoplastic transformation and T-cell factor target gene induction via effects on chromatin remodeling. *Cancer Res.*, **63**, 8726–8734.
44. Chan, H.M., Narita, M., Lowe, S.W. and Livingston, D.M. (2005) The p400 E1A-associated protein is a novel component of the p53--> p21 senescence pathway. *Genes Dev.*, **19**, 196–201.
45. Zheng, H., Seit-Nebi, A., Han, X., Aslanian, A., Tat, J., Liao, R., Yates, J.R. 3rd. and Sun, P. (2013) A Posttranslational modification cascade involving p38, Tip60, and PRAK mediates oncogene-induced senescence. *Mol. Cell*, **50**, 699–710.
46. Berns, K., Hijmans, E.M., Mullenders, J., Brummelkamp, T.R., Velds, A., Heimerikx, M., Kerkhoven, R.M., Madiredjo, M., Nijkamp, W., Weigelt, B. *et al.* (2004) A large-scale RNAi screen in human cells identifies new components of the p53 pathway. *Nature*, **428**, 431–437.
47. Legube, G., Linares, L.K., Tyteca, S., Caron, C., Scheffner, M., Chevillard-Briet, M. and Trouche, D. (2004) Role of the histone acetyltransferase Tip60 in the p53 pathway. *J. Biol. Chem.*, **279**, 44825–44833.
48. Leonart, M., Vidal, F., Gallardo, D., Diaz-Fuertes, M., Rojo, F., Cuatrecasas, M., Lopez-Vicente, L., Kondoh, H., Blanco, C., Camero, A. *et al.* (2006) New p53 related genes in human tumors: significant downregulation in colon and lung carcinomas. *Oncol. Rep.*, **16**, 603–608.
49. Holland, J.D., Klaus, A., Garratt, A.N. and Birchmeier, W. (2013) Wnt signaling in stem and cancer stem cells. *Curr. Opin. Cell Biol.*, **25**, 254–264.
50. Clevers, H. and Nusse, R. (2012) Wnt/beta-catenin signaling and disease. *Cell*, **149**, 1192–1205.
51. Tabas-Madrid, D., Nogales-Cadenas, R. and Pascual-Montano, A. (2012) GeneCodis3: a non-redundant and modular enrichment analysis tool for functional genomics. *Nucleic Acids Res.*, **40**, W478–W483.

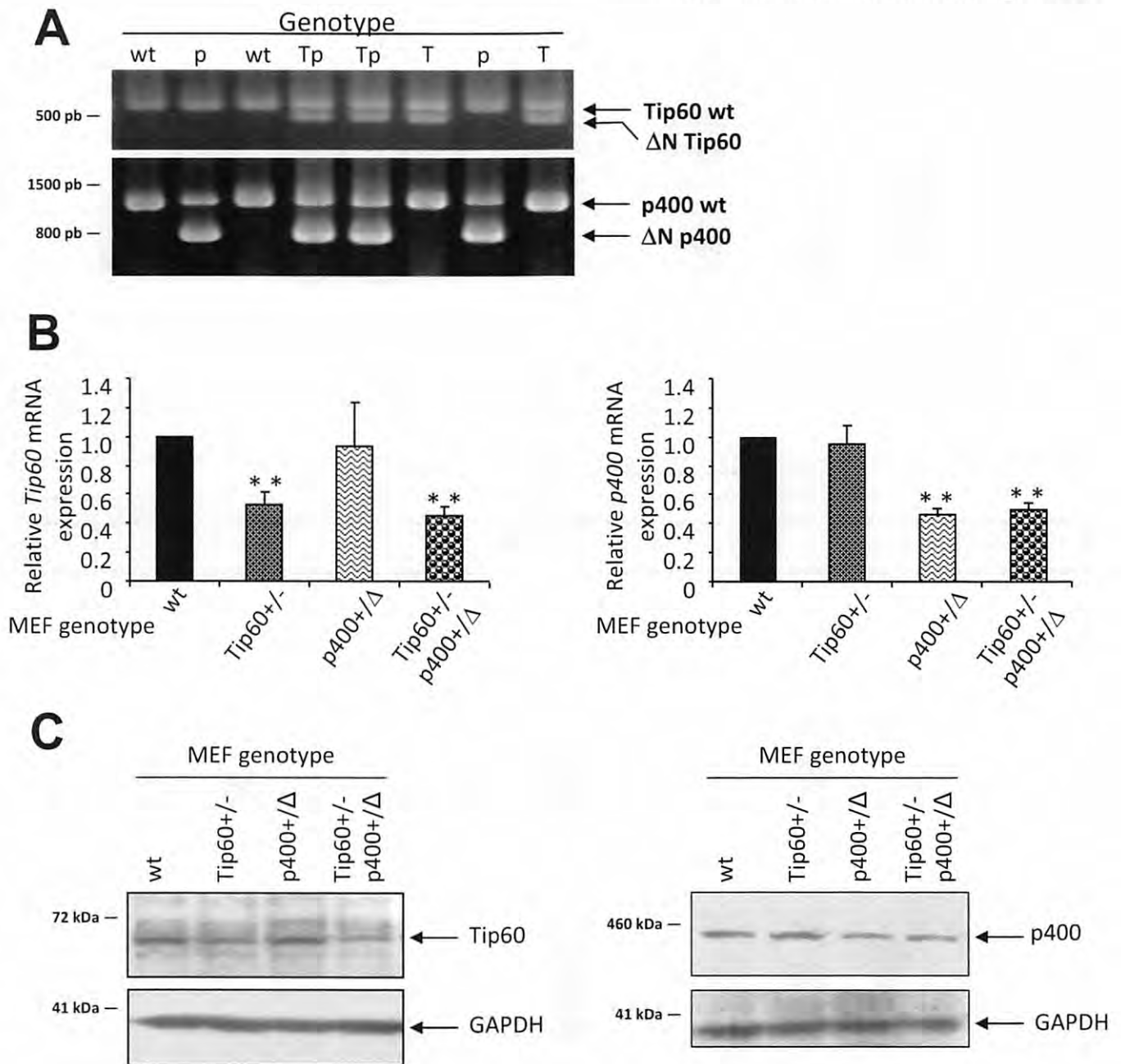


Figure S1: Genotyping of mice strains and quantification of Tip60/p400 mRNA and protein in MEFs.

A) New born mice from mating *Tip60*^{+/-} and *p400*^{+/-} mice were genotyped to distinguish wild-type from ΔN-Tip60 or ΔN-p400 alleles (wt:wild-type; T:*Tip60*^{+/-}, p:*p400*^{+/-}; Tp:*Tip60*^{+/-}&p*p400*^{+/-}). B) MEF from three embryos harboring the indicated genotypes were harvested and total RNA were extracted and submitted to qPCR analysis to quantify Tip60 and full-length p400, after normalization to GAPDH amounts. Results are presented relative to 1 for wild-type genotype. The mean and standard deviation are shown (**, *p*<0.02 versus wild-type genotype)

C) Total protein from indicated MEFs was extracted and Tip60 or full-length p400 protein amounts were measured by western-blot. An anti-GAPDH antibody was used for normalization.

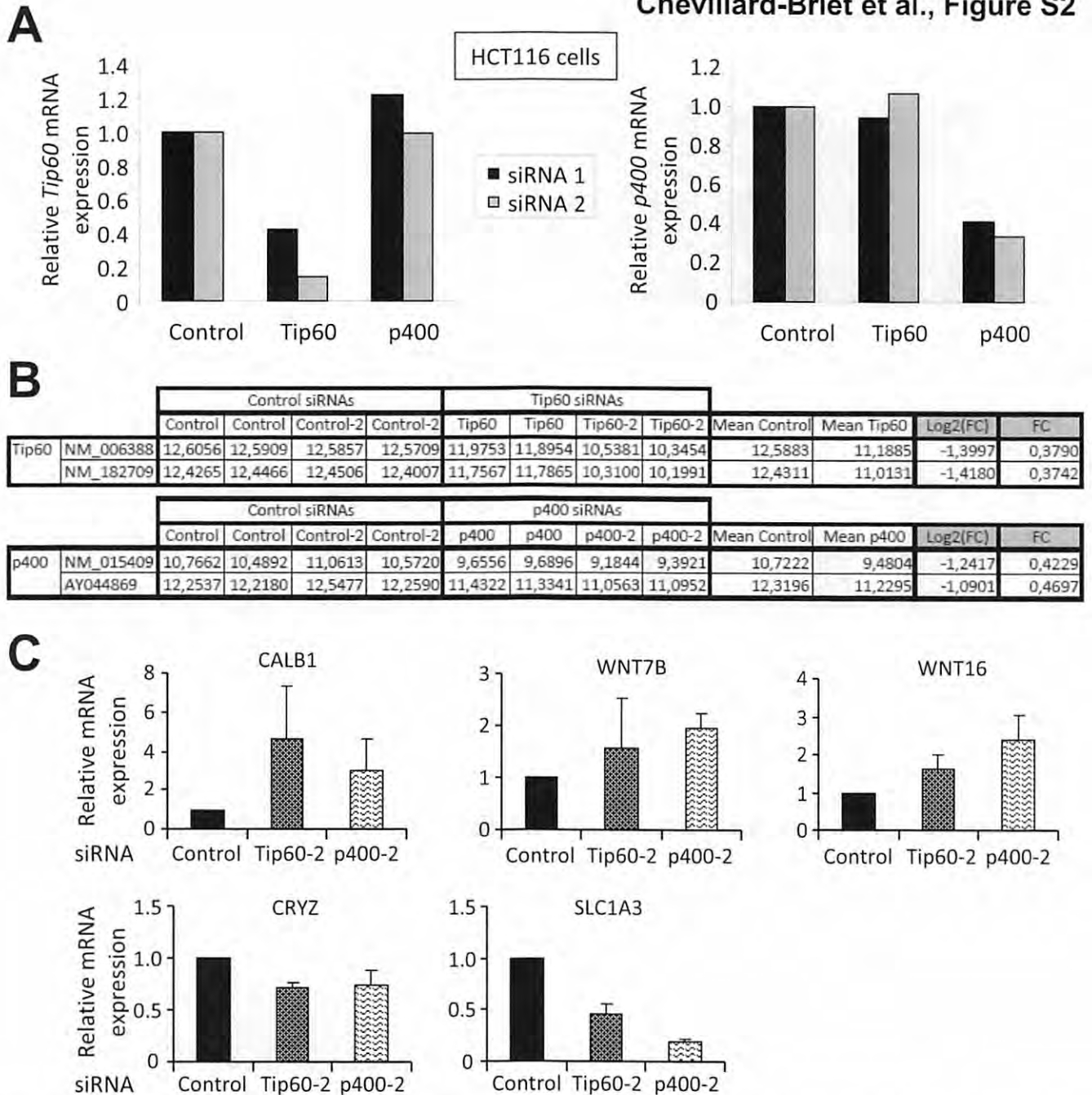


Figure S2: Validation by qPCR of siRNA-mediated silencing and of expression microarrays

A) HCT116 cells were independently transfected with two different series of siRNAs and total RNA was extracted 48h later. After quality control, samples were both used for hybridization on expression microarrays (see Tables S1 and S2) and reverse transcribed and subjected to qPCR analysis. Results of the qPCR are normalized by *GAPDH* and shown relative to 1 for the corresponding control. B) Data obtained from expression microarrays analysis for Tip60 and p400-corresponding RefSeqs, following transfection of the indicated siRNAs. Note that the silencing efficiencies of Tip60 expression by the two sets of Tip60-targetting siRNA are largely different, in accordance with data obtained in A. C) Validation, by qPCR, of the expression arrays analysis using HCT116 cells transfected using the indicated siRNA. We confirmed the co-deregulation of *CALB1*, *CRYZ* and *SLC1A3* upon Tip60 and p400 depletion. We also confirmed the deregulation of *WNT7B* and *WNT16* by p400. The mean and standard deviation from three independent experiments are shown.

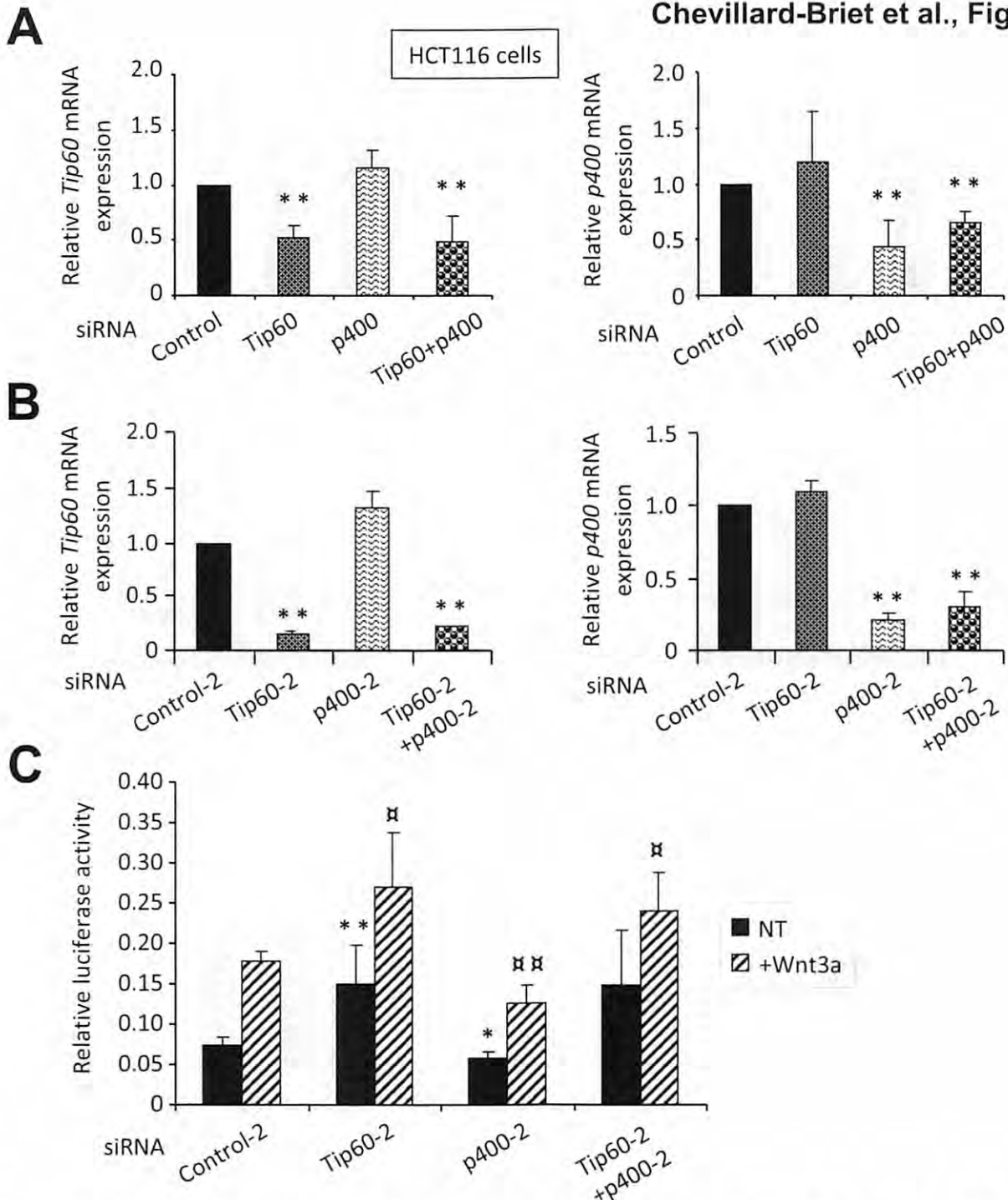


Figure S3: Control of siRNA efficiencies in HCT116 cells and confirmation of the results of the Figure 3 with other siRNAs

A) HCT116 cells were transfected with the indicated siRNAs and total siRNA was extracted 48h later, reverse transcribed and subjected to qPCR analysis. Results are normalized by GAPDH and shown relative to 1 for the control (**, $p < 0.02$). The mean and standard deviation from four independent experiments are shown. B) Same as in A. C) HCT116 cells were transfected using indicated siRNAs and the reporter Tcf/Lef-Firefly vector. 24h later, cells were treated or not with 150ng/ml Wnt3a for 24h before harvesting and measure of luciferase (*, $p < 0.05$ and **, $p < 0.02$ versus untreated control siRNA; \boxtimes , $p < 0.05$ and $\boxtimes\boxtimes$, $p < 0.02$ vs untreated corresponding siRNA). The mean and standard deviation from four independent experiments are shown.

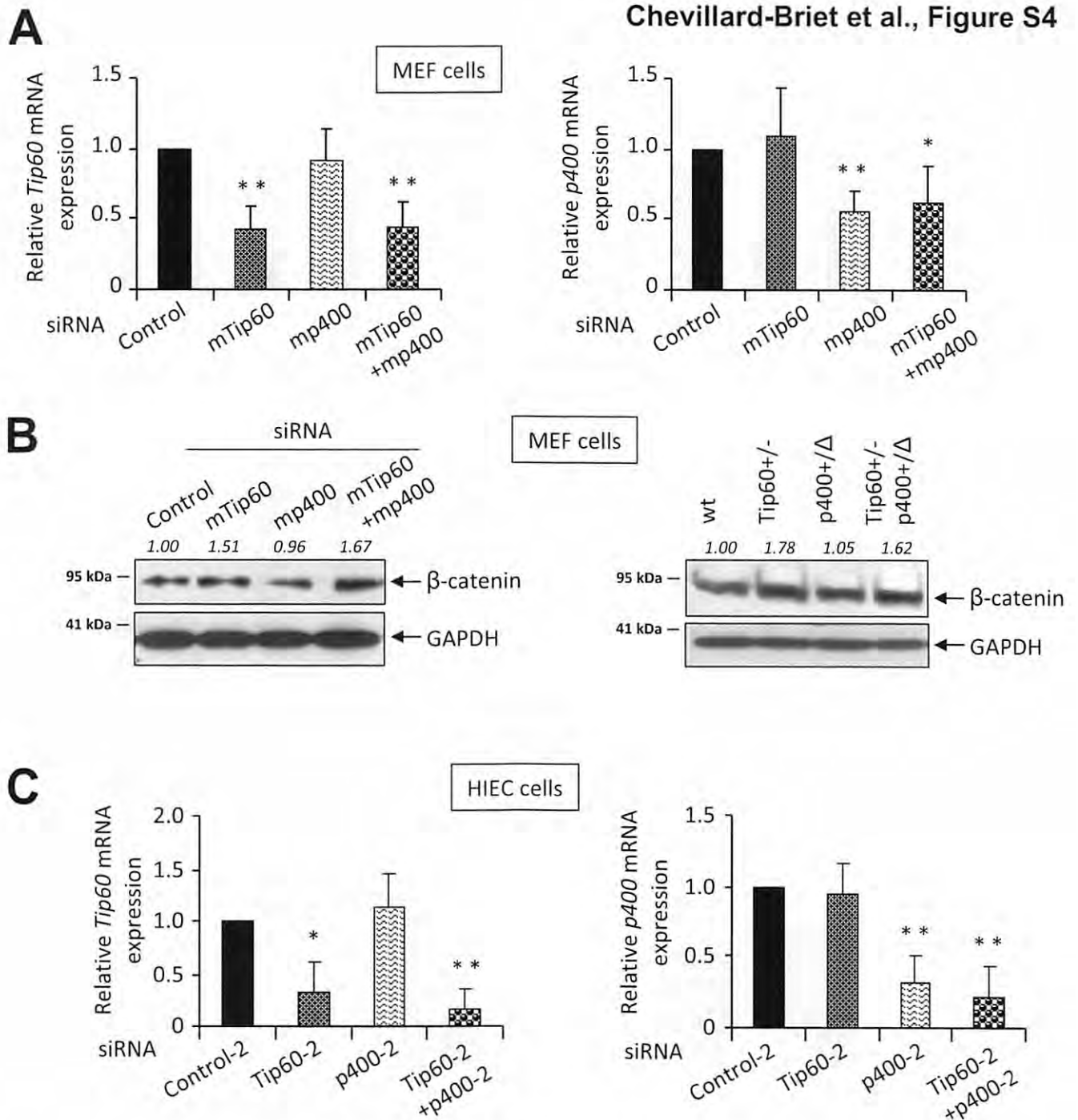


Figure S4: Control of siRNA efficiencies in MEFs and HIEC cells and validation of results from Fig.5A-B using another sample serie

A) Wild-type MEFs were transfected using indicated siRNA and subjected, 48h later, to total RNA extraction, reverse transcription and quantitative PCR analysis. The amount of *Tip60* or *p400* cDNA was divided by the amount of *GAPDH* cDNA and calculated relative to 1 for control siRNA-transfected sample (**, $p < 0.02$; *, $p < 0.05$). The mean and standard deviation from three experiments are shown. B) Western-blot experiments were done, as for Fig.5A-B, using another independent serie of MEF samples transfected with indicated siRNA or heterozygous MEFs. C) Same as in A for HIEC cells.

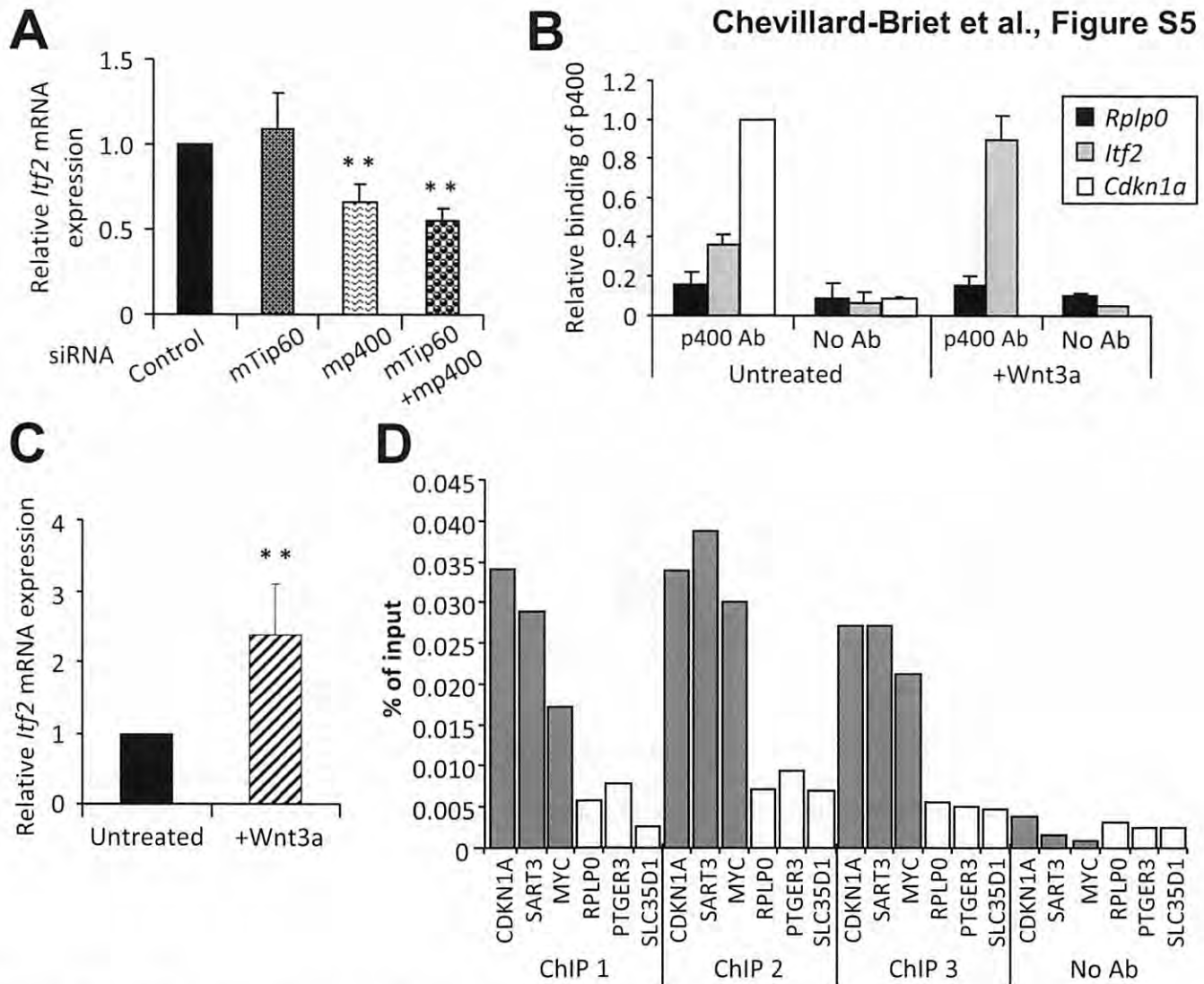


Figure S5: p400 and Wnt3a-dependent control of *Itf2* expression, p400 recruitment to *Itf2* promoter and validation of ChIP-chips experiments

A) Wild-type MEFs were transfected using the indicated siRNAs and total RNA was extracted 48h later to analyze the expression of *Itf2* (normalized to GAPDH and shown relative to 1 for control siRNA-transfected cells (**, $p < 0.02$)). The mean and standard deviation from four experiments are shown. B) Wild-type MEFs were treated or not using 150ng/ml Wnt3a for 24h and then subjected to ChIP experiments using a p400 antibody or no antibody as control. The amounts of *Rplp0*, *Itf2* or *Cdkn1a*^{p21} promoters in the immunoprecipitates were measured by qPCR. The means of 3 experiments were calculated relative to 1 for *Cdkn1a*^{p21} promoter in p400 ChIP of untreated sample. Bars denote standard deviation. C) Wild-type MEFs were treated using 150ng/ml Wnt3a for 24h and total mRNA were subjected to *Itf2* quantification (normalized to GAPDH and shown relative to 1 for untreated condition (**, $p < 0.02$)). The mean and standard deviation from three experiments are shown. D) ChIP samples from three independent samples, similar to those used in large scale analysis (Table S3), were subjected to qPCR analysis of selected promoters. We confirmed the binding of p400 on three ChIP-chips positive promoters (*CDKN1A*, *SART3* or *MYC*), as well as the low specific enrichment of three negative promoters (*RPLP0*, *PTGER3* or *SLC35D1*) compared to No Antibody (No Ab) control. Of note, during the course of this validation, we found two false-negative promoters (promoters which appeared unbound in ChIP-chips experiments but in which specific binding could readily be detected by qPCR). The occurrence of false-negative promoters do not change the main conclusion of the ChIP-chip experiment (that a set of β -catenin target promoters are bound by p400).

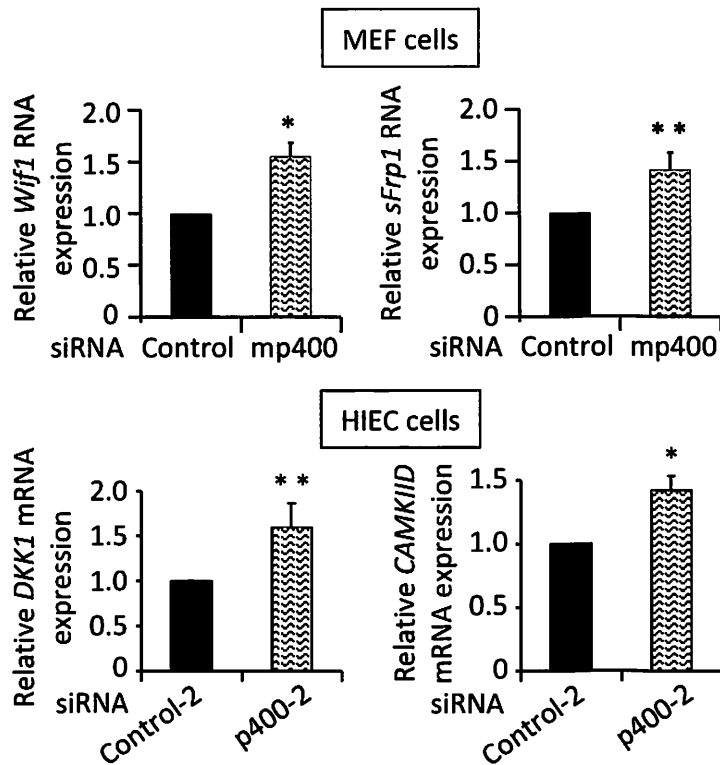


Figure S6: Impact of p400 depletion on Wnt inhibitors expression

Wild-type MEFs or HIEC cells were transfected using indicated siRNA and subjected, 48h later, to total RNA extraction, reverse transcription and quantitative PCR analysis. The amount of Wif1, sFrp1 (for MEFs), DKK1 or CAMKIID (for human HIEC cells) cDNA was quantified, normalized to Gapdh/GAPDH amounts and calculated relative to 1 for control siRNA-transfected sample (*, $p < 0.05$; **, $p < 0.02$). The mean and standard deviation from three experiments are shown.

Supplemental Experimental Procedures:

***Reagents**

The anti-p400 and β -catenin antibodies were purchased from Abcam (Paris, France) and the anti-GAPDH antibody from Chemicon International, Inc (Temecula, CA). The anti-Tip60 antibody was described previously in (Legube *et al.*, 2004) and the anti-acetyl-lysine antibody used in IP experiments was purchased from Upstate (Millipore Corp., Billerica, MA). All secondary antibodies were purchased from Amersham (Piscataway, NJ).

All siRNAs were purchased from Eurogentec (Angers, France). The control siRNA does not recognize any mouse or human mRNA. The efficiency of siRNAs silencing was checked in each experiments by reverse transcription followed by real-time PCR.

The sequences of the top strands of the various siRNAs were as follows:

Control: CAUGUCAUGUGUCACAUCU-dTdT

Control-2: ACUCAAACUCACGAAGGAA-dTdT

Human Tip60: ACGGAAGGUGGAGGUGGUU-dTdT

Human Tip60-2: GGACGUAAGAACAAGAGUU-dTdT

Human p400: UGAAGAAGGUUCCCAAGAA-dTdT

Human p400-2: CGACACAUUGGAUACAGAA-dTdT

Mouse mTip60: UGAGAUUGAUGGACGAAA-dTdT

Mouse mTip60-2: UGAAGAACAUUGAGUGUAU-dTdT

Mouse mp400: GAGUCUCUUCAAGAUGUUC-dTdT

The following primer pairs were used to genotype the mouse litters and MEFs (from 5' to 3'):

Mouse *TIP60* : TCGCCAGAACTGCCTCTAGACAA (wild-type and KO allele)

and GTCCTCAGCCACTCATCTTCGTT (wt) or GCCTGCTCTTACTGAAGGCTCTT (KO)

Mouse *p400* : AGAATGTCCAACATCAGCTGCAGAGGTCTA (wild-type and KO allele)

and ATCATGTTTCCCTGTAGATGTTGCAAGAAG (wt) or GATTTCGAGCGCATCGCCTTCTATCG (KO)
(wt primers target the part of p400 which is absent in the Δ N p400)

The following primer pairs were used to amplify cDNAs following reverse transcription experiments (from 5' to 3'):

Human *GAPDH* : GAAGGTGAAGGTCGGAGTCA and GAAGATGGTGATGGGATTC

Human *TIP60* : TGAGCGTGAAGGACATCAGT and AGAAGTACCACGGCTTGAGG

Human *p400* : CTGCTGCGAAGAAGCTCGTT and CAATTCTTCCCTCTCCTGC

Human *CAMK1ID* : CCTTATGGAAAGCCAGTGGGA and CGTTTGGCAGGGTTGATAGT

Human *CALB1* : ATCCCTCATCACAGCCTCAC and TGCCCATACTGATCCACAAA

Human *CRYZ* : TCTCTGGGGTTATGCAGAG and TCTAGCAATTTGGCATGCTG

Human *DKK1* : ACCCAGGCTCTGCAGTCA and CTGCAGGCGAGACAGATTT

Human *FZD2* : GTCCTCAAGGTGCCATCCTA and CAGCCCGACAGAAAATGAT

Human *PORCN* : TACCTGAAGCATGCAAGCAC and CGGTGTCTACCATGTGCATC

Human *SLC1A3* : CATGCACAGAGAAGGCAAAA and AGAGTCTCCATGGCCTCAGA

Human *WNT16* : TGTCCAGTATGGCATGTGGT and TTCCAGCATGTTTTACAGC

Human *WNT7B* : GAAGCTCGGAGCACTGTTCAT and CTGGTACTGGCACTCGTTGA

Chevillard-Briet et al., SuppExpProc

Mouse *Tip60* : GACCCCTTCTCTTCTACGT and CCGGTCTTCCCTTCTACTTT
Mouse *p400* : same primers used for the genotyping of the wild-type allele
Mouse *Gapdh* : AGGTTGTCTCCTGCGACTTC and ATGTAGGCCATGAGGTCCAC
Mouse *β-catenin* : TATCAGGATGACGCGGAAC and ACAATGGCAGACACCATCTG
Mouse *Itf2* : CTCCAGCGGGATGAATCAG and GACATCGGAGGAAGACTGGA
Mouse *Wif1* : GAGTGTCCGGATGGGTTCTA and TGGTTGAGCAGTTTGCTTTG
Mouse *sFrp1* : TACCACGGAAGCCTTAAGC and TTGTCACCGTTTTCTTCTTC

The following primer pairs were used in ChIP experiments (from 5' to 3'):

Human/Mouse *RPLP0* : GGCGACCTGGAAGTCCAAC and CCATCAGCACCACAGCCTTC
Human *CAMKIID* promoter : CCCCTGAGCCACATTACACT and TGAGGTTGCAGGGGAGTTAC
Human *CDKN1A^{p21}* promoter : GTGGCTCTGATTGGCTTTCTG and CTGAAAACAGGCAGCCCAAGG
Human *FZD2* promoter : GACCTCTCCTTAGGGCAAC and TGGCACCTCAAAGTGAGAAA
Human *MYC* promoter : TTGCGGGTTACATACAGTGC and CCTTCCAGGTCTCTTTCC
Human *PORCN* promoter : CACCACGCCCAGTCTTTATT and GCCAAGGGTAGGAGGATAGC
Human *PTGER3* promoter : TCCTCCAGTTCTCCGCTAAA and TGCTTAAGGACAGGCGATT
Human *SLC35D1* promoter : GGGGGTAAAAACCTTCAA and CCCAAGCTGCTTATCTTGCT
Human *SART3* promoter : GCTTCCATTTTTGAGGTAGG and GCCAGCATCTGTGTCGAGTA
Mouse *Itf-2* promoter : TGGAAGTCTGGTTTTTGG and GTGACCCTGAGCTGGAAGAG
Mouse *Cdkn1a^{p21}* promoter : TAGCTTCTGGCCTCAGGA and TGGGGTCTCTGTCTCCATTC

*Cell culture, treatments and transfections

Culture products were purchased from Invitrogen (Carlsbad, CA). The colorectal carcinoma HCT116 cell line was purchased from the ATCC collection and cultured in DMEM medium supplemented with antibiotics and 10% Fetal Calf Serum, as for HIEC (Beaulieu and Menard, 2012) cells and MEFs.

Wnt3a was purchased from R&D Systems (France) and added on HCT116 cells or MEFs at 150ng/ml. For transfection, cells were electroporated with siRNAs using an Amaxa device (Köln, Germany) according to manufacturer's specifications. Cell number was measured using WST-1 reagent (Roche Diagnostics, Meylan, France) according to manufacturer's specifications. FH535 inhibitor of the β -catenin/Tcf transactivation was purchased from Sigma-Aldrich (St-Quentin Fallavier, France).

For some luciferase experiments, HCT116 cells were co-transfected using siRNA and β -catenin expression vectors (0.5 μ g per million of cells) encoding the T41A stabilized form of the wild-type protein or the additionally mutated K345A or K345R β -catenin (Levy et al, 2004).

*Animal housing and genotyping

All mice were housed at the IPBS (UMR5089 CNRS, Toulouse, France) facility and kept in filter top cages for breeding located in the same animal room at 24 \pm 2°C and 50 \pm 5% humidity with a 12/12h light/dark cycle. Mice were given ad libitum access to water and irradiated mouse feed (SAFE, Augy, France). DNA was extracted from mice tails using RedExtract-N-Amp Tissue PCR kit (Sigma-Aldrich) and submitted to qPCR amplification using relevant primers, followed by the migration on 2% agarose gel, as previously described (Hu et al., 2009; Ueda et al., 2007).

* MEFs preparation

MEFs were prepared from *Tip60*^{+/+}-&#p400^{+/Δ} mice using genotyped E13.5 embryos. Dissected tissues were dissociated and plated in Petri dishes containing DMEM+10%FCS, Penicillin/Streptomycin and 10 μ M β -mercaptoethanol. MEF cells were genotyped using RedExtract-N-Amp kit (Sigma-Aldrich) and maintained for a maximum of five passages.

***RNA extraction and reverse transcription**

Total RNA was extracted using an RNeasy mini kit (Qiagen). 1µg of each purified RNA preparation was reverse-transcribed and cDNAs were analysed by qPCR using relevant primers.

***Real-time quantitative PCR analysis**

qPCR analysis was performed on a CFX96 Real-time system device (Biorad) using the iQ qPCR Mix (BioRad), according to the manufacturer's instructions, and specific primers (see above). All experiments included a standard curve and all samples were analyzed in triplicates.

***Large scale gene expression analysis**

For the microarray experiments, two control, Tip60 or p400 siRNAs were independently transfected in HCT116 cells. 48h after transfection, total RNA for each condition was extracted, reverse-transcribed and subjected to qPCR validation of the silencing or amplified and labelled according to the manufacturer's instructions. Following quantification, normalization using the RMA algorithm, a statistical analysis was carried out to select genes whose expression levels significantly change in knockdown Tip60 or p400 condition compared to controls (p-value < 0.05). The Fold Change (FC) for each gene was calculated for siRNAs p400 relative to siRNAs control. Qualified genes are those found regulated with stringent criteria, i.e. using FDR(Benjamini Hocheberg) analysis for p400-regulated genes, or when their expression was modified more than 1.25 fold, in the same way, in at least three out of four comparisons (Tip60vsControl, Tip60-2vsControl, Tip60vsControl-2 and Tip60-2vsControl-2) for identifying Tip60-dependent genes. Gene co-occurrence analysis was done using GeneCoDis3 online software (<http://genecodis.cnb.csic.es>) (Tabas-Madrid, 2012).

***Western blot analysis**

Nuclear extracts or total cell lysates were prepared as previously described (Mattera *et al.*, 2009). Immunoprecipitation was done on total extracts using anti-acetyl-lysine antibody and agarose-coupled protein A and sepharose-bound protein G (50/50) from Sigma Aldrich. 10µg of total proteins or IP samples were separated by NuPAGE® Novex 3-8% Tris-acetate gel (Invitrogen). Proteins in the gel were transferred on a PVDF membrane. Primary antibodies as well as peroxidase-conjugated secondary antibodies were used according to standard western blot procedure and peroxidase was detected by using the Lumi-LightPLUS Western Blotting Substrate (Roche Diagnostics). Quantification of signals was done using ImageJ software (NIH, Bethesda, MA) and standardized by background.

*** Wnt activity assays**

Wnt pathway activity was assayed using the SignalTMTCF/LEF reporter kit from SABiosciences (Frederick, MD) and DualSystem (Promega, Madison, WI) according to manufacturer's instructions. Briefly, cells were transfected by electroporation with TCF/LEF plasmid (firefly luciferase downstream TCF/LEF response element repeats), negative (without TCF/LEF binding sequences) or positive (CMV-driven luciferase) control plasmids. A constitutively expressing Renilla luciferase vector was co-transfected as internal control (for transfection efficiencies and cell viability). 48h later, Firefly and Renilla luciferases were assayed.

ORIGINAL ARTICLE

MNK kinases facilitate c-myc IRES activity
in rapamycin-treated multiple myeloma cellsY Shi^{1,2}, P Frost^{1,2}, B Hoang^{1,2}, Y Yang^{1,2}, R Fukunaga^{1,2}, J Gera^{1,2} and A Lichtenstein^{1,2}

When mTOR inhibitor rapalogs prevent cap-dependent translation of cell-cycle proteins like c-myc, continuing tumor cell growth depends on cap-independent translation, which is mediated by internal ribosome entry sites (IRESes) located in the 5'-UTR (untranslated region) of transcripts. To investigate if rapalog-induced activation of MNK kinases had a role in such IRES activity, we studied multiple myeloma (MM) cells. Rapamycin (RAP)-activated MNK1 kinase activity in MM cell lines and primary specimens by a mitogen-activated protein kinase-dependent mechanism. Pharmacological inhibition of MNK activity or genetic silencing of MNK1 prevented a rapalog-induced upregulation of c-myc IRES activity. Although RAP, used alone, had little effect on myc protein expression, when combined with a MNK inhibitor, myc protein expression was abrogated. In contrast, there was no inhibition of myc RNA, consistent with an effect on myc translation. In a RAP-resistant MM cell lines as well as a resistant primary MM specimen, co-exposure to a MNK inhibitor or MNK1 knockdown significantly sensitized cells for RAP-induced cytorreduction. Studies in MNK-null murine embryonic fibroblasts additionally supported a role for MNK kinases in RAP-induced myc IRES stimulation. These results indicate that MNK kinase activity has a critical role in the fail-safe mechanism of IRES-dependent translation when mTOR is inhibited. As kinase activity also regulated sensitivity to RAP, the data also provide a rationale for therapeutically targeting MNK kinases for combined treatment with mTOR inhibitors.

Oncogene (2013) 32, 190–197; doi:10.1038/onc.2012.43; published online 27 February 2012

Keywords: multiple myeloma; rapamycin; mTOR inhibitors; c-myc; IRES activity; MNK kinases

INTRODUCTION

Previous work in glioblastoma, prostate cancer and multiple myeloma (MM) models demonstrates that sensitivity of tumor cells to rapalog mTOR inhibitors is, at least in part, dependent upon AKT activity.^{1–4} When rapalogs inhibit cap-dependent translation, tumor cell growth depends on cap-independent translation of critical proteins, which is mediated by internal ribosome entry sites (IRESes) in the 5'-UTR (untranslated region) of mRNAs. Specifically for D-cyclin and c-myc translation occurring during mTOR inhibition, IRES activity of these transcripts is curtailed by AKT.⁵ Thus, hyperactive AKT prevents this fail-safe mechanism of translation and, during mTOR inhibition, cellular levels of cyclin and myc fall precipitously resulting in G1 arrest. In contrast, cells with quiescent AKT activity demonstrate upregulation of cyclin/myc IRES activity upon exposure to rapamycin (RAP) ensuring maintained levels and continual cell-cycle transit.

Our work^{5,6} also demonstrates that both extracellular-signal-regulated kinase (ERK) and p38 mitogen-activated protein kinase (MAPK) pathways are critical for this IRES activity observed during mTOR inhibition. The participation of these pathways in myc IRES function had also previously been shown to be operative during genotoxic and apoptotic responses.^{7,8} The mechanism by which these pathways facilitate IRES activity is unknown. However, possible central candidate are the MNK kinases. These signal proteins are downstream target substrates of both the ERK and p38 MAPK pathway.⁹ In addition, they are activated secondary to mTOR inhibition.¹⁰ Furthermore,

a single report in aplysia neurons demonstrated an elevation of the cap-independent/dependent translation ratio upon MNK overexpression.¹¹ Finally, the MNK kinases have been reported to induce posttranslational modification of hnRNP A1,¹² a bona fide myc/cyclin IRES-transacting factor (ITAF), which binds to the IRES and enhances its activity. In fact, hnRNP A1 presence is required for myc and D-cyclin IRES activation during mTOR inhibition.

The two major MNK kinases, MNK1 and MNK2, both have MAPK-binding motifs. However, differences in their C-termini result in differential functional responses. MNK1 has low basal activity but can be activated by either p38 or ERK signaling.^{9,13,14} Activation is associated with phosphorylation in threonine residues in the T activation loop of the kinase. In contrast, MNK2 has high basal activity that does not increase upon activation of MAPKs and ERK/p38 inhibitors do not affect MNK2 activity.^{13,14} MNK kinases are thought to be the only kinases that phosphorylate eIF-4E on S209.¹⁵ To phosphorylate eIF-4E, MNK kinases must first bind to eIF-4G.^{16,17} Interestingly, MNK1/MNK2 knockout mice appear normal,¹⁵ suggesting that the MNKs are critical for stress responses rather than normal basal physiology. In keeping with that theory, MNK-deficient cells are more sensitive to serum starvation.¹⁸ Thus, it seems possible that these kinases could protect the cell from the stress of mTOR inhibition by supporting the remaining mechanism of protein translation occurring through the IRES. We, thus, in the current study, addressed the role of MNK kinase activation in myeloma cells stressed by exposure to RAP.

¹Department of Medicine, Greater Los Angeles VA Healthcare Center and Jonsson Comprehensive Cancer Center of the UCLA Medical Center, Los Angeles, CA, USA and

²Laboratory of Biochemistry, Department of Biochemistry, Osaka University of Pharmaceutical Sciences, Takatsuki, Japan. Correspondence: Dr A Lichtenstein, Hematology-Oncology, W111H, West LA VA Hospital, 11301 Wilshire Blvd. Bldg.500 Rm. 4237, Los Angeles, CA 90073, USA. E-mail: alan.lichtenstein@med.va.gov

Received 27 September 2011; revised 13 January 2012; accepted 15 January 2012; published online 27 February 2012

RESULTS

RAP activates the MNK1 kinase in MM cells through MAPK-dependent pathways

The response of MM cells to challenge with mTOR inhibitors is, in part, regulated by IRES activity. For example, D-cyclin translation in RAP-treated MM cells can be maintained by cyclin-D IRES activity, which is promoted by the MAPK ERK pathway.⁶ This fail-safe mechanism of cyclin translation affords resistance to RAP-induced G1 arrest. When ERK is inhibited, IRES activity is restricted and, along with reduced cap-dependent translation, cyclin levels rapidly fall and G1 arrest ensues. The c-myc IRES is also a well-characterized IRES¹⁹ and its function is specifically upregulated in myeloma cells.^{20,21} Of interest, myc IRES activity is also regulated by both the ERK and p38 MAPK pathways.^{5,7,8} To test whether myc IRES activity occurring in MM cells during mTOR inhibition was related to MNKs, we first tested the ability of RAP to activate these kinases. ANBL-6, U266 or 8226 MM cell lines were incubated with RAP for 3 h followed by immunoblot assays for expression of phosphorylated MNK. The antibody detects phosphorylated MNK1 as well as MNK2. As shown in Figure 1a, RAP successfully upregulated phosphorylation of MNK in all three cell lines although having no significant effect on total MNK levels. In time course experiments, RAP induced MNK phosphorylation as early as 60 min (Figure 1b). In addition, the activation of MNK kinases was temporally correlated with enhanced phosphorylation of eIF-4E (Figure 1b), a substrate of MNKs,¹⁵ suggesting that RAP enhanced kinase activity of MNKs as well as their phosphorylation state.

To further confirm enhanced kinase function and ascertain if MNK1 or MNK2 was being activated, we performed *in vitro* kinase assays (Figures 1c and d). MM cells were exposed to dimethyl sulfoxide alone (control) or to RAP at 100 nM. After 1 h, either MNK1 or MNK2 was immunoprecipitated from protein lysates and tested for its ability to phosphorylate eIF-4E *in vitro*. As shown by immunoblot (Figure 1c), the immunoprecipitating antibodies were specific for MNK1 or MNK2 without cross reactivity. The immunoprecipitated MNK1 from RAP-treated MM cells demonstrate a significantly increased ability to phosphorylate eIF-4E

relative to control cells. In contrast, MNK2 kinase activity was constitutively higher but there was no effect of RAP. A second limited time course experiment (Figure 1d) further demonstrated the ability of RAP to increase MNK1 kinase activity by 60 min of exposure. These data indicate that RAP primarily stimulates MNK1 kinase activity.

Both ERK and p38 MAPK pathways have been described as potential activators of MNKs.^{5,7,8} In our MM cell model, RAP activated both pathways, demonstrated by the enhanced phosphorylation of ERK or p38 (Figure 2a). The effect on ERK peaked at 30 min whereas the effect on p38 lagged behind, occurring sometime between 30 and 60 min. To identify if these pathways mediate MNK1 activation in MM cells, we used inhibitors of the ERK (U0126) or p38 (SB203580) pathways. Specificity of the inhibitors is presented in Figure 2b. As shown, U0126, used at 1 or 10 μM (U1 and U2, respectively), effectively inhibited ERK phosphorylation but had no effect on phosphorylation of hsp27, a p38 MAPK substrate. Conversely, the SB203580 p38 inhibitor used at 12.5 and 25 μM (SB1 and SB2, respectively) successfully inhibited p38-mediated phosphorylation of hsp27 but had no non-specific inhibitory effect on ERK phosphorylation. In RAP-stimulated cells, MNK phosphorylation was most inhibited by the p38 inhibitor. Thus, the p38 MAPK stress-activated pathway appears more important in MNK phosphorylation than the ERK pathway, at least in MM cells stressed by RAP exposure. Although these data are consistent with previous reports,^{5,7,8} indicating MNK kinases are downstream of the p38 pathway, it should be

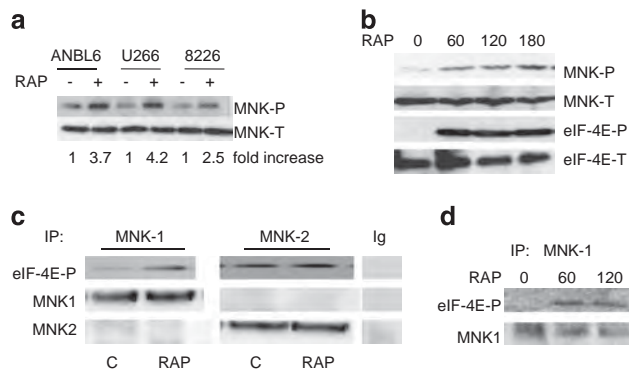


Figure 1. Activation of MNK kinases in MM cells. (a) MM cell lines exposed to RAP (100 nM) for 3 h followed by immunoblot assay for phospho-MNK (MNK-P) and total-MNK expression. Fold increase is determined by densitometric ratio of MNK-P/MNK-total and represents the mean of three independent experiments. RAP-induced increase was significant ($P < 0.05$) in all three cell lines. (b) ANBL-6 cells exposed to RAP for 0, 60, 120 or 180 min, followed by immunoblot assay for phospho-MNK, total-MNK, phospho-eIF-4E and total-eIF-4E expression. (c) MNK1 or MNK2 immunoprecipitated with anti-MNK1, anti-MNK2 antibodies or non-specific IgG, from control or RAP (100 nM for 60 min)-treated ANBL-6 extracts and tested for ability to phosphorylate eIF-4E *in vitro*. eIF-4E phosphorylation determined by immunoblot. (d) MNK1 immunoprecipitated from MM cells after 0, 60 or 120 min of exposure to RAP (100 nM) and tested for phosphorylation of eIF-4E *in vitro*.

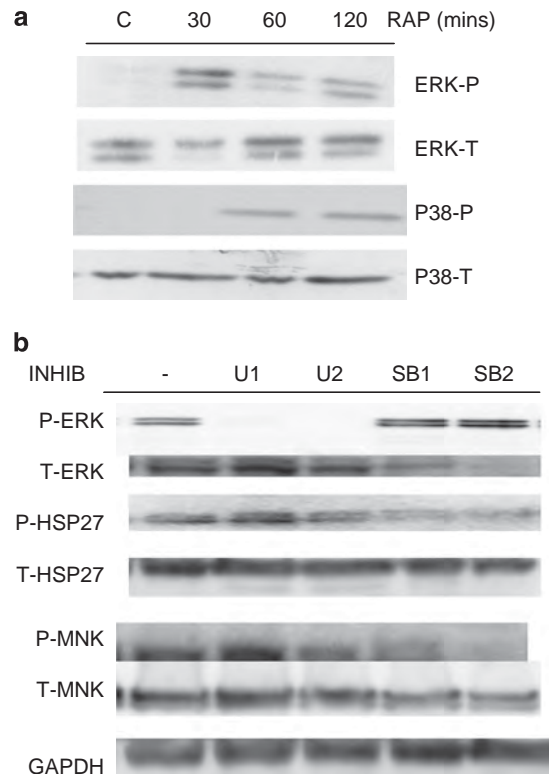


Figure 2. Role of MAPK pathways in MNK phosphorylation. (a) ANBL-6 MM cells exposed to RAP (100 nM) for 30, 60 or 120 min (C = control, no RAP), followed by immunoblot assay for phospho-ERK, total-ERK, phospho-p38 or total-p38 expression. (b) MM cells pretreated for 30 min with U0126 at 1 or 10 μM (U1 and U2) or SB203580 at 12.5 or 25 μM (SB1 and SB2). RAP then added at 100 nM for additional 3 h and immunoblot assay performed for expression of phospho ERK, total ERK, phospho HSP 27, total HSP-27, phospho MNK, total MNK or GAPDH.

noted that, in lung cancer cells, RAP-induced eIF-4E phosphorylation is relatively unaffected by a p38 inhibitor.²²

MNK inhibition curtails RAP-induced myc IRES activity

We initially used the MNK1/MNK2 inhibitor CGP57380 to test effects on IRES activity. Figure 3a demonstrates the ability of CGP to prevent RAP-induced MNK activity as shown by phosphorylation of the eIF-4E MNK substrate. At the lowest concentration (12.5 μM), eIF-4E phosphorylation was decreased by 80% (mean of three separate experiments) whereas it was completely ablated at 25 or 50 μM . At this early time point (3 h), there was no effect of the MNK inhibitor on cell survival. To test effects of the inhibitor on myc IRES activity, MM cells were transfected with either the pRF or pRmF dicistronic reporter constructs as shown in Figure 3b and subsequently treated with RAP \pm CGP. The c-myc 5'-UTR, containing its IRES, was subcloned into the intracistronic space between the Renilla and firefly (FF) luciferase open reading frames in the pRF vector to yield the pRmF vector. The pRmF reporter's FF luciferase translation is driven by the myc 5'-UTR and is a reflection of IRES-dependent, cap-independent translation whereas Renilla expression is because of cap-dependent, IRES-independent translation. Results are normalized for transfection efficiency by co-transfection with a beta-galactosidase construct. A previous study²³ has shown that FF luciferase expression in

these MM cells transfected with pRmF is not due to presence of a cryptic promoter in the 5'-UTR. In addition, the ANBL-6 maintains a relatively low level of activated AKT allowing significant myc IRES activity.²³

Figure 3c is a representative experiment of four separate experiments, each with identical results. In the absence of RAP, the presence of the myc 5'-UTR in the intracistronic space in the pRmF vector increased FF luciferase (black bars) to $4.5 \times$ fold versus that of the pRF control vector. In contrast, the presence of the 5'-UTR had no effect on Renilla expression. RAP exposure significantly stimulated IRES activity as the increase in FF expression because of the myc 5'-UTR was now $9.3 \times$ fold versus that of the pRF vector in RAP-treated cells. This approximate $2 \times$ fold increase in IRES activity was consistent across all four experiments (mean increase of 2.3 ± 0.5 , mean \pm s.d.) and was statistically significant at the $P < 0.05$ level. It is difficult to discern in Figure 3c, but RAP had a modest inhibitory effect on Renilla luciferase activity with an $\sim 25\%$ reduction. In RAP-stressed MM cells, the addition of the CGP MNK inhibitor had a concentration-dependent inhibitory effect on IRES activity assayed by FF luciferase expression. This was statistically significant ($P < 0.05$) at all CGP concentrations. In contrast, the inhibitor had less of an effect on myc IRES activity (FF luciferase expression) in the basal state in the absence of RAP with only 50 μM having a significant effect. There was no consistent effect of the CGP inhibitor on Renilla luciferase expression except

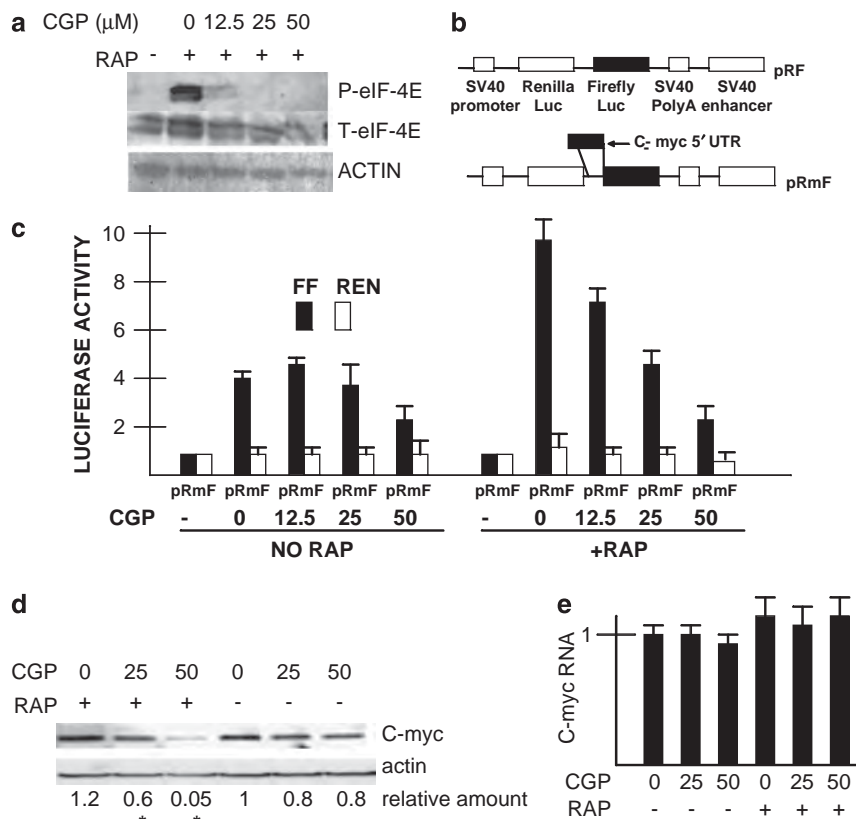


Figure 3. Effect of MNK inhibitor on myc IRES activity and myc expression. **(a)** ANBL-6 MM cells pretreated with the CGP MNK inhibitor for 30 min at varying concentrations. Followed by addition of RAP (100 nM) for 3 h and then immunoblot assay for phospho eIF-4E, total eIF-4E and actin. **(b)** Reporter constructs used to assay for myc IRES activity. **(c)** FF (dark bars) or Renilla (REN, open bars) luciferase expression in pRF versus pRmF-transfected ANBL-6 cells treated \pm RAP (100 nM) and \pm CGP (used at 0, 12.5, 25 or 50 μM). All luciferase activity is normalized to the luciferase values (both REN and FF) obtained for pRF in the absence of added RAP and CGP (designated '1'). Results represent means \pm s.d. of quadruplicate samples. **(d)** ANBL-6 MM cells pretreated with CGP at 0, 25 or 50 μM followed by addition of RAP (or not) at 100 nM for 8 h. Immunoblot assay then performed for c-myc or actin expression. Relative amount of c-myc protein determined densitometrically (ratio of c-myc/actin) and represents means of three independent experiments. Asterisk denotes a value significantly lower ($P < 0.05$) than control (no CGP). **(e)** Experiment performed as in **(d)** but assay is performed by real-time PCR for c-myc RNA expression (data are means \pm s.d. of three experiments).

at the highest concentration (50 μ M) in RAP-treated cells where expression was reduced to 50% of control.

The ability of CGP to inhibit myc IRES activity in RAP-challenged cells is associated with curtailed myc protein expression. As shown in Figure 3d, RAP, used alone, has little effect on c-myc expression presumably because of the stimulation of IRES-mediated cap-independent translation. In addition, the CGP inhibitor, used by itself, has only a minimal effect. However, inhibiting MNK activity with CGP during RAP exposure significantly prevents myc protein expression. As shown in Figure 3e, the CGP-induced inhibition of protein expression is not associated with an inhibition of myc RNA. These results indicate that MNK activity in RAP-treated MM cells has a role in the upregulated myc IRES activity observed and helps maintain myc expression through posttranscriptional activity.

Effects of MNK silencing on myc IRES activity

The above data with the CGP inhibitor suggested a role for MNK1 activation in the RAP-induced upregulation of myc IRES activity.

However, as there may be non-specific effects of the inhibitor, we knocked down MNK1 by shRNA transfection of MM cells. In ANBL-6 MM cells, we targeted two separate sequences of MNK1 (shRNA 1-1 and 1-4). As shown in Figure 4a, knockdown of MNK1 was much more successful with shRNA 1-4 than with 1-1. In addition, the knockdown was relatively specific for MNK1 as MNK2 RNA and protein levels were only minimally affected.

These cell lines were then tested in the myc IRES reporter assay by transiently transfecting either pRF or pRmF reporter plasmids, followed by treatment with or without RAP and assessment of luciferase expression. In control cells transfected with shRNA targeting scrambled sequence, exposure to RAP induced a 1.8 \times fold increase in IRES activity (FF luciferase expression, black bars in Figure 4b). In both MNK1 knockout cell lines, the basal IRES activity was modestly but significantly decreased and the RAP-induced upregulation was blunted. The 1-4 MNK knockout line was more inhibited in its IRES activity. The inhibition of IRES activity in the basal state by the MNK knockouts was comparable to inhibition of activity induced by RAP. However, in a second MM cell lines, U266,

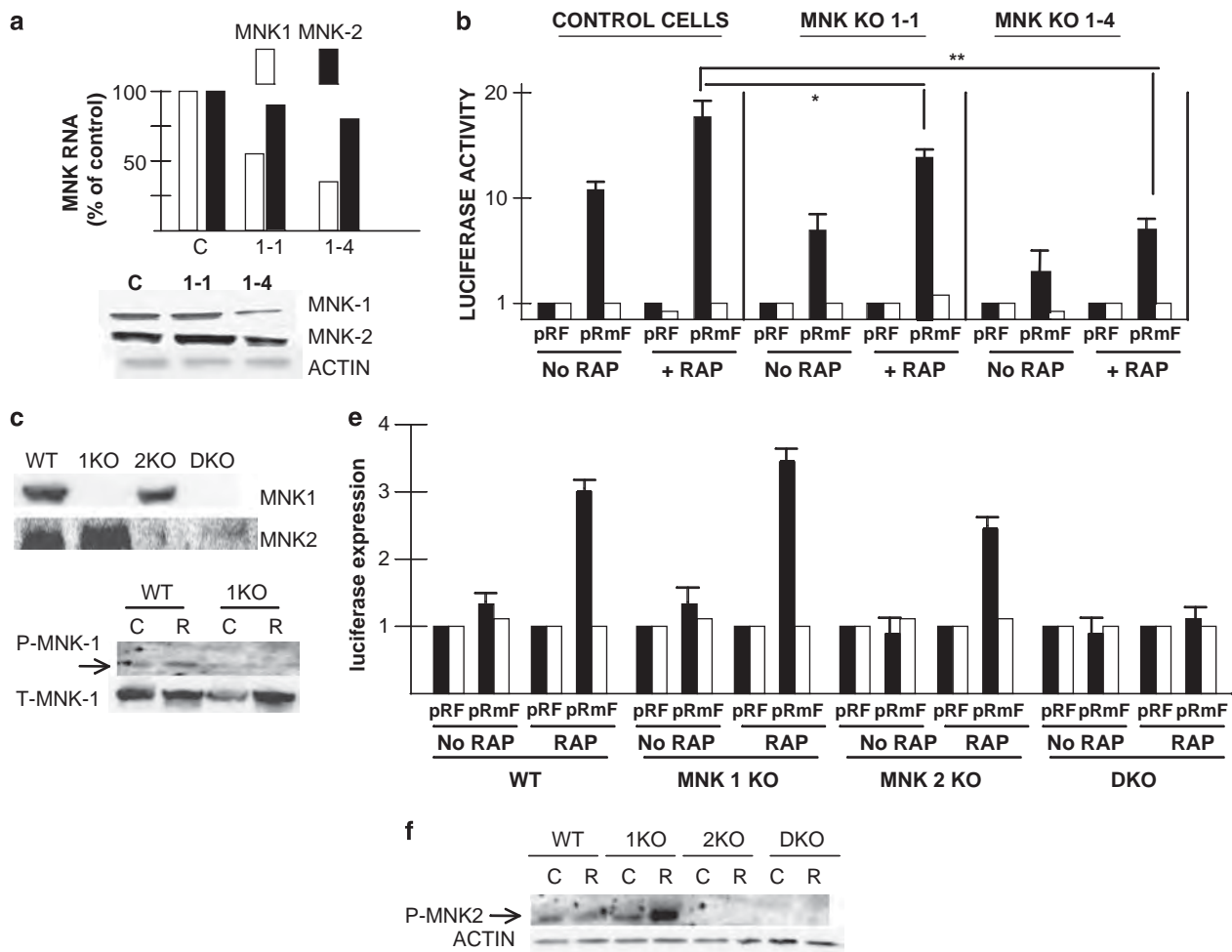


Figure 4. Effect of silencing MNKs on myc IRES activity. (a) MNK1 knocked down in ANBL-6 MM cells by shRNAs targeting two separate sequences (1-1 and 1-4). Control (C) cells infected with shRNA targeting scrambled sequence. Shown is real-time PCR for MNK1 or MNK2 RNA expression and immunoblot for protein expression. (b) Stably knocked down cells transfected with pRF or pRmF reporter plasmids followed by treatment \pm RAP (100 nM) for 3 h and luciferase expression assayed. Black bars are FF and white bars are Renilla luciferase. Data are means \pm s.d. of four separate experiments. * significantly different than control, $P < 0.05$; ** significantly different at $P = 0.01$. (c) MNK WT, MNK1 knocked out (1KO), MNK2 knocked out (2KO) or MNK1/MNK2 double knock out (DKO) MEFs assayed for MNK1 or MNK2 expression. (d) WT or MNK1 knocked out MEFs treated with RAP (R) (100 nM for 3 h) or without (control (C)) followed by immunoblot assay for phospho MNK1 or total MNK1. (e) Different MEF cell lines transiently transfected with pRF or pRmF reporter plasmids, treated with or without RAP (100 nM) and luciferase expression assayed as described above in Figure 3c legend. Data represent means \pm s.d. of three independent experiments. (f) Different MEF cell lines treated with RAP (R; 100 nM for 3 h) or without (control (C)), followed by immunoblot assay for phospho MNK2 and actin.

the RAP-induced IRES response was more inhibited than the basal response (Supplementary Figure 1). In that cell line, we only targeted one sequence of MNK1 with shRNA and obtained a successful knockdown. In control U266 cells (transfected with shRNA against scrambled sequence), RAP increased IRES activity 4 × fold (FF luciferase expression, black bars). In contrast, the RAP-induced increase in IRES activity was significantly curtailed in the MNK1 knocked-out U266 cell line (only 1.8 × fold increase).

In a third MM cell line, OPM-2, a slightly different pattern of IRES responses occurred (Supplementary Figure 2). Although RAP was capable of inducing ERK, MNK and eIF-4E phosphorylation (Supplementary Figure 2A), it did not significantly enhance IRES activity (Supplementary Figure 2C) when used at 20 nM. We have previously demonstrated²⁴ how heightened AKT activity prevents a RAP-induced IRES response because of phosphorylation and inactivation of the myc IRES ITAF, hnRNP A1. This is the likely explanation for the OPM-2 results as this cell line expressed heightened AKT activation due to its PTEN null state.⁴ Nevertheless, the MNK inhibitor CGP, used at 20 μM, significantly inhibited eIF-4E phosphorylation (Supplementary Figure 2B) and myc IRES activity (Supplementary Figure 2C) in OPM-2 cells in the presence or absence of RAP. These data in U266 as well as OPM-2 cells demonstrate MNK-dependent IRES activity is a generalized finding in MM cells and not singular to ANBL-6 cells.

Further support for a role for MNK kinases in myc IRES activity comes from experiments with MNK-null murine embryonic fibroblasts (MEFs). These cell lines have been previously used¹⁰ to demonstrate a RAP-induced activation of MNK activity. Figure 4c confirms the absence of MNK1 or MNK2 in these cell lines. Immunoprecipitation of MNK1 from protein extracts demonstrated *in vitro* kinase activity against eIF-4E when extracts were obtained from wild type (WT) or MNK2 knockout (2KO) lines but not when obtained from MNK1 knockout (1KO) or MNK1/MNK2 double knockout (double) cell lines (Supplementary Figure 3). Conversely, immunoprecipitated MNK2 has kinase activity when obtained from WT or MNK1 knockout (1KO) cell lines but not from 2KO or double knockout cells (Supplementary Figure 3). Figure 4d also demonstrates the ability of RAP to increase MNK1 phosphorylation in WT MEFs, which was ablated in the MNK1 null cells. The cell lines were then transiently transfected with the pRF or pRmF reporter constructs, treated with or without RAP and luciferase expression evaluated (Figure 4e). In WT MEFs, there is very minimal myc IRES activity in the basal state but activity (i.e., FF luciferase expression, black bars) increases 3 × fold following exposure to RAP. There was no increase in Renilla expression seen in RAP-treated cells. A significant RAP-induced increase in FF expression was likewise seen in both MNK1 and MNK2 knockout MEFs. However, this response was ablated in the double knockout cell line (DKO). Thus, in genetically knocked out MEFs, the RAP IRES response can be supported by either MNK1 or MNK2 but the response is lost when both MNKs are absent.

To explain why the MNK1 KO MEFs were not inhibited in RAP induction of myc IRES activity, we considered the possibility that, in these cells, RAP could activate MNK2, which might facilitate IRES activity. We, thus, treated each of the MEF cell lines with and without RAP and tested MNK2 phosphorylation. As shown in Figure 4f, RAP was capable of robust MNK2 phosphorylation in MNK1 knocked out MEFs although no activation was seen in WT MEFs. These data suggest that, in genetically knocked out MEFs, MNK2 can become activated by RAP if MNK1 is absent.

To confirm the specificity of effects of MNK silencing in MEFs, we stably reexpressed either FLAG-tagged MNK1, MNK2 or both MNK1/MNK2 in the double knockout MEF cell line. In Supplementary Figure 4A, a western blot demonstrates expression of the transgenes (top panel) with a corresponding rescuing of eIF-4E phosphorylation, confirming kinase activity of the reexpressed proteins. These cell lines were then transiently transfected with

pRF and pRmF reporter plasmids, treated ± RAP and reporter expression assayed. As shown in Supplementary Figure 4B, reexpression of either MNK1, MNK2 or both MNK1/MNK2, rescued the ability of RAP to significantly enhance myc IRES activity (FF luciferase expression), thus confirming that it is the loss of MNK1/MNK2 in the DKO MEFs that prevents the IRES response.

Effects of MNK inhibition on cellular responses to RAP

To test if paralysis of MNK1 affected cellular growth responses to RAP, the ANBL-6 MM cell line was treated for 48 or 72 h with the CGP MNK inhibitor (25 μM), RAP (100 nM) or the combination of both drugs. ANBL-6 cells were resistant to RAP used alone as shown in Figure 5a. Furthermore, MNK inhibition with CGP used alone had no significant effect on MM cell recovery as well. However, a significant cytoreduction was present when CGP was added to RAP. Relative resistance to RAP, which was reversed by CGP, was also seen in U266 MM cells (Figure 5b).

Further confirmation of a role for MNK1 in MM cell RAP responses was obtained by using the two ANBL-6 MNK1 knockout transfectants, 1-1 and 1-4. Their growth over 120 h in the absence of RAP (black circles, Figure 5c) is comparable to control cells transfected with scrambled sequence. However, the MNK1 knocked-out cell lines are considerably more sensitive to RAP (open squares) as shown in Figure 5c. RAP has no effect on cell growth in control cells but is effective in preventing growth in MNK1 knocked-out cell lines. These data support the notion that the activation of MNK1 in RAP-treated cells serves as a protective factor.

To test if MNKs had a role in RAP responses in primary MM cells, we first tested for induction of MNK phosphorylation. As shown in Figure 6a, western blot analysis demonstrated a RAP-induction of MNK phosphorylation in four primary MM specimens, although the degree of induction was variable. In two MM specimens, we were fortunate to harvest sufficient numbers of purified MM cells for further study. One sample was exposed to RAP (100 nM) ± the CGP MNK inhibitor at 25 or 50 μM. As shown in Figure 6b, both concentrations of CGP successfully prevented MNK activity, shown by abrogated eIF-4E phosphorylation. This specimen is relatively resistant to RAP used alone in terms of c-myc downregulation, similar to ANBL-6 MM cell line. However, CGP can inhibit myc expression in the presence or absence of RAP although myc downregulation is considerably more effective in the presence of RAP. The combination of CGP and RAP is also more effective at preventing survival of primary MM cells (Figure 6c). After 48 h of culture, RAP used at 100 nM or CGP at 50 μM, have no significant effect. However, concurrent exposure to both agents significantly inhibited viable recovery of primary cells.

DISCUSSION

Our previous work has documented the regulatory influence of IRES-dependent, cap-independent translation upon tumor responses to mTOR inhibitors.⁵ TORC1 inhibition, induced by rapalogs, primarily results in restrained cap-dependent translation of cell-cycle proteins like c-myc and D-cyclins with attendant G1 arrest. As the only remaining mechanism for myc/cyclin translation in rapalog-treated cells, IRES activity can determine whether overall myc/cyclin levels are maintained or significantly depressed. The results of the current study demonstrate that MNK kinase activity is a key regulator of RAP-induced IRES activity. MNK activity was enhanced by exposure to RAP in conjunction with myc IRES function and downregulation of MNK activity with the CGP inhibitor or by MNK knockdown, prevented IRES stimulation and sensitized to RAP cytoreduction.

The MAPK-dependence of RAP-induced MNK phosphorylation mirrors the MAPK-dependence of myc IRES activity. Activation of the p38 MAPK cascade during apoptosis⁸ or genotoxic stress⁷ is

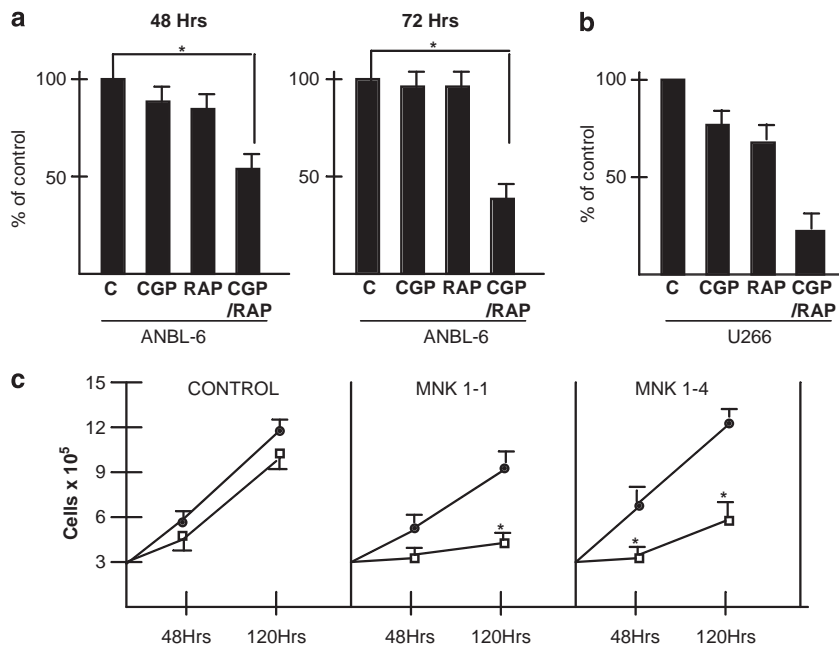


Figure 5. Effect of MNK paralysis on responses to RAP. (a) ANBL-6 MM cells treated \pm CGP (25 μ M) \pm RAP (100 nM) for 48 or 72 h. Viable cell recovery then enumerated by trypan blue exclusion. Data represent means \pm s.d. of four separate experiments. The only significant difference ($P < 0.05$) are in the combined CGP/RAP-treated groups at both time points (designated by an asterisk). (b) U266 cells similarly treated with RAP \pm CGP. Data are means \pm s.d., $n = 3$. Significant differences ($P < 0.05$) designated by asterisk. (c) ANBL-6 MM cells stably transfected with shRNA targeting scrambled sequence (control) or MNK1 sequences (1-1 and 1-4) and treated with or without RAP (100 nM) for 48 or 120 h followed by enumeration of viable cells. Closed circles are control, non-treated cells and open squares are RAP treated. Data represent means \pm s.d. of three separate experiments. * significantly different from control (non-RAP treated), $P < 0.05$.

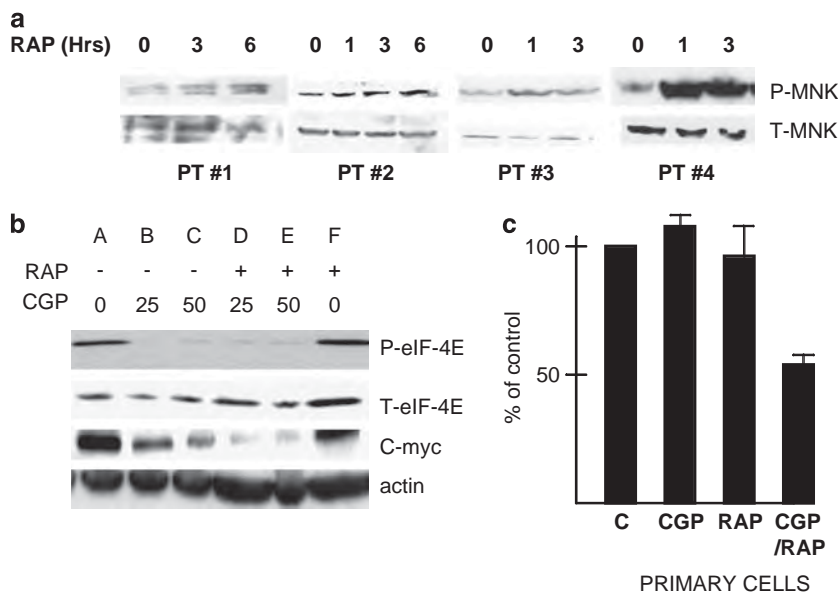


Figure 6. Effect of MNK inhibition in primary MM cells. (a) Primary MM cells obtained from bone marrow biopsies of four patients and treated with or without RAP (100 nM) for 1, 3 or 6 h followed by immunoblot assay for phospho-MNK and total MNK. (b) Primary MM cells pre-treated with CGP at 0, 25 or 50 μ M for 30 min followed by addition of RAP (100 nM) for 6 h and then immunoblot assay performed for phospho-eIF-4E, total eIF-4E, c-myc and actin expression. (c) Primary MM cells exposed to CGP (50 μ M), RAP (100 nM) or the combination of the two drugs for 72 h followed by assessment of viable recovery by trypan blue assay. Data are means \pm s.d. of four wells per group. Control (C) cells not treated represent 100%.

necessary for the stimulation of IRES function. The ERK MAPK pathway also participates in upregulated IRES function during genotoxic stress.⁷ In some RAP-treated MEF cell lines, both MAPK pathways are involved in enhanced myc IRES activity.⁵ The

identification of a role for MNK kinases in IRES activity could explain the involvement of the MAPK cascades. It is likely that which MAPK cascade mediates IRES stimulation is cell line and stimulus dependent. It is also likely that MNK kinases stimulate

IRES activity directly or indirectly via phosphomodulation of one or more ITAFs that are critical for the myc IRES. Alternatively, MNK activity may lead to changes in ITAF expression. Candidate ITAFs include hnRNP A1, which can be phosphorylated by MNK kinases¹² or PCBP1, whose expression is dependent on p38 activity, at least in neuronal cells.²⁵ Both hnRNP A1 and PCBP1 are required for myc IRES activity.^{24,26}

In myeloma cells, RAP primarily stimulated MNK1 activity and MNK1 knockdown curtailed upregulated IRES function. However, significant RAP-mediated stimulation still occurred (Figure 4b). As loss of MNK1 function can be compensated for by MNK2, it is possible that, in MNK1 shRNA-silenced MM cells, RAP could stimulate MNK2 activity with resulting maintenance of some IRES activity. This notion is supported by the results of the IRES reporter assay in MNK-null MEFs. Whereas RAP stimulated MNK1 in these MEFs, loss of MNK1 did not affect RAP-stimulated IRES activity, although double MNK1/MNK2 knockout MEFs had abrogated activity. The ability of RAP to induce MNK2 phosphorylation specifically in MNK-1 knocked out MEFs is consistent with MNK2 compensation for the MNK1-null state.

Myc IRES activity is specifically enhanced in MM cells.^{20,21} IRES activity could be particularly important in this tumor model because continuing ER stress, because of heightened Ig synthesis, restrains mTOR-mediated cap-dependent translation. A recent finding²⁷ of MM-specific overexpression of DEPTOR, an mTOR inhibitor, is consistent with this idea. Heightened MM IRES activity could also be one reason for ineffectiveness of rapalogs in MM patients.²⁸ Although our ANBL-6 MM cell line and primary specimen were resistant to RAP-induced growth inhibition, concurrent paralysis of MNKs with CGP or shRNA knockdown allowed for significant cyto-reduction. In contrast, there was minimal effect of MNK inhibition on MM cells not challenged with RAP. These results suggest that MNK activity may be less critical for IRES function in the basal state, at least for these myeloma cell types. However, in other MM clones, constitutive MAPK signaling, due to MM growth factor stimulation²⁹ or RAS mutation³⁰ could result in upregulated MNK activity and myc IRES function. Nevertheless, these results suggest MNK kinases could be potential therapeutic targets in MM patients.

MATERIALS AND METHODS

Cell lines, reagents, plasmids and transfections

The MM cell lines were obtained from ATCC. The MEF cell lines have been previously described.^{10,15} The pRF construct was a kind gift of Dr A Willis (University of Leicester). The myc IRES was cloned into pRF as previously described⁵ to obtain pRmF. The plko.1 lentiviral vectors targeting MNK1 were purchased from Sigma-Aldrich (St Louis, MO, USA). shRNA 1-1 has the ID# TRCW0000006232 and shRNA 1-4 has TRC0000199013. Virus particles expressing these shRNAs were produced and titers determined by the UCLA viral vector core. Lentiviral infection of MM cells was performed as previously described.³¹ After infection, clones were selected in puromycin. RAP and CGP57380 were purchased from Calbiochem (La Jolla, CA, USA). All antibodies were purchased from Cell Signaling Technology (Danvers, MA, USA), including the anti-phospho-MNK antibody.

Primary myeloma specimens

Primary MM cells were purified from bone marrow of patients by negative selection as described³¹ using the RosettesSep antibody cocktail method (Stem Cell Technologies, Vancouver, Canada). The purity by microscopy and CD138 flow analysis was >99% plasma cells.

Evaluation of protein and RNA expression

Western blot was performed as described.³¹ Real-time PCR for myc RNA and GAPDH RNA was performed as described.²³ All real-time PCR samples were run in triplicate.

MNK *in vitro* kinase assay

The MNK kinase assay was carried out as described³² with modifications. Cells were lysed with ice-cold cell lysis buffer (20 mM Tris-HCl (pH 7.5), 150 mM NaCl, 1 mM Na₂EDTA, 1 mM EGTA, 1% Triton, 2.5 mM sodium pyrophosphate, 1 mM beta-glycerophosphate, 1 mM Na₃VO₄, 1 μg/ml leupeptin and 1 mM PMSF). Direct covalent attachment of MNK1 (Santa Cruz, Santa Cruz, CA, USA, #sc-133107) and MNK2 (Sigma-Aldrich, #M0696) antibodies to the agarose beads were performed with Pierce Direct IP Kit according to the manufacture's protocol (Thermo Fisher Scientific, Pittsburgh, PA, USA, #26468). Labeled beads were washed three times with kinase buffer (20 mM HEPES, 10 mM MgCl₂, 10 mM sodium beta-glycerophosphate, pH 7.4) before 1 μg purified GST fusion eIF-4E protein (purchased from BPS Bioscience, San Diego, CA, USA, #40530) was added. Reaction mixtures were incubated at 30 °C for 30 min in the presence of 25 mM ATP. After SDS-PAGE, phosphorylated eIF-4E proteins were detected on western blots to assay MNKs activity.

Myc IRES activity

The dicistronic pRF or pRmF reporter constructs were transfected into cell lines using Lipofectamine Plus (Invitrogen, Carlsbad, CA, USA) and normalized for transfection efficiency by cotransfection with pSVβGal (Promega, Madison, WI, USA). Transfection efficiency was generally 5–10%. A transfection efficiency of at least 5% was required for carrying out a dicistronic reporter assay. After 12–14 h, cells were treated and were then harvested, followed by detection of Renilla luciferase, FF luciferase and beta-galactosidase activities as previously described.⁵ All luciferase activity is normalized to the luciferase values (both Renilla and FF) obtained for pRF in the absence of any treatment, which is designated as a value of '1'.

Cell survival assays and statistics

Quantitative increases in protein phosphorylation on western blots were evaluated by densitometric analysis of ratio of phosphorylated-protein/total-protein signal of treated MM cells. All western blots were repeated three times and the mean fold increase ($n=3$) in drug-treated groups versus non-treated cells is shown under the gels in the figures. The *t*-test was used to determine significance of differences between groups. The viable recovery data shown in Figures 5 and 6 are means. Percent viable recovery is determined by enumeration of trypan blue-negative viable cells with comparison to that of cells not exposed to any drugs.

CONFLICT OF INTEREST

The authors declare no conflict of interest.

ACKNOWLEDGEMENTS

We thank the UCLA Jonsson Comprehensive Cancer Center vector core lab for assistance in generating the lentiviral shRNA vectors. This work was supported by research funds of the Veteran's Administration, the Multiple Myeloma Research Foundation and the Department of Defense and NIH Grants RO1 CA109312 and RO1 CA111448.

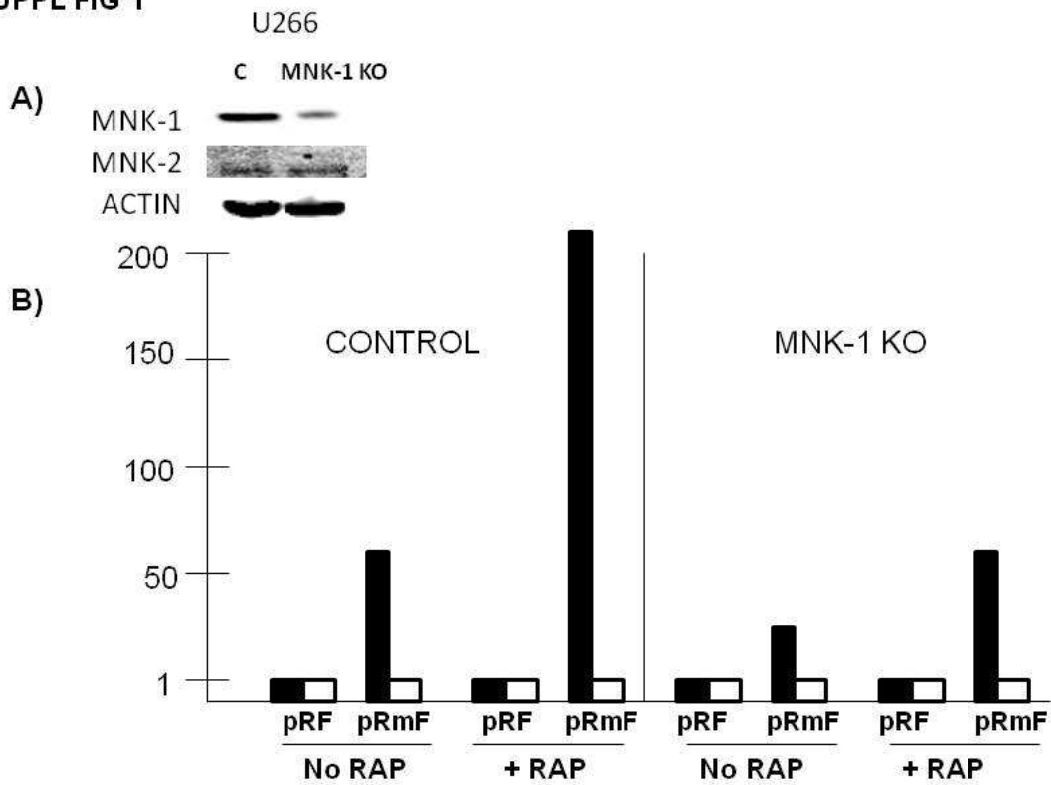
REFERENCES

- Neshat MS, Mellinshoff IK, Tran C, Stiles B, Thomas G, Peterson R et al. Enhanced sensitivity of PTEN-deficient tumors to inhibition of FRAP/mTOR. *Proc Natl Acad Sci* 2001; **98**: 10314–10319.
- Gera J, Mellinshoff I, Shi Y, Rettig M, Tran C, Hsu JH et al. AKT activity determines sensitivity to mTOR inhibitors by regulating cyclin D1 and c-myc expression. *J Biol Chem* 2004; **279**: 2737–2746.
- Frost P, Moatomed F, Hoang B, Shi Y, Gera J, Yan H et al. *In vivo* antitumor effects of the mTOR inhibitor CCI-779 against human multiple myeloma cells in a xenograft model. *Blood* 2004; **104**: 4181–4187.
- Shi Y, Gera J, Hu L, Hsu JH, Bookstein R, Li W et al. Enhanced sensitivity of multiple myeloma cells containing PTEN mutations to CCI-779. *Cancer Res* 2002; **62**: 5027–5034.
- Shi Y, Sharma A, Wu H, Lichtenstein A, Gera J. Cyclin D1 and c-myc IRES-dependent translation is regulated by AKT activity and enhanced by rapamycin

- through a p38 MAPK- and ERK-dependent pathway. *J Biol Chem* 2005; **280**: 10964-109973.
- 6 Frost P, Shi Y, Hoang B, Gera J, Lichtenstein A. Regulation of D-cyclin translation inhibition in myeloma cells treated with mTOR inhibitors: rationale for combined treatment with ERK inhibitors and rapamycin. *Mol Cancer Ther* 2009; **8**: 83-93.
 - 7 Subkhankulova T, Mitchell SA, Willis AE. IRES-mediated initiation of c-myc protein synthesis following genotoxic stress. *Biochem J* 2001; **359**: 183-192.
 - 8 Stoneley M, Chappell SA, Jopling CL, Dickens M, MacFarlane M, Willis AE. C-myc protein synthesis is initiated from the IRES during apoptosis. *Mol Cell Biol* 2000; **20**: 1162-1169.
 - 9 Parra JL, Buxade M, Proud CG. Features of the catalytic domains and C termini of the MAPK signal-integrating kinases MNK1 and MNK2 determine their differing activities and regulatory properties. *J Biol Chem* 2005; **280**: 37623-37633.
 - 10 Wang X, Yue P, Chan C-B, Ye K, Ueda T, Watanabe-Fukunaga R *et al*. Inhibition of mTOR induces PI3-kinase-dependent and MNK-mediated eIF-4E phosphorylation. *Mol Cell Biol* 2007; **27**: 7405-7413.
 - 11 Ross G, Dyer JR, Castellucci VF, Sossin WS. MNK is a negative regulator of cap-dependent translation in Aplysia neurons. *J Neurochem* 2006; **97**: 79-91.
 - 12 Buxade M, Parra JL, Rousseau S, Shpiro N, Marquez R, Morrice N *et al*. The MNKs are novel components in the control of TNF alpha biosynthesis and phosphorylate and regulate hnRNP A1. *Immunity* 2005; **23**: 177-189.
 - 13 Scheper GC, Morrice NA, Kleijn M, Proud CG. The mitogen-activated protein kinase signal-integrating kinase MNK2 is an eIF-4E kinase with high levels of basal activity in mammalian cells. *Mol Cell Biol* 2001; **21**: 743-754.
 - 14 Scheper GC, Parra J-L, Wilson ML, van Kollenburg B, Vertegaal ACO, Han ZG *et al*. The N and C termini of the splice variants of the human MNK2 determine activity and localization. *Mol Cell Biol* 2003; **23**: 5692-5705.
 - 15 Ueda T, Watanabe-Fukunaga R, Fukuyama H, Nagata S, Fukunaga R. MNK2 and MNK1 are essential for constitutive and inducible phosphorylation of eIF-4E but not for cell growth or development. *Mol Cell Biol* 2004; **24**: 6539-6549.
 - 16 Parra-Palau JL, Scheper GC, Wilson ML, Proud CG. Features in the N and C termini of the MAPK-integrating kinase MNK1 mediate its nucleocytoplasmic shuttling. *J Biol Chem* 2003; **278**: 44197-44204.
 - 17 Pyronnet S, Imataka H, Gingras AC, Fukunaga R, Hunter T, Sonenberg N. Human eIF4G recruits MNK1 to phosphorylate eIF-4E. *EMBO J* 1999; **18**: 270-279.
 - 18 Chrestensen CA, Shuman JK, Eschenroeder A, Worthington M, Gram H, Sturgill TW. MNK1 and MNK2 regulation in HER2-overexpressing breast cancer lines. *J Biol Chem* 2007; **282**: 4243-4252.
 - 19 Stoneley M, Willis AE. Cellular IRESes: structures, trans-acting factors and regulation of gene expression. *Oncogene* 2004; **23**: 3200-3207.
 - 20 Paulin FEM, West MJ, Sullivan NF, Whitney RL, Lyne L, Willis AE. Aberrant translational control of the c-myc gene in multiple myeloma. *Oncogene* 1996; **13**: 505-513.
 - 21 Chappell SA, LeQuesne JPC, Paulin FEM, deSchoolmeester ML, Stoneley M, Soutar RL *et al*. A mutation in the c-myc IRES leads to enhanced internal ribosome entry in multiple myeloma: a novel mechanism of oncogene de-regulation. *Oncogene* 2000; **19**: 4437-4440.
 - 22 Sun S-Y, Rosenberg LM, Wang X, Zhou Z, Yue P, Fu H *et al*. Activation of AKT and eIF4E survival pathways by rapamycin-mediated mTOR inhibition. *Cancer Res* 2005; **65**: 7052-7058.
 - 23 Shi Y, Frost PJ, Hoang B, Benavides A, Sharma S, Gera J *et al*. IL-6-induced stimulation of c-myc translation in multiple myeloma cells is mediated by myc IRES function and the RNA-binding protein hnRNP A1. *Cancer Res* 2008; **68**: 10215-10222.
 - 24 Jo OD, Martin PJ, Bernath A, Masri J, Lichtenstein A, Gera J. Heterogeneous nuclear ribonucleoprotein A'1 regulates cyclin D and c-myc IRES function through AKT signaling. *J Biol Chem* 2008; **283**: 23274-23287.
 - 25 Zhu Y, Sun Y, Mao O, Jin KL, Greenberg D. Expression of poly(C) binding proteins is differentially regulated by hypoxia and ischemia in cortical neurons. *Neuroscience* 2002; **110**: 191-198.
 - 26 Evans JR, Mitchell SA, Spriggs KA, Ostrowski J, Bomszyk K, Ostarek D *et al*. Members of the poly (rC) binding protein family stimulate the activity of the c-myc IRES *in vitro* and *in vivo*. *Oncogene* 2003; **22**: 8012-8020.
 - 27 Peterson TR, Laplante M, Thoreen CC, Sancak Y, Kang SA, Kuehl WM *et al*. DEPTOR is an mTOR inhibitor frequently overexpressed in multiple myeloma cells and required for their survival. *Cell* 2009; **137**: 1-14.
 - 28 Farag SS, Zhang S, Jansak BS, Wang X, Kraut E, Chan K *et al*. Phase II trial of temsirolimus in patients with relapsed or refractory multiple myeloma. *Leuk Res* 2009; **33**: 1475-1480.
 - 29 Ogata A, Chauhan D, Teoh G, Treon S, Urashima M, Schlossman RL *et al*. IL-6 triggers cell growth via the RAS-dependent mitogen-activated protein kinase cascade. *J Immunol* 1997; **159**: 2212-2221.
 - 30 Paquette RL, Berenson J, Lichtenstein A, McCormick F, Koeffler HP. RAS mutations in multiple myeloma. *Oncogene* 1990; **5**: 1569-1663.
 - 31 Hoang B, Frost P, Shi Y, Belanger E, Benavides A, Pezeshkpour G *et al*. Targeting TORC2 in multiple myeloma with a new mTOR kinase inhibitor. *Blood* 2010; **116**: 4560-4568.
 - 32 Waskiewicz AJ, Flynn A, Proud CG, Cooper JA. Mitogen-activated protein kinases activate the serine/threonine kinases MNK1 and MNK2. *EMBO J* 1997; **16**: 1909-1920.

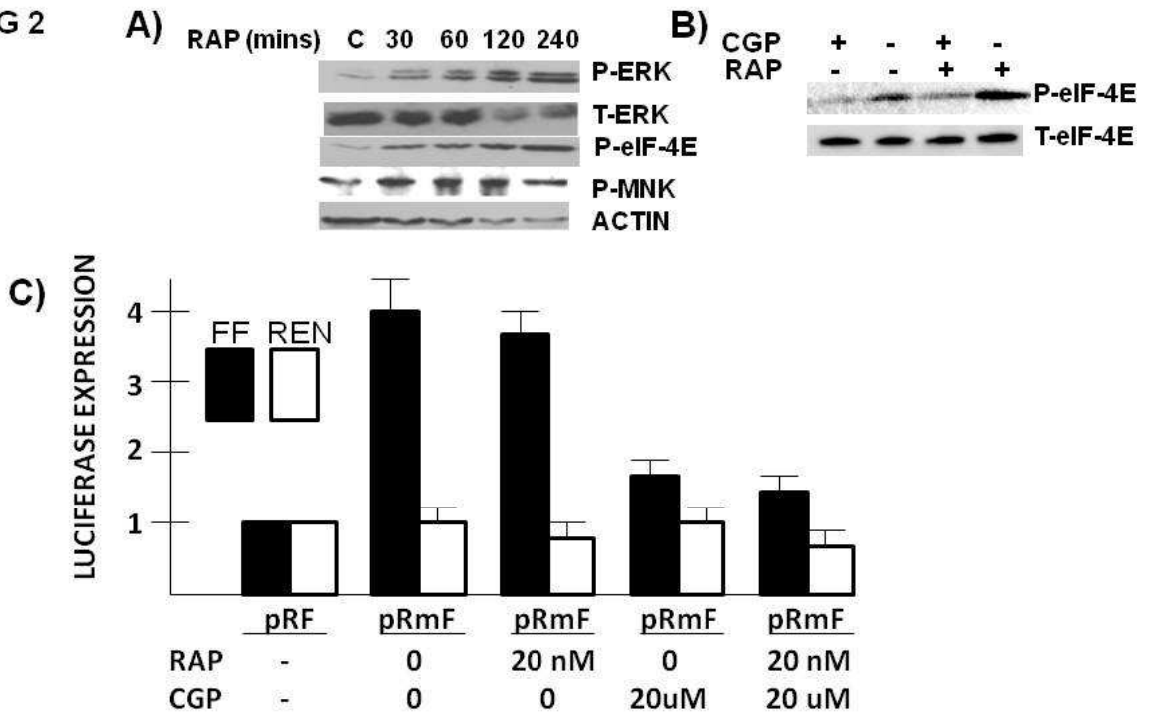
Supplementary Information accompanies the paper on the Oncogene website (<http://www.nature.com/onc>)

SUPPL FIG 1

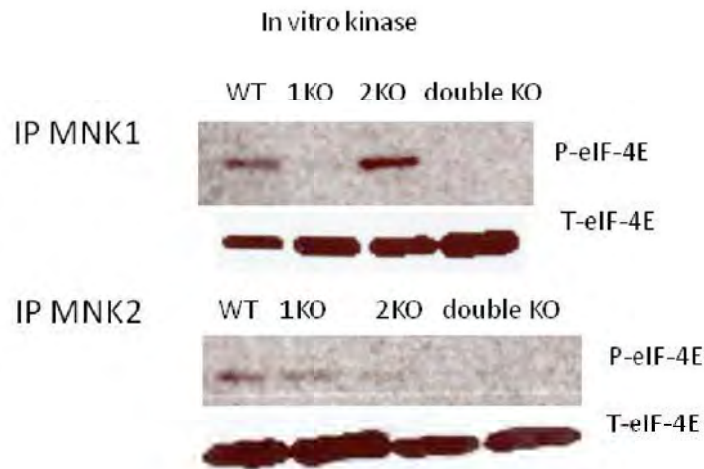


MNK1 knocked-down U266 MM cells have blunted myc IRES response to rapamycin. A) Immunoblot for MNK1, MNK2 or actin in U266 cells infected with control shRNA or MNK1 knockdown shRNA. B) Relative Luciferase expression (black bars=firefly;white bars=Renilla) in the two U266 lines transfected with reporter plasmids and treated +/- rapamycin (100 nM).

Suppl FIG 2

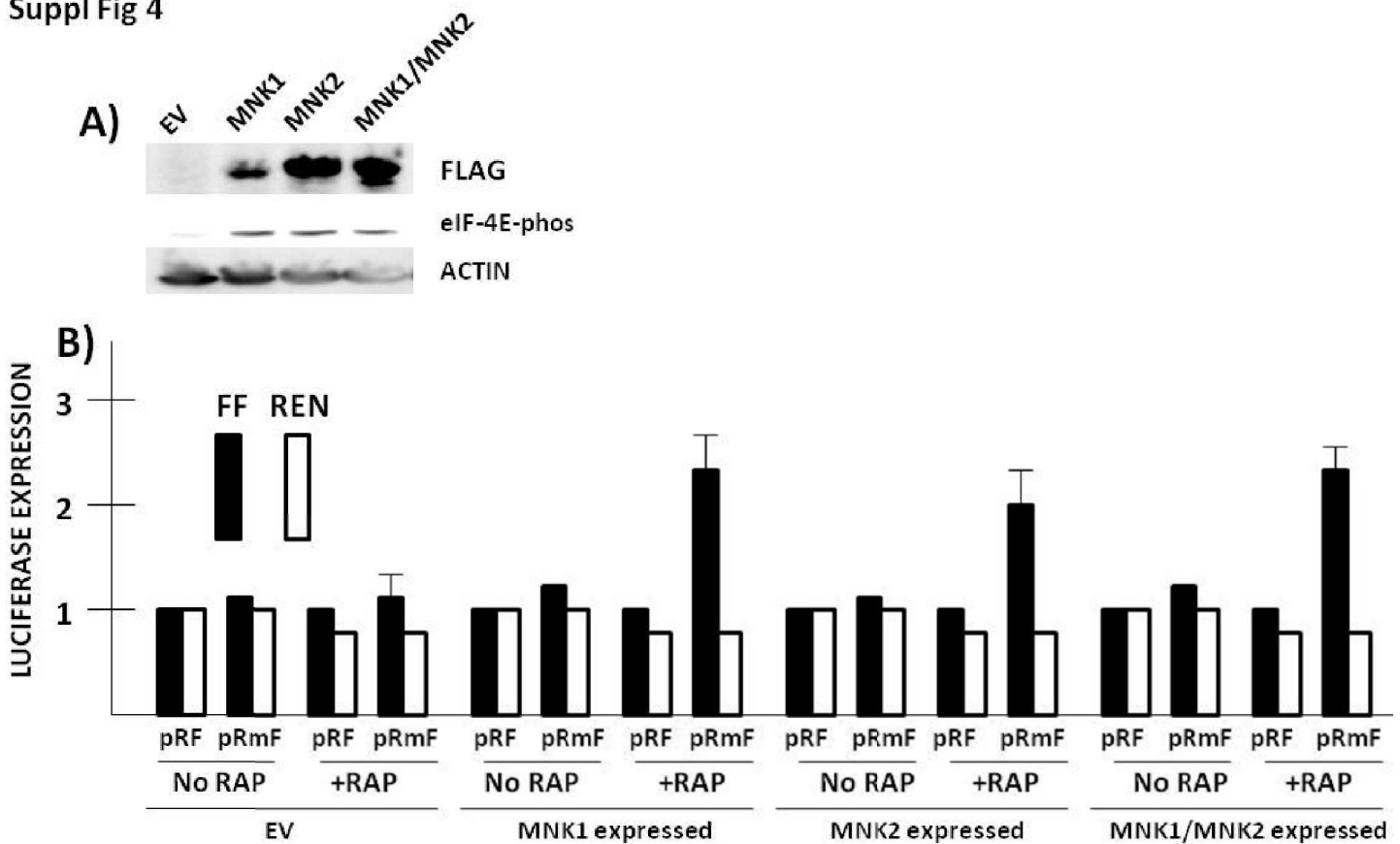


Effect of MNK inhibition on IRES activity in OPM-2 MM cells. In A), OPM-2 cells treated with rapamycin (20nM) For 30, 60, 120 or 240 mins (C=control, no RAP) followed by Western blot assay. In B), OPM-2 cells treated +/- RAP (at 20 nM) and +/- CGP (at 20 uM) followed by Western blot. In C), myc IRES reporter assay performed in OPM-2 cells treated +/- rapamycin (RAP) and +/- CGP. Data are means +/- SD, n=3.



Either MNK1 or MNK2 immunoprecipitated from four MEF cell lines (WT=wild type; 1KO=MNK1 null; 2KO=MNK2 null; double KO=MNK1/MNK2 null) and tested for ability to phosphorylate eIF-4E in vitro.

Suppl Fig 4



Double knock-out (DKO) MEFs re-expressing MNK kinases. In **A)**, DKO MEFs transfected with lentivirus expressing empty vector (EV) or FLAG-tagged MNK1, MNK2 or both MNK1/MNK2. Western blot performed for FLAG, eIF-4E phosphorylation and actin. In **B)**, EV or MNK-transfected MEF cell lines assayed for myc IRES reporter expression in presence (20nM) or absence of rapamycin (RAP). Data are means \pm SD, n=3) (Black bars are firefly (FF) luciferase expression and white bars represent Renilla (REN) luciferase expression).



Mnk1 and 2 Are Dispensable for T Cell Development and Activation but Important for the Pathogenesis of Experimental Autoimmune Encephalomyelitis

This information is current as of January 30, 2013.

Balachandra K. Gorentla, Sruti Krishna, Jinwook Shin, Makoto Inoue, Mari L. Shinohara, Jason M. Grayson, Rikiro Fukunaga and Xiao-Ping Zhong

J Immunol 2013; 190:1026-1037; Prepublished online 26 December 2012;
doi: 10.4049/jimmunol.1200026
<http://www.jimmunol.org/content/190/3/1026>

-
- References** This article **cites 61 articles**, 27 of which you can access for free at: <http://www.jimmunol.org/content/190/3/1026.full#ref-list-1>
- Subscriptions** Information about subscribing to *The Journal of Immunology* is online at: <http://jimmunol.org/subscriptions>
- Permissions** Submit copyright permission requests at: <http://www.aai.org/ji/copyright.html>
- Email Alerts** Receive free email-alerts when new articles cite this article. Sign up at: <http://jimmunol.org/cgi/alerts/etoc>

The Journal of Immunology is published twice each month by The American Association of Immunologists, Inc., 9650 Rockville Pike, Bethesda, MD 20814-3994. Copyright © 2013 by The American Association of Immunologists, Inc. All rights reserved. Print ISSN: 0022-1767 Online ISSN: 1550-6606.



Mnk1 and 2 Are Dispensable for T Cell Development and Activation but Important for the Pathogenesis of Experimental Autoimmune Encephalomyelitis

Balachandra K. Gorentla,^{*,1} Sruti Krishna,^{*,†,1} Jinwook Shin,^{*} Makoto Inoue,[†] Mari L. Shinohara,[†] Jason M. Grayson,[‡] Rikiro Fukunaga,[§] and Xiao-Ping Zhong^{*,†}

T cell development and activation are usually accompanied by expansion and production of numerous proteins that require active translation. The eukaryotic translation initiation factor 4E (eIF4E) binds to the 5' cap structure of mRNA and is critical for cap-dependent translational initiation. It has been hypothesized that MAPK-interacting kinase 1 and 2 (Mnk1/2) promote cap-dependent translation by phosphorylating eIF4E at serine 209 (S209). Pharmacologic studies using inhibitors have suggested that Mnk1/2 have important roles in T cells. However, genetic evidence supporting such conclusions is lacking. Moreover, the signaling pathways that regulate Mnk1/2 in T cells remain unclear. We demonstrate that TCR engagement activates Mnk1/2 in primary T cells. Such activation is dependent on Ras-Erk1/2 signaling and is inhibited by diacylglycerol kinases α and ζ . Mnk1/2 double deficiency in mice abolishes TCR-induced eIF4E S209 phosphorylation, indicating their absolute requirement for eIF4E S209 phosphorylation. However, Mnk1/2 double deficiency does not affect the development of conventional $\alpha\beta$ T cells, regulatory T cells, or NKT cells. Furthermore, T cell activation, in vivo primary and memory CD8 T cell responses to microbial infection, and NKT cell cytokine production were not obviously altered by Mnk1/2 deficiency. Although Mnk1/2 deficiency causes decreased IL-17 and IFN- γ production by CD4 T cells following immunization of mice with myelin oligodendrocyte glycoprotein peptide in complete Freund's adjuvant, correlating with milder experimental autoimmune encephalomyelitis scores, it does not affect Th cell differentiation in vitro. Together, these data suggest that Mnk1/2 has a minimal role in T cell development and activation but may regulate non-T cell lineages to control Th1 and Th17 differentiation in vivo. *The Journal of Immunology*, 2013, 190: 1026–1037.

T cells have a critical role in adaptive immune responses. Activation of T cells is critical for mounting immune responses against foreign Ags and to protect the host from infection (1). However, tight regulation of this process is important for the maintenance of self-tolerance (2). The signal from the

TCR, via multiple intracellular signaling pathways such as the RasGRP1-Ras-Erk1/2-API1, PKC θ -NF- κ B, PI3K-Akt, and Ca⁺⁺-calcineurin-NFAT pathways, has critical roles in T cell maturation and activation (3–5). Orchestrated actions of these signaling cascades ensure proper T cell maturation and T cell activation.

In addition to TCR engagement, various other extracellular stimuli such as growth factors, cytokines, and stress can induce activation of MAPKs. Based on the signals that trigger their activation, MAPKs are categorized as ERKs (Erk1/2), p38 kinases, and C-Jun N-terminal kinase/stress-activated protein kinases (JNK) (6). MAPKs control a wide range of functions including proliferation, differentiation, survival, and apoptosis through direct phosphorylation and activation of substrates (7). These substrates, called MAPK-activated protein kinases (MAPKAPKs), are divided into four families based on the type of phosphorylating MAPK (8, 9). For example, the p90 ribosomal S6 kinase (Rsk) family includes Rsk1, Rsk2, and Rsk3 that are specifically phosphorylated and activated by ERKs (10); MAPKAPKs such as MK2/3 and MK5 are activated by JNKs (11); and mitogen- and stress-activated kinases (MSKs) including MSK1 and MSK2 are phosphorylated by p38 MAPKs (12). Different from these MAPKAPKs, MAPK-interacting kinases 1 and 2 (Mnk1/2) are serine/threonine kinases and are phosphorylated by both ERKs and p38 kinases (13). Murine Mnk1/2 are phosphorylated at threonine 197 and 202 (T197 and T202) or T244 and T249 respectively, which leads to their activation (14–18). Activated Mnk1/2 directly phosphorylates the eukaryotic translation initiation factor 4E (eIF4E) at S209 downstream of growth factor receptors (18). eIF4E binds to 5' methyl guanosine (m⁷GpppN) cap structure found in all eukaryotic mRNAs, and this binding is obligatory for the initiation of cap-dependent translation (19, 20). Cap-dependent translation is the primary

*Division of Allergy and Immunology, Department of Pediatrics, Duke University Medical Center, Durham, NC 27710; [†]Department of Immunology, Duke University Medical Center, Durham, NC 27710; [‡]Department of Microbiology and Immunology, Wake Forest University School of Medicine, Winston-Salem, NC 27157; and [§]Laboratory of Biochemistry, Osaka University of Pharmaceutical Sciences, Osaka 569-1094, Japan

¹B.K.G. and S.K. contributed equally to this work.

Received for publication January 4, 2012. Accepted for publication November 27, 2012.

This work was supported by funding from the National Institutes of Health (AI076357, AI079088, and AI101206), the Food Allergy and Anaphylaxis Network, and the American Cancer Society (RSG-08-186-01-LIB) to X.-P.Z. and National Institutes of Health Grant R01AI068952 (to J.M.G.).

B.K.G. and S.K. were involved in experimental design and execution, data analysis, and preparation of the manuscript. J.S. designed and performed experiments. M.I. and M.L.S. were involved in the experimental autoimmune encephalomyelitis experiments. J.M.G. and R.F. provided essential reagents. X.-P.Z. conceived the project and was involved in experimental design, data analysis, and manuscript preparation.

Address correspondence and reprint requests to Dr. Xiao-Ping Zhong, 133 Medical Sciences Research Building-I, Research Drive, Division of Allergy and Immunology, Department of Pediatrics, Box 2644, Duke University Medical Center, Durham, NC 27710. E-mail address: zhong001@mc.duke.edu

Abbreviations used in this article: DAG, diacylglycerol; DGK, DAG kinase; EAE, experimental autoimmune encephalomyelitis; eIF, eukaryotic translation initiation factor; α -GalCer, α -galactosylceramide; iNKT, invariant NKT; LCMV, lymphocytic choriomeningitis virus; LM-OVA, *Listeria monocytogenes*-expressing recombinant OVA; LN, lymph node; MAPKAPK, MAPK-activated protein kinase; Mnk1/2, MAPK-interacting kinase 1 and 2; MOG, myelin oligodendrocyte glycoprotein; mTOR, mammalian target of rapamycin; Rsk, ribosomal S6 kinase; WT, wild-type.

Copyright © 2013 by The American Association of Immunologists, Inc. 0022-1767/13/\$16.00

mode of eukaryotic translation by which 95% of total cellular mRNAs are translated (21). It has been hypothesized that Mnk1/2 are key protein kinases that can promote cap-dependent translation through eIF4E phosphorylation (22).

The roles of Mnk1/2 were originally studied in *Drosophila*, whose Mnk ortholog is called LK6. Deficiency of this gene was found to impair growth and development, leading to a shortened life span (23). However, in mice, Mnk1/2 double deficiency did not grossly affect development and growth, although eIF4E phosphorylation at S209 was abolished (18). While dispensable for murine development, Mnk1 and Mnk2 have been demonstrated to play an oncogenic role in mice, and their deficiency delays tumor development in a murine tumor model (24). Studies using pharmacologic inhibitors and eIF4E phosphorylation mutants have shown that eIF4E phosphorylation has an important role in cell survival and cancer progression (25).

Using chemical inhibitors, several previous studies have reported that Mnk1/2 could have an important role in immune cells. For example, chemical inhibition of Mnk1/2 was found to decrease the translation of IL-17 in CD4⁺ T cells (26), IFN- γ and IL-4 in invariant NKT (*i*NKT) cells (27), and inflammatory cytokines in macrophages (28). Although these studies provide preliminary evidence that Mnk1/2 activity could have a critical role in immune cell function, possible off-target effects of the chemical inhibitors used cannot be overlooked. In this report, we demonstrate that TCR engagement induces activation of Mnk1/2 and phosphorylation of eIF4E, which is enhanced by Ras signaling, and inhibited by diacylglycerol (DAG) kinases α and ζ that terminate DAG-mediated signaling (29). By using mice deficient in Mnk1/2 (*Mnk1/2DKO*), we show that Mnk1 and Mnk2 are essential for TCR-induced phosphorylation of eIF4E. However, deficiency of both Mnk1 and Mnk2 does not affect gross T cell development, activation, proliferation, or cytokine production. Furthermore, Mnk1/2 activities are dispensable during CD8 T cell-mediated immune responses against *Listeria monocytogenes* and lymphocytic choriomeningitis virus (LCMV) and for *i*NKT cell development and cytokine production.

Materials and Methods

Mice

C57BL/6J mice and TCR-OT1 transgenic mice were purchased from the Jackson Laboratory. Mice expressing a conditional constitutively active form of Ras in a T cell-specific manner (caK_{Ras}-CD4Cre) and *Mnk1/2DKO* mice on a C57BL/6J background were described previously (18, 30–32). DAG kinase (DGK) α and ζ double-knockout mice were reported previously (33, 34). All mice were used according to a protocol approved by the Duke University Institutional Animal Care and Use Committee.

Flow cytometry

Thymocytes, splenocytes, and lymph node (LN) cells were prepared following standard procedures. Cells were stained with fluorochrome-conjugated Abs for CD4, CD8, CD62L, CD44, CD25, TCR β , CD24, NK1.1, and CD69 (BioLegend) as well as CD1d-Tetramer (provided by the National Institutes of Health Tetramer Facility) in 2% FBS-PBS at 4°C for 30 min. In addition, Live/Dead Fixable Violet Dead Cell Stain (Invitrogen) was used to identify the viable cells. The stained cells were collected using a BD FACS Canto II flow cytometer. The collected data were analyzed using Flowjo software. Isolation of liver mononuclear cells and staining of *i*NKT cells were performed as described previously (32, 35).

Activation, anergy, and proliferation assays

Splenocytes from wild type (WT) or *Mnk1/2DKO* mice were left unstimulated or stimulated with anti-CD3 (1 μ g/ml; 2C-11) overnight in the presence or absence of either anti-CD28 (0.5 μ g/ml) or CTLA4-Ig (10 μ g/ml; BioXcell) to assess the upregulation of early activation markers by

FACS. For proliferation assays, splenocytes were labeled with CFSE as described previously (36), left unstimulated or stimulated with anti-CD3 for 72 h. After staining for CD4 and CD8, cells were subjected to FACS analysis. In some experiments, CGP57380 (TOCRIS Bioscience, a Mnk1/2 inhibitor) was added in the culture at the indicated concentrations. To examine T cell anergy, WT and *Mnk1/2DKO* splenocytes were stimulated with anti-CD3 in the presence of either anti-CD28 (0.5 μ g/ml) or CTLA4-Ig (10 μ g/ml) at 37°C for 48 h. Cells were then washed three times and rested in IMDM at 37°C for 24 h. Live cells enriched after Lympholyte (Cedarlane) gradient separation were restimulated with plate-bound anti-CD3 (1 μ g/ml) and soluble anti-CD28 (0.5 μ g/ml) in the presence of 5 μ M GolgiPlug (BD Biosciences) at 37°C for 24 h. Cells were surface-stained for CD4 and CD8 and intracellularly stained for IFN- γ for FACS analysis.

In vitro stimulation of *i*NKT

Thymocytes were cultured in vitro in 10% FBS-complete IMDM with or without α -galactosylceramide (α -GalCer; 125 ng/ml) stimulation at 37°C for 72 h. During the last 5 h of stimulation, PMA (phorbol 12-myristate 13-acetate, 50 ng/ml), ionomycin (500 ng/ml, Sigma) and GolgiPlug were added. After surface staining with anti-TCR- β Ab and the PBS-57-loaded mouse CD1d tetramer (CD1d-Tet), cells were intracellularly stained for IFN- γ and IL-17 followed by FACS analysis. *i*NKT cell proliferation was similarly assessed except that thymocytes were labeled with CFSE and PMA, and ionomycin stimulation was not added.

Immunoblot

Immunoblots were prepared as described previously (31). Thymocytes or splenocytes were washed with PBS. Cells were suspended in PBS with calcium and left unstimulated or stimulated with 5 μ g/ml of anti-CD3 ϵ (500A2; BD Pharmingen) for different times. After stimulation, cells were centrifuged and lysed in 1% Nonidet P-40 buffer (1% Nonidet-40, 150 mM NaCl, and 50 mM Tris, pH 7.4) supplemented with protease and phosphatase inhibitor mixture (Sigma). Total proteins were separated by SDS-PAGE and were transferred to a Trans-Blot Nitrocellulose Membrane (Bio-Rad). To examine protein phosphorylation, the membranes were incubated overnight with Abs specific for phospho Erk1/2, phospho p38, phospho-4E-BP1 (T37/46), phospho-eIF4E (S209), phospho-Mnk1 (T197/202), total Mnk1 (Cell Signaling Technology), total Mnk2 (18), and β -actin (Santa Cruz Biotechnology). Later, the membranes were incubated with the appropriate secondary, peroxidase-conjugated Abs. The blots were developed using the ECL System from Perkin-Elmer. The same blots were stripped and reprobbed using control Abs.

T helper differentiation assay

Naive CD4⁺ T cells were purified from LN cells and cultured with plate-bound anti-CD3 (2C11) 5 μ g/ml, soluble anti-CD28 (1 μ g/ml) and indicated skewing conditions. Skewing conditions were as follows: Th1, IL-12 (5 ng/ml), IFN- γ (100 ng/ml) and anti-IL-4 (100 μ g/ml), with IL-2 (100 U/ml) during the rest period; Th2, IL-4 (1 ng/ml), anti-IL-12 (100 μ g/ml), and anti-IFN- γ (100 μ g/ml), with IL-2 (100 U/ml) during the rest period; Th17, TGF- β (10 ng/ml), IL-6 (10 ng/ml), anti-IFN- γ (100 μ g/ml) and anti-IL-4 (100 μ g/ml); Th9, IL-4 (20 ng/ml) anti-IL-12 (10 μ g/ml), and TGF- β (2 ng/ml) during rest period. Th0, IL-2 (100 U/ml) during the rest period. After culturing for 5 d, cells were stimulated with PMA and ionomycin in the presence of GolgiPlug at 37°C for 5 h. Following surface staining, cells were intracellularly stained for indicated cytokines, followed by FACS analysis.

Adoptive transfer and *L. monocytogenes*-expressing recombinant OVA infection to assess CD8⁺ T cell response *in vivo*

Naive OT1 T cells (α 2⁺CD8⁺ 7AAD⁻CD44⁻) were sorted from LN cells from Thy1.1⁺ WT-OT1 and Thy1.2⁺ *Mnk1/2DKO* OT1 mice. Five thousand sorted WT OT1 cells were mixed with an equal number of sorted *Mnk1/2DKO* OT1 cells in 200 μ l of serum-free IMDM and adoptively transferred by retroorbital injection into sex-matched WT Thy1.1⁺Thy1.2⁺ recipients. After 24 h, recipient mice were injected i.v. with 1×10^4 CFUs of *L. monocytogenes*-expressing recombinant OVA (LM-OVA) (37). Peripheral blood samples (collected in PBS with 5 mM EDTA) and splenocytes were analyzed at 1 and 2 wk after infection. After lysis of RBCs, samples were labeled with fluorochrome-conjugated Abs and analyzed with flow cytometry. Frequencies of Thy1.1⁺ WT-OT1 and Thy1.2⁺ Mnk DKO populations were corrected to account for the deviation of the input ratio from 50:50.

LCMV infection

LCMV Armstrong stocks were propagated on BHK-21 cells and quantitated as described previously (38). LCMV infection and assessment of viral-specific CD8 T cell responses were performed as described previously (39). Mice were infected with 2×10^5 PFU of virus i.p. and monitored by serial bleeding and tetramer staining. For memory experiments, viable CD8⁺CD44⁺ memory cells were sorted from donor mice 8 wk after LCMV infection. While donor mice were Thy1.1⁻Thy1.2⁺, recipients were Thy1.1⁺Thy1.2⁺. Frequency of H-2D^b tetramer loaded with LCMV gp33–41 (TetG)-positive cells in the sorted population was determined by flow cytometry, and an appropriate number of total memory cells was transferred such that each recipient mouse received 5000 TetG⁺ memory cells. Recipients were infected with 2×10^5 PFU of LCMV i.p. the next day and taken 7 d later to assess the memory response.

Induction and scoring of experimental autoimmune encephalomyelitis

Experimental autoimmune encephalomyelitis (EAE) was induced in 6–10-wk-old female mice by s.c. injection of myelin oligodendrocyte glycoprotein (MOG_{35–55}) peptide (100 μg/mouse) emulsified in CFA containing 2 mg/ml *Mycobacterium tuberculosis* (100 μl/mouse). Mice were also injected i.p. with 200 ng of pertussis toxin on day 0 (day of immunization) and day 2. Mice were monitored for ~40 d to assess the development of a clinical score based on the following criteria: 1 = tail limpness; 2 = impaired righting reflex; 3 = hind limb paralysis; 4 = complete paralysis; 5 = death. Some mice were sacrificed on day 7 to assess CD4 T cell differentiation in response to the immunization. Draining LN cells were stimulated with MOG_{35–55} peptide for 3 d to expand the pool of Ag-specific CD4 T cells, followed by stimulation for 5 h with PMA (50 ng/ml) and ionomycin (500 ng/ml) in the presence of GolgiPlug. After stimulation, cells were stained for cell surface CD4 and intracellularly stained for IL-17A and IFN-γ.

Statistical analysis

Statistical significance was determined using the ANOVA or Student *t* test. The *p* values are defined as follows: *p* < 0.05, *p* < 0.01, *p* < 0.001.

Results

Regulation of Mnk1/2 activation and expression in T cells

TCR signaling has been shown to trigger several intracellular signaling pathways leading to phosphorylation and activation of p38 and Erk1/2. We assessed anti-CD3–induced Mnk1 activation in freshly isolated thymocytes or splenic T cells from WT mice. As shown in Fig. 1A, TCR engagement induced Mnk1 and eIF4E phosphorylation in both thymocytes and splenic T cells, correlated with Erk1/2 and p38 activation. In T cells, DAG binds to and activates RasGRP1, which in turn activates the Ras-Mek1/2-Erk1/2 pathway. In the presence of a constitutively active form of Ras (kRas), TCR-induced Erk1/2, Mnk1, and eIF4E phosphorylation were significantly increased, indicating that Ras signaling promotes Mnk1/2 activation in T cells (Fig. 1B). We have previously demonstrated that DGKα and ζ inhibit the activation of the Ras-Erk1/2 signaling (33, 34, 40, 41). In DGKα and ζ double-deficient thymocytes (αζDKO), both Erk1/2 and eIF4E phosphorylation were enhanced (Fig. 1C). Furthermore, this phosphorylation was greatly inhibited by U0126 (UO), a MEK1/2 inhibitor. Together, these observations indicate that TCR engagement induces Mnk1/2 activation, and that such activation is mediated by the Ras-Erk1/2 pathway and is inhibited by DGK activity.

Although Mnk1 and Mnk2 are ubiquitously expressed, their expression is varied in different tissues (17). Using real-time quantitative PCR, we assessed Mnk1/2 mRNA levels in naive and activated CD4⁺ and CD8⁺ T cells. Both Mnk1 and 2 mRNA levels were expressed at higher levels in naive T cells than in activated T cells. Mnk1 was decreased to 45% and 30%, whereas Mnk2 expression was reduced to 50% and 20% in activated CD4 and CD8 T cells, respectively, compared with naive T cells (Fig. 1D). The decreased expression of Mnk1/2 proteins in activated T cells was further confirmed by immunoblotting analysis (Fig. 1E). Naive and activated T cells are drastically different in metabolism

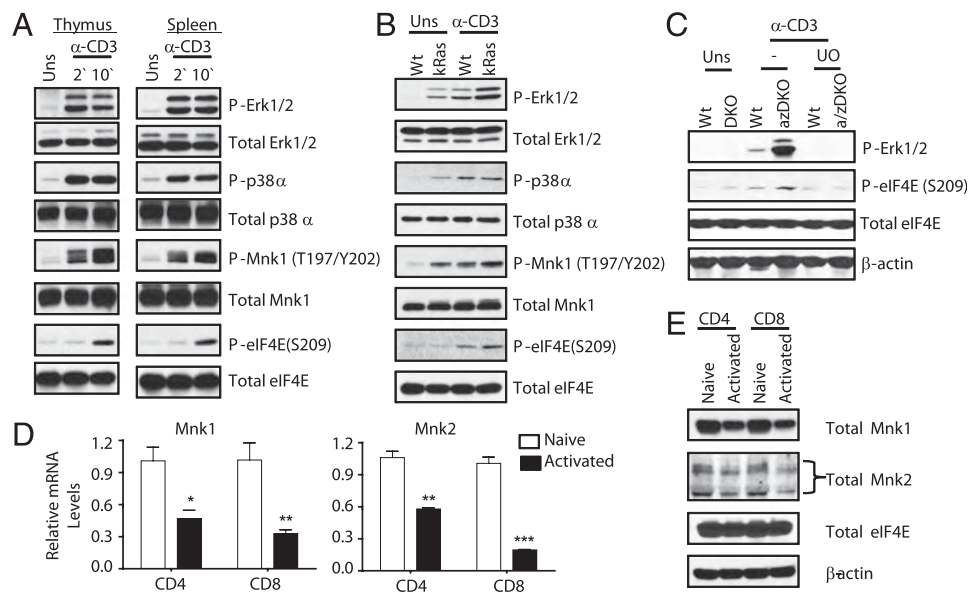
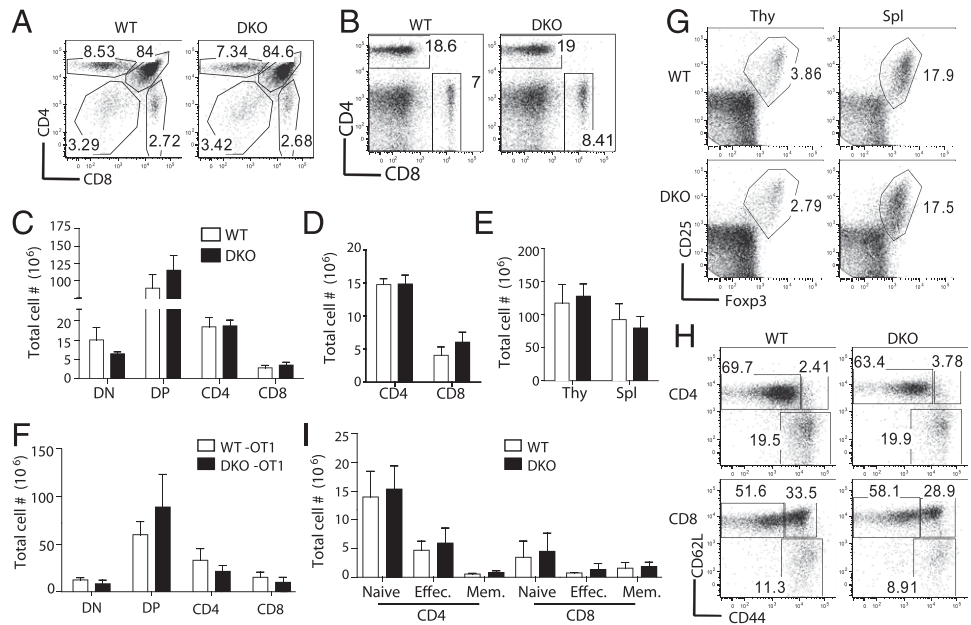


FIGURE 1. Regulation of Mnk1/2 activation in T cells. Thymocytes and splenocytes of indicated genotypes were rested in PBS at 37°C for 30 min and were then left unstimulated or stimulated with 5 μg/ml anti-CD3 (500A2) for the indicated times. Lysates were subjected to immunoblot analysis with the indicated Abs. **(A)** TCR engagement activates Mnk1/2 in WT thymocytes (*left*) and splenocytes (*right*). **(B)** Constitutively active KRas promotes Mnk1/2 activation. Thymocytes from WT and *ca.kRas*-CD4Cre mice were subjected to similar analysis as in **(A)**. **(C)** DGKα and ζ inhibit TCR-induced Mnk1/2 activation in a MEK1/2–dependent manner. WT and in *DGKαζDKO* (*azDKO*) thymocytes were examined as in **(A)** with the addition of groups treated with the MEK1/2 inhibitor U0126 (10 μM). **(D and E)** Differential expression of Mnk1/2 in naive and activated T cells. Mnk1 and Mnk2 mRNA (**D**) and protein (**E**) levels in sorted WT naive and in vitro-activated CD4 and CD8 T cells were examined by real-time quantitative PCR and Western blotting analysis, respectively. **p* < 0.05, ***p* < 0.01, ****p* < 0.001.

FIGURE 2. T cell development in *Mnk1/2DKO* mice. **(A and B)** CD4 and CD8 expression in WT and *Mnk1/2DKO* (DKO) thymocytes (A) and splenocytes (B). Representative dot-plots of CD4 and CD8 staining are shown. **(C and D)** Absolute numbers of thymic (C) and splenic (D) T cell populations in WT and *Mnk1/2DKO* mice ($n = 6$). **(E)** Total thymic and splenic cellularities in WT and *Mnk1/2DKO* mice. **(F)** Absolute numbers of thymic T cell populations in WT-OT1 and *Mnk1/2DKO*-OT1 mice ($n = 3$). **(G)** Regulatory T cell staining in the thymus and spleen. CD25 and Foxp3 staining in CD4⁺ T cells are shown. **(H)** CD44 and CD62L staining of gated WT and *Mnk1/2DKO* CD4⁺ and CD8⁺ T cells. **(I)** Mean \pm SEM presentation of cell numbers of indicated T cell populations ($n = 5$). Data shown are representative of at least three experiments.



and in protein synthesis. Given the proposed role of *Mnk1/2* in cytokine production, it is intriguing that *Mnk1/2* expression is decreased in activated T cells, in which proteins including cytokines are actively translated.

Effect of combined *Mnk1/2* deficiency on T cell development

To investigate the role of *Mnk1/2* in T cells, we analyzed mice with germline deletion of these two genes. Because individual deficiency of *Mnk1* or *Mnk2* did not affect T cell development and activation (data not shown), we examined *Mnk1/2DKO* mice. The percentages and absolute numbers of CD4 and CD8 subsets in the thymus and spleen from *Mnk1/2DKO* mice were similar to those from WT control mice (Fig. 2A–D). The overall thymic and splenic cellularities in *Mnk1/2DKO* mice were also comparable to WT mice (Fig. 2E). To examine the role of *Mnk1/2* in T cell development, we generated *Mnk1/2DKO* mice carrying the OT1 TCR transgene, which directs CD8 T cell development. As shown in Figure 2F, thymocyte numbers were not obviously different between *Mnk1/2DKO* OT1 mice and WT OT1, supporting a minimal role of *Mnk1/2* in intrathymic T cell development. *Mnk1/2DKO* mice did not display an obvious alteration in natural regulatory T cell numbers as compared with WT controls (Fig. 2G). Furthermore, CD44 and CD62L staining showed similar naive and effector T cell populations in WT and *Mnk1/2DKO* mice (Fig. 2H, 2I). These observations indicate that *Mnk1/2* double deficiency does not cause obvious defects in T cell development or homeostasis.

Mnk1/2 are required for TCR induced eIF4E phosphorylation

As mentioned above, TCR engagement induced eIF4E phosphorylation at S209. To determine whether such phosphorylation is dependent on *Mnk1/2*, we compared TCR-induced eIF4E phosphorylation in WT and *Mnk1/2DKO* T cells. Although eIF4E total protein was similar between WT and *Mnk1/2DKO* T cells, TCR-induced eIF4E phosphorylation was virtually abolished in *Mnk1/2DKO* T cells (Fig. 3A). On the contrary, TCR-induced phosphorylation of Erk1/2, Rsk1 (Erk1/2 substrate), and p38 were not affected by *Mnk1/2* deficiency (Fig. 3B), suggesting that *Mnk1/2* deficiency does not cause global signaling defects, and that there is no obvious negative feedback regulation of Erk1/2 and p38 by *Mnk1/2* in T cells. Binding of eIF4E to mRNA is inhibited by its association with 4E-BP1. Mammalian target of rapamycin (mTOR)

phosphorylates 4E-BP1, leading to the release of eIF4E from 4E-BP1 to initiate translation (42). Neither 4E-BP1 protein levels nor its phosphorylation was altered in *Mnk1/2*-deficient T cells compared with WT T cells (Fig. 3C), suggesting that *Mnk1/2*-mediated

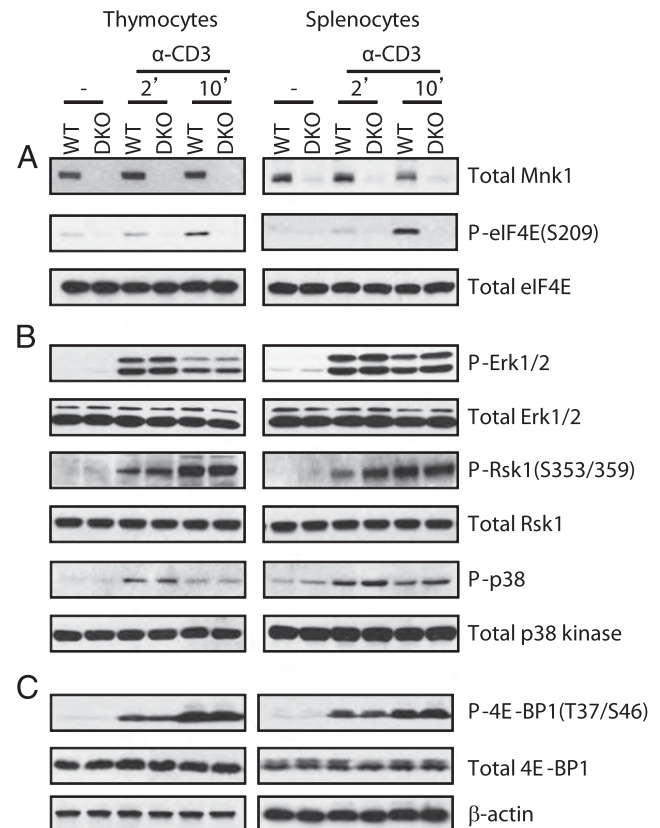


FIGURE 3. Effect of *Mnk1/2* deficiency on TCR-induced signaling. WT and *Mnk1/2DKO* thymocytes and splenocytes were similarly stimulated and analyzed by immunoblot as in Figure 1A. **(A)** *Mnk1/2* are critical for TCR-induced eIF4E phosphorylation at S209. **(B)** *Mnk1/2* deficiency does not alter Erk1/2 and p38 phosphorylation. **(C)** *Mnk1/2* deficiency does not impair mTOR-mediated 4E-BP1 phosphorylation. Data shown are representative of three experiments.

eIF4E phosphorylation does not affect 4E-BP1-mediated suppression of eIF4E or mTOR activity. These results suggest that TCR-induced eIF4E phosphorylation is mediated by Mnk1/2.

Normal *in vitro* T cell activation in the absence of Mnk1/2

To investigate whether Mnk1/2 deficiency affects T cell activation, we first examined the upregulation of early activation markers CD69 and CD25 following overnight anti-CD3 stimulation in the presence or absence of CD28-mediated costimulation. *Mnk1/2DKO* T cells upregulated CD69 and CD25 similarly to WT controls in response

to a wide range of anti-CD3 stimulation in the presence of anti-CD28 (Fig. 4A). The presence of CTLA4-Ig to block CD28-mediated costimulation decreased CD25 and CD69 upregulation in WT T cells. However, the absence of Mnk1/2 did not cause further reduction of CD25 and CD69 expression in T cells.

Mnk1/2DKO T cells also showed comparable proliferation to WT T cells following anti-CD3 stimulation for 72 h as demonstrated by a CFSE dilution assay (Fig. 4B). Moreover, *Mnk1/2DKO* CD4 and CD8 T cells produced similar levels of IFN- γ and TNF- α after stimulation for 48 h, compared with WT controls,

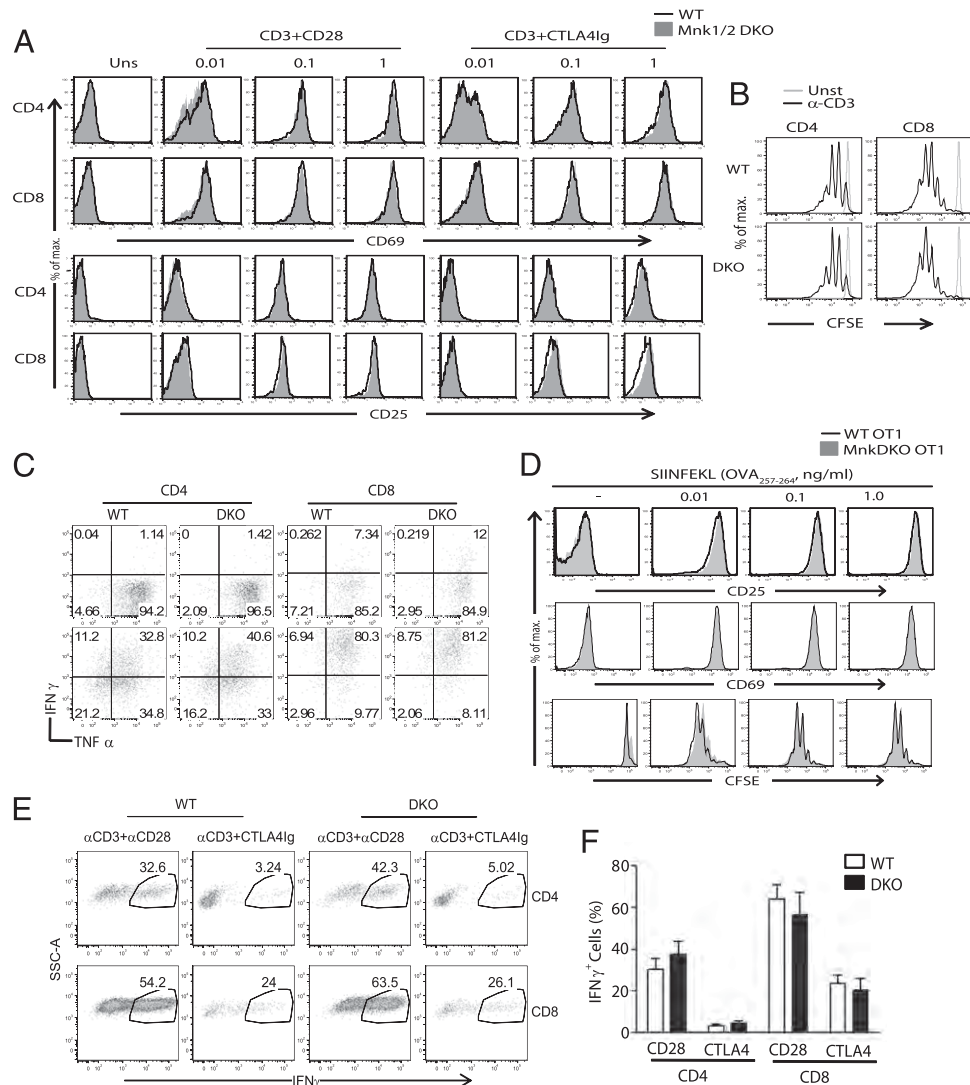


FIGURE 4. Mnk1 and Mnk2 are not essential for *in vitro* T cell activation. **(A)** Upregulation of early activation markers in *Mnk1/2DKO* T cells. WT and *Mnk1/2DKO* splenocytes were left unstimulated or stimulated overnight with an anti-CD3 Ab (2C11) at the indicated concentrations in the presence or absence of an anti-CD28 Ab (37.51, 0.5 μ g/ml) or CTLA4-Ig (10 μ g/ml). Overlaid histograms show CD69 and CD25 expression on gated CD4⁺ and CD8⁺ cells. **(B)** Mnk1/2 deficiency does not affect T cell proliferation. CFSE-labeled WT and *Mnk1/2DKO* splenocytes were unstimulated or stimulated with an anti-CD3 Ab for 72 h. Cultured cells were stained for CD4 and CD8 and analyzed by flow cytometry. Histograms show CFSE intensity on CD4⁺ and CD8⁺ cells. **(C)** Effect of Mnk1/2 deficiency on cytokine production by T cells. Splenocytes from WT or *Mnk1/2DKO* mice were left unstimulated (*top*) or stimulated with an anti-CD3 Ab (*bottom*) for 48 h, followed by PMA (50 ng/ml) and ionomycin (500 ng/ml) stimulation in the presence of a GolgiPlug for 5 h. Cells were stained for surface CD4 and CD8 and intracellular cytokines followed by FACS analysis. IFN- γ and TNF- α expression in gated CD4⁺ and CD8⁺ T cells are shown. **(D)** Mnk1/2 deficiency does not affect OT1 T cell proliferation. Splenocytes from WT OT1 and *Mnk1/2DKO* OT1 mice were either labeled or not labeled with CFSE, and then treated with SIINFEKL peptide at indicated concentrations for 18 or 72 h to assess early T cell activation and proliferation, respectively. Overlaid histograms show CD25 and CD69, and CFSE intensity on live-gated CD8⁺V α 2⁺ T cells. **(E and F)** WT and *Mnk1/2DKO* splenocytes were stimulated with anti-CD3 in the presence or either anti-CD28 (0.5 μ g/ml) or CTLA4-Ig (10 μ g/ml) at 37°C for 48 h. After resting for 24 h, live T cells were restimulated with plate-bound anti-CD3 (1 μ g/ml) and soluble anti-CD28 (0.5 μ g/ml) in the presence of 5 μ M GolgiPlug at 37°C for 24 h. Cells were surface stained for CD4 and CD8 and intracellularly stained for IFN- γ . FACS plots show IFN- γ expression in live gated CD4 and CD8 T cells (E). Bar graph is mean \pm SEM presentation of percentages of IFN- γ ⁺ cells in the indicated populations of cells ($n = 3$). Data shown are representative of three experiments.

based on intracellular staining (Fig. 4C). To study the effect of Mnk1/2 deficiency on Ag-specific T cell activation, we used OT1 T cells, which express the $V\alpha 2^+V\beta 5^+$ TCR and recognize the OVA_{257–264} (SIINFEKL) epitope of OVA presented on H-2K^b. When stimulated with different concentrations of OVA_{257–264} peptide, *Mnk1/2DKO* OT1 T cells upregulated CD25 and CD69, and proliferated similarly to WT OT1 T cells (Fig. 4D). These data indicate that Mnk1/2 double deficiency does not obviously affect T cell activation *in vitro*.

As mentioned earlier, mTORC1 phosphorylates 4E-BP1 to promote eIF4E-mediated translation initiation. Decreased mTORC1 activity causes T cell anergy while enhanced mTORC1 activity leads to resistance to anergy (43–45). We asked further whether Mnk1/2-mediated phosphorylation of eIF4E has a role in T cell anergy. We stimulated WT and *Mnk1/2DKO* splenocytes with anti-CD3 in the presence of CTLA4-Ig to block CD28-mediated costimulation for 48 h. After an additional 24 h of resting, live T cells were restimulated by plate bound anti-CD3 and soluble anti-CD28 overnight, followed by intracellular staining for IFN- γ . As shown in Figure 4E and 4F, similar IFN- γ levels were detected in WT and *Mnk1/2DKO* T cells under anergic conditions, suggesting that Mnk1/2 deficiency does not obviously affect T cell sensitivity to anergy induction *in vitro*.

Minimal effect of Mnk1/2 deficiency on Th differentiation *in vitro*

Using a Mnk1/2 inhibitor, a recent study has implicated Mnk1/2 in IL-17 production by T cells (26). We examined whether deficiency of Mnk1/2 affected Th differentiation. Sorted naive WT and *Mnk1/2DKO* CD4 T cells were subjected to *in vitro* Th1, Th2, Th17, and Th9 differentiation. Intracellular staining was used to assess the production of IFN- γ , IL-17, and IL-9 under different skewing conditions, while IL-4 levels were measured by ELISA. As shown in Figure 5, no obvious difference was observed between WT and *Mnk1/2DKO* T cells in the production of these cytokines. These observations suggest that Mnk1/2 and Mnk1/2-mediated eIF4E phosphorylation are dispensable for Th differentiation *in vitro*.

Mnk1/2 deficiency may impair Th1 and Th17 differentiation *in vivo* in the EAE model

To determine whether Mnk1/2 deficiency could affect CD4 cell differentiation *in vivo*, we used the EAE model because the differentiation of CD4 cells into Th1 and particularly into Th17 lineage is known to have an important role in the pathogenesis of

the disease (46). Spleens and draining lymph nodes from WT and *Mnk1/2DKO* mice immunized with MOG_{35–55} peptide emulsified in CFA showed comparable total cellularity and frequency of CD4 cells 1 wk after immunization (Fig. 6A). When Ag-specific cells were expanded by *ex vivo* stimulation of lymph node cells with MOG_{35–55} for 3 d, stimulation with PMA and ionomycin revealed a marked reduction in the frequency of *Mnk1/2DKO* CD4 T cells that were able to produce IL-17A or IFN- γ (Fig. 6B). Bearing in mind our previous results that Mnk1/2-deficient T cells survive and proliferate similar to WT counterparts (Fig. 4), the reduction in the IFN- γ -producing and IL-17A-producing pools of Ag-specific cells suggests that the absence of Mnk1/2 might somehow impair the differentiation of CD4 T cells into Th1 and Th17 cells in response to Ag stimulation *in vivo*. Correlating with the smaller pool of IFN- γ -producing and IL-17A-producing cells, mice deficient in Mnk1/2 developed milder EAE disease than WT counterparts (Fig. 6C). These results suggest that Mnk1/2 deficiency impairs Th1 and Th17 differentiation *in vivo* to perturb disease development in the EAE model.

Combined Mnk1/2 deficiency does not affect CD8 T cell response to *L. monocytogenes* infection *in vivo*

The data described above have revealed that Mnk1 and Mnk2 are dispensable for T cell activation *in vitro*. We used the *L. monocytogenes* infection model to determine whether Mnk1/2 is required for T cell responses *in vivo*. Equal numbers of sorted naive WT (Thy1.1⁺) and *Mnk1/2DKO* (Thy1.2⁺) $V\alpha 2^+CD8^+$ OT1 cells were mixed and coinjected *i.v.* into WT Thy1.1⁺Thy1.2⁺ recipient mice. Recipients were subsequently infected with LM-OVA (Fig. 7A, 7B). Expansion of OVA-specific OT1 T cells was monitored in the peripheral blood and spleen on days 7 and 14 after LM-OVA infection. No significant difference was observed in the frequency of WT (Thy1.1⁺) and *Mnk1/2DKO* (Thy1.2⁺) OT1 cells in the recipient mice 7 and 14 d after infection (Fig. 7C, 7D). These results suggest that Mnk1/2 might not have a critical role in the expansion and early contraction phases of Ag-specific CD8 T cell responses, at least in the LM-OVA model.

Mnk1/2-deficient mice mount normal primary and memory CD8 responses to LCMV infection

We next sought to better understand the effects of Mnk1/2 deficiency on polyclonal primary and memory CD8 T cell responses to viral infection. To this end, we infected WT and *Mnk1/2DKO* mice with the Armstrong strain of LCMV that causes acute infection (Fig. 8A). We then examined by flow cytometry at 1, 2, and 4 wk

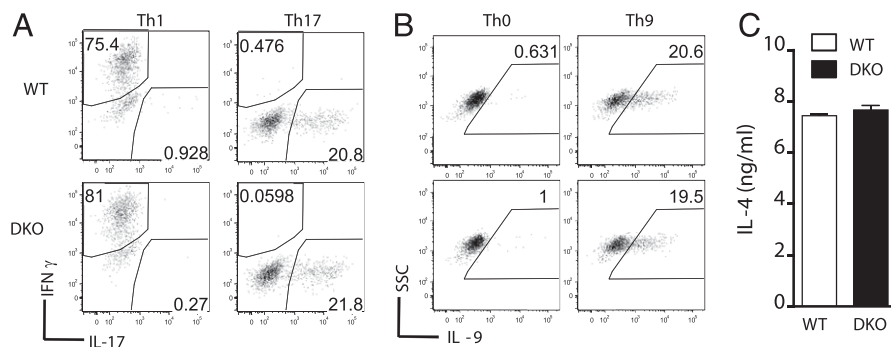
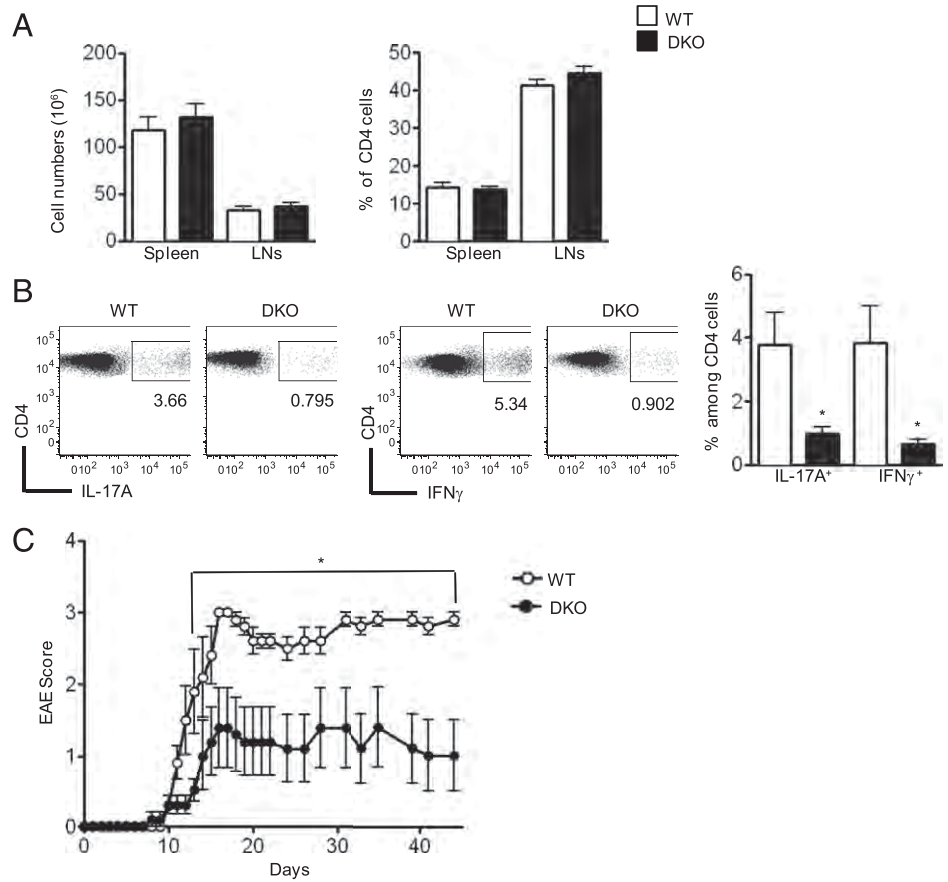


FIGURE 5. Combined Mnk1/2 deficiency does not affect Th differentiation *in vitro*. CD4⁺CD62L⁺ naive CD4 T cells sorted from WT and *Mnk1/2DKO* spleen and LNs were subjected to *in vitro* Th skewing conditions. PMA, ionomycin, and GolgiPlug were added to the culture during the last 5 h of differentiation. At the end of culture, cells were stained with anti-CD4, Live/Dead, and indicated cytokines. Dot plots show IFN- γ and IL-17 staining on gated live CD4 T cells under Th1 or Th17 skewing conditions (**A**) and IL-9 staining under Th0 and Th9 skewing conditions (**B**). IL-4 production by T cells that were under a Th2 skewing condition was determined by ELISA of culture supernatants (**C**). All data shown are representative of at least three experiments.

FIGURE 6. Mnk1/2 deficiency can impair Th1 and Th17 differentiation in vivo. **(A)** Total cell numbers in the spleen and LNs and percentages of CD4 T cells in these organs in WT and *Mnk1/2DKO* mice 7 d after immunization with MOG and CFA. **(B)** IL-17A and IFN- γ -producing cells within CD4 T cells following MOG peptide stimulation for 3 d ex vivo. Dot plots show IFN- γ and IL-17A expression in gated CD4 T cells. Bar graph represents mean \pm SEM of IFN- γ and IL-17A producing cells within CD4 T cells from multiple mice ($n = 6$). **(C)** EAE score of immunized WT and *Mnk1/2DKO* mice monitored at indicated time points and scored as indicated in *Materials and Methods* ($n = 5$). Mean \pm SEM are calculated for the indicated number of mice per group. Data shown are representative of two or more independent experiments. * $p < 0.05$.



after infection the frequency of CD8 cells in the peripheral blood that could recognize the LCMV GP33–41 peptide presented on H-2D^b tetramers (TetG⁺ cells). Our results showed that the fre-

quencies of TetG⁺ cells were comparable in WT and *Mnk1/2DKO* mice at these time points (Fig. 8B, 8C). Similar results were obtained when we determined the frequency of CD8 T cells that

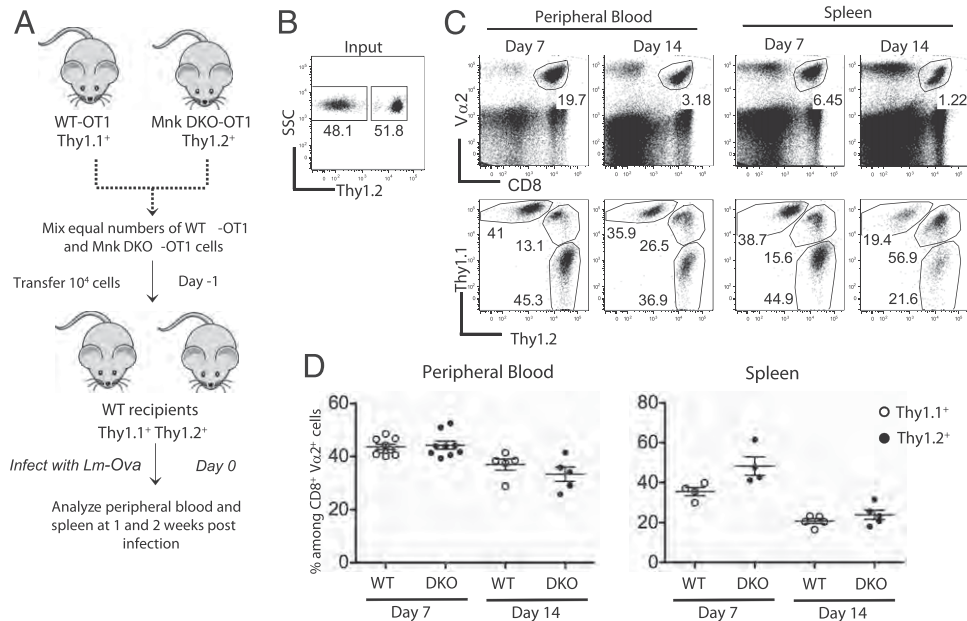
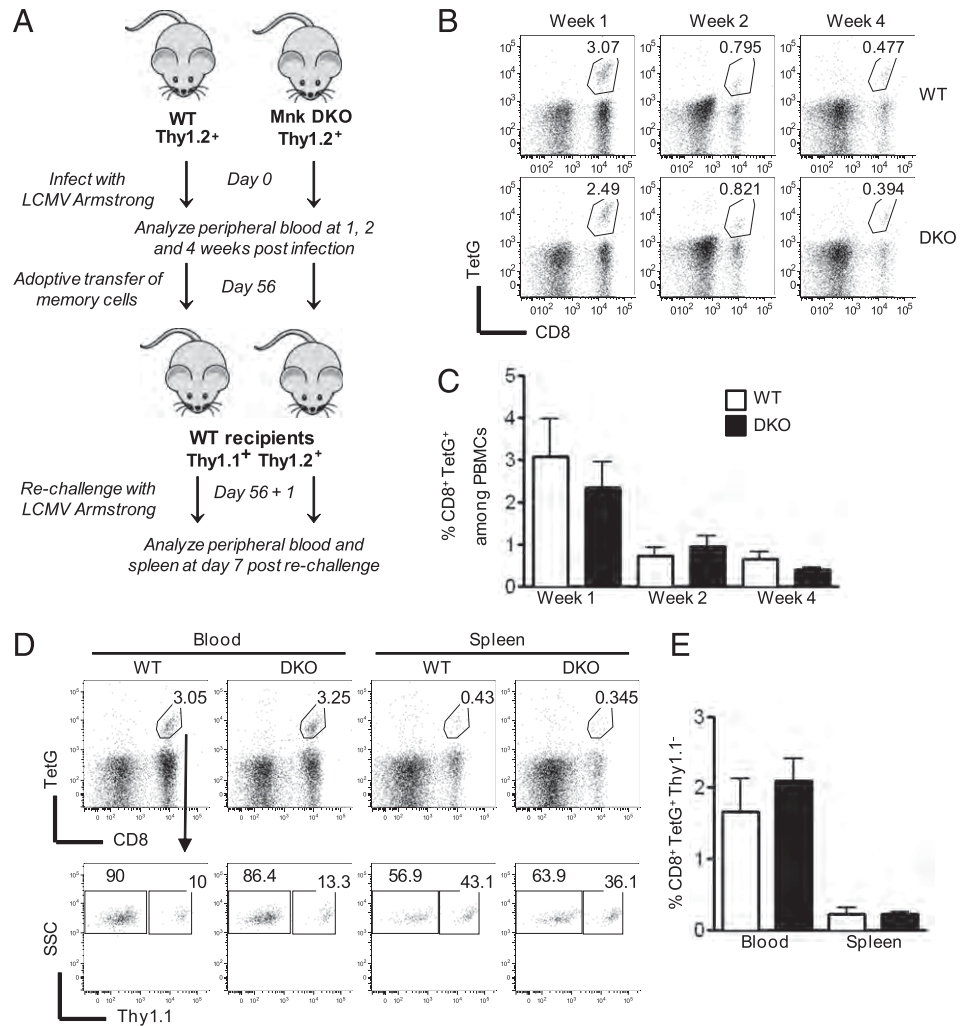


FIGURE 7. Combined Mnk1/2 deficiency does not affect Ag-specific primary CD8 T cell responses in vivo. **(A)** Schematic representation of experimental design showing competitive adoptive transfer of WT Thy1.1⁺ and *Mnk1/2DKO* Thy1.2⁺ OT1 T cells, and the LM-OVA infection model. **(B)** Thy1.1 and Thy1.2 staining of mixture of sorted naive WT and *Mnk1/2DKO* OT1 cells before injection. **(C)** Representative FACS analysis of peripheral blood and splenocytes detecting V α 2⁺ CD8 T cells (top panels), and Thy1.1/Thy1.2 congenic markers within the gated V α 2⁺CD8⁺ T cell population at indicated time points after infection. **(D)** Percentages of WT OT1 (Thy1.1⁺) and *Mnk1/2DKO* OT1 (Thy1.2⁺) cells among total V α 2⁺CD8⁺ cells in the peripheral blood and spleen. Mean \pm SEM was calculated after correcting for the input ratio. Each dot represents one mouse. Data shown are representative of three independent experiments.

FIGURE 8. Mnk1/2 deficiency does not affect primary or memory antiviral CD8 responses in vivo. **(A)** Schematic representation of experimental design showing primary infection with LCMV Armstrong, adoptive transfer of memory cells, and rechallenge. **(B and C)** Primary response. **(B)** Representative FACS plots of peripheral blood samples obtained at indicated time points and stained with anti-CD8 Ab and TetG. **(C)** Mean \pm SEM presentation of percentages of CD8⁺TetG⁺ cells in the peripheral blood at the indicated time points ($n = 6$ WT; $n = 7$ Mnk1/2DKO). **(D and E)** Recall response. **(D)** Representative FACS plots of peripheral blood and spleen samples from recipient mice that received WT or Mnk1/2DKO memory cells. *Top panels* show CD8 and TetG staining of peripheral blood and splenocytes. *Bottom panels* show Thy1.1 expression in the gated CD8⁺TetG⁺ population. **(E)** Mean \pm SEM presentation of percentages of CD8⁺TetG⁺Thy1.1⁻ cells in peripheral blood and spleen samples from recipient mice ($n = 5$). Data shown are representative of two independent experiments.



could recognize the LCMV NP 396–404 peptide presented on H-2D^b tetramers (data not shown). Together, these results suggest that Mnk1/2 deficiency might not alter polyclonal primary CD8 responses, at least in the LCMV model.

To understand whether Mnk1/2-deficient memory CD8 T cells generated after primary LCMV infection can respond robustly to pathogen rechallenge, we sorted out CD8⁺CD44⁺ memory cells from WT (Thy1.1⁻Thy1.2⁺) and Mnk1/2DKO (Thy1.1⁻Thy1.2⁺) mice 8 wk after infection. These memory cells were adoptively transferred into WT Thy1.1⁺Thy1.2⁺ congenic recipients after normalizing the number of TetG⁺ cells. Recipient mice were challenged the next day with LCMV Armstrong, and the memory response was examined in the peripheral blood and spleen 7 d after infection. Results from flow cytometric analysis indicated a comparable expansion of adoptively transferred (Thy1.1⁻) WT and Mnk1/2DKO TetG⁺ memory cells in the peripheral blood and spleen (Fig. 8D, 8E), suggesting that Mnk1/2-deficient memory CD8 cells can respond robustly to rechallenge. Taken together, these results support and extend those from the LM-OVA model, suggesting that Mnk1/2 function is dispensable during primary and memory CD8 responses to intracellular pathogens.

Effects of Mnk1/2 deficiency on iNKT cell development and function

The iNKT cells are a rare subset of T cells with the ability to bridge innate and adaptive immunity by rapidly producing and secreting copious amounts of cytokines. The mechanisms regul-

ating cytokine production in iNKT cells are not well understood. We have recently demonstrated that proper iNKT cell development requires tight regulation of DAG-mediated signaling. Deficiency of RasGRP1 or enhanced activation of DAG-mediated signaling owing to DGK α and ζ deficiency can lead to defects in iNKT cell development (32, 35). Because Mnk1 and Mnk2 are downstream effector molecules of the DAG-RasGRP1-Ras-Erk1/2 pathway, we investigated whether Mnk1 or Mnk2 have a role in regulating iNKT cell development. Like conventional T cells, individual or combined deficiency of Mnk1/2 did not affect the development of iNKT cells in the thymus, spleen, and liver (Fig. 9A). iNKT cell percentages and absolute numbers were similar in WT and Mnk1/2DKO mice (Fig. 9B). Further analysis of iNKT cell developmental stages based on CD44 and NK1.1 expression did not reveal obvious differences between WT and Mnk1/2DKO mice (Fig. 9A), suggesting normal development of iNKT cells in the absence of Mnk1/2.

It has been reported that inhibition of Mnk1/2 by CGP57380 decreased cytokine production from iNKT cells following α -GalCer stimulation (27). We stimulated WT and Mnk1/2DKO iNKT cells with α -GalCer in vitro for 72 h and intracellularly stained for IFN- γ and IL-17 production. The percentages of IFN- γ and IL-17–positive Mnk1/2DKO iNKT cells were similar to those of WT iNKT cells (Fig. 9C). Using a CFSE dilution assay, we also examined iNKT cell proliferation following α -GalCer stimulation for 72 h. Mnk1/2DKO iNKT cells appeared to proliferate slightly better than WT iNKT cells (Fig. 9D). These observations indicate that Mnk1 and

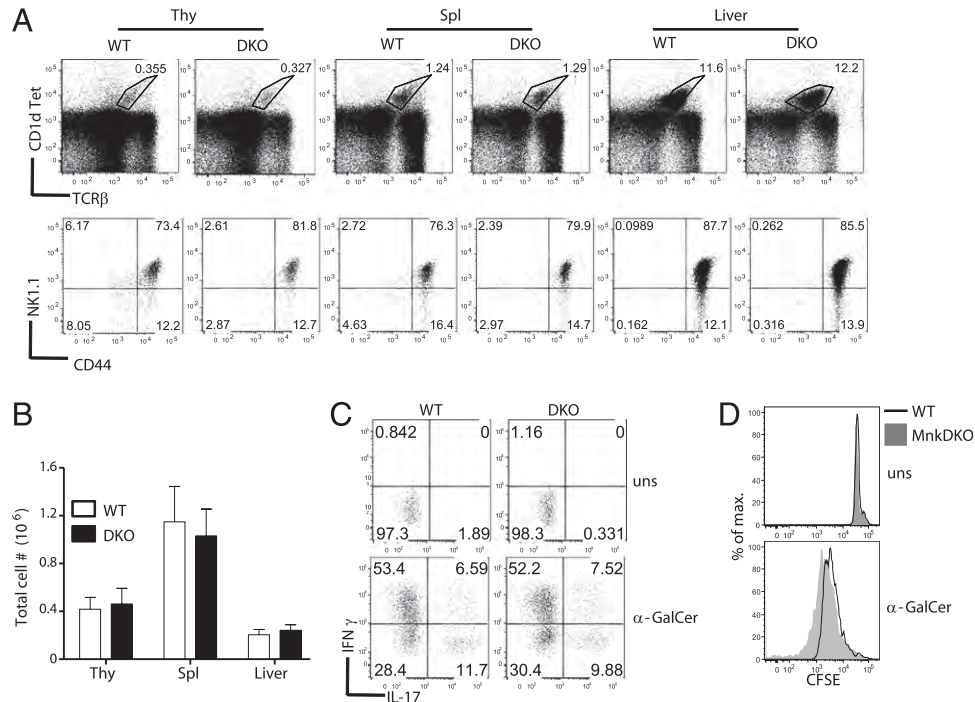


FIGURE 9. Effect of combined Mnk1/2 deficiency on *i*NKT development and activation. **(A)** Normal *i*NKT cell development in the absence of Mnk1/2. Thymocytes, splenocytes, and liver mononuclear cells from age- and sex-matched *Mnk1/2DKO* mice and WT controls were stained with CD1d-Tet, anti-TCR- β , anti-CD24, anti-CD44, and anti-NK1.1 followed by FACS analysis. *Top panels* show CD1d-Tet and anti-TCR- β staining on live cells. *Bottom panels* show NK1.1 and CD44 expression on gated CD1d-Tet⁺CD24⁻ *i*NKT cells. **(B)** Total NKT cell numbers in the indicated organs. **(C)** Mnk1 and Mnk2 are dispensable for IFN- γ and IL-17 production by *i*NKT cells. WT and *Mnk1/2DKO* thymocytes were stimulated with α -GalCer *in vitro* for 72 h with the addition of PMA, ionomycin, and GolgiPlug for the last 5 h. Cultured cells were then stained with CD1d-Tet and anti-TCR- β , and intracellularly stained with anti-IFN- γ and anti-IL-17. Dot plots show IFN- γ and IL-17 expression in live gated CD1d-Tet⁺TCR β ⁺ *i*NKT cells (*bottom panels*). **(D)** Assessment of *i*NKT cell proliferation. CFSE-labeled WT and *Mnk1/2DKO* thymocytes were left unstimulated or were stimulated with α -GalCer for 72 h. Overlaid histograms show CFSE intensity in gated WT and *Mnk1/2DKO* CD1d-Tet⁺TCR β ⁺ *i*NKT cells. Data shown are representative of three experiments.

Mnk2 are dispensable for *i*NKT cell development, production of cytokines, and proliferation.

Effects of Mnk1/2 inhibitor CGP57380 on activation of Mnk1/2 double-deficient T cells

The discrepancies between our data from Mnk1/2 double-deficient mice and those generated by chemical inhibition of Mnk1/2 with CGP57380 raise concerns about the selectivity of CGP57380 for Mnk1/2 and about the conclusions drawn from studies based on this inhibitor. To determine whether CGP57380 contains activities beyond inhibiting Mnk1/2, we examined the effects of CGP57380 on Erk1/2, Mnk1/2, and eIF4E phosphorylation following TCR engagement. As shown in Figure 10A, CGP57380 inhibited not only eIF4E phosphorylation but also Mnk1/2 phosphorylation following TCR engagement. Moreover, it inhibited both WT and Mnk1/2DKO T cell proliferation in similar magnitudes (Fig. 10B), and reduced IFN- γ but not IL-17 production in both WT and Mnk1/2DKO *i*NKT cells (Fig. 10C). These observations are consistent with the findings that CGP57380 is able to inhibit other protein kinases such as MAPK kinase-1, casein kinase 1, and brain-specific kinase 2 (47). Thus, the effects of CGP57380 on T cells might not solely be attributed to Mnk1/2.

Discussion

Mnk1 and Mnk2 are downstream substrates for the Ras-Mek1/2-Erk1/2 and MKK3/MKK6-p38 kinase pathways. The importance of these pathways in T cells, the ability of Mnk1/2 to phosphorylate eIF4E, and the extremely dynamic nature of T cells during development and immune responses raise the possibility that Mnk1 and Mnk2 could have important roles in T cells by promoting

protein translation via eIF4E regulation. Several recent studies lend credence to the idea that Mnk1/2 may be important regulators of the immune system. Inhibition of Mnk1/2 by CGP57380 has been found to reduce the translation of proinflammatory cytokines in keratinocytes (48), macrophages (28), and dendritic cells (49). CGP57380 has also been shown to decrease cytokine production by *i*NKT cells and IL-17 production in CD4⁺ T cells during Th17 differentiation (26, 27). In this report, we have demonstrated that TCR-induced Mnk1/2 activation is promoted by Ras-Erk1/2 signaling and is negatively controlled by DGK α and ζ . In addition, both Mnk1 and Mnk2 are expressed at high levels in naive T cells, but are downregulated in activated T cells. Using Mnk1/2 double-deficient mice, we have demonstrated that Mnk1 and Mnk2 are dispensable for the development of conventional $\alpha\beta$ T cells, natural regulatory T cells, and *i*NKT cells. Moreover, Mnk1/2 double deficiency does not obviously affect activation of conventional T cells and *i*NKT cells, or Th differentiation *in vitro*. The conclusion of a minimal role for Mnk1/2 in T cell activation is further strengthened by the observation that Mnk1/2 deficiency does not impair *in vivo* CD8 T cell responses in a bacterial model and a viral model of infection. Furthermore, our data also raise concerns over CGP57380 as a Mnk1/2-specific inhibitor because CGP57380 reduces eIF4E and Mnk1/2 phosphorylation following TCR engagement, inhibits both WT and Mnk1/2DKO CD4 T cell proliferation, and decreases both WT and Mnk1/2 *i*NKT cell production of IFN- γ .

Mnk1/2 deficiency does not affect Th1 or Th17 differentiation *in vitro*, suggesting that there might be no obvious intrinsic defect of Mnk1/2DKO CD4 T cells in Th differentiation. However, Th1 and Th17 differentiation is diminished in Mnk1/2DKO mice in the

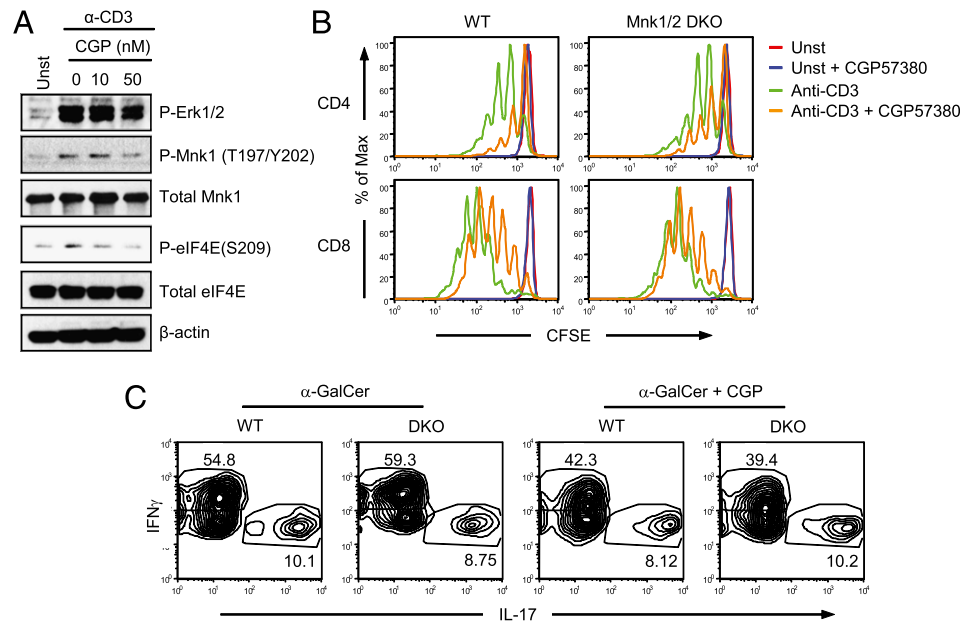


FIGURE 10. Effects of Mnk1/2 inhibitor CGP57380 on T cells. **(A)** Effects of Mnk1/2 inhibitor CGP57380 on TCR signaling. WT thymocytes were rested in PBS at 37°C for 30 min, then either left unstimulated or stimulated with an anti-CD3 ϵ Ab (500A2, 5 μ g/ml) in the presence of CGP57380 of the indicated concentrations (nM) at 37°C for 5 min. Cell lysates were subjected to immunoblotting analysis with the indicated Abs. **(B)** CGP57380 inhibits WT and Mnk1/2DKO T cell proliferation. CFSE-labeled WT and Mnk1/2DKO splenocytes were unstimulated or stimulated with anti-CD3 (2C11, 0.1 μ g/ml) in the presence or absence of CGP57380 (10 nM) at 37°C for 72 h. Cells were then stained for CD4 and CD8. Histograms show CFSE intensity of live-gated CD4 and CD8 T cells. **(C)** Effects of CGP57380 on cytokine production by WT and Mnk1/2DKO iNKT cells. WT and Mnk1/2 thymocytes were stimulated with α -GalCer (125 ng/ml) in the presence or absence of CGP57380 (10 nM) for 72 h. In the last 5 h of stimulation, cells were also treated with PMA plus ionomycin and GolgiPlug. Cells were then stained for TCR- β and CD1d-tetramer followed by intracellular staining for IFN- γ and IL-17A. Contour plots show IL-17A and IFN- γ expression in gated TCR- β^+ CD1d-tetramer $^+$ cells. Data shown represent two independent experiments.

EAE model, suggesting the possibility that Mnk1/2 deficiency affects *in vivo* Th lineage differentiation in a T cell-extrinsic manner. Additional experiments are required to explore these extrinsic mechanisms, including the possibility that Mnk1/2 functions in APCs to shape Th differentiation. This notion is supported by a recent report demonstrating that Mnk1 and Mnk2 regulate innate immune responses by modulating NF- κ B activity (50).

Signals generated from the TCR can trigger the activation of T cells from naive or resting conditions, resulting in a significant increase in transcription, protein synthesis, and DNA synthesis (51, 52). Translation is one of the early events in activated T cells that can contribute to protein synthesis. Translational control is one of the key processes by which cells can generate crucial gene products quickly from preexisting mRNA without delay that results from mRNA transcription and RNA processing (53, 54). Translation is a complex process and involves at least 10 translation initiation factors called eukaryotic translational initiation factors (eIFs), scaffolding or adaptor proteins, and 40S ribosomes. Binding of eIF4E to the mRNA is the foremost regulatory step in the formation of a preinitiation complex that further leads to the formation of complete translational machinery (19). However, how eIF4E is regulated is poorly understood. It has been proposed that recruitment of eIF4E to the 5' cap region can be controlled by at least two intracellular signaling pathways such as the PI3K-mTOR pathway (55) and the Ras-Mek-Erk1/2-Mnk1/2 and MKK3/6-p38-Mnk1/2 pathways (56, 57). 4E-BP1 binds to eIF4E, preventing its association with the 5' cap. Activation of mTOR leads to hyperphosphorylation of 4E-BP1, which results in the dissociation of eIF4E from 4E-BP1 to allow eIF4E binding to the 5' cap of mRNA to drive translation. Inhibition of mTOR results in T cell anergy, whereas deregulation of mTOR renders T cells resistant to anergy induction (43–45), suggesting that mTOR-mediated release of eIF4E from suppression by 4E-BP1 is critical

for T cell activation. Several studies have put forth a notion that Mnk1/2 signaling can regulate cap-dependent translation through phosphorylation of eIF4E at S209 (22, 58). However, the role of eIF4E phosphorylation at S209 for translation initiation has been controversial (59, 60). Similarly, the germ-line deletion of Mnk1/2 in mouse models resulted in ablation in eIF4E phosphorylation without global effects on protein translation in mouse embryonic fibroblasts. In addition, these mouse models display normal growth and development. Consistently, TCR-induced eIF4E phosphorylation is abolished in *Mnk1/2DKO* T cells, suggesting that eIF4E phosphorylation at S209 is not essential for T cell development, proliferation, activation and cytokine expression, and might not globally control protein translation in T cells. It has been demonstrated that mice that carry a non-phosphorylatable form of eIF4E (S209A) allele and Mnk1/2 double-deficient mice are more resistant to tumorigenesis. This resistance was shown to be via translational control of a specific subset of genes related to tumorigenesis, such as vascular endothelial growth factor C, baculoviral IAP repeat-containing protein 2, and matrix metalloproteinase-3 (24, 61). Although we have demonstrated that Mnk1 and Mnk2 are dispensable for T cell development and activation in general, we cannot rule out the possibility that they might be selectively required for efficient translation of specific subsets of proteins that may affect specific T cell responses.

Acknowledgments

We thank Jinhong Wu for help with iNKT cell experiments, Nancy Martin at Duke Cancer Center Flow Cytometry Core Facility for providing sorting services, and the National Institutes of Health tetramer facility for providing CD1d-Tet.

Disclosures

The authors have no financial conflicts of interest.

References

- Cantrell, D. 1996. T cell antigen receptor signal transduction pathways. *Annu. Rev. Immunol.* 14: 259–274.
- Samelson, L. E. 2002. Signal transduction mediated by the T cell antigen receptor: the role of adapter proteins. *Annu. Rev. Immunol.* 20: 371–394.
- Smith-Garvin, J. E., G. A. Koretzky, and M. S. Jordan. 2009. T cell activation. *Annu. Rev. Immunol.* 27: 591–619.
- Zhong, X. P., J. Shin, B. K. Gorentla, T. O'Brien, S. Srivatsan, L. Xu, Y. Chen, D. Xie, and H. Pan. 2011. Receptor signaling in immune cell development and function. *Immunol. Res.* 49: 109–123.
- Weiss, A. 2010. The right team at the right time to go for a home run: tyrosine kinase activation by the TCR. *Nat. Immunol.* 11: 101–104.
- Chen, Z., T. B. Gibson, F. Robinson, L. Silvestro, G. Pearson, B. Xu, A. Wright, C. Vanderbilt, and M. H. Cobb. 2001. MAP kinases. *Chem. Rev.* 101: 2449–2476.
- Kyriakis, J. M., and J. Avruch. 2001. Mammalian mitogen-activated protein kinase signal transduction pathways activated by stress and inflammation. *Physiol. Rev.* 81: 807–869.
- Cargnello, M., and P. P. Roux. 2011. Activation and function of the MAPKs and their substrates, the MAPK-activated protein kinases. *Microbiol. Mol. Biol. Rev.* 75: 50–83.
- Gaestel, M. 2008. Specificity of signaling from MAPKs to MAPKAPKs: kinases' tango nuevo. *Front. Biosci.* 13: 6050–6059.
- Anjum, R., and J. Blenis. 2008. The RSK family of kinases: emerging roles in cellular signalling. *Nat. Rev. Mol. Cell Biol.* 9: 747–758.
- Gaestel, M. 2006. MAPKAP kinases - MKs - two's company, three's a crowd. *Nat. Rev. Mol. Cell Biol.* 7: 120–130.
- Arthur, J. S. 2008. MSK activation and physiological roles. *Front. Biosci.* 13: 5866–5879.
- Buxade, M., J. L. Parra-Palau, and C. G. Proud. 2008. The Mnk: MAP kinase-interacting kinases (MAP kinase signal-integrating kinases). *Front. Biosci.* 13: 5359–5373.
- Fukunaga, R., and T. Hunter. 1997. MNK1, a new MAP kinase-activated protein kinase, isolated by a novel expression screening method for identifying protein kinase substrates. *EMBO J.* 16: 1921–1933.
- Morley, S. J., and L. McKendrick. 1997. Involvement of stress-activated protein kinase and p38/RK mitogen-activated protein kinase signaling pathways in the enhanced phosphorylation of initiation factor 4E in NIH 3T3 cells. *J. Biol. Chem.* 272: 17887–17893.
- Wang, X., A. Flynn, A. J. Waskiewicz, B. L. Webb, R. G. Vries, I. A. Baines, J. A. Cooper, and C. G. Proud. 1998. The phosphorylation of eukaryotic initiation factor eIF4E in response to phorbol esters, cell stresses, and cytokines is mediated by distinct MAP kinase pathways. *J. Biol. Chem.* 273: 9373–9377.
- Waskiewicz, A. J., A. Flynn, C. G. Proud, and J. A. Cooper. 1997. Mitogen-activated protein kinases activate the serine/threonine kinases Mnk1 and Mnk2. *EMBO J.* 16: 1909–1920.
- Ueda, T., R. Watanabe-Fukunaga, H. Fukuyama, S. Nagata, and R. Fukunaga. 2004. Mnk2 and Mnk1 are essential for constitutive and inducible phosphorylation of eukaryotic initiation factor 4E but not for cell growth or development. *Mol. Cell Biol.* 24: 6539–6549.
- Gingras, A. C., B. Raught, and N. Sonenberg. 1999. eIF4 initiation factors: effectors of mRNA recruitment to ribosomes and regulators of translation. *Annu. Rev. Biochem.* 68: 913–963.
- Pause, A., G. J. Belsham, A. C. Gingras, O. Donzé, T. A. Lin, J. C. Lawrence, Jr., and N. Sonenberg. 1994. Insulin-dependent stimulation of protein synthesis by phosphorylation of a regulator of 5'-cap function. *Nature* 371: 762–767.
- Merrick, W. C. 2004. Cap-dependent and cap-independent translation in eukaryotic systems. *Gene* 332: 1–11.
- Pyronnet, S., H. Imataka, A. C. Gingras, R. Fukunaga, T. Hunter, and N. Sonenberg. 1999. Human eukaryotic translation initiation factor 4G (eIF4G) recruits mnk1 to phosphorylate eIF4E. *EMBO J.* 18: 270–279.
- Arquier, N., M. Bourouis, J. Colombani, and P. Léopold. 2005. Drosophila Lk6 kinase controls phosphorylation of eukaryotic translation initiation factor 4E and promotes normal growth and development. *Curr. Biol.* 15: 19–23.
- Ueda, T., M. Sasaki, A. J. Elia, I. I. Chio, K. Hamada, R. Fukunaga, and T. W. Mak. 2010. Combined deficiency for MAP kinase-interacting kinase 1 and 2 (Mnk1 and Mnk2) delays tumor development. *Proc. Natl. Acad. Sci. USA* 107: 13984–13990.
- Mavrakis, K. J., H. Zhu, R. L. Silva, J. R. Mills, J. Teruya-Feldstein, S. W. Lowe, W. Tam, J. Pelletier, and H. G. Wendel. 2008. Tumorigenic activity and therapeutic inhibition of Rheb GTPase. *Genes Dev.* 22: 2178–2188.
- Noubade, R., D. N. Kremontsov, R. Del Rio, T. Thornton, V. Nagaleekar, N. Saligrama, A. Spitzack, K. Spach, G. Sabio, R. J. Davis, et al. 2011. Activation of p38 MAPK in CD4 T cells controls IL-17 production and autoimmune encephalomyelitis. *Blood* 118: 3290–3300.
- Nagaleekar, V. K., G. Sabio, I. Aktan, A. Chant, I. W. Howe, T. M. Thornton, P. J. Benoit, R. J. Davis, M. Rincon, and J. E. Boyson. 2011. Translational control of NKT cell cytokine production by p38 MAPK. *J. Immunol.* 186: 4140–4146.
- Rowlett, R. M., C. A. Chrestensen, M. Nyce, M. G. Harp, J. W. Pelo, F. Cominelli, P. B. Ernst, T. T. Pizarro, T. W. Sturgill, and M. T. Worthington. 2008. MNK kinases regulate multiple TLR pathways and innate proinflammatory cytokines in macrophages. *Am. J. Physiol. Gastrointest. Liver Physiol.* 294: G452–G459.
- Zhong, X. P., R. Guo, H. Zhou, C. Liu, and C. K. Wan. 2008. Diacylglycerol kinases in immune cell function and self-tolerance. *Immunol. Rev.* 224: 249–264.
- Jackson, E. L., N. Willis, K. Mercer, R. T. Bronson, D. Crowley, R. Montoya, T. Jacks, and D. A. Tuveson. 2001. Analysis of lung tumor initiation and progression using conditional expression of oncogenic K-ras. *Genes Dev.* 15: 3243–3248.
- Gorentla, B. K., C. K. Wan, and X. P. Zhong. 2011. Negative regulation of mTOR activation by diacylglycerol kinases. *Blood* 117: 4022–4031.
- Shen, S., J. Wu, S. Srivatsan, B. K. Gorentla, J. Shin, L. Xu, and X. P. Zhong. 2011. Tight regulation of diacylglycerol-mediated signaling is critical for proper invariant NKT cell development. *J. Immunol.* 187: 2122–2129.
- Zhong, X. P., E. A. Hainey, B. A. Olenchock, M. S. Jordan, J. S. Maltzman, K. E. Nichols, H. Shen, and G. A. Koretzky. 2003. Enhanced T cell responses due to diacylglycerol kinase zeta deficiency. *Nat. Immunol.* 4: 882–890.
- Olenchock, B. A., R. Guo, J. H. Carpenter, M. Jordan, M. K. Topham, G. A. Koretzky, and X. P. Zhong. 2006. Disruption of diacylglycerol metabolism impairs the induction of T cell energy. *Nat. Immunol.* 7: 1174–1181.
- Shen, S., Y. Chen, B. K. Gorentla, J. Lu, J. C. Stone, and X. P. Zhong. 2011. Critical roles of RasGRP1 for invariant NKT cell development. *J. Immunol.* 187: 4467–4473.
- O'Brien, T. F., B. K. Gorentla, D. Xie, S. Srivatsan, I. X. McLeod, Y. W. He, and X. P. Zhong. 2011. Regulation of T-cell survival and mitochondrial homeostasis by TSC1. *Eur. J. Immunol.* 41: 3361–3370.
- Dudani, R., Y. Chapdelaine, H. Faassen Hv, D. K. Smith, H. Shen, L. Krishnan, and S. Sad. 2002. Multiple mechanisms compensate to enhance tumor-protective CD8⁽⁺⁾ T cell response in the long-term despite poor CD8⁽⁺⁾ T cell priming initially: comparison between an acute versus a chronic intracellular bacterium expressing a model antigen. *J. Immunol.* 168: 5737–5745.
- Ahmed, R., A. Salmi, L. D. Butler, J. M. Chiller, and M. B. Oldstone. 1984. Selection of genetic variants of lymphocytic choriomeningitis virus in spleens of persistently infected mice. Role in suppression of cytotoxic T lymphocyte response and viral persistence. *J. Exp. Med.* 160: 521–540.
- Shin, J., T. F. O'Brien, J. M. Grayson, and X. P. Zhong. 2012. Differential regulation of primary and memory CD8 T cell immune responses by diacylglycerol kinases. *J. Immunol.* 188: 2111–2117.
- Guo, R., C. K. Wan, J. H. Carpenter, T. Mousallem, R. M. Boustany, C. T. Kuan, A. W. Burks, and X. P. Zhong. 2008. Synergistic control of T cell development and tumor suppression by diacylglycerol kinase alpha and zeta. *Proc. Natl. Acad. Sci. USA* 105: 11909–11914.
- Zhong, X. P., E. A. Hainey, B. A. Olenchock, H. Zhao, M. K. Topham, and G. A. Koretzky. 2002. Regulation of T cell receptor-induced activation of the Ras-ERK pathway by diacylglycerol kinase zeta. *J. Biol. Chem.* 277: 31089–31098.
- Richter, J. D., and N. Sonenberg. 2005. Regulation of cap-dependent translation by eIF4E inhibitory proteins. *Nature* 433: 477–480.
- Xie, D. L., J. Wu, Y. L. Lou, and X. P. Zhong. 2012. Tumor suppressor TSC1 is critical for T-cell energy. *Proc. Natl. Acad. Sci. USA* 109: 14152–14157.
- Zhong, X. P. 2012. An expanded role of the tumor suppressor TSC1 in T cell tolerance. *Cell Cycle* 11: 3909–3910.
- Zheng, Y., S. L. Collins, M. A. Lutz, A. N. Allen, T. P. Kole, P. E. Zarek, and J. D. Powell. 2007. A role for mammalian target of rapamycin in regulating T cell activation versus energy. *J. Immunol.* 178: 2163–2170.
- Pierson, E., S. B. Simmons, L. Castelli, and J. M. Goverman. 2012. Mechanisms regulating regional localization of inflammation during CNS autoimmunity. *Immunol. Rev.* 248: 205–215.
- Bain, J., L. Plater, M. Elliott, N. Shpiro, C. J. Hastie, H. McLauchlan, I. Klevernic, J. S. Arthur, D. R. Alessi, and P. Cohen. 2007. The selectivity of protein kinase inhibitors: a further update. *Biochem. J.* 408: 297–315.
- Kjellerup, R. B., K. Kragballe, L. Iversen, and C. Johansen. 2008. Pro-inflammatory cytokine release in keratinocytes is mediated through the MAPK signal-integrating kinases. *Exp. Dermatol.* 17: 498–504.
- Mikkelsen, S. S., S. B. Jensen, S. Chiliveru, J. Melchjorsen, I. Julkunen, M. Gaestel, J. S. Arthur, R. A. Flavell, S. Ghosh, and S. R. Paludan. 2009. RIG-I-mediated activation of p38 MAPK is essential for viral induction of interferon and activation of dendritic cells: dependence on TRAF2 and TAK1. *J. Biol. Chem.* 284: 10774–10782.
- Herdy, B., M. Jaramillo, Y. V. Svitkin, A. B. Rosenfeld, M. Kobayashi, D. Walsh, T. Alain, P. Sean, N. Robichaud, I. Topisirovic, et al. 2012. Translational control of the activation of transcription factor NF- κ B and production of type I interferon by phosphorylation of the translation factor eIF4E. *Nat. Immunol.* 13: 543–550.
- Cooper, H. L. 1969. Ribosomal ribonucleic acid production and growth regulation in human lymphocytes. *J. Biol. Chem.* 244: 1946–1952.
- Crabtree, G. R., and N. A. Clipstone. 1994. Signal transmission between the plasma membrane and nucleus of T lymphocytes. *Annu. Rev. Biochem.* 63: 1045–1083.
- Gebauer, F., and M. W. Hentze. 2004. Molecular mechanisms of translational control. *Nat. Rev. Mol. Cell Biol.* 5: 827–835.
- Sonenberg, N., and A. G. Hinnebusch. 2009. Regulation of translation initiation in eukaryotes: mechanisms and biological targets. *Cell* 136: 731–745.
- Gingras, A. C., B. Raught, and N. Sonenberg. 2001. Regulation of translation initiation by FRAP/mTOR. *Genes Dev.* 15: 807–826.
- Panja, D., G. Dageyte, M. Bidinosti, K. Wibrand, A. M. Kristiansen, N. Sonenberg, and C. R. Bramham. 2009. Novel translational control in Arc-dependent long term potentiation consolidation in vivo. *J. Biol. Chem.* 284: 31498–31511.
- Chen, Y. J., B. C. Tan, Y. Y. Cheng, J. S. Chen, and S. C. Lee. 2010. Differential regulation of CHOP translation by phosphorylated eIF4E under stress conditions. *Nucleic Acids Res.* 38: 764–777.

58. Pyronnet, S. 2000. Phosphorylation of the cap-binding protein eIF4E by the MAPK-activated protein kinase Mnk1. *Biochem. Pharmacol.* 60: 1237–1243.
59. Scheper, G. C., and C. G. Proud. 2002. Does phosphorylation of the cap-binding protein eIF4E play a role in translation initiation? *Eur. J. Biochem.* 269: 5350–5359.
60. McKendrick, L., S. J. Morley, V. M. Pain, R. Jagus, and B. Joshi. 2001. Phosphorylation of eukaryotic initiation factor 4E (eIF4E) at Ser209 is not required for protein synthesis in vitro and in vivo. *Eur. J. Biochem.* 268: 5375–5385.
61. Furic, L., L. Rong, O. Larsson, I. H. Koumakpayi, K. Yoshida, A. Brueschke, E. Petroulakis, N. Robichaud, M. Pollak, L. A. Gaboury, et al. 2010. eIF4E phosphorylation promotes tumorigenesis and is associated with prostate cancer progression. *Proc. Natl. Acad. Sci. USA* 107: 14134–14139.

Sprouty Proteins Are Negative Regulators of Interferon (IFN) Signaling and IFN-inducible Biological Responses^{*[5]}

Received for publication, July 16, 2012, and in revised form, October 5, 2012. Published, JBC Papers in Press, October 16, 2012, DOI 10.1074/jbc.M112.400721

Bhumika Sharma[‡], Sonali Joshi[‡], Antonella Sassano[‡], Beata Majchrzak[§], Surinder Kaur[‡], Priya Aggarwal[‡], Behnam Nabet[‡], Marinka Bulic[‡], Brady L. Stein[‡], Brandon McMahon[‡], Darren P. Baker[¶], Rikiro Fukunaga^{||}, Jessica K. Altman^{***}, Jonathan D. Licht[‡], Eleanor N. Fish^{§1}, and Leonidas C. Platanias^{‡***2}

From the [‡]Robert H. Lurie Comprehensive Cancer Center and Division of Hematology-Oncology, Feinberg School of Medicine, Northwestern University, Chicago, Illinois 60611, the ^{**}Division of Hematology-Oncology, Department of Medicine, Jesse Brown Veterans Affairs Medical Center, Chicago, Illinois 60612, the [§]Toronto General Research Institute, University Health Network and Department of Immunology, University of Toronto, Toronto, Ontario M5G 2M1, Canada, [¶]Biogen Idec Incorporated, Cambridge, Massachusetts 02142, and the ^{||}Laboratory of Biochemistry, Osaka University of Pharmaceutical Sciences, Osaka 569-1094, Japan

Background: The potential involvement of Spry proteins in IFN signaling is unknown.

Results: Type I IFN treatment results in up-regulation of Spry proteins, which negatively control generation of IFN responses.

Conclusion: Spry proteins play important regulatory roles in IFN signaling and the generation of the biological effects of IFNs.

Significance: This study provides evidence for the existence of a key signaling pathway that controls IFN responses.

Interferons (IFNs) have important antiviral and antineoplastic properties, but the precise mechanisms required for generation of these responses remain to be defined. We provide evidence that during engagement of the Type I IFN receptor (IFNR), there is up-regulation of expression of Sprouty (Spry) proteins 1, 2, and 4. Our studies demonstrate that IFN-inducible up-regulation of Spry proteins is Mnk kinase-dependent and results in suppressive effects on the IFN-activated p38 MAP kinase (MAPK), the function of which is required for transcription of interferon-stimulated genes (ISGs). Our data establish that ISG15 mRNA expression and IFN-dependent antiviral responses are enhanced in Spry1,2,4 triple knock-out mouse embryonic fibroblasts, consistent with negative feedback regulatory roles for Spry proteins in IFN-mediated signaling. In other studies, we found that siRNA-mediated knockdown of Spry1, Spry2, or Spry4 promotes IFN-inducible antileukemic effects *in vitro* and results in enhanced suppressive effects on malignant hematopoietic progenitors from patients with polycythemia vera. Altogether, our findings demonstrate that Spry proteins are potent regulators of Type I IFN signaling and negatively control induction of Type I IFN-mediated biological responses.

Due to the important biological effects of interferons (IFNs) (1–3) and the clinical efficacy of these cytokines in the treatment of various diseases (4), there has been a substantial inter-

est in defining cellular pathways activated by IFN receptors and dissecting their contributions in the generation of the biological effects of IFNs. Although IFNs were originally discovered and described as agents that block replication of different viruses (1–3), subsequent work established that they also act as modulators of innate immune responses and exhibit important growth inhibitory and antineoplastic properties (1–3). Three major IFN groups exist, each of which includes different subgroups and members. These include Type I (α , β , ω , τ , κ , ϵ , and δ); Type II (γ); and the more recently identified class of Type III IFNs ($\lambda 1$, $\lambda 2$, and $\lambda 3$) (1–6). All different IFN classes utilize Jak-Stat pathways to activate elements in the promoters of IFN-stimulated genes (ISGs)³ promoting transcriptional activation and induction of gene expression (7, 8). Common and distinct combinations of receptor-associated Jak kinases and Stat proteins are engaged by Type I, II, and III IFN receptors, and in each case, the coordinated functions of Jak-Stat pathways are essential for ultimate generation of ISG products and associated biological responses (1, 3, 7, 8). Importantly, there is also evidence that unphosphorylated Stats exhibit important functions as transcription factors, as well as modifiers of transcription factors and chromatin structure (9).

In addition to classical Jak-Stat pathways, other signaling cascades engaged by IFN receptors are essential for optimal transcriptional activation and mRNA translation of ISGs, and ultimately, the generation of IFN biological responses. The p38 MAP kinase (MAPK) pathway is activated in parallel to Jak-Stat pathways, and its function is essential for IFN-dependent gene transcription (10, 11), whereas the AKT/mTOR (mammalian target of rapamycin) signaling cascade is also engaged by IFN receptors and is required for mRNA translation of ISGs and ultimate production of ISG proteins (12–15). Other studies have shown that IFN-dependent engagement of the Erk MAP

^{*} This work was supported, in whole or in part, by National Institutes of Health Grants CA155566, CA77816, and CA161796 (to L. C. P.). This work was also supported by a Merit Review grant from the Department of Veterans Affairs (to L. C. P.); by the Lynn Sage Foundation (to J. D. L.); and by Canadian Institutes of Health Research Grant 285791 (to E. N. F.).

^[5] This article contains supplemental Fig. S1.

¹ A Canada Research Chair.

² To whom correspondence should be addressed: Robert H. Lurie Comprehensive Cancer Center, 303 East Superior St., Lurie 3-107, Chicago, IL 60611. Tel.: 312-503-4267; Fax: 312-908-1372; E-mail: l-platanias@northwestern.edu.

³ The abbreviations used are: ISG, IFN-stimulated gene; Spry, Sprouty; mSpry, mouse Spry; MEF, mouse embryonic fibroblast; BFU-E, burst-forming unit, erythroid; CFU-L, colony-forming unit, lymphocyte; Mkk, Map kinase kinase; Mnk, MAPK-interacting kinase.

kinase pathway participates in ISG mRNA translation/protein expression via regulatory effects on the activation of Mnk kinases and eIF4E phosphorylation (16, 17).

In the present study, we provide the first evidence for engagement of Sprouty (Spry) proteins in IFN signaling. The family of Spry proteins includes four members (18–20), all of which are homologues of the *Drosophila melanogaster* Spry, which was originally identified as an inhibitor of FGF signaling (21). These proteins act as negative regulators of growth factor signaling pathways (18–20, 22), and their expression is deregulated in several malignancies (20). Our studies demonstrate that treatment of sensitive cells with IFN α or IFN β results in stabilization/up-regulation of expression of Spry proteins in a Mnk kinase-dependent manner. IFN-activated Spry proteins act as negative feedback regulators and exhibit inhibitory effects on the p38 MAPK pathway and ISG expression. This leads to negative control of IFN-inducible antiviral effects and growth inhibitory responses. Importantly, inhibiting expression of the various Spry proteins results in enhanced IFN-dependent anti-leukemic effects and antiviral responses, suggesting that selective targeting of these proteins may provide an approach to enhance and optimize the therapeutic potential of IFNs.

EXPERIMENTAL PROCEDURES

Cells and Reagents—U937 cells were grown in RPMI supplemented with 10% (v/v) fetal bovine serum and antibiotics. Immortalized Sprouty1,2,4 knock-out MEFs (23) were grown in DMEM supplemented with 10% (v/v) fetal bovine serum and antibiotics. Recombinant human IFN α was obtained from Hoffmann-La Roche. Recombinant human and mouse IFN β were from Biogen Idec. Antibodies against human Spry1 and Spry2 were purchased from Abcam (Cambridge, MA). An antibody against human Spry4 was purchased from Santa Cruz Biotechnology, Inc. (Santa Cruz, CA). Antibodies against mouse Spry1 and Spry2 have been previously described (23). Antibodies against the phosphorylated forms of STAT1, STAT3, ERK1/2 (Thr-202/Tyr-204), and p38 MAPK (Thr-180/Tyr-182), as well as antibodies against ERK1/2 and p38 MAPK, were obtained from Cell Signaling Technology (Danvers, MA). An antibody against GAPDH was obtained from Millipore. siRNAs targeting human Sprouty1, Sprouty2, and Sprouty4 as well nontargeting siRNAs were obtained from Santa Cruz Biotechnology.

Cell Lysis and Immunoblotting—Cells were treated with 5×10^3 or 1×10^4 IU/ml of IFN α and IFN β for the indicated times. For the experiments in which ISG15 expression was assessed, the concentration of IFN used was 2.5×10^3 IU/ml. Cells were then collected and lysed in phosphorylation lysis buffer as in our previous studies (12). Immunoblotting was performed using an enhanced chemiluminescence (ECL) method were performed as in previous studies (12).

mRNA Expression Assays—Cells were treated with 5×10^3 units/ml of IFN α or IFN β for 6 h, and quantitative RT-PCR was carried out as described previously (12). Real-time RT-PCR to determine expression of ISG15 mRNA was carried out by using commercially available 6-carboxyfluorescein-labeled probes and primers (Applied Biosystems). For knockdown experiments, cells were nucleofected with siRNA, and Spry1,2,4

mRNA expression was assessed using real-time RT-PCR. GAPDH was used for normalization.

Overexpression of Murine Spry1 and Murine Spry2 in Spry1,2,4^{-/-} MEFs—For these studies, virus supernatants were generated from a Phoenix packaging cell line that had been transfected with empty vector (pBabe-puro), pBabe-puro murine Spry1 (FLAG/HA), or pBabe-puro murine Spry2 (FLAG/HA) plasmids using FuGENE (Roche Diagnostics). Spry1,2,4^{-/-} MEFs were infected in the presence of Polybrene (8 μ g/ml) with retroviruses and selected for 4 days in puromycin (1 μ g/ml), and protein expression was verified by immunoblotting, as indicated.

Antiviral Assays—The antiviral effects of mouse IFN α in Spry1,2,4^{flox/flox} and Spry1,2,4^{-/-} MEFs were determined in assays using encephalomyocarditis virus as the challenge virus, as in our previous studies (12).

Hematopoietic Cell Progenitor Assays—Peripheral blood from polycythemia vera patients was collected after obtaining consent approved by the Institutional Review Board of Northwestern University. Hematopoietic progenitor colony formation for late erythroid progenitors (BFU-E) was determined in clonogenic assays in methylcellulose, as in our previous studies (16).

RESULTS

In initial studies, we examined the effects of Type I IFNs (IFN α and IFN β) on protein expression of different Spry family members. U937 cells were treated with IFN α or IFN β for different times, and Spry protein levels were assessed by immunoblotting. Type I IFN treatment resulted in the up-regulation of expression of Spry2 that was detectable within 60 min of treatment and persisted for 4–5 h (Fig. 1, A and B). Similarly, IFN treatment resulted in sustained up-regulation of Spry4 (Fig. 1, C and 1D) and Spry1 (Fig. 1, E and F).

Evidence from previous work shows that phosphorylation of Spry2 on serines 112 and 121 by Mnk1 stabilizes the protein and antagonizes c-Cbl binding and polyubiquitination that would otherwise lead to its degradation (24). As we have shown that Mnk1 is engaged in Type I IFN signaling and plays critical roles in the generation of IFN responses (16), we examined whether Mnk kinase activity is required for stabilization/up-regulation of Spry protein expression by the Type I IFN receptor. Immortalized MEFs from mice with targeted disruption of both Mnk1 and Mnk2 (25) or control wild-type (WT) MEFs were treated with mouse IFN β for increasing times, and protein levels of Spry1 and Spry2 were analyzed in parallel. Treatment of WT MEFs with mouse IFN β resulted in rapid up-regulation of Spry1 levels, consistent with stabilization of protein expression, but this up-regulation was not seen in Mnk1/2 double knock-out MEFs (Fig. 2A). Similarly, up-regulation of expression of Spry2 was Mnk kinase-dependent (Fig. 2B), suggesting that IFN-dependent, Mnk-mediated phosphorylation of Spry proteins stabilizes them and promotes their expression (24).

Spry expression is stimulated by growth factors and plays key regulatory roles in growth factor signaling (18–22, 24). By contrast to growth factors, IFNs are cytokines that generally inhibit cell proliferation, and our finding that Spry protein levels are regulated by IFNs raised the possibility that Spry proteins might

Sprouty Proteins in IFN Signaling

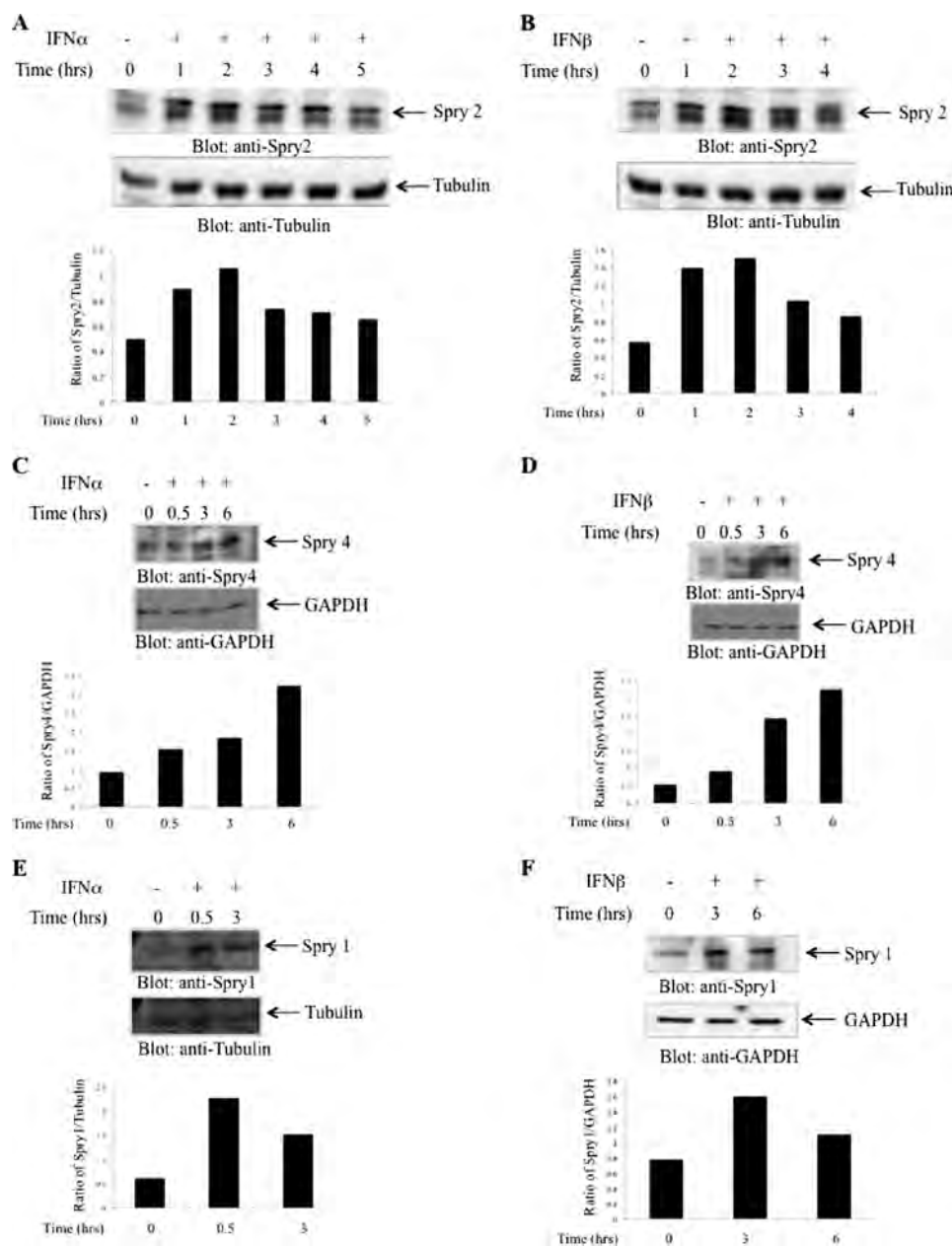


FIGURE 1. Effects of Type I IFNs on Spry protein levels. *A* and *B*, U937 cells were treated with human IFN α or IFN β for the indicated times. Proteins in lysates were resolved by SDS-PAGE and immunoblotted with an antibody against Spry2. The same blots were probed with an antibody against tubulin. The signals for Spry2 and tubulin from the experiments shown in *A* and *B* were quantitated by densitometry, and the intensities of Spry2 relative to tubulin expression were calculated. *C* and *D*, U937 cells were treated with human IFN α or IFN β for the indicated times. Proteins in lysates were resolved by SDS-PAGE and immunoblotted with an antibody against Spry4. The same blots were probed with an antibody against GAPDH. The signals for Spry4 and GAPDH from the experiment shown in *C* and *D* were quantitated by densitometry, and the intensities of Spry4 relative to GAPDH expression were calculated. *E* and *F*, U937 cells were treated with human IFN α or IFN β for the indicated times. Proteins in lysates were resolved by SDS-PAGE and immunoblotted with an antibody against Spry1. The same blots were probed with an antibody against GAPDH. The signals for Spry1 and tubulin (*E*) or GAPDH (*F*) were quantitated by densitometry, and the intensities of Spry1 relative to tubulin or GAPDH expression were calculated.

modulate IFN-mediated growth inhibition. To examine the effects of Spry proteins on Type I IFN-induced signaling, we utilized MEFs created by Cre-mediated excision of lox P-linked alleles deficient for all three Spry proteins up-regulated in response to Type I IFNs (Spry1,2,4^{-/-}) (23). Serum-starved parental Spry1,2,4^{flox/flox} or Spry1,2,4^{-/-} MEFs were treated with mouse IFN β , and phosphorylation/activation of Stat proteins and MAP kinases was determined. As expected, Type I IFN treatment resulted in strong phosphorylation of Stat1 on Tyr-701 (Fig. 3A) and Ser-727 (Fig. 3B) in Spry1,2,4^{flox/flox}

MEFs. This IFN-inducible phosphorylation was intact and similar in Spry1,2,4^{-/-} cells (Fig. 3, *A* and *B*), indicating that Spry proteins do not modulate phosphorylation or protein expression of Stats. In a similar manner, IFN-inducible phosphorylation of Stat3 on Tyr-705 or Ser-727 was similar in Spry1,2,4^{flox/flox} and Spry1,2,4^{-/-} MEFs (Fig. 3, *C* and *D*), indicating that this phosphorylation is independent of Spry activity. Furthermore, in Spry1,2,4^{-/-} cells, IFN-dependent Erk1/2 phosphorylation was enhanced (Fig. 3E), suggesting that, as in the case of growth factor signaling (18–20), Spry proteins act as

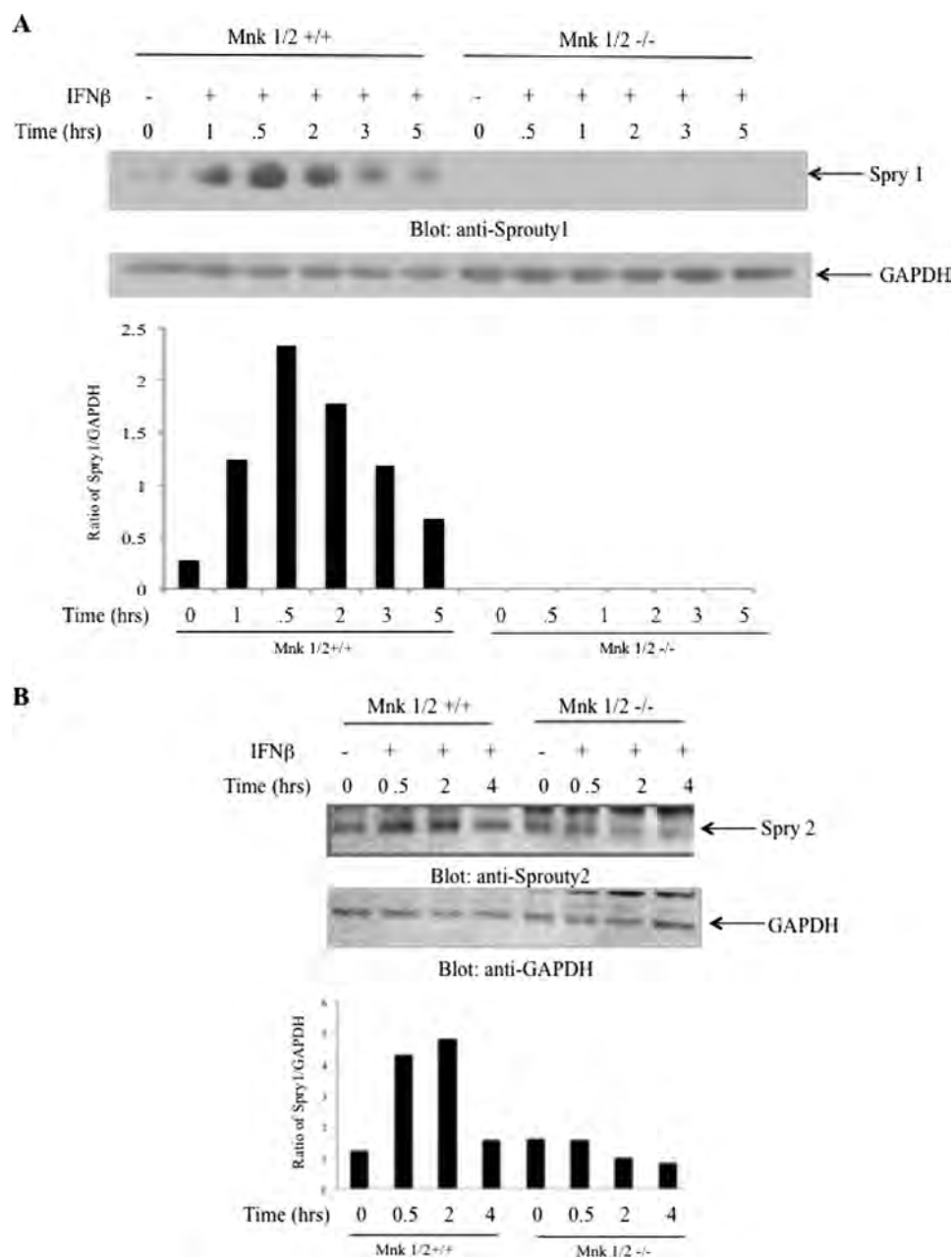


FIGURE 2. Type I IFN-dependent up-regulation of Spry proteins is Mnk kinase dependent. *A*, Mnk1/2 $^{+/+}$ and Mnk1/2 $^{-/-}$ MEFs were treated with mouse IFN β for the indicated times, and proteins in cell lysates were separated by SDS-PAGE and immunoblotted with an antibody against Spry1. The same blot was probed with an antibody against GAPDH. The signals for Spry1 and GAPDH were quantitated by densitometry, and the intensity of Spry1 relative to GAPDH expression was calculated. *B*, Mnk1/2 $^{+/+}$ and Mnk1/2 $^{-/-}$ MEFs were treated with mouse IFN β for the indicated times, and proteins in cell lysates were separated by SDS-PAGE and immunoblotted with an antibody against Spry2. The same blot was probed with an antibody against GAPDH. The signals for Spry2 and GAPDH were quantitated by densitometry, and the intensity of Spry2 relative to GAPDH expression was calculated.

negative feedback regulators of the MEK/Erk pathway. Importantly, targeted disruption of the Spry1, Spry2, and Spry4 genes also resulted in enhancement of phosphorylation/activation of p38 MAPK (Fig. 3*F*), suggesting unique regulatory effects of Spry proteins in IFN signaling.

Previous work established that the p38 MAPK pathway complements the function of Stat pathways and is required for optimal transcription of ISGs with interferon-sensitive response elements in their promoters (26, 27). As our data demonstrated regulatory effects of Spry proteins on p38 MAPK activity, we determined the effects of the targeted disruption of Spry genes

on mRNA expression of the ISG15 gene, the protein product of which accounts for IFN-dependent ISGylation and plays an important role in the control of IFN responses (28). Spry1,2,4 $^{fllox/fllox}$ and Spry1,2,4 $^{-/-}$ MEFs were treated with murine IFN α or IFN β , and ISG15 mRNA expression was determined by quantitative real-time RT-PCR. As shown in Fig. 4*A*, there was strong induction of ISG15 mRNA expression in response to either IFN α or IFN β in Spry1,2,4 $^{fllox/fllox}$ MEFs, but this expression increased further in Spry1,2,4 $^{-/-}$ cells (Fig. 4*A*). Consistent with this, IFN-dependent ISG15 protein expression was strongly enhanced in Spry1,2,4 $^{-/-}$ cells (Fig. 4, *B–C*). To

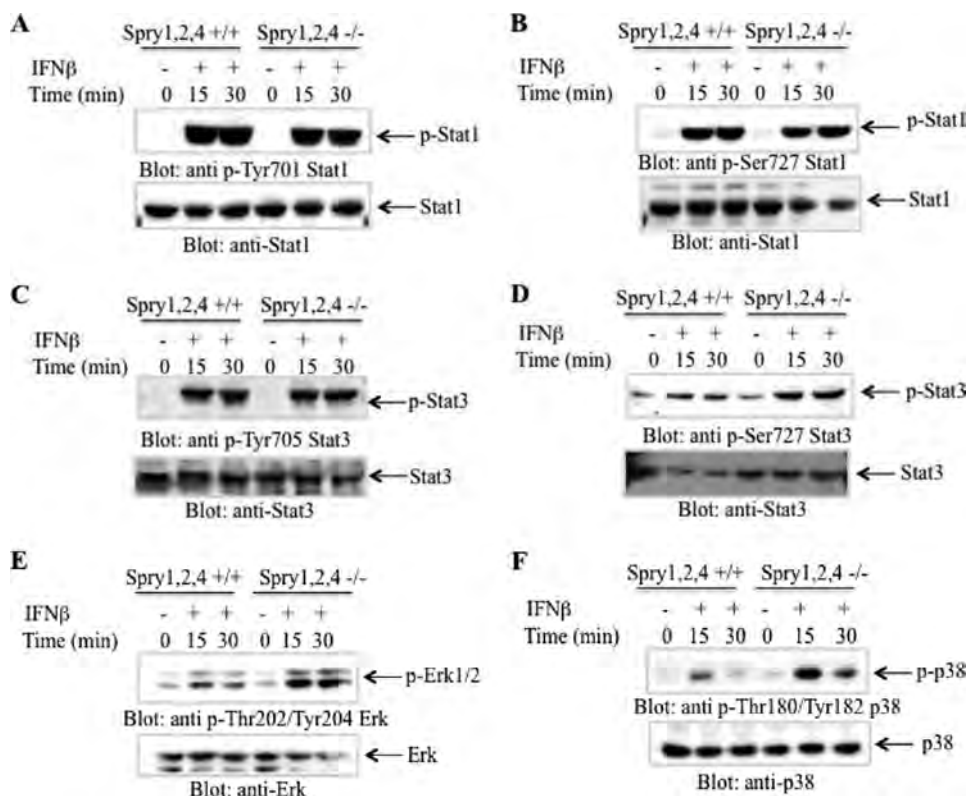


FIGURE 3. Regulatory effects of Spry proteins on elements of Type I IFN signaling. A and B, *Spry1,2,4^{flox/flox}* and *Spry1,2,4^{-/-}* MEFs were treated with mouse IFN β for the indicated times. Equal amounts of protein were resolved by SDS-PAGE and then immunoblotted with antibodies against phosphorylated STAT1 (Tyr-701) (*anti p-Tyr701 Stat1*) (A) or STAT1 (Ser-727) (*anti p-Ser727 Stat1*) (B). The blots were then stripped and reprobed with an antibody against STAT1. C and D, *Spry1,2,4^{flox/flox}* and *Spry1,2,4^{-/-}* MEFs were treated with mouse IFN β for the indicated times. Equal amounts of protein were resolved by SDS-PAGE and then immunoblotted with antibody against phosphorylated STAT3 (Tyr-705) (*anti p-Tyr705 Stat1*) (C) or STAT3 (Ser-727) (*anti p-Ser727 Stat1*) (D). The blots were then stripped and reprobed with an antibody against STAT3. E, *Spry1,2,4^{flox/flox}* and *Spry1,2,4^{-/-}* MEFs were treated with mouse IFN β for the indicated times. Equal amounts of protein were resolved by SDS-PAGE and then immunoblotted with an antibody against phosphorylated Erk1/2 (Thr-202/Tyr-204) (*anti p-Thr202/Tyr204 Erk*). The blot was then stripped and reprobed with an antibody against Erk1/2. F, *Spry1,2,4^{flox/flox}* and *Spry1,2,4^{-/-}* MEFs were treated with mouse IFN β for the indicated times. Equal amounts of protein were resolved by SDS-PAGE and then immunoblotted with an antibody against phosphorylated p38 MAPK (Thr-180/Tyr-182) (*anti p-Thr180/Tyr182 p38*). The blot was then stripped and reprobed with an antibody against p38 MAPK.

further establish the role that Spry proteins play in regulation of ISG15 expression, we ectopically expressed Spry1 (Fig. 4D) or Spry2 (Fig. 4E) in *Spry1,2,4^{-/-}* cells and examined the effects of this complementation on ISG15 protein expression. As shown in Fig. 4F, ectopic expression of either Spry1 or Spry2 substantially decreased the levels of IFN-dependent expression of ISG15 protein (Fig. 4F).

To evaluate the functional relevance of Spry proteins in the biological effects of IFNs, we compared the antiviral properties of mouse IFN α against encephalomyocarditis virus infection in *Spry1,2,4^{-/-}* and *Spry1,2,4^{flox/flox}* MEFs. *Spry1,2,4* triple knock-out MEFs showed enhanced protection from viral infection in response to IFN α when compared with *Spry1,2,4^{flox/flox}* MEFs (Fig. 5A), a finding consistent with the regulatory effects that Spry proteins exhibit on ISG expression.

We next examined the effects of Spry proteins on the ability of Type I IFNs to suppress leukemic progenitor colony formation. Spry1, Spry2, or Spry4 expression was targeted in U937 cells using specific siRNAs (supplemental Fig. S1), and the effects of Spry knockdowns on the generation of the suppressive effects of IFN α or IFN β on leukemic progenitor (CFU-L) colony formation were examined. Treatment with either IFN α or IFN β resulted in partial inhibition of CFU-L colony formation (Fig. 5, B and C), which was significantly enhanced in cells

depleted of Spry1 or Spry2 expression (Fig. 5B). A similar trend was seen in cells in which Spry4 was knocked down (Fig. 5C). Thus, Spry proteins oppose both the antiviral and the antiproliferative/antileukemic effects of Type I IFNs.

To ascertain the clinical importance of this latter effect, we determined the function of Spry proteins on the action of IFN α on primary malignant hematopoietic progenitors from patients with polycythemia vera. As shown in Fig. 5D, selective targeting of Spry1, Spry2, or Spry4 resulted in enhanced IFN-inducible suppressive effects on malignant early erythroid progenitor (BFU-E) colony formation (Fig. 5D), further implicating these proteins as negative regulators of IFN responses, specifically in primary malignant progenitors.

DISCUSSION

The first member of the Sprouty family (dSpry) was originally discovered in *Drosophila* as a novel cysteine-rich protein functioning as an FGF antagonist (21). In that original study, which ultimately defined the existence of the Spry family of proteins, it was demonstrated that the FGF pathway is overactive in *Sprouty* mutant embryos and is associated with ectopic branches, as compared with wild-type embryos (21). Subsequent work identified four mammalian homologs, *Spry1*, *Spry2*, *Spry3*, and *Spry4* (29). Expression of *Spry1*, *Spry2*, and *Spry4*

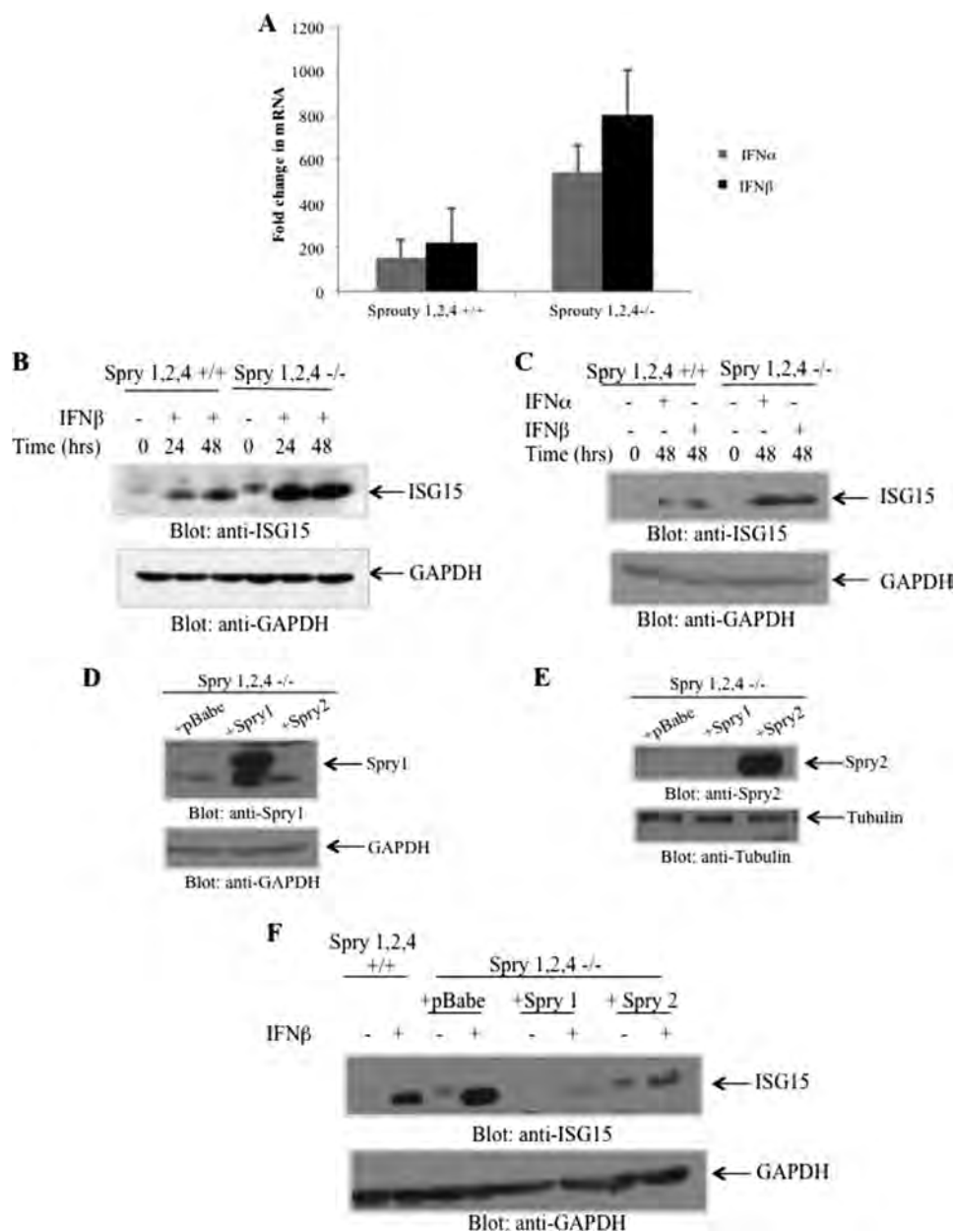


FIGURE 4. Regulatory effects of Spry proteins on ISG expression. *A*, Spry1,2,4^{fllox/fllox} MEFs and Spry1,2,4^{-/-} MEFs were treated with mouse IFN α or IFN β for 6 h, as indicated. The expression of ISG15 mRNA was assessed by quantitative RT-PCR, normalized for GAPDH expression. Data are expressed as -fold induction over corresponding untreated samples and represent means \pm S.E. of three independent experiments. *B*, Spry1,2,4^{fllox/fllox} MEFs and Spry1,2,4^{-/-} MEFs were treated with mouse IFN β for 24 and 48 h, as indicated. Equal amounts of protein were resolved by SDS-PAGE and immunoblotted with antibody against mouse ISG15. The same blot was probed with an antibody against GAPDH. *C*, Spry1,2,4^{fllox/fllox} MEFs and Spry1,2,4^{-/-} MEFs were treated with mouse IFN α or IFN β for 48 h, as indicated. Equal amounts of protein were resolved by SDS-PAGE and immunoblotted with antibody against mouse ISG15. The same blot was probed with an antibody against GAPDH. *D*, Spry null MEFs complemented with empty vector or vectors containing cDNA for mSpry1 or mSpry2 were lysed, and equal amounts of protein were resolved by SDS-PAGE and immunoblotted with an antibody against mSpry1. The same blot was probed with an antibody against GAPDH. *E*, Spry null MEFs complemented with empty vector or cDNA for mSpry1 or mSpry2 vector were lysed, and equal amounts of protein were resolved by SDS-PAGE and immunoblotted with an antibody against mSpry2. The same blot was probed with an antibody against tubulin. *F*, Spry1,2,4^{fllox/fllox} MEFs and Spry1,2,4^{-/-} MEFs in which mSpry1 or mSpry2 were ectopically re-expressed, as indicated, were treated with mouse IFN β 24 h, as indicated. Equal amounts of protein were resolved by SDS-PAGE and immunoblotted with antibody against mouse ISG15. The same blot was probed with an antibody against GAPDH.

proteins is widespread in embryonic and adult tissues, whereas expression of Spry3 is restricted to brain and testes in adult tissues (30, 31). Spry proteins play critical roles in normal cells, and there is accumulating evidence for important regulatory effects during embryogenesis and organ development, including expansion of the organ of Corti (auditory sensory epithelium) (32), diastema tooth development (33), and morphogenesis of the ureteric epithelium in kidney development (34).

These important functions of Spry proteins during development are to a large extent reflections of their properties as modifiers of intracellular pathways and growth factor responses during development.

It is now well established that Spry proteins inhibit signaling from various growth factor receptors, including epidermal growth factor (EGF), fibroblast growth factor (FGF), vascular endothelial growth factor (VEGF), platelet-derived growth fac-

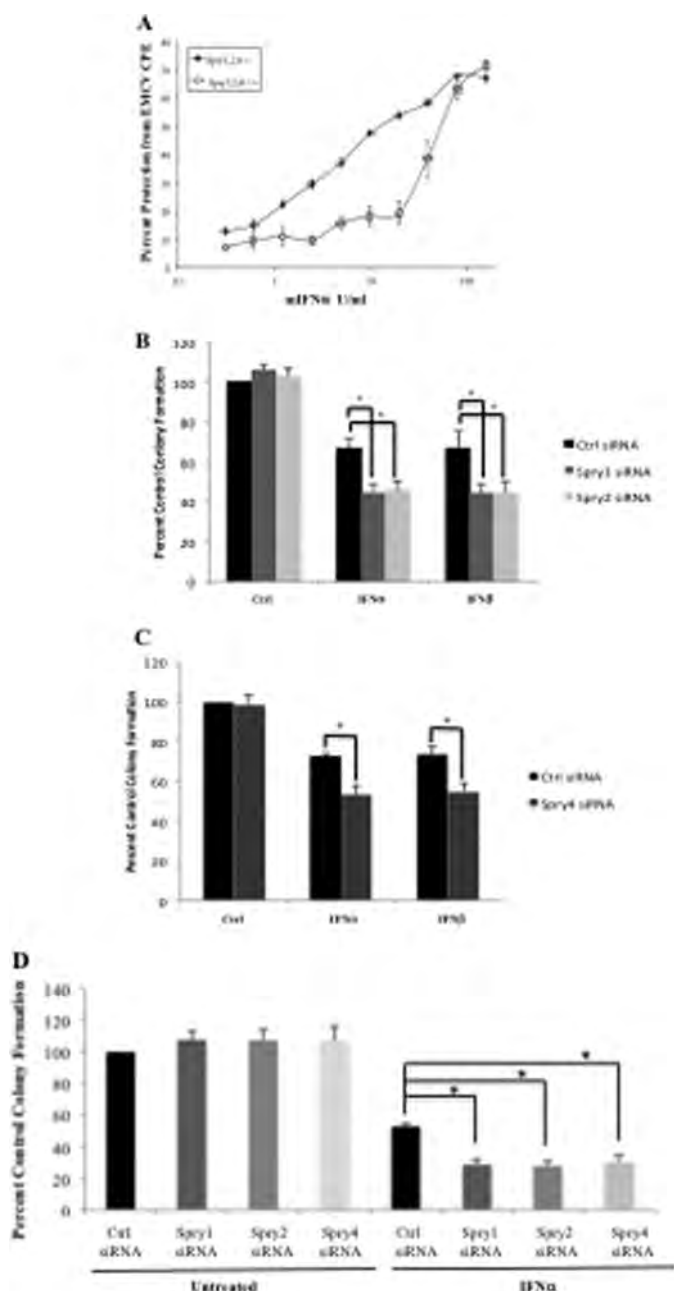


FIGURE 5. Negative regulatory effects of Spry proteins in induction of IFN-dependent antiviral and antileukemic effects. *A*, Spry1,2,4^{lox/lox} MEFs and Spry1,2,4^{-/-} MEFs were incubated with the indicated doses of mouse IFN α . The cells were subsequently challenged with encephalomyocarditis virus (EMCV), and the viral cytopathic effects (CPE) were quantified 4 days later. Data are expressed as the percentage of protection from viral cytopathic effects of encephalomyocarditis virus. *B* and *C*, U937 cells were transfected with the indicated siRNAs and plated in a methylcellulose assay system in the absence or presence of human IFN α and IFN β . Data are expressed as a percentage of the control (Ctrl) siRNA-transfected cell-derived colony formation and represent means \pm S.E. of four independent experiments. For panel *B*, paired *t* test analysis showed $p = 0.001$ for the combination of control siRNA and IFN α versus the combination of Spry1 siRNA and IFN α ; $p = 0.00009$ for the combination of control siRNA and IFN α versus the combination of Spry2 siRNA and IFN α ; $p = 0.019$ for the combination of control siRNA and IFN β versus the combination of Spry1 siRNA and IFN β for CFU-L; and $p = 0.035$ for the combination of control siRNA and IFN β versus the combination of Spry2 siRNA and IFN β for CFU-L colonies. For panel *C*, paired *t* test analysis showed $p = 0.02$ for the combination of control siRNA and IFN α versus the combination of Spry4 siRNA and IFN α ; and $p = 0.008$ for the combination of control siRNA and IFN β versus the combination of Spry4 siRNA and IFN β for CFU-L. *D*, mononuclear cells derived from peripheral blood of patients with

tor (PDGF), and glial cell-derived neurotrophic factor (GDNF) (19–22, 35). A key mechanism by which Spry proteins modulate cell proliferation and survival is by their ability to inhibit the Ras/MEK/Erk pathway (35). Several mechanisms for these responses have been delineated and involve direct interactions with known regulators or effector molecules of this signaling cascade, such as Grb2 (36), SHP2 (37), Raf1 (38), and Gap1 (39). There is also recent evidence that Spry proteins modulate other cellular signals and pathways, such as the phosphatidylinositol-specific phospholipase C- γ , which accounts for regulatory effects on calcium-mediated signaling and T cell proliferation (23). Notably, the effects of Spry proteins on growth factor-activated MAP kinase pathways appear to be limited to the MEK/Erk pathway (20–22), and there have been no reports on effects on other MAP kinase cascades.

In contrast to growth factors, IFNs are cytokines with important antiproliferative properties and tumor suppressive effects on malignant cells (1–3). In addition to the classical Jak-Stat pathways that regulate transcription of IFN-stimulated genes and their products (1, 3–8), IFNs activate several other cellular cascades, the functions of which complement the activities of Jak-Stat pathways in the generation of IFN responses. In recent studies, we demonstrated that activation of the Mnk/eIF4E pathway plays important roles in the generation of IFN-induced biological effects (16, 17). As there is evidence in other systems that phosphorylation of Spry2 on Ser-112 and Ser-121 by Mnk kinase activity stabilizes the protein and antagonizes c-Cbl binding and polyubiquitination (24), we examined the effects of Type I IFN treatment on expression of different members of the Spry family of proteins. Our data established that IFN treatment leads to increased levels of Spry proteins, whereas such expression is defective in Mnk1/2 double knockout MEFs, establishing that Mnk activity is required for the process. In experiments using Spry1/Spry2/Spry4 triple knockout MEFs, we found that IFN-dependent phosphorylation/activation of the MEK/Erk pathway is augmented, in a manner similar to what others have reported previously for growth factor signaling (35). However, the p38 MAPK was also strongly enhanced in the absence of expression of these Spry proteins, establishing regulatory effects of Spry proteins on the p38 MAPK pathway. In parallel studies, we found that induction of *ISG15* gene transcription and ISG15 protein expression are Spry-regulated and that targeted disruption of all three widely expressed Spry genes (*Spry1*, *Spry2*, and *Spry4*) results in enhanced ISG15 expression. Such effects do not reflect effects of Spry proteins on IFN-activated Jak-Stat pathways as IFN-dependent phosphorylation of Stat1 and Stat3 is intact in Spry1,2,4 triple knock-out cells. However, they do correlate

polycythemia vera were transfected with the indicated siRNAs and were then plated in a methylcellulose assay system, in the absence or presence of human IFN α . BFU-E progenitor colonies were scored after 14 days in culture. Data are expressed as the percentage of control colony formation of the control untreated siRNA-transfected cells and represent means \pm S.E. of five independent experiments. For panel *D*, paired *t* test analysis showed $p = 0.0008$ for the combination of control siRNA and IFN α versus the combination of Spry1 siRNA and IFN α ; $p = 0.0017$ for the combination of control siRNA and IFN α versus the combination of Spry2 siRNA and IFN α ; and $p = 0.0074$ for the combination of control siRNA and IFN α versus the combination of Spry4 siRNA and IFN α .

with enhanced p38 MAP kinase activity and are in agreement with previous work that has established that the p38 MAPK pathway plays an essential role in ISG transcription without modulating tyrosine or serine phosphorylation of Stat proteins (26, 27). Such Spry-dependent regulatory effects on the IFN-activated p38 MAPK pathway have important functional consequences as our data demonstrate that knockdown of Spry1, Spry2, or Spry4 potentiates the inhibitory effects of IFN α or IFN β on U937-derived leukemic precursors or primary malignant erythroid hematopoietic progenitors from patients with polycythemia vera. It is of interest that although selective knock-out of distinct Spry proteins only partially enhances the suppressive effects of Type I IFNs on malignant hematopoiesis, different Spry proteins do not appear to compensate for each other in that context. It should also be noted that previous work demonstrated that the p38 MAP kinase pathway is essential for the generation of the suppressive effects of IFN α on normal (40) and leukemic hematopoietic progenitors (41), and recent work has shown that p38 MAPK is required for the inhibitory effects of IFN α on malignant erythroid progenitors from patients with polycythemia vera (42). Taken together with the findings of the current study, the data suggest that the enhancing effects of Spry knockdown on IFN-mediated suppression of malignant hematopoiesis may result from regulatory effects on the p38 MAPK pathway.

The precise protein target(s) of Spry proteins among elements of the IFN-activated p38 MAPK pathway remain to be determined. Putative candidates include various kinases in the p38 MAPK cascade, such as MAP kinase kinase (Mkk) 3, Mkk6, or Mkk4 (10, 11), or various upstream MAP kinase kinases (MAPKKK) that are known to control MKK/p38 MAPK cascades (10, 11). Alternatively, effects on early upstream G-proteins that regulate engagement of the IFN-activated pathway, such as Rac1 (27), may be involved, but this remains to be directly addressed in future studies. Independent of the precise mechanisms involved, the results of this study may prove to have important translational implications in the future use of IFNs in clinical medicine. IFN α/β is used in various clinical settings, such as the treatment of various viral infections, multiple sclerosis, and certain malignancies (4). Importantly, it has major clinical activity, and it is one of the most effective agents in the treatment of Philadelphia negative (Ph⁻) myeloproliferative neoplasms. In recent years, there has been a dramatic emergence of IFN α as an agent with major activity in the treatment of polycythemia vera and essential thrombocytosis (43–45). Nevertheless, not all patients respond or achieve long-term remissions, and efforts to further improve the clinical activity of IFN α should have a substantial impact in the management of patients with myeloproliferative neoplasms. Our studies suggest that Spry proteins are important negative feedback regulators of IFN responses and raise the potential of approaches to block their expression or inhibit their function to enhance and promote the antineoplastic effects of IFNs *in vitro* and *in vivo*.

Acknowledgment—We thank Elisabeth Stecki for expert secretarial assistance.

REFERENCES

1. Stark, G. R., Kerr, I. M., Williams, B. R., Silverman, R. H., and Schreiber, R. D. (1998) How cells respond to interferons. *Annu. Rev. Biochem.* **67**, 227–264
2. Pestka, S., Langer, J. A., Zoon, K. C., and Samuel, C. E. (1987) Interferons and their actions. *Annu. Rev. Biochem.* **56**, 727–777
3. Platanias, L. C. (2005) Mechanisms of type-I- and type-II-interferon-mediated signalling. *Nat. Rev. Immunol.* **5**, 375–386
4. George, P. M., Badiger, R., Alazawi, W., Foster, G. R., and Mitchell, J. A. (2012) Pharmacology and therapeutic potential of interferons. *Pharmacol. Ther.* **135**, 44–53
5. Donnelly, R. P., and Kutenko, S. V. (2010) Interferon- λ : a new addition to an old family. *J. Interferon Cytokine Res.* **30**, 555–564
6. Lasfar, A., Abushahba, W., Balan, M., and Cohen-Solal, K. A. (2011) Interferon λ : a new sword in cancer immunotherapy. *Clin. Dev. Immunol.* **2011**, 349575
7. Stark, G. R. (2007) How cells respond to interferons revisited: From early history to current complexity. *Cytokine Growth Factor Rev.* **18**, 419–423
8. Stark, G. R., and Darnell, J. E. (2012) The JAK-STAT pathway at twenty. *Immunity* **36**, 503–514
9. Cheon, H., Yang, J., and Stark, G. R. (2011) The functions of signal transducers and activators of transcriptions 1 and 3 as cytokine-inducible proteins. *J. Interferon Cytokine Res.* **31**, 33–40
10. Platanias, L. C. (2003) The p38 mitogen-activated protein kinase pathway and its role in interferon signaling. *Pharmacol. Ther.* **98**, 129–142
11. Platanias, L. C. (2003) Map kinase signaling pathways and hematologic malignancies. *Blood* **101**, 4667–4679
12. Kaur, S., Lal, L., Sassano, A., Majchrzak-Kita, B., Srikanth, M., Baker, D. P., Petroulakis, E., Hay, N., Sonenberg, N., Fish, E. N., and Platanias, L. C. (2007) Regulatory effects of mammalian target of rapamycin-activated pathways in type I and II interferon signaling. *J. Biol. Chem.* **282**, 1757–1768
13. Kaur, S., Sassano, A., Dolniak, B., Joshi, S., Majchrzak-Kita, B., Baker, D. P., Hay, N., Fish, E. N., and Platanias, L. C. (2008) Role of the Akt pathway in mRNA translation of interferon-stimulated genes. *Proc. Natl. Acad. Sci. U.S.A.* **105**, 4808–4813
14. Kroczyńska, B., Kaur, S., Katsoulidis, E., Majchrzak-Kita, B., Sassano, A., Kozma, S. C., Fish, E. N., and Platanias, L. C. (2009) Interferon-dependent engagement of eukaryotic initiation factor 4B via S6 kinase (S6K)- and ribosomal protein S6K-mediated signals. *Mol. Cell. Biol.* **29**, 2865–2875
15. Kaur, S., Sassano, A., Majchrzak-Kita, B., Baker, D. P., Su, B., Fish, E. N., and Platanias, L. C. (2012) Regulatory effects of mTORC2 complexes in type I IFN signaling and in the generation of IFN responses. *Proc. Natl. Acad. Sci. U.S.A.* **109**, 7723–7728
16. Joshi, S., Kaur, S., Redig, A. J., Goldsborough, K., David, K., Ueda, T., Watanabe-Fukunaga, R., Baker, D. P., Fish, E. N., Fukunaga, R., and Platanias, L. C. (2009) Type I interferon (IFN)-dependent activation of Mnk1 and its role in the generation of growth inhibitory responses. *Proc. Natl. Acad. Sci. U.S.A.* **106**, 12097–12102
17. Joshi, S., Sharma, B., Kaur, S., Majchrzak, B., Ueda, T., Fukunaga, R., Verma, A. K., Fish, E. N., and Platanias, L. C. (2011) Essential role for Mnk kinases in type II interferon (IFN γ) signaling and its suppressive effects on normal hematopoiesis. *J. Biol. Chem.* **286**, 6017–6026
18. Kim, H. J., and Bar-Sagi, D. (2004) Modulation of signalling by Sprouty: a developing story. *Nat. Rev. Mol. Cell Biol.* **5**, 441–450
19. Mason, J. M., Morrison, D. J., Basson, M. A., and Licht, J. D. (2006) Sprouty proteins: multifaceted negative-feedback regulators of receptor tyrosine kinase signaling. *Trends Cell Biol.* **16**, 45–54
20. Edwin, F., Anderson, K., Ying, C., and Patel, T. B. (2009) Intermolecular interactions of Sprouty proteins and their implications in development and disease. *Mol. Pharmacol.* **76**, 679–691
21. Hacohen, N., Kramer, S., Sutherland, D., Hiromi, Y., and Krasnow, M. A. (1998) Sprouty encodes a novel antagonist of FGF signaling that patterns apical branching of the *Drosophila* airways. *Cell* **92**, 253–263
22. Egan, J. E., Hall, A. B., Yatsula, B. A., and Bar-Sagi, D. (2002) The bimodal regulation of epidermal growth factor signaling by human Sprouty proteins. *Proc. Natl. Acad. Sci. U.S.A.* **99**, 6041–6046

23. Akbulut, S., Reddi, A. L., Aggarwal, P., Ambardekar, C., Canciani, B., Kim, M. K., Hix, L., Vilimas, T., Mason, J., Basson, M. A., Lovatt, M., Powell, J., Collins, S., Quatela, S., Phillips, M., and Licht, J. D. (2010) Sprouty proteins inhibit receptor-mediated activation of phosphatidylinositol-specific phospholipase C. *Mol. Cell. Biol.* **21**, 3487–3496
24. DaSilva, J., Xu, L., Kim, H. J., Miller, W. T., and Bar-Sagi, D. (2006) Regulation of Sprouty stability by Mnk1-dependent phosphorylation. *Mol. Cell. Biol.* **26**, 1898–1907
25. Ueda, T., Watanabe-Fukunaga, R., Fukuyama, H., Nagata, S., and Fukunaga, R. (2004) Mnk2 and Mnk1 are essential for constitutive and inducible phosphorylation of eukaryotic initiation factor 4E but not for cell growth or development. *Mol. Cell. Biol.* **24**, 6539–6549
26. Uddin, S., Majchrzak, B., Woodson, J., Arunkumar, P., Alsayed, Y., Pine, R., Young, P. R., Fish, E. N., and Platanius, L. C. (1999) Activation of the p38 mitogen-activated protein kinase by type I interferons. *J. Biol. Chem.* **274**, 30127–30131
27. Uddin, S., Lekkmine, F., Sharma, N., Majchrzak, B., Mayer, I., Young, P. R., Bokoch, G. M., Fish, E. N., and Platanius, L. C. (2000) The Rac1/p38 mitogen-activated protein kinase pathway is required for interferon α -dependent transcriptional activation but not serine phosphorylation of Stat proteins. *J. Biol. Chem.* **275**, 27634–27640
28. Ritchie, K. J., and Zhang, D. E. (2004) ISG15: the immunological kin of ubiquitin. *Semin. Cell Dev. Biol.* **15**, 237–246
29. Li, X., Wheldon, L., and Heath, J. K. (2003) Sprouty: a controversial role in receptor tyrosine kinase signalling pathways. *Biochem. Soc. Trans.* **31**, 1445–1446
30. Minowada, G., Jarvis, L. A., Chi, C. L., Neubüser, A., Sun, X., Hacohen, N., Krasnow, M. A., and Martin, G. R. (1999) Vertebrate Sprouty genes are induced by FGF signaling and can cause chondrodysplasia when overexpressed. *Development* **126**, 4465–4475
31. Leeksa, O. C., Van Achterberg, T. A., Tsumura, Y., Toshima, J., Eldering, E., Kroes, W. G., Mellink, C., Spaargaren, M., Mizuno, K., Pannekoek, H., and de Vries, C. J. (2002) Human Sprouty 4, a new ras antagonist on 5q31, interacts with the dual specificity kinase TESK1. *Eur. J. Biochem.* **269**, 2546–2556
32. Shim, K., Minowada, G., Coling, D. E., and Martin, G. R. (2005) Sprouty2, a mouse deafness gene, regulates cell fate decisions in the auditory sensory epithelium by antagonizing FGF signaling. *Dev. Cell* **8**, 553–564
33. Klein, O. D., Minowada, G., Peterkova, R., Kangas, A., Yu, B. D., Lesot, H., Peterka, M., Jernvall, J., and Martin, G. R. (2006) Sprouty genes control diastema tooth development via bidirectional antagonism of epithelial-mesenchymal FGF signaling. *Dev. Cell* **11**, 181–190
34. Basson, M. A., Watson-Johnson, J., Shakya, R., Akbulut, S., Hyink, D., Costantini, F. D., Wilson, P. D., Mason, I. J., and Licht, J. D. (2006) Branching morphogenesis of the ureteric epithelium during kidney development is coordinated by the opposing functions of GDNF and Sprouty1. *Dev. Biol.* **299**, 466–477
35. Cabrita, M. A., and Christofori, G. (2008) Sprouty proteins, masterminds of receptor tyrosine kinase signaling. *Angiogenesis* **11**, 53–62
36. Tefft, D., Lee, M., Smith, S., Crowe, D. L., Bellusci, S., and Warburton, D. (2002) mSprouty2 inhibits FGF10-activated MAP kinase by differentially binding to upstream target proteins. *Am. J. Physiol. Lung Cell. Mol. Physiol.* **283**, L700–L706
37. Hanafusa, H., Torii, S., Yasunaga, T., and Nishida, E. (2002) Sprouty1 and Sprouty2 provide a control mechanism for the Ras/MAPK signalling pathway. *Nat. Cell Biol.* **4**, 850–858
38. Sasaki, A., Taketomi, T., Kato, R., Saeki, K., Nonami, A., Sasaki, M., Kuriyama, M., Saito, N., Shibuya, M., and Yoshimura, A. (2003) Mammalian Sprouty4 suppresses Ras-independent ERK activation by binding to Raf1. *Nat. Cell Biol.* **5**, 427–432
39. Casci, T., Vinós, J., and Freeman, M. (1999) Sprouty, an intracellular inhibitor of Ras signaling. *Cell* **96**, 655–665
40. Verma, A., Deb, D. K., Sassano, A., Uddin, S., Varga, J., Wickrema, A., and Platanius, L. C. (2002) Activation of the p38 mitogen-activated protein kinase mediates the suppressive effects of type I interferons and transforming growth factor- β on normal hematopoiesis. *J. Biol. Chem.* **277**, 7726–7735
41. Mayer, I. A., Verma, A., Grumbach, I. M., Uddin, S., Lekkmine, F., Ravandi, F., Majchrzak, B., Fujita, S., Fish, E. N., and Platanius, L. C. (2001) The p38 MAPK pathway mediates the growth inhibitory effects of interferon- α in BCR-ABL-expressing cells. *J. Biol. Chem.* **276**, 28570–28577
42. Lu, M., Zhang, W., Li, Y., Berenzon, D., Wang, X., Wang, J., Mascarenhas, J., Xu, M., and Hoffman, R. (2010) Interferon- α targets JAK2V617F-positive hematopoietic progenitor cells and acts through the p38 MAPK pathway. *Exp. Hematol.* **38**, 472–480
43. Bracarda, S., Eggermont, A. M., and Samuelsson, J. (2010) Redefining the role of interferon in the treatment of malignant diseases. *Eur. J. Cancer.* **46**, 284–297
44. Kiladjian, J. J., Cassinat, B., Chevret, S., Turlure, P., Cambier, N., Roussel, M., Bellucci, S., Grandchamp, B., Chomienne, C., and Fenaux, P. (2008) Pegylated interferon- α -2a induces complete hematologic and molecular responses with low toxicity in polycythemia vera. *Blood* **112**, 3065–3072
45. Quintás-Cardama, A., Kantarjian, H., Manshour, T., Luthra, R., Estrov, Z., Pierce, S., Richie, M. A., Borthakur, G., Konopleva, M., Cortes, J., and Verstovsek, S. (2009) Pegylated interferon α -2a yields high rates of hematologic and molecular response in patients with advanced essential thrombocythemia and polycythemia vera. *J. Clin. Oncol.* **27**, 5418–5424

Essential Role for Mnk Kinases in Type II Interferon (IFN γ) Signaling and Its Suppressive Effects on Normal Hematopoiesis*

Received for publication, October 27, 2010, and in revised form, December 10, 2010. Published, JBC Papers in Press, December 13, 2010, DOI 10.1074/jbc.M110.197921

Sonali Joshi[‡], Bhumika Sharma[‡], Surinder Kaur[‡], Beata Majchrzak[§], Takeshi Ueda[¶], Rikiro Fukunaga^{||}, Amit K. Verma^{**}, Eleanor N. Fish[§], and Leonidas C. Platanias^{‡,1}

From the [‡]Robert H. Lurie Comprehensive Cancer Center and Division of Hematology-Oncology, Northwestern University Medical School and Jesse Brown Veterans Affairs Medical Center, Chicago, Illinois 60611, the [§]Division of Cell and Molecular Biology, Toronto Research Institute, University Health Network and Department of Immunology, University of Toronto, Toronto, Ontario M5G2M1, Canada, the [¶]Department of Disease Model, Research Institute for Radiation Biology and Medicine, Hiroshima University, Hiroshima, 737-8553 Japan, the ^{||}Department of Medical Chemistry, Graduate School of Medicine, Kyoto University, Kyoto 606-8501, Japan, and the ^{**}Division of Hematology-Oncology, Department of Medicine, Albert Einstein College of Medicine, Bronx, New York 10461

IFN γ exhibits potent antitumor effects and plays important roles in the innate immunity against cancer. However, the mechanisms accounting for the antiproliferative effects of IFN γ still remain to be elucidated. We examined the role of Mnk1 (MAPK-interacting protein kinase 1) in IFN γ signaling. Our data demonstrate that IFN γ treatment of sensitive cells results in engagement of Mnk1, activation of its kinase domain, and downstream phosphorylation of the cap-binding protein eIF4E on Ser-209. Such engagement of Mnk1 plays an important role in IFN γ -induced IRF-1 (IFN regulatory factor 1) gene mRNA translation/protein expression and is essential for generation of antiproliferative responses. In studies aimed to determine the role of Mnk1 in the induction of the suppressive effects of IFNs on primitive hematopoietic progenitors, we found that siRNA-mediated Mnk1/2 knockdown results in partial reversal of the suppressive effects of IFN γ on human CD34+-derived myeloid (CFU-GM) and erythroid (BFU-E) progenitors. These findings establish a key role for the Mnk/eIF4E pathway in the regulatory effects of IFN γ on normal hematopoiesis and identify Mnk kinases as important elements in the control of IFN γ -inducible ISG mRNA translation.

The only known member of the Type II IFN family, IFN γ , plays an important role in the innate and adaptive immunity against microbial and viral infections and exhibits potent anti-tumor effects (1–4). IFN γ is a cytokine mainly secreted by T lymphocytes, activated natural killer cells, and antigen-presenting cells such as macrophages and dendritic cells (5, 6) and is known to elicit pleiotropic biological effects on cells and tissues. This cytokine enhances the activity of natural killer cells, facilitates class switching, and regulates immunoglobulin production by B cells (5–7). In addition, it regulates survival and proliferation of T cells, modulates the activity of

antigen presenting cells and, under certain circumstances, can promote differentiation of several distinct cell types (5–7). Importantly, IFN γ facilitates immune responses to tumor cells, although it also inhibits angiogenesis and exerts direct anti-proliferative effects on a number of tumor cells (8). Thus, considering the broad effects of IFN γ , understanding the cellular mechanisms that regulate its biological effects is highly relevant in advancing our overall understanding of the mechanisms of innate immunity against cancer and viral infections.

Previous studies have established that IFN γ transduces signals by binding to its cell surface receptor, which is composed of two distinct subunits; the IFN γ receptor 1 and 2 chains, which are constitutively associated with the JAK family members JAK1 and JAK2 (reviewed in Refs. 2 and 3). Binding of IFN γ to its receptor results in interactions between the receptor chains leading to the phosphorylation of the STAT1 transcriptional activator, followed by its dimerization, translocation to the nucleus, and activation of gene transcription by IFN γ -activated sequences (GAS)² (2, 3). Beyond the classic JAK-STAT pathway, the transcriptional response to IFN γ also involves IFN γ -activated transcription elements (9) that are controlled by the transcription factor CCAAT enhancer-binding protein- β . Notably, the activity of CCAAT enhancer-binding protein- β is positively regulated by the MAP kinases Erk1 and Erk2 (10). There has been also some previous evidence implicating protein kinase pathways in the generation of cellular responses to IFN γ . The phosphatidylinositol 3-kinase regulates transcriptional regulation by IFN γ (11, 12), whereas the Akt/mTOR pathway plays an important role downstream of phosphatidylinositol 3-kinase, promoting mRNA translation of ISGs (13, 14). PKC family members PKC δ , PKC θ , and PKC ϵ have been also shown to play important roles in IFN γ signaling (11, 15, 16). Additionally there is evidence for important functional roles for MAPK pathways in the induction of IFN γ responses (17–20).

We determined whether Mnks (MAPK-interacting protein kinases) 1 and 2 are activated during engagement of the Type

* This work was supported, in whole or in part, by National Institutes of Health Grants CA77816, CA121192, AG029138, and HL08294. This work was also supported by a Merit Review grant from the Department of Veterans Affairs and a Malkin Scholars Award.

¹ To whom correspondence should be addressed: Robert H. Lurie Comprehensive Cancer Center, 303 East Superior St., Lurie 3-107, Chicago, IL 60611. Tel.: 312-503-4267; Fax: 312-908-1372; E-mail: l-platanias@northwestern.edu.

² The abbreviations used are: GAS, IFN γ -activated sequences; MEF, mouse embryonic fibroblast; CFU-GM, colony forming unit-granulocyte monocyte; BFU-E, burst forming unit-erythroid.

Mnk Kinases in the Generation of IFN γ Responses

II IFN receptor and participate in the generation of IFN γ responses. Mnk1 is a downstream effector for both the p38 MAPK and Erk1/2 pathways and along with the related Mnk2 regulates phosphorylation of eIF4E (21, 22). Our data show that IFN γ treatment results in activation of Mnk1 and its downstream target eIF4E in an Mek/Erk-dependent manner. In studies using dual Mnk1/Mnk2 knock-out cells, we found that Mnk activity is essential for IFN γ -dependent mRNA translation of IRF-1 (interferon regulatory factor 1) and plays a critical role in the generation of growth inhibitory responses by the Type II IFN receptor. Altogether, our findings identify Mnk1 as a novel element required for mRNA translation of ISGs and generation of IFN γ antiproliferative responses.

MATERIALS AND METHODS

Antibodies, Cell Lines, and Reagents—The antibodies against p-Mnk1 (Thr-197/202), Mnk1, p-eIF4E (Ser-209), eIF4E, p-Erk1/2 (Thr-202/Tyr-204), Erk1/2, pSTAT1 (Tyr-701), and p-STAT1 (Ser-727) were obtained from Cell Signaling Technology (Danvers, MA). The antibodies against STAT1 and IRF-1 were obtained from Santa Cruz Biotechnology, Inc. (Santa Cruz, CA). The antibody against GAPDH was obtained from Millipore (Billerica, MA). Human and mouse IFN γ were obtained from PBL Interferon Source (Piscataway, NJ). U937 cells were grown in RPMI-1060 supplemented with 10% (v/v) fetal bovine serum and antibiotics. CD34+ cells were obtained from either Lonza (Basel, Switzerland) or Stemcell Technologies (Vancouver, Canada). Immortalized Mnk1^{-/-} MEFs, Mnk2^{-/-} MEFs, and Mnk1/Mnk2^{-/-} MEFs were cultured in DMEM supplemented with 10% (v/v) fetal bovine serum and antibiotics. The Mnk inhibitor CGP57380 and the Mek1/2 inhibitor U0126 were obtained from Calbiochem (Darmstadt, Germany). The siRNAs targeting human Mnk1 and Mnk2 as well as nontargeting siRNAs were obtained from Dharmacon.

Cell Lysis and Immunoblotting—The cells were treated with IFN γ (10³ or 10⁴ IU/ml) for the indicated times and were then lysed in phosphorylation lysis buffer as described in our previous studies (23, 24). In experiments using pharmacological inhibitors, the cells were pretreated with CGP57380 (5–10 μ M) or U0126 (10 μ M) for 1 h followed by IFN γ treatment for the indicated time in the continuous presence of the inhibitors; the cells were then lysed in phosphorylation lysis buffer. Immunoblotting was performed using an ECL method, as in our previous studies (25–27).

Luciferase Reporter Assay—Mnk1/2^{+/+}, Mnk1^{-/-}, Mnk2^{-/-}, and Mnk1/2^{-/-} MEFs were transfected with an 8 \times GAS luciferase construct (containing a luciferase reporter gene with eight GAS elements linked to a minimal prolactin promoter) and a constitutive β -galactosidase expression vector using the SuperFect transfection reagent according to the protocol of the manufacturer (Qiagen). The 8 \times GAS construct was kindly provided by Dr. Christofer Glass (University of California, San Diego, CA) (28). 48 h post-transfection, the triplicate cultures were either left untreated or treated with mouse IFN γ (1,000 units/ml) for 6 h. The cells were then lysed, and the luciferase activity was measured as per the manufacturer's instructions (Promega, Madison, WI) described in previous

studies (23). The luciferase activity was then normalized utilizing the β -galactosidase activity for each sample.

Quantitative RT-PCR—The Mnk1/2^{+/+}, Mnk1^{-/-}, Mnk2^{-/-}, and Mnk1/2^{-/-} MEFs were either left untreated or were with IFN γ (1,000 units/ml) for 6 h and RNA was isolated using the RNeasy kit (Qiagen). Cellular mRNA was reverse transcribed into cDNA using the Omniscript RT kit and oligo(dT) primer (Qiagen) as described previously (16). Quantitative PCR was carried out as described previously (14). Commercially available FAM-labeled probes and primers (Applied Biosystems) to determine *Irf-1* mRNA expression were used. GAPDH was used for normalization. The mRNA amplification was calculated as described previously (14), and the data were plotted as the fold increase as compared with untreated samples.

Isolation of Polysomal Fractions—The Mnk1/2^{+/+}, Mnk1^{-/-}, Mnk2^{-/-}, and Mnk1/2^{-/-} MEFs were treated with mouse IFN γ (1,000 units/ml) for 48 h, and polysomal fractionation was performed as in our previous studies (13, 24).

Hematopoietic Progenitor Cell Assays—CD34+ cells were transfected with either control nontargeting siRNA or siRNA specific to human Mnk1 and/or Mnk2 (Dharmacon, Lafayette, CO). In some experiments the cells were also treated with the Mnk inhibitor CGP57380 (5 μ M) or diluent control DMSO. The cells were then cultured in a methylcellulose assay system in the absence or presence of human IFN γ (1,000 units/ml) for 14 days, and erythroid (BFU-E) or myeloid (CFU-GM) colonies were scored as described previously (27, 29). In the experiments to assess the effects of Mnk inhibition on leukemic CFU-L progenitors, U937 cells were transfected with either control nontargeting siRNA or siRNAs targeting Mnk1, Mnk2, or both or treated with either DMSO or CGP57380 (2.5 μ M). The cells were then cultured in a methylcellulose assay system in the absence or presence of human IFN γ (1,000 units/ml) for 7 days, and colony-forming units were scored as described previously (30).

RESULTS

In initial studies we examined whether IFN γ induces phosphorylation/activation of Mnk1. For these, sensitive U937 cells were treated with human IFN γ for different times, and cell lysates were analyzed by SDS-PAGE and immunoblotted with an antibody that recognizes the phosphorylated/activated form of Mnk1. IFN γ treatment resulted in rapid phosphorylation/activation of Mnk1, which was noticeable at 10 min and was still detectable 50 min post-IFN γ treatment (Fig. 1A), suggesting the involvement of this kinase in IFN γ signaling. We also examined whether IFN γ treatment regulates phosphorylation of the downstream effector of Mnk1, eIF4E, at Ser-209, which is the Mnk phosphorylation site in other systems (31–34). As shown in Fig. 1B, IFN γ treatment of U937 cells resulted in phosphorylation of eIF4E (Fig. 1B). To determine whether Mnk activity is essential for Type II IFN-dependent phosphorylation of eIF4E, we examined whether such induction is blocked in immortalized MEFs from mice with targeted disruption of both the Mnk1 and Mnk2 genes (34). Mnk1/2^{+/+} and Mnk1/2^{-/-} MEFs were serum-starved and then treated with mouse IFN γ for different times. As seen

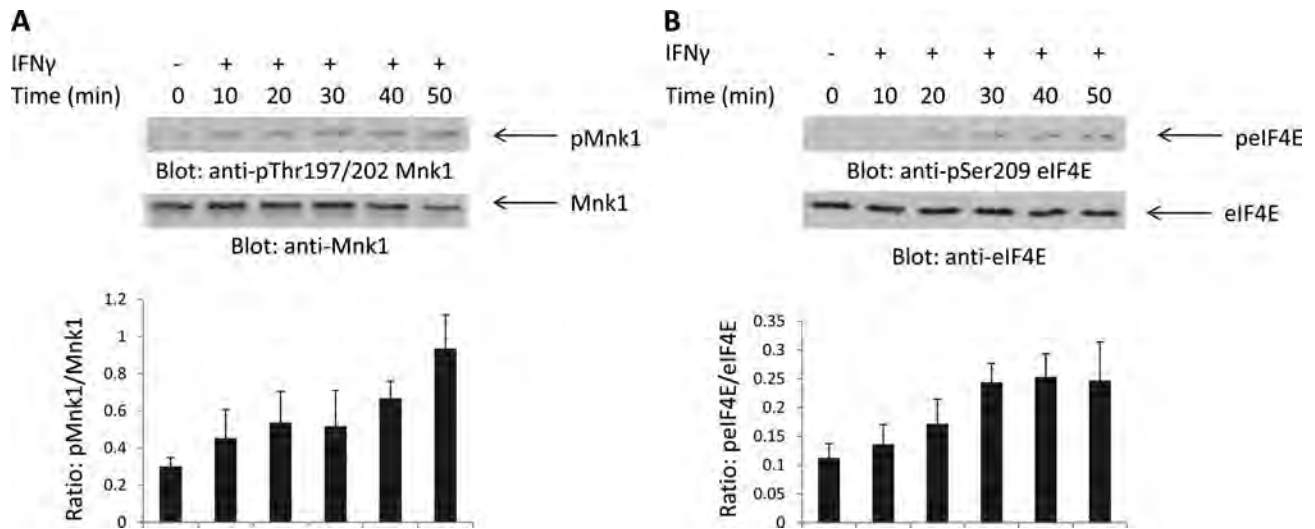


FIGURE 1. IFN γ -mediated engagement of Mnk1 and eIF4E. **A**, U937 cells were treated with human IFN γ for the indicated times. Total lysates were separated by SDS-PAGE and immunoblotted with an antibody against phosphorylated Mnk1 (Thr-197/202). The same blot was stripped and reprobed with an antibody against total Mnk1. The signals for pMnk1 and total Mnk1 from three independent experiments (including the one shown in **A**) were quantitated by densitometry, and the intensity of pMnk1 relative to total Mnk1 expression was calculated. The data are expressed as the means of ratios of pMnk1 to Mnk1 levels \pm S.E. for each experimental condition. **B**, U937 cells were treated with human IFN γ for the indicated times. Total lysates were separated by SDS-PAGE and immunoblotted with an antibody against phosphorylated eIF4E (Ser-209). The same blot was stripped and reprobed with an antibody against total eIF4E. The signals for p-eIF4E and total eIF4E from four independent experiments (including the one shown in **B**) were quantitated by densitometry, and the intensity of p-eIF4E relative to total eIF4E expression was calculated. The data are expressed as the means of ratios of p-eIF4E to eIF4E levels \pm S.E. for each experimental condition.

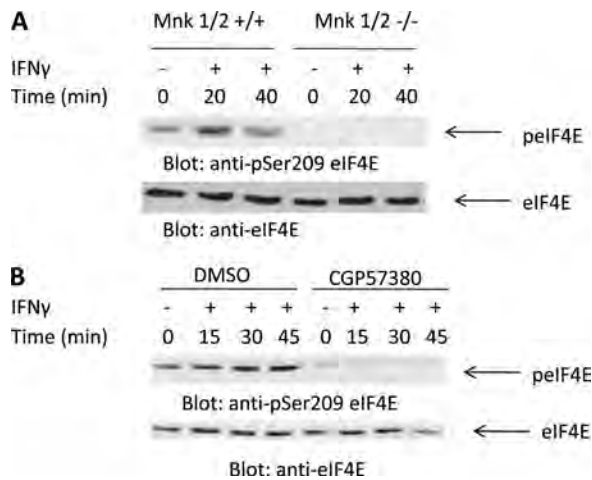


FIGURE 2. Mnk1/2 is required for IFN γ -mediated engagement of eIF4E. **A**, Mnk1/2^{+/+} and Mnk1/2^{-/-} MEFs were serum-starved overnight and treated with mouse IFN γ for the indicated times. Equal amounts of lysates were separated by SDS-PAGE followed by immunoblotting with an antibody against phosphorylated eIF4E (S209). The same blot was stripped and reprobed with an antibody against total eIF4E. **B**, U937 cells were incubated with either DMSO or CGP57380 for 60 min and were then treated with human IFN γ for the indicated times. Equal amounts of lysates were separated by SDS-PAGE and then immunoblotted with an antibody against phosphorylated eIF4E (Ser-209). The blot was then stripped and reprobed with an antibody against eIF4E.

in Fig. 2A, IFN γ treatment resulted in strong phosphorylation of eIF4E in Mnk1/2^{+/+} MEFs, whereas this phosphorylation was not inducible in the Mnk1/2^{-/-} MEFs (Fig. 2A). Consistent with this, in experiments in which the effects of pharmacological inhibition of Mnk were evaluated in U937 leukemic cells, we found that the IFN γ -dependent phosphorylation of eIF4E is Mnk1/2-dependent (Fig. 2B).

We subsequently sought to define upstream signaling events required for activation of Mnk1 and eIF4E during en-

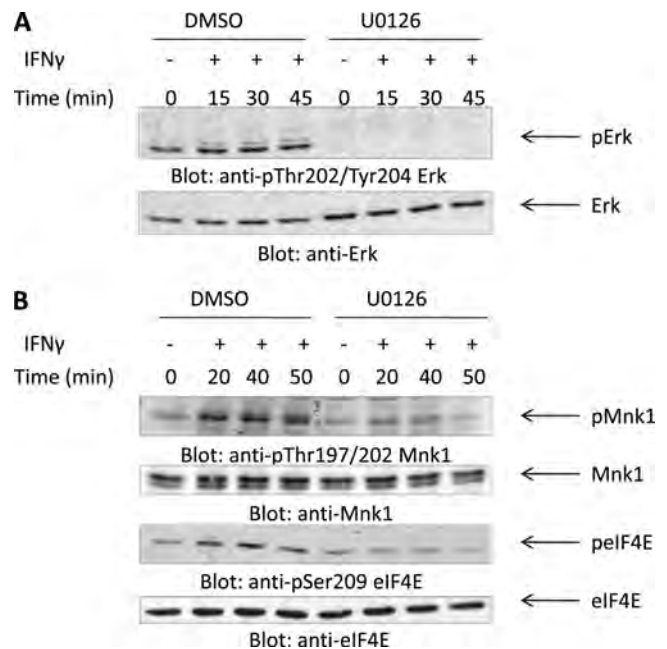


FIGURE 3. IFN γ -mediated engagement of Mnk1 and eIF4E is Mek/Erk-dependent. **A**, U937 cells were incubated with either DMSO or U0126 for 60 min and were then treated with human IFN γ for the indicated times. Equal amounts of protein were separated by SDS-PAGE and then immunoblotted with antibodies against phosphorylated Erk1/2 (Thr-202/Tyr-204). The blot was then stripped and reprobed with an antibody against total Erk1/2. **B**, U937 cells were incubated with either DMSO or U0126 for 60 min and were then treated with human IFN γ for the indicated times. Equal amounts of lysates were separated by SDS-PAGE and then immunoblotted with antibodies against phosphorylated Mnk1 (Thr-197/202) or against phosphorylated eIF4E (Ser-209). The respective blots were then stripped and reprobed with antibodies against total Mnk1 or total eIF4E.

agement of the Type II IFN receptor. Mnk1 has been shown to be phosphorylated by the Erk1 and Erk2 kinases in response to various stimuli (31–33). We examined the phos-

Mnk Kinases in the Generation of IFN γ Responses

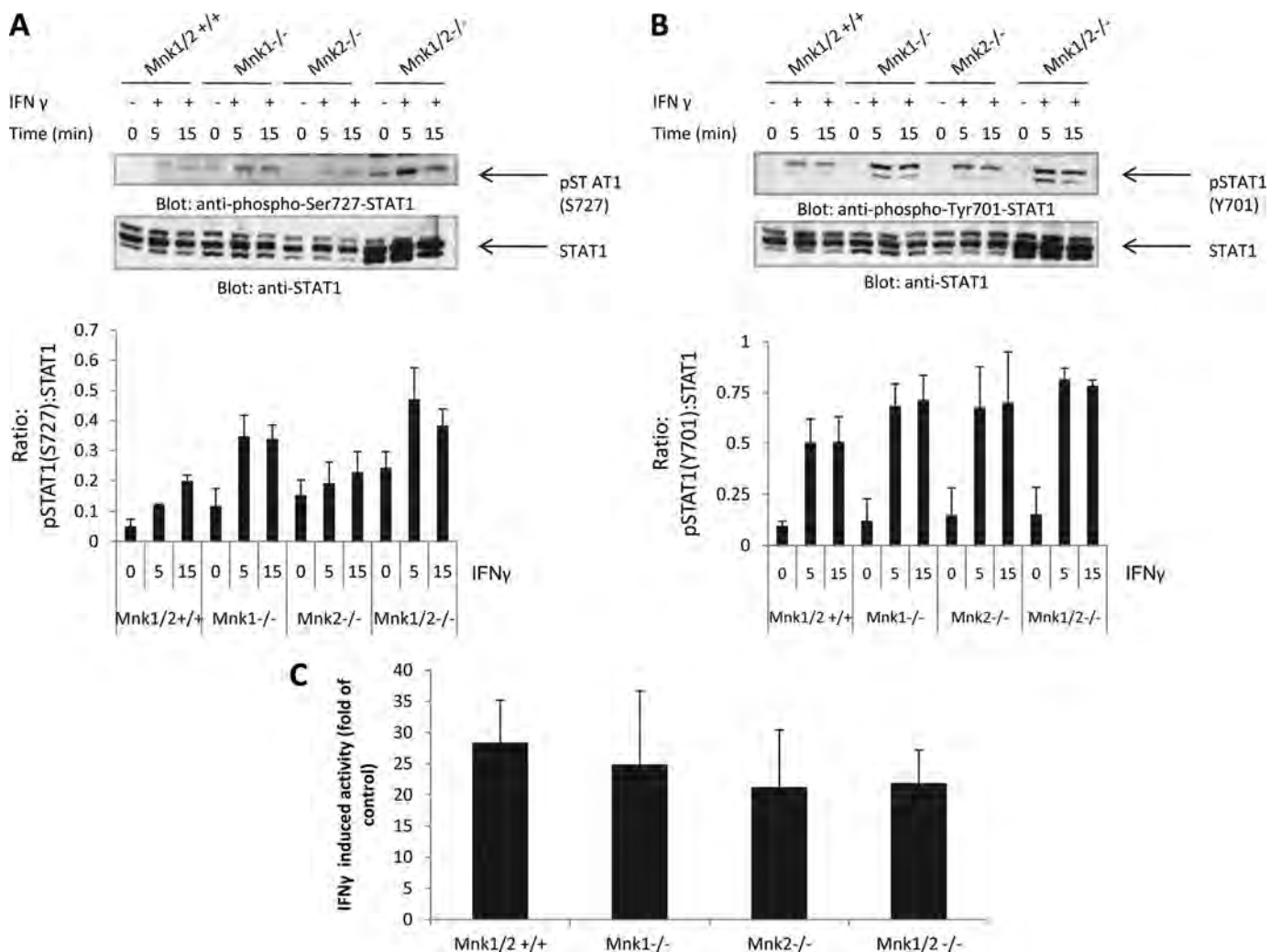


FIGURE 4. Mnk1 and Mnk2 are not required for IFN γ -mediated engagement of STAT1 or activation of transcription via GAS elements. *A*, Mnk1/2^{+/+}, Mnk1^{-/-}, Mnk2^{-/-}, and Mnk1/2^{-/-} MEFs were treated with IFN γ for the indicated times. Equal amounts of total cell lysates were separated by SDS-PAGE and immunoblotted with antibodies against phosphorylated STAT1 (Ser-727). The blot was stripped and reprobed with antibody against total STAT1. The signals for pSTAT1 (Ser-727) and total STAT1 from three independent experiments (including the one shown in *A*) were quantitated by densitometry, and the intensity of pSTAT1 (S727) relative to total STAT1 expression was calculated. The data are expressed as the means of ratios of pSTAT1 (S727) to STAT1 levels \pm S.E. for each experimental condition. *B*, Mnk1/2^{+/+}, Mnk1^{-/-}, Mnk2^{-/-}, and Mnk1/2^{-/-} MEFs were treated with IFN γ for the indicated times. Equal amounts of total cell lysates were separated by SDS-PAGE and immunoblotted with antibodies against phosphorylated STAT1 (Tyr-701). The blot was stripped and reprobed with antibody against total STAT1. The signals for pSTAT1 (Tyr-701) and total STAT1 from three independent experiments (including the one shown in *B*) were quantitated by densitometry, and the intensity of pSTAT1 (Tyr-701) relative to total STAT1 expression was calculated. The data are expressed as the means of ratios of pSTAT1 (Tyr-701) to STAT1 levels \pm S.E. for each experimental condition. *C*, Mnk1/2^{+/+}, Mnk1^{-/-}, Mnk2^{-/-}, and Mnk1/2^{-/-} MEFs were transfected with an 8 \times GAS luciferase construct. 48 h post-transfection, the cells were incubated with or without IFN γ for 6 h. The cells were then harvested and assayed for luciferase activity. The data are expressed as fold increases in luciferase activity in response to IFN γ treatment over control untreated cells and represent the means \pm S.E. of four independent experiments.

phorylation of Mnk1 and Mnk2 in U937 cells in the presence of the Mek/Erk inhibitor U0126. U937 cells were pretreated with either DMSO (control) or U0126 and then treated with IFN γ for the indicated times. IFN γ has been shown to result in the engagement of Erk1 and Erk2 in various systems (35, 36). As expected, U0126 inhibited IFN γ -dependent phosphorylation/activation of Erk1/2 (Fig. 3*A*). In DMSO pretreated cells, Mnk1 and eIF4E were phosphorylated by IFN γ , whereas in U0126-treated cells, the activation of Mnk1 and eIF4E was suppressed (Fig. 3*B*), indicating that the Mek/Erk pathway is required for IFN γ -mediated activation of Mnk1/eIF4E.

We next examined the role of Mnk1 as a putative mediator of IFN γ signaling events. We initially determined whether Mnk1 plays a role in the regulation of phosphorylation/activa-

tion of STAT1 and IFN γ -regulated gene transcription. STAT1 phosphorylation by IFN γ on both Tyr-701 and Ser-727 was intact in the absence of either Mnk1 or Mnk2 and in the absence of both Mnk1 and Mnk2 (Fig. 4, *A* and *B*). Consistent with this, transcriptional activation via GAS elements was intact in luciferase promoter assays (Fig. 4*C*), establishing that Mnk kinases do not play roles in the control of IFN γ -induced STAT1 activation or gene transcription. Interestingly, there was some increase seen in the IFN γ -induced serine phosphorylation of STAT1 (Fig. 4*A*), suggesting a compensatory effect, but the precise mechanism and relevance of this finding remains to be defined in future studies.

IFN γ up-regulates the expression of the IRF-1, which plays an important role in mediating the biological effects of IFN γ

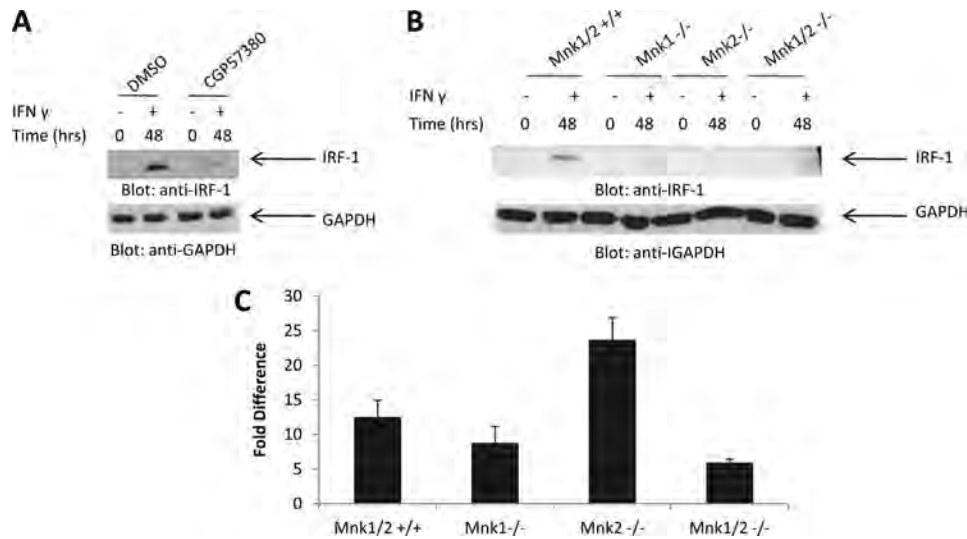


FIGURE 5. Requirement of Mnk1 and Mnk2 for IFN γ -induced IRF1 protein expression. *A*, U937 cells were incubated with either DMSO or CGP57380 for 60 min followed by treatment with human IFN γ for the indicated times. Equal amounts of lysates were separated by SDS-PAGE and immunoblotted with an antibody against IRF-1, and the same blot was also probed with an antibody against GAPDH. *B*, Mnk1/2^{+/+}, Mnk1^{-/-}, Mnk2^{-/-}, and Mnk1/2^{-/-} MEFs were treated with mouse IFN γ for the indicated times. Equal amounts of lysates were separated by SDS-PAGE and immunoblotted with an antibody against IRF-1, and the same blot was also probed with an antibody against GAPDH. *C*, Mnk1/2^{+/+}, Mnk1^{-/-}, Mnk2^{-/-}, and Mnk1/2^{-/-} MEFs were treated with mouse IFN γ . The expression of IRF-1 mRNA was assessed by quantitative RT-PCR, using GAPDH as a control. The data are expressed as the fold induction over corresponding untreated samples and represent the means \pm S.E. of five independent experiments.

(7). To better understand the relevance of the Mnk pathway in the induction of IFN γ responses, we examined and compared the effects of IFN γ on IRF-1 gene transcription and protein expression in single or double Mnk1 and Mnk2 knock-outs and parental cells. IRF-1 protein was clearly IFN γ -inducible in parental MEFs, but such induction was attenuated in the Mnk1^{-/-}, Mnk2^{-/-}, and Mnk1/2^{-/-} MEFs (Fig. 5*B*). Similarly, IFN γ -inducible IRF-1 protein expression was defective in cells treated with the Mnk inhibitor CGP57380 (Fig. 5*A*). These results indicate that Mnk1/2 expression/activity plays an important role in IFN γ -mediated protein expression of IRF-1. Interestingly, when IFN γ -dependent mRNA expression for IRF-1 was assessed in the different Mnk knock-out MEFs, we noticed a significant decrease in Mnk1/2^{-/-} MEFs, whereas there were minimal effects in Mnk1 single knock-out MEFs (Fig. 5*C*). On the other hand, there was an increase in Mnk2^{-/-} MEFs (Fig. 5*C*). Thus, although IRF-1 protein expression in response to IFN γ is defective in single or double Mnk1/Mnk2 knock-outs, there are variable profiles of IRF-1 transcriptional activation/mRNA expression seen in the different Mnk knock-out cells, suggesting that a different mechanism, possibly regulation of mRNA translation, primarily accounts for defective protein expression. To directly determine the role of the Mnk pathway in IRF-1 mRNA translation, Mnk1/2^{+/+} and Mnk1/2^{-/-} MEFs were either left untreated or treated with IFN γ for 48 h. The cells were then subjected to hypotonic lysis and resolved on a sucrose gradient followed by RNA extraction from the polysomal fractions, and IRF-1 polysomal mRNA induction was analyzed by quantitative RT-PCR. As seen in Fig. 6, IRF-1 mRNA translation was attenuated in the Mnk1/2^{-/-} MEFs, indicating that Mnk1 and Mnk2 play important roles in translation of IRF-1 mRNA. Similarly, defective IRF-1 mRNA expression was noticeable in studies using single Mnk1 or single Mnk2 knock-out MEFs, indicating involvement of both kinases in this regulation (Fig. 7).

In subsequent studies, we directly examined the effects of Mnk1 and Mnk2 in the generation of IFN γ -dependent growth inhibitory responses. Leukemic U937 cells were treated with IFN γ , in the presence or absence of the Mnk inhibitor CGP57380, and leukemic progenitor (CFU-L) colony formation was assessed. As shown in Fig. 8*A*, simultaneous treatment with the Mnk inhibitor partially reversed the antiproliferative effects of IFN γ , suggesting a role for Mnk kinases in the generation of IFN γ -dependent antiproliferative responses. To confirm these results, we also used specific siRNAs targeting Mnk1 and/or Mnk2 and determined the effects of these knockdowns on IFN γ -mediated suppression of leukemic progenitor colony formation. There was partial reversal of the suppressive effects of IFN γ on leukemic progenitor colony formation (Fig. 8*B*), definitively establishing a requirement for Mnk1 in the process.

We also performed studies aimed at examining the roles of Mnk1 and Mnk2 as mediators of the suppressive effects of IFN γ on normal human hematopoiesis. Human CD34⁺ bone marrow cells were treated with IFN γ in the presence or absence of CGP57380, and normal myeloid (CFU-GM) or erythroid (BFU-E) colony formation was assessed. The suppressive effects of IFN γ on either CFU-GM and/or BFU-E (Fig. 9*A*) colonies were partially reversed by the CGP57380. Importantly, such reversal of myelosuppressive responses was also seen when CD34⁺ cells were transfected with siRNAs targeting Mnk1, Mnk2, or both (Fig. 9*B*), definitively establishing a role for the Mnk pathway as a mediator of the suppressive effects of IFN γ on normal hematopoiesis.

DISCUSSION

Extensive work over the years has established the relevance of Mnk kinases in stress-activated signaling cascades and as mediators of growth factor and pro-inflammatory signals (37). A major target for Mnk kinases is the initiation factor eIF4E, which undergoes Mnk-mediated phosphorylation on serine

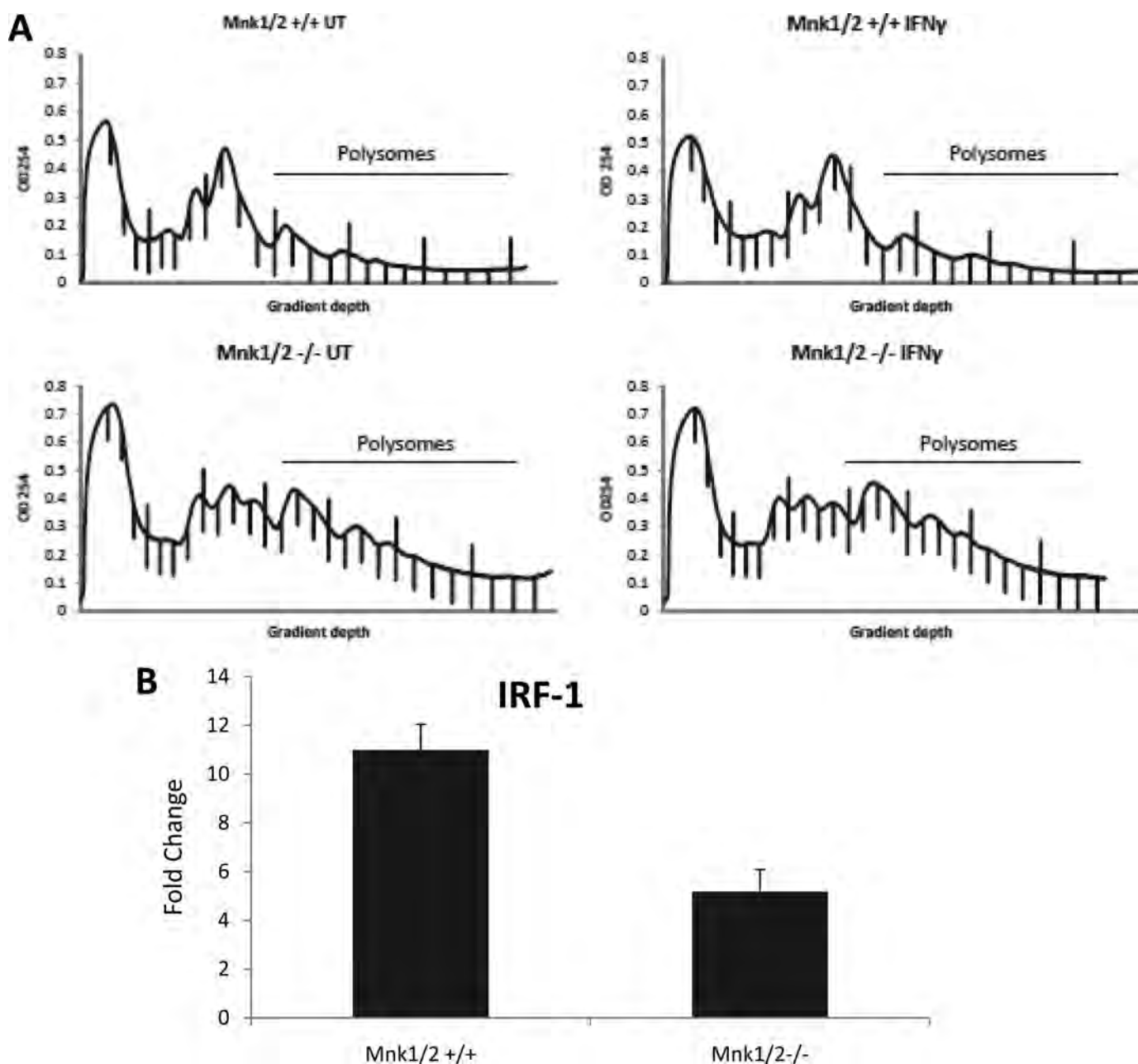


FIGURE 6. Mnk kinases are required for IFN γ -induced IRF1 mRNA translation. *A*, Mnk1/2^{+/+} and Mnk1/2^{-/-} MEFs were either left untreated or treated with mouse IFN γ . The cells were subjected to hypotonic lysis followed by separation on a 10–50% sucrose gradient, and the optical density at 254 nm (OD 254) was recorded. The optical density at 254 nm is shown as a function of gradient depth for each treatment. *B*, IRF-1 mRNA expression in the polysomal fractions was determined by quantitative RT-PCR, using GAPDH for normalization. The data are expressed as fold increases in the IFN γ -treated samples over untreated samples and represent the means \pm S.E. of three independent experiments.

209 (34, 37). Phosphorylation of eIF4E at this site has been shown in different studies to be of importance in the initiation of mRNA translation for certain genes, as well as for oncogenic transformation and malignant cell proliferation (38–42). Mnk kinases have been also implicated in the production of TNF, IL-6, and monocyte chemoattractant protein-1 in response to LPS (43, 44), whereas more recent studies have provided evidence that, under certain circumstances, Mnk1 is involved in cap-independent translation (45, 46). The importance of the Mnk/eIF4E pathway in tumorigenesis was definitively established in recent work using knock-in mice expressing a mutant form of eIF4E, which cannot undergo

phosphorylation on serine 209 (47). These studies demonstrated that phosphorylation on this site is required for tumorigenesis in a prostate cancer mouse model (47). Remarkably, eIF4E phosphorylation on serine 209 was also found to correlate with a high Gleason score, high levels of MMP3 expression, and disease progression in prostate cancer patients (47). Other recent studies demonstrated that Mnk1/2 activity is required for tumor development in the Lck-Pten mouse model (48), underscoring the relevance of the Mnk/eIF4E pathway in malignant tumor development.

The only Type II IFN, IFN γ , exhibits pleiotropic biological functions, including immunomodulatory, antitumor, and an-

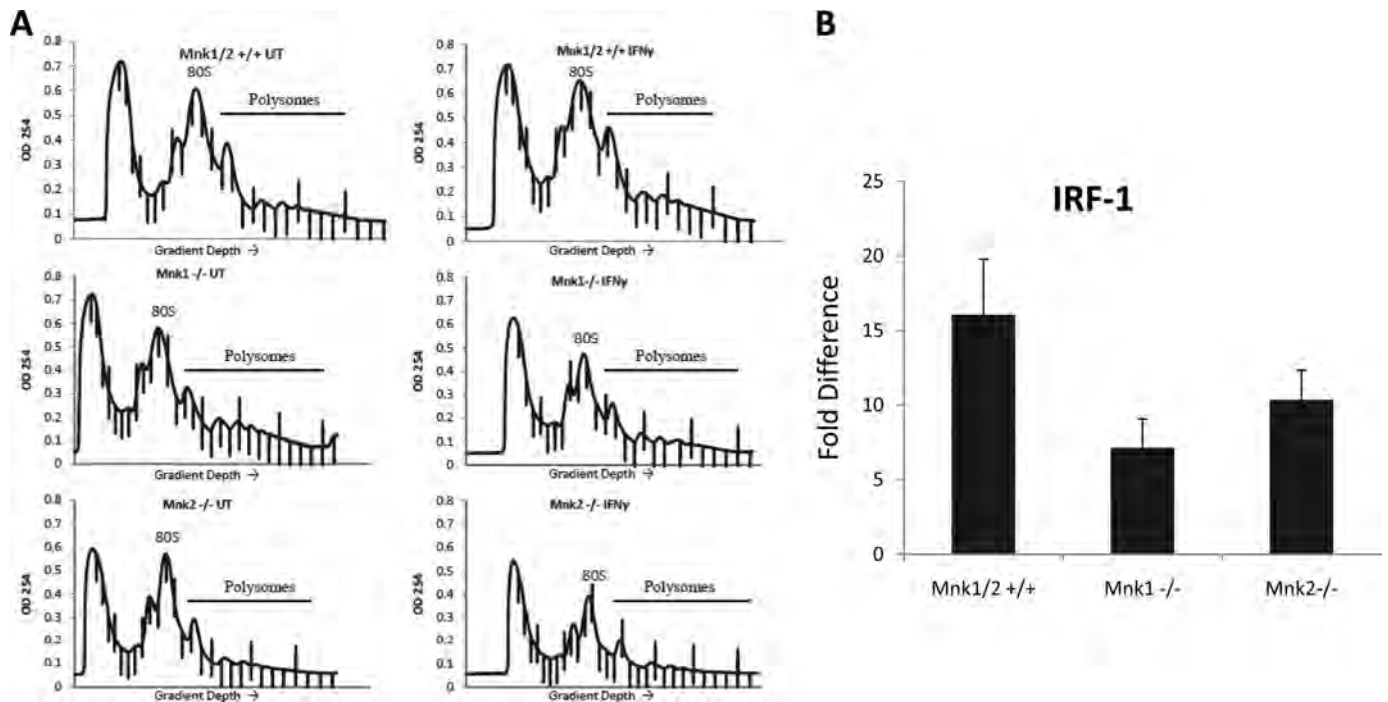


FIGURE 7. **Mnk1 and Mnk2 in IFN γ -induced mRNA translation.** *A*, Mnk1/2^{+/+}, Mnk1^{-/-}, and Mnk2^{-/-} MEFs were either left untreated or treated with mouse IFN γ . The cells were subjected to hypotonic lysis followed by separation on a 10–50% sucrose gradient, and the optical density at 254 nm (*OD* 254) was recorded. The optical density at 254 nm is shown as a function of gradient depth for each treatment. *B*, IRF-1 mRNA expression in the polysomal fractions was determined by quantitative RT-PCR, using GAPDH for normalization. The data are expressed as fold increases in the IFN γ -treated samples over untreated samples and represent the means \pm S.E. of four independent experiments.

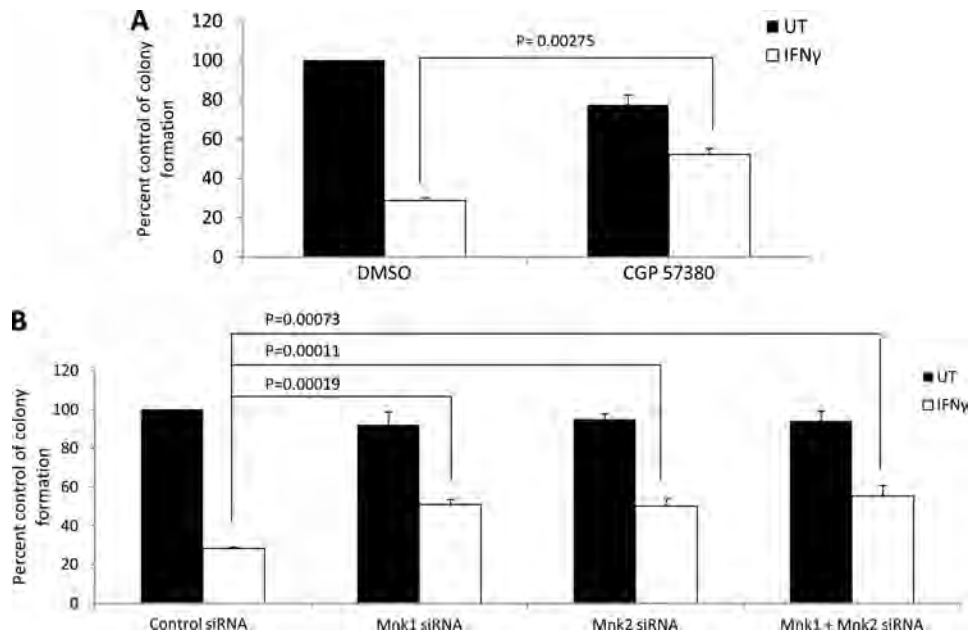


FIGURE 8. **Mnk kinases mediate the antiproliferative effects of IFN γ on U937 cells.** *A*, U937 cells were incubated in clonogenic assays in methylcellulose with or without human IFN γ , in the presence of DMSO or CGP57380, as indicated. Leukemic CFU-L colonies were scored, and the data are expressed as percentages of control DMSO treated colonies and represent the means \pm S.E. of three independent experiments. Paired *t* test analysis showed $p = 0.00275$ for the combination of DMSO and IFN γ versus the combination of CGP57380 and IFN γ . *B*, U937 cells were transfected with the indicated siRNAs and plated in a methylcellulose assay system in the absence or presence of human IFN γ . The data are expressed as percentages of control siRNA transfected cell-derived colony formation and represent the means \pm S.E. of six independent experiments. Paired *t* test analysis showed $p = 0.00019$ for the combination of control siRNA and IFN γ versus the combination of Mnk1-specific siRNA and IFN γ ; $p = 0.00011$ for the combination of control siRNA and IFN γ versus the combination of Mnk2-specific siRNA and IFN γ ; and $p = 0.00073$ for the combination of control siRNA and IFN γ versus the combination of Mnk1- and Mnk2-specific siRNAs and IFN γ . *UT*, untreated.

tiviral activities (49). This cytokine plays key roles in the generation of antineoplastic activities and in the immune surveillance against tumors (49). Interestingly, IFN γ has also been

implicated in diverse pathophysiological states, ranging from bone marrow failure (50) to arteritis (51) or atherosclerosis (52). Such a functional diversity of responses suggests the ex-

Mnk Kinases in the Generation of IFN γ Responses

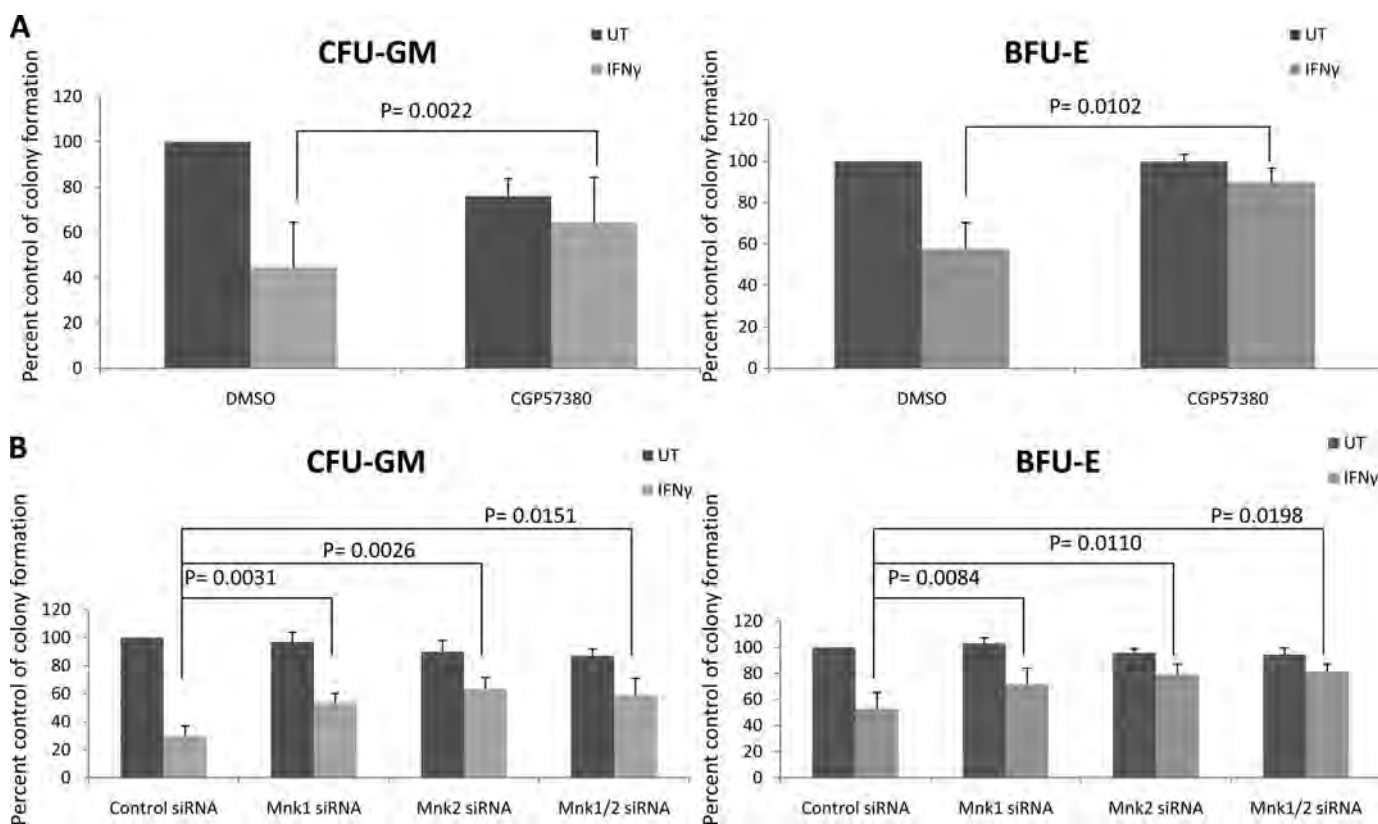


FIGURE 9. Mnk kinases are essential for the generation of the myelossuppressive effects of IFN γ . *A*, CD34⁺ cells derived from normal bone marrow were incubated in clonogenic assays in methylcellulose with or without human IFN γ , in the presence of DMSO or CGP57380, as indicated. CFU-GM and BFU-E progenitor colonies were scored after 14 days in culture. The data are expressed as percentages of control colony formation from DMSO treated cells and represent the means \pm S.E. of five independent experiments. Paired *t* test analysis showed $p = 0.0022$ for the combination of DMSO and IFN γ versus the combination of CGP57380 and IFN γ for CFU-GM colonies. Paired *t* test analysis showed $p = 0.0102$ for the combination of DMSO and IFN γ versus the combination of CGP57380 and IFN γ for BFU-E colonies. *B*, CD34⁺ cells derived from normal bone marrow were transfected with the indicated siRNAs and were then plated in a methylcellulose assay system, in the absence or presence of human IFN γ , as indicated. CFU-GM and BFU-E progenitor colonies were scored after 14 days in culture. The data are expressed as percentages of control colony formation from control siRNA transfected cells and represent the means \pm S.E. of five independent experiments. Paired *t* test analysis showed $p = 0.0031$ for the combination of control siRNA and IFN γ versus the combination of Mnk1 siRNA and IFN γ for CFU-GM colonies; and $p = 0.0084$ for the combination of control siRNAs and IFN γ versus the combination of Mnk1 siRNA and IFN γ for BFU-E colonies. Paired *t* test analysis showed $p = 0.0026$ for the combination of control siRNA and IFN γ versus the combination of Mnk2 siRNA and IFN γ for CFU-GM colonies; and $p = 0.0110$ for the combination of control siRNAs and IFN γ versus the combination of Mnk2 siRNA and IFN γ for BFU-E colonies. Paired *t* test analysis showed $p = 0.0151$ for the combination of control siRNA and IFN γ versus the combination of Mnk1 and Mnk2 siRNAs and IFN γ for CFU-GM colonies and $p = 0.0198$ for the combination of control siRNAs and IFN γ versus the combination of Mnk1 and Mnk2 siRNA and IFN γ for BFU-E colonies. UT, untreated.

istence and coordination of multiple cellular pathways activated by the Type II IFN receptor. It should be noted that the Type II IFN receptor is structurally and functionally distinct from the Type I IFN receptor, and IFN γ has only minimal identity with the family of Type I IFNs (53).

In the current study, we examined whether Mnk kinases are engaged in signaling by the Type II (IFN γ) receptor and their functional relevance in the induction of Type II IFN-mediated mRNA translation of regulated genes and generation of IFN γ responses. Our data demonstrate that Mnk1 is phosphorylated/activated in an IFN γ -inducible manner in sensitive cells and regulates downstream phosphorylation of eIF4E on serine 209. In studies using double knock-out MEFs for both Mnk1 and Mnk2, we identified a requirement for Mnks in the phosphorylation/activation of eIF4E. Moreover, mRNA translation of the IRF-1 gene and expression of the IRF-1 protein was defective in Mnk1 and/or Mnk2 MEFs, indicating a requirement for the Mnk pathway in IRF-1 protein expression. Notably, IRF-1 has been shown to promote induction of anti-tumor activities in a variety of tumors (54–56)

and to play an important role in mediating the antiproliferative effects of IFN γ in malignant mesothelioma cell lines (57) and in oligodendrocyte progenitor cells (58).

Our findings establish that the function of Mnk kinases is essential for generation of the suppressive effects of IFN γ in normal human CD34⁺-derived erythroid (BFU-E) and myeloid (CFU-GM) progenitors, defining a critical and essential role for the pathway in the regulation of normal hematopoiesis by IFN γ . Based on our data, these regulatory effects of the Mnk pathway may reflect the requirement for Mnks in IRF-1 mRNA translation, because previous studies have also shown that IRF-1 plays an important role in mediating IFN γ -induced inhibitory responses in normal human hematopoietic CD34⁺ progenitor cells (59). Thus, as in the case of Type I IFNs (60), Mnk kinases appear to play key and essential roles in mRNA translation of certain ISGs and generation of signals required for antiproliferative responses and the suppression of hematopoiesis. The requirement of the Mnk/eIF4E pathway in the generation of IFN-dependent antiproliferative responses and suppressive effects on normal and leukemic hematopoiesis is

in some ways surprising, because there is extensive evidence implicating this pathway in tumorigenesis and malignant cell proliferation (38–42, 47, 48). It is possible that, in contrast to growth factors and oncogenes, this pathway is used in a selective way by the Type II IFN receptor for mRNA translation of genes, such as IRF-1, that mediate growth inhibitory responses. Coordination of gene transcription by IFN-activated JAK-STAT pathways and IFN-dependent engagement of the Mnk/eIF4E pathway may lead to expression of proteins that mediate growth suppression. Importantly, it is possible that the Type II IFN receptor competes with growth factor receptors for use of this pathway, depriving them of a pathway essential for mitogenic responses and tumorigenesis.

In addition to eIF4E, Mnks are known to regulate the function of several other signaling proteins and effectors. Mnk1 is implicated in the phosphorylation of the heterogenous ribonuclear protein A1 (61), as well as PSF (the polypyrimidine tract-binding protein-associated splicing factor), both of which are AU-rich element-binding proteins that interact with the TNF α mRNA (62). In addition, Mnk1 phosphorylates Sprouty 2, a negative regulator of Erk signaling (63). The phosphorylation of Sprouty 2 by Mnk1 regulates its stability and prevents its degradation, providing an important control point for activation of the Erk pathway by FGF (63). Additionally, Mnk1 has been shown to phosphorylate cytosolic phospholipase A2 on serine 727, resulting in its activation and subsequent arachidonate release (64). The potential regulation of such Mnk-controlled pathways by the IFN γ receptor and implications that such pathways may have in IFN γ -induced, Mnk-dependent, hematopoietic suppression remains to be directly examined in future studies. Nevertheless, independent of the identity of putative downstream effectors that may be involved in the process, our data suggest a central role for this kinase in myelossuppression. Beyond its involvement in Type I (60) and II IFN signaling, Mnk activity is essential for mRNA translation of the gene for TNF α (62), a cytokine that exhibits potent myelossuppressive effects (65, 66). Thus, it is possible that, as is the case for p38 MAPK (17, 25, 66–68), Mnk is a central integrator of signals for the generation of myelossuppressive responses in the regulation of hematopoiesis. If this hypothesis proves to be correct, it would raise the possibility of studies to target this pathway for the treatment of bone marrow failure syndromes involving overproduction of myelossuppressive cytokines (50), and this should be addressed in future studies.

REFERENCES

- Isaacs, A., and Lindenmann, J. (1957) *Proc. R. Soc. Lond. B Biol. Sci.* **147**, 258–267
- Platanias, L. C. (2005) *Nat. Rev. Immunol.* **5**, 375–386
- Borden, E. C., Sen, G. C., Uze, G., Silverman, R. H., Ransohoff, R. M., Foster, G. R., and Stark, G. R. (2007) *Nat. Rev. Drug Discov.* **6**, 975–990
- Schoenborn, J. R., and Wilson, C. B. (2007) *Adv. Immunol.* **96**, 41–101
- Schroder, K., Hertzog, P. J., Ravasi, T., and Hume, D. A. (2004) *J. Leukocyte Biol.* **75**, 163–189
- Boehm, U., Klamp, T., Groot, M., and Howard, J. C. (1997) *Annu. Rev. Immunol.* **15**, 749–795
- Saha, B., Jyothi Prasanna, S., Chandrasekar, B., and Nandi, D. (2010) *Cytokine* **50**, 1–14
- Ikeda, H., Old, L. J., and Schreiber, R. D. (2002) *Cytokine Growth Factor Rev.* **13**, 95–109
- Weihua, X., Kolla, V., and Kalvakolanu, D. V. (1997) *Proc. Natl. Acad. Sci. U.S.A.* **94**, 103–108
- Hu, J., Roy, S. K., Shapiro, P. S., Rodig, S. R., Reddy, S. P., Platanias, L. C., Schreiber, R. D., and Kalvakolanu, D. V. (2001) *J. Biol. Chem.* **276**, 287–297
- Choudhury, G. G. (2004) *J. Biol. Chem.* **279**, 27399–27409
- Nguyen, H., Ramana, C. V., Bayes, J., and Stark, G. R. (2001) *J. Biol. Chem.* **276**, 33361–33368
- Kaur, S., Sassano, A., Dolniak, B., Joshi, S., Majchrzak-Kita, B., Baker, D. P., Hay, N., Fish, E. N., and Platanias, L. C. (2008) *Proc. Natl. Acad. Sci. U.S.A.* **105**, 4808–4813
- Kaur, S., Lal, L., Sassano, A., Majchrzak-Kita, B., Srikanth, M., Baker, D. P., Petroulakis, E., Hay, N., Sonenberg, N., Fish, E. N., and Platanias, L. C. (2007) *J. Biol. Chem.* **282**, 1757–1768
- Srivastava, K. K., Batra, S., Sassano, A., Li, Y., Majchrzak, B., Kiyokawa, H., Altman, A., Fish, E. N., and Platanias, L. C. (2004) *J. Biol. Chem.* **279**, 29911–29920
- Deb, D. K., Sassano, A., Lekmine, F., Majchrzak, B., Verma, A., Kambhampati, S., Uddin, S., Rahman, A., Fish, E. N., and Platanias, L. C. (2003) *J. Immunol.* **171**, 267–273
- Verma, A., Deb, D. K., Sassano, A., Kambhampati, S., Wickrema, A., Uddin, S., Mohindru, M., Van Besien, K., and Platanias, L. C. (2002) *J. Immunol.* **168**, 5984–5988
- Horiuchi, M., Itoh, A., Pleasure, D., and Itoh, T. (2006) *J. Biol. Chem.* **281**, 20095–20106
- Roy, S. K., Hu, J., Meng, Q., Xia, Y., Shapiro, P. S., Reddy, S. P., Platanias, L. C., Lindner, D. J., Johnson, P. F., Pritchard, C., Pagés, G., Pouyssegur, J., and Kalvakolanu, D. V. (2002) *Proc. Natl. Acad. Sci. U.S.A.* **99**, 7945–7950
- Salmenperä, P., Hämmäläinen, S., Hukkanen, M., and Kankuri, E. (2003) *Am. J. Physiol. Cell Physiol.* **284**, C1133–C1139
- Fukunaga, R., and Hunter, T. (1997) *EMBO J.* **16**, 1921–1933
- Waskiewicz, A. J., Flynn, A., Proud, C. G., and Cooper, J. A. (1997) *EMBO J.* **16**, 1909–1920
- Uddin, S., Lekmine, F., Sharma, N., Majchrzak, B., Mayer, I., Young, P. R., Bokoch, G. M., Fish, E. N., and Platanias, L. C. (2000) *J. Biol. Chem.* **275**, 27634–27640
- Kaur, S., Sassano, A., Joseph, A. M., Majchrzak-Kita, B., Eklund, E. A., Verma, A., Brachmann, S. M., Fish, E. N., and Platanias, L. C. (2008) *J. Immunol.* **181**, 7316–7323
- Uddin, S., Yenush, L., Sun, X. J., Sweet, M. E., White, M. F., and Platanias, L. C. (1995) *J. Biol. Chem.* **270**, 15938–15941
- Ahmad, S., Alsayed, Y. M., Druker, B. J., and Platanias, L. C. (1997) *J. Biol. Chem.* **272**, 29991–29994
- Verma, A., Deb, D. K., Sassano, A., Uddin, S., Varga, J., Wickrema, A., and Platanias, L. C. (2002) *J. Biol. Chem.* **277**, 7726–7735
- Horvai, A. E., Xu, L., Korzus, E., Brard, G., Kalafus, D., Mullen, T. M., Rose, D. W., Rosenfeld, M. G., and Glass, C. K. (1997) *Proc. Natl. Acad. Sci. U.S.A.* **94**, 1074–1079
- Mayer, I. A., Verma, A., Grumbach, I. M., Uddin, S., Lekmine, F., Ravandi, F., Majchrzak, B., Fujita, S., Fish, E. N., and Platanias, L. C. (2001) *J. Biol. Chem.* **276**, 28570–28577
- Dolniak, B., Katsoulidis, E., Carayol, N., Altman, J. K., Redig, A. J., Tallman, M. S., Ueda, T., Watanabe-Fukunaga, R., Fukunaga, R., and Platanias, L. C. (2008) *J. Biol. Chem.* **283**, 12034–12042
- Wang, X., Flynn, A., Waskiewicz, A. J., Webb, B. L., Vries, R. G., Baines, I. A., Cooper, J. A., and Proud, C. G. (1998) *J. Biol. Chem.* **273**, 9373–9377
- Waskiewicz, A. J., Johnson, J. C., Penn, B., Mahalingam, M., Kimball, S. R., and Cooper, J. A. (1999) *Mol. Cell Biol.* **19**, 1871–1880
- Scheper, G. C., Morrice, N. A., Kleijn, M., and Proud, C. G. (2001) *Mol. Cell Biol.* **21**, 743–754
- Ueda, T., Watanabe-Fukunaga, R., Fukuyama, H., Nagata, S., and Fukunaga, R. (2004) *Mol. Cell Biol.* **24**, 6539–6549
- Meng, Q., Raha, A., Roy, S., Hu, J., and Kalvakolanu, D. V. (2005) *J. Immunol.* **174**, 6203–6211
- Valledor, A. F., Sánchez-Tilló, E., Arpa, L., Park, J. M., Caelles, C.,

Mnk Kinases in the Generation of IFN γ Responses

- Lloberas, J., and Celada, A. (2008) *J. Immunol.* **180**, 4523–4529
37. Buxade, M., Parra-Palau, J. L., and Proud, C. G. (2008) *Front. Biosci.* **13**, 5359–5373
38. Flynn, A., and Proud, C. G. (1995) *J. Biol. Chem.* **270**, 21684–21688
39. Pyronnet, S., Dostie, J., and Sonenberg, N. (2001) *Genes. Dev.* **15**, 2083–2093
40. Ishida, M., Ishida, T., Nakashima, H., Miho, N., Miyagawa, K., Chayama, K., Oshima, T., Kambe, M., and Yoshizumi, M. (2003) *Circ. Res.* **93**, 1218–1224
41. Wheeler, M. J., Johnson, P. W., and Blaydes, J. P. (2010) *Cancer Biol. Ther.* **10**, 728–735
42. Bianchini, A., Loiarro, M., Bielli, P., Busà, R., Paronetto, M. P., Loreni, F., Geremia, R., and Sette, C. (2008) *Carcinogenesis* **29**, 2279–2288
43. Andersson, K., and Sundler, R. (2006) *Cytokine* **33**, 52–57
44. Rowlett, R. M., Chrestensen, C. A., Nyce, M., Harp, M. G., Pelo, J. W., Cominelli, F., Ernst, P. B., Pizarro, T. T., Sturgill, T. W., and Worthington, M. T. (2008) *Am. J. Physiol. Gastrointest. Liver Physiol.* **294**, G452–G459
45. Origanti, S., and Shantz, L. M. (2007) *Cancer Res.* **67**, 4834–4842
46. Goetz, C., Everson, R. G., Zhang, L. C., and Gromeier, M. (2010) *Mol. Ther.* **18**, 1937–1946
47. Furic, L., Rong, L., Larsson, O., Koumakpayi, I. H., Yoshida, K., Brueschke, A., Petroulakis, E., Robichaud, N., Pollak, M., Gaboury, L. A., Pandolfi, P. P., Saad, F., and Sonenberg, N. (2010) *Proc. Natl. Acad. Sci. U.S.A.* **107**, 14134–14139
48. Ueda, T., Sasaki, M., Elia, A. J., Chio, II., Hamada, K., Fukunaga, R., and Mak, T. W. (2010) *Proc. Natl. Acad. Sci. U.S.A.* **107**, 13984–13990
49. Miller, C. H., Maher, S. G., and Young, H. A. (2009) *Ann. N.Y. Acad. Sci.* **1182**, 69–79
50. Young, N. S., Calado, R. T., and Scheinberg, P. (2006) *Blood* **108**, 2509–2519
51. Weyand, C. M., Younge, B. R., and Goronzy, J. J. (2011) *Curr. Opin. Rheumatol.* **23**, 43–49
52. McLaren, J. E., and Ramji, D. P. (2009) *Cytokine Growth Factor Rev.* **20**, 125–135
53. Pestka, S., Krause, C. D., and Walter, M. R. (2004) *Immunol. Rev.* **202**, 8–32
54. Bouker, K. B., Skaar, T. C., Riggins, R. B., Harburger, D. S., Fernandez, D. R., Zwart, A., Wang, A., and Clarke, R. (2005) *Carcinogenesis* **26**, 1527–1535
55. Bowie, M. L., Ibarra, C., and Seewalt, V. L. (2008) *Adv. Exp. Med. Biol.* **617**, 367–374
56. Kröger, A., Dallügge, A., Kirchhoff, S., and Hauser, H. (2003) *Oncogene* **22**, 1045–1056
57. Buard, A., Vivo, C., Monnet, I., Boutin, C., Pilatte, Y., and Jaurand, M. C. (1998) *Cancer Res.* **58**, 840–847
58. Wang, Y., Ren, Z., Tao, D., Tilwalli, S., Goswami, R., and Balabanov, R. (2010) *Glia* **58**, 195–208
59. Sato, T., Selleri, C., Young, N. S., and Maciejewski, J. P. (1995) *Blood* **86**, 3373–3380
60. Joshi, S., Kaur, S., Redig, A. J., Goldsborough, K., David, K., Ueda, T., Watanabe-Fukunaga, R., Baker, D. P., Fish, E. N., Fukunaga, R., and Platanius, L. C. (2009) *Proc. Natl. Acad. Sci. U.S.A.* **106**, 12097–12102
61. Buxadé, M., Parra, J. L., Rousseau, S., Shpiro, N., Marquez, R., Morrice, N., Bain, J., Espel, E., and Proud, C. G. (2005) *Immunity* **23**, 177–189
62. Buxadé, M., Morrice, N., Krebs, D. L., and Proud, C. G. (2008) *J. Biol. Chem.* **283**, 57–65
63. DaSilva, J., Xu, L., Kim, H. J., Miller, W. T., and Bar-Sagi, D. (2006) *Mol. Cell. Biol.* **26**, 1898–1907
64. Hefner, Y., Borsch-Haubold, A. G., Murakami, M., Wilde, J. I., Pasquet, S., Schieltz, D., Ghomashchi, F., Yates, J. R., 3rd, Armstrong, C. G., Paterson, A., Cohen, P., Fukunaga, R., Hunter, T., Kudo, I., Watson, S. P., and Gelb, M. H. (2000) *J. Biol. Chem.* **275**, 37542–37551
65. Broxmeyer, H. E., Williams, D. E., Lu, L., Cooper, S., Anderson, S. L., Beyer, G. S., Hoffman, R., and Rubin, B. Y. (1986) *J. Immunol.* **136**, 4487–4495
66. Katsoulidis, E., Li, Y., Yoon, P., Sassano, A., Altman, J., Kannan-Thulasiraman, P., Balasubramanian, L., Parmar, S., Varga, J., Tallman, M. S., Verma, A., and Platanius, L. C. (2005) *Cancer Res.* **65**, 9029–9037
67. Platanius, L. C. (2003) *Pharmacol. Ther.* **98**, 129–142
68. Platanius, L. C. (2003) *Blood* **101**, 4667–4679

Amino Acid Sequences of Ferredoxins from Several Species of Genus *Ephedra*[☆]

Yoshiki MINO*, Takashi AZUMA, and Takaji SATO

Laboratory of Analytical Chemistry, Osaka University of Pharmaceutical Sciences
4-20-1 Nasahara, Takatsuki, Osaka 569-1094, Japan.

(Received December 17, 2014; Accepted January 15, 2015)

Abstract The complete amino acid sequences of [2Fe-2S] ferredoxins (Fds) from seven species of genus *Ephedra* (*E. sinica*, *E. distachya*, *E. equisetina*, *E. viridis*, *E. intermedia*, *E. foliate*, and *E. americana*) were determined by automated Edman degradation of the entire S-carboxymethylcysteinyl proteins and of the peptides obtained by enzymatic digestion. *E. sinica*-Fds (I and II), which differ from one another in the amino acid residue at position 95 (Ile for I and Leu for II), have unique amino acid sequences, which include Asn-14, Asp-30, Met-51, Cys-85, Gln-88, and Gln-91, and a deletion of one amino acid residue at the carboxyl terminus. *E. distachya* and *E. equisetina* have the same Fds (I and II) as *E. sinica*-Fds. *E. viridis* and *E. intermedia* only have a Fd that is the same as *E. sinica*-Fd I. *E. foliate*-Fd shows a difference of only one amino acid residue (Val at position 95) compared to other *Ephedra* Fds. In contrast, *E. americana* shows differences in five and six amino acid residues from the other *Ephedra*-Fds, which suggests that *E. americana* is somewhat distantly related to the others. These *Ephedra* Fds have 21-34 differences in their amino acid sequences compared to those of Angiospermous plants except for *Pueraria lobata*. In contrast, 38-40 differences were observed when they were compared to *Equisetum telmateia* and *E. arvense* (horsetail plants). This suggests that *Ephedra* plants are remotely related taxonomically to horsetail plants, although they seem to be morphologically similar. In practice, *Ephedra* plants and horsetail plants belong to different phyla: Spermatophyta and Pterophyta, respectively.

Key words — ferredoxin; *Ephedra sinica*; genus *Ephedra*; Ephedraceae; amino acid sequence; protein chemotaxonomy

INTRODUCTION

Although classical taxonomy, which is based largely on morphological and anatomical characteristics, is still a dominant concept in plant classification, chemical taxonomy has also been used to help clarify the relationships among genera and species when there is a need to confirm or revise an existing taxonomy. We have proposed the term 'protein chemotaxonomy' to describe molecular taxonomy based on the primary structures of common plant proteins, instead of so-called secondary metabolites. To evaluate the effectiveness of this concept, we carried out a series of studies on the family Solanaceae, using ferredoxin

(Fd), an iron-sulfur electron-transfer protein.¹⁾ This protein was chosen because it is easy to isolate and has an appropriate molecular weight for determining the primary structure. Previously, we reported the primary structures of Fds from 14 solanaceous plants,²⁻¹¹⁾ one leguminous plant,¹²⁾ and one alariaceous plant.¹³⁾ Our recent results suggested that their amino acid sequences were related to their taxonomic position among plants that belong to the same genus or family, but not among plants in different families, although there may not be enough sequence data to reach any definite conclusions. It may be worthwhile to determine the amino acid sequences of Fds from many important medicinal plants that belong to different families. These considerations

[☆] Part 14 in the series "Protein Chemotaxonomy".

* e-mail: mino@gly.oups.ac.jp

led us to elucidate the amino acid sequence of Fd from *Ephedra sinica* (Ephedraceae, Ephedrales, Gnetopsida, Gymnospermae, Spermatophyta), the dried aerial part of which is one of the most commonly used traditional medicines in China, Korea, and other Asian countries for the treatment of asthma, allergic rhinitis, upper respiratory infection, and cold.

In this study, we determined the primary structures of Fds from *E. sinica* and several species of genus *Ephedra* and compared them with those of Fds from other higher plants.

MATERIALS AND METHODS

Materials *E. sinica* was cultivated in the herb garden at Osaka University of Pharmaceutical Sciences. The fresh leaves of *E. distachya*, *E. equisetina*, *E. viridis*, *E. foliata*, and *E. americana* were kind gifts from the Nippon Shinyaku Institute for Botanical Research (Kyoto, Japan). The fresh leaves of *E. intermedia* were obtained from the Research Center for Medicinal Plant Resources, National Institute of Biomedical Innovation (Tsukuba, Ibaragi, Japan).

Isolation of ferredoxin Each Fd (*ca.* 4 mg) was purified from the fresh aerial parts (*ca.* 500 g) of each *Ephedra* plant as described previously,^{2,6)} except that 0.02 M Tris-HCl buffer, pH7.5, containing 0.5% Tween 80 was used for the extraction of Fd from the plant sample instead of a buffer without a surface-active agent.

Sequence determination The amino acid sequences of Fds were determined using a gas-phase protein sequencer with automated Edman degradation of S-carboxymethylcysteinyl (Cm) Fd and the peptides obtained by lysyl endopeptidase, trypsin, or endoproteinase Asp-N digestion. The peptides were purified by reversed-phase HPLC using a μ -Bondasphere C₁₈-100Å column (0.39×15cm, Waters) with a solvent system consisting of TFA-

MeCN-H₂O (A=0.1% TFA, B=MeCN containing 0.1% TFA) with a gradient program of 0-40% B in 50 min, flow rate 1 ml min⁻¹. C-terminal analysis was carried out with carboxypeptidase Y.

The details of the procedure and other methods have been described previously.^{2,6)}

Construction of a phylogenetic tree A phylogenetic tree was constructed from the amino acid sequences (97 residues) of higher-plant Fds (39 species) using the unweighed pair-group method with arithmetical averages (UPGMA) as described by Nei (1994) (GENETYX software, Software Development, Japan).¹⁴⁾

RESULTS AND DISCUSSION

Properties of ferredoxins The absorption maxima in the UV-Vis spectrum of *E. sinica* (*Es*)-Fd were at 275, 285(sh), 330, 420, and 465 nm, and showed A_{max}/A_{275nm} ratios of 0.65, 0.44, and 0.38, respectively. This spectrum was characteristic of [2Fe-2S] Fds from other higher plants.¹⁵⁾ The molar absorption coefficient at 420 nm, based on the spectrum and protein determination, was 11000 M⁻¹cm⁻¹, which was similar to those of other higher-plant Fds.^{1,15)} The biological activities and other physico-chemical properties of *Es*-Fd will be published elsewhere. The other *Ephedra* Fds exhibited properties similar to those of *Es*-Fd.

Sequence determination The sequencing strategy for *Es*-Fd is summarized in Fig.1. The analytical results regarding the amino acid compositions of Cm-Fd and the peptides obtained by enzymatic digestion were consistent with the derived sequences. Automated Edman degradation of *Es*-Cm-Fd yielded the amino-terminal sequence up to the 42nd cycle. Lysyl endopeptidase digestion gave two short peptides [L-1 (1-4) and L-2 (5-6)] and four long peptides [L-3 (7-50), L-4 (51-82), L-5 (83-96), and L-5' (83-96)]. Although Lys-91 was conserved in almost all of the

Fds, except for *Gleichenia japonica* (fern)-Fd, in this case the residue was changed to Gln-91. These peptides were isolated by reversed-phase HPLC; their t_R values were 14.4 for L-1(1-4), 29.6 for L-5(83-96), 30.4 for L-5'(83-96), 46.4 for L-3(7-50), and 46.8 min for L-4(51-82), while L-2 was missing. The isolation of L-5 (83-96) and L-5' (83-96) in almost the same amounts clearly indicates the existence of isoforms Fd-I and -II as *Es*-Fd. Sequence analyses of L-5 and L-5' clarified the sequences of 83-96 and a difference in the amino acid residue at position 95 between Fd-I and -II (Ile for I and Leu for II). Edman degradation of L-3-T-2, obtained by tryptic digestion of L-3 (7-50), confirmed the sequence of 41-50. Since there was not enough of the peptides, L-4 (51-82), to determine the sequence near the carboxyl terminus of the peptide, a proper short peptide containing the carboxyl terminus was needed. Endoproteinase Asp-N digestion of L-4 should give several short peptides [L-4-D-1 (51-56), L-4-D-2 (57-59), L-4-D-3 (60-64), and L-4-D-4 (65-82)]. These peptides were also isolated by HPLC;

their t_R values were 20.8 for L-4-D-1,2 (51-59), 31.6 for L-4-D-3, and 41.6 min for L-4-D-4, while L-4-D-1 and L-4-D-2 were missing because of their small yields. Sequence analysis of L-4-D-4 confirmed the end part of 65-82. The N-terminal sequence was confirmed by the isolation of L-1 (Ala-Thr-Tyr-Lys). In addition, carboxypeptidase Y digestion of Cm-Fd for different periods of time suggested that the C-terminal sequence was-Ala-Leu(Ile)-Ala-COOH. This result was reasonably consistent with the C-terminal sequence obtained by Edman degradation of the peptide, L-5 (83-96). These results led to the complete amino acid sequences for *Es*-Fds, as shown in Fig. 1.

In the case of *E. americana* (*Ea*)-Fd, due to the lack of Lys-82, no peak appeared near 30 min (t_R) in the chromatogram of the peptides obtained by lysyl endopeptidase digestion. Instead, the long peptide 51-96 appeared at 46.8 min. Sequence analyses of this peptide clarified the sequences of 51-96 of *Ea*-Fd. This result was confirmed by sequence analyses of the short peptides obtained by Endoproteinase Asp-N digestion

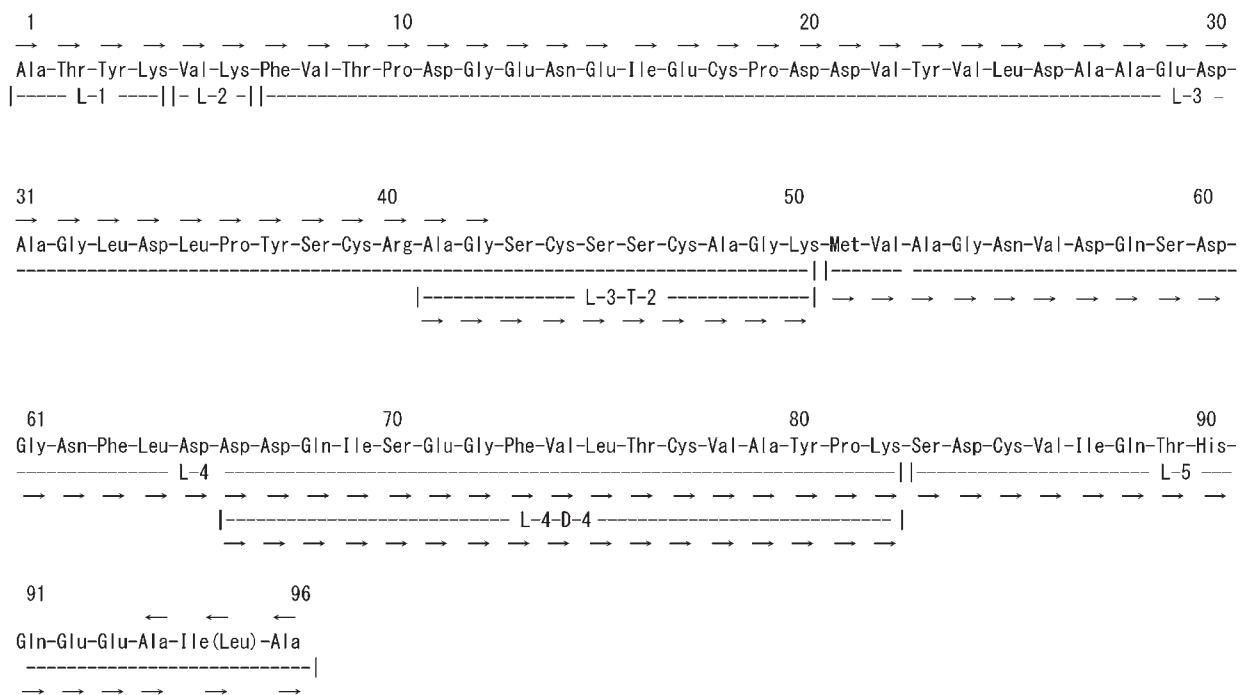


Fig. 1. Amino Acid Sequences of *Ephedra sinica* Ferredoxins

Arrows (\rightarrow) and (\leftarrow) represent residues determined by automated Edman degradation and carboxypeptidase Y digestion, respectively. L (1-5), T-2, and D-4 represent peptides obtained from lysyl endopeptidase, trypsin, and endoproteinase Asp-N digestion, respectively. Only the amino acid sequence of ferredoxin I is shown; for ferredoxin II, the difference in the amino acid residue at position 95 (Leu instead of Ile) is shown in parentheses.

of the long peptide. The other *Ephedra* Fds could be analyzed in almost the same manner as for *Es*-Fd.

Figure 2 shows a comparison of the amino acid sequences among *Ephedra* plant-Fds. *E. sinica* has two isoforms of *Es*-Fd. These isoforms differed from one another in the amino acid residues at position 95; Ile for *Es*-Fd I and Leu for *Es*-Fd II. *E. distachya* and *E. equisetina* also have two isoforms, which have the same amino acid sequences as *Es*-Fds I and II. In contrast, *E. viridis* and *E. intermedia* have only one kind of Fd, which has the same amino acid sequence as *Es*-Fd I. A minor (ca. 20%) *E. intermedia* (*Ei*)-Fd showed differences in two or three amino acids compared to *Es*-Fd I or II. The Fd of *E. foliata* differs from *Es*-Fd I in only one amino acid residue at position 95, which gives Val instead of Ile or Leu. Interestingly, the Fd from *E. americana* had five or six differences in the amino acid sequence compared to the other *Ephedra* Fds, which suggests that *E. americana* is somewhat remotely related to the other *Ephedra* plants, although the other *Ephedra* plants are very closely related to each other. It is also very interesting that only *E. americana* does not contain the alkaloid ephedrine.

In Fig. 3, these amino acid sequences are compared to those of higher-plant Fds.^{2,13,16-18} In comparison to other Fds, a noticeable feature of the present representative sequence, *Es*-Fd, is the isoform with Ile or Leu at position 95 from the amino terminus and a deletion of one amino acid residue at the carboxyl terminus. In comparison to other higher-plant Fds, differences were observed at Phe-7, as with *Brassica napus* (*Bn*) (Cruciferae)-and *Gleichenia japonica* (*Gj*)(Filicales)-

Fds, at Ile-16, as with *Phytolacca americana* (*Pa*)-, *P. esculenta* (*Pe*)(*Phytolaccaceae*)-and *Gj*-Fds, at Val-24, as with *Bn*-, *Petroselinum sativum* (*Ps*)(*Umbelliferae*), *Pa*- and *Pe*-Fds, at Leu-33, as with *Pa*-, *Pe*- and *Gj*-Fds, at Asn-55, as with *Solanum lyratum* (*Solanaceae*)-, *Nicotiana tabacum* (*Solanaceae*)-, and *Trifolium pratense* (*Leguminosae*)-Fds, at Ala-94, as with *Solanum indium* (*Solanaceae*)- and *Lycium chinense* (*Solanaceae*)-Fds, at Ile-95, as with *Ps*-, *Pa*-, and *Pe*-Fds, and at Ala-96, as with *Pe*-Fd. The residues Asn-14, Asp-30, Met-51, Ser-70, Cys-85, Gln-88, and Gln-91 were only observed in the primary structure of this *Es*-Fd among these higher-plant Fds. These residues are characteristic of *Es*-Fd. The residues Met-2 and Leu-8 are also characteristic of *Ea*-Fd. In Fds, the sequence 35-50, including the sequence -C39-C44-C47-, which participates in chelation to iron atoms, the sequence 74-77, which contains the last cysteine ligand (-C77-) for the iron atom, and the region 83-93 are almost perfectly conserved. This was also true in the case of *Ephedra* plant-Fds, except for four differences observed in the region 83-93.

Taxonomic Considerations Ephedrales consist of a single family (Ephedraceae) containing a single genus (*Ephedra*), and are known as the jointfirs because they have long slender branches which bear tiny scale-like leaves at their nodes. The aerial parts of some *Ephedra* plants have been traditionally used as a stimulant, but are controlled substances today in many jurisdictions because of the risk of harmful or even fatal overdosing. The genus *Ephedra*, which contains about 35 species,

	1	2	3	4	5	6	7	8	9
(1) <i>Ephedra sinica</i> I ¶	ATYKVKFVTPDGENEIECPDDVYVLDAAEDAGLDLPYSCRAGSCSSCAGKMWAGNVDSQSDGNFLDDDDQISEGFVLTVCVAYPKSDCVIQTHQEEAIA-	0	0	0	0	0	0	0	0
(2) <i>Ephedra sinica</i> II §	ATYKVKFVTPDGENEIECPDDVYVLDAAEDAGLDLPYSCRAGSCSSCAGKMWAGNVDSQSDGNFLDDDDQISEGFVLTVCVAYPKSDCVIQTHQEEAIA-	0	0	0	0	0	0	0	0
(3) <i>Ephedra foliata</i>	ATYKVKFVTPDGENEIECPDDVYVLDAAEDAGLDLPYSCRAGSCSSCAGKMWAGNVDSQSDGNFLDDDDQISEGFVLTVCVAYPKSDCVIQTHQEEAIA-	0	0	0	0	0	0	0	0
(4) <i>Ephedra intermedia</i> £	ATYKVKFVTPDGENEIECPDDVYVLDAAEDAGLDLPYSCRAGSCSSCAGKMWAGNVDSQSDGNFLDDDDQISEGFVLTVCVAYPKSDCVIQTHQEEAIA-	0	0	0	0	0	0	0	0
(5) <i>Ephedra americana</i>	ATYKVKFVTPDGENEIECPDDVYVLDAAEDAGLDLPYSCRAGSCSSCAGKMWAGNVDSQSDGNFLDDDDQISEGFVLTVCVAYPKSDCVIQTHQEEAIA-	0	0	0	0	0	0	0	0

Fig. 2. Comparison of the Sequences of [2Fe-2S] Ferredoxins from *Ephedra* Plants

Amino acids are represented by one-letter abbreviations. ¶, *E. distachya* I, *E. equisetina* I, *E. viridis*, and *E. intermedia*; §, *E. distachya* II and *E. equisetina* II; £, minor Fd from *E. intermedia*

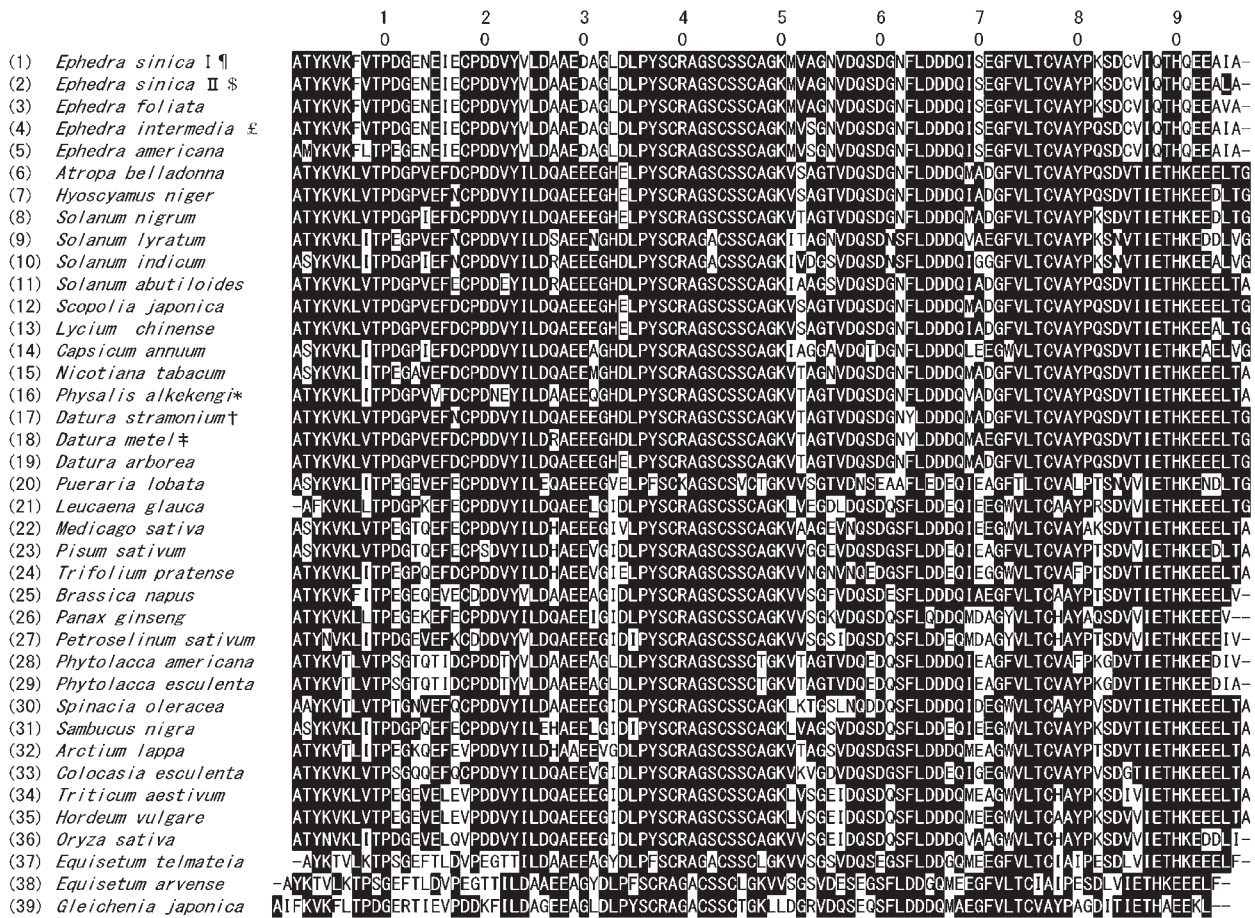


Fig. 3. Comparison of the Sequences of [2Fe-2S] Ferredoxins from Higher Plants

Amino acids are represented by one-letter abbreviations. ¶, *E. distachya* I, *E. equisetina* I, *E. viridis*, and *E. intermedia*; \$, *E. distachya* II and *E. equisetina* II; £, minor Fd from *E. intermedia*;*, *Physalis alkekengi* var. *francheti*; †, var. *stramonium* and var. *tatula*, and *D. quercifolia*, ‡, *D. metel*, *D. innoxia*, and *D. fastuosa*. References for the sequences are: (6) and (7) in (11), (8)–(11) in (10), (12) and (13) in (9), (14) in (8), (15) in (7), (16) in (6), (17) in (2), (18) in (3), (19) in (4), (20) in (12), (21), (22), (25), (27)–(34), and (37)–(39) in (16), (16) in (13), (35) in (18), (36) in (17), and (23) and (24) listed in accession numbers M31713 and AY340639, respectively.

Table 1. Amino Acid Differences Between *Ephedra* Ferredoxins and Other Higher-plant Ferredoxins

	(1)	(2)	(3)	(4)	(5)		(1)	(2)	(3)	(4)	(5)
(1) <i>Ephedra sinica</i> I ¶	0	1	1	2	5	(21) <i>Leucaena glauca</i>	31	30	31	31	31
(2) <i>Ephedra sinica</i> II \$	1	0	1	3	6	(22) <i>Medicago sativa</i>	28	27	28	30	30
(3) <i>Ephedra foliata</i>	1	1	0	3	6	(23) <i>Pisum sativum</i>	26	25	26	26	28
(4) <i>Ephedra intermedia</i> £	2	3	3	0	3	(24) <i>Trifolium pratense</i>	32	31	32	32	32
(5) <i>Ephedra americana</i>	5	6	6	3	0	(25) <i>Brassica napus</i>	22	21	22	21	21
(6) <i>Atropa belladonna</i>	26	25	26	26	29	(26) <i>Panax ginseng</i>	29	29	28	27	26
(7) <i>Hyoscyamus niger</i>	25	24	25	25	28	(27) <i>Petroselinum sativum</i>	30	31	31	29	31
(8) <i>Solanum nigrum</i>	25	24	25	27	30	(28) <i>Phytolacca americana</i>	26	27	27	28	30
(9) <i>Solanum lyratum</i>	29	28	29	31	31	(29) <i>Phytolacca esculenta</i>	24	25	25	26	28
(10) <i>Solanum indicum</i>	28	27	28	29	30	(30) <i>Spinacia oleracea</i>	33	32	33	33	34
(11) <i>Solanum abutiloides</i>	24	23	24	24	27	(31) <i>Sambucus nigra</i>	28	27	28	30	31
(12) <i>Scopolia japonica</i>	26	25	26	26	29	(32) <i>Arctium lappa</i>	32	31	32	33	33
(13) <i>Lycium chinense</i>	24	23	24	24	27	(33) <i>Colocasia esculenta</i>	28	27	28	28	30
(14) <i>Capsicum annuum</i>	29	28	29	28	29	(34) <i>Triticum aestivum</i>	28	27	28	28	29
(15) <i>Nicotiana tabacum</i>	27	26	27	27	26	(35) <i>Hordeum vulgare</i>	27	26	27	27	28
(16) <i>Physalis alkekengi</i> *	28	27	28	28	30	(36) <i>Oryza sativa</i>	30	29	30	30	32
(17) <i>Datura stramonium</i> †	26	25	26	26	29	(37) <i>Equisetum telmateia</i>	39	38	39	38	38
(18) <i>Datura metel</i> ‡	25	24	25	25	28	(38) <i>Equisetum arvense</i>	40	39	40	39	39
(19) <i>Datura arborea</i>	26	25	26	26	29	(39) <i>Gleichenia japonica</i>	31	30	31	31	31
(20) <i>Pueraria lobata</i>	40	39	40	39	38						

See legend to Fig. 3. (1) belongs to Ephedraceae (order: Ephedrales, class: Gnetales, subclass: Gnetales, subphylum: Gymnosperms, phylum: Spermatophyta) (6)–(19) to Solanaceae; (20)–(24) to Leguminosae; (25) to Cruciferae; (26) to Araliaceae; (27) to Umbelliferae; (28) and (29) to Phytolaccaceae; (30) to Chenopodiaceae; (31) to Caprifoliaceae; (32) to Compositae; (33) to Araceae; (34)–(36) to Gramineae; (37) and (38) to Equisetaceae (order: Equisetales, class: Articulatae, phylum: Pteridophyta); and (39) to Gleicheniaceae (order: Filicales, class: Filicinae, phylum: Pteridophyta).

is represented by *E. sinica*.¹⁹⁾

Many primary structures have been reported for chloroplast [2Fe-2S] Fds.^{2-13, 16-18)} The number of amino acid differences is 14-40 for different families and 0 to 4 for the same genus, except for the genus *Solanum*.¹⁰⁾ In our recent study, 2 to 19 amino acid differences were observed among different genera of Solanaceae; *Datura*, *Physalis*, *Nicotiana*, *Capsicum*, *Scopolia*, and *Lycium*. Table 1 shows amino acid differences in *Ephedra* plant-Fds compared to other higher-plant Fds that have been determined so far. These *Ephedra* plant-Fds exhibited 21-34 differences in their amino acid sequences compared to those of Angiosperms, except for *P. lobata* (38-40 differences). In contrast, 38-40 differences were observed compared to *E. telmateia* and *arvensis* (horsetails), respectively. This suggests that *Ephedra* plants are remotely related

taxonomically to horsetails. Note that only 21-24 differences were observed between *Ephedra* plant-Fds and those of several dicotyledonous plants, *B. napus* (Cruciferae) and some solanaceous plants. This does not necessarily indicate a close taxonomic relation between *Ephedra* plants and these dicotyledonous plants. As described by Matsubara and Hase,¹⁶⁾ it may be difficult to deduce the relation at the family or order level based only on Fds. Nevertheless, it is interesting that *Ephedra* plant-Fds showed the lowest similarity to *Equisetum*-Fd (Equisetales) among those of higher plants, despite their morphological similarity. In practice, the genus *Ephedra* (phylum Spermatophyta) is thought to be remotely related to the genus *Equisetum* (phylum Pteridophyta).

Figure 4 shows a phylogenetic tree based on the Fd sequences of higher plants.¹⁴⁾ Fourteen solanaceous



Fig. 4. Phylogenetic Tree Based on the Amino Acid Sequences of Ferredoxins from Higher Plants

The phylogenetic tree was constructed using the UPGMA method of Nei (1987) (GENETYX software).¹⁴⁾ Genetic distances are represented by the proportion of amino acid differences between each taxon (1.0 = 100%).

plants form a cluster that is distinctly separated from other angiospermous plants, ferns, and horsetails by appreciably long branch lengths, which increase in that order. In the solanaceous cluster, five genera, *Atropa*, *Hyoscyamus*, *Scopolia*, *Lycium*, and *Datura*, are separated from each other by short branch lengths, which suggests a close taxonomic relationship among them. On the other hand, *Ephedra* plants (subphylum Gymnospermae) form a small cluster with short branch lengths. This cluster forms a greater cluster together with *B. napus* and two *Phytolacca* plants which belong in a different subphylum (Angiospermae), with a considerably long branch length. Furthermore, this cluster forms a greater cluster with other plants of Angiospermae except for *P. lobata*, which suggests that the correlation between the Fd structures and the taxonomic position of plant taxa is not reasonable. This can be partially accounted for by the rapid evolution of Fds. The number of mutations seems to have been saturated in a relatively short period for a small protein, and differences in the numbers of amino acids in Fds of remotely related plants do not reflect real phylogenetic distances.¹⁶⁾ Nevertheless, it is interesting that differences in the numbers of amino acids in Fds reflect the most remote relation between *Ephedra* plants and horsetails.

In conclusion, *Ephedra* plant-Fds possess unique amino acid sequences that are distinct from those of other Fds based on Asn-14, Asp-30, Met-51, Cys-85, Gln-88, Gln-91, and the deletion of one amino acid residue at the C-terminus. While *E. sinica*, *E. distachya*, *E. equisetina*, *E. viridis*, and *E. intermedia* have identical or very similar Fds, the Fd from *E. americana* was somewhat different from those of the other *Ephedra* plants. These results suggest that *E. americana*, which does not contain ephedrine, is somewhat distantly related to the other ephedrine-containing *Ephedra* plants, although the others are very closely related to each other. A comparison of the amino acid sequence of *Ephedra* plant-Fds to those of other higher plants indicated that *Ephedra* plants (class Gnetopsida, phylum Spermatophyta) and

horsetails (class Articulatae, phylum Pteridophyta) are remotely related. For further discussion, we would need additional information regarding the amino acid sequences of Fds from these two classes.

Acknowledgements The author is grateful to Dr. Tooru Akita, Head of the Nippon Shinyaku Institute for Botanical Research (Kyoto, Japan), for supplying the fresh leaves of several *Ephedra* plants, and for participating in helpful discussions. Thanks are also due to Misses Akiko Ishii, Masumi Yamashita, and Yuko Murata for their technical assistance. This work was supported in part by a Grant-in-Aid for High Technology Research from the Ministry of Education, Culture, Sports, Science, and Technology, Japan.

References

- 1) Palmer G., in "Iron-Sulfur Proteins II," ed. by Lovenberg W., Academic Press, New York, 1973, pp. 285-325.
- 2) Mino Y., Usami, H., Inoue, S., Ikeda, K., Ota, N., *Phytochemistry*, **33**, 601-605 (1993).
- 3) Mino Y., *Phytochemistry*, **35**, 385-387 (1994).
- 4) Mino Y., *Phytochemistry*, **37**, 429-431 (1994).
- 5) Mino Y., *Chem. Pharm. Bull.*, **43**, 1186-1189 (1995).
- 6) Mino Y., Yasuda K., *Phytochemistry*, **49**, 1631-1636 (1998).
- 7) Mino Y., Iwao M., *Biol. Pharm. Bull.*, **22**, 96-99 (1999).
- 8) Mino Y., Iwao M., *Natural Med.*, **53**, 37-41 (1999).
- 9) Mino Y., *Biol. Pharm. Bull.*, **25**, 1367-1369 (2002).
- 10) Mino Y., Hazama T., Machida Y., *Phytochemistry*, **62**, 657-662 (2003).
- 11) Mino Y., Yukita M., Hiratsuka N., Wariishi H., *Biol. Pharm. Bull.*, **28**, 1535-1538 (2005).
- 12) Mino Y., Machida Y., Wariishi H., *Natural Med.*, **59**, 181-185 (2005).
- 13) Mino Y., *Biol. Pharm. Bull.*, **29**, 1771-1774 (2006).
- 14) Nei M., in "Molecular Evolutionary Genetics," ed. by Nei M., Columbia University Press, New York,

- 1987, pp. 287-326.
- 15) Buchanan B. B., Arnon D. I., *Methods Enzymol.*, **23**, 413-440 (1971).
- 16) Matsubara H., Hase T., in "Proteins and Nucleic Acids in Plant Systematics," ed. by Jansen U., Fairbrothers D.E., Springer-Verlag, Berlin, 1983, pp. 168-181.
- 17) Kamo M., Kotani N., Tsugita A., He Y. K., Nozu Y., *Protein Seq. Data Anal.*, **2**, 289-293 (1989).
- 18) Takruri I. A. H., *Phytochemistry*, **30**, 415-418 (1991).
- 19) Tobe H., in "Asahi Encyclopedia, World of Flora," ed. by Suzuki, M., Asahi Shimbun Company, Tokyo, 1994, pp.11-170-11-172.

RESEARCH ARTICLE

Detection of Peramivir and Laninamivir, New Anti-Influenza Drugs, in Sewage Effluent and River Waters in Japan

Takashi Azuma^{1*}, Hirotaka Ishiuchi¹, Tomomi Inoyama¹, Yusuke Teranishi¹, Misato Yamaoka¹, Takaji Sato¹, Naoyuki Yamashita², Hiroaki Tanaka², Yoshiki Mino¹

1 Osaka University of Pharmaceutical Sciences, Takatsuki, Osaka, Japan, **2** Research Center for Environmental Quality Management, Kyoto University, Otsu, Shiga, Japan

* t.azuma@gly.oups.ac.jp



CrossMark
click for updates

Abstract

This is the first report of the detection of two new anti-influenza drugs, peramivir (PER) and laninamivir (LAN), in Japanese sewage effluent and river waters. Over about 1 year from October 2013 to July 2014, including the influenza prevalence season in January and February 2014, we monitored for five anti-influenza drugs—oseltamivir (OS), oseltamivir carboxylate (OC), zanamivir (ZAN), PER, and LAN—in river waters and in sewage effluent flowing into urban rivers of the Yodo River system in Japan. The dynamic profiles of these anti-influenza drugs were synchronized well with that of the numbers of influenza patients treated with the drugs. The highest levels in sewage effluents and river waters were, respectively, 82 and 41 ng/L (OS), 347 and 125 ng/L (OC), 110 and 35 ng/L (ZAN), 64 and 11 ng/L (PER), and 21 and 9 ng/L (LAN). However, application of ozone treatment before discharge from sewage treatment plants was effective in reducing the levels of these anti-influenza drugs in effluent. The effectiveness of the ozone treatment and the drug dependent difference in susceptibility against ozone were further evidenced by ozonation of a STP effluent in a batch reactor. These findings should help to promote further environmental risk assessment of the generation of drug-resistant influenza viruses in aquatic environments.

OPEN ACCESS

Citation: Azuma T, Ishiuchi H, Inoyama T, Teranishi Y, Yamaoka M, Sato T, et al. (2015) Detection of Peramivir and Laninamivir, New Anti-Influenza Drugs, in Sewage Effluent and River Waters in Japan. *PLoS ONE* 10(6): e0131412. doi:10.1371/journal.pone.0131412

Editor: Chon-Lin Lee, NSYSU, TAIWAN

Received: January 6, 2015

Accepted: June 2, 2015

Published: June 25, 2015

Copyright: © 2015 Azuma et al. This is an open access article distributed under the terms of the [Creative Commons Attribution License](https://creativecommons.org/licenses/by/4.0/), which permits unrestricted use, distribution, and reproduction in any medium, provided the original author and source are credited.

Data Availability Statement: All relevant data are within the paper.

Funding: This study was funded by the Lake Biwa-Yodo River Water Quality Preservation Organization (<http://www.byq.or.jp/>). The funders had no role in study design, data collection and analysis, decision to publish, or preparation of the manuscript.

Competing Interests: The authors have declared that no competing interests exist.

Introduction

In recent years, a new environmental pollution problem has been reported whereby residual components of anti-influenza drugs are detected in the river water environment [1,2]. Research has been done into Tamiflu (oseltamivir: OS) and Relenza (zanamivir: ZAN), which are drugs used globally to treat annual seasonal influenza and could be effective in alleviating the potential damage from future global pandemics of new strains of influenza viruses [3–6]. There is concern that oseltamivir carboxylate (OC), which is the pharmacologically active metabolite of OS, could carry environmental risks in terms of increasing the development of drug-resistant viruses in wild waterfowl inhabiting river environments; these resistant viruses could then propagate among humans [7–9]. For this reason, research that aims to determine the status of

OS and ZAN in sewage effluent and river waters [5,6,10,11], as well as the behavior of these drugs in river environments [12–17], is beginning to be actively pursued.

In Japan, two new anti-influenza drugs were introduced clinically in 2010. One of them was Rapiacta (peramivir: PER), which is administered by intravenous drip injection [18–20], and the other is Inavir (laninamivir octanoate), which is administered by inhalation in a way similar to Relenza [19,21,22]. The mechanism of pharmacological action of these two drugs is, similar to that of Tamiflu and Relenza, to inhibit the neuraminidase glycoproteins involved in the proliferation of influenza viruses and suppress the proliferation of these viruses in the human body [19]. Additionally, although Inavir, similarly to Tamiflu, is in an inactive form when taken, it is a prodrug, meaning that its pharmacologically active metabolite, laninamivir (LAN), has medical effects [19,21,22].

Japan accounts for more than 70% of the world's Tamiflu consumption and compared with other countries is extremely highly dependent on anti-influenza drugs [23]. For this reason, it is probable that along with the clinical introduction of the new drugs have come new water environment pollution problems additional to those created by Tamiflu and Relenza [5,6,10,11]. However, to our knowledge there has still been no report of the status of these two new drugs in sewage effluent and river waters, and there are still many factors that need to be revealed before an environmental risk assessment can be conducted. Therefore, it is important to gain an understanding of the status of Rapiacta and Inavir, in addition to Tamiflu and Relenza, in the river environment.

Here, we clarified the status of the new drugs Rapiacta and Inavir in sewage effluent and river waters by performing a year-round detailed monitoring survey of the urban rivers flowing into a representative river basin in Japan, the Yodo River basin, from 2013 to 2014, centering on the height of the influenza outbreak season. In addition, with the aim of finding a water treatment technique effective in removing these drugs, we ran a laboratory-scale removal experiment using ozonation, which is reportedly effective in removing various components of pharmaceutical and personal care products [24–27].

Materials and Methods

2.1 Chemicals and reagents

OS (purity 99%) and ZAN (purity 99%) were purchased from LKT Laboratories (St. Paul, MN, USA). LAN (purity 98%) was purchased from Toronto Research Chemicals Inc. (Toronto, Ontario, Canada). OC (purity 99%) was purchased from Acanthus Research Inc. (Mississauga, Ontario, Canada). PER (purity 99%) was provided by Shionogi & Co., Ltd. (Osaka, Japan) and purchased from ChemScene, LLC. (Monmouth Junction, NJ, USA). The chemical structures and physicochemical properties of these anti-influenza drugs [22,28–37] are shown in Table 1. It is noted in similarities of chemical and physicochemical properties of ZAN and LAN. LC-MS-grade solvents (methanol, acetone, and acetonitrile), formic acid, hydrochloric acid, ascorbic acid, and triethylamine were purchased from Wako Pure Chemical Industries, Ltd. (Osaka, Japan). Individual standard stock solutions of OS, OC, ZAN, PER, and LAN at 1 mg/100 mL were prepared in methanol and stored at -30°C .

2.2 Sampling sites

River waters were collected at four sites on the middle reaches and downstream areas of the Yodo River basin. The locations were R1 (N $34^{\circ}48'52.56''$ E $135^{\circ}37'56.96''$), R2 (N $34^{\circ}45'30.41''$ E $135^{\circ}31'54.90''$), R3 (N $34^{\circ}45'22.35''$ E $135^{\circ}32'12.25''$), and R4 (N $34^{\circ}45'07.48''$ E $135^{\circ}31'30.50''$). The basin is located in the mid-Kansai district; it covers 208 km^2 and is home to 2 million people [38]. We also sampled effluents from public water boundary regions at two

Table 1. Chemical structures and physicochemical properties of the anti-influenza drugs examined [22, 28–37].

Compound	Molecular formula	Molecular mass (g/mol)	pK _a	LogP	Excretion rate (%)
Oseltamivir (OS)	C ₁₆ H ₂₈ N ₂ O ₄	312.41	7.7 [30,31]	0.4 [31]	15 [28]
Oseltamivir carboxylate (OC)	C ₁₄ H ₂₄ N ₂ O ₄	284.35	3.8 (acid) [32,37], 7.8 (base) [32,37]	-2.1 [34]	80 [28]
Zanamivir (ZAN)	C ₁₂ H ₂₀ N ₄ O ₇	332.31	3.8 (acid) [37], 11.3 (base) [37]	-7.1 [35]	80 [29]
Peramivir (PER)	C ₁₅ H ₂₈ N ₄ O ₄	328.41	4.1 (acid) [33], 13.1 (base) [33]	-1.4 [33]	91 [36]
Laninamivir (LAN)	C ₁₃ H ₂₂ N ₄ O ₇	346.34	3.8 (acid) [33], 11.3 (base) [33]	-3.1 [33]	13 [22]

doi:10.1371/journal.pone.0131412.t001

sewage treatment plants (STPs) in the basin, namely S1 (N 34°49'26.93" E 135°37'21.21") and S2 (N 34°46'46.29" E 135°34'14.89"). Both STPs used a conventional activated sludge system (CAS) followed by chlorination for disinfection, and one STP (S2) partly used CAS followed by ozonation (8.6 mg ozone/L). No special permission was required for every sampling location because all waters sampled were of public water body. Locations of the sampling sites are given in Fig 1. Adequateness of the sampling sites is based on the evidence that the STP effluents are the major source of the anti-influenza drug load in the Yodo River system (68–94% of total mass fluxes) due to the high rate of equipment of the sewerage systems in the same area (97–99% in 2010) [16].

Sampling was done over about 1 year from October 2013 to July 2014, including the influenza outbreak season from January to February 2014 on non-rainy days once a week during the influenza outbreak season and once every 2 months for the rest of the year. No rainfall greater than 1 mm was observed in the sampling area during the 2 days before each sampling day. The frequency of the sampling in the present study is the same as that we have done in a year during July 2010 to June 2011 at the similar sites of the Yodo River basin [6] to show synchronous dynamics of observed and predicted values of anti-influenza drugs, OS, OC and ZAN, in environmental waters during a seasonal influenza outbreak in 2011 (January to March). Samples (200 mL) were collected in glass bottles each containing ascorbic acid (1 g/L) as a preservative to keep the sampled solution under reductive state at pH about 3 [39], kept in the refrigerator under dark at 4°C, and processed within 24 h.

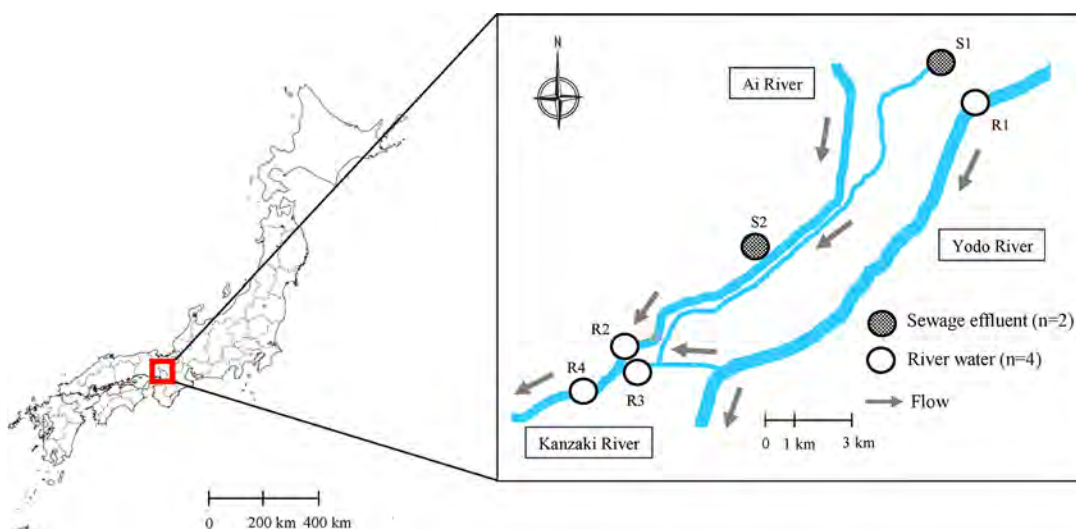


Fig 1. Locations of sampling sites in the Yodo River system.

doi:10.1371/journal.pone.0131412.g001

2.3 Analytical procedures

Water samples were analyzed by using a combination of a strong-cation solid-phase extraction cartridges (Bond Elut SCX, 500 mg; Agilent Technologies, Santa Clara, CA) and liquid chromatography–tandem mass spectrometry (LC-MS/MS) after filtration through a glass fiber filter (GF/B, 1- μ m pore size, Whatman, Maidstone, UK) [40]. Only filtered water samples were used for the analysis, because the adsorption of these drugs onto particulate matter in sewage and river water is negligibly small [7,41]. Aliquots (30 mL for river water and 10 mL for STP effluent) were loaded onto the extraction cartridges.

The materials adsorbed onto the cartridges were eluted with 10% triethylamine in a 1:1 (v/v) mixture of acetone and water after the cartridge had been cleaned up with 6 mL MeOH containing 2% formic acid. Each eluate was concentrated under a gentle stream of nitrogen gas. The residue was then re-dissolved in 200 μ L of a 9:1 (v/v) mixture of aqueous 0.1% formic acid solution and methanol, and 10 μ L of this solution was subjected to LC-MS/MS analysis in a Waters Acquity Ultra Performance LC (UPLC) device fitted with a column (2.1 mm \times 100 mm, 1.7 μ m) of UPLC BEH C₁₈ (Waters Corp., Milford, MA, USA).

A gradient elution program was achieved at 60°C with a mixed solvent system of 0.1% formic acid (v/v) in water (A) and acetonitrile (B) at a flow rate of 0.35 mL/min under a program of 0.0 to 4.0 min (5% B), 4.0 to 4.3 min (25% B), 4.3 to 5.8 min (80% B), 5.8 to 6.0 min (80% B), and 6.0 to 8.0 min (5% B) to condition the column. The UPLC system was coupled to a tandem-quadrupole-detector mass spectrometer (Waters Corp.) equipped with an electrospray ionization source and interface, and it was operated in positive ion mode. Product ions were generated with collision energies of 10 (OS), 10 (OC), 17 (ZAN), 18 (PER), and 16 (LAN) eV. Instrument control and data acquisition and quantification were performed with Mass Lynx 4.1 software (Waters Corp.).

The concentrations of OS, OC, ZAN, PER, and LAN were determined by subtracting the blank data from the data given by the addition of each spiked compound (20 ng/L) to account for matrix effects and loss during sample extraction [5,39,42].

Changes in the numbers of influenza patients per Prefecture per week from October 2013 to July 2014 in Japan were examined by using the surveillance data collected by the National Institute of Infectious Diseases, Japan [43] and the corresponding values in the northern area of Osaka Prefecture including the sampling sites [44].

2.4 Experimental removal of anti-influenza drugs by ozonation

To verify the effectiveness of ozone treatment in removing anti-influenza drugs and obtain kinetic insight of the treatment which will further show drug dependent difference in degradability, as the test water we used secondary effluent from an STP before chlorination for disinfection. Sampling was done on 5 February 2014, at the peak of an influenza outbreak [43,44].

All experiments were performed in a cylindrical stainless-steel reactor with an inside diameter of 23 cm, a height of 40.7 cm, and an effective volume of 1.7 L. Details of the reactor and its operation have been reported previously [45]. The temperature of the test water was maintained at 20°C by using a water circulator to circulate water of controlled temperature into a water jacket outside the reactor. The test water was stirred continuously with a stirrer in the reactor during the treatment experiments.

The experiments started by sparging ozone gas continuously into the reactor filled with the test water. The time before the start of ozone gas sparging was taken to be 0 min (initial conditions), and 60-mL samples were collected from the reactor 2, 5, 10, 15, and 20 min after the start of the reaction. The ozone feed rate was set to 0.6 mg/L/min on the basis of previous research [24,25] that examined the effectiveness of ozone treatment on a wide range of

components used in pharmaceutical and personal care products. The ozone dose in this experiment corresponded to 3 mg/L. Collected samples were analyzed as explained in section 2.3 Analytical procedures.

2.5 Method validation

Seven-point calibration curves were constructed for quantification; the concentrations ranged between 0.5 and 500 ng/mL in a 9:1 (v/v) mixture of 0.1% formic acid solution in methanol. Linear calibration curves for OS, OC, ZNA, PER, and LAN were obtained in the concentration range of 0.5 to 500 ng/L ($r^2 > 0.99$).

The LOD and LOQ values for the environmental water samples were calculated on the basis of the concentrations at signal to noise ratios of 3:1 and 10:1, respectively [2,42]. Rates of recovery from river waters were in the ranges of 65% ± 4% (OS), 76% ± 5% (OC), 62% ± 9% (ZAN), 76% ± 2% (PER), and 59% ± 2% (LAN); for the STP effluents the rates were 61% ± 9% (OS), 56% ± 3% (OC), 42% ± 5% (ZAN), 70% ± 4% (PER), and 45% ± 2% (LAN). Although the rates of recovery of LAN (also ZAN) were relatively lower than those of OS, OC and PER, it is relevant to estimate the close rates of recovery of LAN (59–45%) and ZAN (62–42%) in which latter values were higher than those (39.2–23.3%) previously published [40] by taking similarity of their chemical and physicochemical properties (Table 1) into consideration. Reproducibility for the river water or STP effluent results was in the ranges of 0.3%–0.7% (OS), 0.4%–0.7% (OC), 0.5%–0.7% (ZAN), 0.5%–1.0% (PER), and 0.3%–0.7% (LAN).

Results and Discussion

3.1 Time-dependent dynamics of OS, OC, ZAN, PER, and LAN in river waters and STP effluent

We examined the time-dependent dynamics of OS, OC, ZAN, PER, and LAN concentrations in STP effluent and river waters from July to June 2013–2014, including in the influenza outbreak season (January to March 2014) (Fig 2). We also examined the changes in the numbers of influenza patients (patients/sentinel/week) [44].

OS, OC, ZAN, PER, and LAN were not detected at the end of October 2013. Their levels then began to increase in December by several ng/L synchronously with the increase in the number of influenza patients, peaking at the end of January and in early February 2014. In May 2014, after the end of the outbreak, none of the targeted drugs was detectable. These results were similar to those in a previous report of OS, OC, and ZAN levels in sewage influents and effluents [6].

The maximum concentrations detected in the river water were 10–41 ng/L (OS), 39–125 ng/L (OC), 13–35 ng/L (ZAN), 2–11 ng/L (PER), and 4–9 ng/L (LAN). In the STP effluents they ranged from 74–82 ng/L (OS), 243–347 ng/L (OC), 109–110 ng/L (ZAN), 53–64 ng/L (PER), and 18–21 ng/L (LAN). These results showed that the concentrations of anti-influenza drugs or their metabolites in the STP effluent were roughly two to five times those in the river water; as already indicated in previous surveys of OS, OC, and ZAN [5,16]. Our findings suggested that the STP effluent was a major source of loading of PER and LAN in the river water. Although the levels of PER and LAN were lower than those of OS, OC, and ZAN, it was clear that they were still present in sewage effluent and river water in concentrations from several ng/L to several tens of ng/L during the influenza outbreak season. To our knowledge, this research is the first to report the existence of PER and LAN in sewage effluent and river water. The ratio of OS to OC was in the range of 0.26 ± 0.05 ($n = 18$) for STP effluent and 0.23 ± 0.05 ($n = 36$) for river water; these values agreed with those reported in previous research

(approximately 0.2–0.3 [5,6,41]). This indicated that the source of the OS and OC detected in the urban rivers studied here was Tamiflu ingested by patients.

The maximum concentrations of the drugs in the effluent from STPs that used the CAS process followed by chlorination for disinfection were 82 ng/L (OS), 347 ng/L (OC), 110 ng/L (ZAN), 64 ng/L (PER), and 21 ng/L (LAN). After ozone treatment, the concentrations of all five components were reduced to several to several tens of ng/L, 2 ng/L (OS), 2 ng/L (OC), 29 ng/L (ZAN), 4 ng/L (PER), and 4 ng/L (LAN). Not only was ozone treatment effective for reducing the levels of OS, OC, and ZAN [2,6] as previously reported—it was also effective in removing the new drug components PER and LAN.

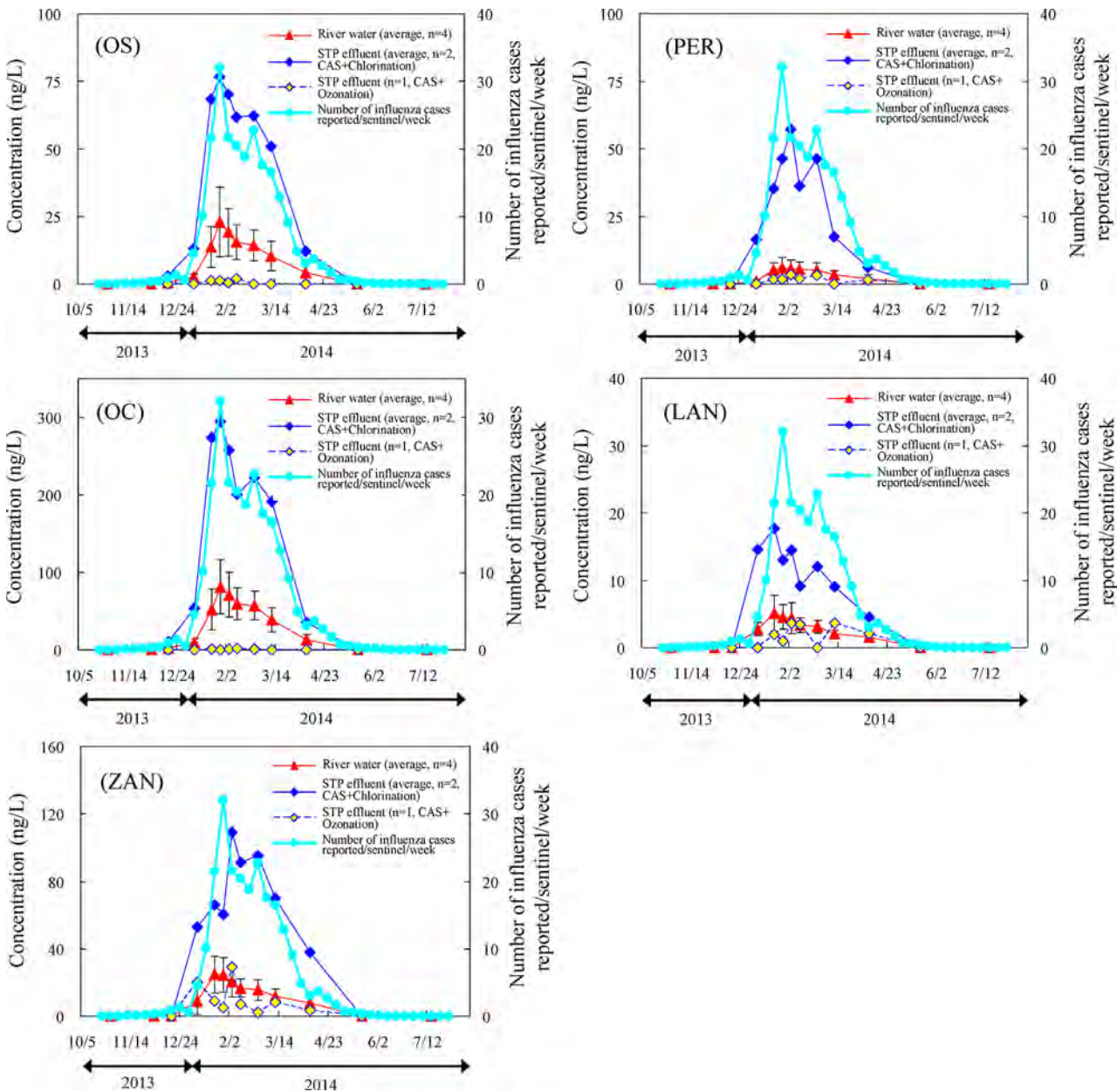


Fig 2. Time-dependent dynamics of OS, OC, ZAN, PER, and LAN average concentrations, with standard deviations, in river waters and STP effluent (CAS: conventional activated sludge systems) from July to June 2013–2014, including in the influenza outbreak season (January to March 2014).

doi:10.1371/journal.pone.0131412.g002

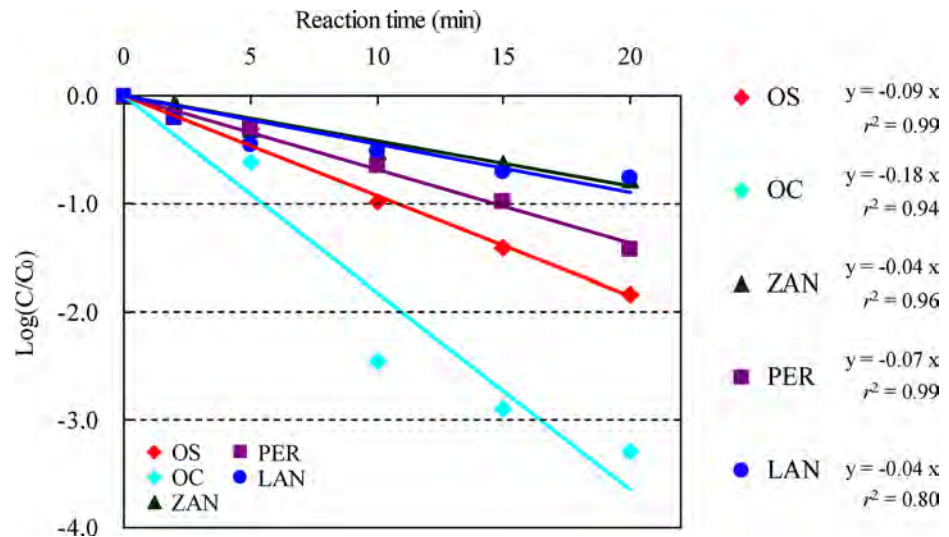


Fig 3. Relative residual concentrations of OS, OC, ZAN, PER, and LAN after experimental ozonation of secondary effluent from an STP at the influenza peak (C₀: Initial concentration, C: Concentration after reaction).

doi:10.1371/journal.pone.0131412.g003

3.2 Experimental ozone treatment of OS, OC, ZAN, PER, and LAN in secondary effluent from STP

We also examined the effectiveness of our experimental ozone treatment of OS, OC, ZAN, PER, and LAN in secondary effluent from an STP (Fig 3) by using a batch ozonation reactor. Although the dose of ozone by using this reactor (3 mg/L) is about 1/3 of the practical level treated at the STP (8.6 mg/L), it may be suffice to show the superiority of the treatment. The changes in concentration due to the removal reaction showed good linearity for all components when evaluated on a logarithmic plot of concentration versus reaction time [$r > 0.99$ (OS), 0.97 (OC), 0.98 (ZAN), 0.99 (PER), and 0.95 (LAN); $r^2 > 0.99$ (OS), 0.94 (OC), 0.96 (ZAN), 0.99 (PER), and 0.80 (LAN)]. After 20-min reaction, all concentrations became below the detection levels. We consider these profiled values adequate in light of a report stating that ozone treatment of a wide range of components in pharmaceutical and personal care products follows pseudo-first-order kinetics [46]. In addition, the half-lives under these ozone treatment conditions were 3.0 (OS), 1.7 (OC), 7.5 (ZAN), 4.3 (PER), and 7.5 (LAN) min; OC was the most easily removed, followed by OS and PER, and then by ZAN and LAN together. This trend corresponded well to the trend in concentration reduction in our survey of the STP that additionally used ozone treatment (see section 3.1). We compared the results with those reported in a previous assessment of the effectiveness of ozone treatment of dozens of pharmaceutical and personal care products, including antibacterial, antipyretic analgesic, and antihypertensive drugs [46,47]; these other reports also suggested that anti-influenza drugs tend to be easily removed. Although unconfirmed, the reason why the rates of removal of ZAN and LAN by ozone treatment were very similar and slower than those of OS, OC, and PER may be because ZAN and LAN have very similar chemical structures. In this regard, further examination of the relationship between chemical structure and removal efficiency by ozone treatment is important.

The environmental risk posed by anti-influenza drugs in the water environment—namely that their presence may increase the development of drug-resistant viruses in wild ducks [7,48,49]—is especially of concern for OC. The OC exposure concentration needed for the

development of Tamiflu-resistant influenza viruses in wild ducks is 1 $\mu\text{g/L}$ [8,9]. In addition, because the pharmacological activity of OS is only about one-hundredth to one-thousandth of that of OC [50,51], even at the time of a large-scale influenza pandemic OS itself probably does not pose an environmental risk [32,52,53]. On the other hand, in the case of ZAN, PER, and LAN there are no available reports on the development of drug-resistant viruses in wild animals. Environmental risk assessments [2,7,48] have been performed on the basis of values in the literature for half-maximal (50%) inhibitory concentrations (IC_{50}) against neuraminidase *in vitro*; these values are used to assay the pharmacological effects of anti-influenza drug components on influenza viruses. The IC_{50} value for OC is about 70–500 ng/L [54–60]; it is about 100–300 ng/L for ZAN, [54–57,59,60], 30–400 ng/L for PER [18,54,57], and 150–700 ng/L for LAN [59,60]. Although the values are somewhat lower for OC than for the others, they are all similar. Comparison of these values with the concentrations we detected in river water at the time of the seasonal influenza outbreak reveals that, even though the components had a broad range of about one-half to one-thirtieth of the IC_{50} values, none had concentrations that could pose an immediate environmental risk and become a problem.

Nevertheless, many studies [32,48,61,62] have pointed out the potential increase in environmental risk due to concentrated administration of anti-influenza drugs, including the risk posed by a large increase in the river concentrations of these drugs in the event of a future worldwide pandemic caused by a new strain of influenza virus. For this reason, it is important to encourage the use of ozone treatment, which can effectively remove a wide range of components, in the sewage treatment process. This can mitigate pollution loads in the river environment, not only from the components of anti-influenza drugs but also from the components of other pharmaceutical and personal care products, thus lessening the risk of drug-resistant viruses developing in the river environment.

Conclusions

We conducted a detailed monitoring survey of river waters and of STP effluent flowing into urban rivers in the highly populated Yodo River basin, Japan. In addition to OS, OC, and ZAN, the survey covered the new drug components PER and LAN, which were clinically introduced in Japan in 2010.

To our knowledge, this is the first research to confirm the presence of PER and LAN in river water and STP effluent during the winter influenza outbreak season. In addition, we confirmed through STP field experiments and laboratory-scale batch experiments that ozone treatment was effective in removing all five anti-influenza drug components and found the drug dependent difference in susceptibility against ozone. These findings should be valuable for conducting detailed environmental assessments of the pollution caused by the components of anti-influenza drugs in the river environment.

Acknowledgments

We thank Shionogi & Co., Ltd. (Japan) for providing the analytical-grade PER. We also thank all of the staff at the STPs for sampling the water.

Author Contributions

Conceived and designed the experiments: TA. Performed the experiments: TA HI TI YT MY. Analyzed the data: TA HI TI YT MY. Contributed reagents/materials/analysis tools: TA NY TS HT YM. Wrote the paper: TA NY YM HT.

References

1. Söderström H, Järhult JD, Olsen B, Lindberg RH, Tanaka H, Fick J (2009) Detection of the antiviral drug Oseltamivir in aquatic environments. *PLoS ONE* 4: e6064. doi: [10.1371/journal.pone.0006064](https://doi.org/10.1371/journal.pone.0006064) PMID: [19557131](https://pubmed.ncbi.nlm.nih.gov/19557131/)
2. Ghosh GC, Nakada N, Yamashita N, Tanaka H (2010) Oseltamivir carboxylate, the active metabolite of oseltamivir phosphate (Tamiflu), detected in sewage discharge and river water in Japan. *Environ Health Perspect* 118: 103–107. doi: [10.1289/ehp.0900930](https://doi.org/10.1289/ehp.0900930) PMID: [20056566](https://pubmed.ncbi.nlm.nih.gov/20056566/)
3. Accinelli C, Caracciolo AB, Grenni P (2007) Degradation of the antiviral drug oseltamivir carboxylate in surface water samples. *Int J Environ Anal Chem* 87: 579–587.
4. Saccà ML, Accinelli C, Fick J, Lindberg R, Olsen B (2009) Environmental fate of the antiviral drug Tamiflu in two aquatic ecosystems. *Chemosphere* 75: 28–33. doi: [10.1016/j.chemosphere.2008.11.060](https://doi.org/10.1016/j.chemosphere.2008.11.060) PMID: [19124147](https://pubmed.ncbi.nlm.nih.gov/19124147/)
5. Prasse C, Schlüsener MP, Schulz R, Ternes TA (2010) Antiviral drugs in wastewater and surface waters: A new pharmaceutical class of environmental relevance? *Environ Sci Technol* 44: 1728–1735. doi: [10.1021/es903216p](https://doi.org/10.1021/es903216p) PMID: [20108960](https://pubmed.ncbi.nlm.nih.gov/20108960/)
6. Azuma T, Nakada N, Yamashita N, Tanaka H (2012) Synchronous dynamics of observed and predicted values of anti-influenza drugs in environmental waters during a seasonal influenza outbreak. *Environ Sci Technol* 46: 12873–12881. doi: [10.1021/es303203c](https://doi.org/10.1021/es303203c) PMID: [23106220](https://pubmed.ncbi.nlm.nih.gov/23106220/)
7. Fick J, Lindberg RH, Tysklind M, Haemig PD, Waldenström J, Wallensten A, et al. (2007) Antiviral oseltamivir is not removed or degraded in normal sewage water treatment: Implications for development of resistance by influenza A virus. *PLoS ONE* 2: e986. PMID: [17912363](https://pubmed.ncbi.nlm.nih.gov/17912363/)
8. Järhult JD, Muradrasoli S, Wahlgren J, Söderström H, Orozovic G, Gunnarsson G, et al. (2011) Environmental levels of the antiviral oseltamivir induce development of resistance mutation H274Y in influenza A/H1N1 virus in mallards. *PLoS ONE* 6: e24742. doi: [10.1371/journal.pone.0024742](https://doi.org/10.1371/journal.pone.0024742) PMID: [21931841](https://pubmed.ncbi.nlm.nih.gov/21931841/)
9. Achenbach JE, Bowen RA (2013) Effect of oseltamivir carboxylate consumption on emergence of drug-resistant H5N2 avian influenza virus in mallard ducks. *Antimicrob Agents Chemother* 57: 2171–2181. doi: [10.1128/AAC.02126-12](https://doi.org/10.1128/AAC.02126-12) PMID: [23459475](https://pubmed.ncbi.nlm.nih.gov/23459475/)
10. Takanami R, Ozaki H, Giri RR, Taniguchi S, Hayashi S (2012) Antiviral drugs zanamivir and oseltamivir found in wastewater and surface water in Osaka, J Water Environ Technol 10: 57–68.
11. Peng X, Wang C, Zhang K, Wang Z, Huang Q, Yu Y, et al. (2014) Profile and behavior of antiviral drugs in aquatic environments of the Pearl River Delta, China. *Sci Total Environ* 466–467: 755–761. doi: [10.1016/j.scitotenv.2013.07.062](https://doi.org/10.1016/j.scitotenv.2013.07.062) PMID: [23973541](https://pubmed.ncbi.nlm.nih.gov/23973541/)
12. Bartels P, von Tümpling W Jr (2008) The environmental fate of the antiviral drug oseltamivir carboxylate in different waters. *Sci Total Environ* 405: 215–225. doi: [10.1016/j.scitotenv.2008.06.032](https://doi.org/10.1016/j.scitotenv.2008.06.032) PMID: [18675443](https://pubmed.ncbi.nlm.nih.gov/18675443/)
13. Accinelli C, Saccà Maria L, Fick J, Mencarelli M, Lindberg R, Olsen B (2010) Dissipation and removal of oseltamivir (Tamiflu) in different aquatic environments. *Chemosphere* 79: 891–897. doi: [10.1016/j.chemosphere.2010.02.022](https://doi.org/10.1016/j.chemosphere.2010.02.022) PMID: [20226496](https://pubmed.ncbi.nlm.nih.gov/20226496/)
14. Gonçalves C, Pérez S, Osorio V, Petrovic M, Alpendurada MF, Barceló D (2011) Photofate of oseltamivir (Tamiflu) and oseltamivir carboxylate under natural and simulated solar irradiation: Kinetics, identification of the transformation products, and environmental occurrence. *Environ Sci Technol* 45: 4307–4314. doi: [10.1021/es1032629](https://doi.org/10.1021/es1032629) PMID: [21495632](https://pubmed.ncbi.nlm.nih.gov/21495632/)
15. Accinelli C, Saccà ML, Mencarelli M, Vicari A (2012) Application of bioplastic moving bed biofilm carriers for the removal of synthetic pollutants from wastewater. *Biores Technol* 120: 180–186.
16. Azuma T, Nakada N, Yamashita N, Tanaka H (2013) Mass balance of anti-influenza drugs discharged into the Yodo River system, Japan, under an influenza outbreak. *Chemosphere* 93: 1672–1677. doi: [10.1016/j.chemosphere.2013.05.025](https://doi.org/10.1016/j.chemosphere.2013.05.025) PMID: [23871592](https://pubmed.ncbi.nlm.nih.gov/23871592/)
17. Zonja B, Gonçalves C, Pérez S, Delgado A, Petrovic M, Alpendurada MF, et al. (2014) Evaluation of the phototransformation of the antiviral zanamivir in surface waters through identification of transformation products. *J Hazard Mater* 265: 296–304. doi: [10.1016/j.jhazmat.2013.10.008](https://doi.org/10.1016/j.jhazmat.2013.10.008) PMID: [24211180](https://pubmed.ncbi.nlm.nih.gov/24211180/)
18. Kohno S, Kida H, Mizuguchi M, Shimada J (2010) Efficacy and safety of intravenous peramivir for treatment of seasonal influenza virus infection. *Antimicrob Age Chemother* 54: 4568–4574.
19. Shobugawa Y, Saito R, Sato I, Kawashima T, Dapat C, Dapat IC, et al. (2012) Clinical effectiveness of neuraminidase inhibitors—oseltamivir, zanamivir, laninamivir, and peramivir—for treatment of influenza A(H3N2) and A(H1N1)pdm09 infection: an observational study in the 2010–2011 influenza season in Japan. *J Infect Chemother* 18: 858–864. doi: [10.1007/s10156-012-0428-1](https://doi.org/10.1007/s10156-012-0428-1) PMID: [22644080](https://pubmed.ncbi.nlm.nih.gov/22644080/)
20. Tanaka A, Seki M, Kosai K, Kawano S (2010) Peramivir (in Japanese). *Jpn J Clin Exp Med* 87: 1702–1706.

21. Watanabe A (2010) Laninamivir (CS-8958, Inavir) (in Japanese). *Jpn J Clin Exp Med* 87: 1707–1712.
22. Ishizuka H, Yoshida S, Okabe H, Yoshihara K (2010) Clinical Pharmacokinetics of Laninamivir, a Novel Long-Acting Neuraminidase Inhibitor, After Single and Multiple Inhaled Doses of Its Prodrug, CS-8958, in Healthy Male Volunteers. *J Clin Pharmacol* 50: 1319–1329. doi: [10.1177/0091270009356297](https://doi.org/10.1177/0091270009356297) PMID: [20145259](https://pubmed.ncbi.nlm.nih.gov/20145259/)
23. Hoffmann-La Roche Inc. Nutley NJ (2005) Roche research report; Pediatric advisory committee executive summary for Tamiflu. 1–22.
24. Kim I, Tanaka H (2010) Use of ozone-based processes for the removal of pharmaceuticals detected in a wastewater treatment plant. *Water Environ Res* 82: 294–301. PMID: [20432647](https://pubmed.ncbi.nlm.nih.gov/20432647/)
25. Kim I, Tanaka H (2011) Energy consumption for PPCPs removal by O₃ and O₃/UV. *Ozone Sci Eng* 33: 150–157.
26. Ternes TA, Stüber J, Herrmann N, McDowell D, Ried A, Kampmann M, et al. (2003) Ozonation: a tool for removal of pharmaceuticals, contrast media and musk fragrances from wastewater? *Water Res* 37: 1976–1982. PMID: [12697241](https://pubmed.ncbi.nlm.nih.gov/12697241/)
27. Rosal R, Rodríguez A, Perdigón-Melón JA, Petre A, García-Calvo E, Gómez MJ, et al. (2010) Occurrence of emerging pollutants in urban wastewater and their removal through biological treatment followed by ozonation. *Water Res* 44: 578–588. doi: [10.1016/j.watres.2009.07.004](https://doi.org/10.1016/j.watres.2009.07.004) PMID: [19628245](https://pubmed.ncbi.nlm.nih.gov/19628245/)
28. George H, Joseph M, Penelope W (1999) Clinical pharmacokinetics of the prodrug Oseltamivir and its active metabolite Ro 64–0802. *Clin Pharmacokinet* 37: 471–484. PMID: [10628898](https://pubmed.ncbi.nlm.nih.gov/10628898/)
29. Lindsey MR, Cass CE, Alan B (1999) Pharmacokinetics of Zanamivir after intravenous, oral, inhaled or intranasal administration to healthy volunteers. *Clin Pharmacokinet Suppl* 36: 1–11.
30. Lindegårdh N, Hien TT, Farrar J, Singhasivanon P, White NJ, Day NPJ (2006) A simple and rapid liquid chromatographic assay for evaluation of potentially counterfeit Tamiflu[®]. *J Pharm Biomed Anal* 42: 430–433. PMID: [16750606](https://pubmed.ncbi.nlm.nih.gov/16750606/)
31. F. Hoffmann-La Roche Ltd. (2008) Product monograph Tamiflu. Mississauga, Ontario, Canada.
32. Straub JO (2009) An environmental risk assessment for oseltamivir (Tamiflu[®]) for sewage works and surface waters under seasonal-influenza- and pandemic-use conditions. *Ecotoxicol Environ Saf* 72: 1625–1634. doi: [10.1016/j.ecoenv.2008.09.011](https://doi.org/10.1016/j.ecoenv.2008.09.011) PMID: [19560203](https://pubmed.ncbi.nlm.nih.gov/19560203/)
33. Chemical Abstracts Service SciFinder. American Chemical Society. SciFinder online database (Subscription database).
34. Widmer N, Meylan P, Ivanyuk A, Aouri M, Decosterd LA, Decosterd LA, Buclin T (2010) Oseltamivir in seasonal, avian H5N1 and pandemic 2009 A/H1N1 influenza: pharmacokinetic and pharmacodynamic characteristics. *Clin Pharmacokinet* 49: 741–765. doi: [10.2165/11534730-000000000-00000](https://doi.org/10.2165/11534730-000000000-00000) PMID: [20923248](https://pubmed.ncbi.nlm.nih.gov/20923248/)
35. GlaxoSmithKline (2006) Zanamivir. Safety data sheet Ver 13: 1–8.
36. Shionogi & Co. Ltd. (2010) Rapiacta[®] for intravenous drip infusion: package insert. (In Japanese.). Shionogi & Co., Ltd, Osaka, Japan.
37. SPARC On-Line Calculator v4.6 (2011) University of Georgia, Atlanta, GA, USA. Available from <<http://sparc.chem.uga.edu/sparc/>>. (accessed April 27, 2015)
38. Osaka Prefectural Government (Japan) (2012) River development project of Kanzaki River in Yodo River system (in Japanese). Osaka: 1–50.
39. Kumar V, Nakada N, Yasojima M, Yamashita N, Johnson AC, Tanaka H (2009) Rapid determination of free and conjugated estrogen in different water matrices by liquid chromatography-tandem mass spectrometry. *Chemosphere* 77: 1440–1446. doi: [10.1016/j.chemosphere.2009.08.052](https://doi.org/10.1016/j.chemosphere.2009.08.052) PMID: [19772979](https://pubmed.ncbi.nlm.nih.gov/19772979/)
40. Azuma T, Nakada N, Yamashita N, Tanaka H (2014) Optimisation of the analysis of anti-influenza drugs in wastewater and surface water. *International Journal of Environ Anal Chem* 94: 853–862.
41. Leknes H, Sturtzel IE, Dye C (2012) Environmental release of oseltamivir from a Norwegian sewage treatment plant during the 2009 influenza A (H1N1) pandemic. *Sci Total Environ* 414: 632–638. doi: [10.1016/j.scitotenv.2011.11.004](https://doi.org/10.1016/j.scitotenv.2011.11.004) PMID: [22127154](https://pubmed.ncbi.nlm.nih.gov/22127154/)
42. Okuda T, Yamashita N, Tanaka H, Matsukawa H, Tanabe K (2009) Development of extraction method of pharmaceuticals and their occurrences found in Japanese wastewater treatment plants. *Environ Int* 35: 815–820. doi: [10.1016/j.envint.2009.01.006](https://doi.org/10.1016/j.envint.2009.01.006) PMID: [19201472](https://pubmed.ncbi.nlm.nih.gov/19201472/)
43. Infectious Disease Surveillance Center (Japan) Infectious Diseases Weekly Report (IDWR) (in Japanese). Available from <<http://idsc.nih.go.jp/index-j.html>>. (accessed April 27, 2015)
44. Osaka Prefecture Infectious Disease Surveillance Center (Japan) Infectious Diseases Weekly Report (in Japanese). Available from <<http://www.iph.pref.osaka.jp/index.html>>. (accessed April 27, 2015)
45. Yoon S, Tanaka H (2014) Optimum conditions for testing N-nitrosamine formation potential (FP) through ozonation in wastewater samples. *J Ind and Eng Chem* 20: 2914–2920.

46. Kim IH, Tanaka H, Iwasaki T, Takubo T, Morioka T, Kato Y (2008) Classification of the degradability of 30 pharmaceuticals in water with ozone, UV and H₂O₂. *Water Sci Technol* 57: 195–200. doi: [10.2166/wst.2008.808](https://doi.org/10.2166/wst.2008.808) PMID: [18235171](https://pubmed.ncbi.nlm.nih.gov/18235171/)
47. Antoniou MG, Hey G, Rodríguez VS, Spiliotopoulou A, Fick J, Tysklind M (2013) Required ozone doses for removing pharmaceuticals from wastewater effluents. *Sci Total Environ* 456–457: 42–49. doi: [10.1016/j.scitotenv.2013.03.072](https://doi.org/10.1016/j.scitotenv.2013.03.072) PMID: [23584032](https://pubmed.ncbi.nlm.nih.gov/23584032/)
48. Singer AC, Nunn MA, Gould EA, Johnson AC (2007) Potential risks associated with the proposed widespread use of Tamiflu. *Environ Health Perspect* 115: 102–106. PMID: [17366827](https://pubmed.ncbi.nlm.nih.gov/17366827/)
49. Renner R (2007) Tamiflu survives sewage treatment. *Environ Sci Technol* 41: 7591. PMID: [18075061](https://pubmed.ncbi.nlm.nih.gov/18075061/)
50. Li W, Escarpe PA, Eisenberg EJ, Cundy KC, Sweet C, Jakeman KJ, et al. (1998) Identification of GS 4104 as an orally bioavailable prodrug of the influenza virus neuraminidase inhibitor GS 4071. *Antimicrob Agents Chemother* 42: 647–653. PMID: [9517946](https://pubmed.ncbi.nlm.nih.gov/9517946/)
51. Williams MA, Kim CU, Lew W, Zhang L, Swaminathan S, Bischofberger N, et al. (1997) GS 4104: A highly potent orally bioavailable influenza neuraminidase inhibitor. *Antiviral Res* 34: 86.
52. Hutchinson TH, Beesley A, Frickers PE, Readman JW, Shaw JP, Straub JO (2009) Extending the environmental risk assessment for oseltamivir (Tamiflu[®]) under pandemic use conditions to the coastal marine compartment. *Environ Int* 35: 931–936. doi: [10.1016/j.envint.2009.04.001](https://doi.org/10.1016/j.envint.2009.04.001) PMID: [19395032](https://pubmed.ncbi.nlm.nih.gov/19395032/)
53. Chen WY, Lin CJ, Liao CM (2014) Assessing exposure risks for aquatic organisms posed by Tamiflu use under seasonal influenza and pandemic conditions. *Environ Pollut* 184: 377–384. doi: [10.1016/j.envpol.2013.09.019](https://doi.org/10.1016/j.envpol.2013.09.019) PMID: [24095813](https://pubmed.ncbi.nlm.nih.gov/24095813/)
54. Hurt AC, Selleck P, Komadina N, Shaw R, Brown L, Barr IG, (2007) Susceptibility of highly pathogenic A(H5N1) avian influenza viruses to the neuraminidase inhibitors and adamantanes. *Antiviral Res* 73: 228–231. PMID: [17112602](https://pubmed.ncbi.nlm.nih.gov/17112602/)
55. Escuret V, Frobert E, Bouscambert-Duchamp M, Sabatier M, Grog I, Valette M, et al. (2008) Detection of human influenza A (H1N1) and B strains with reduced sensitivity to neuraminidase inhibitors. *J Clin Virol* 41: 25–28. PMID: [18055253](https://pubmed.ncbi.nlm.nih.gov/18055253/)
56. Centers for Disease Control and Prevention (USA) (2009) Update: Drug susceptibility of swine-origin influenza A(H1N1) Viruses, April 2009. *Morbidity and Mortality Weekly Report (MMWR)* 58: 421–452.
57. Okomo-Adhiambo M, Sleeman K, Ballenger K, Nguyen HT, Mishin VP, Sheu TG, et al. (2010) Neuraminidase inhibitor susceptibility testing in human influenza viruses: A laboratory surveillance perspective. *Viruses* 2: 2269–2289. doi: [10.3390/v2102269](https://doi.org/10.3390/v2102269) PMID: [21994620](https://pubmed.ncbi.nlm.nih.gov/21994620/)
58. Correia V, de Andrade HR, Santos LA, Lackenby A, Zambon M (2010) Antiviral drug profile of seasonal influenza viruses circulating in Portugal from 2004/2005 to 2008/2009 winter seasons. *Antiviral Res* 86: 128–136. doi: [10.1016/j.antiviral.2010.01.002](https://doi.org/10.1016/j.antiviral.2010.01.002) PMID: [20083142](https://pubmed.ncbi.nlm.nih.gov/20083142/)
59. Itoh Y, Shinya K, Kiso M, Watanabe T, Sakoda Y, Hatta M, et al. (2009) *In vitro* and *in vivo* characterization of new swine-origin H1N1 influenza viruses. *Nature* 460: 1021–1025. doi: [10.1038/nature08260](https://doi.org/10.1038/nature08260) PMID: [19672242](https://pubmed.ncbi.nlm.nih.gov/19672242/)
60. Yamashita M, Tomozawa T, Kakuta M, Tokumitsu A, Nasu H, Kubo S (2009) CS-8958, a prodrug of the new neuraminidase inhibitor R-125489, shows long-acting anti-influenza virus activity. *Antimicrob Agents Chemother* 53: 186–192. doi: [10.1128/AAC.00333-08](https://doi.org/10.1128/AAC.00333-08) PMID: [18955520](https://pubmed.ncbi.nlm.nih.gov/18955520/)
61. Ellis JB (2010) Antiviral pandemic risk assessment for urban receiving waters. *Water Sci Technol* 61: 879–884. doi: [10.2166/wst.2010.002](https://doi.org/10.2166/wst.2010.002) PMID: [20182065](https://pubmed.ncbi.nlm.nih.gov/20182065/)
62. Singer AC, Colizza V, Schmitt H, Andrews J, Balcan D, Huang WE, et al. (2011) Assessing the ecotoxicologic hazards of a pandemic influenza medical response. *Environ Health Perspect* 119: 1084–1090. doi: [10.1289/ehp.1002757](https://doi.org/10.1289/ehp.1002757) PMID: [21367688](https://pubmed.ncbi.nlm.nih.gov/21367688/)

Occurrence and fate of selected anticancer, antimicrobial, and psychotropic pharmaceuticals in an urban river in a subcatchment of the Yodo River basin, Japan

Takashi Azuma¹ · Hiroataka Ishiuchi¹ · Tomomi Inoyama¹ · Yusuke Teranishi¹ · Misato Yamaoka¹ · Takaji Sato¹ · Yoshiki Mino¹

Received: 10 April 2015 / Accepted: 1 July 2015 / Published online: 17 July 2015
© Springer-Verlag Berlin Heidelberg 2015

Abstract Pollution status of six anticancer agents in the river water and effluents of sewage treatment plants (STPs) in Japan was surveyed with comparative analysis of the levels of four microbial and one psychotropic pharmaceuticals widely used for therapeutic medication. The area of survey is located in the Kanzaki–Ai River basin which is a major subcatchment of the Yodo River basin and is centered on a highly populated area that includes the middle and downstream reaches of the Yodo River. Selected cancer agents were bicalutamide, capecitabine, cyclophosphamide, doxifluridine, tamoxifen, and tegafur. A combination of strong anion solid-phase extraction cartridge under pH 11 for adsorption and optimization of liquid chromatography–tandem mass spectroscopy (LC–MS/MS) system was necessary to ensure high recovery rates (63–124 % for river water and 52–115 % for STP effluent). The year-round survey of these compounds in four seasons showed that all anticancer compounds were detected at median concentrations ranged from not detected to 32 ng/L in the river water and from not detected to 245 ng/L in the effluents of sewage treatment plants not using ozonation. In the case of bicalutamide (an active antiandrogen used to treat prostate cancer), the maximum concentration detected was 254 ng/L in river water and 1032 ng/L in non-ozonated sewage treatment plant effluents. Based on the mass balance, sewage treatment plants were the primary sources of anticancer compounds as well as the other pharmaceuticals in the river, and the attenuation effect of the river water was small. Ozonation

at sewage treatment plants was effective in removing these compounds. To the best of our knowledge, this study is the first to report the existence of bicalutamide, doxifluridine, and tegafur in the river environment.

Keywords Ozonation · PPCPs · Urban river · Sewage treatment plant · Solid-phase extraction · UPLC–MS/MS

Introduction

Since the 2000s, the emergence of new problems with pollution of the water environment by pharmaceutical compounds has been reported all over the world (Daughton and Ternes 1999; Kolpin et al. 2002). Trace concentrations of pharmaceutical compounds (roughly in the range of ng/L to µg/L) (López-Serna et al. 2013; Nakada et al. 2007) have been identified in the water environment, but these compounds are designed to have specific bioactivity *in vivo*, even in trace concentrations (Daughton and Ternes 1999). Therefore, a wide range of research is being conducted on, for example, the development of analytical methods applicable to river and sewage water (Grabic et al. 2012; Petrović et al. 2014), the status and behavior of pollutants in rivers and sewage treatment plants (STPs) (Kümmerer 2009; Kolpin et al. 2002; Narumiya et al. 2013), toxic impacts on ecosystems (Carlsson et al. 2006; Komori et al. 2013), and the development of effective water treatment techniques for pollutant removal (Antoniou et al. 2013; Kim et al. 2009a).

Human life is changing in relation to recent developments in science and technology. In Japan, the number one cause of death in 2013 was cancer, accounting for 29 % of deaths. This was almost twice as much as that of the second-highest cause of death, heart disease (16 %) (Ministry of Health Labour and Welfare, Japan 2014). The quantity of pharmaceuticals used in

Responsible editor: Ester Heath

✉ Takashi Azuma
t.azuma@gly.oups.ac.jp; t.azuma.mail@gmail.com

¹ Osaka University of Pharmaceutical Sciences, 4-20-1 Nasahara, Takatsuki, Osaka 569-1094, Japan

Japan is the second largest in the world after that is used by the USA (Ministry of Health Labour and Welfare, Japan 2013). In addition, because of the aging of the Japanese population (Ministry of Health Labour and Welfare, Japan 2014), the number of cancer patients needing treatment is likely to increase in future. Increasing numbers of new pharmaceuticals for chemotherapy (Nussbaumer et al. 2011), which, along with surgery and radiotherapy, is an important treatment for cancer, have been developed in recent years (Ferrando-Climent et al. 2014). The use of anticancer agents in clinical situations is also increasing, whereas the rates of adoption of surgical therapy and chemotherapy in Japan were adopted at about the same rate in 2011 (Social Welfare and Public Health in Tokyo 2012).

Anticancer agents are designed to destroy or inhibit the growth of cancer cells and are therefore often toxic (Besse et al. 2012; Booker et al. 2014). For this reason, if they do exist in the water environment, then it is very important to accumulate information on their aquatic ecotoxicity, beginning with fishes through to planktons and to algae (Besse et al. 2012; Booker et al. 2014; Negreira et al. 2014; Toolaram et al. 2014). Water environment pollution problems due to a wide range of pharmaceutical compounds (more than 100) have already been studied and reported (Ågerstrand et al. 2015; Ferrer et al. 2010; López-Serna et al. 2013; Vasquez et al. 2014). Overseas research into anticancer compounds has found concentrations in STP effluents of not detected (N.D.) to 25 ng/L for cyclophosphamide, N.D. to 100 ng/L for ifosfamide, and N.D. to 147 ng/L for tamoxifen (Besse et al. 2012; Ferrando-Climent et al. 2013; Liu et al. 2010; Martín et al. 2011; Negreira et al. 2014; Rabii et al. 2014); the concentrations of these respective compounds in river water have ranged from N.D. to 65 ng/L, N.D. to 20 ng/L, and N.D. to 10 ng/L (Ashton et al. 2004; Besse et al. 2012; Kosjek and Heath 2011; Martín et al. 2011). In contrast, in Japan, not only has research targeting anticancer compounds been scarce, but also the numbers of compounds targeted have been very limited. Cyclophosphamide has been the only anticancer compound surveyed in aquatic environments in Japan; its concentration in STP effluents was in the range of N.D. to 9 ng/L, and its concentration in river water was N.D. to 1 ng/L (Hanamoto et al. 2013; Narumiya et al. 2013), but many aspects of this pollution remain unknown.

Given this situation, we decided to focus on anticancer agents for which the pollution status in Japanese aquatic environments was unknown and for which it was therefore vital to gather information to conduct environmental risk assessments. As the main target compounds, therefore, selection was made on six anticancer drugs, grouping into antiandrogenic agent (bicalutamide), antimetabolites (capecitabine, doxifluridine, and tegafur), alkylating agent (cyclophosphamide), and antiestrogen agent (tamoxifen), because of their highly frequent therapeutic use in Japan and high excretion rates in unchanged

form (Jiho 2014; Ministry of Health Labour and Welfare, Japan 2012). In addition, as the comparative compounds, selection was also made on four antimicrobial agents (azithromycin, ciprofloxacin, clarithromycin, levofloxacin) and a psychotropic agent (carbamazepine), because of their frequent detection in river and sewage waters and reported to be refractory in river environments (Andreozzi et al. 2003; Hanamoto et al. 2013; Patrolecco et al. 2015). We decided to focus on the Yodo River basin as representative of Japanese drinking water sources and ecosystems requiring conservation (Lake Biwa-Yodo River Water Quality Preservation Organization, Japan 2012). Although their detection levels are in the order of several ng/L to 100 ng/L, issues of appearance of drug-resistant microorganism (Adachi et al. 2013) and growth inhibition to algae (Aristilde et al. 2010) cannot be ignored. To determine the pollution status of these compounds in all four seasons, we conducted a year-round survey in the Kanzaki–Ai River basin. This area is a major subcatchment of the Yodo River basin and is centered on a highly populated area that includes the middle and downstream reaches of the Yodo River. We then used the results we obtained to determine the pollution status of anticancer compounds in the river environment. We estimated the major pollutant load sources and studied the attenuation effects of river water to elucidate the environmental fate of these compounds.

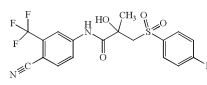
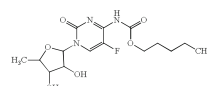
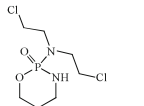
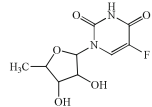
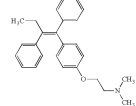
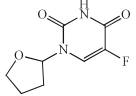
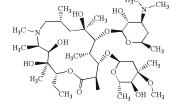
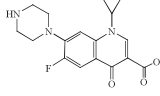
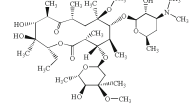
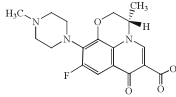
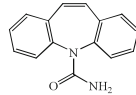
Materials and methods

Chemicals and reagents

Bicalutamide (purity 99 %) was purchased from Santa Cruz Biotechnology, Inc. (Santa Cruz, CA, USA). Capecitabine (purity 99 %) was purchased from LC Laboratories (Woburn, MA, USA). Cyclophosphamide (purity 99 %), azithromycin (purity 99 %), and ciprofloxacin (purity 99 %) were purchased from LKT Laboratories (St. Paul, MN, USA). Doxifluridine (purity 98 %), tegafur (purity 98 %), clarithromycin (purity 98 %), and levofloxacin (purity 98 %) were purchased from Tokyo Chemical Industry Co., Ltd. (Tokyo, Japan). Tamoxifen (purity 98 %) was purchased from Cayman Chemical (Ann Arbor, MI, USA). Carbamazepine (purity 99 %) was purchased from Sigma-Aldrich (St. Louis, MO, USA). The physicochemical properties of the target pharmaceuticals are shown in Table 1.

Liquid chromatography–mass spectrometry (LC–MS) grade solvents (methanol, acetone), formic acid, and ascorbic acid were purchased from Wako Pure Chemical Industries, Ltd. (Osaka, Japan). Individual standard stock solutions of each pharmaceutical at 10 mg/L were prepared in methanol and stored at -20°C . A strong-anion solid-phase extraction (SPE) cartridge, OASIS MAX, 60 mg, was purchased from Waters Corp., Milford, MA, USA.

Table 1 Physicochemical properties of target pharmaceuticals (American Chemical Society SciFinder)

Therapeutic class	CAS registry number	Molecular formula	Molecular mass (g/mol)	Structure	pK_a	$\text{Log}P$	Compound
Anticancer agent	90357-06-5	$\text{C}_{18}\text{H}_{14}\text{F}_4\text{N}_2\text{O}_4\text{S}$	430.4		11.5	4.1	Bicalutamide
	154361-50-9	$\text{C}_{15}\text{H}_{22}\text{FN}_3\text{O}_6$	359.4		5.4	1.0	Capecitabine
	50-18-0	$\text{C}_7\text{H}_{15}\text{Cl}_2\text{N}_2\text{O}_2\text{P}$	261.1		2.8	0.2	Cyclophosphamide
	3094-09-5	$\text{C}_9\text{H}_{11}\text{FN}_2\text{O}_5$	246.2		7.6	-0.7	Doxifluridine
	10540-29-1	$\text{C}_{26}\text{H}_{29}\text{NO}$	371.5		8.7	5.1	Tamoxifen
	17902-23-7	$\text{C}_8\text{H}_9\text{FN}_2\text{O}_3$	200.2		7.6	-0.6	Tegafur
Antibacterial agent	83905-01-5	$\text{C}_{38}\text{H}_{72}\text{N}_2\text{O}_{12}$	749.0		13.3	3.3	Azithromycin
	85721-33-1	$\text{C}_{17}\text{H}_{18}\text{FN}_3\text{O}_3$	331.3		6.0	1.3	Ciprofloxacin
	81103-11-9	$\text{C}_{38}\text{H}_{69}\text{NO}_{13}$	748.0		13.1	3.2	Clarithromycin
	100986-85-4	$\text{C}_{18}\text{H}_{20}\text{FN}_3\text{O}_4$	361.4		5.2	1.6	Levofloxacin
Psychotropic agent	298-46-4	$\text{C}_{15}\text{H}_{12}\text{N}_2\text{O}$	236.3		13.9	2.7	Carbamazepine

CAS chemical abstracts service, pK_a logarithmic acid dissociation constant, $\text{Log}P$ octanol–water partition coefficients

Sampling

Location of the sampling area was settled in the middle to downstream region on the right bank of the Yodo River in the Kansai district of Japan (Lake Biwa-Yodo River Water Quality Preservation Organization, Japan 2012) including the catchments of two rivers, the Kanzaki and the Ai. This area covers an important commercial and urban area of about 790 km² in Osaka and Hyogo prefectures and is home to two

million people (Ministry of the Environment, Japan 2009; Osaka Prefecture, Japan 2012).

Place and number of sampling environmental water were then settled to fit for the present survey. We have selected 14 water samples from 13 sites categorized as three different types (River, Tributary, and STP) as shown in Figure 1. Six sites (R1–R6) were from rivers and four sites (T1–T4) from tributaries of the rivers, and three sites (S1–S3) from STPs, with specification of ID of each site (sample ID) by taking

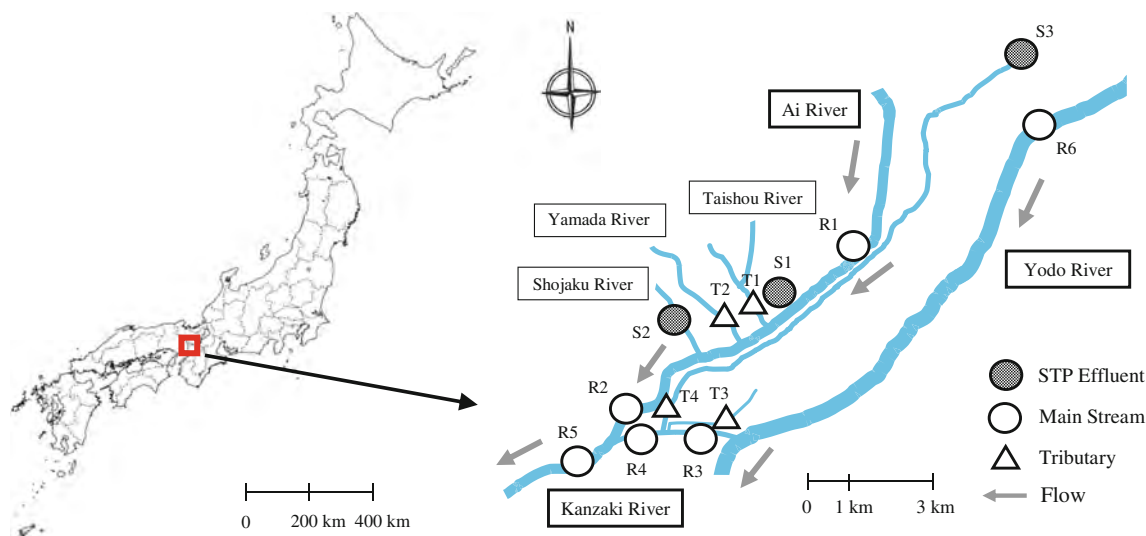


Fig. 1 Locations of sampling sites in the Kanzaki–Ai River basin

each capital letter. Fundamentally, one sample was taken per one site. In the case of S3, however, two sampling sites designated as S3(1) and S3(2) were present because of presence of two effluent sites. All targeted STPs used a conventional activated sludge (CAS) process followed by chlorination for disinfection, and one STP (S3) used partial CAS followed by ozonation (8.6 mg ozone/L). The properties of the STPs surveyed (including populations serviced and average flow rates) are shown in Table 2. In addition, annual flow rates and biological oxygen demand (BOD, mg/L) at the sampling sites on the river are listed in Table 3. To estimate the mass flux of each drug at each site, we multiplied the detected concentration by the mean river flow rate per day or the mean STP discharge (m³ of effluent per day) (Tables 2 and 3).

The survey was conducted once in four different seasons from 2013 to 2014, namely on April 4 (spring), July 29 (summer), December 18 (late autumn), and February 4 (winter). The sampling frequency was selected based on the previous related surveying reports (Kumar et al. 2011; Hanamoto et al. 2013). Sampling was done on rain-free days, and no rainfall greater than 1 mm was observed during the 2 days before the sampling day (Japan Meteorological Agency 2015). Two hundred-milliliter grab samples of river water and STP effluents were collected in glass bottles containing ascorbic acid (1 g/L) as a preservative. All water samples were immediately transported to the laboratory (within 1–2 h), and they were stored at 4 °C under darkness and processed within 24 h of collection.

Analytical procedure

Each water sample was filtered through a glass fiber filter (GF/B, 1-μm pore size, Whatman, Maidstone, UK), and two 30-mL portions were taken out for use as a blank and a practical analysis sample following the combined procedure of SPE and liquid chromatography–tandem mass spectrometry

(LC–MS/MS) as described before (Azuma et al. 2012, 2014; Okuda et al. 2009). The SPE cartridge (OASIS MAX) was preconditioned by washing with 3 mL of methanol and 3 mL of Milli-Q water preadjusted to pH 11 with 1 N NaOH. A known amount of each compound was spiked in the taken out samples to make the final concentration of 200 ng/L and was then transferred to the SPE cartridge at a flow rate of 1 mL/min. Operation of the SPE cartridge (OASIS MAX) under pH 11 is found to be prerequisite to enhance recovery rate because of its strong anion property based on the pre-experiments as described previously (Azuma et al. 2014).

After application of the sample solution, the cartridge had been cleaned up by washing with 6 mL of Milli-Q water preadjusted to pH 11 and dried by using a vacuum pump, and the materials adsorbed onto the cartridges were eluted with 2 mL of acetone, 2 mL of 2 % formic acid in methanol (v/v), and 2 mL of 2 % formic acid in acetone (v/v). Each set of the combined eluted solution was mildly evaporated to dryness under a gentle stream of nitrogen gas at 37 °C. The residue was solubilized in 200 μL of a 90:10 (v/v) mixture of 0.1 % formic acid solution and methanol, and 10 μL of this solution was subjected to LC–MS/MS analysis in multiple reaction monitoring mode by using ultra performance liquid chromatography (UPLC) and a reverse phase UPLC BEH C₁₈ column (2.1 mm×100 mm×1.7 μm) (Waters Acquity, Waters Corp., Milford, MA, USA).

A gradient elution program was achieved at 60 °C with a mixed solvent system of 0.1 % formic acid (v/v) in Milli-Q water (A) and methanol (B) at a flow rate of 0.35 mL/min under a program of 0.0 to 2.0 min (10 % B), 2.0 to 8.0 min (25 % B), 8.0 to 14.0 min (55 % B), 14.0 to 16.0 min (55 % B), 16.0 to 19.0 min (90 % B), 19.0 to 21.0 min (40 % B), and 21.0 to 24.0 min (10 % B) to condition the column. The UPLC system was coupled to a Quattro Micro tandem quadrupole detector (Waters Corp.) equipped with an electrospray

Table 2 Properties of sewage treatment plants surveyed in the Kanzaki–Ai River basin

Sample ID	Service area (ha)	Service population (person)	Flow rate (m ³ /day)		Treatment process
			Mean	SD	
S1	5459	494,974	256,110	31,285	CAS A2O
S2	453	50,732	17,050	2355	CAS
S3(1)	3550	415,364	128,497	11,876	CAS Step AO
S3(2)			2152	18	CAS+ozonation Step AO+ozonation

CAS conventional activated sludge, AO anaerobic/aerobic, A2O anaerobic/anoxic/aerobic

ionization source, and it was operated in positive and negative ion modes. Instrument control and data acquisition and quantification were performed with Mass Lynx 4.1 software (Waters Corp.). By using the same software, initially one precursor ion and one to four product ions were selected for each pharmaceutical (Table 4), and then optimization of the MS/MS parameters for each pharmaceutical was separately done together with determination of the best fit combination of the precursor and product ions in terms of selectivity and intensity for quantification. Finally, a time-scheduled acquisition program was constructed for 11 multiple reaction monitoring (MRM) channels. As a result, sets of the optimized MS/MS parameters and retention times of all pharmaceuticals were listed in Table 4.

Method validation

Six-point standard calibration curves were constructed for quantification, ranging between 0.5 and 200 ng/mL in a 90:10 (v/v) mixture of 0.1 % formic acid solution and methanol. The individual linear calibration curves for all compounds

were obtained in the concentration range from 0.5 to 200 ng/mL ($r^2 > 0.99$). Quantification was made by subtracting the blank data from the corresponding data given by the spiked sample solutions to account for matrix effects and loss during sample extraction (Azuma et al. 2014; Prasse et al. 2010). The recoveries obtained by calculations between the spiked data and the standard data to make calibration were in the ranges of 63 to 124 % for river water and 52 to 116 % for STP effluent; these are generally similar to those reported in a previous study of pharmaceuticals and personal care products (PPCPs) in the water environment (Grabic et al. 2012; Petrović et al. 2014). The limit of detection (LOD) and limit of quantification (LOQ) values for the environmental water samples were calculated on the basis of the concentrations at signal to noise (S/N) ratios of 3 and 10, respectively, according to the methods used for PPCPs (Azuma et al. 2014; Okuda et al. 2009; Schlüsener et al. 2015). The data at $S/N < 3$ and $3 \leq S/N < 10$ were expressed as not detected (N.D.) and not quantified (N.Q.), respectively (Ghosh et al. 2010; Kumar et al. 2009). The LOD and LOQ values were 0.1, 0.2, 0.2, 0.1, 0.1, 0.2, 0.1, 0.1, 0.1, 0.2, and 0.3 ng/L and 0.3, 0.8, 0.7,

Table 3 Flow rates at sampling sites shown in Fig. 1 in the Kanzaki–Ai River basin

Basin	Sample ID	Class	Flow rate (m ³ /day)		BOD (mg/L)
			Mean	SD	
Ai	R1	Main stream	7311	5710	1.2
	T1	Tributary	27,415	19,872	1.6
	T2	Tributary	5751	11,995	4.3
	R2	Main stream	546,352	245,310	1.5
Kanzaki	R3	Main stream	1,180,800	132,832	N.A.
	R4	Main stream	1,379,428	88,647	1.0
	T3	Tributary	N.A.	N.A.	N.A.
	T4	Tributary	198,627	78,298	3.2
	R5	Main stream	1,925,780	286,903	N.A.
Yodo	R6	Main stream	17,815,523	8,742,816	1.1

N.A. not available

Table 4 Retention times of the analytes, and MS/MS parameters optimized for each pharmaceutical

Compound	Retention time (min)	Precursor ion (<i>m/z</i>)	Product ion (<i>m/z</i>)	Cone voltage (V)	Collision energy (eV)	Ionization mode
Bicalutamide	14.8	429.3	<i>255.2</i>	30	16	–
Capecitabine	12.4	360.4	<i>174.2, 244.2</i>	25	16	+
Cyclophosphamide	10.2	261.2	<i>106.2, 139.9, 181.9, 233.4</i>	35	15	+
Doxifluridine	2.0	247.2	<i>73.0, 99.1, 117.0</i>	15	12	+
Tamoxifen	17.9	372.4	<i>72.3</i>	45	15	+
Tegafur	2.8	201.2	<i>71.0, 131.1</i>	15	18	+
Azithromycin	11.5	749.8	<i>573.3, 591.6</i>	52	30	+
Ciprofloxacin	6.2	332.2	<i>288.2, 314.2</i>	40	18	+
Clarithromycin	15.5	748.8	<i>316.6, 553.8, 590.3</i>	38	25	+
Levofloxacin	5.5	362.4	<i>244.9, 261.2, 318.2, 344.5</i>	40	21	+
Carbamazepine	13.0	237.2	<i>192.1, 194.6, 220.2</i>	20	24	+

Product ions in italics were used for quantification

0.2, 0.3, 0.7, 0.4, 0.2, 0.2, 0.5, and 1.1 for bicalutamide, capecitabine, cyclophosphamide, doxifluridine, tamoxifen, tegafur, azithromycin, ciprofloxacin, clarithromycin, levofloxacin, and carbamazepine, respectively.

Calculation of mass loads in the river environment

For estimation of the mass balance of pharmaceuticals discharged into the Kanzaki–Ai River basin, mass flux of each drug at each site was calculated by multiplying the detected concentration by the mean river flow rate per day or the mean STP discharge in terms of cubic meter (m³) of effluent per day. The flow rates at each site are listed in Tables 2 and 3. For analysis of the mass balance, the total mass flux for each drug was found by numerical summing of the mass flux values from the upstream region to the most downstream boundary site, R5. The mass flux of each drug was also estimated at this site.

Results and discussion

Occurrence of target pharmaceutical compounds in river waters and STP effluents

Table 5 shows the concentrations of pharmaceutical compounds detected in the different types of samples, namely main stream, tributary, STP effluent, and STP effluent after ozonation. All 11 compounds, including the six anticancer compounds, were detected in the targeted river waters and STP effluents.

The concentrations of the anticancer compounds were distributed as follows. The median concentrations of bicalutamide, capecitabine, cyclophosphamide, doxifluridine, tamoxifen, and tegafur were, in the mainstream samples, 32, 2, 2, N.D., N.D., and N.D. ng/L, respectively; in the tributaries, 30, 1, 3, N.D.,

N.D., and N.D. ng/L; and in the STP effluents (excluding ozonation) 245, 6, 10, N.D., N.D., and 23 ng/L. The concentrations of bicalutamide, capecitabine, cyclophosphamide, and tegafur in the STP effluents were thus several times higher than those in the river water. Although there were concentration differences among the seasons, the orders of magnitude were about the same throughout the year. Considering the fact that the quantity of water to be treated at these STPs and the river flow rates in the target basin were fairly stable throughout the year (Osaka Prefectural Government, Japan, <http://www.pref.osaka.lg.jp/kankyohozen/osaka-wan/kokyo-status.html>), this finding suggests that the targeted anticancer compounds were being used all year round. The detection frequencies in the mainstream and tributary samples were in the range of 6 to 44 % for doxifluridine, tamoxifen, and tegafur, but they were roughly in the range of 60 to 100 % for all other anticancer compounds. The figures reported previously for cyclophosphamide and tamoxifen have been in the range of N. D. to several tens of ng/L in river water (Ashton et al. 2004; Besse et al. 2012; Kosjek and Heath 2011; Martín et al. 2011) and from N.D. to 100 ng/L in STP effluents (Besse et al. 2012; Ferrando-Climent et al. 2013; Liu et al. 2010; Martín et al. 2011; Negreira et al. 2014; Rabii et al. 2014). Therefore, most of the anticancer compounds were detected here in concentrations of roughly the same order of magnitude as in previous research. However, in the case of bicalutamide (Cockshott 2004), which is an active antiandrogen used to treat prostate cancer, the maximum concentration detected was 254 ng/L in mainstream samples, 151 ng/L in tributaries, and 1032 ng/L in STP effluents (excluding ozonation)—about two to 10 times the concentrations of the other compounds. To the best of our knowledge, this is the first report of the pollution status of bicalutamide, doxifluridine, and tegafur in river and sewage waters.

The detection frequencies of all of the other compounds—namely the antimicrobial and psychotropic compounds—

Table 5 Occurrences of target pharmaceutical compounds in river water and STP effluents ($n=24$ (main stream), $n=16$ (tributary), $n=10$ (STP effluent), $n=10$ (STP effluent (ozonation)))

Compound	Sample type	Concentration (ng/L)				Frequency (%)
		Mean (SD)	Median	Max	Min	
Bicalutamide	Main stream	55 (71)	32	254	N.D.	83
	Tributary	46 (43)	30	151	N.D.	94
	STP effluent	316 (303)	245	1032	49	100
	STP effluent (ozonation)	13 (20)	5	41	N.D.	50
Capecitabine	Main stream	3 (4)	2	20	N.D.	88
	Tributary	3 (4)	1	16	N.D.	100
	STP effluent	6 (3)	6	11	2	100
	STP effluent (ozonation)	2 (2)	2	4	N.D.	50
Cyclophosphamide	Main stream	3 (5)	2	16	N.D.	63
	Tributary	4 (6)	3	20	N.D.	56
	STP effluent	11 (7)	10	20	N.D.	90
	STP effluent (ozonation)	7 (10)	3	22	N.D.	50
Doxifluridine	Main stream	2 (8)	N.D.	39	N.D.	8
	Tributary	1 (3)	N.D.	12	N.D.	6
	STP effluent	1 (3)	N.D.	8	N.D.	20
	STP effluent (ozonation)	N.D. (0)	N.D.	N.D.	N.D.	0
Tamoxifen	Main stream	5 (16)	N.D.	76	N.D.	33
	Tributary	8 (12)	N.D.	33	N.D.	44
	STP effluent	1 (3)	N.D.	9	N.D.	10
	STP effluent (ozonation)	N.D. (0)	N.D.	N.D.	N.D.	0
Tegafur	Main stream	5 (13)	N.D.	56	N.D.	25
	Tributary	6 (12)	N.D.	35	N.D.	25
	STP effluent	20 (16)	23	49	N.D.	70
	STP effluent (ozonation)	4 (8)	N.D.	17	N.D.	25
Azithromycin	Main stream	75 (106)	22	371	N.D.	79
	Tributary	130 (265)	35	1053	N.D.	75
	STP effluent	373 (367)	289	1255	38	100
	STP effluent (ozonation)	10 (17)	3	35	N.D.	50
Ciprofloxacin	Main stream	5 (7)	2	30	N.D.	67
	Tributary	7 (18)	3	76	N.D.	63
	STP effluent	53 (99)	9	300	N.D.	90
	STP effluent (ozonation)	3 (3)	2	6	N.D.	50
Clarithromycin	Main stream	81 (96)	32	333	1	100
	Tributary	160 (311)	46	1268	2	100
	STP effluent	402 (410)	309	1394	58	100
	STP effluent (ozonation)	5 (8)	1	18	1	100
Levofloxacin	Main stream	43 (45)	20	151	2	100
	Tributary	71 (66)	45	203	4	100
	STP effluent	819 (672)	478	2168	170	100
	STP effluent (ozonation)	9 (6)	8	15	4	100
Carbamazepine	Main stream	27 (20)	22	78	4	100
	Tributary	31 (23)	25	74	4	100
	STP effluent	113 (97)	96	383	48	100
	STP effluent (ozonation)	2 (1)	2	4	1	100

N.D. not detected

were roughly in the same range of 60 to 100 % observed for the anticancer compounds. Maximum concentrations ranged from 30 to 333 ng/L in mainstream samples, 76 to 1268 ng/L in tributaries, and 300 to 2168 ng/L in STP effluents (excluding ozonation); as with the anticancer compounds, the concentrations detected in the STP effluents tended to be several times higher than those in the river waters. These concentrations were about the same as, or only about a few times higher than, previously reported values (Hanamoto et al. 2013; Patrolecco et al. 2015; Petrović et al. 2014), probably because our study was conducted in an urban river basin with a high population density. Clarification of the level and mass balance (fate) of the whole discharged pharmaceuticals including anticancer pharmaceuticals and antimicrobial and psychotropic compounds in the urban river environment together with importance of cleaning-up treatment at STPs will have great effects on maintaining local residents in healthy condition by recycling river waters as city tap water, needless to say preventing environmental pollution originating from the discharged anticancer and the other pharmaceuticals.

In the effluent samples from the STP that used ozonation, the mean concentrations of all targeted pharmaceutical compounds ranged from N.D. to several ng/L and were roughly one tenth to one hundredth of the concentrations detected in the STP effluents with chlorination after biological treatment. This result supported those in previous reports (Antoniou et al. 2013; Azuma et al. 2012; Kim et al. 2009b) indicating the effectiveness of ozonation in removing a wide range of pharmaceutical compounds, including refractory compounds, from water samples. Our findings suggest that increased introduction of ozonation in STPs would not only be effective in removing antimicrobial and psychotropic compounds, as has been reported previously (Antoniou et al. 2013; Kim et al. 2009b), but also might be able to mitigate the impacts of anticancer compounds flowing into the river environment.

Source distribution of target pharmaceutical compounds in the Kanzaki–Ai River basin

To determine the major load sources in the Kanzaki–Ai River basin, the amounts of each compound flowing from upstream to the farthest downstream sampling site (R5) were estimated. The percentage contribution of each load source to the total mass flux was then calculated (Fig. 2).

For all compounds except tamoxifen, the percentage contribution of STP effluents as a pollutant loading source was large (about 50 to 98 % of the total load) and the contribution of tributaries was low (a few %). A typical example which supports this criterion is shown in Figure 3 by using the case for bicalutamide as a representative compound. Thus, in the survey area, STP effluent was a major contributor to the pollution of river waters by anticancer and other pharmaceutical compounds. These results were similar to those of studies of

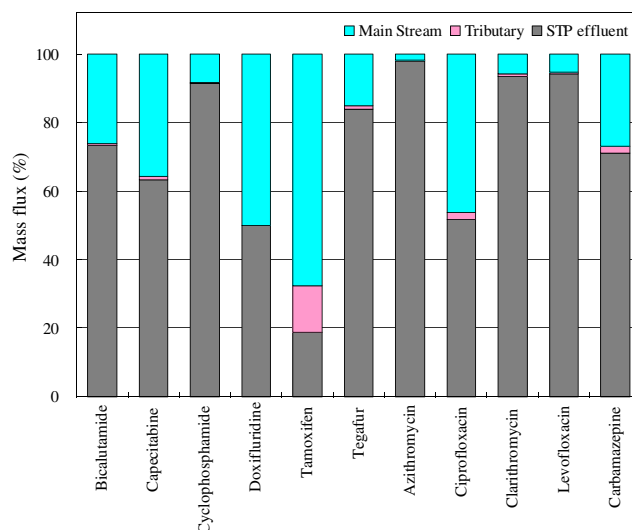


Fig. 2 Source distribution of target pharmaceutical compounds in Kanzaki–Ai River basin

pharmaceutical compounds (Azuma et al. 2013; Hanamoto et al. 2013) and of endocrine-disrupting chemicals such as estrogens (Kumar et al. 2011) in the upper and middle reaches of the Yodo River.

The present results clearly showed that the contribution of STP effluents to the total load of tamoxifen was low (19 %), resulting in its higher contribution of the mainstream and tributary contributions than the other compounds. There are some references which dealt with presence of tamoxifen in the STP effluents and river waters as described in the “Introduction.” Recently, its screening assessment was published (Environment Canada 2015) and a review of its ecotoxicological effect has also been published (Sun et al. 2015). However, owing to the lack of information about the fate of this drug after discharge into the environmental water, further extended investigations are needed for explanation of its exceptional property. In addition, the bulk of the remainder of the

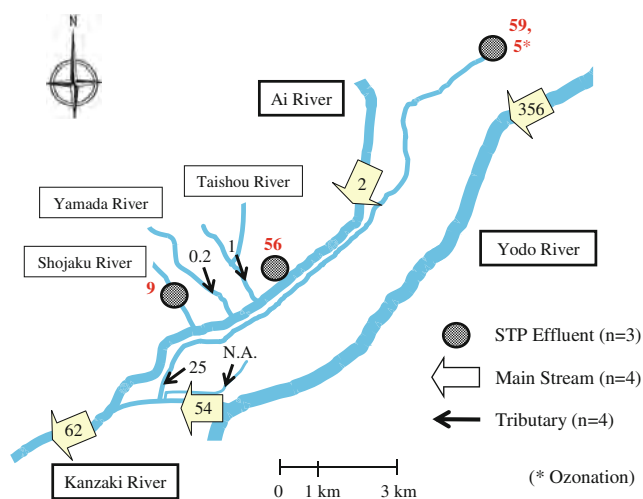


Fig. 3 A typical transition of mass flow from upstream to downstream of Kanzaki–Ai River basin for bicalutamide (N.A. not available)

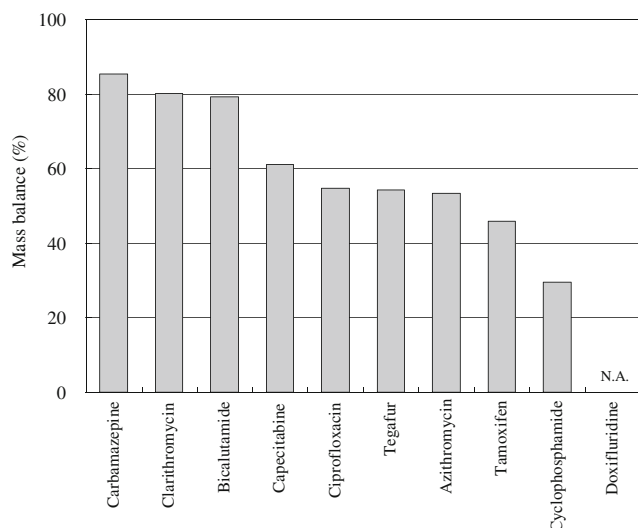


Fig. 4 Mass balance of target pharmaceutical compounds in Kanzaki–Ai River basin (N.A. not available)

contribution to the total mass flux of the compounds studied came from the farther upstream points surveyed in the main stream (Azuma et al. 2013; Hanamoto et al. 2013); thus, pollution loads might have come from areas beyond the sample collection points, because the Kanzaki River originates from a branch on the right bank of the Yodo River. For this reason, to improve the water quality of the Kanzaki–Ai River system, in addition to introducing advanced water-processing techniques at STPs located in the middle and downstream reaches to decrease pollution loads, it is equally important to implement these measures in the upstream reaches.

Mass balance of target pharmaceutical compounds in the Kanzaki–Ai River basin

For each pharmaceutical compound, the mass balance in the Kanzaki–Ai River basin, i.e., the relationship (efflux load/influx load) between the load passing through point R5 (the downstream—most sample collection site) and the total flux upstream of R5 were calculated as a summed up mass flux data of the two data sets at the sites of R3 and T4 (Kanzaki River) and R1, S1, T1, T2, and S2 (Ai River) (Fig. 4).

The load of cyclophosphamide was reduced by 70 % as it flowed downriver, indicating that attenuation had occurred, but the percentage attenuations for the other compounds were smaller—roughly in the range of 15 % to a maximum of 50 %. For clarithromycin and bicalutamide, which tend to be detected in river waters in high concentrations in this study, the results were similar to that of carbamazepine (Andreozzi et al. 2003; Hanamoto et al. 2013; Patrolecco et al. 2015; Yamamoto et al. 2009). Carbamazepine is not very susceptible to photolysis and biodegradation in the river environment (Andreozzi et al. 2003; Löffler et al. 2005) and is therefore

transported down rivers from upstream to downstream sites without being attenuated (Andreozzi et al. 2003; Hanamoto et al. 2013; Patrolecco et al. 2015; Yamamoto et al. 2009). Thus, some of the anticancer compounds that we targeted are attenuated while being transported downriver, but the effect of attenuation is mild and the compounds tend to remain in the river environment. For this reason, to reduce the load of anticancer compounds in rivers, water treatment at STPs is important and the introduction of advanced water treatment techniques such as ozonation (see section “Occurrence of target pharmaceutical compounds in river waters and STP effluents”) is essential. Our findings should be of value for conducting ecotoxicity assessments of anticancer compounds and their risk to human health via drinking water in the future.

Conclusions

We focused here on anticancer compounds used in large quantities in clinical situations in Japan. We studied the pollutant status of these and of antimicrobial and psychotropic compounds in the highly populated Kanzaki–Ai River basin to elucidate pollutant load sources and pollutant movement in the river environment. All six anticancer compounds targeted were detected in sewage and river waters, and the existence of bicalutamide at fairly high concentrations (maximum 254 ng/L in the main stream, 151 ng/L in tributaries, and 1032 ng/L in STP effluents) was identified for the first time. STPs were found to be the main load sources of the target anticancer compounds in the river, and by mass flux evaluation, we found that the effect of attenuation in the river environment was small. We also confirmed the effectiveness of ozonation in the sewage treatment process in removing these compounds. These results should be of value in environmental risk assessments of anticancer compounds in the water environment.

Acknowledgments We thank the staff of the STPs for sampling the water. We acknowledge the River Foundation for the funding in the form of research and scholarships.

References

- Adachi F, Yamamoto A, Takakura K-I, Kawahara R (2013) Occurrence of fluoroquinolones and fluoroquinolone-resistance genes in the aquatic environment. *Sci Total Environ* 444:508–514
- Ågerstrand M, Berg C, Björleinius B, Breitholtz M, Brunström B, Fick J, Gunnarsson L, Larsson DGJ, Sumpter JP, Tysklind M, Rudén C (2015) Improving environmental risk assessment of human pharmaceuticals. *Environ Sci Technol* 49:5336–5345
- American Chemical Society: SciFinder online database (subscription database)

- Andreozzi R, Raffaele M, Nicklas P (2003) Pharmaceuticals in STP effluents and their solar photodegradation in aquatic environment. *Chemosphere* 50:1319–1330
- Antoniou MG, Hey G, Rodríguez Vega S, Spiliotopoulou A, Fick J, Tysklind M, la Cour JJ, Andersen HR (2013) Required ozone doses for removing pharmaceuticals from wastewater effluents. *Sci Total Environ* 456–457:42–49
- Aristilde L, Melis A, Sposito G (2010) Inhibition of photosynthesis by a fluoroquinolone antibiotic. *Environ Sci Technol* 44:1444–1450
- Ashton D, Hilton M, Thomas KV (2004) Investigating the environmental transport of human pharmaceuticals to streams in the United Kingdom. *Sci Total Environ* 333:167–184
- Azuma T, Nakada N, Yamashita N, Tanaka H (2012) Synchronous dynamics of observed and predicted values of anti-influenza drugs in environmental waters during a seasonal influenza outbreak. *Environ Sci Technol* 46:12873–12881
- Azuma T, Nakada N, Yamashita N, Tanaka H (2013) Mass balance of anti-influenza drugs discharged into the Yodo River system, Japan, under an influenza outbreak. *Chemosphere* 93:1672–1677
- Azuma T, Nakada N, Yamashita N, Tanaka H (2014) Optimisation of the analysis of anti-influenza drugs in wastewater and surface water. *Int J Environ Anal Chem* 94:853–862
- Besse J-P, Latour J-F, Garric J (2012) Anticancer drugs in surface waters: what can we say about the occurrence and environmental significance of cytotoxic, cytostatic and endocrine therapy drugs? *Environ Int* 39:73–86
- Booker V, Halsall C, Llewellyn N, Johnson A, Williams R (2014) Prioritising anticancer drugs for environmental monitoring and risk assessment purposes. *Sci Total Environ* 473–474:159–170
- Carlsson C, Johansson A-K, Alvan G, Bergman K, Kühler T (2006) Are pharmaceuticals potent environmental pollutants?: part I: environmental risk assessments of selected active pharmaceutical ingredients. *Sci Total Environ* 364:67–87
- Cockshott I (2004) Bicalutamide: clinical pharmacokinetics and metabolism. *Clin Pharmacokinet* 43:855–878
- Daughton CG, Ternes TA (1999) Pharmaceuticals and personal care products in the environment: agents of subtle change? *Environ Health Perspect* 107:907–938
- Environment Canada (2015) Screening assessment, ethanamine, 2-[4-[(1Z)-1,2-diphenyl-1-butenyl]phenoxy]-N,N-dimethyl-(tamoxifen). 1–63
- Ferrando-Climent L, Rodríguez-Mozaz S, Barceló D (2013) Development of a UPLC-MS/MS method for the determination of ten anticancer drugs in hospital and urban wastewaters, and its application for the screening of human metabolites assisted by information-dependent acquisition tool (IDA) in sewage samples. *Anal Bioanal Chem* 405:5937–5952
- Ferrando-Climent L, Rodríguez-Mozaz S, Barceló D (2014) Incidence of anticancer drugs in an aquatic urban system: from hospital effluents through urban wastewater to natural environment. *Environ Pollut* 193:216–223
- Ferrer I, Zweigenbaum JA, Thurman EM (2010) Analysis of 70 Environmental Protection Agency priority pharmaceuticals in water by EPA Method 1694. *J Chromatogr A* 1217:5674–5686
- Ghosh GC, Nakada N, Yamashita N, Tanaka H (2010) Oseltamivir carboxylate, the active metabolite of oseltamivir phosphate (Tamiflu), detected in sewage discharge and river water in Japan. *Environ Health Perspect* 118:103–107
- Grabic R, Fick J, Lindberg RH, Fedorova G, Tysklind M (2012) Multi-residue method for trace level determination of pharmaceuticals in environmental samples using liquid chromatography coupled to triple quadrupole mass spectrometry. *Talanta* 100:183–195
- Hanamoto S, Nakada N, Yamashita N, Tanaka H (2013) Modeling the photochemical attenuation of down-the-drain chemicals during river transport by stochastic methods and field measurements of pharmaceuticals and personal care products. *Environ Sci Technol* 47:13571–13577
- Social Welfare and Public Health in Tokyo (2012) Summary of medical practices survey in Tokyo. 1–16
- Japan Meteorological Agency, Weather statistics. Available from <<http://www.jma.go.jp/jma/index.html>> (accessed June 12, 2015)
- Jiho (2014) Yakuji Handbook (in Japanese), ISBN: 978-4840743136
- Kim I, Yamashita N, Tanaka H (2009a) Performance of UV and UV/H₂O₂ processes for the removal of pharmaceuticals detected in secondary effluent of a sewage treatment plant in Japan. *J Hazard Mater* 166:1134–1140
- Kim IH, Yamashita N, Kato Y, Tanaka H (2009b) Discussion on the application of UV/H₂O₂, O₃ and O₃/UV processes as technologies for sewage reuse considering the removal of pharmaceuticals and personal care products. *Water Sci Technol* 59:945–955
- Kolpin DW, Furlong ET, Meyer MT, Thurman EM, Zaugg SD, Barber LB, Buxton HT (2002) Pharmaceuticals, hormones, and other organic wastewater contaminants in U.S. streams, 1999–2000: a national reconnaissance. *Environ Sci Technol* 36:1202–1211
- Komori K, Suzuki Y, Minamiyama M, Harada A (2013) Occurrence of selected pharmaceuticals in river water in Japan and assessment of their environmental risk. *Environ Monit Assess* 185:4529–4536
- Kosjek T, Heath E (2011) Occurrence, fate and determination of cytostatic pharmaceuticals in the environment. *TrAC Trends Anal Chem* 30:1065–1087
- Kumar V, Nakada N, Yasojima M, Yamashita N, Johnson AC, Tanaka H (2009) Rapid determination of free and conjugated estrogen in different water matrices by liquid chromatography-tandem mass spectrometry. *Chemosphere* 77:1440–1446
- Kumar V, Nakada N, Yamashita N, Johnson AC, Tanaka H (2011) How seasonality affects the flow of estrogens and their conjugates in one of Japan's most populous catchments. *Environ Pollut* 159:2906–2912
- Kümmerer K (2009) Antibiotics in the aquatic environment—a review—part I. *Chemosphere* 75:417–434
- Lake Biwa-Yodo River Water Quality Preservation Organization, Japan (2012) BYQ (Lake Biwa-Yodo River Water Quality Preservation Organization) Report on water environment in Biwa Lake-Yodo River System 2010 (in Japanese). 1–150
- Liu X, Zhang J, Yin J, Duan H, Wu Y, Shao B (2010) Analysis of hormone antagonists in clinical and municipal wastewater by isotopic dilution liquid chromatography tandem mass spectrometry. *Anal Bioanal Chem* 396:2977–2985
- Löffler D, Römbke J, Meller M, Ternes TA (2005) Environmental fate of pharmaceuticals in water/sediment systems. *Environ Sci Technol* 39:5209–5218
- López-Serna R, Jurado A, Vázquez-Suñé E, Carrera J, Petrović M, Barceló D (2013) Occurrence of 95 pharmaceuticals and transformation products in urban groundwaters underlying the metropolis of Barcelona, Spain. *Environ Pollut* 174:305–315
- Martín J, Camacho-Muñoz D, Santos JL, Aparicio I, Alonso E (2011) Simultaneous determination of a selected group of cytostatic drugs in water using high-performance liquid chromatography–triple-quadrupole mass spectrometry. *J Sep Sci* 34:3166–3177
- Ministry of Health Labour and Welfare, Japan (2012) Annual report on statistics of production by pharmaceutical industry in 2011 (in Japanese)
- Ministry of Health Labour and Welfare, Japan (2013) Vision of medicine industry 2013 (in Japanese). 1–76
- Ministry of Health Labour and Welfare, Japan (2014) Vital statistics in Japan (in Japanese). 1–59
- Ministry of the Environment, Japan (2009) Type of environmental standard for water quality for conservation of aquatic organism, 3rd report

- Nakada N, Komori K, Suzuki Y, Konishi C, Houwa I, Tanaka H (2007) Occurrence of 70 pharmaceutical and personal care products in Tone River basin in Japan. *Water Sci Technol* 56:133–140
- Narumiya M, Nakada N, Yamashita N, Tanaka H (2013) Phase distribution and removal of pharmaceuticals and personal care products during anaerobic sludge digestion. *J Hazard Mater* 260:305–312
- Negreira N, de Alda ML, Barceló D (2014) Cytostatic drugs and metabolites in municipal and hospital wastewaters in Spain: filtration, occurrence, and environmental risk. *Sci Total Environ* 497–498:68–77
- Nussbaumer S, Bonnabry P, Veuthey J-L, Fleury-Souverein S (2011) Analysis of anticancer drugs: a review. *Talanta* 85:2265–2289
- Okuda T, Yamashita N, Tanaka H, Matsukawa H, Tanabe K (2009) Development of extraction method of pharmaceuticals and their occurrences found in Japanese wastewater treatment plants. *Environ Int* 35:815–820
- Osaka Prefecture, Japan (2012) Yodo River System, river construction plan for Kanzaki River (in Japanese). 1–52
- Patrolecco L, Capri S, Ademollo N (2015) Occurrence of selected pharmaceuticals in the principal sewage treatment plants in Rome (Italy) and in the receiving surface waters. *Environ Sci Pollut Res* 22:5864–5876
- Petrović M, Škrbić B, Živančev J, Ferrando-Climent L, Barcelo D (2014) Determination of 81 pharmaceutical drugs by high performance liquid chromatography coupled to mass spectrometry with hybrid triple quadrupole–linear ion trap in different types of water in Serbia. *Sci Total Environ* 468–469:415–428
- Prasse C, Schlüsener MP, Schulz R, Ternes TA (2010) Antiviral drugs in wastewater and surface waters: a new pharmaceutical class of environmental relevance? *Environ Sci Technol* 44:1728–1735
- Rabii FW, Segura PA, Fayad PB, Sauvé S (2014) Determination of six chemotherapeutic agents in municipal wastewater using online solid-phase extraction coupled to liquid chromatography-tandem mass spectrometry. *Sci Total Environ* 487:792–800
- Schlüsener MP, Hardenbicker P, Nilson E, Schulz M, Viergutz C, Ternes TA (2015) Occurrence of venlafaxine, other antidepressants and selected metabolites in the Rhine catchment in the face of climate change. *Environ Pollut* 196:247–256
- Sun L, Chi J, Hu X, Fu Z (2015) Ecotoxicological effects of tamoxifen in the aquatic environment tamoxifen concepts and cancer: new paradigms (cancer etiology, diagnosis and treatments: pharmacology—research, safety testing and regulation). Nova Science Publishers, Inc. Nova Science Publishers, Inc., pp. 47–60
- Toolaram AP, Kümmerer K, Schneider M (2014) Environmental risk assessment of anti-cancer drugs and their transformation products: a focus on their genotoxicity characterization-state of knowledge and short comings. *Mut Res Rev Mutat Res* 760:18–35
- Vasquez MI, Lambrianides A, Schneider M, Kümmerer K, Fatta-Kassinos D (2014) Environmental side effects of pharmaceutical cocktails: what we know and what we should know. *J Hazard Mater* 279:169–189
- Yamamoto H, Nakamura Y, Moriguchi S, Nakamura Y, Honda Y, Tamura I, Hirata Y, Hayashi A, Sekizawa J (2009) Persistence and partitioning of eight selected pharmaceuticals in the aquatic environment: laboratory photolysis, biodegradation, and sorption experiments. *Water Res* 43:351–362



Second- and higher-order structural changes of DNA induced by antitumor-active tetrazolato-bridged dinuclear platinum(II) complexes with different types of 5-substituent

Masako Uemura^a, Yuko Yoshikawa^b, Kenichi Yoshikawa^c, Takaji Sato^d, Yoshiki Mino^d, Masahiko Chikuma^d, Seiji Komeda^{a,*}

^a Faculty of Pharmaceutical Sciences, Suzuka University of Medical Science, Suzuka 513-8670, Japan

^b Department of Biotechnology, College of Life Sciences, Ritsumeikan University, Kusatsu 525-8577, Japan

^c Department of Physics, Graduate School of Science, Kyoto University, Kyoto 606-8501, Japan

^d Faculty of Pharmaceutical Sciences, Osaka University of Pharmaceutical Sciences, Takatsuki 569-1094, Japan

ARTICLE INFO

Article history:

Received 14 December 2012

Received in revised form 2 May 2013

Accepted 2 May 2013

Available online 9 May 2013

Keywords:

Dinuclear Pt complexes

Tetrazole

DNA interaction

Circular dichroism

Fluorescence microscopy

Cancer

ABSTRACT

Here, we used circular dichroism (CD) and fluorescence microscopy (FM) to examine the interactions of a series of antitumor-active tetrazolato-bridged dinuclear platinum(II) complexes, $[[cis-Pt(NH_3)_2]_2(\mu-OH)(\mu-5-R-tetrazolato-N2,N3)]^{n+}$ ($R = CH_3$ (**1**), C_6H_5 (**2**), $CH_2COOCH_2CH_3$ (**3**), CH_2COO^- (**4**), $n = 2$ (**1–3**) or 1 (**4**)), which are derivatives of $[[cis-Pt(NH_3)_2]_2(\mu-OH)(\mu-tetrazolato-N2,N3)]^{2+}$ (**5-H-Y**), with DNA to elucidate the influence of these interactions on the secondary or higher-order structure of DNA and reveal the mechanism of action. The CD study showed that three derivatives, **1–3**, with a double-positive charge altered the secondary structures of calf thymus DNA but that **4**, the only complex with a single positive charge, induced almost no change, implying that the B- to C-form conformational change is influenced by ionic attraction. Unexpectedly, single-molecule observations with FM revealed that **4** changed the higher-order structure of T4 DNA into the compact-globule state most efficiently, at the lowest concentration, which was nearly equal to that of **5-H-Y**. These contradictory results suggest that secondary structural changes are not necessarily linked to higher-order ones, and that the non-coordinative interaction could be divided into two distinct interactions: (1) ionic attraction and (2) hydrogen bonding and/or van der Waals contact. The relationship between diffusion-controlled non-coordinative DNA interactions and cytotoxicities is also discussed.

© 2013 Elsevier Inc. All rights reserved.

1. Introduction

In the 1970s, *cis*-diamminedichloridoplatinum(II) (cisplatin) offered great potential as a platinum-based anticancer drug [1–3] and has since become one of the most important anticancer drugs, especially for ovarian [3–6] and testicular cancers [7–9]. The success of cisplatin promoted the study of structure–activity relationships of mononuclear platinum(II) complexes, leading to the evolution of carboplatin [10–13] and oxaliplatin [14–17], which cause fewer side effects. The platinum-based drugs characteristically possess sharp tumor growth inhibitory ability, which has inspired the development of additional platinum drugs with wider antitumor spectra and fewer potential side effects. It is generally accepted that cisplatin's cytotoxic effect originates from the formation of coordinative Pt–DNA adducts, comprising 1,2-intrastrand cross-links between two adjacent purine bases [18,19]. Carboplatin provides the same Pt–DNA adducts, resulting in a very similar anticancer spectrum and apparent cross-resistance to cisplatin [20].

This fact suggests that, to overcome cisplatin-resistance and to obtain a wider anticancer spectrum, a rational approach would be to prepare platinum complexes that react with DNA via mechanisms distinct from those of cisplatin and its analogs. A series of tetrazolato-bridged dinuclear platinum(II) complexes (tetrazolato-bridged complexes); $[[cis-Pt(NH_3)_2]_2(\mu-OH)(\mu-5-R-tetrazolato-N2,N3)]^{n+}$ (Fig. 1, $R = H$ (**5-H-Y**), CH_3 (**1**), C_6H_5 (**2**), $CH_2COOCH_2CH_3$ (**3**), CH_2COO^- (**4**), $n = 2$ (**5-H-Y** and **1–3**) or 1 (**4**)) was introduced as next-generation platinum-based anticancer drug candidates [21,22]. These complexes differ from widely used clinical platinum drugs in that they have two platinum centers bridged by tetrazolate, have positive charges, and have a relatively stable OH leaving group. Our previous studies revealed that these compounds: (1) overcome *in vitro* cross-resistance to cisplatin, (2) possess totally different cytotoxicity profiles from those of other clinical platinum drugs, and (3) provide effective *in vivo* antitumor activities against xenografted pancreatic cancer, a chemotherapy-resistant cancer [21,22].

For **5-H-Y** and other prototype azolato-bridged complexes, we performed circular dichroism (CD) and fluorescence microscopy (FM) studies to investigate how these complexes interact with DNA

* Corresponding author. Tel.: +81 59 340 0581; fax: +81 59 368 1274.
E-mail address: komedas@suzuka-u.ac.jp (S. Komeda).

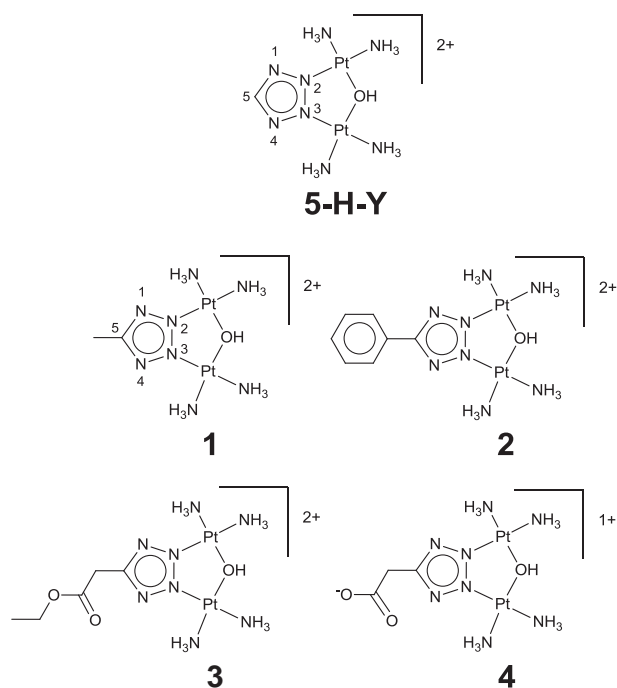


Fig. 1. Schematic representations of tetrazolato-bridged complexes **5-H-Y** and **1-4**.

[23–25]. Using CD, we found that **5-H-Y** reacts with DNA via a two-step interaction that comprises a prompt diffusion-controlled reaction and a relatively slow temperature-dependent reaction [25]. The former reaction may be induced by non-coordinative interactions that may result from the two positive charges of **5-H-Y** and cause conformational changes of calf thymus (CT) DNA from the B- to C-form. In addition, FM observations of higher-order structural changes of T4 phage DNA confirmed that **5-H-Y** induces DNA compactations at a considerably low concentration [24]. These findings also confirmed that cisplatin is less efficient than **5-H-Y** in inducing either second- or higher-order structural changes [26]. Expansion of DNA interaction studies to these derivatives with different types of 5-substituent would provide useful information regarding the relationship between DNA structural changes and the anticancer activities of these compounds, leading to the development of more detailed structure–activity relationships. Therefore, here, we conducted this study with new derivatives **1-4** using CD and FM to obtain a better understanding of their antitumor mechanisms, focusing on how the 5-substituents and differential molecular charges influence the non-coordinative interactions with DNA.

2. Experimental

2.1. Materials

The tetrazolato-bridged dinuclear platinum(II) complexes, $[\{cis-Pt(NH_3)_2\}_2(\mu-OH)(\mu-5-R-tetrazolato-N2,N3)]^{n+}$ ($R = CH_3$ (**1**), C_6H_5 (**2**), $CH_2COOCH_2CH_3$ (**3**), CH_2COO^- (**4**), $n = 2$ (**1-3**) or 1 (**4**)), were prepared and characterized as reported elsewhere [22]. CT DNA was purchased from Sigma (St. Louis, MO, USA). T4 phage DNA (166 kbp, contour length 57 μm) was purchased from Nippon Gene (Toyama, Japan). The fluorescent cyanine dye YOYO-1 (1,1'-[1,3-propanediylbis[(dimethylimino)-3,1-propanediyl]]bis[4-[(3-methyl-2(3H)-benzoxazolylidene)methyl]]-tetraiodide quinolinium) was purchased from Molecular Probes Inc. (Eugene, OR). The antioxidant 2-mercaptoethanol (2-ME) was purchased from Wako Pure Chemical Industries (Osaka, Japan). Other chemicals were of analytical grade and were obtained from various commercial sources.

2.2. Circular dichroism measurements

Each tetrazolato-bridged complex was mixed with CT DNA in various ratios (r) at room temperature in 0.3 mM citrate buffer (pH 7.4) ($r =$ the concentration of complex (μM) / the phosphate concentration of nucleotide ($30 \mu M$) = 0, 0.033, 0.067, 0.17, 0.33, 0.67, 1.0). The spectrum was measured using circular dichroism spectrophotometer (J-805, JASCO, Tokyo, Japan) in the range of the wavelength from 220 to 340 nm immediately after the addition of each complex to the buffered CT DNA solution at 298 K. The cell path length was 0.5 cm and the scan rate was 50 nm/min.

2.3. Direct observation by means of fluorescence microscopy of the structural change of DNA in aqueous solution

T4 phage DNA was dissolved in a 10 mM Tris–HCl buffer and 4% (v/v) 2-ME at pH 7.6 in the presence of various concentrations (1–200 μM) of **1-4**. Measurements were conducted at a low DNA concentration (0.1 μM in nucleotide units). To visualize individual DNA molecules by fluorescence microscopy, the cyanine dye YOYO-1 was added to the DNA solution after incubation with these complexes. To minimize the effect of YOYO-1 on DNA–drug interaction, a low concentration of YOYO-1 (0.05 μM) was added to the samples just before the single-DNA observation. Fluorescent DNA images were obtained using a microscope (Axiovert 200; Carl Zeiss, Oberkochen, Germany) equipped with a 100 \times oil-immersion objective lens and a highly sensitive EBCCD camera (Hamamatsu Photonics, Shizuoka, Japan), which made it possible to record images on DVD. The video images were analyzed with Cosmos image-analysis software (Library, Tokyo, Japan).

3. Results

3.1. Circular dichroism measurements

To study concentration-dependent secondary structural changes of CT DNA (30 μM effective phosphate concentration), we measured the CD spectra of the CT DNA immediately after each addition of **1-4** at various ratios (r), which we defined as the molar ratio of the platinum(II) compound added against the total phosphate concentration of the CT DNA. Fig. 2 shows the concentration-dependent CD spectral changes together with that of **5-H-Y** as previously reported [25].

Each black line shows the spectrum at $r = 0$; the blue, light blue, green, and red lines show the spectra at $r = 0.033, 0.067, 0.17,$ and $0.33,$ respectively. The spectrum in black with a positive band at around 278 nm and a similar magnitude for the negative band at around 248 nm means that the CT DNA is in the B-form. We observed that the positive band at around 278 nm decreased according to the addition of **1-3**. We calculated the difference in ellipticities at 278 nm ($\Delta\theta$) between the ellipticities observed in the absence of a tetrazolato-bridged complex (θ_0) and those obtained at the molar ratio of r (θ_r) defined by the following equation:

$$\Delta\theta = (\theta_0 - \theta_r).$$

The plots of $\Delta\theta$ (mdeg) at 278 nm vs. r ($r = 0, 0.033, 0.067, 0.17, 0.33, 0.67,$ and 1.0) are shown in Fig. 3.

The plots show breaks near $r = 0.33$ in both **1** and **3**, as was also observed in **5-H-Y**, and further addition caused little change in the secondary structure of the CT DNA. Complex **2** provided a characteristic spectrum, in which the ellipticity at around 260 nm increased in parallel with the decrease at around 278 nm. Further addition of **2** induced an increase in the intensity of the positive Cotton effect at around 260 nm with a little red shift, which was more distinct than the changes seen at around 278 nm (see Supplementary data). To obtain a better understanding of this finding, we monitored the CD spectra of **2** at various

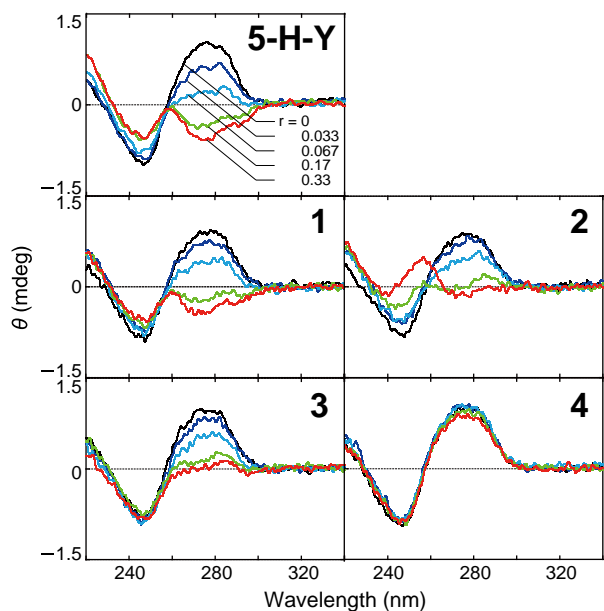


Fig. 2. CD spectrum of CT DNA obtained in the presence of different concentrations of **1–4** together with that of **5-H-Y** as previously reported [25]. The phosphate concentration of the CT DNA was 30 μM and the molar ratios ($r = \text{Pt complex}/P$) were 0 (black), 0.033 (blue), 0.067 (light blue), 0.17 (light green), and 0.33 (red).

concentrations in the absence of CT DNA, and found that there was little circular dichroism at around 260 nm (see Supplementary data). Complex **4**, a singly positively charged compound, provided almost no spectral change in the range of wavelengths observed, whereas the other compounds, with a double positive charge, caused changes in the secondary structure of the CT DNA as mentioned above. Fig. 3 clearly indicates that only modest changes were observed in **4** even at $r = 0.33$.

3.2. Direct observation by means of fluorescence microscopy of the structural change of DNA in aqueous solution

FM observations of T4 DNA were performed to investigate the effects of **1–4** on the higher-order structure of DNA under the same conditions we used to study **5-H-Y** previously [24]. FM enables

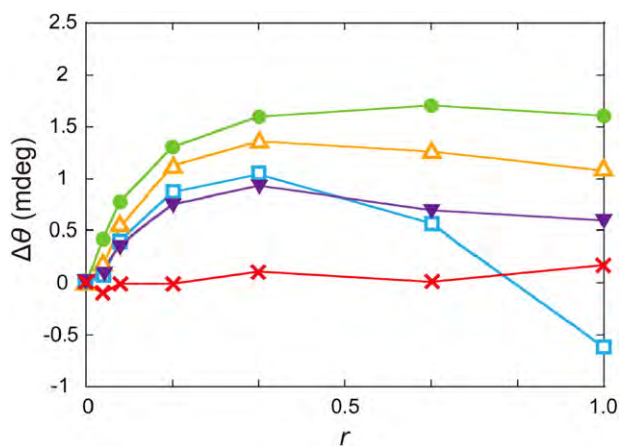


Fig. 3. Plots of $\Delta\theta$ at 278 nm vs. molar ratios (Pt complex/ P): **5-H-Y** (green closed circle), **1** (orange open triangle), **2** (blue open square), **3** (purple closed inverted triangle), and **4** (red cross). Values for **5-H-Y** were previously reported [25]. $\Delta\theta$ is the difference in ellipticities at 278 nm between ellipticities obtained in the absence of platinum(II) complex (θ_0) and those obtained at the molar ratio $= r$ (θ_r).

individual molecular analyses of DNA compaction events [27]. Accordingly, it is more suitable for the direct observation of DNA molecules larger than 100 kbp, which is a realistic model for platinated DNA in living cells [28]. The DNA concentration was low enough (0.1 μM) that multimolecular aggregation was not induced. Representative fluorescence images of individual DNA molecules in aqueous solution together with the corresponding quasi-3D profiles of the fluorescence intensity are shown in Fig. 4.

The higher-order DNA structure can be classified as a coil, partial globule, or compact-globule state on the basis of observations using time-successive FM. DNA exists in an elongated coil conformation in the absence of compounds, as in the control shown in Fig. 4A. Upon addition of **1** or **4** to the DNA solution, the individual DNA molecules undergo a structural transition from the coil state (Fig. 4B) to the compact-globule state (Fig. 4D) via a partial globule state (Fig. 4C) in which elongated and shrunken parts coexist in a single DNA molecule. Complex **4** induced higher-order structural changes into the partial globule state at a relatively low concentration (10 μM).

The distribution of the long-axis length of the T4 DNA is shown in Fig. 5, in which (II) and (III) represent the distribution in the presence of various concentrations of **1** and **4**, respectively.

As the concentrations of the tetrazolato-bridged complexes increased, the long-axis lengths became shorter and the proportion of DNA molecules in the partial or compact-globule state increased, indicating that DNA compaction was induced. Of the tetrazolato-bridged complexes we tested, **1** and **4** efficiently induced DNA compaction, with **4** seemingly the more efficient. This is because, in the presence of **4** at 10 μM (Fig. 5 III), 33% of the DNA molecules were already in the partial globule state, whereas all of the DNA molecules were still in the elongated coil state in the presence of **1** at 10 μM (Fig. 5 II). At 20 μM , **4** changed 87% of the DNA molecules into the compact-globule state, whereas at this concentration **1** changed 74% of the DNA molecules into the partial-globule state. All of the DNA molecules were in the globule state in the presence of 30 μM **1** and **4**, and the DNA long-axis lengths were shorter in the presence of **4** than in that of **1**. Aggregation of DNA molecules on addition of NaCl was observed only for **4**, indicating that the interaction of **4** with DNA is somewhat different from that observed with the other tetrazolato-bridged complexes.

Fig. 6 shows the DNA states in the presence of various concentrations of complexes **1–4** together with those previously reported for **5-H-Y** [24]; the critical concentration to convert more than 80% of the DNA molecules into the compact-globule state is marked with “G”.

Comparing the critical concentrations, we see that **5-H-Y** and **4** seem to induce DNA compaction most efficiently, that is, at the lowest concentration (20 μM), among the complexes listed in Fig. 6. The efficiency of **1** was also high (30 μM). For **2** and **3**, 7.5–10 times as much compound was required to induce the same amount of DNA compaction as that achieved with 20 μM of **5-H-Y** and **4**.

4. Discussion

In cytotoxicity assays for complexes **1–4** in cisplatin-sensitive and -resistant human non-small-cell lung cancer cell lines ([22] and Table S1), **1** was more cytotoxic than cisplatin and cross-resistance to **1** in the cisplatin-resistant cells was largely circumvented. Complex **3** was moderately cytotoxic, whereas **2** and **4** were only marginally cytotoxic. Moreover, complexes **1** and **3** exhibited effective *in vivo* antitumor efficacies in a nude mouse xenografted pancreatic cancer model [22]. Therefore, it is of great interest to see how the cytotoxicities or antitumor efficacies of these complexes are correlated to outcomes of their DNA interactions.

Among the derivatives of **5-H-Y**, **1** and **3** gave similar CD spectral changes to those of the parent compound; however, **2** and **4** showed very different results, as shown in Fig. 2. Complexes **1** and **3** both decreased the magnitude of the positive band at around 278 nm with a

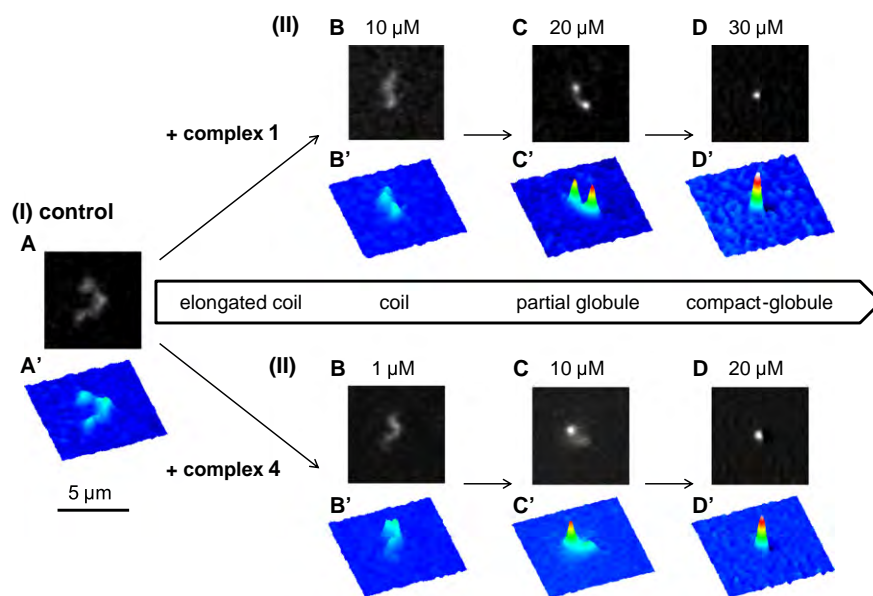


Fig. 4. Images of individual T4 DNA molecules moving freely in solution observed by using fluorescence microscopy (A–D) and corresponding quasi-3D profiles of the fluorescence intensity (A'–D'). (I) Control; time-successive fluorescent image of a single DNA molecule exhibiting Brownian motion in a buffer solution. The concentration-dependent changes of DNA state in the presence of (II) **1** of (B) 10, (C) 20, and (D) 30 μM and (III) **4** of (B) 1, (C) 10, and (D) 20 μM . DNA exists in (A) 'elongated coil', (B) 'coil', (C) 'partial globule' and (D) 'compact-globule' states.

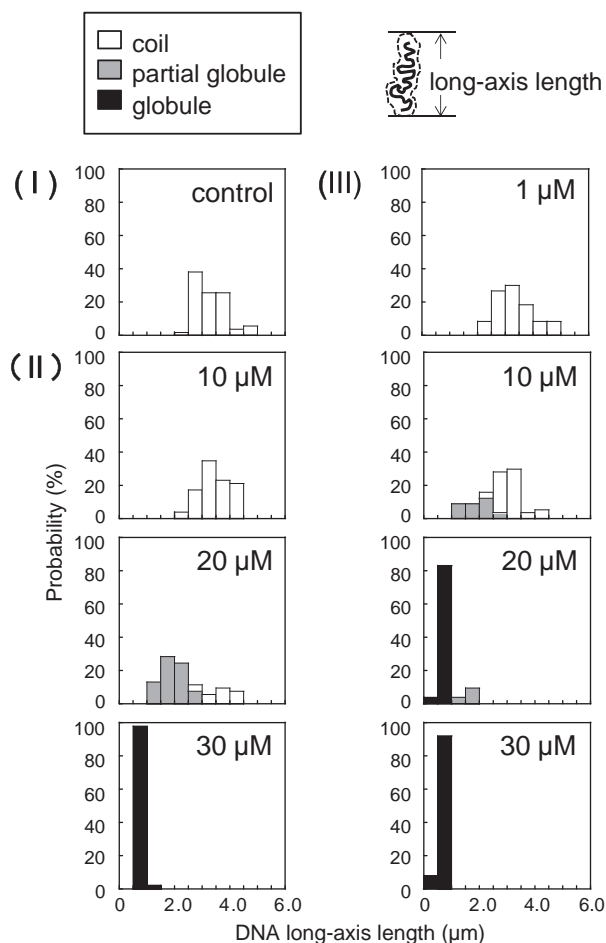


Fig. 5. Comparison of the distribution of the long-axis length of DNA in solution together with assignment of the conformational characteristics of the DNA images: (I) control in a buffer solution, in the presence of (II) **1** and (III) **4**. Top-right illustration shows a schematic representation of a fluorescent image of DNA. The 'coil' state is shown in white, 'partial globule' in gray, and 'compact-globule' in black.

relatively small change in the negative band at around 243 nm after the addition of each compound. In particular, in **1** at $r = 0.17$ and 0.33 , the positive band at around 278 nm decreased into the negative band. This spectral change, which is a characteristic of azolato-bridged complexes [25], was not observed in **3**, indicating that the $\Delta\theta$ given by **3** was considerably smaller than those of **5-H-Y** and **1**, as can be seen in Fig. 3. The band at around 278 nm reflects a change in the number of base pairs per turn [29], and a negative band at around 243 nm without the loss of intensity or Cotton effect at around 278 nm but with a dramatically decreased intensity relative to B-form DNA reflects the characteristic spectrum of C-form DNA [30]. C-form DNA is formed under conditions of rather low relative humidity [31], in association with metal ions such as Li^+ , Mg^{2+} , and Na^+ [29,30], which are densely charged and bind strongly to phosphate oxygen. Consequently, **1** and **3** induce secondary structural changes of DNA from the B- to C-form, with **3** having less potential than **5-H-Y** and **1** to induce such changes.

It is also noteworthy that **2** provided the characteristic spectral change at around 265 nm. The ellipticity at around 265 nm was remarkably increased by the further addition of **2** (see Supplementary data), which led to a drop-off of $\Delta\theta$ at 278 nm over $r = 0.33$ (Fig. 3). However, this change was not observed without CT DNA (see Supplementary data). Therefore, phenyl substitution at the 5-position of the tetrazolate distinguishes **2** from the other tetrazolato-bridged complexes. CD measurements of a double-stranded DNA chain with phenyltetrazoles synthetically attached to consecutive nucleobases produced similar CD spectra, in which ellipticity at around 265 nm and molar ellipticity increased in proportion to the number of phenyltriazoles attached to the DNA chain [32]. Similarly, **3** is probably arranged in some regular manner along the helix of the CT DNA.

On the other hand, **4** induced almost no spectral change. Previous studies have revealed that the concentration-dependent spectral changes observed in other azolato-bridged complexes are induced mainly by electrostatic interactions because these changes are elicited immediately after the compounds are added and even at 277 K where coordinative interactions rarely happen [25]. DNA is highly negatively charged under physiological conditions due to the phosphate groups in the ribose-phosphate backbone, and the tetrazolato-bridged complexes other than **4** are charged in +2. Electrostatic attractions between the negatively charged DNA and the positively charged complexes are, therefore, generated. Among the tetrazolato-bridged

complex \ conc. (μM)	1	2	5	10	20	30	100	150	200
5-H-Y ^[24]	-	-	C	PG(G)	G	-	-	-	-
1	-	-	-	C	PG(C)	G	-	-	-
2	-	-	-	C	-	-	C	PG(G)	G
3	-	-	-	C	C	C(PG)	PG(G)	G	-
4	C	C(PG)	-	PG(C)	G	-	-	-	-

Fig. 6. List of DNA states observed in the presence of various concentrations of **5-H-Y** [24] and **1–4**. The characters in each cell indicate the DNA state under each condition; C is 'coil', PG 'partial globule', and G 'compact-globule' state. '-' means that the experiments were not done at this concentration of the compound.

complexes, only **4** possesses the acetate group, the pK_a of which is 3.23 by titration (see Supplementary data). Accordingly, **4** in each reaction solution almost exists in an ionic form charged at +1 at pH 7.4 (the proportion of ions to total molecules calculated using the Henderson–Hasselbalch eq. is 99.993%). Consequently, the potency of tetrazolato-bridged complexes to induce the B- to C-form transition of DNA may be positively correlated to the magnitude of the positive charge.

FM observation allowed us to see how higher-order structures of DNA molecules were changed into the compact-globule state by the addition of various concentrations of **1–4** as shown in Fig. 4, and whether or not there was a correlation between the secondary structure and the ability to induce higher-order structural changes. Some of us previously reported that the three different mononuclear platinum(II) complexes, cisplatin, cis-diamminedinitratoplatinum(II) and tetraammineplatinum(II), also cause the DNA compaction, but much less efficiently than **5-H-Y** and **1–4** [26]. For instance, the former two mononuclear Pt(II) complexes, which provide the coordinative DNA adducts quickly [33], promoted the compaction weakly and irreversibly, and most of the DNA molecules were in the partial globule state in the presence of each compound at 1 mM. The cationic complex, tetraammineplatinum(II), which associates with DNA mainly by electrostatic attraction, caused complete DNA compaction at 1 mM concentration, which was promptly unfolded upon the addition of 100 mM NaCl. Neither **5-H-Y** nor **1–4** exhibit any marked change in their higher-order structures after the addition of the salt. Therefore, and because coordinative reaction kinetics of the tetrazolato-bridged complexes with a nucleobase derivative were found to be much slower than those of cisplatin [34,35], the diffusion-controlled DNA associations of **1–4** seem not to be caused by a simple electrostatic attraction nor a coordinative Pt–DNA interaction. Accordingly, the tetrazolato-bridged complexes interact with DNA in a manner distinct from that of cisplatin, especially on the diffusion-controlled one. Spermidine is well known to induce DNA compaction in an all-or-none manner, in which DNA molecules are changed from an elongated coil to a compact-globule state without an intermediate state [36]. In contrast, **1–4** induced DNA compaction via a similar process to that of **5-H-Y**, creating an intermediate state, in which both coil and compact parts coexist in a single molecule [24]. Interestingly, as can be clearly seen from Figs. 5 and 6, **4** had the highest DNA compaction potency, which was comparable to that of **5-H-Y**. Thus, **4** efficiently induces large changes in the higher-order structure of DNA, although it yields almost no change in the secondary structure. Therefore, changes in second- and higher-order structures may not be directly connected. Previously, we reported that the interactions of other azolato-bridged complexes with DNA are both coordinative and non-coordinative [23–25]. The results obtained here suggest that the non-coordinative DNA interaction can be further classified into two, one of which changes the secondary DNA structure, and the other causes the higher-order change. A non-coordinative DNA adduct of the prototype complex $[\{cis-Pt(NH_3)_2\}_2(\mu-OH)(\mu-pyazolato)]^{2+}$ (**AMPZ**) has been solved by high-resolution X-ray crystal analysis (Komeda, unpublished observation), in which **AMPZ** is trapped in the AT-tract minor groove in a non-coordinative manner. Given this information, we must take into consideration not only simple electrostatic interactions around

the ribose-phosphate backbone, but also other non-coordinative binding mediated by van der Waals contact and hydrogen bonding. As for hydrogen bond formation, tetrazolato-bridged complexes mainly work as hydrogen-bond donors, because they contain four ammine ligands and a bridging hydroxo ligand; only **4** possesses the potential hydrogen bond acceptor of an acetate group. In other words, **4** could bind more tightly to the minor- or major-grooves of DNA with higher hydrogen bonding potency on the nucleobases compared with other tetrazolato-bridged complexes.

What is the relationship between the diffusion-controlled non-coordinative DNA interactions and the cytotoxicities of these tetrazolato-bridged complexes? Their cytotoxicities are in the order of **1** > **3** > **2** > **4** ([22] and Table S1). At a glance, tetrazolato-bridged complexes that induce the secondary structural change from B- to C-form tend to show higher cytotoxicity. Complex **4** with its marginal cytotoxicity was the most efficient inducer of higher-order structural change, and thus, DNA compaction. Complex **4** could also be a metabolic product of the in vitro or in vivo enzymatic hydrolysis of the highly antitumor-active complex **3**. Chemical drugs containing an ester group generally initiate drug action before or after enzymatic hydrolysis. On the basis of the cytotoxicities of complexes **3** and **4**, complex **3** could be the anti-tumor active form and, **4** appears to be a non-active metabolite. Moreover, it may be that the substitution of acetate at the 5 position of the tetrazolato-bridge does not increase the cytotoxicity of the complex. Nevertheless, our findings suggest a new direction for the development of reagents that are highly efficient at inducing DNA compaction. In the present article, we have described the unique action of the dinuclear platinum(II) complexes on DNA. It may be of scientific value to examine the actual action of these platinum(II) complexes on living cells and also on the body as a whole, and to compare this action with that of mononuclear platinum(II) drugs. As has been demonstrated for the mononuclear complexes, the cellular accumulation of platinum complexes is an essential component of their potential as anticancer drugs [37]. In addition, studies at the whole-body level would need to include an assessment of side effects [38]. We believe that the results presented here will stimulate such future studies that may lead to the development of useful anticancer drugs.

5. Conclusion

Here, we focused on the diffusion-controlled non-coordinative DNA interactions of antitumor-active tetrazolato-bridged dinuclear platinum(II) complexes and revealed that different types of 5-substituents of the tetrazolato ring exert unique or different magnitudes of influence on the second- and higher-order structure of DNA. Our observations suggest that these second- and higher-order DNA structural changes are not necessarily linked to each other. In addition, the non-coordinative interaction could be divided into two distinctive interactions, one originating from ionic attraction, and the other due to hydrogen bonding and/or van der Waals contact. The connection between the outcome of these DNA interactions and cytotoxicity is still ambiguous, unfortunately, and further studies on other important profiles, such as Pt–DNA association/dissociation

constants and cellular uptake (see Table S1 for preliminary data) of the derivatives, are warranted. Furthermore, studies on interactions with biomacromolecules, such as serum proteins, which encounter drugs before they reach cancer cells, would also be useful for drug distribution studies in pharmaceutical science. We are currently synthesizing many more derivatives and investigating their interactions with biomolecules to construct more detailed structure–activity relationships and develop the next generation of anticancer drugs that are effective against chemotherapy-resistant tumors and produce the least potential side effects.

Acknowledgments

This work was supported by JSPS KAKENHI Grant Number 24590063 (MU and SK). We are also grateful to Yakult Honsya Co., Ltd. for financial support.

Appendix A. Supplementary data

Supplementary data to this article can be found online at <http://dx.doi.org/10.1016/j.jinorgbio.2013.05.004>.

References

- [1] B. Rosenberg, L. VanCamp, J.E. Trosko, V.H. Mansour, *Nature* 222 (1969) 385.
- [2] D.M. Hayes, E. Cvitkovic, R.B. Golbey, E. Scheiner, L. Helson, I.H. Krakoff, *Cancer* 39 (2006) 1372–1381.
- [3] E. Cvitkovic, J. Spaulding, V. Bethune, J. Martin, W.F. Whitmore, *Cancer* 39 (1977) 1357–1361.
- [4] E. Wiltshaw, T. Kroner, *Canc. Treat. Rep.* 60 (1976) 55.
- [5] E. Wiltshaw, B. Carr, *Recent Results Cancer Res.* 48 (1974) 178–182.
- [6] R. Young, D. Von Hoff, P. Gormley, R. Makuch, J. Cassidy, D. Howser, *J. Bull. Cancer Treat. Rep.* 63 (1979) 1539.
- [7] D.J. Higby, H.J. Wallace, D. Albert, J. Holland, *Cancer* 33 (1974) 1219–1225.
- [8] E. Cheng, E. Cvitkovic, R.E. Wittes, R.B. Golbey, *Cancer* 42 (1978) 2162–2168.
- [9] G.J. Bosl, R. Gluckman, N. Geller, R. Golbey, W. Whitmore Jr., H. Herr, P. Sogani, M. Morse, N. Martini, M. Bains, *J. Clin. Oncol.* 4 (1986) 1493–1499.
- [10] K.R. Harrap, *Cancer Res.* 55 (1995) 2761–2768.
- [11] K. Harrap, *Cancer Treat. Rev.* 12 (1985) 21–33.
- [12] A. Calvert, D. Newell, L. Gumbrell, S. O'Reilly, M. Burnell, F. Boxall, Z. Siddik, I. Judson, M. Gore, E. Wiltshaw, *J. Clin. Oncol.* 7 (1989) 1748–1756.
- [13] D.S. Alberts, S. Green, E.V. Hannigan, R. O'Toole, D. Stock-Novack, P. Anderson, E.A. Surwit, V.K. Malviya, W.A. Nahhas, C.J. Jolles, *J. Clin. Oncol.* 10 (1992) 706–717.
- [14] E. Raymond, S. Chaney, A. Taamma, E. Cvitkovic, *Ann. Oncol.* 9 (1998) 1053–1071.
- [15] J.M. Extra, M. Espie, F. Calvo, C. Ferme, L. Mignot, M. Marty, *Cancer Chemother. Pharmacol.* 25 (1990) 299–303.
- [16] G. Mathe, Y. Kidani, M. Segiguchi, M. Eriguchi, G. Fredj, G. Peytavin, J. Misset, S. Brienza, F. De Vassals, E. Chenu, *Biomed. Pharmacother.* 43 (1989) 237–250.
- [17] T. Tashiro, Y. Kawada, Y. Sakurai, Y. Kidani, *Biomed. Pharmacother.* 43 (1989) 251–260.
- [18] J. Reedijk, *Proc. Natl. Acad. Sci.* 100 (2003) 3611–3616.
- [19] E.R. Jamieson, S.J. Lippard, *Chem. Rev.* 99 (1999) 2467–2498.
- [20] M. Gore, I. Fryatt, E. Wiltshaw, T. Dawson, B. Robinson, A. Calvert, *Br. J. Cancer* 60 (1989) 767.
- [21] S. Komeda, Y.L. Lin, M. Chikuma, *ChemMedChem* 6 (2011) 987–990.
- [22] S. Komeda, *Metallomics* 5 (2013) 461–468.
- [23] N. Kida, Y. Katsuda, Y. Yoshikawa, S. Komeda, T. Sato, Y. Saito, M. Chikuma, M. Suzuki, T. Imanaka, K. Yoshikawa, *J. Biol. Inorg. Chem.* 15 (2010) 701–707.
- [24] Y. Yoshikawa, S. Komeda, M. Uemura, T. Kanbe, M. Chikuma, K. Yoshikawa, T. Imanaka, *Inorg. Chem.* 50 (2011) 11729–11735.
- [25] M. Uemura, Y. Yoshikawa, M. Chikuma, S. Komeda, *Metallomics* 4 (2012) 641–644.
- [26] Y. Katsuda, Y. Yoshikawa, T. Sato, Y. Saito, M. Chikuma, M. Suzuki, K. Yoshikawa, *Chem. Phys. Lett.* 473 (2009) 155–159.
- [27] Y. Yoshikawa, K. Yoshikawa, *FEBS Lett.* 361 (1995) 277–281.
- [28] Z. Liu, S. Tan, Y. Zu, Y. Fu, R. Meng, Z. Xing, *Micron* 41 (2010) 833–839.
- [29] W.A. Baase, W.C. Johnson, *Nucleic Acids Res.* 6 (1979) 797.
- [30] V.I. Ivanov, L. Minchenkova, A. Schyolkina, A. Poletayev, *Biopolymers* 12 (1973) 89–110.
- [31] G.D. Fasman, *Circular Dichroism and the Conformational Analysis of Biomolecules*, first ed. Springer, Berlin, 1996.
- [32] N.K. Andersen, N. Chandak, L. Brulíková, P. Kumar, M.D. Jensen, F. Jensen, P.K. Sharma, P. Nielsen, *Bioorg. Med. Chem.* 18 (2010) 4702–4710.
- [33] B. Lippert, C. Lock, B. Rosenberg, M. Zvagulis, *Inorg. Chem.* 16 (1977) 1525–1529.
- [34] D.P. Bancroft, C.A. Lepre, S.J. Lippard, *J. Am. Chem. Soc.* 112 (1990) 6860–6871.
- [35] M. Uemura, T. Suzuki, K. Nishio, M. Chikuma, S. Komeda, *Metallomics* 4 (2012) 686–692.
- [36] K. Yoshikawa, Y. Yoshikawa, T. Kanbe, *Chem. Phys. Lett.* 354 (2002) 354–359.
- [37] G.Y. Park, J.J. Wilson, Y. Song, S.J. Lippard, *Proc. Natl. Acad. Sci.* 109 (2012) 11987–11992.
- [38] S. Dhar, N. Kolishetti, S.J. Lippard, O.C. Farokhzad, *Proc. Natl. Acad. Sci.* 108 (2011) 1850–1855.

Note

Adenosine Thiamine Triphosphate (A_{Th}TP) Inhibits Poly(ADP-Ribose) Polymerase-1 (PARP-1) Activity

Takao TANAKA¹, Daisuke YAMAMOTO², Takaji SATO³, Sunao TANAKA⁴, Kazuya USUI⁵, Miki MANABE⁵, Yui AOKI³, Yasuki IWASHIMA³, Yoshihiro SAITO³, Yoshiki MINO³ and Hirofumi DEGUCHI¹

¹Organization of Medical Education, and ²Biomedical Computation Center, Osaka Medical College, 2–7 Daigakuchou, Takatsuki, Osaka 569–8686, Japan

³Laboratory of Analytical Chemistry, and ⁵Laboratory of Pharmacotherapy, Osaka University of Pharmaceutical Sciences, 4–20–1 Nasahara, Takatsuki, Osaka 569–1094, Japan

⁴Human Health Sciences, Graduate School of Medicine Kyoto University, Syogoin Kawaramachi 53, Sakyou-ku, Kyoto 606–8501, Japan

(Received November 5, 2010)

Summary Overactivation of poly(ADP-ribose) polymerase-1 (PARP-1) has been demonstrated to result in various stress-related diseases, including diabetes mellitus. Deficiency of cellular nicotinamide adenine dinucleotide (NAD⁺) content, consumed by PARP-1 to add ADP-ribose moieties onto target proteins, contributes to pathophysiological conditions. Adenosine thiamine triphosphate (A_{Th}TP) exists in small amounts in mammals; however, the function(s) of this metabolite remains unresolved. The structure of A_{Th}TP resembles NAD⁺. Recent experimental studies demonstrate beneficial impacts of high-dose thiamine treatment of diabetic complications. These findings have led us to hypothesize that A_{Th}TP may modulate the activity of PARP-1. We have chemically synthesized A_{Th}TP and evaluated the effect of A_{Th}TP on recombinant PARP-1 enzyme activity. A_{Th}TP inhibited the PARP-1 activity at 10 μM, and a structural model of the PARP-1–A_{Th}TP complex highlighted the A_{Th}TP binding site. The results provide new insights into the pharmacological importance of A_{Th}TP as an inhibitor of PARP-1.

Key Words adenosine thiamine triphosphate, poly(ADP-ribose) polymerase-1

Substantial recent experimental studies demonstrate beneficial impacts of high-dose thiamine on diabetic complications, such as diabetic retinopathy, diabetic nephropathy, diabetic neuropathy and diabetic cardiomyopathy (1–4). However, the pharmacological relevance of high-dose thiamine treatments remains unknown.

Chronic hyperglycemia results in diabetic complications in target organs. The pathogenic effect of high glucose is, at least partially, mediated to a significant extent through increased production of reactive oxygen species and reactive nitrogen species and subsequent oxidative stress (reviewed in Evans et al. (5)). Increased oxidative stress activates the nuclear enzyme, poly(ADP-ribose) polymerase-1 (PARP-1). PARP-1 activation depletes its substrate, nicotinamide adenine dinucleotide (NAD⁺), and also covalently attaches branched nucleic acid-like polymers of poly(ADP-ribose) to various acceptor proteins (reviewed in Kiss and Szabó (6)). A covalently attached ADP-ribose polymer, poly(ADP-ribosylation), affects the function of target proteins. The involvement

of PARP-1 activation in the pathogenesis of diabetes and its complications has recently been emphasized by both *in vivo* and *in vitro* studies (reviewed in Pacher and Szabó (7), and Szabó (8)).

NAD⁺, used as substrate for PARP-1, consists of two nucleotides joined through their phosphate groups, with one nucleotide containing an adenine base and the other containing nicotinamide.

Adenosine thiamine triphosphate (A_{Th}TP), a new thiamine derivative, was recently identified in *Escherichia coli* (9), followed by the identification in small amounts in mouse brain, heart, skeletal muscle, liver and kidneys (10). A_{Th}TP is composed of two molecules, an adenine base and thiamine, which are joined through phosphate groups. The structure of A_{Th}TP appears to closely resemble NAD⁺.

Although the biological role of A_{Th}TP is unknown, the existence of noncoenzyme functions of thiamine derivatives has been speculated (11–14).

In the context of 1) structural resemblance of A_{Th}TP to NAD⁺, 2) the experimental evidence implicating PARP-1 as a causative factor in the pathogenesis of diabetes and diabetic complications *in vitro* and *in vivo* (reviewed in Szabó (8)), and 3) beneficial effects of high-dose thiamine on diabetic complications, we hypothesized that A_{Th}TP could interact with PARP-1 and mod-

E-mail: t.tanaka.md@gmail.com

Abbreviations: A_{Th}TP, adenosine thiamine triphosphate; NAD⁺, nicotinamide adenine dinucleotide; PARP-1, poly(ADP-ribose) polymerase-1.

ulate PARP-1 activity.

Methods

Chemical synthesis and purification of AThTP. AThTP was synthesized according to the method described by Bettendorff et al. (9) The compound was initially purified by solid phase extraction on a MEGA Bond Elut[®] C₁₈ (Varian Inc., Harbor City, CA, USA) cartridge. After passage of the water solution of the crude compound, the cartridge was washed with water. The compound was eluted with 10 v/v% methanol. The eluted fraction was lyophilized, redissolved in water and then purified by size-exclusion chromatography on a Bio-Gel[®] P2 column (2.0×60 cm) equilibrated with water. The elution profile was followed by reading the absorbance at 280 nm to detect the presence of AThTP. The AThTP fraction was lyophilized and redissolved in 50 mM ammonium acetate buffer (pH 7.0). The pure AThTP was obtained using an HPLC system equipped with a semi-preparative COSMOSIL[®] C₁₈-MS-II column (Nacalai Tesque, Inc., Kyoto, Japan) and eluted under isocratic conditions using methanol: 50 mM ammonium acetate buffer (pH 7.0) (5:95) at a flow rate of 3 mL/min. The purity of the preparations was checked by HPLC, MS analysis and NMR.

Evaluation of PARP-1 enzyme activity in a cell-free assay. The effect of AThTP on PARP-1 enzyme activity was evaluated by a HT Universal Colorimetric PARP Assay Kit with Histone-Coated Strip Wells purchased from Trevigen (Gaithersburg, MD, USA), following the manufacturer's instructions. This assay kit measures the incorporation of biotinylated poly(ADP-ribose) onto histone proteins in a 96-well plate.

Molecular modeling of the PARP-1-AThTP complex. For modeling of the human PARP-1 molecule complexed with AThTP, a model of the PARP-1 catalytic domain was prepared by taking the coordinate set, 1A26 including an ADP molecule (15), from the Protein Data Bank (PDB <http://www.rcsb.org/pdb/>). Adenosine and the triphosphate of AThTP were modeled from this ADP molecule. The PARP-1 binding structure of the AThTP thiamin moiety was constructed by referring to the ABT-888 binding to PARP2 (PDB code: 3KJD) (16). The thiazole and pyrimidine rings of the thiamin moiety were positioned in a similar location to the imidazole and pyrrolidine rings of ABT-888. Water molecules were randomly distributed in a 10 Å shell around the complex. After energy minimization using the MMFF94x force field (17), 200-picosecond (ps) molecular dynamics simulations were performed at 300 K using a 0.002 ps time step and the NVT method (18, 19). Finally, the most stable structure during the last 50 ps simulations was optimized by energy minimization. The potential energy of molecular system after final optimization was -4.99×10^4 kcal/mol including the PARP-1 catalytic domain (from Lys662 to Ser1012), AThTP and 2810 water molecules. All operations were performed using the package for molecular structure analyses, MOE (Molecular Operating Environment, Chemical Computing Group Inc., Québec, CA

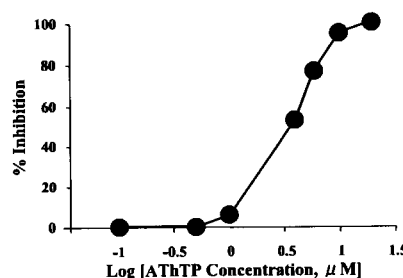


Fig. 1. Graphic representation of the colorimetric read-out of the PARP-1 inhibition curves for AThTP. Each point represents the median value from triplicates.

<http://www.chemcomp.com/>).

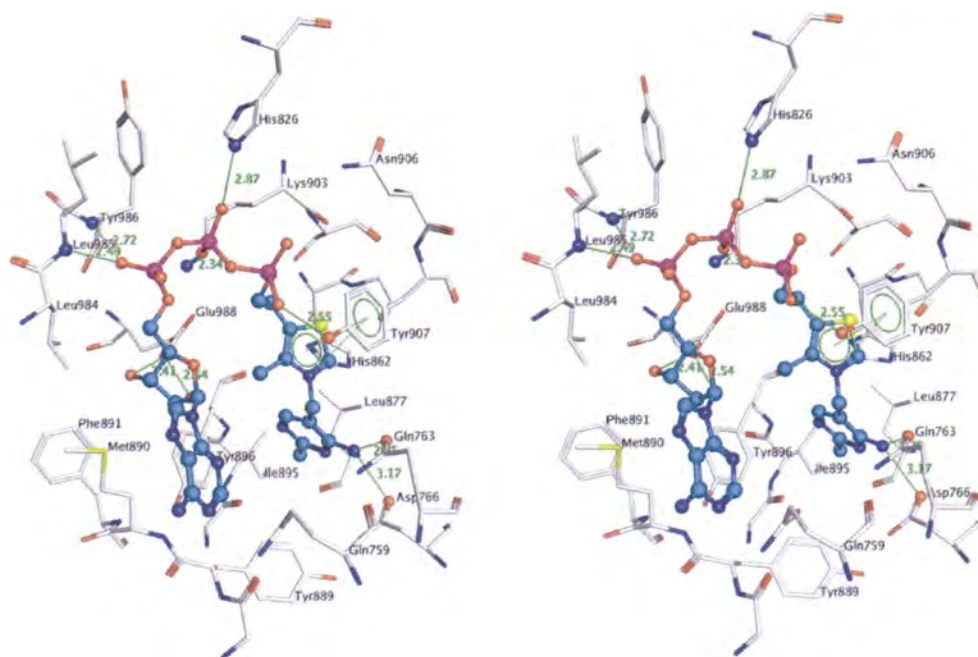
Results and Discussion

To test our hypothesis, we chemically synthesized AThTP and the effect of AThTP on PARP-1 enzyme activity was evaluated using recombinant PARP-1 in a cell-free assay. As expected, PARP-1 activity was markedly reduced by 10 mM 3-aminobenzamide (approximately 80% inhibition, data not shown). AThTP showed a dose-dependent effect on PARP-1 activity, producing almost complete inhibition at 10 μM (Fig. 1). Adenosine thiamine diphosphate (AThDP), thiamine, thiamine diphosphate, and thiamine triphosphate did not inhibit PARP-1 activity at 20 μM (data not shown). It is interesting to examine a synergistic inhibition effect of these materials with ATP and/or ADP, which are not inhibited alone, in detail. A difference of the PARP-1 inhibitory activity between AThTP and AThDP, structurally more close to NAD⁺, is thought to be a difference of interaction with the phosphate to PARP-1 enzyme and a structural flexibility of the phosphate moiety in AThTP.

Although the inhibitory concentration of AThTP (10 μM) is much higher than the concentration in mouse tissues (10), it may be possible that AThTP, synthesized by enzyme, is increased by a mass effect when a tissue concentration of thiamine increases. The hepatic concentration of total thiamine is increased by high-dose thiamine and this phenomenon is robust in streptozotocine-induced diabetic rats (unpublished data). Therefore, AThTP is thought to have pharmacological significance as PARP-1 inhibitor.

In this study, we evaluated the PARP-1 enzyme activity in the commercially available PARP-1 enzyme activity kit, which is used for the screening of PARP-1 inhibitors and for measuring the activity of PARP-1 in cell extracts. Unfortunately the precise inhibitory mechanism could not be evaluated by this kit. Accordingly, to gain further insight, we constructed an initial structural model of the PARP-1-AThTP complex by considering the X-ray structures of the PARP-1-ADP analogue complex (15) and the PARP2-PARP inhibitor (ABT-888) complex (16), deposited in the Protein Data Bank (<http://www.rcsb.org/pdb/>) as 1A26 and 3KJD. The energy-minimized structure after 200 ps of molecular dynamics simulations is shown in Fig. 2A as a ster-

A



B

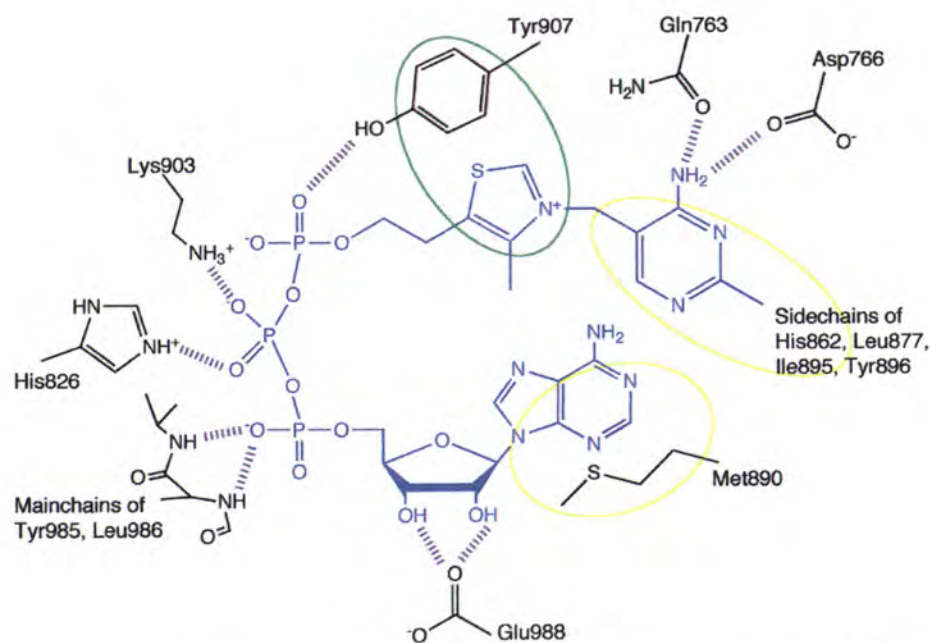


Fig. 2. Predicted interaction between human PARP-1 and AThTP. A simulated complex structure of human PARP-1 with AThTP is shown in (A) without hydrogen atoms. AThTP is presented by a light-blue ball-and-stick model, and PARP-1 residues adjacent to AThTP are shown by white stick models. Nitrogen, oxygen, sulfur and phosphorus atoms are colored blue, red, yellow and purple, respectively. Each hydrogen bond between PARP-1 and AThTP is indicated by a thin green line with its distance (\AA), and the related atoms in PARP-1 are represented by balls. The Ring-stacking interaction between the AThTP thiazole ring and the Tyr907 side-chain is indicated by green circles and dotted lines. An interaction scheme between human PARP-1 and AThTP is shown in (B) with related amino acid residues. AThTP is colored light-blue. Hydrogen bonds, hydrophobic interactions and ring-stacking interactions are illustrated as purple dotted lines, yellow circles and a green circle, respectively.

eo view, and the predicted interaction between PARP-1 and A_{Th}TP is summarized in Fig. 2B. The initial structure of A_{Th}TP was not provided, but the structure of this simulation resulted in a U-shaped conformation of A_{Th}TP. In this structure, the adenine moiety of A_{Th}TP is positioned by hydrophobic interactions with the Met890 side-chain. Two hydroxyl groups of the A_{Th}TP ribose moiety are fixed by hydrogen bonds with the Glu988 side-chain, and the triphosphate is stabilized by hydrogen bonds and electrostatic interactions with a positive charged pocket (His826, Lys903 and the main-chains of Tyr985 and Leu986). These interactions are similar to those observed in the ADP analogue complex (15). Ring-stacking interactions were observed between the A_{Th}TP thiazole ring and the Tyr907 phenyl ring. Furthermore, this phenyl group contributes in fixing a phosphate group of A_{Th}TP via a hydrogen bond. The A_{Th}TP methyl-pyrimidine enters into a hydrophobic hole (His862, Leu877, Ile895 and Tyr896), and the amino group of the pyrimidine moiety appears to interact with Gln763 and Asp766 through hydrogen bonds. Ring-stacking interactions of the thiazole moiety with this enzyme were also similar to the X-ray structure of the PARP2-ABT-888 complex (16) and the PARP-1-PARP-1 inhibitor complexes (20-22).

The ADP and ABT-888 binding sites, described above, were reported as “acceptor” and “donor” binding sites for ADP-ribose elongation by PARP-1 (15). The poly (ADP-ribose) chain (acceptor) and an NAD⁺ molecule (donor) would bind to PARP-1 via the ADP and ABT-888 binding sites, respectively. The NAD⁺ nicotinamide moiety is thought to be stabilized by the ABT-888 binding site, especially Tyr907 via ring-stacking interactions (16), and many PARP-1 inhibitors have been created mainly for binding to this “donor” binding site. By comparing these binding modes, it appears that A_{Th}TP in the structure of the PARP-1 complex could interact with both binding sites at the same time. Furthermore, the A_{Th}TP pyrimidine moiety in the above model could interact with an inner hydrophobic hole near the binding site of the phenoxypropyl group of a quinazoline derivative (PARP-1 inhibitor) (21). However, it is also probable that this pyrimidine ring cannot enter into the hydrophobic hole but covers this hole in a similar manner to other inhibitors (22).

The results herein have reported that A_{Th}TP inhibited PARP-1 activity, providing new insights into the pharmacological relevance of A_{Th}TP as a regulator of PARP-1.

A_{Th}TP is reported to be detectable in the mouse brain, skeletal muscle, heart, kidney, and liver (10) and thiamine diphosphate adenylyl transferase, synthesizing adenosine thiamine triphosphate, has been characterized in *E. coli* (23). We believe that the beneficial impacts of high-dose thiamine on diabetic complications could result from not only the coenzymatic function of thiamine but also, at least partly, from a non-cofactor role for thiamine derivatives in living cells, i.e., the inhibitory function of A_{Th}TP against PARP-1 activity.

The involvement of PARP-1 overactivation has been demonstrated in numerous stress-related diseases (reviewed in Pacher and Szabó (7) and Szabó (8)). Accordingly, high-dose thiamine intervention could be beneficial in treating not only diabetic complications but also in the treatment of various stress-related diseases. Using an obese rat model, we recently found that high-dose thiamine prevented the metabolic syndrome (24) and mitigated the development of hypertension in spontaneous hypertensive rats (SHR) (25), even though the relevance of A_{Th}TP still remains to be verified.

REFERENCES

- 1) Babaei-Jadidi R, Karachalias N, Ahmed N, Battah S, Thornalley PJ. 2003. Prevention of incipient diabetic nephropathy by high-dose thiamine and benfotiamine. *Diabetes* **52**: 2110–2120.
- 2) Brownlee M. 2001. Biochemistry and molecular cell biology of diabetic complications. *Nature* **414**: 813–820.
- 3) Hammes HP, Du X, Edelstein D, Taguchi T, Matsumura T, Ju Q, Lin J, Bierhaus A, Nawroth P, Hannak D, Neumaier M, Bergfeld R, Giardino I, Brownlee M. 2003. Benfotiamine blocks three major pathways of hyperglycemic damage and prevents experimental diabetic retinopathy. *Nat Med* **9**: 294–299.
- 4) Kohda Y, Shirakawa H, Yamane K, Otsuka K, Kono T, Terasaki F, Tanaka T. 2008. Prevention of incipient diabetic cardiomyopathy by high-dose thiamine. *J Toxicol Sci* **33**: 459–472.
- 5) Evans JL, Goldfine ID, Maddux BA, Grodsky GM. 2003. Are oxidative stress-activated signaling pathways mediators of insulin resistance and beta-cell dysfunction? *Diabetes* **52**: 1–8.
- 6) Kiss L, Szabó C. 2005. The pathogenesis of diabetic complications: the role of DNA injury and poly(ADP-ribose) polymerase activation in peroxynitrite-mediated cytotoxicity. *Mem Inst Oswaldo Cruz* **100**: 29–37.
- 7) Pacher P, Szabó C. 2005. Role of poly(ADP-ribose) polymerase-1 activation in the pathogenesis of diabetic complications: endothelial dysfunction, as a common underlying theme. *Antioxid Redox Signal* **7**: 1568–1580.
- 8) Szabó C. 2005. Roles of poly(ADP-ribose) polymerase activation in the pathogenesis of diabetes mellitus and its complications. *Pharmacol Res* **52**: 60–71.
- 9) Bettendorff L, Wirtzfeld B, Makarchikov A, Mazzucchelli G, Frédéric M, Gigliobianco T, Gangolf M, De Pauw E, Angenot L, Wins P. 2007. Discovery of a natural thiamine adenine nucleotide. *Nat Chem Biol* **3**: 211–212.
- 10) Frédéric M, Delvaux D, Gigliobianco T, Gangolf M, Dive G, Mazzucchelli G, Elias B, De Pauw E, Angenot L, Wins P, Bettendorff L. 2009. Thiaminylated adenine nucleotides. *FEBS J* **276**: 3256–3268.
- 11) Bettendorff L. 1994. Thiamine in excitable tissues: reflections on a non-cofactor role. *Metab Brain Dis* **9**: 183–209.
- 12) Singleton CK, Martin PR. 2001. Molecular mechanisms of thiamine utilization. *Curr Mol Med* **1**: 197–207.
- 13) Bâ A. 2008. Metabolic and structural role of thiamine in nervous tissues. *Cell Mol Neurobiol* **28**: 923–931.
- 14) Bettendorff L, Wins P. 2009. Thiamin diphosphate in biological chemistry: new aspects of thiamin metabolism, especially triphosphate derivatives acting other than as cofactors. *FEBS J* **276**: 2917–2925.

- 15) Ruf A, Rolli V, de Murcia G, Schulz GE. 1998. The mechanism of the elongation and branching reaction of poly(ADP-ribose) polymerase as derived from crystal structures and mutagenesis. *J Mol Biol* **278**: 57–65.
- 16) Karlberg T, Hammarström M, Schütz P, Svensson L, Schüler H. 2010. Crystal structure of the catalytic domain of human PARP2 in complex with PARP inhibitor ABT-888. *Biochemistry* **49**: 1056–1058.
- 17) Halgren TA. 1996. Merck molecular force field. I-V. *J Comput Chem* **17**: 490–641.
- 18) Berendsen HJC, Postma JPM, Van Gunsteren WF, DiNola A, Haak JR. 1984. Molecular dynamics with coupling to an external bath. *J Chem Phys* **81**: 3684–3690.
- 19) Bond SD, Leimkuhler BJ, Laird BB. 1999. The Nosé-Poincaré method for constant temperature molecular dynamics. *J Comp Phys* **151**: 114–134.
- 20) Ruf A, de Murcia G, Schulz GE. 1998. Inhibitor and NAD⁺ binding to poly(ADP-ribose) polymerase as derived from crystal structures and homology modeling. *Biochemistry* **37**: 3893–3900.
- 21) Matsumoto K, Kondo K, Ota T, Kawashima A, Kitamura K, Ishida T. 2006. Binding mode of novel 1-substituted quinazoline derivatives to poly(ADP-ribose) polymerase-catalytic domain, revealed by X-ray crystal structure analysis of complexes. *Biochim Biophys Acta* **1764**: 913–919.
- 22) Miyashiro J, Woods KW, Park CH, Liu X, Shi Y, Johnson EF, Bouska JJ, Olson AM. 2009. Synthesis and SAR of novel tricyclic quinoxalinone inhibitors of poly(ADP-ribose) polymerase-1 (PARP-1). *Bioorg Med Chem Lett* **19**: 4050–4054.
- 23) Makarchikov AF, Brans A, Bettendorff L. 2007. Thiamine diphosphate adenylyl transferase from *E. coli*: functional characterization of the enzyme synthesizing adenosine thiamine triphosphate. *BMC Biochem* **8**: 17.
- 24) Tanaka T, Kono T, Terasaki F, Yasui K, Soyama A, Otsuka K, Fujita S, Yamane K, Manabe M, Usui K, Kohda Y. 2010. Thiamine prevents obesity and obesity-associated metabolic disorders in OLETF rats. *J Nutr Sci Vitaminol* **56**: 335–346.
- 25) Tanaka T, Sohmiya K, Kono T, Terasaki F, Horie R, Ohkaru Y, Muramatsu M, Takai S, Miyazaki M, Kitaura, Y. 2007. Thiamine attenuates the hypertension and metabolic abnormalities in CD36-defective SHR: uncoupling of glucose oxidation from cellular entry accompanied with enhanced protein O-GlcNAcylation in CD36 deficiency. *Mol Cell Biochem* **299**: 23–35.

Chemical Degradation of Polychlorinated Biphenyls by the UV-Fe²⁺/Fe³⁺-H₂O₂ System and its Application for Polychlorinated Biphenyl-polluted Electric Insulating Oil

Takashi Azuma and Yoshiki Mino*

Laboratory of Environmental Analysis, Osaka University of Pharmaceutical Sciences, 4-20-1 Nasahara, Takatsuki, Osaka 569-1094, Japan

(Received July 28, 2011; Accepted August 3, 2011; Published online August 19, 2011)

The application of an optimized Fenton reaction and UV irradiation to the degradation of highly chlorinated biphenyls (PCBs) was performed. Recommended conditions were: Fe²⁺/Fe³⁺ concentration (16 mM), H₂O₂ concentration (12%), temperature (70°C), pH (2.0), reaction time under stirring (≥ 2 hr), re-addition of iron solution (1 hr intervals) and H₂O₂ (30 min intervals) and UV irradiation (254 nm, intensity 0.4 mW cm⁻²). When the system was applied to mixtures of PCBs at 5 ppm [PCBs congeners Kanechlor (KC)-400/600], low chlorine substituted biphenyls (Cl: 2–5) were completely decomposed after 2 hr, and even > 90% of high chlorine substituted biphenyls (Cl: 6–8) could be degraded. When the present system was first applied to PCBs present in polluted electric insulating oil (25 ppm), > 80% of PCBs were successfully degraded after 8 hr. These results suggest that the present UV-Fe²⁺/Fe³⁺-H₂O₂ system could be employed as a new technique for combating persistent organic pollutants such as PCBs.

Key words— chemical degradation, polychlorinated biphenyl, UV-Fe²⁺/Fe³⁺-H₂O₂ system, Fenton and Fenton-like reactions, polychlorinated biphenyl-polluted electric insulating oil

INTRODUCTION

Polychlorinated biphenyls (PCBs) are a group of toxic biphenyl compounds that are substituted by chlorines (≤ 10) and exist as a mixture of 209 congeners.¹⁾ PCBs were widely used in industry as heat media and as electric insulating oil. However, the considerable chemical stability and biological toxicity these compounds possess means that they currently pose a severe threat to the natural environment.^{2,3)} Because of their bio-accumulation characteristics and resistance to biodegradation, strict regulations have been implemented against the use of PCBs, and many countries have prohibited their use entirely.³⁾ The signatories of the Stockholm Treaty committed themselves to stopping production of products containing PCBs by 2025 and completing the disposal of stored PCBs by 2028.³⁾ Given the considerable amount of PCBs remaining in the environment and in storage, numerous studies on the degradation of PCBs have been undertaken, including biodegradation using microorganisms,^{4–6)} chemical and physicochemical degradations using TiO₂,⁷⁾ combination of O₃ and UV,⁸⁾ ultrasonication,⁹⁾ UV radiation,¹⁰⁾ hydrodechlorination by palladium on activated carbon (Pd-C),¹¹⁾ and microwave irradiation.¹²⁾ Although these degradation methods are useful for decomposition of PCBs, some are lengthy and/or expensive.¹³⁾

Successful decomposition of PCBs in electric insulating oil has been achieved using γ -ray radiation,¹⁴⁾ sodium dispersion,³⁾ and incineration.¹⁵⁾ However, despite their efficacy, these methods are costly and require the application of specialized techniques in order to perform them safely.

On the other hand, degradation by interaction with radical ·OH generated by Fenton-type reactions is a relatively powerful, safe and economical method for removing decay-resistant organic materials. In fact, for several decades, Fenton/Fenton-like reactions combined with UV or solar radiation have been widely employed to degrade pollutants such as trichloroethylene,¹⁶⁾ phenol,¹⁷⁾ trinitrotoluene,¹⁸⁾ pharmaceuticals in water,¹⁹⁾ pesticides,²⁰⁾ dioxin or dioxin-like pollutants,^{21,22)} as well as to decolorize aqueous pigments,²³⁾ and PCBs.^{13,24)} In most of these studies however, degradation was limited to low chlorine substituted biphenyls (degree of chlorination ≤ 4).

In this study, we employed a combination of the

*To whom correspondence should be addressed: Laboratory of Environmental Analysis, Osaka University of Pharmaceutical Sciences, 4-20-1 Nasahara, Takatsuki, Osaka 569-1094, Japan. Tel.: +81-72-690-1071; Fax: +81-72-690-1005; E-mail: mino@gly.oups.ac.jp

Fenton reaction and UV irradiation (UV-Fe²⁺/Fe³⁺-H₂O₂ system), and applied it to the degradation of PCBs present in electric insulating oil.

MATERIALS AND METHODS

Reagents— Mixtures of PCBs, Kanechlor (KC)-400 and 600, were purchased from GL Science Inc. (Tokyo, Japan) and diluted with *N,N'*-dimethylformamide to make a 0.1% (W/V) solution as a stock solution. Paraffin electric insulating oil was obtained from Cosmo Oil Lubricants Co., Ltd. (Tokyo, Japan). The stock solution of PCBs was diluted with pure insulating oil to make a standard 25 ppm solution of PCBs in insulating oil. The standard solution was used immediately after preparation. Standard 0.4M iron solutions were made by solubilization of solid FeCl₂, FeCl₃, Fe(ClO₄)₂, or Fe(ClO₄)₃ separately in distilled water and were used immediately after preparation. All other chemicals were reagent grade.

Procedures for PCBs Analysis— The reaction mixture was prepared by mixing the stock solution of PCBs, iron solution, and H₂O₂ solution in a 50-ml Erlenmeyer flask. The final volume of the reaction mixture was adjusted to 5 ml with water. The reaction mixture was incubated for 1–4 hr at 30–70°C and concentrations of iron and H₂O₂ were varied from 1 to 16 mM and 1–12%, respectively. The reaction was initiated by addition of the iron solution, then each reaction flask was capped with a silicon rubber stopper with a glass tube (5 × 350 mm) inserted in the stopper as a simple cooling device. The temperature was regulated by a water bath, and the pH of the reaction mixture was adjusted by addition of 1 M NaOH solution.

At the end of the reaction, the deep-red colored precipitates which formed were dissolved by the addition of 2 ml of 1 M HCl before 10 ml of *n*-hexane was added to the flask. After stirring for 5 min, the solution was poured into a funnel flask and the organic layer was separated. The water layer was extracted twice with *n*-hexane (10 ml). The combined organic layer was washed with aqueous saturated NaCl solution (25 ml), dried over anhydrous sodium sulfate, and evaporated to low volume by rotary evaporation at room temperature. The final volume of the solution was adjusted to 2 ml by flash evaporation under nitrogen gas before being used for GC-MS analysis.

Photolysis— Degradation of PCBs was conducted in a 50-ml beaker covered with a poly-chlorovinylidene wrap and irradiated using a handheld UV lamp (254 nm, 0.4 mW cm⁻²; 6 W 100 V, Funakoshi UVGL-58, Funakoshi Co. Ltd., Tokyo, Japan) 4–5 cm from the surface of the beaker. The energy of the UV light was measured with a high-resolution quantum radiometer (Model UVC-254, Sato Shouji Inc., Kawasaki, Japan). The wrap was replaced at hourly intervals. Except for UV irradiation, the reaction mixture was treated as described in "Procedure for PCBs analysis."

Degradation of PCBs in Insulating Oil— The reaction mixture (10 ml) containing PCBs (25 ppm), insulating oil (1 ml), 16 mM FeCl₃ or Fe (ClO₄)₃, and 6% H₂O₂ (as final concentration) in a 50-ml beaker with a wrap was irradiated using UV irradiation as described above. After treatment, *n*-hexane (20 ml) was added to the solution, and the mixture was stirred with a magnetic stirrer for 10 min. The solution was transferred to a funnel flask and the organic layer was separated and manipulated as described elsewhere (Ministry of Health, Labor and Welfare, Japan, July 3rd 1992). Briefly, to this solution, dimethyl sulfoxide (DMSO) saturated with *n*-hexane (25 ml) was added and the solution was shaken for 10 min. After extraction with DMSO (25 ml, three times), the combined DMSO fraction (100 ml) was washed with *n*-hexane (40 ml). The DMSO solution was then back-extracted with a mixture of *n*-hexane (75 ml) and *n*-hexane-washed water (100 ml) by shaking for 5 min, followed by removal of the *n*-hexane layer. The remaining DMSO layer was then extracted twice with *n*-hexane (75 ml). The combined *n*-hexane layers were washed with 2 M KOH (20 ml) and water (20 ml × 2), dried over anhydrous sodium sulfate, and evaporated to 1.0 ml under reduced pressure. This solution was diluted with *n*-hexane (100 ml) and transferred to a funnel flask where the *n*-hexane layer was treated at least three times with 30–40 ml of *c*-H₂SO₄ until the elimination of color in the sulfuric acid layer. After this treatment, the *n*-hexane layer was washed with *n*-hexane-washed water, adjusted to pH 4–5, dried over anhydrous sodium sulfate, and concentrated to 2 ml. This solution was subjected to silica gel chromatography (10 × 300 mm, Wakogel C-200, Wako Pure Chemical Industries, Ltd., Osaka, Japan) and PCB fractions were eluted with *n*-hexane (25 ml). The *n*-hexane recovered was concentrated to 2.0 ml and PCBs in the solution were analyzed by GC-MS.

Table 1. Effect of Fe³⁺ and H₂O₂ Concentration on PCB Degradation

Reagent	Concentration		PCBs Degradation (%)			
	Fe ³⁺ (mM)	H ₂ O ₂ (%)	5Cl-PCB	6Cl-PCB	7Cl-PCB	8Cl-PCB
FeCl ₃	4	1	25	15	0	0
	4	4	29	12	0	0
	4	8	30	13	3	0
	4	12	43	26	15	19
FeCl ₃	8	1	41	18	0	0
	8	4	55	30	5	5
	8	8	45	50	23	20
	8	12	70	55	16	19
FeCl ₃	16	1	39	17	10	8
	16	4	50	36	27	19
	16	8	55	55	30	21
	16	12	80	70	54	60
Fe(ClO ₄) ₃	16	1	47	39	29	18
	16	4	64	50	45	33
	16	8	69	58	46	38
	16	12	84	75	54	55

Conditions; PCBs: 5 ppm, [Fe³⁺]: 4–16 mM, H₂O₂: 1–12%, pH ≈ 2, 70°C, 1 hr.

PCB Analysis by GC-MS— Analysis of PCBs was carried out on a Hitachi 3DQS mass spectrometer M-9000 (Hitachi, Ltd., Tokyo, Japan) coupled to a Hitachi gas chromatograph G-7000. Helium was used as a carrier gas at a flow rate of 1.5 ml/min with a split ratio of 1/50. The injector and transfer line temperatures were set to 280°C. An SGE capillary column forte HT8-PCB 50 m × 0.22 mm, 0.25 μm (SGE Analytical Science, Pty. Ltd., Ringwood, VIC, Australia) was used with a temperature profile of 80°C (2 min hold) to 170°C at a rate of 30°C/min to 299°C (5 min hold) at a rate of 3°C/min.

Identification of PCB peaks was performed according to the method of Matsumura *et al.*²⁵⁾ and quantitative analysis was carried out by measurement of peak areas in the selective ion monitoring (SIM).²⁴⁾ Duplicate measurements were performed and an average value was calculated. For estimating the degradation rates of di- to octa-chlorinated PCBs, peak areas of corresponding components in KC-400/600 solutions [2Cl: 4, 5, 8 (IUPAC No.); 3Cl: 18, 28, 31; 4Cl: 52, 69, 70; 5Cl: 101, 110, 120; 6Cl: 132, 139, 149; 7Cl: 174, 180, 182; 8Cl: 196, 199, 203] were also calibrated in duplicate.

RESULTS AND DISCUSSION

Degradation of PCBs by the Fe³⁺-H₂O₂ System

The effects of reagent concentration on PCB degradation by the present Fenton reactions for 1 hr

at pH 2 and 70°C are shown in Table 1. Since lower ratios of Fenton reagents (iron ion/hydrogen peroxide) have been reported to be important for degradation,^{26,27)} concentration ratios of 1/1–1/3 for Fe³⁺ (4–16 mM)/H₂O₂ (1–12%) were examined. However, the results did not reveal a clear relationship of the Fenton ratio, but rather indicated the reagent concentration dependence. However, at concentrations higher than 16 mM, the reaction proceeded too rapidly to control and loss of PCBs might occur due to generation of gas by H₂O₂. Consequently, the concentration of ferric ion and H₂O₂ for degradation of PCBs was fixed at 16 mM and 12%, respectively. Also, the results showed that Fe(ClO₄)₃ was slightly superior to FeCl₃ as a ferric ion source for the degradation of PCBs.

Next, we analyzed the effect of temperature (30–70°C) on degradation of PCBs. As shown in Fig. 1, the effect of temperature on PCB degradation revealed a negative relationship between the degree of chlorination and decomposition rate as reported by Pignatello and Chapa.²⁴⁾ At 30°C, PCBs having up to 3 degrees of chlorination were successfully decomposed (up to 80%). As the reaction temperature increased, decomposition of PCBs having higher degrees of chlorination also progressed. Taken together, these findings suggest that temperature is an important factor affecting decomposition by the Fe³⁺ (or Fe²⁺)-H₂O₂ system, which is in accordance with previous studies on dioxin²¹⁾ and pesticides.^{28,29)}

The pH of the reaction solution is one of the

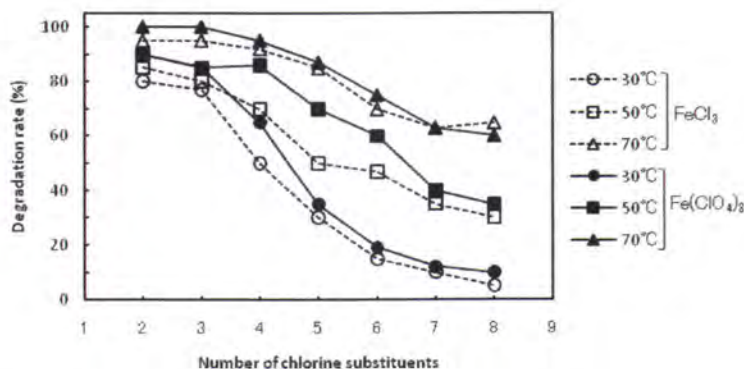


Fig. 1. Effect of Temperature on PCB Degradation

Conditions; PCBs: 5 ppm, $[\text{Fe}^{3+}]$: 16 mM, H_2O_2 : 12%, $\text{pH} \approx 2$, 30–70°C, 1 hr FeCl_3 or $\text{Fe}(\text{ClO}_4)_3$ was used as an iron compound.

most important factors for degradation activity in this reaction system.²¹ The relationship between pH and degradation activity was also investigated. When iron compounds were dissolved in water, the pH of the solution decreased to approximately pH 2, with a slight decrease in pH being observed by the addition of H_2O_2 . For this solution (pH 2.0), strongest activity (degradation rates of > 90% per 1 hr and 70°C for PCBs having 3 degrees of chlorination) was observed, and a clear decrease in activity was seen for pH near 6 or 10 (up to 10%). In fact, a preference for acidic conditions (pH 2.0–2.8) was reported previously.^{23, 30} The reaction in the present Fe^{3+} - H_2O_2 system could therefore be conducted under acidic conditions without any pH adjustment. The reaction at a low pH of 2.0 appeared to be optimal for the degradation of PCBs and we therefore selected pH 2.0 for subsequent experiments.

Degradation of PCBs by the UV- $\text{Fe}^{2+}/\text{Fe}^{3+}$ - H_2O_2 System

The effect of UV irradiation on the degradation of PCBs was analyzed by comparing degradation rates with and without UV irradiation. Irradiation with UV light at 254 nm and 0.4 mW cm^{-2} significantly improved the degradation of PCBs after reaction for 2 hr (Fig. 2). Under this condition, biphenyls having a high number of chlorines (7–8), which are difficult to degrade without UV irradiation, were decomposed at rates exceeding 90% when $\text{Fe}(\text{ClO}_4)_3$ was used as an iron compound. The combined use of UV with the Fenton/Fenton-like system has previously been reported to accelerate the generation of $\cdot\text{OH}$.^{31, 32} The main reason for the improved degradation rate with UV irradiation is attributed to this induction of radical formation and dechlorination by UV.¹⁰

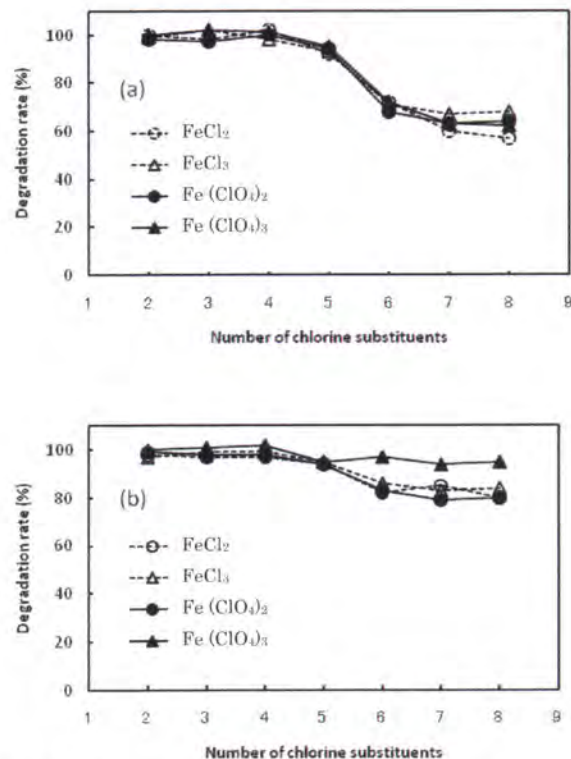


Fig. 2. PCB Degradation under Combined UV Illumination Regimes

(a): Without UV, (b): with UV.

Both iron chloride and iron perchlorate were usable as iron compounds, although the perchlorates were slightly superior to the chlorides for PCBs degradation. No noticeable difference was observed between Fe^{2+} and Fe^{3+} , which suggests the occurrence of not only the classic Fenton reaction catalyzed by Fe^{2+} , but also the reaction in which Fe^{3+} was reduced to Fe^{2+} by perhydroxyl radical ($\text{HO}_2\cdot$) generated from hydrogen peroxide by the Haber-Weiss reaction.³³

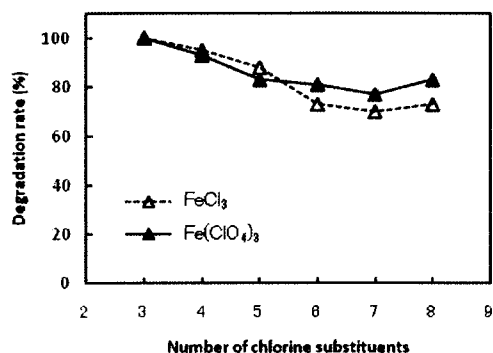


Fig. 3. Degradation of PCBs in Insulating Oil

Conditions; PCBs: 25 ppm, $[\text{Fe}^{2+}/\text{Fe}^{3+}]$: 16 mM, H_2O_2 : 6%, UV intensity $\approx 0.4 \text{ mW cm}^{-2}$, pH ≈ 2 , 50°C , 8 hr, 0.4 ml of 0.4 M iron solution $\times 7$, 2 ml of 30% $\text{H}_2\text{O}_2 \times 15$.

Degradation of Small Amounts of PCBs Contained in Electric Insulating Oil by the UV- $\text{Fe}^{2+}/\text{Fe}^{3+}$ - H_2O_2 System

Figure 3 shows degradation rates of PCBs when the developed UV- $\text{Fe}^{2+}/\text{Fe}^{3+}$ - H_2O_2 system was applied to PCB-polluted paraffin electric insulating oil. The result clearly indicates the efficacy of this chemical method for degrading PCBs in the oil. The rate of PCB degradation in the electric insulating oil was lower than that observed for pure PCBs, particularly in biphenyls having 6–8 chlorine substituents. However, 3–5 chlorine substituted biphenyls were efficiently decomposed to levels exceeding 85% after 8 hr.

Further study might be needed to conduct complete decomposition of PCBs having higher numbers of chlorine substitutions. To elucidate the degradation mechanism of PCBs in this system, GC-MS detection of the intermediates from PCBs in the degradation reaction would be indispensable.

In conclusion, this report demonstrated the application of an improved Fenton reaction for degrading PCBs by combining the $\text{Fe}^{2+}/\text{Fe}^{3+}$ - H_2O_2 system with UV irradiation. Under optimal conditions [16 mM $\text{Fe}^{2+}/\text{Fe}^{3+}$, 12% H_2O_2 , 70°C , 2 hr stirring/reaction, iron ion addition every 1 hr and H_2O_2 every 30 min, and UV irradiation (254 nm, 0.4 mW cm^{-2})], PCBs having low (Cl: 2–5) and high (Cl: 6–8) numbers of chlorine substituents were either decomposed completely or to levels exceeding 90%, respectively. When this system was applied to PCBs in insulating oil, about 80% of PCBs were successfully degraded, even for PCBs having high chlorine substitutions. The main features of our highly effective degradation method are that the reagents are inexpensive and that secondary

environmental pollution is negligible, since H_2O_2 will spontaneously decay into oxygen and water. In addition, the time required for treatments is short. This chemical degradation method using the UV- $\text{Fe}^{2+}/\text{Fe}^{3+}$ - H_2O_2 system has the potential to be applied as a new tool for removing persistent organic pollutants, such as PCBs in electric insulating oil.

Acknowledgement This work was supported in part by a Grant-in-Aid for Scientific Research from the Ministry of Education, Culture, Sports, Science and Technology of Japan.

REFERENCES

- 1) Arensdorf, J. J. and Focht, D. D. (1994) Formation of chlorocatechol meta cleavage products by a pseudomonad during metabolism of monochlorobiphenyls. *Appl. Environ. Microbiol.*, **60**, 2884–2889.
- 2) Seto, M., Kimbara, K., Shimura, M., Hatta, T., Fukuda, M. and Yano, K. (1995) A novel transformation of polychlorinated biphenyls by *Rhodococcus* sp. strain RHA1. *Appl. Environ. Microbiol.*, **61**, 3353–3358.
- 3) Noma, Y., Mitsuhashi, Y., Matsuyama, K. and Sakai, S. (2007) Pathways and products of the degradation of PCBs by the sodium dispersion method. *Chemosphere*, **68**, 871–879.
- 4) Rodrigues, J. L., Maltseva, O. V., Tsoi, T. V., Helton, R. R., Quensen, J. F., Fukuda, M. and Tiedje, J. M. (2001) Development of a *Rhodococcus* recombinant strain for degradation of products from anaerobic dechlorination of PCBs. *Environ. Sci. Technol.*, **35**, 663–668.
- 5) Fuse, H., Takimura, O., Murakami, K., Inoue, H. and Yamaoka, Y. (2003) Degradation of chlorinated biphenyl, dibenzofuran, and dibenzo-*p*-dioxin by marine bacteria that degrade biphenyl, carbazole, or dibenzofuran. *Biosci. Biotechnol. Biochem.*, **67**, 1121–1125.
- 6) Sietmann, R., Gesell, M., Hammer, E. and Schauer, F. (2006) Oxidative ring cleavage of low chlorinated biphenyl derivatives by fungi leads to the formation of chlorinated lactone derivatives. *Chemosphere*, **64**, 672–685.
- 7) Huang, I. W., Hong, C. S. and Bush, B. (1996) Photocatalytic degradation of PCBs in TiO_2 aqueous suspensions. *Chemosphere*, **32**, 1869–1881.
- 8) Vollmuth, S. and Niessner, R. (1995) Degradation of PCDD, PCDF, PAH, PCB and chlorinated phenols during the destruction-treatment of landfill seepage

- water in laboratory model reactor (UV, ozone, and UV/ozone). *Chemosphere*, **30**, 2317–2331.
- 9) Zhang, G. and Hua, I. (2000) Cavitation chemistry of polychlorinated biphenyls: Decomposition mechanisms and rates. *Environ. Sci. Technol.*, **34**, 1529–1534.
 - 10) Chang, F. C., Chiu, T. C., Yen, J. H. and Wang, Y. S. (2003) Dechlorination pathways of *ortho*-substituted PCBs by UV irradiation in *n*-hexane and their correlation to the charge distribution on carbon atom. *Chemosphere*, **51**, 775–784.
 - 11) Kume, A., Monguchi, Y., Hattori, K., Nagase, H. and Sajiki, H. (2008) Pd/C-catalyzed practical degradation of PCBs at room temperature. *Appl. Catal.*, **B 81**, 274–282.
 - 12) Liu, X. and Yu, G. (2006) Combined effect of microwave and activated carbon on the remediation of polychlorinated biphenyl-contaminated soil. *Chemosphere*, **63**, 228–235.
 - 13) Dercova, K., Vrana, B., Tandlich, R. and Subova, L. U. (1999) Fenton's type reaction and chemical pretreatment of PCBs. *Chemosphere*, **39**, 2621–2628.
 - 14) Jones, C. G., Silverman, J., Al-Sheikhly, M., Neta, P. and Poster, D. L. (2003) Dechlorination of polychlorinated biphenyls in industrial transformer oil by radiolytic and photolytic methods. *Environ. Sci. Technol.*, **37**, 5773–5777.
 - 15) Wu, W., Xu, J., Zhao, H., Zhang, Q. and Liao, S. (2005) A practical approach to the degradation of polychlorinated biphenyls in transformer oil. *Chemosphere*, **60**, 944–950.
 - 16) Li, K., Stefan, M. I. and Crittenden, J. C. (2004) UV photolysis of trichloroethylene: product study and kinetic modeling. *Environ. Sci. Technol.*, **38**, 6685–6693.
 - 17) Kavitha, V. and Palanivelu, K. (2004) The role of ferrous ion in Fenton and photo-Fenton processes for the degradation of phenol. *Chemosphere*, **55**, 1235–1243.
 - 18) Liou, M. J., Lu, M. C. and Chen, J. N. (2004) Oxidation of TNT by photo-Fenton process. *Chemosphere*, **57**, 1107–1114.
 - 19) Perez-Estrada, L. A., Malato, S., Gernjak, W., Aguera, A., Thurman, E. M., Ferrer, I. and Fernandez-Alba, A. R. (2005) Photo-Fenton degradation of diclofenac: identification of main intermediates and degradation pathway. *Environ. Sci. Technol.*, **39**, 8300–8306.
 - 20) Pignatello, J. J. (1992) Dark and photoassisted Fe³⁺-catalyzed degradation of chlorophenoxy herbicides by hydrogen peroxide. *Environ. Sci. Technol.*, **26**, 944–951.
 - 21) Mino, Y., Moriyama, Y. and Nakatake, Y. (2004) Degradation of 2,7-dichlorodibenzo-*p*-dioxin by Fe³⁺-H₂O₂ mixed reagent. *Chemosphere*, **57**, 365–372.
 - 22) Katsumata, H., Kaneco, S., Suzuki, T., Ohta, K. and Yobiko, Y. (2006) Degradation of polychlorinated dibenzo-*p*-dioxins in aqueous solution by Fe(II)/H₂O₂/UV system. *Chemosphere*, **63**, 592–599.
 - 23) Hsueh, C. L., Huang, Y. H., Wang, C. C. and Chen, C. Y. (2005) Degradation of azo dyes using low iron concentration of Fenton and Fenton-like system. *Chemosphere*, **58**, 1409–1414.
 - 24) Pignatello, J. J. and Chapa, G. (1994) Degradation in PCBs by ferric ion, hydrogen peroxide and UV light. *Environ. Toxicol. Chem.*, **13**, 423–427.
 - 25) Matsumura, C., Tsurukawa, M., Nakano, T., Ezaki, T. and Ohashi, M. (2002) Elution orders of all 209 PCBs congeners on capillary column "HT8-PCB." *Kankyo Kagaku*, **12**, 855–865.
 - 26) Chan, K. H. and Chu, W. (2003) Modeling the reaction kinetics of Fenton's process on the removal of atrazine. *Chemosphere*, **51**, 305–311.
 - 27) Chu, W., Chan, K. H., Kwan, C. Y. and Lee, C. K. (2004) The system design of UV-assisted catalytic oxidation process—degradation of 2,4-D. *Chemosphere*, **57**, 171–178.
 - 28) Liou, R. M., Chen, S. H., Hung, M. Y. and Hsu, C. S. (2004) Catalytic oxidation of pentachlorophenol in contaminated soil suspensions by Fe³⁺-resin/H₂O₂. *Chemosphere*, **55**, 1271–1280.
 - 29) Lopez, A., Mascolo, G., Detomaso, A., Lovecchio, G. and Villani, G. (2005) Temperature activated degradation (mineralization) of 4-chloro-3-methyl phenol by Fenton's reagent. *Chemosphere*, **59**, 397–403.
 - 30) Chu, W., Kwan, C. Y., Chan, K. H. and Chong, C. (2004) An unconventional approach to studying the reaction kinetics of the Fenton's oxidation of 2,4-dichlorophenoxyacetic acid. *Chemosphere*, **57**, 1165–1171.
 - 31) Lee, C. and Yoon, J. (2004) Temperature dependence of hydroxyl radical formation in the *hv*/Fe³⁺/H₂O₂ and Fe³⁺/H₂O₂ systems. *Chemosphere*, **56**, 923–934.
 - 32) Kusic, H., Koprivanac, N., Bozic, A. L. and Selanec, I. (2006) Photo-assisted Fenton type processes for the degradation of phenol: a kinetic study. *J. Hazard. Mater.*, **136**, 632–644.
 - 33) Motohashi, N. and Mori, I. (1983) Superoxide-dependent formation of hydroxyl radical catalyzed by transferrin. *FEBS Lett.*, **157**, 197–199.

研究論文

硫酸を用いた低温・低 pH 条件における UV-Fe²⁺/Fe³⁺-H₂O₂系による PCBs の化学分解

東 剛志*, 三野 芳紀**
(2010年5月25日受付, 2011年1月17日受理)

Chemical Degradation of PCBs by UV-(H₂SO₄)-Fe²⁺/Fe³⁺-H₂O₂ System under Low Temperature and pH Conditions

Takashi AZUMA*, Yoshiki MINO**

Fenton's reaction using UV-FeSO₄/Fe₂(SO₄)₃-H₂O₂ system was applied to degrade PCBs congeners, Kanechlor (KC)-400/600, at 30°C for 4 hours under adjustment of pH with sulfuric acid to 0.1, more than 80% of degradation rate could be achieved for PCBs having degree of chlorination of 2-4. When this reaction system was applied to PCBs polluted insulating oil, 48-58% of degradation was obtained for PCBs having degree of chlorination of 3 and 6-8, although the corresponding values were relatively low in the case of PCBs having degree of chlorination of 4-5. In order to attain high degradation rate, concentration of Iron ion has to be much higher (480-800 mM) than the usual Fenton's reaction (16 mM).

Key words: chemical degradation, polychlorinated biphenyls, Fenton's reaction, low temperature and pH

1. はじめに

鉄イオンを触媒として過酸化水素が分解されることによって酸化力の非常に強い活性酸素類を発生させる反応はフェントン反応として知られており¹⁾, 有害汚染物質分解の見地から多くの研究がなされている^{2,3)}。難分解性で有害な残留性有機汚染物質であるポリ塩化ビフェニル (Polychlorinated biphenyls: PCBs) に対しても、塩素置換数が低い PCBs (Cl ≤ 4) についてフェントン反応の適用が試みられている⁴⁾。その過程で、フェントン反応は pH 依存性が高いことが判明し、従来反応 pH として 2 ~ 3 付近の酸性条件が最適とされ^{3,5)}、極端な低 pH 条件下では過酸化水素が安定であるためフェントン反応がほとんど起こらないとされてきた⁶⁾。そのため、フェントン反応の持続的な進行には pH の調整が必要となっている。また、共存するイオンによる鉄化合物の形成⁷⁾、スカベンジ作用⁸⁾、有害な塩素化合物の副生⁹⁾等を考慮することも肝要であり、反応の維持に注意を払うことが必要である。また、多くの場合反応の進行に伴って未反応の PCBs を巻き込みながら赤褐色の鉄スラッジを形成するため、定量的な反応が阻害される傾向が認められている^{5,10)}。

さらに、フェントン反応の温度依存性についても研究がなされており、一般的に 70°C で 20 時間程度の加熱反応が用いられているが¹¹⁻¹³⁾、このような温度では水分の蒸発による濃度変化を避けるために冷却管を取り付ける必要があり、反応促進のために紫外線を反応液に直接照射することが困難となる弊害があった。また、低塩素置換 (Cl ≤ 4) ビフェニルでは揮発性が高く、回収率が低下することが報告されている¹⁴⁾ため、反応温度を低く抑えることが望まれる。

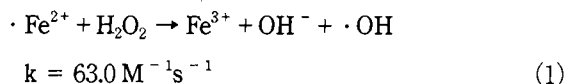
しかしながら、著者らがフェントン反応を用いて PCBs の分解を試みる研究の過程で、硫酸を用いて pH を 0.1 以下に調整し、従来よりも高濃度のフェントン試薬濃度を用いると、反応中に沈殿が発生せず、低温・低 pH 条件下において PCBs の分解が進行することが示唆された¹⁵⁾。硫酸を用いた低温・低 pH 条件における UV-Fe²⁺/Fe³⁺-H₂O₂系を分解反応として用いることには幾つかの優れた利点がある。まず 1 つ目には、最適 pH を維持するための煩雑な pH 調整を必要とせず、簡便に反応を行うことができる。2 つ目には、低 pH 条件下では反応後有色沈殿を生じないので、沈殿溶解の有無の影響を考慮する必要が無く、反応後速やかに抽出操作を行うことが可能となり、実験

操作がより簡便になる利点がある。3つ目には、鉄イオンと過酸化水素の系ではラジカル反応が関与するため、塩化物イオンを含む条件では副生成物として有害な化合物を経由する可能性があるが⁹⁾、硫酸イオンの系ではこれらの危険性の影響を軽減することができる。4つ目は、低温で分解反応を行うため、PCBs中の揮発しやすい成分のロスを低減することができる。さらに、不揮発性の硫酸を用いていることから、反応溶液自体の揮発もより少なくできる利点がある。温度を高く設定して分解反応を行う際には、安全面からより性能の高い恒温装置の併用や、発生する気体を活性炭フィルターを通して排出させる等の対策が必要となるため、安全性の面からも有利であると考えられる。このように、フェントン反応を用いたより簡便で制御がしやすい条件でかつ効果の高いPCBsの分解方法が開発出来る可能性が見出された。

そこで、本研究ではまず硫酸を用いて反応pHを0.1に調整した反応条件下で、温度・鉄イオン触媒の濃度が過酸化水素の分解に及ぼす影響について検討した。次に、この分解系の有効性を様々な塩素置換ビフェニルの同位体を含むカネクロール (Kanechlor) KC-400及び600を用いて評価した。さらに、鉱油系電気絶縁油中に微量混入したPCBsの分解についてその適用を試みた。

2. フェントン反応のメカニズム

Fe^{2+} と過酸化水素から強い酸化力を持つ活性酸素の1つである $\cdot\text{OH}$ を発生させるFenton反応は、Fentonによって1876年に発見され、その後その反応メカニズムの解明とその利用について膨大な研究がなされてきた¹⁶⁾。古典的なフェントン反応は以下の反応式(1)で表される¹⁷⁾。



この反応によって生じたラジカル種は、殆ど全ての化合物と反応する複雑なラジカル連鎖反応を引き起こす¹⁸⁾。一方で、 Fe^{3+} は過酸化水素又は発生したラジカル種により Fe^{2+} へと還元され、連鎖反応が進行する¹⁸⁻²³⁾。 $\cdot\text{OH}$ の酸化力は極めて強く(酸化還元電位 2.38 E° (25°C)/ $V^{24)$)、反応は瞬時に起こり、生成物を生じる²⁵⁾。

本実験では、鉄イオンの供給源として次の分析方法

において述べるように、硫酸鉄(II)及び硫酸鉄(III)を利用する。 HSO_4^- イオン及び SO_4^{2-} イオンは従来型のフェントン反応条件(pH 2~3)下では鉄イオンと化合物(硫酸鉄(II)及びIII))を生成しやすい⁷⁾。しかし、本研究では低pH条件(pH 0.1)下で反応を行うため、これらの塩は溶解し、反応中に鉄スラッジの生成が抑制される利点がある。

3. 実験方法

3.1 PCBsの分解反応

PCBsの分解反応操作は、ダイオキシンの一部(2,7-dichloro dibenzo-*p*-dioxin)についての三野らによる研究²⁶⁾を参考にした。簡単な冷却装置としてシリコン栓にガラス管(5 mm × 35 cm)を付けた50 mLのマイヤーラスコ中に、カネクロール KC-400 及び 600 を *N,N*-dimethylformamide (DMF) に溶解させた PCBs 0.1% (w/v) 溶液をそれぞれ 25 μL ずつ入れ、次いで pH 調整を行った水を加え、鉄イオン溶液(硫酸鉄(II)又は硫酸鉄(III)水溶液)を鉄イオン濃度が 16 ~ 1600 mM となるように加えた後、最後に過酸化水素を 12% (v/v) となるように加え¹³⁾ 分解反応を開始させた。反応液の体積は合計 5 mL となるように水を添加して調整した。反応温度(30 ~ 70 $^\circ\text{C}$)の調節は温浴で行い、温浴の下から攪拌力の強いマグネティックスターラーで攪拌を行った。pHの調整には硫酸又は水酸化ナトリウム水溶液を用いた。

反応終了後、反応溶液を分液ロートに移し、*n*-ヘキサン 10 mL を加えて 5 分間攪拌し、上層の有機層を分取した。この抽出操作を 3 度行った。得られた *n*-ヘキサン 30 mL を飽和食塩水 25 mL で洗浄し、無水硫酸ナトリウム 3 g で脱水した後に減圧下ロータリーエバポレーターで少量まで濃縮し、さらに窒素ガスの吹き付けにより 2 mL に濃縮した後 GC-MS 分析した。

3.2 紫外線の照射

紫外線(UV)の照射を併用したPCBs分解には、ポリクロロビニリデン製のラップを50 mLのピーカーに装着したものを用いた。UV光源にはフナコシ(株)のUVGL-58 6W 100V Handheld UV lampを用いた。UV照射の強度は佐藤(株)の高分解能 Quantum Radiometer (Model UVC-254)を用いて測定し、約0.4

mW/cm²の強さで照射し、波長は254 nmでピーカーの底から4~5 cmの高さから照射を行った。この時ラップが紫外線により劣化して紫外線を通さなくなるので、1時間おきに新しいラップに張り替えた。

3.3 絶縁油中に含まれる PCBs の分解

上記した50 mLのピーカー中の電気絶縁油1 mL (PCBsを25 ppm (mg/L)の濃度で含む)に対して、鉄イオン溶液(硫酸鉄(III):最終鉄イオン濃度800 mM)を加え、pHを硫酸で0.1に調整した後、過酸化水素を12% (v/v)となるように添加して反応を開始した。反応温度は50℃とし、8時間反応させた。紫外線の照射はカネクロールの場合と同様に約0.4 mW/cm²の強度でピーカーの底から4~5 cmの高さから照射を行った。反応終了後、*n*-ヘキサン(20 mL)を加え10分間、2度抽出を行った。攪拌後溶液を分液ロートに移し有機層を別の分液ロートに分取した後、以下に示す厚生省告示の方法(特別管理一般廃棄物及び特別管理産業廃棄物に係る基準の検定方法、厚生省告示第192号別表第3の第1:洗浄液試験法)²⁷⁾に従って抽出操作を行った。

抽出した有機溶媒に*n*-ヘキサンで飽和したdimethylsulfoxide (DMSO) (25 mL)を加え、4度抽出を行い、合計100 mLのDMSOを*n*-ヘキサン(40 mL)で洗浄した。DMSO層は*n*-ヘキサン(75 mL)と*n*-ヘキサン飽和水(分液ロートに*n*-ヘキサンと蒸留水を加え10分間攪拌し、水層を分取したもの:100 mL)を加えて5分間攪拌して逆抽出を行い、*n*-ヘキサン層を分取した。DMSO層はさらに*n*-ヘキサン(75 mL)で2度抽出を行い*n*-ヘキサン層を合わせ、この溶液を2M KOH (20 mL)で洗浄した後、水(20 mL)で二度洗浄し、無水硫酸ナトリウムで脱水後、室温下ロータリーエバポレーターで1 mLまで濃縮した。この溶液を*n*-ヘキサンで希釈し(100 mL)、新しい分液ロートに移し、*n*-ヘキサン層を濃硫酸30~40 mLで硫酸層が着色しなくなるまで少なくとも3度洗浄し、*n*-ヘキサン飽和水でpHが4~5になるまで洗浄し、無水硫酸ナトリウムで脱水後、減圧下ロータリーエバポレーターで少量まで濃縮し、さらに窒素ガスの吹き付けにより2 mLに濃縮した。この溶液をシリカゲルカラム(10 mm × 300 mm, Wakogel C-200)にチャージし、

n-ヘキサン(25 mL)で溶出させ、2.0 mLまで濃縮した後GC-MS分析した。

3.4 PCBs の分析

PCBsの分析は、ガスクロマトグラフG-7000に3DQS質量分析機M-9000を装着したGC-MS(日立ハイテック(株))を用いて行った。ヘリウムガス流量は1.5 mL/min、インジェクターとトランスファーラインの温度を共に280℃、スプリット比を1/50に設定した。キャピラリーカラムにはSGE Analytical Science Pty. Ltd製のHT8-PCB(50 m × 0.22 mm × 0.25 μm)を用い、カラム温度は80℃で2分間保持後、30℃/minで170℃まで昇温し、さらに3℃/minで299℃とし、この温度で5分間保持する昇温プログラムにより変化させた。

PCBsのピークの同定はMatsumura等の報告²⁸⁾に従って行い、定量分析はTICモードで行った。得られたPCBsの各ピークの同定とその構造決定は、松村らが報告したHT8-PCBキャピラリーカラムを用いて測定したPCB全異性体209種の溶出順序に従って行った。分解率の算出には分解処理を行ったサンプルと、分解処理を行わずに抽出操作を行うコントロール間での濃度差を基準に算出した。分解率の算出に用いるPCBs化合物の種類に関しては、実験で用いたカネクロールKC-400及び600中に含まれる各塩化物毎に最も大きく検出される代表的なピーク(2Cl: #4/#5/#8, 3Cl: #18/#28/#31, 4Cl: #52/#69/#70, 5Cl: #101/#110/#120, 6Cl: #132/#139/#149, 7Cl: #174/#180/#182, 8Cl: #196/#199/#203)を用い、1サンプルにつき2度測定し、ピーク高さ平均を用いて計算を行った。PCBsに含まれる各塩素化合物の分解率の再現性は、2Cl, 3Cl, 4Cl, 5Cl, 6Cl, 7Cl及び8Clで各々±0.5%, 0.3%, 4.4%, 4.1%, 5.7%, 4.5%及び11.1%以下であった。

3.5 過酸化水素濃度の分析

過酸化水素の濃度は、各サンプルについて硫酸酸性条件下で過マンガン酸カリウムによる滴定により定量した。

4. 結果及び考察

図1に低pH条件下における、過酸化水素分解の鉄

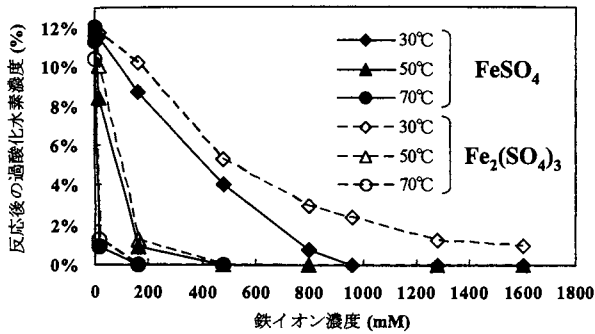


図1 低 pH 条件下における鉄イオン触媒存在下での過酸化水素の分解
(過酸化水素初期濃度：12%，温度：30℃，50℃，70℃，反応時間：1時間，pH：0.1)

イオン触媒濃度依存性を示す。70℃では 16 mM の鉄イオン触媒により 1 時間で過酸化水素の大部分が分解され、50℃では 200 mM 以上の鉄イオン触媒により過酸化水素が急速に分解されたが、30℃の条件では過剰量の鉄イオン触媒 (800 mM 以上) を加えない限り過酸化水素は低 pH 条件下では安定で分解されなかった。30℃の条件下では、硫酸鉄 (II) の方が硫酸鉄 (III) の場合よりも過酸化水素の分解率が高かった。しかし、他の温度では硫酸鉄 (II) と硫酸鉄 (III) の間で過酸化水素の分解率に殆ど変化が認められなかった。これは、30℃以下の低温度では Fe^{2+} は Fe^{3+} よりもはるかに速く過酸化水素と反応する (Fe^{2+} : $k = 63.0 (M^{-1}s^{-1})$, Fe^{3+} : $k = 1.0 \times 10^{-2} (M^{-1}s^{-1})$)^{18,23)} ことが関係していると考えられた。また、鉄 (III) イオンを触媒とした場合には、ハーバーワイス反応²⁹⁾ による過酸化水素の分解が起こるとされているが、この反応と比較して、鉄 (II) イオンが関係する古典的なフェントン反応による過酸化水素の分解の方が反応速度論的に早く起こったものと考えられる。以上の結果から、本研究で用いた条件下で PCBs の分解を進行させるためには、鉄イオンの濃度を従来のフェントン反応で用いている濃度 (16 mM) より遥かに高濃度とする必要があることが明らかとなった。

次に、鉄イオン触媒が存在しない条件下で pH を 0.1, 4.5 及び 10 と変化させるとともに、温度を 30℃, 50℃ 及び 70℃ の範囲で変化させて過酸化水素の安定性を分析した結果を図 2 に示す。低 pH 条件下では 70℃ の条件下でも過酸化水素は殆ど分解されなかったが、高 pH 条件下では 30℃ においても過酸化水素の大部分が分解されることが明らかとなった。

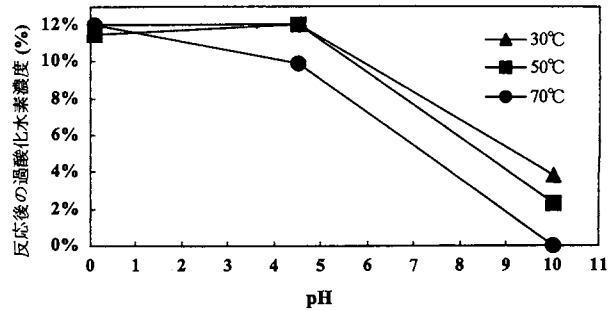


図2 低 pH 条件下、各温度下による過酸化水素の安定性
(鉄イオン触媒非存在下、過酸化水素初期濃度：12%，反応時間：1時間，温度：30℃，50℃，70℃，pH：0.1, 4.5, 10)

表1 低 pH 条件下で UV 照射を併用した場合の過酸化水素の安定性

鉄イオン濃度	pH	温度 (℃)	過酸化水素初期濃度 (%)	反応後残存濃度 (%)	過酸化水素分解率 (%)
16 mM	0.1	30	12.0	11.0	8.3
16 mM	0.1	70	12.0	10.5	12.5

さらに、pH 0.1 の条件下で UV の照射 (波長 254 nm) を併用し、温度を 30℃ 及び 70℃ で 1 時間反応させ、過酸化水素の分解率を分析した結果を表 1 に示す。30℃ では UV 照射により過酸化水素分解が促進される作用は殆ど認められず、温度を 70℃ まで上昇しても濃度はほとんど変化しなかった。

これらの結果から、過酸化水素は低 pH 条件下で温度の上昇や UV 照射に対しては安定であるが、高濃度の鉄イオン触媒の存在により速やかに分解されると結論された。

鉄イオンと過酸化水素を用いたフェントン反応の開始には過酸化水素の分解が必須であり、過酸化水素の分解速度が分解対象物質の分解速度に大きく関係しているため、過酸化水素の分解条件下で PCBs の分解が進行することを検証することは重要であると考えられる。図 3 に硫酸を用いた低温・低 pH 条件下における $Fe^{2+}/Fe^{3+}-H_2O_2$ 系を用いた各塩素置換ジフェニルの分解率に対する pH の影響について示す。pH 2 以下の酸性条件下で PCBs は良好に分解され、pH 0.1 においても PCBs は良好に分解されていた。PCBs の分解率の傾向として、PCBs の塩素置換数が上昇するに従って分解率が減少する傾向がみられた。一方、pH 3 以上では分解率は大きく減少した。この pH 3 で分解率が低下する原因については、pH 3 付近では反応に伴う

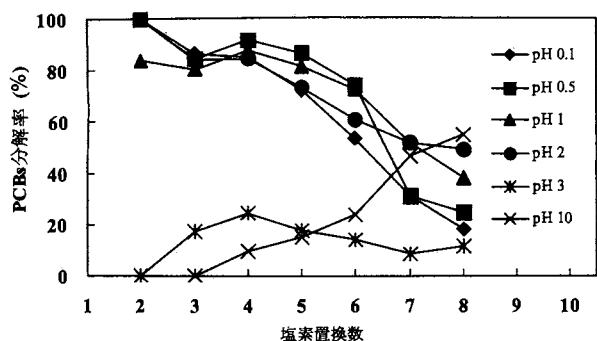


図3 各塩素置換ビフェニルの分解率に対する pH の影響 (鉄イオン濃度: 16 mM, 過酸化水素初期濃度: 12%, 温度: 70°C, 反応時間: 1 時間)

過酸化水素の消費に伴い、反応中に pH ジャンプが起こり、中性付近まで pH が上昇することに原因があると考えられた。

pH が比較的高い領域では多塩素置換ビフェニルが減少する傾向が認められた。この理由については、PCBs や PCDDs 等の塩素置換数が多い化合物をアルカリ条件で処理する際には、温和な条件で処理を行わない限り脱塩素化により多塩素置換ビフェニル ($Cl \geq 8$) の回収率が極端に低下するとの報告があり、本実験でもこの予期せぬ脱塩素化反応が起こっている可能性³⁰⁾ が考えられる。そのため、アルカリ条件下での PCBs 分解反応は望ましくないと考えられた。以上の結果から、非常に低い pH においても PCBs が分解できることが明らかとなった。

図 4 (a, b) に低 pH (0.1), 30°C の低温度下で UV 照射を併用して PCBs 分解実験を行った場合と、UV 照射を行わずに分解反応を行った結果を比較検討した結果を示す。PCBs 分解率については、2~4 塩素置換ビフェニルにおいては 80% 以上の良好な分解率が得られたが、5 塩素置換以上のビフェニルでは殆ど分解されなかった。また、反応時間の増加に伴い PCBs 分解率が上昇する傾向が認められた。硫酸鉄 (II) と硫酸鉄 (III) との形態で分解率に大きな差は認められなかったが、硫酸鉄 (III) の方が硫酸鉄 (II) より 2.4~17.1% 優れていることが分かった。pH が 2~3 付近で行われる鉄塩化物を用いたフェントン反応の系では、UV 照射を併用することにより塩化鉄 (III) から塩化鉄 (II) への還元反応が促進され、多くの場合これに伴って分解率が大きく上昇する傾向が知られている³⁾。しかし、この硫酸を用いた低温・低 pH 条件下における $Fe^{2+}/Fe^{3+}-H_2O_2$ の系では、UV 照射により分解

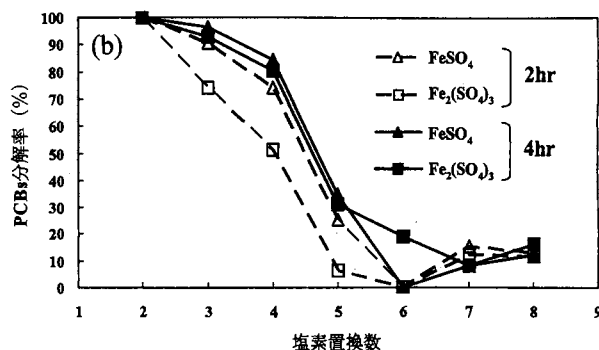
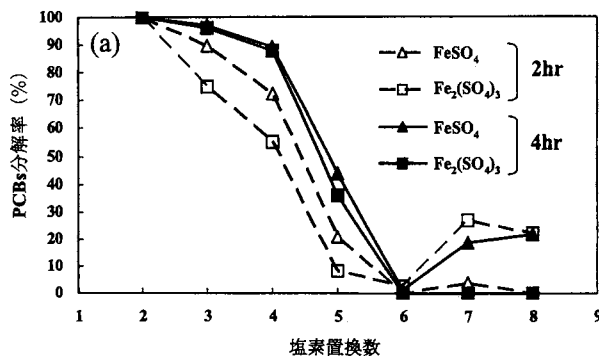


図 4 低 pH (0.1) 条件下における硫酸鉄 (II) / 硫酸鉄 (III) を用いた PCBs 分解 (a) UV 照射無し, (b) UV 照射併用, 鉄イオン濃度: 480 mM, 過酸化水素初期濃度: 12%, 温度: 30°C

率が大きく向上することはなかった。この理由については更なる検討が必要と考えられる。

この実験で得られた PCBs 分解率について、全ての塩素置換ビフェニルに対して良好な分解率を得ることは難しいものの、低塩素置換ビフェニルに対しては非常に有効な分解方法になりうると考えられる。さらに、これまでは分解反応が起こらないとされていた低 pH の条件下で、非常に難分解性の PCBs を分解できることを見出したことは意義のあることで、この反応系を新しい分解反応条件として利用できる可能性が示唆された。

ところで、本研究で対象としている PCBs の問題については、1968年に熱媒体として使われていた PCBs が食用油に混入して多くの深刻な健康被害が起こったカネミ油症事件をきっかけにその製造・使用が禁止されたが、PCBs を含有するトランス・コンデンサの保管・処理の問題は現在まで続いている。また、新しい問題として旧型のトランスを不十分に洗浄せずに PCBs を含まない電気絶縁油を補充した場合に発生する PCBs に微量汚染された電気絶縁油の問題、さらに、過去に環境中に排出された PCBs による環境汚染の問題など様々な問題が存在している。そこで、本研

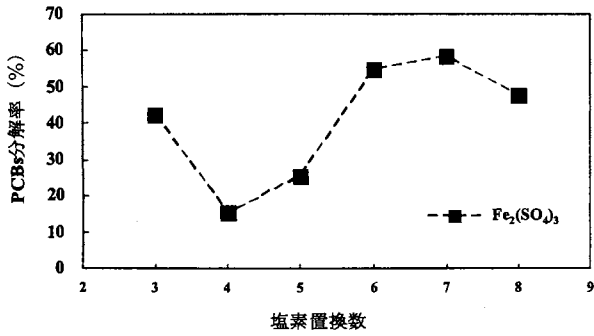


図5 UV-Fe²⁺/Fe³⁺-H₂O₂系を用いた電気絶縁油に混入したPCBs分解への応用
(鉄イオン濃度：800 Mm, 過酸化水素初期濃度：12%, 反応時間：8時間, 温度：30℃, pH：0.1)

究では、次にPCBsを含む電気絶縁油の浄化にこの分解法を適用し、その効果について検討した。

本研究では、鉱油系の電気絶縁油にPCBsを微量混入 (25 ppm) させたものをモデルサンプルとして作成し、このサンプルに対する硫酸を用いた低温・低pH条件におけるUV-Fe²⁺/Fe³⁺-H₂O₂系による分解の効果について検討を行った。図4 (a, b)の結果から硫酸鉄 (II) を用いた場合より硫酸鉄 (III) を用いた場合の方がPCBs分解率が若干高かったため、鉄 (III) 塩のみの系で電気絶縁油の分解反応を行った。その結果を図5に示す。

興味深いことに、電気絶縁油に混入したPCBsに対して分解反応を行った際には、純粋なPCBsのみに対して分解反応を行った場合と比較して4及び5塩素置換ビフェニルにおいて分解率が低く、6以上の塩素置換ビフェニルの場合に48～58%と高くなるという異なった傾向が認められた。この分解率の傾向に関しては、可溶化に用いたDMFの影響、鉱油系電気絶縁油中に含まれている他の成分による影響や、電気絶縁油中からPCBsを抽出・クリーンアップを行う際の予期せぬ脱塩素化反応等が影響している可能性が考えられる³¹⁾。

しかし、本研究の結果は、Dercováら⁴⁾がpH 3.0, 28℃, 30時間の反応により得た4塩素置換体の分解率 (約50%) を高塩素置換体においてやや凌いでいると共に、反応時間を約27%に短縮できたことを意味している。今後は電気絶縁油以外の油に関しても実験を行い、分解率の向上についてさらに検討を行っていく必要があると考えられる。

5. 結 論

本研究では、簡便で制御がしやすい条件で、かつ効果の高いフェントン・フェントン様反応を用いた分解方法について模索を行う目的で硫酸を用いた低温・低pH条件におけるUV-Fe²⁺/Fe³⁺-H₂O₂系によるPCBsの分解反応の有効性について検討を行った。また、鉱油系電気絶縁油中に微量混入したPCBsに対してもその有効性について検討を行った。その結果得られた主要な知見を以下に記す。

- 1) 過酸化水素は低pH条件で非常に安定であり、温度・UV照射の影響を殆ど受けないが、鉄イオン触媒が存在すれば分解反応は速やかに進行した。温度が低い場合でも過剰量の鉄イオン触媒が存在すれば反応は速やかに進行した。
- 2) 硫酸を用いた低pH (pH 0.1), 低温 (30℃) 条件下, 4時間の反応で2～4塩素置換体のPCBsを80%以上分解できることを見出した。また、鉱油系電気絶縁油に混入したPCBsにこの分解方法を適応した結果, 8時間の反応により6～8塩素置換ビフェニルで48～58%の分解率を得ることができた。
- 3) 硫酸を用いた低pH条件 (pH 0.1)・低温 (30℃) におけるフェントン・フェントン様反応を利用することで、従来型のフェントン反応で問題になっていた欠点 (pH調整の必要性・鉄スラッジの生成・有害な副生成物発生の可能性) を解消すると共に、低温条件で硫酸を用いているので反応試薬の揮発による危険性を低減することが出来た。この分解方法が新しいフェントン反応の利用につながる可能性は十分に考えられうることである。

参考文献

- 1) C. Walling, "Fenton's reagent revisited", *Acc. Chem. Res.* 8, 125-131 (1975)
- 2) K. Li, et al., "Trichloroethene degradation by UV/H₂O₂ advanced oxidation process: product study and kinetic modeling", *Environ. Sci. Technol.* 41, 1696-1703 (2007)
- 3) J. J. Pignatello, "Dark and photoassisted Fe³⁺-catalyzed degradation of chlorophenoxy herbicides

- by hydrogen peroxide”, *Environ. Sci. Technol.* 26, 944-951 (1992)
- 4) K. Dercová, et al., “Fenton’s type reaction and chemical pretreatment of PCBs”, *Chemosphere* 39, 2621-2628 (1999)
 - 5) K. A. Baltpurvins, et al., “Effect of pH and Anion Type on the Aging of Freshly Precipitated Iron (III) Hydroxide Sludges”, *Environ. Sci. Technol.* 30, 939-944 (1996)
 - 6) M. Farrokhi, et al., “Oxidation of pentachlorophenol by Fenton’s reagent”, *Iran. J. Public Health* 32, 6-10 (2003)
 - 7) J. De Laat, et al., “A comparative study of the effects of chloride, sulfate and nitrate ions on the rates of decomposition of H_2O_2 and organic compounds by Fe(II)/ H_2O_2 and Fe(III)/ H_2O_2 ”, *Chemosphere* 55, 715-723 (2004)
 - 8) G. G. Jayson, et al., “Some simple, highly reactive, inorganic chlorine derivatives in aqueous solution. Formation using pulses of radiation and their role in the mechanism of the Fricke dosimeter”, *J. Chem. Soc., Faraday Trans 1* 69, 1597-1607 (1973)
 - 9) S. Yamamoto, et al., “Effect of chlorine on direct photodegradation of phosgene in gaseous phase”. *Electrochemistry (Tokyo, Japan)* 70, 425-428 (2002)
 - 10) V. Nadtochenko, J. Kiwi, “Primary Photochemical Reactions in the Photo-Fenton System with Ferric Chloride. 1. A Case Study of Xylidine Oxidation as a Model Compound”, *Environ. Sci. Technol.* 32, 3273-3281 (1998)
 - 11) A. Lopez, et al., “Temperature activated degradation (mineralization) of 4-chloro-3-methyl phenol by Fenton’s reagent”, *Chemosphere* 59, 397-403 (2005)
 - 12) J. J. Pignatello, G. Chapa, “Degradation in PCBs by ferric ion, hydrogen peroxide and UV light”, *Environ. Toxicol. Chem.* 13, 423-427 (1994)
 - 13) K. Matsunaga, et al., “Biomimetic chemical degradation of polychlorobiphenyls below 100°C”, *Chemosphere* 27, 2317-2324 (1993)
 - 14) 鈴木滋, et al. “全 PCB 分析法の検討”, 宮城県保健環境センター年報 24, 165-166 (2006)
 - 15) 東剛志, 三野芳紀, “硫酸を用いた低温・低 pH 条件下での $Fe^{2+}/Fe^{3+}-H_2O_2$ 混合試薬による PCBs の化学分解”, フォーラム2008 衛生薬学・環境トキシコロジー講演要旨集 293 (2008)
 - 16) M. I. Badawy, et al., “Advanced oxidation processes for the removal of organophosphorus pesticides from wastewater”, *Desalination* 194, 166-175 (2006)
 - 17) H. Gallard, et al., “Effect of pH on the rate of oxidation of organic compounds by Fe^{II}/H_2O_2 . Reaction mechanisms and modeling”, *New J. Chem.* 22, 263-268 (1998)
 - 18) C. Walling, A. Goosen, “Mechanism of the ferric ion catalyzed decomposition of hydrogen peroxide. Effect of organic substrates”, *J. Am. Chem. Soc.* 95, 2987-2991 (1973)
 - 19) Y. Lee, et al., “High temperature dependence of 2,4-dichlorophenoxyacetic acid degradation by Fe^{3+}/H_2O_2 system”, *Chemosphere* 51, 963-971 (2003)
 - 20) H. Gallard, et al., “Spectrophotometric study of the formation of iron(III)-hydroperoxy complexes in homogeneous aqueous solutions”, *Water Res.* 33, 2929-2936 (1999)
 - 21) J. De Laat, H. Gallard, “Catalytic Decomposition of Hydrogen Peroxide by Fe (III) in Homogeneous Aqueous Solution: Mechanism and Kinetic Modeling”, *Environ. Sci. Technol.* 33, 2726-2732 (1999)
 - 22) C. Lee, J. Yoon, “Temperature dependence of hydroxyl radical formation in the $hv/Fe^{3+}/H_2O_2$ and Fe^{3+}/H_2O_2 systems”, *Chemosphere* 56, 923-934 (2004)
 - 23) N. Al Ananzeh, et al., “Kinetic Model for the Degradation of MTBE by Fenton’s Oxidation”, *Environ. Chem.* 3, 40-47 (2006)
 - 24) 日本化学会編 (2004) : 改訂 5 版 化学便覧 基礎編 II. 丸善, 580-584
 - 25) X. R. Xu, et al., “Chemical oxidative degradation of methyl *tert*-butyl ether in aqueous solution by Fenton’s reagent”, *Chemosphere* 55, 73-79 (2004)
 - 26) Y. Mino, et al., “Degradation of 2,7-dichlorodibenzo-*p*-dioxin by $Fe^{3+}-H_2O_2$ mixed reagent”, *Chemo-*

- sphere 57, 365-372 (2004)
- 27) 特別管理一般廃棄物及び特別管理産業廃棄物に係る基準の検定方法 (厚生省告示192号), Available from <<http://www.env.go.jp/hourei/syousai.php?id=11000314>>. Accessed 2010, 11/5
- 28) C. Matsumura, et al., "Elution orders of all 209 PCBs congeners on capillary column "HT8-PCB"", *Kankyo Kagaku* 12, 855-865 (2002)
- 29) N. Motohashi, I. Mori, "Superoxide-dependent formation of hydroxyl radical catalyzed by transferrin", *FEBS Lett.* 157, 197-199 (1983)
- 30) 高菅, et al., "アルカリ分解法を用いた PCB, ダイオキシン分析の課題", 第10回環境化学討論会講演要旨集. 日本環境化学会, 愛媛 28-29 (2001)
- 31) J. J. Ryan, et al., "The effect of strong alkali on the determination of polychlorinated dibenzofurans (PCDFs) and polychlorinated dibenzo-*p*-dioxins (PCDDs)", *Chemosphere* 18, 149-154 (1989)

大阪薬科大学
文部科学省私立大学戦略的研究基盤形成支援事業
「組織的研究体系による次世代型感染症治療薬の開発」
平成 23 年度第 1 回公開シンポジウム



平成 23 年 12 月 3 日



主催 大阪薬科大学
協賛 社団法人 日本薬学会
社団法人 日本化学会
社団法人 日本生化学会

ご挨拶

大阪薬科大学では、文部科学省より「平成 23 年度私立大学戦略的研究基盤形成支援事業」として「組織的研究体系による次世代型感染症治療薬の開発」が採択されました。

現在、本学には平成 19 年度に文部科学省より採択されました「生活習慣病を標的とする分子構造と分子間相互作用に基づく合理的創薬システムの開発」をテーマとする「創薬基盤科学技術研究センター」が活動を継続しており、本年度は 5 年計画の最終年度に当たります。このように本学に 2 つの研究センターが設置され、活動していることは大変すばらしいことでもあります。

近年、大腸菌 O-157 を病原体とする出血性大腸菌をはじめとする新興感染症、結核などの再興感染症、病院やデイケアセンター内などでの日和見感染症、さらには医療現場での抗菌薬の濫用が原因とも考えられる多剤耐性菌の発生など多くの問題から、新たな作用機序を有する新規抗菌薬の開発が待ち望まれています。「組織的研究体系による次世代型感染症治療薬の開発」には、分子構造・機能解析学領域に属する微生物学研究室、薬品物理化学研究室、生化学研究室、薬品分析化学研究室、および中央機器研究施設の教員が全員参画し、従来の抗菌薬創製に係るアプローチとは異なる新規感染症治療薬を開発することを目指しています。

研究目的を達成するための具体的な研究課題として、(1) 細菌の増殖機構に関与する新規タンパク質の探索及び特定、(2) 新規タンパク質の構造解析ならびに新規感染症治療薬の分子設計、(3) 新規タンパク質の機能解析ならびに酵素科学的解析、および(4) 細菌の無機元素輸送体を標的とする新規阻害剤の 4 分野を掲げ、従来より関連領域において研究成果を挙げてきた研究室が分担し、効率的に研究を遂行する体制を構築しております。本研究プロジェクトは、従来の抗菌薬療法を大きく変化させ、多剤耐性菌による感染症をも治療することを可能にする極めて社会貢献度の高い研究基盤事業であると考えています。

今回は年一度の開催を予定している公開シンポジウムを、「創薬基盤科学技術研究センター」と合同で開催いたします。「創薬基盤科学技術研究センター」においては、最後のシンポジウムであり、我々の研究センターにおいては最初の記念すべきシンポジウムとなります。

学外からは大阪大学微生物病研究所の飯田哲也先生に、本学からは微生物学研究室の宮本勝城先生に講演をお願いしました。

本シンポジウムが皆様方にとって少しでもお役に立てれば幸甚です。

研究代表者 辻坊 裕

大阪薬科大学
平成 23 年度公開シンポジウム

日 時 : 平成 23 年 12 月 3 日 (土) 14 : 50 ~
会 場 : 大阪薬科大学・C203 教室 (入場無料)

文部科学省私立大学戦略的研究基盤形成支援事業
「組織的研究体系による次世代型感染症治療薬の開発」
第 1 回シンポジウム

大阪薬科大学では、文部科学省より「平成 23 年度私立大学戦略的研究基盤形成支援事業」
として「組織的研究体系による次世代型感染症治療薬の開発」が採択されました。本プロ
ジェクト研究に関連して平成 23 年度の公開シンポジウムを開催いたします。

《 プログラム 》

- | | | |
|-------------------|--|------------|
| 14 : 50 ~ 15 : 00 | ご挨拶 | 研究代表者 辻坊 裕 |
| 15 : 00 ~ 15 : 30 | 宮本 勝城 准教授 (大阪薬科大学)
「病原細菌 <i>Vibrio vulnificus</i> の宿主生体内における生存戦略」
座長 三野 芳紀 | |
| 15 : 30 ~ 16 : 20 | 飯田 哲也 特任教授 (大阪大学微生物病研究所)
「下痢原因細菌の病原性解析と新規治療法への試み」
座長 辻坊 裕 | |
| 18 : 00 ~ | 懇親会 | |

講演要旨

病原細菌 *Vibrio vulnificus* の宿主生体内における生存戦略

大阪薬科大学 宮本勝城

【緒言】

Vibrio vulnificus は、汚染された魚介類の摂食や海水の創傷部曝露等を介して感染し、特に肝機能障害などの基礎疾患をもつヒトに感染すると、急速に全身に広がり、数日以内に敗血症に陥り死亡する。一般に、鉄はほとんどの生物の生存と増殖に不可欠な元素であるが、宿主生体内において病原菌が自由に利用できる遊離鉄は極めて少ない。したがって、宿主生体内で増殖し得る病原菌は、何らかの巧妙な鉄獲得系を保持しているはずである。そこで、鉄獲得系を阻害する新規な抗菌薬の標的タンパク質を探索する目的で、臨床分離株 *V. vulnificus* M2799 株における鉄存在下および欠乏下におけるプロテオーム解析を行った。

【方法】

鉄含有培地としてハートインフュージョン培地、鉄欠乏培地として最終濃度が 10 µg/ml となるように ethylenediamine-di (*o*-hydroxyphenylacetic acid) (EDDA, Sigma) を同培地に添加したものをを用いた。*V. vulnificus* M2799 株を 37°C で攪拌培養後、菌体を細胞溶解緩衝液で溶菌させ、それぞれ 50 µg のタンパク質を Cy2、Cy3 および Cy5 DIGE Fluors minimal dye で標識し、2 次元ディファレンシャルゲル電気泳動(2D-DIGE)を行った。得られたゲルイメージを DeCyder 6.0 Software (GE Healthcare) により解析し、*t* 検定値が 0.01 以下で発現量が 2 倍以上変動するスポットを選択した。同様に調製した 250 µg のタンパク質の 2 次元電気泳動を行い、作成したピックリストに従ってゲルからスポットの切り出しを行った。次に、Montage In-Gel Digest Kit (Millipore) を用いてトリプシン消化後、MALDI-TOF/MS (Voyager DE-STR) でペプチド断片の MS を測定し、PMF 法によりタンパク質の同定を試みた。さらに、鉄欠乏条件下において発現量が 2 倍以上変動したタンパク質遺伝子の欠損株作製を試みた。まず、タンパク質遺伝子の約 1 kb の内部領域が増幅するようにプライマーを作成し、PCR 法により DNA 断片を調製した。調製した DNA 断片を suicide vector pKTN701 に挿入し、大腸菌 SM10 λ pir 株を形質転換した。本形質転換株と M2799 株をフィルター上で 37°C、3 時間接合させた後、フィルター上の菌を LB 液体培地で懸濁し、1.5% NaCl、5.0 µg/ml クロラムフェニコールおよび 100 U/ml ポリミキシン B 含有 LB 寒天培地に塗抹した。37°C で一晩培養後、増殖したコロニーから染色体 DNA およびトータル RNA を調製し、サザンハイブリダイゼーション、PCR 法あるいは逆転写産物の定量的リアルタイム PCR 法により挿入変異が生じているかどうかについて確認した。

【結果および考察】

臨床分離株 M2799 株の細胞内タンパク質のうち、鉄過剰および欠乏下で発現量が 2 倍以上変動したスポットは、対数増殖前期、中期、後期においてそれぞれ 32、53、42 種類存在した。次に、これらタンパク質の同定を試みたところ、対数増殖前期、中期、後期に発現差異が認められたタンパク質のうち、それぞれ 18、31、26 種類を同定することができた(Table)。これらのタンパク質のうち、鉄欠乏下で発現量が 2 倍以上促進された 29 種類のタンパク質について、それらの遺伝子欠損株を作製し、鉄欠乏下における増殖能について検討した。その結果、本菌が産生するシデロフォアであるバルニバク

チンの生合成ならびに鉄獲得機構に関与するタンパク質の遺伝子欠損株において、増殖能の顕著な低下が認められた。特に、バルニバクチンの生合成に必須であり、コリスミン酸をイソコリスミン酸に変換する、イソコリスミン酸合成酵素の遺伝子欠損株は、鉄欠乏下においてほとんど増殖することができなかった。

Table Iron-regulated proteins of *V. vulnificus* M2799.

VV no.	Protein	Predicted molecular mass (Da)/pI	Early	Volume ratio Mid	Late
Information storage and processing					
Transcription regulation					
VV2_0915	Transcriptional regulator IclR	29,668/5.30	4.51	5.88	1.16
Translation, ribosomal structure and biogenesis					
VV1_1338	Elongation factor EF-G	77,469/4.88	4.88	3.01	2.58
VV1_1339	Elongation factor EF-Tu	43,305/4.87	ND ^a	-2.38	ND
Cellular processes					
Posttranslational modification, protein turnover, chaperones					
VV1_0453	Peroxiredoxin	22,456/4.93	1.44	2.14	1.36
VV2_1134	Chaperonin GroEL	55,931/4.93	ND	2.66	ND
Cell envelope biogenesis, outer membrane					
VV1_1811	Outer membrane protein OmpK	30,888/4.98	-1.12	-2.36	-1.53
VV2_0559	Outer membrane protein OmpA	38,728/4.62	1.18	1.08	-2.44
VV2_0578	Outer membrane protein (porin)	37,228/4.80	ND	1.66	4.63
VV2_1529	Hypothetical protein	74,499/5.04	2.01	1.44	3.90
Inorganic ion transport and metabolism					
VV1_1252	Manganese superoxide dismutase SodA	23,015/5.34	8.45	3.73	5.26
VV1_1661	ABC-Type Fe ³⁺ transport system, periplasmic component	37,421/5.88	1.65	3.70	1.37
VV1_2968	Uncharacterized iron-regulated protein	46,799/4.66	4.01	5.95	2.15
VV1_3107	Iron superoxide dismutase SodB	22,168/5.07	-2.26	-2.46	-2.41
VV2_0837	Siderophore-interacting protein ViuB	30,331/4.94	3.42	2.91	2.87
VV2_0842	ABC-Type vulnibactin transport system, periplasmic component FatB	32,706/5.07	7.21	12.93	4.15
VV2_0843	Vulnibactin receptor protein VuuA	75,610/4.77	3.51	11.52	12.53
VV2_1012	ABC-Type aerobactin transport system, periplasmic component VatD	32,342/5.34	2.89	9.04	3.46
VV2_1337	Ferrioxamine B receptor protein DesA	79,594/4.58	5.63	4.72	ND
Signal transduction mechanisms					
VV1_1001	ABC-Type amino acid transport/signal transduction system	27,540/5.24	-2.07	-1.51	-2.34
VV2_0816	ABC-Type amino acid transport/signal transduction system	26,643/4.85	-1.64	-1.20	-2.25
Metabolism					
Energy production and conversion					
VV1_2098	Formate acetyltransferase	84,838/5.30	ND	ND	2.36
VV2_0211	Uncharacterized oxidoreductase	41,742/5.25	1.56	2.11	5.11
Carbohydrate transport and metabolism					
VV1_1541	Fructose/tagatose bisphosphate aldolase	38,975/4.86	ND	ND	2.67
VV2_0569	Phosphomannomutase ManB	62,658/5.67	2.91	7.60	4.42
VV2_0733	TRAP-Type C4-dicarboxylate transport system, periplasmic component	37,800/5.40	ND	1.11	-2.15
VV2_1585	Periplasmic maltose-binding protein	42,260/4.89	-1.19	-3.82	-1.73
Amino acid transport and metabolism					
VV2_0188	Serine hydroxymethyltransferase	46,773/6.07	ND	2.22	1.23
VV2_1400	Oligoendopeptidase F	69,702/5.10	ND	ND	2.02
VV2_1548	Protease II	76,062/5.93	1.79	2.91	2.95
Nucleotide transport and metabolism					
VV1_1465	Aspartate carbamoyltransferase	34,244/5.03	1.46	2.02	3.23
Coenzyme metabolism					
VV2_1484	2-Amino-3-ketobutyrate coenzyme A ligase	72,365/5.28	-1.50	-2.00	ND
Lipid metabolism					
VV1_1237	Acyl-coenzymeA synthase	72,365/5.28	1.01	ND	2.34
Secondary metabolites biosynthesis, transport and catabolism					
VV2_0835	Isochorismate synthase	43,430/5.90	1.05	4.81	ND
Poorly characterized					
General function prediction only					
VV2_0260	Isopenicillin N synthase	31,665/5.03	3.61	2.04	ND
VV2_0985	TRAP-Type uncharacterized transport system, periplasmic component	35,151/6.40	ND	ND	2.57
Unknown					
Intracellular trafficking and secretion					
VV1_2334	FliC pilus assembly protein TadA	47,750/5.55	2.87	3.34	ND
Other					
VV1_0889	Glutamine synthetase	51,941/4.93	ND	2.45	ND
VV1_2326	Unknown	35,685/5.25	9.47	8.01	1.20
VV2_0364	Chromosome segregation ATPase	28,858/6.13	2.63	6.17	3.04
VV2_1399	Hypothetical protein	63,494/4.60	2.28	2.19	1.50
VV2_0196	Outer membrane protein	20,927/4.90	ND	-2.13	-2.33
VV2_1227	Maltoporin	45,354/4.58	1.44	-2.11	-2.03

^a ND, not detected.

略 歴

氏 名	みやもと かつしろ 宮本 勝城
生年月日	1964年2月10日
所属機関	大阪薬科大学准教授 (微生物学研究室)

学 歴

1988年3月	大阪薬科大学薬学部製薬学科卒業
1990年3月	大阪薬科大学大学院薬学研究科博士課程前期修了
2003年3月	博士(薬学) 大阪薬科大学より

職 歴

1990年4月	大阪薬科大学 助手
2005年1月	大阪薬科大学 講師
2011年4月	大阪薬科大学 准教授
	現在に至る

下痢原因細菌の病原性解析と新規治療法への試み

大阪大学微生物病研究所
感染症国際研究センター ゲノム病原細菌学
飯田哲也

腸炎ビブリオ (*Vibrio parahaemolyticus*) は我が国における主要な食中毒原因菌の一つである。魚介類の摂取を通じてヒトに感染し胃腸炎を引き起こす。従来、本菌の産生する耐熱性溶血毒(TDH)およびTDH類似溶血毒(TRH)が本菌の主要な病原因子と考えられ、これらの溶血毒について重点的に研究が行われてきた。我々が本菌の全ゲノム配列を決定した結果、大小2つの染色体上にそれぞれ1セットずつの3型分泌装置遺伝子群が見出され、腸炎ビブリオの病原性研究に新たな展開がもたらされた。ここ数年、腸炎ビブリオ3型分泌装置の病原性への関わりや本装置により分泌されるエフェクターについての解析が急速に進んでおり、様々な知見が得られつつある。我々はごく最近、腸炎ビブリオ3型分泌装置の発現制御機構や発現誘導に関わる宿主側因子を明らかにした。これらは腸炎ビブリオ感染症の新規制御法につながる知見と期待される。本講演では、腸炎ビブリオの病原性発現機構についてオーバービューするとともに、我々の研究室の最近の知見を紹介したい。

参考文献

- Makino, K., Oshima, K., Kurokawa, K., Yokoyama, K., Uda, T., Tagomori, K., Iijima, Y., Najima, M., Nakano, M., Yamashita, A., Kubota, Y., Kimura, S., Yasunaga, T., Honda, T., Shinagawa, H., Hattori, M. and Iida, T.: Genome sequence of *Vibrio parahaemolyticus*: a pathogenic mechanism distinct from that of *V. cholerae*. *Lancet* 361: 743-749, 2003
- Gotoh, K, Kodama, T., Hiyoshi, H., Izutsu, K., Park, K.-S., Dryselius, R., Akeda, Y., Honda, T. and Iida, T. : Bile acid-induced virulence gene expression of *Vibrio parahaemolyticus* reveals a therapeutic potential for bile acid-sequestering agents. *PLoS One* 5: e13365, 2010
- Hiyoshi, H., Kodama, T., Saito, K., Gotoh K., Akeda, Y., Honda, T., and Iida, T. : VopV, an F-actin binding type III secretion effector, is required for *Vibrio parahaemolyticus*-induced enterotoxicity. *Cell Host Microbe* 10: 401-409, 2011

略 歴

氏 名	いいだ てつや 飯 田 哲 也
生年月日	1962年3月15日
所属機関	大阪大学微生物病研究所 感染症国際研究センター ゲノム病原細菌学研究グループ 特任教授

学 歴

1984年3月	京都大学理学部卒業
1987年3月	大阪大学大学院医学研究科修士課程修了
1984年3月	大阪大学大学院医学研究科博士課程修了
1991年3月	医学博士（大阪大学）

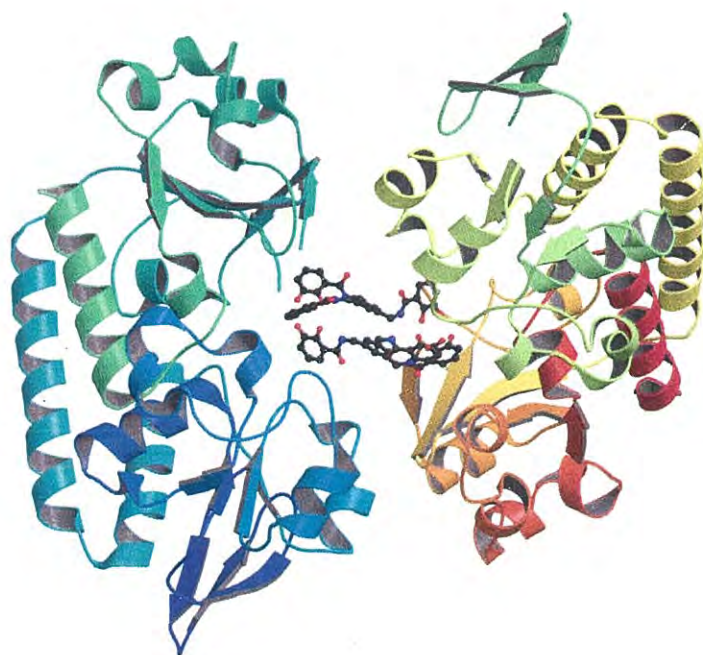
職 歴

1990年4月	日本学術振興会特別研究員
1992年4月	大阪大学微生物病研究所 助手
1999年8月	大阪大学微生物病研究所 助教授
2005年12月	大阪大学微生物病研究所 感染症国際研究センター 特任教授
2010年4月	大阪大学微生物病研究所 遺伝情報実験センター 感染症メタゲノム研究分野兼任 現在に至る

受 賞

1997年	平成9年度日本感染症学会北里柴三郎記念学術奨励賞
2004年	平成16年日本細菌学会小林六造記念賞

大阪薬科大学
文部科学省私立大学戦略的研究基盤形成支援事業
「組織的研究体系による次世代型感染症治療薬の開発」
平成 24 年度公開シンポジウム



平成 24 年 12 月 8 日



主催 大阪薬科大学
協賛 社団法人日本薬学会
社団法人日本化学会
社団法人日本生化学会

ご挨拶

大阪薬科大学では、平成 23 年度に文部科学省の私立大学戦略的研究基盤形成支援事業として採択されました「組織的研究体系による次世代型感染症治療薬の開発」と題したプロジェクト研究を推進しているところです。

平成 23 年度の第 1 回公開シンポジウムは、平成 19 年度に文部科学省により採択されました「生活習慣病を標的とする分子構造と分子間相互作用に基づく合理的創薬システムの開発」をテーマとする「創薬基盤科学技術研究センター」と合同で実施されました。「創薬基盤科学技術研究センター」は昨年最終年を迎えましたので、恒例により本年度は我々のプロジェクト単独で開催する運びとなりました。我々の研究プロジェクトのこれまでの成果を報告するとともに、今回のシンポジウムに相応しい先駆的な研究をなさっている研究者を学外からお招きしております。

大阪薬科大学大学院薬科学専攻博士前期課程は、分子構造・機能解析学領域、創薬化学領域、および生命・環境科学領域から、博士後期課程は分子構造・機能解析学領域および創薬化学領域から構成されています。我々の研究プロジェクトチームは、分子構造・機能解析学領域に属する薬品物理化学研究室、生化学研究室、薬品分析化学研究室、微生物学研究室および中央機器研究施設の教員から構成されていることが特色であり、これらの研究室および施設の全教員が目的を達成するための具体的な研究課題に取り組み、効率的に研究を遂行する体制をとっています。

第 2 回シンポジウムでは、学外から東海大学医学部基礎医学系分子生命科学の良原栄策先生に「多剤耐性グラム陰性菌に対する新規抗菌分子の開発」を、北里大学大学院感染制御科学府北里生命科学研究所の塩見和朗先生に「微生物の生産する新しいターゲットをもつ抗生物質の探索～抗寄生虫・抗細菌～」をテーマにそれぞれご講演をしていただきます。本学からは宮本勝城先生と友尾幸司先生にそれぞれ「病原細菌 *Vibrio vulnificus* の宿主生体内における生存戦略」および「好熱性放線菌由来キシロオリゴ糖輸送に関与するタンパク質群の構造機能解析」について講演をしていただきます。各講演では、独創的な研究展開によって得られた成果についてご披露いただけるものと考えています。また、これらのご講演は、本プロジェクトにおける今後の研究の方向性について、貴重な示唆を与えていただけるものと信じております。皆様方により活発な討論がなされることを期待しております。

なお、シンポジウム終了後、ささやかな懇親会を予定しております。本プロジェクト研究の今後の展開についてご歓談いただけると幸いです。

研究代表者 辻坊 裕

大阪薬科大学
平成 24 年度公開シンポジウム

日 時 : 平成 24 年 12 月 8 日 (土) 13 : 50 ~
会 場 : 大阪薬科大学・C203 教室

文部科学省私立大学戦略的研究基盤形成支援事業
「組織的研究体系による次世代型感染症治療薬の開発」
第 2 回シンポジウム

《 プログラム 》

- : 50 ~ 14 : 00 開会挨拶 研究代表者 辻坊 裕
- : 00 ~ 14 : 30 宮本 勝城 准教授 (大阪薬科大学微生物学研究室)
「病原細菌 *Vibrio vulnificus* の宿主生体内における生存戦略」
座長 佐藤 卓史
- : 30 ~ 15 : 00 友尾 幸司 准教授 (大阪薬科大学薬品物理化学研究室)
「好熱性放線菌由来キシロオリゴ糖輸送に関与するタンパク質群の
構造機能解析」
座長 井上 晴嗣
- : 00 ~ 15 : 50 良原 栄策 准教授 (東海大学医学部基礎医学系分子生命科学)
「多剤耐性グラム陰性菌に対する新規抗菌分子の開発」
座長 福永 理己郎
- : 00 ~ 16 : 50 塩見 和朗 教授 (北里大学大学院感染制御科学府 北里生命科学研究所)
「微生物の生産する新しいターゲットをもつ抗生物質の探索
～抗寄生虫・抗細菌～」
座長 辻坊 裕
- : 00 ~ 懇親会 司会 藤井 忍

講演要旨

病原細菌 *Vibrio vulnificus* の宿主生体内における生存戦略

大阪薬科大学 宮本勝城

【緒言】

当研究室では、臨床分離株 *Vibrio vulnificus* M2799 株の鉄欠乏ストレスに関与するタンパク質群を網羅的に明らかにする目的で研究を行っている。*V. vulnificus* は、汚染された魚介類の摂食や海水の創傷部曝露等を介して、全身性の感染症を引き起こす細菌である。一般に、鉄はほとんどの生物の生存と増殖に不可欠な元素であるが、宿主生体内において病原菌が自由に利用できる遊離鉄は極めて少ない。したがって、宿主生体内で増殖し得る病原菌は、何らかの巧妙な鉄獲得系を保持しているはずである。そこで、臨床分離株 *V. vulnificus* M2799 株の鉄獲得系タンパク質を網羅的に明らかにする目的で、プロテオーム解析を行った。その結果、対数増殖前期、中期、後期に発現差異が認められたタンパク質のうち、それぞれ 18、31、26 種類のタンパク質を同定し、KEGG に基づいて分類を行った¹。それらタンパク質遺伝子を、suicide vector である pKTN701 に連結して相同組換えにより挿入変異株を作製し、鉄欠乏下における増殖能について検討した。その結果、 Δ FeADH (VV2_0211) 株、 Δ VuuA (VV2_0843) 株、 Δ FatB (VV2_0842) 株、 Δ VuuB (VV2_0837) 株、 Δ ICS (VV2_0835) 株、および Δ VV2_1400 株は、鉄欠乏下において増殖能が顕著に抑制された。そこで今回、これら遺伝子産物の機能を明らかにする目的で、高発現系を構築した。また、多重変異株の作製を目的として、M2799 株の遺伝子欠損株作製法を確立した。

【方法】

鉄欠乏下において発現量が変動するタンパク質の諸性質を明らかにする目的で、目的タンパク質が His タグ融合タンパク質として高発現される pProEX HTa (Invitrogen) にそれら遺伝子を導入し、大腸菌 BL21 (DE3) 株を形質転換した。得られた形質転換株を、800 ml のアンピシリン含有 LB 液体培地を用いて、600 nm での吸光度が 0.6 から 0.9 になるまで、37°C、200 rpm で攪拌培養した。これらの培養液に、最終濃度が 0.8 mM となるように 1 M IPTG を加えた後、さらに 20°C で 15 時間攪拌培養した。培養液を 4°C、7,000 rpm で 15 分間遠心分離することにより集菌して超音波破碎した。

遺伝子欠損株の作製は、Miltonら²の方法に従い、suicide vector pDM4 を用いて行った。まず、ターゲット遺伝子内欠失目的領域の上流域および下流域それぞれ 500 bp を PCR で増幅し、これらを連結後、PCR を行い増幅した。増幅した DNA を pDM4 に連結し、大腸菌 SY327 λ pir 株を形質転換した。得られた組換えプラスミドを用いて、*V. vulnificus* 細胞に対する遺伝子伝達能を有する大腸菌 SM10 λ pir 株を形質転換した。得られた SM10 λ pir 株と M2799 株をそれぞれ培養し、メンブレンフィルター上で接合させることでプラスミドの伝達を行わせて 1 回目の相同組換えを誘発した。得られた相同組換え体を 15% スクロース、100 units/ml ポリミキシン B 含有 LB 寒天培地に塗抹し、増殖したコロニーのクロラムフェニコール感受性を確認した。

【結果および考察】

今回、増殖能が顕著に抑制された挿入変異株のうち、ICS および VuuB タンパク質の高

発現系を構築した。その結果、ICS タンパク質は封入体を形成したが、VuuB タンパク質は可溶化で発現した。そこで、本タンパク質を Ni-Sepharose 6FF および HiLoad Superdex 75pg クロマトグラフィーにより、電気泳動的に均一にまで精製した。今後、本タンパク質の諸性質を明らかにし、構造解析を行う予定である。

次に、遺伝子欠損株の作製を試みた。鉄獲得機構に関与するタンパク質群のグローバルレギュレーターである *fur* 遺伝子をターゲット遺伝子とし、pDM4 に本遺伝子上流域および下流域を連結して pDM Δ fur を作製した。得られた pDM Δ fur を有する SM10 λ *pir* 株による接合伝達により、1.5% NaCl、5 μ g/ml クロラムフェニコールおよび 100 units/ml ポリミキシンB 含有 LB 寒天培地を用いて M2799 株の相同組換え体を作製した。pDM4 に存在する *sacB* 遺伝子にコードされる レバンスクララーゼは、本菌株に対して、27°C、15% スクロースの存在下で良好な活性を示したことから、1 回目の相同組換え体を 15% スクロース、100 units/ml ポリミキシンB 含有 LB 寒天培地に塗抹し、27°C で一晩培養した結果、クロラムフェニコール感受性株を得た。2 回目の相同組換え株のうち、リバータントと欠失株の検出は、欠失領域の上流域および下流域の塩基配列に基づき設計したプライマーを用いた PCR により確認した。確立した欠損株作製法を用いて、本菌株のシデロフォアである vulnibactin を介する鉄取り込み機構に関与する遺伝子の欠損株を作製し、鉄欠乏下での増殖能について検討した。その結果、Fe³⁺-vulnibactin 複合体の外膜レセプターである VuuA の欠損株の増殖能は顕著に低下した。一方、Fe³⁺-vulnibactin 複合体のペリプラズム結合タンパク質である FatB の欠損株では、増殖の低下は認められたが、若干の増殖が確認された。そこで、大腸菌の産生するシデロフォアである aerobactin を介する鉄取り込み機構に関与するペリプラズム結合タンパク質である VatD の二重欠損株を作製し、本株の増殖能について検討した結果、顕著に低下した。以上のことから、vulnibactin を介する鉄取り込み機構において、VuuA は必須であるが、FatB については VatD が代替可能であることが示唆された。今後、さらに詳細に検討し、次世代型感染症治療薬開発のターゲットについて模索していきたい。

【参考文献】

1. Milton DL, Norqvist A, Wolf-Watz H. (1992) Cloning of a metalloprotease gene involved in the virulence mechanism of *Vibrio anguillarum*. J. Bacteriol. 174:7235-7244.
2. Miyamoto K, Kosakai K, Ikebayashi S, Tsuchiya T, Yamamoto S, Tsujibo H. (2009) Proteomic analysis of *Vibrio vulnificus* M2799 grown under iron-repleted and iron-depleted conditions. Microb. Pathog. 46:171-177.

略 歴

氏 名 みやもと かつしろ 宮 本 勝 城
生年月日 1964年2月10日
所属機関 大阪薬科大学准教授 (微生物学研究室)

学 歴

1988年3月 大阪薬科大学薬学部製薬学科卒業
1990年3月 大阪薬科大学大学院薬学研究科博士前期課程修了
2003年3月 博士 (薬学) (大阪薬科大学)

職 歴

1990年4月 大阪薬科大学 助手
2005年1月 大阪薬科大学 講師
2011年4月 大阪薬科大学 准教授
現在に至る

賞 罰

なし

好熱性放線菌由来キシロオリゴ糖輸送に関与するタンパク質群の構造機能解析

大阪薬科大学 友尾幸司

好熱性放線菌 *Streptomyces thermoviolaceus* OPC-520 株由来遺伝子中には、キシロオリゴ糖の輸送および分解に関与するタンパク質群を産生する *bxl* オペロンが存在する。その遺伝子産物としては、糖結合タンパク質である Bx1E、2種類の膜貫通型タンパク質 Bx1F、Bx1G、および細胞内 α -xylosidase である Bx1A が存在する。自然界において、セルロースに次いで再生利用可能な資源として多く存在するキシランは、xylanase によってキシロオリゴ糖に分解される。生成したキシロオリゴ糖は、Bx1E によって Bx1F/Bx1G 複合体に受け渡されて細胞内に運ばれ、細胞内にて Bx1A により xylose にまで加水分解されると考えられているが、これら Bx1 タンパク質群による糖輸送機構の構造化学的な詳細はいまだ明らかになっていない。そこで本研究では、X線結晶構造解析法を用いて Bx1 タンパク質群の網羅的構造決定に取り組み、本菌におけるキシロオリゴ糖の細胞内輸送機構を原子レベルで明らかにすることを目的としている。

糖結合タンパク質である Bx1E は 436 アミノ酸残基からなり、単糖、および二糖から六糖までのキシロオリゴ糖との結合親和性が明らかにされている。中でも、二糖であるキシロビオースと最も高い親和性を示す一方で、単糖との親和性は著しく低い。このように、各キシロオリゴ糖に対する Bx1E の親和性の差違や、糖受け渡し機構の詳細について明らかにするために、Bx1E 単独ならびに xylobiose との複合体の立体構造解析を行った。大腸菌を用いた Bx1E の大量発現系を構築し、発現、精製の後、各試料の結晶化および、X線構造解析法による Bx1E 単独、ならびに xylobiose 複合体の立体構造を決定した。その結果、Bx1E は 2つのドメインを有し、そのドメイン間に形成されるクレフトに糖結合部位が存在していた。更に、糖の結合により 2つのドメインが大きく構造変化する事も明らかとなった。また、糖との結合には Bx1E 分子中の 11個のアミノ酸残基が関与し、中でも Trp-102 と Asp-400 の両アミノ酸残基の役割が重要であることが明らかとなった。

一方、細胞内のキシロオリゴ糖の分解に関わる酵素である Bx1A は、770 アミノ酸残基からなるタンパク質で、Glycoside Hydrolase family 3 (GH3) に分類されている。Bx1A のようなヘミセルロース分解酵素は自然界におけるカーボンサイクルの維持にきわめて重要な役割を担っている。また最近ではパルプ製紙工業における漂白作用やリグノセルロース物質を発酵製品(バイオエタノール)に転換するなどの実用的な使用法の可能

性を秘めており関心を集めている。そこで未だ明らかでない Bx1A の酵素触媒機構および立体構造を原子レベルで解明することを目的として、その構造機能解析に取り組んだ。GH3 に属する他の酵素とのアミノ酸配列アライメントより、Bx1A 分子の 286 番目と 316 番目の Asp 残基に着目し、各 Asp 残基を Ala に変換した変異体を作成し、活性発現への影響を調べた。その結果、両変換体は劇的な活性の低下がみられたことから、両残基が Bx1A の活性発現に重要に関与していることが明らかとなった。更に、wild 体については、GST 融合タンパク質として大腸菌の系を用いて大量発現させ、結晶化に成功し、立体構造の決定に至った。構造解析の結果から、先に示した Bx1A の活性発現における Asp-286 と Asp-316 の役割には、大きな違いがあることが明らかとなった。

略 歴

氏 名	ともお こうじ 友尾 幸司
生年月日	1964年1月1日
所属機関	大阪薬科大学准教授 (薬品物理化学研究室)

学 歴

1989年3月	大阪薬科大学大学院薬学研究科博士前期課程修了
1992年3月	大阪薬科大学大学院薬学研究科博士後期課程単位取得退学
1995年1月	博士 (薬学) 大阪薬科大学より

職 歴

1992年4月	大阪薬科大学 助手
1997年11月	ドイツベルリン自由大学結晶解析研究所博士研究員
2004年1月	大阪薬科大学 講師
2007年4月	大阪薬科大学 准教授
	現在に至る

賞 罰

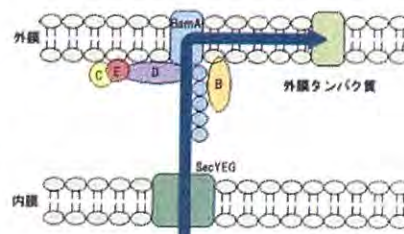
1996年1月	日本薬学会近畿支部奨励賞
---------	--------------

多剤耐性グラム陰性菌に対する新規抗菌分子の開発

良原栄策（東海大学・医学部・基礎医学系分子生命科学）

多くの抗生剤が効かない多剤耐性菌の出現が問題となっている。その中でも特にグラム陰性菌に属する緑膿菌およびアシネトバクターが臨床上深刻な問題を提起している。この状況が続けば医療崩壊に陥ることが危惧される。我々はこの危機的状況を打開することを目的に多剤耐性緑膿菌およびアシネトバクターに対する新規治療薬の開発研究に取り組んだ。

新薬開発で重要な点は新たな薬剤標的分子を見出すことである。そこで我々は BAM 複合体(β -barrel assembly machinery)を新たな標的分子とした。BAM 複合体はグラム陰性菌に特有な外膜の生合成において、新たに合成された外膜タンパク質を受け取り、外膜に挿入する役割を果たす。従って BAM 複合体は菌の生存に必須な装置である。



BAM 複合体の機能

次にではいかに標的分子を阻害するかが問題となる。BAM 複合体は5つのタンパク質 (BamA, -B, -C, -D, -E)が相互作用し集合することで、その機能を果たす。従って複合体のタンパク間相互作用を妨害することができれば、それによって複合体の機能の阻害につながるはずである。

そこで我々は相互作用を妨害する分子としてペプチドを用いることを考えた。タンパク間相互作用を担っているタンパク質の特定の部位の構造を模倣したペプチドはタンパク間相互作用を競争的に阻害できることが予想できる。

我々は BamA と BamB 間相互作用を阻害することを目的に、BamA との相互作用を担っている BamB の領域を特定し、その部位のアミノ酸配列を模倣したペプチドを合成した。このような構造を持つペプチドを緑膿菌に作用させたところ、単独で抗菌活性を示すことが分かった。またこのようなペプチドは培養細胞に対しては毒性作用を示さなかった。このことはこのようなペプチドが抗生剤として機能することを示唆する。

一方、多剤耐性緑膿菌株に対する効果を検討して結果、ペプチドは多剤耐性菌に対しても同様に抗菌活性を示すことが分かった。

また同様の戦略でアシネトバクターに対する抗菌ペプチドの開発ができるのではないかと考えた。そこでアシネトバクターの BAM 複合体の BamB で、BamA と相互作用を担う部位の構造（緑膿菌とは異なるアミノ酸配列を有する）を模倣したペプチドを設計し合成した。このようなペプチドをアシネトバクターに作用させたところ、アシネトバクターに対して選択的な抗菌活性を示すことが分かった。さらに多剤耐性アシネトバクターに対しても同様に抗菌活性を示した。

今回の研究は、世界で大きな問題となっている多剤耐性緑膿菌およびアシネトバクターに対する新規抗菌薬の開発への道を大きく開くものと考えられる。

略 歴

氏 名	よしはら えいさく 良 原 栄 策
生年月日	1950年10月25日
所属機関	東海大学医学部基礎医学系分子生命科学

学 歴

1980年3月	大阪大学大学院博士課程修了 博士(理学) 大阪大学より
---------	--------------------------------

職 歴

1980年11月	Bowman Gray School of Medicine, research associate
1983年3月	東海大学総合医学研究所、助手
1988年4月	東海大学医学部、助手
1990年4月	東海大学医学部、講師
1993年4月	東海大学医学部、准教授
	現在に至る

賞 罰

なし

微生物の生産する新しいターゲットをもつ抗生物質の探索 ー抗寄生虫・抗細菌ー

塩見和朗^{1,2}、大村 智²

¹北里大学大学院感染制御科学府・²北里大学北里生命科学研究所

微生物の培養液中には多種多様な生物活性物質が含まれており、われわれの研究室ではそこから感染症を中心に治療薬のリード化合物となる物質の探索を行っている。今回はその中から、病原体の生育や薬剤耐性に必要な酵素や感染に必須な機能を標的としたスクリーニングにより見いだした化合物をいくつか紹介する。

寄生虫症は先進諸国においては著しく減少してきたが、再興感染症として改めて問題になっている。また発展途上国における寄生虫症は重大な問題であり、薬剤耐性種の出現もその脅威に拍車をかけている。多細胞の寄生虫である蠕虫の成虫の多くは、宿主体内という低酸素環境に適応するため嫌氣的エネルギー代謝を行っている。すなわち、哺乳類では電子伝達系複合体IやIIの反応からIII、IVを経て電子を酸素に伝達しているのに対して、この嫌氣的代謝では複合体Iの反応に続き、糖代謝で産生したフマル酸を用いて複合体IIの逆反応（フマル酸還元酵素）を行い最終的な酸素受容体を揮発性有機酸とすることで、酸素を用いずにエネルギーを産生している。この複合体Iとフマル酸還元酵素を合わせた反応であるNADH-フマル酸還元酵素の阻害物質のスクリーニングを行った結果得られたnafuredin、ukulactoneなどの新規化合物は蠕虫酵素を選択的に阻害した^{1,2)}。

アミノグリコシド抗生物質のアルベカシン（ABK）はメチシリン耐性黄色ブドウ球菌（MRSA）に有効であるが、最近はその耐性菌が問題になっている。ABK耐性MRSAはABKをリン酸化およびアセチル化する二機能酵素を有している。この耐性を克服する物質を探索するため、耐性MRSAをABK添加培地と非添加培地に植菌し、ABK添加培地でのみ抗菌活性を示す試料をスクリーニングした。その結果、biverlactonesと命名した新規物質やaranorosinなどいくつかの化合物を単離し^{3,4)}。それらの化合物は単独では抗MRSA作用を示さない濃度において、ABKと併用することで、耐性MRSAに対するABKの最小生育阻止濃度を低下させた。また他のアミノグリコシド抗生物質との併用においても同様の効果が見られたが、それ以外のグループの抗生物質に対しては全く効果を示さなかった。そしてその耐性克服作用は、二機能酵素のリン酸化活性の阻害によるものであることが解明できた。

サルモネラ属細菌、百日咳菌、緑膿菌、赤痢菌、腸管病原性大腸菌およびO-157に代表される腸管出血性大腸菌など多くのグラム陰性病原細菌は、III型分泌装置（Type 3 secretion system, T3SS）を有している。T3SSは病原菌が宿主に付着し、病原因子を宿主細胞内へ注入させる装置として機能するので、病原性の発揮に必須であるが、病原菌の生育には必須でないことが分かっている。このようにT3SS阻害物質は病原菌の生育に影響を与えず、その感染過程のみを阻害するので、薬剤耐性菌の出現、毒素の大量放出、正常細菌叢の攪乱などを引き起こさない新しい作用メカニズムの感染症治療薬となることが期待される。そこでT3SS阻害物質の探索研究を行った結果、抗生物質aurodoxが抗菌活性を示す濃度よりはるかに低い濃度でT3SSを阻害することを見いだした⁵⁾。さらにaurodoxはT3SS関連タンパク質の転写を抑制しており、感染治療効果も示した。

1) *PNAS* **98**, 60 (2000); 2) *Tetrahedron* **67**, 6582 (2011); 3) *Tetrahedron* **67**, 6644 (2011); 4) *J. Antibiot.* **65**, 527 (2012); 5) *J. Antibiot.* **64**, 197 (2011).

略 歴

氏 名	しおみ かずろう 塩見 和朗
生年月日	1954年5月15日
所属機関	北里大学大学院感染制御科学府・北里生命科学研究so生物機能研究室

学 歴

1979年3月	東京大学農学部農芸化学科卒業
1988年2月	農学博士（東京大学）

職 歴

1979年4月	寶酒造(株)中央研究所 研究員
1980年10月	(財)微生物化学研究会付属微生物化学研究所 客員研究員
1990年4月	寶酒造(株) 退職
1990年5月	(社)北里研究所微生物薬品化学部 研究員
1991年4月	(社)北里研究所生物機能研究所天然物化学研究室 室長代理
1997年4月	(社)北里研究所生物機能研究所天然物化学研究室 室長
2001年4月	北里大学北里生命科学研究so 助教授
2002年4月	北里大学薬学部微生物薬品製造学教室 助教授
2005年11月	北里大学大学院感染制御科学府・北里生命科学研究so生物機能研究室 教授

現在に至る

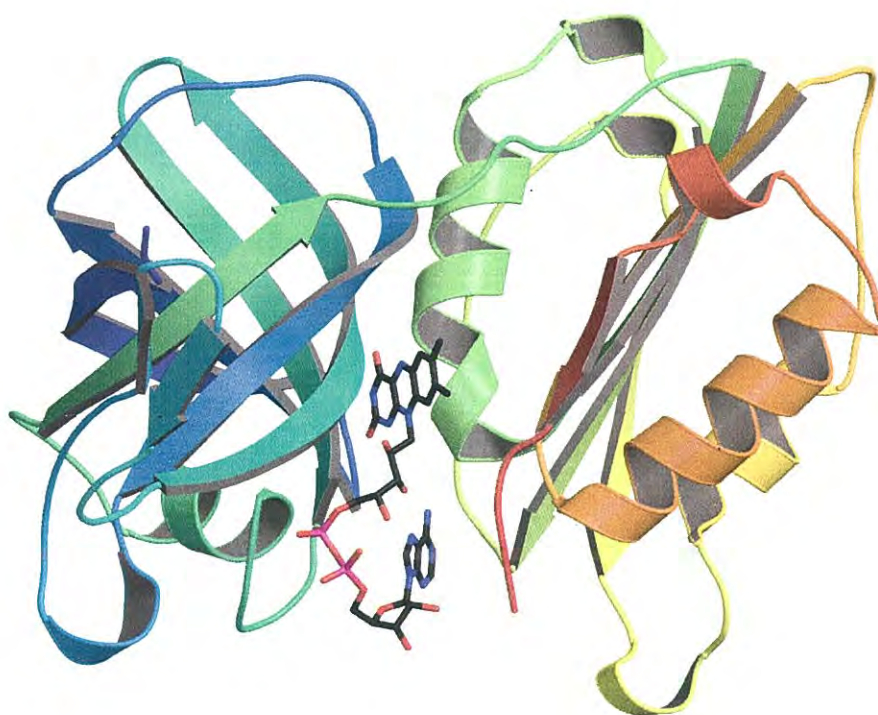
賞 罰

2005年	2005年度住木・梅澤記念賞
-------	----------------

大阪薬科大学

文部科学省私立大学戦略的研究基盤形成支援事業
「組織的研究体系による次世代型感染症治療薬の開発」

平成 25 年度公開シンポジウム



平成 25 年 12 月 7 日



主催 大阪薬科大学
協賛 社団法人 日本薬学会
社団法人 日本化学会
社団法人 日本生化学会

大阪薬科大学

ご挨拶

大阪薬科大学では、平成 23 年度に文部科学省の私立大学戦略的研究基盤形成支援事業として採択されました「組織的研究体系による次世代型感染症治療薬の開発」と題したプロジェクト研究を推進しているところであり、平成 25 年度で 3 年目の節目を迎えます。

本年度の第 3 回シンポジウムでは、我々のプロジェクトのこれまでの研究成果を報告するとともに、今回のシンポジウムに相応しい先駆的な研究を展開されておられる研究者を学外からお招きしております。

大阪薬科大学大学院薬科学専攻博士前期課程は、分子構造・機能解析学領域、創薬化学領域、および生命・環境科学領域の 3 領域から、博士後期課程は分子構造・機能解析学領域および創薬化学領域の 2 領域から構成されています。我々の研究プロジェクトチームは、分子構造・機能解析学領域に属する薬品物理化学研究室、生化学研究室、薬品分析化学研究室、微生物学研究室および中央機器研究施設の教員から構成されており、これらの研究室および施設の全教員が目的を達成するための具体的な研究課題に取り組み、効率的に研究を遂行する体制をとっています。

第 3 回シンポジウムでは、大阪大学 微生物病研究所 分子細菌学分野の堀口安彦先生に「なぜ百日咳菌はヒトだけに感染して激しい咳発作を起こすのか？その基礎細菌学的アプローチ」を、大阪大学 産業科学研究所 生体防御学研究分野の山口明人先生に「多剤排出トランスポーターによる多剤排出機構とその阻害の構造的基礎」をテーマにそれぞれご講演をさせていただきます。本学からは河野広朗先生と佐藤卓史先生にそれぞれ「病原細菌 *Vibrio vulnificus* の宿主生体内における生存戦略」および「次世代型感染症治療薬開発への生物無機化学的アプローチ」についてご講演いただきます。各ご講演では、独創的な研究展開によって得られた成果についてご披露いただけるものと考えています。また、これらのご講演は、本プロジェクトにおける今後の研究の方向性について、貴重な示唆を与えていただけるものと信じております。皆様方により活発な討論がなされることを期待しております。

なお、シンポジウム終了後、ささやかな懇親会を予定しております。本プロジェクト研究の今後の展開についてご歓談いただけると幸いです。

研究代表者 辻坊 裕

平成 25 年度公開シンポジウム

日 時 : 平成 25 年 12 月 7 日 (土) 12 : 50 ~
会 場 : 大阪薬科大学・D304 教室 (入場無料)

文部科学省私立大学戦略的研究基盤形成支援事業
「組織的研究体系による次世代型感染症治療薬の開発」
第 3 回シンポジウム

《 プログラム 》

- 12 : 50 ~ 13 : 00 挨拶 研究代表者 辻坊 裕
- 13 : 00 ~ 13 : 30 河野 広朗 博士 (大阪薬科大学 博士研究員)
「病原細菌 *Vibrio vulnificus* の宿主生体内における生存戦略」
座長 井上 晴嗣
- 13 : 30 ~ 14 : 00 佐藤 卓史 講師 (大阪薬科大学 薬品分析化学研究室)
「次世代型感染症治療薬開発への生物無機化学的アプローチ」
座長 箕浦 克彦
- 14 : 00 ~ 14 : 50 ポスターセッション
- 15 : 00 ~ 16 : 00 堀口 安彦 教授 (大阪大学 微生物病研究所 分子細菌学分野)
「なぜ百日咳菌はヒトだけに感染して激しい咳発作を起こすの
か? その基礎細菌学的アプローチ」
座長 福永 理己郎
- 16 : 00 ~ 17 : 00 山口 明人 特任教授 (大阪大学 産業科学研究所 生体防御学研究分野)
「多剤排出トランスポーターによる多剤排出機構とその阻害の
構造的基礎」
座長 辻坊 裕
- 17 : 10 ~ 懇親会 (無料) 司会 友尾 幸司

講演要旨

病原細菌 *Vibrio vulnificus* の宿主生体内における生存戦略

大阪薬科大学戦略的研究基盤形成支援事業 博士研究員 河野広朗

【緒言】

当プロジェクトでは、臨床分離株 *Vibrio vulnificus* M2799 株の鉄欠乏ストレスに関するタンパク質群を網羅的に明らかにする目的で研究を行っている。*V. vulnificus* は、汚染された魚介類の摂食や海水の創傷部曝露等を介して、全身性の感染症を引き起こす細菌である。一般に、鉄はほとんどの生物の生存と増殖に不可欠な元素であるが、宿主生体内において病原菌が自由に利用できる遊離鉄は極めて少ない。したがって、宿主生体内で増殖し得る病原菌は、何らかの巧妙な鉄獲得系を保持しているはずである。そこで、臨床分離株 *V. vulnificus* M2799 株の鉄獲得系タンパク質を網羅的に明らかにする目的で、プロテオーム解析を行った。その結果、対数増殖前期、中期、後期に発現差異が認められたタンパク質のうち、それぞれ 18、31、26 種類のタンパク質を同定し、KEGG に基づいて分類を行った¹。それらタンパク質遺伝子を、suicide vector である pKTN701 に連結して相同組換えにより挿入変異株を作製し、鉄欠乏下における増殖能について検討した。その結果、 Δ FeADH (VV2_0211) 株、 Δ VuuA (VV2_0843) 株、 Δ FatB (VV2_0842) 株、 Δ VuuB (VV2_0837) 株、 Δ ICS (VV2_0835) 株、および Δ VV2_1400 株は、鉄欠乏下において増殖能が顕著に抑制された。そこで、これら遺伝子の機能をより詳細に明らかにすること及び多重変異株の作製を目的として、M2799 株の遺伝子欠失株作製法を確立した。

【方法】

遺伝子欠失株の作製は、suicide vector pDM4 を用いて行った。まず、ターゲット遺伝子内欠失目的領域の上下流域それぞれ 500 bp を PCR で増幅し、これらをライゲーションで連結後、PCR を行い増幅した。増幅した DNA を pDM4 に連結し、大腸菌 SY327 λ pir 株を形質転換した。得られた組換えプラスミドを用いて、*V. vulnificus* 細胞に対する遺伝子伝達能を有する大腸菌 SM10 λ pir 株を形質転換した。得られた SM10 λ pir 株と M2799 株をそれぞれ培養し、メンブレンフィルター上で接合させることでプラスミドの伝達を行わせて 1 回目の相同組換えを誘発した。得られた相同組換え体を 15% スクロース、100 units/ml ポリミキシン B 含有 LB 寒天培地に塗抹し、増殖したコロニーのクロラムフェニコール感受性を確認した。

【結果および考察】

今回、増殖能が顕著に抑制された挿入変異株のうち、本菌株の産生するシデロフォアである vulnibactin を介する鉄取り込み機構に関与する遺伝子欠損株の作製を試みた。すなわち、ICS、VuuB、Vulnibactin-Fe³⁺ 複合体の外膜レセプター (VuuA)、および Vulnibactin-Fe³⁺ 複合体のペリプラズム結合タンパク質 (FatB) について作製した。これら欠失株の鉄欠乏下における増殖能について検討したところ、ICS および VuuA 遺伝子欠失株では顕著に抑制されたが、VuuB および FatB 遺伝子欠失株においては遅いながらも増殖が確認された。本結果から、これらの代替タンパク質の存在が示唆された。そこで、

ゲノム情報が明らかにされている *V. vulnificus* CMCP6 株において FatB ホモログを探索した結果、Aerobactin-Fe³⁺複合体のペリプラズム結合タンパク質 (VatD) と 17% の相同性が認められた。VatD 遺伝子欠損株、および FatB と VatD の二重遺伝子欠損株を作製し、鉄欠乏下における増殖能について検討した結果、VatD 遺伝子欠損株は野生株とほぼ同様の増殖能を示したが、二重欠損株では FatB 遺伝子欠損株よりもさらに増殖が抑えられた²。以上のことから、Vulnibactin-Fe³⁺複合体のペリプラズム結合タンパク質は FatB が中心となって機能するが、VatD で代替可能であることが推測された。

次に、M2799 株における Vulnibactin 分泌機構に関与するタンパク質遺伝子について検討した。大腸菌において、Enterobactin の分泌に外膜チャネルタンパク質 TolC が関与することが明らかにされており³、TolC を外膜チャネルとする resistance nodulation cell division (RND) 型排出システムが分泌に関与すると推測されている。そこで、M2799 株における TolC ホモログを探索した結果、VV1_0612 及び VV2_1007 を見出した。そこで、これら遺伝子の欠損株を作製し、鉄欠乏下での増殖能について検討したところ、VV1_0612 タンパク質遺伝子欠損株の鉄欠乏下での生育が、顕著に抑制された。以上のことから、*V. vulnificus* M2799 株において、VV1_0612 タンパク質が TolC であると推測した。現在、VV1_0612 タンパク質と協調して機能する RND 内膜タンパク質を探索している。

【参考文献】

1. Miyamoto K, Kosakai K, Ikebayashi S, Tsuchiya T, Yamamoto S, Tsujibo H. (2009) Proteomic analysis of *Vibrio vulnificus* M2799 grown under iron-repleted and iron-depleted conditions. *Microb. Pathog.* 46:171-7.
2. Kawano H, Miyamoto K, Sakaguchi I, Myojin T, Moriwaki M, Tsuchiya T, Tanabe T, Yamamoto S, Tsujibo H. (2013) Role of periplasmic binding proteins, FatB and VatD, in the vulnibactin utilization system of *Vibrio vulnificus* M2799. *Microb. Pathog.* 65:73-81
3. Bleuel C, Grosse C, Taudte N, Scherer J, Wesenberg D, Krauss GJ, Nies DH, Grass G. (2005) TolC is involved in enterobactin efflux across the outer membrane of *Escherichia coli*. *J Bacteriol* 187:6701-7.

略 歴

氏 名 かわの ひろあき
河 野 広 朗
生年月日 1977年8月27日
所属機関 大阪薬科大学戦略的研究基盤形成支援事業

学 歴

2000年3月 東洋大学工学部応用化学科卒業
2002年3月 東洋大学大学院工学研究科博士前期課程修了
2005年3月 博士（工学）東洋大学より

職 歴

2002年4月 独立行政法人海洋研究開発機構極限環境生物圏研究センター 研究推進スタッフ
2005年4月 日本大学歯学部 日本大学助手
2006年11月 協和発酵キリン株式会社フロンティア研究所 研究員
2009年7月 長崎大学大学院医歯薬学総合研究科 助教
2012年4月 大阪薬科大学戦略的研究基盤形成支援事業 博士研究員
現在に至る

受 賞

2004年12月 第4回極限環境生物学会ポスター賞
2005年12月 第5回極限環境生物学会ポスター賞

次世代型感染症治療薬開発への生物無機化学的アプローチ

大阪薬科大学 佐藤卓史

地球上に生命が誕生して 35 億年が経つ。その間、大気、水、土壌などの環境に取り囲まれてきた。これらの環境は極わずかの有機物を含む物のその大部分が無機物で成り立っている。つまり、生物は極めて長い期間、無機環境に曝されてきた。多くの無機物は、生命にとっては、生命の維持にとって危険な存在であった。しかし、生命はしたたかであり、当初は毒物であった酸素をはじめとする無機物を長い年月を掛けて、取捨選択し、逆にうまく利用することで、より効率的で複雑な生命活動を営めるように進化していった。現在では、100 種ほどの元素のうち約 3 分の 1 の元素を利用している。ただ、それらを利用し始めると逆に依存性が高まり、それら 抜きには生命を維持できなくなって行った。これらの元素が現在、必須元素といわれているものである。それらの必須元素のうち、ほぼ全ての生物に必須であり、様々な機能をもつものに鉄がある。鉄はヒトの体内に最も多く含まれる遷移金属である。鉄は生体内での酵素の活性中心に存在して化学反応の場やヘモグロビンのヘムに存在してガス交換の場を提供している。また、DNA の合成に関わるリボヌクレオチド・リダクターゼの活性発現には Fe^{2+} イオンが必要であり、これはヒトだけでなく微生物においても同様で、そのため、鉄がなければ微生物も増殖できない。この生命にとって重要な鉄の酸化数の主たるものは、0、+2 および +3 であり、そのイオンである Fe^{2+} および Fe^{3+} は相互に容易に変換される。この性質が生命にとって重要な役割を果たす大きな要因になっている。現在のヒトの生活環境における酸化的雰囲気下では、 $\text{Fe}^{2+} \rightarrow \text{Fe}^{3+} + e^-$ の方向に反応が進みやすい。一般に Fe^{3+} イオンといわれる $[\text{hexaaquairon(III)}]^{3+}$ は $[\text{hexaaquairon(II)}]^{2+}$ に比べてはるかに不安定で、容易に加水分解してアコ配位子が水酸化物イオンに置換されて電荷を失い、 $\text{trihydroxotriaquairon(III)}$ となり沈殿する。そのため、一般的な水環境における鉄の濃度は低い。ましてや生体内では、鉄はトランスフェリンなどと結合して貯蔵・運搬されているため、その鉄濃度はさらに低い。一方、このような低鉄濃度下で成育する微生物は、宿主のトランスフェリン、フェリチン、ヘムなどの結合している鉄を奪って細胞に供給するシステムをもっている。この鉄を捕捉するために細胞外に分泌される低分子化合物はシデロフォア(siderophore) と総称されている。シデロフォアには多くのものが知られているが、ヒドロキサム酸型とカテコール型の 2 種類に大別される。シデロフォアの鉄に対する結合力は著しく強い。

本プロジェクトにおいては、次世代型の感染症治療薬の開発を目指しているが、最初のターゲットとして、*Vibrio vulnificus* を選んだ。この細菌は、汚染された魚介類の摂食や海水の創傷部曝露等を介して感染し、本来、低鉄濃度環境である血中で爆発的に増殖する。一旦、感染症が成立すると従来型の抗生物質はほぼ無効であり、極めて高い致死率を示す。また、*V. vulnificus* は鉄欠乏下では、*vulnibactin* といわれるカテコール型のシデロフォアを産生する。そこで、この *V. vulnificus* の鉄獲得機構を標的とする新たなタイプの感染症治療薬の開発を計画した。本計画は、様々な知識や技能を有する研究者が集

って、それらが組織的研究体系をくみ上げることで、効率的な研究を行っており、先の標的に対しても、個々の専門領域からのアプローチを行い、その知見を体系的に積み上げ、協力することを主眼としている。そこで、*V. vulnificus*の鉄獲得機構を標的とする次世代型感染症治療薬開発のための当初のアプローチとして、vulnibactinの生合成系や外膜レセプターを介したvulnibactin-Fe(III)取り込み系、細胞内での細胞内のvulnibactin-Fe(III)分解と鉄の取り出し系等の機能性タンパク質の機能を阻害する物質の設計や阻害物質の設計は主に、本プロジェクトに参画している微生物学研究室、生化学研究室、物理化学研究室が中心に、生化学的、構造化学的アプローチを行うこととしている。一方、演者らの薬品分析化学研究室が中心となって、vulnibactinとFe³⁺の結合阻害、vulnibactin-Fe(III)の細胞内輸送機構を介した増殖抑制、*V. vulnificus*の鉄利用の抑制等に関して、生物無機化学的なアプローチを試みている。

本研究では、我々の行うvulnibactinとFe³⁺の結合阻害およびvulnibactinとFe³⁺の結合阻害、さらに、生化学的、構造化学的アプローチにおいてもvulnibactinを安定して入手することが必要なため、その単離・精製法の確立を目指した。鉄欠乏下で*V. vulnificus*を培養し、その培養上清をXAD-7樹脂を用いた吸着クロマトグラフィーで分離後、Cosmosil 5C18 Ar-IIセミ分取カラムを用いたHPLCにより分取することで、vulnibactinの単離に成功した。単離の確認は¹H-NMRおよびFAB-MSにより確認した。本法で培養上清1 Lから0.1~0.6 mgの収量でvulnibactinを得られるようになった。

次いで、vulnibactinとFe³⁺の結合を阻害する物質、あるいは、vulnibactin-Fe(III)からFe³⁺を奪い得る物質を探索するための評価系の構築を検討した。

さらに、入手可能な合成キレート剤等について、*V. vulnificus*の増殖抑制能を検討した。

今後、生物無機化学的見地に基づいて、vulnibactinとFe³⁺の結合を阻害する可能性のある化合物の合成をおこなっており、それらについても発表する予定である。

略 歴

氏 名	さとう たかし 佐 藤 卓 史
生年月日	1963年5月28日
所属機関	大阪薬科大学講師 (薬品分析化学研究室)

学 歴

1990年3月	大阪薬科大学大学院薬学研究科博士前期課程修了
2008年1月	博士 (薬学) 大阪薬科大学より

職 歴

1992年8月	大阪薬科大学 助手
2007年4月	大阪薬科大学 助教
2009年4月	大阪薬科大学 講師
	現在に至る

賞 罰

なし

なぜ百日咳菌はヒトだけに感染して激しい咳発作を起こすのか？ その基礎細菌学的アプローチ

大阪大学微生物病研究所 分子細菌学分野 堀口安彦

百日咳は百日咳菌 (*Bordetella pertussis*) の上部気道感染によって起こる伝染性の疾病である。患者は本症で特徴的な咳発作 (咳嗽) により無呼吸状態に陥るため、チアノーゼや痙攣さらには脳症を起こし、重篤な場合は死に至る。WHOによると、本疾患により毎年世界で約20万人-30万人が死亡している。主に発展途上国での乳幼児感染が最も問題視されているが、先進国においても乳幼児期に接種したワクチン効果の減弱した青年期の感染や、ワクチン成分と抗原性の異なる抗原変異株の出現で罹患者数が増加しており、いわゆる再興感染症の一つに挙げられている。百日咳は古くから知られた病気であるが、その感染成立機構はほとんどわかっていない。この事実は抗原変異株の蔓延が憂慮されている将来に、大きな不安材料を与えている。また、百日咳で見られる発作性咳嗽は患者に多大な負荷を強い、ときに死因に直結するが、その発症機構も不明である。そのため、臨床現場では発作性咳嗽には対症療法を持って処置せざるを得ないのが現状である。さらに基礎細菌学の立場からみた時に、「百日咳はヒトにしか感染しない」という基本的な疑問も目前に横たわる。そこで、本講演では「なぜ百日咳は激しい咳を起こすのか？」と併せて、その解明に迫るための当研究室でのアプローチを紹介したい。

百日咳菌が分類されるボルデテラ属には気管支敗血症菌やパラ百日咳菌といった、いずれも百日咳菌と同じく宿主の上部気道に感染して咳発作を起こす病原細菌がある。全ゲノム配列の解析結果から、これらの3菌種は遺伝学的にきわめて近縁で、主要病原因子は菌種間でほとんど全て共有され、かつその他の共有する遺伝子の相同性も高いことが明らかになっている。しかし、3菌種それぞれの宿主特異性や感染病態は明らかに異なる。百日咳菌はヒトのみを自然宿主として急性の激しい咳発作を起こすのに対し、パラ百日咳菌はヒトあるいはヒツジに急性もしくは亜急性の感染をおこし、気管支敗血症菌は多くの哺乳動物に慢性的に感染する。また、全ゲノム配列解析の結果から、両菌の祖先種は気管支敗血症菌に近く、そこから多数の遺伝子の転移と欠失が繰り返されて百日咳菌が系統分化したと推定されている。百日咳菌で特異的に獲得された明らかな遺伝子領域はみられない。すなわち遺伝子数とゲノムサイズからみて、3菌種の関係は明確に 気管支敗血症菌 > パラ百日咳菌 > 百日咳菌 であることがわかっている。そして興味深いことに、宿主特異性の広狭をみても3菌種は 気管支敗血症菌 > パラ百日咳菌 > 百日咳菌 の関係なのである。すなわち、気管支敗血症菌遺伝子から百日咳菌遺伝子を差し引いた気管支敗血症菌特異的な遺伝子の中に、本菌の広い宿主特異性を許容するのに関係する遺伝子が存在すると考えた。

冒頭で、百日咳の感染・発症機構はいまだ不明であると述べた。その理由のひとつに、百日咳菌がヒトに特化した病原細菌であるために、感染動物モデルを確立し難いという問題が挙げられる。現在のところ、マウスへの大量菌投与の実験系が最も広く利用され、感染病態の解析が進められている。しかし、1) 自然環境ではあり得ない大量の菌数が感染成立に必要である、2) マウスの上部気道には求心性神経が分布していないため咳発作 (咳反射) はそもそもマウスでは起こらない、3) そのため感染度の軽重を肺の炎症度と個体の生死で判定するが、通常の百日咳感染では肺の炎症まで進行するものは稀であり、また感染が直接原因となって患者が死ぬこともない。すなわち、百日咳のマウ

モデルは実験の便宜上作製されたものであり、実際の百日咳感染を再現するものではない。このため、マウスモデルを用いた解析結果を百日咳の感染病態の理解に結びつけることは非常に難しいと、私たちは考えている。

そこで、気管支敗血症菌と種々の動物の組み合わせで、改めて本菌の感染実験スクリーニングを行った結果、少ない投与菌数で一定期間の感染が成立しかつ咳嗽を再現する、という条件を満たす感染動物モデルを作製することに私たちは成功し、さらに咳嗽発作の定量化観察の方法を考案した。この動物モデルでは、多量の百日咳菌による感染においても同様の咳嗽発作が見られることも確認している（ただし感染の維持はできない）。この動物モデルを用いて、感染と咳発作の関連性を調べていたところ、私たちは偶発的に、感染は成立するが宿主の咳嗽発作を起こさない自発性変異株を分離した。この事実は、咳嗽発作発症には特定の（おそらく少数か単一の）遺伝子が関与していること、菌の定着増殖と咳嗽発作の発症は無関係であることを意味している。

以上のような状況において、当研究室ではそれぞれの疑問に対して実験的アプローチを展開している。本講演ではそれぞれについて最新で未発表の研究成果をお話したい。

略 歴

氏 名	ほりぐち やすひこ 堀 口 安 彦
生年月日	1959年10月28日
所属機関	大阪大学微生物病研究所 感染機構研究部門 分子細菌学分野

学 歴

1982年 3月	大阪府立大学農学部獣医学科卒業
1984年 3月	大阪府立大学大学院農学研究科博士前期課程修了
1987年 3月	大阪府立大学大学院農学研究科博士後期課程修了
1987年 3月	農学博士
1990年 6月	大阪大学微生物病研究所研究生

職 歴

1987年 4月	社団法人 北里研究所 研究員
1992年 4月	大阪大学微生物病研究所 助手
1998年 8月	大阪大学微生物病研究所 堀口毒素プロジェクト助教授
2001年 4月	大阪大学微生物病研究所 教授
	現在に至る

受 賞

1996年 3月	平成7年度黒屋奨学賞受賞
----------	--------------

多剤排出トランスポーターによる多剤排出機構と その阻害の構造的基礎

大阪大学産業科学研究所 生体防御学研究分野 山口明人

異物（多剤）排出タンパクは、細菌から高等生物までほとんど全ての細胞に内在する基本的な生体防御装置である。しかし、その過剰発現は多剤耐性を引き起こし、がんや細菌感染症の化学療法における脅威となっている。臨床的に有効な治療薬がほとんど無い多剤耐性緑膿菌（MDRP）においても、RND型異物排出タンパク MexB、MexYの過剰発現が見られ、その阻害剤と抗菌剤の併用により抗MDRP効果が見られるとの報告があるが、阻害剤の実用化には至っていない。

私達は10年前に世界で初めて、大腸菌のRND型異物排出タンパクAcrBの結晶構造決定に成功し¹⁾、以後、薬物結合構造、阻害剤結合構造などの決定を通じて、異物排出輸送機構の解明を進めてきた。また、MexY、MexBとともに阻害する新しいユニバーサル阻害剤の蛋白構造に基づく創薬（SBDD）を進めている。

よく知られているように、異物排出タンパクの最大の特徴は、その非常に広範な排出スペクトルである。排出される基質は薬物・毒物に留まらず、界面活性剤や色素、細菌毒素や老廃物から細胞間情報分子にまで及ぶ。化学構造的には芳香族、脂肪族両方を含み、共通性は見出しがたい。私達は2002年のAcrB構造決定により、異物排出タンパクは脂質二重層表層から基質を取り入れる細胞膜の掃除機（membrane vacuum cleaner）であることを示した¹⁾。その後、他のグループによってなされたABC型異物排出タンパクの構造決定によっても、基質は脂質二重層表層から排出される構造になっていることが証明されている。すなわち、異物は一般に脂質二重層を通過して細胞内に侵入する経路を採る事が多いことから、このメカニズムにより異物を区別するとともに、効率的に水際排除する普遍的な機構となっていると考えられる。

その後、2006年に薬物結合構造を決定し²⁾、ホモ3量体の3つのモノマーが待機、結合、排出という別のコンホメーションを取っていて、順繰りに構造変化することにより基質を排出するという機能的回転輸送モデルを提出した。また、多剤の認識については、マルチサイト結合が基礎にあることを明らかにした。さらに、2011年、大分子量薬物との結合構造を決定し³⁾、マルチサイト結合ポケットが2つあること。基質はこの2つのポケットをタンパク質の蠕動運動によって送られていき、最終的に排出されるペリスタポンプ機構を明らかにした。

さらに、初めてAcrBとMexB双方の阻害剤ピリドピリミジン（ABI-PP）との結合構造決定にも成功し、阻害剤結合ピットを発見した⁴⁾。MexYの対応部位との比較により、ABI-PPがMexYを阻害できない構造的理由がわかり、現在その情報を元にMexYを阻害する化合物を分子設計している。

References

- 1) Murakami et al. *Nature* **419**, 587-593 (2002).
- 2) Murakami et al. *Nature* **443**, 173-179 (2006).
- 3) Nakashima et al. *Nature* **480**, 565-569 (2011)
- 4) Nakashima et al. *Nature* **500**, 102-106 (2013)

略 歴

氏名 やまぐち あきひと
山口 明 人
生年月日 1948年6月25日
所属機関 大阪大学産業科学研究所生体防御学研究分野

学 歴

1972年 東京大学理学部生物化学科卒業
1974年 東京大学大学院薬学系研究科修士課程修了
1977年 東京大学大学院薬学系研究科博士課程修了

職 歴

1977-78 理化学研究所流動研究員
1978-81 千葉大学助手 (生物活性研究所)
1980-81 米国イェール大学博士研究員 (化学部)
1981-83 千葉大学助手 (薬学部)
1983-86 千葉大学講師 (薬学部)
1986-96 千葉大学助教授 (薬学部)
1996- 現在 大阪大学教授 (産業科学研究所)
2013年3月 大阪大学を定年退職 名誉教授
2013- 大阪大学産業科学研究所特任教授 (生体防御学研究分野) CRESTプロジェクトを主宰

受 賞

1993年 日本薬学会奨励賞
2008年 日本細菌学会浅川賞
2008年 日本薬学会賞
2011年 文部科学大臣表彰科学技術賞

ポスター発表要旨

平成 25 年度ポスターセッション目次

- (1) 「*Vibrio vulnificus* M2799 株の鉄獲得機構の解明」
宮本勝城、河野広朗、土屋孝弘、辻坊 裕1
- (2) 「Bam 複合体を標的とした新規抗菌物質の開発」
土屋孝弘、宮本勝城、辻坊 裕2
- (3) 「好熱性放線菌由来キシロオリゴ糖加水分解酵素 Bx1A の構造機能解析」
友尾幸司、尹 康子3
- (4) 「VQIVYK 配列中の CH- π 相互作用がタウの分子会合に与える影響」
箕浦克彦、友尾幸司、尹 康子4
- (5) 「LRG と Cyt c の相互作用」
井上晴嗣、藤井 忍、福永理己郎5
- (6) 「イソコリスミン酸合成酵素の大腸菌による発現とコリスミン酸の調製」
藤井 忍、井上晴嗣、福永理己郎6
- (7) 「*Vibrio vulnificus* が産生するシデロフォア・vulnibactin の単離・精製
および vulnibactin と競合して Fe³⁺ と結合する物質の探索法の確立」
三野芳紀、東 剛志、佐藤卓史7
- (8) 「シスプラチン耐性がん細胞に有効な新規白金(II)二核錯体が培養細胞
および DNA に与える影響」
佐藤卓史、東 剛志、三野芳紀8
- (9) 「鉄-過酸化水素混合試薬による医薬品の分解」
東 剛志、佐藤卓史、三野芳紀9

大阪薬科大学文部科学省私立大学戦略的研究基盤形成支援事業平成25年度研究報告書
「組織的研究体系による次世代型感染症治療薬の開発」

研究課題名	<i>Vibrio vulnificus</i> M2799 株の鉄獲得機構の解明
研究者名	宮本勝城、河野広朗、土屋孝弘、辻坊 裕

研究経過・成果の概要

【研究目的】

当研究室では、臨床分離株 *Vibrio vulnificus* M2799 株の鉄欠乏ストレスに関与するタンパク質群を網羅的に明らかにする目的で研究を行っている。*V. vulnificus* は、汚染された魚介類の摂食や海水の創傷部曝露等を介して、全身性の感染症を引き起こす細菌である。一般に、鉄はほとんどの生物の生存と増殖に不可欠な元素であるが、宿主生体内において病原菌が自由に利用できる遊離鉄は極めて少ない。したがって、宿主生体内で増殖し得る病原菌は、何らかの巧妙な鉄獲得系を保持しているはずである。そこで、臨床分離株 *V. vulnificus* M2799 株の鉄獲得系タンパク質を網羅的に明らかにする目的で、プロテオーム解析を行った。その結果、対数増殖前期、中期、後期に発現差異が認められたタンパク質のうち、それぞれ 18、31、26 種類のタンパク質を同定し、KEGG に基づいて分類を行った。次に、相同組換えによりそれらタンパク質遺伝子の挿入変異株を作製し、鉄欠乏下における増殖能について検討した。その結果、 Δ FeADH (VV2_0211) 株、 Δ VuuA (VV2_0843) 株、 Δ FatB (VV2_0842) 株、 Δ VuuB (VV2_0837) 株、 Δ ICS (VV2_0835) 株、および Δ VV2_1400 株は、鉄欠乏下において増殖能が顕著に抑制された。そこで今回、これら遺伝子産物の機能を明らかにする目的で、高発現系を構築した。また、多重変異株の作製を目的として、M2799 株の遺伝子欠損株作製法を確立した。

【結果および考察】

今回、増殖能が顕著に抑制された挿入変異株のうち、イソコリスミン酸合成酵素(ICS)およびVulnibactin-Fe³⁺複合体を基質とする鉄還元酵素(VuuB)タンパク質の高発現系を構築した。その結果、ICSタンパク質は封入体を形成したが、VuuBタンパク質は可溶化で発現した。そこで、本タンパク質をNi-Sepharose 6FFおよびHiLoad Superdex 75pgクロマトグラフィーにより、電気泳動的に均一にまで精製した。現在、本タンパク質の諸性質を明らかにし、構造解析を行っている。

次に、増殖能が顕著に抑制された挿入変異株のうち、ICS、VuuB、Vulnibactin-Fe³⁺複合体の外膜レセプター(VuuA)、およびVulnibactin-Fe³⁺複合体のペリプラズム結合タンパク質(FatB)について作製した。これら欠失株の鉄欠乏下における増殖能について検討したところ、ICSおよびVuuA遺伝子欠失株では顕著に抑制されたが、VuuBおよびFatB遺伝子欠失株においては遅いながらも増殖が確認された。本結果から、これらの代替タンパク質の存在が示唆された。そこで、ゲノム情報が明らかにされている *V. vulnificus* CMCP6 株においてFatBホモログを探索した結果、Aerobactin-Fe³⁺複合体のペリプラズム結合タンパク質(VatD)と17%の相同性が認められた。VatD遺伝子欠損株、およびFatBとVatDの二重遺伝子欠損株を作製し、鉄欠乏下における増殖能について検討した結果、VatD遺伝子欠失株は野生株とほぼ同様の増殖能を示したが、二重欠失株ではFatB遺伝子欠失株よりもさらに増殖が抑えられた。以上のことから、Vulnibactin-Fe³⁺複合体のペリプラズム結合タンパク質はFatBが中心となって機能するが、VatDで代替可能であることが推測された。

研究課題名	Bam 複合体を標的とした新規抗菌物質の開発
研究者名	土屋孝弘, 宮本勝城, 辻坊 裕.

研究経過・成果の概要

【目的】

グラム陰性細菌の外膜タンパク質の多くは、 β -バレル構造をもつタンパク質である。外膜タンパク質には薬剤排出ポンプなど様々なトランスポーターが含まれており、それらは薬剤耐性やバイオフィーム形成に必須であるため、創薬のターゲットとして注目されている。これらの外膜タンパク質のフォールディングや外膜への挿入には β -barrel assembly machinery (Bam) 複合体が重要な役割を担っている。Bam 複合体は BamA, B, C, D および E から構成されており、BamA のペリプラズム領域である POTRA ドメイン 3 および 5 がそれぞれ BamB と BamD と直接結合している (図)。我々はこの結合を阻害する物質を創製し、*Acinetobacter baumannii* の増殖への影響、抗菌活性、バイオフィーム形成阻害能およびマウスに対する致死活性を調べた。

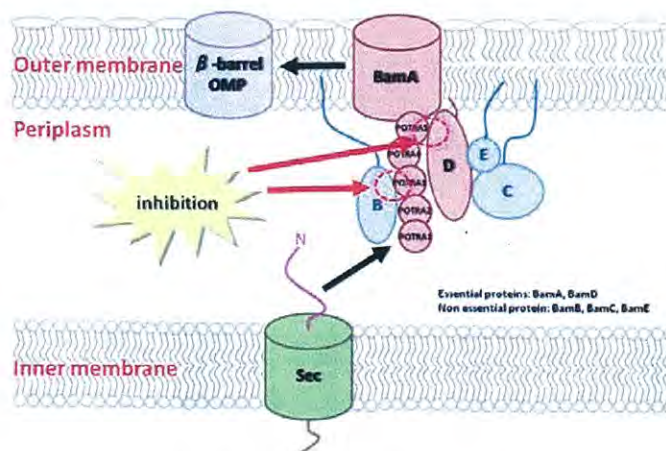


図 外膜タンパク質の膜輸送

【方法】

Acinetobacter baumannii は ATCC19606 株および A112-II-a 株を用い、LB 培地で対数増殖後期まで攪拌培養した。BamA と BamB の結合阻害物質 (K5FS3GN) または BamA と BamD の結合阻害物質 (K5FI2NH) を添加し、各実験を行った。本菌の増殖に及ぼす各阻害物質の影響を 600nm における濁度ならびに生菌数により調べた。バイオフィーム形成能についてはポリスチレンチューブを用いて 24 時間静置培養後、クリスタルバイオレットで染色することにより測定した。マウスに対する致死活性は、抗 Gr1 抗体を前投与した C57BL/6 マウスに本菌と K5FS3GN を経鼻的に投与しその生存率を調べた。

【結果と考察】

BamA と BamB の結合阻害物質 (K5FS3GN) は 10 μ M で本菌の増殖を抑制したが、殺菌活性は認められなかった。また、K5FS3GN はバイオフィームの形成ならびにマウスに対する致死活性を低下させた。BamA と BamD の結合阻害物質 (K5FI2NH) は 5 μ M で本菌の増殖を抑制し、10 μ M で殺菌活性が認められた。これらの結果から、Bam 複合体に対する機能阻害物質は新規抗菌物質として有用であることが明らかとなった。今後は多剤耐性菌に対する評価を行うとともに、より効果的な物質になるよう改良を行う予定である。

大阪薬科大学文部科学省私立大学戦略的研究基盤形成支援事業平成25年度研究報告書
「組織的研究体系による次世代型感染症治療薬の開発」

研究課題名	好熱性放線菌由来キシロオリゴ糖加水分解酵素 Bx1A の構造機能解析
研究者名	友尾幸司、尹 康子

研究経過・成果の概要

好熱性放線菌 *Streptomyces thermoviolaceus* OPC-520 株由来遺伝子中には、キシロオリゴ糖の輸送および分解に関与するタンパク質群を産生する *bx1* オペロンが存在する。その遺伝子産物としては、糖結合タンパク質である Bx1E、2 種類の膜貫通型タンパク質 Bx1F、Bx1G、および細胞内 α -xylosidase である Bx1A が存在する。自然界において、セルロースに次いで再生利用可能な資源として多く存在するキシランは、xylanase によってキシロオリゴ糖に分解される。生成したキシロオリゴ糖は、Bx1E によって Bx1F/Bx1G 複合体に受け渡されて細胞内に運ばれ、細胞内にて Bx1A により xylose にまで加水分解されると考えられているが、これら Bx1 タンパク質群による糖輸送機構の構造化学的な詳細はいまだ明らかになっていない。そこで本研究では、X 線結晶構造解析法を用いて Bx1 タンパク質群の網羅的構造決定に取り組み、本菌におけるキシロオリゴ糖の細胞内輸送機構を原子レベルで明らかにすることを目的としている。

細胞内のキシロオリゴ糖の分解に関わる酵素である Bx1A は、770 アミノ酸残基からなるタンパク質で、Glycoside Hydrolase family 3 (GH3) に分類されている。Bx1A のようなヘミセルロース分解酵素は自然界におけるカーボンサイクルの維持にきわめて重要な役割を担っている。また最近ではパルプ製紙工業における漂白作用やリグノセルロース物質を発酵製品(バイオエタノール)に転換するなどの実用的な使用法の可能性を秘めており関心を集めている。そこで未だ明らかでない Bx1A の酵素触媒機構および立体構造を原子レベルで解明することを目的として、その構造機能解析に取り組んだ。GH3 に属する他の酵素とのアミノ酸配列アライメントより、Bx1A 分子の 286 番目と 316 番目の Asp 残基に着目し、各 Asp 残基を Ala に変換した変異体を作成し、活性発現への影響を調べた。その結果、両変換体は劇的な活性の低下がみられたことから、両残基が Bx1A の活性発現に重要に関与していることが明らかとなった。更に、wild 体については、GST 融合タンパク質として大腸菌の系を用いて大量発現させ、結晶化に成功し、立体構造の決定に至った。構造解析の結果から、活性発現に関わる Asp-286 と Asp-316 の役割には、大きな違いがあることが明らかとなった。各アミノ酸は、当初、活性中心において、求核残基と酸塩基触媒残基の役割をそれぞれ担うと推測していたが、構造解析の結果から、Asp-286 と Glu-509 がそれらの役割を担い、Asp-316 はその活性中心から離れた位置に存在していた。また、Asp-316 の役割は、基質との結合に直接関わるのではなく、活性中心残基である Asp-286 の基質結合における最適な位置に安定化させるという大きく異なった役割を有することが、推測された。

研究課題名	VQIVYK 配列中の CH- π 相互作用がタウの分子会合に与える影響
研究者名	箕浦 克彦、友尾 幸司、尹 康子

研究経過・成果の概要

【緒言】

アルツハイマー型認知症(AD)は、構造異常タンパクの蓄積によって引き起こされる代表的な疾患の一つである。AD患者の脳内では、タウタンパク質が異常自己重合を起こし、PHF (paired helical filaments) と呼ばれる不溶性線維を形成したのち細胞内に蓄積している。PHFの蓄積と認知症状には相関が認められることより、タウの異常自己重合機構の解明に取り組んでいる。PHFの形成には、相同性の高い繰り返し配列で構成された微小管結合部位(MBD)がコアであると考えられている。なかでも3回目の繰り返し配列であるR3 は高い自己重合能を有しているが、特にN末端 6 残基³⁰⁶VQIVYK³¹¹配列はタウの自己重合に極めて重要であると考えられている。我々は、タウのフィラメント形成における³⁰⁶VQIVYK³¹¹配列の重要性について検討し、Tyr残基とIle残基が重要なアミノ酸であることを明らかにした。そこで、両アミノ酸がタウの自己重合にどのように関与しているのかを、主にNMR解析を用いて検討した。

【結果および考察】

フィラメント形成に対する Ile308 と Tyr310 残基の存在意義を明らかにする目的で、さまざまな 4RTau-wild の部位変換体を作成し、それらのフィラメント形性能について、ThS 蛍光強度測定、電子顕微鏡撮影により検討した。その結果、Ile 残基より疎水性の低い残基に置換した 4RTau-I308L や 4RTau-I308T は蛍光強度の低下が認められた。また Tyr 残基と同じ芳香環を有する Phe 残基に置換した Tau-Y310F は 4RTau-wild と同等の蛍光強度を有していた。一方、Tau-I308A や Tau-Y310A は、蛍光強度の上昇を示さなかった。これらの結果は、308 番目の側鎖と 310 番目の芳香環の間に、CH- π 相互作用が形成されている事を示唆している。

次に、Tyr310 と Ile308 側鎖の配向およびCH- π 相互作用に関する構造学的知見を得るために、VQIVYK配列中のIle残基とTyr残基の変換体ペプチドを種々化学合成し、¹H-NMR解析を行った結果、Ileのメチル基とTyrの芳香環プロトンとの間にCH- π 相互作用が形成されていることを明らかにした。この相互作用は、芳香環の電子密度を低下させたVQIVFKペプチドにおけるIle残基の γ CH₃の高磁場シフト変化の低下と、芳香環の電子密度を高くしたVQIVWK ペプチドにおけるIle残基の γ CH₃の高磁場シフト変化の増加よりIle残基の側鎖と芳香環に働く相互作用は、水素結合や疎水力ではなくCH- π 相互作用である事を裏付けている。

次に、R3 配列を有するペプチドおよびその変異体(R3-Y310A, R3-I308A)を化学合成し、それらの TFE 溶液中におけるコンフォメーションについて、NMR および分子動力学計算を用い解析を行った。その結果、R3 に形成されている N 末端配列の両親媒性を保った extended な構造が、2 種の変異体においては崩壊していることが明らかになった。これらのフィラメント形成能を評価した結果、2 種の変異体はフィラメント形成能が消失していることが明らかになった。これらの結果より、R3 の N 末端配列の両親媒性を保った extended な構造がタウの自己重合には重要であり、CH- π 相互作用の存在は、PHF 形成に極めて重要であると考えられる。

研究課題名	LRG と Cyt <i>c</i> の相互作用
研究者名	井上 晴嗣、藤井忍、福永理己郎

研究経過・成果の概要

【緒言】

我々は、機能未知のヒト血清タンパク質であるロイシンリッチ α_2 -グリコプロテイン (LRG) が、インターロイキン 6 刺激により肝臓での発現が促進される急性期タンパク質として働くこと、自己の細胞外シトクロム *c* (Cyt *c*) を内在性リガンドとして非常に強く結合することを明らかにしている。本研究では、大腸菌でヒト Cyt *c* を発現するプラスミド pBTR1 を用いて種々の Cyt *c* 変異体を作製し、これらの変異体と LRG との相互作用を Biacore で測定することにより、LRG による Cyt *c* 認識部位を明らかにすることを目的とした。

【方法】

Cyt *c* の Lys 残基をそれぞれ Ala に置換した pBTR1 変異体を多数作製し、大腸菌で発現させた後、菌体を 0.5% 硫酸アルミニウム存在下で超音波破碎した。変異型 Cyt *c* を含む上清は、CM-Sephadex カラムを用いたイオン交換カラムクロマトグラフィーおよび ResourceRPC カラムを用いた逆相 HPLC によって精製した。次に、ヒト LRG を固定化した CM5 センサーチップをセットした BiacoreT100 装置に、これらの変異型 Cyt *c* (0.6~10nM) をアナライトとして添加し、生じる表面プラズモン共鳴の変化を測定し、1:1 結合モデルで解析した。

【結果および考察】

LRG と Cyt *c* は非常に強く結合し(解離定数は 2-3pM)、K5A, K7A, K22A, K25A, K27A, K39A, K53A, K55A, K86A, K87A, K88A, K99A, K100A の各変異型 Cyt *c* もほぼ同程度の結合を示したが、K8A, K13A, K72A, K73A, K79A では解離定数が大きくなり、結合が低下することがわかった。なかでも K8A は解離定数が 265pM、K72A では 734pM となり、これら 2 つの Lys 残基が Ala に置換することによって 100 倍以上結合が弱くなることがわかった。すなわち Cyt *c* の 8 位、13 位、72 位、73 位、79 位の正電荷が LRG との相互作用に重要であると考えられる。これらの残基は立体構造上では Cyt *c* の露出したヘム *c* を取り囲む位置に存在することがわかった。

研究課題名	イソコリスミン酸合成酵素の大腸菌による発現とコリスミン酸の調製
研究者名	藤井忍、井上晴嗣、福永理己郎

研究経過・成果の概要

【目的】

近年、抗菌薬の乱用などによる多剤耐性菌の発生が問題になっている。そのため、これまでとは異なる作用機序を持つ新規抗菌薬の開発が待ち望まれている。我々のプロジェクトは、敗血症の原因菌である *Vibrio vulnificus* のプロテオーム解析によって、イソコリスミン酸合成酵素 (ICS) 欠損株の増殖が鉄欠乏下で著しく抑制されることを明らかにした。ICS は、コリスミン酸からイソコリスミン酸を産生する酵素であり。イソコリスミン酸は、さらに代謝されてバルニバクチン (総称：シデロフォア) になる。菌体はバルニバクチンを体外へ放出して鉄と結合させて体内に取り込み、生育に必要な鉄を獲得している。ICS 欠損株の増殖抑制はこのような鉄の取り込み阻害に基づくため、ICS を阻害する物質は、新しい作用機序を利用した抗菌薬になり得る。本研究では、ICS 阻害物質の検索のために、ICS の大腸菌による発現系の構築を試みるとともに、ICS の酵素活性測定に必要な基質であるイソコリスミン酸の調製法の確立を行った。

【結果・考察】

Vibrio vulnificus 菌由来 ICS 遺伝子が組み込まれた発現用プラスミド (pProEX HTa) によって形質転換された大腸菌 (BL21(DE3)pLys) を 1mM IPTG で誘導後、20°C で 22 時間振盪培養した。その結果、ICS の発現は確認できたが、その大部分は封入体画分に存在することが明らかになった。今後は、可溶性画分における ICS 活性が存在することの確認や封入体画分からの ICS の再構成を行い、ICS の阻害剤検索に必要な酵素 ICS の入手を目指す。

ICS の阻害剤を検索するためには、ICS の活性測定が必要である。しかし、ICS の基質となるコリスミン酸の市販品は高価で、多量に入手することは困難である。以前、*E. coli* KA12 菌 (表現型は Phe⁻、Tyr⁻、Tet^R、RacA⁻) からのコリスミン酸の調製法が報告されている。そこで、この菌体からのコリスミン酸の調製方法について検討した。

養分を含む培地で *E. coli* KA12 菌を培養することで菌を増殖させ、続いて養分を含まない培地でコリスミン酸を作らせた。培養上清は陰イオンクロマトで分離後、ジクロロメタン洗浄、酢酸エチル抽出を行い、逆相カラムクロマトで分離し凍結乾燥した。この調製方法において、菌を増殖させる温度とコリスミン酸を作らせる温度を検討した結果、前者を 37°C、後者を 27°C で行うことで、最も多量のコリスミン酸を得ることができた。調製したコリスミン酸の構造は ¹H-NMR によって確認し、逆相 HPLC によって分析した。その結果、調製品は、単品であり、その HPLC における保持時間は市販品とほぼ同じであった。

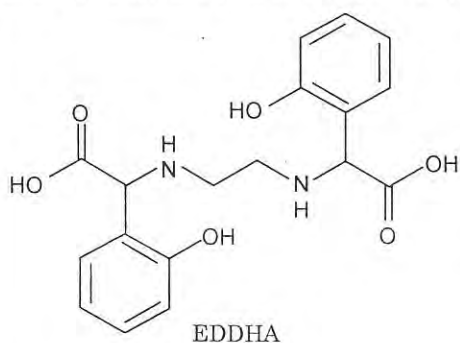
次に、コリスミン酸の溶液中での安定性を確認するため、コリスミン酸を pH7.5 の水溶液に溶解後、4°C または 37°C で 30 時間放置し、HPLC で分析した。その結果、4°C の試料の保持時間は溶解直後の試料と同じであったが、37°C で試料は、コリスミン酸のピークはほぼ消滅していた。この結果から、37°C で酵素活性を測定する場合には、出来る限り短時間での酵素反応の測定にする必要があることがわかった。

研究課題名	<i>Vibrio vulnificus</i> が産生するシデロフォア・vulnibactin の単離・精製および vulnibactin と競合して Fe ³⁺ と結合する物質の探索法の確立
研究者名	三野芳紀、東 剛志、佐藤卓史

研究経過・成果の概要

鉄はヒトの体内に最も多く含まれる遷移金属で、成人男子で4~5g存在している。鉄は、生体内で様々な役割を果たしている必須元素であり、これはヒトだけでなく微生物においても同様である。そのため、鉄がなければ微生物も増殖できない。しかし、現在の環境における酸化的雰囲気下では、比較的水溶性の高いFe²⁺イオンの量は少なく、そのほとんどは3価鉄であり、その大半は水酸化鉄(III)として沈殿している。そのため、微生物は極わずかに存在するFe³⁺イオンを細胞内に取り込む巧妙なシステムをもっている。微生物は、鉄を捕捉するためにシデロフォア(siderophore)と総称されている低分子化合物を細胞外に分泌する。シデロフォアの鉄に対する結合力は著しく強い。病原性微生物もこのシステムを利用して、宿主のトランスフェリン、フェリチン、ヘムなどの結合している鉄を奪って増殖する。本プロジェクトにおいて、次世代型の感染症治療薬の開発のターゲットとしている *Vibrio vulnificus* も汚染された魚介類の摂食や海水の創傷部曝露等を介して感染し、vulnibactinといわれるカテコール型のシデロフォアを産生し、血中で爆発的に増殖する。

そこで、まず、本プロジェクトの研究に不可欠なvulnibactinの単離・精製法の確立を目指した。その結果、鉄欠乏下で *V. vulnificus* を培養し、その培養上清をXAD-7樹脂を用いた吸着クロマトグラフィーで分離後、Cosmosil 5C18 Ar-IIセミ分取カラムを用いたHPLCにより分取することで、vulnibactinの単離に成功した。単離の確認は¹H-NMRおよびFAB-MSにより確認した。本法で培養上清1Lから0.1~0.6mgの収量でvulnibactinを得られるようになった。次いで、vulnibactinとFe³⁺の結合を阻害する物質、あるいは、vulnibactin-Fe(III)からFe³⁺を奪い得る物質を探索するための評価系の構築を検討した。現時点では、評価に用いるのに十分なvulnibactinの入手が不可能なため、入手可能なFe³⁺に対する最強の合成キレーターであるethylenediamine-N,N'-bis(2-hydroxyphenylacetic acid) (EDDHA)を用いた評価系を構築した。方法の概略はエタノールおよび酢酸ナトリウムを含むFe(OH)₃懸濁液にEDDHAを加え、55℃で2時間震蕩した後、上清を取る。その上清に検体溶液を加え、55℃1時間震蕩した後、上清についての吸収スペクトルの測定、あるいはHPLCによる分析を行う。同様に検



体を含まない溶液について同様の操作を行った後、吸収スペクトルを測定、あるいはHPLCによる分析を行う。スペクトル変化あるいはHPLCのピーク値の減少から鉄奪取能を検討する。この評価法によって、EDTA、デスフェリオキサミン、デフェラシクロス、ムギネ酸、クエン酸、トランスフェリン等について、鉄奪取能を検討したところ、ヒドロキサム酸型のシデロフォアであるデスフェリオキサミンにvulnibactin-Fe(III)からFe³⁺を奪い取る能力がある可能性が示唆された。

大阪薬科大学文部科学省私立大学戦略的研究基盤形成支援事業平成25年度研究報告書
「組織的研究体系による次世代型感染症治療薬の開発」

研究課題名	シスプラチン耐性がん細胞に有効な新規白金(II)二核錯体が培養細胞およびDNAに与える影響
研究者名	佐藤卓史、東 剛志、三野芳紀

研究経過・成果の概要

<緒言>

シスプラチンは極めて高い抗腫瘍活性を有し、臨床で最も多く用いられている制がん剤である。しかしながら、治療過程あるいは再発時に腫瘍細胞がシスプラチンに対して耐性を示す例があり、临床上の問題となっている。そのため、シスプラチン耐性がんに対して有効な新たな制がん剤の開発が求められている。演者らは、シスプラチン耐性細胞に対する増殖抑制活性がシスプラチン感受性細胞に対するよりも強い、特異な性質をもつ白金(II)二核錯体を見出した。この錯体について、培養細胞に与える影響を検討した。また、活性発現に関与する可能性の高いDNAとの相互作用を検討した。

<方法>

錯体の構造の決定は¹H-NMRおよびESI-MSにより行った。また、細胞増殖抑制活性はMTT法により、細胞内白金量の測定はICP-MSにより、細胞周期に与える影響はフローサイトメトリーにより評価した。さらに、DNAの二重らせんの安定性に与える影響は融解温度測定により、DNAの構造に及ぼす影響はCDスペクトル測定により、DNAに対する鎖間架橋形成能は直鎖状に切断したCol E1 DNAを用いたアガロースゲル電気泳動により評価した。

<結果・考察>

今回、新たに合成された白金錯体は *trans*-1R,2R-ジアミノシクロヘキサンを担体配位子とし、ジアミノコハク酸で架橋された白金二核錯体 (RR-DASA) であることが確認された。また、この錯体合成の収率は28.5%であった。

RR-DASAの活性は、シスプラチンと同程度であり、ジアミノピメリン酸を架橋配位子とする白金(II)二核錯体RR-DAPAよりも強かった。また、シスプラチン耐性がん細胞に対して、感受性細胞よりも強い活性を示した。さらに、RR-DASAの取り込み量は、感受性細胞の方が多く、活性と細胞内量との相関性は見られなかった。RR-DASAは、感受性細胞の細胞周期をG₂/M期で停止させたが、耐性細胞の細胞周期には特に影響を与えなかった。このように、RR-DASAが感受性細胞より耐性細胞に強い活性を示すのは、耐性細胞がRR-DASAを選択的に取り込むからではないことが分かった。

DNA に対する RR-DASA の作用に関しては、まず、RR-DASA は RR-DAPA と比較して、DNA の二重らせんの安定性に大きな影響及ぼさなかった。また、DNA の構造にも大きな影響を及ぼさなかった。さらに、鎖間架橋の形成も見られなかった。このように RR-DASA は、DNA には結合するものの、その構造に大きな変化を与えないために、DNA 修復系に認識されにくい可能性が高いとより考えられる。

このように、RR-DASA がシスプラチン耐性細胞にも効果を示すのは、DNA 修復機能が本錯体と DNA との結合を認識できないことに起因する可能性が考えられる。今後は、耐性細胞における活性発現機構をより詳細に検討していくとともに、ジアミノコハク酸を架橋配位子とする新たな白金(II)二核錯体を合成し、その作用についても検討していく予定である。

大阪薬科大学文部科学省私立大学戦略的研究基盤形成支援事業平成25年度研究報告書
「組織的研究体系による次世代型感染症治療薬の開発」

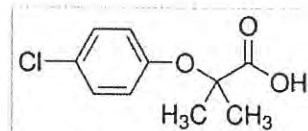
研究課題名	鉄-過酸化水素混合試薬による医薬品の分解
研究者名	東 剛志、佐藤卓史、三野芳紀

研究経過・成果の概要

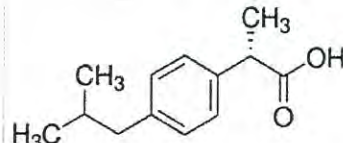
<緒言>

患者が服用した医薬品の一部は代謝を受けずに排泄される。また、医療機関等から排出される可能性もある。これらの医薬品は、通常の下水处理では分解されないことも多い。そのため、生態系に与える影響や生物濃縮を通じて人畜に与える影響などが懸念されている。また、抗生剤や抗ウイルス薬に関しては、対象とする病原体が耐性化する可能性も指摘されている。

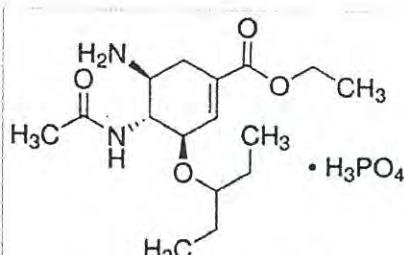
そこで、医薬品による汚染の低減法の開発を目的として、鉄-過酸化水素混合試薬を用いたクロフィブリン酸、イブプロフェン、オセルタミビル・リン酸塩、カルバマゼピンの分解反応について検討を行った。



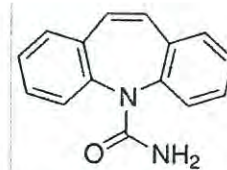
クロフィブリン酸



イブプロフェン



オセルタミビル・リン酸塩



カルバマゼピン

<方法>

各医薬品の1 ppm水溶液10 mLに、種々の濃度の過酸化水素水及び塩化鉄(III)水溶液、あるいは硫酸鉄(III)水溶液を添加し、27 °Cの暗所で24時間静置した。その溶液を固相抽出後、減圧乾固し、HPLCの移動相1 mLで再溶解し、その20 μLをUV検出・逆相HPLCで分析した。

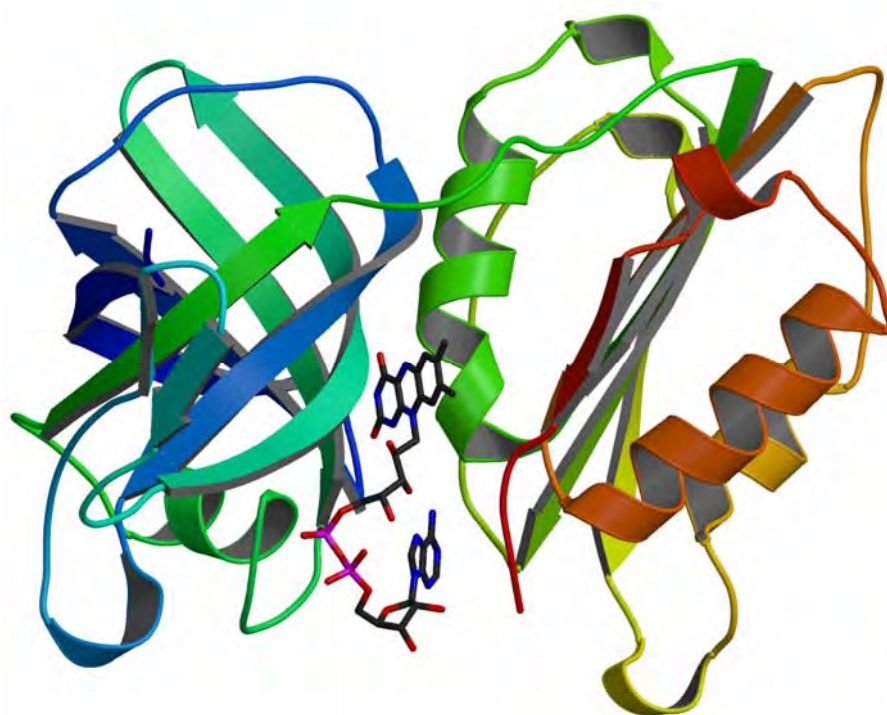
<結果・考察>

塩化鉄(III)水溶液を用いても硫酸鉄(III)水溶液を用いても、ほぼ同程度の分解効率が得られることが明らかとなった。また、Fe³⁺、Fe²⁺の濃度、あるいは過酸化水素の濃度に依存して分解効率が上昇した。さらに、今回検討した鉄-過酸化水素混合試薬系による分解では、同条件ではオセルタミビルが最も高い分解率を示し、他のクロフィブリン酸・イブプロフェン・カルバマゼピンはほぼ同程度の分解率を示した。

大阪薬科大学

文部科学省私立大学戦略的研究基盤形成支援事業
「組織的研究体系による次世代型感染症治療薬の開発」

平成 26 年度公開シンポジウム



平成 26 年 12 月 6 日



主催 大阪薬科大学
協賛 社団法人 日本薬学会
社団法人 日本化学会
社団法人 日本生化学会

大阪薬科大学

ご挨拶

大阪薬科大学では、平成 23 年度に文部科学省の私立大学戦略的研究基盤形成支援事業として採択されました「組織的研究体系による次世代型感染症治療薬の開発」と題したプロジェクト研究を推進しているところであります。平成 25 年度に 3 年目の中間評価を受け、本年度で 4 年目を迎えます。本プロジェクトの期間は、5 年間であり、残すところ 1 年余りとなりました。現在、プロジェクトに参画している教員が力を合わせて、最終目標に向かって鋭意努力しているところでございます。

我々の研究プロジェクトチームは、大阪薬科大学大学院薬科学専攻博士前期・後期課程の分子構造・機能解析学領域に属する薬品物理化学研究室、生化学研究室、薬品分析化学研究室、微生物学研究室および中央機器研究施設の教員から構成されており、これらの研究室および施設の全教員が目的を達成するための具体的な研究課題に取り組み、効率的に研究を遂行する体制をとっています。

本年度の第 4 回シンポジウムでは、我々のプロジェクトのこれまでの研究成果を報告するとともに、今回のシンポジウムに相応しい先駆的な研究を展開されておられる研究者を学外からお招きしております。

千葉大学理学研究科の村田武士先生に「創薬標的膜タンパク質の X 線結晶構造解析に向けた技術開発」を、塩野義製薬（株）コア疾患創薬研究所の山口高広先生に「緑膿菌の抗菌薬耐性とカルバペネム」をテーマにそれぞれご講演をさせていただきます。我々の研究プロジェクトチームからは河野広朗先生と友尾幸司先生にそれぞれ「病原細菌 *Vibrio vulnificus* の宿主生体内における生存戦略」および「*Vibrio vulnificus* における鉄獲得機構関連タンパク質の構造と機能」について研究成果の報告をさせていただきます。各ご講演では、独創的な研究展開によって得られた成果についてご披露いただけるとともに、本プロジェクトにおける今後の研究の方向性について、貴重な示唆を与えていただけるものと信じております。また、各研究室における研究成果をポスターセッションで報告させていただきます。皆様方により活発な討論がなされることを期待しております。

なお、シンポジウム終了後、ささやかな懇親会を予定しております。本プロジェクト研究の今後の展開についてご歓談いただけると幸いです。

研究代表者 辻坊 裕

大阪薬科大学平成 26 年度公開シンポジウム

日時 : 平成 26 年 12 月 6 日 (土) 12 : 50 ~
会場 : 大阪薬科大学・D304 教室 (入場無料)

文部科学省私立大学戦略的研究基盤形成支援事業
「組織的研究体系による次世代型感染症治療薬の開発」
第 4 回シンポジウム

《 プログラム 》

- 12 : 50 ~ 13 : 00 挨拶 研究代表者 辻坊 裕
- 13 : 00 ~ 13 : 30 河野 広朗 博士 (大阪薬科大学 博士研究員)
「病原細菌 *Vibrio vulnificus* の宿主生体内における生存戦略」
座長 佐藤 卓史
- 13 : 30 ~ 14 : 00 友尾 幸司 准教授 (大阪薬科大学 薬品物理化学研究室)
「*Vibrio vulnificus* における鉄獲得機構関連タンパク質の
構造と機能」
座長 藤井 忍
- 14 : 00 ~ 14 : 50 ポスターセッション
- 15 : 00 ~ 16 : 00 山口 高広 研究員 (塩野義製薬(株)コア疾患創薬研究所)
「緑膿菌の抗菌薬耐性とカルバペネム」
座長 宮本 勝城
- 16 : 00 ~ 17 : 00 村田 武士 教授 (千葉大学理学研究科生体構造化学研究室)
「創薬標的膜タンパク質の X 線結晶構造解析に向けた
技術開発」
座長 福永 理己郎
- 17 : 10 ~ 懇親会 司会 箕浦 克彦

講 演 要 旨

病原細菌 *Vibrio vulnificus* の宿主生体内における生存戦略

大阪薬科大学戦略的研究基盤形成支援事業 博士研究員 河野広朗

【緒言】

ヒトに感染症を起こす病原細菌は、宿主生体内で増殖するために鉄を必要とする。したがって、病原細菌の鉄取り込み機構を阻害することにより、ヒトの体内での増殖を抑制することができる。本プロジェクトでは、臨床分離株 *Vibrio vulnificus* M2799 株をモデル細菌として用い、本菌株が産生する鉄キレーターであるシデロフォア (Vulnibactin) を介した鉄取り込み機構に関与するタンパク質群の全容を、プロテオーム解析および挿入変異株の作製により明らかにすることができた¹⁾。さらに、多重変異株を作製する目的で、M2799 株の遺伝子欠失株作製法を確立した。

鉄欠乏下で発現量が増大するタンパク質群のうち、Vulnibactin を介する鉄取り込み機構に関与するタンパク質の遺伝子欠失株を作製した。すなわち、イソコリスミン酸合成酵素 (ICS)、Vulnibactin-Fe³⁺ 複合体を基質とする鉄還元酵素 (VuuB)、Vulnibactin-Fe³⁺ 複合体の外膜レセプター (VuuA)、および Vulnibactin-Fe³⁺ 複合体のペリプラズム結合タンパク質 (FatB) について遺伝子欠失株を作製した。これら欠失株の鉄欠乏下における増殖能について検討したところ、ICS および VuuA 遺伝子欠失 (Δ ics および Δ vuuA) 株では増殖が顕著に抑制されたが、VuuB および FatB 遺伝子欠失株においては遅いながらも増殖が確認された²⁾。以上の結果から、鉄欠乏下において Vulnibactin を介する鉄取り込み能は生育に重要であり、ICS および VuuA は本取り込み機構において必須であることが明らかとなった。そこで、野生株および Vulnibactin 非産生株である Δ ics 株をマウスに腹腔内接種し、致死活性について検討した結果、LD₅₀ 値はそれぞれ 1.0×10^7 および 2.6×10^7 CFU であり、両株において病原性に有意な差は見られなかった。したがって、マウス生体内においては、Vulnibactin を介する鉄獲得機構以外の取り込み機構により鉄を獲得していることが示唆された。そこで今回、本菌株のヘム取り込み機構に着目し、本機構に関与するタンパク質の遺伝子欠失株を作製した。

【方法】

遺伝子欠失株の作製は、suicide vector pDM4 を用いて行った。まず、ターゲット遺伝子内欠失目的領域の上下流域それぞれ 500 bp を PCR で増幅した。得られた PCR 産物を鋳型として、overlapping PCR を行った。増幅した DNA を pDM4 に連結し、大腸菌 SY327 λ pir 株を形質転換した。得られた組換えプラスミドを用いて、*V. vulnificus* に対する遺伝子伝達能を有する大腸菌 SM10 λ pir 株を形質転換した。組換えプラスミドを保持した SM10 λ pir 株と M2799 株をそれぞれ培養し、メンブレンフィルター上で接合させることでプラスミドの伝達を行わせ、1 回目の相同組換えを誘発した。得られた相同組換え体を 15% スクロース、100 units/ml ポリミキシン B 含有 LB 寒天培地に塗抹し、増殖したコロニーのクロラムフェニコール感受性を確認した。

【結果および考察】

類縁菌である *V. vulnificus* CMCP6 株には、ヘム取り込み機構に関与する外膜レセプ

ターとしてHupA (VV2_0276)³⁾およびHvtA (VV2_1549)⁴⁾が存在することが明らかにされている。そこで、M2799株のそれら遺伝子欠失 ($\Delta hupA$ および $\Delta hvtA$) 株を作製した。鉄キレーターであるEDDAと、単一鉄源としてヘミンを添加したCM9培地を用いて、 Δics 、 $\Delta ics\Delta hupA$ 、 $\Delta ics\Delta hvtA$ および $\Delta ics\Delta hupA\Delta hvtA$ 株の増殖試験を行った。本培養条件において、 Δics 株はVulnibactin非産生菌であるため、ヘム取り込み機構を介しての増殖は可能であるが、ヘミンを利用できない欠失株では増殖できない。増殖試験の結果、 $\Delta ics\Delta hvtA$ 株は Δics 株と同様に増殖したが、 $\Delta ics\Delta hupA$ 株では増殖がやや抑制された。さらに、 $\Delta ics\Delta hupA\Delta hvtA$ 株では顕著に増殖が抑制された (図)。以上のことから、本菌株のヘム取り込み機構において、外膜レセプターはHupAが中心となって機能するが、HvtAは補助的役割を有しており、本取り込み機構において、これら2つのレセプターは必須であることが明らかとなった。また、ヘム取り込み機構に関与する新規タンパク質を探索した結果、VV2_1611が唯一のペリプラズム結合タンパク質であり、VV2_1610およびVV2_1609が細胞内膜に存在するABCトランスポーターであることを明らかにした。

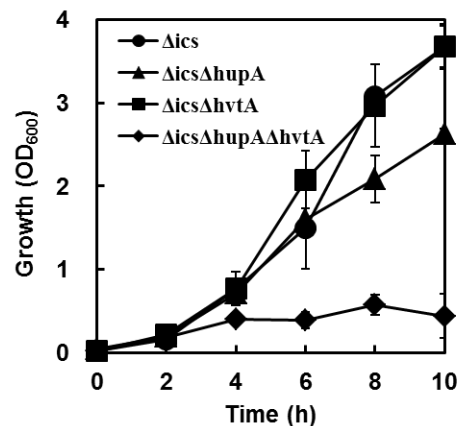


図 EDDAおよびヘミン含有CM9培地における増殖能

【参考文献】

- 1) Miyamoto K, Kosakai K, Ikebayashi S, Tsuchiya T, Yamamoto S, Tsujibo H. (2009) Proteomic analysis of *Vibrio vulnificus* M2799 grown under iron-repleted and iron-depleted conditions. *Microb. Pathog.* **46**:171-7.
- 2) Kawano H, Miyamoto K, Sakaguchi I, Myojin T, Moriwaki M, Tsuchiya T, Tanabe T, Yamamoto S, Tsujibo H. (2013) Role of periplasmic binding proteins, FatB and VatD, in the vulnibactin utilization system of *Vibrio vulnificus* M2799. *Microb. Pathog.* **65**:73-81.
- 3) Litwin CM, Byrne BL. (1998) Cloning and characterization of an outer membrane protein of *Vibrio vulnificus* required for heme utilization: regulation of expression and determination of the gene sequence. *Infect. Immun.* **66**:3134-41.
- 4) Datta S, Crosa JH. (2012) Identification and characterization of a novel outer membrane protein receptor required for heme utilization in *Vibrio vulnificus*. *Biometals* **25**:275-83.

略 歴

氏 名 かわの ひろあき 河野 広朗
生年月日 1977年8月27日
所属機関 大阪薬科大学戦略的研究基盤形成支援事業

学 歴

2000年3月 東洋大学工学部応用化学科卒業
2002年3月 東洋大学大学院工学研究科博士前期課程修了
2005年3月 博士（工学）東洋大学より

職 歴

2002年4月 独立行政法人海洋研究開発機構極限環境生物圏研究センター 研究推進スタッフ
2005年4月 日本大学歯学部 日本大学助手
2006年11月 協和発酵キリン株式会社フロンティア研究所 研究員
2009年7月 長崎大学大学院医歯薬学総合研究科 助教
2012年4月 大阪薬科大学戦略的研究基盤形成支援事業 博士研究員
現在に至る

受 賞

2003年12月 第4回極限環境生物学会ポスター賞
2004年12月 第5回極限環境生物学会ポスター賞

*Vibrio vulnificus*における鉄獲得機構関連タンパク質の構造と機能

大阪薬科大学 友尾幸司

人から細菌に至るまで、鉄はその生存と増殖に不可欠な元素である。その重要性は、一次および二次代謝に関係する 100 以上の酵素が、補因子として鉄イオンを必要とすることからも伺い知ることが出来る。細菌においても、生育に 1 μ M 濃度の鉄が必要とされているが、細胞内で産生することが出来ない鉄の獲得は、その水溶解性が極めて悪いために天然環境からの獲得も困難で、常に不足状態にあるといえる。このような低濃度下の鉄イオンを有効に利用するために細菌は、鉄と強いキレート結合能を有するシデロフォアという低分子物質を自ら産生し、特定のトランスポーターを介した効果的な鉄取り込み機構を有している。病原性細菌においても、利用できる遊離鉄が極めて少ない宿主内での生存において、効果的な鉄の獲得は重要である。よって、病原性細菌の鉄獲得機構の分子・原子レベルでの解明は、細菌性疾患の治療薬や、新たな作用機序を有する抗菌薬の開発に極めて重要な課題である。

臨床分離株 *Vibrio vulnificus* M2799 株は、汚染された魚介類の摂食や海水の創傷部曝露等を介して、全身性の感染症を引き起こす細菌である。これまでの研究から、この病原性細菌においても、シデロフォアを介した鉄取り込み機構が存在し、様々な結合タンパク質や、酵素が関与する非常に複雑なシステムを有することを明らかにしている¹⁾。

そこで、本研究では、*Vibrio vulnificus* M2799 株におけるシデロフォアを介した鉄取り込み機構を解明することにより、従来の抗菌薬とは異なる作用機序を有する新規抗菌薬開発を目的とし、シデロフォア結合タンパク質 VatD の X 線結晶構造解析を行った。

臨床分離株 *Vibrio vulnificus* M2799 株由来シデロフォア結合タンパク質 VatD について、His-tag 融合タンパク質として大腸菌を用いた大量発現系を構築した。IPTG による発現誘導後、20°C において 19 時間培養を行い、菌体破碎後の上清に VatD の発現を確認した。VatD の精製は、アフィニティー、イオン交換、およびゲル濾過の各クロマトグラフィーにより高純度に精製を行った。単離精製した VatD を濃縮し、ヒドロキサメート型シデロフォアである Deferoxamine を結合させ複合体を形成した後、結晶化条件の検討を行った。その結果、良質の複合体結晶を得ることに成功し、X 線回折強度データの収集後、分子置換法により初期構造を構築し、現在 1.85 Å 分解能での構造を得ている。VatD の全体構造は、N-domain と C-domain から構成されており、両ドメインは long α -helix で繋がっていた。VatD-Deferoxamine-Fe³⁺ 複合体の解析により、それら両ドメイン間に Deferoxamine-Fe³⁺ が結合していることが明らかとなった。Deferoxamine-Fe³⁺ は、VatD の Arg69 および Arg177 と直接および水分子を介して水素結合を形成していることが確認できた。また、本結合領域にはトリプトファンやフェニルアラニンなどの疎水性残基が多く存在し、Trp53、Trp205 および Phe263 の側鎖と疎水性相互作用を形成していた。さらに、Apo 体と複合体との構造比較により、両構造において N-domain から long α -helix までは、良く一致した構造であったのに対して、Apo 体の C-domain は外側にシフトしていることが明らかとなった。Apo 体において本結合領域近隣に存在する Gly227、Pro228 の温度因子が高く不安定であることから、Deferoxamine-Fe³⁺ の結合に伴い、VatD の Trp53、Pro228、Arg169、The262 の各アミノ酸残基および隣接する水分子と相互作用ネットワークを形成することにより、C-domain が Deferoxamine-Fe³⁺ 側に動き、結合

サイトの構造を安定化していることが推測された。

【参考文献】

- 1) Miyamoto K, Kosakai K, Ikebayashi S, Tsuchiya T, Yamamoto S, Tsujibo H. (2009) Proteomic analysis of *Vibrio vulnificus* M2799 grown under iron-repleted and iron-depleted conditions. *Microb. Pathog.* **46**:171-177.

略 歴

氏 名	ともお こうじ 友尾 幸司
生年月日	1964年1月1日
所属機関	大阪薬科大学 准教授 (薬品物理化学研究室)

学 歴

1989年3月	大阪薬科大学大学院薬学研究科博士前期課程修了
1992年3月	大阪薬科大学大学院薬学研究科博士後期課程単位取得退学
1995年1月	博士 (薬学) 大阪薬科大学より

職 歴

1992年4月	大阪薬科大学 助手
1997年11月	ドイツベルリン自由大学結晶解析研究所博士研究員
2004年1月	大阪薬科大学 講師
2007年4月	大阪薬科大学 准教授
	現在に至る

賞 罰

1996年1月	日本薬学会近畿支部奨励賞
---------	--------------

緑膿菌の抗菌薬耐性とカルバペネム

塩野義製薬株式会社

コア疾患創薬研究所 感染症部門 抗菌・抗真菌2グループ

山口 高広

緑膿菌は、流し台などの水回りからしばしば分離されるなど、生活環境中に広く常在している「常在菌」であり、健常者には通常、病原性を示さない。細菌学的には、大腸菌や肺炎桿菌と同じくグラム陰性桿菌に分類されることから、エンドトキシンを有している。そのため、緑膿菌が血流中に侵入し、菌血症や敗血症などの血流感染を発症すると、緑膿菌から放出されたエンドトキシンによって、生体の免疫反応が亢進する「エンドトキシンショック」が誘発され、多臓器不全により死亡することがある。特に、抗がん剤治療などにより免疫力の低下した患者や、高齢者の慢性呼吸器疾患患者などにおいては、感染防御能が低下していることが原因で、口腔内や腸管内に常在している緑膿菌が感染症を引き起こし、それらが血流中に侵入することで、菌血症や敗血症などを続発する、典型的な日和見感染症の一つである。

緑膿菌は、大腸菌などの他の細菌に比べ、抗菌薬や消毒剤が細菌の細胞膜を透過しにくいことから、それらに対する感受性が低い「自然耐性」の性質を有する。加えて、菌体内に侵入してきた抗菌薬を菌体外に排出する機構や、抗菌薬を分解・修飾する種々の酵素を産生し、不活化することで、ペニシリンやセファロsporin等のβ-ラクタム薬だけでなく、テトラサイクリン系やマクロライド系抗生物質などの抗菌薬にも耐性を示す傾向が強い。

緑膿菌感染症の治療には、緑膿菌に抗菌力を有するセフェム系であるセフトジジムやセフェピム、或いはイミペネム、メロペネム、ドリペネムなどのカルバペネム系やシプロフロキサシン、レボフロキサシンなどのフルオロキノロン系、さらにアミカシンなどのアミノ配糖体系などが臨床で多用されているが、近年これらの抗菌薬に対しても、耐性を獲得した「多剤耐性緑膿菌」が各地の医療施設で臨床分離され、問題となりつつある。

本講演では、高い安全性と治療効果を有することから、緑膿菌感染症の治療薬として最もよく使用されている抗菌薬の一つであるカルバペネム薬について、その特徴を御紹介させて頂きたい。

略 歴

氏 名 やまぐち たかひろ
山口 高広
生年月日 1967年2月24日
所属機関 塩野義製薬(株) コア疾患創薬研究所 主任研究員

学 歴

1990年3月 大阪薬科大学薬学部薬学科卒業

職 歴

1990年4月 塩野義製薬(株) 研究所 微生物部門 研究員
2009年4月 塩野義製薬(株) 創薬疾患研究所 感染症部門 主任研究員
2011年4月 塩野義製薬(株) コア疾患創薬研究所 主任研究員
現在に至る

賞 罰

なし

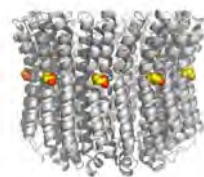
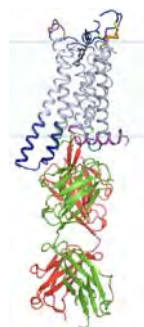
創薬標的膜タンパク質の X 線結晶構造解析に向けた技術開発

千葉大学大学院理学研究科・JST さきがけ 村田武士

膜タンパク質の立体構造情報はドラッグデザインなどの創薬に重要であるが、発現・精製・結晶化が難しく、構造研究が遅れていた。我々は酵母を用いた膜タンパク質の発現システム、大腸菌無細胞タンパク質合成系を用いた複合体再構成システム、有機溶媒を用いた精製結晶化技術、結晶化を促進する機能性抗体の作製技術および共結晶化構造解析技術を開発し、複合体を含む創薬標的膜タンパク質の X 線結晶構造解析を行うためのプラットフォームを整えてきた。この技術を使ってパーキンソン病の薬剤標的であるヒト・アデノシン受容体と機能性抗体との共結晶構造解析に成功し、新たな阻害機構を明らかにした (1)。また、膜タンパク質複合体である V-ATPase の膜リングや回転軸、触媒頭部複合体の高分解能結晶構造解析に世界で初めて成功し、本酵素のイオン輸送機構 (2) や ATP による回転機構 (3) の大枠を明らかにした。本講演では創薬標的膜タンパク質の X 線結晶構造解析に向けた技術開発の現状について世界の動向も含め紹介する。

【参考文献】

- (1) T. Hino *et al.* (2012) G-protein-coupled receptor inactivation by an allosteric inverse-agonist antibody, *Nature*, 482, 7384, 237-240
- (2) T. Murata *et al.* (2005) Structure of the rotor of the V-type Na⁺-ATPase from *Enterococcus hirae*., *Science*, 308, 5722, 654-659
- (3) S. Arai *et al.* (2013) Rotation mechanism of *Enterococcus hirae* V₁-ATPase based on asymmetric crystal structures, *Nature*, 493, 7434, 703-707



略 歴

氏 名 むらた たけし
 村田 武士
生年月日 1971年1月30日
所属機関 千葉大学大学院理学研究科 教授

学 歴

1995年 東京理科大学基礎工学部卒業
1997年 東京理科大学大学院基礎工学研究科修士課程生物工学
 専攻修了
2000年 東京理科大学大学院基礎工学研究科博士課程生物工学
 専攻修了
2000年 博士(工学)(東京理科大学)取得

職 歴

2000-2005年 英国MRC研究所MRC博士研究員、学振海外特別研究員
2005-2006年 理化学研究所基礎科学特別研究員
2007-2009年 京都大学医学研究科助教
2009-2013年 千葉大学理学研究科特任准教授
2013-2014年 千葉大学 理学研究科 准教授
2014年7月 現在に至る

受 賞

特になし

ポスター発表要旨

平成26年度ポスターセッション目次

- (1) 「*Vibrio vulnificus* M2799 株の鉄獲得機構の解明」
宮本勝城、河野広朗、土屋孝弘、辻坊 裕 …………… 1
- (2) 「Bam 複合体を標的とした新規抗菌物質の開発」
土屋孝弘、宮本勝城、辻坊 裕 …………… 2
- (3) 「好熱性放線菌由来キシロオリゴ糖結合タンパク質 BxlE の構造機能解析」
友尾幸司、尹 康子 …………… 3
- (4) 「Tau タンパク質の自己重合抑制能を有する Tau 認識抗体の構造機能解析」
箕浦克彦、尹 康子、土屋孝弘、友尾幸司 …………… 4
- (5) 「VatD と Siderophore の相互作用」
井上晴嗣、藤井 忍、福永理己郎 …………… 5
- (6) 「コリスミ酸の調製とイソコリスミ酸合成酵素 (ICS) の大腸菌による発現」
藤井 忍、井上晴嗣、福永理己郎 …………… 6
- (7) 「*Vibrio* 属シデロホアに関する研究 : vulnibactin の単離・精製とその鉄錯体
の特徴」
三野芳紀、松田尚子、岡田将典、東 剛志、佐藤卓史 …………… 7
- (8) 「鉄-過酸化水素混合試薬によるイブuproフェン及びカルバマゼピンの分解機構」
東 剛志、佐野征太郎、金森理紗、佐藤卓史、三野芳紀 …………… 8

大阪薬科大学文部科学省私立大学戦略的研究基盤形成支援事業平成26年度研究報告書
「組織的研究体系による次世代型感染症治療薬の開発」

研究課題名	<i>Vibrio vulnificus</i> M2799 株の鉄獲得機構の解明
研究者名	宮本勝城、河野広朗、土屋孝弘、辻坊 裕

研究経過・成果の概要

【研究目的】

*Vibrio vulnificus*は、汚染された魚介類の摂食や海水の創傷部曝露等を介して、全身性の感染症を引き起こす細菌である。一般に、鉄はほとんどの生物の生存と増殖に不可欠な元素であるが、宿主生体内において病原菌が自由に利用できる遊離鉄は極めて少ない。したがって、宿主生体内で増殖し得る病原菌は、何らかの巧妙な鉄獲得系を保持しているはずである。そこで、我々は臨床分離株 *V. vulnificus* M2799 株の鉄獲得系タンパク質を網羅的に明らかにする目的で、プロテオーム解析を行った。次に、鉄欠乏下で発現量が増大するタンパク質群のうち、本菌株の産生するシデロフォアであるVulnibactinを介する鉄取り込み機構に関与するタンパク質の遺伝子欠損株を作製した。すなわち、イソコリスミン酸合成酵素 (ICS)、Vulnibactin-Fe³⁺複合体を基質とする鉄還元酵素 (VuuB)、Vulnibactin-Fe³⁺複合体の外膜レセプター (VuuA)、およびVulnibactin-Fe³⁺複合体のペリプラズム結合タンパク質 (FatB) について作製した。これらの欠損株の鉄欠乏下における増殖能について検討したところ、ICSおよびVuuA遺伝子欠損株では顕著に抑制されたが、VuuBおよびFatB遺伝子欠損株においては遅いながらも増殖が確認された。以上の結果から、VuuBおよびFatBにはそれぞれ代替タンパク質が存在することが示唆され、さらなる解析によって、Vulnibactin-Fe³⁺複合体のペリプラズム結合タンパク質はFatBが中心となって機能するが、VatDで代替可能であることが推測された。今回、現在までに明らかにされていない、Vulnibactinの分泌機構について検討を行った。

【結果および考察】

V. vulnificus M2799 株におけるVulnibactin分泌機構に関与するタンパク質遺伝子について検討した。大腸菌において、Enterobactinの分泌に外膜チャネルタンパク質 TolC が関与することが明らかにされており、TolC を外膜チャネルとする resistance nodulation cell division (RND) 型排出システムが分泌に関与すると推測されている。M2799 株における TolC ホモログを探索した結果、VV1_0612 及びVV2_1007 を見出した。そこで、これら遺伝子の欠損株を作製し、鉄欠乏下での増殖能について検討したところ、VV1_0612 タンパク質遺伝子欠損株の鉄欠乏下での生育が顕著に抑制された。また、Vulnibactin 非産生株である ICS 遺伝子欠損株を用いたバイオアッセイを行ったところ、鉄欠乏下において、VV1_0612 タンパク質遺伝子欠損株の培養上清では ICS 遺伝子欠損株は増殖しなかった。以上のことから、*V. vulnificus* M2799 株において、VV1_0612 タンパク質が TolC であると推測された。

次に、VV1_0612 タンパク質と協調して機能する RND タンパク質を探索した。ゲノム情報が明らかにされており類縁菌である、*V. vulnificus* CMCP6 株は 11 種類の RND タンパク質をコードしていた。そこで、これら遺伝子欠損株を作製し、鉄欠乏下における増殖能について検討した結果、VV1_1681 が RND タンパク質としてバルニバクチンの分泌に関与することが示唆された。しかしながら、本遺伝子欠損株では、遅いながらも増殖が確認されたことから、今回解析対象とした RND タンパク質以外の代替タンパク質の存在が示唆された。

研究課題名	Bam 複合体を標的とした新規抗菌物質の開発
研究者名	土屋孝弘, 宮本勝城, 辻坊 裕.

研究経過・成果の概要

【目的】グラム陰性細菌の細胞壁は内膜と外膜から構成されており、外膜にはβ-バレル構造を有する外膜タンパク質が多数存在している。これら外膜タンパク質は生理学的な機能に必須だけでなく、病原性や薬剤排出ポンプなどの機能を有しており、これらの多くが創薬の標的分子となっている。外膜タンパク質は細胞質内で合成されたのち、タンパク質輸送装置を介してペリプラズムに輸送される。輸送されたタンパク質は外膜の内側でβ-barrel assembly machinery (BAM) 複合体に認識され、BAM 複合体によって外膜内にフォールディングされる。BAM 複合体がどのようなメカニズムでタンパク質を外

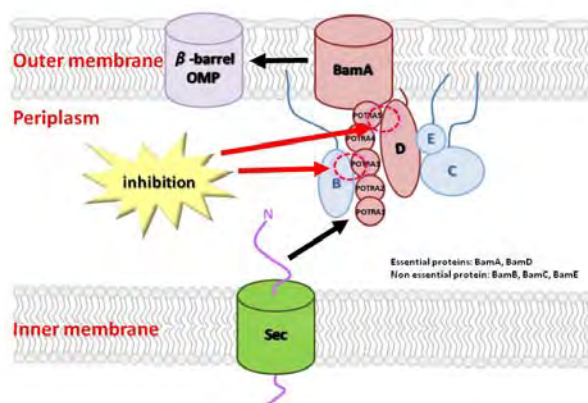


図 外膜タンパク質の膜輸送

膜にフォールディングしているのかは現在までに全く解明されていないが、Bam 複合体が機能しなければ外膜内にタンパク質がフォールディングされず、病原性の低下や薬剤感受性の増大、さらには細菌が生存できなくなることが期待される。BAM 複合体はそれ自身が外膜タンパク質である BamA と、ペリプラズムに存在するその付随タンパク質である BamB, BamC, BamD および BamE から構成されている。BamA にはペリプラズムに 5 つの polypeptide translocation-associated (POTRA) ドメインが存在しており、POTRA ドメインと BamB および BamD が直接結合している。(図)。我々はこの結合を阻害する物質を創製し、*Acinetobacter baumannii* の増殖への影響、抗菌活性、バイオフィーム形成阻害能およびマウスに対する致死活性を調べた。

【方法】*Acinetobacter baumannii* は基準株である ATCC19606 株、臨床分離株である A112-II-a 株および多剤耐性菌である GTC14637 株を用い、LB 培地で対数増殖後期まで攪拌培養した。BamA と BamB の結合阻害物質 (K5FS3GN) または BamA と BamD の結合阻害物質 (K5FI2NH) を添加し、各実験を行った。本菌の増殖に及ぼす各阻害物質の影響を 600nm における濁度ならびに生菌数により調べた。バイオフィーム形成能についてはポリスチレンチューブを用いて 24 時間静置培養後、クリスタルバイオレットで染色することにより測定した。マウスに対する致死活性は、抗 Gr1 抗体を前投与した C57BL/6 マウスに本菌と K5FS3GN を経鼻的に投与しその生存率を調べた。

【結果と考察】BamA と BamB の結合阻害物質 (K5FS3GN) はいずれの菌株に対しても本菌の増殖を抑制したが、殺菌活性は認められなかった。また、K5FS3GN はバイオフィームの形成ならびにマウスに対する致死活性を低下させた。BamA と BamD の結合阻害物質 (K5FI2NH) は本菌の増殖を抑制し、また殺菌活性が認められたが、バイオフィームの形成には影響を与えなかった。これらの結果から、Bam 複合体に対する機能阻害物質は新規抗菌物質として有用であることが明らかとなった。今後はより効果的な物質になるよう改良を行う予定である。

大阪薬科大学文部科学省私立大学戦略的研究基盤形成支援事業平成26年度研究報告書
「組織的研究体系による次世代型感染症治療薬の開発」

研究課題名	好熱性放線菌由来キシロオリゴ糖結合タンパク質 Bx1E の構造機能解析
研究者名	友尾幸司、尹 康子

研究経過・成果の概要

自然界において、セルロースに次いで再生利用可能な資源として多く存在するキシランは、xylanase によってキシロオリゴ糖に分解される。xylanase のようなヘミセルロース分解酵素は自然界におけるカーボンサイクルの維持にきわめて重要な役割を担っている。また最近ではパルプ製紙工業における漂白作用やリグノセルロース物質を発酵製品(バイオエタノール)に転換するなどの実用的な使用法の可能性を秘めており関心を集めている。

好熱性放線菌 *Streptomyces thermoviolaceus* OPC-520 株由来遺伝子中には、キシロオリゴ糖の輸送および分解に関与するタンパク質群を産生する *bxl* オペロンが存在する。その遺伝子産物としては、糖結合タンパク質である Bx1E、2 種類の膜貫通型タンパク質 Bx1F、Bx1G、および細胞内 α -xylosidase である Bx1A が存在する。生成したキシロオリゴ糖は、Bx1E によって Bx1F/Bx1G 複合体に受け渡されて細胞内に運ばれ、細胞内にて Bx1A により xylose にまで加水分解されると考えられているが、これら Bx1 タンパク質群による糖輸送機構の構造化学的な詳細はいまだ明らかになっていない。そこで本研究では、X 線結晶構造解析法を用いて Bx1 タンパク質群の網羅的構造決定に取り組み、本菌におけるキシロオリゴ糖の細胞内輸送機構を原子レベルで明らかにすることを目的としている。

糖結合タンパク質である Bx1E は 436 アミノ酸残基からなり、単糖、および二糖から六糖までのキシロオリゴ糖との結合親和性が明らかにされている。中でも、二糖であるキシロビオースと最も高い親和性を示す一方で、単糖との親和性は著しく低い。このように、各キシロオリゴ糖に対する Bx1E の親和性の差違や、糖受け渡し機構の詳細について明らかにするために、Bx1E 単独ならびに xylobiose との複合体の立体構造解析を行った。大腸菌を用いた Bx1E の大量発現系を構築し、発現、精製の後、各試料の結晶化および、X 線構造解析法による Bx1E 単独、ならびに xylobiose 複合体の立体構造を決定した。その結果、Bx1E は 2 つのドメインを有し、そのドメイン間に形成されるクレフトに糖結合部位が存在していた。更に、糖の結合により 2 つのドメインが大きく構造変化することも明らかとなった。また、糖との結合には Bx1E 分子中の 11 個のアミノ酸残基が関与し、中でも Trp-102 と Asp-400 の両アミノ酸残基の役割が重要であることが明らかとなった。

大阪薬科大学文部科学省私立大学戦略的研究基盤形成支援事業平成26年度研究報告書
「組織的研究体系による次世代型感染症治療薬の開発」

研究課題名	Tau タンパク質の自己重合抑制能を有する Tau 認識抗体の構造機能解析
研究者名	箕浦 克彦 尹 康子 土屋 孝弘 友尾 幸司

研究経過・成果の概要

【緒言】

微小管結合タンパク質の一種である Tau タンパク質は、脳内に多く存在し、微小管の重合促進と安定化に寄与している。しかしながら、異常にリン酸化されると、微小管との結合能を失い、自己重合を起し、PHF (paired helical filament) と呼ばれる不溶性の線維を形成した後、細胞内に蓄積する。この特異な線維の蓄積と認知症状には相関が認められることより、我々は、Tau タンパク質の異常自己重合機構の解明、また自己重合を阻害する物質の開発に取り組んでいる。PHF 形成には Tau 分子中において相同性の高いアミノ酸配列が 4 回繰り返すという特徴的な配列 (R1~R4) である微小管結合ドメイン (MBD 領域) が関与していることが示唆されている。本研究では R2 のアミノ酸配列を特異的に認識して Tau タンパク質の自己重合を阻害する抗体 Tau2r3 を作成し、その Fab フラグメント単体の結晶を得ることに成功した。X 線結晶構造解析より得られた結晶構造を、以前作成した Fab-複合体結晶構造と比較することにより、Fab が R2 の 6 残基 (VQIINK) を認識するメカニズムについて原子レベルで解明し、AD 治療薬の開発に繋げることを目的として研究を進めている。

【方法及び結果】

Tau タンパク質特異的認識抗体 Tau2r3 は、それを産生するマウスハイブリドーマ細胞の上清から、Protein G カラムを用いて精製した。その後、パパイイン処理により高純度 Fab フラグメント (Fab2r3) を得ることに成功した。この Fab フラグメントは、Tau タンパク質に対する特異的認識能、および重合抑制能を保持していることを、ThS 蛍光強度測定や BIAcore などの物理化学的手法により明らかにした。また、エピトープとして用いたペプチドに含まれる VQIINK フラグメントペプチドへの結合は強いが、類似している配列である VQIVYK への結合は弱いことを確認した。Fab フラグメントの結晶化は、ハンギングドロップ蒸気拡散法により行った。種々の条件を検討した結果、2.0 Å の分解能を有する X 線回折データを得ることに成功した。次に、すで取得している Fab-VQIINK 複合体の立体構造を用いた分子置換法により、Fab2r3 単体の結晶化ならびに構造決定に成功した。さらに、今回の Fab2r3 単体と Fab2r3-VQIINK 複合体の構造を比較することにより、Fab2r3 の L3 ドメインの構造柔軟性が抗原ペプチドの認識に重要であることが考えられた。

研究課題名	VatD と Siderophore の相互作用
研究者名	井上 晴嗣、藤井忍、福永理己郎

研究経過・成果の概要

【緒言】

本プロジェクトでは、*Vibrio vulnificus*の鉄欠乏ストレスに関与するタンパク質群を網羅的に調べている。昨年度のシンポジウムで、河野らはVulnibactin-Fe³⁺複合体のペリプラズム結合タンパク質であるFatBの遺伝子欠失株の鉄欠乏下における増殖能について検討し、Aerobactin-Fe³⁺複合体のペリプラズム結合タンパク質であるVatDがFatBの機能を代替している可能性を報告した。そこで、本研究では、VatDと種々のSiderophoreの直接相互作用について、VatDのトリプトファン残基の蛍光変化、およびVatDを固定化したセンサーチップを用いたBiacoreによる表面プラズモン共鳴の変化を利用して調べた。

【方法】

VatDは五十嵐らが*大腸菌*発現系を用いて大量発現し、X線結晶解析用に精製したものをを用いた。0.1M NaClを含む50mM Tris-HCl緩衝液(pH7.5)に溶解した約1 μ M VatDに種々の濃度のDeferoxamine, Deferoxamine-Fe²⁺複合体, Deferoxamine-Fe³⁺複合体, Ferrichrome-Fe³⁺複合体, Enterobactin-Fe³⁺複合体を加え、励起波長280nmで300~400nmの蛍光スペクトル変化を測定した。また、VatDを固定化したCM5 センサーチップをセットしたBiacoreT100装置に、種々の濃度のDeferoxamine, Deferoxamine-Fe³⁺複合体, Enterobactin, Enterobactin-Fe³⁺複合体, Vulnibactin-Fe³⁺複合体をそれぞれアナライトとして添加し、生じる表面プラズモン共鳴の変化を測定した。

【結果および考察】

280nmで励起したときのVatDのトリプトファン残基に由来する蛍光スペクトルを測定すると、蛍光極大波長は342nm付近に見られたが、Deferoxamine-Fe³⁺複合体を添加すると、蛍光極大波長が338nm付近にシフトするとともに蛍光の値が約1/5に大きく減少した。このことはDeferoxamine-Fe³⁺の結合による構造変化によりVatDのトリプトファン残基の存在環境が大きく変化したことを示している。この蛍光変化からVatDとDeferoxamine-Fe³⁺の解離定数 K_d を求めると、 K_d は約0.21 μ Mとなった。鉄を含まないDeferoxamineを添加した場合にも若干の蛍光変化が見られたが、これは非特異的な吸着であると思われる。同様に蛍光変化を利用してEnterobactin-Fe³⁺複合体が K_d 値5.28 μ MでVatDと結合することがわかった。VatDがEnterobactin-Fe³⁺複合体と結合することは、Biacoreを用いた相互作用解析からも確認できたが、BiacoreではDeferoxamine-Fe³⁺複合体やVulnibactin-Fe³⁺複合体とVatDの相互作用は検出できなかった。今後、VatDのみならず、FatBについても種々のSiderophoreとの相互作用を検討したい。

大阪薬科大学文部科学省私立大学戦略的研究基盤形成支援事業平成26年度研究報告書
「組織的研究体系による次世代型感染症治療薬の開発」

研究課題名	コリスミ酸の調製とイソコリスミ酸合成酵素(ICS)の大腸菌による発現
研究者名	藤井忍、井上晴嗣、福永理己郎

研究経過・成果の概要

【目的】

近年、抗菌薬の乱用などによる多剤耐性菌の発生が問題になっている。そのため、これまでとは異なる作用機序を持つ新規抗菌薬の開発が待ち望まれている。我々のプロジェクトは、敗血症の原因菌である *Vibrio vulnificus* のプロテオーム解析によって、イソコリスミ酸合成酵素(ICS)欠損株の増殖が鉄欠乏下で著しく抑制されることを明らかにした。ICSは、コリスミ酸からイソコリスミ酸を産生する酵素であり、イソコリスミ酸は、さらに代謝されてバルニバクチン(総称:シデロフォア)になる。菌体はバルニバクチンを体外へ放出して鉄と結合させて体内に取り込み、生育に必要な鉄を獲得している。ICS欠損株の増殖抑制はこのような鉄の取り込み阻害に基づくため、ICSを阻害する物質は、新しい作用機序を利用した抗菌薬になり得る。本研究では、ICS阻害物質の検索のために、ICSの大腸菌による発現系の構築を試みるとともに、ICSの酵素活性測定に必要な基質であるコリスミ酸の調製法の確立を行った。

【結果・考察】

ICSの阻害物質を検索するためには、ICSの酵素活性を測定する手法を確立しなければならない。しかし、ICSの基質であるコリスミ酸は、市販品として入手するには高価(100mgで約20万円)である。以前、*E. coli* KA12菌(表現型はPhe⁻、Tyr⁻、Tet^R、RacA⁻)を利用してコリスミ酸を産生させる方法が報告されている。そこで、この菌体からのコリスミ酸の調製方法について検討した。

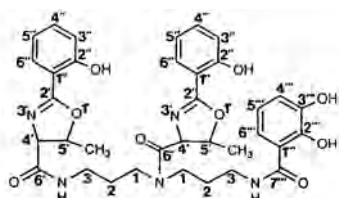
栄養分を含む培地中で*E. coli* KA12菌を培養(37°C、6時間)することで菌を増殖させた後、集菌し、栄養分を含まない培地でコリスミ酸を作らせた(27°C、16時間)。培養上清は陰イオン交換クロマトグラフィーで分離後、ジクロロメタンによる洗浄、酢酸エチルによる抽出を行い、逆相クロマトグラフィーで分離し凍結乾燥した。調製したコリスミ酸の構造は¹H-NMRによって確認し、純度は逆相HPLCによって分析した。その結果、調製品はほぼ純品であることがわかった。次に、水溶液中におけるコリスミ酸の安定性を確認するため、コリスミ酸をpH7.5の水溶液に溶解後、4°Cまたは37°Cにおいて経時的に分取し、逆相HPLCで分析した。その結果、溶解後32時間までは、4°Cの試料は溶解直後の試料とほぼ同じ溶出パターンを示したが、37°Cの試料は、コリスミ酸のピークがほぼ消滅した。また、4°Cで約20日間保存した場合には60%ほど分解していた。

さらに、*Vibrio vulnificus*菌由来ICS遺伝子が組み込まれた発現用プラスミド(pProEX HTa)によって形質転換された大腸菌(BL21(DE3)pLys)を1mM IPTGで誘導後、20°Cで22時間振盪培養した。その結果、ICSの発現は確認できたが、その大部分は封入体画分(IB)に存在した。そこで、IBからのICSの再構成を試みた。IBを6M塩酸グアニジン溶液で溶解後、透析により段階的に塩酸グアニジンの濃度を低くすることで再構成を行った。再構成後の可溶性画分についてSDS-PAGEを行ったところICS(44kDa)のバンドが検出された。発現タンパク質はN末端にHisタグを持つ融合タンパク質であるため、HisTrapカラムによる分離を行ったが、ICS以外の多くのタンパク質を取り除くことはできなかった。今後さらなる精製を行うとともに再構成したICSに活性があることを確認しなければならない。

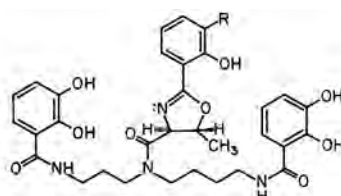
研究課題名	<i>Vibrio</i> 属シデロホアに関する研究： vulnibactin の単離・精製とその鉄錯体の特徴
研究者名	三野芳紀、松田尚子、岡田将典、東 剛志、佐藤卓史

研究経過・成果の概要

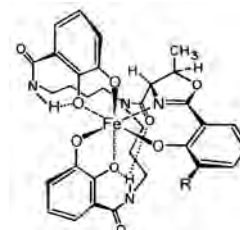
【目的】人食いバクテリアの一種 *Vibrio vulnificus* は、ヒト血液中で増殖するための巧みな鉄獲得系を有している。この鉄獲得系を阻害する化合物は、この病原菌の増殖を抑える薬剤になると考えられる。そこで我々は、*V. vulnificus* が鉄を取り込むときに利用する vulnibactin (以下 VB) と、同等あるいは、それ以上の鉄に対する親和性が期待できる化合物を探索している。また、VB - Fe(III) 錯体の性質は、その構造も含め、ほとんど分っていない。構造類似体の parabactin の鉄(III) 錯体の構造は明らかになっており、VB - Fe(III) 錯体も同様な配位構造が推測される。X線結晶解析、NMR によってその構造を確認する予定である。



vulnibactin(VB)



parabactin(R=H)



parabactin-Fe(III)

これらの研究のためには、何よりも VB の単離・精製法の確立が求められる。ここでは、VB の単離・精製法について報告するとともに、今後の予定も含めて VB - Fe(III) 錯体に関する基礎的な性質について報告する。

【方法】VBの単離・精製：*V. vulnificus*を鉄欠乏下で培養し、その培養液 3 Lをクエン酸溶液でpHを4に調整したのち、Amberlite XAD7に通液した。MeOHで溶出した液を減圧下で濃縮し、セミ分取HPLC (Cosmosil 5C18 AR-II, φ10mm×250mm, 0.5%TFA含有水-CH₃CN勾配溶出) で $t_R=16$ minのピークを分取した。これをNH₃水で中和後、減圧下で濃縮することで、VBを得た。その構造は、NMRとFAB-MSで確認した。

EDDHA-Fe(III)錯体の合成と精製：VBは貴重であるため、その鉄錯体を合成・精製するための基礎実験として、同程度の鉄結合能を有するEDDHAを用いて検討した。等モルのEDDHA(10mg)とFeCl₃を10%MeOH中で混合し、赤紫色の錯体を合成した。これをセミ分取HPLC (pH 6) で分取し、単一ピークのEDDHA-Fe(III)錯体を得た (ca. 6mg)。

【結果および考察】VBの単離・精製は、【方法】に示した方法で可能となった。EDDHA-Fe(III)錯体の精製法を参考にすることで、VB - Fe(III)錯体の精製も可能と思われ、詳細な構造解析も期待できる。また、特発性ヘモクロマトーシスの患者はこの病原菌の感染による死亡率が最も高い。この患者の血中トランスフェリンの鉄飽和度は100% (正常 35%) であり、菌による鉄の利用が容易である。死亡率とトランスフェリン鉄飽和度の関係は興味深い。

大阪薬科大学文部科学省私立大学戦略的研究基盤形成支援事業平成26年度研究報告書
「組織的研究体系による次世代型感染症治療薬の開発」

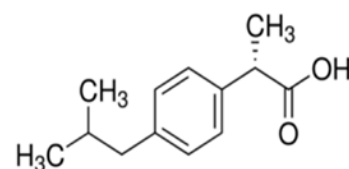
研究課題名	鉄-過酸化水素混合試薬によるイブプロフェン及びカルバマゼピンの分解機構
研究者名	東 剛志、佐野征太郎、金森理紗、佐藤卓史、三野芳紀

研究経過・成果の概要

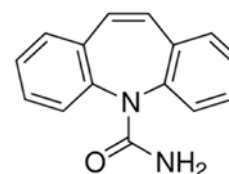
【緒言】

医薬品は服用後、一部は代謝されずに薬効を保ったままの未変化体の形態で体外に排泄される。また、病院等の医療機関で使用される医薬品の一部は、医療廃液として下水道へと排出される。これらの排水は下水処理場や浄化槽で処理されるが、し尿由来の BOD 除去を主目的とした水処理では十分な除去を行うことが困難であり、河川環境中へと放流されているものが多い。そのため、河川環境中に生息する生態系への毒性影響や、飲料水を通じたヒトへの健康影響等が懸念されている。また、抗菌剤や抗ウイルス剤に関しては、薬剤耐性菌や薬剤耐性ウイルスの発生を助長する可能性も指摘されている。

我々の研究室では、鉄-過酸化水素混合試薬が医薬品の分解に有効であることを報告しているが、その分解機構については不明な点が多い。そこで、本研究では世界的にみても河川環境中から検出報告例が多い代表的な医薬品成分として、解熱鎮痛剤のイブプロフェンと向精神薬のカルバマゼピンを対象として、鉄-過酸化水素混合試薬による分解機構について検討を行った。



イブプロフェン



カルバマゼピン

【方法】

蒸留水 1L 中に DMF で溶解させた各医薬品成分の 1% 溶液 1 mL を加え、30% 過酸化水素水 1 mL 及び塩化鉄 (III) 1% 溶液 1 mL を添加し、27°C の暗条件で 24 時間静置し分解反応を行った。反応を行った溶液について固相抽出操作を行い、抽出液を減圧下ロータリーエバポレーターで濃縮乾固し HPLC の移動相 1 mL に再溶解させ、その 20 μL を UV-逆相 HPLC で分析した。また、LC-MS を用いて分解反応によりイブプロフェン又はカルバマゼピンから生成した中間体と考えられる物質について、マススペクトルの測定を行った。

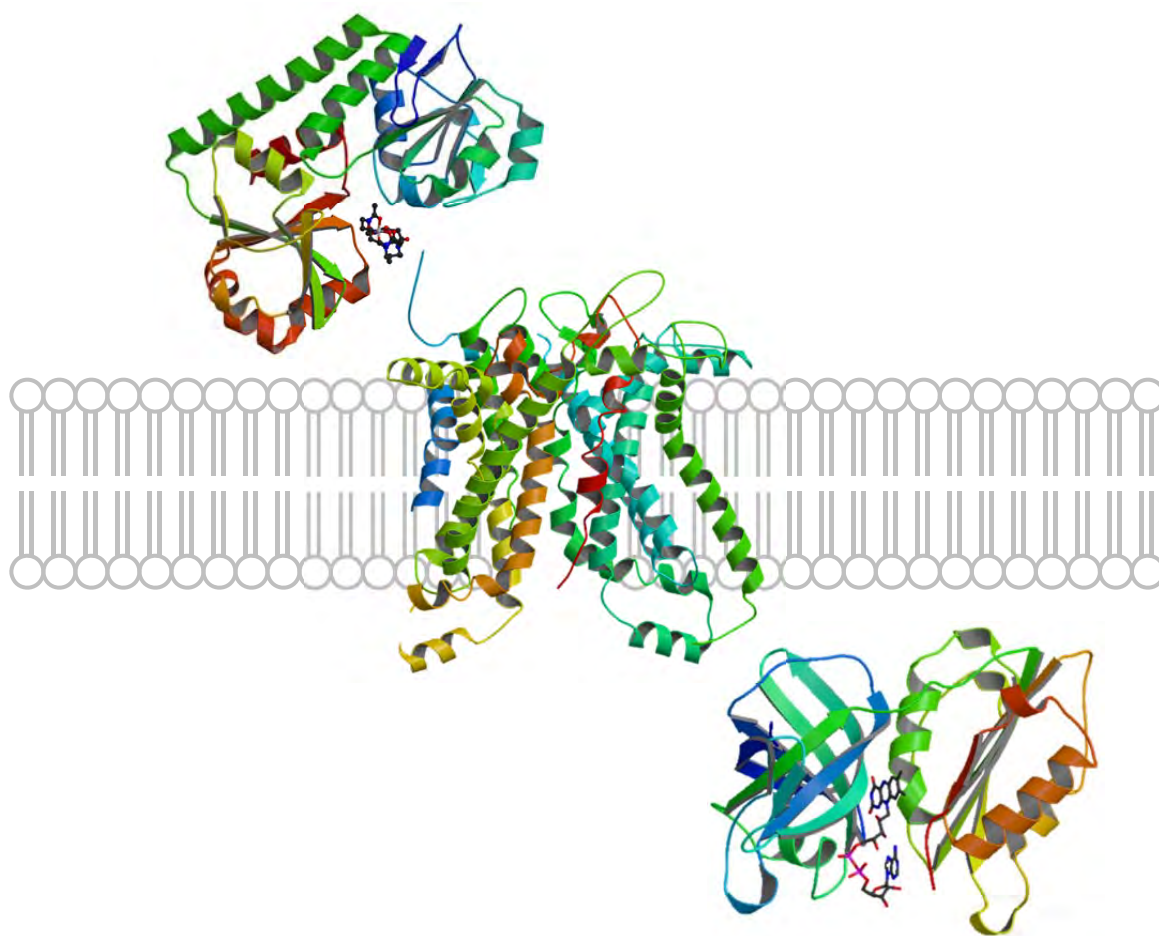
【結果および考察】

分解反応後の溶液中から、分解反応に伴って生成したと考えられる新たなピークがイブプロフェンから 4 つ、カルバマゼピンからは 1 つ検出された。これらの物質のピーク検出時間を基に、分取操作を繰り返して目的物質の単離を行い、LC-MS を用いてマススペクトルの測定を行った。その結果、分解生成物として候補となりうる物質が複数存在すると考えられるものの、大まかな構造推定を行うことが可能であった。今後、NMR 測定等の他の機器分析結果と合わせて、より正確な構造決定を行っていくことが重要であると考えられる。

大阪薬科大学

文部科学省私立大学戦略的研究基盤形成支援事業
「組織的研究体系による次世代型感染症治療薬の開発」

平成 27 年度公開シンポジウム



平成 27 年 12 月 5 日



主催 大阪薬科大学
協賛 公益社団法人 日本薬学会
公益社団法人 日本化学会
公益社団法人 日本生化学会

大阪薬科大学

ご挨拶

大阪薬科大学では、平成 23 年度に文部科学省の私立大学戦略的研究基盤形成支援事業として採択されました「組織的研究体系による次世代型感染症治療薬の開発」と題したプロジェクト研究を推進しているところであります。平成 25 年度に 3 年目の中間評価を受け、本年度は 5 年目の最終年度を迎えます。残すところ僅かではございますが、プロジェクトに参画している教員が力を合わせて、最終目標に少しでも近づけるように鋭意努力しているところでございます。

我々の研究プロジェクトチームは、大阪薬科大学大学院薬科学専攻博士前期・後期課程の分子構造・機能解析学領域に属する薬品物理化学研究室、生化学研究室、薬品分析化学研究室、微生物学研究室および中央機器研究施設の教員から構成されており、これらの研究室および施設の全教員が目的を達成するための具体的な研究課題に取り組み、効率的に研究を遂行する体制をとっています。最終年度を迎えられることは、チームメンバーのご理解・ご協力のお陰であり、ここに感謝申し上げる次第でございます。

本年度の第 5 回シンポジウムでは、我々のプロジェクトのこれまでの研究成果を総括するとともに、今回のシンポジウムに相応しい先駆的な研究を展開されておられる研究者を学外からお招きしております。

東京工業大学大学院生命理工学研究科 生物プロセス専攻の和地正明先生に「新規作用標的を有する抗生物質の探索」を、大阪大学産業科学研究所 生体分子制御科学研究分野 西野邦彦先生に「細菌の多剤排出機構と新規治療戦略」をテーマにそれぞれご講演をしていただきます。我々の研究プロジェクトチームからは、河野先生、知名先生、井上先生、ならびに三野先生にそれぞれ最近の研究成果について報告をしていただきます。各ご講演では、独創的な研究展開によって得られた成果についてご披露いただけるとともに、本プロジェクトにおける今後の研究の方向性について、貴重な示唆を与えていただけるものと信じております。皆様方により活発な討論がなされることを期待しております。

なお、シンポジウム終了後、ささやかな懇親会を予定しております。本プロジェクト研究の今後の展開についてご歓談いただけると幸いです。

研究代表者 辻坊 裕

平成 27 年度公開シンポジウム

日 時 : 平成 27 年 12 月 5 日 (土) 13 : 00 ~
会 場 : 大阪薬科大学・D304 教室 (入場無料)

文部科学省私立大学戦略的研究基盤形成支援事業
「組織的研究体系による次世代型感染症治療薬の開発」
第 5 回シンポジウム

《 プログラム 》

- 13 : 00 ~ 13 : 20 プロジェクトの総括 研究代表者 辻坊 裕
- 13 : 20 ~ 13 : 40 河野 広朗 博士 (大阪薬科大学 博士研究員)
「病原細菌 *Vibrio vulnificus* の宿主生体内における生存戦略」
- 13 : 40 ~ 14 : 00 知名 秀泰 修士 (大阪薬科大学 技術補佐員)
「*Vibrio vulnificus* M2799 株のペリプラズム結合タンパク質
VatD の構造解析」
- 14 : 00 ~ 14 : 20 井上 晴嗣 准教授 (大阪薬科大学 生化学研究室)
「VatD と Siderophore との相互作用」
- 14 : 20 ~ 14 : 40 三野 芳紀 教授 (大阪薬科大学 薬品分析化学研究室)
「微生物の鉄獲得系に作用する新規抗菌剤の開発研究」
- 14 : 40 ~ 15 : 00 休憩
- 15 : 00 ~ 16 : 00 和地 正明 教授
(東京工業大学 大学院生命理工学研究科 生物プロセス専攻)
「新規作用標的を有する抗生物質の探索」
座長 福永 理己郎
- 16 : 00 ~ 17 : 00 西野 邦彦 教授
(大阪大学産業科学研究所 生体分子制御科学研究分野)
「細菌の多剤排出機構と新規治療戦略」
座長 辻坊 裕
- 17 : 10 ~ 懇親会

講 演 要 旨

病原細菌 *Vibrio vulnificus* の宿主生体内における生存戦略

大阪薬科大学戦略的研究基盤形成支援事業 博士研究員 河野広朗

【緒言】

ヒトに感染症を起こす病原細菌は、宿主生体内で増殖するために鉄を必要とする。したがって、病原細菌の鉄取り込み機構を阻害することにより、ヒトの体内での増殖を抑制することができる。本プロジェクトでは、臨床分離株 *Vibrio vulnificus* M2799 株をモデル細菌として用い、本菌株が産生する鉄キレーターであるシデロフォア (Vulnibactin) を介した鉄取り込み機構に関与するタンパク質群の全容を、プロテオーム解析および挿入変異株の作製により明らかにすることができた¹⁾。さらに、多重変異株を作製する目的で、M2799 株の遺伝子欠失株作製法を確立した。

鉄欠乏下で発現量が増大するタンパク質群のうち、Vulnibactin を介する鉄取り込み機構に関与するタンパク質の遺伝子欠失株を作製した。すなわち、生合成に必須な酵素であるイソコリスミン酸合成酵素 (ICS)、Vulnibactin-Fe³⁺ を基質とする鉄還元酵素 (VuuB)、Vulnibactin-Fe³⁺ の外膜レセプター (VuuA)、および Vulnibactin-Fe³⁺ のペリプラズム結合タンパク質 (FatB) について遺伝子欠失株を作製した。これら欠失株の鉄欠乏下における増殖能について検討したところ、*ics* および *vuuA* 遺伝子欠失株では増殖が顕著に抑制されたが、*vuuB* および *fatB* 遺伝子欠失株においては遅いながらも増殖が確認された。以上の結果から、鉄欠乏下において Vulnibactin を介する鉄取り込み機構は生育に重要であり、ICS および VuuA は本取り込み機構において必須であることが明らかとなった。さらに、VuuB および FatB にはそれぞれ代替タンパク質が存在することが示唆された。そこで、FatB 代替タンパク質について探索を行った。また、Vulnibactin 分泌機構に関与するタンパク質についても検討した。

【方法】

遺伝子欠失株の作製は、suicide vector pDM4 を用いて行った。まず、ターゲット遺伝子内欠失目的領域の上下流域それぞれ 500 bp を PCR で増幅し、これらをライゲーションで連結後、PCR により増幅した。増幅した DNA を pDM4 に連結し、大腸菌 SY327λ*pir* 株を形質転換した。得られた組換えプラスミドを用いて、大腸菌 SM10λ*pir* 株を形質転換した。プラスミドを保持した SM10λ*pir* 株と M2799 株をそれぞれ培養し、メンブレンフィルター上で接合させることでプラスミドの伝達を行わせて 1 回目の相同組換えを誘発した。得られた相同組換え体を 15% スクロース、100 units/ml ポリミキシン B 含有 LB 寒天培地に塗抹し、増殖したコロニーのクロラムフェニコール感受性を確認した。

【結果および考察】

ゲノム情報が明らかにされている *V. vulnificus* CMCP6 株において FatB ホモログを探索した結果、Aerobactin-Fe³⁺ のペリプラズム結合タンパク質 (VatD) と 17% の相同性が認められた。*vatD* 遺伝子欠失株、および *fatB* と *vatD* の二重遺伝子欠失株を作製し、鉄欠乏下における増殖能について検討した結果、*vatD* 遺伝子欠失株は野生株とほぼ同様の増殖能を示したが、二重欠失株では *fatB* 遺伝子欠失株よりもさらに増殖が抑えられた。また、二重欠失株に、pRK415 をベクターとして用いて *vatD* 遺伝子を回復させたところ、*fatB* 遺伝子欠失株と同様の増殖が認められた²⁾。以上のことから、Vulnibactin-Fe³⁺ のペリプラズム結合タンパク質は FatB が中心となって機能するが、

VatDで代替可能であることが明らかにされた。

次に、M2799株におけるVulnibactin分泌機構に関与するタンパク質遺伝子について検討した。大腸菌において、Enterobactinの分泌に外膜チャンネルタンパク質To1Cが関与することが明らかにされており、To1Cを外膜チャンネルとするresistance nodulation cell division (RND)型排出システムが分泌に関与すると推測されている。M2799株におけるTo1Cホモログを探索した結果、VV1_0612及びVV2_1007を見出した。そこで、これら遺伝子の欠失株を作製し、鉄欠乏下での増殖能について検討したところ、VV1_0612タンパク質遺伝子欠失株の鉄欠乏下での生育が、顕著に抑制された。以上のことから、*V. vulnificus* M2799株において、VV1_0612タンパク質がTo1Cであると推測した。さらに、CMCP6株にコードされている11種類のRND遺伝子の欠失株を作製し、鉄欠乏下における増殖能について検討した結果、VV1_1681がRNDタンパク質としてVulnibactinの分泌に関与することが明らかとなった³⁾。しかしながら、遅いながらも増殖が確認されたことから、今回解析対象としたRNDタンパク質以外の代替タンパク質の存在が示唆された。

【参考文献】

- 1) Miyamoto K, Kosakai K, Ikebayashi S, Tsuchiya T, Yamamoto S, Tsujibo H. (2009) Proteomic analysis of *Vibrio vulnificus* M2799 grown under iron-repleted and iron-depleted conditions. *Microb. Pathog.* **46**:171-177.
- 2) Kawano H, Miyamoto K, Sakaguchi I, Myojin T, Moriwaki M, Tsuchiya T, Tanabe T, Yamamoto S, Tsujibo H. (2013) Role of periplasmic binding proteins, FatB and VatD, in the vulnibactin utilization system of *Vibrio vulnificus* M2799. *Microb. Pathog.* **65**:73-81.
- 3) Kawano H, Miyamoto K, Yasunobe M, Murata M, Myojin T, Tsuchiya T, Tanabe T, Funahashi T, Sato T, Azuma T, Mino Y, Tsujibo H. (2014) The RND protein is involved in the vulnibactin export system in *Vibrio vulnificus* M2799. *Microb. Pathog.* **75**:59-67.

Vibrio vulnificus M2799 株のペリプラズム結合タンパク質 VatD の構造解析

大阪薬科大学戦略的研究基盤形成支援事業 技術補佐員 知名秀泰

【緒言】

Vibrio vulnificus は、汚染された魚介類の摂食や海水の創傷部曝露等を介して感染する病原細菌であり、驚異的な増殖スピードを有することから感染すると重篤な障害を引き起こす。一般に、鉄はほとんどの生物の生存と増殖に不可欠な元素であるが、宿主生体内において病原菌が自由に利用できる遊離鉄は極めて少ない。しかしながら、*V. vulnificus* のように宿主生体内で急速に増殖し得る病原菌は鉄の取り込みが増殖の鍵因子となっており、何らかの巧妙な鉄獲得系を保持しているはずである。シデロフォアは鉄を細胞内に輸送する有機低分子であり、鉄獲得に重要な役割を担っている。したがって、抗菌薬の開発を指向する上でシデロフォアを介する鉄獲得機構の解明は必要不可欠である。本プロジェクトは、臨床分離株 *V. vulnificus* M2799 株をモデル細菌とし、詳細な鉄獲得機構および細胞増殖機構の解明を目的に開始された。

シデロフォアは、その化学構造から、Vulnibactin などのカテコール型と Deferoxamine などのヒドロキサメート型に大別されており、両者は何れも 1 原子の Fe^{3+} を 1 分子で捕捉する。*V. vulnificus* から生産された Vulnibactin は鉄イオン存在下の細胞外で自発的に Vulnibactin- Fe^{3+} 錯体となり、これはペリプラズム結合タンパク質 FatB などを介して、細胞内に取り込まれる。また本菌は、Deferoxamine も利用することができ、細胞外で形成される Deferoxamine- Fe^{3+} 錯体はペリプラズム結合タンパク質 VatD を介して取り込まれる。近年、VatD が FatB の代替タンパク質として機能することが示唆され¹⁾、VatD の構造と機能に興味を持たれた。本研究では、VatD の構造解析を行うとともに、シデロフォアとの相互作用について検討した。

【方法】

vatD 遺伝子を導入した高発現ベクター pProEX HTa を用いて、可溶性 His タグ融合 VatD (VatD-His) を得た。クロマトグラフィーにより純化された VatD-His は TEV 処理により His タグを除去し、蒸気拡散法により VatD のアポ体およびホロ体の結晶を得た²⁾。種々の結晶において X 線回折強度測定を行い、分子置換法から決定された初期位相を基に結晶構造を決定した。構造解析により、Deferoxamine- Fe^{3+} 錯体との相互作用に重要と考えられた W53、R69、R177 については、それぞれの変異体を作製し、等温滴定カロリーメトリー (ITC) を用いて相互作用解析を行った。

【結果および考察】

分解能 2.6 Å を有するアポ体の VatD および分解能 1.85 Å を有するホロ体の VatD-Deferoxamine- Fe^{3+} 複合体における結晶構造を決定した。図 1 にホロ体の X 線結晶構造を示す。VatD の全体構造は N-domain と C-domain から構成されており、両ドメインは long α -helix で繋がっていた。ホロ体はこれらドメイン間に Deferoxamine- Fe^{3+} 錯体が位置しており、この錯体と R69 および R177 間で水素結合形成が確認できた。また、本結合領域はトリプトファンやフェニルアラニンなどの疎水性残基が多く確認できるため、W53、W205、F263 の 3 残基で疎水性相互作用が形成されていると考えられる。さらに、錯体の結合に伴うアポ体からホロ体への構造変化を明らかにした。ホロ体への構造変化に伴う起動力には W53、P228、R69、T262 などが形成する相互作用ネットワーク

クが関与していると考えられる。ITCを用いた相互作用解析により、W53、R69、R177の3残基がいずれも Deferoxamine-Fe³⁺錯体との相互作用に重要であり、特に R177 がもたらす影響が強いことを明らかにした。

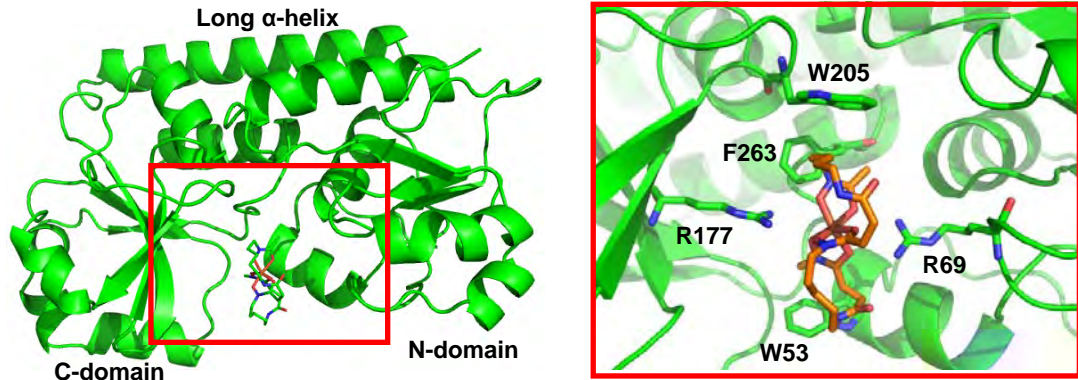


図1. VatD - Deferoxamine - Fe³⁺複合体の X 線結晶構造

【参考文献】

- 1) Kawano H, Miyamoto K, Sakaguchi I, Myojin T, Moriwaki M, Tsuchiya T, Tanabe T, Yamamoto S, Tsujibo H. (2013) Role of periplasmic binding proteins, FatB and VatD, in the vulnibactin utilization system of *Vibrio vulnificus* M2799. *Microb. Pathog.* **65**:73-81.
- 2) Miyano N, Igarashi T, Kawano H, Miyamoto K, Tsuchiya T, Tomoo K, Tsujibo H. (2015) Expression, purification, crystallization and X-ray crystallographic analysis of the periplasmic binding protein VatD from *Vibrio vulnificus* M2799. *Acta Crystallogr. F Struct. Biol. Commun.* **71**:1078-1082.

VatD と Siderophore との相互作用

大阪薬科大学 生化学研究室 井上晴嗣、藤井忍、福永理己郎

【緒言】

本研究室では、本プロジェクト「組織的研究体系による次世代型感染症治療薬の開発」にあたって、2つのテーマを中心に検討してきた。これらのテーマについて、本プロジェクトに直接貢献できる成果はまだ得られていないが、これまでに本研究室で検討してきた結果を報告したい。1つのテーマは藤井グループによる「イソコリスミ酸合成酵素に関する活性測定法の検討」である。イソコリスミ酸合成酵素(ICS)は、コリスミ酸からイソコリスミ酸を産生する酵素であり、イソコリスミ酸は、さらに代謝されてバルニバクチン *Vulnibactin* などの Siderophore になる。*Vibrio vulnificus* は *Vulnibactin* を体外へ放出して鉄と結合させて体内に取り込み、生育に必要な鉄を獲得している。本プロジェクトにおいて、ICS 欠損株の増殖が鉄欠乏下で著しく抑制されることが、宮本らにより明らかされており¹、ICS 阻害剤が新規抗菌薬となる可能性が考えられた。そこで ICS 阻害剤のスクリーニングのため、簡便な ICS 活性測定法の開発について検討した。もう1つのテーマは井上グループによる「*VatD* と Siderophore との相互作用」である。*Vibrio vulnificus* の Siderophore-Fe³⁺複合体の取り込みに関与するペリプラズム結合タンパク質には、*Vulnibactin*-Fe³⁺複合体と結合する *FatB* と *Aerobactin*-Fe³⁺複合体や *Deferoxamine*-Fe³⁺複合体と結合する *VatD* などがある。しかし、本プロジェクトにおいて、*VatD* が *FatB* の機能を代替えており、*VatD* も *Vulnibactin*-Fe³⁺と結合して取り込む可能性が、河野らにより報告された²。そこで、これらのペリプラズム結合タンパク質の Siderophore 結合の特異性を調べるため、*VatD* と種々の Siderophore との相互作用を簡単に調べる方法について検討した。

【結果・考察】

(1)イソコリスミ酸合成酵素に関する活性測定法の検討

まず、ICS の基質であるコリスミ酸は高価であり、*E. coli* KA12 菌(表現型は *Phe⁻*、*Tyr⁻*、*TetR*、*RacA*) を利用してコリスミ酸を産生させる方法が報告されている。そこで、栄養分を含む培地中で *E. coli* KA12 菌を培養(37°C、6時間)することで菌を増殖させた後、集菌し、栄養分を含まない培地でコリスミ酸を作らせた(27°C、16時間)。培養上清を陰イオン交換クロマトグラフィーで分離後、ジクロロメタンによる洗浄、酢酸エチルによる抽出を行い、逆相クロマトグラフィーで分離し凍結乾燥した。最終的に1Lの培養液から約100mgのコリスミ酸を得ることができた。次に、コリスミ酸は非常に不安定であるといわれていることから、水溶液中におけるコリスミ酸の安定性を調べた。コリスミ酸を pH7.5 の水溶液に溶解後、37°Cでは溶解後5分で約50%に減少していたが、4°Cでは32時間まで安定であることが分かった。

また、ICS の生成物であるイソコリスミ酸の定量には、イソコリスミ酸をイソコリスミ酸ピルビン酸リアーゼ (IPL) でサリチル酸に変換し、サリチル酸由来の蛍光強度を測定することで可能になる。そこで、*Vibrio vulnificus* 菌由来 IPL 遺伝子が組み込まれた発現用プラスミド (pProEX HTa) によって形質転換された大腸菌 (BL21(DE3)pLys) を 1mM IPTG で誘導後、37°Cで4時間培養して得られた菌体の

可溶性画分から、HisTrap カラムを用いて組換え IPL をほぼ単一に精製できた。

しかし、肝心の ICS については、*Vibrio vulnificus* 菌由来 ICS 遺伝子が組み込まれた発現用プラスミド (pProEX HTa) を用いた発現系では、産生された組換えタンパク質のほとんどが封入体画分に存在した。そこで、封入体画分を 6M 塩酸グアニジン溶液で溶解後、透析により段階的に塩酸グアニジンの濃度を低くすることで ICS の再構成を行った。再構成後の可溶性画分について、HisTrap カラムによる分離を行ったが、まだ夾雑タンパク質が多く含まれており、さらなる精製が必要であることが示された。今後は、再構成した ICS に活性があるかどうか検討する必要がある。

(2) VatD と Siderophore との相互作用

VatD は本学微生物学研究室によって X線結晶解析用に精製された組換え体を用いた。0.1M NaCl を含む 50mM Tris-HCl 緩衝液 (pH7.5) に溶解した約 1 μ M VatD に、種々の濃度の Siderophore を加え、励起波長 280nm で 300-400nm のトリプトファン由来の蛍光スペクトルを測定した。VatD 単独では、蛍光極大波長は 342nm 付近に見られたが、Deferoxamine-Fe³⁺を添加した場合には、蛍光極大波長が 338nm 付近にシフトするとともに蛍光の値が約 1/5 に大きく減少した。このことは Deferoxamine-Fe³⁺の結合による構造変化によって VatD のトリプトファン残基の存在環境が大きく変化したことを示している。鉄を含まない Deferoxamine を添加した場合にも若干の蛍光変化が見られたが、Tween 20 の添加によってかなり抑えることができたので、この蛍光変化は非特異的な吸着によるものと考えられる。Deferoxamine-Fe³⁺の濃度を変えて 340nm の蛍光変化を測定することにより、VatD と Deferoxamine-Fe³⁺の解離定数 K_d は、 $K_d=7.62\times 10^{-7}$ M と決定された。次に、BiacoreT200 を用いて VatD を固定化したセンサーチップをセットし、Deferoxamine-Fe³⁺の結合に伴う表面プラズモン共鳴の変化を測定したが、変化は見られなかった。おそらく VatD の固定化の際に Deferoxamine-Fe³⁺との結合に関与する構造に変化が起こった可能性が考えられる。

Ferrichrome-Fe³⁺は、蛍光測定においても Biacore においても VatD との相互作用を観察できなかった。Ferrichrome は VatD と結合しないと考えられる。

Enterobactin-Fe³⁺と鉄なしの Enterobactin は蛍光測定で、VatD との相互作用が観察された。しかし、Enterobactin 自体に 340nm の強い吸収をもつため、トリプトファン由来の蛍光が消光された可能性が高く、求めた解離定数の値は信頼できない。Biacore では、VatD との相互作用が観察され、鉄を含まない Enterobactin は結合しないが、Enterobactin-Fe³⁺は結合することが明らかとなり、解離定数 K_d は $K_d=8.21\times 10^{-7}$ M と求められた。

Vulnibactin については、Biacore 測定では VatD との結合を観察できなかった。

【参考文献】

1. Miyamoto K, Kosakai K, Ikebayashi S, Tsuchiya T, Yamamoto S, Tsujibo H. (2009) Proteomic analysis of *Vibrio vulnificus* M2799 grown under iron-repleted and iron-depleted conditions. *Microb. Pathog.* **46**:171-177.
2. Kawano H, Miyamoto K, Sakaguchi I, Myojin T, Moriwaki M, Tsuchiya T, Tanabe T, Yamamoto S, Tsujibo H. (2013) Role of periplasmic binding proteins, FatB and VatD, in the vulnibactin utilization system of *Vibrio vulnificus* M2799. *Microb. Pathog.* **65**:73-81.

微生物の鉄獲得系に作用する新規抗菌剤の開発研究

大阪薬科大学 三野芳紀

【緒言】

地球上に初めて誕生した生命体は周りに豊富にある鉄分を利用し、生命反応に組み入れることで、進化を遂げてきた。ところが、今から 30 億年前にシアノバクテリアが大発生し、地球環境は酸化されやすい状態に変化した。それにより、溶けやすい 2 価鉄が 3 価鉄に酸化され、不溶性 $\text{Fe}(\text{OH})_3$ に変化することで、溶解性の鉄分がほとんどなくなった。多くの微生物は鉄不足に陥り死滅したが、一部の微生物は突然変異により、生き残るための素晴らしい技を手に入れた。すなわち、不溶性の鉄を溶かすことのできる鉄キレーター（シデロホア）を放出することで、必要な鉄分を摂ることができるようになった。自然界では、多くの微生物が自身の種(シ)の繁栄のために他の種と鉄の争奪戦を繰り広げている。ヒトの体内に入った病原性細菌もまた生き残るため鉄を利用しなければならない。身体の中の鉄はヘモグロビン、トランスフェリン、フェリチンのような形でしっかりと固定されており、簡単にそれらの鉄を利用することはできない。しかし、一部の病原菌はトランスフェリンからも鉄を奪えるような強力な鉄キレート能を有するシデロホアを分泌できる。本プロジェクトにおける我々の目的は、微生物の鉄獲得系を阻害(あるいは利用)して、ヒト体内での病原菌の増殖を妨げようとするものである。このシンポジウムでは、まずシデロホアレセプターをターゲットとした、緑膿菌に有効な β -ラクタム剤の開発について紹介する。次に、人食いバクテリアの一種 *Vibrio vulnificus* の鉄獲得系を阻害する化合物の探索のため、①そのシデロホアである vulnibactin の単離・精製、②vulnibactin-Fe(III)錯体の特徴、③*V. vulnificus* の増殖阻害物質の探索 について検討した結果を報告する。

【方法】

vulnibactin の単離・精製: 鉄欠乏条件で *V. vulnificus* を培養し、その培養上清 (2.5L) をクエン酸で pH 4 に調整したのち、Amberlite XAD7 樹脂に通導した。MeOH 溶出液を減圧下濃縮し、分取 HPLC で分取した。条件は、カラム:Cosmosil C₁₈AR-II (10ID ×250 mm)、勾配溶出: A (5%CH₃CN 水溶液、0.05%TFA)、B (100%CH₃CN、0.05%TFA)、B: 50→100% (20min) 波長: 307nm、流速: 2mL/min である。16 分 (t_R) の溶出液を NH₃ 水で中和後、減圧下濃縮することで、vulnibactin 約 2.5mg を得た。なお、培養液中 (注入量: 2mL) の vulnibactin 量をモニターするため、分析 HPLC を行った。分取との相違は、カラムサイズ (4.6ID × 150mm) と勾配溶出の条件 (B: 20→100% [20min]) である。

V. vulnificus の増殖阻害活性: FeCl_3 (最終濃度 0.15 μM) を含む T medium (pH 7.5) に各試料溶液を 1/10 量添加して約 20 時間培養し、濁度から阻害活性を求めた (微生物研究室に依頼)。

【結果および考察】

緑膿菌選択性 β -ラクタム剤の開発: 微生物は鉄欠乏になると独自のシデロホアを分泌し、不溶性の鉄分を Fe(III)錯体として溶かし、レセプターを介して取り込んでいる。シデロホア-Fe(III) はエステラーゼで分解され、鉄を遊離するが、その際シデロホア断片は菌体内に取り込まれてリサイクルされる。このレセプターを介して抗菌剤を菌体内

に効率よく取り込ませる試みが検討され、分子内にカテコール基をもつβ-ラクタム剤が緑膿菌に有効であることが示された。¹⁾ また、同様に分子内にヒドロキサム酸基をもつβ-ラクタム剤も病原菌に有効であることが示された。²⁾ 我々は、更に選択性の高い抗菌剤の開発を目指して、緑膿菌に近縁の蛍光菌のシデロホアである pyoverdine を単離し、β-ラクタム剤とのハイブリッド体の合成を試みたが、その合成には未だ至っていない。将来、標的とする病原菌のシデロホアとβ-ラクタムとのハイブリッド体が合成できれば、その菌だけに効く極めて選択性の高い抗菌剤の開発が可能になると思われる。

vulnibactin の単離・精製：本プロジェクトにおいて、純粋な vulnibactin を確保することは極めて重要である。この化合物は市販されていないため、培養液からの単離・精製を試みた。Okujo らの方法を参考に、分取 TLC 法を分取 HPLC 法に改良した。³⁾ 標品の入手が困難なので、HPLC 上の各ピークを分取し、MS と NMR で構造を確認することで、vulnibactin のピークを見出した。精製法の詳細は【方法】に示した。分析 HPLC で培養液の vulnibactin 量をモニターした結果、些細な培養の条件の違いで、その含有量が大きなばらつきが見られ、培養液毎のモニターが重要であることが示唆された。

vulnibactin-Fe(III) 錯体の特徴：vulnibactin-Fe(III) 錯体は、モル比法により配位子：金属 = 1 : 1 であることが明らかとなった。類似のシデロホア、parabactin-Fe(III) 錯体の構造から、カテコール基、フェノール基の酸素原子 (4 個) とオキサゾリン環の窒素原子 (2 個) が Fe(III) との配位結合に関与していると推定されたが、X線結晶解析による確認が不可欠である。また、その Fe(III) 錯体は、Na₂S₂O₄ により容易に還元され、暗赤紫色から無色の Fe(II) 錯体に変化した。時間経過とともに、元の Fe(III) 錯体に戻ることも確認できた。NADH (E⁰ ≒ -0.32V) による還元が可能なら、enterobactin-Fe(III) (-0.75V) の場合と異なり、ヒドロキサム酸群 (-0.35 ~ -0.45V) と同様、vulnibactin の場合は還元による鉄の受け渡しが可能と思われる。

V. vulnificus の増殖阻害物質の探索：市販の代表的なキレート剤、鉄排泄剤、数種のシデロホアを試料として、*V. vulnificus* に対する増殖阻害活性を調べた。その結果、トロポロン骨格を有するヒノキチオールとトロポロン、TPEN、2,2'-ジピリジル、硝酸ガリウム(III)、クルクミン及びその誘導体に明らかな阻害活性が認められた。最も活性の強かったヒノキチオールは 1 × 10⁻⁵ M の濃度 (最終) でほぼ完全に増殖を阻害した。一方、植物シデロホアのムギネ酸、アポトランスフェリン、経口鉄排泄剤デフェラシロクス、他の多くのキレート剤には活性がなかった。興味深いのは、予備実験から鉄に対する親和性が高いと予測した deferoxamine にほとんど活性が見られなかった点である。この理由として、その Fe(III) 錯体が菌に取り込まれる可能性が考えられる。この点を明らかにするために、菌に取り込めない deferoxamine-dextran70 結合体を合成し、その増殖阻害活性を調べる予定である。今回阻害活性が明らかになった化合物の *in vivo* での活性試験が急がれる。

【参考文献】

1. N. Ohi *et al.*, *J. Antibiotics*, **39**, 230-241 (1986), *Chem. Pharm. Bull.*, **35**, 1903-1909 (1987).
2. J. Miller *et al.*, *J. Med. Chem.*, **34**, 968-978 (1991).
3. N. Okujo *et al.*, *Bio Metals*, **7**, 109-116 (1994).

新規作用標的を有する抗生物質の探索

和地 正明

東京工業大学大学院生命理工学研究科生物プロセス専攻

感染症の化学療法において薬剤耐性菌の出現が大きな問題となっている。薬剤耐性菌の蔓延に対抗するための方策として、既存の抗生物質をいかに有効に使うか、薬剤耐性機構の阻害剤の開発、新規標的の探索などがあげられるであろう。これまでに開発されてきた抗菌剤は、ほとんどすべてが高分子合成過程を標的としたものである。抗生物質市場における販売高上位を見てみても、 β -lactam系抗生物質（細胞壁ペプチドグリカン合成阻害）、macrolide系（タンパク質合成阻害）、fluoroquinolone系（DNA合成阻害）となっている。

我々は、新規標的を有する薬剤の取得を目指して、細菌の無核細胞の放出を指標にしたスクリーニング系を構築した。これまでに、細菌のアクチン様細胞骨格タンパク質 MreB の特異的阻害剤 A22 (*S*-(3,4-dichlorobenzyl)isothiourea) や、ポルフィリン合成の初発段階であるポルフォビリノーゲン合成酵素 (PBGS) を阻害するアラレマイシン (5-acetamido-4-oxo-5-hexenoic acid) を発見した。このスクリーニング系が新規標的を有する薬剤の探索に有効であることが示唆される。本発表では、特にアラレマイシンの作用機構の解析について紹介したい。

アラレマイシンは、ポルフィリン合成の前駆体である 5-アミノレブリン酸 (ALA) と類似の構造を有している (図)。ポルフィリン合成の初発反応は、2 分子の ALA が PBGS の作用により縮合しポルフォビリノーゲンとなる過程である。その構造からアラレマイシンは PBGS を阻害することが期待された。そこで、緑膿菌の PBGS とアラレマイシンの複合体の結晶構造解析を行った結果、アラレマイシンの 4 位の C=O と ALA 結合部位のひとつ (P-部位) の Lys-260 がシッフ塩基を形成し、7 位の C=O がもうひとつの ALA 結合部位 (A-部位) の Lys-205 と水素結合を形成していることが判明した。つまり、PBGS の 2 つの ALA 結合部位をアラレマイシンは 1 分子で効率的にブロックしていたのである。このような阻害様式をもつ PBGS 阻害剤はこれまでに知られておらず、ユニークな阻害剤であるといえる。

ポルフィリンは呼吸を行うすべての好気性生物にとって必須であるが、PBGS は生物種によって大きく二つのタイプに分類される。ヒトを含む動物や細菌の多くの PBGS は Zn^{2+} タイプ、植物や緑膿菌などのある種の病原菌の PBGS は Mg^{2+} タイプに分類される。 Mg^{2+} タイプ PBGS に特異的な阻害剤があれば薬剤として有望であると思われる。そこで、アラレマイシンをリード化合物として様々な誘導体の合成を行った。まず、化学的に高い反応性を示すと言われている α,β -不飽和ケトン形成する 6 位のメチリデン基をメチル基に置換したが、活性はほとんど変化しなかった。次に *N*-アセチル基の 8 位をトリフルオロメチル基に置換したところ、ヒト PBGS に対する阻害活性はほとんど変化せず、緑膿菌 PBGS に対する阻害活性が約 100 倍増大した。また、アラレマイシンに感受性の高い生物を探索したところ、マラリア原虫に対して比較的低濃度で有効であることが判明した (マラリア原虫 PBGS は Mg^{2+} タイプ)。これらのことから、アラレマイシンをリードとした薬剤の開発が有望であると思われる。

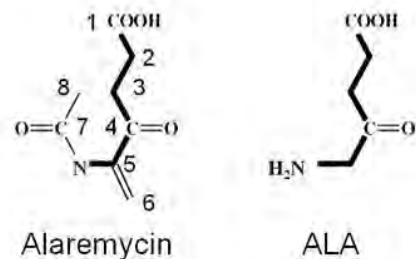


図 アラレマイシンとALAの構造

略 歴

氏 名 わ ち まさあき
和 地 正 明
所属機関 東京工業大学大学院生命理工学研究科 教授

学 歴

1984年3月 東京大学農学部 卒業
1986年3月 同 大学院農学系研究科修士課程 修了
1989年3月 同 大学院農学系研究科博士課程 修了

職 歴

1989年5月 東京工業大学生命理工学 助手
1994年10月 同大学 講師
1997年6月 同大学 助教授
改組等を経て
2012年4月 東京工業大学大学院生命理工学研究科 教授

受 賞

2000年 農芸化学奨励賞（日本農芸化学会）

細菌の多剤排出機構と新規治療戦略

西野邦彦

大阪大学 産業科学研究所・大阪大学大学院 薬学研究科

異物排出トランスポーターは細菌からヒトの細胞にいたるまで多くの生物において見出される膜タンパク質である。特に、複数の薬剤を排出しているものを多剤排出トランスポーターと呼び、多剤耐性の原因の一つであることが知られている。ゲノム解析が進むにつれ、細菌は数多くの多剤排出トランスポーター遺伝子を保有していることが分かってきた。中でも、**AcrAB-TolC** 多剤排出システムは、細菌の獲得耐性と自然耐性の両方に関係している因子として重要であり、数多くのグラム陰性菌において保存されている。耐性因子として同定された経緯から多剤排出トランスポーターの名前がつけられているが、抗菌薬だけではなく、細菌自身を保護するために、環境中に存在する異物や、細菌内に蓄積した代謝産物等を排出していることも分かってきた。また、複数の細菌において、これらトランスポーターと病原性発現との関わりが報告されている。

AcrAB-TolC が属する **RND** ファミリーの多剤排出システムは、マルチコンポーネント型排出システムとも呼ばれ、内膜の排出トランスポーター (**AcrB**) に加えて、外膜チャンネル (**TolC**)、ペリプラズムに存在するタンパク質 (**AcrA**) と複合体を形成することで、一つの多剤排出システムとして機能している。内膜タンパク質の **AcrB** は、複数の抗菌薬をプロトンとの対向輸送により細胞外に排出する。これまでに、**AcrB** とミノサイクリン、ドキシソルビシン、リファンピシンやエリスロマイシン等の薬物との共結晶構造が明らかになっている。**AcrB** 内には複数の基質認識ポケットが存在しており、薬物が、**AcrB** の入り口から、近位ポケット、遠位ポケット、出口へと順番に輸送されるペリスタポンプ排出機構が存在していると考えられている。

細菌では、多剤排出システムをコードしている遺伝子の多くが、複数の制御因子によって、その発現がコントロールされている。近年、**AcrAB** 発現制御に関与するリプレッサータンパク質 **RamR** が、複数の化合物を認識し、その結果、**AcrAB** の発現が誘導されることが分かった。各抗菌性物質は、**RamR** タンパク質の異なるアミノ酸の組み合わせによって、マルチサイト結合を介して認識されていることが分かった。細菌が抗菌性物質に曝されることにより、**AcrAB** 制御に関与するリプレッサータンパク質がこれら物質を認識して、抑制を解除し、多剤排出活性が促進されるというメカニズムが明らかになった。

異物排出トランスポーターは、細菌多剤耐性化と病原性発現の両方に関係していることから、その阻害剤の開発は、感染症の新たな治療戦略にもつながると考えられる。本講演では、これまでに明らかにされた細菌の抗菌薬排出機構に加え、阻害剤による阻害機構とその効果についても紹介したい。

略 歴

氏 名 にし の く に ひ こ
西野 邦彦
所属機関 大阪大学 産業科学研究所
(大阪大学大学院 薬学研究科 兼任) 教授

学 歴

1998年3月 京都薬科大学 薬学部 卒業
2000年3月 大阪大学大学院 薬学研究科 博士前期課程 修了
2001年4月 日本学術振興会 特別研究員 (DC2)
2003年3月 大阪大学大学院 薬学研究科 博士後期課程 修了
2003年3月 博士 (薬学) (大阪大学) 取得
2003年4月 日本学術振興会 特別研究員 (PD)
その間、米国 ワシントン大学医学部 (セントルイス) に
研究留学

職 歴

2005年11月 大阪大学 産業科学研究所 特任助手 (常勤)
2006年10月 科学技術振興機構 さきがけ研究者 (兼任)
2007年4月 大阪大学 産業科学研究所 特任助教 (常勤)
2007年6月 大阪大学 産業科学研究所 助教
2009年1月 大阪大学 産業科学研究所 准教授
2015年2月 大阪大学 産業科学研究所 教授
(大阪大学大学院 薬学研究科 兼任)

受 賞

2005年 Science誌・Young Scientist Award
2006年 Nature誌・Biotechnology Award
2008年 文部科学大臣表彰・若手科学者賞